OPEN ACCESS
ISSN: 2770-6249 (Online)

Complex Engineering Systems

Volume 4, 2024





www.oaepublish.com

EDITORIAL BOARD

Editor-in-Chief

Wenwu Yu (China)

Advisory Board Members

Jinde Cao (China)
Alberto Isidori (Italy)
Zhibin Jiang (China)
Jian Kang (UK)
Marek Pawelczyk (Poland)
Witold Pedrycz (Canada)
Leszek Rutkowski (Poland)

Subject Editors

Kelly Cohen (USA)
Behrad Khamesee (Canada)
Hasan Komurcugil (Turkey)
Yurong Liu (China)
Bidare Divakarachari Parameshachari (India)
Loris Roveda (Switzerland)
Dario Vangi (Italy)
Kalyana C. Veluvolu (South Korea)
Ding Wang (China)
Ning Wang (China)

Associate Editors

Feng Ding (China)
Zhiguang Feng (China)
Len Gelman (UK)
Xiao He (China)
Krzysztof Jóźwik (Poland)
Shaoyuan Li (China)
Jiaqi Ma (USA)
Yilun Shang (UK)
Ning Sun (China)
Shengxiang Yang (UK)
Hao Ying (USA)
Qichun Zhang (UK)
Xudong Zhao (China)
Jizhong Zhu (China)
Quanxin Zhu (China)

Editorial Board Members

Simone Baldi (China)
Stelios Bekiros (Italy)
Gyan Ranjan Biswal (India)
Ruxandra Mihaela Botez (Canada)
Moussa Boukhnifer (France)
Renjie Chai (China)
Duxin Chen (China)
Haifeng Chen (China)
Haoyong Chen (China)
Jinglong Chen (China)
Long Cheng (China)
Xiaochun Cheng (UK)
Zengru Di (China)
Shichang Du (China)
Hassen Fourati (France)
Qingbin Gao (China)
Xiaozhi Gao (Finland)
Zhiqiang Ge (China)
Hongzhi Guo (China)
Mohammad Hammoudeh (UK)
Honggui Han (China)
Shuping He (China)
Huosheng Hu (UK)
Bin Jia (China)
Yu Jiang (China)
Daqing Li (China)
Chang Hua Lien (Taiwan)
Paul P Lin (USA)
Wei Lin (China)
Jinliang Liu (China)
Zhixin Liu (China)
Linyuan Lü (China)
Bomin Mao (China)
Ziyang Meng (China)
Francesco Mercaldo (Italy)
Sangman Moh (South Korea)
Rui Peng (China)
Huihuan Qian (China)
Jiahu Qin (China)
Seyed-Mehdi Rakhtala (Iran)
Roozbeh Razavi-Far (Canada)
Chao Shen (China)
Mouquan Shen (China)
Yung C. Shin (USA)
Wenyan Song (China)
Xiaona Song (China)
Victor Sreeram (Australia)
Vladimir Stojanović (Serbia)
Housheng Su (China)
Jian Sun (China)
Vijayakumar Varadarajan (Australia)
Zhen Wang (China)
Yanling Wei (China)
Zhouchao Wei (China)
Yuanqing Wu (China)
Zhaojing Wu (China)
Zhengguang Wu (China)
Tangbin Xia (China)
Guoqi Xie (China)
Ling Xu (China)
Wenying Xu (China)
Gang Yan (China)
Xinggang Yan (UK)
Dongsheng Yang (China)
Qiang Yang (China)
Qinmin Yang (China)
Tao Yang (China)
Qian Yin (China)
Xiang Yin (China)
Chansu Yu (USA)
Ye Yuan (China)
Meysar Zeinali (Canada)
Chris Zhang (Canada)
Dan Zhang (China)
Youmin Zhang (Canada)
Ali Zolghadri (France)
Yanhua Zou (Japan)

GENERAL INFORMATION

About the Journal

Complex Engineering Systems (*CES*) is an international peer-reviewed, gold open access, online journal.

Information for Authors

Manuscripts should be prepared in accordance with Author Instructions.
Please check www.oaepublish.com/comengsys/author_instructions for details.
All manuscripts should be submitted online at https://oaemesas.com/login?JournalId=comengsys.

Copyright

The entire contents of the *CES* are protected under international copyrights. The journal, however, grants to all users a free, irrevocable, worldwide, perpetual right of access to, and a license to copy, use, distribute, perform and display the work publicly and to make and distribute derivative works in any digital medium for any reasonable purpose, subject to proper attribution of authorship and ownership of the rights. The journal also grants the right to make small numbers of printed copies for their personal use under the Creative Commons Attribution 4.0 License.
Copyright is reserved by © The Author(s) 2024.

Permissions

For information on how to request permissions to reproduce articles/information from this journal, please visit www.comengsys.com.

Disclaimer

The information and opinions presented in the journal reflect the views of the authors and not of the journal or its Editorial Board or the Publisher. Publication does not constitute endorsement by the journal. Neither the *CES* nor its publishers nor anyone else involved in creating, producing or delivering the *CES* or the materials contained therein, assumes any liability or responsibility for the accuracy, completeness, or usefulness of any information provided in the *CES*, nor shall they be liable for any direct, indirect, incidental, special, consequential or punitive damages arising out of the use of the *CES*. The *CES*, nor its publishers, nor any other party involved in the preparation of material contained in the *CES* represents or warrants that the information contained herein is in every respect accurate or complete, and they are not responsible for any errors or omissions or for the results obtained from the use of such material. Readers are encouraged to confirm the information contained herein with other sources.

Publisher

OAE Publishing Inc.
245 E Main Street Ste 107, Alhambra, CA 91801, USA
Website: www.oaepublish.com

Contacts

E-mail: editorial@comengsys.com
Website: https://www.oaepublish.com/comengsys

Complex Engineering Systems

CONTENTS

Volume 4 / Issues 1-4 / 2024/

Volume 4, Issue 1
Research Article

1 **Adaptive neural control for delayed discrete-time switched systems under deception attacks**
Dongke Zhao, Yongjie Tian, Ning Zhao
Complex Eng Syst 2024;4:1
http://dx.doi.org/10.20517/ces.2023.29

2 **Integrated control of anti-lock and regenerative braking for in-wheel-motor-driven electric vehicles**
Jiawang Yong, Yiyao Dong, Zhilin Zhang, Nenglian Feng, Wanting Li
Complex Eng Syst 2024;4:2
http://dx.doi.org/10.20517/ces.2023.36

3 **Fuzzy inference system-assisted human-aware navigation framework based on enhanced potential field**
Shurendher Kumar Sampathkumar, Daegyun Choi, Donghoon Kim
Complex Eng Syst 2024;4:3
http://dx.doi.org/10.20517/ces.2023.34

4 **Continual online learning-based optimal tracking control of nonlinear strict-feedback systems: application to unmanned aerial vehicles**
Irfan Ganie, Sarangapani Jagannathan
Complex Eng Syst 2024;4:4
http://dx.doi.org/10.20517/ces.2023.35

5 **Command filter-based adaptive neural tracking control of nonlinear systems with multiple actuator constraints and disturbances**
Yinguang Li, Jianhua Zhang, Yang Li
Complex Eng Syst 2024;4:5
http://dx.doi.org/10.20517/ces.2023.38

6 **Active manipulation of a tethered drone using explainable AI**
Shraddha Barawkar, Manish Kumar
Complex Eng Syst 2024;4:6
http://dx.doi.org/10.20517/ces.2023.33

Volume 4, Issue 2
Research Article

7 **Layered random fault injection method for the air braking system based on multiple Markov chains**
Zhiwen Chen, Jingke Fan, Lijuan Peng, Hao Luo, Chao Cheng, Zhiyong Chen
Complex Eng Syst 2024;4:7
http://dx.doi.org/10.20517/ces.2024.02

Editorial

8 **Introduction to discrete-time reinforcement learning control in Complex Engineering Systems**
Weiwei Bai
Complex Eng Syst 2024;4:8
http://dx.doi.org/10.20517/ces.2024.18

Research Article

9 **A comprehensive risk prediction method for defense mission planning based on probabilistic reasoning and hierarchical analysis**
WeiWei Du, XiaoWei Chen
Complex Eng Syst 2024;4:9
http://dx.doi.org/10.20517/ces.2024.15

10 **Health status assessment of unmanned aerial vehicle (UAV) attitude control system based on an improved multivariate state**

Complex Engineering Systems

CONTENTS

Volume 4 / Issues 1-4 / 2024/

estimation method
Rong Yuan, Shuyi Shao, Mou Chen
Complex Eng Syst 2024;4:10
http://dx.doi.org/10.20517/ces.2024.13

11 **Intensity enhanced for solid-state-LiDAR in simultaneous localization and mapping**
Xi Tong, Jiaxing Li, Chunhui Zhao
Complex Eng Syst 2024;4:11
http://dx.doi.org/10.20517/ces.2024.06

12 **Synchronization for stochastic switched networks via delay feedback control**
Zebin Li, Fuying Cheng, Juan Tang, Hailing Dong, Jianliang Tang
Complex Eng Syst 2024;4:12
http://dx.doi.org/10.20517/ces.2024.14

Volume 4, Issue 3
Research Article

13 **Extended state observer-based fault-tolerant control for an unmanned surface vehicle under asynchronous injection and deception attacks**
Haiwen Wang, Chun Liu, Xiao Huang, Yuxuan Zhong, Dong Qu, Ron J. Patton
Complex Eng Syst 2024;4:13
http://dx.doi.org/10.20517/ces.2024.19

14 **Enhancing unmanned aerial vehicle communication through distributed ledger and multi-agent deep reinforcement learning for fairness and scalability**
Farman Ali, Muhammad Ahtasham, Zahra Anfaal
Complex Eng Syst 2024;4:14
http://dx.doi.org/10.20517/ces.2024.10

15 **Multiple unmanned aerial vehicle collaborated three-dimensional electromagnetic target situation map construction**
Yuqing Peng, Kun Liu, Xuezhao Cai, Jie Wang, Zhipeng Lin
Complex Eng Syst 2024;4:15
http://dx.doi.org/10.20517/ces.2024.08

16 **Zero trust implementation in the emerging technologies era: a survey**
Abraham Itzhak Weinberg, Kelly Cohen
Complex Eng Syst 2024;4:16
http://dx.doi.org/10.20517/ces.2024.41

Review

17 **AI-enhanced fault-tolerant control and security in transportation and logistics systems: addressing physical and cyber threats**
Hajar Fatorachian, Hadi Kazemi
Complex Eng Syst 2024;4:17
http://dx.doi.org/10.20517/ces.2024.35

Research Article

18 **Path loss prediction for air-to-ground communication links via scenario transfer technology**
Guanjie Zhang, Taiya Lei, Xiaofeng Huo, Yanbin Li, Mengjie Geng, Hongjie Yang, Yuxin Yang, Xiaomin Chen
Complex Eng Syst 2024;4:18
http://dx.doi.org/10.20517/ces.2024.55

Volume 4, Issue 4
Research Article

19 **Tobit Kalman fusion filtering under**

Complex Engineering Systems

CONTENTS

Volume 4 / Issues 1-4 / 2024/

dynamic event-triggering protocol with token bucket specification
Xiangyu Chen, Fei Han, Yanhua Song, Jinnan Zhang
Complex Eng Syst 2024;4:19
http://dx.doi.org/10.20517/ces.2024.37

20 **A performance-centered design method for adaptive cruise control system**
Siya Zhan, Congzhi Liu
Complex Eng Syst 2024;4:20
http://dx.doi.org/10.20517/ces.2024.60

21 **Mapping cracks on port concrete pavements by analyzing structural health monitoring metadata with computer vision-based techniques**
Christina N. Tsaimou, Georgios Kagkelis, Panagiotis Sartampakos, Konstantinos Karantzalos, Vasiliki K. Tsoukala
Complex Eng Syst 2024;4:21
http://dx.doi.org/10.20517/ces.2024.28

Perspective

22 **Dynamic reliability decision-making frameworks: trends and opportunities**
Xiujie Zhao, Yi Luo
Complex Eng Syst 2024;4:22
http://dx.doi.org/10.20517/ces.2024.54

Research Article

23 **Delay-dependent observer based control for uncertain fuzzy-chaotic systems with deception attacks and faulty actuators**
Sekaran Monisha, Venkatesan Nithya, Rathinasamy Sakthivel
Complex Eng Syst 2024;4:23
http://dx.doi.org/10.20517/ces.2024.67

24 **Computation of robust positively invariant set based on direct data-driven approach**
Qian Du, Hongli Yang
Complex Eng Syst 2024;4:24
http://dx.doi.org/10.20517/ces.2024.76

Review

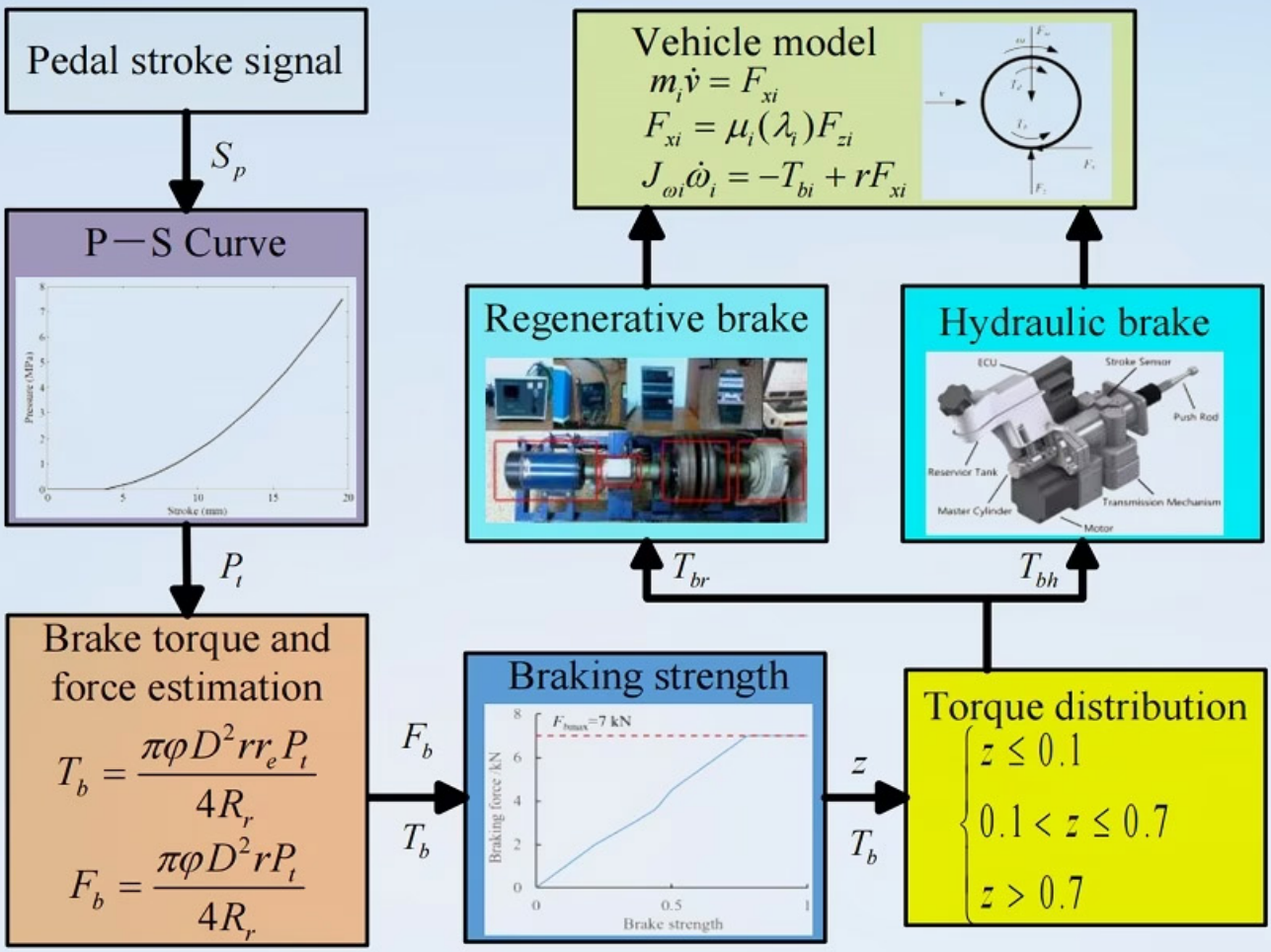
25 **Autonomous vehicles in mixed-autonomy traffic: game theoretic human-like decision making countermeasures**
Qitong Chen, Dong Zhao, Congzhi Liu, Meng Yang, Yehui Shi
Complex Eng Syst 2024;4:25
http://dx.doi.org/10.20517/ces.2024.69

26 **A meta-learning approach for predicting asphalt pavement deflection basin area**
Zhuoxuan Li, Xin Jin, Xinli Shi, Jinde Cao
Complex Eng Syst 2024;4:26
http://dx.doi.org/10.20517/ces.2024.64

Volume 4, Issue 1, March 2024

COMPLEX ENGINEERING SYSTEMS

Editor-in-Chief: Hamid Reza Karimi



Integrated control of anti-lock and regenerative braking for in-wheel-motor-driven electric vehicles

Jiawang Yong, Yiyao Dong, Zhilin Zhang. Nenglian Feng, Wanting Li

Open Access
ISSN 2770-6249 (Online)
www.oaepublish.com/comengsys

Zhao *et al. Complex Eng Syst* 2024;4:1
DOI: 10.20517/ces.2023.29

Complex Engineering Systems

Research Article

Open Access

Check for updates

Adaptive neural control for delayed discrete-time switched systems under deception attacks

Dongke Zhao, Yongjie Tian, Ning Zhao

College of Control Science and Engineering, Bohai University, Jinzhou 121013, Liaoning, China.

Correspondence to: Dr. Ning Zhao, College of Control Science and Engineering, Bohai University, 19 Keji Road, Songshan New District, Jinzhou 121013, Liaoning, China. E-mail: zhaoning_hrbeu@163.com

How to cite this article: Zhao D, Tian Y, Zhao N. Adaptive neural control for delayed discrete-time switched systems under deception attacks. *Complex Eng Syst* 2024;4:1. http://dx.doi.org/10.20517/ces.2023.29

Received: 18 Sep 2023 **First Decision:** 1 Nov 2023 **Revised:** 11 Nov 2023 **Accepted:** 15 Dec 2023 **Published:** 1 Jan 2024

Academic Editor: Hamid Reza Karimi **Copy Editor:** Fangling Lan **Production Editor:** Fangling Lan

Abstract

This paper focuses on the issue of adaptive neural control for discrete-time switched systems with time delay and deception attacks. Firstly, the switching signal is constrained by the dwell time. Considering that the deception attacks are unknown, the neural network technique is employed to approximate the attack signals. Then, an adaptive state feedback controller is established to compensate for the adverse effects of deception attacks for switched systems. Meanwhile, sufficient conditions for the boundedness of the switched system are given through the Lyapunov functional method, and the controller gains can be obtained by resolving the linear matrix inequality. Finally, the feasibility of the proposed method is illustrated via a numerical example.

Keywords: Switched system, deception attacks, adaptive control

1. INTRODUCTION

Switched systems consist of some subsystems and a switching rule that manages these subsystems. Because of their complexity and practicality, switched systems have been used in a wide variety of applications, such as manipulator robots[1], aircraft control systems[2], circuit systems[3], and so on. The switched systems are featured as the stability of each subsystem is not necessarily related to the stability of the closed-loop system. Therefore, designing a correct switching strategy is very significant. In recent years, the approach to constrain a switching strategy has included dwell time (DT)[4] and average DT (ADT)[5].

© The Author(s) 2024. **Open Access** This article is licensed under a Creative Commons Attribution 4.0 International License (https://creativecommons.org/licenses/by/4.0/), which permits unrestricted use, sharing, adaptation, distribution and reproduction in any medium or format, for any purpose, even commercially, as long as you give appropriate credit to the original author(s) and the source, provide a link to the Creative Commons license, and indicate if changes were made.

With the popularity of networking, network control systems (NCSs) have been studied and applied by scholars. In NCSs, control and feedback signals are transmitted through communication networks between sensors, controllers, and actuators. It has the characteristics of high reliability and low cost. Therefore, combining the advantages of NCSs and switched systems is a valuable issue. Despite the evident advantages of NCSs, there are also unavoidable disadvantages such as communication resources and network security problems. In particular, network security is an important problem considered in the open network environment. At present, network attacks can be mainly divided into deception attacks[6,7] and denial-of-service (DoS) attacks. The purpose of the DoS attacks is to prevent the transmission of data. The deception attacks aim to modify real signals and substitute them with false signals. Therefore, the research on how to compensate for the adverse effects of deception attacks on the system is of extraordinary significance. The discrete nonlinear systems with deception attacks were considered, in which Bernoulli distributions were used to describe the adverse effects of deception attacks on the systems[8]. The Takagi-Sugeno fuzzy systems were considered, in which the deception attacks existed in the feedforward and feedback channels, and were modeled independent Bernoulli processes[9]. The problem of network security and communication resources of vehicles under deception attacks were investigated, in which deception attacks were considered as constrained bounded energy signals[10]. In the above articles, deception attacks are supposed to be known or bounded, which is obviously a limitation. Therefore, the deception attacks considered in this paper involve no assumptions but rather focus on the identification and estimation of unknown attack signals. According to the practical situation, deception attacks have been designed as system state-dependent nonlinear functions. Therefore, the deception attack signals can be identified and estimated by applying neural network (NN) techniques, and the approximation function can be employed to design the controller in this article. Currently, the applications of NN techniques to approximate nonlinear functions have yielded numerous research results[11]. In nonlinear systems, these techniques were employed to approximate nonlinear functions that construct adaptive models to save communication resources and address stabilization problems. For the nonlinear switched systems, error terms were approximated by NN technology and compensated with nonlinear filters to solve the adaptive tracking control problem[12]. The adaptive NN observer problem was studied, in which the NN observer is designed to compensate for quantization errors and accurately estimate the state of the actuator[13]. In addition, some existing research results have approximated deception attack signals with NN techniques. The authors investigated the filtering problem of networked switched systems by approximating deception attacks with these techniques[14]. The event-triggered mechanism was designed based on NN, and the deception attacks were approximated by NN, which solved the security control problem[15]. It should be noted that the NN technique has been widely applied to nonlinear systems, but there is little attention paid to the processing of deception attacks as nonlinear functions, which motivates our research. Therefore, the challenge addressed in this paper is how to employ NN techniques to estimate deception attacks occurring in the controller-actuator (C-A) transmission channel, where deception attacks are considered as nonlinear functions.

In this paper, the control problem of discrete-time switched systems with time delay and deception attacks is considered, and a controller design scheme is proposed by using NN techniques to approximate the deception attack signals. The main contributions are as follows:

(1) Different from bounded deception attacks[16], the deception attacks in this paper are approximated using NN techniques, which can better defend against deception attacks.

(2) The switching signals are constrained by the DT, and a new Lyapunov functional method is constructed to ensure the boundedness of the switched systems.

The rest of this paper is structured as follows. In Section 2, the system description and controller design strategy are proposed. The main results of adaptive neural controllers are introduced in Section 3. A numerical example is applied to demonstrate the feasibility of the method in Section 4. Finally, the conclusion is presented in

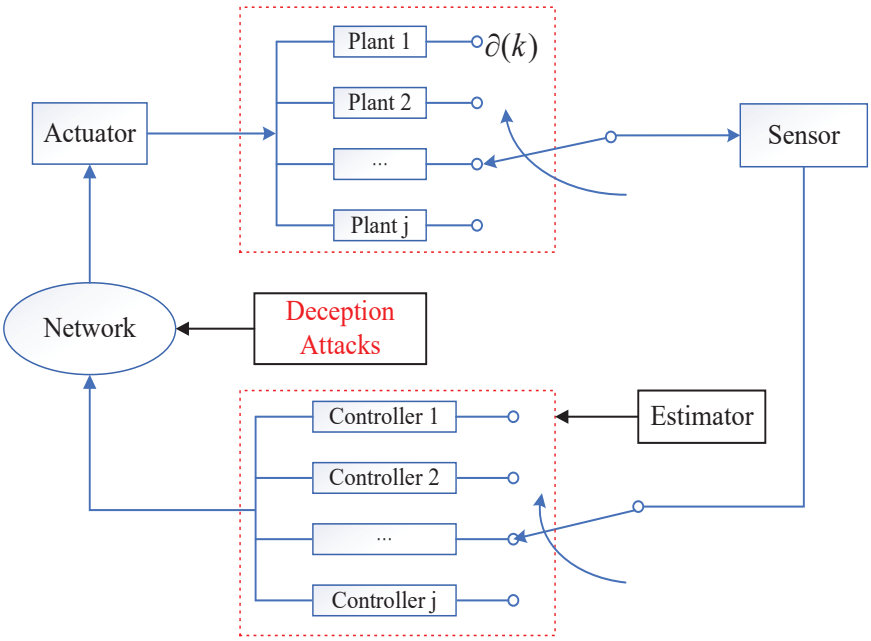


Figure 1. Framework of a switched system under deception attacks.

Section 5.

Notation: $\mathbb{N}$ signifies the set of integers, and the space of $n \times m$ real matrices is represented as $\mathbb{R}^{n\times m}$. In a symmetric block matrix, the symbol $*$ represents the symmetric term. The symbol $\|\cdot\|$ stands for the Euclidean vector norm. The $\|\cdot\|_F$ is Frobenius norm.

2. PROBLEM FORMULATION AND PRELIMINARIES

2.1. System description

Consider a class of discrete-time switched systems with time delay given as

$$\begin{cases} x(k+1) = A_{\partial(k)}x(k) + A^l_{\partial(k)}x(k-l) + B_{\partial(k)}u(k), \\ x(k) = \wp(k), \quad -l \le k \le 0, \end{cases} \tag{1}$$

where $x(k) \in \mathbb{R}^n$ and $u(k) \in \mathbb{R}^p$ denote the state vector and the control input, respectively. $l > 0$ is the time delay of the switched system, $\wp(k)$ is the initial condition for $x(k)$. $\partial\ [0,\infty) \to \mathcal{K} = \{1, 2, \cdots, j\}$ is the switching signal, in which $j \in \mathbb{N}$ is the quantity of subsystems. A_j, A^l_j and B_j are known constant matrices with appropriate dimensions.

Let the switching instants be $\{k_d, d \in \mathbb{N}\}$, then the time interval between two adjacent switching instants is depicted as $k_{d+1} - k_d \ge \varphi$, where φ is the minimum DT.

2.2. Adaptive neural state feedback controller

The C-A transmission channel is influenced by deception attacks, and the authenticity of the data transmission is modified, as shown in Figure 1. Therefore, the actuator input is established as follows:

$$u(k) = \tilde{u}(k) + h(x(k)), \tag{2}$$

where $\tilde{u}(k)$ denotes the control signal, and $h(x(k))$ indicates the signal of deception attacks.

Assuming the signal of deception attacks is the nonlinear function that depends on the system state, then the nonlinear function $h(x(k))$ is expressed as

$$h(x(k)) = M^T L(x(k)) + \gamma(x(k)),\ x(k) \in \Lambda \subset \mathbb{R}^n, \tag{3}$$

where Λ expresses a compact set, $M \in \mathbb{R}^{m\times p}$ is a weight matrix in which m denotes the number of nodes, and $\gamma(x(k))$ stands for the approximation error with $\|\gamma(x(k))\| \le \bar{\gamma}\,\|x(k)\|$. Then, the basis function

$$L(x(k)) = [\ \ell_1(x(k)) \quad \ell_2(x(k)) \quad \cdots \quad \ell_m(x(k))\ ]^T,$$

satisfies $\|L(\cdot)\| \le L_{\max}$ in which $L_{\max}$ is a positive constant. $\ell_i(x(k))$ has the form as follows:

$$\ell_i(x(k)) = \exp\left(-\frac{\|x(k) - f_i\|^2}{\upsilon_i}\right),$$

where υ_i and f_i denote the width and center of function $\ell_i(x(k))$, respectively. And $f_i = [f_{i1}\ \ f_{i2}\ \ \cdots\ \ f_{in}]^T$.

The challenge of defending against deception attacks is recognizing unknown attack signals. In this article, the NN technique is applied to approximate the deception attacks, thereby compensating for the adverse effect of deception attacks on the switched system. Therefore, the adaptive neural controller can be constructed as follows:

$$\tilde{u}(k) = K_{\partial(k)}x(k) - \hat{h}(x(k)), \tag{4}$$

where $K_{\partial(k)}$ is the controller gains to be determined, and $\hat{h}(x(k))$ is the estimation of the deception attack signal $h(x(k))$.

Therefore, the estimation $\hat{h}(x(k))$ of the deception attack signal $h(x(k))$ is constructed as

$$\hat{h}(x(k)) = \hat{M}^T(k)L(x(k)), \tag{5}$$

where $\hat{M}(k)$ is the estimation of M. Then, $\hat{M}(k)$ is designed as

$$\hat{M}(k+1) = -\lambda\hat{M}(k) + \hat{M}(k) - \omega\eta(k)x^T(k)S^T, \tag{6}$$

where $\lambda > 0, \omega > 0$ are two constants, $S \in \mathbb{R}^{n\times p}$ is an adjustment parameter and

$$\eta(k) = L(x(k)) \Big/ (1 + \|L(x(k))\|^2\|Sx(k)\|^2). \tag{7}$$

Let the error $\tilde{M}(k) = \hat{M}(k) - M$, then we have

$$\tilde{M}(k+1) = -\lambda\hat{M}(k) + \tilde{M}(k) - \omega\eta(k)x^T(k)S^T. \tag{8}$$

By means of the above analysis, the system is represented as

$$\begin{cases} x(k+1) = A_{\partial(k)}x(k) + A^l_{\partial(k)}x(k-l) + B_{\partial(k)}K_{\partial(k)}x(k) - B_{\partial(k)}\tilde{M}^T(k)L(x(k)) + B_{\partial(k)}\gamma(x(k)), \\ x(k) = \wp(k), \quad -l \le k \le 0. \end{cases} \tag{9}$$

Remark 1 *Different from the result*[17]*, the NN technique is employed to estimate and approximate the attack signal rather than constrain it to a bounded signal. The approximation capability of the NN is effectively utilized to estimate the attack signal, counteracting the malicious effects brought about by attacks.*

3. MAIN RESULTS

In this section, the sufficient conditions for the uniform and ultimately bounded of the switched system (9) are given subject to deception attacks. Meanwhile, the controller gains are designed.

Theorem 1 *For given constants* $0 < \varpi < 1$, $\lambda > 0$, $h > 0$, $\tau > 0$, $\varsigma > 0$, $\bar{\gamma} > 0$ *and* $\kappa > 1$, *if there exist matrices* $P_j \in \mathbb{R}^{n\times n} > 0$, $Q_j \in \mathbb{R}^{n\times n} > 0$, $F_{j1} \in \mathbb{R}^{n\times n} > 0$,$F_{j2} \in \mathbb{R}^{n\times n} > 0$, *such that*

$$\varpi\kappa^{\frac{1}{\varphi}} < 1, \tag{10}$$

$$\vartheta < 0, \tag{11}$$

$$\begin{bmatrix} \Psi_{j1} & \Psi_{j2} \\ * & -I_p \end{bmatrix} < 0, \tag{12}$$

$$P_j \le \kappa P_i,\ Q_j \le \kappa Q_i, \tag{13}$$

where

$$\begin{aligned}
\Psi_{j1} =& e_1^T(Q_j - \varpi P_j)e_1 + e_2^T P_j e_2 - e_3^T\varpi^l Q_j e_3 - \tau e_4^T e_4 + (e_1^T F_{j1} + e_2^T F_{j2})(F_{j1}e_1 + F_{j2}e_2) \\
&+ \mathrm{He}\{[e_1^T F_{j1} + e_2^T F_{j2}][(A_j + B_j K_j)e_1 - e_2 + A_j^l e_3 - B_j e_4]\}, \\
\Psi_{j2} =& \bar{\gamma} e_1^T B_j, \\
e_1 =& \begin{bmatrix} I_n & 0_{n\times n} & 0_{n\times n} & 0_{n\times m} \end{bmatrix}, \\
e_2 =& \begin{bmatrix} 0_{n\times n} & I_n & 0_{n\times n} & 0_{n\times m} \end{bmatrix}, \\
e_3 =& \begin{bmatrix} 0_{n\times n} & 0_{n\times n} & I_n & 0_{n\times m} \end{bmatrix}, \\
e_4 =& \begin{bmatrix} 0_{m\times n} & 0_{m\times n} & 0_{m\times n} & I_m \end{bmatrix}, \\
\vartheta =& h(1 - \varpi + \frac{1}{4\varsigma} - \lambda) + \tau L_{\max}^2,
\end{aligned}$$

Then, the switched system (9) *is bounded.*

Proof 1 *Construct the Lyapunov functional method as*

$$V_{\partial(k)}(k) = V_{\partial(k)}^1(k) + hV^2(k), \tag{14}$$

where $V_{\partial(k)}^1(k) = x^T(k)P_{\partial(k)}x(k) + \sum_{d=k-l}^{k-1} \varpi^{(k-d-1)} x^T(d)Q_{\partial(k)}x(d)$ *and* $V^2(k) = \mathrm{Tr}\{\tilde{M}^T(k)\tilde{M}(k)\}$. *For convenience, let* $V_{\partial(k)}^1(k) = V_j^1(k)$. *Then the difference of* $V_j^1(k)$ *along the trajectories of the switched system* (9) *can be obtained as*

$$\begin{aligned}
V_j^1(k+1) - \varpi V_j^1(k) =& x^T(k+1)P_j x(k+1) + \sum_{d=k+1-l}^{k} \varpi^{k-d} x^T(d)Q_j x(d) \\
&- \varpi x^T(k)P_j x(k) - \varpi \sum_{d=k-l}^{k-1} \varpi^{k-d-1} x^T(d)Q_j x(d) \\
=& x^T(k)(Q_j - \varpi P_j)x(k) + x^T(k+1)P_j x(k+1) - \varpi^l x^T(k-l)Q_j x(k-l).
\end{aligned} \tag{15}$$

Calculating the difference of $V^2(k)$ *along* (8), *we have*

$$\begin{aligned}
V^2(k+1) - V^2(k) =& \mathrm{Tr}\{\tilde{M}^T(k+1)\tilde{M}(k+1)\} - \mathrm{Tr}\{\tilde{M}^T(k)\tilde{M}(k)\} \\
=& \mathrm{Tr}\{\lambda^2\hat{M}^T(k)\hat{M}(k) - 2\lambda\hat{M}^T(k)\tilde{M}(k) + 2\lambda\omega\hat{M}(k)\eta(k)Sx(k) - 2\omega\tilde{M}(k)\eta(k)Sx(k)\} \\
&+ \omega^2\|\eta(k)\|^2\|Sx(k)\|^2.
\end{aligned} \tag{16}$$

According to the (7)*, we can get*

$$\|\eta(k)\|^2\|Sx(k)\|^2 \leq \frac{1}{4}.$$

Therefore, it is possible to obtain

$$\begin{aligned}
&\mathrm{Tr}\{2\lambda\omega\hat{M}(k)\eta(k)Sx(k)\} \leq \lambda\mathrm{Tr}\{\hat{M}^T(k)\hat{M}(k)\}+\frac{\lambda\omega^2}{4},\\
&-\mathrm{Tr}\{2\omega\tilde{M}(k)\eta(k)Sx(k)\} \leq \frac{\mathrm{Tr}\{\tilde{M}^T(k)\tilde{M}(k)\}}{4\varsigma}+\varsigma\omega^2,\\
&\mathrm{Tr}\{-2\lambda\hat{M}^T(k)\tilde{M}(k)\} = \mathrm{Tr}\{\lambda M^T M-\lambda\tilde{M}^T(k)\tilde{M}(k)-\lambda\hat{M}^T(k)\hat{M}(k)\}.
\end{aligned} \tag{17}$$

Combining (16) *and* (17)*, it can yield*

$$\Delta V^2(k) \leq (\frac{1}{4\varsigma}-\lambda)\left\|\tilde{M}(k)\right\|_F^2+\delta, \tag{18}$$

where $\delta = \lambda\|M\|_F^2+(\varsigma+\frac{1+\lambda}{4})\omega^2$.

For the free-weighting matrices F_{j1} *and* F_{j2}*, we can deduce that*

$$\begin{aligned}
0 =&2[x^T(k)F_{j1}+x^T(k+1)F_{j2}]\\
&\times[-x(k+1)+A_jx(k)+A_j^lx(k-l)+B_jK_jx(k)-B_j\tilde{M}^T(k)L(x(k))+B_j\gamma(x(k))]\\
=&2\xi^T(k)[e_1^TF_{j1}+e_2^TF_{j2}][(A_j+B_jK_j)e_1-e_2+A_j^le_3-B_je_4]\xi(k)\\
&+2\xi^T(k)[e_1^TF_{j1}+e_2^TF_{j2}]B_j\gamma(x(k)),
\end{aligned} \tag{19}$$

where $\xi(k) = [x^T(k), x^T(k+1), x^T(k-l), L^T(x(k))\tilde{M}(k)]^T$*, we have*

$$\begin{aligned}
0 =&\xi^T(k)\mathrm{He}\{[e_1^TF_{j1}+e_2^TF_{j2}][(A_j+B_jK_j)e_1-e_2+A_j^le_3-B_je_4]\}\xi(k)\\
&+2\xi^T(k)[e_1^TF_{j1}+e_2^TF_{j2}]B_j\gamma(x(k)),
\end{aligned} \tag{20}$$

in which

$$\begin{aligned}
2\xi^T(k)[e_1^TF_{j1}+e_2^TF_{j2}]B_j\gamma(x(k)) \leq&\xi^T(k)(e_1^TF_{j1}+e_2^TF_{j2})(F_{j1}e_1+F_{j2}e_2)\xi(k)\\
&+\xi^T(k)(\bar{\gamma}^2e_1^TB_jB_j^Te_1)\xi(k).
\end{aligned} \tag{21}$$

For any positive constant τ*, one obtains*

$$-\tau L^T(x(k))\tilde{M}(k)\tilde{M}^T(k)L(x(k))+\tau L_{\max}^2\mathrm{Tr}\{\tilde{M}^T(k)\tilde{M}(k)\} \geq 0. \tag{22}$$

Combining (14)*,* (15)*,* (18) *and* (22)*, we can obtain*

$$V_j^1(k+1)-\varpi V_j^1(k)+h(V^2(k+1)-\varpi V^2(k)) \leq \xi^T(k)[\Psi_{j1}+\Psi_{j2}^T\Psi_{j2}]\xi(k)+\vartheta\left\|\tilde{M}(k)\right\|_F^2+h\delta \tag{23}$$

Based on the sufficient condition (11) *and the Schur complement of sufficient condition* (12)*, we can deduce that*

$$V(k+1) \leq \varpi V(k)+\bar{\delta}, \tag{24}$$

where $\bar{\delta} = h\delta$.

For $k \in [k_d, k_{d+1}]$, according to condition (13), we can obtain

$$\begin{aligned} V(k) \leq & \varpi^{k-k_d} V(k_d) + \bar{\delta}[1 + \varpi + \cdots \varpi^{k-k_d-1}], \\ \leq & \kappa\varpi^{k-k_d} V(k_d^-) + \bar{\delta}[1 + \varpi + \cdots \varpi^{k-k_d-1}], \\ \leq & \kappa\varpi^{k-k_{d-1}} V(k_{d-1}) + \bar{\delta}[1 + \varpi + \cdots \varpi^{k-k_d-1}] \\ & + \kappa\bar{\delta}[\varpi^{k-k_d} + \varpi^{k-k_d+1} + \cdots + \varpi^{k-k_{d-1}+1}], \\ & \vdots \\ \leq & \kappa^{D(0,k)} \varpi^k V(0) + \bar{\delta}[1 + \varpi + \cdots \varpi^{k-k_d-1}] \\ & + \kappa\bar{\delta}[\varpi^{k-k_d} + \varpi^{k-k_d+1} + \cdots + \Omega^{k-k_d-1}] \\ & + \cdots + \kappa^{D(0,k)} \bar{\delta}[\varpi^{k-k_1} + \varpi^{k-k_1+1} + \cdots + \varpi^{k-k_0-1}], \\ \leq & \kappa^{D(0,k)} \varpi^k V(0) + [\bar{\mu}_0 + \bar{\mu}_1 + \cdots \bar{\mu}_{D(0,k)}], \end{aligned} \tag{25}$$

in which

$$\begin{aligned} \bar{\mu}_0 = & \bar{\delta}[1 + \varpi + \cdots \varpi^{k-k_d-1}] = \frac{\bar{\delta}(1-\varpi^{k-k_d})}{1-\varpi} \leq \frac{\bar{\delta}}{1-\varpi}, \\ \bar{\mu}_1 = & \kappa\bar{\delta}[\varpi^{k-k_d} + \varpi^{k-k_d+1} + \cdots + \varpi^{k-k_{d-1}-1}] \leq \frac{\kappa\bar{\delta}\varpi^{k-k_d}(1-\varpi^{k_d-k_{d-1}})}{1-\varpi} \leq \frac{\kappa\bar{\delta}\Omega^{\varphi}}{1-\varpi}, \\ \bar{\mu}_2 = & \kappa^2\bar{\delta}[\varpi^{k-k_{d-1}} + \varpi^{k-k_{d-1}+1} + \cdots + \varpi^{k-k_{d-2}-1}] \leq \frac{\kappa^2\bar{\delta}\varpi^{k-k_{d-1}}(1-\varpi^{k_{d-1}-k_{d-2}})}{1-\varpi} \\ \leq & \frac{\kappa^2\bar{\delta}(1-\varpi)^{k-k_{d-1}}}{1-\varpi} \leq \frac{\kappa^2\bar{\delta}(1-\varpi)^{2\varphi}}{1-\varpi}, \\ & \vdots \\ \bar{\mu}_{D(0,k)} = & \kappa^{D(0,k)}\bar{\delta}[\varpi^{k-k_1} + \varpi^{k-k_1+1} + \cdots + \varpi^{k-k_0-1}] \leq \frac{\kappa^{D(0,k)}\bar{\delta}\varpi^{k-k_1}(1-\varpi^{k-k_1})}{1-\varpi} \\ \leq & \frac{\kappa^{\frac{k}{\varphi}}\bar{\delta}(1-\varpi)^{k-k_1}}{1-\varpi} \leq \frac{\kappa^d\bar{\delta}(1-\varpi)^{d\varphi}}{1-\varpi}. \end{aligned} \tag{26}$$

Based on (25) and (26), we can get

$$V(k) \leq (\varpi\kappa^{\frac{1}{\varphi}})^k V(0) + \tilde{\delta}, \tag{27}$$

where $\tilde{\delta} = \sum_{m=0}^{d} \frac{\kappa^m\bar{\delta}(1-\varpi)^{m\varphi}}{1-\varpi}$.

The sufficient condition (10) is satisfied, implying that the switched system (9) is bounded. The proof is finished.

Theorem 2 *For given constants $0 < \varpi < 1$, $\lambda > 0$, $h > 0$, $\tau > 0$, $\varsigma > 0$, $\alpha_j > 0$, $\varepsilon_p > 0$, $\varepsilon_q > 0$, $\bar{\gamma} > 0$ and $\kappa > 1$, if there exist matrices $\tilde{P}_j \in \mathbb{R}^{n\times n} > 0$, $\tilde{Q}_j \in \mathbb{R}^{n\times n} > 0$, $Z_{j1} \in \mathbb{R}^{n\times n} > 0$, $Y_j \in \mathbb{R}^{n\times n}$, such that*

$$\begin{bmatrix} \tilde{\Psi}_1 & \tilde{\Psi}_2 \\ * & -I_p \end{bmatrix} < 0, \tag{28}$$

$$\begin{bmatrix} -\kappa\tilde{P}_i & Z_{i1} \\ * & \bar{P}_j \end{bmatrix} \leq 0, \quad \begin{bmatrix} -\kappa\tilde{Q}_i & Z_{i1} \\ * & \bar{Q}_j \end{bmatrix} \leq 0, \tag{29}$$

where

$$\begin{aligned}\tilde{\Psi}_1 =& e_1^T(\tilde{Q}_j - \varpi\tilde{P}_j)e_1 + e_2^T\tilde{P}_j e_2 - e_3^T\varpi^l\tilde{Q}_j e_3 - \tau e_4^T e_4 + (e_1^T + \alpha e_2^T)(e_1 + \alpha e_2)\\ &+ \mathrm{He}\{[e_1^T + \alpha e_2^T][(A_j + B_jK_j)Z_{j1}e_1 - Z_{j1}e_2 + A_j^l Z_{j1}e_3 - B_j e_4]\},\\ \tilde{\Psi}_2 =& \bar{\gamma}e_1^T Z_{j1}B_j,\\ \bar{P}_j =& \varepsilon_p^2\tilde{P}_j - 2\varepsilon_p Z_{j1},\\ \bar{Q}_j =& \varepsilon_q^2\tilde{Q}_j - 2\varepsilon_q Z_{j1},\end{aligned}$$

Then, switched system (9) is bounded. Moreover, the controller gains are designed as

$$K_j = Y_j Z_{j1}^{-1}.$$

Proof 2 *Let*

$$\begin{cases} Z_{j1} = F_{j1}^{-1},\\ F_{j2} = \alpha_j F_{j1}.\end{cases}$$

According to Theorem 1, we define $\Phi_j = [Z_{j1}, Z_{j1}, Z_{j1}, I_p, I_p]$, *pre-multiplying and post-multiplying both sides of inequality* (12) *with* Φ_j. *We assume* $\tilde{P}_j = Z_{j1}P_j Z_{j1}$, $\tilde{Q}_j = Z_{j1}Q_j Z_{j1}$.

In addition, it is easy to see that

$$\begin{aligned}-P_j^{-1} &= -Z_{j1}\tilde{P}_j^{-1}Z_{j1} \le \varepsilon_p^2\tilde{P}_j - 2\varepsilon_p Z_{j1},\\ -Q_j^{-1} &= -Z_{j1}\tilde{Q}_j^{-1}Z_{j1} \le \varepsilon_q^2\tilde{Q}_j - 2\varepsilon_q Z_{j1}.\end{aligned} \tag{30}$$

Similarly, pre-multiplying and post-multiplying both sides of inequalities in (13) *with* Z_{j1} *and using the Schur complement lemma, then* (29) *is ensured by* (13) *holds. The inequality* (12) *can be guaranteed by* (28). *This proof is completed.*

4. NUMERICAL EXAMPLES

Consider a discrete-time switched system with time delay (1) as follows:

$$\begin{aligned}A_1 &= \begin{bmatrix} -0.2 & 1\\ 0.1 & 0.6\end{bmatrix},\ A_1^l = \begin{bmatrix} 0.01 & 0.3\\ 0.1 & 0\end{bmatrix},\ B_1 = \begin{bmatrix} 0.2 & 0\end{bmatrix}^T,\\ A_2 &= \begin{bmatrix} -0.2 & 0.5\\ -0.8 & 0.8\end{bmatrix},\ A_2^l = \begin{bmatrix} 0.01 & 0\\ 0.1 & 0.3\end{bmatrix},\ B_2 = \begin{bmatrix} 0.2 & 0.1\end{bmatrix}^T.\end{aligned}$$

When $l = 1$, the parameters are given as $\bar{\gamma} = 1.5$, $\varepsilon_q = 0.4$, $\varepsilon_q = 0.5$, $\alpha_1 = 1.8$, $\alpha_2 = 2$, $\varpi = 0.9$, $\kappa = 1.8$, $\varphi = 6$, $\tau = 0.1$, $L_{\max}^2 = 81$, $\lambda = 0.6$, $\varsigma = 100$, $h = 1400$. Then, $\vartheta = -40.4$ and $\varpi\kappa^{\frac{1}{\varphi}} = 0.9926$ can be obtained through calculations, so conditions (10) and (11) in Theorem 1 are satisfied. By solving Theorem 2, we obtain

$$K_1 = \begin{bmatrix} 1.7615 & -5.4597\end{bmatrix},\ K_2 = \begin{bmatrix} 3.8378 & -3.9402\end{bmatrix}.$$

The attack signal is set as $h(x(k)) = \sqrt{x_1^2(k) + x_2^2(k)} - 6\sin(x_1(k))$. The NN technique applied to approximate the attack signal $h(x(k))$ consists of 81 nodes whose centers f_i are evenly spaced in $\underbrace{[-6, 6] \times \cdots [-6, 6]}_{81}$ and the widths are $\upsilon_i = 1$ with $i \in \langle 81\rangle$.

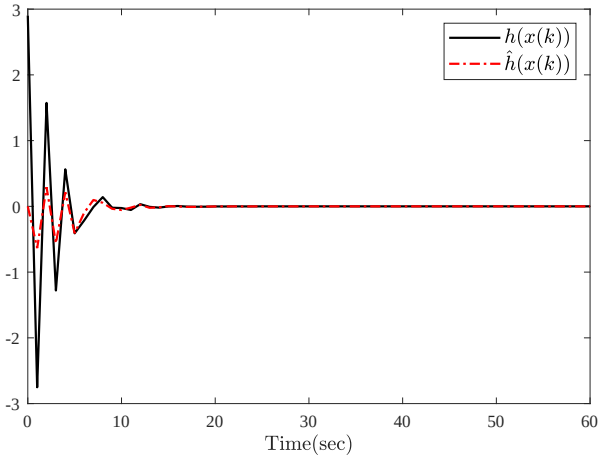


Figure 2. Trajectories of the attack signal and its estimation signal where $\lambda = 0.5$ and $\omega = 0.7$.

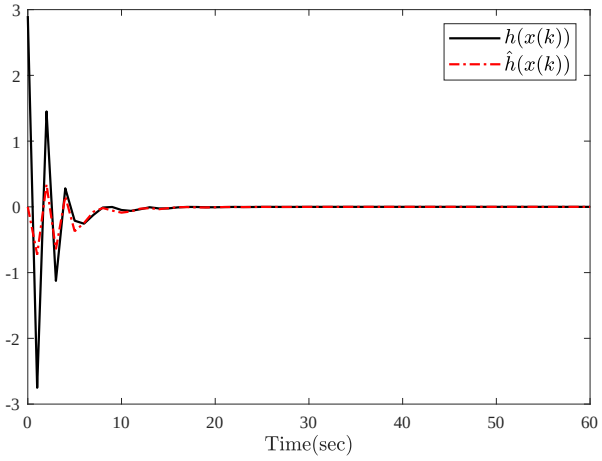


Figure 3. Trajectories of the attack signal and its estimation signal where $\lambda = 0.5$ and $\omega = 0.8$.

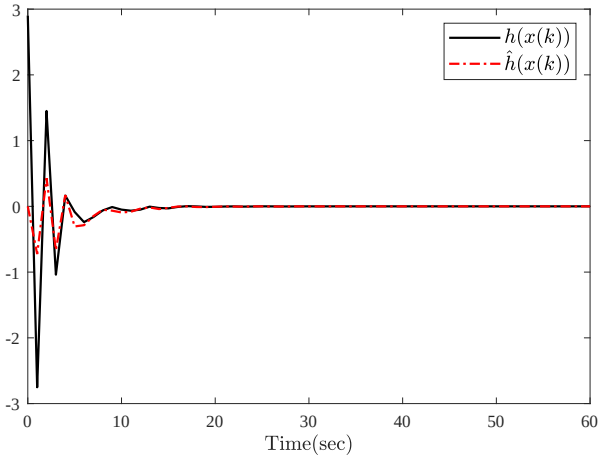


Figure 4. Trajectories of the attack signal and its estimation signal where $\lambda = 0.6$ and $\omega = 0.8$.

Let the initial conditions be $x(0) = [-0.4 \ \ 0.4]^T$, $\hat{M}(0) = 0_{81\times1}$ and $W = [-1 \ \ 1]$. The parameters λ and ω play an important role in the updated law of $\hat{M}$. To demonstrate the impact of parameters on performance,

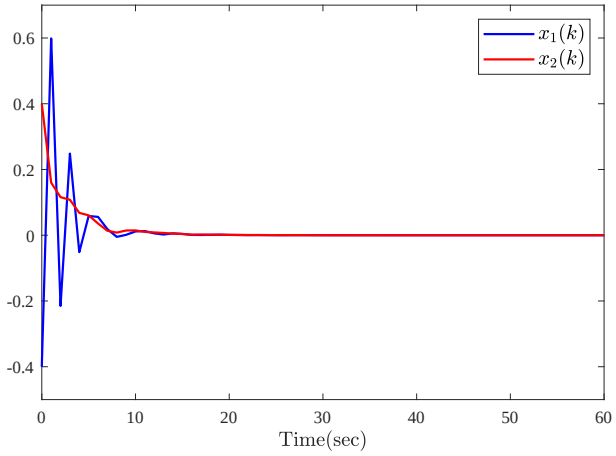


Figure 5. The state responses $x(k)$.

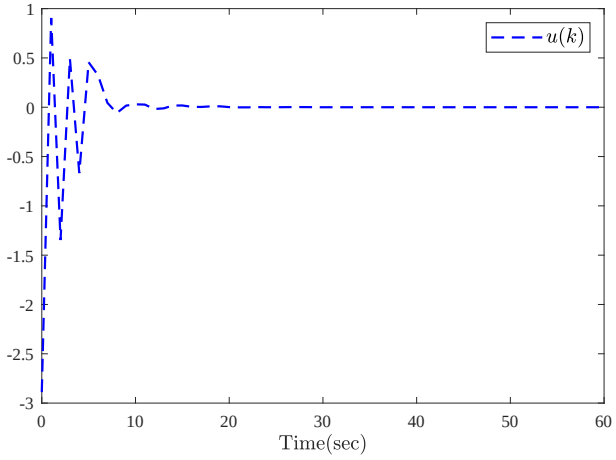


Figure 6. The control signal $u(k)$.

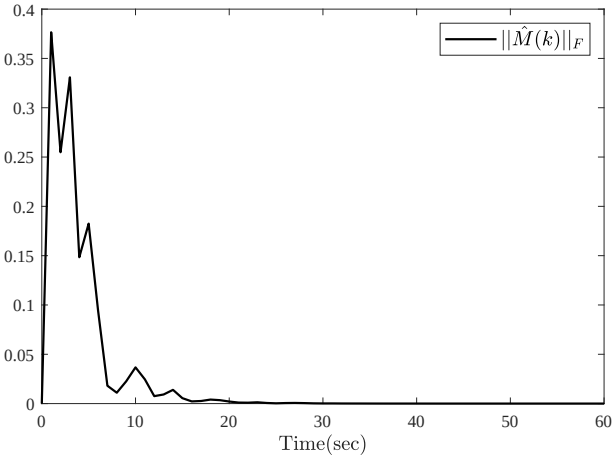


Figure 7. The responses of adaptive parameter $\|\hat{M}(k)\|_F$.

we introduce a performance metric $\tilde{h}$, where $\tilde{h} = \sum_{k=1}^{60} \left| h(x(k)) - \hat{h}(x(k)) \right|$. Therefore, it is necessary to choose

Table 1. $\tilde{h}$ **for different** (λ, ω)

(λ, ω)	$(0.5, 0.8)$	$(0.5, 0.7)$	$(0.6, 0.8)$
$\tilde{h}$	7.3253	8.2059	6.9905

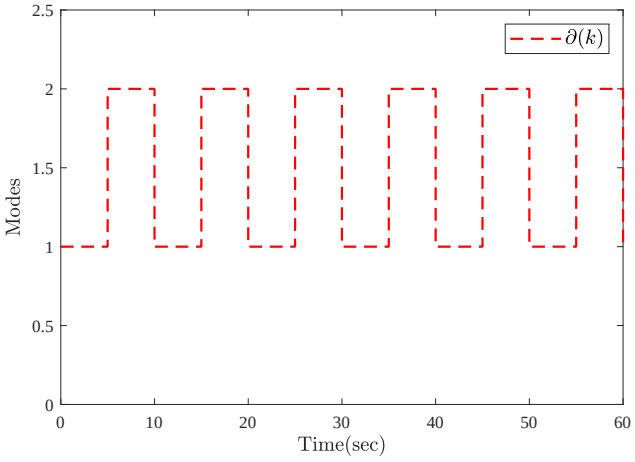


Figure 8. The switching modes of the switched system.

appropriate values for λ and ω. Trajectories for the attack signal $h(x(k))$ and its estimation $\hat{h}(x(k))$ at $\lambda = 0.5$ and $\omega = 0.7$ are depicted in Figure 2, while the corresponding paths at $\lambda = 0.5$ and $\omega = 0.8$ are shown in Figure 3. Additionally, trajectories for $\lambda = 0.6$ and $\omega = 0.8$ are presented in Figure 4. From Table 1, it can be observed that a smaller value of $\tilde{h}$ corresponds to better parameter convergence. Then, the parameters are selected as $\lambda = 0.6$ and $\omega = 0.8$.

Based on the parameters given above, we have the following simulation results. Figure 5 and Figure 6 depict the state responses $x(k)$ and the control signal $u(k)$, which indicate the ability of the controller to resist the adverse effects of deception attacks to bring the system to stability. The response of adaptive parameter $\left\|\hat{M}(k)\right\|_F$ is illustrated in Figure 7. The switching modes of the switched system are shown in Figure 8. Therefore, the feasibility of the proposed method is demonstrated.

5. CONCLUSIONS

In this article, we have addressed the problem of adaptive neural control for discrete-time switched systems with time delay and deception attacks. To counteract the impact of deception attacks, the NN technique has been employed to approximate the attack signal. An adaptive state controller, which incorporates the attack estimation signal and the approximation error, effectively eliminating malicious influences, has been proposed. Sufficient conditions for the boundedness of the switched system under deception attacks have been attained by using the Lyapunov functional and the DT methods. Additionally, a design strategy for controller gains has been presented. Finally, the feasibility of the proposed method has been demonstrated through a numerical example. Future work will focus on filtering and memory feedback control for hybrid systems.

DECLARATIONS

Authors' contributions

Methodology, Writing - original draft, investigation, and conceptualization: Zhao D
Conceptualization and visualization: Tian Y

Conceptualization, investigation, and visualization: Zhao N

Availability of data and materials
Not applicable.

Financial support and sponsorship
None.

Conflicts of interest
All authors declared that there are no conflicts of interest.

Ethical approval and consent to participate
Not applicable.

Consent for publication
Not applicable.

Copyright
© The Author(s) 2024.

REFERENCES

1. Gans NR, Hutchinson SA. Stable visual servoing through hybrid switched-system control. *IEEE Trans Robot* 2007;23:530-40. DOI
2. Wang B, Yan J, Cheng J, Zhong S. New criteria of stability analysis for generalized neural networks subject to time-varying delayed signals. *Appl Math Comput* 2017;314:322-33. DOI
3. Liu L, Liu YJ, Li D, Tong S, Wang Z. Barrier lyapunov function-based adaptive fuzzy FTC for switched systems and its applications to resistance-inductance-capacitance circuit system. *IEEE Trans Cybern* 2020;50:3491-502. DOI
4. Yang D, Zhao J. Dissipativity for switched LPV systems and its application: a parameter and dwell time-dependent multiple storage functions method. *IEEE Trans Syst Man Cybern Syst* 2020;50:502-13. DOI
5. Qi W, Park JH, Cheng J, Kao Y, Gao X. Exponential stability and L1-gain analysis for positive time-delay Markovian jump systems with switching transition rates subject to average dwell time. *Inf Sci* 2018;424:224-34. DOI
6. Cheng J, Huang W, Park JH, Cao J. A hierarchical structure approach to finite-time filter design for fuzzy markov switching systems with deception attacks. *IEEE Trans Cybern* 2022;52:7254-64. DOI
7. Cheng J, Wang Y, Park JH, Cao J, Shi K. Static output feedback quantized control for fuzzy markovian switching singularly perturbed systems with deception attacks. *IEEE Trans Fuzzy Syst* 2022;30:1036-47. DOI
8. Ding D, Wang Z, Han QL, Wei G. Security control for discrete-time stochastic nonlinear systems subject to deception attacks. *IEEE Trans Syst Man Cybern Syst* 2018;48:779-89. DOI
9. Sun HY, Han HG, Sun J, Yang HY, Qiao JF. Security control of sampled-data T-S fuzzy systems subject to cyberattacks and successive packet losses. *IEEE Trans Fuzzy Syst* 2023;31:1178-88. DOI
10. Gu Z, Yin T, Ding Z. Path tracking control of autonomous vehicles subject to deception attacks via a learning-based event-triggered mechanism. *IEEE Trans Neural Netw Learn Syst* 2021;32:5644-53. DOI
11. Ao W, Zhang H, Zhao N, Minchala LI. Adaptive neural security control for networked singular systems under deception attacks. *IEEE Access* 2022;10:33230-37. DOI
12. Xu N, Zhao X, Zong G, Wang Y. Adaptive control design for uncertain switched nonstrict-feedback nonlinear systems to achieve asymptotic tracking performance. *Appl Math Comput* 2021;408:126344. DOI
13. Chen L, Zhu Y, Ahn CK. Adaptive neural network-based observer design forswitched systems with quantized measurements. *IEEE Trans Neural Netw Learn Syst* 2023;34:5897-910. DOI
14. Shang H, Zong G, Shi K. Neural-network-based distributed security filtering for networked switched systems. *Int J Robust Nonlinear Control* 2022;32:2791-804. DOI
15. Gao X, Deng F, Zeng P, Zhang H. Adaptive neural event-triggered control of networked markov jump systems under hybrid cyberattacks. *IEEE Trans Neural Netw Learn Syst* 2023;34:1502-12. DOI
16. Liu K, Guo H, Zhang Q, Xia Y. Distributed secure filtering for discrete-time systems under round-robin protocol and deception attacks. *IEEE Trans Cybern* 2020;50:3571-80. DOI
17. Zhang L, Guo G. Observer-based adaptive event-triggered sliding mode control of saturated nonlinear networked systems with cyber-attacks. *Inf Sci* 2021;543:180-201. DOI

Yong *et al*. *Complex Eng Syst* 2024;4:2
DOI: 10.20517/ces.2023.36

Complex Engineering Systems

Research Article

Open Access

Integrated control of anti-lock and regenerative braking for in-wheel-motor-driven electric vehicles

Jiawang Yong[1], Yiyao Dong[1], Zhilin Zhang[2], Nenglian Feng[3], Wanting Li[1]

[1]Department of Traffic Engineering, Beijing University of Technology, Beijing 100124, China.
[2]Hefei SEEKTOP Automotive Technology Co., Ltd, Hefei 230601,Anhui, China.
[3]Faculty of Environment and Life, Beijing University of Technology, Beijing 100124, China.

Correspondence to: Dr. Jiawang Yong, Department of Traffic Engineering, Beijing University of Technology, No. 100 Pingleyuan, Chaoyang District, Beijing 100124, China. E-mail: yongjw@bjut.edu.cn

How to cite this article: Yong J, Dong Y, Zhang Z, Feng N, Li W. Integrated control of anti-lock and regenerative braking for in-wheel-motor-driven electric vehicles. *Complex Eng Syst* 2024;4:2. http://dx.doi.org/10.20517/ces.2023.36

Received: 10 Oct 2023 **First Decision:** 8 Nov 2023 **Revised:** 23 Nov 2023 **Accepted:** 5 Dec 2023 **Published:** 12 Jan 2024

Academic Editor: Hamid Reza Karimi **Copy Editor:** Fangling Lan **Production Editor:** Fangling Lan

Abstract

The in-wheel motor is increasingly used in electric vehicles due to the significantly improved controllability, response capability, and energy recovery efficiency based on this technology. However, the independent control of in-wheel motors will lead to braking torque distribution problems, especially in a situation where anti-lock braking systems (ABS) are triggered, which may cause the braking energy to be unrecoverable without the coordinated control between anti-lock and RB for two in-wheel motor-driven electric vehicles based on the RB efficiency map. Control-oriented wheel dynamics and slip ratio models of the system are generated. A sliding mode intervention of regenerative braking (RB) control. This paper presents an integrated algorithm to realize the control-based ABS controller is designed to prevent the wheels from locking and to maintain the slip ratio within a desired level, and the stability and robustness of the controller to uncertainties and disturbances are discussed. Moreover, the braking strength of the driver is calculated and divided into different modes to derive a dynamic braking torque distribution to improve the energy recovery efficiency. The hardware-in-the-loop simulation results show that the recovered energy of the proposed strategy under ABS-triggered maneuver is increased by 52.9% than that of the Proportional, Integral, and Derivative controller and can effectively improve the braking performance and stability.

Keywords: Anti-lock braking system, regenerative braking, sliding mode control, energy recovery, braking torque distribution, electric vehicle

© The Author(s) 2024. **Open Access** This article is licensed under a Creative Commons Attribution 4.0 International License (https://creativecommons.org/licenses/by/4.0/), which permits unrestricted use, sharing, adaptation, distribution and reproduction in any medium or format, for any purpose, even commercially, as long as you give appropriate credit to the original author(s) and the source, provide a link to the Creative Commons license, and indicate if changes were made.

1. INTRODUCTION

Many studies imply that almost one-half of the driving energy is dissipated during braking, especially in urban driving circumstances with frequent acceleration and deceleration manipulations[1,2]. The energy consumption during braking processes in different driving cycles is shown in Table 1[3], where UDDS and ECE stand for urban dynamometer driving schedule and Economic Commission of Europe, respectively. Therefore, regenerative braking systems (RBS), which could recapture kinetic energy and greatly reduce power consumption[5], are widely researched in electric or hybrid vehicles[4–6], and brake-by-wire systems[7,8] that support the application of regenerative braking (RB) are investigated as well[7–10]. Xu *et al.* divided the braking into four different modes for hybrid electric vehicles, and a hierarchical controller is designed to switch the braking mode and to realize optimal efficiency control[11]. Guo *et al.* presented a piecewise RB strategy for safety and energy-saving control of intelligent electric vehicles[12]. However, the above strategies do not take the vehicle braking stability into consideration, which will cause the vehicle instability in limited conditions. Biao *et al.* proposed an optimization distribution algorithm-based RB strategy considering vehicle stability during braking situations[13]. The torque distribution ratio is determined by the braking strength and related constraint conditions, and the energy recapture efficiency of the proposed strategy was raised by about fifty percent, but the stability effect of the vehicle was not reflected in the verification part.

The in-wheel motor, which is located directly in the wheels, will significantly enhance controllability and response speed by removing all the intermediate mechanical connections. Additionally, it acquires high efficiency both in motor and generator modes[14]. Therefore, the control strategies for in-wheel motor-driven electric vehicles (IWMDEV) have been widely studied. Karabacak *et al.* designed a fuzzy logic controller in the motor mode and a pulse width modulation controller in the RB mode for two IWMDEV (2IWMDEV), and the algorithm is embedded in a DSP microcontroller[15]. Gang and Zhi proposed an RB control method for four IWMDEV (4IWMDEV) under urban scenes using motor efficiency maps, and the simulation results validated the effectiveness of the proposed method under urban driving cycles[16]. A feedback hierarchical controller for 4IWMDEV is presented by Chen *et al.* to control the vehicle to track the desired velocity and assign braking torque to increase energy recovery[17]. However, in addition to improving recovery efficiency, the braking performance and stability should also be considered, especially under heavy braking strength request conditions, which will cause the braking torque distribution problem[18–21].

Dadashnialehi *et al.* estimated wheel speed accurately based on the back electromotive force of the brushless DC (BLDC) motor, and proposed a sensorless anti-lock braking system (ABS) for IWMDEVs both theoretically and experimentally[22]. Wang and He presented an improved linear quadratic Gaussian controller to derive braking torques for ABS control, and a varying charge voltage in steps control is designed to recover more energy[23]. Yang *et al.* employed a combination method of logic threshold and phase plane theory to generate the braking torque for ABS control and then proposed a coordination strategy of RBS and ABS to increase recovery efficiency for ABS-triggered scenarios[24]. Although these methods integrate the RBS and ABS control together to improve the braking performance and recover more energy, rarely do these methods address the stability problem during braking situations. He *et al.* took the braking stability into consideration and designed a combined sliding mode controller to realize ABS control[25]. Tang *et al.* presented a comprehensive controller: the braking torque distribution strategy. This strategy considers safety and recovery efficiency optimization while also involving a coordinated strategy of RBS and ABS based on model predictive control[26]. Pei *et al.* proposed a coordinated controller to realize optimal energy regeneration and braking stability for distributed electric vehicles by regulating hydraulic and RB torques[27]. However, the braking intension is rarely considered during the coordinated control of energy recovery and braking stability.

The above studies indicate that the problem of how to simultaneously improve the braking stability and regeneration efficiency for 2IWMDEVs considering braking intension is still not resolved. This paper aims to present an integrated control method to combine ABS and RBS control, even in emergency braking situa-

Table 1. Energy consumption during braking processes

Drive Cycle	UDDS	Japanal015	ECE
Total energy consumption, kJ	28241	1814	395
Braking energy consumption, kJ	13432	938	207
Rate, %	47.6	51.7	52.3

UDDS: Urban dynamometer driving schedule; ECE: Economic Commission of Europe.

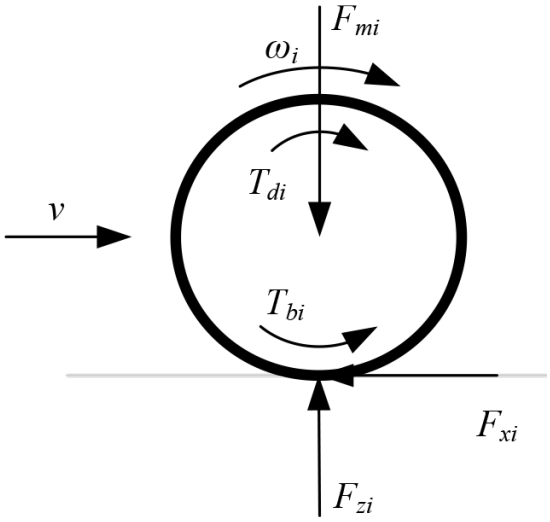


Figure 1. Wheel dynamic.

tions, and synthetically improve braking performance, recovery efficiency, stability, and road adaptability of 2IWMDEVs. The main contributions of the paper include a robust SMC-based ABS controller to make full use of the road conditions under different adhesion coefficients and an RBS strategy to distribute the regenerative and hydraulic braking torques to recapture more energy.

The rest of the paper is organized as follows: In the second section, a SMC-based ABS controller is proposed for 2IWMDEVs, including wheel dynamics models, slip ratio models, ABS controllers, and stability and robustness analysis of the controller. The distribution method of regenerative and frictional braking torques is designed in the third section. In the fourth section, the RB efficiency map is generated through bench experiments. Hardware-in-the-loop (HIL) simulations are conducted in the fifth section to validate the proposed algorithm. Finally, within the same section, conclusions are made, and a future work outlook is provided.

2. SMC-BASED ABS CONTROLLER

2.1 Wheel dynamics

An electric vehicle equipped with two front in-wheel motors and RBSs is applied in the paper, and the two rear wheels are driven by a traction motor. Figure 1 shows rotational dynamics of single wheels, where T_{di} and T_{bi} represent drive and brake torques on the i-th wheel, respectively, F_{mi}, F_{xi}, and F_{zi} denote gravity, longitudinal force, and vertical force on the tire, respectively. ω_i stands for velocity of the i-th wheel, and v is vehicle velocity.

The following assumptions are made.

- The tire rolling resistance and vehicle aerodynamics are negligible during braking processes.
- Tire self-aligning torque is negligible.
- The chamber angle of each wheel is zero.

The dynamic equations are as follows.

$$m_i \dot{v} = F_{xi} \tag{1}$$

$$J_{\omega i} \dot{\omega}_i = -T_{bi} + r F_{xi} \tag{2}$$

$$F_{xi} = \mu_i (\lambda_i) F_{zi} \tag{3}$$

where $J_{\omega i}$ represents the rotational inertia of the i-th in-wheel motor, m_i is the total mass distributed on the i-th wheel, r is the effective wheel rolling radius, and μ_i and λ_i present longitudinal utilized friction coefficient and the slip ratio of the i-th wheel, respectively.

Combining Equations (1), (2), and (3) yields

$$\begin{cases} \dot{\omega}_i = \frac{-T_{bi} + r\mu_i(\lambda_i) F_{zi}}{J_{\omega i}} \\ \dot{v} = \frac{-\sum \mu_i(\lambda_i) F_{zi}}{m_i} \end{cases} \tag{4}$$

where the slip ratio could be expressed as follows during braking situations

$$\lambda_i = \frac{v - r \cdot \omega_i}{v} \tag{5}$$

Taking the derivative of Equation (5) with respect to time and substituting Equation (4) into it, we have

$$\dot{\lambda}_i = \frac{r}{J_{\omega i} v} T_{bi} - \frac{r^2}{J_{\omega i} v} \mu_i (\lambda_i) F_{zi} - \frac{r \omega_i}{m_i v^2} \sum \mu_i (\lambda_i) F_{zi} \tag{6}$$

Figure 2 represents experimental results based on JAC iEV7S, a four-wheel double-drive electric vehicle; it shows the relationship between slip ratios and longitudinal utilized friction coefficients, and the curve could be simplified with two lines intersecting at the peak utilized friction coefficient point. The longitudinal utilized friction coefficient can be described as follows

$$\mu_i (\lambda_i) = \begin{cases} k_{\mu it} \lambda_i, & \lambda_i \le \lambda_{di} \\ \mu_{\text{imax}} - k_{\mu ih} (\lambda_i - \lambda_{di}), & \lambda_i > \lambda_{di} \end{cases} \tag{7}$$

where k_{uit} and k_{uih} denote the slope of lines corresponding to linear and nonlinear areas, respectively, λ_{di} stands for reference slip ratios for the i-th wheel, and μ_{imax} represents peak longitudinal utilized friction coefficients of the i-th wheel.

Substituting Equation (7) into Equation (6), after some manipulations, we have

$$\dot{\lambda}_i = \begin{cases} \frac{r}{J_{\omega i} v} T_{bi} - \frac{r^2}{J_{\omega i} v} \lambda_i k_{uit} F_{zi} - \frac{r \cdot \omega_i}{m_i v^2} \sum k_{\mu it} \lambda_i F_{zi}, & \lambda_i \le \lambda_{di} \\ \frac{r}{J_{\omega i} v} T_{bi} - \frac{r^2}{J_{\omega i} v} \left(\mu_{imax} - k_{\mu ih} (\lambda_i - \lambda_{di})\right) F_{zi} - \frac{r \cdot \omega_i}{m_i v^2} \sum \left(\mu_{imax} - k_{\mu ih} (\lambda_i - \lambda_{di})\right) F_{zi}, & \lambda_i > \lambda_{di} \end{cases} \tag{8}$$

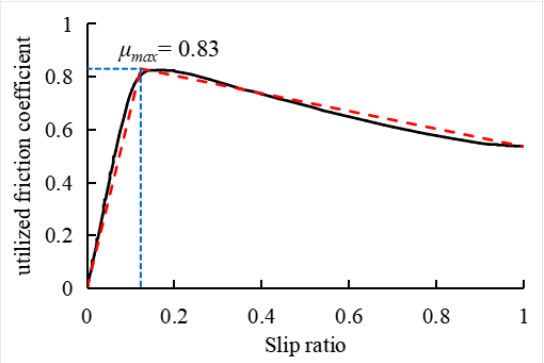


Figure 2. The curve of μ_i and λ_i.

2.2 ABS controller

ABS controllers are designed to maintain the slip ratios of wheels at a particular level, where both the longitudinal and lateral adhesion forces reach their maximum value. To this end, we define the sliding surface in terms of slip ratio tracking errors as

$$S_i = \lambda_{di} - \lambda_i \tag{9}$$

It is apparent that if we find a control law to make S_i converge to zero or maintain small, then the slip ratio will match very well with the desired one. However, a drastic change of the control law will occur when S_i is near the sliding surface. To eliminate the chattering problem and smooth the control law, for the system motion on the sliding surface, control rules are designed below.

$$\dot{S}_i = -K_i \,\mathrm{sat}\,(S_i/\varphi) \tag{10}$$

$$\mathrm{sat}\,(S_i/\varphi) = \begin{cases} S_i/\varphi, & |S_i/\varphi| \le 1 \\ \mathrm{sgn}\,(S_i/\varphi)\,, & |S_i/\varphi| > 1 \end{cases} \tag{11}$$

where K_i is positive and denotes the factor of convergence; $sat(S/\varphi)$ stands for the switching function, and φ represents the boundary layer thickness.

Differentiating Equation (9) with respect to time and combining Equation (8) yield

$$\dot{S}_i = \begin{cases} \dot{\lambda}_{di} - \frac{r}{J_{\omega i} v} T_{bi} - \frac{r^2}{J_{\omega i} v} k_{\mu it} \lambda_i F_{zi} - \frac{r \cdot w_i}{m_i v^2} \sum k_{\mu it} \lambda_i F_{zi}, & \lambda_i \le \lambda_{di} \\ \dot{\lambda}_{di} - \frac{r}{J_{\omega i} v} T_{bi} - \frac{r^2}{J_{\omega i} v} \left(\mu_{imax} - k_{\mu ih} \left(\lambda_i - \lambda_{th}\right)\right) F_{zi} - \frac{r \cdot w_i}{m_i v^2} \sum \left(\mu_{imax} - k_{\mu ih} \left(\lambda_i - \lambda_{di}\right)\right) F_{zi}, & \lambda_i > \lambda_{di} \end{cases} \tag{12}$$

Since λ_{di} is a constant, which means $\dot{\lambda}_{d_i} = 0$, substituting Equation (10) into Equation (12), the control law will be derived.

$$T_{bi}=\begin{cases} rk_{\mu it}\lambda_i F_{zi}+\frac{J_{\omega i}\omega_i}{m_i v}\sum k_{\mu it}\lambda_i F_{zi}+K_i\frac{J_{\omega i}v}{r}\,\mathrm{sat}\left(\frac{\lambda_{di}-\lambda_i}{\varphi}\right), & \lambda_{di}>\lambda_i \\ r\left(\mu_{imax}-k_{\mu ih}\left(\lambda_i-\lambda_{di}\right)\right)F_{zi}+K_i\frac{J_{\omega i}v}{r}\,\mathrm{sat}\left(\frac{\lambda_{di}-\lambda_i}{\varphi}\right)+\frac{J_{\omega i}\omega_i}{m_i v}\sum(\mu_{imax}-k_{\mu ih}\left(\lambda_i-\lambda_{di}\right)F_{zi}, & \lambda_{di}>\lambda_i \end{cases} \tag{13}$$

2.3 Stability analysis of the ABS controller

The Lyapunov function is designed as follows:

$$W_i=\left(\lambda_{di}-\lambda_i\right)^2 \tag{14}$$

Thus,

$$\dot{W}_i=2\left(\lambda_{di}-\lambda_i\right)\left(\dot{\lambda}_{di}-\dot{\lambda}_i\right) \tag{15}$$

Substituting Equation (8) into Equation (15), after some manipulations, we have

$$\dot{W}_i=\begin{cases} -2\left(\lambda_{di}-\lambda_i\right)\left(\frac{r}{J_{\omega i}v}T_{bi}-\frac{r^2}{J_{\omega i}v}k_{\mu it}\lambda_i F_{zi}-\frac{r\omega_i}{m_i v^2}\sum k_{\mu it}\lambda_i F_{zi}\right), & \lambda_i\le\lambda_{di} \\ -2\left(\lambda_{di}-\lambda_i\right)\left(\frac{r}{J_{\omega i}v}T_{bi}-\frac{r^2}{J_{\omega i}v}\left(\mu_{imax}-k_{\mu ih}\left(\lambda_i-\lambda_{di}\right)\right)F_{zi}-\frac{r\omega_i}{m_i v^2}\sum\left(\mu_{imax}-k_{\mu ih}\left(\lambda_i-\lambda_{th}\right)\right)F_{zi}\right), & \lambda_i>\lambda_{di} \end{cases} \tag{16}$$

Substituting Equation (13) into Equation (16) yields

$$\dot{W}_i=-2\left(\lambda_{di}-\lambda_i\right)K_i\,\mathrm{sat}\left(\frac{\lambda_{di}-\lambda_i}{\varphi}\right)\le 0 \tag{17}$$

The stability of the proposed ABS controller has been proved, and the system will move to the surface according to Equation (17). Assume that the initial slip ratio tracking error is finite, and then, S_i will arrive at the sliding surface S_i=0 in a finite time.

2.4 Robustness analysis of the ABS controller

Nonlinear characteristics, disturbances, and uncertainties always exist in practice control systems, e.g., motor torques, estimated vehicle velocity, and sensor noise. Therefore, if the controller is to be applied in practice, it is essential to analyze its robustness.

2.4.1 Disturbance analysis of motor torque

In the actual motor control process, it is generally difficult to achieve real-time precise implementation of the desired motor torque listed in Equation (13), and the torque tracking error may reduce the control performance or even cause the controller instability. Moreover, the additive disturbance will affect the design value of convergence factor K_i. Therefore, the desired motor torque is redesigned with a torque disturbance item added in Equation (13) as

$$T_{bia}=T_{bi}+\Delta T_{bi} \tag{18}$$

Replacing T_{bi} with T_{bia} in Equation (16) and combining Equation (13), we have

$$\dot{W}_i = -2\left(\lambda_{di} - \lambda_i\right)\left[\frac{r}{J_{\omega i} v}\Delta T_{bi} + K_i \,\mathrm{sat}\left(\frac{\lambda_{di} - \lambda_i}{\varphi}\right)\right] \tag{19}$$

Note that the first derivative of the Lyapunov function should be negative definite to ensure the system stability; the torque disturbance should satisfy the following inequality constraints.

$$\left|\Delta T_{bi}\right| \le \left|K_i \frac{J_{wi} v}{r}\,\mathrm{sat}\left(\frac{\lambda_{di} - \lambda_i}{\varphi}\right)\right| \tag{20}$$

The above equation means that the factor of convergence K_i should be large enough to cover the disturbance caused by the control error, and then the stability of the controller will be guaranteed.

2.4.2 Disturbance analysis of vehicle velocity

The actual vehicle velocity is normally obtained from the transmission output shaft speed sensor or estimated based on the wheel speed sensor. However, the above methods will cause velocity error, which leads to slip ratio error $\Delta\lambda_i$, and with Equation (5), we have

$$\Delta\lambda_i = \frac{v + \Delta v - v_{wi}}{v + \Delta v} - \frac{v - v_{wi}}{v} \approx \frac{\Delta v}{v} \tag{21}$$

For the controller, the actual slip ratio is expressed as λ_i+$\Delta\lambda_i$, considering torque disturbance, Equation (17) is updated.

$$\dot{W}_i = -2\left(\lambda_{th} - \lambda_i - \Delta\lambda_i\right) K_i \,\mathrm{sat}\left(\frac{\lambda_{th} - \lambda_i - \Delta\lambda_i}{\varphi}\right) \le 0 \tag{22}$$

From the above equation, $\dot{W}_i$ will always be negative definite no matter if the velocity error is large or small, which implies that the controller has strong robustness under velocity disturbance.

2.4.3 Disturbance analysis of sensor noise

Sensor noise has a significant influence on the stability of a closed-loop system, and the signal fluctuation will degrade measurement accuracy and affect state parameter calculation; e.g., the fluctuation of wheel velocity signals will influence the slip ratio calculation according to Equation (5). High-frequency filters[7] are adopted to estimate the actual value, decrease measurement noise, and guarantee the system stability.

3. DISTRIBUTION OF REGENERATIVE AND FRICTIONAL BRAKING TORQUES

With two front in-wheel motors, the regenerative and frictional blending brake is related, and the optimal objective is to improve energy recovery efficiency and braking stability. To this end, the distribution of the regenerative and frictional braking torques should be first discussed. As shown in Figure 3, the requested braking pressure of the driver is calculated according to brake pedal stroke and the characteristics of brake pressure *vs*. pedal stroke (P-S curve) shown in reference[7], and then the requested braking force F_b and torque T_b are estimated. A braking torque distribution controller is designed to generate the desired regenerative and frictional braking torques according to the braking strength. The RB torque is executed by the in-wheel motors,

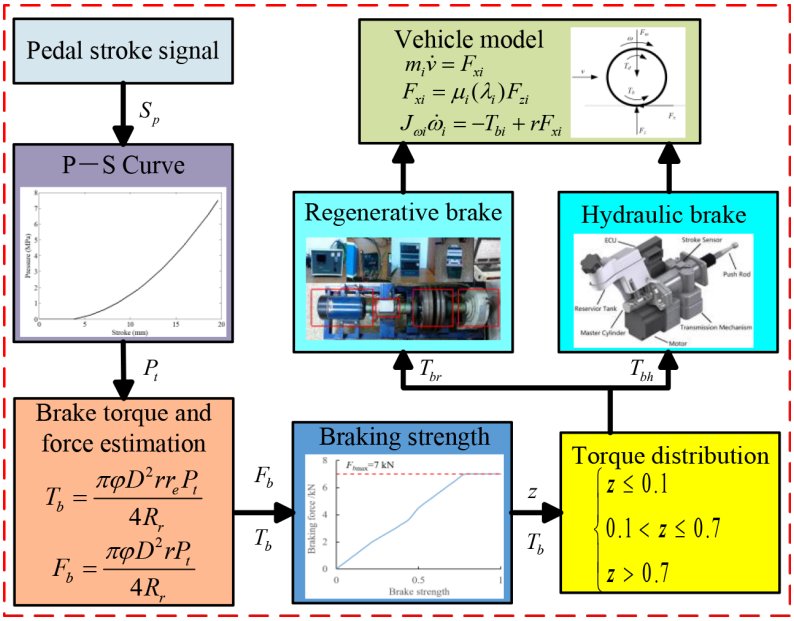


Figure 3. Braking torque control schematic.

while the frictional braking torque is realized by a novel electro-hydraulic actuator illustrated in reference[28], and the novel electro-hydraulic actuator generates braking force fast and has a fast and good pressure-tracking performance.

To improve tire-road friction coefficient (TRFC) utilization efficiency and directional stability during braking situations, both the front and rear wheels should be locked simultaneously, and the desired braking forces of the front and rear axles are expressed as follows

$$\begin{cases} F_{\mu 1} + F_{\mu 2} = F_b \\ F_{\mu 2} = \frac{1}{2}\left[\frac{G}{h_g}\sqrt{b^2 + \frac{4h_g L}{G}F_{\mu 1}} - \left(\frac{Gb}{h_g} + 2F_{\mu 1}\right)\right] \end{cases} \tag{23}$$

where $F_{\mu 1}$ and $F_{\mu 2}$ denote the desired braking forces of the front and rear axles, respectively, G stands for the weight of vehicles, L represents wheelbase, b is the horizontal distance between the rear axle and center of gravity, and h_g indicates the height of the center of gravity with respect to the ground.

With manipulations of Equation (23), we have

$$\begin{cases} F_{\mu 1} = \frac{F_b^2 h_g + F_b G b}{GL} \\ F_{\mu 2} = F_b - F_{\mu 1} \end{cases} \tag{24}$$

As shown in Figure 3, the braking strength z is achieved according to the requested braking force and F_b-z lookup table. The braking mode is divided into three levels: mild ($z \le 0.1$), moderate ($0.1 < z \le 0.7$), and emergency ($z > 0.7$), and the braking torque distribution strategy is discussed based on different modes.

(A) When $z \le 0.1$, the requested braking torque of the front axle will be offered only by the two front regenerative motors; the braking torque distribution of axles and blended braking system are derived

$$\begin{cases} T_{bfr} = F_{\mu 1} r, T_{bfh} = 0 \\ T_{br} = F_{\mu 2} r \end{cases} \tag{25}$$

where T_{bfr} and T_{bfh} represent regenerative and hydraulic braking torques of the front axle, respectively, and the braking torque of the left and right wheels of the front axle is allocated averagely; T_{br} denotes the braking torque of the rear axle.

(B) When $0.1 < z \leq 0.7$, the RB torque may not meet the request one, and the braking torques are distributed as follows

$$\begin{cases} T_{bfr} = F_{\mu 1} r, T_{bfh} = 0, T_{br} = F_{\mu 2} r; & T_{bf} \leq T_{bfr\max} \\ T_{bfr} = T_{bfr\max}, T_{bfh} = T_{bf} - T_{bfr\max}, T_{br} = F_{\mu 2} r; & T_{bf} > T_{bfr\max} \end{cases} \tag{26}$$

where $T_{bf} = (F_b^2 h_g + F_b G b) r / GL$ is the braking torque calculated by Equation (24), T_{bfrmax} stands for the maximum RB torque that both the left and right motors could be applied for at the same time.

(C) When $z > 0.7$, the braking torque distribution is the same as Equation (26) if the wheels are not locked. However, the ABS will probably be triggered in this large deceleration request situation, and the braking torques of the front and rear axles will not be decided by Equation (24) but rather by the results generated from ABS controllers. In this case, the torque distribution is determined by

$$\begin{cases} T_{bffr} = T_{bffA}, T_{bfih} = 0, T_{bri} = T_{briA}; & T_{bffA} \leq T_{bfr\max} \\ T_{bfir} = T_{bfr\max}, T_{bfh} = T_{bfiA} - T_{bfr\max}, T_{bri} = T_{briA}; & T_{bffA} > T_{bfr\max} \end{cases} \tag{27}$$

where T_{bfiA} and T_{briA} stand for desired braking torques of the four wheels generated by the ABS controller, T_{bfir} and T_{bfih} represent distributed regenerative and hydraulic braking torques of the front two wheels, and T_{bri} is braking torque of two rear wheels.

4. EFFICIENCY MAP OF THE RB SYSTEM

An optimal energy recovery method should be designed based on an efficiency map by minimizing the transfer loss during blending brake, and the motor-to-battery efficiency is calculated by the following expression.

$$\eta = \frac{U_C I_C}{T_b \omega} \tag{28}$$

where U_C and I_C are the measured battery charging voltage and current during RB, respectively.

Figure 4 shows the test bench; a motor with the same characteristics is used instead of the in-wheel one, and a magnetic powder brake is adopted to simulate the vehicle rolling resistance to prevent the motor from moving or to supply kinetic energy during braking. Batteries and sensors are installed to collect energy recapture information. With Equation (28), the RB efficiency map is generated from bench tests under different braking torques and wheel velocities and is fitted, as shown in Figure 5, based on the experimental data.

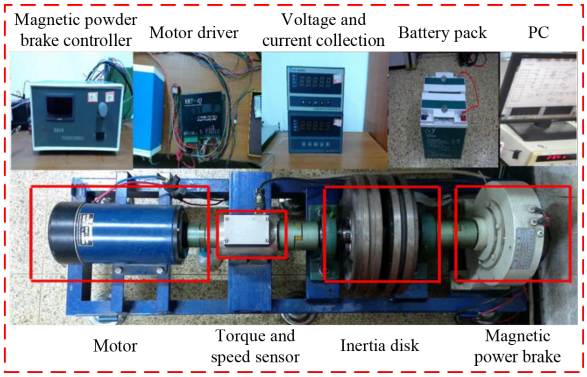


Figure 4. Test bench.

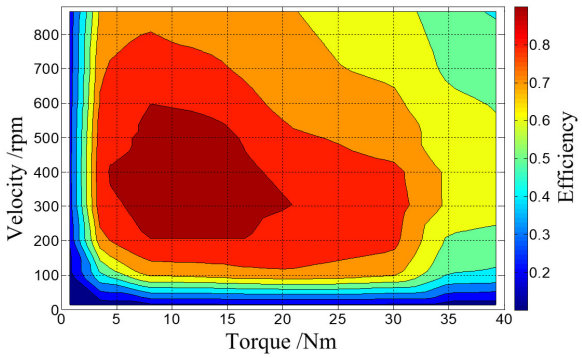


Figure 5. RB efficiency map.

Table 2. Vehicle model and controller parameters

Parameters	Value
Vehicle mass (m)	1,855 kg
Rotational inertia of the front/rear tire ($J_{\omega i}$)	1.5 kg·m^2
Effective wheel rolling radius (r)	316 mm
Height of the center of gravity (h_g)	530 mm
Distance between the front and rear axles (L)	2,490 mm
Front axle to the center of gravity (a)	1,100 mm
Rear axle to the center of gravity (b)	1,390 mm
Effective radius of the front brake disc (r_b)	105 mm
Piston radius of the front wheel cylinder (r_w)	27 mm
Friction coefficient of the front brake pad (μ_f)	0.4
Maximum RB torque (T_{hfrmax})	1,200 N
Convergence factor (K_i)	0.02
Boundary layer thickness (ϕ)	0.1

5. HIL SIMULATION AND RESULTS ANALYSIS

A HIL simulation system equipped with vehicle-manipulator systems, steering systems, and hydraulic braking system is developed to evaluate the performance of the proposed integrated algorithm.Figure 6 displays the system composition. Figure 7 illustrates the algorithm block diagram. In this diagram, the steering angle and braking torque are requested by the driver. The vehicle model is then simulated using the CarSim software. The torque distribution and ABS algorithm code are generated using MATLAB/Simulink and downloaded to the dSPACE/SCALEXIO for execution. Finally, the recaptured energy is stored in the battery pack.The vehicle model and controller parameters are listed in Table 2.



Figure 6. HIL simulation system.

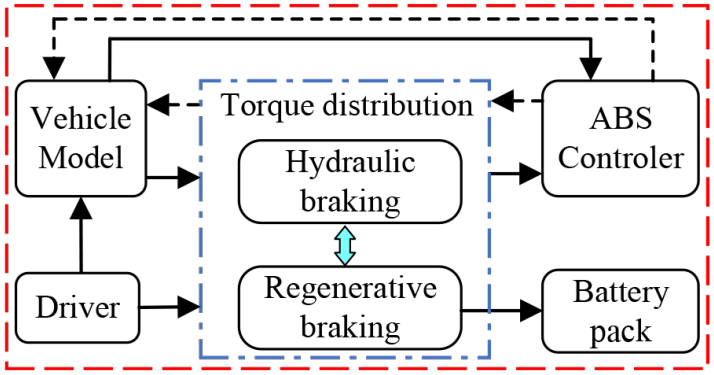


Figure 7. Algorithm block diagram.

5.1 Results on homogeneous surface

A steering-braking maneuver with a 75 km/h initial forward velocity is performed on a high-*mu* homogeneous surface to verify the proposed algorithm, and a Proportional, Integral, and Derivative (PID) controller is also simulated to compare with the proposed one. Figure 8 shows the time histories of vehicle and wheel velocities derived from the two controllers under the specified simulation maneuver. At the end of the simulation, the four wheels of the PID controller are locked, while those of the SMC controller are not during the whole simulation, which indicates that the proposed SMC controller achieves better anti-lock performance than the PID controller. As shown in Figure 8A and B, compared with PID controllers, the regulation frequency of the front wheels of SMC controllers is lower, which will improve the vehicle stability and comfort.

Figure 9 depicts the comparison of wheel slip ratios derived from the two controllers. Slip ratios of all the wheels of both the controllers are within a reasonable range near the optimal value in the beginning, and then, the fluctuation of the PID controller dramatically rises to approximately one while that of the SMC controller is still reasonable. The high braking torque regulation frequency of front wheels leads to frequent and dramatic chattering of the slip ratio. The results illustrate that the SMC controller acquires a significantly better tracking performance of the optimal slip ratio.

Figure 10 presents the time histories of sideslip angular velocities and yaw rates. In Figure 10A, although the fluctuations of both two controllers are large in the beginning because of the steering input, the sideslip angular velocity derived from the SMC controller is constrained within a very small boundary in the remaining simulation process, while that of the PID method is still variate intensive. As shown in Figure 10B, the magnitude of the yaw rate of the PID controller is much larger than that of the SMC controller, especially at the

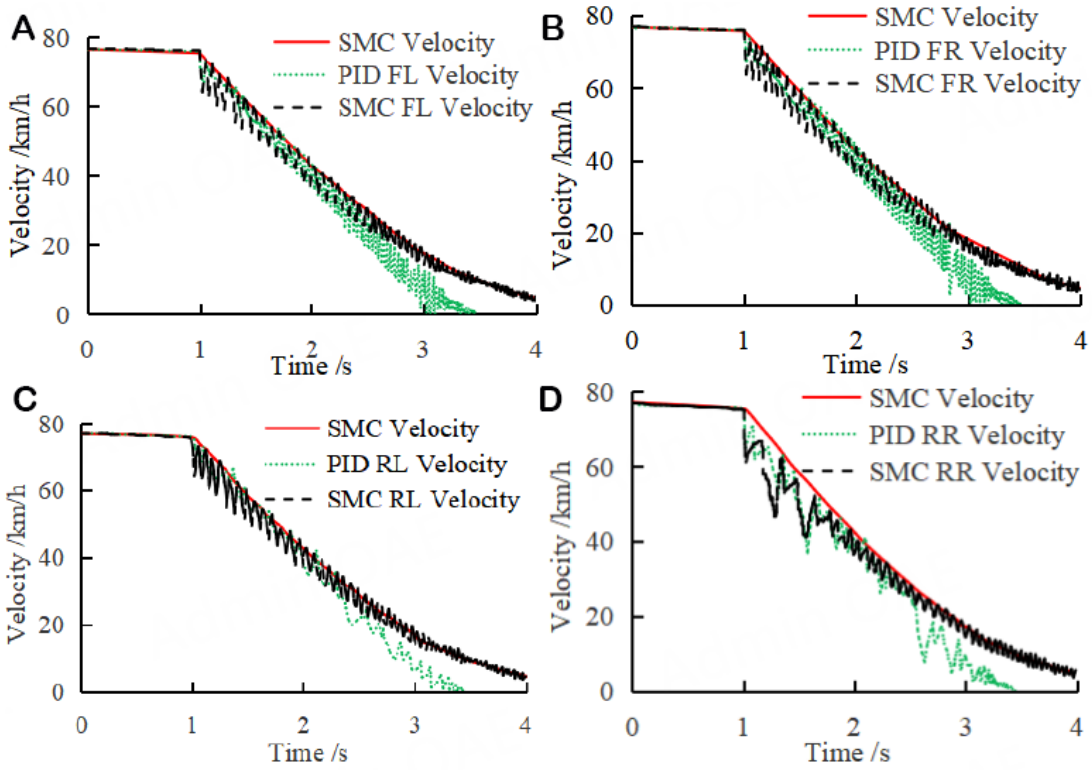


Figure 8. Velocities of vehicles and wheels. (A) Front left wheel; (B) Front right wheel; (C) Rear left wheel; (D) Rear right wheel.

end of the simulation. The results indicate that the proposed method achieves a better handling and stability performance than that of the PID controller.

Figure 11 and Figure 12 reveal the comparison of energy recovery between the SMC and PID controllers. Since the braking torque generated by the SMC controller is much bigger than that of the PID controller before about 1.5 s, the recapture energy of the SMC controller is larger during the beginning period. After about 2.4 s, the braking torque derived from PID is larger than SMC, which causes a greater wheel velocity variation even to lock, as shown in Figure 8. However, the recaptured energy by SMC grows faster than by PID due to the distribution of braking torques, and the main growth of recovery energy by SMC lies in this period. Overall, the SMC-based energy recovery efficiency is significantly higher than that of PID-based, and the efficiency increases by 52.9%.

5.2 Results on the split surface

A driver-in-the-loop simulation on the split surface with a 70 km/h initial forward velocity is conducted to evaluate the effectiveness of the proposed algorithm in non-ideal scenarios, and the TRFCs of the left and right sides are 0.3 and 0.8, respectively.Figure 13A shows the master cylinder pressure applied by the driver and the wheel cylinder pressures generated by the ABS controller. The applied pressure (about 8 MPa) is too big to anti-lock the wheels, and the ABS is triggered to regulate the wheel pressures. Furthermore, the generated pressures of the left wheels change more frequently than the right wheels due to the lower TRFC, and the pressure increasement times of the front left (FL) and rear left (RL) wheels are 25 and 26 in approximately eight seconds, whereas that of the front right (FR) and rear right (RR) are two and 24 times, respectively. Although the left wheels are easier to lock up due to their huge fluctuations of slip ratios, the frequent regulation of braking pressures keeps the wheels in anti-lock status, as shown in Figure 13B. The maximum equivalent braking pressure generated by the RB motor is calculated by the following expression.

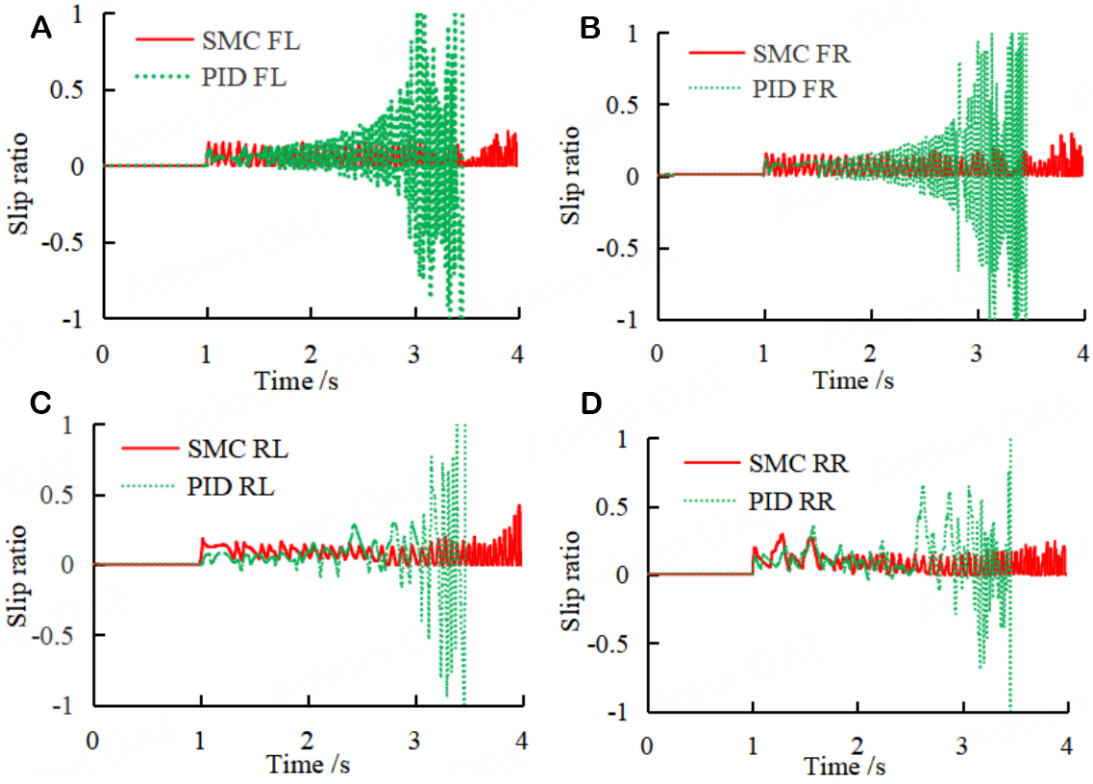


Figure 9. Slip ratio of the wheels.(A) Front left wheel; (B) Front right wheel; (C) Rear left wheel; (D) Rear right wheel.

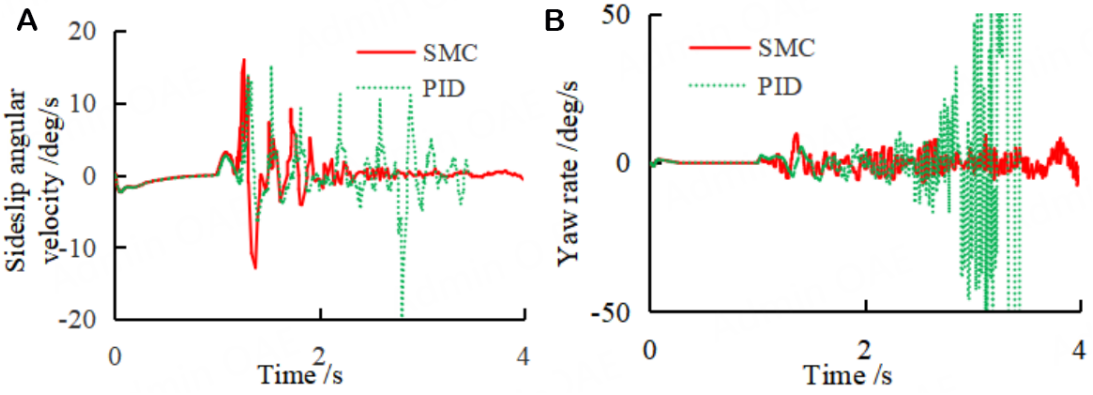


Figure 10. Vehicle sideslip angular velocity and yaw rate. (A) Sideslip angular velocity; (B) Yaw rate.

$$P_{mr} = \frac{F_{bfr\max} r}{2\pi r_w^2 \mu r_b} \tag{29}$$

With the parameter values listed in Table 2, the value of P_{mr} is calculated as 2 MPa. Figure 13C and D indicates the braking distribution results of the front wheels derived from the proposed algorithm; only RB is applied if the pressure generated by the ABS controller is less than 2 MPa, and the residual pressure is generated by the hydraulic braking system.

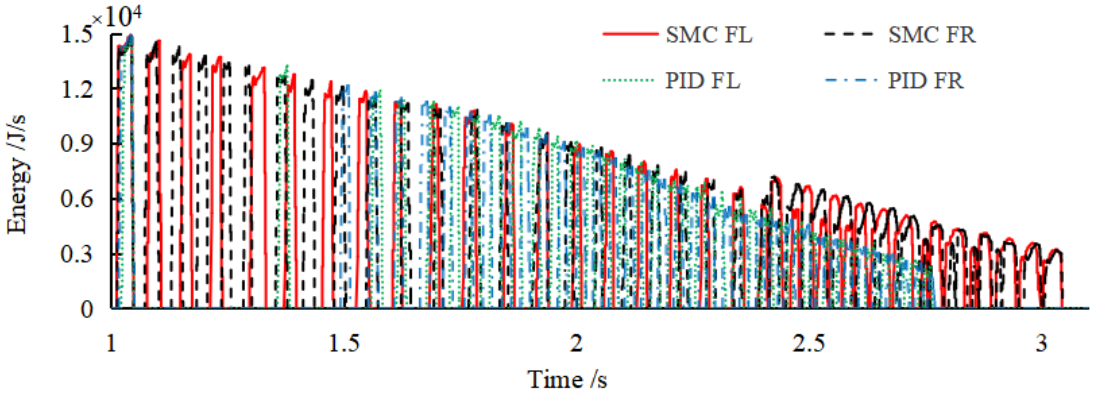


Figure 11. Distribution of the regenerative braking energy.

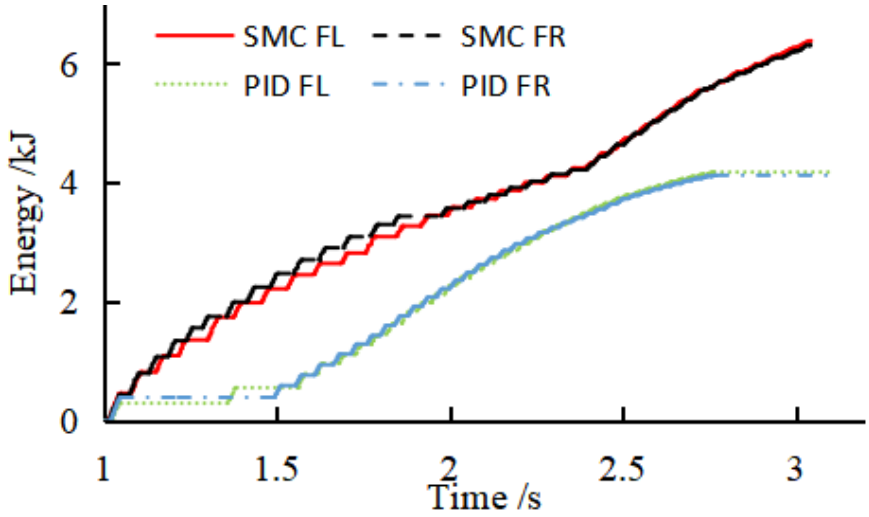


Figure 12. Comparison of total recaptured energy.

6. CONCLUSIONS AND FUTURE WORK

An integrated algorithm is proposed for ABS and RBS coordinated control of 2IWMDEVs to improve vehicle braking stability and energy recovery efficiency, including both RB control on the front two wheels and anti-lock braking control on all four wheels. HIL simulations are carried out to verify the effectiveness of the integrated algorithm, and the results show that the ABS controller can prevent wheels from being locked to ensure braking performance and vehicle stability. With the distribution strategy of braking torques among in-wheel motors and friction brakes considering the required braking torque and strength, the recovered energy of the proposed strategy under ABS-triggered maneuver is increased by 52.9% than that of the PID controller. Therefore, the presented integrated algorithm can not only maintain the slip ratio within the desired range and braking stability but also achieve excellent energy recapture efficiency, which is significant to ensure safety and economy of the 2IWMDEVs.

Our future work will concentrate on adaptive threshold value design for braking modes division, experimental validation of the proposed algorithm through in-vehicle field and road tests with the consideration of uncertainties, and modification of the proposed algorithm to adapt to 4IWMDEVs.

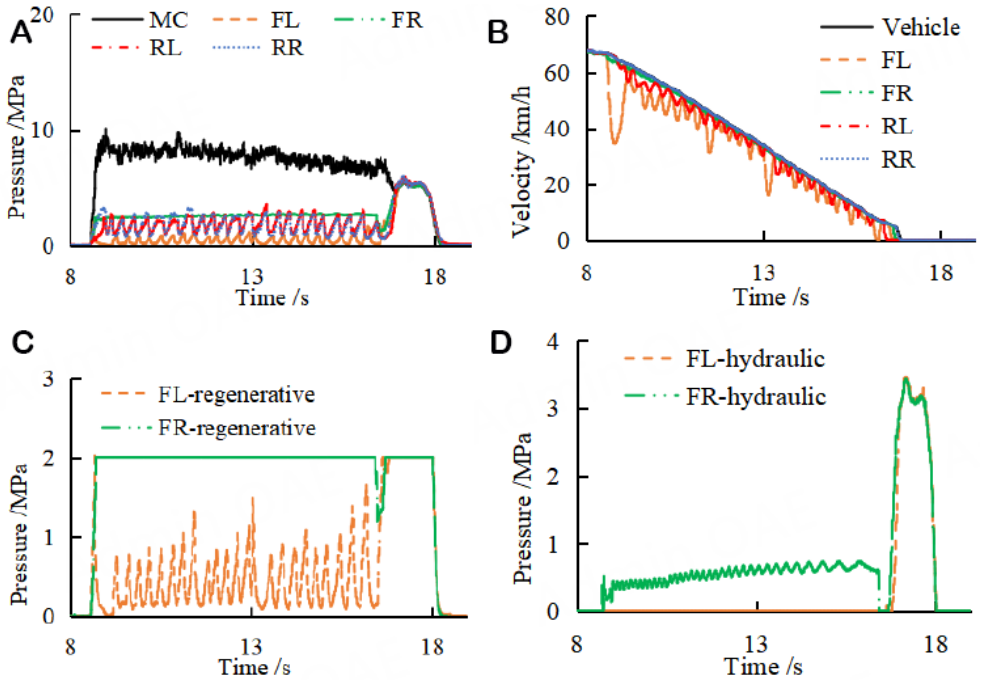


Figure 13. Simulation results on the split surface. (A) Braking pressure; (B) Velocities; (C) Regenerative braking; (D) Hydraulic braking.

DECLARATIONS

Acknowledgments

The authors would like to thank the anonymous reviewers for their valuable comments.

Authors' contributions

Made substantial contributions to the conception and design of the study and performed data analysis and interpretation: Yong J, Dong Y, Zhang Z

Performed data acquisition and provided administrative, technical, and material support: Zhang Z, Feng N, Li W

Availability of data and materials

Not applicable.

Financial support and sponsorship

This work was supported by the National Natural Science Foundation of China (No. 52002009), Beijing Natural Science Foundation (No. 3222003), and the State Key Laboratory of Automotive Safety and Energy under Project No. KF2010.

Conflicts of interest

All authors declared that there are no conflicts of interest.

Ethical approval and consent to participate

Not applicable.

Consent for publication

All the authors have agreed to publish the paper.

Copyright
© The Author(s) 2024.

REFERENCES

1. Feng N, Yong J, Zhan Z. A direct multiple shooting method to improve vehicle handling and stability for four hub-wheel-drive electric vehicle during regenerative braking. *J Automot Eng* 2019;234:1047-56. DOI
2. Zhao W, Wu G, Wang C, Yu L, Li Y. Energy transfer and utilization efficiency of regenerative braking with hybrid energy storage system. *J Power Sources* 2019;427:174-83. DOI
3. Bravo RRS, De Negri VJ, Oliveira AAM. Design and analysis of a parallel hydraulic-pneumatic regenerative braking system for heavy-duty hybrid vehicles. *Appl Energy* 2018;225:60-7. DOI
4. Xu M, Peng J, Ren X, Yang X, Hu Y. Research on braking energy regeneration for hybrid electric vehicles. *Machines* 2023;11:347. DOI
5. Choo KM, Won CY. Design and analysis of electrical braking torque limit trajectory for regenerative braking in electric vehicles with PMSM drive systems. *IEEE Trans Power Electron* 2020;35:13308–21. DOI
6. Hamada AT, Orhan MF. An overview of regenerative braking systems. *J Energy Stor* 2022;52:105033 DOI
7. Yong J, Gao F, Ding N, He Y. Design and validation of an electro-hydraulic brake system using hardware-in-the-loop real-time simulation. *Int J Automot Technol* 2017;18:603-12. DOI
8. Han W, Xiong L, Yu Z. A novel pressure control strategy of an electro-hydraulic brake system via fusion of control signals. *J Automot Eng* 2019;233:3342-57. DOI
9. Chen Q, Lv Z, Tong H, Xiong Z. Clamping force control strategy of electro-mechanical brake system using VUF-PID controller. *Actuators* 2023;12:272. DOI
10. Wang Z, Ding X, Zhang L. Chassis coordinated control for full X-by-wire four-wheel-independent-drive electric vehicles. *IEEE Trans Veh Technol* 2023;72:4394-410. DOI
11. Xu Q, Wang F, Zhang X, Cui S. Research on the efficiency optimization control of the regenerative braking system of hybrid electrical vehicle based on electrical variable transmission. *IEEE Access* 2019;7:116823-34. DOI
12. Guo J, Li W, Wang J, Luo Y, Li K. Safe and energy-efficient car-following control strategy for intelligent electric vehicles considering regenerative braking. *IEEE Trans Intell Transport Syst* 2022;23:7070-81. DOI
13. Biao J, Xiangwen Z, Yangxiong W, Wenchao H. Regenerative braking control strategy of electric vehicles based on braking stability requirements. *Int J Automot Technol* 2021;22:465-73. DOI
14. Hosseini Salari A, Mirzaeinejad H, Fooladi Mahani M. A new control algorithm of regenerative braking management for energy efficiency and safety enhancement of electric vehicles. *Energy Convers Manag* 2023;276:116564. DOI
15. Karabacak Y, Uysal A. An embedded controller application with regenerative braking for the electric vehicle. *Elektron ElektroTech* 2020;26:10-17. DOI
16. Gang L, Zhi Y. Energy saving control based on motor efficiency map for electric vehicles with four-wheel independently driven in-wheel motors. *Adv Mech Eng* 2018;10:1-18. DOI
17. Chen J, Yu J, Zhang K, Ma Y. Control of regenerative braking systems for four-wheel-independently-actuated electric vehicles. *Mechatronics* 2018;50:394-401. DOI
18. Lupberger S, Degel W, Odenthal D, Bajcinca N. Nonlinear control design for regenerative and hybrid antilock braking in electric vehicles. *IEEE Trans Contr Syst Technol* 2022;30:1375-89. DOI
19. Ma Z, Sun D. Energy recovery strategy based on ideal braking force distribution for regenerative braking system of a four-wheel drive electric vehicle. *IEEE Access* 2020;8:136234-42. DOI
20. Zhang Z, Ma R, Wang L, Zhang J. Novel PMSM control for anti-lock braking considering transmission properties of the electric vehicle. *IEEE Trans Veh Technol* 2018;67:10378-86. DOI
21. Chen Y, Chen S, Zhao Y, Gao Z, Li C. Optimized handling stability control strategy for a four in-wheel motor independent-drive electric vehicle. *IEEE Access* 2019;7:17017-32. DOI
22. Dadashnialehi A, Bab-hadiashar A, Cao Z, Kapoor A. Intelligent sensorless antilock braking system for brushless in-wheel electric vehicles. *IEEE Trans Ind Electron* 2015;62:1629-38. DOI
23. Wang J, He R. Varying charge voltage in the steps control method of ABS for in-wheel motors driven electric vehicles based on an improved LQG scheme. *IEEE Access* 2018;6:15039-50. DOI
24. Yang Y, Tang Q, Bolin L, Fu C. Dynamic coordinated control of regenerative braking system and anti-lock braking system for electrified vehicles under emergency braking conditions. *IEEE Access* 2020;8:172664-77. DOI
25. He L, Ye W, He Z, Song K, Shi Q. A combining sliding mode control approach for electric motor anti-lock braking system of battery electric vehicle. *Control Eng Pract* 2020;102:104520. DOI
26. Tang Q, Yang Y, Luo C, Yang Z, Fu C. A novel electro-hydraulic compound braking system coordinated control strategy for a four-wheel-drive pure electric driven by dual motors. *Energy* 2022;241:122750. DOI
27. Pei X, Pan H, Chen Z, Guo X, Yang B. Coordinated control strategy of electro-hydraulic braking for energy regeneration. *Control Eng Pract* 2020;96:10434. DOI
28. Yong JW, Gao F, Ding NG, He YP. Pressure-tracking control of a novel electro-hydraulic braking system considering friction compensation. *J Cent South Univ* 2017;24:1909-21. DOI

Sampathkumar *et al*. *Complex Eng Syst* 2024;4:3
DOI: 10.20517/ces.2023.34

Complex Engineering Systems

Research Article

Open Access

Fuzzy inference system-assisted human-aware navigation framework based on enhanced potential field

Shurendher Kumar Sampathkumar[1], Daegyun Choi[2], Donghoon Kim[2]

[1]Department of Mechanical and Materials Engineering, University of Cincinnati, Cincinnati, OH 45221, USA.
[2]Department of Aerospace Engineering and Engineering Mechanics, University of Cincinnati, Cincinnati, OH 45221, USA.

Correspondence to: Dr. Donghoon Kim, Department of Aerospace Engineering and Engineering Mechanics, University of Cincinnati, 2600 Clifton Ave, Cincinnati, OH 45221, USA. E-mail: Donghoon.Kim@uc.edu; ORCID: 0000-0003-3142-4458

How to cite this article: Sampathkumar SK, Choi D, Kim D. Fuzzy inference system-assisted human-aware navigation framework based on enhanced potential field. *Complex Eng Syst* 2024;4:3. http://dx.doi.org/10.20517/ces.2023.34

Received: 29 Sep 2023 **First Decision:** 24 Nov 2023 **Revised:** 9 Dec 2023 **Accepted:** 21 Dec 2023 **Published:** 13 Jan 2024

Academic Editor: Hamid Reza Karimi **Copy Editor:** Fangling Lan **Production Editor:** Fangling Lan

Abstract

With the advent of Autonomous Mobile Robots (AMRs) in public areas such as malls and airports, their harmonious coexistence with humans is crucial. AMRs must operate in a manner that ensures human safety, comfort, and acceptability to reduce stress. This is called Human Aware Navigation. This study introduces a framework for AMR navigation that prioritizes safety and human comfort in such environments, utilizing an enhanced Potential Field approach augmented by Fuzzy Inference Systems. To achieve a smooth AMR trajectory, the framework employs these systems based on AMR, human, and obstacle information. The proposed approach is tested across various scenarios, including complex, cluttered environments that mimic practical situations. Simulation results demonstrate that AMRs using the proposed method navigate human-rich environments safely and comfortably while mitigating common issues associated with Potential Field-based approaches, such as local minima and obstacles near the goal.

Keywords: Human Aware Navigation (HAN), Potential Field (PF), Fuzzy Inference System (FIS), Autonomous Mobile Robot (AMR)

1. INTRODUCTION

Asimov's first law of robotics [1] explicitly states that "A robot may not injure a human being or, through inaction, allow a human being to come to harm", serving as a foundational principle in human-robot interaction. While

© The Author(s) 2023. **Open Access** This article is licensed under a Creative Commons Attribution 4.0 International License (https://creativecommons.org/licenses/by/4.0/), which permits unrestricted use, sharing, adaptation, distribution and reproduction in any medium or format, for any purpose, even commercially, as long as you give appropriate credit to the original author(s) and the source, provide a link to the Creative Commons license, and indicate if changes were made.

this rule primarily concerns physical harm, the significance of safeguarding a person's psychological well-being cannot be understated. Currently, there is no established technology allowing robots to interpret the human mind, but research has been ongoing since the early 2000s to understand how robot actions may influence human psychological safety[2].

Traditionally, robots, especially Autonomous Mobile Robots (AMRs), have been utilized in factories and warehouses due to their efficiency in handling repetitive tasks[3]. However, recent years have witnessed the widespread deployment of AMRs in diverse settings, including restaurants[4,5], airports[6,7], and hospitals[3,8]. Surprisingly, despite the presence of humans in these environments, AMRs have often operated without due consideration for human safety. Nevertheless, some researchers[9,10] have concentrated on two generalized levels of safety: (i) physical safety, which involves avoiding collisions with humans; and (ii) psychological safety, which entails adhering to specific human norms, such as maintaining a safe distance from humans[9] and refraining from navigating certain areas near humans[10]. To mitigate the risk of collision with humans and alleviate human discomfort caused by AMRs' operation, proper navigation approaches for the AMRs are required.

In a typical AMR setup, the core components are often referred to as the "3P's", which play a critical role in its functionality[11]: Perception, Prediction, and Path planning. Here, perception represents mapping the AMR's surrounding environment, while prediction involves forecasting the future states of all the agents within that environment. Finally, path planning focuses on determining the safe course of action for the AMR to reach its next state. Scholars have frequently explored the interplay of these three components in the context of AMRs. For instance, Mateus *et al*. proposed a vision-based perception approach employing deep convoluted neural networks[12] for pedestrian detection. Their work featured a convolutional neural network-based aggregate channel features detector for pedestrian detection, alongside using asymmetric Gaussian functions to model human-aware constraints. The path planning was accomplished using the A* algorithm. Similarly, Bruckschen *et al*. delved into prediction, considering how humans navigate based on observations from the AMR and prior knowledge of human interactions with objects[13]. Hansen *et al*. developed an adaptive method for detecting a person's interest in interacting with the robot, relying on case-based reasoning and two-dimensional (2D) laser range measurements[14]. They further incorporated a time-dependent cost map for planning the AMR's path based on human future movement. In other works, such as the research by Ah *et al*.[15], a Probabilistic Road Map (PRM)-based algorithm was employed for the global path planner, while deep reinforcement learning was used for the local planner. The results obtained after evaluation with different environments and pedestrian behaviors exhibited improved AMR navigation with a reduced likelihood of colliding with humans.

In previous studies, it has become evident that the 3P's are intricately interconnected. However, the focus of this work predominantly centers on AMR's path planning, emphasizing the critical aspect of collision-free navigation while assuming the successful attainment of perception and prediction. In the domain of path planning research, diverse conditions and considerations have been employed by different researchers in designing their algorithms, encompassing aspects such as the nature of humans, algorithms, Human-Aware Navigation (HAN) models, and environmental factors. A summary of these variations is presented in Table 1.

The "nature of human" category relates to whether the human's position and heading exhibit changes over time. Meanwhile, the HAN model encompasses various constraints, including considerations such as respecting the human's intimate zone [Proxemics (PR)], avoiding navigation in the human's frontal space [Field of View (FV)], or refraining from traversing the area immediately behind the human [Back Space (BS)].

For instance, in the research conducted by Korkmaz *et al*., emphasis was placed on utilizing the A* algorithm as a primary planner, introducing a dynamic path planning method for HAN[16]. Their comparison between A* and PRM as navigation bases revealed that PRM could function as a quicker planner for HAN in comparison to A*. However, it often resulted in longer travel distances, steering the AMR away from humans. Notably, they

Table 1. Comparison of related works

Ref.	Nature of human	HAN model considered	Algorithm	Advantages	Disadvantages
[16]	Static	PR	PRM	Fast path planning compared to A*	Consideration of only static human and PR
[17]	Dynamic	PR	A*	Natural behavior of AMR, reduced planning time, time-dependent cost map	Consideration of PR only, planning timeout, computational burden
[18]	Dynamic	PR, FV	A*	Natural behavior of AMR, time-dependent cost map	Planning time-out, higher computational burden compared to [17]
[19]	Static	PR, FV, BS	APF	Smooth path compared to A*, no path planning timeout	Local minima and GNRON, consideration of only static human

did not consider that human moves over time and solely relied on PR. Moreover, the paths generated by both A* and PRM were found to be significantly influenced by the number of nodes [16,20]. Attempts to reduce the number of nodes in the A* map to alleviate computational burdens could compromise the path's smoothness. Similarly, Kirby *et al.* implemented a conventional A* path planner enhanced with social conventions, such as passing humans on the right [21]. Additionally, Kollmitz *et al.* designed a time-dependent deterministic planner using A*, which accounted for human motion [17]. However, this method solely relied on PR for navigation. They introduced a planning timeout within the algorithm, allowing it to stop after a fixed time and return the least-cost path to the destination. While this aids in timely algorithm termination, it occasionally yields sub-optimal paths or no path at all. Nonetheless, this algorithm ensures the AMR exhibits natural behaviors, such as avoiding close proximity to humans,

waiting for humans to pass, and adjusting its path in response to humans. Moreover, Briamonte *et al.* explored the application of the time-dependent deterministic A* path planning method for AMRs navigating in confined spaces around groups of humans, incorporating considerations of PR and FV [18]. However, their study observed longer navigation times compared to [17]. In another study by Sampathkumar *et al.*, the authors adopted the Artificial Potential Field (APF) for path planning, integrating human-associated factors through adjustable coefficients [19]. They optimized the path planning model using a genetic algorithm, fine-tuning coefficients such as scaling factors and Potential Field (PF) orders to minimize the AMR's path length while adhering to human-prescribed rules. Despite these improvements, their APF-based approach still encountered challenges related to local minima and difficulties reaching goals due to nearby obstacles, termed as goal non-reachable with obstacle nearby (GNRON) issues [22]. In short, the aforementioned studies include some level of limitations, such as a lack of consideration of sufficient human factors or human movement, planning timeout, or navigation issues (local minima and GNRON).

In light of these considerations, this work employs Enhanced PF (EPF) [23] as the foundational path planning technique. Furthermore, three human factors (PR, BS, and FV) are considered in this study, along with no planning timeout. The integration of EPF with HAN effectively addresses the limitations of APF while adhering to the principles of HAN in the AMR navigation. Additionally, the coefficients of EPF highly govern the behavior of AMRs. Hence, this research incorporates a Fuzzy Inference System (FIS) to dynamically adjust the coefficients within the HAN-EPF framework based on the system knowledge. This adaptive coefficient adjustment equips AMRs to effectively navigate within dynamically changing environments, accommodating the presence of humans with PR, BS, and FV considered human factors. The efficacy of the proposed approach is subsequently evaluated based on the AMR's ability to navigate to its destination while strictly adhering to HAN constraints, ensuring proper human-robot interaction and safety.

Overall, the main contributions of this work are

- To design a diverse human factors-employed HAN framework based on EPF that effectively overcomes local minima and GNRON issues.
- To employ the FISs to adaptively determine coefficients that enable the AMR to safely navigate in a dynam-

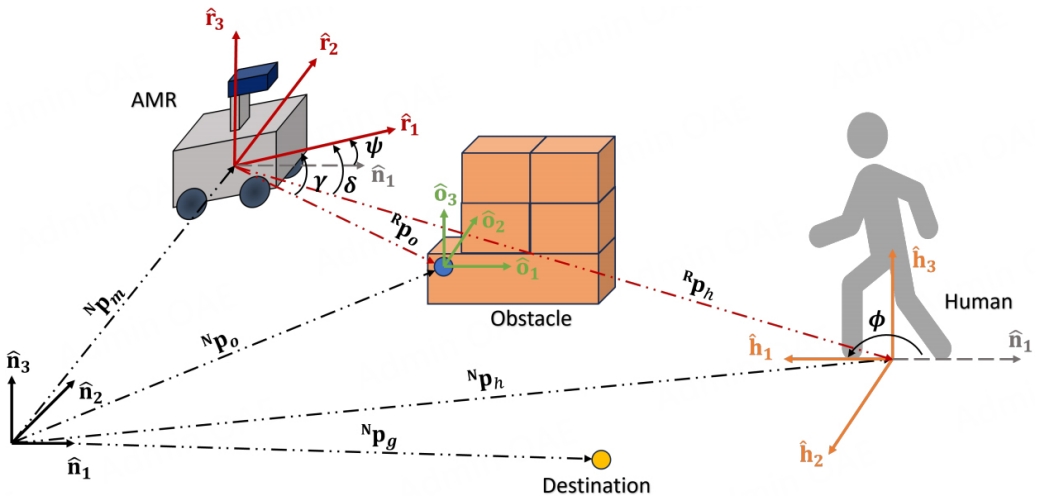


Figure 1. Definition of frames representation of vectors.

ically changing human-rich environment.

The paper is structured as follows: Section 2 lays the groundwork by defining frames and providing a concise overview of the EPF and FISs. Section 3 elaborates on the integration of HAN principles into the EPF framework and outlines the design of the FISs. In Section 4, the authors present and explore simulation results aimed at validating the performance of the proposed approach. Finally, Section 5 offers concluding remarks on this work.

2. PRELIMINARIES

2.1. Definition of frames and states

To describe the motion of the AMR, the reference frames, as shown in Figure 1, are established. The inertial frame is represented by $\hat{\mathbf{n}}_k$ for $k = 1, 2,$ and 3. The AMR's body frame is denoted by $\hat{\mathbf{r}}_k$, with its origin centered on the center of mass of the AMR's body. The AMR's primary movement direction aligns with $\hat{\mathbf{r}}_1$, while $\hat{\mathbf{r}}_3$ coincides with $\hat{\mathbf{n}}_3$. Accordingly, $\hat{\mathbf{r}}_2$ is determined using the right-hand rule. Similarly, the human's body frame is defined through $\hat{\mathbf{h}}_k$, with its origin situated at the center of mass of the human. Similar to the AMR's body frame, the forward direction of the human corresponds to $\hat{\mathbf{h}}_1$, and $\hat{\mathbf{h}}_3$ aligns with $\hat{\mathbf{n}}_3$. It is important to note that, given that the AMR generally lacks translational motion along $\hat{\mathbf{n}}_3$ and rotational motion along $\hat{\mathbf{n}}_1$ and $\hat{\mathbf{n}}_2$, this study adopts a 2D position vector and accounts for a rotational component about $\hat{\mathbf{n}}_3$.

The positions of the AMR, human, obstacle, and the AMR's destination in the inertial frame are denoted as ${}^N\mathbf{p}_m \in \mathbb{R}^2$, ${}^N\mathbf{p}_h \in \mathbb{R}^2$, ${}^N\mathbf{p}_o \in \mathbb{R}^2$, and ${}^N\mathbf{p}_g \in \mathbb{R}^2$, respectively. Here, the superscripts N, R, and H denote that the vector is represented in the inertial, AMR's body, and human's body frames, respectively. Note that the position vectors for the human and obstacle expressed in the AMR frame are described as

$$ {}^R\mathbf{p}_h = C_{RN}\, {}^N\mathbf{p}_h, \tag{1} $$

$$ {}^R\mathbf{p}_o = C_{RN}\, {}^N\mathbf{p}_o, \tag{2} $$

where C_{RN} represents the rotation matrix that maps from the inertial frame to the body frame, defined as

$$ C_{RN} = \begin{bmatrix} \cos\psi & \sin\psi \\ -\sin\psi & \cos\psi \end{bmatrix}. \tag{3} $$

Here, ψ represents the heading angle of the AMR, while the orientation of the human is denoted as ϕ. Also,

the relative angle between the AMR and the human in the AMR frame is expressed as δ, and the relative angle between the AMR and the obstacle within the AMR frame is defined as γ, as shown in Figure 1.

2.2. Enhanced potential field

The APF serves as a widely adopted method for robot collision avoidance owing to its mathematical efficiency and its capability to generate smooth obstacle-avoiding trajectories. This approach comprises two primary components: attraction and repulsion. An AMR is steered toward its destination by an attractive PF while being simultaneously pushed away from environmental obstacles through repulsive PFs. Consequently, a net PF emerges, which is the sum of both attractive and repulsive PFs, influencing the AMR's motion. The total potential function, denoted as Q_t governing the PFs, is defined as [23]

$$Q_t({}^N\mathbf{p}_m) = Q_a({}^N\mathbf{p}_m) + Q_r({}^N\mathbf{p}_M), \tag{4}$$

where

$$Q_a({}^N\mathbf{p}_m) = \frac{1}{2}k_a d({}^N\mathbf{p}_m, {}^N\mathbf{p}_g)^2, \tag{5}$$

$$Q_r({}^N\mathbf{p}_M) = \begin{cases} \frac{1}{2}k_r \left(\frac{1}{d({}^N\mathbf{p}_m, {}^N\mathbf{p}_o)} - \frac{1}{d_o}\right)^2 d({}^N\mathbf{p}_m, {}^N\mathbf{p}_g)^{n_g}, & \text{if } d({}^N\mathbf{p}_m, {}^N\mathbf{p}_o) \le d_o, \\ 0, & \text{if } d({}^N\mathbf{p}_m, {}^N\mathbf{p}_o) > d_o. \end{cases} \tag{6}$$

Here, $Q_a({}^N\mathbf{p}_m)$ is the attractive potential function, $Q_r({}^N\mathbf{p}_m)$ is the repulsive potential function, k_a and k_r are the attractive and repulsive coefficients, respectively, n_g is the potential order, $d(\mathbf{a}, \mathbf{b})$ is the distance between two generic position vectors $\mathbf{a}$ and $\mathbf{b}$, and d_o is the distance of influence. An essential improvement to note in the presented equation is the inclusion of an additional term $d({}^N\mathbf{p}_m, {}^N\mathbf{p}_g)^{n_g}$, which effectively addresses a well-known issue of the conventional APF known as GNRON [23]. Also, by taking the negative gradient of the respective terms, the total PF is derived as [23]

$$\mathbf{f}_t({}^N\mathbf{p}_m) = \mathbf{f}_a({}^N\mathbf{p}_m) + \mathbf{f}_r({}^N\mathbf{p}_m). \tag{7}$$

Note that the attractive and repulsive PFs are found by

$$\mathbf{f}_a({}^N\mathbf{p}_m) = -\nabla Q_a({}^N\mathbf{p}_m) = k_a d({}^N\mathbf{p}_m, {}^N\mathbf{p}_g) \frac{\partial d({}^N\mathbf{p}_m, {}^N\mathbf{p}_g)}{\partial\, {}^N\mathbf{p_m}}, \tag{8}$$

$$\mathbf{f}_r({}^N\mathbf{p}_m) = -\nabla Q_r({}^N\mathbf{p}_m) = \begin{cases} \mathbf{f}_{r_o}({}^N\mathbf{p}_m) + \mathbf{f}_{r_g}({}^N\mathbf{p}_m), & \text{if } d({}^N\mathbf{p}_m, {}^N\mathbf{p}_o) \le d_o, \\ 0, & \text{if } d({}^N\mathbf{p}_r, {}^N\mathbf{p}_o) > d_o, \end{cases} \tag{9}$$

where

$$\mathbf{f}_{r_o}({}^N\mathbf{p}_m) = -k_r \frac{d({}^N\mathbf{p}_m, {}^N\mathbf{p}_g)^{n_g}}{d({}^N\mathbf{p}_m, {}^N\mathbf{p}_o)^2} \left(\frac{1}{d({}^N\mathbf{p}_m, {}^N\mathbf{p}_o)} - \frac{1}{d_o}\right) \frac{\partial d({}^N\mathbf{p}_m, {}^N\mathbf{p}_o)}{\partial\, {}^N\mathbf{p_m}}, \tag{10}$$

$$\mathbf{f}_{r_g}({}^N\mathbf{p}_m) = -\frac{1}{2} n_g k_r d({}^N\mathbf{p}_m, {}^N\mathbf{p}_o)^{n_g - 1} \left(\frac{1}{d({}^N\mathbf{p}_m, {}^N\mathbf{p}_o)} - \frac{1}{d_o}\right)^2 \frac{\partial d({}^N\mathbf{p}_m, {}^N\mathbf{p}_g)}{\partial\, {}^N\mathbf{p_m}}. \tag{11}$$

Note that $\partial d({}^N\mathbf{p}_m, {}^N\mathbf{p}_g)/\partial\, {}^N\mathbf{p_m}$ is the direction from the AMR to the destination position, and $\partial d({}^N\mathbf{p}_m, {}^N\mathbf{p}_o)/\partial\, {}^N\mathbf{p_m}$ is the direction from the AMR to the obstacle. Nonetheless, a persistent challenge with the APF approach is

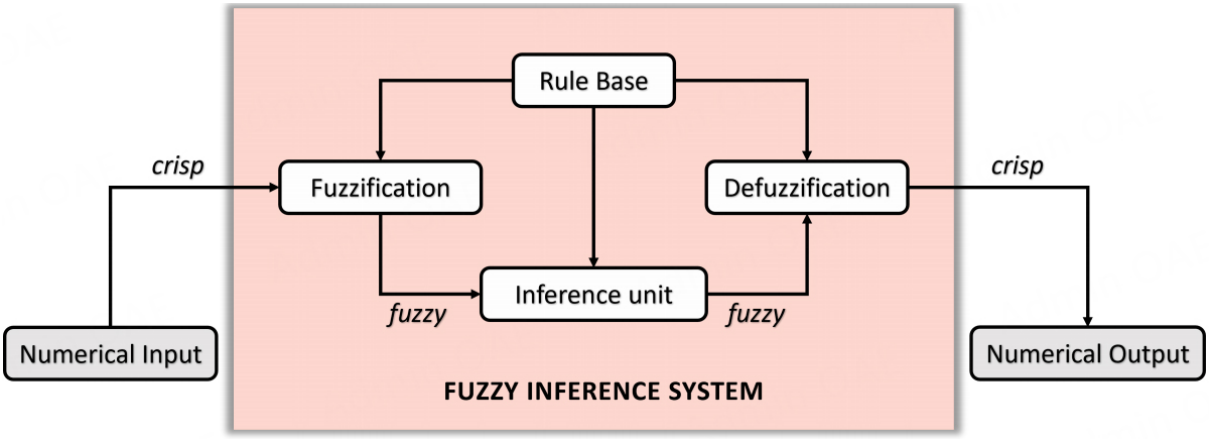


Figure 2. Schematic diagram of FIS.

the occurrence of local minima, particularly when one or more obstacles obstruct the AMR's path symmetrically. This issue stems from the criteria used to determine the direction of the repulsive PF. To mitigate this challenge, the following modification is introduced, replacing $\mathbf{f}_{r_o}({}^N\mathbf{p}_r)$ with a new term, as outlined in [23]:

$$\mathbf{f}_{r_e}({}^N\mathbf{p}_m) = -k_r \frac{d({}^N\mathbf{p}_m, {}^N\mathbf{p}_g)^{n_g}}{d({}^N\mathbf{p}_m, {}^N\mathbf{p}_o)^2} \left(\frac{1}{d({}^N\mathbf{p}_m, {}^N\mathbf{p}_o)} - \frac{1}{d_o} \right) \hat{\mathbf{q}}, \tag{12}$$

where $\hat{\mathbf{q}} \in \mathbb{R}^2$ is a newly defined repulsive PF direction vector given by

$$\hat{\mathbf{q}} = \frac{\mathbf{q}}{||\mathbf{q}||}, \tag{13}$$

where

$$\mathbf{q} = R_e({}^N\mathbf{p}_o - {}^N\mathbf{p}_m). \tag{14}$$

Note that $R_e \in \mathbb{R}^{2x2}$ is the rotation matrix given by

$$R_e = \begin{cases} R, & \text{if } \gamma < 0 \\ R^{\mathrm{T}}, & \text{if } \gamma \geq 0 \end{cases}, \tag{15}$$

where

$$R = \begin{bmatrix} \cos\theta & -\sin\theta \\ \sin\theta & \cos\theta \end{bmatrix}. \tag{16}$$

Here, θ represents a rotation angle responsible for altering the direction of the repulsive PF.

2.3. Fuzzy inference system

A FIS is an approach that employs a rule base and fuzzy set theory [24] to map inputs to outputs, as shown in Figure 2. When numerical data is input into the FIS, it undergoes a transformation into fuzzy inputs through fuzzification. This process involves assigning a degree of membership to each Membership Function (MF) corresponding to the numeric value. An MF precisely defines the degree to which an input value belongs to a fuzzy set. It maps input values from a precise domain onto a scale of the degree of membership, mostly ranging between 0 and 1. This scale indicates how strongly an element is associated with the set, allowing for a smooth transition between membership and non-membership states. Subsequently, the inference unit derives outputs based on user-defined rules, typically expressed in linguistic form; for example, "*If* Input 1 is Category 1 *AND* Input 2 is Category 2, *then* Output is Category 3". These outputs are associated with varying degrees

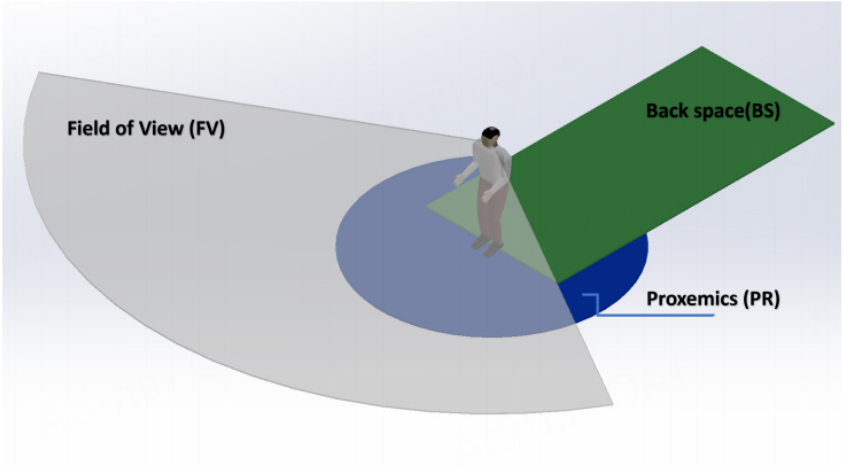


Figure 3. Representation of HAN factors with respect to a human.

of membership within output MFs. Finally, a process called defuzzification is employed to convert these fuzzy outputs back into numerical outputs. In this study, Mamdani-type FISs[24] are used and are referred to as FIS. One of the key advantages of FIS-based systems is their capacity to provide explainability, which can be attributed to the linguistically defined rules and MFs[25].

3. METHODOLOGY

3.1. Human aware navigation

HAN represents the convergence of robot motion planning and human-robot interactions[9]. While the primary aim of robot motion planning is to guide the robot to its destination, HAN prioritizes AMR's ability to minimize stress and prevent harm to humans. Therefore, it can be defined as "navigation of the AMRs based on human-centered PFs, aiming to minimize discomfort and prevent harm"[19].

Human discomfort stemming from AMRs can arise from various sources, including the robot's appearance, unnatural movement, production of discomforting noise, close proximity to humans, and failure to adhere to cultural norms[9]. Kruse *et al.* classified discomfort in HAN into three main categories: human comfort, AMR naturalness, and AMR sociability[9]. Human comfort revolves around ensuring maximum comfort and safety for humans in the presence of AMRs. Examples include AMRs maintaining a specified distance from humans at all times and refraining from traversing specific spaces near humans. AMR naturalness entails the robot's movement resembling that of humans, such as following smooth trajectories and having a friendly appearance, thereby enhancing acceptance. AMR sociability implies that the robot should adhere to cultural norms, such as traveling on a specific side (left/right) of humans depending on the country and overtaking humans along a certain direction. Among these categories, this work primarily focuses on human comfort concerning AMR navigation, as the robot's appearance and noise levels are not significantly related to its navigation. Safety takes precedence in this context.

This study introduces three important terms in HAN: PR, FV, and BS, as shown in Figure 3. PR signifies that the AMR must not only maintain a predetermined relative distance from humans at all times but also avoid collisions with them. BS denotes the region behind the human, where the presence of the AMR may cause discomfort to humans when traversing. FV represents the region in front of the human where the AMR could potentially obstruct the human's path. Consequently, a successful HAN planner must ensure that the AMR avoids these defined regions.

3.2. Proposed approach: HAN-EPF

3.2.1 Definitions of HAN factors

The primary focus of this study centers on the integration of factors associated with humans into the navigation of the AMR. To streamline collision-free path planning, it is assumed that the relative positions of humans with respect to the AMR are known, as this information can be obtained through optical or infrared sensors equipped with perception algorithms. Similarly, the relative position information of obstacles is obtained through lidar sensors. Note that obstacles are represented as a collection of points resembling cloud points. Data from the sensor, in the form of cloud points, is utilized to outline the boundaries of obstacles within the sensor's range. To account for HAN factors related to humans, this work introduces virtual cloud points surrounding a human. These virtual points are positioned along the perimeters of the HAN factors. To illustrate the formation of these virtual cloud points, Figure 4 depicts a parametric representation of the HAN factors in relation to a human, as introduced in the previous section.

The threshold distance for PR can vary considerably, depending on factors such as human age, the type of social interaction, and cultural norms[26]. However, in this work, PR is treated as a constant α_{PR} around the human center, in alignment with relevant studies[9,12,13]. Furthermore, the dimensions of the BS are defined using α_{BS_1} and α_{BS_2}, determined based on survey results[13]. Similarly, the angle and distance parameters for FV (α_{FV_1} and α_{FV_2}) are chosen considering the characteristics of human vision. Beyond a certain limit, known as the monocular vision area, human vision reduces to approximately one-fifth of normal human vision, leading to limited 3D perception and difficulty in viewing[27]. It is important to note that the generation of virtual cloud points for each HAN factor depends on the position and orientation of the human. Consequently, when the AMR detects a human within its sensing range, it generates virtual cloud points around the humans, taking into account the relevant HAN factors. These virtual cloud points for each HAN factor, as illustrated in Figure 4, are compactly formulated as

$$\begin{bmatrix} f_x \\ f_y \end{bmatrix} = D_j \, \Omega_j, \tag{17}$$

where f_x and f_y are the x and y coordinates of the virtual cloud point, respectively, D_j encompasses the geometric formulations involving varying δ angle, and Ω_j contains the dimensional information for each HAN factor, denoted as j and covering PR, BS, and FV. Here, Ω_j for each j is defined as $\Omega_{PR} = \alpha_{PR}$, $\Omega_{BS} = \begin{bmatrix} \alpha_{BS_1} & 0.5\alpha_{BS_2} \end{bmatrix}^{\mathrm{T}}$, and $\Omega_{FV} = \alpha_{FV2}$, and D_j is defined as

$$D_{PR} = \begin{bmatrix} \cos\delta \\ \sin\delta \end{bmatrix} \text{ for } 0 \le \delta < 2\pi, \tag{18}$$

$$D_{BS} = \begin{cases} \begin{bmatrix} 0 & 0 \\ 0 & 0 \end{bmatrix}, & \text{if } \delta < \frac{\pi}{2} \text{ or } \delta > \frac{3\pi}{2}, \\ \begin{bmatrix} -\tan(\delta - \pi/2) & 1 \\ 0 & 0 \end{bmatrix}, & \text{if } \delta \ge \frac{\pi}{2} \text{ or } \delta < \frac{\pi}{2} + \tan^{-1}\left(\frac{\alpha_{BS_1}}{0.5\alpha_{BS_2}}\right), \\ \begin{bmatrix} \tan(\delta - \pi/2) & -1 \\ 0 & 0 \end{bmatrix}, & \text{if } \delta > \frac{3\pi}{2} - \tan^{-1}\left(\frac{\alpha_{BS_1}}{0.5\alpha_{BS_2}}\right) \text{ or } \delta \le \frac{3\pi}{2}, \\ \begin{bmatrix} 0 & 0 \\ -1 & 1/\tan(\delta - \pi/2) \end{bmatrix}, & \text{if } \delta \ge \frac{\pi}{2} + \tan^{-1}\left(\frac{\alpha_{BS_1}}{0.5\alpha_{BS_2}}\right) \text{ or } \delta \le \frac{3\pi}{2} - \tan^{-1}\left(\frac{\alpha_{BS_1}}{0.5\alpha_{BS_2}}\right), \end{cases} \tag{19}$$

$$D_{FV} = \begin{cases} \begin{bmatrix} \cos\delta & \sin\delta \\ 0 & 0 \end{bmatrix}, & \text{if } \delta \leq \frac{\alpha_{FV_1}}{2} \text{ or } \delta \geq 2\pi - \frac{\alpha_{FV_1}}{2}, \\ \begin{bmatrix} 0 & 0 \\ 0 & 0 \end{bmatrix}, & \text{if } \frac{\alpha_{FV_1}}{2} < \delta < 2\pi - \frac{\alpha_{FV_1}}{2}. \end{cases} \tag{20}$$

To generate a specific virtual cloud point within the FV region, denoted as (f_x, f_y), the parameters Ω_{FV} and D_{FV} are used. Likewise, virtual cloud points for PR and BS are obtained based on the relative angle between the human and the AMR in the AMR frame.

3.2.2 Formulation of HAN-EPF

To account for human comfort in the AMR's navigation, an additional repulsive PF term is incorporated into the total PF. Consequently, the total PF of the HAN-EPF is expressed as

$$\mathbf{f}_t({}^N\mathbf{p}_m) = \mathbf{f}_a({}^N\mathbf{p}_r) + \mathbf{f}_r({}^N\mathbf{p}_m) + \mathbf{f}_h({}^N\mathbf{p}_m), \tag{21}$$

where $\mathbf{f}_h({}^N\mathbf{p}_m)$ is the repulsive PF associated with humans, serving as an additional component. The definition of $\mathbf{f}_h({}^N\mathbf{p}_m)$ is as follows:

$$\mathbf{f}_h({}^N\mathbf{p}_m) = \mathbf{f}_{h_g}({}^N\mathbf{p}_m) + \mathbf{f}_{h_e}({}^N\mathbf{p}_m), \tag{22}$$

where

$$\mathbf{f}_{h_g}({}^N\mathbf{p}_m) = -\frac{1}{2} n_g k_h d({}^N\mathbf{p}_m, {}^N\mathbf{p}_f)^{n_g - 1} \left(\frac{1}{d({}^N\mathbf{p}_m, {}^N\mathbf{p}_f)} - \frac{1}{d_o} \right)^2 \frac{\partial d({}^N\mathbf{p}_m, {}^N\mathbf{p}_g)}{\partial\, {}^N\mathbf{p_m}}, \tag{23}$$

$$\mathbf{f}_{h_e}({}^N\mathbf{p}_m) = -k_h \frac{d({}^N\mathbf{p}_m, {}^N\mathbf{p}_g)^{n_g}}{d({}^N\mathbf{p}_m, {}^N\mathbf{p}_f)^2} \left(\frac{1}{d({}^N\mathbf{p}_m, {}^N\mathbf{p}_f)} - \frac{1}{d_o} \right) \hat{\mathbf{q}}. \tag{24}$$

It is important to note that, at any given time step, only the closest virtual cloud point related to human factors and the closest obstacle point are considered. For instance, in Figure 5, all the HAN factors are detected in the left figure. However, the AMR is closer to FV than PR and BS. Hence, only FV is considered when generating $\mathbf{f}_h({}^N\mathbf{p}_m)$. Similarly, the obstacle point that is closer to AMR is used to compute $\mathbf{f}_r$. In the right figure, only BS is considered among the HAN factors.

The HAN-EPF contains several unknown parameters, but the dominant factors influencing the AMR's collision avoidance behavior are the coefficients k_a, k_r, and k_h. As determining proper suitable scaling factors typically involves trial and error and is a time-consuming process, this study introduced new variables, specifically the scaling factors μ_r and μ_h, to reduce the number of parameters and analyze the AMR's behavior concerning changes in those parameters. These variables replace k_r and k_h and are defined as follows:

$$k_r = \frac{k_a}{\mu_r}, \tag{25}$$

$$k_h = \frac{k_a}{\mu_h}. \tag{26}$$

Note that k_r and k_h are only dependent on the scaling factors once k_a is fixed. In this work, the scaling factors μ_r and μ_h, along with the coefficient k_a, are determined through the FISs proposed.

3.3. Preliminary study for understanding HAN-EPF

Before designing the FISs for the scaling factors, it is crucial to gain insights into how these scaling factors influence the AMR's behavior. This foundational understanding is essential for creating the MFs and rules for

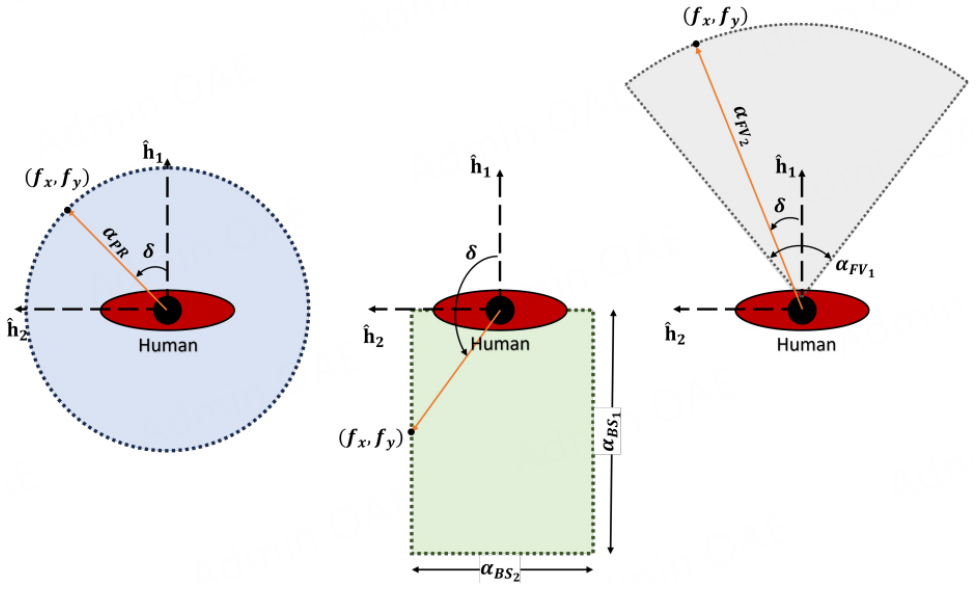


Figure 4. Virtual cloud points for each HAN factor (left - PR, middle - BS, right - FV).

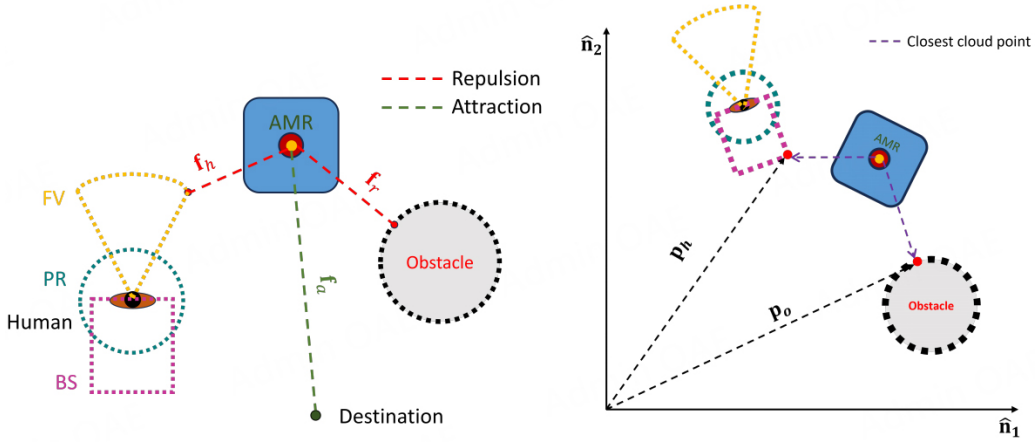


Figure 5. Illustrations for selecting HAN factors.

the proposed FISs. To achieve this, preliminary simulation studies were conducted to investigate the AMR's behavior in terms of its path length and relative distance from obstacles during avoidance maneuvers, with a focus on changes in the scaling factors. These preliminary results serve as the basis for designing the proposed FIS and help to establish reasonable ranges for the scaling factors. The simulation parameters introduced in Section 4 were utilized for these preliminary studies. Note that the coefficient k_a in the attractive PF was set to 1 to specifically observe how the AMR's behavior changes with varying μ_r values. The following observations were made from these preliminary studies. When the value of μ_r decreases beyond a certain value, the AMR's position starts to oscillate, as illustrated in Figure 6 (left). This oscillation occurs because the AMR traverses the boundary of the obstacle's distance of influence (d_o). On the other hand, increasing μ_r beyond a certain value causes the AMR to collide with the obstacle, as shown in Figure 6 (right). A threshold distance of 0.5 m was assumed to indicate a physical collision.

Due to the dominant attractive PF compared to the repulsive PF, the AMR is not effectively repelled from the obstacle. Consequently, when μ_r is high, the AMR travels closer to the obstacle, while a low μ_r results in a

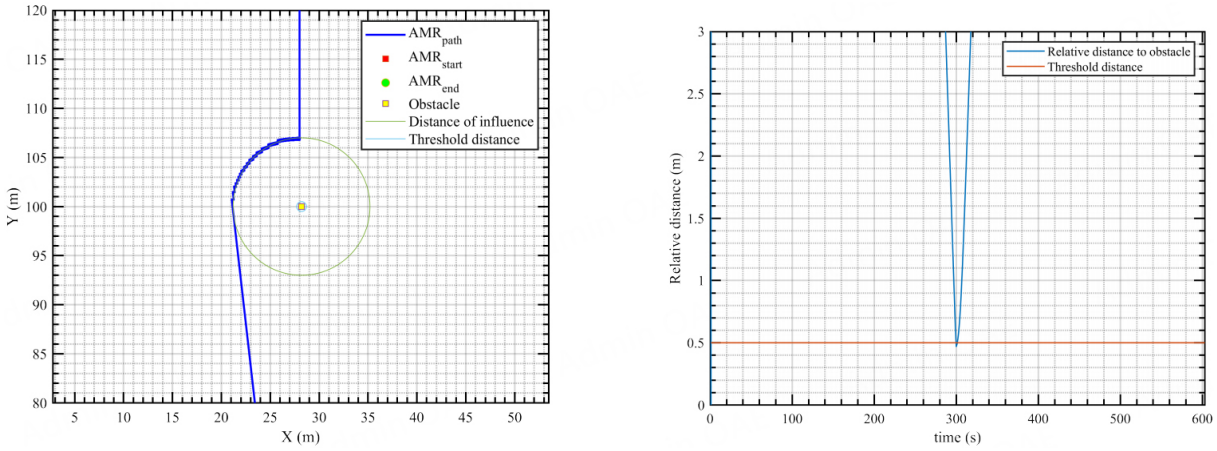


Figure 6. AMR's trajectory with very small μ_r (left) and relative distance between the AMR and the obstacle with very high μ_r (right).

longer path for the AMR, as shown in Figure 7.

It is noteworthy that the appropriate range for μ_r was found to be between 0.01 and 55, where neither collisions nor oscillations occurred. These preliminary simulations maintained k_a at 1 and the fixed distance of influence (d_o) at 25 m, reflecting typical lidar sensor sensing ranges. In addition, these analysis results can be applied to the scaling factor μ_h for humans, employing the same scaling factor range.

3.4. FIS design

This study employs three FISs to determine the coefficient k_a and scaling factors μ_r and μ_h. The first step in designing these FISs involves defining the appropriate inputs and outputs for each FIS. The structure of the FISs considered in this work is illustrated in Figure 8. For FIS 1, which determines the coefficient k_a (the output of the FIS 1), two inputs are selected: the relative distance between the AMR and the destination position and the relative distance between the AMR and either the obstacle or the human (whichever is closer). This choice is made because the magnitude of the attractive PF is closely tied to the AMR's motion toward the goal position. FIS 2 is responsible for determining the scaling factor μ_r, which governs the repulsive PF for obstacle avoidance. The inputs selected for FIS 2 include the relative distance of the AMR from the obstacle and the relative angle between the AMR's heading and the direction to the obstacle. These inputs are chosen to appropriately determine μ_r in relation to obstacle avoidance. FIS 3 derives the scaling factor μ_h, which is associated with interactions involving humans. The inputs for FIS 3 consist of the relative distance between the AMR and the human and the relative velocity of the AMR in relation to the human. These inputs are used to determine μ_h, which, in turn, influences the repulsive PF concerning human interactions.

For each input and output of the FISs, three MFs are considered, which are Low, Medium, and High. In particular, this work considers two sets of the MFs, as shown in Figure 9. The first set of the MFs in Figure 9 (left) is used for the inputs of all three FISs. These MFs normalize input numeric values within the range of 0 to 1. This normalization allows the FISs to be applicable across different environments and AMR velocities, provided that the maximum values are known. For FIS 1, the output uses the first set of MFs. On the other hand, the outputs of FIS 2 and FIS 3 use the second set of MFs defined in Figure 9 (right). The range of these output MFs, ranging from 0.01 to 55, is determined based on the preliminary studies described in the previous section.

The next step in designing the FISs is to build the rules that define the relationship between the inputs and outputs for each FIS, aiming to achieve the desired behavior of the AMR. As stated previously, FIS 1 determines the magnitude of the attractive PF. For example, if the AMR is in close proximity to obstacles or humans while

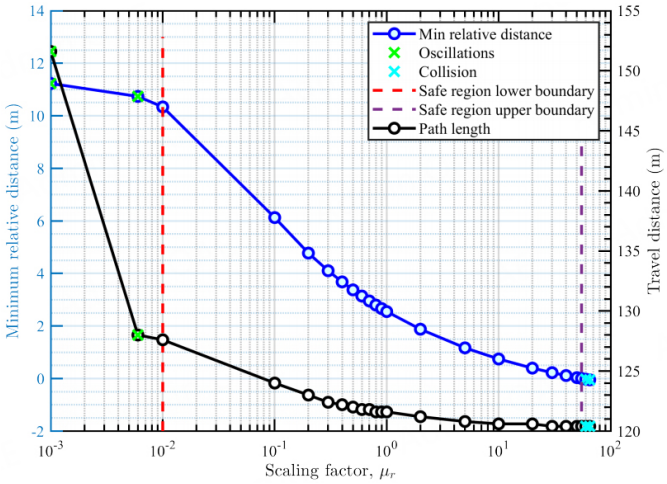


Figure 7. Minimum relative distance and the travel distance with respect to the scaling factor.

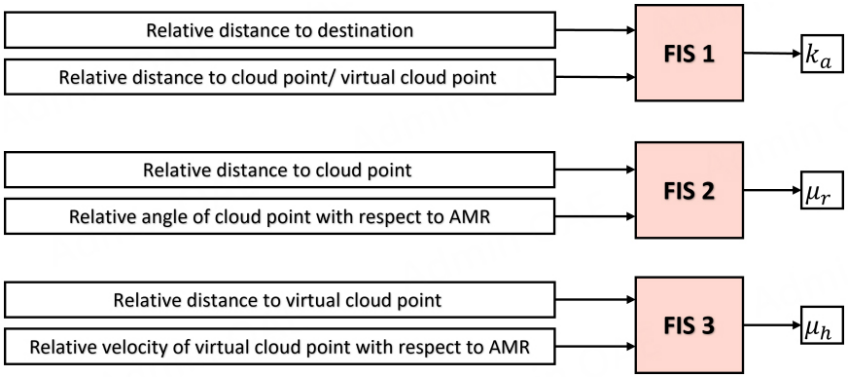


Figure 8. Structure of each FIS.

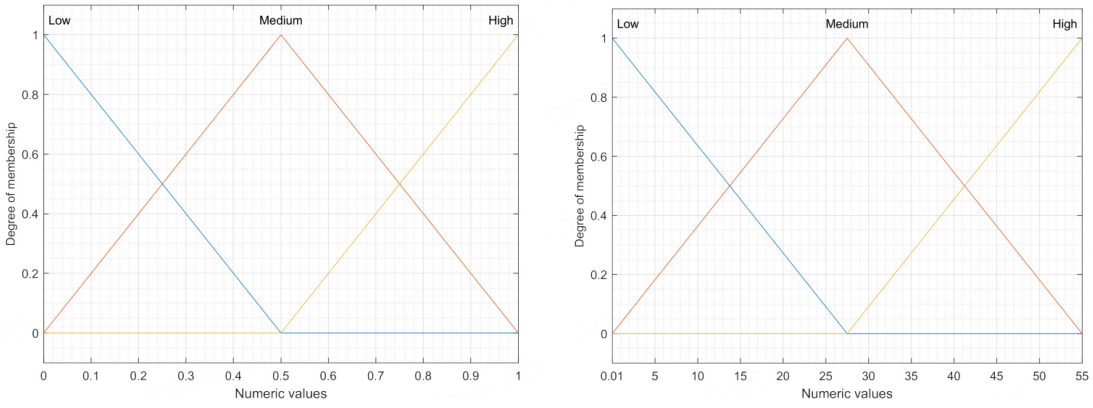


Figure 9. Two sets of the MFs considered.

being far from the goal position, it is desirable for the AMR to generate a smaller attractive PF than the repulsive one to avoid collisions, even if the relative distance to the goal is large. Conversely, if the AMR is far from both the destination and obstacles, it should generate a large attractive PF, which corresponds to a large value of k_a. Based on knowledge of the desired behavior of the AMR, the rules for FIS 1 are defined as shown in Table 2.

The next step in designing the FISs is to establish the rules for FIS 2, which determines μ_r and, consequently, k_r for the obstacle-associated repulsive PF. In contrast to FIS 1, FIS 2 takes into account the relative angle between the AMR and the obstacle. When the AMR is in close proximity to the obstacle and the relative angle is small, the AMR should generate a strong repulsive PF because a small relative angle indicates that the AMR is approaching the obstacle head-on. Consequently, μ_r should be set to "Low", resulting in a high value of k_r. The rules for FIS 2 are defined in Table 3 based on the desired avoidance maneuvers of the AMR.

Similar to FIS 2, FIS 3's rule matrix is designed to govern the desired avoidance maneuver of the AMR with respect to humans. For instance, when the AMR is in close proximity to a human and the relative velocity is high, a significant repulsive PF is needed. In such a case, where the human is approaching the AMR's direction, the AMR should have the capability to maneuver without violating HAN rules. This significant repulsive PF can be generated by setting μ_h to a small value. The rule matrix for FIS 3 is defined based on the AMR's motion concerning the input values, as shown in Table 4.

The entire process is summarized in the flowchart, as shown in Figure 10. Initially, once the parameters are defined, the human positional information is utilized to generate the virtual cloud points. Concurrently, the parameters used in the calculations concerning the AMR frame are inputted into the FIS to derive the outputs: k_a, μ_r, and μ_h. These resulting outputs, along with the virtual cloud points, are then fed into the EPF framework to calculate the total PF exerted on the AMR.

4. SIMULATION STUDIES

To validate the effectiveness and the performance of the proposed approach, simulation studies are performed, considering different environments using the parameters listed in Table 5.

To make the simulation realistic, the maximum human velocity is limited to 1.2 m/s, which is the preferred walking speed of humans [28]. In addition, in all scenarios, a threshold distance of 0.5 m is maintained between the AMR and obstacles or virtual cloud points. Crossing this threshold is considered a collision. This work considers three scenarios in the simulation studies. In Scenario 1, the AMR encounters three well-known issues sequentially: local minima, GNRON, and a moving human at distinct time steps. Scenario 2 takes into consideration a complex environment where the AMR encounters both obstacles and humans. Scenario 3 mimics a crowded real-life environment, such as an airport, where the AMR needs to navigate amidst many humans and obstacles, similar to a real-world infrastructure.

4.1. Scenario 1

In this scenario, the AMR maneuvers in an environment designed to introduce challenges such as local minima, GNRON, and the presence of a moving human. The environment includes a circular obstacle placed to block the AMR's head-on, causing a local minima issue, and a rectangular obstacle positioned near the destination position to create a GNRON issue. The parameters for the position information of the AMR and human are listed in Table 6.

Figure 11 (left) shows the AMR's trajectory in Scenario 1, demonstrating that the AMR adaptively avoids both the obstacle and the human during its travel. Also, Figure 11 (right) provides a visual representation of the scenario, highlighting that the AMR successfully maintains a relative distance greater than the collision threshold value of 0.5 m from both obstacles and the human. The closest relative distance between the AMR and the obstacle (purple dot) is 1.6 m, while the closest distance to the virtual cloud points (red dot) is 1.07 m. Furthermore, Figure 12 shows a close-up view of the AMR's interaction with the human. At 41 s, the AMR starts a maneuver when it encounters the human. Notably, the closest virtual cloud point corresponds to the FV, and based on the relative angle δ, the AMR navigates towards the back of the human. At 42 s and 44 s,

Table 2. Rule matrix for FIS 1

k_a		Relative distance to the goal		
		LOW	MEDIUM	HIGH
Relative distance to the obstacle	LOW	Medium	Medium	Low
	MEDIUM	Medium	Medium	High
	HIGH	High	High	High

Table 3. Rule matrix for FIS 2

μ_r		Relative distance to the obstacle		
		LOW	MEDIUM	HIGH
Relative angle to obstacle	LOW	Low	Low	Low
	MEDIUM	Low	Medium	Medium
	HIGH	High	High	High

Table 4. Rule matrix for FIS 3

μ_h		Relative distance to the virtual cloud point		
		LOW	MEDIUM	HIGH
Relative velocity to human	LOW	Low	Low	Low
	MEDIUM	Low	Medium	Medium
	HIGH	High	High	High

after navigating away from FV, the AMR successfully avoids PR and BS, respectively. Hence, throughout the simulation, the AMR reaches the destination position while avoiding the human and navigating safely without violating any HAN rules.

4.2. Scenario 2

Scenario 2 presents a more complex environment compared to Scenario 1, involving obstacles and moving humans. This environment consists of two humans, one in motion and the other rotating to change gaze, along with three obstacles. The parameters related to the positions of the AMR and human are given in Table 7.

Figure 13 displays the trajectory traveled by the AMR in Scenario 2. Despite facing two humans simultaneously near a static obstacle, the AMR adeptly navigates through this complex situation. Following this maneuver, the AMR safely reaches its destination while avoiding two static obstacles. Figure 13 (right) provides a visual representation of the relative distance between the AMR, obstacles, and humans. It can be observed that the closest relative distance between the AMR and the obstacles and the virtual cloud points are 1.15 and 1.06 m, respectively, both exceeding the collision threshold distance. Consequently, no collision occurs during the maneuver.

Figure 14 (top left) depicts the initial encounter between the AMR and human-1, who starts to rotate the AMR approaches. The AMR spends a significant portion of time navigating close to the FV of human-1, primarily because of the continuous rotation of their gaze. In response, the AMR adjusts its path, avoiding human-1 and subsequently encountering a rectangular obstacle near 58 s, as shown in Figure 14 (top right). When encountering the rectangular static obstacle, the robot prioritizes avoiding collision with it. Depending on the relative angle, the robot adjusts its navigation towards the right to circumvent the obstacle. Around 60 s, as shown in Figure 14 (bottom left), the AMR approaches a moving human and successfully navigates to the right side of the human, even though the human is moving toward the AMR. Note that the closest relative distance between the AMR and human-2 is highlighted by a red dot in Figure 13 (right), which occurs near the FV of human-2. Finally, at 70 s, as shown in Figure 14 (bottom right), the AMR bypasses human-2 and proceeds toward its destination, encountering both the rectangular obstacle and the circular obstacle along the way.

Table 5. Simulation parameters for the proposed HAN-EPF approach

Description	Value (unit)
Time interval, Δt	0.1 (s)
Order of potential, n_g	2
Distance of influence, d_o	25 (m)
Collision threshold distance	0.5 (m)
Repulsive field rotational angle, θ	45 (deg)
Sensing range	25 (m)
Maximum AMR velocity	1 (m/s)
Maximum human velocity	1.2 (m/s)
Proxemics range, α_{PR}	4 (m)
Back space range, α_{BS_1}	5 (m)
Back space width, α_{BS_2}	2.4 (m)
Field of view angle, α_{FV_1}	120 (deg)
Field of view range, α_{FV_2}	6 (m)

Table 6. Simulation parameters - Scenario 1

Description	Value (unit)
AMR start position	$\begin{bmatrix}90 & 160\end{bmatrix}^T$ (m)
AMR destination position	$\begin{bmatrix}90 & 40\end{bmatrix}^T$ (m)
Human start position	$\begin{bmatrix}47 & 34\end{bmatrix}^T$ (m)

Table 7. Simulation parameters - Scenario 2

Description	Value (unit)
AMR start position	$\begin{bmatrix}10 & 110\end{bmatrix}^T$ (m)
AMR destination position	$\begin{bmatrix}110 & 10\end{bmatrix}^T$ (m)
Human-1 start position	$\begin{bmatrix}38 & 79\end{bmatrix}^T$ (m)
Human-2 start position	$\begin{bmatrix}100 & 57\end{bmatrix}^T$ (m)

Table 8. Simulation parameters - Scenario 3

Description	Value (unit)
AMR start position	$\begin{bmatrix}20 & 10\end{bmatrix}^T$ (m)
AMR destination position	$\begin{bmatrix}5 & 65\end{bmatrix}^T$ (m)
Human-1 start position	$\begin{bmatrix}55 & 40\end{bmatrix}^T$ (m)
Human-2 start position	$\begin{bmatrix}60 & 70\end{bmatrix}^T$ (m)
Human-3 start position	$\begin{bmatrix}30 & 58\end{bmatrix}^T$ (m)
Human-4 start position	$\begin{bmatrix}12.5 & 5\end{bmatrix}^T$ (m)
Human-5 start position	$\begin{bmatrix}10 & 50\end{bmatrix}^T$ (m)
Human-6 start position	$\begin{bmatrix}62.5 & 15\end{bmatrix}^T$ (m)

Table 9. Closest relative distance from the AMR to humans and obstacles for each scenario

Scenario	Closest distance to human (m)	Closest distance to obstacles (m)
Scenario 1	1.07	1.6
Scenario 2	1.06	1.15
Scenario 3	0.55	0.89

4.3. Scenario 3

Scenario 3 considers a more realistic environment, resembling an airport setting with various humans and infrastructure-like obstacles. Circular obstacle-1 and circular obstacle-2 can be envisioned as pillars in an

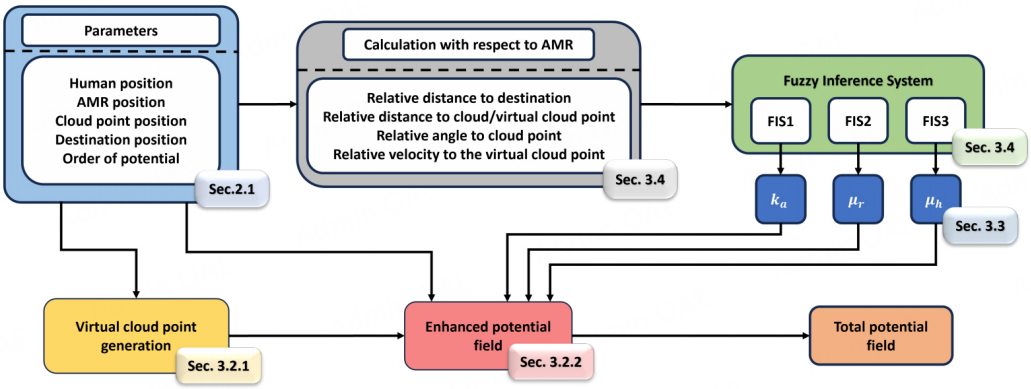


Figure 10. Overall procedure of the proposed approach.

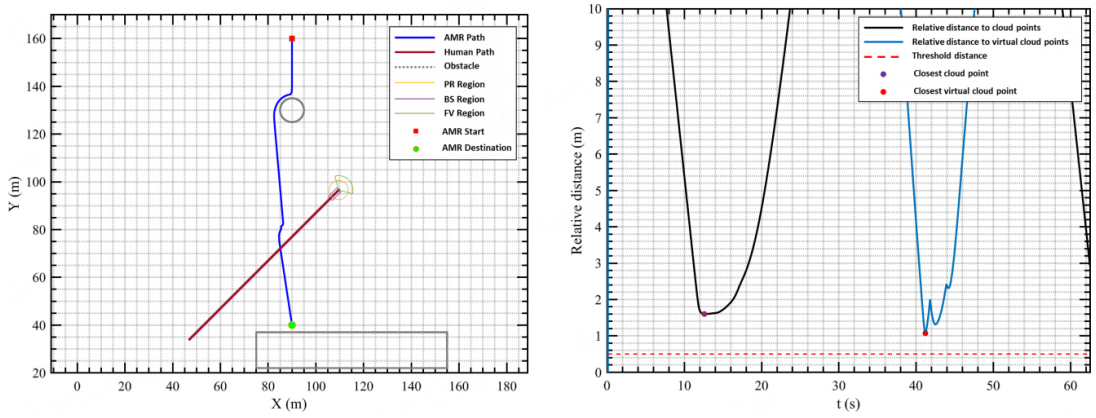


Figure 11. AMR's trajectory and relative distance from the AMR to obstacles and humans (Scenario 1).

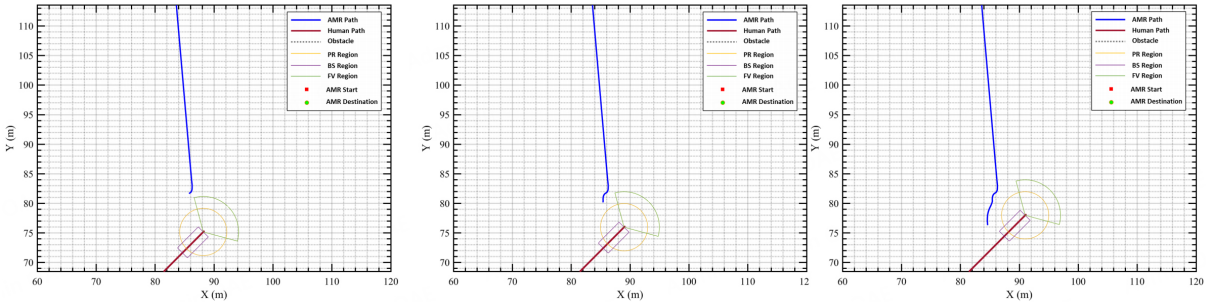


Figure 12. AMR's trajectories near humans (Scenario 1): (left) 41 s, (middle) 42 s, and (right) 44 s.

airport hallway, with humans following the convention of moving along the right side. In addition, there are two rectangular obstacles that represent passenger waiting regions. The simulation includes six human agents, and their positions are listed in Table 8.

From Figure 15 (right), one can observe that throughout the simulation, the AMR never crosses the collision threshold. The minimum relative distance between the AMR and obstacles, as well as the virtual cloud points around humans, are 0.89 m and 0.55 m, respectively. Figure 16 (top left) shows the initial encounter between the AMR and human-1, where the AMR maneuvers to the right at 10.5 s. However, it becomes evident that human-1 is moving faster than the AMR at 14.5 s, as shown in Figure 16 (top right). Consequently, the AMR

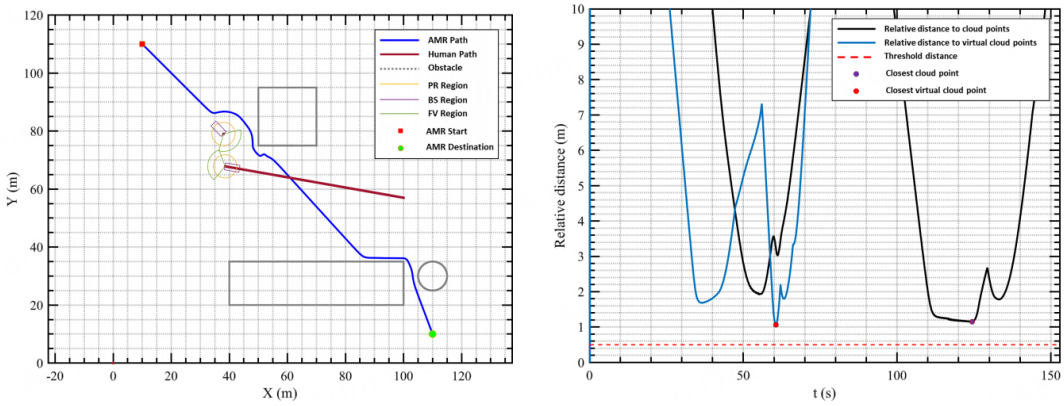


Figure 13. AMR's trajectory and relative distance from the AMR to obstacles and humans (Scenario 2).

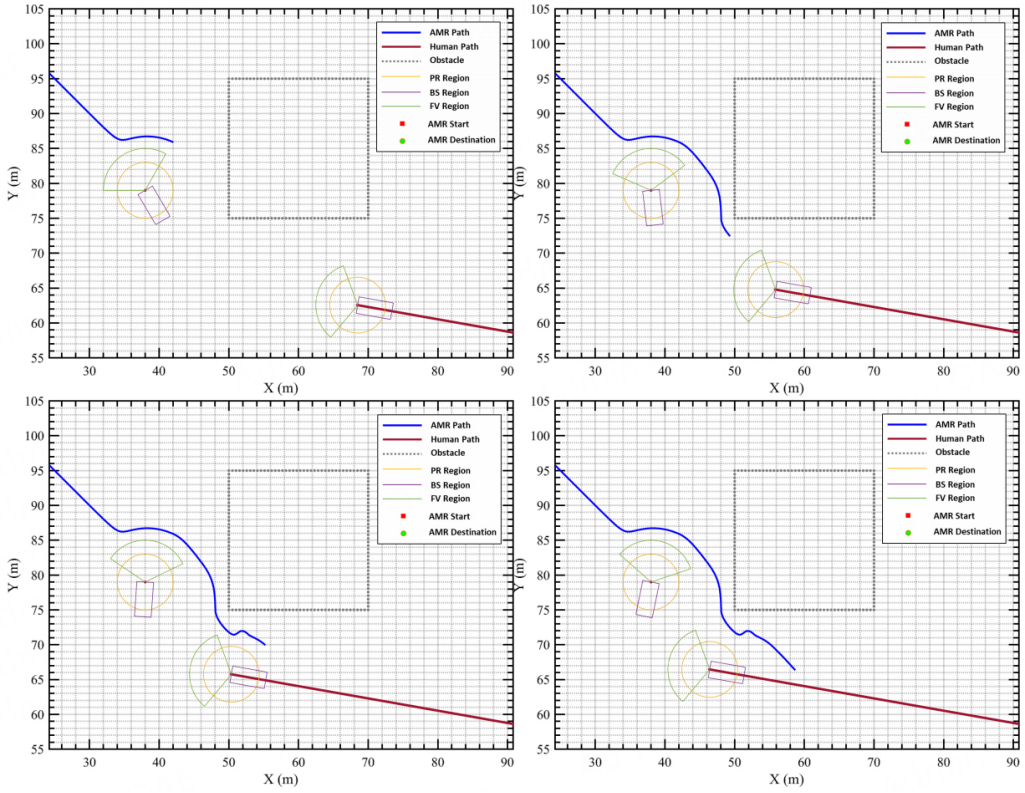


Figure 14. AMR's trajectories near obstacles and humans (Scenario 2): (top left) 42 s, (top right) 58 s, (bottom left) 65 s, and (bottom right) 70 s).

stops and maneuvers to the left to avoid a collision at 20 s, as shown in Figure 16 (middle left). Subsequently, the AMR prioritizes steering away from pillar-1 by choosing to navigate toward the left side. At around 35 s, the AMR faces human-2, who moves into its path and gazes in the AMR's direction, as shown in Figure 16 (middle right). The AMR successfully navigates the gap between FV of human-2 and the circular obstacle-1 during this maneuver, as depicted in Figure 16 (bottom left). Since the gap is small, the closest relative distance occurs during this maneuver of the AMR when the AMR encounters the FV of human-2. At 45 s, the AMR steers clear of human-2, as shown in Figure 16 (bottom left), and Figure 16 (bottom right) shows that at 65 s, it encounters human-3, who is moving in the same direction as the AMR but at a slower pace. Consequently, the AMR overtakes human-3 and reaches its destination. Note that human-4, located near the destination,

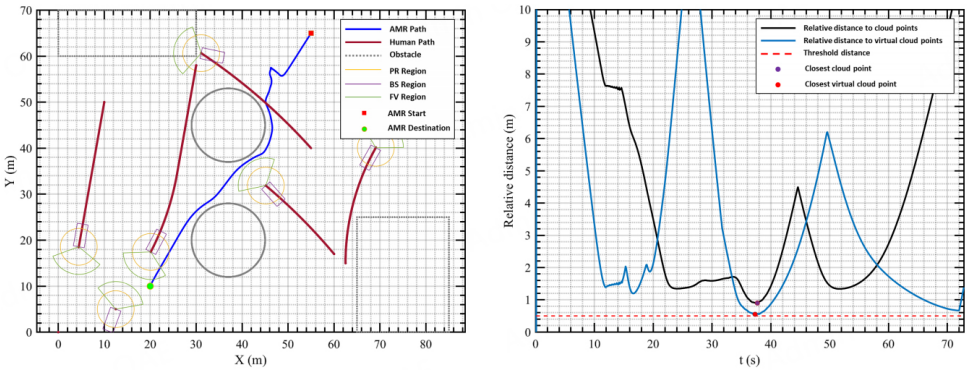


Figure 15. AMR's trajectory and relative distance from the AMR to obstacles and humans (Scenario 3).

presents a situation similar to GNRON.

To summarize the findings of the simulation study, the closest relative distances from the AMR to humans and obstacles obtained are tabulated in Table 9. Upon comparing various scenarios, it is observed that the relative distance from the AMR to humans is smaller than the distance from the AMR to obstacles. Since humans are moving, unlike static obstacles, during the operation of the AMR, there is a high possibility that the AMR navigates around humans closely. Furthermore, it is observed that the AMR comes closest to both humans and obstacles in Scenario 3 compared to the others. These results are natural as the AMR must navigate in a complex environment, dealing with dynamically moving humans and multiple static obstacles. Despite these challenges, it is noteworthy that in all scenarios, the AMR adeptly navigates to the destination position without violating any HAN constraints.

5. CONCLUSIONS

In this study, the authors introduce a HAN approach for AMRs through the integration of an EPF framework, referred to as HAN-EPF. The HAN-EPF method is designed by incorporating a repulsive PF that considers the impact of social constraints on human comfort during navigation. The concept of virtual cloud points is introduced when the AMR detects a human presence, effectively addressing these social constraints and ensuring safe and respectful interactions with humans. To simplify parameter selection, the coefficients of the repulsive PF are redefined in terms of the coefficient of the attractive PF and analyzed based on minimum relative distances and travel distances. Three FISs are employed to adaptively determine these redefined coefficients, guided by the design of MFs and rules based on analysis results. The approach's validation through simulation studies in diverse scenarios demonstrates effective AMR navigation, adherence to HAN rules, and avoidance of collisions with obstacles. Summarizing the important contributions of this work:

- Introducing the EPF as a foundational method for path planning, considering human factors, specifically PR, BS, and FV.
- Designing the FISs for the determination of the EPF's coefficients, assisting the AMR in successfully navigating in a human-populated environment that undergoes continuous changes.

In the future, the integration of a global planner alongside HAN-EPF as a local planner will be considered. This exploration involves testing this combined setup in environments characterized by an increased number of static obstacles.

Additionally, future plans involve delving into parameter optimization for the developed FISs using learning capabilities offered by optimization algorithms to achieve optimal routes for AMRs while adhering to the principles of the HAN framework.

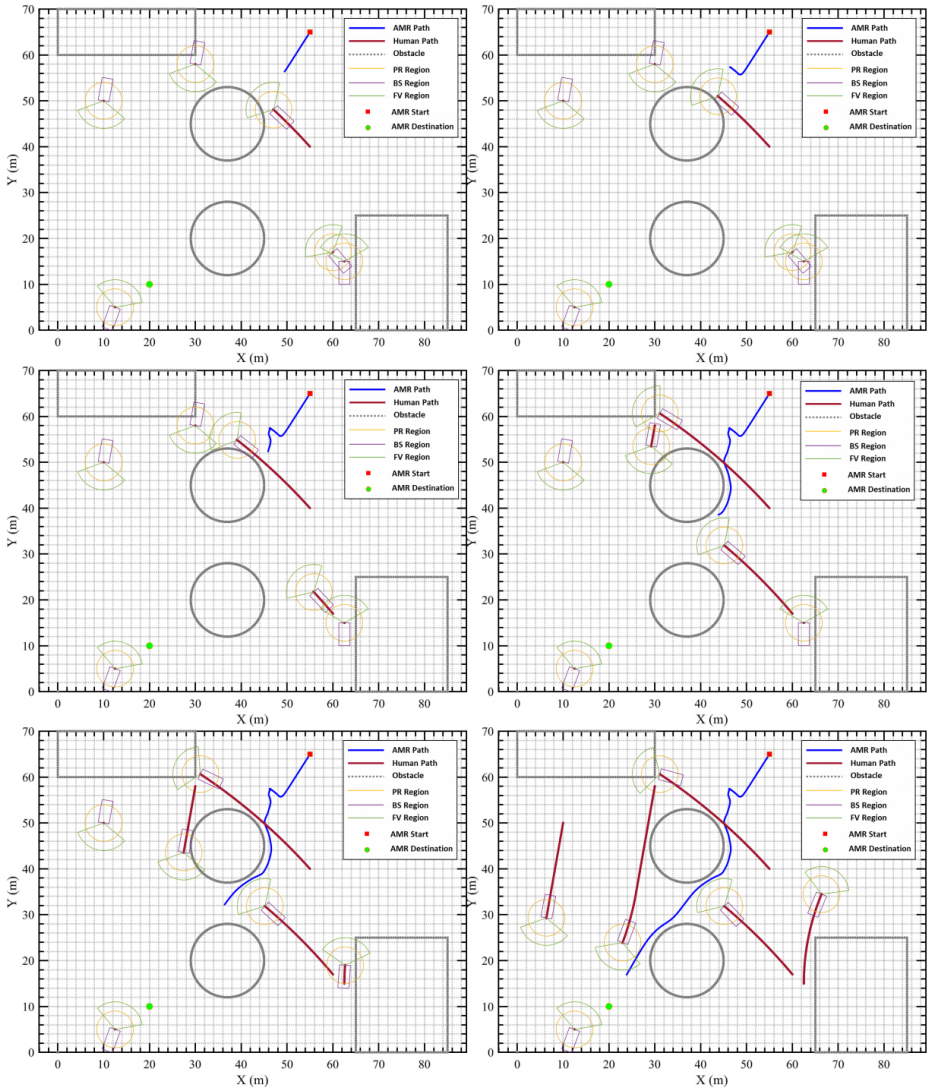


Figure 16. AMR's trajectories near obstacles and humans (Scenario 3): (top left) 10.5 s, (top right) 14.5 s, (middle left) 20 s, (middle right) 35 s, (bottom left) 45 s, and (bottom right) 65 s.

DECLARATIONS

Authors' contributions

Made substantial contributions to the conceptualization, methodology, and analysis: Sampathkumar SK, Choi D, Kim D

Contributed to approach validation, software simulation, and writing - original draft preparation: Sampathkumar SK, Choi D

Contributed to the investigation, supervision, and writing - review and preparation: Kim D

Availability of data and materials

Not applicable.

Financial support and sponsorship

None.

Conflicts of interest

All authors declared that there are no conflicts of interest.

Ethical approval and consent to participate

Not applicable.

Consent for publication

Not applicable.

Copyright

© The Author(s) 2024.

REFERENCES

1. Robertson N. The future of teaching? Asimov's three laws and the hypothetical robot teacher. *PRISM J* 2022;4:29-40. DOI
2. Butler JT, Agah A. Psychological effects of behavior patterns of a mobile personal robot. *Auton Robot* 2001;10:185-202. DOI
3. Fragapane G, Hvolby HH, Sgarbossa F, Strandhagen JO. Autonomous mobile robots in hospital logistics. In: IFIP international conference on advances in production management systems. Cham: Springer; 2020. pp. 672-79. DOI
4. Guo P, Shi H, Wang S, Tang L, Wang Z. An ROS architecture for autonomous mobile robots with UCAR platforms in smart restaurants. *Machines* 2022;10:844. DOI
5. Hasan OA, Alhakeem ZM, Armash MK, et al. Designing smart restaurant for reopening during the relaxation of lockdown in the time of corona pandemic. In: 2022 5th international conference on information and communications technology (ICOIACT), Yogyakarta, Indonesia; 2022. pp. 301-6. DOI
6. Wang J, Meng MQH. Path planning for nonholonomic multiple mobile robot system with applications to robotic autonomous luggage trolley collection at airports. In: 2020 IEEE/RSJ international conference on intelligent robots and systems (IROS), Las Vegas, NV, USA; 2020. pp. 2726-33. DOI
7. Tran HT, Vo TC, Nguyen QNA, et al. A novel design of a smart interactive guiding robot for busy airports. *Int J Smart Sens Intell Syst* 2022;15. DOI
8. Cheng L, Zhao N, Wu K, Chen Z. The multi-trip autonomous mobile robot scheduling problem with time windows in a stochastic environment at smart hospitals. *Appl Sci* 2023;13:9879. DOI
9. Kruse T, Pandey AK, Alami R, Kirsch A. Human-aware robot navigation: a survey. *Robot Auton Syst* 2013;61:1726-43. DOI
10. Nonaka S, Inoue K, Arai T, Mae Y. Evaluation of human sense of security for coexisting robots using virtual reality - 1st report: evaluation of pick and place motion of humanoid robots. In: IEEE international conference on robotics and automation, New Orleans, LA, USA; 2004. pp. 2770-75. DOI
11. Xin L. Dynamic path planning of multiple mobile robots. 2007. pp. 1-140. Available from: http://scholarbank.nus.edu.sg/handle/10635/13405 [Last accessed on 27 Dec 2023].
12. Mateus A, Ribeiro D, Miraldo P, Nascimento JC. Efficient and robust pedestrian detection using deep learning for human-aware navigation. *Robot Auton Syst* 2019;113:23-37. DOI
13. Bruckschen L, Bungert K, Dengler N, Bennewitz M. Human-aware robot navigation by long-term movement prediction. In: 2020 IEEE/RSJ international conference on intelligent robots and systems (IROS), Las Vegas, NV, USA; 2020. pp. 11032-37. DOI
14. Hansen ST, Svenstrup M, Andersen HJ, Bak T. Adaptive human aware navigation based on motion pattern analysis. In: RO-MAN 2009-The 18th IEEE international symposium on robot and human interactive communication, Toyama, Japan; 2009. pp. 927-32. DOI
15. Ah Sen N, Carreno-Medrano P, Kulić D. Human-aware subgoal generation in crowded indoor environments. In: Lecture notes in computer science. Cham: Springer; 2022. pp. 50-60. DOI
16. Korkmaz M. Human-aware dynamic path planning. In: 2021 international conference on INnovations in intelligent sysTems and applications (INISTA), Kocaeli, Turkey; 2021. pp. 1-5. DOI
17. Kollmitz M, Hsiao K, Gaa J, Burgard W. Time dependent planning on a layered social cost map for human-aware robot navigation. In: 2015 European conference on mobile robots (ECMR), Lincoln, UK; 2015. pp. 1-6. DOI
18. Briamonte A. Human-aware robot navigation around groups in narrow spaces. 2020. pp. 1-80. Available from: http://kth.diva-portal.org/smash/record.jsf?pid=diva2%3A1470222&dswid=-8798 [Last accessed on 27 Dec 2023].
19. Sampathkumar SK, Chhabra A, Choi D, Kim D. Optimization of artificial potential field using genetic algorithm for human-aware navigation of autonomous mobile robots. In: North American fuzzy information processing society annual conference. Cham: Springer; 2023. pp. 160-71. DOI
20. Zhang Y, Li Ll, Lin HC, Ma Z, Zhao J. Development of path planning approach using improved A-star algorithm in AGV system. *J Int Technol* 2019;20:915-24. Available from: https://jit.ndhu.edu.tw/article/view/2069 [Last accessed on 27 Dec 2023].
21. Kirby R, Simmons R, Forlizzi J. COMPANION: a constraint-optimizing method for person-acceptable navigation. In: RO-MAN 2009 - The 18th IEEE international symposium on robot and human interactive communication, Toyama, Japan; 2009. pp. 607-12. DOI
22. Khatib O. Real-time obstacle avoidance for manipulators and mobile robots. *Int J Robot Res* 1986;5:90-8. DOI

23. Choi D, Kim D, Lee K. Enhanced potential field-based collision avoidance in cluttered three-dimensional urban environments. *Appl Sci* 2021;11:11003. DOI
24. Mamdani EH. Application of fuzzy algorithms for control of simple dynamic plant. *IET* 1974;121:1585–88. DOI
25. Choi D, Chhabra A, Kim D. Collision avoidance of unmanned aerial vehicles using fuzzy inference system-aided enhanced potential field. Reston, VA: AIAA; 2022. p. 0272. DOI
26. Rios-Martinez J, Spalanzani A, Laugier C. From proxemics theory to socially-aware navigation: a survey. *Int J Soc Robot* 2015;7:137-53. DOI
27. Wheelwright B, Sulai Y, Geng Y, et al. Field of view: not just a number. In: Digital optics for immersive displays, Strasbourg, France; 2018. DOI
28. Shaganan T, Liu R, Yuen C, et al. Follow a human using a mobile robot regardless of the walking speed. In: 2018 3rd international conference on advanced robotics and mechatronics (ICARM), Singapore; 2018. pp. 351-56. DOI

Ganie *et al. Complex Eng Syst* 2024;4:4
DOI: 10.20517/ces.2023.35

Complex Engineering Systems

Research Article

Open Access

Continual online learning-based optimal tracking control of nonlinear strict-feedback systems: application to unmanned aerial vehicles

Irfan Ganie, Sarangapani Jagannathan

Electrical and Computer Engineering, Missouri University of Science and Technology, Rolla, MO 65409, USA.

Correspondence to: Irfan Ganie, Electrical and Computer Engineering, Missouri University of Science and Technology, 141 Emerson Electric Co. Hall, 301 W. 16th St., Rolla, MO 65409, USA. E-mail: iag76b@mst.edu

How to cite this article: Ganie I, Jagannathan S. Continual online learning-based optimal tracking control of nonlinear strict-feedback systems: application to unmanned aerial vehicles. *Complex Eng Syst* 2024;4:4. http://dx.doi.org/10.20517/ces.2023.35

Received: 8 Oct 2023 **First Decision:** 6 Dec 2023 **Revised:** 4 Jan 2024 **Accepted:** 23 Jan 2024 **Published:** 20 Feb 2024

Academic Editors: Ding Wang, Hamid Reza Karimi **Copy Editor:** Fangling Lan **Production Editor:** Fangling Lan

Abstract

A novel optimal trajectory tracking scheme is introduced for nonlinear continuous-time systems in strict feedback form with uncertain dynamics by using neural networks (NNs). The method employs an actor-critic-based NN backstepping technique for minimizing a discounted value function along with an identifier to approximate unknown system dynamics that are expressed in augmented form. Novel online weight update laws for the actor and critic NNs are derived by using both the NN identifier and Hamilton-Jacobi-Bellman residual error. A new continual lifelong learning technique utilizing the Fisher Information Matrix via Hamilton-Jacobi-Bellman residual error is introduced to obtain the significance of weights in an online mode to overcome the issue of catastrophic forgetting for NNs, and closed-loop stability is analyzed and demonstrated. The effectiveness of the proposed method is shown in simulation by contrasting the proposed with a recent method from the literature on an underactuated unmanned aerial vehicle, covering both its translational and attitude dynamics.

Keywords: Continual lifelong learning, optimal control, neural networks, unmanned aerial vehicles, strict-feedback systems

© The Author(s) 2023. **Open Access** This article is licensed under a Creative Commons Attribution 4.0 International License (https://creativecommons.org/licenses/by/4.0/), which permits unrestricted use, sharing, adaptation, distribution and reproduction in any medium or format, for any purpose, even commercially, as long as you give appropriate credit to the original author(s) and the source, provide a link to the Creative Commons license, and indicate if changes were made.

1. INTRODUCTION

Optimal control of nonlinear dynamical systems with known and uncertain dynamics is an important field of study due to numerous practical applications. Traditional optimal control methods[1,2] for nonlinear continuous-time (CT) systems with known dynamics often require the solution to a partial differential equation, referred to as Hamilton-Jacobi-Bellman (HJB) equation, which cannot be solved analytically. To address this challenge, actor-critic designs (ACDs) combined with approximate dynamic programming (ADP) have been proposed as an online method[3,4]. Numerous optimal adaptive control (OAC) techniques for nonlinear CT systems using strict-feedback structure have emerged, leveraging backstepping design as outlined in[5,6]. These approaches, however, require predefined knowledge of the system dynamics. In real-world industrial settings, where system dynamics might be partially or completely unknown, the application of neural network (NN)-based optimal tracking for uncertain nonlinear CT systems in strict feedback form has been demonstrated in[5,7], utilizing the policy/value iterations associated with ADP. However, these policy/value iteration methods often require an extensive number of iterations within each sampling period to solve the HJB equation and ascertain the optimal control input, leading to a significant computational challenge.

The optimal trajectory tracking of nonlinear CT systems involves obtaining a time-varying feedforward term to ensure precise tracking and a feedback term to stabilize the system dynamics. Recent optimal tracking efforts[7,8], have utilized a backstepping-based approach with completely known or partially unknown system dynamics, but the design of feedforward term while minimizing a cost function has not been addressed. Instead, a linear term is used to design the control input. A more recent study[8,9] employed a positive function for obtaining simple weight update laws of the actor and critic NN, which also relaxes the persistency of excitation (PE) condition. However, finding such a function for the time-varying trajectory tracking problem of a nonlinear CT system will be challenging by using an explicit time-dependent value function and HJB equation at each stage of backstepping design since the Hamiltonian is nonzero along the optimal trajectory[10]. In simplified and optimized backstepping control schemes were developed for a class of nonlinear strict feedback systems[8,11,12]. These approaches are different from the one proposed in[5]. However, they either require complete knowledge of the system dynamics or do not assume that the system dynamics are completely unknown.

Moreover, all control techniques rooted in NN-based learning, whether aimed at regulation or tracking, routinely face the issues of catastrophic forgetting[13]. This is understood as the system's ability to lose previously acquired knowledge while assimilating new information[13,14]. Continual lifelong learning (CLL) is conceived as the sustained ability of a nonlinear system to acquire, assimilate, and retain knowledge over prolonged periods without the interference of catastrophic forgetting. This concept is particularly critical when delving into the realm of online NN control strategies for nonlinear CT systems, as these systems are often tasked with navigating and managing complex processes within dynamic and varying environments and conditions. Nonetheless, the lifelong learning (LL) methodologies shown in[13,15] operate in an offline mode and have not been applied to real-time NN control scenarios yet. This scenario offers a promising direction to leverage the advantage of LL in online control systems, addressing catastrophic forgetting and thus enhancing the efficacy of the control system progressively. Implementing LL-oriented strategies in online NN control enables persistent learning and adaptation without discarding prior knowledge, thereby improving its overall performance. By developing an LL-based NN trajectory tracking scheme, it is possible to continuously learn and track trajectories of interest without losing information about previous tasks.

This paper presents an optimal backstepping control approach that incorporates reinforcement learning (RL) to design the controller. The proposed method utilizes an augmented system to address the tracking problem, incorporating both feedforward and feedback controls, which sets it apart from prior work such as[8,16]. This approach uses a trajectory generator to generate the trajectories and hence deals with the non-stationary condition in the HJB equation that arises in optimal tracking problems due to the time-varying reference trajectory. In addition, the proposed weight update laws are direct error driven based, obtained using Hamiltonian and

control input error, in contrast to where the weight update laws are obtained using some positive functions[8,16]. Furthermore, the control scheme incorporates an identifier where the approximation error is bounded above by system states to approximate the unknown system dynamics, as opposed to prior work, such as[8,16], where the system dynamics are either completely known or partially known. Additionally, the utilization of an HJB equation at each step of the backstepping process is intended to ensure that the entire sequence of steps is optimized.

The paper also examines the impacts of LL and catastrophic forgetting on control systems and proposes strategies for addressing these challenges in control system-based applications. Specifically, the proposed method employs a weight velocity attenuation (WVA)-based LL scheme in an online manner, in contrast to prior work, such as[13,15], which utilizes offline learning. Additionally, the proposed method demonstrates the stability of the LL scheme via Lyapunov analysis in contrast to offline-based learning[13,15], where the weight convergence is not addressed. To validate the effectiveness of the proposed method, an unmanned aerial vehicle (UAV) application is considered, and the proposed method is contrasted with the existing approach. Lyapunov stability shows the uniform ultimate boundedness (UUB) of the overall closed-loop continual lifelong RL (LRL) scheme.

The contributions include

(1) A novel optimal trajectory tracking control formulation is presented, utilizing an augmented system approach for nonlinear strict-feedback systems within an ADP-based framework, offering a novel perspective.

(2) An NN-based identifier is employed, wherein the reconstruction error is presumed to be upper-bounded by the norm of the state vector, providing an enhanced approximation of the system dynamics. The new weight update laws are introduced, incorporating Hamiltonian and the NN identifier within an actor-critic framework at each step of the backstepping process.

(3) An online LL method is developed in the critic NN weight update law, mitigating both catastrophic forgetting and gradient explosion, with the significance of weights for NN layers obtained using Fisher Information Matrix (FIM) determined by the Bellman error, as opposed to offline LL-based methods with targets.

(4) Lyapunov stability analysis is undertaken for the entire closed-loop tracking system, involving the identifier NN and the LL-based actor-critic NN framework to show the UUB of the closed-loop system.

2.CONTINUAL LIFELONG OPTIMAL CONTROL FORMULATION

In this section, we provide the problem formulation and the development of our proposed LRL approach for uncertain nonlinear CT systems in strict feedback form.

2.1 System description

Consider the following strict feedback system

$$\begin{aligned} \dot{x}_1(t) &= f_1(x_1) + g_1(x_1)x_2, \\ \dot{x}_2(t) &= f_2(\bar{x}_2) + g_2(\bar{x}_2)u, \end{aligned} \tag{1}$$

where $\bar{x}_2(t) = [x_1(t), x_2(t)]^\top \in \mathbb{R}^2$ is the system state, $u \in \mathbb{R}$ is the control input, and $f_i(.), g_i(.), i = 1, 2$ are unknown yet Lipschitz continuous functions on Ω_x and satisfying $f_i(0) = 0$. The standard following assumptions are stated to proceed.

Assumption 1 ([17]) *The nonlinear CT system is controllable and observable. In addition, the control coefficient matrix satisfies* $\|g_i(.)\| \leq g_{iM}$, *where* g_{iM} *is an unknown positive constant.*

Assumption 2 ([4]) *The state vector is considered measurable. The desired trajectory $\xi_r \in \mathbb{R}$ is bounded, and there exists a Lipschitz continuous command generator function $h_d(\xi_r(t))$ such that $\dot{\xi}_r(t) = h_d(\xi_r(t))$ and $h_d(0) = 0$.*

Next, the LRL control design is introduced. The goal of the LRL control scheme is to achieve satisfactory tracking and maintain the boundedness of all closed-loop system signals while minimizing the control effort and addressing the issue of catastrophic forgetting.

The design of the control system begins by implementing an optimal backstepping approach using augmented system-based actor-critic architecture and then using an online LL to mitigate catastrophic forgetting.

2.2 Optimal backstepping control

To develop optimal control using the backstepping technique, first, a new augmented system is expressed in terms of tracking error as follows. Define the tracking error as $e_{tr1}(t) = x_1(t) - \xi_r(t)$. Taking the time derivative and using the value of $\dot{x}_1$ to obtain

$$\dot{e}_{tr1}(t) = f_1(x_1) + g_1(x_1)x_2 - h_d(\xi_r(t)), \tag{2}$$

where $x_2(t)$ is the virtual control.

In order to get both the feedforward and feedback part of the controller, the tracking problem is changed to a regulation problem by defining a new augmented state as $z_1 = \begin{bmatrix} e_{tr1}^\top & \xi_r^\top \end{bmatrix}^\top$. Then, we can write

$$\dot{z}_1(t) = \mathcal{F}_{s1}(z_1) + \mathcal{G}_{s1}(z_1)\alpha_1, \tag{3}$$

where $\mathcal{F}_{s1}(z_1) = \begin{bmatrix} f_1(x_1) - h_d(\xi_r(t)) \\ h_d(\xi_r(t)) \end{bmatrix}$ and $\mathcal{G}_{s1}(z_1) = \begin{bmatrix} g_1(x_1) \\ 0 \end{bmatrix}$, with $z_1(0) = \begin{bmatrix} e_{tr1}^\top(0) & \xi_r^\top(0) \end{bmatrix}^\top$ and α_1 is virtual control. From Assumption 1, it follows that $0 < \|\mathcal{G}_{si}(.)\| \leq \bar{G}_i$, where $\bar{G}_i > 0$ for $i = 1, 2$. The design is presented in two steps.

Step 1: For the first backstepping step, let α_1 and α_1^* be the virtual and optimal virtual control inputs, respectively. The optimal performance index function $J_1^*(z_1)$ is defined as

$$J_1^*(z_1) = \min_{\alpha_1 \in \Psi(\Omega_{z1})} \left(\int_t^\infty e^{-\gamma_1(s-t)} h_1(z_1, \alpha_1)\, ds \right) = \int_t^\infty e^{-\gamma_1(s-t)} h_1\left(z_1, \alpha_1^*\right) ds, \tag{4}$$

where $\Psi(\Omega_{z1})$ denotes the set of admissible control policies over a compact set Ω_{z1}, $J_1(z_1) = \left(\int_t^\infty e^{-\gamma_1(s-t)} h_1(z_1, \alpha_1)\, ds \right)$, and $h_1(z_1, \alpha_1) = z_1(s)^\top q_1 z_1(s) + \alpha_1(z_1)^\top r_1 \alpha_1(z_1)$ with , q_1 is a positive definite, $r_1 > 0$, γ_1 is the discount factor, $\gamma_1 > 0$.

Remark 1 *Generally, addressing trajectory tracking control problems poses considerable challenges, particularly when dealing with a system characterized by nonlinear dynamics and a trajectory that evolves over time. In such instances, a prevalent approach is to employ a discounted cost function, denoted as (4), to render the cost index, J_1^*, finite. The control input, consisting of both feedforward and feedback components, is obtained simultaneously by minimizing the performance function (4) along the trajectories of the augmented system (3). In addition, the performance function is not explicitly dependent on time.*

By taking the time derivative on both sides of the optimal performance function (4), the tracking Bellman equation is obtained as

$$J_1^*(z_1) = \int_t^\infty \frac{\partial}{\partial t} e^{-\gamma_1(s-t)} h_1\left(z_1, \alpha_1^*\right)) ds - h_1(z_1, \alpha_1^*) \tag{5}$$

By noting that the first term of (5) is $\gamma_1 J_1$, therefore, (5) can be rewritten as

$$h_1\left(z_1, \alpha_1^*\right) + \frac{dJ_1^{*\top}(z_1)}{dz_1} \dot{z}_1(t) - \gamma_1 J_1^* = 0. \tag{6}$$

Therefore, the tracking HJB equation is generated as

$$\begin{aligned} H_1\left(z_1, \alpha_1^*, \frac{dJ_1^*}{dz_1}\right) &= h_1\left(z_1, \alpha_1^*\right) + \frac{dJ_1^{*\top}(z_1)}{dz_1} \dot{z}_1(t) - \gamma_1 J_1^* \\ &= \frac{dJ_1^{*\top}(z_1)}{dz_1}\left(\mathcal{F}_{s1}(z_1) + \mathcal{G}_{s1}(z_1)\alpha_1^*\right) + Q_1 + \bar{\alpha}_1 - \gamma_1 J_1^* = 0. \end{aligned} \tag{7}$$

where $H_1\left(z_1, \alpha_1^*, \frac{dJ_1^*}{dz_1}\right)$ is the Hamiltonian function for the first step, $Q_1 = z_1(s)^\top q_1 z_1(s)$, $\bar{\alpha}_1 = \alpha_1^*(z_1)^\top r_1 \alpha_1^*(z_1)$. The optimal control solution α_1^* can be obtained by solving $\frac{\partial H_1}{\partial \alpha_1^*} = 0$. This equation represents the condition for finding the optimal control that minimizes the performance index and satisfies the HJB equation as

$$\alpha_1^* = -\frac{1}{2} r_1^{-1} \mathcal{G}_{s1}^\top(z_1) \frac{dJ_1^*(z_1)}{dz_1}. \tag{8}$$

It is well known that NNs have universal function approximation abilities and can approximate a nonlinear continuous function $\mathcal{H}(z) : \mathbb{R}^n \to \mathbb{R}^m$ on a compact set Ω_z as $\mathcal{H}(z) = W^\top \sigma(z)$, where $W \in \mathbb{R}^{p \times m}$ is the weight matrix, p is the number of neurons, and $\sigma(z)$ is the basis function vector.

Since J_1^* is unknown, an NN and its derivative will be used to approximate it on a compact set as

$$J_1^* = W_{c1}^{*\top} \sigma_{c1}(z_1) + \varepsilon_{c1}(z_1) \tag{9}$$

$$\frac{dJ_1^*(z_1)}{dz_1} = \nabla \sigma_{c1}^\top(z_1) W_{c1}^* + \nabla \varepsilon_{c1}^\top(z_1), \tag{10}$$

where W_{c1}^*, σ_{c1}, and ε_{c1} are the target weights, basis function vector, and the NN reconstruction error, respectively, $\nabla \sigma_{c1}$ and $\nabla \varepsilon_{c1}$ are the partial derivative of σ_{c1} and ε_{c1}, respectively, with respect to input z_1. Substituting (8) and (9) into the HJB equation (6) to get

$$\begin{aligned} H_1^* &= \frac{1}{4}(W_{c1}^{*\top} \nabla \sigma_{c1} + \nabla \varepsilon_{c1}) \wedge_1 (\nabla \sigma_{c1}^\top W_{c1}^* + \nabla \varepsilon_{c1}^\top) - \gamma_1 (W_{c1}^{*\top} \sigma_{c1}(z_1) + \varepsilon_{c1}) \\ &+ (W_{c1}^{*\top} \nabla \sigma_{c1}(z_1) + \nabla \varepsilon_{c1}) \times \left(\mathcal{F}_{s1}(z_1) - (\frac{1}{2} \wedge_1 (\nabla \sigma_{c1}^\top(z_1) W_{c1}^* + \nabla \varepsilon_{c1}^\top)\right) + Q_1, \end{aligned} \tag{11}$$

where optimal Hamiltonian function $H_1^* = H_1\left(z_1, \alpha_1^*, \frac{dJ_1^*}{dz_1}\right)$, and $\wedge_1 = \mathcal{G}_{s1} r_1^{-1} \mathcal{G}_{s1}^\top$. Since the target weight matrix, W_{c1}^*, is unknown, an actor-critic NN and its derivative will be designed to find the solution as follows

$$\begin{aligned} \hat{J}_1 &= \hat{W}_{c1}^\top(t) \sigma_{c1}(z_1) \\ \frac{d\hat{J}_1(z_1)}{dz_1} &= \nabla \sigma_{c1}^\top(z_1) \hat{W}_{c1}, \end{aligned} \tag{12}$$

where $\hat{W}_{c1}$ is the estimate of the weight matrices for critic NN, and $\sigma_{c1}(z_1)$ is the basis function vector. Next, using (12), we can rewrite (11) as

$$\hat{H}_1 = \frac{1}{4}\hat{W}_{c1}^{\top}\nabla\sigma_{c1}\hat{\wedge}_1\nabla\sigma_{c1}^{\top}\hat{W}_{c1} - \gamma_1\hat{W}_{c1}^{\top}\sigma_{c1}(z_1) + (\hat{W}_{c1}^{\top}\nabla\sigma_{c1})\left(\hat{\mathcal{F}}_{s1}(z_1) - (\frac{1}{2}\hat{\wedge}_1\nabla\sigma_{c1}^{\top}\hat{W}_{c1})\right) + Q_1, \tag{13}$$

where the estimated Hamiltonian function $\hat{H}_1 = H_1\left(z_1, \hat{\alpha}_1, \frac{d\hat{J}_1}{dz_1}\right)$, $\hat{\wedge}_1 = \hat{\mathcal{G}}_{s1}r_1^{-1}\hat{\mathcal{G}}_{s1}^{\top}$ and $\hat{\mathcal{F}}_{s1}(z_1), \hat{\mathcal{G}}_{s1}$ are the estimate of augmented internal dynamics and input dynamics to be generated in the subsequent section by using an NN identifier. From (8), α_1 is unknown, continuous on a compact set Ω_{z1}, and an NN is used to approximate it over a compact set, as shown in the subsequent steps. We can write

$$-\frac{1}{2}r_1^{-1}\mathcal{G}_{s1}^{\top}(z_1)\frac{dJ_1^*(z_1)}{dz_1} = -\frac{1}{2}\mathcal{V}_1^*(z_1), \tag{14}$$

where $\mathcal{V}_1^*(z_1) = r_1^{-1}\mathcal{G}_{s1}^{\top}(z_1)\frac{dJ_1^*(z_1)}{dz_1}$. where $\mathcal{G}_{s1}(z_1) \in \mathbb{R}^2$, and $\frac{dJ_1^*(z_1)}{dz_1} \in \mathbb{R}^2$ which makes $\mathcal{V}_1^*(z_1)$ a scaler. To achieve the tracking, decompose the term $\mathcal{V}_1^*$ into following two parts

$$\mathcal{V}_1^* = 2\beta_1 z_1 + \mathcal{V}_1^0, \tag{15}$$

where $\mathcal{V}_1^0 = -2\beta_1 z_1 + \mathcal{V}_1^*$, where β_1 is a $[\bar{\beta}_1, 0]$ i.e $\beta_1 \in \mathbb{R}^{1\times 2}$, $\bar{\beta}_1 > 0$, $z_1 \in \mathbb{R}^2$. The optimal virtual controller α_1^* can be written as

$$\alpha_1^* = -\beta_1 z_1 - \frac{1}{2}\mathcal{V}_1^0. \tag{16}$$

Therefore, $\mathcal{V}_1^0$ can be approximated using NN,

$$r_1^{-1}\mathcal{G}_{s1}^{\top}(z_1)\frac{dJ_1^*(z_1)}{dz_1} = 2\beta_1 z_1 + (W_{a1}^{*\top}\sigma_{a1}(z_1) + \varepsilon_1), \tag{17}$$

where $W_{a1}^* \in \mathbb{R}^{p\times m}$ are the target bounded unknown weights, and $\varepsilon_1 \in \mathbb{R}^m$ denotes the function reconstruction error; $\sigma_{a1}(z_1)$ with $z_1 \in \Omega_{z_1}$ is the basis function vector. Hence, the virtual controller (8) can be written as

$$\alpha_1^* = -\beta_1 z_1 - \frac{1}{2}(W_{a1}^{*\top}\sigma_{a1}(z_1) + \varepsilon_1(z_1)), \tag{18}$$

where $W_{a1}^* \in \mathbb{R}^{p\times m}$ are the target bounded unknown weights, and $\varepsilon_1 \in \mathbb{R}^m$ denotes the function reconstruction error; $\sigma_{a1}(z_1)$ with $z_1 \in \Omega_{z_1}$ is the basis function vector. Since the target weights are unknown, the actor NN will be designed to estimate the optimal virtual control as

$$\hat{\alpha}_1 = -\beta_1 z_1 - \frac{1}{2}\hat{W}_{a1}^{\top}\sigma_{a1}(z_1), \tag{19}$$

where $\hat{W}_{a1}, \sigma_{a1}(z_1), z_1 \in \Omega_{z1}$ are the estimated weights and the basis function of actor NN. According to the HJB equation (11) and its approximation (13), define the HJB residual error $e_1(t)$ as

$$e_1(t) = \hat{H}_1 - H_1^* = \hat{H}_1, \tag{20}$$

since the optimal Hamiltonian value is zero. Notice that the estimated Hamiltonian, $\hat{H}_1$, requires the estimate of unknown dynamics from the identifier. The second step is discussed next.

Remark 2 *The subsequent section will leverage the HJB residual error (20) to formulate the weight update laws for the critic NN. Additionally, the control input error u_e, delineated in Lemma 1, will facilitate the derivation of the actor NN weight update laws.*

Employing the HJB residual error and the control input error for formulating the weight update laws is pivotal as it enables efficient optimization of the weights in NN. This methodology ensures more accurate and reliable learning processes, allowing the network to better approximate the desired functions or policies, thereby enhancing the overall performance and robustness of the system.

Step 2: This is the second step, and the actual controller $\hat{u}$ will be derived. Define $e_{tr2}(t) = x_2(t) - \hat{\alpha}_1$; then using (1), the error dynamics are written as

$$\dot{e}_{tr2}(t) = f_2(\bar{x}_2) + g_2(\bar{x}_2)u - \dot{\hat{\alpha}}_1. \tag{21}$$

Since $\hat{\alpha}_1 = -\beta_1 z_1 - \hat{W}_{a1}^\top \sigma_z$, on using the values from step 1, $\dot{\hat{\alpha}}_1$ can be calculated by using a virtual generator $h_d(\hat{\alpha}_1)$. Let $z_2 = [e_{tr2}^\top, \hat{\alpha}_1^\top]^\top \in \mathbb{R}^2$. One can write

$$\dot{z}_2(t) = \mathcal{F}_{s2}(z_2) + \mathcal{G}_{s2}(z_2)u, \tag{22}$$

where $\mathcal{F}_{s2}(z_2) = \begin{bmatrix} f_2(\bar{x}_2) - h_d(\hat{\alpha}_1) \\ h_d(\hat{\alpha}_1) \end{bmatrix}$ and $\mathcal{G}_{s2}(z_2) = \begin{bmatrix} g_2(\bar{x}_2) \\ 0 \end{bmatrix}$. Letting u^* be the optimal control, the optimal integral cost function is defined as

$$J_2^*(z_2) = \min_{u \in \Psi(\Omega_{z2})} \left(\int_t^\infty e^{-\gamma_2(s-t)} h_2(z_2(s), u(z_2))\, ds \right) = \int_t^\infty e^{-\gamma_2(s-t)} h_2(z_2(s), u^*(z_2))\, ds, \tag{23}$$

where $h_2 = z_2(s)^\top q_2 z_2(s) + u^*(z_2)^\top r_2 u^*(z_2)$ is the cost function. The user-defined penalties, q_2 and r_2, are positive definite and $\gamma_2 > 0$.

The HJB equation for step 2 is given by

$$H_2\left(z_2, u^*, \frac{dJ_2^*}{dz_2}\right) = Q_2 + \bar{u} + \frac{dJ_2^{*\top}}{dz_2}\left(\mathcal{F}_{s2}(z_2) + \mathcal{G}_{s2}(z_2)u^*\right) - \gamma_2 J_2^* = 0, \tag{24}$$

where $H_2\left(z_2, u^*, \frac{dJ_2^*}{dz_2}\right)$ is the Hamiltonian function for the second step, $Q_2 = z_2(s)^\top q_2 z_2(s)$, $\bar{u} = u^*(z_2)^\top r_2 u^*(z_2)$. Similar to previous steps, solving $(\partial H_2 / \partial u^*) = 0$ yields

$$u^* = -\frac{1}{2} r_2^{-1} \mathcal{G}_{s2}^\top(z_2) \frac{dJ_2^*}{dz_2}. \tag{25}$$

Since J_2^* is unknown, an NN will be used to approximate it on a compact set given by

$$J_2^* = W_{c2}^{*\top} \sigma_{c2}(z_2) + \varepsilon_{c2}(z_2). \tag{26}$$

Therefore, $\frac{dJ_2^*(z_2)}{dz_2} = \nabla \sigma_{c2}^\top(z_2) W_{c2}^* + \nabla \varepsilon_{c2}^\top$, where $W_{c2}^*, \sigma_{c2}, \varepsilon_{c2}$ are the NN weights, activation function, and the reconstruction error, respectively. Substituting (25) and (26) into the HJB equation (24) gets

$$\begin{aligned} H_2^* = {} & \frac{1}{4}(W_{c2}^{*\top} \nabla \sigma_{c2} + \nabla \varepsilon_{c2}) \wedge_2 (\nabla \sigma_{c2}^\top W_{c2}^* + \nabla \varepsilon_{c2}^\top) + Q_2 - \gamma_2 (W_{c2}^{*\top} \sigma_{c2}(z_2) + \varepsilon_{c2}) \\ & + (W_{c2}^{*\top} \nabla \sigma_{c2}(z_2) + \nabla \varepsilon_{c2}) \left(\mathcal{F}_{s2}(z_2) - \frac{1}{2} \wedge_2 (\nabla \sigma_{c2}^\top(z_2) W_{c2}^* + \nabla \varepsilon_{c2}^\top) \right), \end{aligned} \tag{27}$$

where $H_2^* = H_2\left(z_2, \alpha_2^*, \frac{dJ_2^*}{dz_2}\right)$ is the optimal Hamiltonian for the second step, $\wedge_2 = \mathcal{G}_{s2} r_2^{-1} \mathcal{G}_{s2}^\top$. Since the target weight matrix, W_{c2}^*, is unknown, an actor-critic NN will be designed to find the solution as follows

$$\begin{aligned} \hat{J}_2 &= \hat{W}_{c2}^\top(t)\sigma_{c2}(z_2) \\ \frac{d\hat{J}_2(z_2)}{dz_2} &= \nabla\sigma_{c2}^\top(z_2)\hat{W}_{c2}, \end{aligned} \tag{28}$$

where $\hat{W}_{c2}$ is the estimate of the weight matrices for critic NN, and $\sigma_{c2}(z_2), z_2 \in \Omega_{z2}$ is the basis function vector. Next, we can rewrite (27) as follows

$$\hat{H}_2 = \frac{1}{4}\hat{W}_{c2}^\top \nabla\sigma_{c2}\hat{\wedge}_2\nabla\sigma_{c2}^\top\hat{W}_{c2} + Q_2 - \gamma_2\hat{W}_{c2}^\top\sigma_{c2}(z_2) + \left(\hat{W}_{c2}^\top\nabla\sigma_{c2}\right)\left(\hat{\mathcal{F}}_{s2}(z_2) - \left(\frac{1}{2}\hat{\wedge}_2\nabla\sigma_{c2}^\top\hat{W}_{c2}\right)\right), \tag{29}$$

where $\hat{H}_2 = H_2\left(z_2, \hat{\alpha}_2, \frac{d\hat{J}_2}{dz_2}\right)$ is the estimated Hamiltonian, $\hat{\wedge}_2 = \hat{\mathcal{G}}_{s2} r_2^{-1} \hat{\mathcal{G}}_{s2}^\top$ and $\hat{\mathcal{F}}_{s2}(z_2), \hat{\mathcal{G}}_{s2}$ are the estimate of augmented internal and input dynamics to be generated in the subsequent section by using the NN identifier.

Since $\mathcal{G}_{s2}(z_2)$ and $\frac{dJ_2^*(z_2)}{dz_2}$ are unknown, continuous on a compact set Ω_{z2}, an NN is used to approximate them over a compact set, we can write

$$-\frac{1}{2}r_2^{-1}\mathcal{G}_{s2}^\top(z_2)\frac{dJ_2^*(z_2)}{dz_2} = -\frac{1}{2}\mathcal{V}_2^*(z_2), \tag{30}$$

where $\mathcal{V}_2^*(z_2) = r_2^{-1}\mathcal{G}_{s2}^\top(z_2)\frac{dJ_2^*(z_2)}{dz_2}$. To achieve tracking, decompose the term $\mathcal{V}_2^*$ into following two parts

$$\mathcal{V}_2^* = 2\beta_2 z_2 + \mathcal{V}_2^0, \tag{31}$$

where $\mathcal{V}_2^0 = -2\beta_2 z_2 + \mathcal{V}_2^*, \beta_2 = [\bar{\beta}_2, 0]$ i.e $\beta_2 \in \mathbb{R}^{1\times 2}, \bar{\beta}_2 > 0, z_2 \in \mathbb{R}^2$. The optimal controller u^* can be written as $u^* = -\beta_2 z_2 - \frac{1}{2}\mathcal{V}_2^0$. Therefore, we can write

$$r_2^{-1}\frac{\mathcal{G}_{s2}^\top(z_2)}{2}\frac{dJ_2^*(z_2)}{dz_2} = 2\beta_2 z_2 + (W_{a2}^{*\top}\sigma(z_2) + \varepsilon_2), \tag{32}$$

where $W_{a2}^* \in \mathbb{R}^{p\times m}$ are the target bounded unknown weights, and $\varepsilon_2 \in \mathbb{R}^m$ denotes the function reconstruction error; $\sigma(z_2)$ with $z_2 \in \Omega_{z_2}$ is the basis function vector. Therefore, the actual controller (16) can be written as

$$u^* = -\beta_2 z_2 - \frac{1}{2}(W_{a2}^{*\top}\sigma_{a2}(z_2) + \varepsilon_2(z_2)). \tag{33}$$

Similarly, the actor NN will be designed to estimate the optimal control as

$$\hat{u} = -\beta_2 z_2 - \frac{1}{2}\hat{W}_{a2}^\top\sigma_{a2}(z_2), \tag{34}$$

where $\hat{W}_{a2}, \sigma_{a2}(z_2), z_2 \in \Omega_{z2}$ are the estimated weights and the basis function of actor NN. According to the HJB equation (27) and its approximation (29), define the HJB residual error $e_2(t)$ as follows

$$e_2(t) = \hat{H}_2 - H_2^* = \hat{H}_2, \tag{35}$$

since the optimal Hamiltonian for the second step is zero, notice that the estimated Hamiltonian, $\hat{H}_2$, requires the estimate of unknown dynamics from the identifier. Similar to the two steps, the proposed method can be extended to nth order.

Remark 3 *The optimal control input can be obtained by utilizing the gradient of the optimal value function (26) and an NN identifier. As a result, the critic NN outlined in (26) may be utilized to determine the actor input without the need for an additional NN. However, for the purpose of simplifying the derivation of weight update rules and subsequent stability analysis, separate NNs are employed for the actor and critic.*

Next, an NN identifier will be used to approximate the unknown dynamics given by (3) and (22).

2.3 NN identifier

A single-layer NN is used to approximate both the nonlinear functions $\mathcal{F}_{sj}$ and $\mathcal{G}_{sj}$ where $j = 1, 2$, that govern the augmented dynamics[17]. Then, by using $\hat{\mathcal{G}}_{sj}$, which is obtained from the NN identifier, the estimated control policy is applied to the nonlinear system. The approximations are represented as $\mathcal{F}_{sj}(z_j) = {V_{F_j}}^\top \sigma_{F_j}(z_j) + \varepsilon_{F_j}(z_j)$ and $\mathcal{G}_{sj}(z_j) = V_{G_j}^\top \sigma_{G_j}(z_j) + \varepsilon_{G_j}(z_j)$, where V_{F_j} and V_{G_j} are the NN's weight matrices, $\sigma_{F_j}(z_j)$ and $\sigma_{G_j}(z_j)$ are the activation functions, and $\varepsilon_{F_j}(z_j)$ and $\varepsilon_{G_j}(z_j)$ are the NN's reconstruction errors respectively. The estimated values of the internal dynamics and control coefficient matrix of the augmented system are given by $\hat{\mathcal{F}}_{sj}(z_j) = \hat{V}_{F_j}^\top \sigma_{F_j}(z_j)$ and $\hat{\mathcal{G}}_{sj}(z_j) = \hat{V}_{G_j}^\top \sigma_{G_j}(z_j)$, where $\hat{V}_{F_j}$ and $\hat{V}_{G_j}$ are the estimated NN's weight matrices. Define

$$\dot{z_j}(t) = Z_j^\top \boldsymbol{\sigma}(\boldsymbol{\xi_j})\bar{\alpha}_j + \varepsilon_I(z_j), \tag{36}$$

where $\bar{\alpha}_j = \left[1, \alpha_j\right]^\top$, is the augmented control input, α_j is given by (19), (34), $Z_j = \begin{bmatrix} V_{F_j}^\top & V_{G_j}^\top \end{bmatrix}^\top \in \mathbb{R}^{2l \times n}$ represents the augmented NN identifier weights, and $\boldsymbol{\sigma}(\boldsymbol{\xi_1}) = \text{diag}\{\sigma_{F_j}\left(z_j\right), \sigma_{G_j}(z_j)\}$ denotes the augmented activation function for the NN identifier. The reconstruction error of the NN identifier, denoted by $\varepsilon_I(z_j)$, is defined as $\varepsilon_I(z_j) = (\varepsilon_{F_j}(z_j) + \varepsilon_{G_j}(z_j)\alpha_j)$. Next, the following assumption is stated.

Assumption 3 ([17]) *The NN identifier is of single-layer, and its reconstruction error is bounded above such that* $\|\varepsilon_I(z_1)\|^2 \leq b_0\|z_1\|^2$ *and* $\|Z_1\| \leq Z_{m_1}$.

Remark 4 *Because $\varepsilon_I(z_j)$ depends on input α_j and the system state $z_j(t)$, it is assumed to be bounded above by the norm of the state vector unlike[18], where $\varepsilon_I(z_j)$ is bounded by a constant value.*

Define the dynamics of the NN identifier as

$$\dot{\hat{z}}_j(t) = \hat{Z}_j^\top \boldsymbol{\sigma}(\boldsymbol{\xi}_j)\bar{\alpha}_j + K(z_j - \hat{z}_j), \tag{37}$$

where $\hat{z}_j(t)$ represents the estimated augmented state vector, K is a user defined constant gain matrix, and $\hat{Z}_j = \begin{bmatrix} \hat{V}_{F_j}^\top & \hat{V}_{G_j}^\top \end{bmatrix}^\top$ represents the augmented NN identifier estimated weights. The state estimation error is defined as $e_{i_j} = z_j - \hat{z}_j$. The weight update law for the NN identifier is given by

$$\dot{\hat{Z}}_j = -\alpha_{vj}\hat{Z}_j + \sigma(\boldsymbol{\xi}_j)\bar{\alpha}_j e_{i_j}^\top, \tag{38}$$

where $\alpha_{vj} > 0$ is a tuning parameter.

Remark 5 *The NN identifier weights are tuned by using both augmented state estimation error and the input vector. The boundedness of the control input is needed to show the convergence of the NN identifier if proof is shown separately, whereas this assumption is relaxed when the identifier is combined with the LRL control scheme, as shown in the next section.*

Remark 6 *Since the control input error and the HJB error used to tune the actor-critic NN weights require the system dynamics which are uncertain, the NN identifier is used to approximate the unknown dynamics of an*

augmented system. The estimated values from the identifier are used in the actor-critic weight update laws to tune the NN weights, as shown in the subsequent section.

2.4 Actor critic NN weight tuning

In this section, the actor-critic weight update laws are obtained using the gradient descent method to the Hamiltonian-based performance function. The following Lemma is stated.

Lemma 1 *Consider a system* (1)*, transformed system* (3)*, NN identifier weight update laws* (38)*, the update laws for the critic NN* (12)*,* (26) *and actor NN* (19)*,* (34)*. They can be written as*

$$\dot{\hat{W}}_{cj} = \gamma_{cj}\hat{\psi}_j(t)\left(e_j^\top(t) - \frac{1}{4}\hat{W}_{cj}^\top\nabla\sigma_{cj}\hat{\wedge}_j\nabla\sigma_{cj}^\top\hat{W}_{cj} - \hat{W}_{cj}^\top\nabla\sigma_{cj}\hat{\mathcal{F}}_{sj}\right) - \sigma_{1j}\hat{W}_{cj} \tag{39}$$

$$\dot{\hat{W}}_{aj}(t) = \beta_{aj}(S_{aj}u_{ej}^\top) - \sigma_{2j}\hat{W}_{aj} \tag{40}$$

where j denotes the number of steps in backstepping, $\gamma_{cj} = \frac{\beta_{cj}\hat{\psi}_j}{\|\hat{\psi}_j\|^2+1}$, $\beta_{cj}, \beta_j, \beta_{aj} > 0$ are the learning rates, $S_{aj} = \sigma_{aj}(z_j)$, $S_{cj} = \sigma_{cj}(z_j)$, and $\hat{\psi}_j(t) = \gamma_j S_{cj} - \nabla\sigma_{cj}(\hat{\mathcal{F}}_{sj} + \hat{\mathcal{G}}_{sj}\hat{\alpha}_j)$, where $\sigma_{1j} > 0, \sigma_{2j>0}$ are the design constants, u_{ej} is the error between estimated control and actual control and is given by $u_{ej} = -\beta_j z_j - \frac{1}{2}\hat{W}_{aj}^\top\sigma_{aj}(z_j) + \frac{1}{2}r_j^{-1}\hat{\mathcal{G}}_{sj}^\top\frac{d\hat{J}_j}{dz_j}$, e_j is the HJB error for each step given by (20)*,*(35)*, $\hat{\wedge}_j = \hat{\mathcal{G}}_{sj}r_j^{-1}\hat{\mathcal{G}}_{sj}^\top$, and $\hat{\mathcal{F}}_{sj}, \hat{\mathcal{G}}_{sj}$ are approximated by using NN identifier.*

Proof: The weight update laws for critic NN in step j are obtained by defining the performance function as

$$E_j = \frac{1}{2}e_j^2. \tag{41}$$

By using the gradient descent algorithm, the weight update law can be obtained as

$$\dot{\hat{W}}_{cj} = -\frac{\beta_{cj}\hat{\psi}_j}{(1+\hat{\psi}_j^\top\hat{\psi}_j)}\frac{\partial E_j(t)}{\partial\hat{W}_{cj}}. \tag{42}$$

On simplifying (42), we will get the weight update law for critic NN, as shown in Lemma. The weight update law for actor NN is obtained by defining the performance function as

$$E_{aj} = \frac{1}{2}u_{ej}^2. \tag{43}$$

By using the gradient descent approach, the weight update law for an actor NN is obtained as

$$\dot{\hat{W}}_{aj}(t) = -\frac{\partial E_{aj}(t)}{\partial\hat{W}_{aj}}. \tag{44}$$

On further solving and adding the stabilization terms, we will get the weight update law shown in Lemma 1.

Remark 7 . *The weight update laws are obtained using the gradient descent method to the Hamiltonian-based performance function. The weight update equations for the critic and actor have additional terms to ensure stability and facilitate convergence proof. The last term, known as the sigma modification term, relaxes the PE condition needed to ensure weight convergence. It is important to note that the right-hand side terms in the weight update equation can be measured.*

The following assumption is stated next.

Assumption 4 ([4]) *It is assumed that the ideal weights exist and are bounded over a compact set by an unknown positive constant, such that* $\left\|W_{cj}^*\right\| \leq \bar{W}_{M1j}$, $\left\|W_{aj}^*\right\| \leq \bar{W}_{M2j}$ *where* $\bar{W}_{M1j}, \bar{W}_{M2j}$ *are unknown constant values. The basis function* $\sigma(\cdot)$*, function reconstruction error* $\varepsilon_j(\cdot)$*, and their derivatives with respect to their arguments are assumed to be bounded over a compact set, with unknown bounds as* $\|\sigma\| \leq \bar{\sigma}, \|\dot{\sigma}\| \leq \bar{\dot{\sigma}}, \varepsilon_j(\cdot) \leq \varepsilon_m, \dot{\varepsilon}_j(\cdot) \leq \bar{\varepsilon}_m$.

Next, the following theorem is stated.

Theorem 1 *Consider the nonlinear system in strict-feedback form defined by* (1)*. By using the augmented system* (3)*, consider the optimal virtual control* (19) *and actual control terms* (34)*, along with the identifier, actor-critic updating laws* (38), (39)*, and* (40)*. Further, assume that the design parameters are selected as per the conditions stated and that Assumptions 1 through 4 hold. If the system input is PE and its initial value,* u_0*, is admissible, then tracking errors, augmented state* z_j*, the actual state* x_j *and NN weight estimation errors,* $\tilde{Z}_j = Z_j - \hat{Z}_j$*,* $\tilde{W}_{cj} = W_{cj} - \hat{W}_{cj}$*, and* $\tilde{W}_{aj} = W_{aj} - \hat{W}_{aj}$ *are guaranteed to be bounded. This, in turn, ensures that the actual system output tracks the desired trajectory and estimated/actual control inputs are bounded close to their optimal values.*

Proof: See Appendix.

Remark 8 *In the proposed optimal backstepping technique, the RL/ADP is employed at every step to obtain the optimal virtual and actual control inputs. We have derived the backstepping for a two-step process; however, it can be implemented up to n steps using a similar procedure.*

Remark 9 *The sigma modification term does serve to alleviate the PE condition and assists in the process of forgetting; however, it does not prove effective in multitasking scenarios to minimize forgetting. Subsequently, a novel online LL strategy is presented to address the issue of catastrophic forgetting.*

Next, an online regularization-based approach to LL is introduced.

2.5 Continual lifelong learning

To mitigate the issues of catastrophic forgetting[13], a novel technique called WVA was proposed[15]. However, WVA has only been used in an offline manner, which cannot be applied to NN-based online techniques.

In contrast, this study introduces a new online LL technique that can be integrated into an online NN-based trajectory tracking control scheme by identifying and safeguarding the most critical parameters during the optimization process. To achieve this, the proposed technique employs a performance function given by

$$L_j(\hat{W}_{cj}) \approx E_{bj} + \frac{\lambda_j}{2}\left\|\hat{W}_{cj} - \hat{W}_{cjp}^*\right\|_{\bar{\Omega}_{kj}}^2, \tag{45}$$

where E_{bj} is the loss function for the current task B in step j (41), $\bar{\Omega}_{kj} = diag\{\frac{\Omega_{w1}}{\Omega_{w1}+1} \cdots \frac{\Omega_{wn}}{\Omega_{wn}+1}\}$, Ω_{wi} represents the significance of the i-th weight, where $i = 1, \ldots, n$, of the NN in step j after learning from prior tasks, the diagonal elements of the FIM $\bar{\Omega}_{kj}$, with k denoting the task, are estimated using HJB error since targets are unavailable in online learning, λ_j is the design parameter controlling the strength of the regularization, $\left\|\hat{W}_{cj} - \hat{W}_{cjp}^*\right\|_{\bar{\Omega}_{kj}} = (\hat{W}_{cj} - \hat{W}_{cjp}^*)\bar{\Omega}_{kj}(\hat{W}_{cj} - \hat{W}_{cjp}^*)^\top$, $\hat{W}_{cjp}^*$ is the optimized bounded weight vector of the previous task, and $\hat{W}_{cj}$ is the weight vector of the current task that needs to be optimized. The FIM for each

task is calculated by defining the log-likelihood function as:

$$\ell(\hat{W}_{cjp}, z_{jp}) = \log p(e_{jp}|\hat{W}_{cjp}, z_{jp}), \tag{46}$$

where e_{jp} represents the HJB residual error, as defined by (20) and (35) from the previous task. The term $p(e_{jp}|\hat{W}_{cjp}, z_{jp})$ denotes the probability density function of the HJB error, given the input z_{jp} from the previous task and the weights $\hat{W}_{cjp}$ at step j from the previous task. Calculate the Jacobian matrix as

$$J(\hat{W}_{cjp}, z_{jp}) = \frac{\partial \ell(\hat{W}_{cjp}, z_{jp})}{\partial \hat{W}_{cjp}}, \tag{47}$$

where $\frac{\partial \ell(\hat{W}_{cjp}, z_{jp})}{\partial \hat{W}_{cjp}}$ denotes the partial derivative of the log-likelihood function with respect to the weights from the previous task. Therefore, the estimation of FIM is obtained as

$$\bar{\Omega}_{kj} = \frac{1}{t_1 - t_0} \int_{t_0}^{t_1} J\left(\hat{W}_{cjp}, z_{jp}\right) J\left(\hat{W}_{cjp}, z_{jp}\right)^{\top} dt, \tag{48}$$

where t_0 denotes the task start time, t_1 denotes the task end time. The elements of the FIM illustrate the extent of information concerning the HJB error that is conveyed by every weight within the network. Sure! Here's a clearer and more structured way to convey the information. For the first task, the FIM is zero. When estimating the FIM for the second task using data from the first task, the estimate remains bounded. This bounded behavior is due to the fact that the closed-loop system associated with task 1 is also bounded, as demonstrated in Theorem 1.

Subsequently, leveraging normalized gradient descent allows us to formulate an additional term in the critic weight update law. This term is derived as follows

$$-\frac{\partial}{\partial \hat{W}_{cj}}(L_j(\hat{W}_{cj})) = -\frac{\partial E_j(t)}{\partial \hat{W}_{cj}} - \lambda_j \bar{\Omega}_{kj}(\hat{W}_{cj} - \hat{W}^*_{cjp}). \tag{49}$$

For LL, the terms from (49) are combined with the terms from the previously defined update law that is given in Theorem 1. Next, the following theorem is stated.

Theorem 2 *Consider the hypothesis stated in Theorem 1, and let Assumptions 1 to 4 hold, with the LRL critic NN tuning law for j step optimal backstepping, given by*

$$\dot{\hat{W}}_{cj} = \gamma_{cj}\hat{\psi}_j(t)\left(e_j(t) - \frac{1}{4}\hat{W}_{cj}^{\top}\nabla\sigma_{cj}\hat{\wedge}_j\nabla\sigma_{cj}^{\top}\hat{W}_{cj} - \hat{W}_{cj}^{\top}\nabla\sigma_{cj}\hat{\mathcal{F}}_{sj}\right) - \sigma_{j1}\hat{W}_{cj} - \alpha_j\lambda_j\bar{\Omega}_{kj}(\hat{W}_{cj} - \hat{W}^*_{cjp}), \tag{50}$$

where j denotes the number of steps in backstepping, λ_j is the design parameter, and α_j are the NN learning rates; then, $\tilde{W}_{cj}$ and all closed-loop signals, including those in Theorem 1, are UUB.

Proof: See Appendix.

Remark 10 *From (49), when the significance of the weights increases, Ω_{w_i} can become infinite; therefore, $\frac{\Omega_{wi}}{\Omega_{w_i}+1}$ will become 1; hence, the gradient explosion can be avoided.*

Remark 11 *The first part of the NN weight update law in Theorem 2 is the same as in Theorem 1, whereas the second part includes regularization terms resulting from LL. Notice that the tracking and weight estimation error bounds increase due to the LRL-based control scheme because the bounding constant, $\bar{C} = \bar{C}_{0j} + \gamma_{penj}$, includes additional terms that are obtained from the penalty function from LL, where $\bar{C}_{0j}$ is bound when LL is absent, and γ_{penj} is because of LL in jth step. The overall stability is unaffected due to LL.*

Remark 12 *The proposed LL method is scalable to encompass n tasks. A third task, C, aims to maintain network weights in alignment with the learned weights from the preceding two tasks, implementable via single or dual penalties, given the quadratic nature of the penalties.*

Remark 13 *The efficacy of the LL method is pronounced when Tasks 1 and 2 share informational overlap reflected in the weights, facilitating the knowledge transfer for Task 2. However, in the absence of shared weights or knowledge between non-overlapping tasks, the visible enhancement in Task 2 performance might be negligible with online LL, albeit it mitigates the catastrophic forgetting of Task 1, offering long-term benefits when reverting to Task 1.*

3. UAV TRACKING SIMULATION OUTCOMES

This section delineates the outcomes of optimal tracking control founded on LRL, applied on an underactuated UAV system.

3.1 Unmanned aerial vehicle (UAV) problem formulation and control design

Consider the UAV model depicted in Figure 1, which is characterized by two reference frames: the inertial frame $I = \{x_I, y_I, z_I\}$ fixed to the earth and the body-fixed frame $A = \{x_A, y_A, z_A\}$. The UAV is steered using four forces $F_{j=1,2,3,4}$, each produced by a respective rotor. To negate the yaw drift due to the reactive torque, rotors are arranged in two pairs, with $(1, 3)$ spinning clockwise and $(2, 4)$ spinning counterclockwise.

The quadrotor dynamics can be modeled by two unique equations: (1) translational; and (2) rotational. However, these dynamic equations interrelate via the rotation matrix, rendering them as two cohesive subsystems. A holistic control strategy involves both outer and inner loop controls, corresponding to the two subsystems. The outer loop aims to execute positional control by managing the state variables of x, y, and z while concurrently generating command inputs for roll and pitch states in the inner loop through a correction block, dependent on a predefined yaw reference signal. The inner loop's objective is to achieve attitude control by managing the state variables of roll, pitch, and yaw.

Define $\zeta_1(t) = [x(t), y(t), z(t)]^\top \in \mathbb{R}^3$ as the UAV's positional state and $\zeta_2(t) = [\dot{x}(t), \dot{y}(t), \dot{z}(t)]^\top \in \mathbb{R}^3$ as its velocity state within the inertial frame I. A transformation relation exists: $\zeta_2(t) = R(\eta_1)V$. Consequently, the translational dynamic equation can be represented as

$$\dot{\zeta}_1(t) = \zeta_2(t)$$
$$\dot{\zeta}_2(t) = -\begin{bmatrix} 0 \\ 0 \\ g \end{bmatrix} + R(\eta_1)\begin{bmatrix} 0 \\ 0 \\ 1/m \end{bmatrix} u_c.$$

Given the underactuated nature of UAV translational dynamics, an intermediate control vector

$$V = R(\eta_1)\begin{bmatrix} 0 \\ 0 \\ 1/m \end{bmatrix} u_c$$

is introduced for optimal position control derivation, and the translational dynamic can thus be reformulated

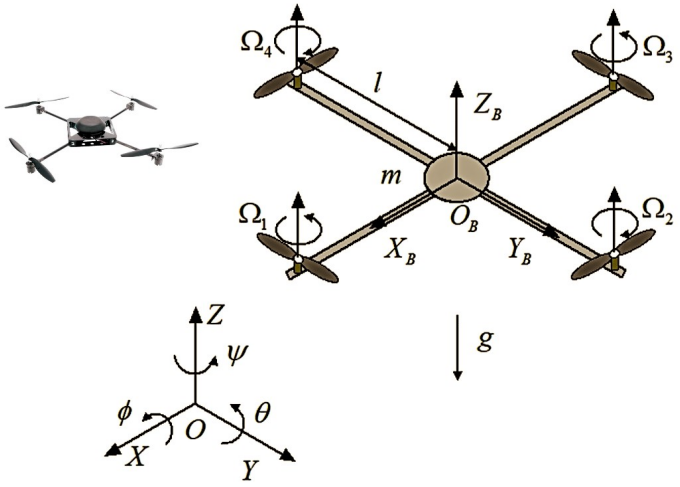


Figure 1. Quadrotor UAV.

as

$$\dot{\zeta}_1(t) = \zeta_2(t)$$
$$\dot{\zeta}_2(t) = -\begin{bmatrix} 0 \\ 0 \\ g \end{bmatrix} + V.$$

Remark 14 *The relation between* $V = [V_1, V_2, V_3]^\top \in \mathbb{R}^3$ *and* u_c *is given by*

$$V_1 = (\cos(\phi)\sin(\theta)\cos(\psi) + \sin(\phi)\sin(\psi))\frac{u_c}{m}$$
$$V_2 = (\cos(\phi)\sin(\theta)\sin(\psi) - \sin(\phi)\cos(\psi))\frac{u_c}{m}$$
$$V_3 = \cos(\phi)\cos(\theta)\frac{u_c}{m}$$

Solving yields the control u_c *as*

$$u_c = m\left(V_1^2 + V_2^2 + V_3^2\right)^{\frac{1}{2}}$$

Using the reference trajectory vector $\zeta_{\text{ref}}(t) = [x_{\text{ref}}(t), y_{\text{ref}}(t), z_{\text{ref}}(t)]^\top \in \mathbb{R}^3$, we define the tracking error variables as $e_{\zeta_1}(t) = \zeta_1(t) - \zeta_{\text{ref}}(t)$ and $e_{\zeta_2}(t) = \zeta_2(t) - \alpha_\zeta$, where α_ζ is the virtual control.

For the coordinate transformation of rotational dynamic, the transformation relationship between rotational velocity Ω and the Euler angles rate of change $\eta_2(t) = \dot{\eta}_1(t) = [\dot{\phi}(t), \dot{\theta}(t), \dot{\psi}(t)]^\top \in \mathbb{R}^3$ is represented as:

$$\eta_2(t) = \dot{\eta}_1(t) = \Phi(\eta_1)\,\Omega$$

with

$$\Phi(\eta_1) = \begin{bmatrix} 1 & s(\phi)t(\theta) & c(\phi)t(\theta) \\ 0 & c(\phi) & -s(\phi) \\ 0 & s(\phi)\sec(\theta) & c(\phi)\sec(\theta) \end{bmatrix}.$$

Applying time derivation to both sides yields the attitude dynamic as:

$$\ddot{\eta}_1(t) = -\Phi(\eta_1)\,I^{-1}\left(\Phi^{-1}(\eta_1)\,\eta_2(t)\dot{\times}I\Phi^{-1}(\eta_1)\,\eta_2(t)\right) + \dot{\Phi}(\eta_1)\,\Phi^{-1}(\eta_1)\,\eta_2(t) + \Phi(\eta_1)\,I^{-1}\tau.$$

The function $f(\eta_1, \eta_2)$ is represented as:

$$f(\eta_1, \eta_2) = -\Phi(\eta_1) I^{-1} \left(\Phi^{-1}(\eta_1) \eta_2(t) \dot{\times} I \Phi^{-1}(\eta_1) \eta_2(t) \right) + \dot{\Phi}(\eta_1) \Phi^{-1}(\eta_1) \eta_2(t)$$

So, the attitude dynamic can be rephrased in strict feedback form as

$$\begin{aligned} \dot{\eta}_1(t) &= \eta_2(t) \\ \dot{\eta}_2(t) &= f(\eta_1, \eta_2) + \Phi(\eta_1) I^{-1} \tau. \end{aligned}$$

Reference signals are denoted as $\eta_{\text{re}}(t) = [\phi_{\text{re}}(t), \theta_{\text{re}}(t), \psi_{\text{re}}(t)]^\top$. The yaw command element $\psi_{\text{re}}(t)$ is predefined, and the roll and pitch command angles are derived as

$$\begin{aligned} \phi_{\text{re}}(t) &= \arcsin\left(m \frac{V_1 \sin(\psi_{\text{re}}) - V_2 \cos(\psi_{\text{re}})}{u_c} \right) \\ \theta_{\text{re}}(t) &= \arctan\left(\frac{V_1 \cos(\psi_{\text{re}}) + V_2 \sin(\psi_{\text{re}})}{V_3} \right). \end{aligned}$$

Tracking error variables are designated as $e_{\eta 1}(t) = \eta_1(t) - \eta_{\text{re}}(t)$ and $e_{\eta 2}(t) = \eta_2(t) - \alpha_\eta$, where $\alpha_\eta \in \mathbb{R}^3$ is the virtual control.

Therefore, using the control law (34) and the weight update laws shown in Theorems 1 and 2 for translational and attitude dynamics will drive the UAV system to track the reference trajectory, as shown in the simulations.

3.2 Simulation parameters and results

The desired position trajectory for $\xi_{\text{re}}(t) = [2t - 20, 5, 0]^\top$ and, for task 2, is $\xi_{\text{re}}(t) = [5\sin(t), 5\cos(t), t]^\top$. The yaw command angle is predefined as $\psi_{\text{re}} = \pi/4$; then, the roll and pitch command signals ϕ_{re} and θ_{re} can be produced. The design parameter $\beta_1 = [6, 0]$, $\beta_2 = [4.2, 0]$, $m = 5$, $\sigma_{1j} = 0.75$ and $\sigma_{2j} = 0.82$, $\beta_{ci} = 0.6$, $\beta_{ai} = 0.6$, $\lambda_w = 2$, $\alpha_w = 0.85$. The initial values are set as $z_1(0) = [1.7, 3.8, 0.41]^\top$, $z_2(0) = [2.31, 3, 0.4]^\top$. In this configuration, the NN is based on a Random Vector Functional Link (RVFL) architecture. The network is structured with a single layer, where the input layer is directly connected to the output layer, bypassing traditional hidden layers. The interlayer connections are facilitated by a weight matrix V, which is randomly initialized. This matrix V effectively represents the neurons in the network. Specifically, the network comprises ten neurons, each corresponding to a column in the V matrix. These neurons functionally link the input to the output through the RVFL mechanism. The transformation from the input to the output layer is given by $W^\top \sigma(V^\top X)$, where σ denotes the activation function applied element-wise, and X is the input and W is tuned using the weight update laws in Theorems 1 and 2. Similarly, seven neurons are used for the identifier; sigmoid is used as an activation function, $\epsilon_0 = 0.65$. For attitude control, the initial values are set as $z_3(0) = [\pi/4, \pi/4, \pi/4]^\top$, $z_4(0) = [\pi/3, \pi/3, \pi/3]^\top$.

We consider two task scenarios in which the reference trajectory is changed in each task as if the UAV is moving in a different path or environment. In the simulations, we have shown task 1 again to demonstrate that when the UAV returns to task 1, the LL-based control will help mitigate the catastrophic forgetting. The proposed method is able to drive the UAV to track the reference trajectory accurately, even on changing tasks. Figure 2 shows the performance of the position and attitude tracking; it indicates that using the proposed LRL method shown by the blue color, and the UAV position states can accurately follow the reference trajectory shown by the red color. The attitude tracking performance demonstrates that the UAV attitudes can also follow the reference attitudes better as compared to recent literature[9] shown by green color. Figure 3 illustrates the tracking errors, indicating that the tracking performance of the proposed method is superior when compared with recent literature, referred to as 'r-lit'[9]. Figure 4 illustrates the position and attitude tracking errors.

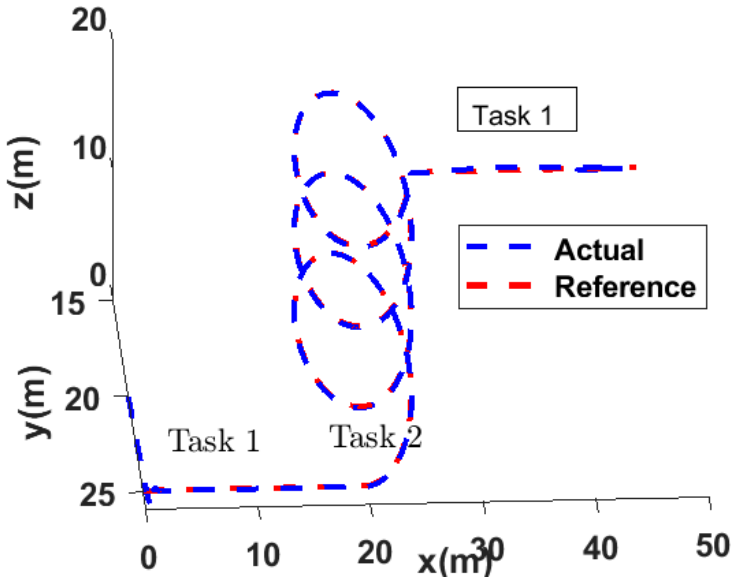


Figure 2. Actual and reference trajectories using the proposed LL-based method.

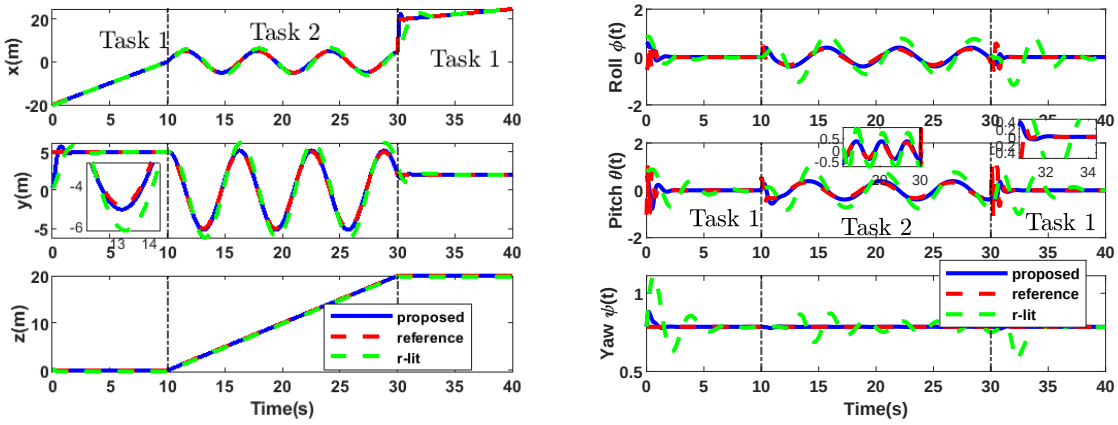


Figure 3. Tracking performance of position and attitude subsystems using LRL and recent literature (r-lit) [9] methods.

Both the system state tracking plots and positional error plots in Figure 2 and Figure 3 demonstrate the superior performance of the proposed LL method, represented by blue lines. However, the recent literature [9] exhibits higher error, thus showing the need for LL. In contrast, the 'Lit' method, as shown in green, has a higher error rate when compared to other methods. Notably, the total average error shown in Figure 4 is low when the proposed LL method is employed over the 'Lit' method, indicating a substantial enhancement in tracking accuracy.

Figure 5 depicts torque inputs and cumulative costs where it can be seen that the cost of using the proposed method is minimal, and all the closed-loop signals are bounded. The control effort demanded by the 'Lit' method is higher in comparison to the proposed LL-based method. Figure 5 also showcases the cumulative cost. It is observed that the cost associated with Lit (shown in green color) is higher compared to the proposed LL method (represented in blue) during the tasks and as the tasks change.

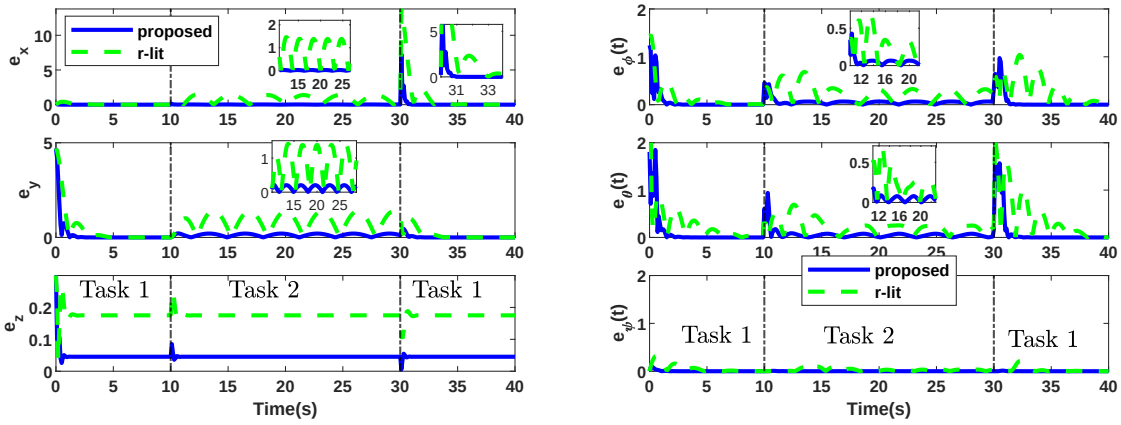


Figure 4. Position and attitude tracking errors using proposed LRL and recent literature (r-lit) [9] methods.

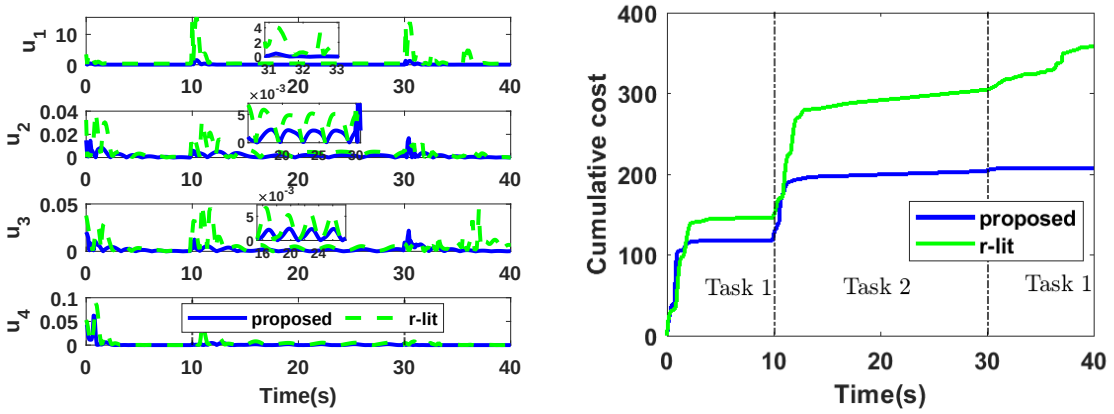


Figure 5. Torque inputs and cumulative cost using proposed LRL and recent literature (r-lit) [9] methods.

4. CONCLUSION AND DISCUSSION

This paper proposed an innovative LL tracking control technique for uncertain nonlinear CT systems in strict feedback form. The method combined the augmented system, trajectory generator, and optimal backstepping approach to design both feedforward and feedback terms of the tracking scheme. By utilizing a combination of actor-critic NN and identifier NN, the method effectively approximated the solution to the HJB equations with unknown nonlinear functions. The use of RL at each step of the backstepping process allows for the development of virtual and actual optimal controllers that can effectively handle the challenges posed by uncertain, strict feedback systems. The proposed work highlighted the significance of considering catastrophic forgetting in online controller design and developed a new method to address this issue. Simulation results on a UAV tracking a desired trajectory show acceptable performance. The proposed approach can be extended by using deep NNs for better approximation. In addition, the integral RL (IRL)-based approach can relax the drift dynamics. Dynamic surface control can be included to minimize the number of NNs used.

DECLARATIONS

Authors' contributions

Made substantial contributions to the conception and design of the study: Ganie I, Jagannathan S
Made contributions in writing, reviewing, editing, and methodology: Ganie I, Jagannathan S

Availability of data and materials

Not applicable.

Financial support and sponsorship

The project or effort undertaken was or is sponsored by the Office of Naval Research Grant N00014-21-1-2232 and Army Research Office Cooperative Agreements W911NF-21-2-0260 and W911NF-22-2-0185.

Conflicts of interest

Both authors declared that there are no conflicts of interest.

Ethical approval and consent to participate

Not applicable.

Consent for publication

Not applicable.

Copyright

© The Author(s) 2024.

REFERENCES

1. Abu-Khalaf M, Lewis FL. Nearly optimal control laws for nonlinear systems with saturating actuators using a neural network HJB approach. *Automatica* 2005;41:779–91. DOI
2. McLain TW, Beard RW. Successive galerkin approximations to the nonlinear optimal control of an underwater robotic vehicle. In Proceedings of the1998 IEEE international conference on robotics and automation (Cat. No.98CH36146). Leuven, Belgium. 20-20 May 1998. DOI
3. Vrabie D, Pastravanu O, Abu-Khalaf M, Lewis FL. Adaptive optimal control for continuous-time linear systems based on policy iteration. *Automatica* 2009;45:477–84. DOI
4. Modares H, Lewis FL. Optimal tracking control of nonlinear partially-unknown constrained-input systems using integral reinforcement learning. *Automatica* 2014;50:1780–92. DOI
5. Gao W, Jiang ZP. Learning-Based adaptive optimal tracking control of strict-feedback nonlinear systems. *IEEE Trans Neural Netw Learn Syst* 2018;29:2614–24. DOI
6. Zargarzadeh H, Dierks T, Jagannathan S. Optimal control of nonlinear continuous-time systems in strict-feedback form. *IEEE Trans Neural Netw Learn Syst* 2015;26:2535–49. DOI
7. Huang Z, Bai W, Li T, et al. Adaptive reinforcement learning optimal tracking control for strict-feedback nonlinear systems with prescribed performance. *Inf Sci* 2023;621:407–23. DOI
8. Wen G, Chen CLP, Ge SS. Simplified optimized backstepping control for a class of nonlinear strict-feedback systems with unknown dynamic functions. *IEEE Trans Cybern* 2021;51:4567–80. DOI
9. Wen G, Hao W, Feng W, Gao K. Optimized backstepping tracking control using reinforcement learning for quadrotor unmanned aerial vehicle system. *IEEE Trans Syst Man Cybern Syst* 2022;52:5004–15. DOI
10. Bryson AE. Applied optimal control: optimization, estimation and control. New York: Routledge; 1975. p. 496. DOI
11. Wen G, Ge SS, Tu F. Optimized backstepping for tracking control of strict-feedback systems. *IEEE Trans Neural Netw Learn Syst* 2018;29:3850–62. DOI
12. Wu J, Wang W, Ding S, Xie X, Yi Y. Adaptive neural optimized control for uncertain strict-feedback systems with unknown control directions and pre-set performance. *Commun Nonlinear Sci Numer Simul* 2023;126:107506. DOI
13. Kirkpatrick J, Pascanu R, Rabinowitz NC,et al. Overcoming catastrophic forgetting in neural networks. *Proc Natl Acad Sci USA* 2017;114:3521–6. DOI
14. Ganie I, Jagannathan S. Adaptive control of robotic manipulators using deep neural networks. *IFAC-PapersOnLine* 2022;55:148–53. DOI
15. Kutalev A, Lapina A. Stabilizing elastic weight consolidation method in practical ML tasks and using weight importances for neural network pruning. *ArXiv* 2021. Available from: https://arxiv.org/abs/2109.10021 [Last accessed on 2 Feb 2024].
16. Liu Y, Zhu Q, Wen G. Adaptive tracking control for perturbed strict-feedback nonlinear systems based on optimized backstepping technique. *IEEE Trans Neural Netw Learn Syst* 2022;33:853–65. DOI
17. Moghadam R, Jagannathan S. Optimal adaptive control of uncertain nonlinear continuous-time systems with input and state delays. *IEEE Trans Neural Netw Learn Syst* 2023;34:3195–204. DOI
18. Mishra A, Ghosh S. Simultaneous identification and optimal tracking control of unknown continuous-time systems with actuator constraints. *Int J Control* 2022;95:2005–23. DOI

APPENDICES

Proof of Theorem 1

Step1: Consider the Lyapunov function as follows

$$L_1 = J_1(z_1) + \frac{1}{2}e_{i1}^{\top}e_{i1} + \frac{1}{2}tr\left\{\tilde{Z}_1^{\top}\tilde{Z}_1\right\} + \frac{1}{2}tr\{\tilde{W}_{c1}\tilde{W}_{c1}^{\top}\} + \frac{1}{2}tr\{\tilde{W}_{a1}\tilde{W}_{a1}^{\top}\}. \tag{51}$$

The time derivative of L_1 is

$$\dot{L}_1 = \dot{J}_1(z_1) + tr\{e_{i1}^{\top}\dot{e}_{i1}\} + tr\{\tilde{Z}_1^{\top}\dot{\tilde{Z}}_1\} + tr\{\tilde{W}_{c1}^{\top}\dot{\tilde{W}}_{c1}\} + tr\{\tilde{W}_{a1}^{\top}\dot{\tilde{W}}_{a1}\}. \tag{52}$$

Where tr denotes the trace operator. Let $\dot{L}_1 = \dot{L}_{11} + \dot{L}_{12} + \dot{L}_{13} + \dot{L}_{14} + \dot{L}_{15}$. where $L_{11} = J_1(z_1), L_{12} = \frac{1}{2}e_{i1}^{\top}e_{i1}, L_{13} = \frac{1}{2}tr\left\{\tilde{Z}_1^{\top}\tilde{Z}_1\right\}, L_{14} = \frac{1}{2}tr\{\tilde{W}_{c1}\tilde{W}_{c1}^{\top}\}, L_{15} = \frac{1}{2}tr\{\tilde{W}_{a1}\tilde{W}_{a1}^{\top}\}$.

Considering the first term of (51), we can write it as $\dot{J}_1(z_1) = \nabla J_1 \dot{z}_1$.

Substituting (3), (9) in (52) gives

$$\dot{J}_1(z_1) = (W_{c1}^{\top}\nabla\sigma_{c1} + \nabla\varepsilon_{c1})(\mathcal{F}_{s1}(z_1) + \mathcal{G}_{s1}(z_1)\alpha_1). \tag{53}$$

Substituting the value of α from (8) in (53) leads to

$$\dot{J}_1(z_1) = (W_{c1}^{\top}\nabla\sigma_{c1} + \nabla\varepsilon_{c1})\big(\mathcal{F}_{s1}(z_1) - \frac{1}{2}\mathcal{G}_{s1}(z_1)r^{-1}\hat{\mathcal{G}}_{s1}^{\top}(z_1)(\nabla\sigma_{c1}^{\top}\hat{W}_{c1})\big). \tag{54}$$

Using $\hat{W}_{c1} = W_{c1} - \tilde{W}_{c1}$ in (54), and simplifying, one will get

$$\dot{J}_1(z_1) = (W_{c1}^{\top}\nabla\sigma_{c1} + \nabla\varepsilon_{c1})\left(\mathcal{F}_{s1}(z_1) - \frac{1}{2}\mathcal{G}_{s1}(z_1)r^{-1}\mathcal{G}_{s1}^{\top}(z_1)\nabla\sigma_{c1}^{\top}(W_{c1} - \tilde{W}_{c1})\right) \tag{55}$$

Separating the terms in (55) w.r.t actual NN weights and the terms w.r.t weight estimation error gives

$$\begin{aligned}\dot{J}_1(z_1) &= W_{c1}^{\top}\nabla\sigma_{c1}\mathcal{F}_{s1}(z_1) - \frac{1}{2}W_{c1}^{\top}\nabla\sigma_{c1}\mathcal{G}_{s1}(z_1)r^{-1}\hat{\mathcal{G}}_{s1}^{\top}(z_1)\nabla\sigma_{c1}^{\top}W_{c1}\\ &+ \frac{1}{2}W_{c1}^{\top}\nabla\sigma_{c1}\mathcal{G}_{s1}(z_1)r^{-1}\hat{\mathcal{G}}_{s1}^{\top}(z_1)\nabla\sigma_{c1}^{\top}\tilde{W}_{c1} + \nabla\varepsilon_{c1}\mathcal{F}_{s1}(z_1)\\ &- \frac{\nabla\varepsilon_{c1}}{2}\mathcal{G}_{s1}(z_1)r^{-1}\hat{\mathcal{G}}_{s1}^{\top}(z_1)\nabla\sigma_{c1}^{\top}W_{c1} + \frac{\nabla\varepsilon_{c1}}{2}\mathcal{G}_{s1}(z_1)r^{-1}\hat{\mathcal{G}}_{s1}^{\top}(z_1)\nabla\sigma_{c1}^{\top}\tilde{W}_{c1}.\end{aligned} \tag{56}$$

Substituting $\hat{\mathcal{G}}_{s1} = \mathcal{G}_{s1} - \tilde{\mathcal{G}}_{s1}$ in (56) leads to

$$\begin{aligned}\dot{J}_1(z_1) &= W_{c1}^{\top}\nabla\sigma_{c1}\mathcal{F}_{s1}(z_1) - \frac{1}{2}W_{c1}^{\top}\nabla\sigma_{c1}\mathcal{G}_{s1}(z_1)r^{-1}(\mathcal{G}_{s1} - \tilde{\mathcal{G}}_{s1})^{\top}\nabla\sigma_{c1}^{\top}W_{c1} + \frac{1}{2}W_{c1}^{\top}\nabla\sigma_{c1}\mathcal{G}_{s1}(z_1)r^{-1}\\ &(\mathcal{G}_{s1} - \tilde{\mathcal{G}}_{s1})^{\top}\nabla\sigma_{c1}^{\top}\tilde{W}_{c1} + \nabla\varepsilon_{c1}\mathcal{F}_{s1}(z_1) - \frac{\nabla\varepsilon_{c1}}{2}\mathcal{G}_{s1}(z_1)r^{-1}(\mathcal{G}_{s1} - \tilde{\mathcal{G}}_{s1})^{\top}\nabla\sigma_{c1}^{\top}W_{c1}\\ &+ \frac{\nabla\varepsilon_{c1}}{2}\mathcal{G}_{s1}(z_1)r^{-1}(\mathcal{G}_{s1} - \tilde{\mathcal{G}}_{s1})^{\top}\nabla\sigma_{c1}^{\top}\tilde{W}_{c1}.\end{aligned} \tag{57}$$

One can further simplify (57), as follows

$$\begin{aligned}\dot{J}_1(z_1) = tr\{&W_{c1}^\top \nabla\sigma_{c1}\mathcal{F}_{s1}(z_1) - \frac{1}{2}W_{c1}^\top \nabla\sigma_{c1}\mathcal{G}_{s1}(z_1)r^{-1}\mathcal{G}_{s1}^\top \nabla\sigma_{c1}^\top W_{c1} \\ &+ \frac{1}{2}W_{c1}^\top \nabla\sigma_{c1}\mathcal{G}_{s1}(z_1)r^{-1}\mathcal{G}_{s1}^\top \nabla\sigma_{c1}^\top \tilde{W}_{c1} + \nabla\varepsilon_{c1}\mathcal{F}_{s1}(z_1) \\ &- \frac{\nabla\varepsilon_{c1}}{2}\mathcal{G}_{s1}(z_1)r^{-1}\mathcal{G}_{s1}^\top \nabla\sigma_{c1}^\top W_{c1} + \frac{\nabla\varepsilon_{c1}}{2}\mathcal{G}_{s1}(z_1)r^{-1}\mathcal{G}_{s1}^\top \nabla\sigma_{c1}^\top \tilde{W}_{c1} \\ &+ \frac{1}{2}W_{c1}^\top \nabla\sigma_{c1}\mathcal{G}_{s1}(z_1)r^{-1}\tilde{\mathcal{G}}_{s1}^\top \nabla\sigma_{c1}^\top W_{c1} - \frac{1}{2}W_{c1}^\top \nabla\sigma_{c1}\mathcal{G}_{s1}(z_1)r^{-1}\tilde{\mathcal{G}}_{s1}^\top \nabla\sigma_{c1}^\top \tilde{W}_{c1} \\ &+ \frac{\nabla\varepsilon_{c1}}{2}\mathcal{G}_{s1}(z_1)r^{-1}\tilde{\mathcal{G}}_{s1}^\top \nabla\sigma_{c1}^\top W_{c1} - \frac{\nabla\varepsilon_{c1}}{2}\mathcal{G}_{s1}(z_1)r^{-1}\tilde{\mathcal{G}}_{s1}^\top \nabla\sigma_{c1}^\top \tilde{W}_{c1}\}.\end{aligned} \tag{58}$$

Using (11), we have $W_{c1}^\top \nabla\sigma_{c1}\mathcal{F}_{s1}(z_1) - \frac{1}{2}W_{c1}^\top \nabla\sigma_{c1}\mathcal{G}_{s1}(z_1)r^{-1}\mathcal{G}_{s1}(z_1)W_{c1}\nabla\sigma_{c1} \leq -k\|z_1\|^2$. Additionally, it is also assumed that the effect of the NN approximation error in the system dynamics is bounded above, i.e., $\nabla\varepsilon_{c1}\mathcal{F}_{s1}(z_1) - \frac{1}{2}\nabla\varepsilon_{c1}\mathcal{G}_{s1}(z_1)r^{-1}\mathcal{G}_{s1}(z_1)W_{c1}\nabla\sigma_{c1} \leq -\bar{\epsilon}\|z_1\|^2$. One can write (58), as follows

$$\dot{J}_1(z_1) = -(k+\bar{\epsilon})z_1^2 + k_1\tilde{W}_{c1} + k_2\tilde{W}_{c1} + k_3\tilde{\mathcal{G}}_{s1} + k_4\tilde{\mathcal{G}}_{s1} + k_5\tilde{W}_{c1}\tilde{\mathcal{G}}_{s1} + k_6\tilde{W}_{c1}\tilde{\mathcal{G}}_{s1}. \tag{59}$$

which can be further written as

$$\dot{J}_1(z_1) = -\bar{k}_1 z_1^2 + \bar{k}_2\tilde{W}_{c1} + \bar{k}_3\tilde{\mathcal{G}}_{s1} + \bar{k}_4\tilde{W}_{c1}\tilde{\mathcal{G}}_{s1}, \tag{60}$$

where $\frac{1}{2}W_{c1}^\top \nabla\sigma\mathcal{G}_{s1}(z_1)r^{-1}\mathcal{G}_{s1}\nabla\sigma \leq k_1$, $\frac{\nabla\varepsilon_{c1}}{2}\mathcal{G}_{s1}(z_1)r^{-1}\mathcal{G}_{s1}\nabla\sigma \leq k_2$, $\frac{1}{2}W_{c1}^\top \nabla\sigma\mathcal{G}_{s1}(z_1)r^{-1}W\nabla\sigma \leq k_3$,

$\frac{\nabla\varepsilon_{c1}}{2}\mathcal{G}_{s1}(z_1)r^{-1}W_{c1}\nabla\sigma \leq k_4$, $\frac{1}{2}W_{c1}^\top \nabla\sigma\mathcal{G}_{s1}(z_1)r^{-1}\nabla\sigma \leq k_5$, $\frac{\nabla\varepsilon_{c1}}{c2}\mathcal{G}_{s1}(z_1)r^{-1}\nabla\sigma \leq k_6$. Consider the second and third term of (52)

$$\dot{L}_{12} + \dot{L}_{13} = tr\{e_{i1}^\top \dot{e}_{i1}\} + tr\{\tilde{Z}_1^\top \dot{\tilde{Z}}_1\} \tag{61}$$

On substituting the value of $\dot{e}_{i1}$ and $\dot{\tilde{Z}}_1$ from Theorem 1, one can write RHS of (83) as follows

$$tr\left\{e_{i1}^\top(-Ke_{i1} + \tilde{Z}_1\boldsymbol{\sigma}(\boldsymbol{\xi})\hat{\tilde{u}} + \varepsilon_I(z_1)) + \tilde{Z}_1^\top\left(-\alpha_v\tilde{Z}_1 - \boldsymbol{\sigma}(\boldsymbol{\xi})\hat{\tilde{u}}e_{i1}^\top + \alpha_v Z_1\right)\right\}. \tag{62}$$

which can be further simplified by using the cyclic property of traces as

$$tr\{e_{i1}^\top(-Ke_{i1} + \varepsilon_I(z_1)) + \tilde{Z}_1^\top\left(-\alpha_v\tilde{Z}_1 + \alpha_v Z_1\right)\}. \tag{63}$$

To simplify, we have

$$\dot{L}_{12} + \dot{L}_{13} \leq -K\|e_{i1}\|^2 - \alpha_v\|\tilde{Z}_1\|^2 + \|e_{i1}\|^2 + \|z_1\|^2 + \|\alpha_v\tilde{Z}_1^\top Z_1\| \tag{64}$$

Consider the fourth term of (52),

$$\dot{L}_{14} = tr\left\{\tilde{W}_{c1}^\top\left(\gamma_c\hat{\psi}_1(t)(-e_1(t) + \frac{1}{4}\hat{W}_{c1}^\top \nabla\sigma_{c1} \wedge \nabla\sigma_{c1}^\top\hat{W}_{c1} + \hat{W}_{c1}^\top \nabla\sigma_{c1}\mathcal{F}_{s1}) + \sigma_{11}\hat{W}_{c1}\right)\right\} \tag{65}$$

Therefore, one can further simplify (65) by using Young's inequality in cross-product terms as follows

$$\dot{L}_{14} \leq c_1\|\tilde{W}_{c1}\|^2 + c_2\|\tilde{W}_{c1}\| + c_3\|\tilde{Z}_1\|^2 + c_4\|\tilde{W}_{c1}\| - c_5\|\tilde{W}_{c1}\|^2 \tag{66}$$

Consider the fifth term of (52) $\dot{L}_{15} = tr\{\tilde{W}_{a1}^{\top}\dot{W}_{a1}\}$. On using the weight update law from Theorem 2, one can write

$$\dot{L}_{15} = tr\left\{\tilde{W}_{a1}^{\top}(\beta_a S_3(\beta_1 z_1 + \frac{1}{2}\hat{W}_{a1}^{\top}\sigma_{a1}(\bar{z}_1) - \frac{1}{2}r^{-1}\hat{\mathcal{G}}_{s1}^{\top}\nabla\sigma_{c1}^{\top}\hat{W}_{c1}) + \sigma_{22}\hat{W}_{a1})\right\} \tag{67}$$

Using $\tilde{W}_{c1} = W_{c1} - \hat{W}_{c1}$,$\tilde{W}_{a1} = W_{a1} - \hat{W}_{a1}$, $\tilde{G}_{s1} = \mathcal{G}_{s1} - \hat{\mathcal{G}}_{s1}$

$$\dot{L}_{15} = tr\left\{\tilde{W}_{a1}^{\top}(\beta_a S_3(\beta_1 z_1 + \frac{1}{2}(W_{a1} - \tilde{W}_{a1})^{\top}\sigma_{a1}(\bar{z}_1) - \frac{1}{2}r^{-1}(\mathcal{G}_{s1} - \tilde{\mathcal{G}}_{s1})^{\top}\nabla\sigma_{c1}^{\top}(W_{c1} - \tilde{W}_{c1}) + \sigma_{22}\tilde{W}_{a1}(W_{a1} - \tilde{W}_{a1})\right\} \tag{68}$$

Considering a last term, we can write

$$\tilde{W}_{a1}(W_{a1} - \tilde{W}_{a1}) = \tilde{W}_{a1}W_{a1} - \tilde{W}_{a1}^2$$

Using Young's inequality in the cross product terms, we can write

$$\dot{L}_{15} = c_5\|\tilde{W}_{a1}\|^2 + c_6\|z_1\|^2 + c_7\|\tilde{Z}_1\|^2 + c_8\|W_{c1}\|^2 + c_9\|\tilde{Z}_1\| + c_{10}\|\tilde{W}_{c1}\| + c_{11}\|\tilde{W}_{a1}\| - c_{12}\|\tilde{W}_{a1}\|^2 \tag{69}$$

Combining (60), (64),(66) and (69) and simplifying, we have

$$\dot{L}_1 \leq -\bar{c}_1\|z_1\|^2 + \bar{k}_2\|\tilde{W}_{c1}\| + \bar{k}_3\|\tilde{Z}_1\| - \bar{c}_2\|\tilde{W}_{c1}\|^2 - \bar{c}_3\|\tilde{Z}_1\|^2 - \bar{c}_5\|e_{i1}\|^2 + c_0\|\tilde{W}_{a1}\| - \bar{c}_4\|\tilde{W}_{a1}\|^2, \tag{70}$$

where $\bar{c}_1 = \bar{k}_1 - c_{13}, \bar{k}_1 > c_{13}, \bar{c}_2 = c_4 - \bar{k}_4, c_4 > \bar{k}_4, \bar{c}_3 = \alpha_v - k_4, \alpha_v > \bar{k}_4, \bar{c}_4 = c_{12} - c_5, c_{12} > c_5$. We can simplify it further as follows

$$\dot{L}_1 < -\bar{c}_1\|z_1\|^2 - \bar{c}_2(\|\tilde{W}_{c1}\| - \frac{\bar{k}_2}{\bar{c}_2})^2 - \bar{c}_3(\|\tilde{Z}_1\| - \frac{k_3}{\bar{c}_3})^2 - \bar{c}_4(\|\tilde{W}_{a1}\| - \frac{c_0}{\bar{c}_4})^2 - \bar{c}_5\|e_{i1}\|^2 + \bar{C}_{01}, \tag{71}$$

where $\bar{C}_{01} = \frac{k_2^2}{c_2} + \frac{k_3^2}{c_3} + \frac{c_0^2}{c_4}$. Therefore, we can write

$$\begin{cases} \|z_1\| > \sqrt{\frac{\bar{C}_{01}}{c_1}} or \|\tilde{W}_{c1}\| > \sqrt{\frac{\bar{C}_{01}}{c_2}} + \frac{k_2}{c_2} or \\ \|\tilde{W}_{a1}\| > \sqrt{\frac{\bar{C}_{01}}{c_4}} + \frac{c_0}{c_4} or \|\tilde{Z}_1\| > \sqrt{\frac{\bar{C}_{01}}{c_3}} + \frac{k_3}{c_3} or \|e_{i1}\| > \sqrt{\frac{\bar{C}_{01}}{c_5}}. \end{cases} \tag{72}$$

This demonstrates that the overall closed-loop system is bounded. Since $\tilde{G}$ is a function of the weight estimation error of the NN identifier, or $\tilde{Z}$, and from (72), $\tilde{Z}$ is bounded; as a consequence, $\hat{G}$ is bounded. From (72) $\tilde{W}$, identification error and system state are bounded. As a result, the control input error becomes bounded.

Step 2:

This is the final step. Consider the Lyapunov function as follows

$$L_2 = L_1 + J_2(z_2) + \frac{1}{2}e_{i2}^{\top}e_{i2} + \frac{1}{2}tr\left\{\tilde{Z}_2^{\top}\tilde{Z}_2\right\} + \frac{1}{2}tr\{\tilde{W}_{c2}\tilde{W}_{c2}^{\top}\} + \frac{1}{2}tr\{\tilde{W}_{a2}\tilde{W}_{a2}^{\top}\}. \tag{73}$$

The time derivative of L_2 is

$$\dot{L}_2 = \dot{L}_1 + \dot{J}_2(z_2) + tr\{e_{i2}^{\top}\dot{e}_{i2}\} + tr\{\tilde{Z}_2^{\top}\dot{\tilde{Z}}_2\} + tr\{\tilde{W}_{c2}^{\top}\dot{\tilde{W}}_{c2}\} + tr\{\tilde{W}_{a2}^{\top}\dot{\tilde{W}}_{a2}\}. \tag{74}$$

Let $\dot{L}_2 = L_1 + \dot{L}_{21} + \dot{L}_{22} + \dot{L}_{23} + \dot{L}_{24} + \dot{L}_{25}$. where $L_{21} = J_2(z_2), L_{22} = \frac{1}{2}e_{i2}^\top e_{i2}, L_{23} = \frac{1}{2}tr\left\{\tilde{Z}_2^\top \tilde{Z}_2\right\}, L_{24} = \frac{1}{2}tr\{\tilde{W}_{c2}\tilde{W}_{c2}^\top\}, L_{25} = \frac{1}{2}tr\{\tilde{W}_{a2}\tilde{W}_{a2}^\top\}$.

Considering the second term of (74), substituting (3) in $\dot{J}_2(z_2)$, it gives

$$\dot{J}_2(z_2) = (W_{c2}^\top \nabla\sigma_{c2} + \nabla\varepsilon_{c2})(\mathcal{F}_{s2}(z_2) + \mathcal{G}_{s2}(z_2)u). \tag{75}$$

which on further solving leads to

$$\dot{J}_2(z_2) = (W_{c2}^\top \nabla\sigma_{c2} + \nabla\varepsilon_{c2})(\mathcal{F}_{s2}(z_2) - \frac{1}{2}\mathcal{G}_{s2}(z_2)r_2^{-1}(\hat{\mathcal{G}}_{s2}^\top(z_2)(\nabla\sigma_{c2}^\top \hat{W}_{c2})). \tag{76}$$

Using $\hat{W}_{c2} = W_{c2} - \tilde{W}_{c2}$ in (76), and simplifying, one will get

$$\dot{J}_2(z_2) = (W_{c2}^\top \nabla\sigma_{c2} + \nabla\varepsilon_{c2})(\mathcal{F}_{s2}(z_2) - \frac{1}{2}\mathcal{G}_{s2}(z_2)r_2^{-1}\mathcal{G}_{s2}^\top(z_1)\nabla\sigma_{c2}^\top(W_{c2} - \tilde{W}_{c2})). \tag{77}$$

Separating the terms in (77) w.r.t actual NN weights and the terms w.r.t weight estimation error gives

$$\begin{aligned}\dot{J}_2(z_2) &= W_{c2}^\top \nabla\sigma_{c2}\mathcal{F}_{s2}(z_2) - \frac{1}{2}W_{c2}^\top \nabla\sigma_{c2}\mathcal{G}_{s2}(z_2)r_2^{-1}\hat{\mathcal{G}}_{s2}^\top(z_2)\nabla\sigma_{c2}^\top W_{c2} \\ &+ \frac{1}{2}W_{c2}^\top \nabla\sigma_{c2}\mathcal{G}_{s2}(z_2)r_2^{-1}\hat{\mathcal{G}}_{s2}^\top(z_2)\nabla\sigma_{c2}^\top \tilde{W}_{c2} + \nabla\varepsilon_{c2}\mathcal{F}_{s2}(z_2) \\ &- \frac{\nabla\varepsilon_{c2}}{2}\mathcal{G}_{s2}(z_2)r_2^{-1}\hat{\mathcal{G}}_{s2}^\top(z_2)\nabla\sigma_{c2}^\top W_{c2} + \frac{\nabla\varepsilon_{c2}}{2}\mathcal{G}_{s2}(z_2)r_2^{-1}\hat{\mathcal{G}}_{s2}^\top(z_2)\nabla\sigma_{c2}^\top \tilde{W}_{c2}.\end{aligned} \tag{78}$$

Substituting $\hat{\mathcal{G}}_{s2} = \mathcal{G}_{s2} - \tilde{\mathcal{G}}_{s2}$ in (78) leads to

$$\begin{aligned}\dot{J}_2(z_2) &= W_{c2}^\top \nabla\sigma_{c2}\mathcal{F}_{s2}(z_2) - \frac{1}{2}W_{c2}^\top \nabla\sigma_{c2}\mathcal{G}_{s2}(z_2)r_2^{-1}(\mathcal{G}_{s2} - \tilde{\mathcal{G}}_{s2})^\top \nabla\sigma_{c2}^\top W_{c2} \\ &+ \frac{1}{2}W_{c2}^\top \nabla\sigma_{c2}\mathcal{G}_{s2}(z_2)r_2^{-1}(\mathcal{G}_{s2} - \tilde{\mathcal{G}}_{s2})^\top \nabla\sigma_{c2}^\top \tilde{W}_{c2} + \nabla\varepsilon_{c2}\mathcal{F}_{s2}(z_2) - \frac{\nabla\varepsilon_{c2}}{2}\mathcal{G}_{s2}(z_2)r_2^{-1}(\mathcal{G}_{s2} - \tilde{\mathcal{G}}_{s2})^\top \nabla\sigma_{c2}^\top W_{c2} \\ &+ \frac{\nabla\varepsilon_{c2}}{2}\mathcal{G}_{s2}(z_2)r_2^{-1}(\mathcal{G}_{s2} - \tilde{\mathcal{G}}_{s2})^\top \nabla\sigma_{c2}^\top \tilde{W}_{c2}.\end{aligned} \tag{79}$$

One can further simplify (79), as follows

$$\begin{aligned}\dot{J}_2(z_2) &= tr\{W_{c2}^\top \nabla\sigma_{c2}\mathcal{F}_{s2}(z_2) - \frac{1}{2}W_{c2}^\top \nabla\sigma_{c2}\mathcal{G}_{s2}(z_2)r_2^{-1}\mathcal{G}_{s2}^\top \nabla\sigma_{c2}^\top W_{c2} \\ &+ \frac{1}{2}W_{c2}^\top \nabla\sigma_{c2}\mathcal{G}_{s2}(z_2)r_2^{-1}\mathcal{G}_{s2}^\top \nabla\sigma_{c2}^\top \tilde{W}_{c2} + \nabla\varepsilon_{c2}\mathcal{F}_{s2}(z_2) \\ &- \frac{\nabla\varepsilon_{c2}}{2}\mathcal{G}_{s2}(z_2)r_2^{-1}\mathcal{G}_{s2}^\top \nabla\sigma_{c2}^\top W_{c2} + \frac{\nabla\varepsilon_{c2}}{2}\mathcal{G}_{s2}(z_2)r_2^{-1}\mathcal{G}_{s2}^\top \nabla\sigma_{c2}^\top \tilde{W}_{c2} \\ &+ \frac{1}{2}W_{c2}^\top \nabla\sigma_{c2}\mathcal{G}_{s2}(z_2)r_2^{-1}\tilde{\mathcal{G}}_{s2}^\top \nabla\sigma_{c2}^\top W_{c2} - \frac{1}{2}W_{c2}^\top \nabla\sigma_{c2}\mathcal{G}_{s2}(z_2)r_2^{-1}\tilde{\mathcal{G}}_{s2}^\top \nabla\sigma_{c2}^\top \tilde{W}_{c2} \\ &+ \frac{\nabla\varepsilon_{c2}}{2}\mathcal{G}_{s2}(z_2)r_2^{-1}\tilde{\mathcal{G}}_{s2}^\top \nabla\sigma_{c2}^\top W_{c2} - \frac{\nabla\varepsilon_{c2}}{2}\mathcal{G}_{s2}(z_2)r_2^{-1}\tilde{\mathcal{G}}_{s2}^\top \nabla\sigma_{c2}^\top \tilde{W}_{c2}\}.\end{aligned} \tag{80}$$

Using (11), we have $W_{c2}^\top \nabla\sigma_{c2}\mathcal{F}_{s2}(z_2) - \frac{1}{2}W_{c2}^\top \nabla\sigma_{c2}\mathcal{G}_{s2}(z_2)r_2^{-1}\mathcal{G}_{s2}(z_2)W_{c2}\nabla\sigma_{c2} \leq -k\|z_2\|^2$. Additionally, it is also assumed that the effect of the NN approximation error in the system dynamics is bounded above, i.e., $\nabla\varepsilon_{c2}\mathcal{F}_{s2}(z_2) - \frac{1}{2}\nabla\varepsilon_{c2}\mathcal{G}_{s2}(z_2)r_2^{-1}\mathcal{G}_{s2}(z_2)W_{c2}\nabla\sigma_{c2} \leq -\bar{\epsilon}\|z_2\|^2$. One can write (80), as follows

$$\dot{J}_2(z_2) = -(k + \bar{\epsilon})z_2^2 + k_1\tilde{W}_{c2} + k_2\tilde{W}_{c2} + k_3\tilde{\mathcal{G}}_{s2} + k_4\tilde{\mathcal{G}}_{s2} + k_5\tilde{W}_{c2}\tilde{\mathcal{G}}_{s2} + k_6\tilde{W}_{c2}\tilde{\mathcal{G}}_{s2}. \tag{81}$$

which can be further written as

$$\dot{J}_2(z_2) = -\bar{k}_1 z_2^2 + \bar{k}_2 \tilde{W}_{c2} + \bar{k}_3 \tilde{\mathcal{G}}_{s2} + \bar{k}_4 \tilde{W}_{c2} \tilde{\mathcal{G}}_{s2}, \tag{82}$$

where $\frac{1}{2} W_{c2}^{\top} \nabla\sigma \mathcal{G}_{s2}(z_2) r_2^{-1} \mathcal{G}_{s2} \nabla\sigma \leq k_1$, $\frac{\nabla\varepsilon}{2} \mathcal{G}_{s2}(z_2) r_2^{-1} \mathcal{G}_{s2} \nabla\sigma \leq k_2$, $\frac{1}{2} W_{c2}^{\top} \nabla\sigma \mathcal{G}_{s2}(z_2) r_2^{-1} W_{c2} \nabla\sigma \leq k_3$, $\frac{\nabla\varepsilon}{2} \mathcal{G}_{s2}(z_2) r_2^{-1} W_{c2} \nabla\sigma \leq k_4$, $\frac{1}{2} W_{c2}^{\top} \nabla\sigma \mathcal{G}_{s2}(z_2) r_2^{-1} \nabla\sigma \leq k_5$, $\frac{\nabla\varepsilon}{2} \mathcal{G}_{s2}(z_2) r_2^{-1} \nabla\sigma \leq k_6$.

Consider the second and third term of (52)

$$\dot{L}_{22} + \dot{L}_{23} = tr\{e_{i2}^{\top} \dot{e}_{i2}\} + tr\{\tilde{Z}_2^{\top} \dot{\tilde{Z}}_2\} \tag{83}$$

On substituting the value of $\dot{e}_{i2}$ and $\dot{\tilde{Z}}_2$ from Theorem 1, one can write (83) as follows

$$\dot{L}_{22} + \dot{L}_{23} = tr\left\{ e_{i2}^{\top}(-K e_{i2} + \tilde{Z}_2 \boldsymbol{\sigma}(\boldsymbol{\xi}) \hat{\dot{u}} + \varepsilon_I(\zeta)) + \tilde{Z}_2^{\top} \left(-\alpha_v \tilde{Z}_2 - \boldsymbol{\sigma}(\boldsymbol{\xi}) \hat{\dot{u}} e_{i2}^{\top} + \alpha_v Z_2 \right) \right\}. \tag{84}$$

which can be further simplified by using the cyclic property of traces as

$$\dot{L}_{22} + \dot{L}_{23} = tr\{e_{i2}^{\top}(-K e_{i2} + \varepsilon_I(\zeta)) + \tilde{Z}_2^{\top} \left(-\alpha_v \tilde{Z}_2 + \alpha_v Z_2 \right)\}. \tag{85}$$

To simplify, we have $\varepsilon_I^2(z_2) \leq \|z_2\|^2$. Therefore, on using Young's inequality in $e_{i2} z_2$, we have

$$\dot{L}_{22} + \dot{L}_{23} \leq -K\|e_{i2}\|^2 - \alpha_v \|\tilde{Z}_2\|^2 + \|e_{i2}\|^2 + \|z_2\|^2 + \alpha_v \|\tilde{Z}_2^{\top} Z_2\| \tag{86}$$

Consider the fourth term of (52),

$$\dot{L}_{24} = tr\left\{ \tilde{W}_{c2}^{\top} \left(\gamma_c \hat{\psi}_2(t)(-e_2(t) + \frac{1}{4} \hat{W}_{c2}^{\top} \nabla\sigma_{c2} \wedge \nabla\sigma_{c2}^{\top} \hat{W}_{c2} + \hat{W}_{c2}^{\top} \nabla\sigma_{c2} \mathcal{F}_{s2}) + \sigma_{21} \hat{W}_{c2} \right) \right\} \tag{87}$$

Therefore, one can further simplify (87) by using Young's inequality in cross-product terms as follows

$$\dot{L}_{24} \leq c_1 \|\tilde{W}_{c2}\|^2 + c_2 \|\tilde{W}_{c2}\| + c_3 \|\tilde{Z}_2\|^2 + c_4 \|\tilde{W}_{c2}\| - c_5 \|\tilde{W}_{c2}\|^2 \tag{88}$$

Consider the fifth term of (52) $\dot{L}_{25} = tr\{\tilde{W}_{a2}^{\top} \dot{W}_{a2}\}$. On using the weight update law from Theorem 2, one can write

$$\dot{L}_{25} = tr\left\{ \tilde{W}_{a2}^{\top} (\beta_a S_3(\beta_1 z_2 + \frac{1}{2} \hat{W}_{a2}^{\top} \sigma_{a2}(\bar{z}_2) - \frac{1}{2} r_2^{-1} \hat{\mathcal{G}}_{s2}^{\top} \nabla\sigma_{c2}^{\top} \hat{W}_{c2}) + \sigma_{22} \hat{W}_{a2}) \right\} \tag{89}$$

Using $\tilde{W}_{c2} = W_{c2} - \hat{W}_{c2}$, $\tilde{W}_{a2} = W_{a2} - \hat{W}_{a2}$, $\tilde{\mathcal{G}}_{s2} = \mathcal{G}_{s2} - \hat{\mathcal{G}}_{s2}$

$$\dot{L}_{25} = tr\left\{ \tilde{W}_{a2}^{\top} (\beta_a S_3(\beta_1 z_2 + \frac{1}{2} (W_{a2} - \tilde{W}_{a2})^{\top} \sigma_{a2}(\bar{z}_2) - \frac{1}{2} r_2^{-1} (\mathcal{G}_{s2} - \tilde{\mathcal{G}}_{s2})^{\top} \nabla\sigma_{c2}^{\top} (W_{c2} - \tilde{W}_{c2}) + \sigma_{22} \tilde{W}_{a2} (W_{a2} - \tilde{W}_{a2}) \right\} \tag{90}$$

Considering a last term, we can write

$$\tilde{W}_{a2}(W_{a2} - \tilde{W}_{a2}) \leq \|\tilde{W}_{a2} W_{a2}\| - \|\tilde{W}_{a2}\|^2$$

Using Young's inequality in the cross product terms, we can write

$$\dot{L}_{25} \leq c_5\|\tilde{W}_{a2}\|^2 + c_6\|z_2\|^2 + c_7\|\tilde{Z}_2\|^2 + c_8\|W_{c2}\|^2 + c_9\|\tilde{Z}_2\| + c_{10}\|\tilde{W}_{c2}\| + c_{21}\|\tilde{W}_{a2}\| - c_{22}\|\tilde{W}_{a2}\|^2 \tag{91}$$

Combining (82), (86),(88) and (91) and simplifying, we have

$$\begin{aligned}\dot{L} \leq & -c_{z1}(\|z_1\| - \frac{k_{11}}{c_{z1}})^2 - c_{z2}(\|z_2\| - \frac{k_{21}}{c_{z2}})^2 \\ & - C_{c1}(\|\tilde{W}_{c1}\| - \frac{k_{12}}{C_{c1}})^2 - C_{c2}(\|\tilde{W}_{c2}\| - \frac{k_{22}}{C_{c2}})^2 \\ & - C_{a1}(\|\tilde{W}_{a1}\| - \frac{k_{13}}{C_{a1}})^2 - C_{a2}(\|\tilde{W}_{a2}\| - \frac{k_{23}}{C_{a2}})^2 \\ & - C_{f1}(\|\tilde{W}_{f1}\| - \frac{k_{f1}}{C_{f1}})^2 - C_{f2}(\|\tilde{W}_{f2}\| - \frac{k_{f2}}{C_{f2}})^2 + \bar{C}_{02},\end{aligned} \tag{92}$$

where $\bar{C}_{02} = \frac{k_{11}^2}{c_{z1}} + \frac{k_{21}^2}{c_{z2}} + \frac{k_{12}^2}{C_{c1}} + \frac{k_{13}^2}{C_{a1}} + \frac{k_{23}^2}{C_{a2}} + \frac{k_{f1}^2}{C_{f1}} + \frac{k_{f2}^2}{C_{f2}}$. Therefore, from (92), the bounds for $\|z_k\|, \|\tilde{W}_{ck}\|, \|\tilde{W}_{ak}\|, \|\tilde{W}_{fk}\|$ can be obtained as

$$\begin{cases} \|z_1\| > \sqrt{\frac{\bar{C}_{01}}{c_{z1}}} + \frac{k_{11}}{c_{zk}} \quad or \|z_2\| > \sqrt{\frac{\bar{C}_{02}}{c_{z2}}} + \frac{k_{21}}{c_{z2}} or \\ \|\tilde{W}_{c1}\| > \sqrt{\frac{\bar{C}_{01}}{C_{c1}}} + \frac{k_{12}}{C_{c1}} or \|\tilde{W}_{c2}\| > \sqrt{\frac{\bar{C}_{02}}{C_{c2}}} + \frac{k_{22}}{C_{c2}} or \\ \|\tilde{W}_{a1}\| > \sqrt{\frac{\bar{C}_{01}}{C_{a1}}} + \frac{k_{13}}{C_{a1}} or \|\tilde{W}_{a2}\| > \sqrt{\frac{\bar{C}_{02}}{C_{a2}}} + \frac{k_{23}}{C_{a2}} \\ or \|\tilde{W}_{f1}\| > \sqrt{\frac{\bar{C}_{01}}{C_{f1}}} + \frac{k_{f1}}{C_{f1}} or \|\tilde{W}_{f2}\| > \sqrt{\frac{\bar{C}_{02}}{C_{f2}}} + \frac{k_{f2}}{C_{f2}}. \end{cases} \tag{93}$$

This demonstrates that the overall closed-loop system is bounded. Since $\tilde{\mathcal{G}}_{sj}$ is a function of the weight estimation error of the NN identifier, or $\tilde{Z}_j$, and from (93), $\tilde{Z}_j$ is bounded; as a consequence, $\hat{\mathcal{G}}_{sj}$ is bounded. From (93) $\tilde{W}_{aj}, \tilde{W}_{cj}$, identification error and system state are bounded. As a result, the control input error $u_{ej} = -\beta_j z_j - \frac{1}{2}\hat{W}_{aj}\sigma_{aj}(z_j) + \frac{1}{2}r_j^{-1}\mathcal{G}_{sj}\frac{dJ_j}{dz_j}$ becomes bounded with bound e_b which can be obtained by using the bounds from (93) and Assumption 4. Therefore, the actual control inputs are bounded close to their optimal values.

Proof of Theorem 2

The convergence of weights for Task 1 remains in alignment with Theorem 1. For Task 2, an additional term emerges in the Lyapunov proof (92) due to the regularization penalty, denoted as

$$\gamma_{\text{pen1}_j} = \tilde{W}_j(\hat{W}_j - {W_{A_j}}^*), \tag{94}$$

where ${W_{A_j}}^*$ is indicative of the optimized weights for the primary task, as verified to be bounded in Theorem 1.

Substituting $\hat{W}_j = W_j^* - \tilde{W}_j$, we can rearrange equation (94) to

$$\tilde{W}_j W_j^* - \tilde{W}_j^2 - \tilde{W}_j {W_{A_j}}^* \leq \|\tilde{W}_j\|\|W_j^*\| - \|\tilde{W}_j\|^2 + \|\tilde{W}_j W_{A_j}^*\|. \tag{95}$$

Employing Young's inequality to the first and third terms of (95), we get

$$\|\tilde{W}_j\|\|W_j^*\| \leq \frac{\|\tilde{W}_j\|^2}{2} + \frac{\|W_j^*\|^2}{2},$$
$$\|\tilde{W}_j W_{A_j}^*\| \leq \frac{\|\tilde{W}_j\|^2}{2} + \frac{\|W_{A_j}^*\|^2}{2}.$$

Substituting $\|\tilde{W}_j\|\|W_j^*\|, \|\tilde{W}_j W_{A_j}^*\|$ back into (95) provides

$$\tilde{W}_j W_j^* - \tilde{W}_j^2 - \tilde{W}_j {W_{A_j}}^* \leq \frac{\|W_{A_j}^*\|^2}{2} + \frac{\|W_j^*\|^2}{2}. \tag{96}$$

Thus, the integration of this term into the proof solely modifies the error bound to $\gamma_{\text{pen}_j} \leq \frac{\|W_j^*\|^2}{2} + \frac{\|W_{A_j}^*\|^2}{2}$, without impacting the overarching stability of the system.

The aggregate contribution to the error bounds is calculated by adding γ_{penj_j} to (92), resulting in a comprehensive error bound $C_j = \bar{C}_{0j} + \gamma_{\text{penj}_j}$. It is, therefore, clear from the derived equations that the error bounds experience an increase as the weights deviate from their optimal points; however, the comprehensive stability of the system remains intact.

Li *et al. Complex Eng Syst* 2024;4:5
DOI: 10.20517/ces.2023.38

Complex Engineering Systems

Research Article

Open Access

Command filter-based adaptive neural tracking control of nonlinear systems with multiple actuator constraints and disturbances

Yinguang Li, Jianhua Zhang, Yang Li

School of Information and Control Engineering, Qingdao University of Technology, Qingdao 266520, Shandong, China.

Correspondence to: Dr. Jianhua Zhang, School of Information and Control Engineering, Qingdao University of Technology, No. 777, East Jialingjiang Road, Huangdao District, Qingdao 266520, Shandong, China. E-mail: Jianhuazhang@qut.edu.cn

How to cite this article: Li Y, Zhang J, Li Y. Command filter-based adaptive neural tracking control of nonlinear systems with multiple actuator constraints and disturbances. *Complex Eng Syst* 2024;4:5. http://dx.doi.org/10.20517/ces.2023.38

Received: 16 Oct 2023 **First Decision:** 7 Dec 2023 **Revised:** 5 Jan 2024 **Accepted:** 15 Jan 2024 **Published:** 21 Feb 2024

Academic Editors: Yurong Liu, Hamid Reza Karimi **Copy Editor:** Fangling Lan **Production Editor:** Fangling Lan

Abstract

In this paper, the adaptive practical finite-time tracking control problem for a class of strictly feedback nonlinear systems with multiple actuator constraints is investigated using backstepping techniques and practical finite-time stability theory. The effects of deadband and saturated nonlinear constraints on the controller design of nonlinear systems are addressed by the equivalent transformation method. The problem of complexity explosion due to the derivatives of virtual control signals is solved by using the virtual control signals as inputs to the command filters and using the outputs of the command filters to perform the corresponding control tasks. An adaptive neural network tracking backstepping control strategy based on the command filter technique and the backstepping design algorithm is proposed by approximating an unknown nonlinear function using a neural network. The control strategy ensures the boundedness of all variables in the closed-loop system, and the output tracking error fluctuates in a small region near the origin. Finally, simulations verify the effectiveness of the control strategy designed in this paper.

Keywords: Nonlinear systems, actuator constraint, command filtering, neural network, adaptive

1. INTRODUCTION

The control theory of nonlinear systems has been widely developed in the past two decades, and how to design controllers that are more reasonable and meaningful for nonlinear systems has gradually become an active

© The Author(s) 2024. **Open Access** This article is licensed under a Creative Commons Attribution 4.0 International License (https://creativecommons.org/licenses/by/4.0/), which permits unrestricted use, sharing, adaptation, distribution and reproduction in any medium or format, for any purpose, even commercially, as long as you give appropriate credit to the original author(s) and the source, provide a link to the Creative Commons license, and indicate if changes were made.

topic, such as the design of tracking control for nonlinear systems[1–4]. The backstepping method is a practical approach to nonlinear control problems and was proposed by Kanellakopoulos *et al.* at the end of the last century[5]. Combining the backstepping method with the fuzzy or neural adaptive technique yields an effective control tool for solving uncertain nonlinear systems[6]. Due to the Characteristics of the adaptive backstepping method, it is possible to achieve asymptotic sedimentation of nonlinear systems and guarantee boundedness of the signal under parameter uncertainty, which has led to many fruitful results[7–9]. The adaptive neural fault-tolerant decentralized tracking control problem for switching stochastic uncertain nonlinear systems has been studied in the literature[10]. The article[11] investigates the design of discounted iterative adaptive critic for tracking control of affine nonlinear systems by introducing a new cost function. The authors[12] investigate the output consensus control of heterogeneous multiagent systems (MASs) by designing a distributed adaptive observer for each follower and introducing an additional tracking error observer. The article[13] deals with the attitude and vibration problems of flexible spacecraft simultaneously by proposing a novel adaptive control strategy. In the literature[14], adaptive tracking control of nonlinear systems with unknown input constraints and unpredictable variables is studied. In the literature[15], a controller design strategy based on separation of variables is designed for non-strict feedback nonlinear systems. The neural adaptive FTC technique allows the controlled system to achieve good tracking performance in finite time, and the whole variables of the closed-loop system are bounded[16]. The article[17] addresses the problem of finite-time control of non-triangular uncertain stochastic nonlinear systems. The authors[18] investigate adaptive finite-time control for nonlinear systems with input quantization and full-state constraints.

Although the fuzzy/neural adaptive inversion algorithm is one of the most general methods for controller design of nonlinear systems and has solved many problems in the field of control[19]. However, it should be noted that since the virtual control inputs in the controller design process need to be differentiated and iterated repeatedly, the design of controllers for nonlinear systems using adaptive inversion algorithms will become more and more computationally intensive along with the increase in the order of the system, a phenomenon we refer to as "complexity explosion"[20]. In order to solve the defect of "complexity explosion" of traditional backstepping algorithms, two methods of dynamic surface control (DSC)[21] and command filter backstepping control[22] have emerged. However, as DSC ignores the errors introduced by the filter, it affects the control accuracy of the controlled system[23]. Since then, the backstepping command filtering method has been combined with the adaptive technique to achieve significant results in eliminating the filter errors[24,25]. The article[26] investigates the work on life prediction of lithium-ion batteries using adaptive techniques and filtering methods. In this article, the problem of tracking control of uncertain higher-order nonlinear systems with input saturation is investigated based on the command filtering technique[27].

Compared with asymptotic sedimentation methods, finite-time control methods have the advantages of fast convergence, high accuracy, good performance, and robustness to uncertainty and have achieved fruitful results[28]. In practical engineering applications, nonlinear problems, such as hysteresis, deadband, saturation, and external disturbances, often occur. Deadband and saturation, as non-smooth functions, have a large impact on system control performance. Therefore, special attention should be paid to the controller design process of nonlinear systems. Li *et al.* combined the obstacle Lyapunov function with an adaptive backstepping control method to solve a FTC problem for nonlinear systems with dead zones[29]. In recent years, many effective results have emerged for nonlinear systems with different input constraints[30,31]. However, to our knowledge, few research results use a combination of neural adaption and command filtering to solve simultaneous input deadband, saturation, and nonlinear disturbances. Therefore, it is an interesting task to study finite-time stabilized controllers for nonlinear systems with simultaneous multiple input constraints and Nonlinear disturbances.

In summary, it can be seen that external disturbances and the presence of input constraints on the actuator

can have a significant impact on system control performance and safety, especially in control processes, such as Mars drones far from Earth and chemical reactions with major safety incidents. Therefore, in this paper, for a class of uncertain nonlinear systems with multiple actuator constraints and external disturbances, a practical adaptive neural network (NN) FTC method is designed to reduce the effects of actuators and disturbances on the tracking performance of the system. Compared with the current research results, the main contributions can be summarized as follows:

1: In this paper, the problem of adaptive NN backstepping control for nonlinear systems with multiple actuator constraints and external disturbances is investigated by combining neural adaptive and command filtering techniques. Under the combined influence of multiple actuator constraints and external disturbances, the controller design task is accomplished, and good tracking control performance is achieved.

2: The use of command filtering and compensation mechanisms solves the complexity explosion problem while eliminating the effect of filtering errors. Deadband and saturation are grouped into one model, simplifying the difficult problem of designing controllers under multiple constraints.

3: With the control method used in this paper, all signals of the controlled system are bounded, which meets the realistic requirements of the actual physical control process, and the output tracking error can be quickly converged to within a bounded and adjustable tight set in finite time.

The rest of this paper is described below. Section 2 provides an introduction to the problem description and preparatory knowledge. Section 3 presents the controller design and stability analysis of the adaptive NN tracking control. Section 4 gives the numerical simulations and the result analysis. Finally, Section 5 analyzes and concludes the paper.

2. PROBLEM FORMULATION AND PRELIMINARIES

In this section, the system model and NN and preparatory knowledge are described. For convenience, the following notations are used in this paper. $|*|$ represents the absolute value of $*$. $y^{(j)}$ is the j-order differentiation of y. x^T denotes the transpose of matrix x. R^n and $R^{n\times n}$ denote the n-dimensional Euclidean space and the real $n \times n$-matrix spaces, respectively. Ω_Z represents the compact set.

2.1. System model

Consider the following strictly feedback nonlinear system [32].

$$\begin{cases} \dot{x}_i = x_{i+1} + f_i(\bar{x}_i) + d_i(t), 1 \le i \le n-1, \\ \dot{x}_n = u(t) + f_n(\bar{x}_n) + d_n(t), \\ y = x_1 \end{cases} \tag{1}$$

in which $\bar{x}_i = [x_1(t), \ldots, x_i(t)]^T \in R^n, i = 1, \ldots, n$ expresses the system state variables, and y indicates the system output; $f_i(\bar{x}), i = 1, \ldots, n$ displays the unknown smooth nonlinear functions. $d_i(t)$ represents unknown bounded external interference with $x_{i+1} + f_i(x) \neq 0$. $u(t)$ represents control inputs subject to nonlinearities of multiple actuator constraints and is described as

$$u = m(v)v + \pi(v) \tag{2}$$

where v represents the input signal for dead zone and saturation nonlinear models. Select l_+, l_-, u_+, u_- as positive design constants, and $u_H > 0 and u_L > 0$ denote the normal number to be designed. $m(v)$ called the dead zone slope, and $m(v), \pi(v)$ are expressed by

$$m(v) = \begin{cases} \frac{u_H}{v}, v > u_H \\ l_+, \ u_+ < v < u_H \\ l_+, \ -u_- < v < u_+ \\ l_-, \ -u_L < v < u_- \\ -\frac{u_L}{v}, v < -u_L \end{cases} \tag{3}$$

$$\pi(v) = \begin{cases} 0, v > u_H \\ -l_+u_+, u_+ < v < u_H \\ -l_+v, \ -u_- < v < u_+ \\ -l_-u_-, -u_L < v < u_- \\ 0, v < -u_L \end{cases} \tag{4}$$

2.2. Mathematical preparation

The objective of this paper is to design a new finite-time tracking control algorithm for nonlinear systems with tight feedback so that the system output can trace the wanted trajectory signal in finite time and all the variables of the considered system are well bounded, so the below assumptions and lemmas are implemented without loss of generality.

Assumption 1: [33] The positive and negative slopes of the dead zone and saturation nonlinear models are equal; i.e., $l_+ = l_- = l$. Dead-zone parameters of the controller, u_+, u_-, and l, are bounded; that is, there are known parameters $u_{+\max}, u_{-\max}$, and $l_{\max}$ that $|u_+| < u_{+\max}, |u_-| < u_{-\max}$, and $|l| < l_{\max}$.

Remark 1: In real production process environments, special requirements are usually imposed on the inputs to the system actuators, such as controlling the maximum amplitude of the inputs within a certain range and avoiding fluctuations near zero as much as possible in order to minimize the consumption. Deadband and saturation constraints are direct manifestations of the above problems in real physical systems. In order to place limits on the control inputs and retain the control capability of the controller, the parameters associated with the deadband and saturation models must be bounded; otherwise, the controller will lose its control capability. For example, if u_+, u_- is infinite, the control input is always in the dead zone, and the ability to control is disabled. From Assumption 1, It is not difficult to obtain that $\pi(v)$ is bounded, and $|\pi(v)| \leq D$, in which D represents the upper limit value.

Assumption 2: [34] The anticipated tracking trace signal y_d and its first derivative considered in this paper are continuous and bounded.

Remark 2: Consider the actual situation; the control input signal v cannot be infinite. Therefore, consider that $m(v)$ satisfies the following inequality

$$0 < \gamma \leq \min\left\{\frac{u_H}{v_{\max}}, l\right\} \leq m(v) \leq \max\{1, l\} \tag{5}$$

in which $v_{\max}$ represents the maximum value of the designed controller.

Lemma 1:[35] In this paper, RBF NNs will be utilized to approximate unknown nonlinear functions. For a continuous function $h(Z)$, there exists that

$$h_i(Z) = \phi_i{}^T R_i(x) + \delta_i(x) \tag{6}$$

where $Z \in \Omega_Z \subset R^{\mathrm{n}}$ denotes the input vector, $\phi = [\phi_1, \phi_2, \ldots, \phi_m]^T \subset R^m$ expresses the ideal weight vectors, in which $m > 1$ is the NN node number. $\delta(x)$ indicates the approaching error, and $R(Z) = [R_1(Z), R_2(Z), \ldots, R_m(Z)]^T$ represents the vectors of RBF basis functions.

Lemma 2:[36] The filters used in this paper are described as follows

$$\begin{cases} \dot{\omega}_i = \omega_\tau \omega_{i,2} \\ \dot{\omega}_{i,2} = -2\varsigma\omega_\tau\omega_{i,2} - \omega_\tau(\dot{\omega}_i - \alpha_{i-1}) \end{cases} \tag{7}$$

where $\varsigma \in (0, 1]$ and $\omega_\tau > 0$ indicate positive filter parameters. Consider Virtual Controller α_{i-1} and ω_i as input and output of the filter, respectively, in which $\omega_i(0) = \alpha_{i-1}(0), \omega_{i,2}(0) = 0$.

Remark 3: In the process of designing a controller using the backstepping method, the computational burden of the controller design increases dramatically with the system scale due to the repeated differentiation of the virtual control inputs. In order to overcome this complexity explosion, this paper uses the command filtering technique to perform filtering operations on the virtual control signals in order to eliminate the repetitive differentiation of the virtual control signals. The virtual control signal is used as the input to the command filter, and a good filtered output signal can be obtained by adjusting the ω_τ and ς parameters. In order to demonstrate the effect of the command filter parameters on the filtered output, the output of the command filter is plotted compared to the trajectory of the input signal using the following three different sets of filter parameters (1) ω_1 ($\omega_\tau = 60, \varsigma = 0.85$); (2) ω_2 ($\omega_\tau = 20, \varsigma = 0.85$); (3) ω_3 ($\omega_\tau = 60, \varsigma = 0.2$), which are displayed in Figure 1. Figure 1 illustrates the filtered output traces corresponding to different filter parameters. It can be seen that parameter ω_τ affects the tracking error of the filtered output, and parameter ς affects the tracking performance in the pre-period.

Lemma 3:[37] For any positive constants b_1, b_2, b_3 and real variables x, y, the below inequality holds

$$|x|^{b_1}|y|^{b_2} \le \frac{b_1}{b_1 + b_2} b_3 |x|^{b_1+b_2} + \frac{b_2}{b_1 + b_2} b_3^{-\frac{b_1}{b_2}} |y|^{b_1+b_2} \tag{8}$$

Lemma 4:[38] Consider a dynamic system $\dot{x} = f(x, u), x(t_0) = x_0$, in which $f : R^n \to R^n$ represents a smooth mapping. If there exists a Radically unbounded and deterministic positive scalar function $V(x), \mu_1 > 0, \mu_1 > 0$ and $0 < q < 1, 0 < \delta < \infty$ such that

$$\dot{V}(x, t) \le -\mu_1 V(x) - \mu_2 V^q(x) + \delta \tag{9}$$

Then, the output of this system $\dot{x} = f(x, u)$ is practical finite-time stable, and the set of residuals of the system solution is shown below

$$\lim_{t\to T_r} V(x) \leq \min\left\{\frac{\sigma}{(1-\varphi)\alpha}, \left(\frac{\sigma}{(1-\varphi)\beta}\right)^{\frac{1}{q}}\right\} \tag{10}$$

in which $\varphi \in (0,1)$. Then, one can obtain the settling time bounded by

$$\begin{aligned} T_r \leq \max\Bigg\{ & t_0 + \frac{1}{\varphi\mu_1(1-q)} \ln \frac{\varphi\mu_1 V^{1-q}(t_0) + \mu_2}{\mu_2}, \\ & t_0 + \frac{1}{\mu_1(1-q)} \ln \frac{\mu_1 V^{1-q}(t_0) + \varphi\mu_2}{\varphi\mu_2} \Bigg\} \end{aligned} \tag{11}$$

Remark 4: The above Lemma 4 gives a practical finite-time stability criterion for nonlinear systems. Next, this paper will use Lemma 4 as a basis for designing command-filtered adaptive NN tracking controllers for strict-feedback nonlinear systems with dead-zone and saturation constraints.

3. CONTROLLER DESIGN AND STABILITY ANALYSIS

3.1. Finite-time controller design

In this subsection, an adaptive NN controller will be designed for system 1 by backstepping algorithms. The controller will handle both the tracking performance of the system and the boundedness of the variables. Moreover, the complexity explosion of the classical backstepping algorithm is conquered by the command filtering method. The controller consists of some basic stages, and the design is built on the following coordinate transformation

$$\begin{cases} z_1 = x_1 - y_d \\ z_i = x_i - \omega_i \end{cases} \tag{12}$$

in which y_d expresses the desired reference trajectory signal, and ω_i with $i = 2, 3, \ldots, n$ represents the introduced command filter variable.

Remark 5: Note that the command filter will increase the operational burden of the actuator due to the error defect introduced. To address this drawback, a compensation signal will be designed to compensate for the tracking error $(\omega_i - \alpha_{i-1})$ incurred by the command filter.

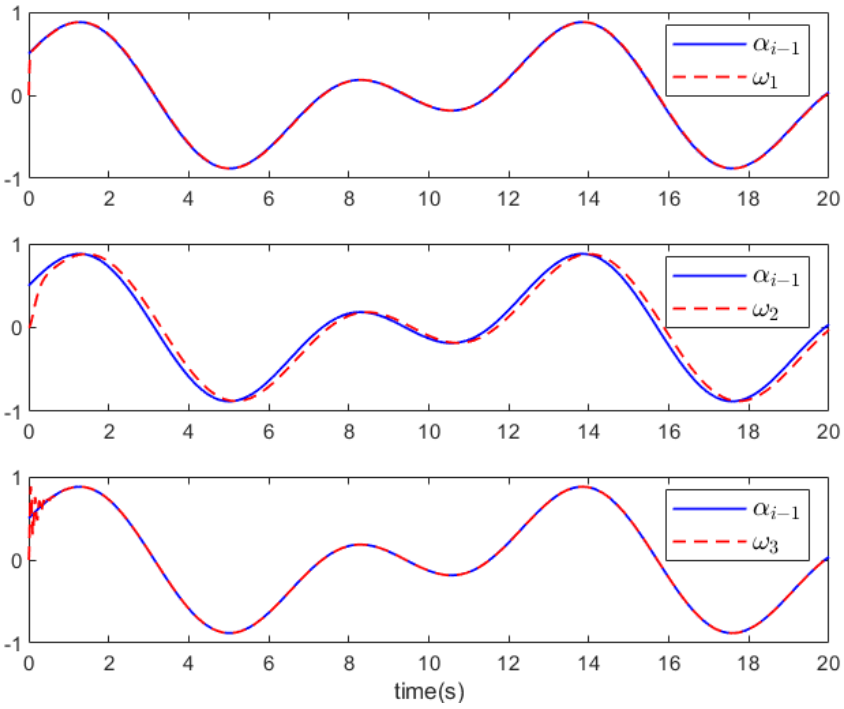


Figure 1. Command filter output.

In addition, in order to reduce the computation of controller design, the following compensation tracking error is constructed based on the idea of coordinate transformation:

$$\xi_i = z_i - r_i, i = 1, \ldots, n \tag{13}$$

where r_i indicates the compensated signal.

Step 1: With the aid of (1), (12), and (13), the following equation can be obtained

$$\dot{\xi}_1 = \xi_2 + r_2 + \omega_2 + f_1 + d_1 - \dot{y}_d - \dot{r}_1 \tag{14}$$

Select a Lyapunov function V_1 as

$$V_1 = \frac{1}{2}\xi_1^2 + \frac{1}{2\lambda_1}\tilde{\theta}_1^2 \tag{15}$$

where $\lambda_1 = 2\rho_1/(2\rho_1 - 1), \rho_1 > 1/2$ denotes the parameters to be constructed. $\tilde{\theta}_1 = \theta_1 - \hat{\theta}_1$, in which $\hat{\theta}_1$ denotes the estimate of the uncertain parameter θ_1.

Taking the time derivative of V_1, for $\forall q \in \left(\frac{1}{2}, 1\right)$, it follows that

$$\dot{V}_1 = \xi_1(-k_{1,2}\xi_1^{2q-1} + \xi_2 + r_2 + \omega_2 + h_1(Z_1) - \dot{r}_1 - \dot{y}_d) - \frac{1}{\lambda_1}\tilde{\theta}_1\dot{\hat{\theta}}_1 \tag{16}$$

where $h_1(Z_1) = f_1 + d_1 + k_{1,2}\xi_1^{2q-1}$ is not available for feedback due to the existence of unknown nonlinear functions. Then, $h_1(Z_1)$ will be approximated by RBF NNs as

$$h_1(Z_1) = {\phi_1}^{*T} R_1(x) + \delta_1(x), , \quad |\delta_1(\zeta_1)| \leq \varepsilon_1 \tag{17}$$

where $Z_1 = [x_1, y_d, \dot{y}_d]^T$, and $\delta_1(Z_1)$ represents the estimate error, with arbitrary constants $\varepsilon_1 > 0$. Applying Young's inequality, it produces

$$\xi_1 h_1(Z_1) \leq \frac{1}{2a_1^2}\xi_1^2\theta_1 R_1^T R_1 + \frac{a_1^2}{2} + \frac{1}{2}\xi_1^2 + \frac{1}{2}\varepsilon_1^2 \tag{18}$$

where $\theta_1 = \left\|\phi_1^*\right\|^2, a_1 > 0$.

Next, the virtual controller is introduced as α_1, and a compensating signal r_1 is designed as

$$\alpha_1 = -k_{1,1}z_1 - \frac{1}{2a_1^2}\xi_1\hat{\theta}_1 R_1^T R_1 - \frac{1}{2}\xi_1 + \dot{y}_d \tag{19}$$

$$\dot{r}_1 = -k_{1,1}r_1 + r_2 + \omega_2 - \alpha_1 \tag{20}$$

where $k_{1,1}$ indicates a parameter to be built.

With the aid of (17)–(20), the following inequality holds

$$\dot{V}_1 \leq -k_{1,1}\xi_1^2 - k_{1,2}\xi_1^{2q} + \frac{\tilde{\theta}_1}{\lambda_1}\left(\frac{\lambda_1}{2a_1^2}\xi_1^2 R_1^T R_1 - \dot{\hat{\theta}}_1\right) + \xi_1\xi_2 + \frac{1}{2}a_1^2 + \frac{1}{2}\varepsilon_1^2 \tag{21}$$

Then, building an adaptive law $\dot{\hat{\theta}}_1$ as

$$\dot{\hat{\theta}}_1 = \frac{\lambda_1}{2a_1^2}\xi_1^2 R_1^T R_1 - \eta_1\hat{\theta}_1 \tag{22}$$

Thus, on the basis of the above equation, the following inequality holds

$$\dot{V}_1 \leq -k_{1,1}\xi_1^2 - k_{1,2}\xi_1^{2q} + \frac{\eta_1}{\lambda_1}\tilde{\theta}_1\hat{\theta}_1 + \xi_1\xi_2 + \frac{1}{2}a_1^2 + \frac{1}{2}\varepsilon_1^2 \tag{23}$$

Step i: With the aid of (1), (12), and (13), similar to step 1 as

$$\dot{\xi}_i = \xi_{i+1} + r_{i+1} + \omega_{i+1} + f_i + d_i - \dot{\omega}_i - \dot{r}_i \tag{24}$$

Select a Lyapunov function V_i as

$$V_i = V_{i-1} + \frac{1}{2}\xi_i^2 + \frac{1}{2\lambda_i}\tilde{\theta}_i^2 \tag{25}$$

where $\lambda_i = 2\rho_i/(2\rho_i - 1), \rho_i > 1/2$ represents a parameter to be constructed.

Then, similarly to step 1, the following inequality holds

$$\begin{aligned}\dot{V}_i \leq & -\sum_{j=1}^{i-1} k_{j,1}\xi_1^2 - \sum_{j=1}^{i-1} k_{j,2}\xi_1^{2q} + \sum_{j=1}^{i-1}\frac{\eta_j}{\lambda_j}\tilde{\theta}_j\hat{\theta}_j + \xi_i(\xi_{i-1} - k_{i,2}\xi_i^{2q-1} + \xi_{i+1} + r_{i+1} + \omega_{i+1} \\ & + h_i(Z_i) - \dot{r}_i - \dot{\omega}_i) - \frac{1}{\lambda_i}\tilde{\theta}_i\dot{\hat{\theta}}_i - \frac{1}{2}\xi_i^2 + \frac{1}{2}\sum_{j=1}^{i-1}(a_j^2 + \varepsilon_j^2)\end{aligned} \tag{26}$$

in which $h_i(Z_i) = f_i + d_i + k_{i,2}\xi_i^{2q-1} - \xi_{i-1}$. Similarly, there exists NNs and $\forall\varepsilon_i > 0$. Consequently, $h_i(Z_i) = \phi_i^{*T} R_i(x) + \delta_i(x)$ with $|\delta_i(Z_i)| \leq \varepsilon_i$.

Combining Young's inequality, the following inequality holds

$$\xi_i h_i(Z_i) \leq \frac{1}{2a_i^2}\xi_i^2\theta_i R_i^T R_i + \frac{a_i^2}{2} + \frac{1}{2}\xi_i^2 + \frac{1}{2}\varepsilon_i^2 \tag{27}$$

where $\theta_i = \left\|\phi_i^*\right\|^2, a_i > 0$.

Next, the virtual controller is introduced as α_1, and the compensating signal is constructed as $\dot{r}_1$, along with the adaptive law $\dot{\hat{\theta}}_i$, as follows:

$$\alpha_i = -k_{i,1}z_i - \frac{1}{2}\xi_i - \frac{1}{2a_i^2}\xi_i\hat{\theta}_i R_i^T R_i + \dot{\omega}_i \tag{28}$$

$$\dot{r}_i = -k_{i,1}r_i + r_{i+1} + \omega_{i+1} - \alpha_i \tag{29}$$

$$\dot{\hat{\theta}}_i = \frac{\lambda_i}{2a_i^2}\xi_i^2 R_i^T R_i - \eta_i\hat{\theta}_i \tag{30}$$

where $k_{i,1}$ indicates a normal number to be constructed. With the help of (27)–(30), the following inequality holds

$$\dot{V}_i \leq -\sum_{j=1}^{i} k_{j,1}\xi_1^2 - \sum_{j=1}^{i} k_{j,2}\xi_1^{2q} + \sum_{j=1}^{i}\frac{\eta_j}{\lambda_j}\tilde{\theta}_j\hat{\theta}_j + \frac{1}{2}\sum_{j=1}^{i}(a_j^2 + \varepsilon_j^2) + \xi_i\xi_{i+1} \tag{31}$$

Step n: With the aid of (1), (12), and (13), one can get the derivative of ξ_n as

$$\dot{\xi}_n = u(t) + f_n - \dot{\omega}_n - \dot{r}_n + d_n = m(v) + \pi(v) + f_n + d_n - \dot{\omega}_n - \dot{r}_n \tag{32}$$

Select a Lyapunov function V_n as

$$V_n = V_{n-1} + \frac{1}{2}\xi_n^2 + \frac{1}{2\lambda_n}\tilde{\theta}_n^2 \tag{33}$$

Then, we obtain the $\dot{V}_i$ by (32) and (33) as:

$$\begin{aligned}\dot{V}_i \leq -\sum_{j=1}^{n-1} k_{j,1}\xi_1^2 - \sum_{j=1}^{n-1} k_{j,2}\xi_1^{2q} + \sum_{j=1}^{n-1}\frac{\eta_j}{\lambda_j}\tilde{\theta}_j\hat{\theta}_j + \xi_n(\xi_{n-1} - k_{n,2}\xi_n^{2q-1} + m(v)v + \pi(v) + h_n(Z_n) \\ - \dot{\omega}_n - \dot{r}_n) - \frac{1}{\lambda_n}\tilde{\theta}_n\dot{\hat{\theta}}_n - \frac{1}{2}\xi_n^2 + \frac{1}{2}\sum_{j=1}^{n-1}(a_j^2 + \varepsilon_j^2)\end{aligned} \tag{34}$$

where $h_n(Z_n) = f_n + d_n + k_{n,2}\xi_n^{2q-1} - \xi_{n-1}$. Similar to (17) and (27), we can get

$$\xi_n h_n(Z_n) \leq \frac{1}{2a_n^2}\xi_n^2\theta_n R_n^T R_n + \frac{a_n^2}{2} + \frac{1}{2}\xi_n^2 + \frac{1}{2}\varepsilon_n^2 \tag{35}$$

$$\xi_n\pi(v) \leq \frac{1}{2}\xi_n^2 + \frac{1}{2}D^2 \tag{36}$$

where $|\pi(v)| < D$.

Now, as obtained from Remark 2, the actual control signal v, compensation signal $\dot{r}_n$, and adaptive law $\dot{\hat{\theta}}_n$ can be constructed as follows:

$$v = \frac{1}{\gamma}(-k_{n,1}z_n - \xi_n - \frac{1}{2a_n^2}\xi_n\hat{\theta}_n R_n^T R_n + \dot{\omega}_n) \tag{37}$$

$$\dot{r}_n = -k_{n,1}r_n \tag{38}$$

$$\dot{\hat{\theta}}_n = \frac{\lambda_n}{2a_n^2}\xi_n^2 R_n^T R_n - \eta_n\hat{\theta}_n \tag{39}$$

where $k_{n,1}$ indicates a normal number to be constructed. With the help of (35)–(39), the following inequality holds

$$\dot{V}_n \leq -\sum_{j=1}^{n} k_{j,1}\xi_1^2 - \sum_{j=1}^{n} k_{j,2}\xi_1^{2q} + \sum_{j=1}^{n}\frac{\eta_j}{\lambda_j}\tilde{\theta}_j\hat{\theta}_j + \frac{1}{2}\sum_{j=1}^{n}(a_j^2 + \varepsilon_j^2) + \frac{1}{2}D^2 \tag{40}$$

Algorithm 1 Proposed Control Algorithm

Initialize: $i = 1$, selecting the desired trajectory signal y_d
while $i \leq n$ **do**
  Choose the Lyapunov function V_i and derive it to obtain the derivative $\dot{V}_i$.
  Approximating the nonlinear function in $\dot{V}_i$ using RBF NNs.
  Constructing the virtual controller α_i or the final actual controller v.
  while $i < n$ **do**
    Take the virtual control signal α_{i-1} into the command filter to get the filtered output signal ω_i.
  end while
  Construct the compensation signal $\dot{r}_i$, which compensates for the filtering error due to the command filter.
  Choose the adaptive laws $\dot{\hat{\theta}}_i$.
end while
return α_i, v, $\dot{r}_i$, $\dot{\hat{\theta}}_i$.

3.2. Stability analysis

Now, after the above n-step controller design, the controller construction has been completed. This section will be concluded by the following theorem.

Theorem 1: For the uncertain nonlinear system (1) that meets the conditions of Assumptions 1 and 2, under adopting the controller (19), (28), (37) and the adaptive law (30), the controlled system is practically finite-time stable, and the signals of the system are bounded almost surely.

Proof: Recalling the definition $\tilde{\theta}_1 = \theta_1 - \hat{\theta}_1$, for any $\rho_j > 1/2$, the following inequality can be obtained

$$\tilde{\theta}_j\hat{\theta}_j \leq \frac{\rho_i}{2}\theta_j^2 - \frac{1}{\lambda_j}\tilde{\theta}_j^2 \tag{41}$$

With the aid of (41), yields

$$\begin{aligned}\dot{V}_n \leq & -\sum_{j=1}^{n} k_{j,1}\xi_1^2 - \sum_{j=1}^{n} k_{j,2}\xi_1^{2q} - \sum_{j=1}^{n}\frac{\eta_j}{2\lambda_j}\tilde{\theta}_j^2 - \sum_{j=1}^{n}\frac{\eta_j}{2\lambda_j}\tilde{\theta}_j^2 + \frac{1}{2}\sum_{j=1}^{n}(a_j^2+\varepsilon_j^2+\rho_j\eta_j\theta_j^2) + \frac{1}{2}D^2 \\ = & -a\sum_{j=1}^{n}\frac{1}{2}\xi_j^2 - a(\sum_{j=1}^{n}\frac{1}{2}\xi_j^2)^q - a\sum_{j=1}^{n}\frac{\tilde{\theta}_j^2}{2\lambda_j} - a(\sum_{j=1}^{n}\frac{\tilde{\theta}_j^2}{2\lambda_j})^q + \sum_{j=1}^{n}\eta_j(\frac{\tilde{\theta}_j^2}{2\lambda_j})^q - \sum_{j=1}^{n}\frac{\eta_j}{2\lambda_j}\tilde{\theta}_j^2 \\ & + \frac{1}{2}\sum_{j=1}^{n}(a_j^2+\varepsilon_j^2+\rho_j\eta_j\theta_j^2) + \frac{1}{2}D^2\end{aligned} \tag{42}$$

where $a = \min\left\{2k_{j,1}, 2^q k_{j,2}, \eta_j, j = 1, \ldots, n\right\}$.

By applying Lemma 3, the following equation can be obtained

$$(\sum_{j=1}^{n}\frac{1}{2\lambda_j}\tilde{\theta}_j^2)^q \leq \sum_{j=1}^{n}\frac{1}{2\lambda_j}\tilde{\theta}_j^2 + (1-q)q^{\frac{q}{1-q}} \tag{43}$$

where $x = 1, y = \sum_{j=1}^{n}\frac{1}{2\lambda_j}\tilde{\theta}_j^2, b_1 = \frac{1}{4}, b_2 = \frac{3}{4}$.

With the aid of (41)-(43), the following equation can be obtained

$$\dot{V}_n \leq -\alpha V_n - \beta V_n^q + \delta_1 \tag{44}$$

in which $\alpha = \beta = a, \delta_1 = \frac{1}{2}\sum_{j=1}^{n}(a_j^2+\varepsilon_j^2+\rho_j\eta_j\theta_j^2) + \frac{1}{2}D^2 + (1-q)q^{\frac{q}{1-q}}$.

By using the formulation of Theorem 4, it can be easily obtained that the system (1) considered in this paper is practically finite-time stable and converges to the following compact set

$$\xi_i \in \min\left\{V(x) \leq \frac{\delta_1}{(1-\varphi)\alpha}, (\frac{\delta_1}{(1-\varphi)\beta})^{\frac{1}{q}}\right\} \tag{45}$$

where $\varphi \in (0,1)$. Then, the upper limit of the settling time can be expressed as

$$\begin{aligned}T \leq T_r = \max\Bigg\{ & t_0 + \frac{1}{\varphi\alpha(1-q)}\ln\frac{\varphi\alpha V^{1-q}(t_0)+\beta}{\beta}, \\ & t_0 + \frac{1}{\alpha(1-q)}\ln\frac{\alpha V^{1-q}(t_0)+\varphi\beta}{\varphi\beta}\Bigg\}\end{aligned} \tag{46}$$

Since the boundedness of the error $\xi_i = z_i - r_i$ is closely related to z_i and r_i. Therefore, in order to obtain the convergence of z_i, the boundedness of r_i has to be considered. To demonstrate the convergence of the error compensation system, the Lyapunov function is constructed as follows

$$V_r = \frac{1}{2}\sum_{j=1}^{n} r_j^2 \tag{47}$$

According to (20), (29), and (38), the derivative of V_r is obtained as

$$\dot{V}_r = r_1\left(-k_{1,1}r_1 + r_2 + (\omega_2 - \alpha_1)\right) + r_2\left(-k_{2,1}r_2 + r_3 + (\omega_3 - \alpha_2)\right) + \cdots + r_n\left(-k_{n,1}r_n\right) \tag{48}$$

Based on Young's inequality, it yields

$$r_j r_{j+1} \leq \frac{1}{2} r_j^2 + \frac{1}{2} r_{j+1}^2 \tag{49}$$

$$r_j \left(\omega_{j+1} - \alpha_j\right) \leq \frac{1}{2\eta} r_j^2 + \frac{\eta}{2} H_j^2 \tag{50}$$

where η is a positive constant, and H satisfies $\left|\omega_{j+1} - \alpha_j\right| \leq H_j$. Substituting (49) and (50) into (48) yields

$$\dot{V}_r \leq -\sum_{j=1}^{n} \kappa r_j^2 + \frac{n-1}{2} \eta H^2 \leq -\frac{\kappa}{2} V_r^2 + \frac{n-1}{2} \eta H^2 \tag{51}$$

in which $\kappa = \min\left\{k_{j,1} - \frac{1}{2} - \frac{1}{2\eta}\right\}$, $H = \max\left\{\sqrt{\eta} H_j\right\}$. Thus, from Gronwall's Lemma, it follows that

$$0 \leq V_r \leq \left(V_r(0) - \frac{(n-1)\eta H^2}{\kappa}\right) e^{-\frac{\kappa}{2} t} + \frac{(n-1)\eta H^2}{\kappa} \tag{52}$$

From the above discussion, it can be concluded that ξ_i, $\tilde{\theta}_i$, and r_i are bounded. Because $\hat{\theta}_i$ denotes the estimate of the uncertain parameter θ_i and $\tilde{\theta} = \theta - \hat{\theta}$, one has $\hat{\theta}_i$ is bounded. From the definition of the compensation error $\xi_i = z_i - r_i$, it follows that z_i is bounded. From (19) and (28), it follows that α_i are bounded because they are composed of $z_i, \xi_i, \hat{\theta}_i$. Since α_i is bounded, ω_i must also be bounded. Thus, by the definition of the tracking error $z_i = x_i - \omega_i$, x_i is also bounded. The boundedness of the controller can be deduced, too. Thus, we prove the boundedness of all closed-loop signals of the system.

By the above description, it is proven to be completed. For a clearer understanding of the controller designed in this paper and to facilitate the simulation design in the next section, the adaptive NN command filtering control algorithm scheme is shown in Figure 2 and Algorithm 1. □

4. SIMULATION

In the above formulation of the paper, the research work has been completed. In this section, the simulation verification of the designed finite-time controller will be done using matlab.

Example 1: The following second-order nonlinear system is used as the simulation object:

$$\begin{cases} \dot{x}_1 = (1 + 0.1\cos(x_1))x_2 + x_1 x_2^2 + d_1(t) \\ \dot{x}_2 = u + x_2^2 \sin(x_1) + d_2(t) \\ y = x_1 \end{cases} \tag{53}$$

where $d_1(t) = 0.1\sin(0.1t)$,$d_2(t) = 0.1\sin(0.5t)$. The desired trajectory tracking signal is $y_d = 0.5\sin(1.5t)$, and the control objective is to utilize a controller u designed to enable the input to track the expected target path y_d.

The relationship between the actual input signal u and the actual control signal v of the system is defined as follows

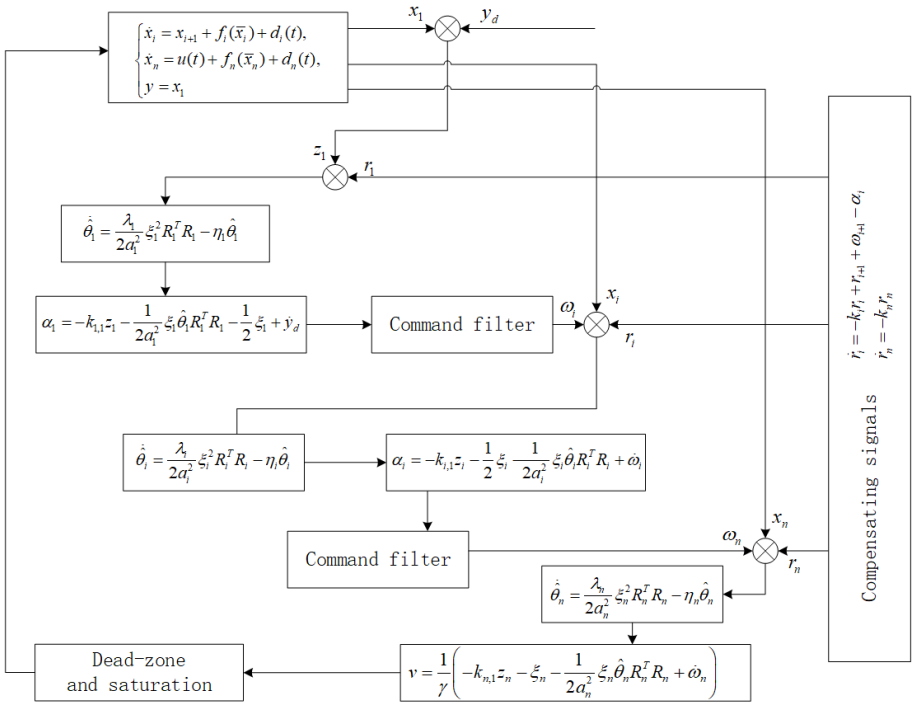


Figure 2. The block diagram of the control scheme.

$$u = \begin{cases} 20, & v > 20 \\ 0.6(v - 0.6), & 0.6 < v < 20 \\ 0, & -0.6 < v < 0.6 \\ 0.6(v + 0.6), & -20 < v < -0.6 \\ -20, & v < -20 \end{cases} \tag{54}$$

The control law, the adaptive law, and its related parameters are designed as follows: $k_1 = 10$, $k_2 = 15$, $a_1 = a_2 = 10$, $\gamma = 1$, $\omega_\tau = 60$, $\varsigma = 0.85$, $\lambda_1 = 0.5$, $\lambda_2 = 0.1$, $\eta_1 = 1$, $\eta_2 = 0.8$. The initial states and updating laws are selected as $[x_1(0), x_2(0)]^T = [0.3, 0.5]^T$, $\left[\hat{\theta}_1(0), \hat{\theta}_2(0)\right]^T = [0.2, 0.3]^T$.

Since RBF NNs have excellent approximation performance, they are often used as approximate models for unknown nonlinearities. In the present study, the RBF NNs are used to approximate the unknown nonlinear term $h(Z)$. The following Gaussian function is chosen as the basis function of RBF NNs, and its expression as

$$R_i(Z) = \exp\left(-\frac{(Z - c_i)^T (Z - c_i)}{2}\right) \tag{55}$$

where $i = 1, 2, \ldots, 8$, The distribution interval of the center c_i of the Gaussian function is [-1,1].

The simulation results in this example are presented in Figure 3, Figure 4, and Figure 5. Figure 4A illustrates the trajectory of the system output and reference signals. To demonstrate the effectiveness of the controller designed in this paper, the control strategy from the literature[38] is used as a comparison to plot its system

Table 1. Example 2 Parameters of a single-link robotic arm system

Parameter	Description	Value
J	torsion coefficient	$0.5\ \mathrm{kg}\cdot\mathrm{m}^2$
M	mess of the link	1 kg
g	acceleration of gravity	$9.8\ \mathrm{m/s}^2$
l_0	length of the connecting rod	1 m
B	coefficient of friction	$0.5\ \mathrm{N/m}^2$

output tracking curve as trajectory y_c in Figure 4A. From Figure 4A, it can be seen that the control strategy designed in this paper using command filters has better tracking performance than the control strategy in the literature[38] using DSC. Figure 4B demonstrates the tracking error trajectory plots of the control strategy and the comparison control scheme in this paper. It is obvious from Figure 4 that the command filtered adaptive controller designed in this paper has better tracking performance and smaller tracking errors.

Figure 3A illustrates the trajectory of the controller signals and control inputs. After the dead zone and saturated nonlinear constraints, the amplitude of the control input becomes smaller and the input curve becomes smoother, which meets the actual needs of the real physical system. Figure 3B illustrates the trajectory of the adaptive parameters $\hat{\theta}_1, \hat{\theta}_2$. Figure 5A depicts the trajectory of the system state x_2 and the command filter output ω_2. As can be seen in Figure 5A, the command filter output avoids the computational complexity of virtual control signal derivation while completely replacing the virtual controller. The compensation signal is used to compensate for the filtering error introduced due to the command filter, the trajectory of which is depicted in Figure 5B.

Example 2: In this section, a single-link manipulator system containing stochastic perturbations is used as an example to demonstrate the effectiveness and practicality of the designed controller. The single-link manipulator system schematic is exhibited in Figure 6A. The single-link manipulator system dynamic model[39] is given as:

$$J\ddot{q} = -Mgl_0\sin(q) - B\dot{q} + u(v) \tag{56}$$

in which q, $\dot{q}$, and $\ddot{q}$ are the coordinates, velocity, and acceleration of angles, respectively. $u(v)$ is the input torque subject to saturation and deadband. Table 1 lists all the parameters of the single-link manipulator system.

We can rewrite the system (56) as follows:

$$\begin{cases} \dot{x}_1 = x_2 \\ \dot{x}_2 = 2u(v) - 19.6\sin(x_1) - x_2 - d(t) \\ y = x_1 \end{cases} \tag{57}$$

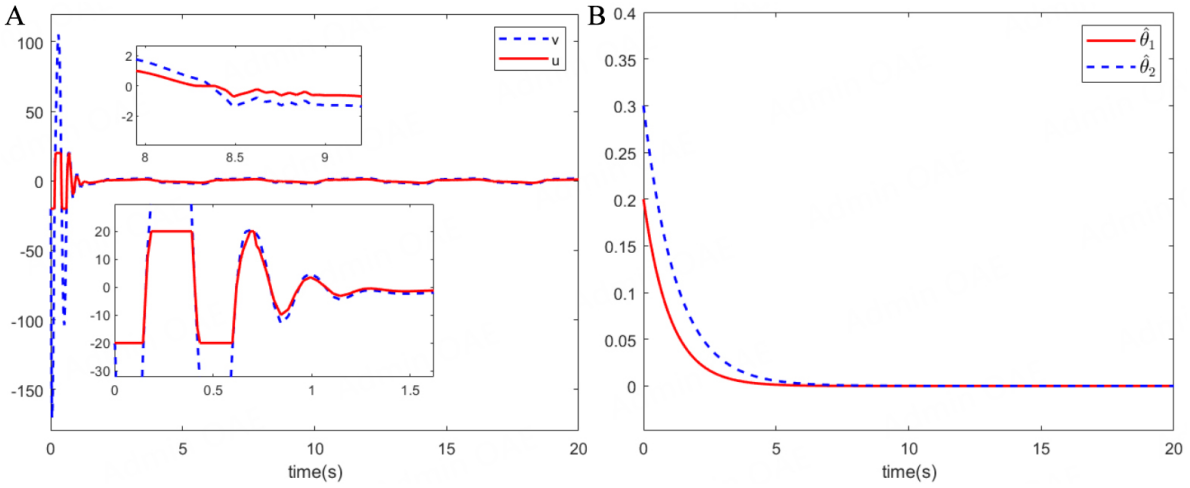


Figure 3. (A) Control input. (B) adaptive parameters.

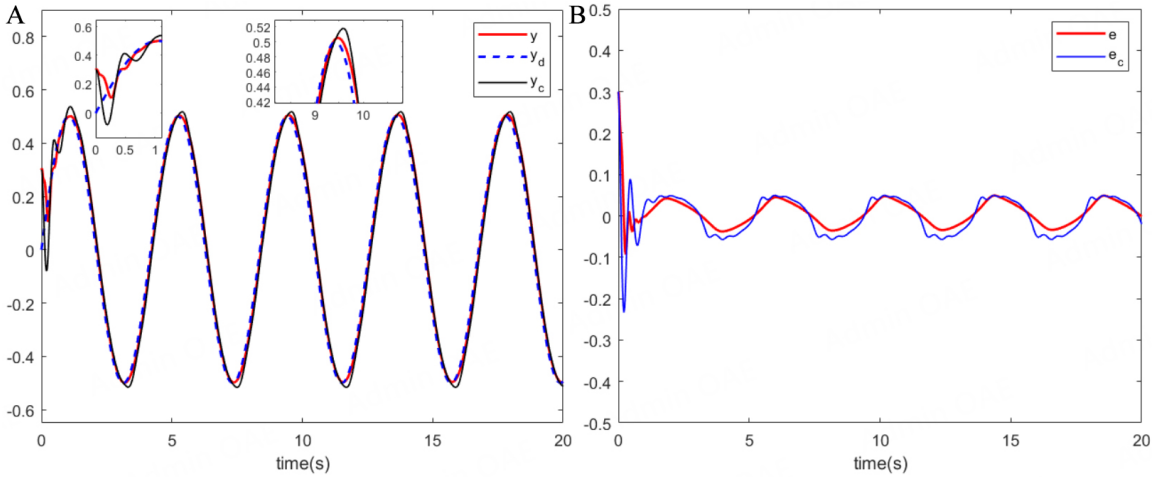


Figure 4. (A) System output and desired trajectory. (B) tracking error.

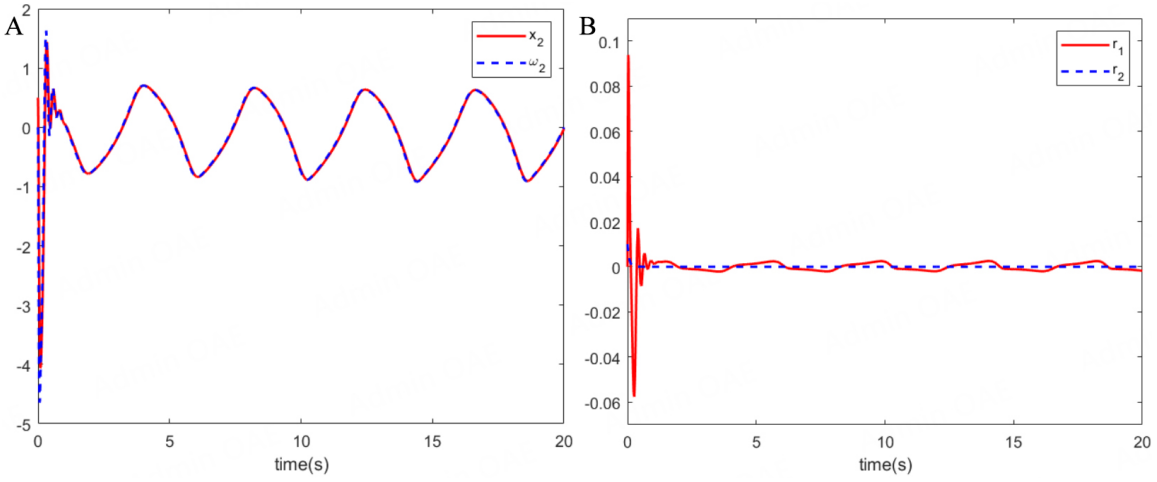


Figure 5. (A) State variable x_2 and filter output ω_2. (B) compensatory signal.

where $d(t)$ is a bounded white noise signal, which is exhibited in Figure 6B. The desired trajectory tracking signal is $y_d = 0.5\sin(t)+0.5\sin(0.5t)$. The dead zone and saturation nonlinear models are described as follows

$$u = \begin{cases} 10, & v \geq 10 \\ 0.85(v-0.6), & 0.5 < v < 10 \\ 0, & -0.5 < v < 0.5 \\ 0.85(v+0.6), & -10 < v < -0.5 \\ -10, & v \leq -10 \end{cases} \tag{58}$$

The control law, the adaptive law, and its related parameters are designed as follows: $k_1 = 15$, $k_2 = 15$, $a_1 = a_2 = 10$, $\gamma = 1$, $\omega_\tau = 60$, $\varsigma = 0.85$, $\lambda_1 = 0.5$, $\lambda_2 = 0.2$, $\eta_1 = 1$, $\eta_2 = 0.8$. The initial states and updating laws are selected as $[x_1(0), x_2(0)]^T = [0.3, 0.5]^T$,$\left[\hat{\theta}_1(0), \hat{\theta}_2(0)\right]^T = [0.15, 0.08]^T$.

The simulation results in this example are presented in Figure 6, Figure 7, and Figure 8. Figure 7A displays the trajectory of the system output and reference signals for the control scheme in this paper and the control strategy in the literature[38]. The tracking errors of the control strategies in this paper and the comparative literature are plotted in Figure 7B. Figure 7 demonstrates that the control strategy, using command filters and compensation mechanisms in this paper, has better tracking performance and smaller tracking errors. Figure 8A demonstrates the controller trajectory and the trajectory of the control input, from which it is clear that after the deadband and saturation constraints, the control input amplitude is greatly reduced while ensuring good tracking performance.

In order to demonstrate the robustness and stability of the adaptive NN tracking control algorithm proposed in this paper, perturbations $d(t) = 1.5\sin(5t)$ are added to the control input signal u. Figure 9 gives a comparison of the trajectories of the control input signal and the system output for additional disturbances and no disturbances. From the figure, it can be seen that the adaptive NN controller designed in this paper has good robustness and stability.

From the simulation results shown in this section, it is easy to see that by applying the finite-time NN tracking controller designed in this paper and choosing appropriate parameters, the system can obtain good tracking performance when all signals are bounded and the actual control inputs satisfy the deadband and saturation constraints, and the use of command filters and compensation mechanisms overcomes the problem of exploding computational complexity due to the derivation of the virtual control signals, which proves the practicability and validity of the controller we designed.

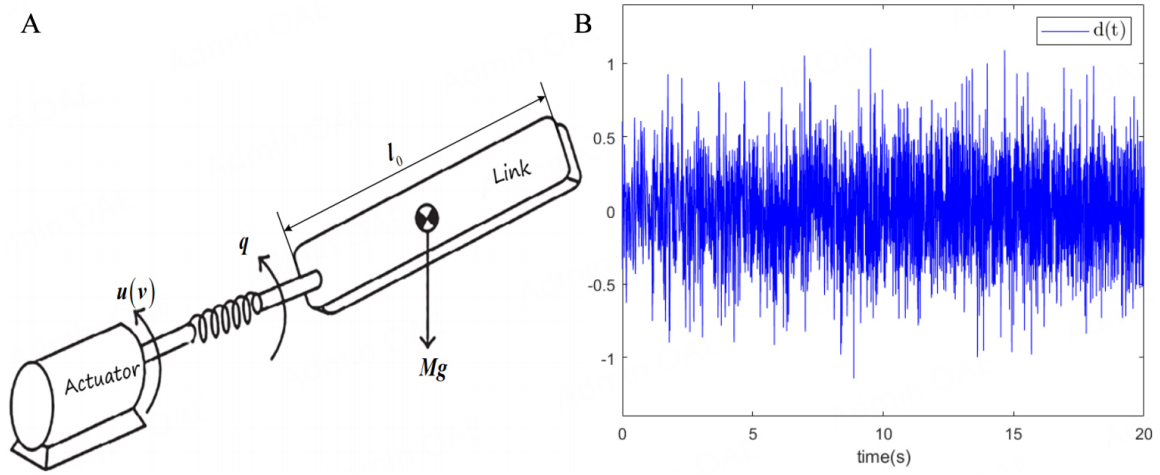


Figure 6. Example 2: (A) Single-link manipulator. (B) curves of bounded interference signals.

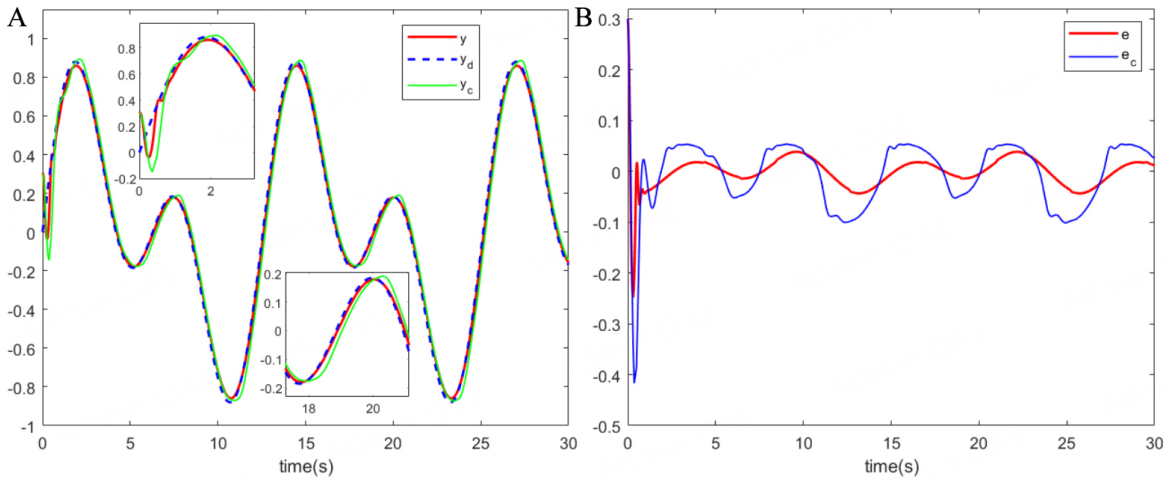


Figure 7. Example 2: (A) System output. (B) tracking error.

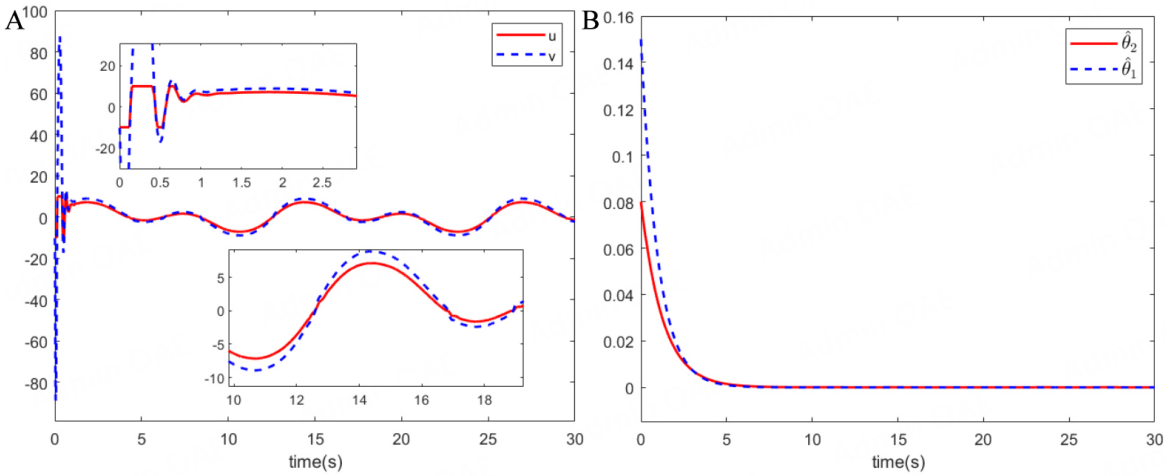


Figure 8. Example 2: (A) Control input. (B) adaptive parameters.

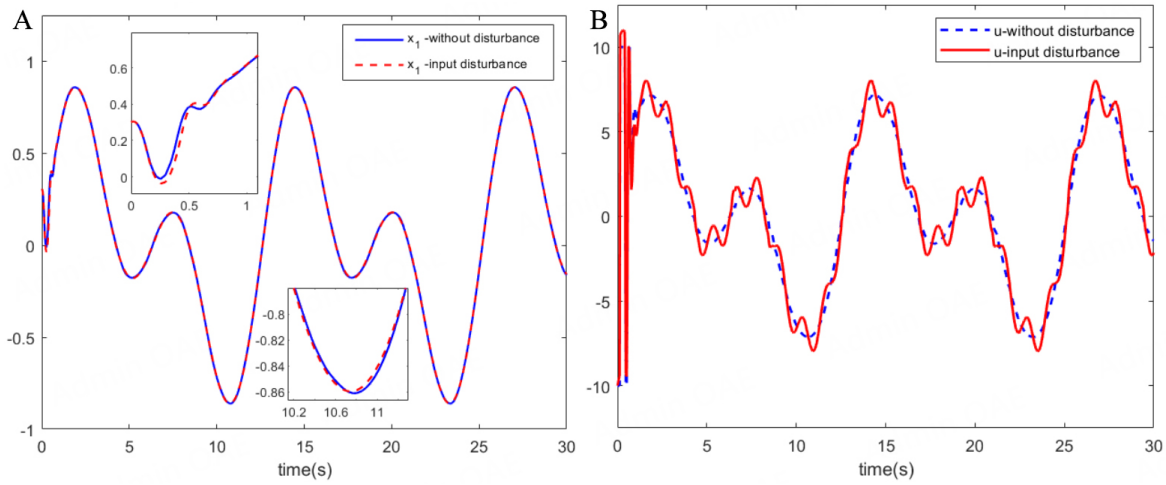


Figure 9. Example 2: system output and control input with disturbance and without disturbance.

5. CONCLUSIONS

In real production process environments, special requirements are usually imposed on system actuator inputs, such as limiting the maximum amplitude of the inputs to a certain range to ensure safe and reliable operation of the system and avoiding fluctuations of the control inputs near zero as much as possible to minimize consumption and reduce actuator losses. Deadband and saturation constraints are specific manifestations of the above problems in real physical systems, which are commonly found in many practical systems, such as unmanned aircraft systems, electromechanical systems, and robotic systems. In order to solve the effects of multi-actuator constraints and external disturbances on nonlinear systems, an adaptive NN finite time tracking controller based on command filtering is designed in this paper. The effects of dead zones and saturated nonlinear constraints on the controller design are eliminated through an equivalent transformation. Using the command filtering technique, the problem of exploding computational complexity due to virtual control signal derivatives is overcome while accomplishing the virtual controller control task. The controller can guarantee the boundedness of all signals in the controlled system, and the output of the system can quickly track the desired reference trajectory. Simulation results verify the effectiveness and rationality of the designed control strategy.

DECLARATIONS

Acknowledgments

Special thanks to the School of Information and Control Engineering, Qingdao University of Technology, China, for providing technical support for this research.

Authors' contributions

Made substantial contributions to the conception and design of the study and performed validation analysis and interpretation: Li Y (Li Yinguang), Zhang J

Provided simulation design and administrative and technical support: Li Y (Li Yang)

Financial support and sponsorship

This work was supported in part by the National Natural Science Foundation (62203247) from China.

Availability of data and materials
Not applicable.

Conflicts of interest
All authors declared that there are no conflicts of interest.

Ethical approval and consent to participate
Not applicable.

Consent for publication
Not applicable.

Copyright
© The Author(s) 2024.

REFERENCES
1. Yin X, Zhang Q. Backstepping-based state estimation for a class of stochastic nonlinear systems. *Complex Eng Syst* 2022;2:1. DOI
2. Liu Q, Cai Z, Chen J, Jiang B. Observer-based integral sliding mode control of nonlinear systems with application to single-link flexible joint robotics. *Complex Eng Syst* 2021;1:8. DOI
3. Li Y, Zhu Q, Zhang J. Distributed adaptive fixed-time neural networks control for nonaffine nonlinear multiagent systems. *Sci Rep* 2022;12:8459. DOI
4. Chen M, Wang H, Liu X. Adaptive fuzzy practical fixed-time tracking control of nonlinear systems. *IEEE Trans Fuzzy Syst* 2021;29:664–73. DOI
5. Kanellakopoulos I, Kokotovic PV, Morse AS. Systematic design of adaptive controllers for feedback linearizable systems. In: 1991 American Control Conference; Boston, MA, USA, 26-28 June 1991. pp. 649–54. DOI
6. Ba D, Li YX, Tong S. Fixed-time adaptive neural tracking control for a class of uncertain nonstrict nonlinear systems. *Neurocomputing* 2019;363:273–80. DOI
7. Wang F, You Z, Liu Z, Chen CLP. A fast finite-time neural network control of stochastic nonlinear systems. *IEEE Trans Neural Netw Learn Syst* 2023;34:7443–52. DOI
8. He W, Mu X, Zhang L, Zou Y. Modeling and trajectory tracking control for flapping-wing micro aerial vehicles. *IEEE/CAA J Automat Sin* 2021;8:148–56. DOI
9. Dong H, Yang X. Adaptive neural finite-time control for space circumnavigation mission with uncertain input constraints. *J Franklin Inst* 2021;358:3353–75. DOI
10. Cui D, Zou W, Guo J, Xiang Z. Adaptive fault-tolerant decentralized tracking control of switched stochastic uncertain nonlinear systems with time-varying delay. *Int J Adapt Control Signal Process* 2022;36:2971–87. DOI
11. Ha M, Wang D, Liu D. Discounted iterative adaptive critic designs with novel stability analysis for tracking control. *IEEE/CAA J Automat Sin* 2022;9:1262–72. DOI
12. Lv Y, Fu J, Wen G, Huang T, Yu X. Distributed adaptive observer-based control for output consensus of heterogeneous mass with input saturation constraint. *IEEE Trans Circuits Syst I Regul Pap* 2020;67:995–1007. DOI
13. Liu Z, Han Z, Zhao Z, He W. Modeling and adaptive control for a spatial flexible spacecraft with unknown actuator failures. *Sci China Inf Sci* 2021;64:152208. DOI
14. Tong S, Li Y. Adaptive fuzzy output feedback tracking backstepping control of strict-feedback nonlinear systems with unknown dead zones. *IEEE Trans Fuzzy Syst* 2012;20:168–80. DOI
15. Li Y, Liu L, Feng G. Robust adaptive output feedback control to a class of non-triangular stochastic nonlinear systems. *Automatica* 2018;89:325–32. DOI
16. Li YX. Finite time command filtered adaptive fault tolerant control for a class of uncertain nonlinear systems. *Automatica* 2019;106:117–23. DOI
17. Sui S, Chen CLP, Tong S. Fuzzy adaptive finite-time control design for nontriangular stochastic nonlinear systems. *IEEE Trans Fuzzy Syst* 2019;27:172–84. DOI
18. Lu C, Pan Y, Liu Y, Li H. Adaptive fuzzy finite-time fault-tolerant control of nonlinear systems with state constraints and input quantization. *Int J Adapt Control Signal Proces* 2020;34:1199–219. DOI
19. Yu J, Cheng S, Shi P, Lin C. Command-filtered neuroadaptive output-feedback control for stochastic nonlinear systems with input constraint. *IEEE Trans Cybern* 2023;53:2301–10. DOI
20. Li YX. Command filter adaptive asymptotic tracking of uncertain nonlinear systems with time-varying parameters and disturbances. *IEEE Trans Automat Contr* 2022;67:2973–80. DOI
21. Shi X, Lim CC, Shi P, Xu S. Adaptive neural dynamic surface control for nonstrict-feedback systems with output dead zone. *IEEE Trans*

Neural Netw Learn Syst 2018;29:5200–13. DOI
22. Zhao S, Pan Y, Du P, Liang H. Adaptive control for non-affine nonlinear systems with input saturation and output dead zone. *Appl Math Comput* 2020;386:125506. DOI
23. Wang L, Wang H, Liu PX, Ling S, Liu S. Fuzzy finite-time command filtering output feedback control of nonlinear systems. *IEEE Trans Fuzzy Syst* 2022;30:97–107. DOI
24. Yu J, Shi P, Dong W, Lin C. Adaptive fuzzy control of nonlinear systems with unknown dead zones based on command filtering. *IEEE Trans Fuzzy Syst* 2018;26:46–55. DOI
25. Yu H, Yu J, Wang QG, Lin C. Time-varying BLFs-based adaptive neural network finite-time command-filtered control for nonlinear systems. *IEEE Trans Syst Man Cybern Syst* 2023;53:4696–704. DOI
26. Zhang J, Jiang Y, Li X, Luo H, Yin S, Kaynak O. Remaining useful life prediction of lithium-ion battery with adaptive noise estimation and capacity regeneration detection. *IEEE/ASME Trans Mechatron* 2023;28:632–43. DOI
27. Zhao L, Yu J, Wang QG. Finite-time tracking control for nonlinear systems via adaptive neural output feedback and command filtered backstepping. *IEEE Trans Neural Netw Learn Syst* 2021;32:1474–85. DOI
28. Li Y, Yang T, Tong S. Adaptive neural networks finite-time optimal control for a class of nonlinear systems. *IEEE Trans Neural Netw Learn Syst* 2020;31:4451–60. DOI
29. Li H, Zhao S, He W, Lu R. Adaptive finite-time tracking control of full state constrained nonlinear systems with dead-zone. *Automatica* 2019;100:99–107. DOI
30. Liu J, Wang C, Li X, Cai X. Adaptive finite-time practical consensus protocols for second-order multiagent systems with nonsymmetric input dead zone and uncertain dynamics. *J Franklin Inst* 2019;356:3217–44. DOI
31. Wang J, Zhang H, Ma K, Liu Z, Chen CLP. Neural adaptive self-triggered control for uncertain nonlinear systems with input hysteresis. *IEEE Trans Neural Netw Learn Syst* 2022;33:6206–14. DOI
32. Liu Y, Chen Y. Dynamic memory event-triggered adaptive control for a class of strict-feedback nonlinear systems. *IEEE Trans Circuits Syst II Express Briefs* 2022;69:3470–74. DOI
33. Wang H, Kang S, Zhao X, Xu N, Li T. Command filter-based adaptive neural control design for nonstrict-feedback nonlinear systems with multiple actuator constraints. *IEEE Trans Cybern* 2022;52:12561–70. DOI
34. Chen M, Wang H, Liu X. Adaptive practical fixed-time tracking control with prescribed boundary constraints. *IEEE Trans Circuits Syst I Regul Pap* 2021;68:1716–26. DOI
35. Yuan X, Chen B, Lin C. Neural adaptive fixed-time control for nonlinear systems with full-state constraints. *IEEE Trans Cybern* 2023;53:3048–59. DOI
36. Farrell JA, Polycarpou M, Sharma M, Dong W. Command filtered backstepping. *IEEE Trans Automat Contr* 2009;54:1391–95. DOI
37. Liang Y, Li YX, Hou Z. Adaptive fixed-time tracking control for stochastic pure-feedback nonlinear systems. *Int J Adapt Control Signal Process* 2021;35:1712–31. DOI
38. Wang H, Xu K, Liu PX, Qiao J. Adaptive fuzzy fast finite-time dynamic surface tracking control for nonlinear systems. *IEEE Trans Circuits Syst I Regul Pap* 2021;68:4337–48. DOI
39. Xu B, Li YX, Tong S. Neural learning fixed-time adaptive tracking control of complex stochastic constraint nonlinear systems. *J Franklin Inst* 2023;360:13671–91. DOI

Barawkar *et al. Complex Eng Syst* 2024;4:6
DOI: 10.20517/ces.2023.33

Complex Engineering Systems

Research Article

Open Access

Active manipulation of a tethered drone using explainable AI

Shraddha Barawkar[1], Manish Kumar[1,2]

[1]Maryland Robotics Center, University of Maryland, College Park, MD 20740, USA.
[2]Mechanical and Materials Engineering, University of Cincinnati, Cincinnati, OH 45221, USA.

Correspondence to: Dr. Shraddha Barawkar, Maryland Robotics Center, University of Maryland, 8125 Paint Branch Dr, College Park, MD 20740, USA. E-mail: sbarawka@umd.edu

How to cite this article: Barawkar S, Kumar M. Active manipulation of a tethered drone using explainable AI. *Complex Eng Syst* 2024;4:6. http://dx.doi.org/10.20517/ces.2023.33

Received: 29 Sep 2023 **First Decision:** 4 Jan 2024 **Revised:** 31 Jan 2024 **Accepted:** 7 Mar 2024 **Published:** 25 Mar 2024

Academic Editor: Hamid Reza Karimi **Copy Editor:** Fanglin Lan **Production Editor:** Fanglin Lan

Abstract

Tethered drones are currently finding a wide range of applications such as for aerial surveillance, traffic monitoring, and setting up ad-hoc communication networks. However, many technological gaps are required to be addressed for such systems. Most commercially available tethered drones hover at a certain position; however, the control task becomes challenging when the ground robot or station needs to move. In such a scenario, the drone is required to coordinate its motion with the moving ground vehicle without which the tether can destabilize the drone. Another challenging aspect is when the system is required to operate in GPS denied environments, such as in planetary exploration. In this paper, to address these issues, we take advantage of passive or force-based control in which the tension in the tether is sensed and used to drive the drone. Fuzzy logic is used to implement the force-based controller as a tool for explainable Artificial Intelligence. The proposed fuzzy logic controller takes tether force and its rate of change as the inputs and provides desired attitudes as the outputs. Via simulations and experiments, we show that the proposed controller allows effective coordination between the drone and the moving ground rover. The rule-based feature of fuzzy logic provides linguistic explainability for its decisions. Simulation and experimental results are provided to validate the novel controller. This paper additionally develops an adaptive controller for estimating unknown constant winds on these tethered drone systems using a proportional controller. The simulation results demonstrate the effectiveness of the proposed adaptive control scheme in addressing the effect of wind on a tethered drone.

Keywords: Active manipulation, tethered drone, fuzzy logic, explainable AI, force control

© The Author(s) 2024. **Open Access** This article is licensed under a Creative Commons Attribution 4.0 International License (https://creativecommons.org/licenses/by/4.0/), which permits unrestricted use, sharing, adaptation, distribution and reproduction in any medium or format, for any purpose, even commercially, as long as you give appropriate credit to the original author(s) and the source, provide a link to the Creative Commons license, and indicate if changes were made.

1. INTRODUCTION

Today, artificial intelligence (AI) is seeing widespread applications in sectors such as defense, finance, law, in healthcare and in robotics. This has been facilitated by recently developed diverse tools and methods, tremendous improvement in computational resources, and ability to gather data. Random forests[1], reinforcement learning[2,3], recurrent neural nets[4], probabilistic graphical models, and deep learning[5] are a few of the recent methods that have fueled the growth of the AI field. The performance and accuracy of many of these methods have an inverse relation with the explainability. The higher performance or more accurate methods, such as deep learning, are less explainable while the most explainable techniques, such as decision trees, are less accurate[6–9]. The question is how to convert the current machine learning techniques from black box to at least partial or fully explainable solutions. This step is necessary to be addressed given the advent of AI and its widespread use is expected to be seen in the future. Moreover, it is desired to have improved accuracy with increasingly explainable models. This paper proposes the use of a fuzzy logic controller for the control of an actively tethered drone. Fuzzy logic forms a qualitative approach and a unique tool of AI used to interpret and understand complex numerical data since it can efficiently deal with inaccuracies and uncertainties[10]. The fuzzy rules are typically designed using human intuitive knowledge, and the fuzzy controller provides full interpretability to the decisions it takes as compared to limited explainability/transparency of other machine learning models. Fuzzy logic also shows better sensor noise handling capacity which enables the use of low-cost noisy sensors[11–13]. Due to the above-mentioned advantages, it was chosen as the proposed method to address the complexity and uncertainties associated with force-based coordination between a moving vehicle/robot and a tethered drone. Moreover, its widespread use in the robotics field forms an added advantage and provides more reason to exploit it as an AI tool[14–16].

Tethered drone systems form the future of the drone industry. Such systems will be seen tomorrow providing next generation ad-hoc wireless networks[17], carrying out infrastructure inspections, for disaster mitigation[3] or to monitor ground traffic. The need of this technology is also evident from the current market of such systems. Elistair[18], Fotokite[19], and Hoverfly[20] are a few of the leading companies in the area of tethered drones. As compared to traditional drones, tethered drones offer various perks such as unlimited flight time (continuous power via tether), faster and secure data transmission, safer operation, better aerial surveillance, and no fear of communication loss. Active manipulation of tethered drones, where tension in tether controls the drone actuation so the drone can be maneuvered using the tether, forms the need of the hour. This is because, to the best of our knowledge, existing tethered drone solutions are not designed to move/coordinate with a moving ground station or rover which forms a technological gap this paper attempts to address. Moreover, active manipulation of drones alleviates the need of knowledge of drone piloting skills[11,21]. Such actively manipulated tethered drones can be attached to a moving emergency vehicle, robot, or even a ship. When the ground entity (car, robot, etc.) moves, the drone is required to coordinate with the motion of the ground entity. Given the benefits offered by such systems, these drones can be leashed with ground rovers in space too for interplanetary exploration where there are no obstacles such as trees, buildings and electric wires. Such systems are especially suited for space applications due to unlimited flight time and safer operation during an emergency or technical malfunction.

Active manipulation of the tethered drone can be achieved via either position control (using sensors such as GPS or cameras to estimate the relative position of the ground robot with respect to the drone) or force control (based on the tether tension). The paper focuses on a force-based control method that enables the use of such systems in GPS denied environments such as mines, space and remote construction sites. In this approach, the tethered drone is not required to know its position or the position of the ground robot. A force sensor can be attached to the drone or the ground vehicle to implement the controller. This research is inspired by force-based control or passive control used for applications such as multi-drone cooperative transport (CT) and human-drone interaction (HDI) tasks. Both these tasks have recently been investigated by multiple researchers via schemes of admittance and fuzzy controllers[22–24]. Barawkar *et al.*[11] show both these tasks using fuzzy logic

via a low-cost imprecise force-torque sensor. In all these schemes, leader-follower strategy is utilized where the leader can either be another drone (for CT) or a human operator (for HDI). The same concept can be utilized for active manipulation of tethered drones where the motion of a ground robot controls the motion of the drone via force feedback. However, now, the coupled dynamics between the ground robot and the drone changes the challenges as compared to that of multi-drone CT and HDI tasks. For example, the maintenance of a certain tension in the tether, development of controllers for force-based coordination between the ground and aerial robots and wind disturbances form a few of the challenges associated with tethered drone systems.

In the context of force-based control of tethered drones, relatively little has been carried out in literature. Breese *et al.*[25] present a fuzzy logic force-based control of a tethered drone; however, the inputs to the fuzzy controller are different from the ones of the proposed controller of this paper. Moreover, the approach and the utilized principle are different and experiments have not been conducted. The minimization principle of forces and their rates (indicated in the Approach Section) has not been used by Breese *et al.*[25]. Wind disturbance handling is also not examined by them[25].

Drone-ground rover cooperation has been a topic of immense interest recently among the robotics research community[26,27]. However, the system dynamics and, hence, modeling and control significantly change upon introducing a tether as a means of connecting the ground robot and the drone. Further, diverse research has been conducted on tethered drone systems with different control approaches, configurations and applications. Research by Fagiano *et al.*[28] shows a control approach for chain of multiple tethered drones where the first drone is tethered to the ground station while the last drone acts as an end effector. The tethers are assumed to be elastic and their length can be varied via actuated winches installed on ground stations and drones. Each drone uses a distributed linear controller, and a high-level model predictive controller is employed to control the formation. On the other hand, Martinez Rocamora Jr *et al.*[29] develop "Oxpecker", a tethered drone for inspection of stone-mine pillars. A multi-agent Q-learning approach is examined in another research[17] for using an optimal tethered drone in A2G communication network. Work of Lee *et al.*[30] implements a geometric controller that shows asymptotic stability of the coupled dynamics of the drone and tether of a tethered drone system.

Work of Kourani *et al.*[31] presents surge velocity control of an unmanned aerial vehicle manipulating the velocity of a buoy via tether. Further, Glick *et al.*[32] present a unified model approach to control tethered drones with state and input constraints. Work of Sandino e*et al.*[33] investigates tether configurations for stability during hovering of small helicopters. The taut cable is considered as a control input which makes sure the helicopter is stable in windy environments, while an actuated winch controls the tether tension as the drone controls its position. Work of Nicotra *et al.*[34] presents nonlinear control of a tethered drone specially analyzing the taut cable case. The paper shows that the tethered drone maintains a non-zero attitude hovering at a constant position. The control objective of Nicotra *et al.*[34] is to stabilize the drone and keep the tether taut at all times which forms as a constraint. Stability is ensured by a cascade controller scheme using thrust vectoring while a reference governor ensures constraint satisfaction. Their work[34] uses a winch system to control the length of the tether, while the drone maintains its desired orientation and the tether tension. In this paper, for simplicity purposes, we do not use a winch system. The tether is assumed to be elastic and its length is fixed (not varying, as seen in winch systems). In summary, apart from our previous work[25], hardly any methods available in literature focus on developing a controller that would allow the drone to follow a ground vehicle based on tether tension inputs.

In the analysis of wind disturbances on tethered drones, very little work exists in literature. For drones in general, Mokhtari *et al.*[35] investigate the effect of wind on rotational dynamics of a drone; however, presence of tether changes the dynamics significantly. Ali *et al.*[36] discuss control of the hexrotor drone equipped with a cable-driven gripper, subject to wind disturbances, using model reference adaptive control with an integrator.

On the other hand, Escareno *et al.*[37] present trajectory control of a drone under two-dimensional wind disturbances using hierarchical, sliding mode and adaptive control techniques with an approach different from what is presented in this paper in terms of analysis of dynamics of a tethered drone. In another work, Kumar *et al.*[38] have demonstrated the performance of a tethered tilt-rotor quadcopter in rejecting wind disturbances.

In this paper, we propose a fuzzy logic-based force feedback controller for the tethered drone. We assume the contact forces and their rates between the drone and the tether are measurable. The inputs to the fuzzy logic force feedback controller are the contact forces and their rates while the output of the controller is the desired orientation required to be commanded to the attitude controller of the drone. The fuzzy rules are designed to provide effective force-based coordination between the drone and the ground robot. Both extensive simulations and experimental results are provided to validate the proposed controller. It should be noted that fuzzy logic was chosen as it enables incorporation of human intuitive knowledge (thus providing explainability) into controller design, allows for the use of noisy force sensors, and has also shown promising results previously for multi-drone CT[11].

Moreover, as external wind disturbances can mislead a force feedback controller, this paper additionally proposes an adaptive control method based on proportional force feedback for controlling an actively tethered drone in presence of constant or slowly varying unknown winds. The overall dynamic model is provided and examined thoroughly in simulations for the scenario of wind disturbance on a tethered drone. The estimation of unknown wind speed is achieved by a novel adaptive strategy that requires the drone to know the position and velocity of the ground robot. The estimated wind velocity is used by a proportional controller to control the drone.

To summarize, the primary contribution of this paper is to develop a novel and explainable force-based fuzzy logic controller for actively manipulating a tethered drone. To the best of our knowledge, this work forms one of the first instances to experimentally demonstrate force-based control of a tethered drone using low-cost imprecise force sensors. Secondly, as discussed earlier, wind disturbances can affect the force-based controller of a tethered drone. This paper additionally implements an adaptive controller on a tethered drone to estimate constant unknown wind, which forms the second primary contribution of this paper. To develop the adaptive control for the scenario of wind disturbances, we take motivation from previously utilized adaptive controllers for multi-ground robot CT where such controllers were utilized to estimate uncertainties in the object and the ground robots. However, extending previous work to a tethered drone with wind disturbances is a novel contribution due to significant difference in dynamics and control objectives. The proposed control schemes are resilient in handling wind disturbance through adaptive controllers and managing force sensor noise by employing fuzzy logic[11].

2. PROBLEM FORMULATION

Consider a drone tethered to a ground rover [Figure 1]. Let $\eta_o = \begin{bmatrix} \phi_o & \theta_o & \psi_o \end{bmatrix}^T$ be the orientation of the drone with angles roll (ϕ_o), pitch (θ_o), and yaw (ψ_o). Three primary challenges are associated with operating this system. First, irrespective of stationary or moving ground rover, the drone is required to maintain a desired tension T^d in the tether and a desired tether inclination angle with the ground α^d. Second, when the ground rover is moving, the drone is required to coordinate with the ground rover based on the measured tether forces and their rates (F^m and $\dot{F}^m$) exerted by the ground rover on the tethered drone. This can be achieved by changing the attitude of the drone, which would allow the drone to move in order to comply with the tension in the tether. Thus, the net desired orientation η_o^d of the tethered drone should be a function:

$$\eta_o^d = f(T^d, \alpha^d, F^m, \dot{F}^m) \tag{1}$$

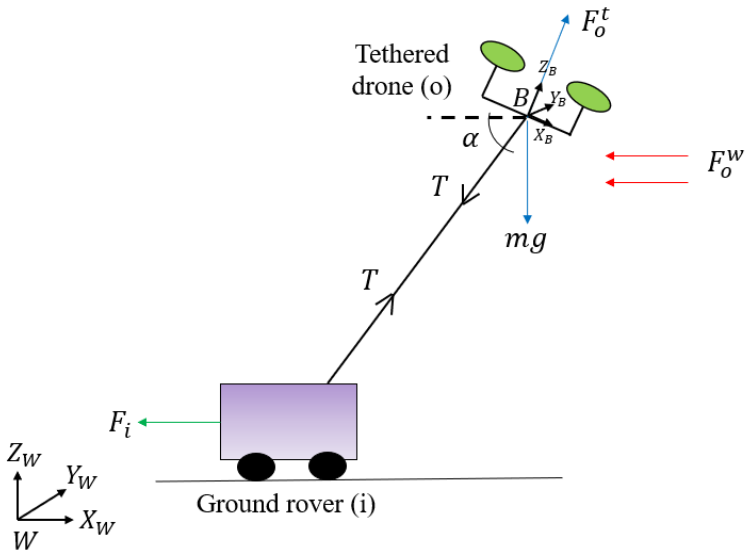


Figure 1. Schematic diagram of a drone tethered to a ground rover in equilibrium/hovering position.

Lastly, the next problem consists of evaluating f.

3. DYNAMICS

3.1. General system dynamics

Figure 1 shows a schematic diagram of a drone of mass m tethered to a ground robot. W and B are the world frame of the system and the body frame of the drone, respectively. The diagram also presents different forces acting on both the drone and the ground rover at equilibrium condition in which the drone is moving at constant speed with the magnitude and the direction of motion same as that of the ground rover. The drone is assigned symbol 'o' while the ground rover is assigned symbol 'i'. At equilibrium, the control of the drone is designed to align the pitch axis of its body frame to the direction of motion of the ground vehicle. Thus, it does not need to roll or yaw in this state (the desired roll and yaw angles, ϕ_o^d=ψ_o^d=0). In the equilibrium condition, the drone only pitches by angle θ_o^{eq} (equilibrium pitch angle of the drone) to create the required tension in the tether and the motion of the drone. In order to compute the desired pitch angle at equilibrium or hovering position, we perform the following analysis.

Overall, three forces act on the drone in the tethered position, viz., the tether tension (T), the drone actuation force or thrust force due to rotors (F_o^t), and the weight of the drone (mg), respectively, where g is the acceleration due to gravity. It should be noted that F_o^w denotes the force due to wind disturbance which will be considered later in sections of wind disturbance analysis. Now, the force acting on the drone $F_o^a = \begin{bmatrix} F_x^a & F_y^a & F_z^a \end{bmatrix}^T$ (in world frame W) due to actuation of the rotors is given by:

$$F_o^a = R_B^W \begin{bmatrix} 0 \\ 0 \\ F_o^t \end{bmatrix} \tag{2}$$

where $F_o^t = (f_1 + f_2 + f_3 + f_4)$ is the thrust force (in frame B) created by the drone which corresponds to the summation of rotor forces (f_1, f_2, f_3, f_4), and R_B^W is the rotation matrix to go from body (B) to world frame (W) (see Figure 1). We use the Euler sequence of $Z - X - Y$ to model the rotation matrix of the system in the

world frame. The rotation matrix R_B^W is:

$$R = \begin{bmatrix} c\psi c\theta - s\phi s\psi s\theta & -c\phi s\psi & c\psi s\theta + s\phi s\psi c\theta \\ c\theta s\psi + c\psi s\phi s\theta & c\phi c\psi & s\psi s\theta - c\psi c\theta s\phi \\ -c\phi s\theta & s\phi & c\phi c\theta \end{bmatrix} \tag{3}$$

where $c(.)$ and $s(.)$ are the cosine and sine terms, respectively. Upon analysis of the free body diagram, at equilibrium, we have:

$$F_x^a = Tcos(\alpha) \tag{4}$$

$$F_z^a = Tsin(\alpha) + mg \tag{5}$$

By linearizing Equation 2, we can compute the desired pitch angle (θ_o^{eq}) to maintain a desired tension ($T^{eq} = \begin{bmatrix} T_x^{eq} & T_y^{eq} & T_z^{eq} \end{bmatrix}^T$) in tether and desired angle (α^{eq}) of tether with the ground. Thus, θ_o^{eq} can be computed using:

$$\theta_o^{eq} = tan^{-1}\left(\frac{T^{eq}cos(\alpha^{eq})}{T^{eq}sin(\alpha^{eq}) + mg}\right) \tag{6}$$

To compute the hovering rotor speed ω_o^h of the drone, we compute the total equilibrium force F_o^{eq} acting on the drone as follows:

$$F_o^{eq} = \sqrt{(T^{eq}cos(\alpha^d))^2 + (T^{eq}sin(\alpha^d) + mg)^2} \tag{7}$$

The hovering speed ω_o^h of the drone is,

$$\omega_o^h = \sqrt{\frac{F_o^{eq}}{4k_f}} \tag{8}$$

Here, $k_f = 2.2 \times 10^{-4}$ is the chosen motor constant ([39]). The next step consists of writing the equations of motion of the drone and the ground rover. The translational and rotational equations of motion of the tethered drone are given by,

$$m\ddot{r}_o = R_B^W \begin{bmatrix} 0 \\ 0 \\ F_o^t \end{bmatrix} + \begin{bmatrix} 0 \\ 0 \\ -mg \end{bmatrix} - T \tag{9}$$

$$I\ddot{\eta}_o = \begin{bmatrix} L(f_2 - f_4) \\ L(f_3 - f_1) \\ M_1 - M_2 + M_3 - M_4 \end{bmatrix} - \dot{\eta}_o \times I\dot{\eta}_o \tag{10}$$

where r_o is the position of the drone in world frame (W). I and L are the mass moment of inertia and the arm length of the drone, respectively. M_1, M_2, M_3, and M_4 are the moments created by the four rotors of the drone. $\eta_o = \begin{bmatrix} \phi_o & \theta_o & \psi_o \end{bmatrix}^T$ is the orientation of the drone. It should be noted that a small angle approximation is assumed in the entire paper. Thus, angular velocity and angular acceleration of the drone are $\dot{\eta}$ and $\ddot{\eta}$, respectively. We then compute the net desired pitch angle θ_o^d and yaw angle ψ_o^d as follows:

$$\theta_o^d = \theta_o^{eq} + \theta_o^f \tag{11}$$

$$\psi_o^d = \psi_o^f \tag{12}$$

where,

$$\theta_o^f = func_1(F_x^m - T_x^{eq}, \dot{F}_x^m) \tag{13}$$

$$\psi_o^f = func_2(F_y^m, \dot{F}_y^m) \tag{14}$$

where $F^m = \begin{bmatrix} F_x^m & F_y^m & F_z^m \end{bmatrix}^T$ is the measured force at the point of contact between the drone and the tether. Here, θ_o^f and ψ_o^f are the pitch and yaw commands (additional to being applied at equilibrium) to enable the

drone to follow the ground robot. It is worth noting that we calculate this sensed force mathematically for simulation analysis, while for experiments, we use a force sensor using load cells. $func_1$ and $func_2$ are the proposed fuzzy logic functions that evaluate the desired pitch θ_o^f and yaw ψ_o^f angles based on the contact forces and their rates. The net desired pitch and yaw angles, θ_o^d and ψ_o^d, are then commanded to the attitude controller of the drone thus making the drone coordinate with the ground robot based on the measured forces. The ground rover actively manipulates the drone without requiring to know the three-dimensional position of the drone. Such techniques are especially beneficial for GPS denied environments and planetary explorations. Note that we assume that the tether is elastic and there is no separately implemented controller for the vertical Z_W axis of the drone. The drone is made to operate at hovering speed ω_o^h and the desired orientation that allows it to obtain its position along vertical Z_W direction based on the tether length.

3.2. System dynamics in presence of wind disturbance

This section formulates dynamics of the system considering force due to wind disturbance. Referring to Figure 1, we first write the general nonlinear form of dynamical equations of the drone as:

$$u_o - T = M_o(p_o)\ddot{p}_o + C_o(p_o, \dot{p}_o)\dot{p}_o + g_o(p_o) \tag{15}$$

where, $p_o = \begin{bmatrix} r_o^T & \eta_o^T \end{bmatrix}^T$ is the position and orientation vector of the drone in the world fame W. M_o, C_o, g_o, and u_o are the symmetric positive definite inertia matrix, damping coefficient matrix, gravity force term, and the input to the drone, respectively. Note that $\dot{M}_o - 2C_o$ is skew-symmetric for a certain C_o. Now, for a given arbitrarily defined velocity ν_o, we can write

$$F_o^w = M_o(p_o)\dot{\nu}_o + C_o(p_o, \dot{p}_o)\nu_o + g_o(p_o) \tag{16}$$

where F_o^w is the force due to wind which we propose to estimate using an adaptive control strategy as presented in the next section. The input u_o provides asymptotic stability in wind disturbance and makes the drone cooperate with the ground robot; it is obtained using:

$$u_o = \hat{F}_w + T^d - K_o s_o \tag{17}$$

$\hat{F}_w$ is the estimated force due to wind, T^d is the desired tension required to be maintained in the tether for force-based coordination between the drone and the ground rover and $K_o > 0$ is the feedback gain matrix. s_o is the velocity error of the drone and is obtained as[40,41]:

$$s_o = \begin{bmatrix} \dot{r}_o^T & \dot{\eta}^T \end{bmatrix}^T - \begin{bmatrix} \dot{r}_{or}^T & (\dot{\eta_{or}})^T \end{bmatrix}^T \tag{18}$$

Here, $\dot{r}_{or}$ and $\dot{\eta}_{or}$ are the reference linear and angular velocities of the drone. Similarly, we can write a simple general form of dynamical equations of the ground robot as,

$$F_i + T = M_i(p_i)\ddot{p}_i \tag{19}$$

where, $p_i = \begin{bmatrix} r_i^T & \eta_i^T \end{bmatrix}^T$ is the position (r_i) and orientation (η_i) vector of the ground robot in the world fame W. M_i is the symmetric positive definite inertia mass matrix of the ground robot. Since this paper does not focus on developing a lower-level controller for the ground robot, it is assumed that $F_i^d = F_i$; i.e., its actual actuating force matches the desired actuating force of the ground robot. In other words, the ground robot actuators and controller perform perfectly in producing the desired force. The velocity error of the ground robot is $s_i = \begin{bmatrix} \dot{r}_i^T & \dot{\eta_i}^T \end{bmatrix}^T - \begin{bmatrix} \dot{r}_{ir}^T & (\dot{\eta_{ir}})^T \end{bmatrix}^T$. Where $\dot{r}_{ir}$ and $\dot{\eta}_{ir}$ are the reference linear and angular velocities of the drone. We use the control law for $\dot{p}_{ir} = \begin{bmatrix} \dot{r}_{ir}^T & \dot{\eta}_{ir}^T \end{bmatrix}^T$ as,

$$\dot{p}_{ir} = \rho(p_i^d - p_i) + \dot{p}_i^d \tag{20}$$

where p_i^d is the desired goal position and orientation of the ground robot. Note that we obtain the desired tension in the tether during wind disturbance as:

$$T^d = mk_o(\ddot{r}_{ir} - \ddot{r}_o) \tag{21}$$

where k_o is a proportional constant.

4. ADAPTIVE CONTROL FOR ESTIMATION OF WIND FORCE

The following theorem is used in this paper to implement the proposed adaptive controller.

Theorem 1. *Consider a tethered drone system whose dynamics are given by Equations 15 and 19. The given system, using the control law given by 17, is asymptotically stable if the following adaptation law is used:*

$$\dot{\hat{F}}_w = -\Gamma s_o \tag{22}$$

where Γ *is a symmetric positive definite matrix of tunable parameters.*

Proof. Using equations 15, 16, 18,

$$M_o\dot{s}_o + C_o s_o = \tilde{F}_w + \Delta T - K_o s_o \tag{23}$$

where $\tilde{F}_w = \hat{F}_w - F_w$ is the wind parameter error vector, and $K_o > 0$ is a feedback gain matrix of the drone and $\Delta T = T^d - T$. Similarly, for the ground robot, we use Equation 19 to obtain:

$$M_i\dot{s}_i = -\Delta T - K_i s_i \tag{24}$$

Now, we choose the candidate Lyapunov function as follows:

$$V = \frac{1}{2}\left(s_o^T M_o s_o + \tilde{F}_w^T \Gamma^{-1}\tilde{F}_w + s_i^T M_i s_i\right) \tag{25}$$

Then, Equations 22, 23, and 24 are used to compute the time derivative of Equation 25. It should be noted that considering the duality of force and velocity and the fact that the force applied by the ground rover via the tether is equal and opposite to the force exerted on the drone (due to the assumption of the mass-less tether), we consider $s_i = s_o$. Refer to work of[40] for further details. Thus, we have:

$$\begin{aligned}\dot{V} &= s_o^T(\tilde{F}_w + \Delta T - K_o s_o) + s_i^T(-K_i s_i - \Delta T) + \tilde{F}_w^T\Gamma^{-1}\dot{\hat{F}}_w \\ &= -s_o^T K_o s_o - s_i^T K_i s_i \leq 0\end{aligned} \tag{26}$$

$\dot{V}$ is negative semi-definite. Thus, s_o, $\tilde{F}_w$ and s_i are bounded. Since $\tilde{F}_w$ is bounded, $\hat{F}_w$ is also bounded as F_w is considered constant in this paper. From Equation 18, p_{or}, $\dot{p}_{or}$, $\ddot{p}_{or}$, p_o, $\dot{p}_o$ and $\ddot{p}_{or}$ are bounded considering the operating regime under the small angle approximation. Similarly, from definition of s_i, we have p_{ir}, $\dot{p}_{ir}$, $\ddot{p}_{ir}$, p_i, $\dot{p}_i$ and $\ddot{p}_i$ to be bounded. Thus, from Equation 21, T^d is bounded. Hence, referring to Equation 17, u_o is bounded, and thus, from Equation 15, T is bounded, which makes ΔT bounded. Taking the second derivative of V, we get,

$$\ddot{V} = -2(\dot{s}_o^T K_o s_o + \dot{s}_i^T K_i s_i) \tag{27}$$

From Equations 23 and 24, $\dot{s}_i$ and $\dot{s}_o$ are bounded. Thus, $\ddot{V}$ is bounded according to Barbalat's lemma. Therefore, $\dot{V} \to 0$ as $t \to \infty$ making $s_i \to 0$, $s_o \to 0$, $\dot{p}_o \to \dot{p}_{or}$, $\dot{p}_i \to \dot{p}_{ir}$, $\ddot{p}_{or} \to 0$ as $t \to \infty$. Thus, $p_i \to p_i^d$ and $T \to T^d$ as $t \to \infty$. It should be noted that this analysis does not guarantee parameter convergence to true values as condition for persistent excitation has not been implemented.

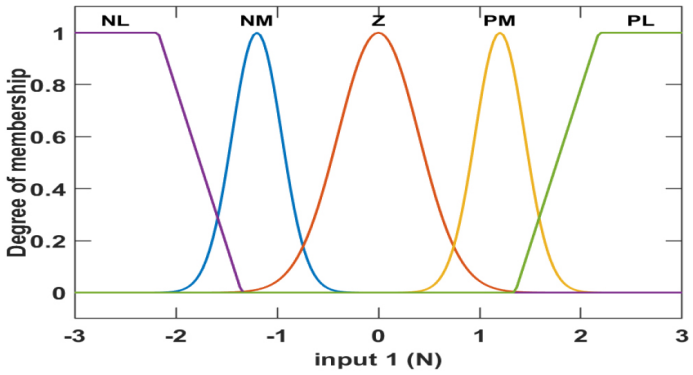
5. APPROACH

5.1. Fuzzy logic force feedback controller

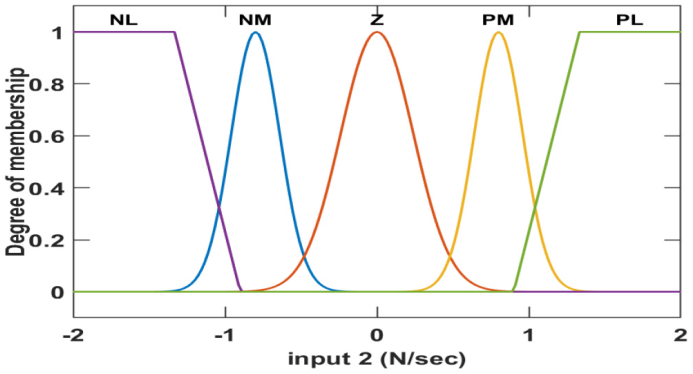
Based on our earlier work[11,42], we propose a fuzzy logic-based force feedback controller to control the pitch and yaw angles of the drone based on the tether forces and their rates acting on the drone due to the motion of the ground rover. Initially, before the ground robot starts moving, the drone goes into its equilibrium position with orientation as $\eta_o = \begin{bmatrix} 0 & \theta_o^{eq} & 0 \end{bmatrix}^T$. This orientation maintains an equilibrium tension $T^{eq} = \begin{bmatrix} T_x^{eq} & 0 & T_z^{eq} \end{bmatrix}^T$ in the tether and also makes the tether inclined to the ground at an angle α^{eq} (see Equations 4 to 8). After reaching this equilibrium position, the ground robot starts navigating towards its goal location. The next step consists of computing the desired pitch θ_o^f and yaw ψ_o^f angles of the drone based on contact forces and their rates thus making the drone coordinate with the rover via force feedback. Consequently, when the rover moves along the X_W direction, the drone pitches accordingly, while when the rover moves along the Y_w axis, it creates a force on the drone along the Y_w axis making the drone yaw with an objective of aligning its body pitch direction (X_B) with the current direction of motion of the rover. Finally, the net desired pitch θ_o^d is calculated and commanded to the attitude controller of the drone.

This section presents the fuzzy-based approach used to find θ_o^f and ψ_o^f. Two fuzzy controllers are implemented for pitching and yawing actions, respectively. For calculating θ_o^f, two inputs to the fuzzy logic force feedback controller are considered: i) force $F_x^m - T_x^{eq}$, and ii) rate of force change $\dot{F}_x^m$. Since the first input of the fuzzy logic controller for pitch axis $F_x^m - T_x^{eq}$ is proportional to the sensed force along the X_W axis by the drone, we call this controller a force feedback controller. Five membership functions are considered for both the inputs and the output of this controller. The membership functions are negative large (NL), negative medium (NM), Zero (Z), positive medium (PM), and positive large (PL). Table 1 summarizes the fuzzy rule base. The rule base is built using human intuition which can be understood as follows. Let us consider an example when the input $F_x^m - T_x^{eq}$ is PL and another input $\dot{F}_x^m$ is NL. In such a scenario, a PL first input $F_x^m - T_x^{eq}$ means that high force is acting on the drone due to motion of the rover and the drone is supposed to move faster with a large pitch value. However, the second NL input to the fuzzy controller $\dot{F}_x^m$ means that the rate of contact force change is large in the opposite manner; thus, the contact force is expected to increase in magnitude in a negative direction, which means that the drone should pitch negatively. The net effect of the two inputs is that the drone should not pitch at all; thus, the desired pitch angle (output) θ_o^f should then be Z. Similarly, when $F_x^m - T_x^{eq}$ is PM and $\dot{F}_x^m$ is PL, θ_o^f is chosen as PL. The drone thus compromises between the applied force and its rate of change. This approach is termed the minimization principle of contact forces, where, in order for the drone to move cooperatively with the ground rover, the drone must minimize the contact forces acting at its end due to motion of the ground rover[11]. The fuzzy logic controller provides interpretability by providing a linguistic representation where output (control action) is related to inputs (force and rate of change of force) via an intuitive rule base. Figures 2 and 3 show the membership functions and control surface of the fuzzy logic-based force feedback controller along pitch direction while Table 1 shows the fuzzy rules used in simulations. It should be noted that the membership functions were chosen to be Gaussian to maintain continuity and enable gradual transition from one membership function to another during control; this avoids peaks/spikes in output signal.

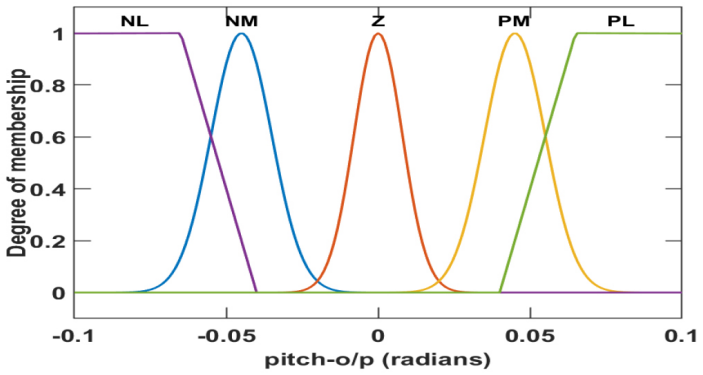
The yaw motion controller is similar to the pitch axis controller except that the first input is F_y^m. The yaw axis figures are not indicated here for brevity purposes. The outputs of fuzzy-based force feedback controllers along pitch and yaw axes are used to obtain the net desired attitude commands using Equations 11 and 12. The net desired attitude commands are used by the attitude controller of the drone to control the rotor speeds using Proportional-Derivative controllers (see[39,43] for more details). Figure 4 illustrates the control architecture of the system with fuzzy logic force feedback controller for a tethered drone, and more details are provided.



(a) Membership functions of input 1 ($F_x^m - T_x^{eq}$).



(b) Membership functions of input 2 ($\dot{F}_x^m$).



(c) Output membership functions of desired pitch angle θ_o^f.

Figure 2. Simulations: Membership functions for fuzzy logic force feedback controller in pitch direction.

5.2. Proportional controller for wind disturbance

We now present another controller for the tethered drone for wind disturbance analysis. Once the input u_o is computed, the desired pitch θ_o^f and yaw ψ_o^f angles based on forces are then calculated using a proportional controller as

$$\theta_o^f = k_{t,\theta}^p (u_{o,x} + F_x^m) \tag{28}$$

and

$$\psi_o^f = k_{t,\psi}^p (u_{o,y} + F_y^m) \tag{29}$$

where $k_{t,\theta}^p$ and $k_{t,\psi}^p$ are the proportional gains. Please note that the symbols used in all sections have been kept the same to maintain consistency. The wind analysis control part of this paper is different from the fuzzy logic

Table 1. Simulations: Fuzzy logic rules of force feedback controller for the pitch direction

		input 1				
		NL	**NM**	**Z**	**PM**	**PL**
input 2	**NL**	NM	NM	NM	Z	Z
	NM	NL	NM	Z	Z	Z
	Z	NM	NM	Z	PM	PM
	PM	NM	Z	PM	PM	PM
	PL	Z	Z	PM	PL	PL

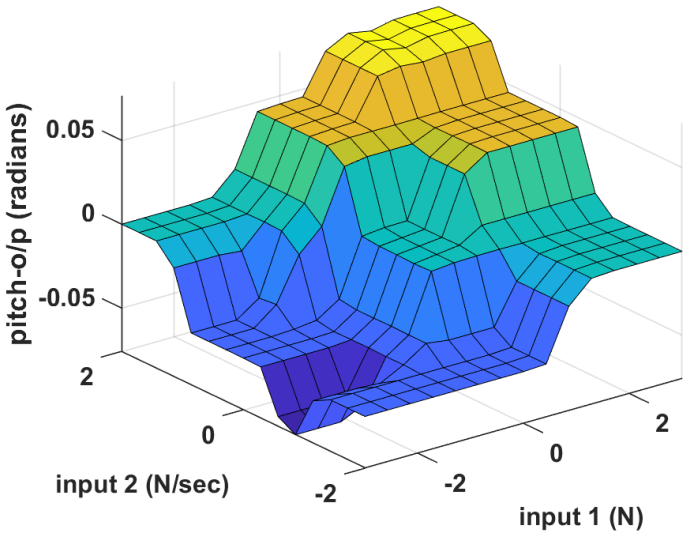


Figure 3. Simulations: Control surface of the fuzzy logic force feedback controller along pitch direction.

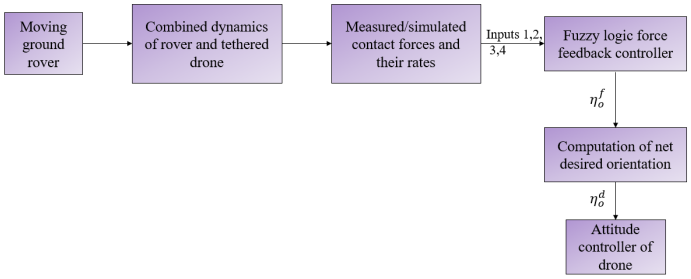


Figure 4. Fuzzy logic force feedback controller: Control architecture of the entire system.

control part presenting the active control of the tethered drone without presence of wind. The wind analysis section is just proposed as an additional preliminary work, and in the future, we plan to apply a fuzzy scheme for it.

5.3. Attitude controller of drone

Based on the computed ϕ_o^d, θ_o^d and ψ_o^d, we compute the deviations from ω_0^h for different rotors used to navigate the drone along different directions. These deviations $\Delta\omega_o^\phi$, $\Delta\omega_o^\theta$ and $\Delta\omega_o^\psi$ are computed by implementing

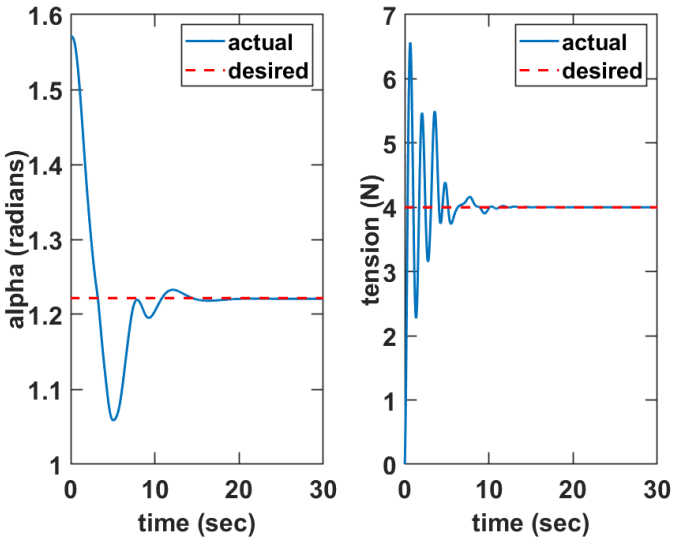


Figure 5. Simulations: Graph showing the angle (α) the tether makes with the ground and the tether tension (T).

proportional-derivative (PD) controllers as follows,

$$\Delta\omega_o^{\phi} = k_{\eta,\phi}^{p}(\phi_o^d - \phi) + k_{\dot{\eta},\dot{\phi}}^{d}(\dot{\phi}_o^d - \dot{\phi}) \tag{30}$$

$$\Delta\omega_o^{\theta} = k_{\eta,\theta}^{p}(\theta_o^d - \theta) + k_{\dot{\eta},\dot{\theta}}^{d}(\dot{\theta}_o^d - \dot{\theta}) \tag{31}$$

$$\Delta\omega_o^{\psi} = k_{\eta,\psi}^{p}(\psi_o^d - \psi) + k_{\dot{\eta},\dot{\psi}}^{d}(\dot{\psi}_o^d - \dot{\psi}) \tag{32}$$

where, $k_{\eta,\phi}^{p}$, $k_{\eta,\theta}^{p}$ and $k_{\eta,\psi}^{p}$ are the proportional gains and $k_{\dot{\eta},\dot{\phi}}^{d}$, $k_{\dot{\eta},\dot{\theta}}^{d}$ and $k_{\dot{\eta},\dot{\psi}}^{d}$ are the derivative gains of the PD controller. The desired individual rotor speeds of the drone are then computed based on $\Delta\omega_o^{\phi}$, $\Delta\omega_o^{\theta}$ and $\Delta\omega_o^{\psi}$ using a control allocation matrix[39].

6. RESULTS

This section presents results for simulations and experiments of the proposed controller. The simulation results consist of implementation of a fuzzy logic force feedback controller and validation of a proportional controller for wind disturbance analysis. MATLAB is used to simulate the system. Experimental work comprises validation of the proposed fuzzy logic force feedback controller using a Crazyflie drone attached to a TurtleBot.

6.1. Simulations

Fuzzy logic force feedback controller

Simulation setup and parameters - A drone of mass $m = 1kg$ is tethered to a ground rover of mass $3kg$. The desired tension in the tether is chosen as $T^d = T^{eq} = 4N$, while the desired angle of the tether with the ground is $\alpha^d = \alpha^{eq} = 70° = 1.22rad$. The desired pitch angle at equilibrium position is $\theta_o^{eq} = 5.75° = 0.1rad$. The ground robot is required to reach the goal location of $(-5m, 5m)$. The tether is chosen to have stiffness $K = 20N/m$, damping $C = 1Nsec/m$, and length $l = 5m$. Other parameters used in simulation are: $L = 0.12m$, $k_{\eta}^{p} = \begin{bmatrix}100 & 100 & 100\end{bmatrix}^T$, $k_{\dot{\eta}}^{d} = \begin{bmatrix}20 & 20 & 20\end{bmatrix}^T$, $k_{g}^{p} = \begin{bmatrix}0.4 & 0.4\end{bmatrix}^T$, $k_{g}^{d} = \begin{bmatrix}1 & 1\end{bmatrix}^T$. The fuzzy membership functions were chosen to be Gaussian to maintain continuity and enable gradual transition from one membership function to another during control; this avoids peaks/spikes in the output signal.

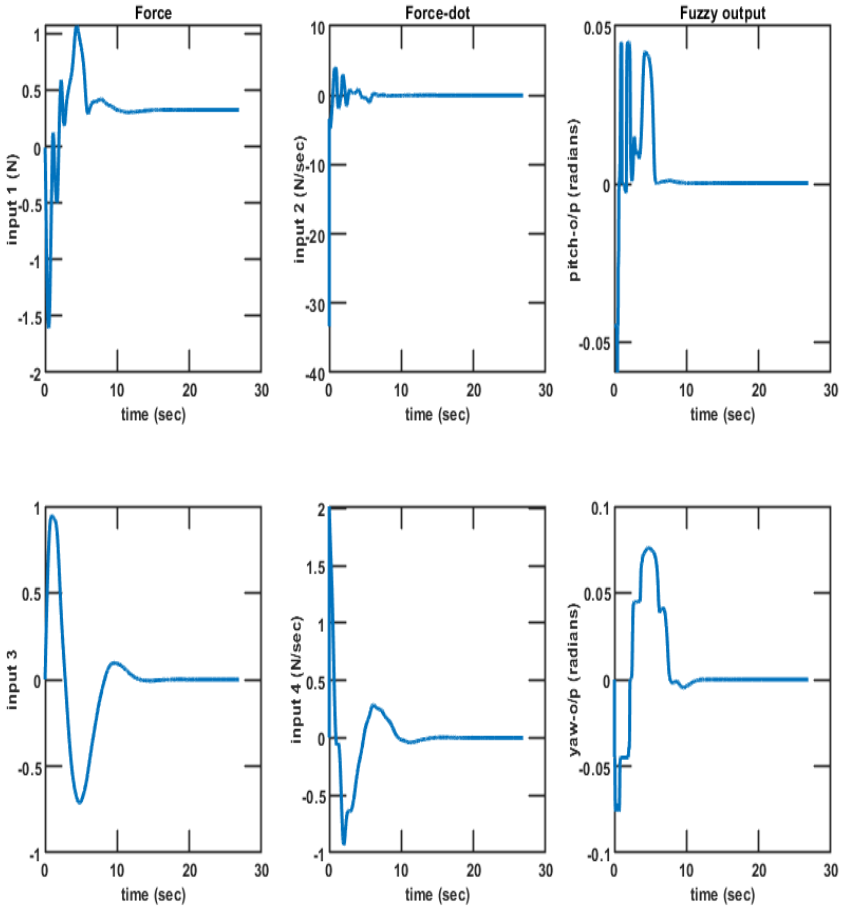


Figure 6. Simulations: Graph showing the inputs and outputs of fuzzy logic force feedback controllers for pitch (top row) and yaw angles (bottom row). Input 1 is $F_x^m - T_x^{eq}$, Input 2 is $\dot{F}_x^m$, Input 3 is F_y^m and Input 4 is $\dot{F}_y^m$.

Results - Figure 5 shows the tension change in the tether and the angle α made by the tether with the ground. It can be seen that the drone tries to maintain the desired values of tension and angle with the ground. Figure 6 presents the inputs and outputs generated by the fuzzy controller for both pitch and yaw axes. The top row demonstrates the inputs and output for the pitch controller, and the bottom row indicates the inputs and output for the yaw controller. Figure 7 exhibits the position of the ground robot and the drone during the simulation period. It can be seen that both the ground rover and the drone stably reach their specified goal locations starting from their initial points. Please note the slight offset between desired and actual position values along the Z_W direction. This is expected since we do not implement any controller along the vertical Z_W axis of the drone. The rightmost column of Figure 7 shows the net desired pitch and yaw angles (θ_o^d and ψ_o^d) commanded to the attitude controller of the drone. It can be observed that the attitude controller of the drone stably tracks the desired values.

Proportional controller for wind disturbance analysis

Simulation setup and parameters - For simulation study of the system under wind disturbance, we chose the following system parameters. The mass of a drone is taken as $m = 1kg$, while the ground rover has a mass of $3kg$. The desired tension in the tether is chosen as $T^d = T^{eq} = 4N$, while the desired angle of the tether with the ground is $\alpha^d = \alpha^{eq} = 70^\circ = 1.22rad$. The desired pitch angle at equilibrium position is $\theta_o^{eq} = 5.75^\circ = 0.1rad$. The ground robot is required to reach the goal location of $(-5m, 3m)$. The tether is chosen to have stiffness

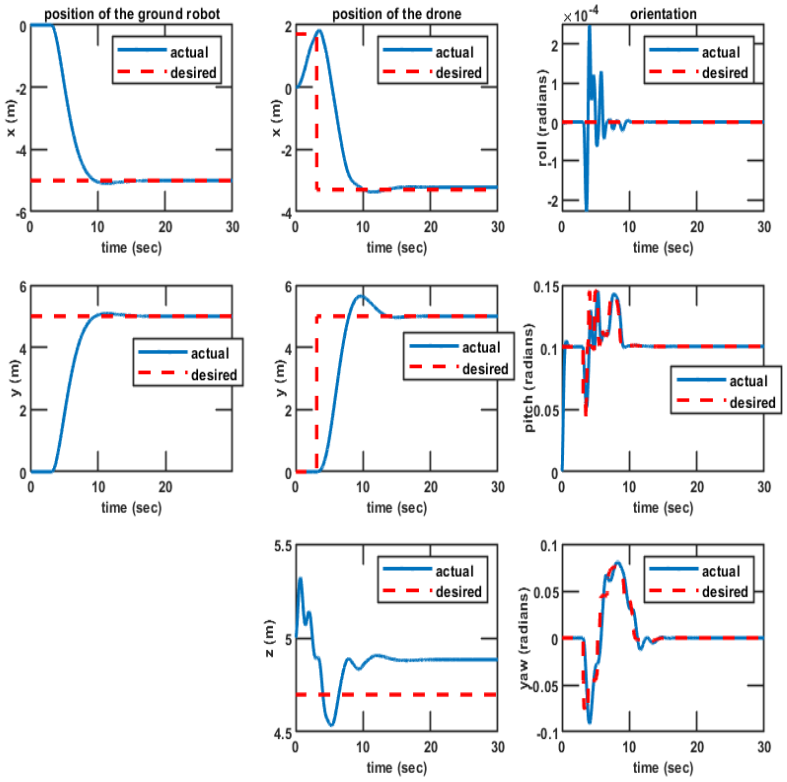


Figure 7. Simulations: Graph showing the desired and actual position of the ground rover and the drone. The left column shows the ground robot position (actual and desired). The middle column shows the drone position (actual and desired). The rightmost column shows the net desired and actual roll, pitch, and yaw angles.

$K = 20N/m$, damping $C = 1Nsec/m$, and length $l = 5m$. A constant wind force of 6N along the X_W direction and 1N along the Y_W direction is applied at t=4 sec and persists till the end of the simulation. Other parameters are: $L = 0.12m$, $k_\eta^p = \begin{bmatrix}100 & 100 & 100\end{bmatrix}^T$, $k_\eta^d = \begin{bmatrix}20 & 20 & 20\end{bmatrix}^T$, $k_{t,\theta}^p = 0.01$, $k_{t,\psi}^p = 0.01$, $k_g^p = \begin{bmatrix}1 & 0.1\end{bmatrix}^T$, $k_g^d = \begin{bmatrix}1 & 1\end{bmatrix}^T$, $K_o = diag\begin{pmatrix}0.01 & 0.01 & 0\end{pmatrix}$, $\Gamma = diag\begin{pmatrix}0.22 & 1 & 0\end{pmatrix}$.

Results - The results for this subsection are shown in Figures 8 and 9. It can be seen from Figure 8 that both the ground robot and the drone reach their respective goal locations in presence of wind disturbance. The vertical motion along the Z_W axis is not controlled; hence, slight offset is seen between the desired and actual altitude values. The attitude controller of the drone also tracks its desired orientation well. Figure 9 shows that the adaptive controller computes the estimate of the unknown wind disturbance effectively. Adaptive estimate of wind force is then used to control the tethered drone, as presented in Section 5. Figure 10 further presents the stable flight of the tethered drone in windy environments. The green dashed line indicates the trajectory of the drone, while the red denotes the path of the ground robot. The blue and the red arrows depict the lateral wind forces acting on the drone. It should be noted that the wind disturbance is assumed to be along the lateral $X_W Y_W$ plane.

6.2. Experiments to validate the fuzzy logic controller

For experimental validation of the fuzzy logic controller, TurtleBot 3 Burger[44] and Crazyflie 2.1[45] were used as the ground robot and quadrotor drone, respectively. The drone was tethered to the turtle bot by a tether. Figure 11 shows the system of the Crazyflie tethered to the TurtleBot. We use Raspberry Pi (Rpi) as

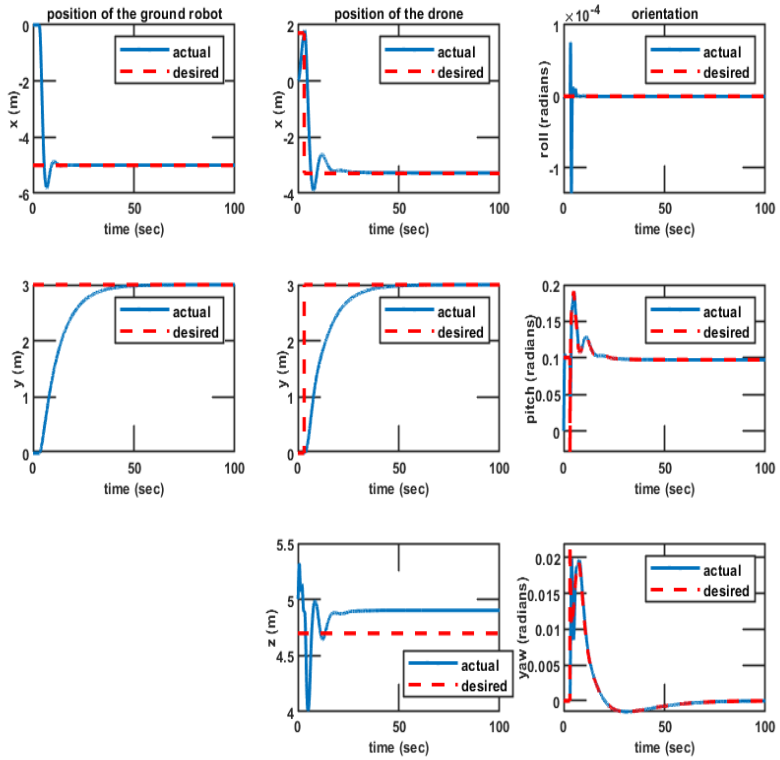


Figure 8. Simulations: Graph showing the position of the drone and the ground robot under wind disturbances. The left column shows the ground robot position (actual and desired). The middle column shows the drone position (actual and desired). The rightmost column shows the net desired and actual roll, pitch, and yaw angles.

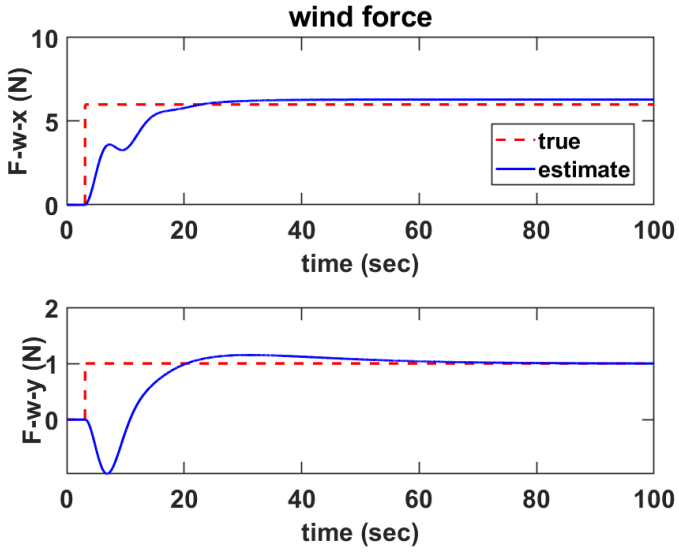


Figure 9. Simulations: Graph showing the estimate of the constant unknown wind force/disturbance on the drone using the proposed adaptive control strategy.

an onboard computer on the TurtleBot which sends commands to the Crazyflie via a Radio attached to the Rpi. Two inexpensive noisy load cells (attached to the ground rover) are employed to measure forces in the

$X_W Y_W$ plane. A/D amplifying converters are also applied along with the load cells. Notably, since tension in tether is equal and opposite at the two ends, i.e., the drone and the ground rover, this allows us to attach the force sensor to the ground rover instead of the drone. It may be noted that this requires properly taking care of the directions of the forces when controlling the drone based on them. Further, the onboard computer, Rpi, gathers load cell data, applies a Kalman filter for the data, and then implements the proposed fuzzy logic force feedback controller. The fuzzy controller then generates the desired pitch and yaw angles and then uses them to calculate the net desired pitch and yaw angles. The net desired pitch and yaw angles are then commanded to the attitude controller of the Crazyflie. It should be noted that the Crazyflie is made to fly at constant thrust. The parameters used in experiments for the Crazyflie platform are $thrust = 40000$ and $\theta_o^{eq} = 4^\circ = 0.07rad$.

Figures 12 and 13 demonstrate the membership functions and control surface of the fuzzy logic force feedback controller used in experiments. The fuzzy rules are similar to those used for simulations and, thus, are not indicated in this subsection. Two cases are evaluated in the experiments: i) Case 1: Straight line motion and ii) Case 2: Circular trajectory tracking. The results along the X_W or pitch axis for Case 1 are shown in Figure 14. It can be seen that the fuzzy logic controller effectively generates the pitch output based on forces and their rates ($F_x^m - T_x^{eq}$ and $\dot{F}_x^m$). Moreover, the attitude tracking controller of the Crazyflie tracks the desired pitch angle well. The black dashed line marked on the bottom plot of Figure 14 shows the equilibrium pitch angle θ_o^{eq} for Case 1 about which the net desired pitch angle θ_o^d varies. Figure 15 presents the results for yaw control for Case 1 based on forces and their rates (F_y^m and $\dot{F}_y^m$). The yaw rate controller of the Crazyflie shows successful tracking of the desired yaw rate. It should be noted that, given hardware constraints, we decided to command the yaw rate to the Crazyflie instead of the desired yaw angle based on force feedback. It can be seen from these results that the drone can be actively manipulated by the ground rover as if the ground robot is flying the drone akin to a kite. Figures 16 and 17 exhibit similar results for Case 2 when the ground robot is made to move along a circular path performing the trajectory tracking. These results show that irrespective of whether the ground robot moves in a straight line or tracks a trajectory, the drone can coordinate with it via forces and their rates.

The results in this section validate the performance of the proposed approach for an actively manipulated tethered drone.

7. CONCLUSIONS

This paper focuses on developing and demonstrating a control approach for actively manipulating drones tethered to a ground robot. We presented a fuzzy logic-based force feedback controller for such a tethered drone system where the drone coordinated with the moving ground rover using the measured contact forces due to the tether. Fuzzy logic allows effective force coordination between the ground rover and the drone, incorporation of human knowledge in controller design, and use of noisy, inexpensive force sensors. Additionally, fuzzy logic provides explainability to the control engineer regarding the decisions the controller takes. Both simulation and experimental results are provided, which validate the performance of the proposed controller. This paper additionally implements a proportional force-based controller to control a tethered drone during wind disturbances. The proposed technique uses an adaptation law to estimate unknown winds and uses that information to control the drone. The simulation results of wind disturbance analysis are presented to support the proposed approach. Future work consists of implementing a fuzzy logic controller for the system during wind disturbances and developing adaptive strategies for such a system during time-varying winds. Current novel state-of-the-art on channel estimation, link and parameters for drone and ground rover communication with posture variation, fuselage scattering effect and utilization of machine learning for 3D channel monitoring is worth noting and can also be incorporated in this research as a part of future work[46–48].

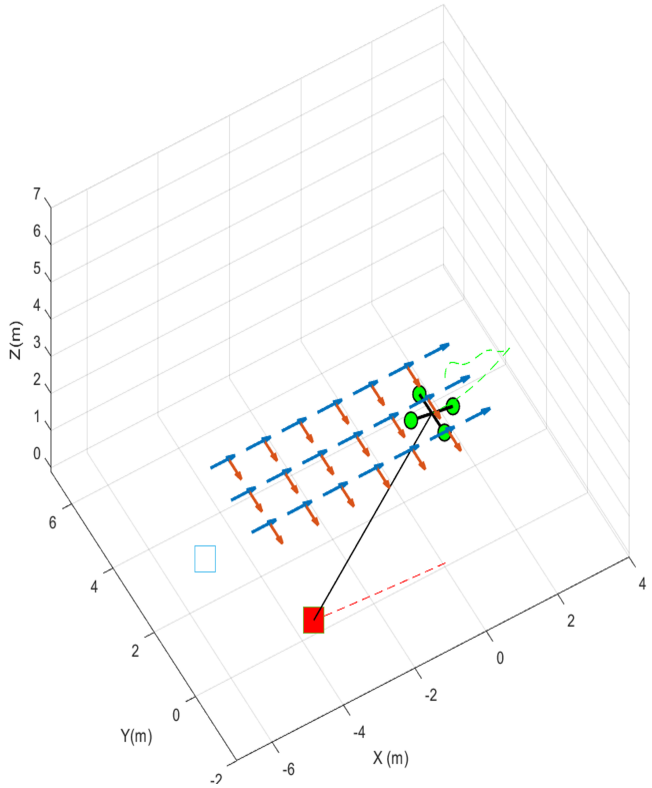


Figure 10. Simulations: Tethered drone flying in a simulated environment with wind disturbance.

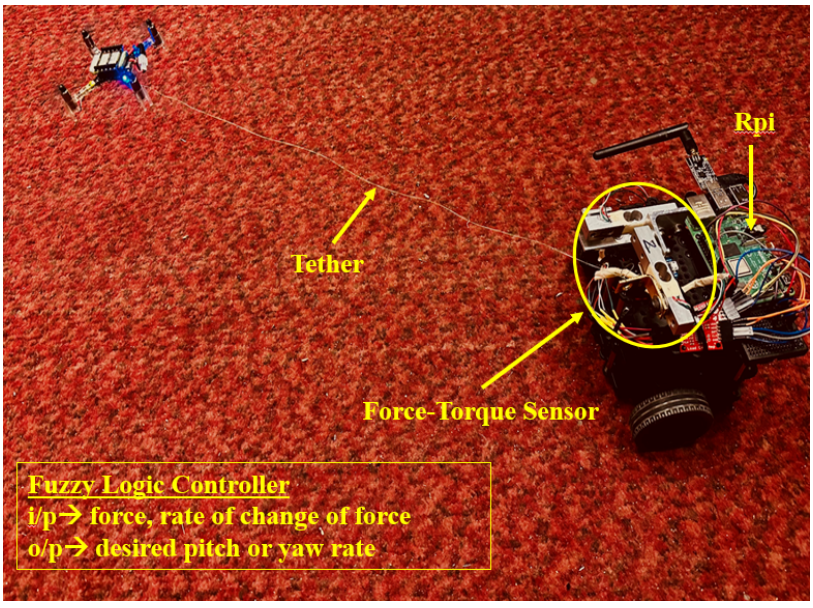
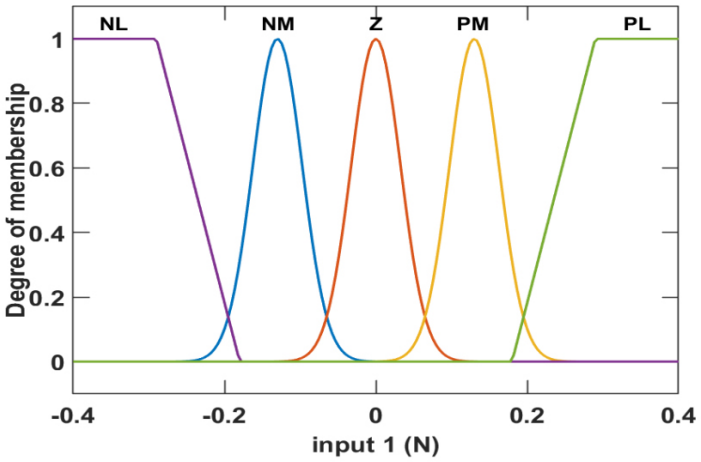
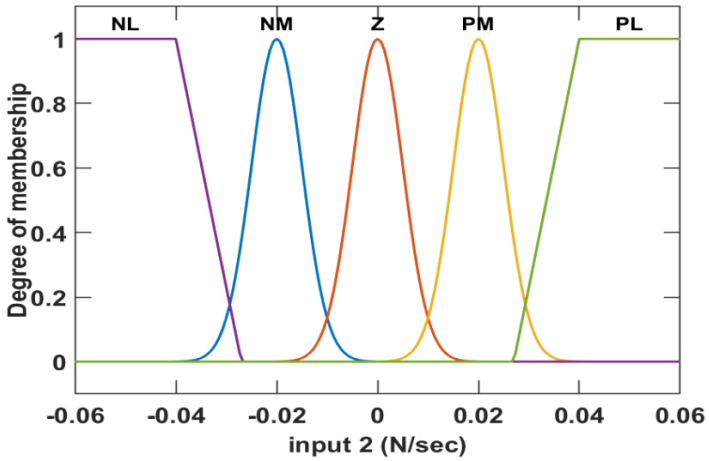


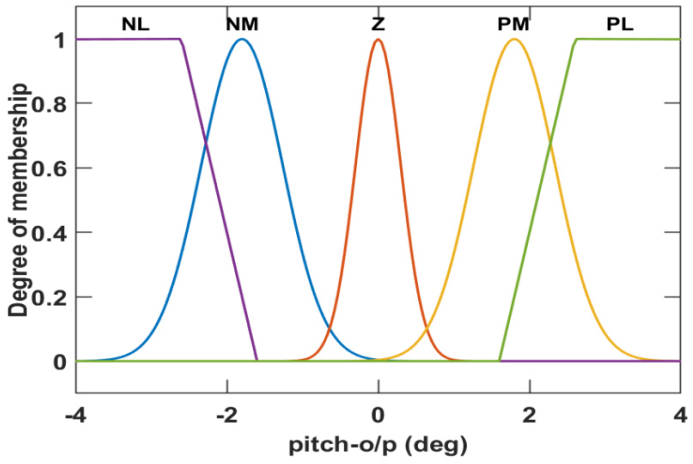
Figure 11. Experiments: Schematic diagram of the system used in experiments.



(a) Membership functions of input 1 ($F_x^m - T_x^{eq}$).



(b) Membership functions of input 2 ($\dot{F}_x^m$).



(c) Output membership functions of desired pitch angle θ_o^f.

Figure 12. Experiments: Membership functions for fuzzy logic force feedback controller in pitch direction.

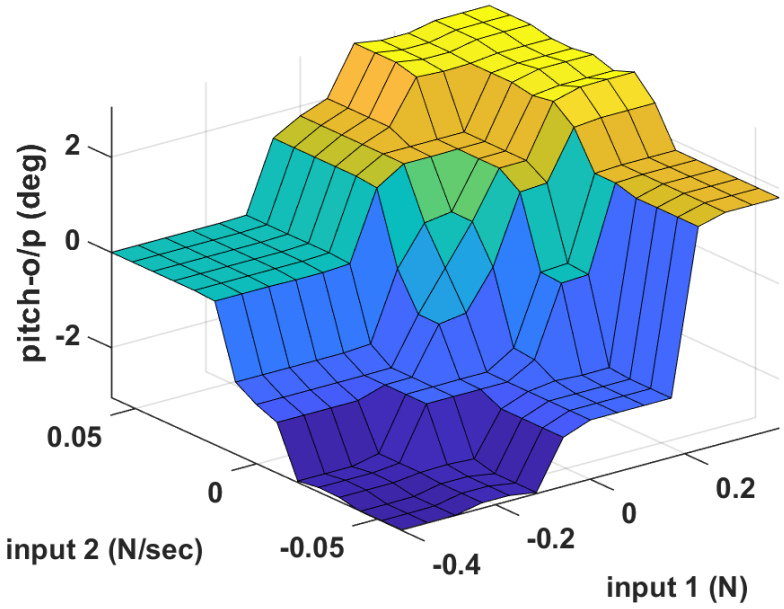


Figure 13. Experiments: Control surface of the fuzzy logic force feedback controller along pitch direction.

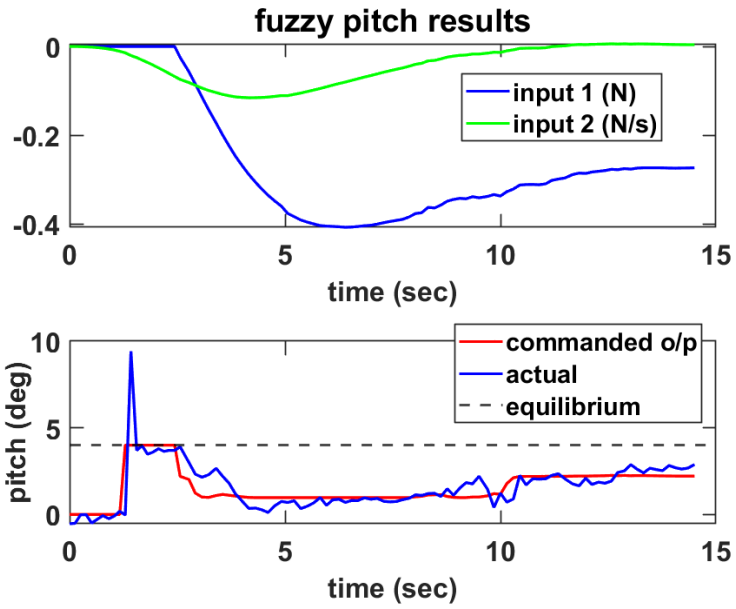


Figure 14. Experiments (Case 1: Straight line motion): Graph showing the inputs - forces and their rates (F_x^m – T_x^{eq} and $\dot{F}_x^m$) -acting on the drone along the pitch direction. The bottom plot shows the desired net pitch angle θ_o^d and the actual pitch angle θ_o. The black dashed line on the bottom plot shows marks the desired equilibrium pitch angle θ_o^{eq}.

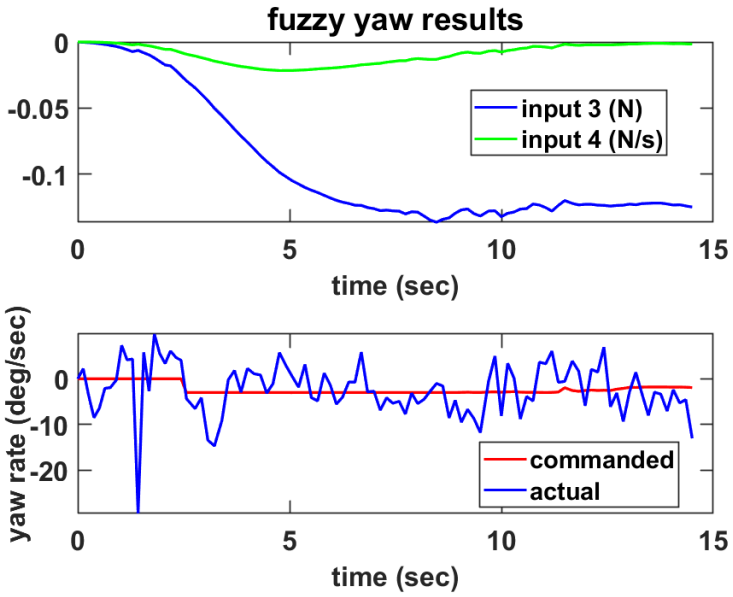


Figure 15. Experiments (Case 1: Straight line motion): Graph showing the inputs - forces and their rates (F_y^m and $\dot{F}_y^m$) -acting on the drone for yaw control. The bottom plot shows the desired yaw rate $\dot{\psi}_o^d$ and the actual yaw rate $\dot{\psi}_o$.

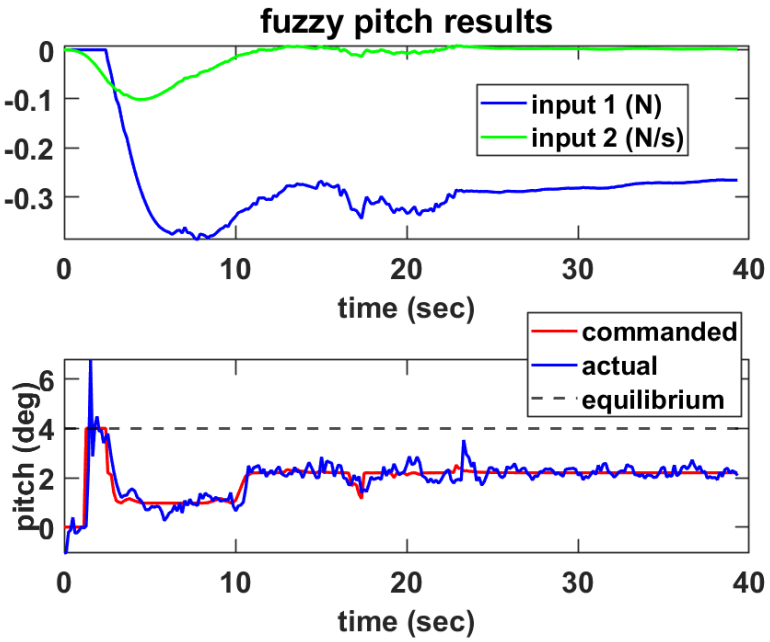


Figure 16. Experiments (Case 2: Circular trajectory tracking): Graph showing the inputs - forces and their rates ($F_x^m - T_x^{eq}$ and $\dot{F}_x^m$) -acting on the drone along the pitch direction. The bottom plot shows the desired net pitch angle θ_o^d and the actual pitch angle θ_o. The black dashed line on the bottom plot shows marks the desired equilibrium pitch angle θ_o^{eq}.

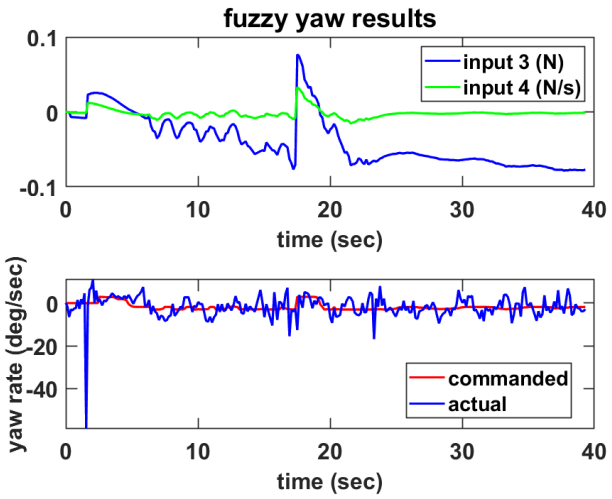


Figure 17. Experiments (Case 2: Circular trajectory tracking): Graph showing the inputs - forces and their rates (F_y^m and $\dot{F}_y^m$) - acting on the drone for yaw control. The bottom plot shows the desired yaw rate $\dot{\psi}_o^d$ and the actual yaw rate $\dot{\psi}_o$.

8. PATENTS

This work is based on our recent patent [21].

DECLARATIONS

Acknowledgments

We would like to acknowledge the University of Cincinnati's Space Research Institute for Discovery and Exploration (SRIDE) for supporting this research in the form of SRIDE Fellowship to the first author of this paper for the years 2022-23.

Authors' contributions

Contributed to the proposed methodology, simulation and experimental validation, and draft writing: Barawkar S

Provided regular feedback on all aspects of research, and assisted in writing the manuscript (The second author is the faculty advisor who investigated and supervised the first author): Kumar M

Availability of data and materials

Not applicable.

Financial support and sponsorship

The University of Cincinnati's Space Research Institute for Discovery and Exploration (SRIDE) funding support was utilized for this research in the form of SRIDE Fellowship to the first author of this paper for the years 2022-23.

Conflicts of interest

All authors declared that there are no conflicts of interest.

Ethical approval and consent to participate

Not applicable.

Consent for publication

Not applicable.

Copyright
© The Author(s) 2024.

REFERENCES

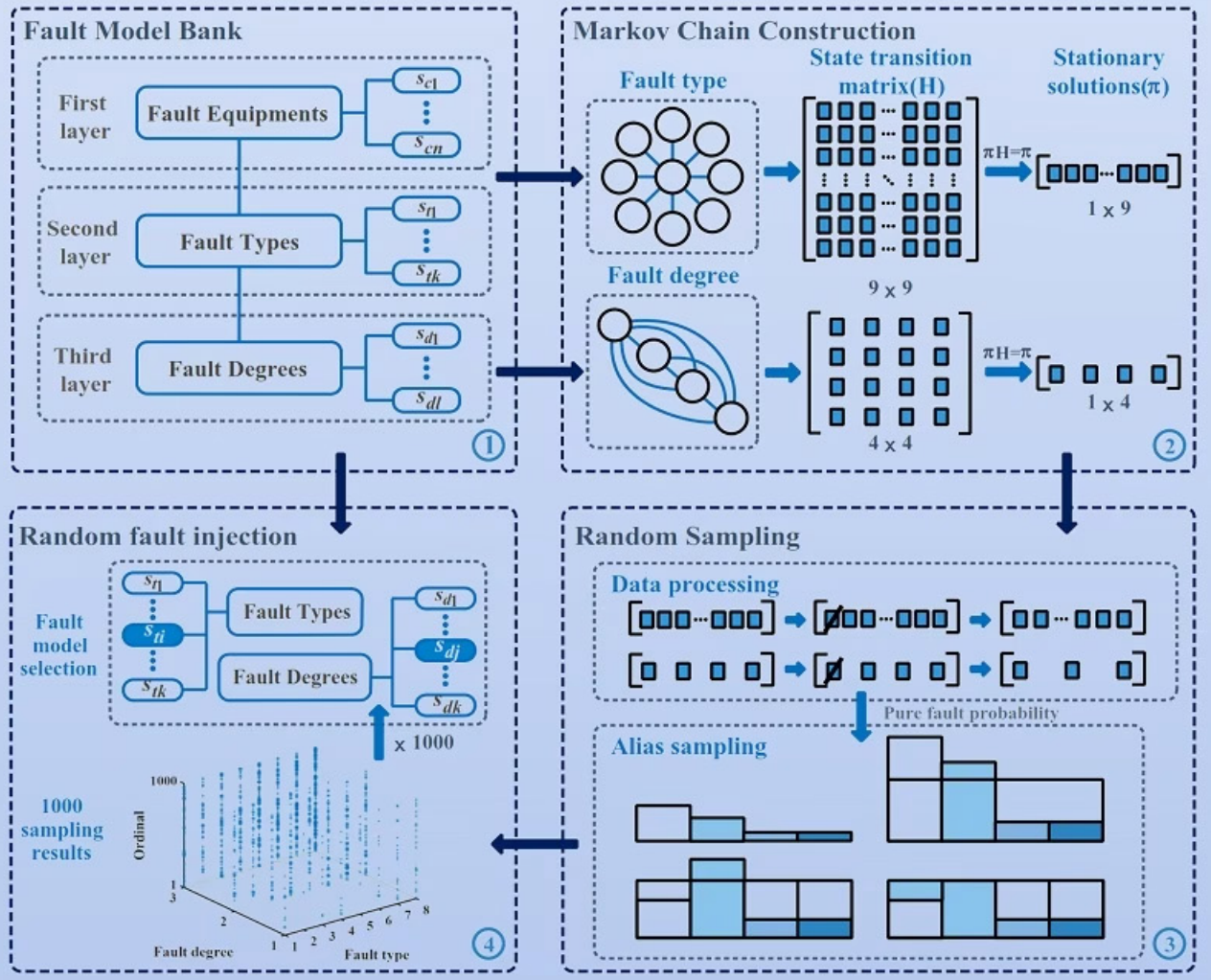
1. Yoo S, Kim S, Kim S, Kang BB. AI-HydRa: advanced hybrid approach using random forest and deep learning for malware classification. *Inf Sci* 2021;546:420–35. DOI
2. Park JH, Farkhodov K, Lee SH, Kwon KR. Deep reinforcement learning-based DQN agent algorithm for visual object tracking in a virtual environmental simulation. *Appl Sci* 2022;12:3220. DOI
3. Fragkos G, Tsiropoulou EE, Papavassiliou S. Disaster management and information transmission decision-making in public safety systems. In: 2019 IEEE Global Communications Conference (GLOBECOM). IEEE; 2019. pp. 1–6. DOI
4. Salehinejad H, Sankar S, Barfett J, Colak E, Valaee S. Recent advances in recurrent neural networks. *arXiv preprint arXiv:180101078* 2017. DOI
5. Osco LP, Junior JM, Ramos APM, et al. A review on deep learning in UAV remote sensing. *Int J Appl Earth Obs Geoinf* 2021;102:102456. DOI
6. Gunning D, Stefik M, Choi J, et al. XAI—Explainable artificial intelligence. *Sci Robot* 2019;4:eaay7120. DOI
7. Keneni BM, Kaur D, Al Bataineh A, et al. Evolving rule-based explainable artificial intelligence for unmanned aerial vehicles. *IEEE Access* 2019;7:17001–16. DOI
8. Došilović FK, Brčić M, Hlupić N. Explainable artificial intelligence: A survey. In: 2018 41st International convention on information and communication technology, electronics and microelectronics (MIPRO). IEEE; 2018. pp. 0210–15. DOI
9. Samek W, Müller KR. Towards explainable artificial intelligence. Explainable AI: Interpreting, Explaining and Visualizing Deep Learning. Cham: Springer International Publishing; 2019. pp. 5-22. DOI
10. Lima BN, Balducci P, Passos RP, et al. Artificial intelligence based on fuzzy logic for the analysis of human movement in healthy people: a systematic review. *Artif Intell Rev* 2021;54:1507–23. DOI
11. Barawkar S, Kumar M. Force-torque (FT) based multi-drone cooperative transport using fuzzy logic and low-cost and imprecise FT sensor. *Proc Inst Mech Eng G J Aerosp Eng* 2023:09544100231153686. DOI
12. De Reus N. Assessment of benefits and drawbacks of using fuzzy logic, especially in fire control systems. FYSISCH EN ELEKTRONISCH LAB TNO THE HAGUE (NETHERLANDS); 1994.
13. Albertos P, Sala A. Fuzzy logic controllers. Advantages and drawbacks. In: VIII international congress of automatic control. vol. 3; 1998. pp. 833–44.
14. Dewi T, Nurmaini S, Risma P, Oktarina Y, Roriz M. Inverse kinematic analysis of 4 DOF pick and place arm robot manipulator using fuzzy logic controller. *Int J Electr Comput Eng* 2020;10:1376. DOI
15. Štefek A, Pham VT, Krivanek V, Pham KL. Optimization of fuzzy logic controller used for a differential drive wheeled mobile robot. *Appl Sci* 2021;11:6023. DOI
16. Mishra DK, Thomas A, Kuruvilla J, et al. Design of mobile robot navigation controller using neuro-fuzzy logic system. *Comput Electr Eng* 2022;101:108044. DOI
17. Lim S, Yu H, Lee H. Optimal tethered-UAV deployment in A2G communication networks: Multi-agent Q-learning approach. *IEEE Internet Things J* 2022;9:18539–49. DOI
18. Elistair;. Available from: https://elistair.com/. [Last accessed on 18 Mar 2024]
19. Fotokite;. Available from: https://fotokite.com/. [Last accessed on 18 Mar 2024]
20. Hoverfly; 2021. Available from: https://hoverflytech.com/. [Last accessed on 18 Mar 2024]
21. Barawkar S, Kumar M, Cohen K. Tether controlled drone. Google Patents; 2022. US Patent App. 17/385,026.
22. Barawkar S, Radmanesh M, Kumar M, Cohen K. Fuzzy logic based variable damping admittance control for multi-UAV collaborative transportation. In: 2018 Annual American Control Conference (ACC). IEEE; 2018. pp. 2084–89. DOI
23. Barawkar S, Radmanesh M, Kumar M, Cohen K. Admittance based force control for collaborative transportation of a common payload using two uavs. In: ASME 2017 Dynamic Systems and Control Conference. American Society of Mechanical Engineers Digital Collection; 2017. DOI
24. Augugliaro F, D'Andrea R. Admittance control for physical human-quadrocopter interaction. In: 2013 European Control Conference (ECC). IEEE; 2013. pp. 1805–10. DOI
25. Breese B, Scott D, Barawkar S, Kumar M. Fuzzy logic controller for force feedback control of quadcopter via tether. In: Dynamic Systems and Control Conference. vol. 84287. American Society of Mechanical Engineers; 2020. p. V002T36A008. DOI
26. Ghamry KA, Dong Y, Kamel MA, Zhang Y. Real-time autonomous take-off, tracking and landing of UAV on a moving UGV platform. In: 2016 24th Mediterranean conference on control and automation (MED). IEEE; 2016. pp. 1236–41. DOI
27. Guérin F, Guinand F, Brethé JF, et al. UAV-UGV cooperation for objects transportation in an industrial area. In: 2015 IEEE International Conference on Industrial Technology (ICIT). IEEE; 2015. pp. 547–52. DOI
28. Fagiano L. Systems of tethered multicopters: modeling and control design. *IFAC-PapersOnLine* 2017;50:4610–15. DOI
29. Martinez Rocamora Jr B, Lima RR, Samarakoon K, et al. Oxpecker: A tethered uav for inspection of stone-mine pillars. *Drones* 2023;7:73. DOI
30. Lee T. Geometric controls for a tethered quadrotor UAV. In: 2015 54th IEEE conference on decision and control (CDC). IEEE; 2015. pp.

2749–54. DOI
31. Kourani A, Daher N. Marine locomotion: A tethered UAV-buoy system with surge velocity control. *Rob Auton Syst* 2021;145:103858. DOI
32. Glick T, Arogeti S. Control of tethered drones with state and input constraints-a unified model approach. In: 2018 International Conference on Unmanned Aircraft Systems (ICUAS). IEEE; 2018. pp. 995–002. DOI
33. Sandino LA, Bejar M, Kondak K, Ollero A. On the use of tethered configurations for augmenting hovering stability in small-size autonomous helicopters. *J Intell Robot Syst* 2013;70:509–25. DOI
34. Nicotra MM, Naldi R, Garone E. Nonlinear control of a tethered UAV: The taut cable case. *Automatica* 2017;78:174–84. DOI
35. Mokhtari A, Benallegue A. Dynamic feedback controller of Euler angles and wind parameters estimation for a quadrotor unmanned aerial vehicle. In: IEEE International Conference on Robotics and Automation, 2004. Proceedings. ICRA'04. 2004. vol. 3. IEEE; 2004. pp. 2359–66. DOI
36. Ali ZA, Zhangang H. Maneuvering control of hexrotor UAV equipped with a cable-driven gripper. *IEEE Access* 2021;9:65308–18. DOI
37. Escareño J, Salazar S, Romero H, Lozano R. Trajectory control of a quadrotor subject to 2D wind disturbances: Robust-adaptive approach. *J Intell Robot Syst* 2013;70:51–63. DOI
38. Kumar R, Agarwal SR, Kumar M. Modeling and Control of a Tethered Tilt-Rotor Quadcopter with Atmospheric Wind Model. *IFAC-PapersOnLine* 2021;54:463–68. DOI
39. Michael N, Mellinger D, Lindsey Q, Kumar V. Experimental evaluation of multirobot aerial control algorithms. *IEEE Robot Autom Mag* 2010;17:56–65. DOI
40. Kawasaki H, Ito S, Ramli RB. Adaptive decentralized coordinated control of multiple robot arms. *IFAC Proc Vol* 2003;36:387–92. DOI
41. Barawkar S, Kumar M. Fuzzy logic force-torque feedback controller for multi-drone cooperative transport with offset cg. *IFAC-PapersOnLine* 2021;54:605–10. DOI
42. Barawkar S. Collaborative transportation of a common payload using two UAVs based on force feedback control. University of Cincinnati; 2017. Available from: http://rave.ohiolink.edu/etdc/view?acc_num=ucin1505125636211596. [Last accessed on 18 Mar 2024]
43. Barawkar S, Kumar M. Cooperative Transport of a Payload With Offset CG Using Multiple UAVs. In: Dynamic Systems and Control Conference. vol. 59162. American Society of Mechanical Engineers; 2019. p. V003T21A008. DOI
44. Robotis. TurtleBot 3 Burger; 2023. Available from: https://www.robotis.us/turtlebot-3-burger-us/. [Last accessed on 18 Mar 2024]
45. Bitcraze. Crazyflie 2.1; 2023. Available from: https://www.bitcraze.io/products/crazyflie-2-1/. [Last accessed on 18 Mar 2024]
46. Hua B, Ni H, Zhu Q, et al. Channel modeling for UAV-to-ground communications with posture variation and fuselage scattering effect. *IEEE Trans Commun* 2023;71:3103-16. DOI
47. Mao K, Zhu Q, Song M, et al. Machine-learning-based 3-D channel modeling for U2V mmWave communications. *IEEE Internet Things J* 2022;9:17592–607. DOI
48. Mao K, Zhu Q, Qiu Y, et al. A uav-aided real-time channel sounder for highly dynamic non-stationary a2g scenarios. *IEEE Trans Instrum Meas* 2023;72:1-15. DOI

Volume 4, Issue 2, June 2024

COMPLEX ENGINEERING SYSTEMS

Editor-in-Chief: Hamid Reza Karimi



Layered random fault injection method for the air braking system based on multiple Markov chains

Zhiwen Chen, Jingke Fan, Lijuan Peng, Hao Luo, Chao Cheng, Zhiyong Chen

Open Access
ISSN 2770-6249 (Online)
www.comengsys.com

Chen *et al*. *Complex Eng Syst* 2024;4:7
DOI: 10.20517/ces.2024.02

Complex Engineering Systems

Research Article

Open Access

Check for updates

Layered random fault injection method for the air braking system based on multiple Markov chains

Zhiwen Chen[1], Jingke Fan[1], Lijuan Peng[1], Hao Luo[2], Chao Cheng[3], Zhiyong Chen[4]

[1]School of Automation, Central South University, Changsha 410083, Hunan, China.
[2]Department of Control Science and Engineering, Harbin Institute of Technology, Harbin 150006, Heilongjiang, China.
[3]School of Computer Science and Engineering, Changchun University of Technology, Changchun 130012, Jilin, China.
[4]School of Engineering, The University of Newcastle, Callaghan, NSW 2308, Australia.

Correspondence to: Dr. Zhiwen Chen, School of Automation, Central South University, No. 932, Lushan South Road, Changsha, 410083, Hunan, China. E-mail: zhiwen.chen@csu.edu.cn

How to cite this article: Chen Z, Fan J, Peng L, Luo H, Cheng C, Chen Z. Layered random fault injection method for the air braking system based on multiple Markov chains. *Complex Eng Syst* 2024;4:7. http://dx.doi.org/10.20517/ces.2024.02

Received: 7 Jan 2024 **First Decision:** 31 Jan 2024 **Revised:** 21 Feb 2024 **Accepted:** 11 Mar 2024 **Published:** 1 Apr 2024

Academic Editor: Hamid Reza Karimi **Copy Editor:** Fanglin Lan **Production Editor:** Fanglin Lan

Abstract

The air braking system is crucial for the safe operation of high-speed trains but is susceptible to faults from harsh environments and prolonged use. However, faulty data in practice are still rare because of the "safety oriented principle". For this purpose, fault injection is regularly employed. Due to the stochastic nature of faults in the system, random fault injection can more realistically simulate faulty scenarios compared to the deterministic fault injection. The traditional method entails analyzing a significant amount of raw data to extract the fault distribution function, followed by random sampling. However, the obstacles lie in the scarcity of raw fault data and the labor-intensive nature of constructing the fault distribution function. This paper proposes a layered random fault injection method based on multiple Markov chains. First, a multi-layer structured fault model base is established for the system, followed by the implementation of layered fault injection. Then, the random fault types and degrees are realized using Markov chains, in which the fault probability function is determined by the state transition matrix. Subsequently, a low-complexity Alias sampling algorithm is proposed for discrete random sampling. The nominal model is transformed into a corresponding fault model based on the sampling outcomes, facilitating the acquisition of fault data. Finally, a graphical user interface is developed to present and visualize the validation results.

Keywords: Air braking system, fault simulation, fault injection, Markov chain, random sampling

© The Author(s) 2024. **Open Access** This article is licensed under a Creative Commons Attribution 4.0 International License (https://creativecommons.org/licenses/by/4.0/), which permits unrestricted use, sharing, adaptation, distribution and reproduction in any medium or format, for any purpose, even commercially, as long as you give appropriate credit to the original author(s) and the source, provide a link to the Creative Commons license, and indicate if changes were made.

1. INTRODUCTION

High-speed trains play an essential role in both railway passenger transportation and the economic development of regions[1,2]. However, owing to their elevated speeds, the braking system has emerged as a critical safety consideration[3,4]. The air braking system (ABS) serves as the central subsystem; however, its intricate operational conditions and prolonged usage frequently result in wear, aging, and sudden abnormalities in certain components. ABS constitutes a primary origin of train malfunctions, and the failure to promptly detect and address these faults can result in significant safety incidents, causing substantial casualties and property damage[5]. The derailment incident of the Talgo 250 Hybrid high-speed train in Spain on July 24, 2013, was attributed to a braking system malfunction, leading to a substantial number of casualties. However, simulating faults on real high-speed trains is expensive and challenging, with the majority of existing platforms primarily concentrating on modeling regular train operations[6]. Therefore, investigating fault injection in ABS of high-speed trains holds significant importance. To fulfill the criteria of minimizing risk, reducing costs, and achieving short development cycles, simulation-based fault injection is often used to simulate and inject faults into ABS. Fault injection is a fault simulation technique proposed in the 20th century[7]. Its essence is to artificially introduce faults into the target system with a certain strategy for a specified fault type so as to observe and analyze the operation behavior of the target system under the condition of injected faults. It has garnered significant attention[8,9].

In the fault injection of automotive systems: Abboush *et al.*[10] proposed a new method based on hardware in the loop (HIL) simulation and automatic real-time fault injection method for generating, analyzing, and collecting data samples in the presence of single and concurrent faults. In the fault injection of aviation control systems: Joshi *et al.*[11] first proposed the application of Microsoft baseline security analyzer to the fault modeling and verification process of aviation control systems. Linnosmaa *et al.*[12] used architecture analysis and design language or its fault extension language to verify the safety requirements of aviation control system fault models. In the fault injection of hydraulic systems: Liu[13] used AMESim to establish a simulation model of the hydraulic control module of the drilling machine loop and studied the fault tolerance and fault detection of hydraulic systems. Karpenko and Sepehri[14] built mathematical models and physical experiments of servo-hydraulic positioning systems and studied leakage between actuator cavities. Niksefat and Sepehri[15] established the mathematical model of the electro-hydraulic servo system and analyzed the influence of sensor fault and hydraulic pump fault on the system through experiments. In the fault injection of heating, ventilation, and air-conditioning (HVAC) systems, Kiamanesh Bahareh[16] presents modeling patterns of numerous faults in HVAC systems based on data from field failure rates and maintenance records. The extended fault injection framework supports the injection of multiple faults with exact control of the timing, locality, and values in fault-injection vectors. A multi-dimensional fault model is defined, including the probability of the occurrence of different sensor and actuator faults. Comprehensive experimental results provide insights into the behavior of the system for concrete example scenarios using multiple fault patterns. In the fault injection of the train system: Zhou *et al.*[17] built a 1:1 electric multiple-unit platform. The brake cylinder leakage fault is realized by adding components to the platform. This fault injection method simulates a single fault type and causes a certain degree of damage to the components when simulating the fault, which hinders the feasibility of conducting experiments repeatedly. Gou *et al.*[18] and Youssef *et al.*[19] reported fault injection of open-circuit faults of rectifiers, gain and noise faults of grid-side current sensors and direct current voltage sensors in a hardware-in-the-loop simulation platform. Chen *et al.*[20] used Simulink/AMESim co-simulation to realize the fault injection of brake cylinders, train pipes and other components in the train braking system and developed a new open-source benchmark for validating the fault diagnosis methods of the electro-pneumatic brake system (EPBS). Yang *et al.*[8] proposed a fault injection strategy based on signal conditioning that realized the simulation of fault scenarios, such as sensors, traction converters, and motors, in the traction drive system. The fault injection simulations mentioned above all involve deterministic faults. By observing the behavior of the system under specific fault scenarios and acquiring faulty data, it becomes possible to formulate targeted fault diagnosis algorithms[21,22]. Presently, the majority of validation methods for diagnostic algo-

rithms entail the establishment of deterministic experiments to assess fault scenarios. Given the stochastic nature of fault occurrences in the system, random fault injection simulates the fault occurrences of the entire system in real-world scenarios. This enhances the objectivity of fault injection and introduces greater flexibility in the injection process. Therefore, employing random fault injection represents a more convenient and efficient approach for validating fault diagnosis algorithms [23]. Presently, the prevalent approach for injecting random faults into a system involves fitting a fault injection model density function using an extensive dataset derived from the system. Subsequently, the fault parameters are randomly sampled based on this function to accomplish the random fault injection [24]. However, the creation of the fault injection model density function involves multiple steps, including data processing, parameter estimation, and function fitting, rendering it a laborious process. Furthermore, the existing challenge for ABS lies in the absence of comprehensive and accurate raw statistical data on fault distribution. This scarcity hampers the comprehensive construction of the fault injection model density function. Therefore, finding a convenient and effective method for conducting random fault injection on ABS is a pressing issue.

The main contributions of this paper are as follows:
1. A layered random fault injection method based on multiple Markov chains (MCs) is proposed, leveraging multiple MCs to systematically represent fault scenarios. This approach constructs both convergent fault type MCs and fault degree MCs, effectively diminishing reliance on initial fault data and significantly streamlining the laborious process of establishing fault distribution.
2. The Alias Sampling (A-S) algorithm has been augmented, incorporating queue operations in lieu of arrays, which serves to decrease the computational complexity involved in constructing Alias tables. This adjustment enhances the efficiency of conducting random sampling within fault distributions.
3. A random fault injection and fault diagnosis platform for the ABS is designed and developed based on Simulink/AMESim co-simulation, including modules for the underlying simulation model, random fault injection, fault diagnosis, and visual display.

Preliminary research has been reported at [25]. The rest of this paper is organized as follows: Section 2 describes the construction of ABS fault model base. Section 3 proposes the method of constructing a random fault distribution based on steady-state MCs and uses the A-S algorithm for random sampling. In Section 4, the simulation results are given. Finally, Section 5 presents the main conclusions.

2. PRELIMINARY

2.1. Typical faults

ABS comprises diverse components, including EP valves, train pipes, brake cylinders, and sensors. Subject to diverse and intricate operational environments and factors, each device category is inevitably prone to encountering various types and degrees of faults. This paper simulates typical fault scenarios of ABS, including sensors, EP valves, brake cylinders, and train pipes. For the sensor, four kinds of faults, including offset, gain, drift and impact, are simulated. For the EP valve, external leakage, internal leakage and spring damage are simulated. For the brake cylinder, the air leakage fault is simulated. For the train pipe, the air leakage fault is simulated. The fault parameters for each fault type are categorized into specific ranges, classifying the fault degrees into three categories based on the national standard GB/T709-2006, which divides equipment status into four levels: normal, mild, average, and severe. Train pipe fault: Compressed air is transmitted in the train pipe. Due to wear and tear over long periods of operation, the walls of the train pipe are thinned or even damaged, eventually leading to gas leaks. This means that the braking system lacks adequate air pressure, resulting in prolonged braking response time as the air pressure decreases within the braking system, thereby delaying the desired braking effect. This leads to a sluggish response of the braking system to braking commands issued by the train driver, consequently affecting the overall braking performance of the train. Sensor offset fault: This particular fault typically induces a fixed deviation in the measurement of the raw signal. The braking system

Table 1. Summary of typical faults

Fault component	Fault type	Fault degree	Changes
Sensor	Offset fault	Normal/ Mild/ Average/ Severe	The output signal increases by a fixed offset
	Gain fault	Normal/ Mild/ Average/ Severe	The output signal is multiplied proportionally
	Drifting fault	Normal/ Mild/ Average/ Severe	The output signal adds an extra signal that is proportional to time
	Shock fault	Normal/ Mild/ Average/ Severe	The output signal is added with a pulse signal at a certain time
EP valve	External air leakage	Normal/ Mild/ Average/ Severe	The pressure values of the four brake cylinders are reduced
	Internal air leakage	Normal/ Mild/ Average/ Severe	The pressure values of the four brake cylinders increase and the exhaust time becomes longer
	Spring fault	Normal/ Mild/ Average/ Severe	The speed of gas-filled changes in the charging time of the brake cylinders
Brake cylinder	Air leakage fault	Normal/ Mild/ Average/ Severe	The corresponding brake cylinder pressure value decreases
Train pipe	Air leakage fault	Normal/ Mild/ Average/ Severe	The pressure values of the four brake cylinders are reduced

relies on sensor data to ensure precise control and distribution of braking force to the wheels. Sensor offset can lead to erroneous detection of wheel speed or other parameters, causing uneven distribution of braking force across the wheels. This can result in an imbalance in the vehicle during braking, affecting both the effectiveness of braking and overall stability. Brake cylinder fault: The realization of air braking ultimately depends on the gas pressure in the brake cylinder through which the basic braking device is propelled. However, after prolonged operation, tiny gaps inevitably develop between the piston and the housing. These tiny gaps allow the gradual infiltration of gas from the gas chamber, leading to a reduction in chamber pressure. As a result, the force applied to the basic braking device is also reduced, ultimately affecting the overall braking effect. The impact of other faults is briefly summarized in Table 1.

2.2. Multi-layer fault injection model base

In order to guarantee coverage of the diverse fault scenarios outlined above, it is essential for the fault injection system to encompass a maximal number of faults. If the foundation of the fault model relies on directly enumerating fault cases, four types of fault devices are involved, with a total of eight fault types for each device, and each type has three degrees of severity. Therefore, there are a total of 24 corresponding fault scenarios. Following this enumerative method would occupy a significant amount of storage resources. Moreover, generating a significant quantity of random fault cases during subsequent fault injection and diagnosis proves to be inconvenient.

To solve the above problems, Fang *et al.*[24] have created a fault model base for the train traction system with a multi-layer structure, organized into three layers. This paper establishes a fault model base for ABS. The first layer stores the fault components; the following layer encompasses the fault types, and the subsequent layer accommodates the fault degrees, denoted as $(\boldsymbol{SC}, \boldsymbol{ST}, \boldsymbol{SD})$. The first layer stores the fault components, and there are n kinds of fault components, which constitute the fault component set $\boldsymbol{SC} = \{s_{c1}, s_{c2}, s_{c3}, \ldots, s_{cn}\}$. The second layer stores fault types, including normal operation and fault states composed of k fault types, which form a fault type set $\boldsymbol{ST} = \{s_{t1}, s_{t2}, s_{t3}, \ldots, s_{tk}\}$. The third layer stores the fault degrees, including the fault state composed of normal and l fault degrees, which forms the fault degree state set $\boldsymbol{SD} = \{s_{d1}, s_{d2}, s_{d3}, \ldots, s_{dl}\}$. A comprehensive fault injection can be denoted as $(s_{ci}, s^i_{tj}, s^j_{dk})$.

Within the three-layer fault model base, real-world scenarios allow for clear classification of both fault devices and fault types. For example, fault devices may consist of train pipes, sensors, and similar components, whereas fault types may cover leakage faults, blockage faults, and so forth. However, the differentiation of fault severity demands distinctions based on the parameter ranges influencing the fault, spanning from mild to average to

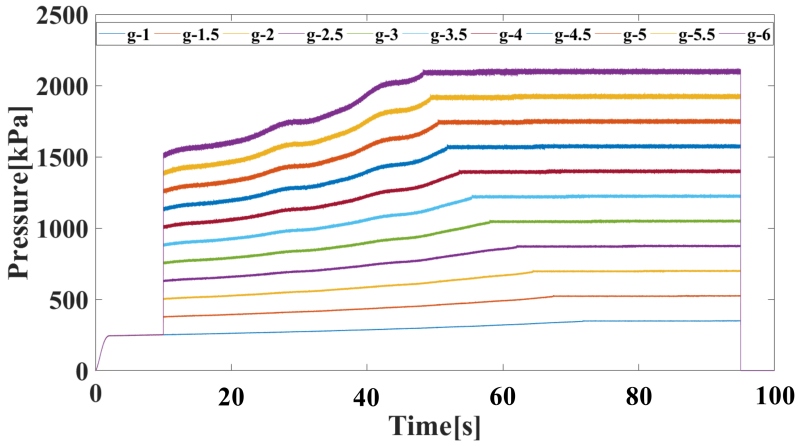


Figure 1. Sensor gain fault at different parameters.

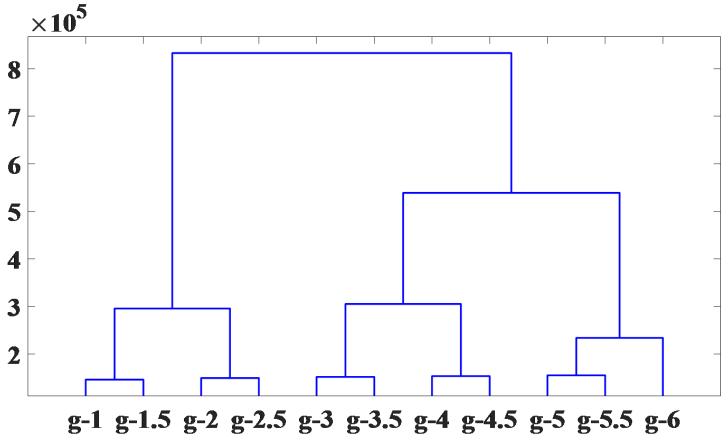


Figure 2. Cluster tree of sensor gain faults.

severe. This paper tackles this challenge by employing spectral clustering algorithms[26], which have become one of the most popular modern clustering algorithms. It is simple to implement and very often outperforms traditional clustering algorithms.

Using the gain fault of the sensor as an illustration, the fault curve is generated by selecting the gain coefficient parameter (ranging from 1 to 6 with a step size of 0.5), and the results are shown in Figure 1. Subsequently, the spectral clustering algorithm is applied for classification, and Figure 2 represents the dendrogram obtained from the classification. Due to the need to categorize the fault severity into three classes, the classification results are outlined as follows: minor (1-2.5), moderate (2.5-4.5), and severe (4.5, 6).

2.3. MC

MC[27] illustrates the interrelated transition process among different states once the system is initiated. Given the determination of the previous state of the system, the probability of the next state is independent of the previous state. In ABS, owing to the fault and repair of diverse components, there is a bidirectional transition between the normal and fault states at each level, with the probability of the next state contingent upon the previous state. As shown in Figure 3, the fault state transition in ABS can be viewed as a MC.

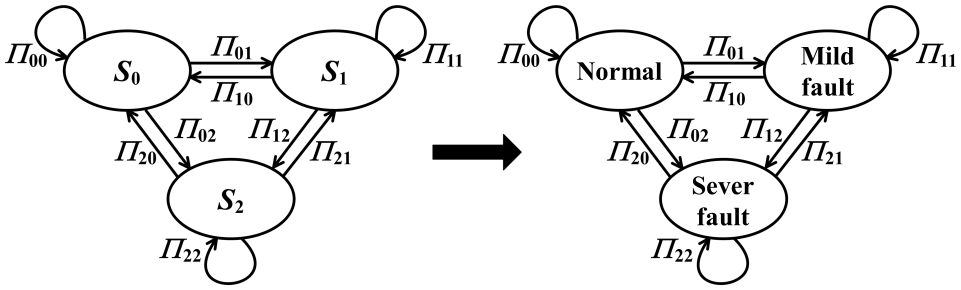


Figure 3. MC of fault. MC: Markov chain.

The MC possesses a distinct "memoryless" attribute, signifying that once the random variables in the nth step are known, those in the $(n+1)$th step are independent of others [28]. For the random variable set $\boldsymbol{X} = \{X_n : n > 0\}$ in the probability space with a one-dimensional countable set as the exponent set, the values of random variables are included in the countable set $\boldsymbol{S} = \{s_0, s_1, s_2, \ldots, s_m\}$, which is called the state set. The "homogeneity" in a homogeneous MC is evident in the fact that the transition probability is solely connected to the state before and after the transition, rather than being dependent on the two time points. A homogeneous MC can be expressed as follows:

$$\text{Prob}\,(X_{n+1} \mid X_n, \ldots, X_1) = \text{Prob}\,(X_{n+1} \mid X_n) \tag{1}$$

$\boldsymbol{\pi}_i$ is defined as its probability distribution and $\boldsymbol{\Pi}_{i,j}$ as its one-step transition probability. The mathematical expression is as follows:

$$\boldsymbol{\pi}_i = \text{Prob}(X_n = s_i), s_i \in \boldsymbol{S}. \tag{2}$$

$$\boldsymbol{\Pi}_{i,j} = \text{Prob}(X_{n+1} = s_j \mid X_n = s_i), \quad s_i, s_j \in \boldsymbol{S}. \tag{3}$$

When all objects of a MC satisfy the following properties: recurrence, aperiodicity and pairwise connectivity, it has a unique steady-state solution [29,30], which is independent of the initial state, and can be expressed as [31]:

$$\lim_{n\to\infty} \text{Prob}\,(X_n = s_i) = \pi_i \tag{4}$$

The algorithm for solving the steady-state probability of MC is shown in Algorithm 1.

Algorithm 1: Steady-state probability of MC (SM)

Input: A state-transition matrix M.
Output: A steady-state probability matrix.
$Phase_n = M$
$Phase_n1 = Phase_n1 * M$
while *not (Phase_n == Phase_n1).all( )* **do**
    $Phase_n = Phase_n1$
    $Phase_n1 = Phase_n1 * M$
Return the matrix: $Phas_n$.

3. LAYERED RANDOM FAULT INJECTION METHOD BASED ON MULTIPLE MCS

3.1. Fault probability distribution construction

In this paper, a multi-layer fault injection model base is established, which is divided into fault components, types and degrees. However, considering the background of ABS, the majority of components exhibit only a single type of fault. Therefore, the combination of fault components and types is called a fault type. In the

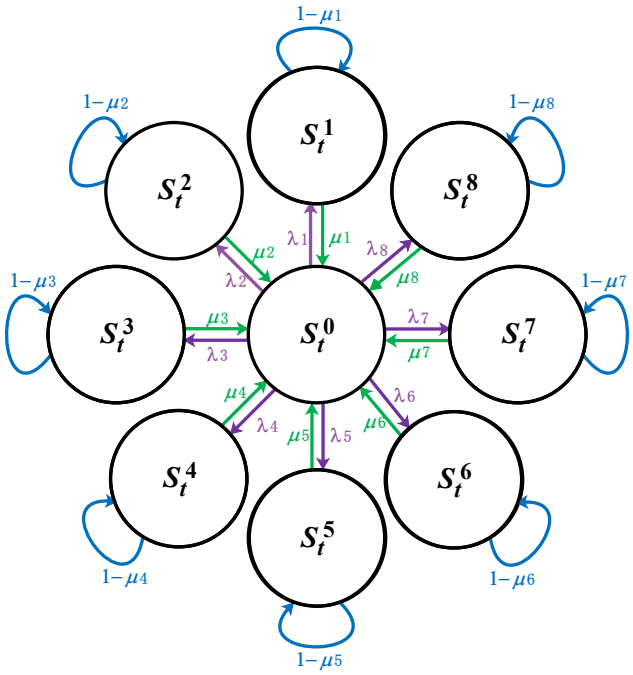


Figure 4. Fault type state transition diagram.

subsequent construction of a MC model, only the construction of fault type and fault degree MC is considered, which simplifies the model.

3.1.1 Fault type transfer MC model construction

When constructing the state transition diagram for fault types, the following conditions must be satisfied:

① When examining the state transition of an individual fault within the system, every fault state and the normal state should be mutually reachable and interconnected. However, distinct fault states should not be mutually reachable. Because the faults addressed in this manuscript are all individual faults and do not involve compound faults, that is, scenarios where two or more faults occur simultaneously. The state transition diagram must adhere to the following formula:

$$s_t^i \leftrightarrow s_t^0 \quad i = 1, 2, \ldots, k \tag{5}$$

② In the case of single fault state transfer, different fault states are unreachable, and the state transition diagram must adhere to the following formula:

$$s_t^i \nrightarrow s_t^j \quad i, j = 1, 2, \ldots, k,\ i \neq j \tag{6}$$

For fault type MC in Figure 4: there are k fault types except for the normal operation state. The state transition probability matrix $\boldsymbol{H_t}$ of the fault type MC can be constructed by using the steady-state probability distribution of the fault degree MC.

In Figure 4, λ_i(i=1,2,...,k) is defined as the probability of fault occurrence of the ith fault type, specifically, the probability of transition from state s_t^0 to state s_t^i. $\mu_i(i = 1, 2, ..., k)$ represents the probability of transition from

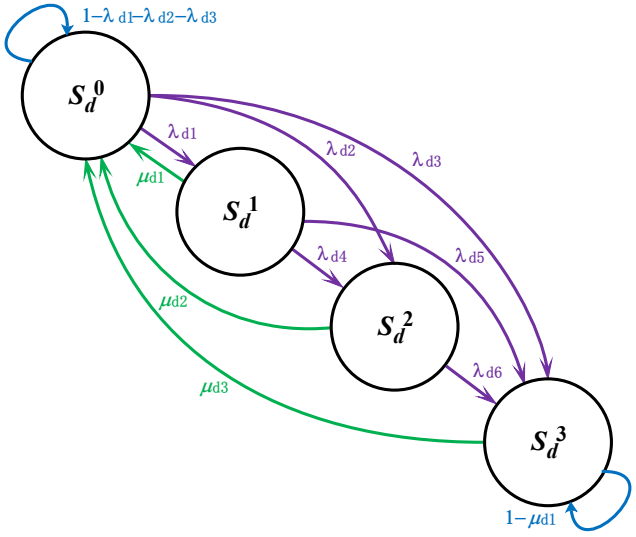


Figure 5. Fault degree state transition diagram.

state s_t^i to state s_t^0. The state transition probability matrix $\boldsymbol{H_t}$ of the fault type MC is constructed as follows:

$$\boldsymbol{H_t} = \begin{bmatrix} 1-\sum_{i=1}^{k}\lambda_i & \lambda_1 & \cdots & \lambda_k \\ \mu_1 & 1-\mu_1 & \cdots & 0 \\ \vdots & \vdots & \ddots & \vdots \\ \mu_k & 0 & \cdots & 1-\mu_k \end{bmatrix} \tag{7}$$

$\boldsymbol{\pi_t}$ is defined as the stationary probability distribution of MC with fault type, and $\pi_{t0}, \pi_{t1}, ..., \pi_{tk}$ are respectively the steady-state probability of normal operation state and k fault states.

$$\boldsymbol{\pi_t} = [\pi_{t0}, \pi_{t1}, ..., \pi_{tk}] \tag{8}$$

$$\boldsymbol{\pi_t H_t} = \boldsymbol{\pi_t} \tag{9}$$

$$\sum_{i=0}^{k} \pi_{ti} = 1 \tag{10}$$

The specific value of $\pi_{ti}(i = 0, 1, ..., k)$ can be determined by simultaneously solving Eqs. (8)-(10), representing the steady-state solution. At this point, the steady-state probabilities corresponding to the aforementioned $k+1$ states have been acquired.

3.1.2 Fault degree transfer MC model construction

When constructing the state transition relationships for the fault degree state transition diagram, the following conditions must be satisfied:

① Without accounting for the repairability of the system, faults consistently progress in a more severe direction, and the state transition diagram must adhere to the following formula:

$$s_d^i \rightarrow s_d^j \quad i, j = 1, 2, \ldots, l, \ i \leq j \tag{11}$$

② Taking into account the reparability of the system, any fault state can be directly restored to the normal state, and the state transition diagram must adhere to the following formula:

$$s_d^i \rightarrow s_d^0 \quad i = 1, 2, \ldots, l \tag{12}$$

In Figure 5, $\boldsymbol{H_d}$ is defined as the state transition probability matrix of the fault degree MC. Using $l = 3$ as an illustration, the expression of $\boldsymbol{H_d}$ is as follows:

$$\boldsymbol{H_d} = \begin{bmatrix} 1 - \sum_{i=1}^{3} \lambda_{di} & \lambda_{d1} & \lambda_{d2} & \lambda_{d3} \\ \mu_{d1} & 1 - \gamma_{14} - \lambda_{d5} & \lambda_{d4} & \lambda_{d5} \\ \mu_{d2} & 0 & 1 - \gamma_{26} & \lambda_{d6} \\ \mu_{d3} & 0 & 0 & 1 - \mu_{d3} \end{bmatrix} \tag{13}$$

where $\gamma_{ij} = \mu_{di} + \lambda_{dj}$. $\lambda_{dj}(j = 1, 2, ..., 2l)$ represents the probability of transition from state s_d^{j-1} to state s_d^j, which is recorded as the fault rate. $\mu_{di}(i = 1, 2, ..., 2l)$ represents the probability of transition from state s_d^i to state s_d^0, which is recorded as the repair rate.

$\boldsymbol{\pi_d}$ is defined as the stationary probability distribution of MC with fault degree, and $\pi_{d0}, \pi_{d1}, ..., \pi_{dl}$ represent the steady-state probability of normal and l fault degree, respectively.

$$\boldsymbol{\pi_d} = [\pi_{d0}, \pi_{d1}, ..., \pi_{dl}] \tag{14}$$

$$\boldsymbol{\pi_d} \boldsymbol{H_d} = \boldsymbol{\pi_d} \tag{15}$$

$$\sum_{i=0}^{l} \pi_{di} = 1 \tag{16}$$

The specific value of $\pi_{di}(i = 1, 2, ..., l)$ can be obtained by solving Eqs. (14)-(16). The steady-state probabilities corresponding to the aforementioned four fault levels have been determined.

3.2. Random sampling of probability distribution

Upon acquiring the probability distribution of faults in ABS, efficiently simulating this distribution and conducting a substantial number of sampling tests have emerged as pivotal challenges.

3.2.1 Data processing

Random sampling from the calculated failure probability distribution may result in around 70% of the 1000 samples being in normal conditions, leading to significant resource wastage. Considering that faults are not introduced from the outset, the fault data inherently comprises both normal operational and fault data. Subsequently, following the acquisition of the steady-state probability distribution for fault types, the normal operational state can be eliminated, and a re-computation of the probability distribution can be conducted.

Eq. (8) and Eq. (14) are transformed into:

$$\boldsymbol{\pi_t} = [\pi_{t1}, \pi_{t2}, ..., \pi_{tk}]/(1 - \pi_{t0}) \tag{17}$$

$$\boldsymbol{\pi_d} = [\pi_{d1}, \pi_{d2}, ..., \pi_{dl}]/(1 - \pi_{d0}) \tag{18}$$

3.2.2 Random sampling method based on Alias algorithm

The Simple sampling (S-S) method shows a substantial discrepancy with the actual probability, particularly as the actual probability decreases. Additionally, each sampling operation in the S-S method has a complexity of O(K); even if the binary search method is used, the complexity is O(log(K)). Given the necessity for hundreds of samplings in a single test, a lower-complexity algorithm is required. The A-S algorithm [32] is a cutting-edge sampling algorithm that significantly mitigates the time complexity of sampling. Given a discrete random probability distribution Prob($X = x_i$) = p_i, the A-S algorithm treats the entire probability distribution as N rectangles with an area of $1 * p_i$, and all events are converted into corresponding rectangular areas. Next, the area of each rectangle is normalized by $1/N$ to obtain N rectangles with an area of $N * p_i$. Fill the rectangles with an area of more than 1 into the rectangles with an area of less than 1, and record the details of the filling

operation. Finally, N rectangles with a total area of $1 * 1$ are formed. Two arrays are constructed according to the original area and filling condition of the rectangle. One is the probability array, which is recorded as $prob$ and stores the original probability of the corresponding event of each rectangle. The other is an alias array. It stores the event number of the rectangle that is not filled enough, which is recorded as $alias$. If it is not filled, it is represented by $NULL$.

The algorithm constructed using the above method has a time complexity of $O(K^2)$. A more efficient approach involves using two queues, A and B, to separately store node labels greater and less than 1. In each iteration, a node is selected from each queue, and the larger one is merged into the smaller one. The smaller node is then dequeued. Subsequently, the merged node is examined, and if its value is greater than 1, it is enqueued into queue A. If the value is equal to 1, it is dequeued. If the value is less than 1, it is enqueued into queue B. This algorithm achieves a time complexity of $O(K)$. The algorithm for constructing the above A-S table and sampling process is shown in Algorithm 2. From the aforementioned process, it is evident that the A-S algorithm is designed to trade space for time. Despite having a space complexity of $O(K)$, its time complexity is merely $O(1)$. Given sufficient physical space, this results in a significant reduction in time complexity and an acceleration in sampling speed.

This section combines the model built in Section 2 with the fault model to extract specific faults hierarchically

Algorithm 2: Alias Sampling

Input: A list P of length n, store the discrete distribution
Output: An integer in range $[0, n)$
Create arrays $Alias$ and $Prob$, each of size n
Create two queues, $Small$ and $Large$.
Multiply each probability by n.
if $p_i < 1$ **then**
  add i to $Small$
else
  add i to $Large$
while *$Small$ and $Large$ are not empty* **do**
  Remove the first element from $Small$, and call it l
  Remove the first element from $Large$, and call it g
  Set $Prob[l] = p_l$. And set $Alias[l] = g$
  Set $p_g := (p_g + p_l) - 1$
  if $pg<1$ **then**
    add g to $Small$
  else
    add g to $Large$
while *$Large$ is not empty* **do**
  Remove the first element from $Large$, and call it g. And set $Prob[g] = 1$
while *$Small$ is not empty* **do**
  Remove the first element from $Small$, and call it l. And set $Prob[l] = 1$
Generation a fair die roll from an n-sided die, call the side i
Flip a biased coin that comes up head with probability $Prob[i]$
if *the coin comes up heads* **then**
  return i
else
  return $Alias[i]$

from the fault model library according to sampling results, to achieve effective fault injection. The specific operational process is as follows:

① A layered fault injection model ($\boldsymbol{ST}, \boldsymbol{SD}$) for the ABS is established according to Section 2, storing collections of fault types and degrees separately;

② Users set the MC state transition matrix for fault types and degrees according to requirements and use it as input parameters; this matrix must meet certain conditions; for instance, the sum of elements in each row must equal 1;

③ The steady-state probability calculation module is responsible for calculating the steady-state probabilities of the MC state transition matrices for fault types and degrees and uses them as the fault probability distribution;

④ In the random fault generation module, the improved A-S algorithm is applied to randomly sample from the fault type probability distribution and the fault degree probability distribution, successively, obtaining (s_{ti}, s_{dj}^{i});

⑤ Upon receiving a model switching signal, the model switching module will switch the switch from the normal state model to the corresponding fault model, thus implementing the injection of random faults. The model switching signal refers to a signal when the system's randomly preset or user-defined fault injection time arrives.

Following these steps allows for the single instance of random fault injection into the ABS; repeating these steps can achieve multiple instances of random fault injections.

3.3. Overview

Most fault injections are deterministic, requiring users to manually set fault parameters for each injection. In contrast, random fault injection can more accurately simulate real-world fault scenarios, providing robust data support for subsequent fault detection and diagnosis research while reducing manual labor in extensive experiments. The prevalent method for implementing random fault injections involves fitting a large volume of raw sample data to obtain a distribution function that meets certain conditions. Then, based on this function, fault parameters are randomly sampled to achieve random fault injection. However, constructing a fault distribution function is a tedious process that requires data processing and parameter estimation. Additionally, a significant challenge in current research is the lack of raw fault data for ABSs, making it difficult to fit a fault distribution function comprehensively and accurately.

To address these issues, this chapter introduces a hierarchical random fault injection method based on multiple MCs. By leveraging the steady-state characteristics of MCs, users only need to provide the system's state transition matrix to construct a fault probability distribution, circumventing the need for complete raw data and tedious function fitting. Following the probability distribution acquisition, an improved A-S algorithm is proposed to sample the fault probability distribution accurately, efficiently, and with minimal repetition. This approach effectively resolves the challenges of constructing fault probability distributions and sampling fault probabilities, facilitating convenient and effective random fault injection into ABSs. The overall process is shown in Figure 6, and the algorithm is given in Algorithm 3.

4. SIMULATION AND ANALYSIS

4.1. Platform introduction

For the convenience of user verification, a fault injection and diagnosis platform for ABS is designed and implemented in this paper. The operational interface of this platform is illustrated in Figure 7, allowing the selection of position ② for deterministic and random fault injections. It incorporates the multiple MCs-based layered random fault injection method proposed in this paper. Click ② in Figure 7, select Random fault injection, and the random fault injection parameter setting interface, as shown in Figure 8, will pop up. ① Introduction describes the use process of the interface. ② Fault type state transition matrix setting on the left

Algorithm 3: Multiple MCs-based layered random fault injection method

Input: A fault type state-transition matrix Mt. A fault degree state-transition matrix Md. The sample size n

Output: An array of fault type sample results Res_t. An array of fault degree sample results Res_d

$Pt = \mathrm{SM}(Mt)$

$Pd = \mathrm{SM}(Md)$

for $i = 1$ *to* n **do**

  $Res_t(end + 1) = \mathrm{A\text{-}S}(Pt)$

for $i = 1$ *to* n **do**

  $Res_d(end + 1) = \mathrm{A\text{-}S}(Pd)$

Return the array of fault degree sample results Res_t

Return the array of fault degree sample results Res_d

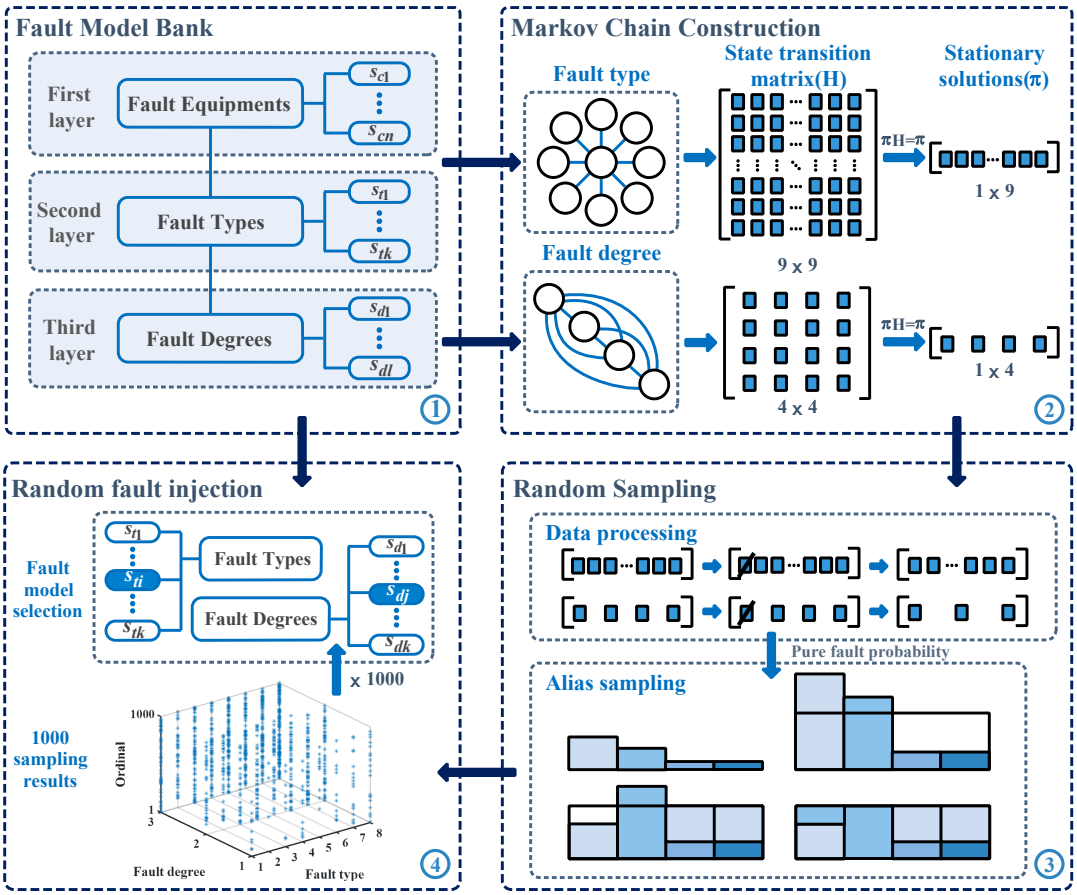


Figure 6. Multiple MCs-based layered random fault injection method. MC: Markov chain.

should be filled in. ④ Fault degree state transition matrix setting on the right should be filled in. Click OK after filling in; the platform will automatically calculate the steady-state solution of the MC according to the state transition matrix filled in by the user and display it in ③ Steady state probability of fault types and ⑤ Steady state probability of fault degrees below. Click ⑥ Start Fault Injection; the platform will automatically conduct random fault injection according to user settings, and the final simulation results will be displayed in the ⑱ data visualization module and ⑲ fault diagnosis module in Figure 7. In addition, for the specific operation process, please refer to the platform's help document for details, which is available at http://gfist.csu.

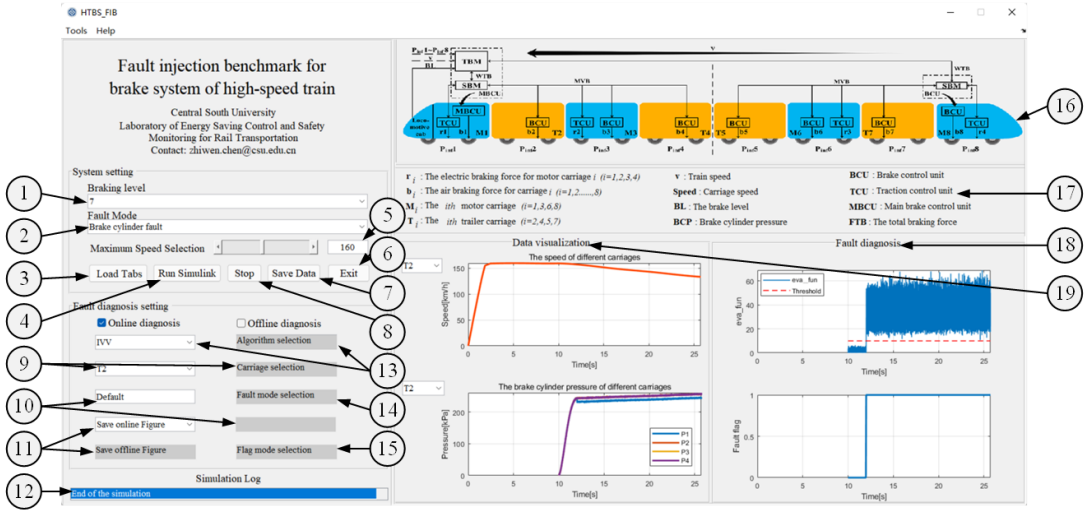


Figure 7. EPBS_FIDMV main function model diagram. ①Set up the fault level. ②Set the fault type. ③Load form. ④Run the simulation. ⑤Set up the initial braking speed. ⑥Exit interface. ⑦Save observation point data. ⑧Stop the simulation. ⑨Select carriage. ⑩Display user-defined algorithm path. ⑪Save the online and offline fault diagnosis results. ⑫Lists simulation logs. ⑬Select fault diagnosis algorithms. ⑭Load offline fault data. ⑮Set the offline fault flag mode. ⑯Display train operation structure diagram. ⑰Introduce abbreviations. ⑱Display the online and offline fault diagnosis results. ⑲Display the data curve of the fault observation point.

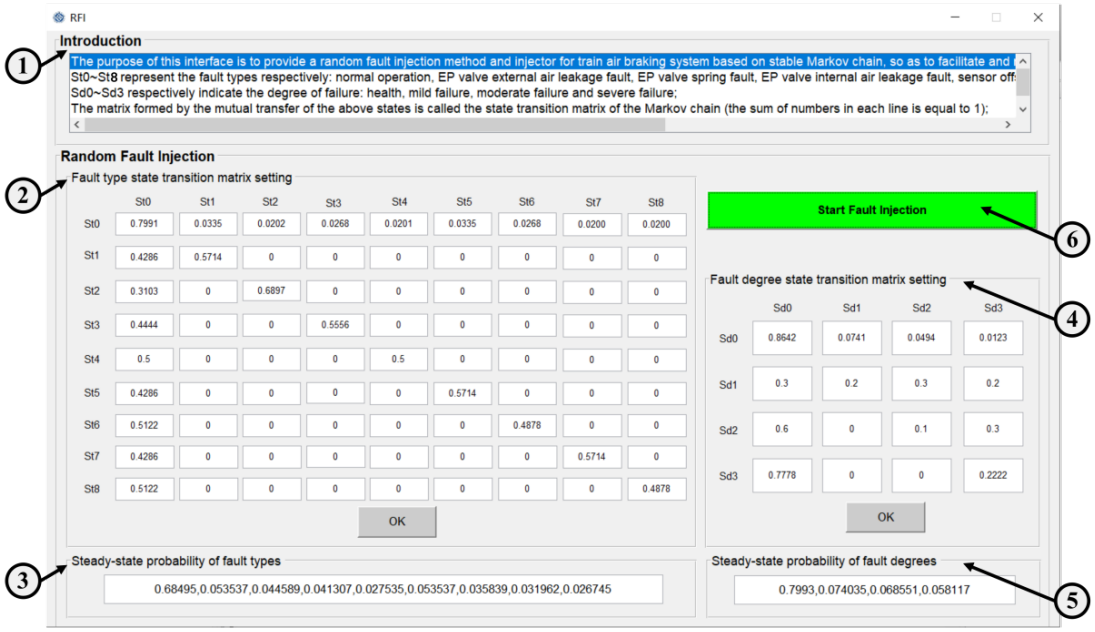


Figure 8. Fault injection and diagnosis platform of ABS. ①Introduce the operation process. ②Set the fault type state transition matrix. ③ Display steady-state probability of fault type. ④Set the fault degree state transition matrix. ⑤Display steady-state probability of fault degree. ⑥Start fault injection.

edu.cn/Download.html.

4.2. Simulation results and comparative analysis

One test in the above figure is taken as an example. The fault types include normal operation state, sensor deviation fault, sensor gain fault, EP valve external leakage, train pipe air leakage fault, and so on. The above states form the fault type state set $\boldsymbol{S_t} = \{s_t^0, s_t^1, s_t^2, s_t^3, s_t^4, s_t^5, s_t^6, s_t^7, s_t^8\}$ in turn. The fault degree in-

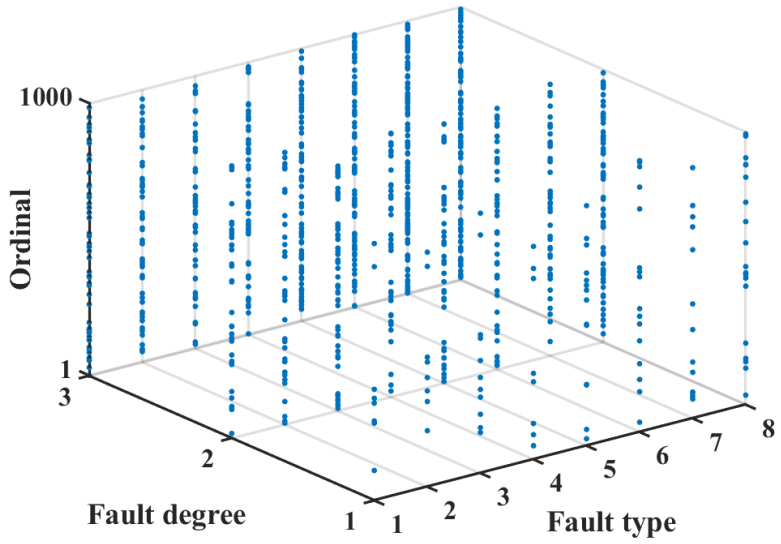


Figure 9. 1000 sampling results based on A-S.

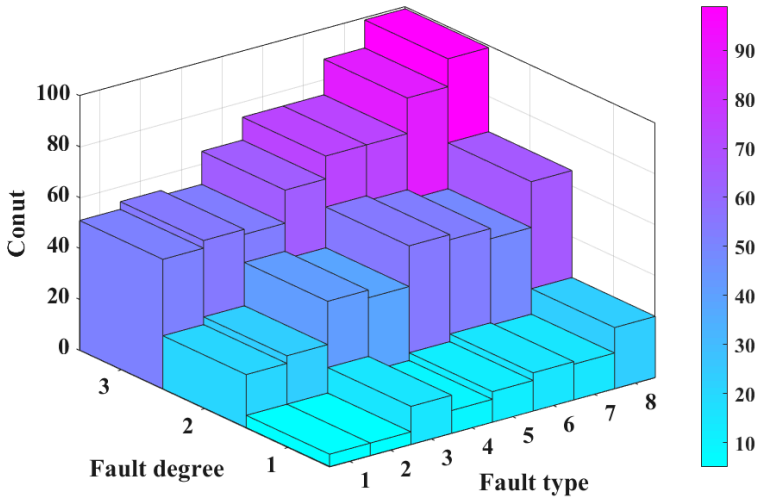


Figure 10. Frequency distribution histogram based on A-S.

cludes normal, minor, general, and severe. The above states, in turn, constitute the fault degree state set $\boldsymbol{S_d} = \{s_d^0, s_d^1, s_d^2, s_d^3, s_d^4, s_d^5, s_d^6\}$. For the fault type MC, the state transition probability matrix $\boldsymbol{H_t}$ of the fault type MC is constructed as follows:

Table 2. Frequency statistics of A-S and S-S

Fault type	Truth	Frequency statistics (1000times)		Frequency statistics (100times)	
		Alias	Simple	Alias	Simple
1	17%	17.00%	15.90%	17.00%	12.00%
2	14%	14.90%	12.70%	13.00%	16.00%
3	13%	13.50%	15.50%	15.00%	17.00%
4	9%	8.80%	9.80%	10.00%	5.00%
5	17%	16.80%	17.50%	15.00%	14.00%
6	11%	11.40%	11.20%	12.00%	9.00%
7	10%	10.00%	9.90%	8.00%	15.00%
8	9%	7.60%	7.50%	10.00%	12.00%

Table 3. Comparison of run time between A-S and S-S under different sample sizes

Sample size	100	500	1000	5000	10000	50000	100000
A-S time[ms]	0.627	1.274	1.492	2.131	2.518	6.827	12.187
S-S time[ms]	6.819	10.329	10.890	10.954	12.233	19.164	26.633

$$\boldsymbol{H_t} = \begin{bmatrix} 0.7991 & 0.0335 & 0.0202 & 0.0268 & 0.0201 & 0.0335 & 0.0269 & 0.0200 & 0.0200 \\ 0.4286 & 0.5714 & 0 & 0 & 0 & 0 & 0 & 0 & 0 \\ 0.3103 & 0 & 0.6897 & 0 & 0 & 0 & 0 & 0 & 0 \\ 0.4444 & 0 & 0 & 0.5556 & 0 & 0 & 0 & 0 & 0 \\ 0.5000 & 0 & 0 & 0 & 0.5000 & 0 & 0 & 0 & 0 \\ 0.4286 & 0 & 0 & 0 & 0 & 0.5714 & 0 & 0 & 0 \\ 0.5122 & 0 & 0 & 0 & 0 & 0 & 0.4878 & 0 & 0 \\ 0.4286 & 0 & 0 & 0 & 0 & 0 & 0 & 0.5714 & 0 \\ 0.5122 & 0 & 0 & 0 & 0 & 0 & 0 & 0 & 0.4878 \end{bmatrix} \tag{19}$$

The specific value of π_{ti}(i=0,1,...,8) can be obtained by solving Eqs. (8)–(10) simultaneously: [0.68495, 0.053537, 0.044589, 0.041307, 0.027535, 0.053537, 0.035839, 0.031962, 0.026745], which is the steady-state solution.

For the MC of fault degree of EP valve solenoid valve leakage, the state transition probability matrix is expressed as follows:

$$\boldsymbol{H_d} = \begin{bmatrix} 0.8642 & 0.0741 & 0.0494 & 0.0123 \\ 0.3000 & 0.2000 & 0.3000 & 0.2000 \\ 0.6000 & 0 & 0.1000 & 0.3000 \\ 0.7778 & 0 & 0 & 0.2222 \end{bmatrix} \tag{20}$$

The specific value of π_{di}(i=0,1,2,3) can be obtained by solving Eqs. (14)-(16) simultaneously is [0.7993, 0.1141, 0.0685, 0.0181], which is the steady-state solution. After excluding the normal operational state, the probability distribution for pure fault types is recalculated as [0.1699, 0.1415, 0.1312, 0.0875, 0.1699, 0.1137, 0.1014, 0.0849]. Similarly, excluding the normal status, the probability distribution for pure fault degrees is recalculated as [0.5687, 0.3413, 0.0900]. These two probability distributions are subjected to 1000 tests simultaneously using the A-S algorithm. The sampling results are illustrated in Figure 9.

The graph displays three data columns on the fault degree axis, denoted as 1 - 3 representing three fault levels. Additionally, eight data columns on the fault type axis are labeled as 1 - 8 representing eight fault types. Observing the graph, it is evident that among the 1000 sampling points, the method achieves a uniform distribution of sampling points for fault types and degrees. No substantial clustering is observed, indicating a high degree of randomness. The fault type and degree are arranged in ascending order based on their probabilities, and the frequency statistics results are presented in Figure 10. It can be seen that the probabilities of various fault degrees and types are different. The frequency distribution histogram exhibits a step-like pattern, with lower probabilities associated with higher fault degrees, aligning with the anticipated expectations for the frequency

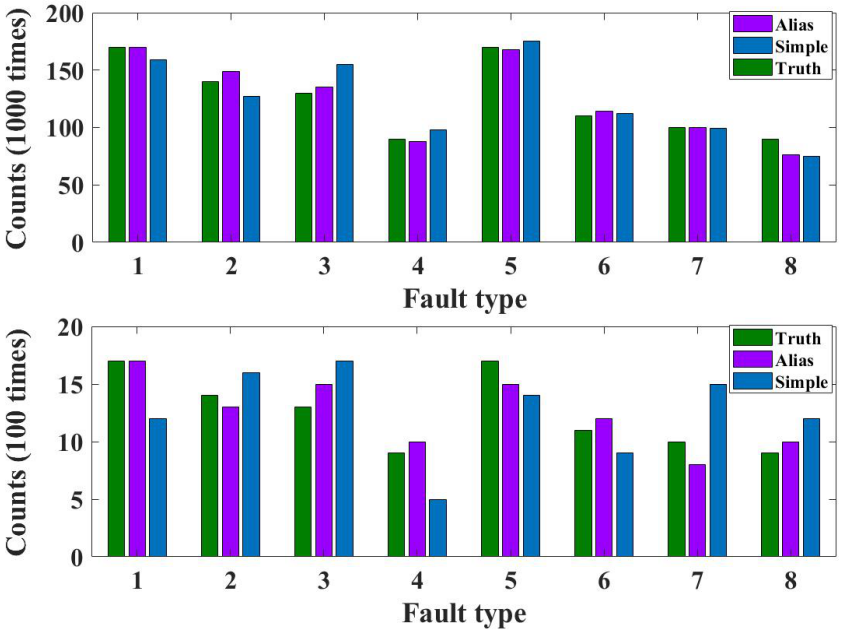


Figure 11. Frequency histogram of A-S and S-S.

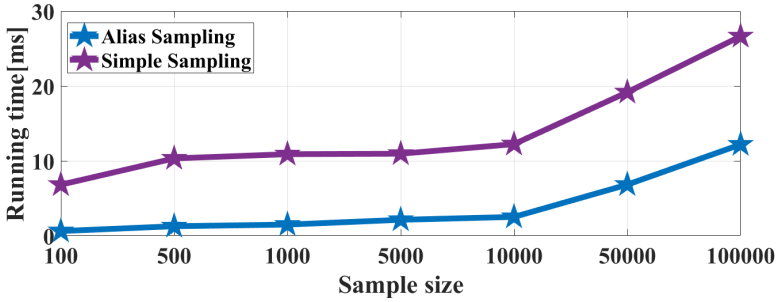


Figure 12. Run time comparison of A-S and S-S.

distribution based on fault degrees and types. The following compares A-S and S-S based on three aspects: accuracy, run time, and repetition rate.

4.2.1 Accuracy

The accuracy rate evaluation ensures that the random fault injection process closely resembles the real system situation and is more reliable. After 1000 and 100 samples, respectively, the fault type is sampled for frequency statistics and compared with the real value calculated based on MC, the frequency statistics table of A-S and S-S shown in Table 2 and the frequency histogram shown in Figure 11. The results indicate that with a large sampling volume (1000 times), the error between the frequency statistics and the actual values is small. However, with a smaller sampling amount (100 times), S-S exhibits greater errors than A-S, and the magnitude of the error amplifies with a decrease in sample probability.

4.2.2 Run time

Run time evaluation aims to minimize waiting time when injecting a large number of faults, enhancing efficiency. A-S and S-S undergo joint sampling of fault types and degrees, and the running time for sampling n

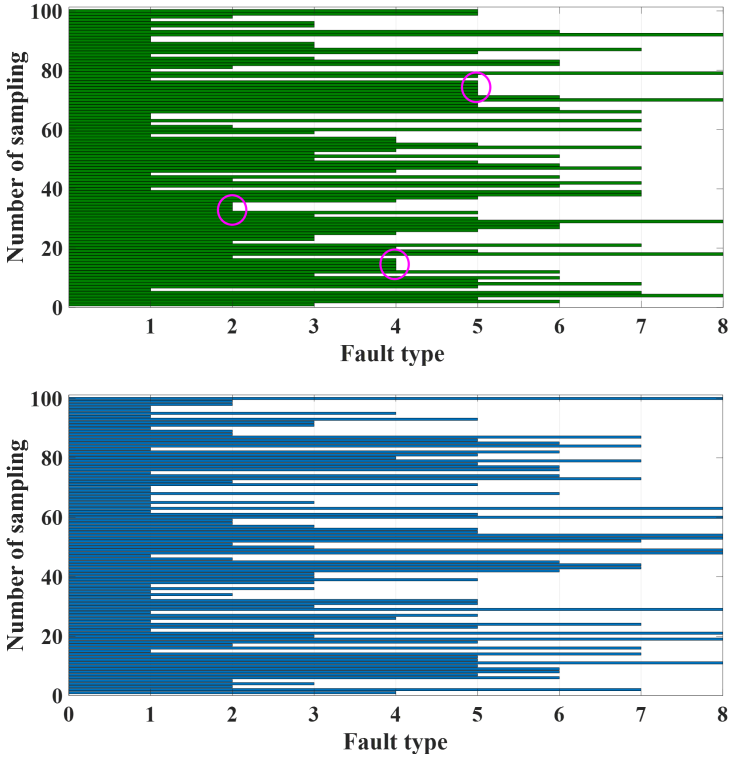


Figure 13. Repetition rate comparison of A-S and S-S.

times is computed. The results, as shown in Table 3 and Figure 12, indicate that A-S outperforms S-S in terms of sampling run time, enhancing the overall efficiency of random fault injection. This significantly contributes to reducing user waiting times and improving the overall user experience.

4.2.3 Repetition rate

The repetition rate evaluation ensures that redundant workload caused by multiple occurrences of the same fault can be avoided during small-scale random fault injection. The fault types are sampled 100 times by A-S and S-S, respectively, and the results of 100 sampling are shown in Figure 13. Any repeated sampling occurring three times or more is deemed unacceptable. The results reveal that both A-S and S-S exhibit two consecutive sampling repetitions. However, S-S has three consecutive sampling repetitions of three or more. While a high repetition rate may not influence fault injection and subsequent fault diagnosis, repeated faults can result in redundant and inconsequential fault diagnosis, leading to a waste of time and space resources.

Random fault sampling is performed using the A-S method described above, and the corresponding fault is injected into the ABS simulation model. The resulting speed curve and brake cylinder pressure curve are illustrated in Figure 14. The graph depicts that the high-speed train undergoes an acceleration phase from 0 km/h to 160 km/h within the time interval of 0 - 10 s, with the brake cylinder pressure remaining at 0 kPa. Between 10 - 105 s, the train gradually decelerates, reducing its speed from 160 km/h to 0 km/h. Throughout this process, the pressure within the brake cylinder steadily increases. In a fault-free operation of a high-speed train, the pressure across all four brake cylinders should be uniform. However, the P1 curve in the figure deviates from the overall trend, indicating a system failure during this period. To substantiate the injection of a fault into the system, Inter-variable Variance (IVV)[17,33] is employed. IVV is a statistical metric that

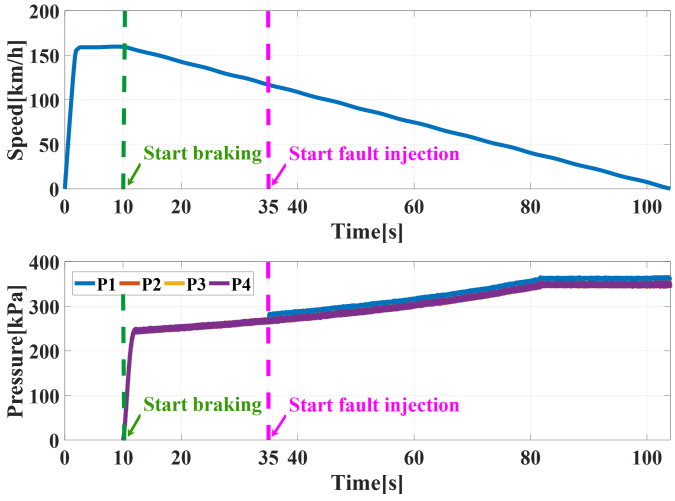


Figure 14. The speed and brake cylinder pressure of the train.

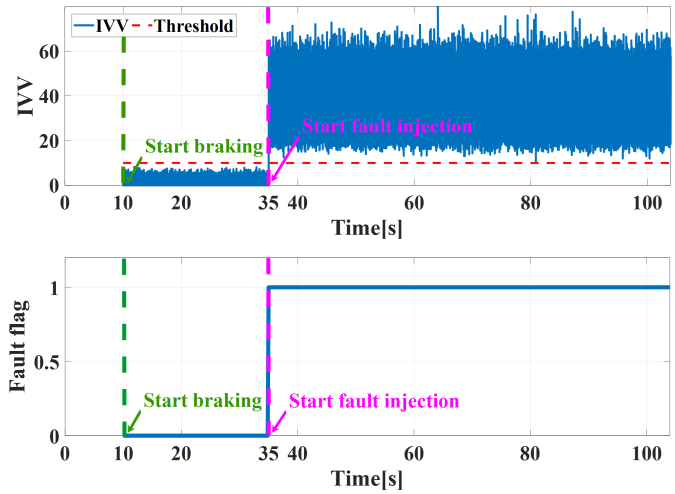


Figure 15. The result of fault diagnosis.

quantifies the variability or dispersion among different variables within a dataset. This measure is instrumental in gauging the extent of variance across the variables under examination, which is pivotal for tasks such as feature selection, elucidating the interrelations among variables, and in the realm of predictive modeling, where the independence of variables could influence the efficacy of the model. Utilizing IVV for fault detection during braking demonstrates a shift in the fault flag bit from 0 (indicating a no-fault state) to 1 (indicating a fault state), as illustrated in Figure 15.

5. CONCLUSIONS

This paper proposes a layered random fault injection method based on multiple MCs for ABS and provides a platform for fault injection and diagnosis. The random fault types and degrees are realized using MCs, in which the fault probability function is determined by the state transition matrix. The A-S algorithm is then

employed for random sampling of the fault distribution, enabling efficient fault injection due to its low complexity. Additionally, a graphical user interface (GUI) is developed to present and visualize the validation results, including modules for the underlying simulation model, random fault injection, fault diagnosis, and visual display. The test results show that the proposed method can achieve more comprehensive and efficient random fault injection for ABS. The current version mainly includes the functions of random fault injection and fault diagnosis. In the future, the function of evaluating fault diagnosis algorithms will be added based on this, providing evaluation indicators suitable for ABS.

DECLARATIONS

Acknowledgments
The authors are grateful to the Guest Editors and anonymous reviewers for their constructive comments based on which the presentation of this paper has been greatly improved.

Authors' contributions
Writing-original draft and conceptualization: Chen Z, Fan J
Technical support: Luo H, Cheng C, Peng L
Validation and supervision: Chen Z

Availability of data and materials
Not applicable.

Financial support and sponsorship
This work was supported by the National Natural Science Foundation of China (Nos. U20A20186, 62173349), the Natural Science Foundation of Hunan Province (2022JJ20076), the Science and Technology Innovation Program of Hunan Province (2022RC1090), and the Key Laboratory of Energy Saving Control and Safety Monitoring for Rail Transportation under Grant (2017TP1002).

Conflicts of interest
All authors declared that there are no conflicts of interest. Zhiwen Chen is a Junior Editorial Board member in Complex Engineering Systems.

Ethical approval and consent to participate
Not applicable.

Consent for publication
Not applicable.

Copyright
© The Author(s) 2024.

REFERENCES

1. Yong Q, Hui M, Li-Min J. Development trend and active safety technology for advanced rail transit system. *China Railway* 2015;2015:77–81. DOI
2. Cheng C, Sun X, Song Y, et al. A just-in-time manifold-based fault detection method for electrical drive systems of high-speed trains. *Simu Model Prac Theor* 2023;127:102778. DOI
3. Wei W, Lin Y. Simulation of a freight train brake system with 120 valves. *Proc Inst Mech Eng Part F J Rail Rapid Transit* 2009;223:85–92. DOI
4. Wu Z, Huang NE. Ensemble empirical mode decomposition: a noise-assisted data analysis method. *Adv Adapt Data Anal* 2009;1:1–41. DOI

5. Su S, She J, Wang D, Gong S, Zhou Y. A stabilized virtual coupling scheme for a train set with heterogeneous braking dynamics capability. *Transp Res Part C: Emerg Technol* 2023;146:103947. DOI
6. Dong H, Ning B, Cai B, Hou Z. Automatic train control system development and simulation for high-speed railways. *IEEE Circuits Syst Mag* 2010;10:6–18. DOI
7. Wang T, Wang W, Zio E, Tang T, Zhou D. Analysis of configuration data errors in Communication-based Train Control systems. *Simul Model Pract Theory* 2019;96:101941. DOI
8. Yang C, Yang C, Peng T, Yang X, Gui W. A fault-injection strategy for traction drive control systems. *IEEE Trans Ind Electron* 2017;64:5719–27. DOI
9. Ding M, Chen B. Secure consensus control for multi-agent systems under communication constraints via adaptive sliding mode technique. *Complex Eng Syst* 2023;3:7. DOI
10. Abboush M, Knieke C, Rausch A. Representative real-time dataset generation based on automated fault injection and HIL simulation for ML-assisted validation of automotive software systems. *Electronics* 2024;13:437. DOI
11. Joshi A, Miller SP, Whalen M, Heimdahl MP. A proposal for model-based safety analysis. In: 24th Digital Avionics Systems Conference. vol. 2. IEEE; 2005. pp. 13–pp. DOI
12. Linnosmaa J, Pakonen A, Papakonstantinou N, Karpati P. Applicability of AADL in modelling the overall I&C architecture of a nuclear power plant. In: IECON 2020 The 46th Annual Conference of the IEEE Industrial Electronics Society, Singapore, 2020, pp. 4337-4344 DOI
13. Liu T, Yu J, Sun WJ. Study on fault-tolerant technique based on knowledge modules of hydraulic fault theory. In: Advanced Materials Research. vol. 712. Trans Tech Publ; 2013. pp. 2043–50. DOI
14. Karpenko M, Sepehri N. Fault-tolerant control of a servohydraulic positioning system with crossport leakage. *IEEE Trans Control Syst Technol* 2004;13:155–61. DOI
15. Niksefat N, Sepehri N. Fault tolerant control of electrohydraulic servo positioning systems. In: Proceedings of the 2001 American Control Conference.(Cat. No. 01CH37148). vol. 6. IEEE; 2001. pp. 4472–77. DOI
16. Kiamanesh Bahareh BAOR. Fault Injection with Multiple Fault Patterns for Experimental Evaluation of Demand-Controlled Ventilation and Heating Systems. *Sensors* 2022;22:8180. DOI
17. Zhou D, Ji H, He X, Shang J. Fault Detection and Isolation of the Brake Cylinder System for Electric Multiple Units. *IEEE Trans Contr Syst Technol* 2018;26:1744-57. DOI
18. Gou B, Ge X, Wang S, et al. An open-switch fault diagnosis method for single-phase PWM rectifier using a model-based approach in high-speed railway electrical traction drive system. *IEEE Trans Power Electron* 2016;31:3816-26. DOI
19. Youssef AB, El Khil SK, Slama-Belkhodja I. State Observer-Based Sensor Fault Detection and Isolation, and Fault Tolerant Control of a Single-Phase PWM Rectifier for Electric Railway Traction. *IEEE Trans Power Electron* 2013;28:5842-53. DOI
20. Chen Z, Peng L, Fan J, et al. EPBSFIDMV: A fault injection and diagnosis methods validation benchmark for EPBS of EMU. *Contr Eng Pract* 2024;145:105873. DOI
21. Qin SJ. Survey on data-driven industrial process monitoring and diagnosis. *Annu Rev Control* 2012;36:220-34.. DOI
22. Huang M, Yin J, Yan S, Xue P. A fault diagnosis method of bearings based on deep transfer learning. *Simul Model Pract Theory* 2023;122:102659. DOI
23. He J, Lv Z, Chen X. Rolling bearing fault diagnosis method based on 2D grayscale images and Wasserstein Generative Adversarial Nets under unbalanced sample condition. *Complex Eng Syst* 2023;3:13. DOI
24. Fang D, Peng T, Yang C, Chen Z, Tao H. Random-Sampling-Based Performance Evaluation Method of Fault Detection and Diagnosis for Railway Traction System. In: 2019 CAA Symposium on Fault Detection, Supervision and Safety for Technical Processes (SAFEPROCESS). IEEE; 2019. pp. 570–74. DOI
25. Chen Z, Fan J, Peng L, et al. Multiple Markov chains-based layered random fault injection method for the air braking system. In: 2023 IEEE 2nd Industrial Electronics Society Annual On-Line Conference (ONCON), SC, USA, 2023, pp. 1-6. DOI
26. Von Luxburg U. A tutorial on spectral clustering. *Stat Comput* 2007;17:395-416. DOI
27. Mcginnis R, Isaacson DL, Madsen RW. Markov Chains Theory and Applications. *Contemp Sociol* 1977;6:322. DOI
28. Sericola GRB. Markov Chains and Dependability Theory. Cambridge: Cambridge University Press; 2014. DOI
29. Grassmann WK, Taksar MI, Heyman DP. Regenerative analysis and steady state distributions for Markov chains. *Oper Res* 1985;33:1107-16. DOI
30. Azimi S, Hassannayebi E, Boroun M, Tahmoures M. Probabilistic analysis of long-term climate drought using steady-state Markov chain approach. *Water Resour Manage* 2020;34:4703-24. DOI
31. Bod LWM. Introduction to probability theory and formal stochastic language theory. *Probabilistic Linguistic* 2003. DOI
32. Smith JC, Jacobson SH. An analysis of the alias method for discrete random-variate generation. *INFORMS J Comput* 2005;17:321-7. DOI
33. Ji H. Optimization-Based Incipient Fault Isolation for the High-Speed Train Air Brake System. *IEEE Trans Instrum Meas* 2022;71:1-9. DOI

Bai. *Complex Eng Syst* 2024;4:8
DOI: 10.20517/ces.2024.18

Complex Engineering Systems

Editorial

Open Access

Check for updates

Introduction to discrete-time reinforcement learning control in Complex Engineering Systems

Weiwei Bai

Navigatioin College, Dalian Maritime University, Dalian 116026, Liaoning, China.

Correspondence to: Prof. Weiwei Bai, Navigation College, Dalian Maritime University, No. 1 Linghai Road, Dalian 116026, Liaoning, China. E-mail: baiweiweidl@dlmu.edu.cn

How to cite this article: Bai W. Introduction to discrete-time reinforcement learning control in Complex Engineering Systems. *Complex Eng Syst* 2024;4:8. https://dx.doi.org/10.20517/ces.2024.18

Received: 22 Apr 2024 **Accepted:** 25 Apr 2024 **Published:** 28 Apr 2024

Academic Editor: Hamid Reza Karimi **Copy Editor:** Fangling Lan **Production Editor:** Fangling Lan

Within the context of the Complex Engineering Systems (CES), this editorial aims to describe the recent progress of discrete-time reinforcement learning (RL) control.

Considering the widespread application of the digital computer in the CES, which process the data in discrete-time form, and the nonlinearity inherent in the engineering, the nonlinear discrete-time control design has garnered growing attention in the modern control engineering. For instance, when the backstepping method is employed to design the controller for a nonlinear discrete-time system, it may suffer from a noncausal problem. As the authors claimed, the causality contradiction problem may arise[1], where the future signal is embedded in the current control signal, leading to controller design failure. To solve this problem, various system transformations were developed, making them one of the perennial topics for nonlinear discrete-time systems.

The control design is one of the most important topics of CES; as an optimal control strategy, RL has received increasing attention. It can not only make a compromise between the control cost and performance but also decrease the impact of external environment through continuous exploration[2]. Many RL techniques exist, such as Q-learning, adaptive dynamic programming (ADP), policy iteration, *etc.* Among them, actor-critic is one of the classical RL techniques, which is simple and easy to apply. However, it should be noted that the gradient descent method is employed to learn the weight vector that searches for

© The Author(s) 2024. **Open Access** This article is licensed under a Creative Commons Attribution 4.0 International License (https://creativecommons.org/licenses/by/4.0/), which permits unrestricted use, sharing, adaptation, distribution and reproduction in any medium or format, for any purpose, even commercially, as long as you give appropriate credit to the original author(s) and the source, provide a link to the Creative Commons license, and indicate if changes were made.

the optimal solution from a single point, and it may easily fall into the local optimal. Therefore, solving the local optimal problem is one of the hot topics in the RL control design. In the following section, the above control topics of research progress will be introduced.

1. SYSTEM TRANSFORMATION

The noncausal problem was first pointed out by Yeh[3] and it was solved using a time-varying mapping technique for the parameter-strict-feedback and parameter-pure-feedback systems. Based on this result, it was further extended to the time-varying parameters and nonparametric uncertainty systems[4]. However, this transformation is inapplicable to a class of more general nonlinear strict feedback systems. To address this issue, Ge *et al.* transformed the nonlinear strict feedback system into a novel sequential decrease cascade form, and the noncausal problem was solved[5]. Notably, the nonlinear function $f_i(\bar{x}_i(k))$ only includes partial states $\bar{x}_i(k) = [x_1(k), \ldots, x_i(k)]^{\mathrm{T}}$ (refer to[6] for more details). However, it may incorporate all the states of the control system $\bar{x}_n(k) = [x_1(k), \ldots, x_n(k)]^{\mathrm{T}}$, which is the so-called non-strict feedback system that is more general than the strict one. The system transformation in[5] is no longer applicable again. In[7], the discrete-time non-strict feedback system was transformed into a time instant recursive form, requiring all the past information at the current time, which will lead to great difficulty for the application. Subsequently, a universal system transformation was recently devised[8], and the noncausal problem was solved thoroughly. This is the main research progress about the system transformation up to now, and this is a perennial topic.

2. LOCAL OPTIMAL PROBLEM

Another hot topic within the control field is the issue of local optimal. As previously stated, the gradient descent method searches for the optimal solution from a single point, which may easily fall into the local optimal. Therefore, the local optimal problem should be considered in the controller design. Genetic (GA) and evolutionary algorithms can effectively tackle this problem by exploring optimal solutions from multiple points of view. However, the evolutionary algorithms have a heavy computation burden when it has a large population rendering them unsuitable for the online learning. After that, the experience replay technique is developed, involving repeatedly learning the past information, allowing the parameters to converge to the true value[9]. Nevertheless, this technique is a traditional adaptive technique that cannot realize the optimization. Based on the key idea of the experience replay technique, a multi-gradient recursive approach is developed to learn the weight vector and solve the local optimal problem[10]. Consequently, this issue has received much attention in the adaptive control field recently, emerging as a prominent subject in adaptive RL control.

DECLARATIONS

Authors' contributions

The author contributed solely to the article.

Availability of data and materials

Not applicable.

Financial support and sponsorship

This work was supported by the National Natural Science Foundation of China (No. 52271360), the Dalian Outstanding Young Scientific and Technological Talents Project (No. 2023RY031), and the Basic Scientific Research Project of Liaoning Education Department (Grant No. JYTMS20230164).

Conflicts of interest

The author declared that there are no conflicts of interest.

Ethical approval and consent to participate

Not applicable.

Consent for publication

Not applicable.

Copyright

© The Author(s) 2024.

REFERENCES

1. Bai W, Li T, Long Y, Chen CLP. Event-triggered multigradient recursive reinforcement learning tracking control for multiagent systems. *IEEE Trans Neural Netw Learn Syst* 2023;34:366-79. DOI PubMed
2. Yang Q, Cao W, Meng W, Si J. Reinforcement-learning-based tracking control of waste water treatment process under realistic system conditions and control performance requirements. *IEEE Trans Syst Man Cybern Syst* 2022;52:5284-94. DOI
3. Yeh PC, Kokotović PV. Adaptive control of a class of nonlinear discrete-time systems. *Int J Control* 1995;62:303-24. DOI
4. Zhang Y, Wen C, Soh YC. Discrete-time robust backstepping adaptive control for nonlinear time-varying systems. *IEEE Trans Automat Control* 2000;45:1749-55. DOI
5. Ge SS, Li GY, Lee TH. Adaptive NN control for a class of strict-feedback discrete-time nonlinear systems. *Automatica* 2003;39:807-19. DOI
6. Li YM, Min X, Tong S. Adaptive fuzzy inverse optimal control for uncertain strict-feedback nonlinear systems. *IEEE Trans Fuzzy Syst* 2020;28:2363-74. DOI
7. Bai W, Li T, Tong S. NN reinforcement learning adaptive control for a class of nonstrict-feedback discrete-time systems. *IEEE Trans Cybern* 2020;50:4573-84. DOI PubMed
8. Bai W, Li T, Long Y, et al. A novel adaptive control design for a class of nonstrict-feedback discrete-time systems via reinforcement learning. *IEEE Trans Syst Man Cybern Syst* 2024;54:1250-62. DOI
9. Modares H, Lewis FL, Naghibi-Sistani MB. Adaptive optimal control of unknown constrained-input systems using policy iteration and neural networks. *IEEE Trans Neural Netw Learn Syst* 2013;24:1513-25. DOI PubMed
10. Bai W, Zhou Q, Li T, Li H. Adaptive reinforcement learning neural network control for uncertain nonlinear system with input saturation. *IEEE Trans Cybern* 2020;50:3433-43. DOI

Du *et al. Complex Eng Syst* 2024;4:9
DOI: 10.20517/ces.2024.15

Complex Engineering Systems

Research Article

Open Access

A comprehensive risk prediction method for defense mission planning based on probabilistic reasoning and hierarchical analysis

WeiWei Du[1,2], XiaoWei Chen[3,4]

[1]School of Mechanical and Electrical Engineering, Beijing Institute of Technology, Beijin 100081, China.
[2]North Automatic Control Technology Institute, Taiyuan 030006, Shanxi, China.
[3]State Key Laboratory of Explosion Science and Technology, Beijing Institute of Technology, Beijing 100081, China.
[4]Institute of Frontier Interdisciplinary Sciences, Beijing Institute of Technology, Beijing 100081, China.

Correspondence to: Prof. XiaoWei Chen, State Key Laboratory of Explosion Science and Technology, Beijing Institute of Technology, 5 Zhongguancun South Street, Haidian District, Beijing 100081, China. E-mail: chenxiaoweintu@bit.edu.cn

How to cite this article: Du W, Chen X. A comprehensive risk prediction method for defense mission planning based on probabilistic reasoning and hierarchical analysis. *Complex Eng Syst* 2024;4:9. http://dx.doi.org/10.20517/ces.2024.15

Received: 29 Mar 2024 **First Decision:** 9 May 2024 **Revised:** 21 May 2024 **Accepted:** 24 May 2024 **Published:** 31 May 2024

Academic Editor: Hamid Reza Karimi **Copy Editor:** Fangling Lan **Production Editor:** Fangling Lan

Abstract

Most existing risk prediction methods focus on constructing risk element sets and analyzing their uncertainties but do not deeply explore the correlation types and intensities of factors, resulting in large errors in the comprehensive risk prediction results. In this paper, a new integrated risk prediction method is proposed based on the correlation types of tasks in defense task planning and execution. The approach mainly includes the following steps: First, based on the difference of the sequence and mode of action of link tasks, three correlation types (hierarchical, synergistic, and independent) are defined among them, and various correlation measurement techniques are proposed to model these abstract correlation relations and provide data basis for constructing risk decision graphs. Secondly, the rotation extraction strategy is introduced to excavate the internal correlation law between link tasks and generate their hierarchical topology to ensure the rational distribution of their hierarchy positions in defense missions. Then, the intra-layer risk weight is determined based on the centrality of each node in the topology structure, and then the comprehensive risk prediction weighting graph is constructed. Finally, the path analysis is used to assess the rationality of the hierarchical topology structure of the link tasks, and the validity of the proposed method is verified using the test sample set. The results show that compared with other approaches, the predicted results of the proposed method more closely approximate the actual outcomes.

© The Author(s) 2024. **Open Access** This article is licensed under a Creative Commons Attribution 4.0 International License (https://creativecommons.org/licenses/by/4.0/), which permits unrestricted use, sharing, adaptation, distribution and reproduction in any medium or format, for any purpose, even commercially, as long as you give appropriate credit to the original author(s) and the source, provide a link to the Creative Commons license, and indicate if changes were made.

Keywords: Defense mission planning, risk prediction, associative relationships, hierarchical topology, decision mapping

1. INTRODUCTION

Defense task planning[1–3] involves the comprehensive layout and detailed strategizing of specific defense measures by commanders before executing a specific task. This process mainly includes task understanding, analysis and judgment, formulation of concepts, program development, program selection, plan development, and other links. Each stage aims to achieve the overall objective with a clear purpose and specific function. The reasonableness of mission planning and the effectiveness of its execution directly determine the outcome of the entire defense mission. Therefore, risk decision-making for the specific defense mission is a necessary precondition to ensure its successful implementation.

Scholars have achieved certain research results on risk prediction in defense mission planning[4], medical system research and development[5], commercial project risk management[6], and risk assessment of construction projects[7], mainly in the methods of multi-attribute decision-making[8], decision tree analysis[9], and so on. Wu *et al.* analyzed various factors influencing the slope stability, including hydrological conditions of open-pit mines, the geologic formations of slopes, the internal structure[10], *etc.* They identified the attribute sets affecting slope stability and proposed a large-scale multi-attribute group decision-making model based on intuitionistic fuzzy sets. This kind of decision model requires relative independence among the attributes in the set. Decision tree analysis is an analytical method for systematic decision-making after a unified combination arrangement on the premise of classifying the attributes affecting the event; e.g., Ikwan *et al.* constructed a decision tree from the attributes of environmental impacts, management constraints, human/equipment failure factors, and risk factors of the tanks themselves and put forth a fishbone diagram-decision tree-risk matrix analysis strategy, which realized an effective prediction of the effective prediction of tank leakage risk[11]. Zheng *et al.* explored the composition of the mission conception risk assessment system from the levels of thoroughness, mobility, and protection by combining the conception elements and research and judgment data and solved the problem of quantifying the risk of defense conception by establishing the quantitative analysis model of each assessment index[12]. Song *et al.* proposed a program based on the task derivation by establishing a program index system under the background of the joint task risk analysis model[13]. Ryczy□ski *et al.* proposed a risk analysis technique integrating the Kaplan method, the Garrick method, and fuzzy theory to realize the risk management decision-making in the liquid fuel material supply program during military operations[14]. Kim *et al.* introduced the Risk Management Framework (RMF) and developed an assessment model of the weapon system, which offers a theoretical foundation for the mission plan formulation[15]. Most of the above research results focus on constructing risk element sets and analyzing their uncertainty; however, comprehensive prediction is needed on the premise that risk factors are independent.

Subsequently, researchers have made significant efforts in comprehensive risk prediction based on factor associations; e.g., Zhang *et al.*[16] proposed the project portfolio risk (PPR) evolution and response model to solve the problem of project risk interaction, which effectively reflected the real-time interaction in the evolution process of PPRs and helped decision makers quickly identify key strategic intrusion nodes[16]. Zhang *et al.*[16] proposed a category-based association measurement technology (the Measuring Attractiveness by a Categorical-Based Evaluation Technique (MACBETH)) to measure the associative relationships between risks and construct a risk response model for the selection of risk relationships in the medical system research and development project (Risk Response Actions (RRA)), so as to maximize the expectations of the management of medical system research and development project under budget constraints[5] . Abedzadeh *et al.* used fuzzy decision tree analysis to determine the possible combinatorial relationships among social, economic, environmental, and water damage index attributes to achieve an integrated risk management decision for developing

water resources [17]. These methods provide a quantitative assessment of the similarity of risk associations and, to some extent, reveal the linkages and impacts between various risks. In fact, in defense mission planning, not only do the tasks adhere to a strict time sequence, but they also follow layer-by-layer refinement. Directly applying the correlation method mentioned to the defense mission planning for risk prediction will lead to large errors in the prediction results. Hierarchical directed topology lays out the nodes of a complex system according to a hierarchical structure. Inspired by this, hierarchical topology is used in the integrated risk prediction of defense tasks. This technique not only effectively highlights the inter-association relationship among link tasks but also reveals the roles of each task on the defense missions, thereby enhancing the accuracy of the integrated risk prediction.

The main contributions of this paper are as follows: (1) oriented to the task execution process in defense mission planning, the association relationship between tasks in different planning links is studied, and the normalized description of hierarchical, synergistic, and independent relationships and the measurement calculation method are defined; (2) the hierarchical topology between link tasks is generated using the rotational extraction method; (3) on the premise of clarifying the role of each link task on the whole defense mission, a new integrated risk prediction approach is proposed by constructing a weighted map of integrated risk prediction; and (4) combined with specific defense tasks, the proposed method is analyzed qualitatively and quantitatively, and its effectiveness and feasibility are verified.

The structure of this paper is outlined as follows: Section 2 gives the research idea and schematic diagram for constructing a model of the integrated risk prediction problem for defense mission planning; Section 3 defines the three association types and their quantification techniques; Section 4 describes the process of generating the hierarchical topology for link missions; Section 5 proposes a new integrated risk prediction method based on weighted mapping; Section 6 analyzes and validates the proposed approach; Section 7 provides the conclusion.

2. PROBLEM MODELING

To improve the reliability of risk prediction of defense mission planning, this paper, based on the "OODA" (Observe, Orient, Decide, and Act) ring, decomposes the tasks involved into six links and further divides them into four aspects: acquiring information about the defense mission, analyzing the composition of the execution force, evaluating the capability of the attacking entity, and assessing the execution program and plan. The paper specifically examines 15 links of task risk, such as clarifying the defense information, identifying the force of our unit, determining the scale of the attacking entity, and evaluating the resilience of the program. Aimed at the strong temporal sequence of link tasks and their complexity and intertwined relationships, this paper mainly examined the following three aspects: determining their relationships, constructing their hierarchical topology, and developing a comprehensive risk prediction model. The schematic diagram of this prediction model is shown in Figure 1.

The functions of each part are as follows:

(i) As each link follows a strict timing sequence and contains various subtasks, many complex associations may exist between different link tasks. Rationally distinguishing and describing these relationships is the basis for improving the reliability of comprehensive risk prediction. In this paper, we determine the associations by mining the relationship between their time sequences and hierarchies. We specify the association types, give a normalized description of these relationships, and outline the calculation method of the association measures to provide numerical inputs for establishing the probability association matrix between link tasks.

(ii) The relationship between link tasks directly determines the mode and intensity of the role of each link to the total task, and the correlation type varies among various link tasks, which directly affects the comprehensive

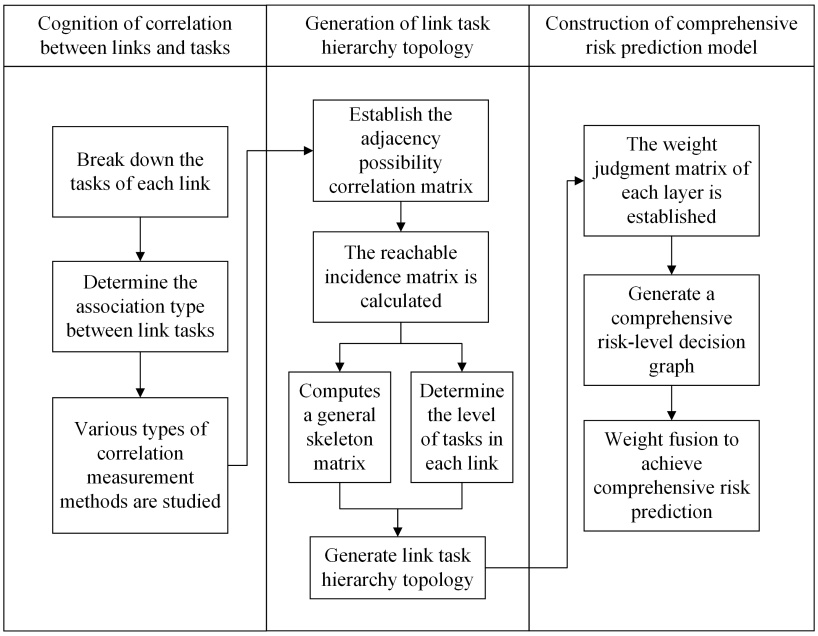


Figure 1. Schematic diagram of the integrated risk prediction model.

risk prediction. The correct construction of link task hierarchical topology is the key to improving the reliability of comprehensive risk prediction. Therefore, this paper clarifies the role and intensity of link tasks on the whole defense task based on the association measurement size of each task in (i), establishes the possibility association matrix, and introduces the rotation extraction method to determine the hierarchical position of the link tasks, which provides a theoretical basis for constructing the comprehensive risk decision-making mapping.

(iii) The risk of each link task acts on the total risk of the defense task based on the topology between link tasks. However, the correlation strength between link tasks is independent, so determining the link task risk weights based on the correlation distribution is a guarantee to enhance the reliability of the comprehensive risk prediction. In this paper, a three-scale hierarchical analysis is conducted based on the centrality of each link task to determine its hierarchical weights, and then a weighted map is constructed to ensure the reliability of the comprehensive risk prediction results.

3. PERCEPTION OF THE CORRELATION BETWEEN LINK TASKS

3.1. Analysis of the correlation between the link tasks

Defense task planning needs to strictly follow the chronological order of the specific measures taken by each link to gradually refine; when a subsequent link task depends on a preceding task, there is a hierarchical relationship between them [18]; when multiple tasks converge into a single task, they share a synergistic relationship; when there is no intrinsic link between the link tasks, they have an independent relationship [19]. The specific description is as follows:

(1) Hierarchical relationship: the correlation between link tasks R_i and R_j is submissive transfer, and R_j needs to depend on the information passed in one direction by R_i to execute, noted as HR.

(2) Synergy relationship: link tasks R_i and R_j act synergistically on link task R_k; then, the correlation between R_i, R_j and R_k is called synergy relationship, and R_k needs to depend on the output information of both R_i and R_j to execute, denoted as SR.

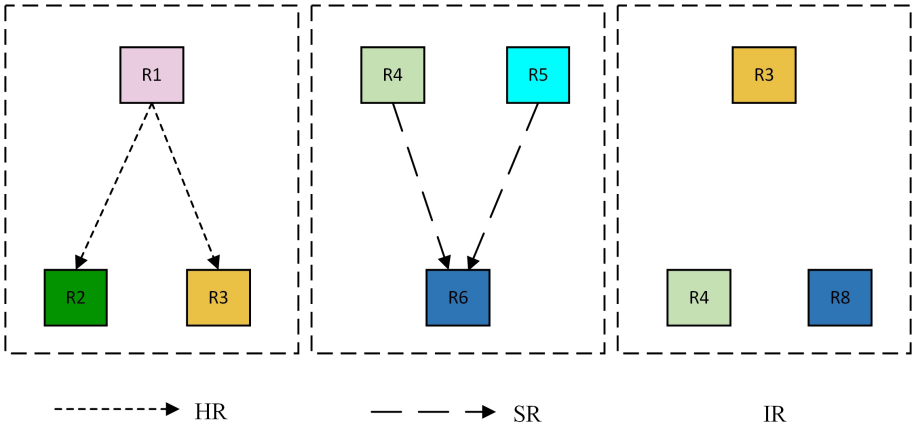


Figure 2. Schematic diagram of the correlation between the link tasks

(3) Independent relationship: there is no interaction of information between link tasks R_i and R_j; there is no dependency between them, and each can execute independently, which is recorded as IR.

In principle, the three types of relationships mentioned are unique: only one type can exist between tasks of the same link. Meanwhile, given the sequential execution of the link tasks and the gradual elaboration of the planning content, all these relationships are unidirectional, from previous to subsequent link tasks.

The schematic diagram of the correlation between the link tasks is depicted in Figure 2. The colors represent the specific link in which each task is located, such as the hierarchical relationship between R_1 and R_2, R_3, the synergistic relationship between R_4, R_5 and R_6, and no obvious relationship between R_3, R_4 and R_8.

3.2. Measurement of the degree of correlation between link tasks

This study uses the degree of association to measure the relationship between link tasks. Subsequently, we determine this degree from the nature of various association relationships.

(1) Calculation of HR relevance

Since the information between the tasks of each link in HR has one-way transferability and the correlation between tasks increases with the similarity of the situational information affecting them, the number of basic situational information inputs to any two link tasks is analyzed using the ensemble similarity measure function [20–22], which measures the HR correlation between the link tasks, expressed as

$$\zeta_{i\to j}^{(\mathrm{HR})} = \frac{2\left\{SI(R_i)\cap SI(R_j)\right\}}{\{SI(R_i)\}+\left\{SI(R_j)\right\}} \tag{1}$$

where $SI(g)$ is the basic situation information input when performing the g-th session task, $\{SI(g)\}$ is the number of situation posture information input when performing the g-th session task, and $\left\{SI(R_i)\cap SI(R_j)\right\}$ denotes the number of intersections of $SI(R_i)$ and $SI(R_j)$.

(2) SR relevance calculation

Unlike HR, SR is more inclined to the joint impact of the execution effect of two or more link tasks on another. Fuzzy hierarchical analysis [23–25] is considered to measure the effect factor of each link task on its acted task,

that is, to calculate the SR correlation between link tasks from a functional perspective.

Assuming that a total of n session tasks have a common effect on R_k when a defense task is planned, the SR correlation between the i-th session task R_i and the k-th session task R_k ($i \in [1, n]$, $k \in [1, n]$ $(k \neq i)$) is

$$\zeta_{i\to k}^{\mathrm{SR}} = \frac{\mathrm{Im}\,(R_i \to R_k)}{\sum_{i=1}^{n} \mathrm{Im}\,(R_i \to R_k)} \tag{2}$$

where $\mathrm{Im}(R_i \to R_k)$ denotes the action factor of the i-th link task R_{i} on R_k, which needs to be inferred using fuzzy hierarchical analysis to derive the extent to which each of the n link tasks acts on R_k.

(3) IR relevance calculation

When the link task R_i is related to R_j as IR, there is no interdependence between these two tasks. Therefore, for any link task, when the relationship between them is IR, then there is $\zeta_{i\to j}^{(\mathrm{IR})} = 0$.

In summary, for a particular defense task, the correlation $\Gamma(R_i, R_j)$ between the link tasks in its planning can be expressed in a triple as follows:

$$\Gamma(R_i, R_j) = \left\langle R_i, \zeta_{i\to j}^{(*)}, R_j \right\rangle \tag{3}$$

where R_i and R_j are the i-th and j-th link tasks, respectively; $\zeta_{i\to j}^{(*)}$ denotes the degree of association, when the association between R_i and R_j is a $*$-relationship, and $* \in \{\mathrm{HR}, \mathrm{SR}, \mathrm{IR}\}$, $\zeta_{i\to j}^{(*)} \in [0, 1]$.

4. LINK TASK HIERARCHY TOPOLOGY GENERATION

4.1. Adjacency probability correlation matrix

Assuming that a total of n link tasks are involved in planning a specific defense task, for two link tasks R_i and R_j, since HR, SR, and IR are unique, the correlation between them can be expressed as

$$\zeta_{i\to j} = \zeta_{i\to j}^{(\mathrm{HR})} \quad or \quad \zeta_{i\to j}^{(\mathrm{SR})} \quad or \quad \zeta_{i\to j}^{(\mathrm{IR})} \tag{4}$$

In addition, due to the temporal nature of the adjacent links in planning, for the convenience of the subsequent study, the link tasks are sorted in strict time order of execution. Thus, the adjacency correlation matrix between the link tasks is established based on the values of the degree of correlation between them. Considering that the degree of correlation takes values between 0 and 1, instead of only 0 and 1, we distinguish it from the traditional adjacency correlation matrix, which is called the adjacency possibility correlation matrix $\Gamma_{n\times n}$ here.

$$\Gamma_{n\times n} = \left(\zeta_{i\to j}\right)_{n\times n} = \begin{bmatrix} 0 & \cdots & \cdots & \zeta_{1\to j} & \cdots & \zeta_{1\to n} \\ 0 & 0 & \cdots & \cdots & \cdots & \cdots \\ 0 & 0 & 0 & \zeta_{i\to j} & \cdots & \zeta_{i\to n} \\ 0 & 0 & 0 & 0 & \cdots & \cdots \\ 0 & 0 & 0 & 0 & 0 & \cdots \\ 0 & 0 & 0 & 0 & 0 & 0 \end{bmatrix} \tag{5}$$

Since the adjacency possibility association matrix $\Gamma_{n\times n}$ emphasizes the unidirectional association between different link tasks and does not consider the own association of the link task, Equation (5) is a triangular array with diagonal elements of zero.

4.2. Calculation of the possibility hierarchy position for the link tasks

To ensure that the link tasks directly related to the total task are classified in the innermost layer, while the fundamental link tasks that affect the total task are classified in the outermost layer, the concept of rotational extraction [26] is used to calculate the possibility hierarchy position of each link task in the total task [27,28]; that is, the innermost and outermost layers are determined first. Subsequently, the next inner and outer layers are followed by the next-sub-inner and -outer layers until all link tasks are assigned. The implementation process is as follows:

(i) Combining the unit matrix I, the adjacency possibility correlation matrix $\Gamma_{n\times n}$ is concatenated until the matrix does not change to obtain the reachable correlation matrix $M_{n\times n}^{i\to j}$:

$$M_{n\times n}^{i\to j} = \left(\left(\zeta_{i\to j}\right)_{n\times n} + (I)_{n\times n}\right)^{k+1} = \left(\left(\zeta_{i\to j}\right)_{n\times n} + (I)_{n\times n}\right)^{k} \neq \left(\left(\zeta_{i\to j}\right)_{n\times n} + (I)_{n\times n}\right)^{k-1} \tag{6}$$

(ii) The link tasks in each column and row corresponding to all elements in row t and column t of $M_{n\times n}^{i\to j}$ that are not zero are noted as the sets $A(R_t)$ and $B(R_t)$, respectively. Let the intersection of the two sets be $C(R_t)$. Subsequently, the link tasks in the innermost and outermost layers are determined according to the following rules.

$$\begin{cases} \text{Divide the extracted session tasks to the innermost layer when } C\left(R_t\right) = A\left(R_t\right) \bigcap B\left(R_t\right) = A\left(R_t\right) \\ \text{Divide the extracted session tasks to the outermost layer when } C\left(R_t\right) = A\left(R_t\right) \bigcap B\left(R_t\right) = B\left(R_t\right) \end{cases} \tag{7}$$

(iii) The link tasks set as the innermost and outermost layers in Step (2) are removed from the reachable association matrix $M_{n\times n}^{i\to j}$. If m link task items are removed at this point, a reachable association matrix $M_{(n-m)\times(n-m)}^{i\to j(1)}$ of order $n-m$ is obtained, and Step (2) is repeated to determine the link tasks located in the next inner and outer layers.

(iv) The sub-inner and sub-outer link tasks identified in Step (3) are removed from the reachable association matrix $M_{(n-m)\times(n-m)}^{i\to j(1)}$. If c link task items are removed at this point, a reachable association matrix $M_{(n-m-c)\times(n-m-c)}^{i\to j(2)}$ of order $n-m-c$ is obtained, and Step (2) is repeated to identify the link tasks located in the sub-inner and sub-outer layers until all link task items have been set.

(v) The following operations are performed on the reachable correlation matrix $M_{n\times n}^{i\to j}$ to create a general skeleton matrix $E_{n\times n}$:

$$E_{n\times n}=\left(e_{ij}\right)_{n\times n} = M_{n\times n}^{i\to j} - \left(M_{n\times n}^{i\to j} - (I)_{n\times n}\right)^2 - (I)_{n\times n} \tag{8}$$

The position of the possibility hierarchy for each link task is determined based on Step (4).

5. INTEGRATED RISK PREDICTION MODELING

5.1. Calculation of task risk weights and integrated risk

The process of realization is as follows:

(i) With the link task risk as the sub-node and the total task risk as the root node, the link task level position determined in Section 4 is taken as the position of each sub-node relative to the root node, and the hierarchical decision graph of the comprehensive risk is preliminarily determined. Determine the total number of layers K. If the $h \in [1, K]$ layer contains g_{hv} child nodes, calculate the centrality of each child node according to the general skeleton matrix $E_{n\times n}$ as follows:

$$C(F_t) = \sum_{j=1}^{n} e_{tj} + \sum_{i=1}^{n} e_{it} \tag{9}$$

where F_t is the tth child node, e_{tj} is the degree of association between the tth child node and the j $(j = 1, 2, \cdots, n)$th child node, and e_{it} is the degree of association between the ith child node and the tth child node.

The child node centrality at layer h is compared pairwise and assigned on a three-scale degree:

$$b_{lk} = \begin{cases} 2 & C(F_l) > C(F_k) \\ 1 & C(F_l) = C(F_k) \\ 0 & C(F_l) < C(F_k) \end{cases}, l, k = 1, 2, ..., g_{hv} \tag{10}$$

Then, the weight judgment matrix of the hth layer sub-node is built.

$$B_h = \begin{bmatrix} b_{11} & \cdots & b_{1j} & \cdots & b_{1g_{hv}} \\ \cdots & \cdots & \cdots & \cdots & \cdots \\ b_{i1} & \cdots & b_{ij} & \cdots & b_{ig_{hv}} \\ \cdots & \cdots & \cdots & \cdots & \cdots \\ b_{g_{hv}1} & \cdots & b_{g_{hv}j} & \cdots & b_{g_{hv}g_{hv}} \end{bmatrix} \tag{11}$$

(ii) According to the weight judgment matrix B_h, the proposed optimal transfer matrix[29] $U_h=(u_{lk})_{g_{hv}\times g_{hv}}$ is established, and the element u_{lk} is determined using

$$u_{lk} = \exp\left(\frac{1}{g_{hv}} \sum_{q=1}^{g_{hv}} (b_{lq} - b_{kq})\right) \tag{12}$$

The maximum eigenvalue $\lambda_{\max}$ of U_h is calculated and its corresponding eigenvector $\xi_h=(\xi_{h1}, \xi_{h2}, ..., \xi_{hg_{hv}})$ is obtained and normalized to obtain the intra-layer weight vector of the $g_h$sub-nodes of the hth layer, as expressed below:

$$\xi_h{'}=(\xi_{hg_{h1}}{'}, \cdots \xi_{hg_{h2}}{'}, ..., \xi_{hg_{hv}}{'}) \tag{13}$$

where $\xi_{hg_{hr}}{'}$ denotes the intra-layer weight coefficient of the $r \in [1, v]$th child node in the h-th layer. The intra-layer risk weight of each link is used as the connection edge strength between the child nodes to represent

the degree of influence of the previous on the subsequent child nodes. In this way, the weighted graph of comprehensive risk prediction is generated.

(iii) Combining the weight vectors of the child nodes within all the layers, the weight of the impact of each link's risk on the total risk is determined from the top level downwards, and the combined weight of the r-th child node in the h-th layer in the root node is calculated by

$$\omega_{g_{hr}} = \frac{\xi_{hg_{hr}}'}{\sum_{h=1}^{K}\sum_{r=1}^{g_{hv}} \xi_{hg_{h1}}'+\xi_{hg_{h2}}'+\ldots+\xi_{hg_{hr}}'} \tag{14}$$

(iv) The weighted fusion of task risks for each segment yields a combined risk prediction of

$$F = \sum\nolimits_{h=1}^{K} \sum\nolimits_{r=1}^{g_{hv}} F_{hg_{hr}} \times \omega_{g_{hr}} \tag{15}$$

where $F_{hg_{hr}}$ represents the value at risk corresponding to the tasks in each session.

5.2. Comprehensive risk prediction based on weighted mapping

The pseudo-code of the integrated risk prediction model based on weighted mapping is shown in Table 1.

6. CASE VERIFICATION AND COMPARATIVE ANALYSIS

To verify the feasibility and superiority of the proposed method, this section presents an example of defense mission planning.

Assuming that an attacking entity is expected to strike our T-area at a certain time, the commanders plan defense tasks with the acquired basic situational information. A total of 15 tasks within six planning segments are involved in this planning process. The values of risk incurred by the link tasks are shown in Table 2.

6.1. Calculation of the correlation between the link tasks

Here, the reasonableness of resource coordination R_9 is used as an example to illustrate the calculation of its correlation with the others of the tasks. To formulate resource coordination rationality, it is necessary to combine the indicators expected to be achieved by the overall defense task, such as the coverage of the defense area and destruction requirements. The rationality of task indicator setting R_7 is a specific description of the indicators expected to be achieved by the task. Thus, the relationship between R_9 and R_7 belongs to a hierarchy. When combining the basic situational information involved in R_7 and R_9, and their intersection [Table 3], the hierarchical correlation between R_7 and R_9 can be calculated as $\zeta_{7\to9}^{(\mathrm{HR})} = 0.769$ using Equation (1).

Table 1. Integrated risk prediction model pseudo-code

		Integrated risk prediction model pseudo-code
Perceived linkages between session tasks	Step 1	Determine the types of interlinked relationships between link tasks based on the concepts of hierarchical, synergistic and independent relationships.
	Step 2	Using Equations (1) and (2) to calculate the link inter-task correlation, respectively.
Hierarchical topology generation	Step 3	Using Equations (5) and (6) to obtain the adjacency likelihood correlation matrix and the reachability correlation matrix, respectively.
	Step 4	Use Equation (7) to determine the hierarchical position of the tasks in each session.
	Step 5	The general skeleton matrix is computed using Equation (8) and the hierarchical topology is generated.
Consolidated risk projections	Step 6	Using Equations (9-11) to construct the weight judgment matrix of task risk for each layer of the link B_h.
	Step 7	Calculate the weighting coefficients of each segment's task risk in the composite risk using Equations (12-14) to construct a composite risk decision weighting map.
	Step 8	The combined risk is predicted using Equation (15).

Table 2. Information about the session tasks and their corresponding risk items in a given scenario

Session task	Corresponding risk items	Risk value
Defensive message clarity R_1	Unclear defensive information F_1	0.658
Comprehensive information on the attacking entity R_2	Incomplete information about the attacking entity F_2	0.790
Our defense unit strength determination R_3	Our defense unit strength was incorrectly determined F_3	0.566
Judgment of the direction of movement of the attacking entity R_4	Inaccurate judgment of the direction of movement of the attacking entity F_4	0.778
Attack entity size determination R_5	The size of the attacking entity was incorrectly identified F_5	0.721
Unit platform response capability R_6	Inadequate response capability of the unitary platform F_6	0.618
Reasonable setting of task indicators R_7	Unreasonable setting of task indicators F_7	0.692
Reasonableness of the selection of the target of fire collection R_8	Unreasonable selection of fire target F_8	0.764
Rationalization of resource integration R_9	Unreasonable resource integration F_9	0.625
Protective capability in conception R_{10}	Insufficient conceptual protection F_{10}	0.750
Reasonableness of programming standards R_{11}	Unreasonable standards for program development F_{11}	0.615
Program Resilience R_{12}	Inadequate program resilience F_{12}	0.632
Reasonableness of the index system of program preference R_{13}	The index system of program preference is not reasonable F_{13}	0.625
Execution of branch plans R_{14}	Inadequate execution of branch plans F_{14}	0.724
Monitoring capabilities of the program R_{15}	Insufficient monitoring power of the plan F_{15}	0.625

Table 3. Basic situation information related to R_7 and R_9

Serial number	$SI(R_7)$	$SI(R_9)$	$SI(R_7) \cap SI(R_9)$
1	Expected means of mission defense	Expected means of mission defense	1
2	Expected Achievement Goals	Expected Achievement Goals	1
3	Destruction parameter requirements	Destruction parameter requirements	1
4	Coverage	Coverage	1
5	Duration of mission	Duration of mission	1
6	The capability of reconnaissance and early warning unit capability	The capability of reconnaissance and early warning unit capability	1
7	The capability of firepower unit capability	The capability of firepower unit capability	1
8	The capability of electronic countermeasures unit capability	The capability of electronic countermeasures unit capability	1
9	The capability of integrated assurance unit	The capability of integrated assurance unit	1
10	The capability of interceptor strike unit capability	The capability of interceptor strike unit capability	1
11	–	Attack entity equipment type	0
12	–	Number of attacking entity equipment	0
13	–	Attack entity incoming main direction	0
14	–	Attack entity incoming sub-direction	0
15	–	Attack entity incoming proximity direction	0
16	–	Attack entity incoming intent	0

In addition to the hierarchical relationship between R_9 and R_7, R_9 also has a synergistic relationship with defense information clarity R_1, our defense unit strength determination R_3, and attack entity size determination

R_5. For example, when planning a mission, if we ignore the determination of the strength of the specific unit defense measures available to us and the overall determination of the size of the attacking entity of the opponent and directly conceptualize the unit strength, the allocation of unit strength resources will likely be unreasonable and even cause the deployment to fail. In other words, the clarity of defense information, the determination of our defense unit forces, and the determination of the size of the attacking entity all affect the rationality of resource coordination in the conceptualization process, which, together, determine the rationality of our resource coordination. Therefore, a synergistic relationship exists between them and the reasonableness of our resource integration.

To measure the degree of synergy between link tasks, ten experts in related fields determined the role factors of link tasks R_1, R_3 and R_5 on R_9 using fuzzy hierarchical analysis, the fuzzy complementary judgment matrix is as follows:

$$\begin{pmatrix} 0.5 & 0.55 & 0.15 \\ 0.45 & 0.5 & 0.1 \\ 0.85 & 0.9 & 0.5 \end{pmatrix}\begin{pmatrix} 0.5 & 0.5 & 0.2 \\ 0.5 & 0.5 & 0.1 \\ 0.8 & 0.9 & 0.5 \end{pmatrix}\begin{pmatrix} 0.5 & 0.6 & 0.15 \\ 0.4 & 0.5 & 0.05 \\ 0.85 & 0.95 & 0.5 \end{pmatrix}\begin{pmatrix} 0.5 & 0.5 & 0.2 \\ 0.5 & 0.5 & 0.2 \\ 0.8 & 0.8 & 0.5 \end{pmatrix}\begin{pmatrix} 0.5 & 0.6 & 0.1 \\ 0.4 & 0.5 & 0.15 \\ 0.9 & 0.85 & 0.5 \end{pmatrix}$$

$$\begin{pmatrix} 0.5 & 0.55 & 0.15 \\ 0.45 & 0.5 & 0.2 \\ 0.85 & 0.8 & 0.5 \end{pmatrix}\begin{pmatrix} 0.5 & 0.5 & 0.1 \\ 0.5 & 0.5 & 0.05 \\ 0.9 & 0.95 & 0.5 \end{pmatrix}\begin{pmatrix} 0.5 & 0.55 & 0.2 \\ 0.45 & 0.5 & 0.1 \\ 0.8 & 0.9 & 0.5 \end{pmatrix}\begin{pmatrix} 0.5 & 0.6 & 0.15 \\ 0.4 & 0.5 & 0.2 \\ 0.85 & 0.8 & 0.5 \end{pmatrix}\begin{pmatrix} 0.5 & 0.55 & 0.2 \\ 0.45 & 0.5 & 0.05 \\ 0.8 & 0.95 & 0.5 \end{pmatrix}$$

Calculating the action factors of the link tasks R_1, R_3 and R_5 on R_9 based on the above matrix, as shown in Table 4. Based on Table 4, the degrees of correlation between R_1, R_3, R_5 and R_9 were calculated using Equation (2) to obtain $\zeta_{1\to9}^{(SR)} = 0.283$, $\zeta_{3\to9}^{(SR)} = 0.258$, and $\zeta_{5\to9}^{(SR)} = 0.459$.

Since program resilience is not associated with other link tasks, it is considered an independent relationship and acts directly on the total task. The degrees of synergy between all tasks can be calculated based on the analysis of the remaining tasks, which will not be repeated here owing to length constraints. Thus, the adjacency probability correlation matrix $\Gamma_{15\times15}$ [30,31] between the 15 link tasks can be generated, as shown in Table 5:

Where data followed by "*" indicates that the type of relationship between tasks in the session is hierarchical; data followed by "/" denotes that the relationship type between tasks in the session is synergistic.

In turn, the reachable correlation matrix $M_{15\times15}^{i\to j}$ [32–34] and the general skeleton matrix $(E)_{15\times15}$ can be determined, as provided in Tables 6 and 7, respectively:

Therefore, according to the results of link task relevance calculation, the link task relevance structure model can be obtained, as given in Figure 3.

This paper adopts the path analysis method to test the accuracy and reliability of the link task association structure model. Several domain experts are invited to assess the risk value of each link task and use it as a basis for judgment, and the risk value of the corresponding risk item of each link task is imported into the path analysis model for analysis to verify the validity of the association path between each task and the total task [35–37], where the standardized coefficient specifically reflects the degree of influence between the two risks; when the p-value is $< 5\%$, it can be considered significant, representing a valid path between the risks. The specific results are shown in Table 8.

From the results of Table 8, it can be seen that the p-value of paths $R_1 \to R_9$, $R_3 \to R_9$, $R_{12} \to R$ is less than 5%, and that of the rest of the paths is less than 1%, which indicates that the paths existing between risks in the

Table 4. The action factors of the link tasks R_1, R_3 and R_5 on R_9 obtained from FAHP

	$\mathrm{Im}(R_1 \to R_9)$	$\mathrm{Im}(R_3 \to R_9)$	$\mathrm{Im}(R_5 \to R_9)$
Action factor	0.283	0.258	0.459

Table 5. The adjacency probability correlation matrix

$\Gamma_{15\times15} = (\zeta_{i\to j})_{15\times15}$	R_1	R_2	R_3	R_4	R_5	R_6	R_7	R_8	R_9	R_{10}	R_{11}	R_{12}	R_{13}	R_{14}	R_{15}
R_1	0	0	0	0	0	0	0.275/	0	0.283/	0	0	0	0.4*	0	0
R_2	0	0	0.75*	0.462*	0	0	0.6/	0	0	0	0	0	0	0	0
R_3	0	0	0	0	0	0.913*	0.125/	0	0.258/	0	0	0	0	0	0
R_4	0	0	0	0	0	0	0	0.7/	0	0	0	0	0	0	0
R_5	0	0	0	0	0	0	0	0.3/	0.459/	0	0	0	0	0	0
R_6	0	0	0	0	0	0	0	0	0	0.606*	0	0	0	0.92*	0.467*
R_7	0	0	0	0	0	0	0	0	0.769*	0	0	0	0.324*	0	0
R_8	0	0	0	0	0	0	0	0	0	0	0	0	0	0	0
R_9	0	0	0	0	0	0	0	0	0	0	0.64*	0	0	0	0
R_{10}	0	0	0	0	0	0	0	0	0	0	0	0	0	0.541*	0
R_{11}	0	0	0	0	0	0	0	0	0	0	0	0	0	0	0
R_{12}	0	0	0	0	0	0	0	0	0	0	0	0	0	0	0
R_{13}	0	0	0	0	0	0	0	0	0	0	0	0	0	0	0
R_{14}	0	0	0	0	0	0	0	0	0	0	0	0	0	0	0
R_{15}	0	0	0	0	0	0	0	0	0	0	0	0	0	0	0

Table 6. The reachable correlation matrix

$M_{15\times15}^{i\to j}$	R_1	R_2	R_3	R_4	R_5	R_6	R_7	R_8	R_9	R_{10}	R_{11}	R_{12}	R_{13}	R_{14}	R_{15}
R_1	1	0	0	0	0	0	0.275	0	0.283	0	0.283	0	0.4	0	0
R_2	0	1	0	0.75	0.462	0	0.6	0.7	0.6	0	0.6	0	0.324	0	0
R_3	0	0	1	0	0	0.913	0.125	0	0.258	0.606	0.258	0	0.125	0.913	0.467
R_4	0	0	0	1	0	0	0	0.7	0	0	0	0	0	0	0
R_5	0	0	0	0	1	0	0	0.3	0.459	0	0.459	0	0	0	0
R_6	0	0	0	0	0	1	0	0	0	0.606	0	0	0	0.92	0.467
R_7	0	0	0	0	0	0	1	0	0.769	0	0.64	0	0.324	0	0
R_8	0	0	0	0	0	0	0	1	0	0	0	0	0	0	0
R_9	0	0	0	0	0	0	0	0	1	0	0.64	0	0	0	0
R_{10}	0	0	0	0	0	0	0	0	0	1	0	0	0	0.541	0
R_{11}	0	0	0	0	0	0	0	0	0	0	1	0	0	0	0
R_{12}	0	0	0	0	0	0	0	0	0	0	0	1	0	0	0
R_{13}	0	0	0	0	0	0	0	0	0	0	0	0	1	0	0
R_{14}	0	0	0	0	0	0	0	0	0	0	0	0	0	1	0
R_{15}	0	0	0	0	0	0	0	0	0	0	0	0	0	0	1

link task association structure model are effective. And the degree of influence between risks can be reflected by the standardized coefficient value; the larger the standardized coefficient value is, the higher the degree of validity of the existence of paths between risks; according to the results of Table 8, it can be seen that each path distance presents a significant positive correlation (standardized coefficient > 0). Thus, the reliability of the link task association structure model paths is verified.

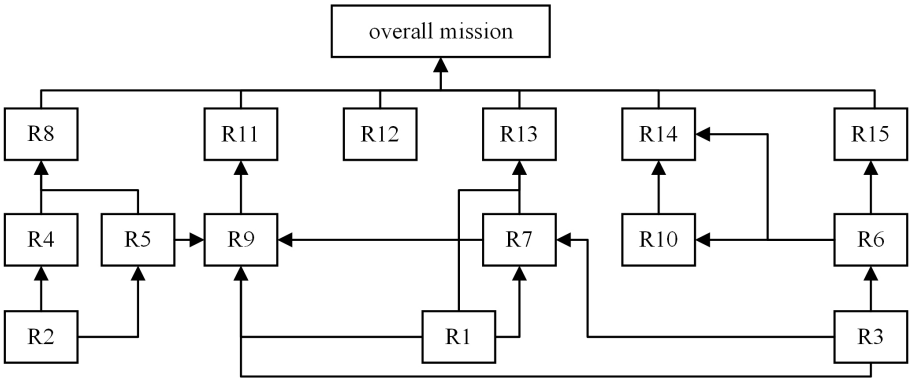


Figure 3. Structural modeling of link task associations

Table 7. The general skeleton matrix

$(E)_{15\times15}$	R_1	R_2	R_3	R_4	R_5	R_6	R_7	R_8	R_9	R_{10}	R_{11}	R_{12}	R_{13}	R_{14}	R_{15}
R_1	0	0	0	0	0	0	0.275	0	0.008	0	0	0	0.125	0	0
R_2	0	0	0	0.75	0.462	0	0.6	0	0	0	0	0	0	0	0
R_3	0	0	0	0	0	0.913	0.125	0	0.133	0	0	0	0	0	0
R_4	0	0	0	0	0	0	0	0.7	0	0	0	0	0	0	0
R_5	0	0	0	0	0	0	0	0.3	0.459	0	0	0	0	0	0
R_6	0	0	0	0	0	0	0	0	0	0.606	0	0	0	0.379	0.467
R_7	0	0	0	0	0	0	0	0	0.769	0	0	0	0.324	0	0
R_8	0	0	0	0	0	0	0	0	0	0	0	0	0	0	0
R_9	0	0	0	0	0	0	0	0	0	0	0.64	0	0	0	0
R_{10}	0	0	0	0	0	0	0	0	0	0	0	0	0	0.541	0
R_{11}	0	0	0	0	0	0	0	0	0	0	0	0	0	0	0
R_{12}	0	0	0	0	0	0	0	0	0	0	0	0	0	0	0
R_{13}	0	0	0	0	0	0	0	0	0	0	0	0	0	0	0
R_{14}	0	0	0	0	0	0	0	0	0	0	0	0	0	0	0
R_{15}	0	0	0	0	0	0	0	0	0	0	0	0	0	0	0

Table 8. Regression coefficients for structural modeling of link task associations

Path	Standardized coefficient	P	Path	Standardized coefficient	P
$R_2 \to R_4$	0.961	<1% (0.000***)	$R_9 \to R_{11}$	0.983	<1% (0.000***)
$R_2 \to R_5$	0.953	<1% (0.000***)	$R_1 \to R_{13}$	0.147	<5% (0.042**)
$R_3 \to R_6$	0.963	<1% (0.000***)	$R_7 \to R_{13}$	0.843	<1% (0.000***)
$R_1 \to R_7$	0.447	<1% (0.000***)	$R_6 \to R_{14}$	0.499	<1% (0.001***)
$R_3 \to R_7$	0.547	<1% (0.000***)	$R_{10} \to R_{14}$	0.495	<1% (0.01***)
$R_4 \to R_8$	0.515	<1% (0.000***)	$R_6 \to R_{15}$	0.974	<1% (0.000***)
$R_5 \to R_8$	0.479	<1% (0.000***)	$R_8 \to R$	0.154	<1% (0.000***)
$R_1 \to R_9$	0.201	<5% (0.029**)	$R_{11} \to R$	0.269	<1% (0.000***)
$R_3 \to R_9$	0.229	<5% (0.023**)	$R_{12} \to R$	0.081	<5% (0.025**)
$R_5 \to R_9$	0.181	<1% (0.07***)	$R_{13} \to R$	0.127	<1% (0.07***)
$R_7 \to R_9$	0.430	<1% (0.01***)	$R_{14} \to R$	0.251	<1% (0.000***)
$R_6 \to R_{10}$	0.976	<1% (0.000***)	$R_{15} \to R$	0.190	<1% (0.01***)

6.2. Risk hierarchy decision weighting mapping construction

Based on the general skeleton matrix $(E)_{15\times15}$, the rotational extraction concept described in Section 4 is used to determine the possibility hierarchy position of the link task in the total task and then generate a risk hierarchy decision weighting mapping $G \updownarrow$ for defense task planning, as shown in Figure 4A. It can be observed from Figure 4A that F_8, F_{11}, F_{12}, F_{13}, F_{14}, and F_{15} act directly on the total risk F, while $F_1 \sim F_7$ and $F_9 \sim F_{10}$ need to act indirectly on F through other intermediate nodes.

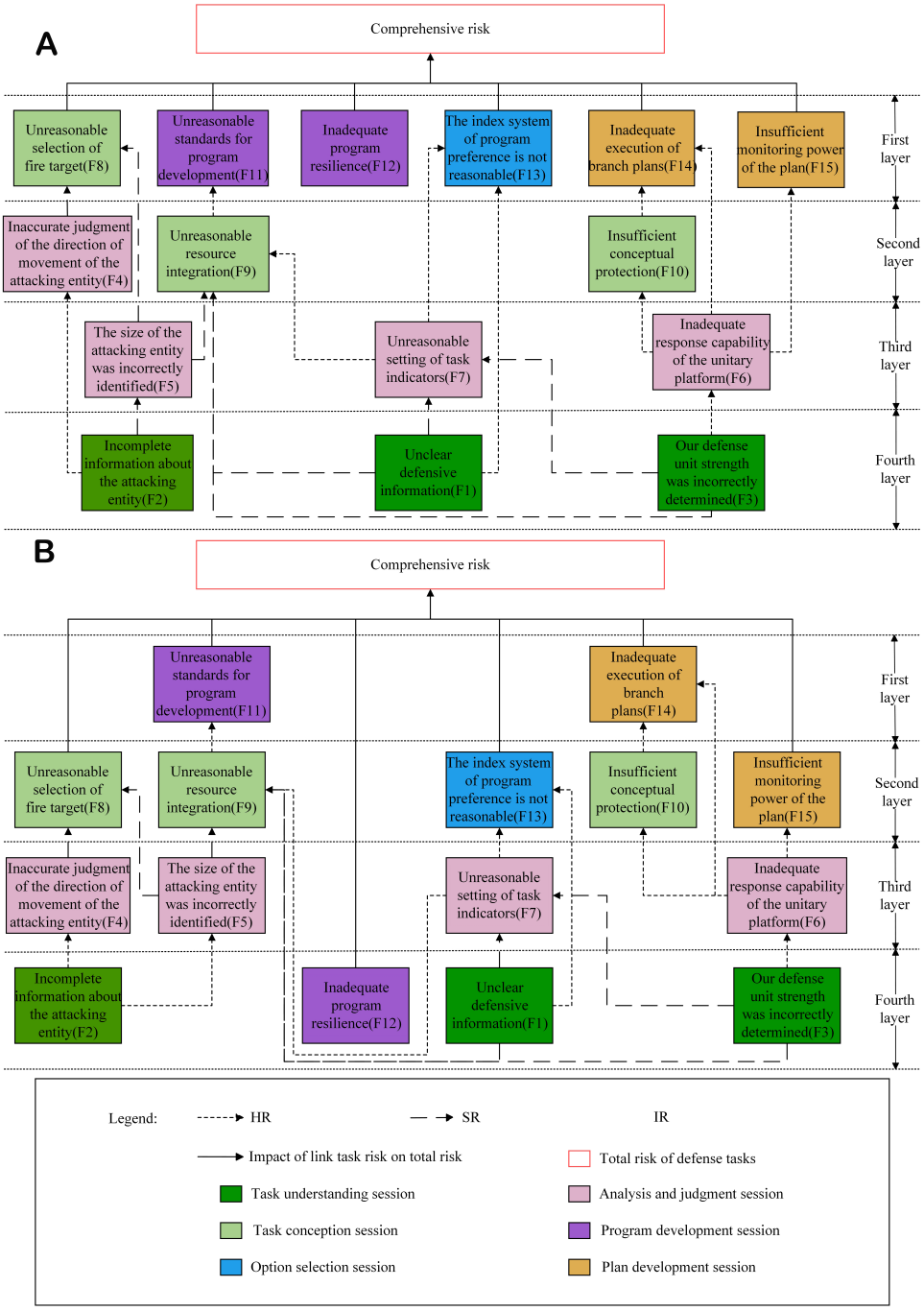


Figure 4. Decision mapping generated by the two methods. (A) Decision mapping of the possibility hierarchy determined by the rotattional extractional method; (B) Decision mapping of the possibility hierarchy determined by bottom-upextractional method.

To illustrate that the generated risk hierarchy decision weighting mapping $G\updownarrow$ is more conducive to the prediction of integrated risks, the rationality of the approach in this study is analyzed by comparing it with the risk hierarchy decision weighting mapping $G\uparrow$[38,39] (shown in Figure 4B) constructed based on the bottom-up explanatory structure model[40].

By comparing Figure 4A and B, we can find that in the $G\uparrow$ generated based on the bottom-up explanation structure model, F_8, F_{12}, F_{13}, and F_{15}, which play a direct role in the total risk, are not assigned to the first layer,

which is closer to the total risk; however, F_8, F_{13}, and F_{15} are assigned to the second and F_{12} is assigned to the forth layer. Moreover, F_4 is influenced by the position of the F_8 layer and is assigned to the third layer that is further away from the total risk. To a certain extent, the direct influence of F_4, F_8, F_{12}, F_{13}, and F_{15} on the total task is weakened, making the corresponding risks of each link task relatively more diffuse in the decision, thereby making it difficult for the decision weighting mapping to be clustered to the total risk. In contrast, $G\updownarrow$ generated by the proposed method, F_8 and $F_{11} \sim F_{15}$, which play a direct role in the total task, are both assigned to the first layer nearest to the total risk. F_4 is assigned to the second layer which is relatively far from the total risk, because it indirectly acts on F through a node F_8. The proposed method is more conducive to clustering each link task to the total task.

To visualize the aforementioned phenomenon, firstly, according to the general skeleton matrix $(E)_{15\times15}$ obtained in Section 5.1, the elements in each nonzero row and column are summed up to obtain the impact value $\sum_{i=1}^{15} e_{ij}$ of other tasks on the ith link task and the impact value $\sum_{j=1}^{15} e_{ij}$ of the ith link task on other tasks. Subsequently, the impact values of each link task are processed in combination with its different levels N ($N = 1, 2, 3, 4$) as follows:

$$\begin{cases} \sum_{i=1}^{15} e_{ij} + (N-1) & \text{The impact value of the other tasks on the } i\text{th link task} \\ \sum_{j=1}^{15} e_{ij} + (N-1) & \text{The impact value of the } i\text{th link task on other tasks} \end{cases} \tag{16}$$

Taking $\sum_{i=1}^{15} e_{ij} + (N-1)$ and $\sum_{j=1}^{15} e_{ij} + (N-1)$ as the horizontal and vertical coordinates of the ith link task, respectively, the possibility hierarchy position distribution of each link task of $F_1 \sim F_{15}$ can be calculated, as shown in Figure 5. Among them,"0, 1, 2, 3, 4" on the coordinate axis represent the boundaries of the four layer task hierarchy established in the defense task planning process, and their physical meaning is the number of hierarchical levels.

It can be intuitively observed from Figure 5 that in the hierarchical decision map $G\updownarrow$ generated by our proposed method, the link tasks are more aggregated to the root node F. In contrast, the link tasks in the method in the literature[40], are more inclined to spread to the branch nodes, which weakens the comprehensive effect on the risk to a certain extent. Therefore, it is more reasonable and feasible to use the decision mapping generated by the proposed method for subsequent integrated risk prediction.

6.3. Forecasting methodology for integrated risk

Based on the general skeleton matrix $(E)_{15\times15}$ and the integrated risk hierarchical decision weighting mapping generated in Section 5.1, the centrality of the link task risk is calculated using Equation (9) (as shown in Table 9), and the numerical comparison is used to establish the link task risk weight judgment matrix $B_h = \left(b_{ij}\right)_{g_h\times g_h}$ for the hth layer, where $h = 1, 2, 3, 4$. Then, Equations (11-14) are used to determine the intra-layer weight and comprehensive weight of the task risk of each layer in the total task risk.

To illustrate the rationality of the above weight determination method, the weights obtained from the bottom-up extraction method[40] and entropy method[41] are compared for analysis, respectively, as shown in Table 10.

Compared to the bottom-up extraction method, the weight values of F_1, F_2, and F_3 in F obtained by the proposed method are higher, which is in line with the needs of defense task planning. The main reason is that the link tasks F_1, F_2, and F_3 are all basic situational information. Only by fully grasping them can the emergence of risks in the execution of the later link tasks be avoided and the completion of the total task be ensured. The risks corresponding to F_8, F_{13}, and F_{15} are raised from the second to the first level in the proposed method, and the weight values are increased because they act directly on F. Simultaneously, the risk corresponding to F_4 increases from the third to the second level, and the weight value is also improved. The

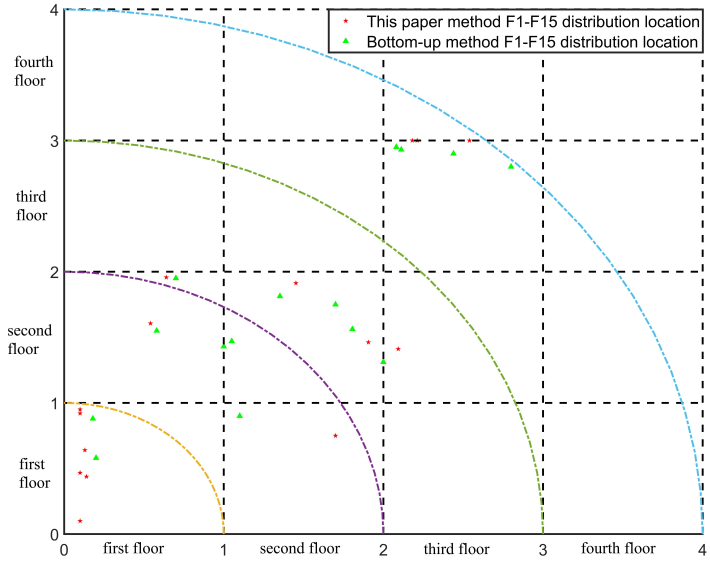


Figure 5. Distribution of link task likelihood hierarchy positions based on two methods.

aforementioned adjustments are reasonable when combined with the comprehensive risk prediction results calculated in this section.

Compared to the entropy method, the weight value of F_2 obtained using the proposed method is relatively low. The main reason is that the link task F_2 has higher value-at-risk when using the entropy method. If the information of the attacking entity is not fully understood, it will seriously hinder the total task execution and even cause a fatal blow. However, this paper argues that F_2 is very important. More importantly, we must allocate our forces and respond to physical attacks based on our knowledge of the enemy's posture when making comprehensive risk predictions. Therefore, it is reasonable that the combined weight of F_2 obtained by the proposed method is lower than that obtained using the entropy method.

In addition, compared to the scenario strain shortage capacity risk F_{12}, the impact of the unreasonable indicators system of program preference risk F_{13} on the overall program performance is relatively large, and the weight of F_{12} in F should be lower than the weight of F_{13} in F. Compared with the literature[40], it is more effectively reflected in the proposed method.

According to the risk weight value of each link task given by the defense expert system, the link task weight value obtained by each method in Table 10 is analyzed by using the Technique for Order of Preference by Similarity to Ideal Solution (TOPSIS) ideal point method[42–44], and the decision matrix[45] constructed is shown in Table 11, where the elements indicate the difference between the weights of each link task given by different methods and expert systems. Based on Table 11, the calculated TOPSIS evaluation results are shown in Table 12.

As can be seen from the results in Table 12, compared with the other two methods, the comprehensive score index of the method proposed in this paper is higher and is the optimal program, indicating that the risk weight value of each link of the task obtained by our technique is most consistent with the actual situation.

Table 9. The centrality of the link task risk

F_i	$C(F_i)$	F_i	$C(F_i)$	F_i	$C(F_i)$
F_1	0.4080	F_6	2.3650	F_{11}	0.6400
F_2	1.8120	F_7	2.0930	F_{12}	0.0000
F_3	1.1710	F_8	1.0000	F_{13}	0.4490
F_4	1.4500	F_9	2.0090	F_{14}	0.9200
F_5	1.2210	F_{10}	1.1470	F_{15}	0.4670

Table 10. Table of intra-tier weights for the link tasks

Weight judgment matrix $B_h = (b_{ij})_{g_h \times g_h}$							Methodology of this study			Bottom-up extraction method			Entropy method
							Levels	Intra-layer weights	Composite weights	Levels	Intra-layer weights	Composite weights	
F_8	1	2	2	2	2	2		0.3278	**0.0822**	2nd Floor	0.1713	**0.0443**	0.0480
F_{11}	0	1	2	2	0	2	1st Floor	0.1684	0.0422	1st Floor	0.7311	0.1887	0.0631
F_{12}	0	0	1	0	0	0		**0.0619**	**0.0156**	4th Floor	**0.1015**	**0.0262**	**0.0725**
F_{13}	0	0	2	1	0	0		**0.0864**	**0.0217**	2nd Floor	**0.0770**	**0.0199**	**0.0674**
F_{14}	0	2	2	2	1	2		0.2349	0.0589	1st Floor	0.2689	0.0694	0.0343
F_{15}	0	0	2	2	0	1		0.1206	**0.0303**	2nd Floor	0.1148	**0.0296**	0.0451
F_4	1	0	2				2nd Floor	0.2889	0.0822	3rd Floor	0.1674	0.0074	0.0842
F_9	2	1	2					0.5628	0.0422	2nd Floor	0.3813	0.1887	0.0654
F_{10}	0	0	1					0.1483	0.0589	2nd Floor	0.2556	0.0694	0.0535
F_5	1	0	0				3rd Floor	0.1483	0.0492	3rd Floor	0.1015	0.0236	0.0631
F_6	2	1	2					0.5628	0.1481		0.4551	0.0990	0.0720
F_7	2	0	1					0.2889	0.0339		0.2760	0.0719	0.0474
F_1	1	0	0				4th Floor	0.5627	**0.1315**	4th Floor	0.4551	**0.0310**	0.1244
F_2	2	1	2					**0.1484**	**0.0330**		0.1674	**0.0121**	**0.0642**
F_3	2	0	1					0.2889	**0.1701**		0.2760	**0.1188**	0.0954

Table 11. TOPSIS decision-making matrix

Segment task risk items	Methodology of this article	Bottom-up extraction method	Entropy method	Segment task risk items	Methodology of this article	Bottom-up extraction method	Entropy method
F_1	0.0015	0.099	0.081	F_9	0.0578	0.0887	0.0348
F_2	0.003	0.0179	0.0404	F_{10}	0.0089	0.0194	0.0135
F_3	0.0002	0.0515	0.0995	F_{11}	0.0578	0.0887	0.0288
F_4	0.0022	0.0726	0.0219	F_{12}	0.0026	0.0132	0.0701
F_5	0.0292	0.0036	0.0336	F_{13}	0.0044	0.0062	0.0605
F_6	0.0171	0.032	0.0762	F_{14}	0.0369	0.0474	0.0387
F_7	0.0039	0.0419	0.0472	F_{15}	0.0087	0.008	0.0442
F_8	0.0062	0.0317	0.006				

Table 12. TOPSIS evaluation results

Method	Positive ideal solution distance	Negative ideal solution distance	Composite score index	Arrange in order
Methodology of this article	**1.06422349**	**3.52206885**	**0.76795559**	1
Bottom-up extraction method	2.85681912	2.18487242	0.43336099	2
Entropy method	2.98084338	2.11787522	0.41537402	3

Combining the link task risk values in Table 2 and the link task weights in Table 10, the risk value of the total

Table 13. Comparison of integrated risk forecast results

	Actual combined risk value	Bottom-up extraction method	Entropy method	Methodology of this article
Comprehensive Risk	0.6621	0.6485	0.6764	0.6676

Table 14. Deviation between the predicted value of each integrated risk and the actual integrated risk value

	Bottom-up extraction method	Entropy method	Methodology of this article
Deviation	13.82%	15.83%	**6.08%**

task is obtained using Equation (15). The integrated risk value evaluated by the air defense expert system was taken as the actual integrated risk value, and was compared and analyzed with the risk values obtained by each of the aforementioned methods, as shown in Table 13.

Table 13 shows that the relative error rate between the integrated risk value obtained by the proposed method and the actual risk value is 0.82%, while the relative error rates of the other two approaches are 2.1% and 2.11%.

6.4. Comparative analysis of different methods

To further illustrate the overall advantages of the proposed method, the risk values of 20 test samples are predicted; the detection samples are obtained by collecting basic data of the defense side in exercise tasks in different scenarios. The real comprehensive risk values based on the expert system were 0.5327, 0.6745, 0.8871, 0.7125, 0.6265, 0.5292, 0.7715, 0.4858, 0.6142, 0.5383, 0.7627, 0.5475, 0.4965, 0.6057, 0.7322, 0.8447, 0.5737, 0.7124, 0.5325, and 0.6581. The risk values predicted by the proposed method, bottom-up extraction method, and fuzzy hierarchical analysis were compared. The validation outcomes illustrate the feasibility and reasonableness of the proposed method. The actual integrated risk values of the 20 test samples and the predicted integrated risk values obtained by different methods are shown in Figure 6. The deviation of each predicted value from the actual integrated risk value is calculated, as given in Table 14.

It can be seen from Table 14 that the deviation between the proposed method and the actual comprehensive risk value is minimal. Compared with bottom-up extraction, the relative deviation is reduced by 56%. Compared with the entropy weight method, the relative deviation is reduced by 61.6%. It shows that this method can predict the comprehensive risk of defense mission planning more accurately and exhibits certain feasibility.

7. CONCLUSION

In this paper, the relation between links and tasks is systematically expounded. On the premise of considering different association types, the hierarchy determination method of the link task in the whole defense task is explored. The decision graph of link task risk level for efficient defense task planning is generated. Then, a comprehensive risk prediction model is constructed. The problem of inaccurate risk prediction results caused by non-independence between tasks is solved. Through the simulation of test samples, the feasibility and rationality of the proposed method are compared and analyzed. The work and innovation of this paper are mainly reflected in:

(i) Defining the types of link inter-task associations as hierarchical, synergistic and independent relationships, further deepening the connotation of associative relationships, and proposing a calculation method for link tasks.

(ii) Introducing the idea of hierarchical topology, a method for determining the hierarchical position of link tasks based on rotational extraction is proposed, and the reasonableness of the generated hierarchical topology paths is analyzed based on the level of significance in the path analysis method.

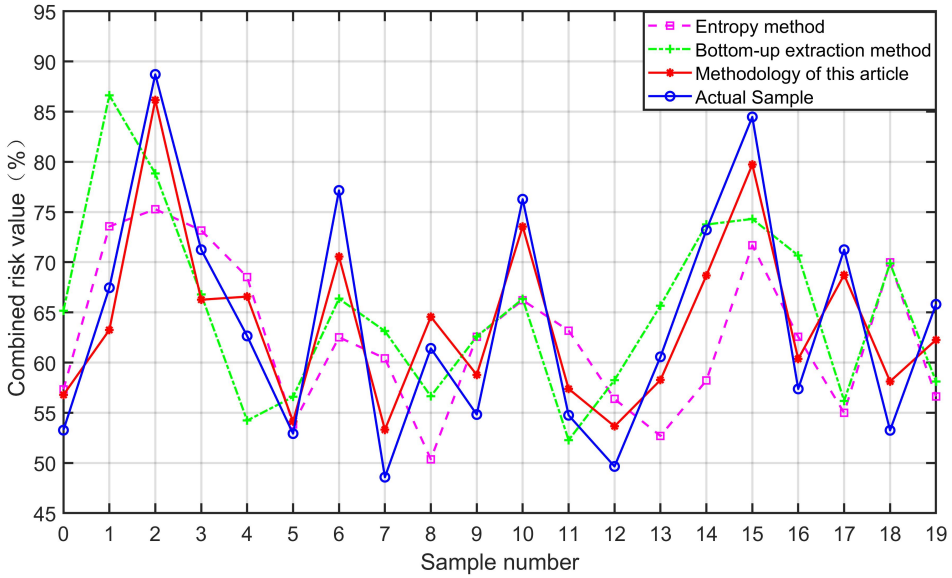


Figure 6. Comparative chart of integrated risk forecast results

(iii) A hierarchical decision weighted mapping of integrated risk is constructed using the link task centrality degree. Compared with the entropy weight method, this paper considers the correlation type and intensity of tasks in weight calculation. The result is more consistent with the actual situation, and the relative deviation of risk is reduced by 61.6%. Compared with the bottom-up extraction method, the nodes in the graph constructed in this paper are more centralized to the root node, and the relative risk deviation is reduced by 56%. To some extent, the proposed method solves the problem that the existing decision-making methods are difficult to reflect the correlation strength of link tasks, which leads to unreasonable prediction results.

In summary, the integrated risk prediction method for defense mission planning with hierarchical weighted mapping proposed in this paper shows significant advantages in dealing with the complex risk environment of planning missions in the field of national defense and can provide scientific decision support for strategic deployment. At the same time, the method can also be applied to risk decision-making in financial investment, emergency management, urban planning and construction. However, the construction of risk terms proposed in this paper is not comprehensive enough, and we will further improve the accuracy of comprehensive risk prediction by refining and expanding the risk terms in the future.

DECLARATIONS

Acknowledgments

The authors would like to thank the reviewers for their thoughtful comments and efforts towards improving this manuscript.

Authors' contributions

Methodology, experiment, data analysis, and manuscript drafting: Du W
Conceptualization, manuscript edition and review, and supervision: Chen X

Availability of data and materials

Not applicable.

Financial support and sponsorship
None.

Conflicts of interest
Both authors declared that there are no conflicts of interest.

Ethical approval and consent to participate
Not applicable.

Consent for publication
Not applicable.

Copyright
© The Author(s) 2024.

REFERENCES

1. Gong J, Lu C, Liu Q, Huang J. Uncertain mission planning for earthquake rescue based on scenario. Proceedings of the 2022 IEEE 2nd international conference on electronic technology, communication and information (ICETCI), Changchun, China, 27-29 May 2022; pp. 586-92. DOI
2. Yue L, Yang R, Zhang Y, Yu LX, Wang Z. Deep reinforcement learning for UAV intelligent mission planning. *Complexity* 2022;2022:3551508. DOI
3. Kase SE, Hung CP, Krayzman T, Hare JZ, Rinderspacher BC, Su SM. The future of collaborative human-artificial intelligence decision-making for mission planning. *Front Psychol* 2022;13:850628. DOI
4. Xu J, Liu T, Tian W, Wang X, Zhang J, Chen Y. Safety risk assessment based on reloading airdrop mission. *E3S Web Conf* 2021;257:02084. DOI
5. Zhang Y, Zuo F. Selection of risk response actions considering risk dependency. *Kybernetes* 2016;45:1652-67. DOI
6. Dixit V. Risk assessment of different sourcing contract scenarios in project procurement. *Int J Constr Manag* 2022;22:1537-49. DOI
7. Lin SS, Shen SL, Zhou A, Xu YS. Risk assessment and management of excavation system based on fuzzy set theory and machine learning methods. *Automat Constr* 2021;122:103490. DOI
8. Li Y, Hu Z. A review of multi-attributes decision-making models for offshore oil and gas facilities decommissioning. *J Ocean Eng Sci* 2022;7:58-74.DOI
9. Duan L, He J, Li M, et al. Based on a decision tree model for exploring the risk factors of smartphone addiction among children and adolescents in China during the COVID-19 pandemic. *Front Psychiatry* 2021;12:652356. DOI
10. Wu J, Gong H, Liu F, Liu Y. Risk Assessment of open-pit slope based on large-scale group decision-making method considering non-cooperative behavior. *Int J Fuzzy Syst* 2023;1:245-63. DOI
11. Ikwan F, Sanders D, Hassan M. Safety evaluation of leak in a storage tank using fault tree analysis and risk matrix analysis. *J Loss Prevent Proc Ind* 2021;73:104597. DOI
12. Zheng HL, Du WW, Zhao XX, Shi H. Operational conception risk assessment model. *Fire Control Command Control* 2021;4:110-5;121. DOI
13. Song YB, He JL, Sun JZ, Xu T. Evaluation on joint operation determination scheme. *Command Inf Syst Technol* 2016;4:49-54. DOI
14. Ryczynski J, Tubis AA. Tactical risk assessment method for resilient fuel supply chains for a military peacekeeping operation. *Energies* 2021;14:4679. DOI
15. Kim I, Kim S, Kim H, Shin D. Mission-based cybersecurity test and evaluation of weapon systems in association with risk management framework. *Symmetry* 2022;14:2361. DOI
16. Zhang Y, Liu J, Xie X, Wang C, Bai L. Modeling of project portfolio risk evolution and response under the influence of interactions. *Mathematics* 2023;11:4091.DOI
17. Abedzadeh S, Roozbahani A, Heidari A. Risk assessment of water resources development plans using fuzzy fault tree analysis. *Water Resour Manag* 2020;34:2549-69. DOI
18. Du WW, Chen XW. Operational task hierarchical decomposition. *Acta Armamentarii* 2021;42:2771. DOI
19. Lei S, Peng XR, Li XS. Research on the evaluation of national defense science and technology strategic intelligence research capability based on QFD. *Inf Stud Theory Appl* 2022;2:55-60. DOI
20. Costa LF. Further generalizations of the Jaccard index. *arXiv* 2021. DOI
21. Zhang D, You X, Liu S, Yang K. Multi-colony ant colony optimization based on generalized jaccard similarity recommendation strategy. *IEEE Access* 2019;7:157303-17. DOI
22. Chung NC, Miasojedow B, Startek M, Gambin A. Jaccard/Tanimoto similarity test and estimation methods for biological presence-absence data. *BMC Bioinformatics* 2019;20:1-11. DOI

23. Hsu WK, Chen J, Huynh NT, Lin Y. Risk assessment of navigation safety for ferries. *J Mar Sci Eng* 2022;5:700. DOI
24. Yu Y, He X, Wan F, Bai Z, Fu C. Dynamic risk assessment of karst tunnel collapse based on fuzzy-AHP: a case study of the LianHuaShan tunnel, China. *Adv Civil Eng* 2022;2022:4426318. DOI
25. Li K, Xiahou X, Huang H, et al. AHP-FSE-Based risk assessment and mitigation for slurry balancing shield tunnel construction. *J Environ Public Health* 2022;2022:1666950. DOI
26. Fan C, Deng B, Yin Y. Hierarchical structure and transfer mechanism to assess the scheduling-related risk in construction of prefabricated buildings: an integrated ISM–MICMAC approach. *Eng Constr Archit Manag* 2023;30:2991-3013. DOI
27. Chen Y, Lou N, Liu G, Luan Y, Jiang H. Risk analysis of ship detention defects based on association rules. *Mar Policy* 2022;142:105123. DOI
28. Song W, Zhu Y, Li S, Wang L, Zhang H. Risk evaluation of information technology outsourcing project: an integrated approach considering risk interactions and hierarchies. *Eng Appl Artif Intell* 2022;113:104938. DOI
29. Wei DT, Liu XD, Guo R. Research on strategic consistency evaluation method of equipment system based on improved DEMATEL-ISM-FCA. *Military Oper Res Assess* 2021;3:29-35. DOI
30. Mathiyazhagan K, Govindan K, NoorulHaq A, Geng Y. An ISM approach for the barrier analysis in implementing green supply chain management. *J Clean Prod* 2023;47:283-297. DOI
31. Ajmera P, Jain V. A fuzzy interpretive structural modeling approach for evaluating the factors affecting lean implementation in Indian healthcare industry. *Int J Lean Six Sigma* 2019;2:376-97. DOI
32. Wang M, Zhang Y, Tian Y, Zhang K. An integrated rough-fuzzy WINGS-ISM method with an application in ASSCM. *Expert Syst Appl* 2023;212:118843. DOI
33. Amini A, Alimohammadlou M. Toward equation structural modeling: An integration of interpretive structural modeling and structural equation modeling. *J Manag Anal* 2021;4:693-714. DOI
34. Ahmad N, Qahmash A. Smartism: implementation and assessment of interpretive structural modeling. *Sustainability* 2021;16:8801. DOI
35. Niati DR, Siregar ZME, Prayoga Y. The effect of training on work performance and career development: the role of motivation as intervening variable. *BIRCI J* 2021;2:2385-93. DOI
36. Heri S, Nur AY, Mohd H, Rico NI, Irada S. Relationship between budget participation, job characteristics, emotional intelligence and work motivation as mediator variables to strengthening user power performance: an emperical evidence from indonesia government. *Morfai J* 2021;1:36-48. DOI
37. Hirdinis M. Capital structure and firm size on firm value moderated by profitability. *Int J Econ Business Admin* 2019;VII:174-91. DOI
38. Poduval PS, Pramod VR, Raj VPJ. Interpretive structural modeling (ISM) and its application in analyzing factors inhibiting implementation of total productive maintenance (TPM). *Int J Qual Reliab Manag* 2015;3:308-31. DOI
39. Sarabi S, Han Q, Romme AGL, de Vries B, Valkenburg R, den Ouden B. Uptake and implementation of nature-based solutions: an analysis of barriers using interpretive structuralmodeling. *J Environ Manag* 2020;270:110749. DOI
40. Sharma A, Abbas H, Siddiqui MQ. Modelling the inhibitors of cold supply chain using fuzzy interpretive structural modeling and fuzzy MICMAC analysis. *Plos One* 2021;16:e0249046. DOI
41. Zhu Y, Tian D, Yan F. Effectiveness of entropy weight method in decision-making. *Math Problems Eng* 2020;2020:3564835. DOI
42. Nor-Al-Din SM, Razali NK, Sukri NM, Rosli MA. Application of TOPSIS method for decision making in selecting the best new car in Malaysia. *IOP Conf Ser Mater Sci Eng* 2021;1176:012040. DOI
43. Chakraborty S. TOPSIS and modified TOPSIS: a comparative analysis. *Decis Anal J* 2022;2:100021. DOI
44. Siregar VMM, Sonang S, Purba AT, Sugara H, Siagian NF. Implementation of TOPSIS algorithm for selection of prominent student class. *J Phys Conf Ser* 2021;1783:012038. DOI
45. Watrobski J, Baczkiewicz A, Ziemba E, Sałabun W. Sustainable cities and communities assessment using the DARIA-TOPSIS method. *Sustain Cities Soc* 2022;83:103926. DOI

Yuan *et al*. *Complex Eng Syst* 2024;4:10
DOI: 10.20517/ces.2024.13

Complex Engineering Systems

Research Article

Open Access

Health status assessment of unmanned aerial vehicle (UAV) attitude control system based on an improved multivariate state estimation method

Rong Yuan, Shuyi Shao, Mou Chen

College of Automation Engineering, Nanjing University of Aeronautics and Astronautics, Nanjing 211106, Jiangsu, China.

Correspondence to: Prof. Mou Chen, College of Automation Engineering, Nanjing University of Aeronautics and Astronautics, Jiangjun Road No. 29, Nanjing 211106, Jiangsu, China. E-mail: chenmou@nuaa.edu.cn; ORCID: 0000-0001-9458-661X

How to cite this article: Yuan R, Shao S, Chen M. Health status assessment of unmanned aerial vehicle (UAV) attitude control system based on an improved multivariate state estimation method. *Complex Eng Syst* 2024;4:10. http://dx.doi.org/10.20517/ces.2024.13

Received: 16 Mar 2024 **First Decision:** 30 May 2024 **Revised:** 13 Jun 2024 **Accepted:** 19 Jun 2024 **Published:** 28 Jun 2024

Academic Editor: Hamid Reza Karimi **Copy Editor:** Fangling Lan **Production Editor:** Fangling Lan

Abstract

In this paper, a health status assessment scheme is studied for the attitude control system (ACS) of fixed-wing unmanned aerial vehicle (FWUAV) based on an improved multivariate state estimation technology that incorporates a dynamic memory matrix. Firstly, the parameters of the FWUAV representing the health status of the ACS are selected as feature parameters, and the historical health data of the feature parameters for the FWUAV is compared with the real-time test data. At the same time, the multivariate state estimation technology is applied to obtain the abnormal degree of components for the ACS. Based on the analytic hierarchy process and the expert experience, the weights are obtained for the different elements at the same functional level of the ACS. Secondly, the functional structure of the ACS is analyzed, and the abnormal degree is calculated for the ACS by combining the concept of reconfigurability and the weight information of each element, and the health status assessment indicators are further established. The health status result for the ACS of the FWUAV is acquired according to the efficiency value of the indicators and the abnormal degree of the ACS. Finally, the effectiveness of the developed algorithm is verified by the simulation analysis.

Keywords: Fixed-wing unmanned aerial vehicle, health status assessment, health assessment index system, state estimation

© The Author(s) 2023. **Open Access** This article is licensed under a Creative Commons Attribution 4.0 International License (https://creativecommons.org/licenses/by/4.0/), which permits unrestricted use, sharing, adaptation, distribution and reproduction in any medium or format, for any purpose, even commercially, as long as you give appropriate credit to the original author(s) and the source, provide a link to the Creative Commons license, and indicate if changes were made.

1. INTRODUCTION

The health status of the system refers to its ability to maintain normal functions[1], and the health status of the attitude control system (ACS) for the fixed-wing unmanned aerial vehicle (FWUAV) is the ability of the ACS to maintain the stable operation of the FWUAV and achieve the attitude control effect with certain accuracy. As everyone knows that the ACS of FWUAV has a complex structure and is composed of multiple subsystems[2] and components. Once a subsystem or component fails or the status is abnormal, the efficiency or reliability of the entire ACS will decline. Therefore, for the health status management of the ACS for the FWUAV, if the key factors affecting the health status of the system can be extracted from the complex physical structure of the FWUAV, the effective abnormal status information can be quickly screened, and the reasonable decisions can be made using scientific methods, which will be helpful to improve the effectiveness and real-time of the health status management of the ACS for the FWUAV.

The concept of system health management was proposed by the National Aeronautics and Space Administration, which refers to the process, technology and method of preventing or minimizing the impact of system failures during the whole life cycle. The concept of the system health has been closely related to "reliability" since its birth[3], so the assessment of the health status of the FWUAV system is conducive to the prevention of the system failure and improves the reliability of the system. As a key subsystem for the stable operation of the FWUAV, the ACS consists of sensors, actuators and controllers, which coordinate and cooperate to maintain and adjust the attitude of the FWUAV. Its health status plays an important role in the smooth flight of the FWUAV. Due to the complex and uncertain flight environment of the FWUAV[4], the possibility for abnormal ACS of the FWUAV is increased. Its control system plays an important role in flight tasks, and once its health status is abnormal, it will lead to huge losses. Therefore, it is of great significance to evaluate the health status of the FWUAV control system.

At present, the development of health status assessment technology mainly includes three stages. The first stage is mainly the way of human observation in the environment, and the assessment is mainly based on the experience of experts. The assessment results are the product of the simple data processing based on the empirical knowledge[5]. The second stage is mainly based on the vigorous development of the sensing technology, the signal acquisition, the data analysis and the dynamic testing technology and the rise of computer technology; the health assessment technology combined with data processing has been rapidly developed. The third stage is the current development status; that is, the data processing technology[6,7] of the second stage is combined with the intelligent diagnostic technology[8–10] and the cross-integration with multi-disciplines[11]. Based on the above health status assessment technologies, the health status assessment works of the aircraft have been reported in large numbers.

For instance, a machine learning-based battery management system was constructed for the state-of-charge prediction and state-of-health estimation of the UAV[12]. The fault diagnosis method was studied for the actuator damage of the UAV based on the embedded recorded data and stacked machine learning models[13]. An adaptive two-stage unscented Kalman filter algorithm was explored for the actuator health assessment of the quadrotor UAV[14]. A health evaluation method was investigated for the multicopters based on the stochastic hybrid system[15]. The reliable flight performance assessment scheme was designed for the multirotor based on the interaction of the multiple model particle filter and the health degree[16]. The problems of the fault diagnosis and the reconstruction were analyzed for the spacecraft ACS[17]. An efficient nonlinear actuator fault detection and isolation system was designed for the UAV[18]. The flight validation was shown for an embedded structural health monitoring system of the UAV[19]. A supervised learning algorithm was proposed for the spacecraft ACS health monitoring[20]. The battery health management approach was developed for the electric UAV[21]. Although the above studies have proposed many methods for the health management of aircraft, there are few reports on the strategies for the health status assessment of the FWUAV control system using the multivariate state estimation technology (MSET)[22]. As the MSET is an advanced pattern recognition

technology that can complete the status assessment by measuring the similarity between the various monitoring parameters in the normal operating range, the better assessment results can be obtained by applying this technology to the design of the ACS health assessment method [23]. Therefore, the health assessment method for the ACS of the FWUAV based on the dynamic memory matrix MSET is worthy of further research.

With the above analysis as the research motivation, a health status assessment approach is designed based on an improved MSET for the ACS of the FWUAV, and the health status assessment indicators are also built. Finally, the simulation analysis is given to illustrate the effectiveness of the studied approach. The most important contributions in this paper are shown as follows:

(i) A double-K method [the K-means & the K-nearest neighbor (KNN)] is employed to construct the dynamic memory matrix;

(ii) The abnormal degree of components for the ACS of the FWUAV is obtained based on an improved MSET;

(iii) The health assessment index system for the ACS of the FWUAV is constructed by extracting the key measurement parameters.

The rest of this paper is organized as follows. In Section 2, the analysis of the structure composition for the ACS of the FWUAV is described, the component abnormal status assessment method is presented, the health status assessment system for the ACS of the FWUAV is established, and the weights of health assessment indicators are determined. In Section 3, the simulation results are given. Finally, a conclusion is given in Section 4.

2. FWUAV ATTITUDE CONTROL SYSTEM STRUCTURE COMPOSITION AND HEALTH STATUS ASSESSMENT ALGORITHM

2.1 The structure composition of the FWUAV attitude control system

The ACS is very important for the FWUAV, and its health depends on the health of the device groups and components that make up the system. The ACS of the FWUAV mainly comprises the sensors, the onboard controllers, and the servo actuation devices, i.e., the actuators. The role of the sensor is to collect information such as the angular velocity, the attitude, the position, the altitude, the airspeed, *etc*., which is the basis of the ACS, while the role of the controller is to calculate and generate the control instructions by calculating the attitude information obtained from the sensors, outputting control signals to the actuators to maintain the attitude stability performance or to track the desired attitude signals; the role of the actuator is to execute the action according to the instructions of the controller to generate force and torque to act on the airframe, so as to satisfy the health and safety of the FWUAV. The components of a typical FWUAV attitude system and the proposed health status assessment algorithm are shown in Figure 1.

The following is an analysis of the components for the ACS of the FWUAV, and the characteristic parameters are selected based on their functions. Firstly, the sensors mainly include the angle of attack (AOA) sensor and the inertial measurement unit (IMU), which are mainly used to measure the airspeed, the attitude angle, the attitude angle rate, and other information. The output information of the sensors is very important as the feedback information for the attitude control computer to solve its own attitude and output control signals. However, under the unknown disturbances such as the complex electromagnetic environment, the sensor output is prone to noise mixing. Therefore, when the conditions are available, it is necessary to detect the output noise of the sensor to ensure the correctness and reliability of the attitude control closed-loop data. Taking IMU as an example, the current and the output noise during the normal operation should be within the required range and changed smoothly. If there is a large oscillation, even if it is within the normal range, it characterizes that the performance of the device has deteriorated, which will be the cause of FWUAV failure

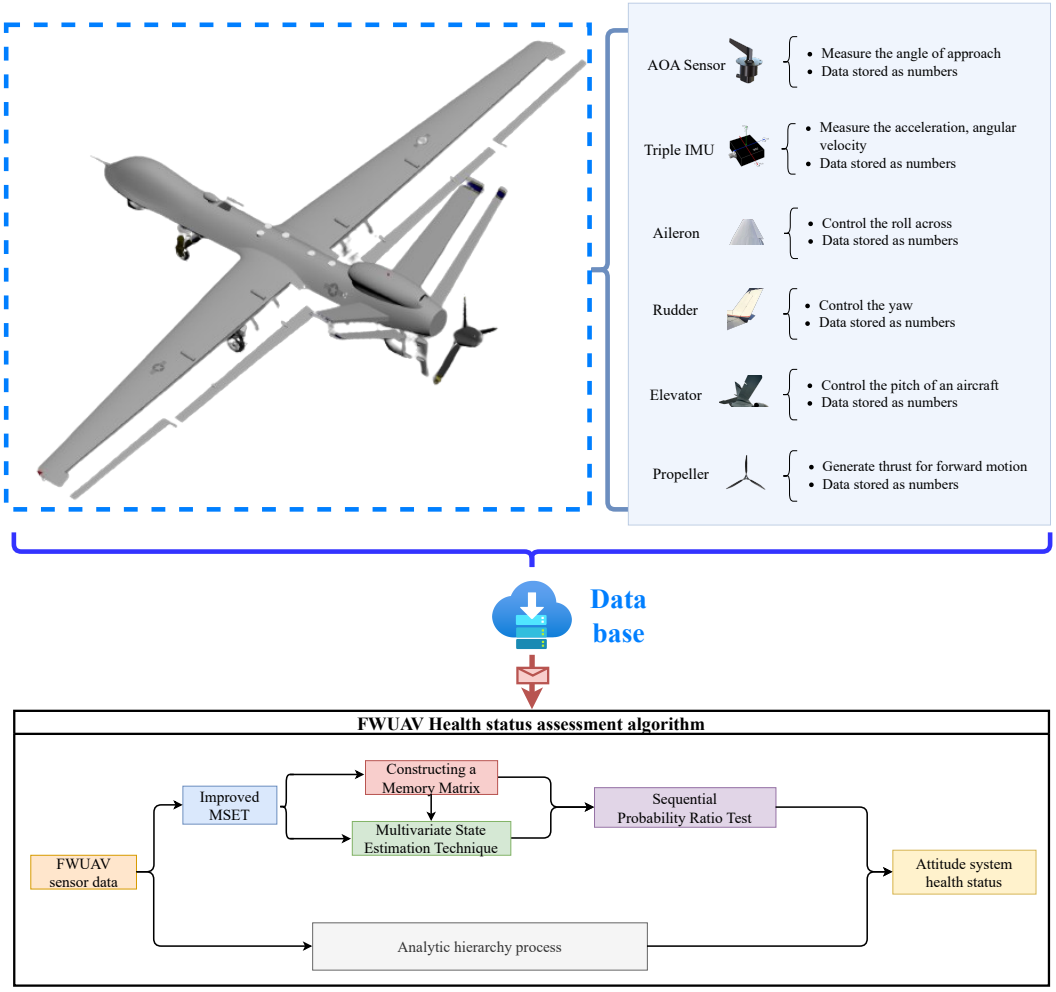


Figure 1. Composition of FWUAV attitude control system.

and should be paid enough attention. Therefore, the characteristic parameters of the IMU are selected as supply voltage and power consumption.

Secondly, the controller for the ACS of the FWUAV is the control computer, which provides the control law in different working modes and working states, and the possible failures are reset or crash, and the backup function for the important parameters such as the attitude control time, the control mode, and the dynamics parameter does not cause major abnormalities in general, but the control computer still has reset and other cases. The characteristic parameter of the controller is selected as the power supply voltage. In the case of normal power supply, the ability of the controller to calculate the control law depends on the soft design such as the control law, so the power supply voltage is selected from the returned data as the characterization parameter to assess whether the controller is working normally.

Thirdly, the actuators mainly include ailerons, elevators, rudders, and propellers, and their main functions are to output the attitude control torque according to the control commands to control the attitude. Most of the actuators are driven by servo motors, so the actuator failures can be caused by the short-circuit or the broken circuit problems, as well as the overheating and software failures due to coupling with other subsystems. Once a failure occurs, the control system will experience a health degradation, which may seriously affect the flight safety of the FWUAV, so the health status of the actuator components needs to be focused on. Therefore, the

power supply voltage, the speed, the current and the temperature of the servo actuator device are selected as the characteristic parameters of the actuators.

2.2 Component abnormal condition assessment

Once the faults occur for the actuators and sensors of the FWUAV, even if the FWUAV has a certain fault tolerance ability, the status of some components will still be different from the usual situations, that is, in an abnormal status. However, the faults of the components do not mean that they are in a normal status. There are many reasons for the abnormal status of the component, such as the environmental changes, the system behavior changes, and the command input errors. To sum up, the abnormal status of components includes the failure of UAV components, but is not limited to the failure situation. Therefore, the analysis for the abnormal status of components comprehensively considers the impact of more aspects, including the failure, and that can reflect the health status of FWUAV in a more comprehensive way.

2.2.1 An improved multivariate state estimation algorithm for the ACS of the FWUAV

First of all, the status observation needs to select the data to characterize the internal characteristics, which are generally reflected directly or indirectly based on the feedback signal data by the sensor of ACS. The status data generated by the normal operation of the system is taken as the historical health data set. By analyzing the relationships between the parameters in historical health data sets, the MSET[24] applies the learned relationships between parameters to the observation of the test data, while using the learned patterns to assess the current status of the current test system data. Although there may be coupling and redundancy among the parameters, each quantity can reflect certain characteristics of the actual physical process. The results of the status estimation are obtained by comparing the patterns in the historical health data with the current test data and weighting the states of each parameter. The weights are determined by applying the learned patterns to the overlapping degree of the historical health data and the current test data of each parameter. To sum up, the MSET has certain learning ability and is a machine learning regression technology with supervision ability. In the field of machine learning, the historical health data is labeled as "normal state" and used as the training data, and the current test data is used as the observation data to be evaluated for obtaining final assessment results, which is the essential feature of supervision ability.

The basic principle of MSET is as follows: Supposing that the n-dimensional measurement data of a part up to time t_m is obtained, and the data is expressed as a matrix form, in which the observation data of characteristic parameters at any time is a column vector, then the $n \times m$ order observation matrix is obtained. For the ACS of the FWUAV, which is shown in Figure 2, where n is the number for the selected characteristic parameters of the ACS sensor ($n = 19$), and m is the number of time points observed.

Taking x_{ji} to denote the observed value of the parameter j at the moment t_i, then the observed value of each feature parameter at the moment t_i constitutes the observation vector $X(t_i) = [x_{1i}, x_{2i}, ..., x_{ni}]^{\mathrm{T}}$, where $n = 19$. In addition to the observation data, it is set that all the historical data under the normal operation of the component for the ACS can be obtained, which is denoted as T and called the training data; i.e., T covers the dynamic range of the feature parameter values during the normal operation of the ACS, but it is not required to obtain all the values of the feature parameters under the normal state of the components for the ACS. A number of typical values of the feature parameters are selected from the training data T, and the resulting matrix is called the memory matrix, denoted as $\aleph$. If the training data that are not selected into the memory matrix, which are called the remaining training data, denoted as L, then $T = \aleph \cup L$. The linear weighting of the data in the memory matrix is used as an estimation of the state of the evaluation object, denoted as X_{est}; i.e., $X_{est} = \aleph \cdot W$, W is a weight vector, and the value is obtained by minimizing the estimation error vector ϵ_X.

Defining the state estimation error as $\varepsilon_X = X_{obs} - X_{est}$, where X_{obs} is the observed value, and the minimization

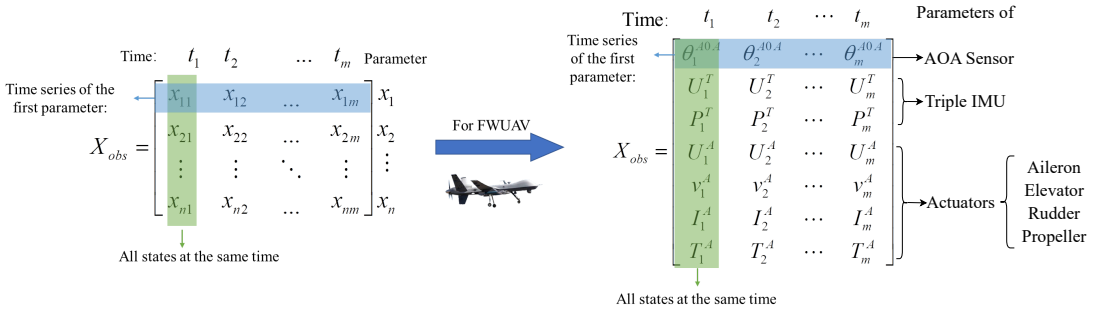


Figure 2. The observation matrix for FWUAV.

of ϵ_X implies the shortest length of the error vector, which can be written as

$$\min_W \|\epsilon_X\| = \min_W \|X_{obs} - X_{est}\| \tag{1}$$

Clearly, (1) is equivalent to[24]:

$$\min_W \{\epsilon_X^{\mathrm{T}} \epsilon_X\} = \min_W \{\{X_{obs} - X_{est}\}^{\mathrm{T}} \{X_{obs} - X_{est}\}\} \tag{2}$$

Because of $X_{est} = \aleph \cdot W$, calculating the derivative of (2) with respect to W and setting it to zero to obtain the minimum value of the squared error, one has

$$\frac{d\{\epsilon_X^{\mathrm{T}} \epsilon_X\}}{dW} = \frac{d\left\{\{X_{obs} - X_{est}\}^{\mathrm{T}} \{X_{obs} - X_{est}\}\right\}}{dW} = 2\aleph^{\mathrm{T}}(\aleph W - X_{obs}) = 0 \tag{3}$$

Then, the weight vector W is obtained by solving (3); we have

$$W = (\aleph^{\mathrm{T}} \cdot \aleph)^{-1} \cdot (\aleph^{\mathrm{T}} \cdot X_{obs}) \tag{4}$$

The state estimation X_{est} can be obtained from the weight vector obtained as follows[24]:

$$X_{est} = \aleph \cdot (\aleph^{\mathrm{T}} \cdot \aleph)^{-1} \cdot (\aleph^{\mathrm{T}} \cdot X_{obs}) \tag{5}$$

Then, the residual of the estimation can be described as

$$R_X = X_{est} - X_{obs} = (\aleph \cdot (\aleph^{\mathrm{T}} \cdot \aleph)^{-1} \cdot \aleph^{\mathrm{T}} - I) \cdot X_{obs} \tag{6}$$

where R_X is the actual residual.

Applying the above estimation procedure to the remaining training data yields the following estimations:

$$L_{est} = \aleph \cdot (\aleph^{\mathrm{T}} \cdot \aleph)^{-1} \cdot (\aleph^{\mathrm{T}} \cdot L) \tag{7}$$

Similarly, the residual of the remaining training data is obtained as

$$R_L = L_{est} - L \tag{8}$$

where R_L is the health residual.

Remark 1: In the estimation of the weight vector, $\aleph^{\mathrm{T}} \cdot \aleph$ is required to be invertible, which is generally difficult to be satisfied in practical applications. For example, when the number of states (columns of $\aleph$) in the memory matrix $\aleph$ is smaller than the number of state parameters (rows of $\aleph$), $\aleph$ is not full rank. To solve the matrix invertibility problem, it is common to use the MSET method with the nonlinear operator "$\otimes$" instead of the vector product "$\cdot$". In practice, the Euclidean distance operator[25] and the Manhattan distance operator[26] are often used as the nonlinear operators, which are defined respectively as

$$x \otimes y = \sqrt{\sum_{m=1}^{k} (x_m - y_m)^2}, x \otimes y = \sum_{m=1}^{k} |x_m - y_m| \tag{9}$$

2.2.2 Dynamic Memory Matrix Construction Algorithm Based on Double-K Algorithm

The construction of the memory matrix is the key to the performance of MSET[24]. The traditional method usually uses a fixed memory matrix, and the construction method is prone to cause information redundancy to reduce the overall computational speed on the one hand, and on the other hand, the estimation accuracy based on a fixed memory matrix may degrade over time because the operating conditions are constantly changing and may require frequent maintenance[27]. Therefore, it is necessary to improve the flexibility of memory matrix construction.

Due to the similarity among many data points in the memory matrix, which are all derived from normal operation of the device, especially with a large sample size, the redundancy within the memory matrix can be significantly reduced by representing one data point as a representative for a cluster of highly similar data. A dynamic memory matrix construction method is designed based on the K-means and KNN algorithms. As two typical clustering methods, the K-means demonstrates the high computational efficiency and the strong adaptability, enabling the partitioning of the dataset into multiple categories based on their attributes[28]. The core of the KNN algorithm is to infer the output based on the characteristics of several known samples that are nearest to the input[29].

In this paper, the K-means algorithm is selected for constructing the initial dynamic memory matrix and the KNN algorithm is utilized for constructing the dynamic memory matrix based on different observations. To construct the initial memory matrix, the m_1 clustering centers in the normalized ACS training matrix are selected as the state vectors to construct the initial memory matrix, where m_1 is not more than 50% of the state vectors of the training matrix. This method is implemented using Euclidean distance and the improved K-means algorithm as given below:

Step 1: The same method of normalization is chosen for all matrices and vectors, which can be expressed as $z_{ij} = \frac{x_{ij} - \mu_i}{\sigma_i}$ and $z_{ij} = \frac{x_{ij} - min_i}{max_i - min_i}$, where x_{ij} is the initial matrix vectors.

Step 2: The m_1 state vectors are randomly selected as clustering centers in the normalized ACS training matrix, $A = \left[A_1, A_2, \cdots, A_{m_1}\right]$.

Step 3: The distance $d\left(X_i, A_j\right)$ between the remaining samples X_i to each cluster center A_j is calculated separately using Euclidean distance and classified into the class corresponding to the cluster center with the smallest distance.

$$d\left(X_i, A_j\right) = \sqrt{\sum_{k=1}^{p} \left(x_{i,k} - A_{j,k}\right)^2}, \quad (i = 1, \cdots, m; j = 1, \cdots, m_1) \tag{10}$$

$$X_i \in \arg\min_{A_j} d\left(X_i, A_j\right) \tag{11}$$

Step 4: For each category A_j, recalculating the cluster center (i.e., the mean value $\mu_j = \left(\mu_{j,1}, \mu_{j,2}, \cdots, \mu_{j,p}\right)^T$ of each feature), finding the Euclidean distance $d\left(X_i, \mu_j\right)$ of the respective state vectors to the cluster center and selecting the closest state vector to the mean value as the new cluster center A'_j. Then, we have

$$\mu_j = \left(\mu_{j,1}, \mu_{j,2}, \cdots, \mu_{j,p}\right)^T = \left(\sum_{i=1}^{k_j} x_{i,1}^j \Big/ k_j, \sum_{i=1}^{k_j} x_{i,2}^j \Big/ k_j, \cdots, \sum_{i=1}^{k_j} x_{i,p}^j \Big/ k_j\right)^T, \quad (j = 1, \cdots, m_1) \tag{12}$$

$$d\left(X_i, \mu_j\right) = \sqrt{\sum_{k=1}^{p} \left(x_{i,k} - \mu_{j,k}\right)^2}, \quad (i = 1, \cdots, m; j = 1, \cdots, m_1) \tag{13}$$

$$A'_j = \arg\min_{X_i} d\left(X_i, \mu_j\right) \tag{14}$$

where k_j denotes the number of state vectors in the j-th cluster, and $x_{i,l}^j$ indicates the l-th characteristic parameter of the i-th state vector in cluster A_j, and $l = 1, \cdots, p$.

Step 5: Repeating steps 3 and 4 until the sum of squares of the errors I_{SSE} in the cluster no longer changes, one has

$$I_{SSE} = \sum_{j=1}^{m_1} \sum_{X_i \in A_j} \left\|X_i, A_j\right\|^2 \tag{15}$$

Step 6: The initial memory matrix $\aleph$ is constructed by taking the final m_1 cluster centers of state vectors.

The initial memory matrix constructed using this method not only has better flexibility, but also helps remove redundant vectors in the matrix by clustering, and it can reduce useless calculations in the traditional MSET [27]. Moreover, to obtain the dynamic memory matrix, the steps for calculating the dynamic memory matrix of the observation process using the KNN algorithm are as follows:

Step 1: The same method of normalization is chosen for all matrices and vectors.

Step 2: For the observation input $X_{obs} = [X_1 \cdots X_m]$, the Euclidean distance $d_i\left(X_{obs_i}, Y_j\right)$ between each of the state vectors X_{obs_i} and each of the state vector Y_j in the training set T is calculated separately, which can be written as

$$d_i\left(X_{obs_i}, Y_j\right) = \sqrt{\sum_{k=1}^{p} \left(x_{obs_{i,k}} - y_{j,k}\right)^2}, \quad (i, j = 1, \cdots, m; k = 1, \cdots, p) \tag{16}$$

where $x_{obs_{i,k}}$ is the k-th characteristic parameter of the i-th state vector in the observation matrix, and $y_{j,k}$ is the k-th characteristic parameter of the j-th state vector in the training matrix.

Step 3: Upon arranging the distance vector $D_i = \left(d_{i,1}, d_{i,2}, \cdots, d_{i,m}\right)^T$, the k samples with the smallest distances are selected from the training set T, thereby identifying the k nearest neighbors denoted as $T_i = \left[Y_{i,1}, Y_{i,2}, \cdots, Y_{i,k}\right]$.

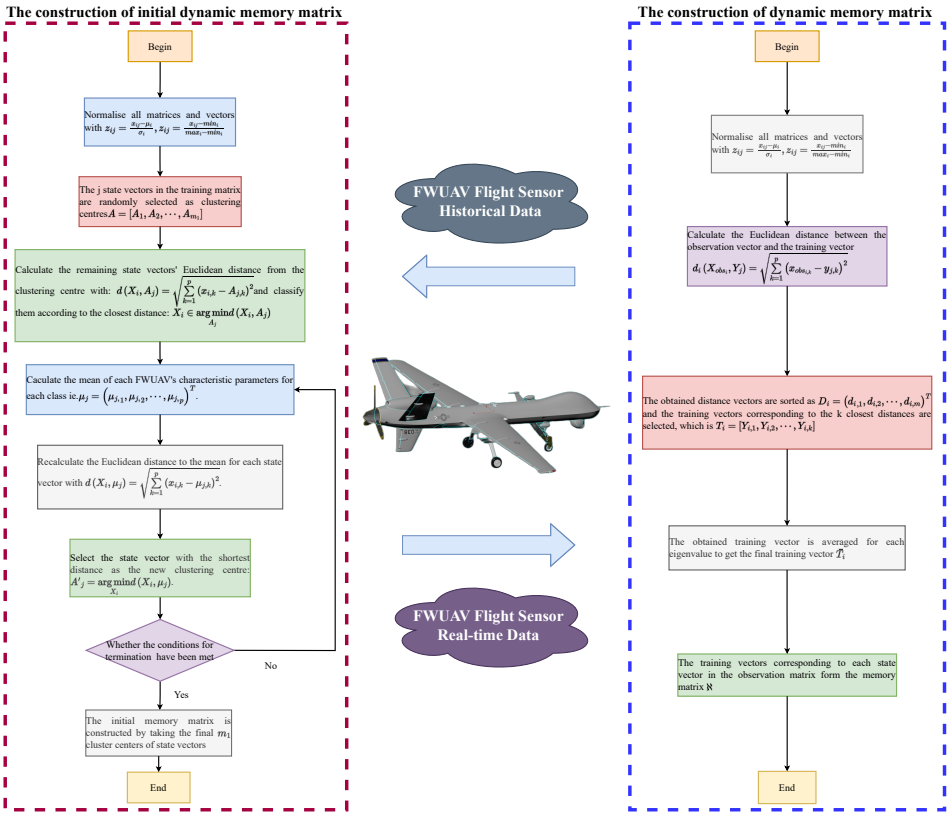


Figure 3. Dynamic memory matrix construction process.

Step 4: For the training matrix constructed to the observation vector X_{obs_i}, the mean value for each characteristic parameter is taken as the corresponding training vector element, and finally, the corresponding training vector $\bar{Y}_i$ will be obtained as follows:

$$\bar{Y}_i=\sum_{j=1}^{k}Y_{i,j}\Big/k=\left[\begin{array}{cccc}\sum\limits_{j=1}^{k}y_{i,j}^{1}\Big/k & \sum\limits_{j=1}^{k}y_{i,j}^{2}\Big/k & \cdots & \sum\limits_{j=1}^{k}y_{i,j}^{p}\Big/k\end{array}\right]^T,\quad (i=1,\cdots,m) \tag{17}$$

Step 5: The matrix consisting of the training vectors corresponding to each observation vector is used as the memory matrix $\aleph$.

According to the analysis above, the double-K algorithm is used to construct the dynamic memory matrix, which plays a pivotal role in minimizing information redundancy within the matrix. This construction process is paramount for optimizing the performance of the algorithm, as it systematically identifies and retains only the most relevant and non-repetitive data points from the input dataset. The resulting dynamic memory matrix serves as a refined representation of the dataset, which can facilitate more precise and efficient computation during the algorithm's execution. The specific construction process can be represented by Figure 3.

2.2.3 MSET based on double-K dynamic memory matrix

Assuming that the object to be evaluated has p feature quantity, the implementation steps of the MSET based on the optimization of the double-K algorithm are as follows:

Step 1: Obtain the training data set and its statistical characteristics. The characteristic parameter data generated under normal working conditions is regarded as health status data, and the health status data of the

ACS is taken as training data T to obtain the statistical characteristics of each characteristic quantity, including the mean value, the standard deviation, the maximum value and the minimum value. The training data T is a matrix containing the state quantity of each characteristic parameter at each moment, and the number of columns for the matrix T is the number of moments K, the number of rows is the number of characteristic parameters p; then, the dimension of the matrix T is $p \times K$ as follows:

$$T = [Y_1 \quad \dots \quad Y_K] = \begin{bmatrix} y_{11} & y_{12} & \cdots & y_{1K} \\ y_{21} & y_{22} & \cdots & y_{2K} \\ \vdots & \vdots & \ddots & \vdots \\ y_{p1} & y_{p2} & \cdots & y_{pK} \end{bmatrix} \tag{18}$$

where $K > 2p + 2$.

In the step of obtaining the mean value, the standard deviation and the maximum and minimum values of the typical statistical characteristics for the assessment object under the health status from the historical health data, the health status does not need to contain all the historical health data, but the selection of health data sets needs to have certain typical significance. Then, the estimation of the mean and standard deviation for the i-th characteristic quantity can be expressed as

$$min_i = \min_{k=1}^{K} (y_{ik}), max_i = \max_{k=1}^{K} (y_{ik}) \tag{19}$$

Remark 2: In practice, the entire historical data of the ACS may not necessarily contain the full dynamic range, so the selection of the training data T needs to be addressed. The selection can consider part of the observation data and the proposed observations generated using these observations as the training data, and the data updating can take a moving window approach; i.e., after each time the observation data are obtained, the last columns of the observation matrix are used as the training data T. This selection of T can help monitor the abnormal trend of the ACS.

Step 2: Obtain the current test data set of the ACS. The data set of the ACS is selected from the test data of the current state characteristics to form the $p \times m$-dimensional observation matrix $X_{obs} = (x_{ij})_{p \times m}$, where p is also the number of characteristic parameters, m denotes the number of time points in the current time period, and the matrix element $x_i j$ stands for the x_{ij} observation of the j-th observed value, and the observation matrix X_{obs} is as follows:

$$X_{obs} = [X_1 \cdots X_m] = \begin{bmatrix} x_{11} & x_{12} & \cdots & x_{1m} \\ x_{21} & x_{22} & \cdots & x_{2m} \\ \vdots & \vdots & \ddots & \vdots \\ x_{p1} & x_{p2} & \cdots & x_{pm} \end{bmatrix} \tag{20}$$

Step 3: Standardization of the historical health data and the test data. Since the characteristic parameters are all FWUAV system parameters, but are of different types and involve diverse aspects of physical concepts, and, thus, have varying scales and levels of quantity. Thus, the training data T and the observation matrix X_{obs} need to be standardized first if the historical health data and test data are to be used to obtain the assessment results. The standardization method can adopt the z-score or min-max standardization formula, and the results of x_{ij} standardizing the observation matrix are $z_{ij} = \frac{x_{ij} - \mu_i}{\sigma_i}$ and $z_{ij} = \frac{x_{ij} - min_i}{max_i - min_i}$, respectively. The obtained normalized observation data is denoted as $Z_{obs} = (Z_1 \cdots, Z_m)^{\mathrm{T}}$. Similarly, the normalized training data set is T', and the same normalization method needs to be used for the training data and the test data; otherwise, it may cause the problem of different data scales.

Step 4: The observation residual estimation method based on MSET is as follows: The dynamic memory matrix $\aleph$ is constructed according to the double-K algorithm, where $\aleph$ is a $p \times M$ matrix; due to the dynamic memory matrix constructed by the double-K algorithm, the number of columns m of the matrix may change during the operation, but it must be guaranteed that $M > 2p + 2$ during the operation. The data from the data matrix T' that is removed from the memory matrix $\aleph$ is called residual data and is denoted by the capital letter L, i.e., $T'_{p\times K} = \aleph_{p\times M} \cup L_{p\times N}$, where $M + N = K$.

Remark 3: The construction of the memory matrix is key to the performance of the algorithm. In order to avoid the overfitting problem, the memory matrix should not have too much data.

In addition, the observation residuals R_x and Z_{est} are calculated. The observation residual estimation R_X is obtained from the observation matrix Z_{obs} and the memory matrix $\aleph$ with:

$$\begin{aligned} Z_{est} &= \aleph \cdot (\aleph^{\mathrm{T}} \cdot \aleph + \alpha I)^{-1} \aleph^{\mathrm{T}} \cdot Z_{obs} \\ R_X &= [\aleph \cdot (\aleph^{\mathrm{T}} \cdot \aleph + \alpha I)^{-1} \aleph^{\mathrm{T}} - I] \cdot Z_{obs} \end{aligned} \tag{21}$$

where $\alpha > 0$ is the constant regularization factor to be selected.

2.2.4 Component anomaly state estimation based on MEST & SPRT

The sequential probability ratio test (SPRT)[30] is a method of measuring the degree of deviation for an observation from the normal state by comparing the probability of the observation occurring in the normal state and the abnormal state with the ratio of the probabilities. The basic principle is as follows: Assuming that $H_0 : \theta = \theta_0$, $H_1 : \theta = \lambda\theta_0 \triangleq \theta_1(\lambda > 1)$, denoting $Y_n = (Y_1, ..., Y_n)$ as the sample data, and taking the likelihood function as $L(Y_n; H_i) = \prod_{i=1}^{n} f(y_i|H_i)$, where $f(y_i|H_i)$ is the density function of the distribution for Y_i. Defining the likelihood ratio as $\Lambda(Y_n) = \frac{L(Y_n;H_1)}{L(Y_n;H_0)}$, the determination of H_0 and H_1 is obtained by comparing $\Lambda(Y_n)$ with an upper limit value $\mathcal{B}$ and a lower limit value $\mathcal{A}$. The decision-making rules are as follows: (i) If $\Lambda(Y_n) \geq \mathcal{B}$, then H_1 is accepted; (ii) If $\Lambda(Y_n) \leq \mathcal{A}$, then H_1 is accepted; (iii) If $\mathcal{A} < \Lambda(Y_n) < \mathcal{B}$, then make no decision, continue with the observation and repeat the above steps. Moreover, the upper limit value $\mathcal{B}$ and lower limit value $\mathcal{A}$ are defined as $\mathcal{A} \approx \frac{\beta}{1-\alpha}$ and $\mathcal{B} \approx \frac{1-\beta}{\alpha}$, respectively, for a given false alarm rate α and missed alarm rate β.

The input data of SPRT-based anomaly detection are health residuals R_L and actual residuals R_x, and the basic idea of the test is to examine whether they come from the same object, if so, the assessment object is in a normal state; otherwise, it is in an abnormal state. The realization process of SPRT is given below for the two cases of normal overall and non-parametric. It should be noted that the following test method is only for one-dimensional scalar; for the detection of multi-dimensional observation vectors, one way is to introduce weight vectors to turn multi-dimensional vectors into one-dimensional vectors, and the other way is to test each feature parameter separately. In the traditional MSET&SPRT method, it is assumed that the residuals follow a normal distribution. The null hypothesis describes the health status of the assessment object, i.e., the mean value is 0 and the standard deviation is σ. And the four following alternative assumptions describe the degradation state of the ACS: (i) the mean value shifts to $+\mathcal{M}$, the standard deviation is σ; (ii) the mean value shifts to -$\mathcal{M}$, the standard deviation is σ; (iii) the mean value is 0, and the standard deviation is $\mathcal{V}\sigma$; (iv) the mean value is 0, and the standard deviation is $\sigma/\mathcal{V}$, where $\mathcal{M}$ and $\mathcal{V}$ are disturbance parameters determined before testing, which need to be analyzed according to the specific system and the behavior. In addition, the mean value of the healthy residuals R_L is first obtained and the null hypothesis is acquired by subtracting the mean value from the healthy residuals R_L before implementing the SPRT; the observation residuals of the observed data are used as inputs, and the mean value of the healthy residuals needed to be subtracted before performing the SPRT test. The SPRT implementation algorithm is as follows:

Step 1: The observation residual R_X is obtained.

Step 2: The health residual R_L is calculated. The estimation matrix of the remaining training data L_{est} and the health residual R_L are obtained from the remaining data L and the memory matrix $\aleph$, the expressions for L_{est} and R_L are

$$\begin{aligned} L_{est} &= \aleph \cdot (\aleph^{\mathrm{T}} \cdot \aleph + \alpha I)^{-1} \aleph^{\mathrm{T}} \cdot L \\ R_L &= [\aleph \cdot (\aleph^{\mathrm{T}} \cdot \aleph + \alpha I)^{-1} \aleph^{\mathrm{T}} - I] \cdot L \end{aligned} \tag{22}$$

Step 3: Calculate the degree of anomaly Θ from the historical health status based on the SPRT. Calculating SPRT as an indicator of an abnormal state, and the $p \times m$-dimensional observation residual matrix and $p \times N$-dimensional health observation residual matrix are written in the following vector form:

$$\begin{aligned} R_X &= [R_{X_1}, R_{X_2}, \cdots, R_{X_m}] \\ R_L &= [R_{L_1}, R_{L_2}, \cdots, R_{L_N}] \end{aligned} \tag{23}$$

Supposing that each column vector of the observation residual matrix R_X and the health residual matrix R_L have the multivariate normal distribution, we have

$$\begin{aligned} R_{x_j} &= [R_{X_{1j}}, R_{X_{2j}}, \cdots, R_{X_{pj}}]^{\mathrm{T}} \sim N_p(\mu, \sum R_{X_j})(j = 1, 2, \cdots, m) \\ R_{L_n} &= [R_{L_{1n}}, R_{L_{2n}}, \cdots, R_{L_{pn}}]^{\mathrm{T}} \sim N_p(\mu, \sum R_{L_n})(n = 1, 2, \cdots, N) \end{aligned} \tag{24}$$

The probability ratio of the R_X to the R_L is taken as the anomaly degree as follows:

$$\Theta = SPR = \frac{\prod_{j=1}^{m} f(R_{X_j}; \mu, \sum R_{x_j})}{\prod_{n=1}^{N} f(R_{L_n,}; \mu, \sum R_{L_n})} \tag{25}$$

where $f(\cdot)$ is the p-dimensional multivariate normal distribution function, representing the probability density of the p-dimensional vector ξ, and its expression can be written as

$$f(\xi) = (2\pi)^{-p/2} \left| \sum \xi \right|^{-1/2} \exp((-\frac{1}{2}(\xi - \mu)^T \sum_{\xi}^{-1} (\xi - \mu)) \tag{26}$$

where μ and $\sum_{\xi}$ are the mean value and the covariance of the distribution for ξ subject to the multivariate normal distribution, respectively.

Step 4: Calculate the component abnormal state index H. The logistic function of the degree of deviation Θ from the normal state of the component is used as the component abnormal state indicator, i.e., $H = \frac{2}{1+e^{\Theta}}$.

2.3 Establishment of a health status assessment system for ACS

2.3.1 Establishment of a set of indicators for assessing the ACS health status

The health status assessment indexes are both the direct parameters for assessing the health status of components and the basic parameters for assessing the overall health status of the ACS. The ACS enables the FWUAV to follow the attitude desired signal, and the dynamic performance, the steady-state performance, and the cumulative effect of time involved in the tracking process, as well as the key measurement parameters of each component for the control system, collectively constitute the set of health assessment indexes for the ACS of the FWUAV. Therefore, the index parameters are chosen in the health status assessment index system as the steady-state tracking error, the overshooting amount, the regulation time and the time error integral related to the attitude angle. Next, the above indicators are explained as follows:

(i) The steady-state error is an important dynamic measure of the accuracy for a system and is usually expected to be zero or not to exceed a certain range. It refers to the deviation from the commanded attitude signal and the actual attitude after the FWUAV has returned to a steady state after perturbations.

(ii) The overshoot is an indicator describing the maximum degree of the deviation for the controlled variable from the steady state, and it is a dynamic indicator reacting to the stability of the transient process. The overshoot is one of the important dynamic indicators of the attitude maneuvering, and the overshooting too much may result in the attitude angle being too large and exceeding the flight envelope, which will affect the flight safety.

(iii) The regulation time mainly measures whether the system can quickly return to a stable state when it is subjected to frequent perturbations, reflecting the rapidity of the system's response. After the system encounters perturbations, a shorter regulation time implies a stronger attitude maneuvering performance, while a longer regulation time implies a poor attitude maneuvering performance.

(iv) The time integral index is the integral of the controlled quantity deviation from the static value along the time axis in the transient process, and the absolute value error e integral is chosen here, and the integral model is $f(e,t) = |e|, J = \int_0^\infty |e|dt$, which is increased by the increase of the error amplitude and the growth of time. The larger the integral value, the control effect will be worse, and the control effectiveness will gradually become weaker with time.

Once the assessment hierarchy of the system has been determined, the data for the indicators to be assessed can be normalized and the weights assigned to the indicators can be determined.

2.3.2 Determination of the weights for the health assessment indicators based on the analytic hierarchy process

Health assessment indicators are juxtaposed, but the importance of each indicator to the ACS of the FWUAV is different, so the establishment of the health assessment indicator methodology actually needs to analyze the importance of each indicator parameter in the indicator set. The determination of indicator weights can enable the health assessment algorithm to effectively capture the important aspects of FWUAV system health. The determination of the weights for the health assessment indicators in this paper will be based on the analytic hierarchy process (AHP) method[31]. The steps of the AHP methodology applied to health status assessment are as follows:

Step 1: Establish a hierarchical model based on the functional structure. A hierarchical structure model is constructed based on the functional components of the assessment system. Taking the ACS of the FWUAV as the top level, and the systematically expanding downward layer by layer according to the functional structure. Then, the complete system hierarchy is obtained and the appropriate assessment indicators are defined for each level.

Step 2: Normalize the indicators based on utility functions. A suitable utility function is selected based on the physical meaning of each indicator to normalize the indicator data. The choice of utility functions should comprehensively consider the impact of the indicator on the system. Additionally, the threshold values for the indicator attributes should be determined in accordance with practical considerations.

Step 3: Construct all judgment matrices for each level. The process of constructing judgment matrices involves applying pairwise comparison methods. The constructed judgment matrices are positive reciprocal matrices. The definition of a judgment matrix B is as follows:

$$B = (c_{ij})_{n\times n} = \begin{bmatrix} C_{11} & C_{12} & \cdots & C_{1n} \\ C_{21} & C_{22} & \cdots & C_{2n} \\ \cdots & \cdots & \cdots & \cdots \\ C_{n1} & C_{n2} & \cdots & C_{nn} \end{bmatrix} \tag{27}$$

where $n = 19$ represents the number of indicators; $C_{ij} = f(x_i, x_j)$ denotes the scale of importance for com-

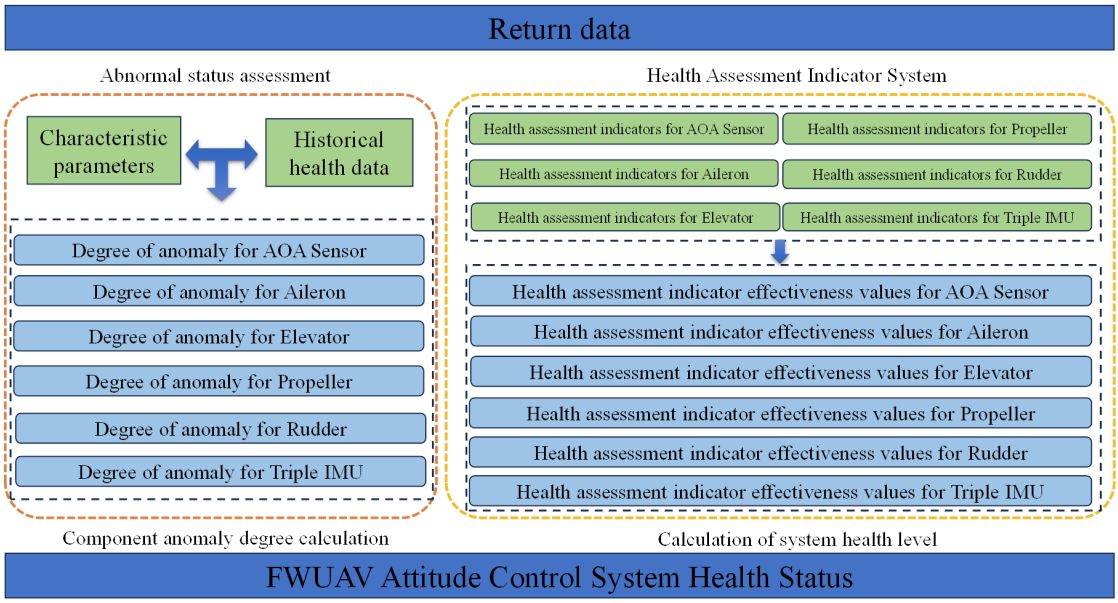


Figure 4. Schematic diagram of attitude control system health assessment for FWUAV.

paring indicators x_i and x_j, when $i = j$, $C_{ij} = 1$; and when $i \neq j$, $C_{ij} = 1/C_{ji}$. The selection of $f(x_i, x_j)$ is determined by the importance level between indicators x_i and x_j.

Step 4: Consistency Check. After constructing judgment matrix B, a consistency check is required to ensure the logical validity of the weight selection. The consistency index (CI) is calculated based on the maximum eigenvalue $\lambda_{\max}$ of the judgment matrix B using $CI = \frac{\lambda_{\max} - n}{n-1}$. Then, the consistency ratio (CR) is calculated using $CR = \frac{CI}{RI}$, where RI is the random index corresponding to the order of the matrix. If $CR < 0.1$, the judgment matrix is considered consistent[32]. If it does not meet this criterion, the matrix needs to be updated to achieve consistency.

Step 5: Perform the assessment based on the weights. The weight vector is calculated for a single layer using the following formula, known as the eigenvector method:

$$\omega_i = \frac{1}{n} \sum_{j=1}^{n} \frac{a_{ij}}{\sum_{k=1}^{n} a_{kj}} \tag{28}$$

where ω_i is the weight parameter and the a_{ij} is element of the eigenvector.

3. SIMULATION ANALYSIS

3.1 The overall flow of the algorithm

The FWUAV health assessment algorithm in this paper is designed in terms of the abnormal degree of deviation for the returned data from the historical health data and the effectiveness of the ACS in accomplishing the FWUAV attitude angle maneuvering task, which not only describes whether the system is functioning properly by combining the actual data of the system components in operation at the detailed level, but also describes the health status of the ACS from the macroscopic perspective for the effectiveness of the ACS. The overall structure of the FWUAV health assessment algorithm that combines the returned data and health assessment indicators is schematically shown in Figure 4.

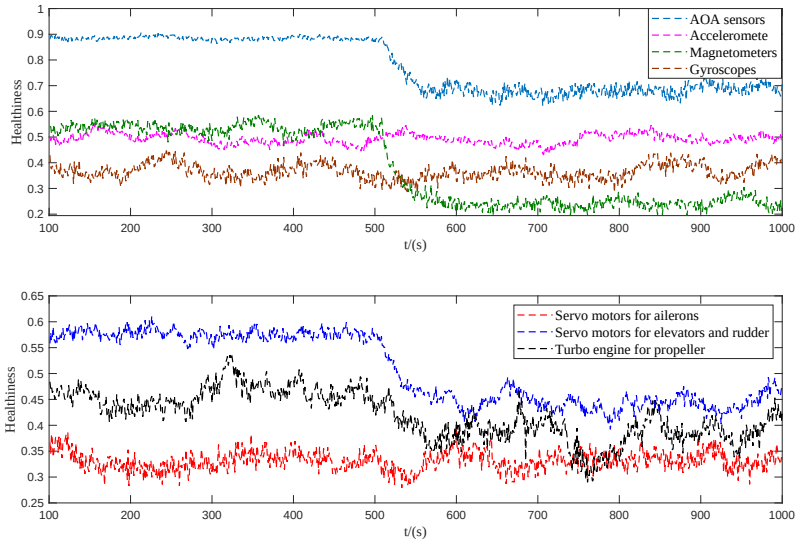


Figure 5. Healthiness of sensor components and actuator components.

3.2 Simulation results

The configuration of the ACS includes an attitude control computer, three magnetometers, three gyroscopes, three accelerometers, two AOA sensors, and actuators including two servo motors for the ailerons, one servo motor for the elevator and rudder, one servo motor for the rudder, and a set of turboprop engines. The experimental data are 1000 sets of return data and 1000 sets of historical health data, mainly including FWUAV attitude system steady-state error, overshoot, integrated time and absolute error (ITAE) and regulation time.

Setting the K value of the KNN algorithm as 6 and the cluster of K-means as $m - 3$, and setting the constant regularization factor of the MSET algorithm as 1, and the weights for the characteristic parameters of the attitude system are set based on the AHP method. Firstly, the weights of the controller, the actuator group and the sensor group are computed as $W_C = 0.1858$, $W_A = 0.6568$ and $W_S = 0.1575$, respectively. The weights of each component of sensors are calculated as $S_1 = 0.6231$, $S_2 = 0.1963$, $S_3 = 0.1638$, and $S_4 = 0.01689$, respectively. The weights of each component of actuators are $A_1 = 0.7903$, $A_2 = 0.1327$, and $A_3 = 0.07692$. The weights of the health assessment indicators are calculated separately as $I_1 = 0.6089$, $I_2 = 0.2274$, $I_3 = 0.1419$, and $I_4 = 0.02178$.

The data deviation from the healthy state is set at 500s and 900s in the test data, where the lowest data health is injected at 500s. Based on the health assessment algorithm proposed in this paper to calculate the health degree, the final results obtained for the health status of the ACS are shown in Figure 4-Figure 8

As shown in Figure 5, the healthiness of the AOA sensors and magnetometers in the sensor components plummeted at the 500th second, corresponding to the unhealthy data injected at that time. Similarly, the healthiness of all components in the actuator dropped significantly at 500 s. In Figure 6, the overall healthiness of both the sensor and actuator groups declined at 500 and 900 s, with the most significant drop occurring at 500 s. This indicates that the injected faults are effectively detected by the algorithm. According to the results in Figure 7, the individual health assessment indicators for various components also showed varying degrees of decline at these times, further validating the sensitivity of the method to detect faults. Figure 8 shows the overall healthiness of the ACS of the FWUAV. The healthiness decreases at the corresponding moments (500 and 900 s), which demonstrates that the assessment algorithm can effectively reflect the health status of the

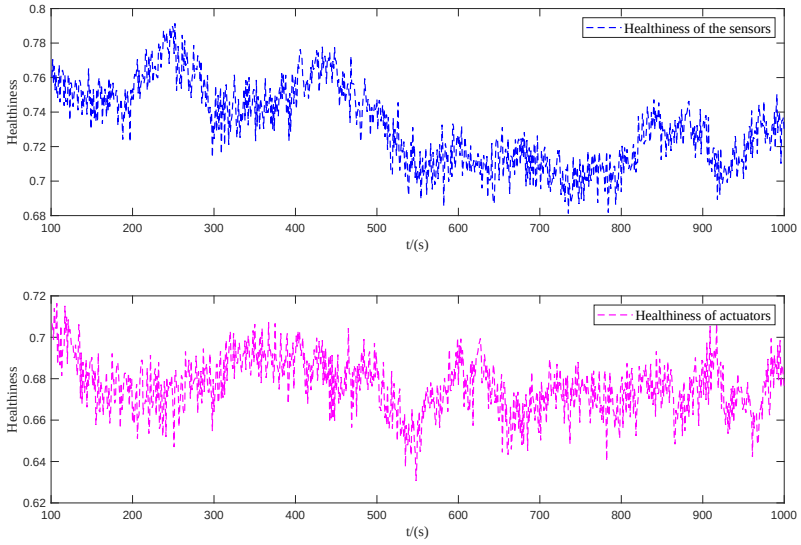


Figure 6. Healthiness of the sensor group and actuator group.

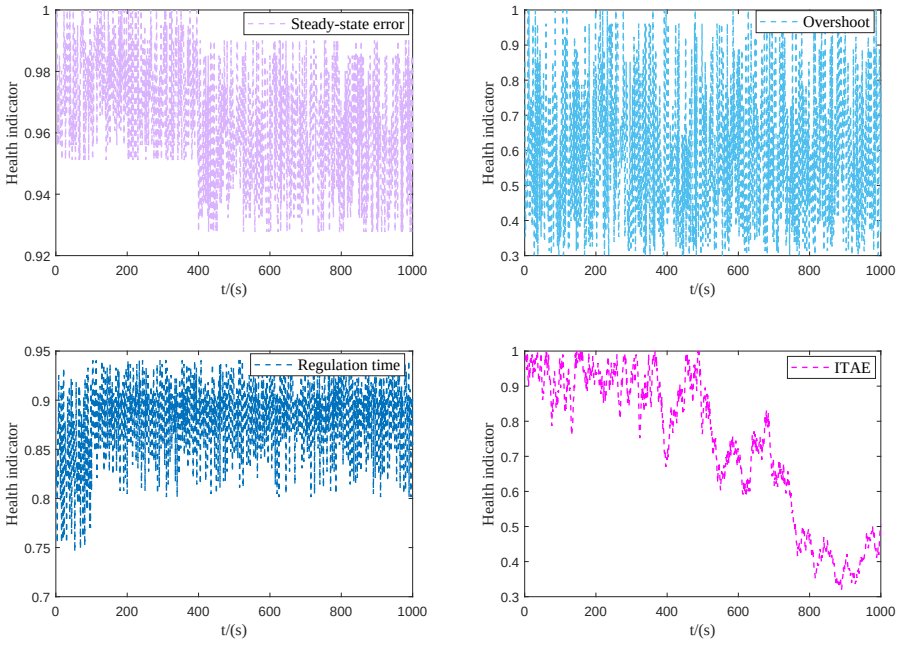


Figure 7. Effectiveness values of health assessment indicators.

ACS. These results illustrate the superiority of the proposed estimation algorithm for detecting and reflecting health status changes in real time, compared to existing methods. The significant drops in healthiness at the times of injected faults demonstrate accuracy and reliability of the algorithm in health assessment.

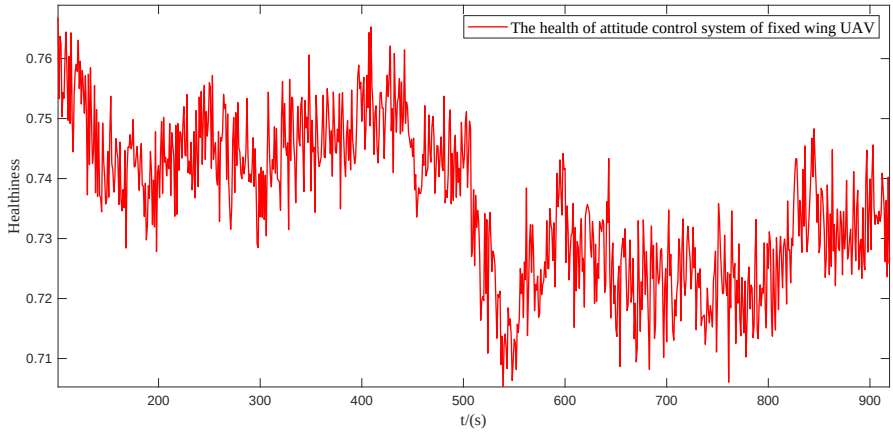


Figure 8. Healthiness of attitude control systems for FWUAVs.

4. CONCLUSIONS

In this paper, an algorithm has been designed for evaluating the health status of the ACS. The parameters that can characterize the health status for the ACS of the FWUAV have been selected as feature parameters, and the state fluctuation characteristics have been obtained. The abnormal degree of the ACS components has been obtained by applying the dynamic memory matrix MSET to calculate the feature parameters. Further, based on the functional structure of the ACS, the abnormal state of the component group and the system can be calculated based on the abnormal state of the component, and the health state indication system of the ACS can be established based on the AHP and SPRT methods, so as to confirm whether the ACS is in a healthy state. Finally, the health status assessment process of the ACS is demonstrated by the simulation analysis to verify the effectiveness of the algorithm.

DECLARATIONS

Authors' contributions

Made significant contributions to the conception, writing and simulation: Yuan R
Made significant contributions to the writing: Shao S
Made substantial contributions to the revision: Chen M

Availability of data and materials

Not applicable.

Financial support and sponsorship

This work was supported by the Science and Technology on Space Intelligent Control Laboratory Foundation (No. HTKJ2023KL502002), the China Postdoctoral Science Foundation (No. 2020M681587), and the Jiangsu Province Postdoctoral Science Foundation (No. 2020Z112).

Conflicts of interest

All authors declared that there are no conflicts of interest.

Ethical approval and consent to participate

Not applicable.

Consent for publication

Not applicable.

Copyright

© The Author(s) 2024.

CITATIONS

REFERENCES

1. Liu D, Peng L, Zhao Z. A review of intelligent methods of health assessment technology.*Intell Robot* 2023;3:355-73. DOI
2. Zhang B, Sun X, Liu S, Lv M, Deng X. Event-triggered adaptive fault-tolerant synchronization tracking control for multiple 6-DOF fixed-wing UAVs. *IEEE Trans Vehi Technol* 2021;71:148-61. DOI
3. Petritoli E, Leccese F, Ciani L. Reliability and maintenance analysis of unmanned aerial vehicles. *Sensors* 2018;18:3171. DOI
4. Zhen Z, Chen Y, Wen L, Han B. An intelligent cooperative mission planning scheme of UAV swarm in uncertain dynamic environment. *Aerosp Sci Technol* 2020;100:105826. DOI
5. Wang C, Lu N, Cheng Y, Jiang B. A telemetry data based diagnostic health monitoring strategy for in-orbit spacecrafts with component degradation. *Adv Mech Eng* 2019;11:1-14. DOI
6. Chen J, Zhao Y, Xue X, Chen R, Wu Y. Data-driven health assessment in a flight control system under uncertain conditions. *Appl Sci* 2021;11:10107. DOI
7. Wang B, Liu D, Peng Y, Peng X. Multivariate regression-based fault detection and recovery of UAV flight data. *IEEE Trans Instrum Meas* 2019;69:3527-37. DOI
8. Li C, Li S, Zhang A, et al. A Siamese hybrid neural network framework for few-shot fault diagnosis of fixed-wing unmanned aerial vehicles. *J Comput Des Eng* 2022;9:1511-24. DOI
9. Garcia DF, Perez AE, Moncayo H, et al. Spacecraft heath monitoring using a biomimetic fault diagnosis scheme. *J Aerosp Inf Syst* 2018;15:396-413. DOI
10. Cui A, Zhang Y, Zhang P, Dong W, Wang C. Intelligent health management of fixed-wing UAVs: a deep-learning-based approach. In: 2020 16th International Conference on Control, Automation, Robotics and Vision (ICARCV); 2020. pp. 1055-60. DOI
11. Guo K, Liu L, Shi S, Liu D, Peng X. UAV sensor fault detection using a classifier without negative samples: a local density regulated optimization algorithm. *Sensors* 2019;19:771. DOI
12. Shibl MM, Ismail LS, Massoud AM. A machine learning-based battery management system for state-of-charge prediction and state-of-health estimation for unmanned aerial vehicles. *J Energy Storage* 2023;66:107380. DOI
13. Al-Haddad LA, Jaber AA, Al-Haddad SA, Al-Muslim YM. Fault diagnosis of actuator damage in UAVs using embedded recorded data and stacked machine learning models. *J Supercomputing* 2023;80:3005-24. DOI
14. Zhang Z, Zhang M, Li G, Qin S, Xu C. ATSUKF-based actuator health assessment method for quad-copter unmanned aerial vehicles. *Drones* 2023;7:12. DOI
15. Zhao Z, Quan Q, Cai KY. A health evaluation method of multicopters modeled by Stochastic Hybrid System. *Aerosp Sci Technolo* 2017;68:149-62. DOI
16. Zhiyao Z, Peng Y, Xiaoyi W, et al. Reliable flight performance assessment of multirotor based on interacting multiple model particle filter and health degree. *Chinese J Aeronaut* 2019;32:444-53. DOI
17. Yang Z, Ma J, Ji R, Yang B, Fan X. IAR-STSCKF-based fault diagnosis and reconstruction for spacecraft attitude control systems. *IEEE Trans Instrum Meas* 2022;71:3526112. DOI
18. Ducard G, Geering HP. Efficient nonlinear actuator fault detection and isolation system for unmanned aerial vehicles. *J Guid Control Dynam* 2008;31:22-37. DOI
19. Kressel I, Dorfman B, Botsev Y, et al. Flight validation of an embedded structural health monitoring system for an unmanned aerial vehicle. *Smart Mater Struct* 2015;24:075022. DOI
20. Nassar B, Hussein W, Medhat M. Supervised learning algorithms for spacecraft attitude determination and control system health monitoring. *IEEE Aerosp Electron Syst Mag* 2017;32:26-39. DOI
21. Sierra G, Orchard M, Goebel K, Kulkarni C. Battery health management for small-size rotary-wing electric unmanned aerial vehicles: an efficient approach for constrained computing platforms. *Reliab Eng Syst Safety* 2019;182:166-78. DOI
22. Zhang W, Liu J, Gao M, Pan C, Huusom JK. A fault early warning method for auxiliary equipment based on multivariate state estimation technique and sliding window similarity. *Comput Ind* 2019;107:67-80. DOI
23. Lopez L. Advanced electronic prognostics through system telemetry and pattern recognition methods. *Microelectron Reliab* 2007;47:1865-73. DOI
24. Wang Z, Liu C. Wind turbine condition monitoring based on a novel multivariate state estimation technique. *Measurement* 2021;168:108388. DOI
25. Liu HC, Liu L, Li P. Failure mode and effects analysis using intuitionistic fuzzy hybrid weighted Euclidean distance operator. *Int J Syst Sci* 2014;45:2012-30. DOI
26. Jiang W, Wang M, Deng X, Gou L. Fault diagnosis based on TOPSIS method with Manhattan distance. *Adv Mech Eng*

2019;11:1687814019833279. DOI
27. Li Y, Dai W, Zhu L, Zhao B. A novel fault early warning method for mechanical equipment based on improved MSET and CCPR. *Measurement* 2023;218:113224. DOI
28. Yu K, Lin TR, Ma H, Li X, Li X. A multi-stage semi-supervised learning approach for intelligent fault diagnosis of rolling bearing using data augmentation and metric learning. *Mech Syst Signal Proces* 2021;146:107043. DOI
29. Wu X, Kumar V, Ross Quinlan J, et al. Top 10 algorithms in data mining. *Knowledge Inf Syst* 2008;14:1-37. DOI
30. Mohammadi M, Kavousi-Fard A, Dabbaghjamanesh M, Farughian A, Khosravi A. Effective management of energy internet in renewable hybrid microgrids: a secured data driven resilient architecture. *IEEE Trans Ind Inform* 2022;18:1896-904. DOI
31. Tavana M, Soltanifar M, Santos-Arteaga FJ. Analytical hierarchy process: revolution and evolution. *An Oper Res* 2023;326:879-907. DOI
32. Chu P, Liu JKH. Note on consistency ratio. *Math Comput Model* 2002;35:1077-80. DOI

Tong *et al. Complex Eng Syst* 2024;4:11
DOI: 10.20517/ces.2024.06

Complex Engineering Systems

Research Article

Open Access

Check for updates

Intensity enhanced for solid-state-LiDAR in simultaneous localization and mapping

Xi Tong, Jiaxing Li, Chunhui Zhao

Northwestern Polytechnical University, Xi'an 710072, Shaanxi, China.

Correspondence to: Prof. Chunhui Zhao, Northwestern Polytechnical University, Youyi West Road 127, Xi'an 710072, Shaanxi, China. E-mail: zhaochunhui@nwpu.edu.cn; ORCID: 0000-0001-8664-9609

How to cite this article: Tong X, Li J, Zhao C. Intensity enhanced for solid-state-LiDAR in simultaneous localization and mapping. *Complex Eng Syst* 2024;4:11. http://dx.doi.org/10.20517/ces.2024.06

Received: 29 Jan 2024 **First Decision:** 28 Apr 2024 **Revised:** 22 May 2024 **Accepted:** 26 Jun 2024 **Published:** 28 Jun 2024

Academic Editors: Hamid Reza Karimi, qiuming Zhu **Copy Editor:** Fangling Lan **Production Editor:** Fangling Lan

Abstract

Solid-state light detection and ranging (LiDAR) has the advantages of low cost, small size and strong practicability. However, it faces challenges in simultaneous localization and mapping applications due to its small field of view and irregular scanning patterns. A solid-state LiDAR simultaneous localization and mapping system containing intensity information is proposed. In order to solve the irregular scanning characteristics of solid-state LiDAR, we introduce a data preprocessing framework and add intensity feature points to the front-end odometer. This improves the accuracy and robustness of positioning when geometric feature points are scarce, thus solving the problem of feature point degradation caused by a finite field of view. In the back-end optimization stage, we combine the geometric feature residuals with the intensity feature residuals through the proposed consistent difference function, so that the system can maintain good performance even in challenging environments. Finally, we conducted an extensive evaluation of the proposed algorithm on official datasets and various datasets collected from multiple platforms, and the results confirmed the validity of our approach. Compared with the corresponding method, in indoor scenes, the absolute trajectory error and relative attitude error are decreased by 54.5% and 5.3%. In outdoor scenes, the absolute trajectory error and relative attitude error are decreased by 29.6% and 58.8%.

Keywords: Solid-state lidar, intensity, localization, optimization

© The Author(s) 2024. **Open Access** This article is licensed under a Creative Commons Attribution 4.0 International License (https://creativecommons.org/licenses/by/4.0/), which permits unrestricted use, sharing, adaptation, distribution and reproduction in any medium or format, for any purpose, even commercially, as long as you give appropriate credit to the original author(s) and the source, provide a link to the Creative Commons license, and indicate if changes were made.

1. INTRODUCTION

Autonomous robotics is a rapidly developing field and has a good application prospect in various fields. Simultaneous localization and mapping (SLAM) is a fundamental aspect of robotics. Visual SLAM[1] solutions rely heavily on external lighting conditions to capture images and estimate the robot's pose by extracting or matching visual features. However, vision-based SLAM systems often fail in low-light or no-light conditions. Lidar, on the other hand, which uses light detection and ranging (LiDAR) technology, is more robust to environmental changes, including weather and lighting conditions. LiDAR-based SLAM[2] can generate accurate maps that can be used directly for robot navigation and obstacle avoidance, making it increasingly popular in the field.

In recent years, solid-state lidar has garnered increasing attention and development. Compared to mechanical lidar, solid-state lidar offers significant advantages in terms of cost, resolution, and performance that cannot be ignored. However, it also faces several challenges, particularly in SLAM applications. Firstly, its scanning method is often irregular, which means that higher demands are placed on data processing. Unlike the regular scanning of mechanical lidar, irregular scanning requires more complex algorithms for point cloud data processing to achieve accurate localization and map construction[3]. Secondly, the field of view of most solid-state lidars is relatively small, which can lead to feature matching degradation. In situations with a limited field of view, there may be insufficient matching, resulting in reduced performance of the SLAM system. Furthermore, during the continuous movement of the lidar, intra-frame motion can cause distortion in the point cloud data. This distortion can potentially affect the accuracy of the SLAM system and, therefore, requires compensatory measures to address the issue, such as motion distortion correction.

To solve all these problems, in this paper, we propose an inertial SLAM method for solid-state LiDAR that includes intensity information. The method enables accurate, robust, real-time positioning and mapping, and can also operate effectively in challenging degraded environments. In summary, our main contributions are as follows: (a) We propose a point cloud preprocessing framework specifically designed for the irregular scanning of solid-state LiDAR. The framework solves the problems of excessive noise caused by irregular scanning and difficulty in extracting geometric feature points; (b) An intensity normalization method suitable for solid-state LiDAR is proposed to facilitate the subsequent use of intensity information; and (c) An odometer and mapping algorithm that includes intensity information as an aid. With more abundant information, the localization accuracy and robustness in the scenario of scarce geometric feature points are improved.

The rest of this article is organized as follows. In Section 2, we discuss the relevant literature. In Section 3, algorithms for solid-state LiDAR - inertial range measurement and mapping are introduced. Section 3.1 describes the point cloud data preprocessing framework. See Section 3.2 for the feature extraction method. State estimates with intensity information are presented in Section 3.3. All experimental studies are discussed in Section 4. Finally, Section 5 summarizes the thesis.

2. RELATED WORKS

Limited computing resources on mobile platforms result in time-consuming processing of large amounts of raw LiDAR data in SLAM systems. As a solution, several LiDAR-based SLAM frameworks have been proposed that utilize feature extraction. A pioneering work in this field is lidar odometry and mapping (LOAM)[4], which extracts geometric edges and surfaces based on the smoothness of raw LiDAR data, and enables real-time odometry and mapping[5] through plane-to-plane and edge-to-line matching. In order to speed up the calculation, lightweight and ground-optimized LOAM (LEGO-LOAM)[6] extracts the ground features by segmental clustering of geometric plane points, and adopts two-stage optimization for attitude estimation. Using lidar alone can lead to motion distortion and low system output frequency issues. Combining IMU (Inertial Measurement Unit) with lidar can effectively address these problems and significantly improve the system's

robustness and accuracy. Unlike the approach of selecting features by sampling uniformity in space, Implicit Moving Least Squares (IMLS)-SLAM[7] employs a unique sampling strategy that considers the contribution of points to the observability of the robot's state. This strategy is designed to ensure both time efficiency and accuracy. On the other hand, Pan *et al.* focuses on extracting various classified geometric features from the scan data and proposes an efficient registration algorithm[8]. This algorithm can perform pose optimization using point-to-point, plane, and line error metrics. IMU typically acquires data at a much higher rate than lidar. Scholars have proposed various methods to handle high-rate IMU measurements. Zhang[4] and Shan[6] employed the IMU to correct the skew in point clouds and initialize motion estimates for LiDAR odometry based on scan matching. The most straightforward approach is to use IMU for state propagation in methods based on Extended Kalman[9,10]. In the field of graph optimization theory, an effective IMU preintegration technique has been introduced[11]. This technique, which uses Euler angles to parameterize rotation errors, aims to prevent redundant integration of IMU measurements. Shen *et al.* derived covariance propagation using continuous-time error state dynamics[12]. Forster *et al.* further enhanced the preintegration theory by incorporating posterior IMU bias corrections[13,14]. Qin *et al.* represents the pioneering tightly-coupled LiDAR-inertial odometry (LIO) approach that calculates the 6 degrees of freedom (6 DOF) ego-motion through iterated Kalman filtering[15]. LIO-Smoothing and Mapping (SAM)[16] introduces a tightly-coupled LiDAR-Inertial SLAM framework that utilizes redundant information from multiple sensors to achieve more accurate and robust positioning and mapping results. The above methods are specially designed for rotating LiDAR. To address the challenges posed by solid-state lidar, such as limited field of view and irregular scanning patterns, Loam-Livox[17] has developed a software package that can be efficiently integrated with the Livox Mid-40 LiDAR. Another approach, FAST-LIO[18], uses a tightly coupled iterative extended Kalman filter to combine LiDAR functionality with IMU data to achieve an efficient and accurate LiDAR inertial odometer. The new version of FAST-LIO 2.0[19] eliminates the need for feature extraction and directly matches the original point cloud to the entire map, enabling powerful and efficient LiDAR localization and mapping using the ikd-Tree toolkit. CamVox[20] uses a dense point cloud to automatically calibrate the Livox Lidar and camera, taking advantage of the features of the non-repeat scan mode. In order to improve the accuracy and computational efficiency, LiLi-OM[21] proposes a keyframe-based LiDAR - Inertial SLAM sliding window optimization method. In solving optimization-based problems, Zhang *et al.* proposes an online method to mitigate degradation by analyzing the geometry of the problem constraints and explaining the impact of environmental degradation on state estimation[22]. In a separate study, Zhao *et al.* analyzed the characteristics of the Livox MID-40 LiDAR, evaluating the intensity distribution of the laser points in the field of view, the accuracy measurement, and the effect of the color of the target surface on the reflection intensity[23]. This analysis inspired the combination of geometry and intensity information, providing additional constraints for state estimation. Using intensity readings from imaging LiDAR, Shan *et al.* obtains intensity images that aid in real-time robust positioning[24]. Finally, Li *et al.* introduces two multiple weighting functions in the optimization process to deal with geometry and intensity factors, which shows strong robustness in degraded environments[25].

In recent years, in addition to extracting geometric features, there has been exploration into semantic-based SLAM[26,27]. These approaches go beyond utilizing just geometric plane and edge features; they also extract semantic information to gain a more comprehensive understanding of the surrounding environment.

3. METHODS

The proposed SLAM framework for solid-state LiDAR is shown in Figure 1. In the figure, red boxes and text mark the main process position of the innovation point in this paper. In order to cope with the challenge of irregular scanning and the need for intensity points in subsequent processing, a feature point extraction algorithm based on intensity and geometric information is proposed. The frame solves the problem of motion distortion by clutter filtering and motion compensation. Firstly, geometric feature points are extracted based on spatial distribution to deal with irregular scanning. In order to ensure the accuracy of extraction, the

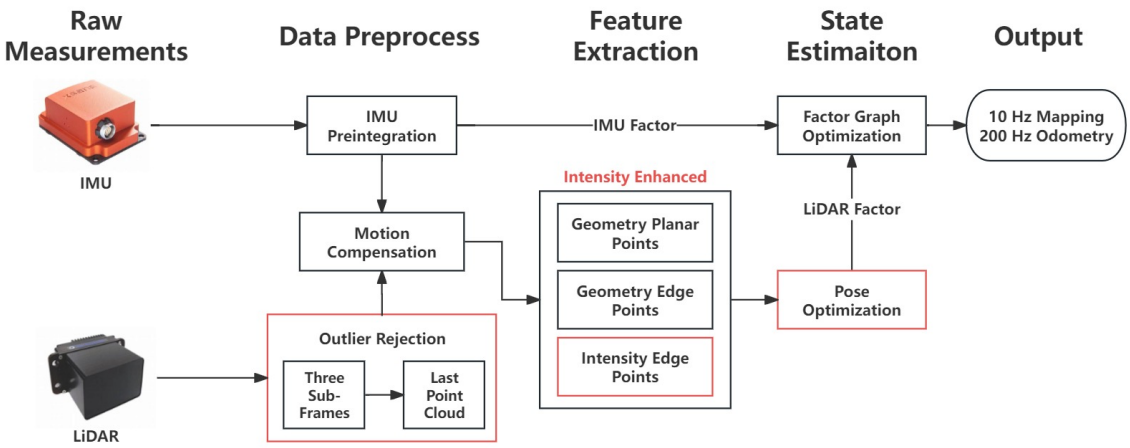


Figure 1. System pipeline of solid-state-LiDAR-inertial SLAM with intensity information assistance.

quadratic plane feature confirmation method is adopted. To solve the problem that the small field of view of solid-state LiDAR leads to the loss of feature points and the degradation of positioning performance, the intensity information is used to extract the intensity feature points. Then, feature point matching is carried out, and a matching algorithm containing intensity information is used to mitigate the wrong plane point matching caused by a limited field of view. Finally, the residual equation is formed by combining the intensity point residual with the original geometric point residual, and the accurate and robust solid-state LiDAR positioning output is obtained.

3.1. LiDAR data preprocess

Generally, in solid-state LiDAR systems, in order to improve the accuracy and robustness of positioning, mapping and closed-loop detection modules, it is necessary to remove outliers such as points near the blind spot of the field of view, points with too high or too low intensity values, horizontal incidence angles, shielding points, and ground points.

Since the point cloud data within a single frame of the Lidar sensor are not generated at the same time, the intra-frame motion distorts the point cloud and causes motion blur, and some outliers appear. The fast elimination of outliers will improve the accuracy of positioning and mapping. In this paper, a piecewise linear method is proposed to divide the data of each frame into three segments in chronological order. The incoming frame is divided into three consecutive subframes, each of which matches independently with the currently constructed map. For each subframe, use the pose of the last point in the subframe to project all points onto the global map. This method reduces the sampling time of each frame to one-third of the original time, speeds up the processing speed, and can effectively compensate for the motion distortion to reduce the motion blur. Segmentation technology can take advantage of the multi-core architecture of the CPU by processing each subframe in parallel in a separate thread. Each subframe matches the global map on a dedicated thread, and once the match is complete, the matched subframe is registered as part of the global map. To speed up the process, a new thread is created to receive the newly registered subframe and a kd tree is constructed to efficiently match the data for the next frame.

For solid-state lidar, due to its unique scanning mode, no beam segmentation, and higher vertical resolution, points in the vertical direction can be considered when calculating curvature. In this paper, a region-based feature point extraction algorithm is proposed to obtain the edge and surface features of point clouds efficiently.

The kth LiDAR input scan frame $\mathcal{P}_i$ maps in two dimensions according to horizontal and vertical resolutions. Given a point in the nth LiDAR input scan frame $P_i = \{x_i, y_i, z_i\} \in \mathcal{P}_i$, the horizontal angle α_i and vertical angle θ_i are formulated as:

$$\alpha_i = \arctan\left(\frac{y_i}{x_i}\right) \tag{1}$$

$$\theta_i = \arctan\left(\frac{z_i}{x_i}\right) \tag{2}$$

Based on horizontal and vertical detection areas, the entire point cloud frame is divided into $M \times N$ rectangular areas. The horizontal region range is $[\alpha_{min}, \alpha_{max}]$, and the vertical region range is $[\theta_{min}, \theta_{max}]$. For a solid-state LiDAR, assuming its horizontal resolution is α_r and vertical resolution is θ_r, the formula for calculating the parameters of the rectangular area is as follows:

$$M = \frac{\alpha_{\max} - \alpha_{\min}}{\alpha_r} \tag{3}$$

$$N = \frac{\theta_{\max} - \theta_{\min}}{\theta_r} \tag{4}$$

3.2. Robust feature extraction

Calculate the curvature after mapping the point cloud to the $M \times N$ rectangular region. The distance difference between the points in the square search area around the current point is calculated to obtain the local smoothness. Taking the current point $P_k^{(m,n)}$ as an example, the calculation formula is as follows:

$$c_k^{(m,n)} = \frac{1}{\lambda} \cdot \sum_{P_k^{(i,j)} \in S_k^{(m,n)}} \left(\left\| P_k^{(i,j)} \right\| - \left\| P_k^{(m,n)} \right\| \right) \tag{5}$$

where $\mathcal{S}_k^{(m,n)} = \left\{ \mathbf{p}_k^{(i,j)} \mid i \in [m-L, m+L], j \in [n-L, n+L] \right\}$, L is predefined square search area side length, and λ is the number of points in that region. $c_k^{(m,n)}$ represents the local smoothness of the point; the larger the value, the steeper the local surface, and the corresponding point is the edge point. Conversely, a lower value indicates that the corresponding point is a plane point.

In order to ensure the accuracy of the selected plane features and edge features, the two-stage geometric distribution verification method is used to determine whether the feature points meet the criteria by relying on the geometric distribution of the point cloud. For the current point, select a certain number of adjacent points, calculate their covariance matrix, and get the eigenvalue. The eigenvalues are arranged in ascending order λ_1, λ_2, and λ_3. If the set of these points satisfies the geometry of the plane, then $\lambda_1/\lambda_2 < \alpha$. If the set of these points satisfies the geometric characteristics of the edge, then $\lambda_2/\lambda_3 < \beta$. In this study, $\alpha$is set to 0.22 and $\beta$is set to 0.2 through experimental testing. Intensity feature extraction needs to use the intensity information of point cloud. Intensity measurements are determined by:

$$I = \frac{P_r}{P_e} = \frac{D_r^2 \rho}{4R^2} \eta_{\text{sys}} \eta_{\text{atm}} \cos\theta = \eta_{\text{all}} \frac{\rho \cos\theta}{R^2} \tag{6}$$

where η_{all} is a constant. Therefore, the surface reflectivity ρ is only related to the incident angle θ and the measurement distance R.

$$\rho \propto \frac{IR^2}{\cos\theta} \tag{7}$$

Before extracting the intensity features, it is necessary to normalize the intensity values of the point cloud to obtain a unified intensity feature, and its distance can be directly calculated to correspond with the intensity

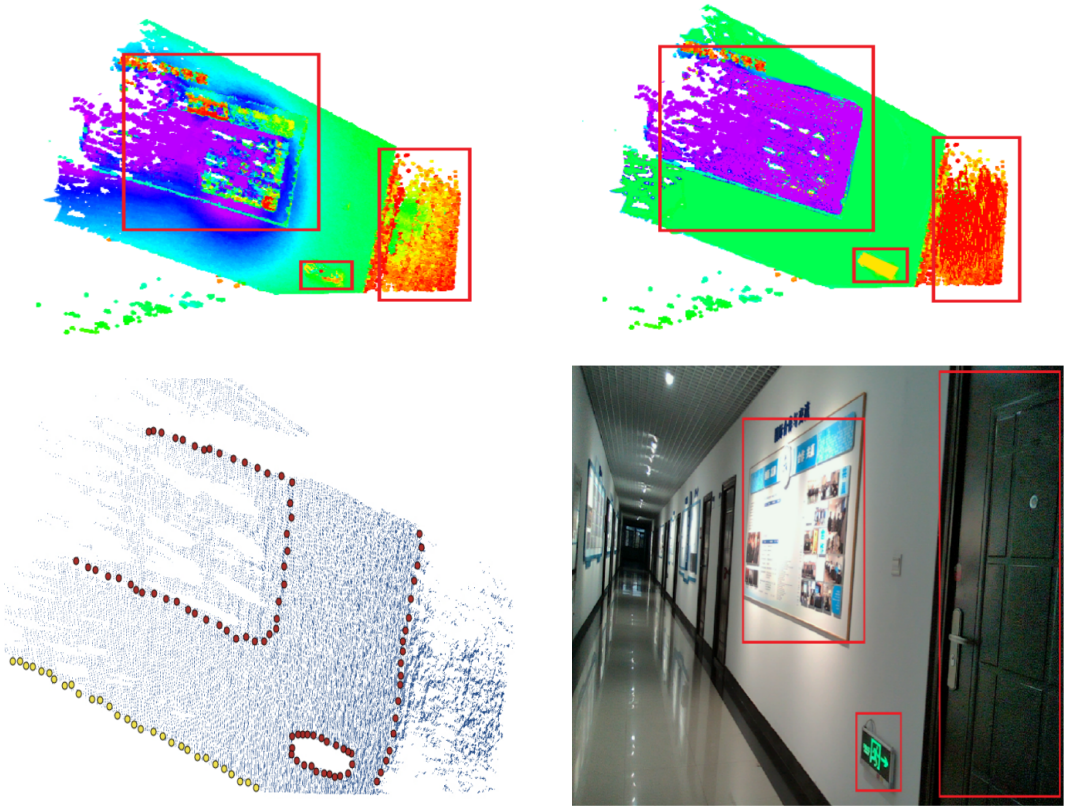


Figure 2. Intensity normalization and feature extraction. The upper left corner is the distribution map before the intensity normalization, the upper right corner is the distribution map after the intensity normalization, the lower left corner is the feature extraction, and the lower right corner is the real scene with a camera.

information. When a point is identified as a plane point by two-stage spatial feature determination, the incidence Angle of the point is calculated according to the normal vector of the point. Select the point P_a farthest from the solid-state laser radar source point from the plane point set, and then find the point P_b farthest from the point P_a. According to the following geometric formula, we can determine the point P_c.

$$\mathbf{p}_c = \underset{\mathbf{p}_i \in \mathbb{P}}{\operatorname{argmax}} \left\| (\mathbf{p}_a - \mathbf{p}_b) \times (\mathbf{p}_a - \mathbf{p}_i) \right\|_2 \tag{8}$$

Planes can be represented by plane equations:

$$\Pi : n_x \cdot x + n_y \cdot y + n_z \cdot z + \bar{d}_i = 0 \tag{9}$$

where n_x, n_y, n_z, and $\bar{d}_i$ are the parameters of the plane, and the calculation formula is as follows:

$$\overline{\mathbf{n}}_i = \left[n_x, n_y, n_z \right]^T = \frac{(\mathbf{p}_a - \mathbf{p}_b) \times (\mathbf{p}_a - \mathbf{p}_c)}{\left\| (\mathbf{p}_a - \mathbf{p}_b) \times (\mathbf{p}_a - \mathbf{p}_c) \right\|_2} \tag{10}$$

$$\bar{d}_i = - \left(n_x \cdot p_x + n_y \cdot p_y + n_z \cdot p_z \right) \tag{11}$$

$$\overline{\mathbf{p}} = \left[p_x, p_y, p_z \right]^T = \frac{1}{m} \sum_{\mathbf{p}_i \in \mathbb{P}} \mathbf{p}_i \tag{12}$$

Where $\overline{\mathbf{n}}_i$ is the unit normal vector of the plane, and $\overline{\mathbf{p}}$ is the center of the plane. The formula for calculating the incident angle of the point is as follows:

$$\cos \theta = \frac{\mathbf{p}^T \cdot \mathbf{n}}{|\mathbf{p}|} \tag{13}$$

In order to avoid redundancy of point selection based on intensity Angle and geometric Angle, only the normalized intensity information of plane points is considered in calculating the incidence Angle. After intensity calibration, the intensity value reflects the reflectivity of the point, indicating its material properties. The point cloud image after intensity processing is shown in Figure 2.

The previous section explains in detail the intensity preprocessing steps and mapping point cloud frames onto a two-dimensional matrix plane. Based on the surface smoothness of the point, the intensity smoothness is introduced as a measure to describe the local intensity distribution of the surface. Taking the current point $P_k^{(m,n)}$ as an example, the intensity smoothness is calculated by:

$$c_{ik}^{(m,n)} = \frac{1}{\lambda} \cdot \sum_{I_k^{(i,j)} \in S_k^{(m,n)}} \left(\left\| I_k^{(i,j)} \right\| - \left\| I_k^{(m,n)} \right\| \right) | \tag{14}$$

The diagram in Figure 2 illustrates the process of feature extraction. Blue denotes geometric plane feature points, yellow represents geometric edge feature points, and red indicates intensity edge feature points.

3.3. State estimation

For geometric feature points, the matching method can be referenced from Li[21]. However, unlike geometric information, intensity information differs in the dimensions and cannot be calculated on the original data, so it needs to be unified under one dimension for fusion. Considering that the range interval of the negative exponential function is 0-1, the consistency difference function which can integrate the intensity information and the geometry information is designed. Under the same geometric consistency, the closer the intensity of two points, the higher their correspondence. The consistency difference function they match is:

$$w_i^o = e^{-\left(d + d^I\right)} \tag{15}$$

$$d = \left| \hat{\mathbf{p}}_k - \mathbf{p}^I \right| \tag{16}$$

$$d^I = \| I - \bar{I} \| \tag{17}$$

The final consistent difference function w_i^o, the geometric consistent difference function d, and the intensity consistent difference function d^I are used in the calculation process of intensity residuals, which is similar to that of geometric residuals. Each plane point in the current frame $\mathbf{p}_k \in P_k$ is mapped to the local coordinate system using:

$$\hat{\mathbf{p}}_k = \mathbf{T}_k \cdot \mathbf{p}_k \tag{18}$$

Where $\hat{\mathbf{p}}_k$ denotes the point mapped to the local map, and $\mathbf{T}_k$ represents the attitude change estimated in the previous frame. For intensity feature points, select the point $\mathbf{p}^I$ that corresponds to the smallest consistency cost function in the intensity local plot for calculating the intensity residual D. The intensity residual $f_I\left(\hat{\mathbf{p}}_k\right)$ is computed using:

$$f_I\left(\hat{\mathbf{p}}_k\right) = \left| \hat{\mathbf{p}}_k - \mathbf{p}^I \right| \tag{19}$$

The final residual equations of the system include geometric edge point residuals $f_{\mathcal{E}}\left(\hat{\mathbf{p}}_i\right)$, geometric planar point residuals $f_{\mathcal{S}}\left(\hat{\mathbf{p}}_i\right)$, and intensity feature point residuals $f_I\left(\hat{\mathbf{p}}_i\right)$:

$$\mathbf{T}^* = \arg\min_{\mathbf{T}^*} \sum_{\mathbf{p}_i \in \mathcal{P}_{\mathcal{E}}} \left| f_{\mathcal{E}}\left(\hat{\mathbf{p}}_i\right) \right| + \sum_{\mathbf{p}_i \in \mathcal{P}_{\mathcal{S}}} \left| f_{\mathcal{S}}\left(\hat{\mathbf{p}}_i\right) \right| + \sum_{\mathbf{p}_i \in \mathcal{P}_I} \left| f_I\left(\hat{\mathbf{p}}_i\right) \right| \tag{20}$$

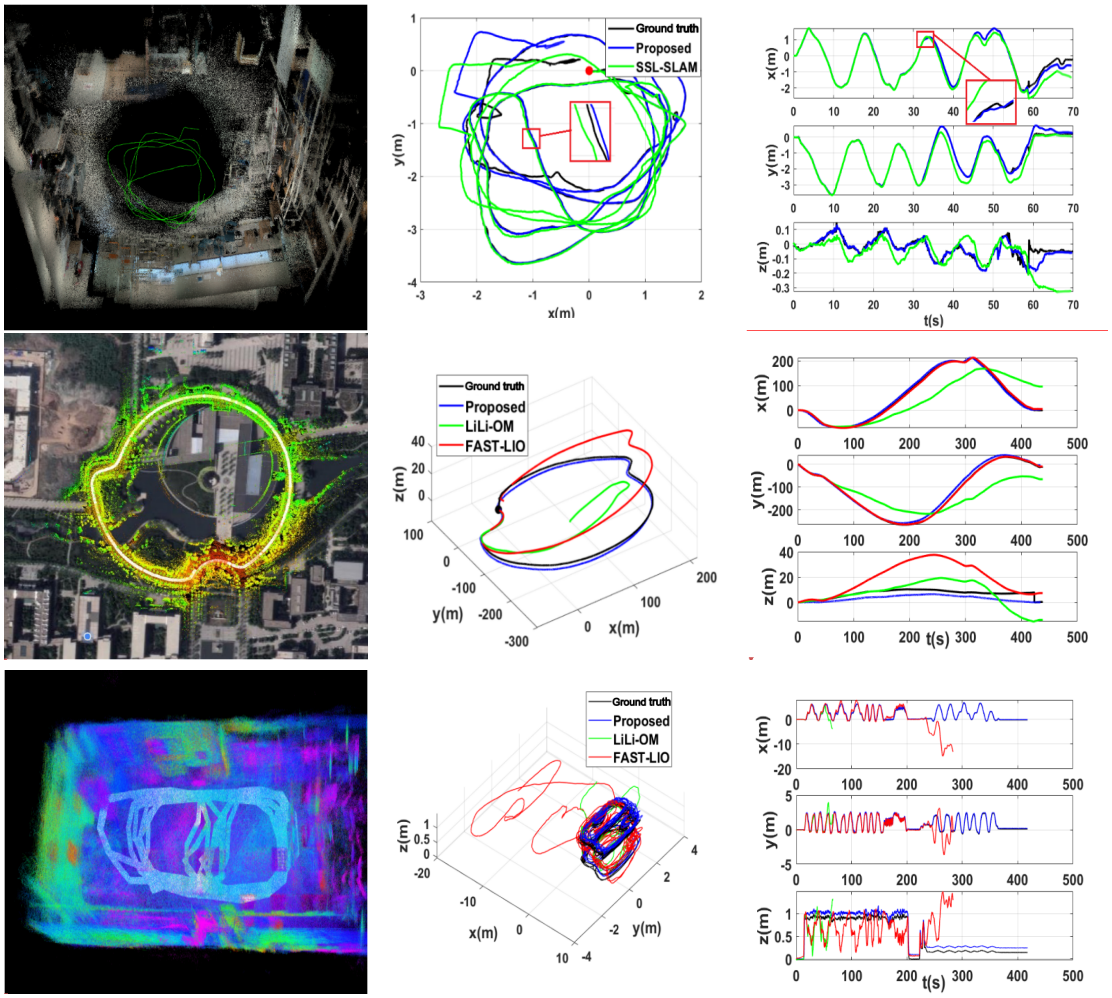


Figure 3. Experimental results. The first column is the localization and mapping performance in Scenes 1,2,3, respectively, from top to bottom. The second column is the trajectory plot in every Scene. The third column is the comparison of three-axis positions in every Scene.

4. RESULTS

In order to validate the accuracy and robustness of the proposed solid-state LiDAR location algorithm, this section conducts an experimental evaluation using both publicly available and customized datasets. The computational cost and evaluation metrics of different algorithms were measured on laptops equipped with AMD 6-core 5800H processors and Nvidia 3050 graphics cards.

To quantitatively evaluate the accuracy of the algorithm, two widely used SLAM evaluation indexes, absolute trajectory error (ATE) and relative attitude error (RPE), are introduced. ATE provides an intuitive representation of overall positioning accuracy, while RPE compares relative attitude increments rather than absolute attitude, providing insight into local accuracy. These two indexes effectively measure the accuracy and robustness of the algorithm.

The selection of parameters is based on a comprehensive understanding of the algorithm and results from experiments across various scenarios. The robustness of the algorithm is verified through systematic experiments in different environmental settings. Additionally, comparative experiments with existing algorithms are conducted to demonstrate the superiority of our method. Same as Zhao [28], we test the proposed method in three scenarios.

Table 1. Experimental error evaluation in Scene 1

Index	SSL_SLAM	Proposed
ATE	0.33 m	0.1 5m
RPE	0.019 m	0.018 m

Table 2. Experimental error evaluation in Scene 2

Index	LiLi-OM	FAST-LIO	Proposed
ATE	49.44 m	10.88 m	7.6 6m
RPE	0.65 m	0.34 m	0.14 m

We selected three scenarios to evaluate our approach. Scenario 1 involved capturing the indoor environment of a warehouse using an automated guided vehicle (AGV) equipped with an Intel-L515 solid-state Lidar. Scenario 2 entailed recording an outdoor environment on a university campus library using an AGV with a Livox-Xsens suite. Scenario 3 depicted a de-escalation scene recorded in an indoor hallway. To showcase the effectiveness of our method, we compared it with several traditional algorithms in LiDAR systems, including Solid-State LiDAR SLAM (SSL-SLAM), LIvox Lidar-inertial Odometry and Mapping (LLI-OM), and Fast LiDAR-inertial Odometry.

In Scene 1, the ground truth is provided by the VICON system. The data set used in the indoor scene is the public data set supporting the SSL-SLAM project. The acquisition device is Intel RealSense l,515 solid-state Lidar, and SSL-SLAM is the only open source algorithm suitable for l,515 solid-state LiDAR. Other algorithms are not applicable, so we only use this algorithm to compare with our method. The algorithm is evaluated against ground truth and SSL-SLAM algorithms to assess the localization results. The experimental findings are presented in Figure 3. It is evident that the SSL-SLAM algorithm exhibits a significant deviation from the actual ground truth at 35 s, whereas the algorithm proposed in this study only deviates during the final turn. Towards the end of the experiment, the robot platform moves backward and then forward. For such short trajectory segments, SSL-SLAM fails to provide accurate localization, whereas our proposed algorithm closely aligns with real-world conditions on the ground. The error comparison of experimental results is detailed in Table 1. It can be observed that our proposed algorithm demonstrates superior accuracy and robustness compared to state-of-the-art algorithms in indoor scenarios. The error level is one order of magnitude lower due to the introduction of the intensity information of the algorithm in this paper. Especially for indoor scenes, due to less interference and more one-dimensional data, the accuracy of regular features will be greatly improved, reflecting the advantages of the algorithm in this paper. The ATE and RPE are decreased by 54.5% and 5.3%.

Scene 2 is an outdoor. Because the data set used in the outdoor scene is Livox solid-state LiDAR, and the SSL-SLAM algorithm is inapplicable, so it is not compared with this algorithm. The Livox-Avia LiDAR is used in sync with the Xsens MTi-G-700 IMU (six-axis, 150 Hz). The ground truth is provided by Real-Time Kinematic (RTK). It can be seen from the result figure that compared with the advanced LiLi-OM and FAST-LIO algorithms, the proposed algorithm has smaller error and higher positioning accuracy and robustness. The error comparison of experimental results is shown in Table 2. It can be seen that in outdoor scenes, compared with LiLi-OM and FAST-LIO algorithms, the proposed algorithm has higher accuracy and robustness. Outdoor scenes are much more complex than indoor ones. In the back-end optimization stage, the geometric and intensity feature residuals are combined to enhance the robustness of the system. The experimental results show the importance of this step for outdoor scenes. The ATE and RPE are decreased by 29.6% and 58.8%.

Scene 3 is a challenging scenario, the actual length is 274 m, and the duration is 417 s. The LiDAR is directed toward the ceiling, where there are hardly any geometric edge points. In this scene, the other two algorithms

Table 3. Experimental error evaluation in Scene 3

Index	LiLi-OM	FAST-LIO	Proposed
ATE	∞	∞	0.23 m
RPE	∞	∞	0.14 m

Table 4. The computational complexity of each method

Index	SSL_SLAM	LiLi-OM	FAST-LIO	Proposed
Scene 1	16%			17%
Scene 2		20%	19%	23%
Scene 3		2.3%	2.1%	21%

have data at the beginning. In the operation process, due to the challenging scene, the positioning failed successively, so there is no data. The results show that the LiLi-OM and FAST-LIO algorithms fail at 65 and 240 s, respectively, due to the lack of geometric feature points on the ceiling. However, the algorithm successfully achieved positioning in 417 s, with an acceptable error range. The error comparison of experimental results is shown in Table 3. In challenging environments, the algorithm manages to keep the error within an acceptable range when the other two algorithms fail. Because the intensity information is added to the algorithm, and the residuals of geometric features and intensity features are fused in the residual part, the proposed method can still obtain a good positioning effect in the degenerate environment with fewer features.

Regarding the complexity of the algorithm, we conducted a comprehensive analysis. All algorithms were tested on a laptop equipped with an AMD 6-core 5800H processor and Nvidia 3050 graphics card. We recorded the percentage of CPU usage of each method at execution time and calculated the average usage to evaluate the computational complexity of each method. The conclusions are shown in Table 4. In Scene 1, only the SSL-SLAM method is available, and it is found that it occupies the same proportion of resources as the proposed method. In Scene 2, the LiLi-OM and FAST-LIO methods and the proposed method can successfully complete all the positioning functions, while the resource proportion of the proposed method is slightly higher because the algorithm complexity of the proposed method is slightly higher and there are too many feature points in the scene which need more computing resource. In Scene 3, both LiLi-OM and FAST-LIO methods failed to complete their tasks and failed to stop after only running for a period of time at the beginning, so the resource proportion is very small. The proposed method also takes up a smaller proportion of resources than that in Scene 2 due to fewer feature points.

Despite the introduction of new computational steps, the overall complexity of our algorithms did not increase significantly due to our skillful optimization of the data processing workflow. In a complex environment, the algorithm has a fast convergence speed. This is due to the introduction of an adaptive feature extraction mechanism in the algorithm, which enables it to better adapt to environmental changes and integrate new observational data faster.

5. CONCLUSIONS

A localization and mapping algorithm for solid-state LiDAR is proposed. To address the problem of irregular scanning modes of solid-state lidar, a geometric feature extraction strategy suitable for solid-state lidar is proposed. To solve the problem of feature point loss and degradation caused by a limited field of view in solid-state lidar location, an intensity normalization method is designed, and an intensity-based feature point extraction and matching algorithm is proposed. In the process of position update, the intensity point residual is introduced and combined with the geometric point residual to form a complete residual equation, which realizes the accurate and robust positioning output of solid-state Lidar. Tests using open source datasets and

self-collected datasets validate the effectiveness and reliability of the algorithm, which is more accurate and robust than the most advanced solid-state LiDAR localization algorithms. Compared with the corresponding method, in indoor scenes, the ATE and RPE are decreased by 54.5% and 5.3%. In outdoor scenes, the ATE and RPE are decreased by 29.6% and 58.8%. The proposed method can be well adapted to indoor and outdoor scenes, but only for relatively stable scenes. In addition, due to the small field of view of solid-state lidar, although the proposed algorithm can have relatively good positioning results, there will be drags during map construction, which will lead to the accumulation of continuous positioning accuracy errors. These are the areas that should be improved in the future.

DECLARATIONS

Acknowledgments
Part of this work was presented at the 3rd ICAUS 2023 (Nanjing China, September 2023, pp.129-139) and all authors agree to submit and publish it in this new article.

Authors' contributions
Contributed to the study conception and design, material preparation, data collection and analysis were performed, commented on previous versions: Tong X, Li J, Zhao C
The first draft of the manuscript was written: Tong X
All authors read and approved the final manuscript.

Availability of data and materials
Not applicable.

Financial support and sponsorship
This work was supported by NSFC No. 62073264.

Conflicts of interest
All authors declared that there are no conflicts of interest.

Ethical approval and consent to participate
Not applicable.

Consent for publication
Not applicable.

Copyright
© The Author(s) 2024.

REFERENCES

1. Taketomi T, Uchiyama H, Ikeda S. Visual SLAM algorithms: a survey from 2010 to 2016. *IPSJ Trans Comput Vis Appl* 2017;9:16. DOI
2. Labbé M, Michaud F. Rtab-Map as an open-source lidar and visual simultaneous localization and mapping library for large-scale and long-term online operation. *J Field Robot* 2018;36:416-46. DOI
3. Jiao J, Zhu Y, Ye H, et al. Greedy-based feature selection for efficient LiDAR SLAM. In: 2021 IEEE International Conference on Robotics and Automation (ICRA); 2021, pp. 5222-8. DOI
4. Zhan J, Sing S. LOAM: lidar odometry and mapping in real-time. In: Robotics: science and system. 2014. Available from: https://api.semanticscholar.org/CorpusID:18612391 [Last accessed on 26 Jun 2024]
5. Lo KL. Linear least-squares optimization for point-to-plane ICP surface registration. 2004. Available from: https://api.semanticscholar.org/CorpusID:122873316 [Last accessed on 26 Jun 2024]
6. Sha T, Englo B. LeGO-LOAM: lightweight and ground-optimized lidar odome-try and mapping on variable terrain. In: 2018 IEEE/RSJ International Conference on Intelligent Robots and Systems (IROS); 2018, pp. 4758-65. DOI

7. Deschau JE. IMLS-SLAM: scan-to-model matching based on 3D data. In: 2018 IEEE International Conference on Robotics and Automation (ICRA); 2018, pp. 2480-5. DOI
8. Pa Y, Xiao P, He Y, Shao Z, Li Z. MULLS: versatile LiDAR SLAM via multi-metric linear least square. In: 2021 IEEE International Conference on Robotics and Automation (ICRA); 2021, pp. 11633-40. DOI
9. Weiss S, Achtelik MW, Lynen S, Chli M, Siegwart R. Real-time onboard visual-inertial state estimation and self-calibration of mavs in unknown environments. In: 2012 IEEE International Conference on Robotics and Automatio; 2012, pp. 957-64. DOI
10. Mouriki AI, Roumelioti SI. A multi-state constraint kalman filter for vision-aided inertial navigation. In: Proceedings 2007 IEEE International Conference on Robotics and Automatio; 2007, pp. 3565-72. DOI
11. Lupto T, Sukkarie S. Visual-inertial-aided navigation for high-dynamic motion in built environments without initial conditions. *IEEE Trans Robot* 2012;28:61-76. DOI
12. Shen S, Michael N, Kumar V. Tightly-coupled monocular visual-inertial fusion for autonomous flight of rotorcraft MAVs. In: 2015 IEEE International Conference on Robotics and Automation (ICRA); 2015, pp. 5303-10 DOI
13. Forster C, Carlone L, Dellaert F, Scaramuzza D. On-manifold preintegration for real-time visual-inertial odometry. *IEEE Trans Robot* 2017;33:1-21. DOI
14. Forster C, Carlone L, Dellaert F, Scaramuzza D. IMU preintegration on manifold for efficient visual-inertial maximum-a-posteriori estimation. 2015. DOI
15. Qin C, Ye H, Pranata CE, Han J, Zhang S, Liu M. LINS: a lidar-inertial state estimator for robust and efficient navigation. In: 2020 IEEE International Conference on Robotics and Automation (ICRA); 2020, pp. 8899-906. DOI
16. Shan T, Englot B, Meyers D, Wang W, Ratti C, Rus D. LIO-SAM: tightly-coupled lidar inertial odometry via smoothing and mapping. In: 2020 IEEE/RSJ International Conference on Intelligent Robots and Systems (IROS); 2020, pp. 5135-42. DOI
17. Lin J, Zhang F. Loam livox: a fas, robus, high-precision lidar odometry and mapping package for lidars of small fov. In: 2020 IEEE International Conference on Robotics and Automation (ICRA); 2020, pp. 3126-31. DOI
18. Xu W, Zhang F. FAST-LIO: a fas, robust lidar-inertial odometry package by tightly-coupled iterated kalman filter. *IEEE Robot Autom Lett* 2021;6:3317-24. DOI
19. Xu W, Cai Y, He D, Lin J, Zhang F. FAST-LIO2:fast direct lidar-inertial odometry. *IEEE Trans Robot* 2022;38:2053-73. DOI
20. Zhu Y, Zheng C, Yuan C, Huang X, Hong X. CamVox: a low-cost and accurate lidar-assisted visual slam system. In: 2021 IEEE International Conference on Robotics and Automation (ICRA); 2021, pp. 5049-55. DOI
21. Li K, Li M, Hanebeck UD. Towards high-performance solid-state-lidar-inertial odometry and mapping. *IEEE Robot Autom Lett* 2021;6:5167-74. DOI
22. Zhang J, Kaess M, Singh S. On degeneracy of optimization-based state estimation problems. In: 2016 IEEE International Conference on Robotics and Automation (ICRA); 2016, pp. 809-16. DOI
23. Zhao Y, Huang K, Lu H, Xiao J. Extrinsic calibration of a small FoV LiDAR and a camera. In: 2020 Chinese Automation Congress (CAC); 2020, pp. 3915-20. DOI
24. Shan T, Englot B, Duarte F, Ratti C, Rus D. Robust place recognition using an imaging lidar. In: 2021 IEEE International Conference on Robotics and Automation (ICRA); 2021, pp. 5469-75. DOI
25. L, H, Tia, B, She, H, L, J. An intensity-augmented LiDAR-inertial SLAM for solid-state LiDARs in degenerated environments. *IEEE Trans Instrum Meas* 2022;71:1-10. DOI
26. Chen X, Milioto A, Palazzolo E, Giguère P, Behley J, Stachniss C. Suma++: efficient LiDAR-based semantic SLAM. In: 2019 IEEE/RSJ International Conference on Intelligent Robots and Systems (IROS); 2019, pp. 4530-4537. DOI
27. Chen G, Wang B, Wang X, Deng H, Wang B, Zhang S. PSF-LO: parameterized semantic features based lidar odometry. In: 2021 IEEE International Conference on Robotics and Automation (ICRA); 2021, pp. 5056-62. DOI
28. Zhao C, Li J, Chen A, Lyu Y, Hua L. Intensity augmented solid-state-LiDAR-inertial SLAM. In: Proceedings of 3rd 2023 International Conference on Autonomous Unmanned Systems (3rd ICAUS 2023); pp. 129-39. Available from: https://link.springer.com/chapter/10.1007/978-981-97-1103-1_12 [Last accessed on 26 Jun 2024]

Li *et al. Complex Eng Syst* 2024;4:12
DOI: 10.20517/ces.2024.14

Complex Engineering Systems

Research Article

Open Access

Synchronization for stochastic switched networks via delay feedback control

Zebin Li[1], Fuying Cheng[2], Juan Tang[3], Hailing Dong[1], Jianliang Tang[1]

[1]School of Mathematical Sciences, Shenzhen University, Shenzhen 518060, Guangdong, China.
[2]Shenzhen Pinghu No. 2 Experimental School, Shenzhen 518100, Guangdong, China.
[3]Pingshan School Affiliated to Sustech, Shenzhen 518118, Guangdong, China.

Correspondence to: Prof. Hailing Dong, Science of Mathematics College, Shenzhen University, 3688 Nanhai Avenue, Nanshan District, Shenzhen 518060, Guangdong, China. E-mail: hailing@szu.edu.cn

How to cite this article: Li Z, Cheng F, Tang J, Dong H, Tang J. Synchronization for stochastic switched networks via delay feedback control. *Complex Eng Syst* 2024;4:12. http://dx.doi.org/10.20517/ces.2024.14

Received: 25 Mar 2024 **First Decision:** 16 May 2024 **Revised:** 28 May 2024 **Accepted:** 18 Jun 2024 **Published:** 28 Jun 2024

Academic Editor: Hamid Reza Karimi **Copy Editor:** Fangling Lan **Production Editor:** Fangling Lan

Abstract

In this paper, asymptotical synchronization in mean square, H_∞-synchronization, and almost sure exponential synchronization are developed for a class of stochastic switched networks with Markov switching and Brown noise using a delay feedback controller that depends on the past state. By utilizing some inequality techniques, Itô formula and Borel-Cantelli Lemma, we show that the stochastic switched network model can achieve asymptotical synchronization in mean square, H_∞-synchronization, and almost sure exponential synchronization when the delay of the control is smaller than a given upper bound. Finally, the effectiveness of the theory is verified by a numerical simulation.

Keywords: Delay feedback control, Markov switching, asymptotical synchronization in mean square, almost sure exponential synchronization, H_∞-synchronization

1. INTRODUCTION

Complex networks are ubiquitous in society and nature because they can abstractly describe almost all actual complex systems, such as the relationship between bacteria and cells, cooperation among academia, intelligent systems, Internet communication, biological engineering, power systems, Brownian motion, and others (see, e.g., [1–3] and reference therein). Therefore, they have become an irreplaceable framework and natural phe-

© The Author(s) 2024. **Open Access** This article is licensed under a Creative Commons Attribution 4.0 International License (https://creativecommons.org/licenses/by/4.0/), which permits unrestricted use, sharing, adaptation, distribution and reproduction in any medium or format, for any purpose, even commercially, as long as you give appropriate credit to the original author(s) and the source, provide a link to the Creative Commons license, and indicate if changes were made.

nomenon in many complex social studies, which provides us with a new perspective and method of complexity research[4,5]. So, the research on complex networks is of great significance.

At present, the research content of complex networks mainly focuses on the following aspects: the formation mechanism of the network, the geometric nature of the network, the nature of the network model, the stability of the network, the synchronization and consistency of the network, and other issues[6–12]. Synchronization is a common collective behavior phenomenon in nature. In recent years, the synchronization theory and application research of complex networks have received extensive attention from domestic and foreign scholars. In terms of application research, synchronization mechanisms are applied to issues such as secure communications, nervous systems, superconducting materials, transportation networks, the Internet, and so on[13–17]. The most common synchronization problems in life are the glow of fireflies, the behavior of fish swimming in the ocean, and the gradual regular applause when the audience applauds. Therefore, the synchronization study of complex networks is of great significance in revealing the universal laws of network dynamics.

In the existing literature, people have studied various synchronization problems of the network model. In most of the literature, a commonly used and taken-for-granted method is to design a controller to synchronize the network. However, a more practical problem is the difference between the time to observe the state and the time to control the system. The time interval is greater than zero, so a more reasonable explanation is to set a controller with a time delay for the system. The paper[18] first proposed feedback control with time delays and applied it in the study of the stabilization of stochastic differential equations (SDEs). As we know, the delay feedback has not been used in the study of the synchronization issue for Markov switched stochastic networks. However, there are a large number of time-delay feedbacks in reality, such as monetary policy in economic systems, control systems in industrial processes, and neural systems in biology. Therefore, we study time-delay feedback control in Markov switching stochastic networks.

In addition, the existing research on Markov switching networks mainly focuses on the exponential mean square synchronization, such as[19]. Although exponential mean square synchronization provides convergence characteristics, it cannot guarantee that every orbit can be synchronized. In contrast, almost sure exponential synchronization has more advantages, because it not only ensures that all orbits are synchronized but also enables the synchronization speed to be faster in comparison. We not only study almost sure exponential synchronization but also investigate asymptotical synchronization in mean square and H_∞-synchronization.

Based on the theory of SDEs, the properties of Markov processes, and the Itô formula by designing a delay feedback controller, the almost sure exponent is established with stochastic synchronization of noisy complex networks. Next, we will introduce the contribution of this article:

1.We design a suitable controller with time delay to achieve almost sure exponential synchronization, asymptotical synchronization in mean square and H_∞-synchronization in the Markov switched stochastic networks, which is more consistent with the actual situation and differs from the previous control strategies.

2.From a practical point of view, almost sure exponential convergence is almost certainly more effective, because it can ensure that each orbit of the stochastic process reaches convergence. The synchronization problem of complex networks with random noise and Markov switching under time-delay feedback control discussed in this paper is an infinite-dimensional problem, which is more difficult than a finite-dimensional problem.

3.Developing almost sure convergence in network synchronization is inherently challenging due to the need for estimating the time tail probability. As far as our current knowledge extends, there has not been any study addressing the almost sure convergence for complex networks involving a controller with time delay in the existing literature.

2.PROBLEM FORMULATION AND PRELIMINARIES

The notion diag $\{p_1, p_2, \cdots, p_n\}$ denotes the diagonal matrix with entries $p_1, p_2, \cdots, p_n$ on the diagonal. I_N stands for the identity matrix with dimension N. 1_n is a n-dimension vector whose entries are 1. The notions $\lambda_{min}(\cdot), \lambda_{max}(\cdot)$ represent the minimum and maximum eigenvalue of a given matrix, respectively. For a vector x, let $x^\top$ denote the transpose vector and $\|x\|$ denote L_2-vector norm. Let $\mathbb{R}$ be the set of real numbers, $\mathbb{N} = \{1, 2, 3, \cdots\}$ be the set of natural numbers, $\mathbb{R}^n$ be the n-dimensional Euclidean space and $\mathbb{R}^{n\times n}$ be the set of all $n \times n$ real matrices. The symbol $\otimes$ denotes the standard Kronecker product.

Let $B_i(t) = [B_1(t), B_2(t), \ldots, B_m(t)]^T$ be an $\mathcal{F}_t$ -adapted Brownian motion and $\{\sigma(t), t \geq 0\}$ be a continuous time Markov process, where the state space of $\sigma(t)$ is $\mathbb{S} = \{1, 2, \cdots, m\}$. The generator $Q = (q_{ij})_{(m\times m)}$ of Markov process is given by

$$\mathrm{P}\{\sigma(t+\Delta t) = \ell \mid \sigma(t) = r\} = \begin{cases} q_{r\ell}\Delta t + o(\Delta t), & \text{if } \ell \neq r\,, \\ 1 + q_{r\ell}\Delta t + o(\Delta t), & \text{if } \ell = r\,, \end{cases}$$

where $\lim_{\Delta t\to 0^+} o(\Delta t)/\Delta t = 0$, $0 \leq q_{r\ell}$, $(\ell \neq r)$, and $q_{\ell\ell} = -\sum_{r=1,r\neq\ell}^{m} q_{r\ell}$.

Assume that $\sigma(\cdot)$ and $B(\cdot)$ are independent of each other. By using a delay pinning feedback controller, we study the Markovian switched stochastic network as follows:

$$dx_i(t) = h(x_i(t), \sigma_t)dt + r(x_i(t), \sigma_t)dB(t) + c\sum_{j=1}^{M} a_{ij}(\sigma_t)x_j(t)dt + u(x_i(t-\tau), \sigma_t)dt, \tag{1}$$

$$u(x_i(t-\tau), \sigma_t) = -\rho d_i(\sigma_t)(x_i(t-\tau) - s(t-\tau)), \tag{2}$$

where $i = 1, 2, 3, \cdots, M, x_i(t) \in \mathbb{R}^n$ represents the state vector of the ith node; $h(x_i(t), \sigma_t)$ and $r(x_i(t), \sigma_t, t)$ are continuous functions, and they separately describe the dynamics and noise intensity. The coupling matrix $A(\sigma_t) = (a_{ij}(\sigma_t))_{N\times N}$ is irreducible, which also satisfies: $a_{ij}(\sigma_t) \geq 0$, $a_{ij}(\sigma_t) = a_{ji}(\sigma_t)$, $i \neq j$ and $a_{ii}(\sigma_t) = -\sum_{j=1,j\neq i}^{M} a_{ij}(\sigma_t)$; where $d_i(\sigma_t) = I_{i\in\mathcal{D}(\sigma_t)}$ is the indication function for the pinned node subset $\mathcal{D}(\sigma_t) \subset \{1, 2, \cdots, N\}$, ρ is the control gain, $u(0, i, t) \equiv 0$. The initial data are $\{x(t) : -\tau \leq t \leq 0\} = \xi \in C([-\tau, 0]; R^n)$ and $\sigma(0) = \sigma_0 \in S$.

Denote $s(t)$ as a desirable state solution that satisfies:

$$ds(t) = H(s(t), \sigma_t)dt + R(s(t), \sigma_t)dB(t), \tag{3}$$

The set $s(t) \times 1_n$ is used as the synchronization manifold. The initial value of $s(t)$ is given by $s(t) = \psi(t) \in C^b_{\mathcal{F}_0}([-\tau, 0], \mathbb{R}^n)$. The error system of this network can be written as follows:

$$de(t) = \hat{H}(e(t), \sigma_t)dt + \hat{R}(e(t), \sigma_t)dB(t) + cA(\sigma_t)e(t)dt - \rho D(\sigma_t)e(t-\tau)dt, \tag{4}$$

where: $e(t) = (e_1^\top(t), \cdots, e_N^\top(t))^\top$, $\hat{H}(e(t), \sigma_t) = H(x(t), \sigma_t) - H(s(t), \sigma_t)$, $\hat{R}(e(t), \sigma_t) = R(x(t), \sigma_t) - R(s(t), \sigma_t)$. $H(x(t), \sigma_t) = (h(x_1(t), \sigma_t), \cdots, h(x_N(t), \sigma_t))^\top$, $R(x(t), \sigma_t) = (r(x_1(t), \sigma_t), \cdots, r(x_N(t), \sigma_t))^\top$, $H(s(t), \sigma_t) = (h(s(t), \sigma_t) \times 1_N)^\top$, $R(s(t), \sigma_t) = (h(s(t), \sigma_t) \times 1_N)^\top$, $D(\sigma_t)$ =diag$[d(\sigma_t), d(\sigma_t), \cdots, d(\sigma_t)]$.

Definition 1.[20] (H_∞-Synchronization) The network (4) achieves H_∞-synchronization, if we have

$$\int_0^\infty E\|e(t)\|^2 dt < \infty.$$

Definition 2.[20] (Synchronization in Mean Square) The solution of the network (4) satisfies

$$\lim_{t\to+\infty} E\|e(t)\|^2 = 0,$$

for $\forall\, \psi(t)$, namely, the network (1) achieves synchronization in mean square.

Definition 3.[16] (Exponential Synchronization) System (1) is said to achieve exponential synchronization, if there exist constants $\varepsilon > 0$ and $G > 0$ such that

$$E\|e(t)\|^2 \leq Ge^{-\varepsilon t}.$$

Definition 4.[16] (Almost Surely Exponentially Synchronization) The solution of the network (1) with the initial has the property that:

$$\limsup_{t\to\infty} \frac{1}{t}\log(\|e(t)\|) < 0, \qquad a.s.$$

That is, the network (1) is almost surely exponentially synchronization.

Definition 5. ($QUAD$ Condition) The function $h(x,\ell)$ is said to satisfy the $QUAD$ condition, denoted as $h(x,\ell) \in QUAD(P_\ell, \Delta_\ell, \varphi_\ell)$, if we can find positive define diagonal matrices P_ℓ and Δ_ℓ, for $\ell = 1, 2, \cdots, m$ and a positive constant φ_ℓ, such that for any $x, y \in \mathbb{R}^n$, the following condition holds:

$$(x-\bar{x})^\top P_\ell[h(x,\ell) - h(\bar{x},\ell) - \Delta_\ell(x-\bar{x})] \leq -\varphi_\ell(x-\bar{x})^\top P_\ell(x-\bar{x}).$$

Assumption 1.[21] If we can find $\eta_\ell > 0$ and $\alpha_\ell > 0$ such that

$$\|h(x,\ell) - h(\bar{x},\ell)\|^2 \leq \eta_\ell(\|x-\bar{x})\|^2),$$
$$\|r(x,\ell) - r(\bar{x},\ell)\|^2 \leq \alpha_\ell(\|x-\bar{x})\|^2).$$

Assumption 2. [9,18] The function $r(x,\ell)$ satisfies the Lipschitz condition and we can find $\omega_l > 0$ such that for $l = 1, 2, \ldots, N$,

$$\text{trace}[r(x,\ell) - r(\bar{x},\ell)]^T[r(x,\ell) - r(\bar{x},\ell)] \leq \omega_\ell(x-\bar{x})^2.$$

Assumption 3. [20] If we can find $\gamma > 0$ such that

$$\|u(x,\ell) - u(\bar{x},\ell)\| \leq \gamma\|x-\bar{x}\|,$$

for all $(x,\ell) \in R^n$ and $t \geq 0$. This assumption, together with $u(0,\ell) \equiv 0$, implies

$$\|u(x,\ell)\| \leq \gamma\|x\|.$$

Assumption 4. [22] If we can find $K > 0$ such that

$$\|h(x,\ell)\| \leq K(1+\|x\|) \; and \; \|r(x,\ell)\| \leq K(1+\|x\|), \tag{5}$$

for all $(x,\ell) \in R^n \times S$.

Assumption 5.[20] If we can choose functions W and Λ, as well as a positive number c and $q \geq 2$, such that

$$|x|^2 \leq W(x,\ell) \leq \Lambda(x) \quad \forall (x,\ell) \in R^n \times S, \tag{6}$$

and

$$\begin{aligned}\mathcal{L}W(x,\ell) :=& W_t(x,\ell) + W_x(x,\ell)u(x,\ell) + \frac{1}{2}trace[R^T(x,\ell)\mathrm{P}(l)r(x,\ell)] + \frac{1}{2}\sum_{l=1}^{m} q_{\sigma_t l}e^T(t)\mathrm{P}(l)e(t)\\ &\leq -c\Lambda(x),\end{aligned} \tag{7}$$

for all $(x,\ell) \in R^n \times S$, $W \in C^{2,1}(R^n \times S; R_+)$, $\Lambda \in C(R^n \times [-\tau, \infty))$.

3 SYNCHRONIZATION ANALYSIS

For studying the problem of the synchronization of the controlled complex network system (4), we define two segments: $\hat{e}_t := e(t+s) : -\tau \le s \le 0$ and $\hat{\sigma}_t := \sigma(t+s) : -\tau \le s \le 0$ for $t \ge 0$. For $\hat{e}_t$ and $\hat{\sigma}_t$ to be well defined for $0 \le t \le \tau$, we set $e(s) = e_0$ and $\sigma_s = \sigma_0$ for $s \in [-\tau, 0)$.

We choose the Lyapunov-Krasovskii function as follows:

$$\begin{aligned} V(\hat{e}_t, \hat{\sigma}_t) =& U(e(t), \sigma_t) + \frac{2\gamma^2}{\beta} \int_{-\tau}^{0} \int_{t+s}^{t} [\tau \|\hat{H}(e(v), \sigma_v) + cA(\sigma_v)e(v) - \rho D(\sigma_v)e(v-\tau)\|^2 \\ &+ \|\hat{R}(e(v), \sigma_v)\|^2] dv ds, \end{aligned} \tag{8}$$

where for $t \ge 0$, $U(e(t), \sigma_t) = \frac{1}{2} e^{\top}(t)\mathbf{P}(\sigma_t)e(t)$, $\mathbf{P}(\sigma_t) = I_N \otimes P(\sigma_t)$.

We claim that $V(\hat{e}_t, \hat{\sigma}_t)$ is an Itô process on $t \ge 0$, In fact, according to the generalized Itô formula [22], we have

$$dV(e(t), \sigma_t) = \mathcal{L}V(e(t), \sigma_t)dt + dM(t). \tag{9}$$

For $t \ge 0$, where $M(t)$ is a martingale, with the initial value is 0, and

$$\mathcal{L}V(\hat{e}_t, \hat{\sigma}_t) = \mathcal{L}U(e(t), \sigma_t) + I(t). \tag{10}$$

where $I(t) = U_x(e(t), \sigma_t)[u(e(t-\tau), \sigma_t) - U(e(t), \sigma_t)] + \frac{2\gamma^2}{\beta}\tau[\tau\|\hat{H}(e(t), \sigma_t) + cA(\sigma_t)e(t) - \rho D(\sigma_t)e(t-\tau)\|^2 + \|\hat{R}(e(t), \sigma_t)\|^2] - \frac{2\gamma^2}{\beta}\int_{t-\tau}^{t}[\tau\|\hat{H}(e(v), \sigma_v) + cA(\sigma_v)e(v) - \rho D(\sigma_v)e(v-\tau)\|^2 + \|\hat{R}(e(v), \sigma_v)\|^2]dv$.

Lemma 1. Under Assumptions (1)-(6), then we have the following inequality:

$$\mathcal{L}U(e(t), \sigma_t) \le \left(-\rho\bar{p}\underline{\lambda} - \lambda_1 + \frac{\bar{p}\omega}{2} + \pi \right) \|e(t)\|^2,$$

where $\lambda_1 = \lambda_{min}[\varphi\mathbf{P}(\sigma_t) - I_N \otimes P(\sigma_t)\Delta]$.

Proof: Step 1, for $u(x, \ell)$, we will let $U_t(x, \ell) = \frac{\partial u(x,\ell)}{\partial t}$,$U_x(x, \ell) = \left(\frac{\partial u(x,\ell)}{\partial x_1}, \cdots, \frac{\partial u(x,\ell)}{\partial x_n} \right)$, and $\mathcal{L}U$:$R^n \times S \longrightarrow R$ is defined by

$$\begin{aligned} \mathcal{L}U(e(t), \sigma_t) =& U_x(e(t), \sigma_t)U(e(t), \sigma_t) + e^{\top}(t)\mathbf{P}(\sigma_t)[\hat{H}(e(t), \sigma_t) + cA(\sigma_t)e(t) - \rho D(\sigma_t)e(t-\tau)] \\ &+ \frac{1}{2} tr[\hat{R}^{\top}(e(t), \sigma_t)\mathbf{P}(\sigma_t)\hat{R}(e(t), \sigma_t)] + \frac{1}{2}\sum_{l=1}^{m} q_{\sigma_t l} e^{T}(t)\mathbf{P}(l)e(t) \\ \triangleq& \mathcal{L}U_1(t) + \mathcal{L}U_2(t) + \mathcal{L}U_3(t) + \mathcal{L}U_4(t). \end{aligned} \tag{11}$$

Step 2, we compute the $\mathcal{L}U_1(t) - \mathcal{L}U_4(t)$ respectively. For the $\mathcal{L}U_1(t)$, $U_x(e(t), \sigma_t) = e^{\top}(t)\mathbf{P}(\sigma_t)$, $U(e(t), \sigma_t) = -\rho D(\sigma_t)e(t)$, we obtain that

$$\mathcal{L}U_1(t) \le -\rho\bar{p}\underline{\lambda}\|e(t)\|^2, \tag{12}$$

where $\bar{p} = \lambda_{max}\{P(\sigma_t)\}$, $\underline{p} = \lambda_{min}\{P(\sigma_t)\}$, $\bar{\lambda} = \lambda_{max}\{D(\sigma_t)\}$, $\underline{\lambda} = \lambda_{min}\{D(\sigma_t)\}$. For the $\mathcal{L}U_2(t)$, one can see

$$\mathcal{L}U_2(t) = e^{\top}(t)\mathbf{P}(\sigma_t)\hat{H}(e(t), \sigma_t) + ce^{\top}(t)(\mathbf{P}(\sigma_t) \otimes A(\sigma_t))e(t) - \rho e^{\top}(t)\mathbf{P}(\sigma_t)D(\sigma_t)e(t-\tau). \tag{13}$$

From the definition of $A(r)$, we know that $\lambda(A(r)) \leq 0$, which yields

$$ce^{\top}(t)(\mathbf{P}(\sigma_t) \otimes A(\sigma_t))e(t) \leq 0. \tag{14}$$

According to Assumption 2, we obtain

$$\begin{aligned} & e^{\top}(t)\mathbf{P}(\sigma_t)\hat{H}(e(t),\sigma_t) - \rho e^{\top}(t)\mathbf{P}(\sigma_t)D(\sigma_t)e(t-\tau) \\ \leq & -\varphi e^{\top}(t)\mathbf{P}(\sigma_t)e(t) + e^{\top}(t)(I_N \otimes P(\sigma_t)\Delta)e(t) \\ \leq & -\lambda_1\|e(t)\|^2, \end{aligned} \tag{15}$$

where $\lambda_1 = \lambda_{min}[\varphi\mathbf{P}(\sigma_t) - I_N \otimes P(\sigma_t)\Delta]$. By substituting (14), (15) into (13), we then obtain

$$\mathcal{L}U_2(t) \leq -\lambda_1\|e(t)\|^2. \tag{16}$$

Furthermore, by Assumption 3, one can see

$$\mathcal{L}U_3(t) \leq \frac{\bar{p}\omega}{2}\|e(t)\|^2 R(x(t),\sigma_t) - R(s(t),\sigma_t), \tag{17}$$

where $\omega = max\{\omega_\ell\}$. Based on the properties of the Markov process, we can obtain

$$\begin{aligned} \mathcal{L}U_4(t) &= \frac{1}{2}\sum_{l=1}^{m} q_{\sigma_t l} e^T(t)\mathbf{P}(l)e(t) \\ &\leq \frac{1}{2}\sum_{l=1,l\neq\sigma_t}^{m} \bar{p}q_{\sigma_t l} e^T(t)e(t) + q_{ll}\underline{p}e^T(t)e(t) \\ &\leq \pi\|e(t)\|^2, \end{aligned} \tag{18}$$

where $\pi = \frac{1}{2}\sum_{l=1,l\neq\sigma_t}^{m} \bar{p}q_{\sigma_t l} + \underline{p}q_{ll}$.

Step 3, substituting (12)-(18) into (11), we can get;

$$\mathcal{L}U(e(t),\sigma_t) \leq -c\|e(t)\|^2, \tag{19}$$

where $c = [\rho\bar{p}\underline{\lambda} + \lambda_1 - \frac{\bar{p}\omega}{2} - \pi]$.

The proof of Lemma 1 is, therefore, completed.

Lemma 2.

Given that Assumptions (5) and (6) hold, the solution of the complex (4) satisfies

$$\sup_{-\tau\leq t<\infty} E\|e(t)\|^q < \infty. \tag{20}$$

Theorem 1. Under Assumptions (1)-(6), if $U_x(e(t),\sigma_t)$ satisfies that $U_x(e(t),\sigma_t) \leq \|e(t)\|^2$, the delay pinning feedback control and $d > 0$, the coupled network (1) can achieve H_∞-synchronization.

Proof: Step 1: According to (19) and (10), one can see that

$$\mathcal{L}V(\hat{e}_t,\hat{\sigma}_t) \leq -c\|e(t)\|^2 + I(t). \tag{21}$$

By Assumption 4, it is easy to see that

$$U_x(e(t),\sigma_t)[u(e(t-\tau),\sigma_t)-u(e(t),\sigma_t)] \le \frac{\beta}{2}U_x(e(t),\sigma_t)^2+\frac{1}{2\beta}|u(e(t-\tau),\sigma_t)-u(e(t),\sigma_t)|^2$$
$$\le \frac{\beta}{2}\|e(t)\|^2+\frac{\gamma^2}{2\beta}\|e(t)-e(t-\tau)\|^2. \tag{22}$$

According to the inequality $(a+b)^2 \le 2(a^2+b^2)$ and Assumption 1,

$$\begin{aligned}
&\frac{2\gamma^2}{\beta}\tau[\tau\|\hat{H}(e(t),\sigma_t)+cA(\sigma_t)e(t)-\rho D(\sigma_t)e(t-\tau)\|^2+\|\hat{R}(e(t),\sigma_t)\|^2]\\
\le&\frac{4\gamma^2\tau^2}{\beta}\|\hat{H}(e(t),\sigma_t)\|^2+\frac{4\gamma^2\tau^2\rho^2\overline{\lambda}^2}{\beta}\|e(t-\tau)\|^2+\frac{2\gamma^2\tau}{\beta}\|\hat{R}(e(t),\sigma_t)\|^2\\
\le&\frac{4\gamma^2\tau^2}{\beta}\|H(x(t),\sigma_t)-H(s(t),\sigma_t)\|^2+\frac{4\gamma^2\tau^2\rho^2\overline{\lambda}^2}{\beta}\|e(t-\tau)\|^2+\frac{2\gamma^2\tau}{\beta}\|R(x(t),\sigma_t)-R(s(t),\sigma_t)\|^2\\
\le&\frac{2\gamma^2}{\beta}(2\tau^2\eta+\tau\alpha)\|e(t)\|^2+\frac{4\gamma^2\tau^2\rho^2\overline{\lambda}^2}{\beta}\|e(t-\tau)\|^2.
\end{aligned} \tag{23}$$

where $\eta=\max\{\eta_1,\eta_2,\cdots,\eta_N\}$, $\alpha=\max\{\alpha_1,\alpha_2,\cdots,\alpha_N\}$,$\ell=1,2,\cdots,N$, η_ℓ and α_ℓ are defined in Assumption 1. Noting $\tau \le \sqrt{\frac{\beta}{16\rho^2\overline{\lambda}^2}}$, we have

$$\frac{4\gamma^2\tau^2\rho^2\overline{\lambda}^2}{\beta^2}\|e(t-\tau)\|^2 \le \frac{8\gamma^2\tau^2\rho^2\overline{\lambda}^2}{\beta^2}\|e(t)\|^2+\frac{8\gamma^2\tau^2\rho^2\overline{\lambda}^2}{\beta^2}\|e(t)-e(t-\tau)\|^2$$
$$\le \frac{8\gamma^2\tau^2\rho^2\overline{\lambda}^2}{\beta^2}\|e(t)\|^2+\frac{\gamma^2}{2\beta}\|e(t)-e(t-\tau)\|^2. \tag{24}$$

Substituting (22), (23), (24) into (21), we can obtain

$$\mathcal{L}V(\hat{e}_t,\hat{\sigma}_t) < -\chi\|e(t)\|^2+\frac{\gamma^2}{\beta}\|e(t)-e(t-\tau)\|^2-\frac{2\gamma^2}{\beta}\int_{t-\tau}^{t}(\tau\|\hat{H}(e(v),\sigma_v)+cA(\sigma_v)e(v)$$
$$-\rho D(\sigma_v)e(v-\tau)\|^2+\|\hat{R}(e(v),\sigma_v)\|^2)dv, \tag{25}$$

where $\chi=[c-\frac{\beta\bar{p}^2}{2}-\frac{8\gamma^2\tau^2\rho^2\overline{\lambda}^2}{\beta^2}-\frac{2\gamma^2}{\beta}(2\tau^2\eta+\tau\alpha)]$.

Follows from the error system (4) that, for $t \ge \tau$

$$\begin{aligned}
&\|e(t)-e(t-\tau)\|^2\\
=&\left\|\int_{t-\tau}^{t}[\hat{H}(e(v),\sigma_v)+cA(\sigma_v)e(v)-\rho D(\sigma_v)e(v-\tau)]dv+\int_{t-\tau}^{t}\hat{R}(e(v),\sigma_v)dB(v)\right\|^2\\
\le&2\int_{t-\tau}^{t}(\tau\|\hat{H}(e(v),\sigma_v)+cA(\sigma_v)e(v)-\rho D(\sigma_v)e(v-\tau)\|^2+\|\hat{R}(e(v),\sigma_v)\|^2)dv.
\end{aligned} \tag{26}$$

Substituting (26) into (25), we can obtain

$$\mathcal{L}V(\hat{e}_t,\hat{\sigma}_t) < -\chi\|e(t)\|^2. \tag{27}$$

Step 2: Using a similar method in Theorems 3 and 4[23], we define the stopping time as follows

$$\zeta_k = inf\{t \ge 0 : \|e(t)\| \ge k\}. \tag{28}$$

According to Lemma 1, $U(e(t), \sigma_t)$ satisfied assumption 6, and $h(x, \ell)$ satisfied assumption 5; by lemma 2, ζ_k is increasing to infinity almost surely as $k \to \infty$. Where $t \geq 0$, $H \in C^{2,1}(R^n \times S; R_+)$.
Then, we can obtain

$$EV(\hat{e}_{t\wedge\zeta_k}, \hat{\sigma}_{t\wedge\zeta_k}) \leq V(\hat{e}_0, \hat{\sigma}_0) + E\int_0^{t\wedge\zeta_k} \mathcal{L}V(\hat{e}_s, \hat{\sigma}_s)ds. \tag{29}$$

for any $t \geq 0$ and $k \geq k_0$, we can let $k \to \infty$ and then apply the Fubini theorem to get

$$EV(\hat{e}_t, \hat{\sigma}_t) \leq V(\hat{e}_0, \hat{\sigma}_0) + \int_0^t E\mathcal{L}V(\hat{e}_s, \hat{\sigma}_s)ds, \tag{30}$$

for any $t \geq 0$, substituting (27) into (30), we obtain

$$EV(\hat{e}_t, \hat{\sigma}_t) \leq V(\hat{e}_0, \hat{\sigma}_0) - \chi\int_0^t E\|e(s)\|^2 ds. \tag{31}$$

We can get from (31)

$$\chi\int_0^t E\|e(s)\|^2 ds \leq V(\hat{e}_0, \hat{\sigma}_0). \tag{32}$$

Step 3: Noting that $\chi > 0$, we see from the above inequality that

$$\int_0^t E\|e(s)\|^2 ds \leq \frac{V(\hat{e}_0, \hat{\sigma}_0)}{\chi}. \tag{33}$$

Letting $t \to \infty$, we obtain that

$$\int_0^\infty E\|e(s)\|^2 ds < +\infty. \tag{34}$$

The proof is, therefore, complete.

Theorem 2. Under Assumptions (1)-(6), the solution of the controlled network (4) for any given initial data, the controlled system (1) is asymptotical synchronization in mean square.

Proof: For any $0 \leq t_1 < t_2 < \infty$, according to Assumptions 4 and 5, we can apply the Itô formula to show

$$\begin{aligned}
&|E\|e(t_2)\|^2 - E\|e(t_1)\|^2| \\
\leq &\int_{t_1}^{t_2} 2K \sup_{-\tau\leq t<\infty} E\|e(t)\| + 2K \sup_{-\tau\leq t<\infty} E\|e(t)\|^2 + 2\gamma \sup_{-\tau\leq t<\infty} E\|e(t)\|\|e(t-\tau)\| + K^2 \sup_{-\tau\leq t<\infty} (1 + \|e(t)\|)^2 \\
\leq &\Theta(t_2 - t_1),
\end{aligned} \tag{35}$$

where Θ is a constant independent of t_1 and t_2. That is, $\lim_{t\to+\infty} E\|e(t)\|^2 = 0$.

Lemma 3.(Hanalay inequality) Let w(t) be a nonnegative function defined on the interval $[t_0 - \tau, \infty)$, and be continuous on the subinterval $[t_0, \infty)$. If there exist two positive constants a, b satisfying $a > b$, such that:

$$\dot{w(t)} \leq -aw(t) + bw(t-\tau), \qquad t \geq t_0,$$

then $w(t) \leq w_{t_0}e^{-\gamma(t-t_0)}$, $t \geq t_0$, there $w_{t_0} = \sup_{t_0-\tau\leq t\leq t_0} w(t)$. $\gamma > 0$ is the smallest real root of the equation $a - \gamma - be^{\gamma\tau} = 0$.

Theorem 3. Under Assumptions (1)-(6), and the delay feedback pinning control given by (2). $\varepsilon\tau \leq \frac{1}{2}$ exists; the coupled network (1) can achieve exponential synchronization.

Proof: We choose Lyapunov function $V(\hat{e}_t, \hat{\sigma}_t)$ as defined by (8). Similar to the proof in Step 2 of Theorem 1 and according to the formula (30), we can show that

$$e^{\varepsilon t}EV(\hat{e}_t, \hat{\sigma}_t) \leq V(\hat{e}_0, \hat{\sigma}_0) + \int_0^t e^{\varepsilon s}E\Big(\varepsilon V(\hat{e}_s, \hat{\sigma}_s) + \mathcal{L}V(\hat{e}_s, \hat{\sigma}_s)\Big)ds. \tag{36}$$

Let $h_1 = \min_{\ell\in S} \underline{p}_\ell$, $h_2 = \max_{\ell\in S} \bar{p}_\ell$. From (8), we can get

$$V(\hat{e}_s, \hat{\sigma}_s) \leq \frac{h_2}{2}\|e(s)\|^2 + J_1, \tag{37}$$

where

$$J_1 = \frac{2\gamma^2}{\beta}\int_{-\tau}^{0}\int_{t+s}^{t}[\tau\|\hat{H}(e(v), \sigma_v) + cA(\sigma_v)e(v) - \rho D(\sigma_v)e(v-\tau)\|^2 + \|\hat{R}(e(v), \sigma_v)\|^2]dvds.$$

Similar to what we did in Theorem 1, we can show that:

$$\mathcal{L}V(\hat{e}_s, \hat{\sigma}_s) \leq -\Phi\|e(s)\|^2 + \frac{\gamma^2}{2\beta}\|e(s) - e(s-\tau)\|^2 + \frac{4\gamma^2\tau^2\rho^2\overline{\lambda}^2}{\beta^2}\|e(s-\tau)\|^2 - J_2, \tag{38}$$

where: $J_2 = \frac{2\gamma^2}{\beta}\int_{s-\tau}^{s}(\tau\|\hat{H}(e(v), \sigma_v) + cA(\sigma_v)e(v) - \rho D(\sigma_v)e(v-\tau)\|^2 + \|\hat{R}(e(v), \sigma_v)\|^2)dv$,$\Phi = [c - \frac{\beta\bar{p}^2}{2} - \frac{2\gamma^2}{\beta}(2\tau^2\eta + \tau\alpha)]$. For all $t \geq 0$, where ε is a sufficiently small positive number to be determined later. Substituting (37) and (38) into (36), then we have

$$\begin{aligned}
e^{\varepsilon t}\frac{h_1}{2}E(\|e(t)\|^2) \leq\ & V(\hat{e}_0, \hat{\sigma}_0) + \int_0^t e^{\varepsilon s}E\Big(\varepsilon\frac{h_2}{2}\|e(s)\|^2 + \varepsilon J_1 - \Phi\|e(s)\|^2 + \frac{\gamma^2}{2\beta}\|e(s) - e(s-\tau)\|^2 \\
&+ \frac{4\gamma^2\tau^2\rho^2\overline{\lambda}^2}{\beta^2}\|e(s-\tau)\|^2 - J_2\Big)ds \\
\leq\ & V(\hat{e}_0, \hat{\sigma}_0) + \int_0^t e^{\varepsilon s}E\Big((\varepsilon\frac{h_2}{2} - \Phi)\|e(s)\|^2 + \frac{\gamma^2}{2\beta}\|e(s) - e(s-\tau)\|^2 \\
&+ \frac{4\gamma^2\tau^2\rho^2\overline{\lambda}^2}{\beta^2}\|e(s-\tau)\|^2 + \varepsilon J_1 - J_2\Big)ds.
\end{aligned} \tag{39}$$

Making use of (26), we can see:

$$\frac{\gamma^2}{2\beta}\|e(s) - e(s-\tau)\|^2 \leq \frac{1}{2}J_2. \tag{40}$$

According to the definitions of J_1 and J_2, we can get

$$J_1 \leq \tau J_2. \tag{41}$$

Substituting (41) and (40) into (39), we can get

$$\begin{aligned}
e^{\varepsilon t}\frac{h_1}{2}E(\|e(t)\|^2) \leq & V(\hat{e}_0, \hat{\sigma}_0) - (\Phi - \frac{\varepsilon h_2}{2})\int_0^t e^{\varepsilon s}E(\|e(s)\|^2)ds + \frac{4\gamma^2\tau^2\rho^2\overline{\lambda}^2}{\beta^2}\int_0^t e^{\varepsilon s}E(\|e(s-\tau)\|^2)ds \\
&+ (\varepsilon\tau - \frac{1}{2})\int_0^t e^{\varepsilon s}E(J_2)ds.
\end{aligned} \tag{42}$$

We can choose a sufficiently small $\varepsilon > 0$, such that:

$$\varepsilon\tau \le \frac{1}{2} \quad , \quad \Phi - \frac{\varepsilon h_2}{2} > \frac{4\gamma^2\tau^2\rho^2\overline{\lambda}^2}{\beta^2}.$$

According to Lemma 3, we can then easily show that

$$E(\|e(t)\|^2) \le Ge^{-\varepsilon t}. \tag{43}$$

Where: $G = \frac{2}{h_1}\left(V(\hat{e}_0, \hat{\sigma}_0) + \sup_{-\varepsilon\le s\le 0} E\|e(s)\|^2\right)$.

The proof is complete.

Theorem 4. Under the same condition of Theorem 3, the network (1) is almost surely exponentially synchronization.

Proof: Let k be any nonnegative integer. According to Assumption 1, the Hölder inequality and the Doob martingale inequality, we can obtain that

$$E\left(\sup_{k\le t\le k+1}\|e(t)\|^2\right) \le 3E\|e(k)\|^2 + 3\int_k^{k+1} E\left(\|\eta e(t) - \rho\underline{\lambda}e(t-\tau)\|^2\right)dt + 12\alpha^2\int_k^{k+1} E\|e(t)\|^2 dt.$$

By the inequality $(a+b)^2 \le 2a^2 + 2b^2$, it is then to show that

$$E\left(\sup_{k\le t\le k+1}\|e(t)\|^2\right) \le 3E\|e(k)\|^2 + (6\eta^2 + 12\alpha^2)\int_k^{k+1} E\|e(t)\|^2 dt + 6\rho^2\underline{\lambda}^2\int_k^{k+1} E\|e(t-\tau)\|^2 dt.$$

According to (43), we can get

$$\begin{aligned} E\left(\sup_{k\le t\le k+1}(\|e(t)\|^2\right) &\le 3Ge^{-\varepsilon k} + G[6\eta^2 + 12\alpha^2]\int_k^{k+1} e^{-\varepsilon t}dt + 6G\rho^2\underline{\lambda}^2\int_k^{k+1} e^{-\varepsilon(t-\tau)}dt \\ &\le 3Ge^{-\varepsilon k} + G[6\eta^2 + 12\alpha^2]e^{-\varepsilon k} + 6G\rho^2\underline{\lambda}^2 e^{\frac{1}{2}}e^{-\varepsilon k} \\ &= Ce^{-\varepsilon k}. \end{aligned}$$

where $C = 3G[1 + 2\eta^2 + 4\alpha^2 + 2\rho^2\underline{\lambda}^2 e^{\frac{1}{2}}]$. According to Chebyshev's inequality, consequently:

$$\sum_{k=0}^{\infty} P\left(\sup_{k\le t\le k+1}\|e(t)\| > e^{-0.25\varepsilon k}\right) \le \sum_{k=0}^{\infty} Ce^{-0.5\varepsilon k} < \infty.$$

By Borel-Cantelli lemma, for almost all $\omega \in \Omega$, there is positive integer $k_0 = k_0(\omega)$ such that

$$\sup_{k\le t\le k+1}\|e(t)\| \le e^{-0.25\varepsilon k}, \qquad k \ge k_0.$$

Then, for almost all $\omega \in \Omega$

$$\frac{1}{t}\log(\|e(t)\|) \le -\frac{0.25\varepsilon k}{k+1}, \qquad t \in [k, k+1], k \ge k_0.$$

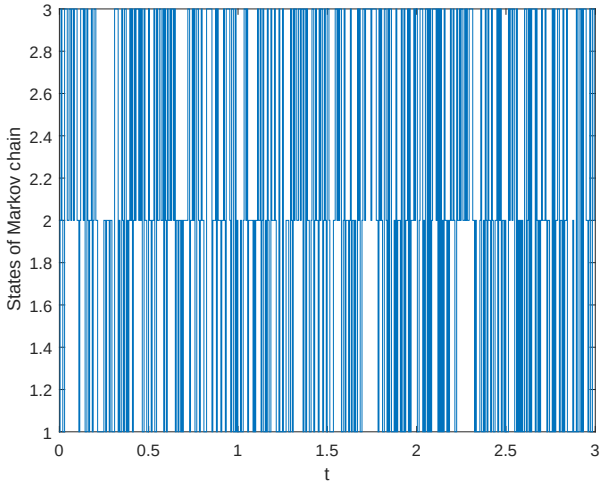


Figure 1. Time evolution of Markov chain $\{\sigma_t | t \in [0,3]\}$ that switches between the three states with generator $\mathcal{Q}$.

This implies

$$\limsup_{t\to\infty} \frac{1}{t} \log(\|e(t)\|) \leq -0.25\varepsilon < 0, \qquad a.s.$$

The proof is complete.

Remark. Our new result in this paper has removed the restrictive condition of existing research, which enables us to design a delay feedback control in order to stabilize a given unstable hybrid SDE. Furthermore, our new result can be used to achieve synchronization conditions for stochastic switched networks with Lévy noise.

4. EXAMPLE

Let us consider a linear n-dimensional unstable stochastic coupled network with delay pinning adaptive feedback control:

$$dx_i(t) = h(x_i(t), \sigma_t)dt + r(x_i(t), \sigma_t)dB(t) + c\sum_{j=1}^{5} a_{ij}(\sigma_t)x_j(t)dt + u(x_i(t-\tau), \sigma_t)dt \tag{44}$$

$$u(x_i(t-\tau), \sigma_t) = -\rho d_i(\sigma_t)(x_i(t-\tau) - s(t-\tau)) \tag{45}$$

where $x_i(t) = (x_i^1(t), x_i^2(t), x_i^3(t)) \in \mathbb{R}^2$; $d_i(\sigma_t) = I_{i\in\mathcal{D}(\sigma_t)}$ is the indication function for the pinned node subset $\mathcal{D}(\sigma_t) \subset \{1,2,3,4,5\}$. Let $c = 0.84$ and the control strength gain be $\rho = 8$. The desirable trajectory $s(t) = (s^1(t), s^2(t), s^3(t))^\top$ is described by (3).

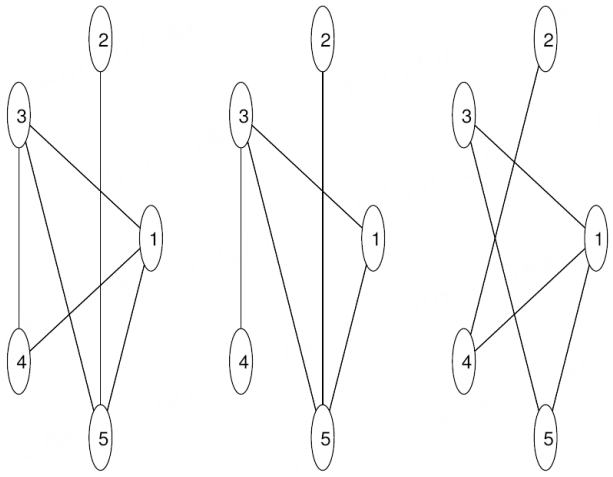


Figure 2. The topological structures $A_i (i = 1, 2, 3)$ of the complex network.

The state space of the Markov chain σ_t is $\mathbb{S} = \{1, 2, 3\}$ with generator as $Q = \begin{bmatrix} 8 & -3 & -5 \\ -2 & 5 & -3 \\ -4 & -5 & 9 \end{bmatrix}$. The time evolution of Markov chain σ_t is depicted in Figure 1, showing the underlying switching. And the coupling matrix $A(\sigma_t) = (a_{ij}(\sigma_t))_{5\times5}$ is switched according to σ_t as follows: $\sigma_t = \ell$, then $A(\ell) = A_\ell$; one of possible topological structures is shown in Figure 2.

The coupling matrix corresponding to Figure 2 is shown as follows,

$$A_1 = \begin{bmatrix} -3 & 0 & 1 & 1 & 1 \\ 0 & -1 & 0 & 0 & 1 \\ 1 & 0 & -3 & 1 & 1 \\ 1 & 0 & 1 & -2 & 0 \\ 1 & 1 & 1 & 0 & -3 \end{bmatrix}, A_2 = \begin{bmatrix} -2 & 0 & 1 & 0 & 1 \\ 1 & -1 & 0 & 0 & 1 \\ 1 & 0 & -3 & 1 & 1 \\ 0 & 0 & 1 & -1 & 0 \\ 1 & 1 & 1 & 0 & -3 \end{bmatrix}, A_3 = \begin{bmatrix} -3 & 0 & 1 & 1 & 1 \\ 0 & -1 & 0 & 1 & 0 \\ 1 & 0 & -2 & 0 & 1 \\ 1 & 1 & 0 & -2 & 0 \\ 1 & 0 & 1 & 0 & -2 \end{bmatrix}$$

The noise is described by Brownian motion $B_i(t)$, which is given in Figure 3.

Consider a network of Chua's circuits. The individual node dynamics of Chua's circuit can be expressed as follows:

$$h(x_i(t), \sigma_t) = \begin{pmatrix} z_1(\sigma_t)(-x_1(t) + x_2(t) - h_1(x_1(t))) \\ x_1(t) - x_2(t) + x_3(t) \\ -z_2(\sigma_t)x_2(t) \end{pmatrix}$$

where $h_1(x) = \sigma_1 x + 1/2(\sigma_2 - r_1)(|x + 1| - |x - 1|), z_1(1) = 9.78, z_1(2) = 3.38, z_1(3) = 9.98, z_2(1) = 100.24, z_2(2) = 30.24, z_2(3) = 1.4, \sigma_1(1) = -0.3, \sigma_1(2) = -0.5, \sigma_1(3) = -2.35, \sigma_2(1) = -0.1, \sigma_2(2) = -1.6, \sigma_2(3) = 0.6$.
$r(x_i(t), \sigma_1) = tanh(x), r(x_i(t), \sigma_2) = tanh(x) - 1, r(x_i(t), \sigma_3) = tanh(x) - 2$. In order to make $h(x_i(t), \sigma_t)$ and $r(x_i(t), \sigma_t)$ satisfies Assumption 1, we choose $\eta = 3.421$. $\alpha = 2.854$.

Let $P = I_3, \Delta = 12.6I_3$ and $\varphi = 2.9846, \gamma = 0.2437, \beta = 0.427, \overline{\lambda} = 0.143, \bar{p} = 1.06, \rho = 12.4, h_2 = 8.37$, Then, $\tilde{H}(x(t), \sigma_t)$ satisfied Assumption 2; $u(x, i)$ satisfied Assumption 4.

Considering the intensity functions $R(\cdot)$, we select $R(x_i(t), \sigma_t) = 0.1 \cdot \sigma_t \cdot \text{diag}\{x_i^1(t), x_i^2(t), x_i^3(t)\}$. Then, we can get $\text{trace}(R^T R) \leq 0.03 e_i^T(t) e_i(t)$. Let $\omega = 0.03$, then Assumption 3 holds

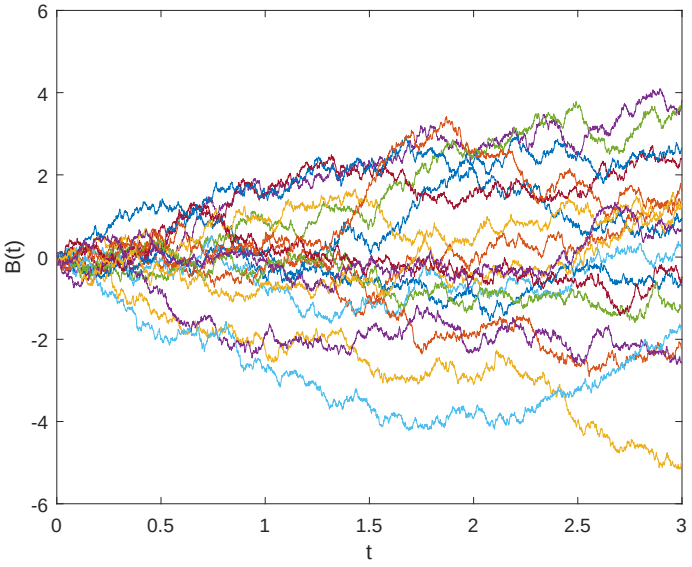


Figure 3. Time evolution of Brownian motion $B(t)$.

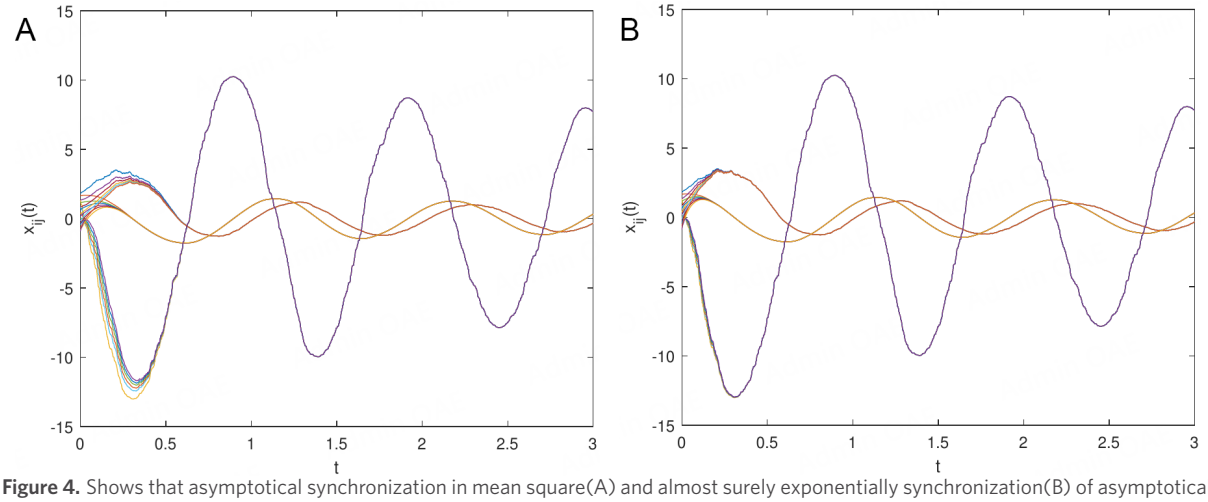


Figure 4. Shows that asymptotical synchronization in mean square(A) and almost surely exponentially synchronization(B) of asymptotical synchronization in mean square and almost surely exponentially synchronization of the State trajectories $x_i^j(t)(i = 1, 2, \cdots, 5, j = 1, 2, 3)$ for networks system (44) under delay pinning feedback control in [0,3] separately.

According to Theorem 1, we can see $\tau \leq \sqrt{\frac{\beta}{16\rho^2\bar{\lambda}^2}} \approx 0.3366$. From Theorem 3, $\varepsilon\tau \leq \frac{1}{2}$, then $\varepsilon \leq \frac{1}{2\tau} \approx 1.4854$. Then, it follows that $\Phi = [c - \frac{\beta\bar{p}^2}{2} - \frac{2\gamma^2}{\beta}(2\tau^2\eta + \tau\alpha)] \approx 0.1337$ and $\Phi - \frac{\varepsilon h_2}{2} > \frac{4\gamma^2\tau^2\rho^2\bar{\lambda}^2}{\beta^2}$.

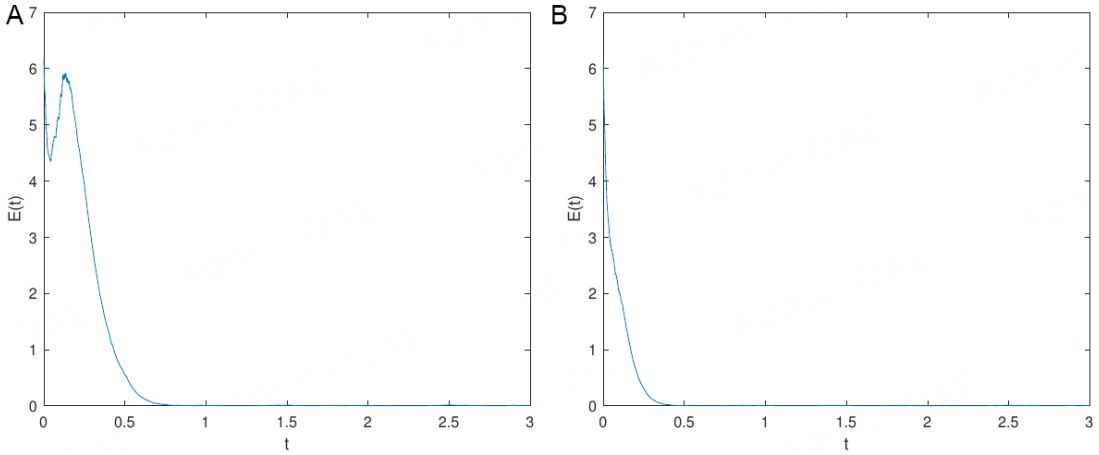


Figure 5. The trajectory of synchronization error $E(t)$ of asymptotical synchronization in mean square (A) and almost surely exponentially synchronization (B) networks system (44) under delay pinning feedback control in [0,3] separately.

As demonstrated by Figure 4, Figure 4A shows that the State trajectories for networks system (44) under Theorem 2; Figure 4B presents that the State trajectories for networks system (44) under Theorem 4; the state variables of all nodes of the Markov switched stochastic complex networks can achieve the synchronization in a very short time.

Denote the total synchronization error $E(t)$ by $E(t) = \sqrt{\sum_{i=1}^{5}\sum_{j=1}^{3}(x_i^j(t) - s_j(t))^2}$.

Figure 5 demonstrates that the total error converges to zero after a very short time. Figure 5A illustrates that all nodes in the stochastic complex network (44) achieve the asymptotical synchronization in mean square, which also indicates the convergent efficiency under the proposed framework. Figure 5B shows the complex network (44) achieves the almost surely exponentially synchronization; $E(t)$ converges to zero after a very short time.

5. CONCLUSION

By using a time-delay feedback controller that depends on the past state, we study a class of Stochastic Switched Networks with Markov switching and Brown noise in this paper. We obtain the sufficient condition of asymptotical synchronization in mean square, H_∞-synchronization and almost sure exponential synchronization in our framework. The main method includes inequality techniques, Itô formula and Borel-Cantelli Lemma. Finally, we illustrate our theory with an example of simulation. Our future effort will focus on the asymptotical synchronization in mean square, H_∞-synchronization and almost sure exponential synchronization of highly nonlinear Markov switched stochastic network. If Assumptions (1) - (6) do not hold, the delay feedback control method in this article will be inapplicable and new methods need to be introduced for exploration. General feedback control may need to be set up, which will be our next consideration.

DECLARATIONS

Authors' contributions

Writing the manuscript: Li Z, Tang J (Juan Tang), Cheng F, Dong H
Organizing the manuscript: Li Z, Cheng F, Tang J (Juan Tang), Dong H, Tang J (Jianliang Tang)
Experimental data presented in the manuscript: Cheng F, Tang J (Juan Tang), Li Z
Discussion of the manuscript: Dong H, Cheng F, Li Z, Tang J (Juan Tang), Tang J (Jianliang Tang)

Availability of data and materials

Not applicable.

Financial support and sponsorship
This work is supported in part by the National Key R&D Program of China under Grant 2023YFE0126800 and the NNSF of China under Grant 12371448.

Conflicts of interest
All authors declared that there are no conflicts of interest.

Ethical approval and consent to participate
Not applicable.

Consent for publication
Not applicable.

Copyright
© The Author(s) 2024.

REFERENCES

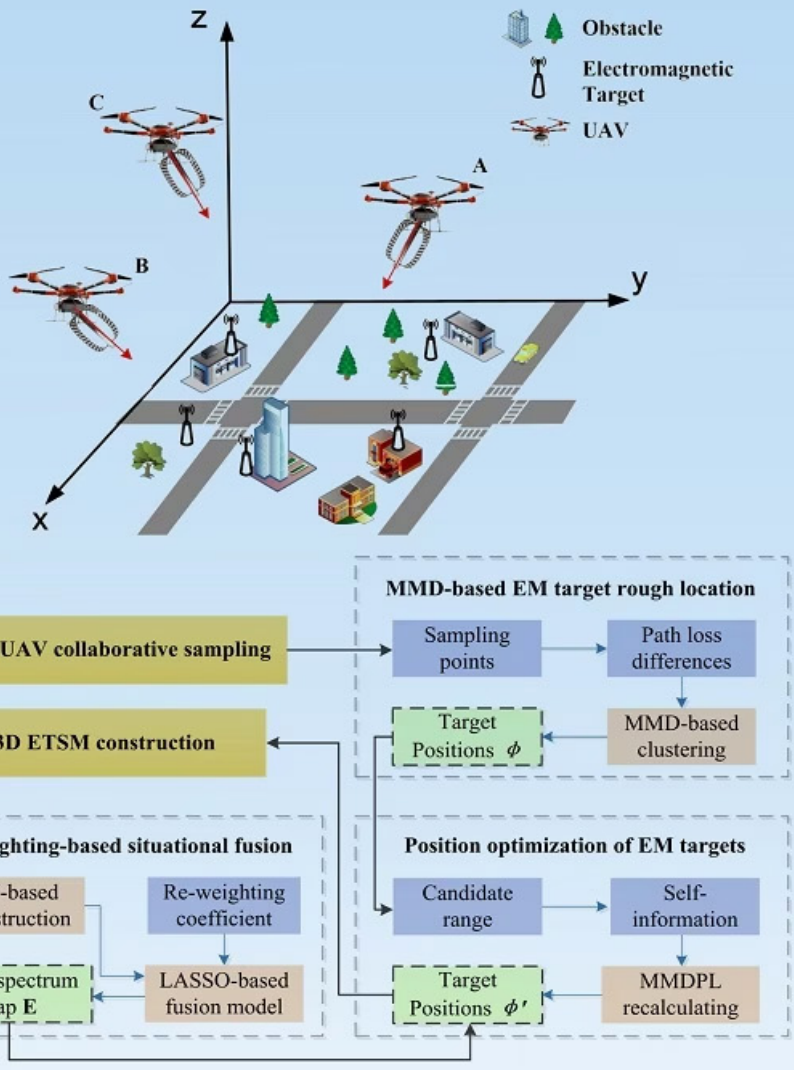
1. Ahmed HM, Ahmed AMS, Ragusa MA. On some non-instantaneous impulsive differential equations with fractional brownian motion and Poisson jumps. *TWMS J Pure Appl Math* 2023;14:125-40. DOI
2. Al-Askar FM. Impact of fractional derivative and brownian motion on the solutions of the Radhakrishnan-Kundu-Lakshmanan equation. *J Funct Space* 2023;2023:8721106. DOI
3. Benkabdi Y, Lakhel EH. Exponential stability of delayed neutral impulsive stochastic integro-differential systems perturbed by fractional Brownian motion and Poisson jumps. *Filomat* 2023;37:8829-44. DOI
4. Ghosh D, Frasca M, Rizzo A, et al. The synchronized dynamics of time-varying networks. *Phys Rep* 2022;949:1-63. DOI
5. Li M, Liu RR, Lü L, Hu MB, Xu S, Zhang YC. Percolation on complex networks: theory and application. *Phys Rep* 2021;907:1-68. DOI
6. Dutta S, Khanna A, Assoa AS, et al. An ising hamiltonian solver based on coupled stochastic phase-transition nano-oscillators. *Nat Electron* 2021;4:502-12. DOI
7. Somers VLJ, Manchester IR. Sparse resource allocation for spreading processes on temporal-switching networks. *IFAC-PapersOnLine* 2023;56:7387-93. DOI
8. Zhong J, Ho DWC, Lu J. A new approach to pinning control of Boolean networks. *IEEE Trans Control Network Syst* 2021;9:415-26. DOI
9. Zhou W, Zhu Q, Shi P, Su H, Fang J, Zhou L. Adaptive synchronization for neutral-type neural networks with stochastic perturbation and Markovian switching parameters. *IEEE Trans Cybern* 2014;44:2848-60. DOI
10. Giap VN, Nguyen QD, Huang SC. Synthetic adaptive fuzzy disturbance observer and sliding-mode control for chaos-based secure communication systems. *IEEE Access* 2021;9:23907-28. DOI
11. Dong H, Luo M, Xiao M. Synchronization for stochastic coupled networks with Lévy noise via event-triggered control. *Neural Netw* 2021;141:40-51. DOI
12. Wu Y, Shen B, Ahn CK, Li W. Intermittent dynamic event-triggered control for synchronization of stochastic complex networks. *IEEE Trans Circuits Syst I* 2021;68:2639-50. DOI
13. Gambuzza LV, Di Patti F, Gallo L, et al. Stability of synchronization in simplicial complexes. *Nat Commun* 2021;12:1255. DOI
14. Lin H, Wang C, Chen C, et al. Neural bursting and synchronization emulated by neural networks and circuits. *IEEE Trans Circuits Syst I* 2021;68:3397-410. DOI
15. Jo J, Lee S, Hwang SJ. Score-based generative modeling of graphs via the system of stochastic differential equations. *Int Conf Mach Learn* 2022;10362-83. DOI
16. Luo D, Tian M, Zhu Q. Some results on finite-time stability of stochastic fractional-order delay differential equations. *Chaos Solitons Fractals* 2022;158:111996. DOI
17. Vaseghi B, Hashemi SS, Mobayen S, Fekih A. Finite time chaos synchronization in time-delay channel and its application to satellite image encryption in OFDM communication systems. *IEEE Access* 2021;9:21332-44. DOI
18. Zhou L, Zhu Q, Wang Z, Zhou W, Su H. Adaptive exponential synchronization of multislave time-delayed recurrent neural networks with levy noise and regime switching. *IEEE Trans Neural Netw Learn Syst* 2017;28:2885-98. DOI
19. Qi W, Hou Y, Zong G, Ahn CK. Finite-time event-triggered control for semi-Markovian switching cyber-physical systems with FDI attacks and applications. *IEEE Trans Circuits Syst I* 2021;68:2665-74. DOI
20. Lu Z, Hu J, Mao X. Stabilisation by delay feedback control for highly nonlinear hybrid stochastic differential equations. *Discrete Cont Dyn Syst* 2019;24:4099-116. DOI
21. Liptser RS, Shiryayev AN. Theory of martingales. Kluwer Academic Publishers; 1982, p. 49. DOI
22. Mao X. Stochastic differential equations and applications. Elsevier; 2008. Available from: https://www.sciencedirect.com/book/9781904275343/stochastic-differential-equations-and-applications [Last accessed on 25 Jun 2024]

23. Fei W, Hu L, Mao X, Shen M. Delay dependent stability of highly nonlinear hybrid stochastic systems. *Automatica* 2017;82:65-70. DOI

Volume 4, Issue 3, September 2024

COMPLEX ENGINEERING SYSTEMS

Editor-in-Chief: Hamid Reza Karimi



Multiple unmanned aerial vehicle collaborated three-dimensional electromagnetic target situation map construction

Yuqing Peng, Kun Liu, Xuezhao Cai, Jie Wang, Zhipeng Lin

Open Access
ISSN 2770-6249 (Online)
www.oaepublish.com/comengsys

Wang *et al. Complex Eng Syst* 2024;4:13
DOI: 10.20517/ces.2024.19

Complex Engineering Systems

Research Article

Open Access

Extended state observer-based fault-tolerant control for an unmanned surface vehicle under asynchronous injection and deception attacks

Haiwen Wang[1], Chun Liu[1], Xiao Huang[1], Yuxuan Zhong[2], Dong Qu[3], Ron J. Patton[4]

[1]School of Mechatronic Engineering and Automation, Shanghai University, Shanghai 200444, China.
[2]China Ship Development and Design Center, Wuhan 430064, Hubei, China.
[3]School of Future Technology, Shanghai University, Shanghai 200444, China.
[4]School of Engineering, University of Hull, Hull HU6 7RX, UK.

Correspondence to: Prof. Chun Liu, School of Mechatronic Engineering and Automation, Shanghai University, No. 99, Shangda Road, Baoshan District, Shanghai 200444, China. E-mail: Chun Liu@shu.edu.cn

How to cite this article: Wang H, Liu C, Huang X, Zhong Y, Qu D, Patton RJ. Extended state observer-based fault-tolerant control for an unmanned surface vehicle under asynchronous injection and deception attacks. *Complex Eng Syst* 2024;4:13. http://dx.doi.org/10.20517/ces.2024.19

Received: 23 Apr 2024 **First Decision:** 21 Jun 2024 **Revised:** 2 Jul 2024 **Accepted:** 18 Jul 2024 **Published:** 24 Jul 2024

Academic Editor: Hamid Reza Karimi **Copy Editor:** Fangling Lan **Production Editor:** Fangling Lan

Abstract

This paper explores the problem of fault-tolerant control concerning an underactuated unmanned surface vehicle affected by actuator faults and disturbances in the physical layer and multiple cyber threats (time-varying delays, injection attacks, and deception attacks) in the networked layer. Firstly, an extended state observer is designed to estimate the relative state and fault information by constructing the estimation error term based on the output information affected by injection attack and delay. Secondly, a novel fault-tolerant controller is designed to deal with random Bernoulli deception attacks and compensate for time-varying delay and actuator faults by using the estimated information and considering the probability dynamics of deception attacks. Assuming that dual-channel asynchronous independent injection and deception attacks occur on the sensor-to-observer and observer-to-controller channels. A sufficient condition for asymptotic stability of the unmanned surface vehicle is derived by using Lyapunov-Krasovskii functional within the co-design framework of fault estimation and fault-tolerant control, and ensured by eliminating the equality constraint. Finally, the efficacy of the proposed algorithm is assessed through simulations of the unmanned surface vehicle under two distinct scenarios: low forward speed and high forward speed.

Keywords: Extended state observer, fault-tolerant control, unmanned surface vehicle, injection attacks, deception attacks

© The Author(s) 2023. **Open Access** This article is licensed under a Creative Commons Attribution 4.0 International License (https://creativecommons.org/licenses/by/4.0/), which permits unrestricted use, sharing, adaptation, distribution and reproduction in any medium or format, for any purpose, even commercially, as long as you give appropriate credit to the original author(s) and the source, provide a link to the Creative Commons license, and indicate if changes were made.

1. INTRODUCTION

For the past few years, the relevant technology of unmanned surface vehicles (USVs) has undergone rapid advancements, garnering substantial attention across various fields including military operations[1], ocean exploration[2], and maritime monitoring[3]. An overview of control methods for USVs can be seen[4]. Notably, considerable attention has been devoted to the fault-tolerant control (FTC) of nonlinear steering controlled[5], underactuated[6], and fully actuated[7] USVs. An active FTC method for the USV is discussed[8], while[9] provides insights into a passive FTC approach. More cutting-edge research on FTC can be seen[10–12]. Consequently, further exploration of FTC strategies for USVs is imperative to bolster reliability and stability of the system.

Given the intricacies of the marine environment, numerous accidents, including sensor faults (dead fault, biased fault, and random drift) and actuator faults (stuck steering mechanism-type fault and noise-type fault) along with insufficient thrust due to external disturbances, are prone to occur during mission execution. The smooth movement of USVs hinges upon various factors such as environmental perception and attitude control. These physical threats not only degrade the overall performance of USVs but also pose the risk of severe accidents. Hence, the FTC issues of USVs under physical threats are now receiving considerable attention[13–15]. An observer is constructed based on an intermediate variable and an FTC protocol is designed for a USV with actuator faults and partial transmission data loss[15]. Specifically, the FTC of USVs under actuator faults[16], sensor faults[17], thruster faults[18], actuator faults and disturbances[19] is investigated. In the FTC research, the observer-based active FTC method stands as a prominent choice[8,20,21]. This approach revolves around extracting fault information from the fault estimation (FE) and subsequently designing an FTC strategy based on the estimated information. However, prevailing observer-based FTC methods conventionally separate the front-end FE from the back-end FTC which complicates the research of USVs. Conversely, the co-design of FE and FTC not only mitigates complexity but also abbreviates fault response durations, rendering it more conducive for a USV to move in complex environments. Therefore, it is necessary to further explore the applicability of FE and FTC co-design framework within the realm of USVs.

In addition to the adverse effects stemming from the aforementioned physical threats, the advancement of USV intelligence is also accompanied by cyber risks. On the one hand, attacks in the networked layer damage the connectivity of transmission channels and the integrity of data, diminishing the reliability of the USV and potentially leading to the deviation from prescribed routes and loss of control. Therefore, when facing such malicious attacks as denial of service (DoS) attack, deception attack, injection attack, how to design a suitable FTC scheme to withstand the impact is crucial. A concise summary of cyber threats faced by USVs across different domains is provided, and a data protection scheme is presented[22]. Under the framework of co-design, a distributed control method based on the distributed unknown input observer is adopted to solve the distributed security control problem of multiple USVs under aperiodic DoS attacks[23]. An event-triggered communication scheme and an event-based switching control system are proposed to deal with both delayed and aperiodic DoS attacks[24]. A new defense and tolerance technology is adopted to deal with malicious connection hybrid attacks in the networked layer and solve the distributed tracking control problem of multiple USVs[25]. However, the predominant focus of current research lies in the FTC for USVs under periodic/aperiodic DoS attacks[23,24,26]. Different from DoS attacks which lead to serious communication interruption, deception attacks and injection attacks compromise the integrity and confidentiality of transmitted data by manipulating them, which causes misoperation of USVs and brings substantial security risks. On the other hand, the presence of network-induced delay significantly influences the real-time efficacy of USV control instructions, which greatly limits the flexibility of the system when performing tasks requiring rapid response such as obstacle avoidance. An event-triggered control design method for multiple USVs constrained by communication delay and drive resources is proposed to solve the dynamic target tracking problem[27]. A novel nonlinear networked predictive control approach, leveraging the discrete sliding mode framework, is introduced to address the trajectory tracking challenges encountered by USVs in the presence of

communication limitations, encompassing network delay, packet loss, and packet disorder[28]. The dynamic nature and inherent uncertainty associated with network-induced delay exert a notable influence on control precision, which establishes it as one of the key factors in USV control research. Furthermore, apart from the types of cyber threats, it is pertinent to contemplate the location of their influence. Most cyber threats involved in the research are imposed on the controller-actuator channel[13,26,29] or sensor-to-fault detection filter channel[30,31], ignoring other cases, particularly the sensor-to-observer (SO) and observer-to-controller (OC) channels. In the case of SO and OC channels facing cyber threats, the control system receives imprecise estimated information, thereby causing incorrect fault response. Consequently, in scenarios where both SO and OC channels encounter cyber attacks and delays and the system is subjected to physical threats, the design of an observer-based FTC strategy is significant to safeguard the security and stability of a USV in complex environments.

The primary contributions of this paper are as follows. (1) In contrast to previous investigations of USVs focusing on the single side such as faults[17,18] or cyber attacks[31,32], this paper presents a more comprehensive analysis by considering the combined impact of multiple cyber-physical threats. Different from the independent design of FE and FTC, this paper deduces the co-design criteria of FE and FTC under the unified framework based on Lyapunov-Krasovskii functional, and eliminates equality constraints, which alleviates the dilemma of solving nonlinear matrix inequalities; and (2) Unlike the prevailing emphasis on deception attacks and injection attacks[31–33], the complex case of dual-channel asynchronous injection and deception attacks is considered, with the attacks specifically aimed at SO and OC channels. The fault-tolerant controller devised in this paper diverges from conventional active FTC configurations predicated on pure estimation data[21,34]. Instead, it integrates adversarial and benign scenario considerations. Leveraging damaged estimation information, it strengthens the resilience of the USV to multiple cyber threats, rendering it more practical.

2. PROBLEM FORMULATION

2.1. USV modeling

The movement challenges encountered by a USV on the horizontal plane are examined within this paper, with due attention given to disturbances arising from environmental factors. Emphasis is placed exclusively on the sway-yaw-roll motion pattern of USV, illustrated in Figure 1, with the repercussions of the heave-surge-pitch motion treated as perturbations. The dynamic model representing the USV is given as follows:

$$\begin{cases} \dot{r}(t) = K_{vr}v(t)/T_r + \omega_\psi(t)/T_r + K_{ar}\delta(t)/T_r - r(t)/T_r \\ \dot{p}(t) = \omega_n^2 K_{ap}\delta(t) - 2\zeta\omega_n p(t) + \omega_n^2\omega_\phi(t) - \omega_n^2\phi(t) + \omega_n^2 K_{vp}v(t) \\ \dot{v}(t) = K_{av}\delta(t)/T_v - v(t)/T_v \\ \dot{\psi}(t) = r(t) \\ \dot{\phi}(t) = p(t) \end{cases} \tag{1}$$

where $r(t)$, $v(t)$, $p(t)$, $\phi(t)$, $\delta(t)$, and $\psi(t)$ represent the yaw velocity, sway velocity, roll velocity, roll angle, rudder angle, and heading angle, respectively. $\omega_\psi(t)$ and $\omega_\phi(t)$ signify the external disturbances influencing the heading and roll velocity channels due to wave-induced effects. ω_n and ζ stand for the undamped natural frequency and damping ratio, respectively. The channel gains are denoted by K_{ap}, K_{ar}, K_{vp}, K_{vr}, and K_{av}, while T_r and T_v represent the time constants. To simplify the analysis, it is assumed that the speed of the USV remains the same.

During the propulsion of USVs, occurrences of actuator faults, such as noise-type faults and stuck steering mechanism-type faults, are inevitable. Consequently, the USV subject to external disturbances and actuator faults is modeled as:

$$\begin{cases} \dot{x}(t) = Ax(t) + Bu(t) + E\omega(t) + Ff(t) \\ y(t) = Cx(t) \end{cases} \tag{2}$$

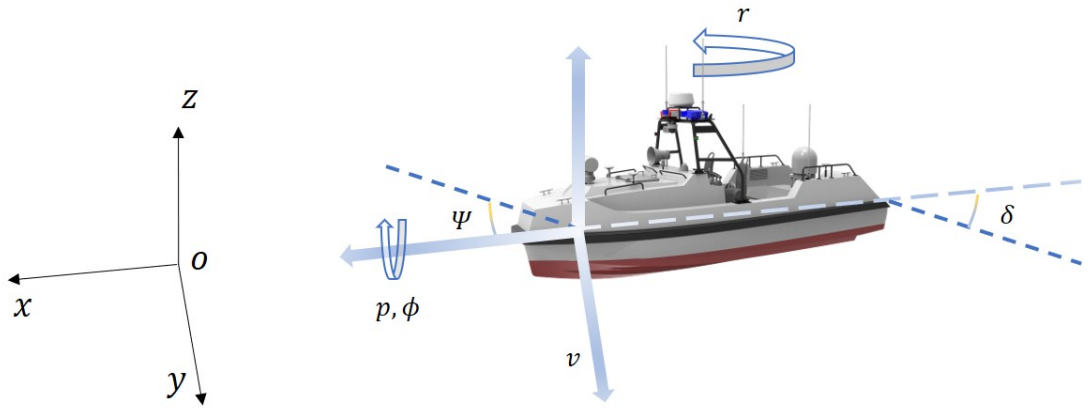


Figure 1. The sway-yaw-roll motion of USV illustrated in body-fixed coordinate frame.

where $x(t) = [v(t)\ r(t)\ \psi(t)\ p(t)\ \phi(t)]^T$ is the state of the USV. $u(t) = \delta(t)$ and $y(t)$ represent the input and output of the system, respectively. $\omega(t) = \left[\omega_\psi(t)\ \omega_\phi(t)\right]^T$ and $f(t)$ characterize the wave-induced disturbances and actuator faults. Matrices A, B, C, E and F are constant matrices, with A, B, and E derived from (1),

$$A = \begin{bmatrix} -1/T_v & 0 & 0 & 0 & 0 \\ K_{vr}/T_r & -1/T_r & 0 & 0 & 0 \\ 0 & 1 & 0 & 0 & 0 \\ \omega_n^2 K_{\text{vp}} & 0 & 0 & -2\zeta\omega_n & -\omega_n^2 \\ 0 & 0 & 0 & 1 & 0 \end{bmatrix}, \quad B = \begin{bmatrix} K_{av}/T_v \\ K_{ar}/T_r \\ 0 \\ \omega_n^2 K_{\text{ap}} \\ 0 \end{bmatrix}, \quad E = \begin{bmatrix} 0 & 0 \\ 1/T_r & 0 \\ 0 & 0 \\ 0 & \omega_n^2 \\ 0 & 0 \end{bmatrix}. \tag{3}$$

2.2. Asynchronous injection and deception attacks modeling

Concerning threats in the networked layer, considerable focus has been directed toward assessing the combined impact of network-induced delays, as well as asynchronous injection and deception attacks targeting transmitted signals across SO and OC channels, as portrayed in Figure 2.

Under the joint impact of time-varying delays and injection attacks, the output signal $y(t)$ transmitted on the SO channel is transformed into the following form,

$$\bar{y}(t) = y(t - \beta(t)) + \alpha y(t - \beta(t)) = \bar{\alpha} y(t - \beta(t)) \tag{4}$$

where $\bar{y}(t)$ indicates the affected output signal, and $\beta(t)$ represents the time-varying delay caused by network transmission process. The scaling factor α denotes the attack amplitude.

In intricate maritime settings, direct acquisition of the state information of the USV is unfeasible owing to the prevalence of interferences such as magnetic fields and waves. Hence, an extended state observer is proposed to simultaneously estimate state and fault information. The extended state observer is constructed as follows:

$$\begin{cases} \dot{\hat{x}}(t) = A\hat{x}(t) + Bu(t) + F\hat{f}(t) - L(\bar{y}(t) - \hat{y}(t)) \\ \hat{y}(t) = C\hat{x}(t) \\ \dot{\hat{f}}(t) = Q(\bar{y}(t) - \hat{y}(t)) \end{cases} \tag{5}$$

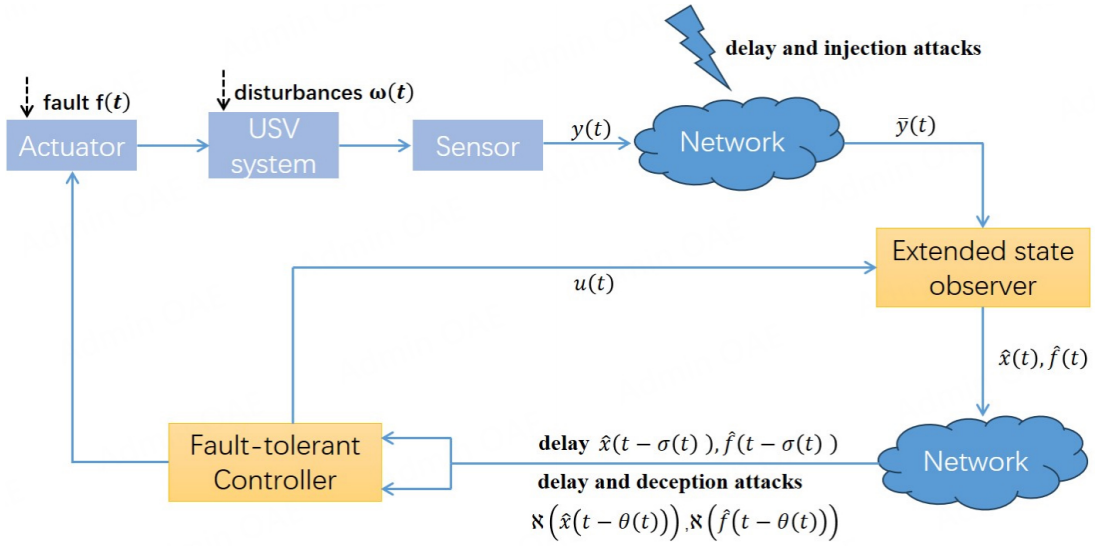


Figure 2. Dual-channel time-varying delays and asynchronous injection and deception attacks

where $\hat{x}(t)$ and $\hat{f}(t)$ represent the estimation of state information and fault information, respectively, which are transmitted to the fault-tolerant controller through OC channel. L and Q both are gain matrices to be determined.

In the context of deception attacks occurring on the OC channel, a stochastic variable denoted as $\rho(t)$ is introduced to delineate the probability associated with attack occurrences. The stochastic variable $\rho(t)$ is governed by the Bernoulli distribution and embodies the mathematical expectation formulated as follows:

$$\Pr(\rho(t) = 1) = \mathbb{E}\{\rho(t)\} = \bar{\rho}, \mathbb{E}\{(\rho(t) - \bar{\rho})^2\} = \bar{\rho}(1 - \bar{\rho}), \bar{\rho} \in [0, 1] \tag{6}$$

In addition to deception attacks, the existence of time-varying delays is also taken into account within the OC channel. When the estimated information $\hat{x}(t)$ and $\hat{f}(t)$ are transmitted through the OC channel to the fault-tolerant controller without being subjected to Bernoulli deception attacks, the received data are denoted as $\hat{x}(t-\sigma(t))$ and $\hat{f}(t-\sigma(t))$, respectively. Conversely, in the event of attacks, the data integrity is damaged, resulting in post-attack signals represented as $\aleph(\hat{x}(t-\theta(t)))$ and $\aleph\left(\hat{\dot{f}}(t-\theta(t))\right)$. Both $\sigma(t)$ and $\theta(t)$ represent the time-varying delay on the OC channel.

Remark 1: The injection attacks on the SO channel and the deception attacks on the OC channel give rise to an asynchronous independent attacks phenomenon attributed to varying delays across channels. The disparity in delays and attack modalities poses challenges to the investigation of the controllability and reliability of the USV. Concerning the injection attack on the SO channel, it injects the attack signal by combining with the state information, which is more targeted and elusive than the attack that directly injects irrelevant information. In addition, in contrast to other researches focusing on Bernoulli deception attacks on channels[35,36], no analogous constraint is imposed on the attacks.

Assumption 1:[5,6,37] The time-varying delays occurring on either SO or OC channels have known upper bounds, i.e., $\beta(t) \in [0, \beta_M]$, $\sigma(t) \in [0, \sigma_M]$, $\theta(t) \in [0, \theta_M]$. In addition, both the derivative of the fault vector $\dot{f}(t)$ and the disturbance vector have an unknown upper bound, i.e., $\left\|\dot{f}(t)\right\| \leq \bar{f}$, $\bar{f} > 0$, $\|\omega(t)\| \leq \bar{\omega}$, $\bar{\omega} > 0$.

Assumption 2:[24] The system matrix C^T satisfies full column rank.

Lemma 1:[37] For the provided matrix $C^T \in \mathbb{R}^{n\times l}$ and positive definite matrix $W \in \mathbb{R}^{n\times n}$, there is a matrix $N \in \mathbb{R}^{l\times l}$ such that $WC^T = C^T N$ if and only if

$$W = J^T \begin{bmatrix} W_{11} & 0 \\ 0 & W_{22} \end{bmatrix} J \tag{7}$$

where $W_{11} \in \mathbb{R}^{l\times l}$, $W_{22} \in \mathbb{R}^{(n-l)\times(n-l)}$, and J is an orthogonal matrix.

Control objective: The main purpose is to design a fault-tolerant controller $u(t)$ within the FE and FTC co-design framework that enables the USV system (2) to achieve asymptotic stability under multiple cyber-physical threats such as disturbances, actuator faults, time-varying delays, injection attacks, and deception attacks.

3. MAIN RESULTS

In this section, the $u(t)$ is designed using the information estimated by the extended state observer. A sufficient condition for asymptotic stability of the USV system (2) is derived under the framework of FE and FTC co-design, and a method to eliminate the equality constraints is proposed to solve the unknown gain matrix to ensure the sufficient condition.

The state estimation error and FE error are respectively defined as $e_x = \hat{x}(t) - x(t)$, $e_f = \hat{f}(t) - f(t)$. The dynamics of the estimation errors are deduced by using (2) and (5) as follows:

$$\begin{cases} \dot{e}_x(t) = Ae_x(t) + Fe_f(t) - E\omega(t) + \bar{\alpha}LCe_x(t-\beta(t)) - \bar{\alpha}LC\hat{x}(t-\beta(t)) + LC\hat{x}(t) \\ \dot{e}_f(t) = -\bar{\alpha}QCe_x(t-\beta(t)) + \bar{\alpha}QC\hat{x}(t-\beta(t)) - QC\hat{x}(t) - \dot{f}(t) \end{cases} \tag{8}$$

When time-varying delays and Bernoulli deception attacks exist within the OC channel, the state estimation information $\hat{x}(t)$ and FE information $\hat{f}(t)$ are utilized to construct the fault-tolerant controller $u(t)$ for the USV system (2), formulated as follows:

$$\begin{aligned} u(t) = {} & (1-\rho(t))K\hat{x}(t-\sigma(t)) + \rho(t)K\aleph(\hat{x}(t-\theta(t))) \\ & - (1-\rho(t))G\hat{f}(t-\sigma(t)) - \rho(t)G\aleph\left(\hat{f}(t-\theta(t))\right) \end{aligned}$$

In combination with (5), (8), and (9), the augmented system is constructed as follows:

$$\begin{aligned} \dot{\xi}(t) = {} & \hat{A}\xi(t) + \hat{C}\xi(t-\beta(t)) + (1-\rho(t))\hat{B}M\xi(t-\sigma(t)) \\ & + \rho(t)\hat{B}\aleph(M\xi(t-\theta(t))) + \hat{E}\varpi(t) \end{aligned} \tag{9}$$

where $\xi(t) = \left[e_x^T(t)\ e_f^T(t)\ \hat{x}^T(t)\ \hat{f}^T(t)\right]^T$, and $\varpi(t) = \left[\ \omega^T(t)\ \dot{f}^T(t)\ \right]^T$ are the augmented vectors. $\hat{A} = \begin{bmatrix} A & F & LC & 0 \\ 0 & 0 & -QC & 0 \\ 0 & 0 & A+LC & F \\ 0 & 0 & -QC & 0 \end{bmatrix}$, $\hat{B} = \begin{bmatrix} 0 & 0 \\ 0 & 0 \\ BK & -BG \\ 0 & 0 \end{bmatrix}$, $M = \begin{bmatrix} 0 & 0 & I & 0 \\ 0 & 0 & 0 & I \end{bmatrix}$, $\hat{C} = \begin{bmatrix} \bar{\alpha}LC & 0 & -\bar{\alpha}LC & 0 \\ -\bar{\alpha}QC & 0 & \bar{\alpha}QC & 0 \\ \bar{\alpha}LC & 0 & -\bar{\alpha}LC & 0 \\ -\bar{\alpha}QC & 0 & \bar{\alpha}QC & 0 \end{bmatrix}$, and $\hat{E} = \begin{bmatrix} -E & 0 \\ 0 & -I \\ 0 & 0 \\ 0 & 0 \end{bmatrix}$ are the augmented matrices.

Given the positive parameter $\gamma > 0$, the asymptotic stability of the USV system (2) is equivalent to the augmented system (9) satisfying the following H_∞ performance index.

$$\mathbb{E}\{\int_0^t \xi^T(s)\xi(s)ds\} \leq \gamma^2\mathbb{E}\{\int_0^t \varpi^T(s)\varpi(s)ds\} \tag{10}$$

Theorem 1: Given the known parameters $\beta_M, \sigma_M, \theta_M, \bar{\rho}, \gamma$, and matrices $\hat{A}, \hat{B}, \hat{C}, \hat{E}, M$, the augmented system (9) can achieve asymptotic stability under the zero initial condition with an H_∞ index γ, if there exist positive definite matrices P, Θ_i, and $\Psi_i (i = 1, 2, 3)$ satisfying the following matrix inequality:

$$\Omega(s) = \begin{bmatrix} \Omega_{11} & * & * & * \\ \Omega_{21} & \Omega_{22} & * & * \\ \Omega_{31} & 0 & \Omega_{33} & * \\ \Omega_{41} & 0 & 0 & \Omega_{44} \end{bmatrix} < 0 \tag{11}$$

where

$$\Omega_{11} = \begin{bmatrix} \Upsilon & * & * & * & * & * & * & * \\ \hat{C}^T P & 0 & * & * & * & * & * & * \\ 0 & 0 & -\Theta_1 & * & * & * & * & * \\ (1-\bar{\rho})M^T\hat{B}^T P & 0 & 0 & 0 & * & * & * & * \\ 0 & 0 & 0 & 0 & -\Theta_2 & * & * & * \\ 0 & 0 & 0 & 0 & 0 & -\Theta_3 & * & * \\ \bar{\rho}\hat{B}^T P & 0 & 0 & 0 & 0 & 0 & 0 & * \\ \hat{E}^T P & 0 & 0 & 0 & 0 & 0 & 0 & -\gamma^2 I \end{bmatrix}$$

$$\Upsilon = P\hat{A} + \hat{A}^T P + \Theta_1 + \Theta_2 + \Theta_3 + I, \Omega_{22} = \Omega_{33} = \Omega_{44} = \text{Diag}\left\{-P\Psi_1^{-1}P, -P\Psi_2^{-1}P, -P\Psi_3^{-1}P\right\}$$

$$\Omega_{21} = \begin{bmatrix} \beta_M P \\ \sigma_M P \\ \theta_M P \end{bmatrix} \begin{bmatrix} \hat{A} & \hat{C} & 0 & (1-\bar{\rho})\hat{B}M & 0 & 0 & \bar{\rho}\hat{B} & \hat{E} \end{bmatrix}, m = \sqrt{\bar{\rho}\,(1-\bar{\rho})}$$

$$\Omega_{31} = \begin{bmatrix} m\beta_M P \\ m\sigma_M P \\ m\theta_M P \end{bmatrix} \begin{bmatrix} 0 & 0 & 0 & \hat{B}M & 0 & 0 & -\hat{B} & 0 \end{bmatrix}, \Omega_{41} = \begin{bmatrix} P & 0 & -P & 0 & 0 & 0 & 0 & 0 \\ P & 0 & 0 & 0 & -P & 0 & 0 & 0 \\ P & 0 & 0 & 0 & 0 & -P & 0 & 0 \end{bmatrix}.$$

Proof: The Lyapunov-Krasovskii functional $V(t)$ is framed as $V(t) = V_1(t) + V_2(t) + V_3(t)$ with the following form

$$\begin{aligned} V_1(t) &= \xi^T(t)P\xi(t) \\ V_2(t) &= \int_{t-\beta_M}^t \xi^T(s)\Theta_1\xi(s)ds + \int_{t-\sigma_M}^t \xi^T(s)\Theta_2\xi(s)ds + \int_{t-\theta_M}^t \xi^T(s)\Theta_3\xi(s)ds \\ V_3(t) &= \beta_M \int_{-\beta_M}^0 \int_{t+v}^t \dot{\xi}^T(z)\Psi_1\dot{\xi}(z)dzdv + \sigma_M \int_{-\sigma_M}^0 \int_{t+v}^t \dot{\xi}^T(z)\Psi_2\dot{\xi}(z)dzdv \\ &\quad + \theta_M \int_{-\theta_M}^0 \int_{t+v}^t \dot{\xi}^T(z)\Psi_3\dot{\xi}(z)dzdv \end{aligned} \tag{12}$$

Then, the $\mathbb{E}\{\dot{V}(t)\}$ can be formulated as $\mathbb{E}\{\dot{V}(t)\} = \mathbb{E}\{\dot{V}_1(t)\} + \mathbb{E}\{\dot{V}_2(t)\} + \mathbb{E}\{\dot{V}_3(t)\}$, as delineated by the

subsequent expressions.

$$\begin{aligned}
\mathbb{E}\{\dot{V}_1(t)\} &= 2\xi^T(t)P\Xi \\
\mathbb{E}\{\dot{V}_2(t)\} &= \xi^T(t)\left(\Theta_1+\Theta_2+\Theta_3\right)\xi(t) - \xi^T\left(t-\beta_M\right)\Theta_1\xi\left(t-\beta_M\right) \\
&\quad - \xi^T\left(t-\sigma_M\right)\Theta_2\xi\left(t-\sigma_M\right) - \xi^T\left(t-\theta_M\right)\Theta_3\xi\left(t-\theta_M\right) \\
\mathbb{E}\{\dot{V}_3(t)\} &= -\beta_M\int_{t-\beta_M}^{t}\dot{\xi}^T(s)\Psi_1\dot{\xi}(s)ds - \sigma_M\int_{t-\sigma_M}^{t}\dot{\xi}^T(s)\Psi_2\dot{\xi}(s)ds \\
&\quad - \theta_M\int_{t-\theta_M}^{t}\dot{\xi}^T(s)\Psi_3\dot{\xi}(s)ds + \mathbb{E}\{\dot{\xi}^T(t)\Psi\dot{\xi}(t)\}
\end{aligned} \tag{13}$$

where

$$\begin{aligned}
&\mathbb{E}\{\dot{\xi}^T(t)\Psi\dot{\xi}(t)\} = \mathbb{E}\{[\Xi+(\bar{\rho}-\rho(t))\Xi_1]^T\Psi[\Xi+(\bar{\rho}-\rho(t))\Xi_1]\} = \Xi^T\Psi\Xi + m^2\Xi_1^T\Psi\Xi_1 \\
&\Xi = \hat{A}\xi(t) + \hat{C}\xi(t-\beta(t)) + (1-\bar{\rho})\hat{B}M\xi(t-\sigma(t)) + \bar{\rho}\hat{B}\aleph(M\xi(t-\theta(t))) + \hat{E}\varpi(t) \\
&\Xi_1 = \hat{B}M\xi(t-\sigma(t)) - \hat{B}\aleph(M\xi(t-\theta(t))), \Psi = {\beta_M}^2\Psi_1 + {\sigma_M}^2\Psi_2 + {\theta_M}^2\Psi_3.
\end{aligned}$$

From the Jensen inequality, the following inequalities hold

$$\begin{aligned}
-\beta_M\int_{t-\beta_M}^{t}\dot{\xi}^T(s)\Psi_1\dot{\xi}(s)ds &\le -[\xi(t)-\xi(t-\beta_M)]^T\Psi_1[\xi(t)-\xi(t-\beta_M)] \\
-\sigma_M\int_{t-\sigma_M}^{t}\dot{\xi}^T(s)\Psi_2\dot{\xi}(s)ds &\le -[\xi(t)-\xi(t-\sigma_M)]^T\Psi_2[\xi(t)-\xi(t-\sigma_M)] \\
-\theta_M\int_{t-\theta_M}^{t}\dot{\xi}^T(s)\Psi_3\dot{\xi}(s)ds &\le -[\xi(t)-\xi(t-\theta_M)]^T\Psi_3[\xi(t)-\xi(t-\theta_M)]
\end{aligned} \tag{14}$$

In order to ensure that the augment system (9) satisfies H_∞ index (10), the following calculation is performed under the zero initial condition,

$$\begin{aligned}
&\mathbb{E}\{\int_0^t\xi^T(s)\xi(s)ds\} - \gamma^2\mathbb{E}\{\int_0^t\varpi^T(s)\varpi(s)ds\} = \mathbb{E}\{\int_0^t(\xi^T(s)\xi(s)-\gamma^2\varpi^T(s)\varpi(s))ds\} \\
&\le \int_0^t\mathbb{E}\{\xi^T(s)\xi(s)-\gamma^2\varpi^T(s)\varpi(s)+\dot{V}(s)\}ds \le 2\xi^T(t)P\Xi + \xi^T(t)\left(\Theta_1+\Theta_2+\Theta_3\right)\xi(t) \\
&- \xi^T\left(t-\beta_M\right)\Theta_1\xi\left(t-\beta_M\right) - \xi^T\left(t-\sigma_M\right)\Theta_2\xi\left(t-\sigma_M\right) + \Xi^T\Psi\Xi + \xi^T(t)\xi(t) \\
&+ m^2\Xi_1^T\Psi\Xi_1 - \xi^T\left(t-\theta_M\right)\Theta_3\xi\left(t-\theta_M\right) - [\xi(t)-\xi(t-\beta_M)]^T\Psi_1[\xi(t)-\xi(t-\beta_M)] \\
&- \gamma^2\varpi^T(t)\varpi(t) - [\xi(t)-\xi(t-\sigma_M)]^T\Psi_2[\xi(t)-\xi(t-\sigma_M)] \\
&- [\xi(t)-\xi(t-\theta_M)]^T\Psi_3[\xi(t)-\xi(t-\theta_M)]
\end{aligned} \tag{15}$$

The inequality (11) is a sufficient condition for $\mathbb{E}\{\dot{V}(t)+\xi^T(t)\xi(t)-\gamma^2\varpi^T(t)\varpi(t)\} < 0$ with the definition of $s(t) = [\xi^T(t)\ \xi^T(t-\beta(t))\ \xi^T(t-\beta_M)\ \xi^T(t-\sigma(t))\ \xi^T(t-\sigma_M)\ \xi^T(t-\theta_M)\ \aleph^T(M\xi(t-\theta(t)))\ \varpi^T(t)]^T$ through using the Schur complement in the inequality (15).

Remark 2: In formulating the aforementioned Lyapunov-Krasovskii functional $V(t)$, the parameters β_M, σ_M and θ_M signify the upper bounds of the corresponding channel delays to model worst-case scenarios. Thus, inequality (10) persists under the condition that the time-varying delays of the channels remain within the prescribed upper bounds in all cases.

The resolution of matrix inequalities (11) poses challenges in directly solving the unknown matrix parameters employing the linear matrix inequalities (LMI) technique, attributed to the inclusion of partial nonlinear terms. Consequently, a method is introduced in the following theorem to eliminate equality constraints,

thereby linearizing the nonlinear terms, and subsequently resolving multiple undetermined matrix parameters via a matrix inequality.

Theorem 2: Given the scalars $\beta_M, \sigma_M, \theta_M, \bar{\rho}, \gamma, \epsilon_i (i = 1, 2, 3, 4)$ and matrices $\hat{A}$, $\hat{B}$, $\hat{C}$, $\hat{E}$, after eliminating the equality constraint, the augmented system (9) achieves the H_∞ performance index (10) if there exist positive definite matrices W, $\tilde{\Theta}_i$, $\Psi_i (i = 1, 2, 3)$ and matrices $\tilde{Q}$, $\tilde{L}$, $\tilde{K}$, G such that the following inequalities can be solved,

$$\tilde{\Omega}(s) = \begin{bmatrix} \tilde{\Omega}_{11} & * & * & * \\ \tilde{\Omega}_{21} & \tilde{\Omega}_{22} & * & * \\ \tilde{\Omega}_{31} & 0 & \tilde{\Omega}_{33} & * \\ \tilde{\Omega}_{41} & 0 & 0 & \tilde{\Omega}_{44} \end{bmatrix} < 0 \tag{16}$$

where

$$\tilde{\Omega}_{11} = \begin{bmatrix} \tilde{\Upsilon} & * & * & * & * & * & * & * \\ \tilde{C} & 0 & * & * & * & * & * & * \\ 0 & 0 & -\tilde{\Theta}_1 & * & * & * & * & * \\ (1-\bar{\rho})\tilde{B} & 0 & 0 & 0 & * & * & * & * \\ 0 & 0 & 0 & 0 & -\tilde{\Theta}_2 & * & * & * \\ 0 & 0 & 0 & 0 & 0 & -\tilde{\Theta}_3 & * & * \\ \bar{\rho}\tilde{B}_1 & 0 & 0 & 0 & 0 & 0 & 0 & * \\ \hat{E}^T & 0 & 0 & 0 & 0 & 0 & 0 & -\gamma^2 I \end{bmatrix}$$

$$\tilde{\Upsilon} = \tilde{A} + \tilde{A}^T + \tilde{\Theta}_1 + \tilde{\Theta}_2 + \tilde{\Theta}_3 + I, \tilde{\Omega}_{22} = \tilde{\Omega}_{33} = \tilde{\Omega}_{44} = \text{Diag}\left\{-\Psi_1^{-1}, -\Psi_2^{-1}, -\Psi_3^{-1}\right\}$$

$$\tilde{\Omega}_{21} = \begin{bmatrix} \beta_M \\ \sigma_M \\ \theta_M \end{bmatrix} \begin{bmatrix} \tilde{A} & \tilde{C}^T & 0 & (1-\bar{\rho})\tilde{B}^T & 0 & 0 & \bar{\rho}\tilde{B}_1^T & \hat{E} \end{bmatrix}$$

$$\tilde{\Omega}_{31} = \begin{bmatrix} m\beta_M \\ m\sigma_M \\ m\theta_M \end{bmatrix} \begin{bmatrix} 0 & 0 & 0 & \tilde{B}^T & 0 & 0 & -\tilde{B}_1^T & 0 \end{bmatrix}, \tilde{\Omega}_{41} = \begin{bmatrix} P^{-1} & 0 & -P^{-1} & 0 & 0 & 0 & 0 & 0 \\ P^{-1} & 0 & 0 & 0 & -P^{-1} & 0 & 0 & 0 \\ P^{-1} & 0 & 0 & 0 & 0 & -P^{-1} & 0 & 0 \end{bmatrix}$$

$$\tilde{A} = \hat{A}P^{-1} = \begin{bmatrix} \epsilon_1 AW & \epsilon_2 F & \epsilon_3 \tilde{L}^T C & 0 \\ 0 & 0 & -\epsilon_3 \tilde{Q}^T C & 0 \\ 0 & 0 & \epsilon_3 AW + \epsilon_3 \tilde{L}^T C & \epsilon_4 F \\ 0 & 0 & -\epsilon_3 \tilde{Q}^T C & 0 \end{bmatrix}, \tilde{B} = P^{-1} M^T \hat{B}^T = \begin{bmatrix} 0 & 0 & 0 & 0 \\ 0 & 0 & 0 & 0 \\ 0 & 0 & \epsilon_3 \tilde{K} B^T & 0 \\ 0 & 0 & -\epsilon_4 G^T B^T & 0 \end{bmatrix}$$

$$\tilde{B}_1 = P_1^{-1} \hat{B}^T = \begin{bmatrix} 0 & 0 & \epsilon_3 \tilde{K} B^T & 0 \\ 0 & 0 & -\epsilon_4 G^T B^T & 0 \end{bmatrix}, \tilde{\Theta}_i = P^{-1} \Theta_i P^{-1}, (i = 1, 2, 3)$$

$$\tilde{C} = P^{-1} \hat{C}^T = \begin{bmatrix} \epsilon_1 \bar{\alpha} C^T \tilde{L} & -\epsilon_1 \bar{\alpha} C^T \tilde{Q} & \epsilon_1 \bar{\alpha} C^T \tilde{L} & -\epsilon_1 \bar{\alpha} C^T \tilde{Q} \\ 0 & 0 & 0 & 0 \\ -\epsilon_1 \bar{\alpha} C^T \tilde{L} & \epsilon_1 \bar{\alpha} C^T \tilde{Q} & -\epsilon_1 \bar{\alpha} C^T \tilde{L} & \epsilon_1 \bar{\alpha} C^T \tilde{Q} \\ 0 & 0 & 0 & 0 \end{bmatrix}$$

$$P^{-1} = \begin{bmatrix} \epsilon_1 W & 0 & 0 & 0 \\ 0 & \epsilon_2 I & 0 & 0 \\ 0 & 0 & \epsilon_3 W & 0 \\ 0 & 0 & 0 & \epsilon_4 I \end{bmatrix}, P_1^{-1} = \begin{bmatrix} \epsilon_3 W & 0 \\ 0 & \epsilon_4 I \end{bmatrix}.$$

Proof: For the matrix $C^T \in \mathbb{R}^{n\times l}$ of the full column rank, there exist two orthogonal matrices $J \in \mathbb{R}^{n\times n}$ and $Y \in \mathbb{R}^{l\times l}$ such that

$$JC^TY = \begin{bmatrix} J_1 \\ J_2 \end{bmatrix} C^TY = \begin{bmatrix} \Delta \\ 0 \end{bmatrix} \tag{17}$$

where $J_1 \in R^{l\times n}$, $J_2 \in R^{(n-l)\times n}$, and $\Delta = \text{Diag}\{\sigma_1, \cdots, \sigma_l\}$ for $\sigma_1, \cdots, \sigma_l$ being nonzero singular values of C^T. Constructing the following matrix W,

$$W = J^T \begin{bmatrix} W_{11} & 0 \\ 0 & W_{22} \end{bmatrix} J = J_1^T W_{11} J_1 + J_2^T W_{22} J_2 \tag{18}$$

where W_{11} and W_{22} are symmetric positive definite matrices with J_1 and J_2 defined in (17).

It follows from Lemma 1 that for the full column rank matrix $C^T \in \mathbb{R}^{n\times l}$, there exists the nonsingular matrix N such that $WC^T = C^TN$ holds. The inequality (16) is verified by the premultiplication and postmultiplication of (11) with Γ and Γ^T, respectively. The correlation matrices are constructed as follows:

$$\Gamma_1 = \text{Diag}\{\underbrace{P^{-1}, \cdots P^{-1}}_{6}, P_1^{-1}, I\}, \Gamma_2 = \text{Diag}\{P^{-1}, P^{-1}, P^{-1}\}, \Gamma = \text{Diag}\{\Gamma_1, \Gamma_2, \Gamma_2, \Gamma_2\}$$

Finally, solving the LMI (16) and the following equation (19) enables the determination of the extended state observer gain matrices Q, L and the controller gain matrix K within the co-design framework of FE and FTC.

$$Q = \tilde{Q}^T N^{-T}, L = \tilde{L}^T N^{-T}, K = \tilde{K}^T W^{-1} \tag{19}$$

The proof is completed.

4. SIMULATION

In this section, since the forward speed is the key parameter, simulations are conducted under two distinct scenarios: low speed and high speed of the USV. The parameters corresponding to the low-speed V = 3.8 m/s and high-speed V = 7.8 m/s configurations are delineated in Table 1. To align with practical scenarios and demonstrate the proposed algorithm's robustness to initial condition deviations, the initial state of the USV is set as $x(0) = \begin{bmatrix} 0.8 & -0.5 & 0.5 & -0.5 & 0.6 \end{bmatrix}^T$.

The system matrices A, B, E in (3) derived from the parameters in Table 1 are shown in Table 2. It is noteworthy that in both scenarios, the system matrix C and the fault coefficient matrix F in (2) are chosen to be the same. At the same time, C satisfies the full column rank condition in Assumption 2. The specific values of C and F are also shown in Table 2. According to Lemma 1, the correlation matrices with the singular value decomposition of the matrix C manifest as follows.

$$\begin{aligned} J_1 &= \begin{bmatrix} 0.5000 & -0.4000 & -0.5000 & 0.5000 & -0.3000 \end{bmatrix}, N = 1, \\ J_2 &= \begin{bmatrix} 0.4000 & 0.8933 & -0.1333 & 0.1333 & -0.0800 \\ 0.5000 & -0.1333 & 0.8333 & 0.1667 & -0.1000 \\ -0.5000 & 0.1333 & 0.1667 & 0.8333 & 0.1000 \\ 0.3000 & -0.0800 & -0.1000 & 0.1000 & 0.9400 \end{bmatrix}, \Delta = 2. \end{aligned} \tag{20}$$

Table 1. The relevant parameters of USV under the two scenarios [37]

Lowforwardspeed	Highforwardspeed
$T_v = 2/V, T_r = 1.6/V, K_{av} = 0.01V,$ $K_{ar} = -0.0027V, K_{ap} = -0.0014V^2,$ $K_{vp} = 0.21V, K_{vr}$ = -0.46 m/s, ω_n = 1.63 rad/s, ζ = 0.64 + 0.38V	$T_v = 1.8/V, T_r = 2/V, K_{av} = 0.06V,$ $K_{ar} = -0.0036V, K_{ap} = -0.0022V^2,$ $K_{vp} = 0.16V, K_{vr}$ = -0.58 m/s, ω_n = 2.2 rad/s, ζ = 0.58 + 0.67V

Table 2. The system matrices of USV under the two scenarios

Low forward speed	High forward speed
$A = \begin{bmatrix} -1.9000 & 0 & 0 & 0 & 0 \\ -1.0925 & -2.3750 & 0 & 0 & 0 \\ 0 & 1.0000 & 0 & 0 & 0 \\ 2.1202 & 0 & 0 & -6.7938 & -2.6569 \\ 0 & 0 & 0 & 1.0000 & 0 \end{bmatrix}$	$A = \begin{bmatrix} -4.3333 & 0 & 0 & 0 & 0 \\ -2.2620 & -3.9000 & 0 & 0 & 0 \\ 0 & 1.0000 & 0 & 0 & 0 \\ 6.0403 & 0 & 0 & -25.5464 & -4.8400 \\ 0 & 0 & 0 & 1.0000 & 0 \end{bmatrix}$
$B = \begin{bmatrix} 0.0722 & -0.0244 & 0 & -0.0537 & 0 \end{bmatrix}^T$	$B = \begin{bmatrix} 2.0280 & -0.1095 & 0 & -0.6478 & 0 \end{bmatrix}^T$
$C = \begin{bmatrix} 1 & 0.8 & 1 & -1 & 0.6 \end{bmatrix}$	$C = \begin{bmatrix} 1 & 0.8 & 1 & -1 & 0.6 \end{bmatrix}$
$E = \begin{bmatrix} 0 & 2.3750 & 0 & 0 & 0 \\ 0 & 0 & 0 & 2.6569 & 0 \end{bmatrix}^T$	$E = \begin{bmatrix} 0 & 3.9000 & 0 & 0 & 0 \\ 0 & 0 & 0 & 4.8400 & 0 \end{bmatrix}^T$
$F = \begin{bmatrix} 0.6 & -1 & 2 & 0.8 & 1 \end{bmatrix}^T$	$F = \begin{bmatrix} 0.6 & -1 & 2 & 0.8 & 1 \end{bmatrix}^T$

The disturbances are selected as $\omega_\psi(t) = \omega_1(t)0.9s/(s^2 + 2.2s + 1)$ and $\omega_\phi(t) = 0.15\cos(t)$, where ω_1 represent a vector of zero-mean Gaussian white noises. The upper bound of the delays on the SO and OC channels is selected as $\beta_M = 0.2, \sigma_M = 0.1, \theta_M = 0.15$. For Bernoulli deception attacks on the OC channel, the probability is set to $\bar{\rho} = 0.3$ and a smooth nonlinear function $\tanh(\cdot)$ is introduced to characterize the attacks. The specific forms of the deception attacks are as follows.

$$\aleph\left(\hat{f}(t)\right) = -\tanh\left(0.2\hat{f}(t)\right), \aleph(\hat{x}(t)) = \begin{pmatrix} -\tanh(0.3\hat{x}_1(t)) \\ -\tanh(0.6\hat{x}_2(t)) \\ -\tanh(0.5\hat{x}_3(t)) \\ -\tanh(0.4\hat{x}_4(t)) \\ -\tanh(0.8\hat{x}_5(t)) \end{pmatrix} \tag{21}$$

According to Theorem 2, the relevant parameters given are set as $\gamma = 1.2, \epsilon_1 = 0.6, \epsilon_2 = 1.8, \epsilon_3 = 0.9, \epsilon_4 = 1.8$. The gain matrices L and Q of the observer and the gain matrices K and G of the controller are obtained by solving inequality 16 and equation 19, as shown in Table 3.

To assess the efficacy of the algorithm when the USV faces the above multiple cyber-physical threats, four comparative simulation cases under two scenarios are given. In all subsequent experiments, the units of the components of the state vector $x(t)$ are $v(t)(m/s)$, $r(t)(rad/s)$, $\psi(t)(rad)$, $p(t)(rad/s)$ and $\phi(t)(rad)$.

Case 1: In this situation, the USV is solely considered to face pure physical threats such as noise-type faults and disturbances. The specific form of noise-type fault is as follows. The state response $x(t)$ of the USV under noise-type actuator faults and disturbances is illustrated in Figure 3. Upon observation of the Figure 3, it is evident that the USV under the high-speed condition is significantly affected by disturbances and noise-type faults, resulting in a longer time for the system to achieve asymptotic stability compared to the low-speed condition. Nevertheless, across both low- and high-speed scenarios, the curves converge to bounded within a certain period of time, which verifies the effectiveness of the proposed algorithm in USV against physical threats.

Table 3. The correlation gain matrices of FE and FTC co-design under the two scenarios

Low forward speed	High forward speed
$Q = 0.65,\ G = 1.35$	$Q = 0.35,\ G = 1.05$
$L = \begin{bmatrix} -3.1626 & -1.5543 & 0.9668 & 0.9255 & -2.3214 \end{bmatrix}^T$	$L = \begin{bmatrix} -3.1530 & -1.0647 & 0.7674 & 1.0257 & -2.5214 \end{bmatrix}^T$
$K = \begin{bmatrix} 0.3642 & -1.3235 & 1.5725 & 0.4126 & 1.2125 \end{bmatrix}$	$K = \begin{bmatrix} 0.2642 & -1.2325 & 2.1125 & 0.3924 & 1.1225 \end{bmatrix}$

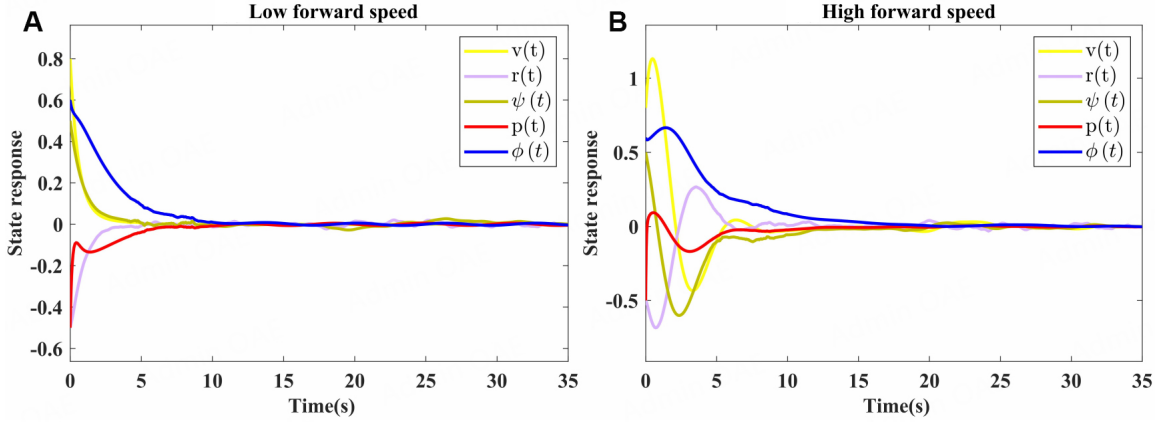


Figure 3. The state response $x(t)$ to disturbances and noise-type faults under two scenarios.

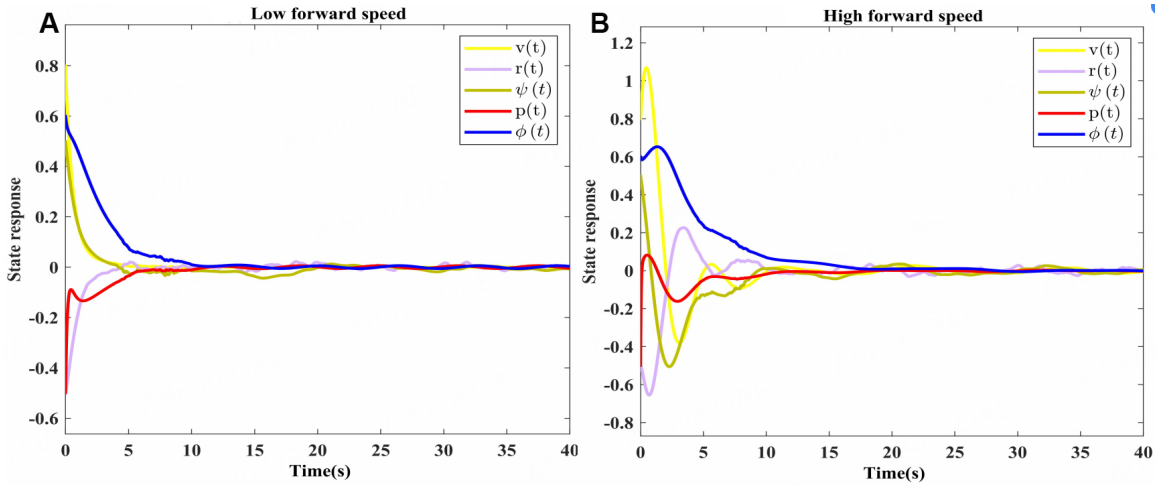


Figure 4. The state response $x(t)$ to noise-type actuator faults, disturbances, time-varying delays and constant injection attacks under two scenarios.

$$f(t) = \begin{cases} 0.3\omega_1(t)\sin(\mathrm{t}), & \mathrm{t} \in [4\mathrm{s}, 10\mathrm{s}] \\ 0, & \text{otherwise} \end{cases} \tag{22}$$

Case 2: This case is based on Case 1 to verify the effectiveness of the algorithm in the case of constant injection attacks and time-varying delays occurring within SO channel. The state response $x(t)$ of the USV under noise-type actuator faults, disturbances, time-varying delays and constant injection attacks is illustrated in Figure 4. Figure 4 shows that the curve fluctuates more frequently when the SO channel suffers from time-varying delays and constant injection attacks, but even under the high-speed scenario, the state response $x(t)$ still starts to stabilize at about 20s under the influence of the proposed algorithm.

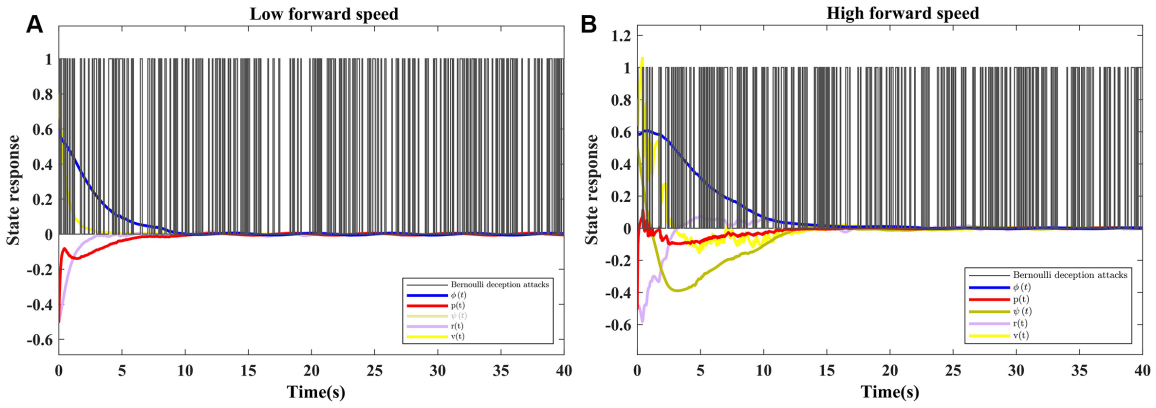


Figure 5. The state response $x(t)$ to noise-type actuator faults, disturbances, and dual-channel asynchronous injection and deception attacks under two scenarios.

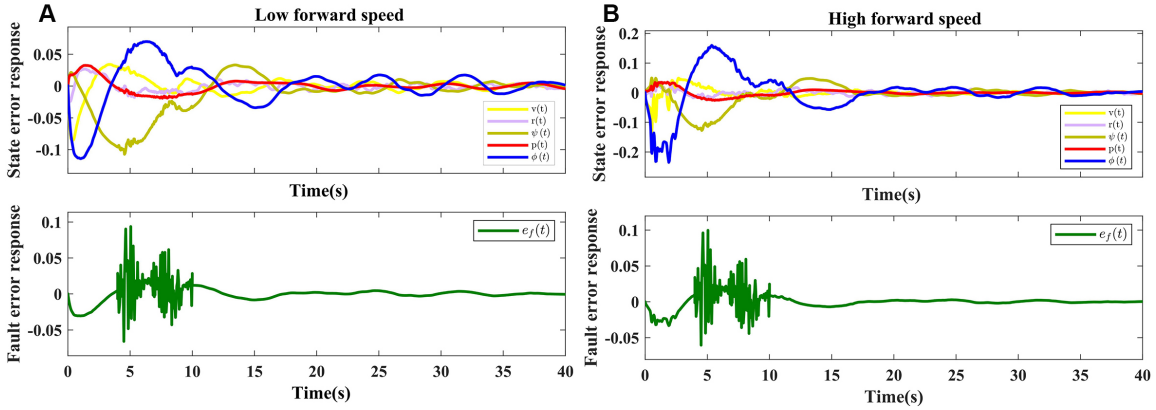


Figure 6. The state error response $e_x(t)$ and the fault error response $e_f(t)$ to noise-type actuator faults, disturbances, and dual-channel asynchronous injection and deception attacks under two scenarios.

Case 3: Based on Case 2, this case considers the existence of Bernoulli deception attacks and time-varying delays on OC channel, thus forming dual-channel asynchronous independent injection and deception attacks. Figure 5 illustrates the trend of the state $x(t)$ of the USV in the face of multiple cyber-physical threats (noise-type actuator faults, disturbances, dual-channel asynchronous independent injection and deception attacks) under the two scenarios. It can be seen from Figure 5 that even though Bernoulli deception attacks occur frequently, the state of the USV tends to be stable quickly and fluctuates less under both low- and high-speed scenarios, which verifies the feasibility of the proposed algorithm. Figure 6 illustrates the state estimation error $e_x(t)$ and FE error $e_f(t)$ of the USV under the two scenarios, respectively. It can be seen from Figure 6 that both the state estimation error $e_x(t)$ and the FE error $e_f(t)$ only fluctuate within a small range regardless of the low or high speed, even with many influences, thus demonstrating the good performance of the extended state observer proposed in this paper. Figure 7 illustrates the variation in the control input response $u(t)$ of the USV under the specified physical threat scenario. It is observed that as the USV's state reaches stabilization, the control input progressively stabilizes. It is noteworthy that the inclusion of disturbances and integrators within the simulation framework leads to the generation of FE even in the absence of actual faults.

Case 4: In this situation, firstly, the noise-type actuator faults in case 3 are replaced with stuck steering mechanism-type faults. Figure 8 and Figure 9 show the state response $x(t)$ and the error response $e_x(t)$ and $e_f(t)$ under the influence of stuck steering mechanism-type faults, disturbance, dual-channel asynchronous constant injection and Bernoulli deception attacks, respectively. Compared with the noise-type faults in Case

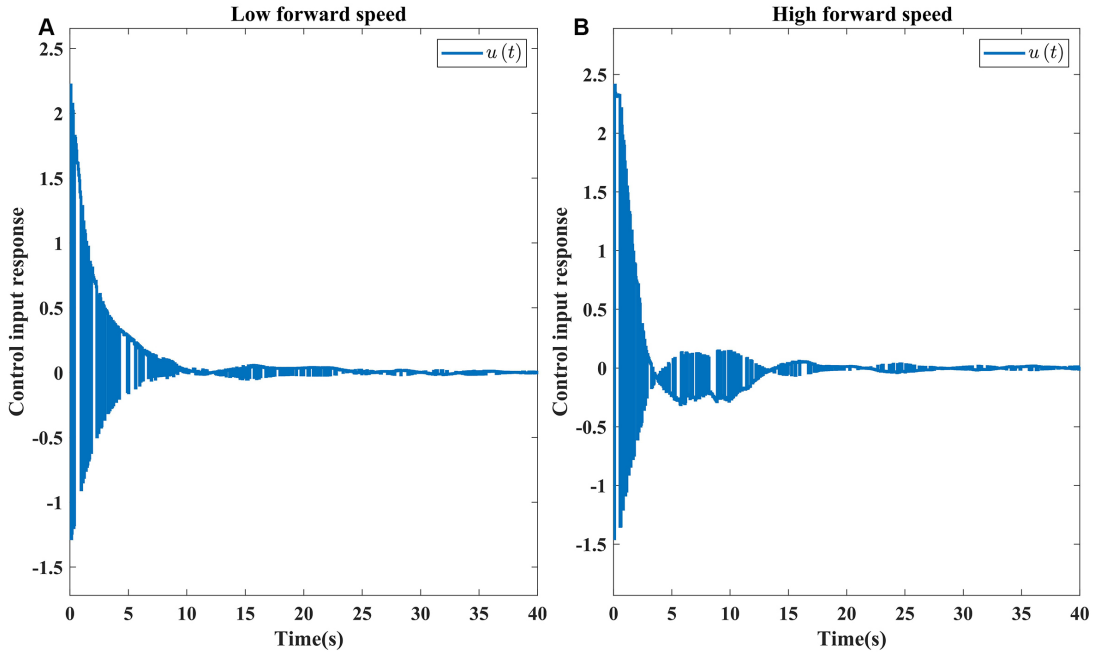


Figure 7. The control input response $u(t)$ under two scenarios.

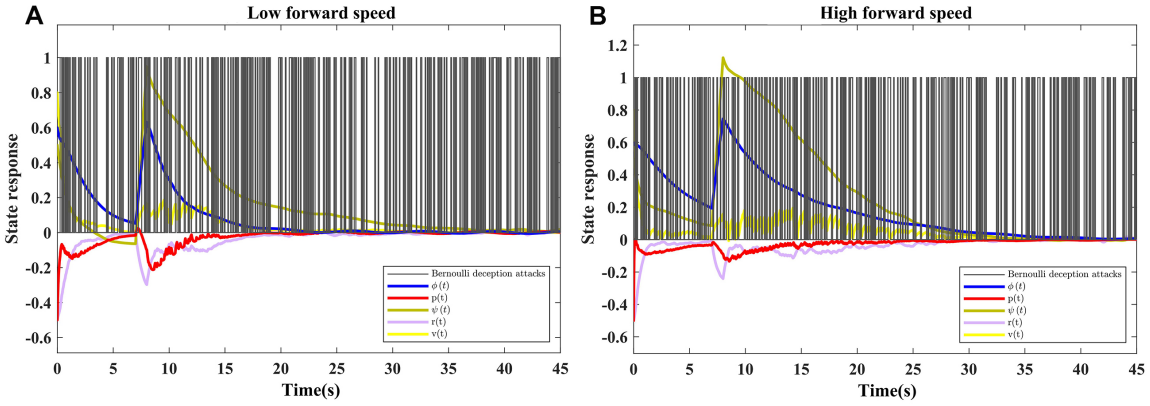


Figure 8. The error response $x(t)$ to stuck steering mechanism-type faults, disturbances, and dual-channel asynchronous injection and deception attacks under two scenarios.

3, the abrupt change of the stuck steering mechanism-type faults makes the stability of the USV more difficult, but the algorithm proposed in this paper still makes the USV tend to be stable in a certain period of time under the two scenarios. At the same time, the stuck steering mechanism-type faults also make the convergence of estimation error become relatively slow in the high-speed scenario. Secondly, in order to better characterize the impact of injection attacks, the constant injection attacks are replaced by time-varying or adaptive injection attacks. The specific forms of the stuck steering mechanism-type faults and the two types of injection attacks are as follows. It can be seen from Figure 10 and Figure 11 that the existence of time-varying injection attacks makes the state response $x(t)$ and error responses $e_x(t)$ and $e_f(t)$ fluctuate more sharply, but these fluctuations are still maintained in a tolerable range. Figure 12 and Figure 13 show that the adopted FTC scheme based on the extended state observer performs well against the adaptive injection attack.

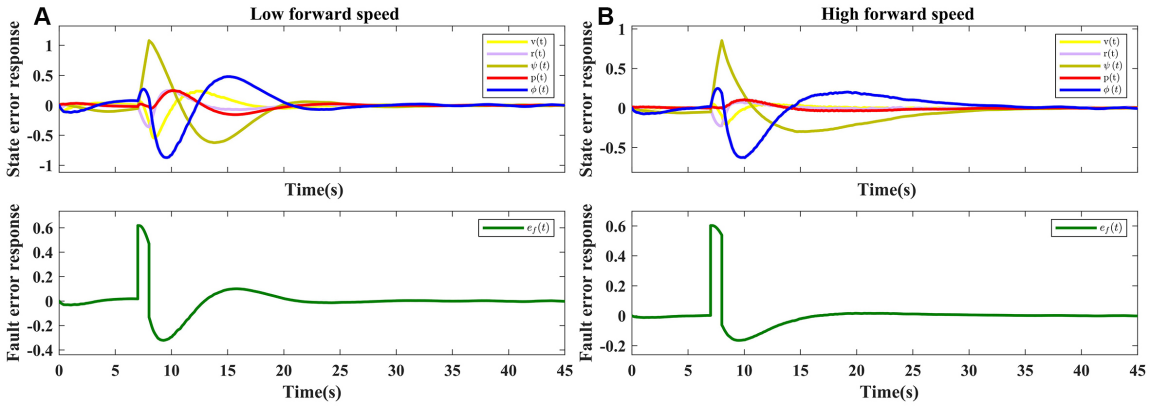


Figure 9. The error response $e_x(t)$ and $e_f(t)$ to stuck steering mechanism-type faults, disturbances, and dual-channel asynchronous injection and deception attacks under two scenarios.

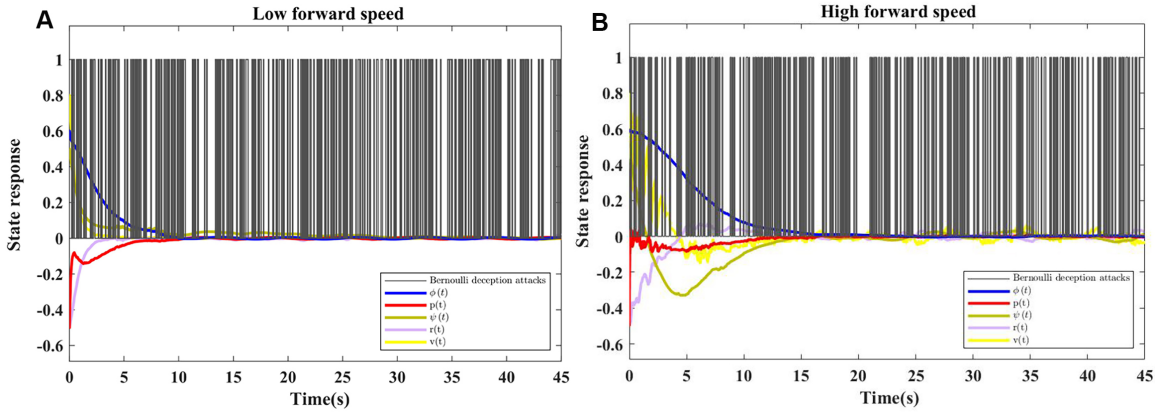


Figure 10. The state response $x(t)$ to noise-type faults, disturbances, and dual-channel asynchronous time-varying injection and deception attacks under two scenarios.

$$\begin{cases} \alpha = 0.1\sin t \\ \dot{\alpha} = -2\alpha + 3\omega_2 \end{cases}, f(t) = \begin{cases} 0.6, \ t \in [7\text{s}, 8\text{s}] \\ 0, \quad \text{otherwise} \end{cases} \tag{23}$$

where ω_2 is also a Gaussian white noise with variance 1.

5. CONCLUSIONS

A co-design method of FE and FTC for an underactuated USV under actuator faults, disturbances and cyber threats is proposed in this paper to achieve the smooth movement of the USV. To address the delays, uncertainties, and signal disruptions caused by dual-channel independent asynchronous injection and deception attacks, an extended state observer and a fault-tolerant controller were constructed using the compromised information, ensuring robust control of the USV under multiple cyber-physical threats. Utilizing the Lyapunov-Krasovskii functional, a sufficient condition for the integrated design was derived, and a method for eliminating equality constraints was proposed to overcome the challenges of solving nonlinear matrix inequalities. Simulation results validate the efficacy of the extended state observer-based FTC approach.This study advances theoretical foundations for the design of integrated FTC strategies and stability analysis of USVs under multi-layered adverse conditions. At the same time, it provides valuable insights for USVs to reliably navigate in modern complex network environments. Prospective research is encouraged to introduce the idea

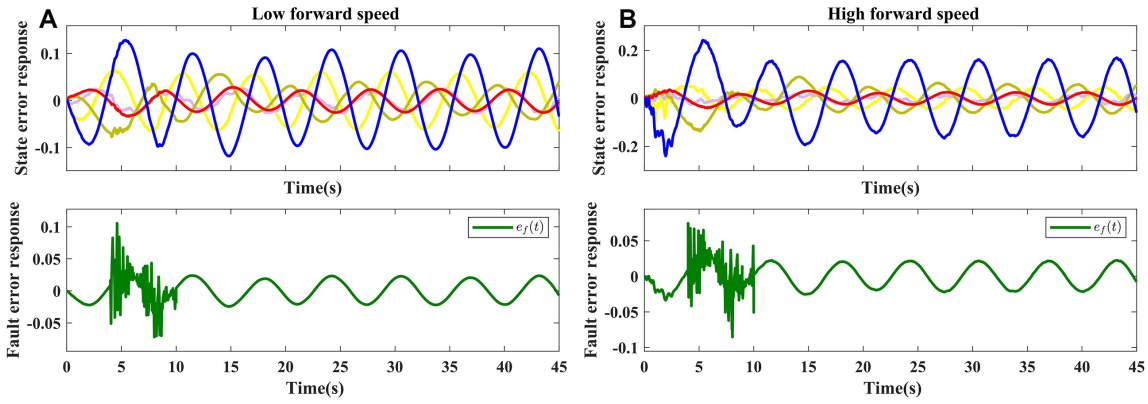


Figure 11. The error response $e_x(t)$ and $e_f(t)$ to noise-type faults, disturbances, and dual-channel asynchronous time-varying injection and deception attacks under two scenarios.

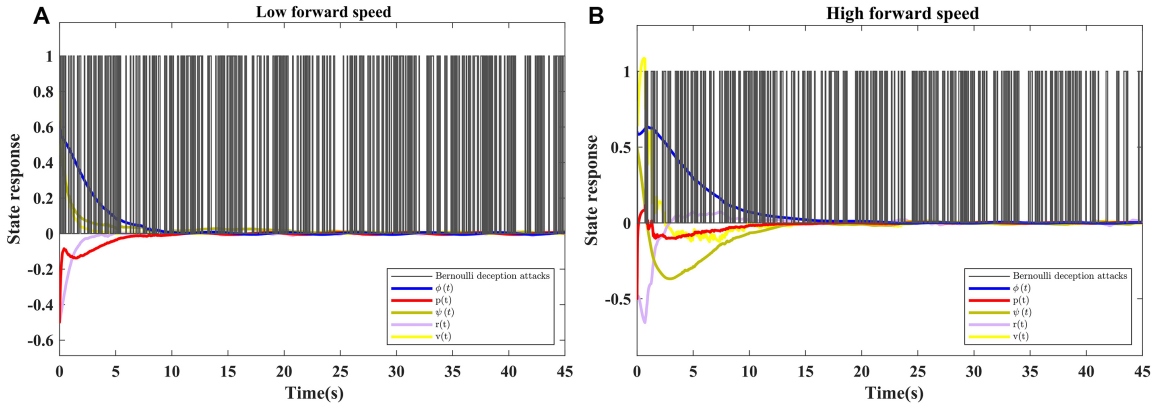


Figure 12. The state response $x(t)$ to noise-type faults, disturbances, and dual-channel asynchronous adaptive injection and deception attacks under two scenarios.

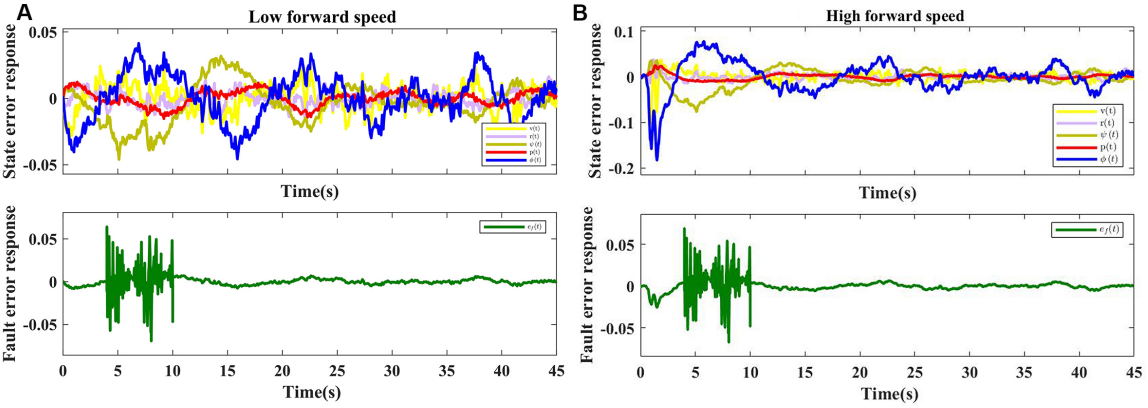


Figure 13. The error response $e_x(t)$ and $e_f(t)$ to noise-type faults, disturbances, and dual-channel asynchronous adaptive injection and deception attacks under two scenarios.

of the co-design into the cooperative control scenario of multi-USVs, aiming to enhance overall performance amidst the presence of diverse cyber-physical threats. In addition, insights from advanced control methods, such as reinforcement learning[38], can further enhance the adaptability of USVs in complex environments.

DECLARATIONS

Authors' contributions

Writing-original draft and conceptualization: Wang H, Liu C
Technical support: Huang X, Zhong Y, Qu D
Validation and supervision: Patton RJ

Availability of data and materials

Not applicable.

Financial support and sponsorship

This work was supported by the National Natural Science Foundation of China (62103250, 62273223, 62333011, and 62336005); Shanghai Sailing Program (21YF1414000); Project of Science and Technology Commission of Shanghai Municipality, China (22JC1401401); Joint Research Fund of Shanghai Academy of Spaceflight Technology (USCAST2023-22).

Conflicts of interest

Chun Liu and Ron J. Patton are the guest editors of the Special Issue of "Advancements in Fault-Tolerant Control and Security of Complex Systems", while the other authors have declared that they have no conflicts of interest.

Ethical approval and consent to participate

Not applicable.

Consent for publication

Not applicable.

Copyright

© The Author(s) 2024.

REFERENCES

1. Rao J, Xu X, Bian H, et al. A modified random network distillation algorithm and its application in USVs naval battle simulation. *Ocean Eng* 2022;261:112147. DOI
2. Rumson AG. The application of fully unmanned robotic systems for inspection of subsea pipelines. *Ocean Eng* 2021;235:109214. DOI
3. Wu J, Li R, Li J, Zou M, Huang Z. Cooperative unmanned surface vehicles and unmanned aerial vehicles platform as a tool for coastal monitoring activities. *Ocean Coastal Manage* 2023;232:106421. DOI
4. Er MJ, Ma C, Liu T, Gong H. Intelligent motion control of unmanned surface vehicles: a critical review. *Ocean Eng* 2023;280:114562. DOI
5. Zhang X, Xu X, Li J, et al. Observer-based fuzzy adaptive fault-tolerant control for NSC system of USV with sideslip angle and steering machine fault. *IEEE Trans Intell Veh* 2024;9:372-82. DOI
6. Meng X, Zhang G, Han B. Robust adaptive finite-time course tracking control of vessel under actuator attacks. *Complex Eng Syst* 2023;3:12 DOI
7. He S, Dai SL, Luo F. Asymptotic trajectory tracking control with guaranteed transient behavior for MSV with uncertain dynamics and external disturbances. *IEEE Trans Ind Electron* 2019;66:3712-20. DOI
8. Zhang G, Chu S, Zhang W, Liu C. Adaptive neural fault-tolerant control for USV with the output-based triggering approach. *IEEE Trans Veh Technol* 2022;71:6948-57. DOI
9. Yu XN, Hao LY. Integral sliding mode fault tolerant control for unmanned surface vessels with quantization: less iterations. *Ocean Eng* 2022;260:111820. DOI
10. Wu W, Li Y, Tong S. Neural network output-feedback consensus fault-tolerant control for nonlinear multiagent systems with intermittent actuator faults. *IEEE Trans Neural Netw Learn Syst* 2023;34:4728-40. DOI
11. Zhao XQ, Guo S, Long Y, Zhong GX. Simultaneous fault detection and control for discrete-time switched systems under relaxed persistent dwell time switching. *Appl Math Comput* 2022;412:126585. DOI
12. Li JN, Feng H, Wang Y, Liu GY. A novel failure-distribution-dependent non-fragile H_∞ fault-tolerant load frequency control for faulty multi-area power systems. *IEEE Trans Power Syst* 2024;39:2936-46. DOI
13. Zhou Z, Zhong M, Wang Y. Fault diagnosis observer and fault-tolerant control design for unmanned surface vehicles in network environ-

ments. *IEEE Access* 2019;7:173694-702. DOI
14. Wang N, Deng Z. Finite-time fault estimator based fault-tolerance control for a surface vehicle with input saturations. *IEEE Trans Ind Inform* 2020;16:1172-81. DOI
15. Li K, Feng K, Li Y. Fuzzy adaptive fault-tolerant formation control for USVs with intermittent actuator faults. *IEEE Trans Intell Veh* 2024:1-10. DOI
16. Wan L, Cao Y, Sun Y, Qin H. Fault-tolerant trajectory tracking control for unmanned surface vehicle with actuator faults based on a fast fixed-time system. *ISA Trans* 2022;130:79-91. DOI
17. Li J, Zhang G, Zhang X, Zhang W. Integrating dynamic event-triggered and sensor-tolerant control: application to USV-UAVs cooperative formation system for maritime parallel search. *IEEE Trans Intell Transp Syst* 2023:1-13. DOI
18. Hao LY, Yu Y, Li TS, Li H. Quantized output-feedback control for unmanned marine vehicles with thruster faults via sliding-mode technique. *IEEE Trans Cybern* 2022;52:9363-76. DOI
19. Zhang G, Liu S, Zhang X. Adaptive distributed fault-tolerant control for underactuated surface vehicles with bridge-to-bridge event-triggered mechanism. *Ocean Eng* 2022;262:112205. DOI
20. Meng X, Zhang G, Han B. Fault-tolerant control of underactuated MSVs based on neural finite-time disturbance observer: an event-triggered mechanism. *J Frankl Inst Eng Appl Math* 2024;361:106603. DOI
21. Liu Q, Cai Z, Chen J, Jiang B. Observer-based integral sliding mode control of nonlinear systems with application to single-link flexible joint robotics. *Complex Eng Syst* 2021;1:8 DOI
22. Zeng H, Su Z, Xu Q, Li R. Security and privacy in space-air-ocean integrated unmanned surface vehicle networks. *IEEE Netw* 2024;38:48-56. DOI
23. Liu C, Jiang B, Wang X, Zhang Y, Xie S. Event-based distributed secure control of unmanned surface vehicles with DoS attacks. *IEEE Trans Syst Man Cybern Syst* 2024;54:2159-70. DOI
24. Ma Y, Nie Z, Hu S, et al. Fault detection filter and controller co-design for unmanned surface vehicles under DoS attacks. *IEEE Trans Intell Transp Syst* 2021;22:1422-34. DOI
25. Liu C, Xia Z, Tian Y, Patton RJ. Defense and tolerance technique against attacks and faults on leader-following multi-USVs. *IEEE Trans Intell Transp Syst* 2024;25:5450-61. DOI
26. Zhang D, Ye Z, Feng G, Li H. Intelligent event-based fuzzy dynamic positioning control of nonlinear unmanned marine vehicles under DoS attack. *IEEE Trans Cybern* 2022;52:13486-99. DOI
27. Gao S, Peng Z, Liu L, Wang H, Wang D. Coordinated target tracking by multiple unmanned surface vehicles with communication delays based on a distributed event-triggered extended state observer. *Ocean Eng* 2021;227:108283. DOI
28. Lei T, Wen Y, Yu Y, Tian K, Zhu M. Predictive trajectory tracking control for the USV in networked environments with communication constraints. *Ocean Eng* 2024;298:117185. DOI
29. Nemati A, Peimani M, Mobayen S, Sayyedfattahi S. Adaptive non-singular finite time control of nonlinear disturbed cyber-physical systems with actuator cyber-attacks and time-varying delays. *Inf Sci* 2022;612:1111-26. DOI
30. Fei Z, Wang X, Wang Z. Event-based fault detection for unmanned surface vehicles subject to denial-of-service attacks. *IEEE Trans Syst Man Cybern Syst* 2022;52:3326-36. DOI
31. Wu C, Zhu G, Lu J. Indirect adaptive neural tracking control of USVs under injection and deception attacks. *Ocean Eng* 2023;270:113641. DOI
32. Yin T, Gu Z, Park JH. Event-based intermittent formation control of multi-UAV systems under deception attacks. *IEEE Trans Neural Netw Learn Syst* 2024;35:8336-47. DOI
33. Liu ZQ, Ge X, Han QL, Wang YL, Zhang XM. Secure cooperative path following of autonomous surface vehicles under cyber and physical attacks. *IEEE Trans Intell Veh* 2023;8:3680-91. DOI
34. Zhao D, Tian Y, Zhao N. Adaptive neural control for delayed discrete-time switched systems under deception attacks. *Complex Eng Syst* 2024;4:1 DOI
35. Wang D, Chen F, Meng B, Hu X, Wang J. Event-based secure $\mathcal{H}_\infty$ load frequency control for delayed power systems subject to deception attacks. *Appl Math Comput* 2021;394:125788. DOI
36. Dai S, Zha L, Liu J, Xie X, Tian E. Fault detection filter design for networked systems with cyber attacks. *Appl Math Comput* 2022;412:126593. DOI
37. Wang YL, Han QL. Network-based fault detection filter and controller coordinated design for unmanned surface vehicles in network environments. *IEEE Trans Ind Inform* 2016;12:1753-65. DOI
38. Bai W. Introduction to discrete-time reinforcement learning control in Complex Engineering Systems. *Complex Eng Syst* 2024;4:8 DOI

Ali *et al*. *Complex Eng Syst* 2024;4:14
DOI: 10.20517/ces.2024.10

Complex Engineering Systems

Research Article

Open Access

Enhancing unmanned aerial vehicle communication through distributed ledger and multi-agent deep reinforcement learning for fairness and scalability

Farman Ali[1,2], Muhammad Ahtasham [2], Zahra Anfaal[2]

[1]School of Electronics and Information Engineering, Nanjing University of Aeronautics and Astronautics, Nanjing 211106, Jiangsu, China.
[2]Department of Electrical Engineering, Qurtuba University of Science and IT, Dera Ismail Khan 29050, Pakistan.

Correspondence to: Dr. Farman Ali, Department of Electrical Engineering, Qurtuba University of Science and IT, Dera Ismail Khan 29050, Pakistan. E-mail: drfarmanali.optics@qurtuba.edu.pk

How to cite this article: Ali F, Ahtasham M, Anfaal Z. Enhancing unmanned aerial vehicle communication through distributed ledger and multi-agent deep reinforcement learning for fairness and scalability. *Complex Eng Syst* 2024;4:14. http://dx.doi.org/10.20517/ces.2024.10

Received: 2 Mar 2024 **First Decision:** 22 May 2024 **Revised:** 22 Jun 2024 **Accepted:** 17 Jul 2024 **Published:** 25 Jul 2024

Academic Editor: Hamid Reza Karimi **Copy Editor:** Fangling Lan **Production Editor:** Fangling Lan

Abstract

Unmanned Aerial Vehicles (UAVs) are pivotal in enhancing connectivity in diverse applications such as search and rescue, remote communications, and battlefield networking, especially in environments lacking ground-based infrastructure. This paper introduces a novel approach that harnesses Multi-Agent Deep Reinforcement Learning to optimize UAV communication systems. The methodology, centered on the Independent Proximal Policy Optimization technique, significantly improves fairness, throughput, and energy efficiency by enabling UAVs to autonomously adapt their operational strategies based on real-time environmental data and individual performance metrics. Moreover, the integration of Distributed Ledger Technologies with Multi-Agent Deep Reinforcement Learning enhances the security and scalability of UAV communications, ensuring robustness against disruptions and adversarial attacks. Extensive simulations demonstrate that this approach surpasses existing benchmarks in critical performance metrics, highlighting its potential implications for future UAV-assisted communication networks. By focusing on these technological advancements, the groundwork is laid for more efficient, fair, and resilient UAV systems.

Keywords: Unmanned aerial vehicles-to-ground communication, multi-agent deep reinforcement learning, fairness and throughput, distributed ledger technologies

© The Author(s) 2023. **Open Access** This article is licensed under a Creative Commons Attribution 4.0 International License (https://creativecommons.org/licenses/by/4.0/), which permits unrestricted use, sharing, adaptation, distribution and reproduction in any medium or format, for any purpose, even commercially, as long as you give appropriate credit to the original author(s) and the source, provide a link to the Creative Commons license, and indicate if changes were made.

1. INTRODUCTION

Unmanned Aerial Vehicles (UAVs) have significantly revolutionized communication in different areas, including wireless sensor networks (WSN), cellular networks, the Internet of Things (IoT), and Space-Air-Ground Integrated Networks (SAGIN). These flexible platforms facilitate the rapid implementation of communication services to users on the ground in situations when terrestrial infrastructure is not accessible or has been compromised, including in disaster-impacted areas or conflict-ridden battlefields. UAVs are versatile and can be used for various purposes such as improving communication coverage, serving as mobile relays, enabling edge computing, and performing data collection. These applications have advanced UAV-assisted technology to the forefront of research in wireless communications and network sectors[1–4]. The benefits of UAVs are distinctive and can be credited to several significant advancements. Advancements in industrial technology have enabled the downsizing of electronic equipment, enhancing their capacity and facilitating the integration of more advanced modules on UAVs at a lower cost. Furthermore, the great mobility of UAVs allows them to be deployed in difficult terrains such as mountains and rivers, where setting up ground-based infrastructure is not feasible. This guarantees thorough and smooth communication capacities. Thirdly, UAVs provide excellent visibility for ground communication systems, minimizing signal route loss caused by barriers and improving Line-of-Sight (LoS) connections. In recent years, substantial research has been dedicated to enhancing the control systems of UAVs to address the challenges associated with their deployment. Notable among these advancements is the development of distributed adaptive fuzzy formation control for multiple UAVs, which can handle uncertainties and actuator faults while operating under switching topologies. This method utilizes fuzzy logic to adaptively manage the formation of UAVs, ensuring robust performance despite the presence of system uncertainties and potential faults[5]. Additionally, neural adaptive distributed formation control has emerged as a significant approach for managing nonlinear multi-UAV systems with unmodeled dynamics. By leveraging neural networks, this control strategy can adapt to complex, nonlinear interactions within the UAV network, ensuring stable formation control even when the system dynamics are not fully known or are subject to change. These neural adaptive methods provide a high degree of flexibility and robustness, making them suitable for dynamic and uncertain environments[6]. Furthermore, other advanced control techniques, such as Model Predictive Control (MPC) and Reinforcement Learning (RL), have been applied to UAV systems to enhance their autonomous capabilities. MPC allows UAVs to predict and optimize their trajectories based on future states, ensuring efficient navigation and collision avoidance. RL, on the other hand, enables UAVs to learn optimal control policies through interaction with their environment, adapting to new scenarios and improving performance over time[7,8]. These advancements in UAV control systems are critical for enabling UAVs to operate autonomously and efficiently in various applications, from disaster response to commercial delivery services. The integration of these sophisticated control techniques ensures that UAVs can maintain stable formations, handle dynamic changes, and operate reliably even in the presence of uncertainties and external disturbances.

1.1. Related work

Cutting-edge research is being conducted on UAV-assisted communication, fairness, and energy efficiency in wireless networks. These studies are aimed at devising new and inventive solutions and strategies to enhance the performance, reliability, and security of UAV communication systems. The[5] investigated the utilization of UAVs as aerial base stations for Ground Users (GUs) and proposes cooperative jamming by UAV jammers to counter ground eavesdroppers. It leveraged Multi-Agent Deep Reinforcement Learning (MADRL) to optimize UAV trajectories, transmit power, and jamming power. The research[6] has focused on optimizing UAV trajectories, user association, and GUs' transmit power to achieve fairness-weighted throughput.The research has emphasized the importance of balancing fairness and throughput in UAV-Base Stations (BSs)-assisted communication and introduces the UAV-Assisted Fair Communication (UAFC) algorithm based on multi-agent deep reinforcement learning[7]. Moreover, it proposes sharing neural networks to reduce decision-making uncertainty. The authors in have explored energy-efficient UAV trajectories for uplink communication and employ reinforcement learning for load balancing[8]. The challenge of secure communication in the presence

of multiple eavesdroppers is addressed in [9], and the utilization of UAV jammers and artificial noise signals is proposed. The study [10] considered fairness alongside coverage and throughput, introducing the UAFC algorithm for fair throughput optimization. Additionally, the work proposed the sharing of neural networks for distributed decision-making. The study investigated the use of UAVs as mobile relays between GUs and a macro base station, utilizing reinforcement learning for trajectory optimization [11]. The authors in [12] addressed wiretapping by ground eavesdroppers and propose cooperative jamming and multi-agent reinforcement learning as countermeasures. The study [13] has focused on the investigation of UAV-BSs for efficient wireless communication, balancing coverage, throughput, and fairness. A MADRL approach for UAV-BSs serving GUs is proposed in [14], considering fair throughput, coverage, and flight status. Additionally, in the context of integrating UAVs into 6G networks, several key areas of innovation and study have been identified, such as the exploration of UAV capabilities, base station offloading, emergency response, intelligent telecommunication, and mobile edge computing [15–18]. In addition to the current body of knowledge on UAV communication systems and their optimization through deep learning and distributed ledger (DL) technologies, it is pertinent to consider advancements in multi-agent network applications. One notable study in this domain is mentioned in [19]. This research addresses the challenges in multi-agent networks where the ability to perform collective activities is crucial. The study investigates the containment and consensus tracking problems within a network of continuous-time agents characterized by state constraints. These endeavors aim to address the challenges and opportunities associated with UAV-assisted communications, contributing to the development of efficient, secure, and scalable UAV communication systems. Several limitations exist in the current works related to UAV-to-ground communication. These limitations include fairness, complex structure, reliability, security, privacy, and scalability. Furthermore, there are other unresolved issues and limitations in the field of UAV-assisted communications that require additional research. A concern is the lack of emphasis on supporting multiple users in emergency communication situations, requiring equitable service delivery. Innovative methods are required to ensure effective cooperation and connectivity among UAVs that can maintain UAV connectivity without relying on fixed infrastructure. Centralized methodologies now in use pose notable scalability and complexity issues, highlighting the necessity for more adaptable and scalable methods in UAV communication systems. As a result, we have identified a significant research gap that needs to be addressed. To enhance UAV communication systems, we have explored the potential of DL technology and MADRL.

1.2. Major contribution

The major contribution of this paper is summarized as follows.

1. The paper proposed a new system model that utilizes multiple UAVs to provide fair communication services to ground users without ground-based stations. Our approach addresses the challenges of UAV network connectivity and equitable throughput by optimizing fair throughput and energy efficiency.

2. A MADRL framework for UAV communication scenarios is used, with an Independent Proximal Policy Optimization (IPPO) technique. This enables decentralized learning for individual observations, promoting a more in-depth investigation of tactics. The reward system encourages fairness and energy efficiency.

3. The challenges posed by limited load capacities and energy resources in UAVs are addressed through the utilization of MADRL and Distributed Ledger Technologies (DLT). The MADRL framework, specifically employing the IPPO technique, enables UAVs to optimize their energy usage and load management by making efficient, decentralized decisions based on real-time observations. The reward function within the MADRL framework is designed to incentivize energy efficiency, ensuring that UAVs conserve energy during prolonged missions. Additionally, the integration of DLT ensures secure and efficient data management, thereby reducing computational and communication overhead, which, in turn, aids in conserving energy and effectively managing load capacities.

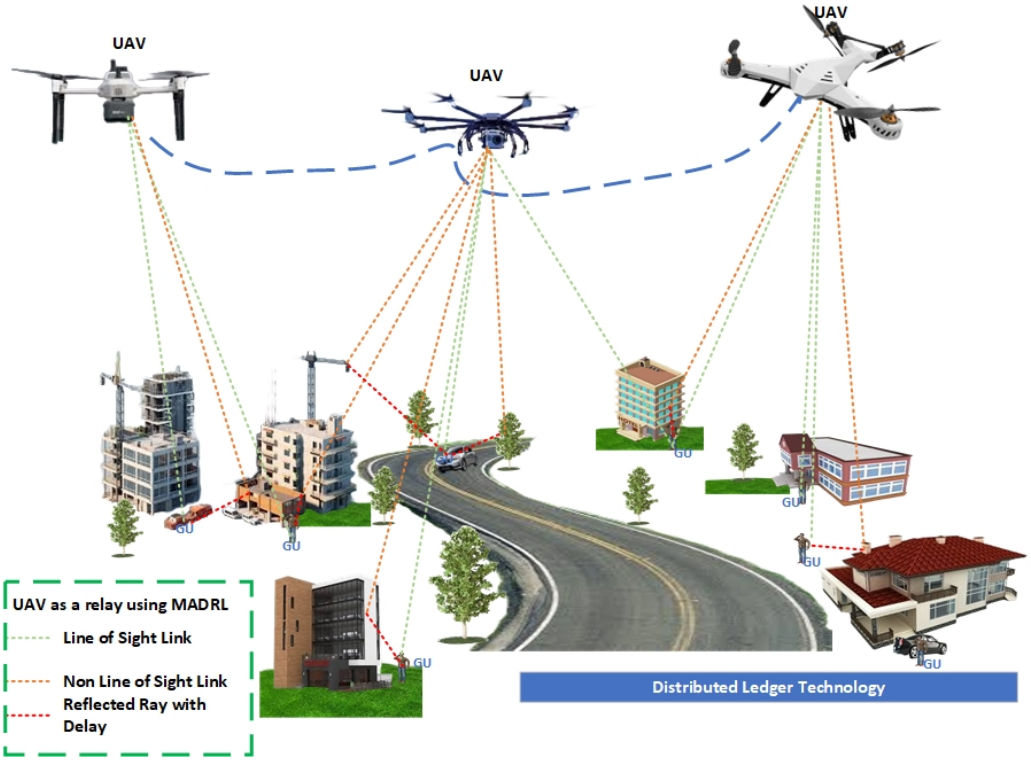


Figure 1. Proposed system model using integrated MADRL and distributed ledger techniques.

4. The MADRL-based solution incorporating DL technology has been rigorously evaluated through experimental validation and compared against traditional benchmarks. The results demonstrate superior performance in terms of fairness, throughput, and energy efficiency. Furthermore, the actual outcomes highlight notable enhancements in scalability, security, and fairness for UAV communications. This presents a substantial advancement in the field, effectively showcasing the technology's capacity to establish new standards for UAV-assisted communication systems.

The rest part of the paper is organized as follows. Section 2 develops the system model; problem formulation and objective function is explained in Section 3; Section 4 discusses the combined features of MADRL DL. Results and discussion are explored in Section 5, and finally, Section 6 provides the conclusion.

2. SYSTEM MODEL

The framework illustrated in Figure 1 presents an advanced system for communication that consists of a group of UAVs, each equipped with DLT and MADRL capabilities. The purpose of this design is to overcome the limitations of traditional communication networks, particularly in areas where conventional infrastructure is insufficient or degraded. In this innovative network, UAVs act as independent aerial relay stations, forming a robust mesh network to provide connectivity to GUs across different terrains. Each UAV m from the fleet M has a position $\mathbf{w}_{u_m}(t)$ at time t, which includes altitude H. The movement of UAVs between time slots is limited by their maximum speed V_{max} and the time slot duration δ [20,21].

$$\|\mathbf{w}_{u_m}(t) - \mathbf{w}_{u_m}(t-1)\|_2 \leq (V_{max} \cdot \delta), \quad \forall m \in M, t \in T \tag{1}$$

The UAVs manage communication links with GUs using a Time Division Multiple Access (TDMA) scheme. The binary indicator variables $\alpha_{src_{m,k}}(t)$ and $\beta_{dst_{m,k}}(t)$ denote whether a source k_{src} or destination k_{dst} GU is connected to UAV m during time slot t [22,23].

$$\alpha_{src_{m,k}}(t), \beta_{dst_{m,k}}(t) \in \{0, 1\}, \quad \forall m \in M, k \in K, t \in T \tag{2}$$

The constraints C1 and C2 for access control are expressed as

$$\sum_{m \in M} \alpha_{src_{m,k}}(t) \leq 1, \quad \forall k \in K, t \in T \tag{3}$$

$$\sum_{m \in M} \beta_{dst_{m,k}}(t) \leq 1, \quad \forall k \in K, t \in T \tag{4}$$

The integration of DLT ensures a secure and unchangeable exchange of data, while MADRL enables UAVs to make informed decisions for enhancing the network's performance. In MADRL, the Q-function is used to measure the effectiveness of a particular action taken in a specific state, represented as $\Theta(s, a)$, where s denotes the state and a represents the action. The primary goal is to optimize the policy parameters Θ such that the total future rewards are maximized. This optimization process involves using an update function U, which modifies Θ iteratively according to a specific update rule.

$$U(\Theta|s, a) = \Theta(s, a) + \Delta\Theta \tag{5}$$

The change $\Delta\Theta$ in the policy parameters is defined as

$$\Delta\Theta = \alpha \cdot \left(\mathcal{R}(s, a) + \gamma \cdot \max_{a' \sim \pi(\cdot|s')} \Theta(s', a') - \Theta(s, a) \right) \tag{6}$$

In this particular formulation, the learning rate α represents the extent to which new information overrides old information. The function $\mathcal{R}(s, a)$ provides the immediate reward after taking an action a in a particular state s. The discount factor γ balances the significance of immediate and future rewards. The policy $\pi(\cdot|s')$, which can potentially be an ϵ-greedy strategy, guides the selection of the subsequent action a' in the next state s', and the operation $\max_{a' \sim \pi(\cdot|s')}$ identifies the action that maximizes the expected Q-value given the policy π and the new state s'. By means of this mechanism, the algorithm gradually approaches an optimal policy that prescribes the best action to take in any given state to maximize long-term rewards. Dual transmitters on UAVs and Orthogonal Frequency-Division Multiple Access (OFDMA) can reduce interference with a factor η that mitigates its impact in UAV-to-UAV communication.

$$I_{total} = \sum_{i=1}^{N} \eta \cdot I_i \tag{7}$$

where I_{total} represents the overall interference experienced by a GU. The value of N refers to the total number of interfering signals, and the value of I_i is the interference generated by the $i - th$ signal. The term η (where $0 < \eta < 1$) indicates the effectiveness of interference reduction techniques.

2.1. UAV to UAV channel

In the system model illustrated in Figure 1, the communication channel between UAVs plays a crucial role in ensuring efficient data transfer in scenarios where ground infrastructure is lacking or non-existent, such as in search and rescue missions or in remote communication setups. This model addresses the challenges of providing equal access and uninterrupted connectivity among UAVs, while also taking into account the

limitations imposed by their load capacities and energy resources. The channel model is based on the principles of free space propagation, adapted to the dynamic and versatile nature of UAVs enabled by MADRL [24–26].

The channel gain or path loss between two UAVs, m_i and m_j, at a particular time slot t, is characterized by the following equation, which adheres to the free space propagation model.

$$g_{m_i,m_j}(t) = \frac{p_0}{\|\mathbf{w}_{m_i}(t) - \mathbf{w}_{m_j}(t)\|^2} \tag{8}$$

where p_0 is the channel gain at a reference distance of one meter under ideal conditions, $\mathbf{w}_{m_i}(t)$ and $\mathbf{w}_{m_j}(t)$ represent the position vectors of UAV m_i and m_j at time slot t, respectively. The expression $\|\mathbf{w}_{m_i}(t) - \mathbf{w}_{m_j}(t)\|$ stands for the Euclidean distance between two UAVs at time t, which reflects the spatial connection impacting signal quality. The signal-to-noise ratio (SNR) at UAV m_j caused by the transmission from UAV m_i is determined to handle communication links and potential interference when many UAVs are operating close to each other.

$$\gamma_{m_i,m_j}(t) = \frac{P_{max} \cdot g_{m_i,m_j}(t)}{n_0 \cdot b_u} \tag{9}$$

where P_{max} is the maximum transmit power of the UAV, determining the strength of the transmitted signal; n_0 is the noise spectral density, reflecting the background noise level that can impact signal reception and b_u signifies the bandwidth allocated for the UAV-to-UAV communication link, which influences the data rate.

To maintain the quality of the communication link, the communication strategy must keep the SNR above a predetermined threshold. This creates a communication range R_c that serves as a key distance for UAVs to communicate efficiently. When the distance between two UAVs exceeds R_c, signal quality may drop, affecting the reliability of the communication link.

Using MADRL, each UAV independently changes its position and communication settings to optimize the network's total data transfer rate while ensuring equal treatment of all GUs being serviced. The MADRL architecture, via its IPPO technique, enables individual observation-based learning to tackle the non-convex nature and hybrid variable difficulties found in traditional systems. Integrating DLT into this architecture enhances security and immutability by openly and permanently recording all communication transactions.

2.1.1 Handling NLoS conditions

In urban environments where obstacles are prevalent, Non-Line-of-Sight (NLoS) conditions are common and significantly influence UAV-to-UAV communication. To address this, our model incorporates both LoS and NLoS conditions by adapting the path loss model accordingly. The probability of LoS $P_{LoS_{m_i,m_j}}$ and NLoS $P_{NLoS_{m_i,m_j}}$ conditions is modeled based on environmental factors such as building density and height. The average path loss $PL_{m_i,m_j}(t)$ considering both LoS and NLoS conditions is given by

$$PL_{m_i,m_j}(t) = P_{LoS_{m_i,m_j}} \times PL_{LoS_{m_i,m_j}} + P_{NLoS_{m_i,m_j}} \times PL_{NLoS_{m_i,m_j}} \tag{10}$$

where $P_{LoS_{m_i,m_j}}$ is the probability of LoS condition, $P_{NLoS_{m_i,m_j}} = 1 - P_{LoS_{m_i,m_j}}$ is the probability of NLoS condition, $PL_{LoS_{m_i,m_j}}$ is the path loss under LoS condition, and $PL_{NLoS_{m_i,m_j}}$ is the path loss under NLoS condition.

The path loss values for LoS and NLoS conditions are calculated based on empirical models suitable for urban environments. The LoS probability $P_{LoS_{m_i,m_j}}$ is influenced by the elevation angle θ_{m_i,m_j} and the density of obstacles, modeled as:

$$P_{LoS_{m_i,m_j}} = \frac{1}{1 + a\exp(-b(\theta_{m_i,m_j} - a))} \tag{11}$$

where a and b are constants that depend on the urban environment.

2.2. UAV-to-ground channel

The UAV-to-ground channel in the proposed model includes the probability of LoS communication, which is essential for signal strength and reliability and is influenced by the environment. Urban environments with many buildings tend to have a lower LoS probability compared to open rural areas. The probability is modeled as

$$P_{LoS_{k(\cdot),m(t)}} = \frac{1}{1 + a\exp(-b(\theta_{k(\cdot),m[t]} - a))} \tag{12}$$

where a and b are environment-dependent constants, and θ represents the elevation angle between the GU and the UAV. The average path loss considers both LoS and NLoS conditions, and is calculated as

$$PL_{k(\cdot),m(t)} = P_{LoS_{k(\cdot),m(t)}} \times PL_{LoS_{k(\cdot),m(t)}} + (1 - P_{LoS_{k(\cdot),m(t)}}) \times PL_{NLoS_{k(\cdot),m(t)}} \tag{13}$$

The path loss for both LoS and NLoS scenarios is calculated based on the carrier frequency f_1, the distance $d_{k(\cdot),m(t)}$, and the speed of light c. The average path losses for LoS and NLoS situations are denoted by η_{LoS} and η_{NLoS} correspondingly.

$$PL_{LoS_{k(\cdot),m(t)}} = 20\log\left(\frac{4\pi f_1 d_{k(\cdot),m(t)}}{c}\right) + \eta_{LoS} \tag{14}$$

$$PL_{NLoS_{k(\cdot),m(t)}} = 20\log\left(\frac{4\pi f_1 d_{k(\cdot),m(t)}}{c}\right) + \eta_{NLoS} \tag{15}$$

The SNR for the uplink from GU to UAV and the signal-to-noise interference ratio (SINR) for the downlink from UAV to GU are computed considering the transmit power of the GU (p_G), the channel gain (h), the bandwidth allocated to each GU (b_u), and the interference from other UAVs. The SNR for uplink from GU to UAV is defined as

$$\gamma_{kG2U_{src,m1(t)}} = \frac{p_G \cdot h_{k_{src},m1(t)}}{n_0 \cdot b_u} \tag{16}$$

where $h_{k_{src},m1(t)} = 10^{-PL_{k_{src},m(t)}/10}$ is the channel gain.

The SINR for downlink from UAV to GU takes into account the interference from other UAVs.

$$\gamma_{U2G_{m2,k_{dst}(t)}} = \frac{p_U \cdot h_{m2,k_{dst}(t)}}{I_{m2,k_{dst}(t)} + n_0 \cdot b_u} \tag{17}$$

The transmission rate for uplink and downlink is calculated using the logarithmic function of $1 + \gamma$, where γ is the SNR or SINR, as appropriate.

It is assumed that the bottleneck in transmission rate is either on the uplink or downlink, not on the UAV to UAV link, due to high-quality links between UAVs. The instant transmission rate between the kth pair is determined by the minimum of the uplink or downlink transmission rates, considering the hovering time ($\tau_{m_{hover}(t)}$) and the ratio of source (q_1) and destination (q_2) allocation factors.

3. PROBLEM FORMULATION AND OBJECTIVE FUNCTION

We define the accumulative throughput for the k-th user pair at time slot t as

$$TP_k(t) = \sum_{r=1}^{t} r_k(r) \tag{18}$$

Here, $r_k(r)$ represents the throughput for user pair k at time slot r.

Subsequently, the sum accumulative throughput for all user pairs is given by

$$SUM_TP(t) = \sum_{k \in K} TP_k(t) \tag{19}$$

To ensure fairness, we utilize Jain's index[26] to measure fair throughput

$$f(t) = \frac{(\sum_{k \in K} TP_k(t))^2}{K \sum_{k \in K} (TP_k(t))^2} \tag{20}$$

The parameter e represents the energy consumed by each UAV m at each time slot t. where the fairness index $f(t)$ ranges between $\frac{1}{K}$ and 1.

The access policies of GUs and the locations of UAVs at time slot t are represented by $A = \{\alpha^{src}_{m,k}(t), \beta^{dst}_{m,k}(t)\}_{m \in M, k \in K, t \in T}$ and $W = \{w^m_u(t)\}_{m \in M, t \in T}$, respectively.

Our objective function aims to maximize

$$S_{max} = \frac{\sum_{t \in T} f(t) \cdot SUM_TP(t)}{\sum_{t \in T} \sum_{m \in M} e_m[(t)} \tag{21}$$

Subject to constraints (1)–(4), where $C1$ enforces a safe distance d_{safe} between any two UAVs to avoid collisions, for any m, n in M and t in T, and $C2$ secures the network's algebraic connectedness with a positive measure λ_2. The target function aims to enhance equity and efficiency, as well as decrease the energy usage of all UAVs, in accordance with system needs. Constraint $C1$ controls the spatial mobility of UAVs, while constraints (2)–(4) manage the access control for GUs. Constraint $C2$ is based on the second smallest eigenvalue of the Laplacian matrix to guarantee that the UAVs sustain a linked network topology.

4. COMBINED MADRL AND DISTRIBUTED LEDGER

The IPPO method improves trajectory optimization for many UAVs by employing a decentralized approach. Every UAV functions within a partially observable Markov Decision Process (MDP) framework, making decisions based on its own observations rather than a common global state. The system's state is determined by

aggregating all UAV observations, while actions are decided independently in each location.

1. Observation Space Every UAV has a specific observation area that contains crucial environmental data, including the locations of all UAVs and GUs, total throughput, satisfaction levels, and access regulations. This extensive observation space is created to avoid execution problems in simulation and acts as a placeholder because of the fixed input dimensions needed by neural networks. Let O_i represent the observation space for UAV i. The information can be expressed as a vector containing environmental data.

$$O_i = [\mathbf{p}_1, \ldots, \mathbf{p}_N, \mathbf{g}_1, \ldots, \mathbf{g}_M, \tau, \sigma, \alpha] \tag{22}$$

where $\mathbf{p}_j$ is the location of UAV j, $\mathbf{g}_k$ is the position of GU k, τ is the accumulative throughput, σ is satisfaction levels, and α is access policies.

2. Action Space A UAV's action space is defined by the direction and distance of movement. The collective action space for all UAVs is the combination of individual actions, with a dimensionality equal to twice the number of UAVs. The action space for UAV i, represented as $\mathcal{A}_i$, comprises movement direction θ_i and distance d_i. The communal action space $\mathcal{A}$ is determined by

$$\mathcal{A} = \bigtimes_{i=1}^{N} \mathcal{A}_i = \bigtimes_{i=1}^{N} (\theta_i, d_i) \tag{23}$$

where N is the number of UAVs.

3. Reward Function The incentive function integrates a cooperative element shared by all UAVs and an individual element that encompasses penalties for border breaches, unsafe distances, connectivity problems, and energy usage. The incentive function design ensures that UAVs work together to optimize fair throughput while minimizing energy consumption and penalty infractions. The reward function for UAV i is denoted as R_i.

$$R_i(O_i, \mathcal{A}_i) = w_c C + w_i I - w_b B - w_d D - w_e E \tag{24}$$

where C is the cooperative component, I is the individual throughput, B represents border violation penalties, D represents unsafe distance penalties, E represents energy consumption, and w_c, w_i, w_b, w_d, w_e are the corresponding weights.

4. Actor-Critic Networks This methodology maintains distinct actor-critic networks for each UAV, updating them exclusively based on individual observations, in contrast to classic centralized training and exploration (CTDE) systems that could restrict the diversity of agent policies. This encourages a wider range of actions and decreases policy similarity among actors. Each UAV i has actor π_i and critic Q_i networks, which are defined by parameters θ_i and ϕ_i correspondingly.

$$\pi_i(a|O_i;\theta_i) \tag{25}$$

$$Q_i(O_i,a;\phi_i) \tag{26}$$

The networks are updated using gradients from the collected experiences:

$$\Delta\theta_i \propto \nabla_{\theta_i} \log \pi_i(a|O_i;\theta_i) A_i \tag{27}$$

$$\Delta\phi_i \propto \nabla_{\phi_i} (R_i - Q_i(O_i,a;\phi_i))^2 \tag{28}$$

where A_i is the advantage function for UAV i.

5. Algorithms The training algorithm requires UAVs to observe the state, make judgments using the actor network, execute actions, receive rewards, and update their networks with knowledge stored in memory. IPPO differs from MAPPO in that it utilizes only the buffered information of each agent during the update phase, instead of aggregating information from all agents. The IPPO algorithm is defined by the following iterative phases.

Algorithm
- Observe state O_i for UAV i.
- Choose action a_i using actor network: $a_i \sim \pi_i(\cdot|O_i;\theta_i)$.
- Execute action a_i and observe reward r_i and new state O_i'.
- Store transition (O_i, a_i, r_i, O_i') in memory.
- Sample random mini-batch from memory and update θ_i and ϕ_i using stochastic gradient descent.

The key distinction of IPPO in the update phase is in the use of the experiences:

$$\text{For each UAV } i: \theta_i \leftarrow \theta_i + \eta \Delta\theta_i(O_i, a_i, R_i, O_i') \tag{29}$$

where η is the learning rate.

4.1. Computational complexity analysis

The computational complexity of the proposed MADRL algorithm with the IPPO technique involves several components, including observation space processing, action space exploration, reward calculation, and the update of actor-critic networks.

1. Observation Space Processing: Each UAV has an observation space of size $O(N + M)$, where N is the number of UAVs and M is the number of GUs. This space includes the positions, battery levels, and other relevant state information of all UAVs and GUs. The processing of the observation space, which involves gathering and updating this information, is $O(N + M)$ per UAV.

2. Action Space Exploration: The action space for each UAV includes movement direction and distance. The exploration of the action space, which involves selecting an action based on the current policy, is $O(1)$ per UAV since the action space's dimensionality remains constant regardless of the number of UAVs and GUs.

3. Reward Calculation: The reward function involves cooperative components, individual throughput, border violations, unsafe distances, and energy consumption. These calculations involve linear operations on the observations and actions. Therefore, the complexity for calculating the reward function is $O(N+M)$ per UAV.

4. Update of Actor-Critic Networks: The update of the actor and critic networks involves backpropagation through neural networks. Let L be the number of layers and D be the maximum number of neurons per layer. The complexity of updating each network is $O(LD^2)$. Given that each UAV has its separate networks, the total complexity for updating all UAVs is $O(NLD^2)$.

Combining all components, the overall computational complexity per time step per UAV is written as

$$O(N+M)+O(1)+O(N+M)+O(LD^2)=O(N+M)+O(LD^2) \tag{30}$$

Given that the number of layers L and the number of neurons D per layer are typically constants for a fixed neural network architecture, the primary factors influencing computational complexity are the number of UAVs N and the number of GUs M. In scenarios with a large number of UAVs and GUs, the complexity scales linearly with $N+M$. However, the quadratic term LD^2 related to the neural network updates can become significant if the network architecture is very deep or wide. Thus, the overall computational complexity of the MADRL algorithm with the IPPO technique for the entire system (considering N UAVs) is:

$$O(N\cdot(N+M+LD^2))=O(N^2+NM+NLD^2) \tag{31}$$

5. RESULTS AND DISCUSSION

UAV-assisted communication network simulation is a technology that aims to connect locations without ground-based infrastructure. It uses a 10 km x 10 km 3D simulated environment to replicate both rural and urban terrains. UAVs fly between 100 and 300 meters to communicate directly with ground users for optimal transmission. To simulate real-world user dispersal, 50 GUs are randomly dispersed over the simulation territory. The MADRL algorithm is used to balance current and future rewards with a learning rate of 0.01 and a discount factor of 0.95. The communication technicalities include a noise spectral density of -174 dBm/Hz and a transmit power of 20 dBm for UAVs and 23 dBm for GUs. The implementation details of the IPPO algorithm describe the MADRL model: Each UAV agent's policy and value networks are updated depending on observations and rewards to imitate learning. Each UAV contains a blockchain module that imitates DL technology for secure and immutable communication transactions. The networks have densely linked layers with Restricted Linear Unit (ReLU) activation and a softmax layer for action probability. The observation space contains important data such as the UAV's location, battery level, adjacent GUs, and network throughput. Specific actions describe UAV direction and distance motions for the next time slot, defining the action space. The incentive function encourages GUs to improve throughput, energy efficiency, and fairness.

The simulation results depicted in Figure 2 illustrate the comparative performance of four UAV communication strategies across a sequence of time slots. The primary strategy, MADRL with DL, is shown to achieve the highest throughput, a testament to the efficacy of integrating DL technology with advanced RL algorithms. This strategy exhibits a rapid ascent in throughput that stabilizes as it approaches the system's capacity limit, forming an S-shaped logistic curve that represents a realistic growth pattern in network throughput. The second strategy, standalone MADRL, although effective, does not reach the peak performance achieved by its

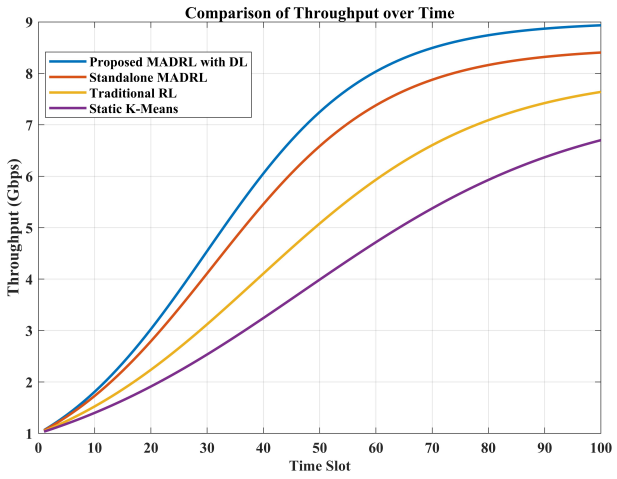


Figure 2. Comparison investigation proposed framework based on MADRL with DL, standalone MADRL, traditional RL and static K-means.

DL-enhanced counterpart, suggesting that while MADRL is a robust approach, its integration with DL technologies offers significant improvements. This curve parallels the top performer at a slightly subdued growth rate, demonstrating substantial but not maximal efficiency. The traditional RL strategy curve rises at a more modest pace, reflecting a lower growth rate and capacity. This indicates that traditional RL, while capable, falls short of the more sophisticated MADRL techniques, particularly in environments that demand dynamic and complex decision-making. Lastly, the Static K-Means strategy lags behind, with the least growth rate and capacity, suggesting its relative inadequacy in adapting to the evolving demands of UAV communication networks. Its performance trajectory, while still positive, is the most gradual and plateaus at the lowest throughput level, underscoring the limitations of less dynamic optimization methods. The results collectively encapsulate the cumulative throughput achievements of the UAV networks over time, measured in Gbps.

Figure 3 presents a comparison of four UAV communication optimization techniques across four metrics, including cumulative rewards, fairness index, cumulative throughput, and energy consumption. After 5000 episodes, the proposed MADRL with DL approach demonstrates the highest rewards in the cumulative rewards graph, indicating its superior performance in accumulating benefits over time. The data analysis shows a steady and significant rise in rewards, suggesting that this strategy is highly effective in achieving the desired outcomes in the simulated scenario. The fairness index graph evaluates the fair distribution of resources among users or agents. The proposed MADRL with DL consistently exhibits good performance, with a fairness index close to one, indicating optimal fairness. This method effectively distributes resources in a fair manner, guaranteeing that no individual or group is given special treatment. The cumulative throughput graph demonstrates the amount of data successfully transmitted over the network. The proposed MADRL with DL approach achieves the highest throughput, indicating efficient network traffic management. This technique shows a consistent and substantial increase in throughput, indicating an effective optimization strategy for maximizing data flow in the network. The energy consumption graph compares the energy needed by each technique to achieve its objectives. The proposed MADRL with DL technique is notable for its minimal energy usage, emphasizing its effectiveness. It is essential to focus on energy efficiency for UAV operations to ensure sustainability and cost-effectiveness. The proposed technique is designed to be high-performing and energy-efficient. The proposed MADRL with DL approach outperforms the standalone MADRL, traditional RL, and static K-Means strategies in all performance metrics. These findings highlight the advantages of incorporating deep learning with DL technology in UAV communication systems, resulting in improved performance, fairness, throughput, and energy efficiency. Utilizing effective analysis rather than relying on a curve can highlight the enhanced benefits of using advanced algorithms to oversee intricate communication networks.

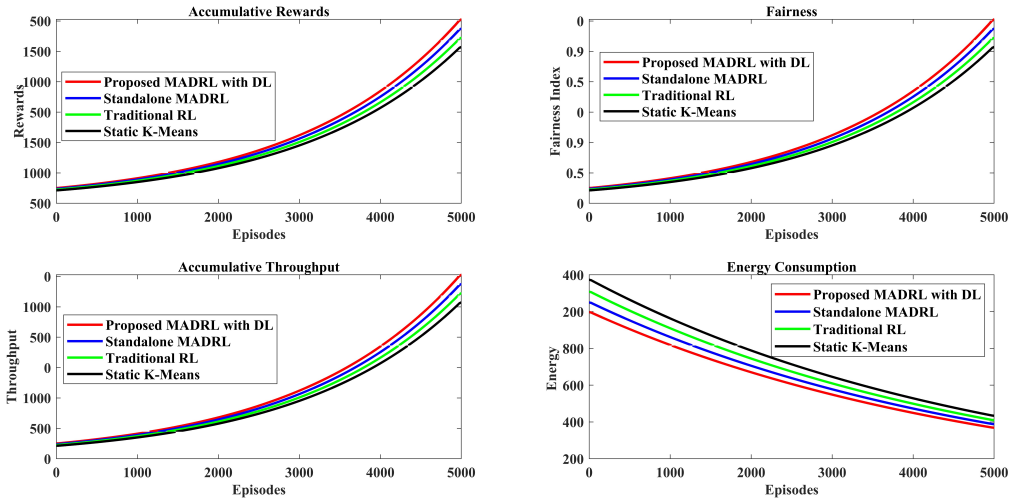


Figure 3. Throughput, rewards, fairness index and energy estimations.

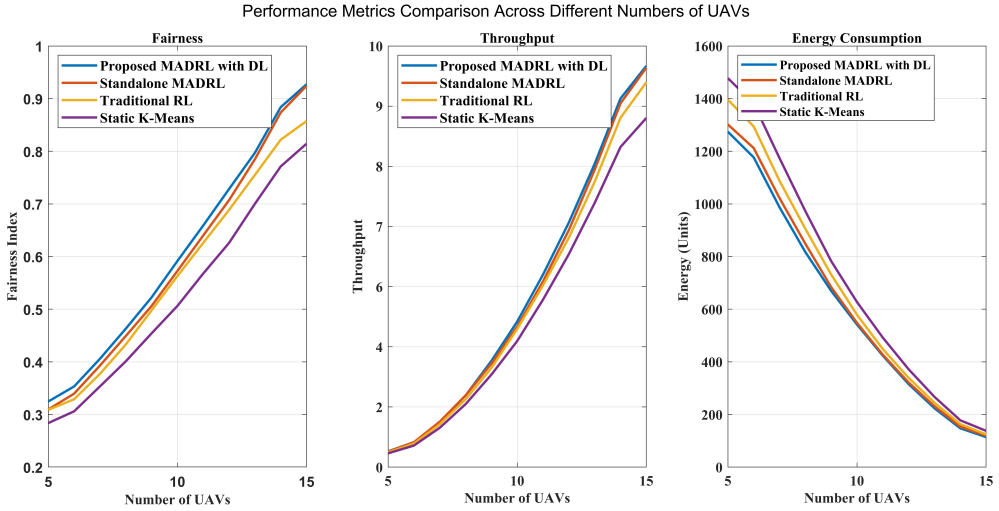


Figure 4. Number of UAVs evaluation in terms of energy, throughput and fairness index.

Figure 4 compares the performance of various communication mechanisms using different numbers of UAVs. The methods evaluated are the proposed MADRL with DL, Standalone MADRL, Traditional RL, and Static K-Means. The fairness index is used to assess the equitable allocation of resources among UAVs or network users. The MADRL with DL proposal shows the highest fairness index, indicating its effectiveness in ensuring equitable conditions throughout the network. As the number of UAVs increases, fairness grows, demonstrating the effectiveness of the proposed MADRL with Deep Learning as the UAV fleet size scales up. The Standalone MADRL has a higher fairness index compared to the Traditional RL and Static K-Means, indicating a more equitable distribution of resources. The throughput represents the data transmission rate controlled by each approach. The graph shows that as the number of UAVs increases, all techniques enhance throughput, but the Proposed MADRL with DL performs better than the other methods, showcasing its superior capacity to efficiently manage more intricate connections and larger data transfers. The Standalone MADRL outperforms Traditional RL, while Static K-Means has the lowest throughput, indicating that advanced dynamic techniques can effectively utilize more UAVs to enhance network capacity. Similarly, energy consumption shows the

energy usage for each technique. Reduced energy usage is favorable as it indicates a more effective use of resources. The Proposed MADRL with DL consumes more energy compared to previous options, but it offers a trade-off for increased fairness and throughput. The Standalone MADRL has somewhat greater efficiency compared to the Proposed MADRL with DL, while Traditional RL consumes less energy than both MADRL approaches. The Static K-Means algorithm, while highly energy-efficient, may exhibit lower performance compared to other algorithms, as seen by preceding measures. The data indicates that the Proposed MADRL with DL method achieves superior performance in fairness and throughput, albeit with increased energy usage. The Standalone MADRL method is characterized by a balanced combination of moderate energy consumption and performance. Traditional RL and Static K-Means are more energy-efficient but lag in network performance, showing a trade-off between energy efficiency and operational efficacy. This research can help identify the optimal technique for UAV network communication based on the specific needs for fairness, throughput, and energy efficiency.

6. CONCLUSIONS

This research marks a significant advancement in UAV communication systems, particularly beneficial in environments lacking ground-based infrastructure. By integrating MADRL with DLT, we have significantly enhanced the performance, fairness, and energy efficiency of UAV networks. The proposed system architecture leverages a cluster of UAVs to deliver equitable communication services, striking an optimal balance between network connectivity and resource utilization. The decentralized learning strategy, based on the IPPO technique, enables UAVs to tailor their operational strategies based on individual observations, fostering a dynamic and adaptive communication environment. While our findings demonstrate that the MADRL with DLT approach substantially outperforms traditional methods across various metrics, this study also opens several avenues for future research. Future work could explore the integration of more complex adaptive algorithms to further enhance the system's responsiveness to changing environmental conditions and user demands. Additionally, further research is needed to address potential challenges in scalability and manageability as the size and complexity of UAV networks increase. The complexities involved in real-world implementations, such as regulatory hurdles and varying environmental conditions, also present substantial challenges that require innovative solutions. Moreover, as UAV technologies and the frameworks for their operation evolve, continuous improvements in security measures will be essential to safeguard against increasingly sophisticated cyber threats. The adoption of newer cryptographic techniques and advanced security protocols will be crucial to ensure the integrity and confidentiality of the data transmitted within these networks.

DECLARATIONS

Authors' contributions

Made substantial contributions to conception and design of the study and performed data analysis and interpretation: Ali F

Performed data acquisition and provided administrative, technical, and material support: Ahtasham M, Anfaal Z

Availability of data and materials

The data can be provided as per request.

Financial support and sponsorship

None.

Conflicts of interest

Ali F is a Guest Editor of the journal *Complex Engineering Systems*, while the other authors have declared that they have no conflicts of interest.

Ethical approval and consent to participate

Not applicable.

Consent for publication

Not applicable.

Copyright

© The Author(s) 2024.

REFERENCES

1. Mahen MA, Anirudh SA, Chethana HD, Shashank AC. Design and development of amphibious quadcopter. *Int J Mech Prod Eng* 2014;2:30-4. DOI
2. Zhang D, Li C, Zhang Y. Dual-hand gesture controlled quadcopter robot. In: 2017 36th Chinese Control Conference (CCC). Dalian, China, 2017, pp. 6869-74. DOI
3. Marwan M, Han M, Dai Y, Cai M. The impact of global dynamics on the fractals of a quadrotor unmanned aerial vehicle (QUAV) chaotic system. *Word Sci* 2024;32:2450043. DOI
4. Elmas EE, Alkan M. Bir İnsansız Hava Aracı Sisteminin Tasarımı, Benzetimi ve Gerçekleştirilmesi. *Politeknik Dergisi* 2023;26:929-40. DOI
5. Zhang Y, Mou Z, Gao F, Jiang J, Ding R, Han Z. UAV-enabled secure communications by multi-agent deep reinforcement learning. *IEEE Trans Veh Technol* 2020;69:11599-611. DOI
6. Lu J, Guo X, Huang T, Wang Z. Consensus of signed networked multi-agent systems with nonlinear coupling and communication delays. *App Math Comput* 2019;350:153-62. DOI
7. Zhou Y, Jin Z, Shi H, et al. UAV-assisted fair communication for mobile networks: a multi-agent deep reinforcement learning approach. *Remote Sens* 2022;14:5662. DOI
8. Abohashish SMM, Rizk RY, Elsedimy EI. Trajectory optimization for UAV-assisted relay over 5G networks based on reinforcement learning framework. *J Wireless Com Network* 2023;55:2023. DOI
9. Li H, Li J, Liu M, Gong F. UAV-assisted secure communication for coordinated satellite-terrestrial networks. *IEEE Commun Lett* 2023;27:1709-13. DOI
10. Luo X, Xie J, Xiong L, Wang Z, Liu Y. UAV-assisted fair communications for multi-pair users: a multi-agent deep reinforcement learning method. *Comput Netw* 2024;242:110277. DOI
11. Agrawal N, Bansal A, Singh K, Li CP, Mumtaz S. Finite block length analysis of RIS-assisted UAV-based multiuser IoT communication system with non-linear EH. *IEEE Trans Commun* 2022;70:3542-57. DOI
12. Sun G, Zheng X, Sun Z, et al. UAV-enabled secure communications via collaborative beamforming with imperfect eavesdropper information. *IEEE Trans Mobile Comput* 2024;23:3291-308. DOI
13. Li J, Liu A, Han G, Cao S, Wang F, Wang X. FedRDR: federated reinforcement distillation-based routing algorithm in UAV-assisted networks for communication infrastructure failures. *Drones* 2024;8:49. DOI
14. Zhang Z, Liu Q, Wu C, Zhou S, Yan Z. A novel adversarial detection method for UAV vision systems via attribution maps. *Drones* 2023;7:697. DOI
15. Zhang Y, Zhuang Z, Gao F, Wang J, Han Z. Multi-agent deep reinforcement learning for secure UAV communications. In: 2020 IEEE Wireless Communications and Networking Conference (WCNC), Seoul, Korea (South); 25-28 May 2020. DOI
16. Tang, D, Zhang Q. UAV 5G: enabled wireless communications using enhanced deep learning for edge devices. *Wireless Netw* 2023. DOI
17. Oubbati OS, Atiquzzaman M, Baz A, Alhakami H, Ben-Othman J. Dispatch of UAVs for urban vehicular networks: a deep reinforcement learning approach. *IEEE Trans Veh Technol* 2021;70:13174-89. DOI
18. Ansari S, Taha A, Dashtipour K, Sambo Y, Abbasi QH, Imran MA. Urban air mobility-a 6G use case? *Front Comms Net* 2021;2:729767. DOI
19. Shang Y. Consensus tracking and containment in multiagent networks with state constraints. *IEEE Trans Syst Man Cybern Syst* 2023;53:1656-65. DOI
20. Zhang G. 6G enabled UAV traffic management models using deep learning algorithms. *Wireless Netw* 2023;1-11. DOI
21. Elamin A, El-Rabbany A. UAV-based multi-sensor data fusion for urban land cover mapping using a deep convolutional neural network. *Remote Sens* 2022;14:4298. DOI
22. Kuutti S, Fallah S, Katsaros K, Dianati M, Mccullough F, Mouzakitis A. A survey of the state-of-the-art localization techniques and their potentials for autonomous vehicle applications. *IEEE Int Things J* 2018;5:829-46. DOI
23. Al-Hourani A, Kandeepan S, Lardner S. Optimal LAP altitude for maximum coverage. *IEEE Wireless Commun Lett* 2014;3:569-72. DOI
24. Ge J, Zhang S. Adaptive inventory control based on fuzzy neural network under uncertain environment. *Complexity* 2020;2020:1-10. DOI
25. Sun Q, Ren J, Zhao F. Sliding mode control of discrete-time interval type-2 fuzzy Markov jump systems with the preview target signal. *Appl Math Comput* 2022;435:127479. DOI
26. Zhong W, Xu L, Zhu Q, Chen X, Zhou J. MmWave beamforming for UAV communications with unstable beam pointing. *China Commun*

2019;16:37-46 DOI

Peng *et al*. *Complex Eng Syst* 2024;4:15
DOI: 10.20517/ces.2024.08

Complex Engineering Systems

Research Article

Open Access

Multiple unmanned aerial vehicle collaborated three-dimensional electromagnetic target situation map construction

Yuqing Peng[1], Kun Liu[1], Xuezhao Cai[1], Jie Wang[1], Zhipeng Lin[1]

[1]College of Electronic and Information Engineering, Nanjing University of Aeronautics and Astronautics, Nanjing 211106, Jiangsu, China.

Correspondence to: Dr. Zhipeng Lin, College of Electronic and Information Engineering, Nanjing University of Aeronautics and Astronautics, 29 Jiangjun Road, Jiangning District, Nanjing 211106, Jiangsu, China. E-mail: linlzp@nuaa.edu.cn; ORCID: 0000-0001-5941-2163

How to cite this article: Peng Y, Liu K, Cai X, Wang J, Lin Z. Multiple unmanned aerial vehicle collaborated three-dimensional electromagnetic target situation map construction. *Complex Eng Syst* 2024;4:15. http://dx.doi.org/10.20517/ces.2024.08

Received: 21 Feb 2024 **First Decision:** 6 Jun 2024 **Revised:** 9 Jul 2024 **Accepted:** 22 Jul 2024 **Published:** 26 Jul 2024

Academic Editor: Hamid Reza Karimi **Copy Editor:** Fangling Lan **Production Editor:** Fangling Lan

Abstract

The electromagnetic (EM) target situation map can visualize the situation and locations of multiple EM targets in the three-dimensional (3D) space. It is vital for the spectrum activity monitoring, radiation source localization, frequency resource management, and so on. Traditional studies focused on the radio environment map construction, and the characteristics such as locations of EM targets are not accurate due to reconstruction deviation and environmental noise. This paper presents a 3D EM target situation map construction scheme based on multiple unmanned aerial vehicle collaboration. Firstly, an improved maximum and minimum distance clustering-based algorithm is proposed to estimate the number and rough location of EM targets directly by utilizing the original sparse sampling data. Then, to improve the accuracy of situational awareness, a re-weighted map fusion algorithm is used to update the raw EM characteristics results. Finally, we calculate the self-information of different targets and optimize the previous location results. Compared with other conventional methods, numerical results demonstrate that the proposed method has higher mapping accuracy under the same low sampling rate.

Keywords: Multi-UAV collaboration, 3D electromagnetic target situation map, clustering algorithm, re-weighted fusion

© The Author(s) 2023. **Open Access** This article is licensed under a Creative Commons Attribution 4.0 International License (https://creativecommons.org/licenses/by/4.0/), which permits unrestricted use, sharing, adaptation, distribution and reproduction in any medium or format, for any purpose, even commercially, as long as you give appropriate credit to the original author(s) and the source, provide a link to the Creative Commons license, and indicate if changes were made.

1. INTRODUCTION

With the rapid development of wireless communication, plenty of radio, mobile phones, navigation and other equipment and systems have been integrated into the electromagnetic (EM) network, resulting in an increasingly complex EM environment[1–4]. The spatial distribution of EM targets is one of the important characteristic pieces of information in EM space. An electromagnetic target situation map (ETSM) can quantitatively characterize and visualize the quantity, position, power, and other information of EM targets[5]. It effectively solves the monitoring and locating of multiple EM targets in complex scenarios.

Take the traditional radio environment map (REM) as an example, whose composition process is also known as spectrum mapping. The construction process of REM accounts for the variations in the spatial distribution of EM environments in practical applications, making a realistic description of the EM environment possible. A complete REM construction system can achieve the perception, reconstruction, storage, and visualization of EM environment information[6]. The REM system is primarily composed of four main modules: measurement capable devices (MCDs), prior information database, cognitive engine, and storage and retrieval unit[7]. Depending on the type of platform used in MCDs, the REM mapping systems can be divided into three categories: space-based, ground-based, and air-based. Among these, space-based mapping systems, such as Kleos Space in France and HawkEye360 in the United States, use artificial satellites to gather global spectrum information. Researches on ground-based mapping systems are more mature currently, most of which use handheld spectrum analyzers, spectrum monitoring vehicles, and spectrum sensing sensors arranged in interested areas to obtain ground spectrum information. The German unmanned aerial vehicle (UAV) monitoring system Colibrex LS OBSERVER AMU is a typical air-based mapping system; however, the measurement range is extremely limited due to its tethered structure. Du *et al.* proposed an aerial spectrum situational mapping system based on UAV platform, which can achieve the construction of air-ground spectrum situational maps[8–10].

The restoration of EM environment based on sparse sampling spectrum data, i.e., map completion, is the key component of the above system. The completion methods for REMs can be classified into two categories: data-driven and model-driven[11]. Data-driven methods mainly include spatial interpolation algorithms, matrix (tensor) completion algorithms, and machine learning-based methods. Inverse distance weighted (IDW)[12], also known as Shepard method, is a classic spatial interpolation technique with fast completing speed and high smoothness. To solve the problem of completing multidimensional spectrum data, tensor-based completion methods are proposed[13]. Hashimoto *et al.* propose a spatial interpolation with convolutional neural networks (SICNN) method based on deep learning[14]. Above all, these data-driven methods can directly estimate the spectrum data of unsampled positions without any prior knowledge, but usually require a large amount of observation spectrum data and with lower accuracy. The models in model-driven methods mainly refer to the propagation loss (PL) model of wireless channels. Classic model-driven methods contain active transmitter location estimation-based method (LIvE)[15], Received Signal Strength Difference (RSSD)-based method[16], *etc*. However, both LIvE and RSSD assume that there is only one EM target in the monitored area, which cannot solve the spectrum completion problem in complex environments. Compared with data-driven methods, model-driven methods usually have superior completion accuracy; however, they require prior information such as the position, number of EM targets, and the precise channel propagation model[17–19]. In recent years, multi-channel spectrum sensing studies based on deep learning neural networks have begun to emerge, but such methods are overly dependent on datasets and often ignore the actual EM propagation rules[20–22].

In order to obtain precise information about EM targets, it is necessary to address the localization problem of EM targets[23]. At present, source-free positioning methods represented by Direction of Arrival (DOA) and Time Difference of Arrival (TDOA) have been applied in various studies[24,25]. However, these methods require multiple antenna signal receiving devices and have high hardware costs. Thus, single antenna localization methods based on Received Signal Strength (RSS) have been paid much more attention in recent years.

Liu *et al.* used an UAV system equipped with a single antenna to collect data and achieved rapid localization in urban scenes based on RSS method[26]. On the other hand, due to the correlation and similarity between spectrum data, clustering methods such as K-means, DBSCAN (Density-Based Spatial Clustering of Applications with Noise), Gaussian Mixture Model (GMM), *etc.* are widely used in RSS-based localization[27]. With the development of deep learning, neural network structure is introduced into clustering algorithms. Aiming to solve the problem of large-scale high-dimensional spectrum data that are difficult to handle through traditional clustering methods, a semi-supervised K-means algorithm is proposed[28]. However, the above clustering methods did not consider the propagation characteristics of EM waves, making it difficult to accurately classify spectrum data and obtain the position of EM targets.

Overall, the main contributions of this paper are summarized as follows:

• An EM target awareness system based on collaborative multiple UAVs (multi-UAVs) is designed for collecting spectrum data, which solves the issue of sampling errors that are prone to occur in complex environments or at high altitudes. And a mathematical model of the three-dimensional (3D) ETSM combined with actual EM propagation rules is constructed.

• A map fusion algorithm based on re-weighting is proposed. The algorithm enhances the reconstruction results of data-driven method by modeling the fusing process as a least absolute shrinkage and selection operator (LASSO) regression problem.

• An improved maximum and minimum distance (MMD)-based EM target staged-location method is proposed. By optimizing the characteristic parameter of MMD with a proper PL model, the rough positions of EM targets can be fast derived based on raw spectrum data. The ultimate location result is modified with fused spectrum data.

The rest of this paper is organized as follows. Section 2 gives the composition of the collaborative multi-UAV system and the 3D ETSM model. In Section 3, the details of the proposed 3D ETSM construction scheme are given and demonstrated. Simulation results and analysis are provided in Section 4. Finally, we make a summary and conclusion in Section 5.

2. SYSTEM MODEL

2.1. Collaborative multi-UAV system

In recent years, UAVs have been widely used in various communication systems due to their advantages of high maneuverability, low risk, and low cost. However, it is challenging to build lightweight systems because of load and storage capacity limits. The proposed hardware EM target awareness system is shown in Figure 1. It consists of three parts: autonomous control of UAVs, aerial spectrum measurement, and fuse-construction of EM target situation. The details of each part are as follows.

The UAV platform subsystem includes a Global Positioning System (GPS) receiving module, an integrated communication and remote control module, a flight control module, and an image module. Via information exchanges through the integrated communication and remote control module, the GPS receiving module receives GPS position information obtained from the ground. The flight control module controls the flight of UAVs. The image module transmits the collected images to the ground processing terminal. Note that an UAV platform subsystem is equipped with a spectrum measurement subsystem.

The spectrum measurement subsystem includes a spectrum receiver, measurement antenna, and microcomputer. It is responsible for collecting and analyzing spectrum information.

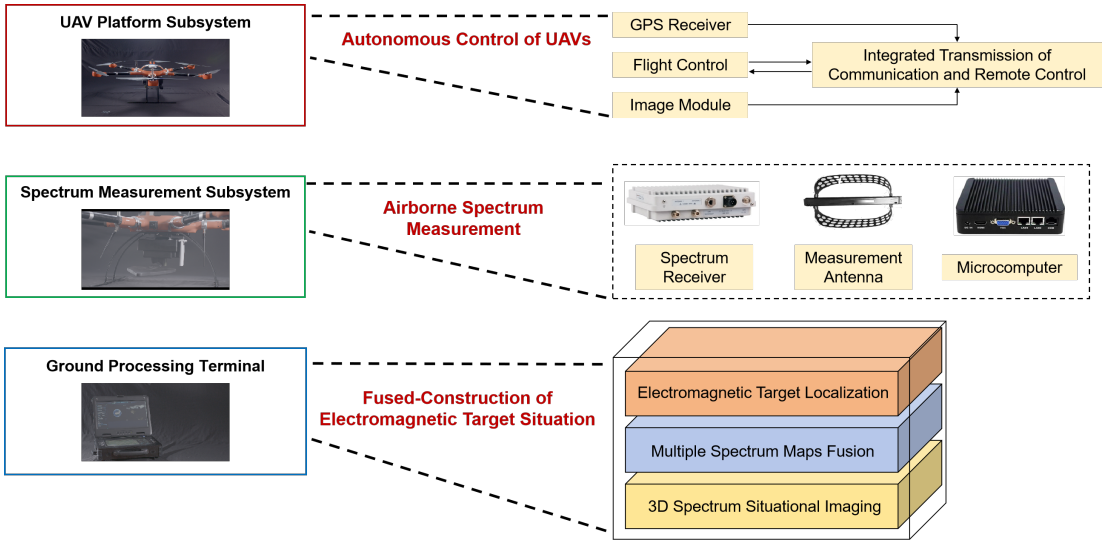


Figure 1. UAV-assisted system of EM target awareness.

The ground processing terminal sends the information gathered from the integrated communication and remote transmission module to the ground station. The ground station is equipped with a software platform to integrate, process, analyze the sampling data, and construct the 3D ETSM of the interested area.

2.2. 3D ETSM model

In this paper, multi-UAVs loaded spectrum measurement modules are used to obtain the initial spectrum data, and the collaborative sampling model is shown in Figure 2. In order to simplify the data volume to be processed in the following steps, the monitored area is divided into $N = N_x \times N_y \times N_z$ cubes, and each cube is numbered as (n_x, n_y, n_z). Assuming that the grid scale of the cubes is m, ETSM of the entire area can be modeled as a third-order tensor $\boldsymbol{\varphi} \in \mathbb{R}^{N_x \times N_y \times N_z}$.Then, in a 3D Cartesian coordinate system, center point of each cube can be expressed as

$$S(x, y, z) = ((n_x - 0.5) \times m, (n_y - 0.5) \times m, (n_z - 0.5) \times m). \tag{1}$$

According to the distribution of obstacles, the ground terminal sends GPS information through the integrated communication and remote control module for route planning of UAVs. Each UAV conducts uniform sparse sampling of spectrum data along the pre-set trajectory respectively, i.e., RSS values are observed at R positions, which can be expressed as a transposed matrix $\boldsymbol{\varphi} = [\varphi_1, ..., \varphi_R]^{\mathrm{T}}$. Assume that the number of UAVs is G, and the number of sampling points for the g-th UAV is R_g. The sampling rate of the ETSM system can be defined as

$$SR_{\text{aver}} = \frac{1}{G} \sum_{g=1}^{G} (R_g / N). \tag{2}$$

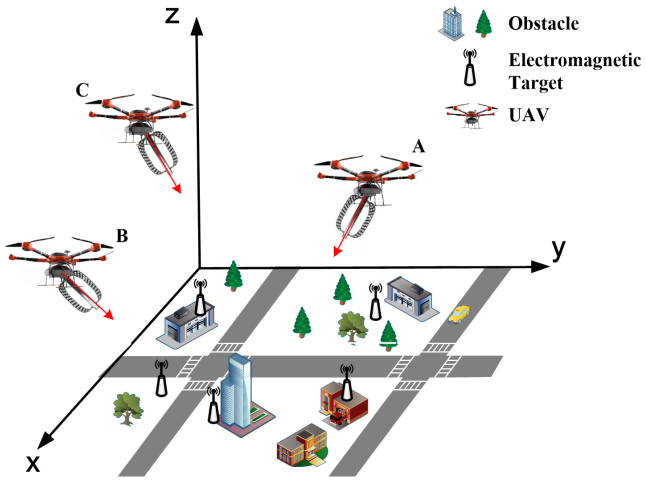


Figure 2. Multi-UAV collaborative sampling model.

3. 3D ETSM CONSTRUCTION WITH MULTI-UAV COLLECTED DATA

The construction scheme of 3D ETSM is shown in Figure 3. We first propose an improved MMD-based clustering algorithm to obtain a preliminary estimate of target positions. Then, we design a map fusion algorithm to reconstruct the fused spectrum map. Finally, we modify the preliminary estimation of target positions and obtain the precise positions.

3.1. MMD-based electromagnetic target rough location

An improved MMD-based clustering algorithm is proposed in this section for the approximate localization of EM targets. MMD is a pattern recognition probing-based clustering technique, which is based on Euclidean distance and takes objects as far as possible as the cluster center. Therefore, compared with K-means method, it prevents the chance of cluster centers being too close to each other when selecting initial values[17]. In addition to finding the number of the initial clustering centers rapidly, this method can increase the efficiency of spectrum data partition.

The basic MMD algorithm first starts with a sample object as the first cluster center, then selects a sample that is the farthest from the first cluster center as the second cluster center. Afterwards, other cluster centers are determined based on the maximum distance in succession, until no new cluster centers are generated. Finally, classify the samples into the nearest class according to the principle of minimum distance, and the division of the dataset is completed. However, in actual scenarios, the RSS value may be affected by the transmission distance, reflection, refraction, diffraction, and dispersion of EM waves during propagation, *etc.*[29]. Additionally, the attenuation of EM wave strength during transmission varies greatly with distance. The basic MMD method only considers the distance factor to cluster RSS data within the monitored area and cannot locate EM targets.

To accomplish the estimation of the EM target position within the monitored area, we improve the MMD algorithm by the PL rules in this paper. Given that the 3D ETSM of the monitored area contains N cubes, we consider the average RSS value within each cube representing a region as the RSS value at the center of that cube, denoted as $P_n(x_n, y_n, z_n)$, $n = 1, 2, ..., N$. Since the prior knowledge of EM targets is unknown, we take the total sampling spectrum data of multi-UAVs as the input dataset, and select an arbitrary sampling cube $S_i(x_i, y_i, z_i)$, $i = 1, 2, ..., R'$ as the first clustering center $Z_1(x_1, y_1, z_1)$, where R' is the total number of sampling points corresponding to the multi-UAV system. To ensure that the next selected cluster center has a higher

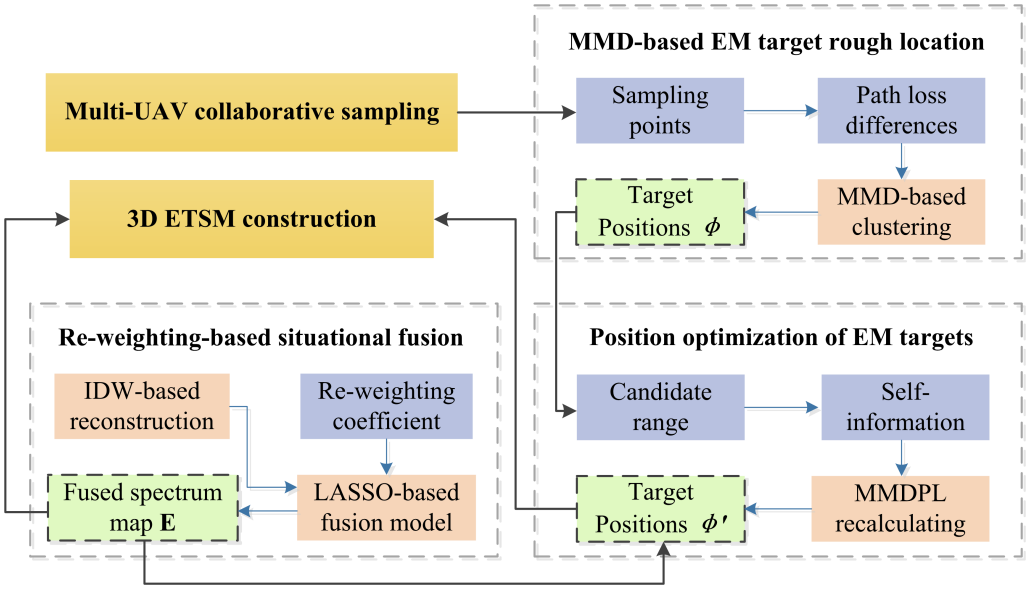


Figure 3. Overview of 3D ETSM construction.

possibility of being the location of the EM target, the path loss difference calculation is chosen to replace the distance calculation in the clustering algorithm. Path loss between the k-th clustering center and the i-th cube can be expressed as

$$\Delta\hat{P}_{ki} = \left|\Delta P_{ki} - L_i\right|, \quad k < N, \tag{3}$$

where

$$\Delta P_{ki} = \left|P_k - P_i\right|, \tag{4}$$

which denotes the difference of RSS between the k-th clustering center and the i-th cube. L_i is the path loss of EM wave strength in free space, which can be calculated as

$$L_i(\mathrm{dB}) = 32.45 + 20\lg(f) + 20\lg(d_{ki}), \tag{5}$$

$$d_{ki} = \sqrt{(x_{Z_i} - x_i)^2 + (y_{Z_i} - y_i)^2 + (z_{Z_i} - z_i)^2}, \tag{6}$$

where f is the frequency of EM targets, d_{ki} is the Euclidean distance between the k-th clustering center and the i-th cube. Next, calculate the path loss from all other sampling points to Z_1, if

$$\Delta\hat{P}_{k1} > \max_i\{\Delta\hat{P}_{i1}\}, \tag{7}$$

Algorithm 1: MMPLD

Input: iteration counter k=0, sampled data $\mathbf{P}$.
Output: EM target positions $\boldsymbol{\phi} = [\phi_1, ..., \phi_K]^{\mathrm{T}}$
Initialization: set of clustering centers $\mathbf{Z} = \emptyset$
Randomly select an arbitrary sampling point from $\boldsymbol{S}$ as the first clustering center Z_1 and add it to $\mathbf{Z}$.
For $k = 1$ to the desired number of EM targets, do:
  a. Initialize the maximum path loss difference $\max_i\{\Delta\hat{P}_{i1}\} = 0$
  b. For each sampling point S_i in $\boldsymbol{S}$, do:
    i. If S_i is not assigned to any cluster center yet, then:
      - Calculate the path loss difference P_{ki} between S_i and all cluster centers in $\mathbf{Z}$ by Equation (7)
    ii. If $\Delta\hat{P}_{k1} > \max_i\{\Delta\hat{P}_{i1}\}$, then:
      - Update $\max_i\{\Delta\hat{P}_{i1}\} = \Delta\hat{P}_{k1}$
      - Set the current sampling point S_i as the next cluster center candidate
  c. Add the next cluster center candidate to $\mathbf{Z}$
  d. Assign all sampling points in $\boldsymbol{S}$ to the nearest cluster center based on the path loss difference
Return $\boldsymbol{\phi} = [\phi_1, ..., \phi_K]^{\mathrm{T}}$

then, S_k is taken as the second clustering center Z_2. Then, the $(k+1)$-th clustering center can be determined by

$$\begin{aligned} & Z_{k+1} = Z_j, \\ s.t. \quad & \Delta\hat{P}_{pj} = \max\{\min(\Delta\hat{P}_{1i}, \Delta\hat{P}_{2i}, ..., \Delta\hat{P}_{ki})\}, \\ & (p = 1, 2, ..., k), \end{aligned} \tag{8}$$

where $\Delta\hat{P}_{ki}$ denotes the path loss from the k-th clustering center to the i-th cube. For fast convergence, when $\Delta\hat{P}_{pj} \leq \theta \cdot \Delta\hat{P}_{12}$, the calculating process ends, where $\Delta\hat{P}_{12}$ is the path loss from Z_1 to Z_2. θ is a clustering parameter that determines the number of clusters, usually determined by probing. All sampling points are divided based on the differences of path losses according to K-Nearest Neighbor (KNN) principle, and the clustering centers are considered as EM targets; i.e., the rough position estimation result $\boldsymbol{\phi} = [\phi_1, ..., \phi_K]^{\mathrm{T}}$ of EM targets is obtained. In this case, the improved MMD algorithm is recalled as Maximum Minimum Propagation Loss Difference (MMPLD) method. Algorithm 1 summarizes the process of MMD-based EM target rough location.

3.2. Re-weighting-based situational fusion

In this section, we design a map fusion algorithm based on re-weighting to enhance the accuracy of spectrum data, which can significantly improve the accuracy of ETSM construction and further localization of EM targets.

3.2.1 spectrum reconstruction based on IDW

Since the sampling data are sparsely distributed in the monitored area, we first get the initial spectrum maps corresponding to each single-UAV by IDW.

Classic IDW method assumes that the influence of the sampling value of a known point on the estimated value of an unknown point depends on the distance between the sampling point and the unknown point. To obtain the RSS value $\hat{P}_{S_0}$ of the unknown cube S_0, the weight coefficient ω_n is calculated by using the weighted average of RSS data $P_{S_n}, n = 1, 2, ..., N$ of its nearest N known cubes S_n, which can be expressed as

$$\omega_n = \frac{d_n^p}{\sum_{i=1}^{N} d_i^p}, \tag{9}$$

where d_n is the distance between S_0 and S_n, parameter p controls the decrease rate of the weight coefficient ω_n with distance, which usually taken as -2. The IDW method is called inverse distance squared weighting method at this time. Thus, the RSS value of the unknown point S_0 can be calculated by

$$P_0(x_0, y_0, z_0) = \sum_{n=1}^{N} \omega_n P_n(x_n, y_n, z_n). \tag{10}$$

Traditional IDW method only considers the effect of distance, ignoring the influences of other factors (*e.g.*, frequency) on the RSS in actual EM propagation environment. In order to improve the performance of the traditional IDW, the weight coefficient can be improved based on the PL model as

$$\omega_n = \frac{\left(10 \lg\left(\frac{4\pi f d_n}{c}\right)\right)^{-2}}{\sum_{n=1}^{N}\left(10 \lg\left(\frac{4\pi f d_n}{c}\right)^{-2}\right)}, \tag{11}$$

where f is the frequency of the received signal, c is the speed of light, and $d_n = \sqrt{(x_0 - x_n)^2 + (y_0 - y_n)^2 + (z_0 - z_n)^2}$ is the Euclidean distance from the n-th sampling point (x_n, y_n, z_n) to the interpolated point (x_0, y_0, z_0). Define χ_n as the tensor of the 3D ETSM and assign the RSS value of the sampled point P_i and the RSS value of the unknown point P_n obtained by IDW inference to the map tensor χ_n. Then, calculating Equations (10) and (11), multiple independent spectrum maps based on sparse sampling of single-UAVs are completed for the next fusion processing.

3.2.2 Fusion model based on LASSO regression

In order to reduce the limitation of the information provided by single-UAVs, a LASSO regression fusion model is proposed to process the above initial maps.

We define the initial maps corresponding to G UAVs as $(\mathbf{M}_1, \mathbf{M}_2, ...\mathbf{M}_G)$, and the map obtained by the g-th UAV can be vectorized as spectrum data to be fused as $\mathbf{m}_g \in \mathbb{R}^N$. The fused data are defined as $\boldsymbol{\varepsilon}_g \in \mathbb{R}^N$, which are initialized to zero vectors. By applying the ℓ_1 - norm to describe the spatial correlation degree of the fused data, the LASSO regression problem can be expressed as

$$\arg\min_{\boldsymbol{\varepsilon}_g}\left(\sum_{g}^{G}\left(\mathbf{m}_g - \mathbf{I}_N\boldsymbol{\varepsilon}_g\right)^2 + \tau\left\|\boldsymbol{\varepsilon}_g\right\|_1\right), \tag{12}$$

where $\mathbf{I}_N$ is the identity matrix, τ is the penalty coefficient, $\left\|\boldsymbol{\varepsilon}_g\right\|_1$ can be calculated as

$$\left\|\boldsymbol{\varepsilon}_g\right\|_1 = \sum_{g}^{G}\left|\boldsymbol{\varepsilon}_g\right|. \tag{13}$$

Combined with the EM propagation model, when the targets are observed with different strengths, the performance of Equation (13) can be enhanced by exploiting another weighting function. Large weights are used

to discourage nonzero entries, while small weights are used to encourage zero entries. Then, the weighting function $\mathbf{v}_N$ can be expressed as

$$\mathbf{v}_N^{(i)} = \begin{cases} \left(\sum_g^G \left(\boldsymbol{\varepsilon}_g^{(i-1)} \right)^2 \right)^{-1/2}, & \text{if } \left\| \boldsymbol{\varepsilon}_g \right\|_1 > 0, \\ 1/\rho, & \text{if } \left\| \boldsymbol{\varepsilon}_g \right\|_1 = 0, \end{cases} \tag{14}$$

where $\mathbf{v}_N^{(i)}$ denotes the re-weighting coefficient for the i-th iteration, and ρ is a constant slightly greater than zero. By introducing the re-weighting term $\mathbf{v}_N$ in Equation (14), the optimization problem proposed in Equation (12) can be rewritten as a re-weighting fusion model as

$$\arg\min_{\boldsymbol{\varepsilon}_g} \left(\sum_g^G \left(\mathbf{m}_g - \mathbf{I}_N \boldsymbol{\varepsilon}_g \right)^2 + \mathbf{v}_N \cdot \tau \left\| \boldsymbol{\varepsilon}_g \right\|_1 \right), \tag{15}$$

which can be solved by Least Angle Regression (LARS)[30]. Finally, we can obtain the ultimate fused spectrum situation map $\mathbf{E}$ by

$$\mathbf{E} = \text{ivec} \left(\frac{1}{G} \sum_g^G \boldsymbol{\varepsilon}_g \right), \tag{16}$$

where ivec(·) is the inverse of vectorization. By calculating Equation (16), the fused RSS data $\boldsymbol{\varphi}$ for position optimization can be obtained.

3.3. Position optimization of electromagnetic targets

In this section, the localization results in Section 3.1 are modified based on the fused map data. Since the number of EM targets is K, taking the k-th estimated target as an example, we extend a distance of the total length outward by 10% along the x-axis, y-axis and z-axis, respectively. We use this range as a candidate range Υ_k. The sampled data $\boldsymbol{\upsilon}_k = [\upsilon_{k_1}, ..., \upsilon_{k_n}]^{\mathrm{T}} \in \mathbb{C}^{N_k}$ contained in the range Υ_k is used to locate the accurate position of the EM target in that range. υ_{k_n} corresponding to ϕ_{i_n} satisfies

$$\begin{aligned} \phi_{i_x} - 0.1 \cdot L_x \le \varphi_{k_{nx}} \le \phi_{i_x} + 0.1 \cdot L_x, \\ \phi_{i_y} - 0.1 \cdot L_y \le \varphi_{k_{ny}} \le \phi_{i_y} + 0.1 \cdot L_y, \\ \phi_{i_z} - 0.1 \cdot L_z \le \varphi_{k_{nz}} \le \phi_{i_z} + 0.1 \cdot L_z, \end{aligned} \tag{17}$$

Taking the central point of a certain ϕ_k cube as the origin point, we first extend a distance of the total length outward by 10% along the x-axis, y-axis and z-axis, respectively. Then, we get a correction range for ϕ_k.

If there are other candidate targets within the range, the completed data within the range need to be corrected by

$$\hat{\upsilon}_{k_n} = \upsilon_{k_n} - \frac{\lambda^2}{\left(4\pi \cdot d \left(\phi_i', \varphi_{k_n} \right) \right)^2}, \tag{18}$$

where ϕ_i' is the location of other candidate targets within the range, φ_{k_n} is the location of the cube to be modified in the range that corresponds to ϕ_i, and υ_{k_n} is the fused data at a certain grid.

Next, the amount of self-information can be measured by calculating the entropy in the range for measuring[31],

$$\boldsymbol{\upsilon}_k = \left[\left\lfloor 10\lg \widehat{\upsilon}_{k_1} \right\rfloor, \left\lfloor 10\lg \widehat{\upsilon}_{k_2} \right\rfloor, \ \ldots, \left\lfloor 10\lg \widehat{\upsilon}_{k_n} \right\rfloor\right]^{\mathrm{T}}. \tag{19}$$

We take the fused data of the grids at the top 70% of the information entropy as the effective sampling data for correcting the position of the EM targets. The localization results can be updated by recalculating Equation (8); i.e., initial positioning result $\boldsymbol{\phi} = [\phi_1, \ldots, \phi_K]^{\mathrm{T}}$ is modified to $\boldsymbol{\phi'} = \left[\phi_1', \ldots, \phi_K'\right]^{\mathrm{T}}$. Finally, the EM target localization is annotated on the fused map, and the ultimate 3D ETSM is constructed.

4. SIMULATION RESULTS AND ANALYSIS

In this section, the performance of the proposed 3D ETSM construction method is analyzed and verified under the campus scenario. The satellite map of the monitored area is shown in Figure 4. To validate the performance of the proposed method in complex environments while maintaining clarity, we only show the simulation results of the example region (ER). The ER includes various environmental factors such as grass, trees, and buildings that affect signal propagation. This allows us to verify the performance of the proposed method in complex environments. Moreover, the smaller range of the area helps to display the results more clearly. Assuming that the ER is 100 m × 100 m × 50 m. The 3D area is divided into 10 × 10 × 10 cubes, and each cube is 10 m × 10 m × 5 m. We utilize Radio Frequency (RF) transmitters to simulate EM targets. We can choose any frequency of interest to obtain the 3D ETSM at that frequency. Since many wireless devices currently operate in the 2.4 GHz band, we set the working frequency of each signal RF transmitter as 2.4 GHz. The other simulation parameters are shown in Table 1, where the positions of the RF transmitters are randomly selected. In other words, EM targets may be placed in various locations such as grasslands, roads, indoors, rooftops, *etc*. The transmitting power of different RF transmitters can be set arbitrarily. To more clearly display the simulation results, we set the transmitter power as 30 dBm in the simulation. The numbers of RF transmitters and UAVs in ETSM construction performance can also be set arbitrarily. Considering the limitations of existing equipment for future measurements, we set them to 5 and 3, respectively.

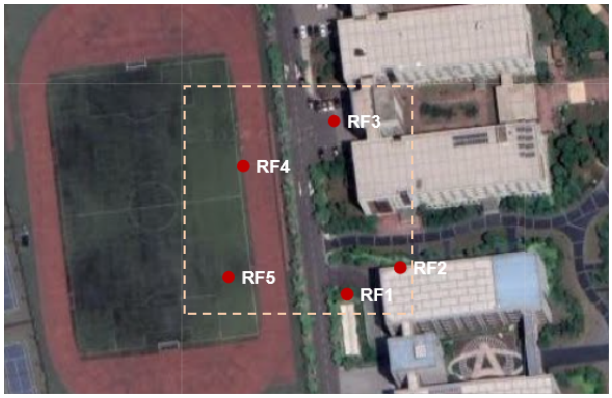


Figure 4. 3D ETSM construction scenario.

Table 1. The main simulation parameters

Parameters	Value
The monitored area	100 m × 100 m × 50 m
ETSM tensor size	10 × 10 × 10
Granularity of ETSM tensor	10 m × 10 m × 5 m
Number of RF transmitters (κ)	5, 7, 9, 11
Transmitting power	30 dBm
Transmitting frequency (f)	2.4 GHz
Sampling rate, number of RF transmitters, and number of UAVs in ETSM construction performance	$SR_{\text{aver}} = 0.1, K = 5, G = 3$
The heights of UAVs	5 m, 10 m, 20 m
Positions of RF transmitters (x, y, z)	(91 m, 68 m, 13.9 m), (79 m, 293.5 m, 47 m), (236.5 m, 127.5 m, 34.6 m), (327.5 m, 423.5 m, 18.7 m), (459 m, 166.5 m, 3 m)

As shown in Figure 5 (left), the ideal ETSM is calculated by Ray Tracing (RT) method. Assuming that three UAVs sample the ideal map along different paths, with the sampling rate of each UAV set to 10%, an original spectrum map obtained by a random single-UAV is shown in Figure 5 (middle). The ultimate 3D ETSM constructed by our method is shown in Figure 5 (right). As shown in Figure 5, one single-UAV system cannot accurately recover the ETSM, especially when the distance between two adjacent EM targets is too close. The performance of the ultimate ETSM is superior to that of the single-UAV system. This is because we fuse the observation data from multi-UAVs and eliminate outliers. When using the observation data from a single-UAV to construct the map, the presence of outliers in the data affects the accuracy of map construction.

Next, taking a two-dimensional plane at a certain height in the 3D ETSM as an example, the process and performance of the staged EM target positioning method are demonstrated in Figure 6. Firstly, we set three EM targets at the same XoY plane, which is re-divided into 50 × 50 grids, and size of each grid is 2 m × 2 m. The ideal map of the XoY plane is shown in Figure 6 (left). Then, maintain the sampling rate as 10%, rough positions based on raw data are shown in Figure 6 (middle), and the ultimate result is shown in Figure 6 (right). The red spiders denote the estimated positions of EM targets. Results show that the accuracy of the estimated EM target positions based on MMPLD can be improved by the fused ETSM, which effectively reduces mistakes in the first step of localization. This is because the RSS values used for localization become more accurate after fusion.

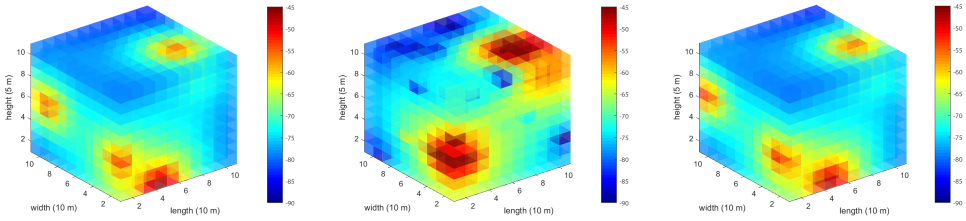


Figure 5. Simulation results of 3D ETSM construction: (left) Ideal 3D ETSM; (middle) Original 3D ETSM obtained by random single-UAV; (right) Ultimate 3D ETSM.

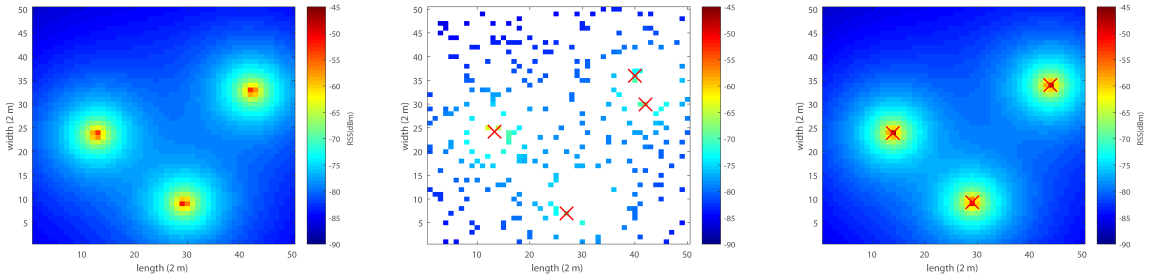


Figure 6. Simulation results of target positioning: (left) Ideal 2D plane; (middle) MMPLD-based rough positioning; (right) Ultimate positioning result.

The root mean squared error (RMSE) is introduced to evaluate the accuracy of 3D ETSM construction, as given by

$$RMSE_{\mathrm{ETSM}} = \sqrt{\frac{1}{N}\sum_{n=1}^{N}|P_{\mathrm{est}}(n) - P_{\mathrm{ide}}(n)|}, \tag{20}$$

$$RMSE_{\mathrm{ET}} = \frac{1}{K}\sum_{k=1}^{K}\sqrt{\left\|\phi_k - \widehat{\phi}_k\right\|^2}, \tag{21}$$

where $RMSE_{\mathrm{ETSM}}$ denotes the accuracy of spectrum map recovery, and P_{est} and P_{ide} are the estimated and the ideal RSS values in dBm at the n-th cube, respectively. $RMSE_{\mathrm{ET}}$ denotes the accuracy of EM target positioning; K is the total number of EM targets; ϕ_k and $\widehat{\phi}_k$ are the estimated and the real position of the k-th EM target, respectively. $RMSE$s of the result in Figure 4 are listed in Table 2; this highlights that the proposed spectrum data fusion algorithm provides greater performance improvements.

In the simulations, the accuracy of the proposed 3D ETSM construction is compared with IDW, alternating direction method of multipliers (ADMM)[13], and iterative completion method of difference of measurement (ICDM)[32]. Figure 7 (left) shows the RMSEs of spectrum map recovery versus signal-to-noise ratios (SNRs) at 10% sampling rate. The localization performance is also compared with several multi-objective localization methods, including orthogonal matching pursuit (OMP)[33], Bayesian compressed sensing (BCS)[34], and adaptive grid multiple targets localization (AGMTL)[35]. Figure 7 (right) shows the RMSEs of target locations versus SNRs at 10% sampling rate. When the SNR increases from -10 dB to 20 dB, the RMSEs of spectrum map recovery and target location of different methods all decrease. This is because we use the fusion algorithm based on re-weighting, eliminating some outliers generated in the process of spectrum completion.

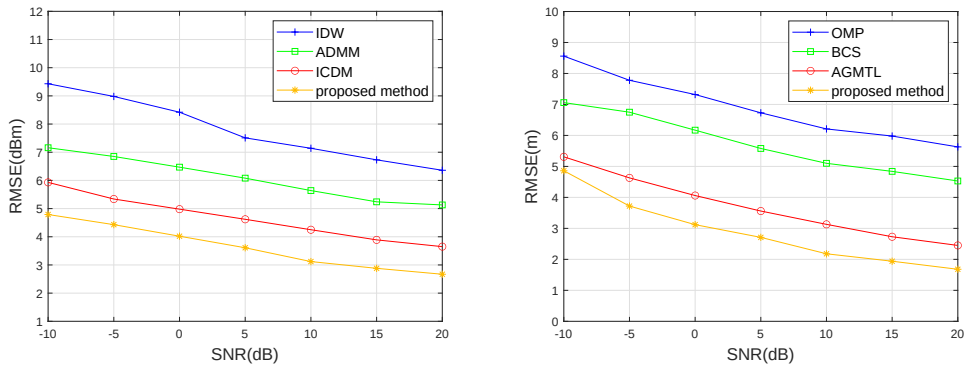


Figure 7. (left) The RMSEs of spectrum map recovery of all the methods versus SNRs; and (right) the RMSEs of target locations of all the methods versus SNRs.

Table 2. RMSEs of 3D ETSM construction

Type	$RMSE_{\mathrm{ETSM}}$ (dBm)	Type	$RMSE_{\mathrm{ET}}$(m)
ETSM before fusion	7.6	rough positioning	2.62
ETSM after fusion	2.24	ultimate positioning	1.33

5. CONCLUSIONS

This paper has proposed a 3D ETSM construction method based on multi-UAV collaboration. Through situational fusion based on re-weighting, complementation of spectrum information has been achieved by multi-UAVs, and the fault tolerance of the ETSM construction system has increased. Furthermore, a staged EM target positioning algorithm based on MMPLD has been proposed for EM target perception. The algorithm rapidly locates multiple EM targets while retaining a certain degree of computing complexity. Compared with existing methods, the simulation results have demonstrated that the proposed 3D ETSM construction method effectively improves the accuracy of spectrum map construction and EM target localization. However, due to the experimental constraints, we only discuss and compare the simulation performance in this paper. In the future research, we will further carry out more field experiments and verify the performance of the proposed construction method.

DECLARATIONS

Authors' contributions

Made substantial contributions to conception and design of the study and performed data analysis and interpretation: Peng Y, Liu K, Cai X

Contributed to approach validation, software simulation, and writing-original draft preparation: Peng Y, Wang J

Contributed to the investigation, supervision, and writing-review and preparation: Lin Z

Availability of data and materials

Not applicable.

Financial support and sponsorship

This work was supported in part by the National Natural Science Foundation of China under Grant No. 62271250, in part by Natural Science Foundation of Jiangsu Province, No. BK20211182, in part by the Key Technologies R&D Program of Jiangsu (Prospective and Key Technologies for Industry) under Grants BE2022067, BE2022067-1 and BE2022067-3, in part by the States Key Laboratory of Air Traffic Management

System under Grant No. SKLATM202305 and in part by the Shanghai Aerospace Science and Technology Fund under Grant No. SAST2023-023.

Conflicts of interest

All authors declared that there are no conflicts of interest.

Ethical approval and consent to participate

Not applicable.

Consent for publication

Not applicable.

Copyright

© The Author(s) 2024.

REFERENCES

1. Ding G, Wu Q, Zhang L, Lin Y, Tsiftsis TA, Yao YD. An amateur drone surveillance system based on the cognitive internet of things. *IEEE Commun Mag* 2018;56:29-35. DOI
2. Huang Y, Zhu X, Wu Q. Intelligent spectrum anti-jamming with cognitive software-defined architecture. *IEEE Syst J* 2023;17:2686-97. DOI
3. Pan J, Ye N, Yu H, et al. AI-driven blind signature classification for IoT connectivity: a deep learning approach. *IEEE Trans Wireless Commun* 2022;21:6033-47. DOI
4. Liu J, Yu J, Niyato D, Zhang R, Gao X, An J. Covert ambient backscatter communications with multi-antenna tag. *IEEE Trans Wireless Commun* 2023;22:6199-212. DOI
5. Höyhtyä M, Mämmelä A, Eskola M, et al. Spectrum occupancy measurements: a survey and use of interference maps. *IEEE Commun Surv Tutorials* 2016;18:2386-414. DOI
6. Phillips C, Ton M, Sicker D, Grunwald D. Practical radio environment mapping with geostatistics. In: 2012 IEEE International Symposium on Dynamic Spectrum Access Networks; 2012. pp. 422-33. DOI
7. Yilmaz HB, Tugcu T, Alagöz F, Bayhan S. Radio environment map as enabler for practical cognitive radio networks. *IEEE Commun Mag* 2013;51:162-9. DOI
8. Du XF, Zhu QM, Wu QH, et al. UAV-assisted spectrum mapping system based on tensor completion scheme. In: MLICOM 2020: Machine Learning and Intelligent Communications; 2021. pp. 16-26. DOI
9. Zhu Q, Zhao Y, Huang Y, et al. DEMO abstract: an UAV-based 3D spectrum real-time mapping system. In: IEEE INFOCOM 2022 - IEEE Conference on Computer Communications Workshops (INFOCOM WKSHPS); 2022. pp. 1-2. DOI
10. Agrawal N, Bansal A, Singh K, Li CP, Mumtaz S. Finite block length analysis of RIS-assisted UAV-based multiuser IoT communication system with non-linear EH. *IEEE Trans Commun* 2022;70:3542-57. DOI
11. Üreten S, Yongaçoğlu A, Petriu E. A comparison of interference cartography generation techniques in cognitive radio networks. In: 2012 IEEE International Conference on Communications (ICC); 2012. pp. 1879-83. DOI
12. Denkovski D, Atanasovski V, Gavrilovska L, Riihijärvi J, Mähönen P. Reliability of a radio environment Map: Case of spatial interpolation techniques. In: 2012 7th International ICST Conference on Cognitive Radio Oriented Wireless Networks and Communications (CROWNCOM); 2012. pp. 248-53. DOI
13. Tang M, Ding G, Wu Q, Xue Z, Tsiftsis TA. A joint tensor completion and prediction scheme for multi-dimensional spectrum map construction. *IEEE Access* 2016;4:8044-52. DOI
14. Hashimoto R, Suto K. SICNN: spatial interpolation with convolutional neural networks for radio environment mapping. In: 2020 International Conference on Artificial Intelligence in Information and Communication (ICAIIC); 2020. pp. 167-70. DOI
15. Yilmaz HB, Tugcu T. Location estimation-based radio environment map construction in fading channels. *Wireless Commun Mob Comput* 2015;15:561-70. DOI
16. Alfattani S, Yongacoglu A. Indirect methods for constructing radio environment map. In: 2018 IEEE Canadian Conference on Electrical & Computer Engineering (CCECE); 2018. pp. 1-5. DOI
17. Wang J, Zhu Q, Lin Z, et al. Sparse bayesian learning-based 3-D radio environment map construction-sampling optimization, scenario-dependent dictionary construction and sparse recovery. *IEEE Trans Cogn Commun Netw* 2023;10:80-93. DOI
18. Zhao Y, Zhu Q, Lin Z, et al. Temporal prediction for spectrum environment maps with moving radiation sources. *IET Commun* 2023;17:538-48. DOI
19. Liu K, Lin Z, Liu Y, Zhu Q, Wu Q, Cai X. A new spectrum map fusing method based on difference group sparsity. In: 2023 IEEE/CIC International Conference on Communications in China (ICCC); 2023. pp. 1-6. DOI
20. Zhang H, Tian Q, Han Y. Multi channel spectrum prediction algorithm based on GCN and LSTM. In: 2022 IEEE 96th Vehicular

Technology Conference (VTC2022-Fall); 2022. pp. 1-5. DOI
21. Zhang H, Peng S, Zhang J, Lin Y. Big data analysis and prediction of electromagnetic spectrum resources: a graph approach. *Sustainability* 2022;15:508. DOI
22. Li S, Sun Y, Zhang H, Wang M, Zhang Z. MTF^{2}N: multi-channel temporal-frequency fusion network for spectrum prediction. In: GLOBECOM 2022 - 2022 IEEE Global Communications Conference; 2022. pp. 4703-9. DOI
23. Cai X, Lin Z, Peng Y, et al. A new variational bayesian-based radiation source positioning method with multistage parameter modification. In: 2023 IEEE/CIC International Conference on Communications in China (ICCC); 2023. pp. 1-6. DOI
24. Trinh-Hoang M, Viberg M, Pesavento M. Partial relaxation approach: an eigenvalue-based DOA estimator framework. *IEEE Trans Signal Proc* 2018;66:6190-203. DOI
25. Zhang Y, Wang M, Tan Z, et al. Design of wireless sensor network location algorithm based on TDOA. In: 2019 IEEE 3rd Information Technology, Networking, Electronic and Automation Control Conference (ITNEC); 2019. pp. 70-75. DOI
26. Liu B, Zhu X, Jiang Y, Wei Z, Huang Y. UAV and piecewise convex approximation assisted localization with unknown path loss exponents. *IEEE Trans Veh Technol* 2019;68:12396-400. DOI
27. Min E, Guo X, Liu Q, Zhang G, Cui J, Long J. A survey of clustering with deep learning: from the perspective of network architecture. *IEEE Access* 2018;6:39501-14. DOI
28. Jordan Y, Carey EP. Semi-supervised K-means++. *arXiv* 2017;87:2597-608. DOI
29. Umer M, Kulik L, Tanin E. Spatial interpolation in wireless sensor networks: localized algorithms for variogram modeling and Kriging. *Geoinformatica* 2010;14:101-34. DOI
30. Bradley E, Trevor H, Iain J, Robert T. Least angle regression. *Ann Stat* 2004;32:407-99. DOI
31. Sun B, Guo Y, Li N, Fang D. Multiple target counting and localization using variational bayesian EM algorithm in wireless sensor networks. *IEEE Trans Commun* 2017;65:2985-98. DOI
32. Lu J, Zha S, Huang J, Liu PG, Chen G, Xu S. The iterative completion method of the spectrum map based on the difference of measurement values. In: 2018 IEEE 3rd International Conference on Signal and Image Processing (ICSIP). IEEE; 2018. pp. 255-59. DOI
33. Tropp JA, Gilbert AC. Signal recovery from random measurements via orthogonal matching pursuit. *IEEE Trans Infor Theory* 2007;53:4655-66. DOI
34. Chi Y, Pezeshki A, Scharf L, Calderbank R. Sensitivity to basis mismatch in compressed sensing. In: 2010 IEEE International Conference on Acoustics, Speech, and Signal Processing; 2010. pp. 3930-33. DOI
35. You K, Yang L, Liu Y, Guo W, Wang W. Adaptive grid multiple sources localization based on sparse bayesian learning. *J Elect Infor Technol* 2018;40:2150-7. DOI

Weinberg *et al*. *Complex Eng Syst* 2024;4:16
DOI: 10.20517/ces.2024.41

Complex Engineering Systems

Research Article

Open Access

Check for updates

Zero trust implementation in the emerging technologies era: a survey

Abraham Itzhak Weinberg[1], Kelly Cohen[2]

[1]AI-WEINBERG, AI Experts, Tel-Aviv 90850, Israel.
[2]Department of Aerospace Engineering, University of Cincinnati, Cincinnati, OH 45231, USA.

Correspondence to: Dr. Abraham Itzhak Weinberg, AI-WEINBERG, AI Experts, Tel-Aviv 90850, Israel. E-mail: aviw2010@gmail.com; ORCID: 0000-0002-2505-9653

How to cite this article: Weinberg AI, Cohen K. Zero trust implementation in the emerging technologies era: a survey. *Complex Eng Syst* 2024;4:16. http://dx.doi.org/10.20517/ces.2024.41

Received: 3 Jul 2024 **First Decision:** 22 Aug 2024 **Revised:** 1 Sep 2024 **Accepted:** 19 Sep 2024 **Published:** 26 Sep 2024

Academic Editors: Shuping He, Hamid Reza Karimi **Copy Editor:** Fangling Lan **Production Editor:** Fangling Lan

Abstract

This paper presents a comprehensive analysis of the shift from the traditional perimeter model of security to the Zero Trust (ZT) framework, emphasizing the key points in the transition and the practical application of ZT. It outlines the differences between ZT policies and legacy security policies, along with the significant events that have impacted the evolution of ZT. Additionally, the paper explores the potential impacts of emerging technologies, such as Artificial Intelligence and quantum computing, on the policy and implementation of ZT. The study thoroughly examines how Artificial Intelligence can enhance ZT by utilizing Machine Learning algorithms to analyze patterns, detect anomalies, and predict threats, thereby improving real-time decision-making processes. Furthermore, the paper demonstrates how a chaos theory-based approach, in conjunction with other technologies such as eXtended Detection and Response, can effectively mitigate cyberattacks. As quantum computing presents new challenges to ZT and cybersecurity as a whole, the paper delves into the intricacies of ZT migration, automation, and orchestration, addressing the complexities associated with these aspects. Finally, the paper provides a best practice approach for the seamless implementation of ZT in organizations, laying out the proposed guidelines to facilitate organizations in their transition towards a more secure ZT model. The study aims to support organizations in successfully implementing ZT and enhancing their cybersecurity measures.

Keywords: Zero trust, policy, eXtended detection and response (XDR), artificial intelligence (AI), quantum computing, chaos theory

© The Author(s) 2024. **Open Access** This article is licensed under a Creative Commons Attribution 4.0 International License (https://creativecommons.org/licenses/by/4.0/), which permits unrestricted use, sharing, adaptation, distribution and reproduction in any medium or format, for any purpose, even commercially, as long as you give appropriate credit to the original author(s) and the source, provide a link to the Creative Commons license, and indicate if changes were made.

1. INTRODUCTION

In recent years, several phenomena have been observed in which their interactions lead to the proliferation of the Zero Trust (ZT) approach. The first is an increase in the number of devices connected to the network, such as Internet of Things (IoTs)[1]. The second is poised emerging technologies, such as Artificial Intelligence (AI), Generative AI (GenAI), and quantum computing. The third is the rapid growth of cyberattacks, attack surfaces, and sophistication levels of attacks[2]. In addition, the COVID-19 pandemic has accelerated the adoption of cloud-based technologies and technologies that enable workers to work from anywhere they would like to. In addition, the White House Executive Order (WHEO) published definitions and migration steps for ZT to agencies[3].

In this paper, we focus on recent technological developments in ZT. The paper will focus on the influences of emerging technologies such as AI, and quantum computing on ZT implementation, elucidating their effects on the formulation of tailored ZT strategies. Additionally, we elaborate on their impact on ZT automation orchestration and migration in the context of new emerging technologies. To the best of our knowledge, only a few ZT survey papers relate to this aspect[4] and this is the first time that the combination between them has been surveyed.

This paper presents the challenges, approaches, and implementation of ZT for Detection and Response (DR) layers, such as Endpoint DR (EDR), eXtended DR (XDR), and Network DR (NDR) also known as Network Traffic Analysis (NTA). As can be learned from its name, DR has two purposes: detecting and responding to security incidents that aim to bypass the End Point Protection Platforms (EPP). ZT is a crucial framework for EDR as it is one of the most exposed points to cyberspace.

The paper is organized as follows: First, we introduce ZT, discussing its history and evolution over the years. Next, we elaborate on the ZT policy and its principles. In the subsequent section, we explore the challenges that ZT faces. Following that, we delve into discussions on ZT implementation methods. Subsequently, we address the integration of ZT with cutting-edge technologies such as AI, chaos theory, and quantum computing, as well as cybersecurity. We also discuss approaches for evaluating ZT. Finally, we conclude by summarizing the main issues and outlining future directions.

While dealing with defense approaches, it is important to bear in mind that while the attack can be considered a success story, even after many failures, the defense must always be successful. Hence, defense capabilities must be better than potential attacks. Cybersecurity experts claim that an attack will eventually occur, and practically, the chances of 100% are only theoretical[5]. Risk can be mitigated by early detection and response to an attack when it occurs. ZT is expected to solve this gap. Since ZT plays a practical role in many organizations, we find in the literature design principles such as designing architecture from the inside out, determination of the access needs at a preliminary stage, focusing on the required organizational outcomes, and using the EDR as a source for inspecting the log traffic[6].

The ZT can help protect against Operational Technology (OT) attacks. OT attacks are designed to exploit systems that are directly on the plant floor[7]. ZT can be applied to Industrial Control Systems (ICS) to ensure that only authorized devices and users can access the system[8,9]. For example, in the case of the 2017 NotPetya attack[10], which caused millions of dollars in damage to industrial sites, ZT principles could have prevented the spread of malware by limiting lateral movement between systems. In addition, ZT can improve Remote Access Security (RAS) by enforcing strict authentication and access control policies[11,12]. ZT can help protect against supply chain attacks by limiting third-party vendors' access to critical systems and data. It can also help protect against IoT-based attacks by ensuring that only authorized devices can access the network[13,14].

Finally, OT attacks using open Application Programming Interface (API) can pose a serious threat to indus-

trial control systems, allowing attackers to gain unauthorized access to OT systems and data[15]. ZT model includes strict access control and authentication policies, network segmentation, and security measures that specifically target open APIs, such as using API gateways to enforce authentication and access control policies. The implementation of a ZT can effectively complement Digital Twin (DT) configurations. DTs create a virtual representation of a physical system, facilitating various purposes such as monitoring, optimization, planning, and decision-making[16,17].

By replicating key aspects of physical objects or systems using sensors and real-time data, DT enables modeling, analysis, and testing of changes prior to real-world implementation. To ensure the protection and segmentation of DT, the application of ZT principles is essential, encompassing strong authentication, authorization, microsegmentation of sensitive data, and centralized monitoring of logs and events[18]. Using DT can increase integration of real-time data and, as a result, ensure robust security measures. This can lead to mitigation of the risks associated with tampering and cyberattacks. ZT principles guarantee that only authorized access is granted, enhancing the security, resilience, and effectiveness of information technology (IT) and operational systems by integrating virtual models with granular, context-aware access controls and monitoring mechanisms[19]. The integration between the two can serve as a valuable test bed for simulating cyberattacks and evaluating the effectiveness of ZT in handling such threats.

1.1. Zero trust history and evolution

The phrase ”Zero Trust” was coined by Stephen Paul Marsh in 1994[20]. The next step occurred approximately a decade later in 2003. The Jericho Forum consortium defined de-perimeterization[21]. They claimed that ZT can be used as a security strategy for de-perimeterization. De-perimeterization is practically the removal of a boundary between an organization and the outside world. Only six years later, in 2009, Google implemented ZT architecture BeyondCorp and published it in 2014[22]. BeyondCorp uses an authentication-based combination of the device and the user. Thus, it eliminates the need for privileged corporate networks.

In 2010, Kindervag *et al*.from Forrester used ZT for access control[23,24]. In their report, Forrester claimed that firewalls are not sufficient in the endeavor effort to cope with cyber attacks[24]. In addition, they coined one of the main premise principles of ZT: “never trust, always verify”[24]. In 2015, ZT analysts reported augmentation in the adaptation of ZT by technology vendors[25,26].

In 2017, Forrester and Gartner published the ZT frameworks: Zero Trust eXtended (ZTX) ecosystem[27] and Continuous Adaptive Risk and Trust Assessment (CARTA)[28] respectively. ZTX is a framework that maps ZT to organizational applications. CARTA is considered a strategic framework that enables organizations to continuously assess their risk of cyberattacks. CARTA also enables the assessment of the trust level of organizational systems. In 2018, the National Institute of Standards and Technology (NIST) and National Cybersecurity Center of Excellence (NCCoE) published the cornerstone paper SP800-207. It defines cybersecurity metrics with a focus on ZT components and principles. In this way, it helps abstractly design the organizational network architecture in the light of ZT without drilling into a specific implementation[29]. In 2019, Gartner introduced the terms Zero-Trust Network Access (ZTNA) and Secure Access Service Edge (SASE) to describe new defenses considered part of the emerging ZT framework[30]. These new models added available layers of protection beyond the traditional network perimeter.

In 2020, the COVID-19 pandemic accelerated widespread adoption of remote work, increasing the need for ZT approaches to secure hybrid workforces[30]. NIST published updated guidance on applying ZT principles in Federal networks in Special Publication 800-207.

In 2021, a Microsoft report found 96% of organizations saw ZT as critical to success due to security and compliance needs[30]. Meanwhile, federal orders and strategies laid the groundwork for public sector adoption to

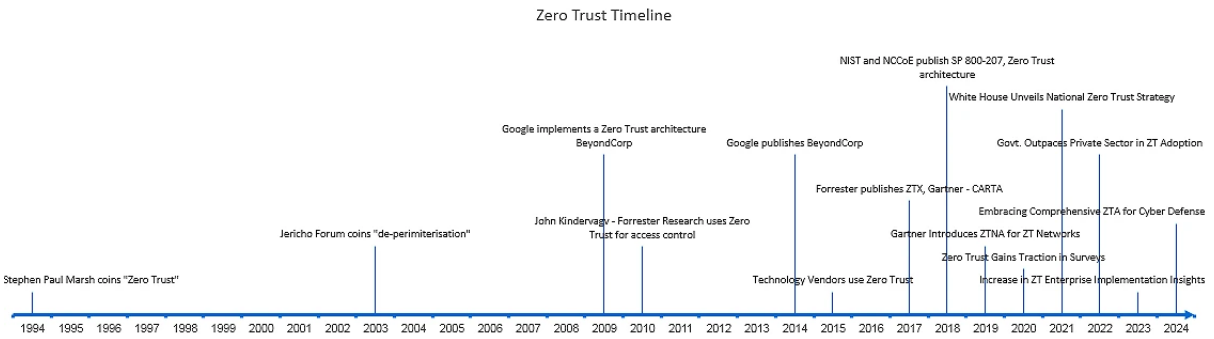


Figure 1. Zero trust timeline.

strengthen national cyber defenses and transition to ZT.

In early 2022, the U.S. government accelerated its adoption of ZT frameworks [30]. United States Office of Management and Budget (OMB) released details of the federal ZT strategy and set requirements for agencies to meet five security goals by September 2024. Acting Director Young issued a memorandum stressing defenses against evolving threats. Additionally, Cybersecurity and Infrastructure Security Agency (CISA) published an expanded Cloud Security Technical Reference Architecture in June 2022, co-authored with two other agencies to guide adoption of ZT in cloud environments. Such proactive government efforts, combined with initiatives worldwide, indicated public sector leaders in ZT according to an Okta (company) report. It found that 72% of surveyed government organizations had active or planned ZT programs compared to 55% of private companies.

By 2023, OKTA reported ZT had gone mainstream [31], with adoption more than doubling in two years and 61% of organizations reporting a defined initiative. Another 35% planned to implement one soon, showing over 90% recognized its importance. The swift rise underscored how ZT strategies delivered stronger security as hybrid work became standard.

By 2024, ZT security reached a critical stage [32]. Adopting comprehensive Zero Trust Architecture (ZTA) became recommended to align defenses with evolving threats. ZT transformed from isolated tools to a foundational change, moving beyond legacy perimeter views. Full ZTA verified all users, assets and applications continuously, strengthening protections while boosting productivity as risks grew distributed and dynamic.

In Figure 1, we present the history and evolution of ZT.

Currently, ZT is widespread and has growing market potential. It is implemented in organizations worldwide that use different architectures and systems on both premise and cloud architectures. It has a prospect of 60.7 billion dollars by 2027, with an annual growth of 17.3% [33]. This is evident in the growth of ZT implementation and usage - horizontally all over the world and vertically - in many market segments and technologies. We can observe the invasion of ZT into 5G networks for healthcare devices [34].

2. ZERO TRUST POLICY AND PRINCIPLES

The ZT policy is a security framework that aims to protect organizations from cyberattacks. As a result, it encompasses all the organizational systems' users, regardless of their physical location. ZT continually validates the system security configuration, as well as authentication and authorization processes [35,36].

ZT changed the architecture of separation between different levels of security zones such as the Internet, De-

Militarized Zone (DMZ), and Trusted and Privileged zones to a controlled architecture[37,38]. ZT employs a Control Plane (CP) to effectively classify and distinguish between trusted and untrusted clients. When the CP acknowledges the client, it accepts the traffic. Typically, ZT uses an encrypted tunnel based on temporary one-time credentials to communicate with a trusted client. ZT transferred the traditional perimeter model and removed the borders between the different zones while maintaining secured communication only with trusted clients.

The CISA proposed the ZT Maturity Model[39] which divides ZT into eight pillars: users, infrastructure, devices, data, applications, networks, visibility and analytics, and orchestration and automation. The model relates to human factors, devices, and data usage. Each pillar indicates an identification process implemented before accessing the data or required services. ZT relates to both the static aspect of security that resides as data in devices and infrastructure, and to the dynamic aspect of data streams in networks and applications.

To achieve the ZT policy, the organization must relate to the security and authentication aspects of each pillar. Missing one of the pillars' security aspects might influence the ZT policy and, hence, breach the organizational security level. The first and most fundamental stage of ZT is user identification. This stage is critical because most breaches use compromised identities, which are difficult to detect[40].

This stage is implemented before accessing organizational resources. ZT defines a ZTNA policy that defines which of the remote workers are eligible to connect to specific resources. In recent years, the commonly used technique for identification has been based on Multi-Factor Authentication (MFA), such as Passkey. MFA is based on asking the user for two or more pieces of evidence for authentication.

ZT defines authorized devices and infrastructure only after going through a compliance process that stands under the Compliance Management (CM) spec. Thus, ZT ensures that the organization aligns with the required industrial cybersecurity regulations. To protect organizational data from exfiltration threats, ZT usually recommends encrypting data and using access control regulation policies, such as least privilege. ZT policy applies to applications in several ways such as legitimacy of the application, authorized user access to the application, and the environment in which the application can run. NIST defines the regulations for the ZT Application workload. Workload is a resource that supports application capability. ZT obligates organizations to define which resources are essential for each application and how they work in the most secure way.

To protect the network, ZT uses techniques such as explicit policies or variable trust. The variable trust uses a score to define the trust of the transferred data when an action is required. An additional ZT pillar involves visibility and analytics[36]. Visibility and analytics focuses on users and network traffic. To enable analytics and visibility, ZT guides organizations to enable network traffic inspection and store the history of logged users, asset logs, and actions. NIST ZT regulations advise the division of on-premise data centers and cloud, as well as workloads to traffic segments. Thus, ZT prevents lateral movement. In this way, the organization can investigate attacks and detect them online.

The eighth pillar of ZT in our list is orchestration and automation[41]. Automation and orchestration are the upper levels of ZT. They aim to deploy and apply ZT security policy. Automation focuses on making a process run without human intervention. It usually includes pipelines and scheduling parts, such as coordinating endpoint security. Orchestration adds optimization to automation. Orchestration usually includes AI components for each pillar. It helps in detecting attacks, identifying users, and responding to cyberattacks. To the best of our knowledge, orchestration has the highest level of ZT technology.

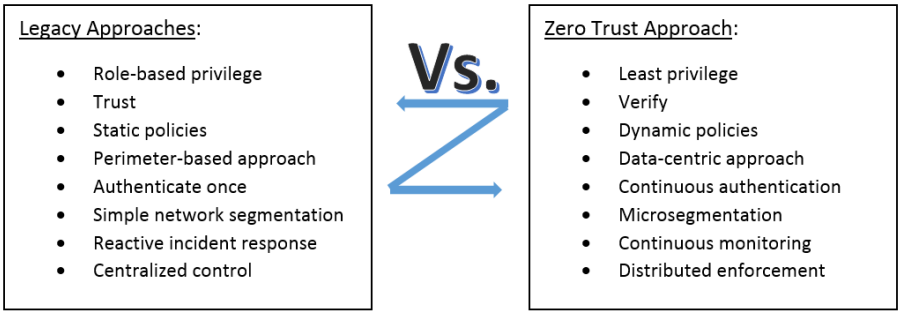


Figure 2. Legacy *vs.* Zero trust approaches.

2.1 From legacy policies and models to zero trust

ZT is considered a new approach compared to other policies and models that have been used for many years in the industry. This section discusses the relationship between them and ZT. One of the main characteristics of the ZT is its trustworthiness. To achieve this, ZT uses the Forrester's paradigm "never trust, always verify"[42]. The journey for achieving trustworthiness from security systems started many years ago by enforcing policies and access control. Access control techniques can be divided into Attribute Based Access Control (ABAC), Role Based Access Control (RBAC), and Fine Grained Access Control (FGAC)[43]. The main difference between the first approaches is whether the access control depends on the access user's attributes or organizational roles. Typically, RBAC is more popular because the same user can have several organizational roles. On the other hand, FGAC uses conditions or entitlements for user access confirmation.

The most popular and well-known models for enforcing access control in industry are the Bell-LaPadula (BLP) and Biba. Both Biba and BLP relate to the Confidentiality, Integrity and Availability (CIA) model. CIA is designed to guide policies for information security within an organization. Biba's main strength is to ensure the integrity of data in an organization, where BLP ensures confidentiality. In order to achieve it, Biba enforces two main rules: "no write up, no read down"[44] while BLP enforces "write up, read down" (WURD) or "no read up, no write down". In this way, Biba's principles prevent data modification by unauthorized objects, while the BLP's rules prevent the leakage of information. To enforce the required results, both models must be implemented as Mandatory Access Control (MAC) or Mandatory Integrity Control (MIC). However, in practice, it is a challenging task to enforce the models because many situations are considered grey zones. To solve these issues, Tidjon *et al.* proposed a ZT model that relied on and combined Biba and BLP[42]. The authors attached trust scores to each object (such as servers, files, and data channels). The scores use weights for each object based on Biba's integrity and BLP's confidentiality levels. ZT can rely on old models and can be implemented as a top layer in organizations that have already used these approaches.

2.1.1 Zero Trust in comparison to legacy policies and models

As mentioned before, ZT is based on solid grounds of legacy policies. The adoption of ZT dictates changes in the concepts and cybersecurity worldviews. Some of the main changes are summarized in Figure 2. The main differences are based on the following points: role-based *vs.* least privilege, trust *vs.* verification, static policies *vs.* dynamic policies, perimeter-based *vs.* data-centric, authenticate once *vs.* continuous authentication, simple network segmentation *vs.* microsegmentation, reactive incident response *vs.* continuous monitoring, and centralized control *vs.* distributed enforcement[4,45,46].

Legacy access control systems often rely on static roles and groups, implementing a role-based approach rather

than a least-privileged one. ZT follows the principle of "least privilege", granting only the minimum access required for a specific task or context. Legacy models typically adopt an initial "trust but verify" approach, where devices and users are granted trust by default within the perimeter. ZT starts with "never trust, always verify" and requires continuous validation.

Legacy policies are typically static and undergo infrequent updates, in contrast to dynamic policies that adapt and evolve more frequently. On the other hand, ZT policies are more dynamic and situation-aware, changing based on context, such as location, task, and risk level. Legacy models primarily prioritize securing the network perimeter, in contrast to data-centric approaches that emphasize safeguarding the data itself. Instead, ZT focuses on securing individual data assets and granting only the necessary access on a per-request basis.

In legacy models, users are typically authenticated once and remain trusted until they log out, as opposed to continuous authentication methods that maintain ongoing verification throughout user sessions. ZT requires the continuous authentication and re-validation of access rights. Legacy network approaches often exhibit coarse segmentation, with simple network segmentation practices in place, as opposed to the more granular and precise microsegmentation methods. ZT leverages fine-grained microsegmentation-based methods, for example, on data, applications, users, and tasks.

Legacy security practices typically rely on reactive incident response strategies that address threats after they have been detected, in contrast to the proactive and continuous monitoring approaches that provide real-time threat awareness and prevention. ZT enables proactive threat detection and containment through continuous monitoring. Legacy security models typically depend on centralized control for policy enforcement, as opposed to distributed enforcement mechanisms that distribute policy enforcement throughout the network. ZT distributes enforcement points, such as EDR, across the full technology stack for increased resilience.

3. ZERO TRUST CHALLENGES

ZT challenges stem from continual changes in the organizational environment. These changes can be endogenous or exogenous. Organizational management decides on internal changes and reacts to environmental changes.

These decisions and other factors cause organizations to constantly change workers' positions and, as a result, their roles in the computational systems are changed. Worker status also changed on a frequent basis. New workers join organizations where others leave. In addition, each worker usually uses more than one device for his work and connects it to the organizational network. Moreover, in each device, several installed applications were used by their owners. The overall number of applications and devices is growing. An additional trend that has been evident in recent decades is data and service distributions. Organizational data and services are distributed in a wide variety of places. Some of them are located in the cloud, whereas others are on-premise.

The implementation of ZT in organizations is a phased project. Each phase depends on the previous phase, and the final prospective results can be achieved only after years[47]. During the implementation of the ZT project, the environment constantly changes. New technologies are added, and source allocation is changed. In addition, there are many changes in budget allocations in the organization, as well as in projects and ZT levels.

An additional aspect of project implementation is its impact on organizational policy. As ZT is a cornerstone in organizational security, it is supposed to influence its security policy. Consequently, it can cause a domino effect on other computational and security systems, as well as attack surfaces. ZT also influences organizational standards and procedures. It is necessary to close the gap between the pre and post-implementation stages

of ZT. One of the main approaches for closing this gap requires integration between departments, teams of workers, products, and legacy systems. This is usually supported by new standards and procedures. A common solution for such an integration is the creation of an organizational repository that integrates the relevant information and helps coordinate between ZT project users and leaders.

The ZT project requires inspecting both inside and outside the perimeter of an organization. Since ZT is based on the continual inspection of organizational security, continual inspection of the relevant network components is required. It requires defining tools and metrics to monitor the security status. It also has an impact on organizational risk management. Last but not least, it requires a thorough inspection of network edges such as EDR, Internet Service Provider (ISP) components, organizational IoTs, and employees' applications and devices under the Bring Your Own Device (BYOD) policy. The challenges of ZT require not only an overall inspection of the current organizational systems but also looking outside the perimeter of an organization. It involves not only systems but also organizational workers and management, as well as every entity that works with the organization.

Emerging network attack techniques present key challenges to current ZT frameworks. Side-channel attacks exploit implementation vulnerabilities, bypassing authentication and encryption safeguards, undermining the principle of verifying every request[48]. Addressing novel side-channel risks is crucial. Password guessing attacks, stemming from compromised credentials, necessitate robust credential policies and passwordless authentication for mitigation[49,50].

There is a unique solution for authentication that provides a strong defense against account compromise such as Attribute-Based Password Authenticated Key Exchange (AB-PAKE) protocol, ensuring that only two legitimate users with desired attributes and correct passwords can establish a shared session key. However, ZT may not fully resolve issues in initial credential management. Techniques such as deepfakes pose detection challenges for existing methods such as behavioral analytics, requiring ZT strategies to identify manipulated requests. Distributed and encrypted threats obscure network visibility, demanding enhanced endpoint data for accurate risk identification. To combat the rapid pace of new attacks, ZT must blend segmentation for resilience with rapid threat containment strategies based on user behaviors.

Blockchain technology can serve several vital roles in supporting ZT architectures[51]. It excels in identity management by offering a decentralized approach to handling digital identities and credentials, mitigating single points of failure and enabling identity verification without central authority reliance. Through smart contracts, blockchain can enforce detailed, dynamic access control policies, including context-based rules and trust attestations. The immutable ledger of blockchain ensures data integrity, aiding in detecting unauthorized changes and anomalies within a ZT framework.

Moreover, blockchain facilitates trust establishment through transparent cryptographic verification, aligning with ZT's principle of verifying access trust without internal system visibility. By encoding ownership and lifecycle details on blockchain, asset management gains enhanced visibility into device identities, postures, and authorization levels for informed access decisions. Smart contracts also streamline policy enforcement, automating complex access policies in alignment with business rules stored on blockchain, ensuring consistent policy application in decentralized business environments.

The impact of ZT on operational overhead varies based on organizational implementation[52]. Initial setup and policy configuration may demand substantial effort initially, but ongoing operations typically do not impose significant overhead once established. While granular access controls and asset visibility add processing and storage requirements, these costs are balanced by long-term breach mitigation and enhanced access management efficiency.

Leveraging existing infrastructure minimizes additional hardware/software expenses, and automation through APIs and policy engines reduces manual workload. Workload segmentation and least privilege access optimize resource usage, while enhancing organizational agility and enabling secure cloud/remote access. Although there are upfront costs, a well-designed ZT approach focused on automation and efficient access management generally does not result in intolerable ongoing operational burdens at scale, emphasizing the importance of strategic resource planning.

In the next subsections, we divide the most fundamental ZT challenges into migration, automation, and orchestration. For each challenge, we will explain how emerging technologies, such as AI, can help organizations fulfill the challenge.

3.1 The role of AI in zero trust security

The AI revolution is already in place, with wide use in many fields, including cybersecurity. The AI is a double-edged sword. This is evident in malware generation using generative pre-trained transformer (GPT) tools[53]. The endless race between attackers and defenders relies on advances in AI technologies and solutions. In this section, we identify the way in which AI can integrate with ZT and elevate it to a higher level.

Usage in the ZT field can be classified into four main categories: CP, identity verification, attack detection, and monitoring[41]. The CP is the ZT brain responsible for decision making regarding whether to grant object access[35].

ZT goes hand-in-hand with the AI technology. AI can help in the implementation of ZT, as described before, and the symmetrical implementation of ZT intensifies the need for AI. The adoption of ZT policies enhances the need to use AI based on security ecosystems. Implementing ZT in an organization creates more data that stream from more objects and sources. This also affects the microsegmentation process and intensifies the need to analyze the data at a more granular level. By implementing ZT, there is a strict need to enforce policies. AI and automation can be leveraged to dynamically define and enforce fine-grained, context-aware access policies required for a ZT model. In addition, AI can be used to continuously analyze the risk levels associated with different entities, such as users, devices, events, and processes. AI dynamically adjusts ZT policies and responses in real-time.

The continuous verification requirements of ZT make it a natural fit for AI technologies that can monitor user and device behavior in real-time and detect anomalies. This includes behavioral analytics. Rapid changes in ZT environments require fast responses to security incidents. Fast responses to security incidents can be achieved by AI-driven automation, for instance. The implementation of ZT increases the number of system alerts. Only a small portion of alerts are relevant and must be handled. AI system reduces alert fatigue by reducing false alarms and highlighting and forwarding important issues. The nature of ZT increases the operational costs. AI enables automation of the tedious and routine operation of the ZT system and, as a result, can decrease operational costs.

3.2 Common AI algorithms for supporting zero trust cybersecurity

ZT classification and clustering are important techniques used in cybersecurity to identify potential security threats and protect against cyberattacks. These algorithms can be divided into supervised and unsupervised algorithms, which are also known as classification and clustering.

Classification algorithms can be used in ZT security models for purposes such as user and entity classification, anomaly classification, network traffic classification, file classification, and email classification. Machine Learning (ML) algorithms can classify users, devices, workloads, and applications into risk categories (such as high, medium, and low risk) based on their attributes and behaviors. This aids in access control and segmentation

decisions. Anomaly classification can be trained based on normal behavior and activity patterns to classify new observations as normal or anomalous. This enabled the detection of threats and policy violations. Network traffic analysis can classify traffic into known categories, such as web, email, and Voice over Internet Protocol (VoIP), to enforce microsegmentation policies and detect abnormal traffic. File classification algorithms can classify files as malicious or benign to detect malware and block harmful files from entering a network. Email classifications can be used to detect phishing emails. The ML algorithms can be used to detect and filter threats before they reach the users.

The common classification algorithms used for ZT include Support Vector Machines (SVM)[54], Decision Trees (DT)[55], Linear Discriminant Analysis (LDA)[56], Artificial Neural Networks (ANN)[55], Convolutional Neural Networks (CNN)[57], Recurrent Neural Networks (RNN)[58], AutoEncoders (AE)[59] and Bidirectional Encoder Representations from Transformers (BERT)[60].

Clustering algorithms can be used in ZT security models in several ways, such as device and user grouping (where the groups are unknown in advance), application workload clustering, anomaly detection, threat hunting, and segmentation optimization. Clustering algorithms can group users and devices with no prior knowledge of relevant groups. These algorithms use similar attributes, access needs, and risk profiles. This can be used to assign them to roles and enforce the least privileged access controls. In addition, the algorithms can be used for clustering workloads based on their communication patterns, and dependencies can help optimize network microsegmentation and isolate workloads with different security requirements. Similar to classification algorithms, clustering algorithms can be used for anomaly detection where the groups are not explicit in advance. These algorithms can detect deviations in clustering patterns over time. For instance, if a node suddenly changes in a cluster, it can indicate anomalies and potentially suspicious behaviors. Threat hunting can be performed by clustering entities based on their network behaviors, and threats that exhibit different patterns can be identified and flagged for further investigation. An additional method to use clustering algorithms in the context of ZT is segmentation optimization. Network traffic patterns can be clustered to identify natural segmentation boundaries within the network, thereby aiding the design of the microsegments.

The commonly used algorithms for ZT clustering tasks are Affinity Propagation (AP)[61], Density-Based Spatial Clustering of Applications with Noise (DBSCAN)[62], Hierarchical clustering[63], Gaussian mixture modeling (GMM)[64,65], Self Organizing Map (SOM)[66] and K-Means[67].

A combination of supervised and unsupervised learning, classification, clustering, and neural network algorithms can be leveraged to implement the core functions required for ZT security model tasks, such as anomaly detection, role-based access, and behavior analysis.

3.3 Combating GPT and AI-based attacks with zero trust cybersecurity framework

In recent years, there has been a breakthrough and profileration of AI models and GPT. Side by side, they enable novel attack vectors. ZT, as a cybersecurity framework, has to adapt itself to these types of attacks and provide policies and solutions for mitigating them. AI-generated attacks are a growing cybersecurity threat that can be used by malicious actors to bypass the traditional security measures. These attacks can be generated using ML models and can include a variety of tactics such as spear-phishing, malware, and social engineering. To protect against AI-generated attacks, organizations can implement a ZT model that limits access to critical systems and data, and continuously monitors potential threats. This can include strict access controls, such as MFA and role-based access controls, and the continuous monitoring of network traffic and user behavior.

Additionally, organizations can use security solutions that are specifically designed to detect and respond to AI-generated attacks, such as AI-based threat detection systems that use ML algorithms to analyze network traffic and identify suspicious activities. The chaos theory-based approach can also be used to handle AI- and

GPT-based attacks. GPT has many useful applications and can also be used maliciously by hackers to generate realistic-looking phishing emails, social engineering messages, and other types of attacks. Malware generation using GPT tools is already available in [53]. We dedicate the next section on how chaos theory techniques can be used to detect and respond to these attacks [68]. To protect against AI- and GPT-generated attacks, organizations can implement a ZT model that limits access to critical systems and data, and continuously monitors potential threats. Additionally, organizations can use security solutions specifically designed to detect and respond to GPT-generated attacks, such as anti-phishing solutions that use ML algorithms to analyze the content and context of emails to identify suspicious messages.

4. ZERO TRUST STRATEGY AND APPROACHES

In this section, we describe several common ZT approaches that organizations can adopt, including the strategies and technologies they employ as part of a comprehensive ZT approach. The first approach is identity-based access control [69,70], which grants access based on verified user or device identities rather than network location, using MFA and strong identity management systems.

The second method was microsegmentation [71,72], which isolates the systems, workloads, and data within the network to minimize lateral movement if one asset is compromised. This method enforces strict control of network traffic. Additionally, the least-privileged access approach ensures that users and services only have the minimal access rights necessary to perform their assigned tasks. Privileges are granted on a just-in-time and as-needed basis. An additional relevant access approach is adaptive access [73,74], which dynamically adjusts access privileges based on real-time factors such as location, device health, and authentication strength, applying more stringent access controls for high-risk situations.

While minimizing access to entities, it is necessary to continuously monitor organizational systems and networks. Continuous monitoring and analytics enables this feature [35], as it constantly monitors network traffic, assets, and user behavior for anomalies that could indicate threats. AI and ML were used to detect deviations from normal patterns. To continually monitor organizational data traffic, gateways and service edges must be secured and monitored. Secure service edges enable the strict control of access to APIs and other external touchpoints [34,35]. The identity, permissions, and context of each request should be verified. In addition to implementing continuous monitoring, the organization can implement User and Entity Behavior Analytics (UEBA) [29,75]. It plays an important role in continuous monitoring. UEBA solutions can detect anomalies and deviations in things, such as user login and access patterns, device usage and communication patterns, privileged account activity API, and application usage. The other security aspect is related to data.

ZT requires data encryption [4,76]. Encrypting data at rest and in transit to prevent unauthorized access, even if the system is compromised. Therefore, key management and robust policies are critical. In recent years, there has been a transformation from an on-premise infrastructure and services to the cloud. ZT strategy involves securing a cloud workload [35,38,77]. ZT principles are applied to Infrastructure as a Service (IaaS), Platform as a Service (PaaS), and Software as a Service (SaaS), including verifying managed identities, encrypting data, and enabling activity monitoring.

The aforementioned common approaches and technologies are part of a comprehensive, general ZT strategy. It is important to implement multiple types of controls instead of relying on a single technique in isolation. An additional approach to ZT involves the training and education of teams and users. Training and education are crucial for creating ZT environments [78]. Users must understand why policies have changed and how their workflows may have been impacted. This could reduce friction and encourage adoption. From the perspective of implementation and project management, the organization must consider that ZT extends beyond technology. It also requires changes in processes, governance, and organizational culture. These include establishing a

ZT Center of Excellence (ZTX CoE) and creating a ZT roadmap and milestones[29,35]. This section described some of the common strategies and technologies that organizations employ as part of a comprehensive ZT approach. Implementing multiple types of control instead of relying on any single technique in isolation is crucial. Moreover, it is essential to remember that ZT is an ongoing journey rather than a final destination. Organizations must consistently evaluate and optimize their ZT posture in response to evolving threats and improving security maturity.

5. ZERO TRUST IMPLEMENTATION BEST PRACTICE

Earlier, we described the ZT migration. ZT implementation establishes a ZT posture from the start of a new environment. ZT migration transitions from an existing traditional security model to ZT architecture over time.

Organizations can make a smooth transition to ZT security over time by using several principles. To successfully adopt a ZT model, organizations should begin with small-scale pilots to gain experience, validate the value proposition, and troubleshoot any issues before gradually expanding[28,29,79,80]. The management and leading team should conduct a comprehensive inventory of all assets, including users, applications, devices, and data, to establish visibility and a baseline for the ZT model.

Several success stories illustrate the impact of ZT on the organization. Airbus[81], Capital One[82], and NASA[83] successfully implemented models for enhanced security and operational efficiency. Airbus witnessed that ZT was extended to corporate data across email, collaborative applications, and custom-built solutions while maintaining a balance between security and productivity. Mobile endpoints were securely protected from cyber threats through proactive visibility, detection, and remediation of potential issues from a cloud-based platform that enabled smooth, simple deployment to over 100,000 corporate devices. An easy-to-use, non-intrusive interface allowed field workers to remain productive while accessing resources with the confidence of robust protection everywhere.

Capital One's adoption of ZT reflects an IT security approach mandating thorough identity validation for all users and devices attempting to access network assets, irrespective of their location within or beyond the network perimeter, showcasing the importance of such measures in bolstering overall network security. Additionally, ZTNA serves as a critical facet within the SASE framework, emphasizing the significance of adaptive security protocols within contemporary network architectures.

NASA adopted ZT principles to securely enable hybrid workforces to collaborate from anywhere, using any device at any time as guided by its Future of Work strategy. Well-implemented ZT architectures streamlined cybersecurity efforts by providing consistent security controls and user experiences regardless of location. As a guiding principle for security architectures aimed at improving security posture and increasing cyber resilience, ZT both reduced risks from malware infections and minimized potential impacts of attacks. Partial ZT deployments within NASA nonetheless yielded dramatic security enhancements by guiding more secure cloud computing through identity-based adaptive controls and demonstrating that perfect implementations should not preclude considerable improvements from good progress toward a ZT model.

While success stories illuminate the path for some ZT projects, a different narrative emerges when considering the potential pitfalls that could lead to failure in US federal agencies, as predicted by Gartner[84]. Gartner Predicts 75% of U.S. Federal Agencies Will Fail to Implement ZT Security Policies Through 2026. These pitfalls include funding shortfalls causing implementation delays, a cybersecurity skills shortage impeding recruitment efforts, struggles to meet policy deadlines amidst budget constraints, limited progress reporting complicating transparency, and the looming risk of incomplete ZT adoption leaving agencies vulnerable to threats,

potentially resulting in service disruptions or costly data breaches.

To achieve the desired end state, a clear vision and roadmap should be articulated and broken down into manageable phases and priorities. It is equally important to focus on changes in security policies, procedures, and people, as it is on technologies to ensure buy-in from all stakeholders. Automation should be used wherever possible to minimize manual effort and human error, starting with easy wins to build momentum and validate the concept[39].

Incorporating API-based access for applications can help minimize fragile and centralized components. A risk-based approach should be adopted, prioritizing high-risk users, assets, and access for initial ZT implementations to maximize the impact[85]. Careful planning and testing should be performed when integrating various zero-trust solutions to avoid these issues. A clear change management plan should be developed, communicating changes to employees, predicting impacts, and formulating a plan to minimize disruptions while providing adequate training[86,87].

A governance model should be created, defining roles, processes, policies, and guidelines around ZT to manage and maintain it in the long term. Regular progress measurement using metrics can help evaluate the effectiveness and identify areas for improvement, allowing for necessary adjustments. Finally, a multi-year roadmap should be developed to guide ZT implementation and achieve the desired end state over time[80].

In addition, it is always beneficial to follow the best practice guidelines that have already been tried in other organizations. The first principle is to start small but think big. It is recommended to begin with small-scale pilots to prove value and address any issues before gradually expanding to the entire organization. Conducting a full inventory of all assets, users, devices, applications, networks, and data provides visibility and a baseline for ZT models.

Creating a clear vision and roadmap for the desired end state, and breaking it down into actionable phases and priorities, helps organizations achieve their goals and minimizes risk and complexity.

6. AI AS A SUPPORTIVE SOLUTION FOR ZERO TRUST CHALLENGES

In this section, we will explore the primary ZT challenges of migration, automation, and orchestration. We will discuss and demonstrate how AI can enhance the solutions for these challenges.

6.1 Migration challenges and how AI can help

ZT migration refers to the transition of an existing traditional network security model to ZT architecture. We can identify several potential challenges that organizations face when transitioning to a ZT security model, including complexity[25,88], resistance to change[89], cost[90,91], visibility[92], compatibility of legacy systems[73], integration[72], technology immaturity[93], lack of skills and expertise[94] and implementation time[92]. Navigating the complexities of ZT implementation requires a holistic multilayered approach that encompasses numerous changes across networks, systems, applications, processes, and policies. This level of change is inherently complex to implement[25,88]. Furthermore, resistance to change can pose a challenge, as some organizations face pushback from employees who are comfortable with the status quo and are reluctant to adopt new security practices and policies. Effective communication and change management strategies are crucial[89]. AI plays a significant role in addressing these challenges. By automatically enforcing dynamic policies, AI is well suited for implementing fine-grained, context-aware, and continually adapting access policies at the core of ZT. Additionally, AI's scalability surpasses that of humans, reducing resistance to change.

Another aspect to consider is the cost of implementing a comprehensive ZT model. The inclusion of vari-

ous components such as MFA, microsegmentation, and continuous monitoring can be financially demanding, particularly for large organizations[90,91]. Nevertheless, leveraging AI and ML to automate complex tasks can help lower the operational costs involved in establishing and maintaining a strict ZT architecture. Moreover, many organizations realize a lack of visibility in their existing networks, systems, and access rights during the planning stage of ZT implementation. This lack of visibility adds further complexity to the planning and implementation processes[92]. AI can contribute to improving visibility by utilizing ML techniques to analyze network traffic, endpoint data, log files, and other relevant data sources, thereby providing a clearer understanding of the existing environment.

In addition, the incompatibility of legacy systems with ZT features, such as continuous authentication and device posture checks, presents another challenge. Overcoming this requires the implementation of workarounds, replacements, or even the creation of air gaps to bridge the compatibility gap[73]. Furthermore, integrating ZT solutions and technologies can be a challenging task, particularly when dealing with multiple point products from various vendors. This requires careful planning and rigorous testing to ensure successful integration.

In addition to the challenges of integrating ZT solutions and technologies from multiple vendors, organizations may face the hurdle of dealing with relatively immature technologies. Technologies such as identity management, microsegmentation, and other related components may still be in the early stages of development, demanding that organizations consistently update and enhance their implementation. Therefore, careful planning, rigorous testing, and a proactive approach to technology updates are essential for overcoming these obstacles and ensuring successful ZT implementation[72].

In addition, the lack of skills and expertise in areas such as identity, access management, segmentation, and cryptography can pose a hurdle for organizations adopting ZT[94]. AI can alleviate this challenge by automating complex authentication, authorization, access control, and monitoring processes, thereby reducing the manual effort and training required by workers. Implementing a full ZT transformation across an entire organization is a time-consuming endeavor, often taking months or years. The scale and complexity involved necessitate careful planning, phased implementation, and creation of roadmaps to ensure a successful and efficient transition[92].

In addition to the aforementioned challenges, AI can significantly contribute to ZT in various areas such as continuous verification, risk-based decisions, reducing alert fatigue, and detecting anomalies. Continuous verification, a key tenet of ZT, can be achieved through AI technologies such as behavioral analytics and anomaly detection. These AI capabilities enable continuous monitoring of user and device activities, ensuring the ongoing verification of trustworthiness.

The role of AI in ZT extends to risk-based decisions as it can continuously analyze risk levels associated with different users, devices, applications, network segments, and events. By dynamically adjusting ZT policies and responses in real time based on this analysis, organizations can effectively manage and mitigate risks. AI-powered solutions have been developed to combat alert fatigue. These solutions can filter and prioritize ZT alerts, allowing human analysts to focus on critical issues. By reducing mental exhaustion and human error, organizations can maintain a high level of vigilance in their security operations. Furthermore, AI techniques such as ML and deep learning excel in detecting anomalies and outliers in large datasets. As ZT relies on continuous monitoring and verification, these AI capabilities are critical for identifying potential threats and security breaches.

By leveraging continuous verification, risk-based decisions, alert fatigue reduction, and anomaly detection enabled by AI, organizations can enhance the overall security of their ZT implementation, effectively mitigate risks, and ensure a robust security posture. In summary, AI should be leveraged wherever possible during ZT

migration to provide better insight, automate processes, enforce dynamic policies, continuously verify trust, make risk-based decisions, accelerate remediation, reduce costs, and detect anomalies. AI can help address many of these challenges and streamline the transition to a ZT model.

6.2 Automation challenges and how AI can help

ZT automation uses automated technologies and processes to implement the principles of ZT architecture. Several automation challenges are associated with ZT security models. The main automation challenges revolve around integrating solutions, orchestrating policies and scaling operations, and gaining full visibility. ZT principles require the continuous verification of trust, but current technologies still rely heavily on human intervention for many tasks. Automation is an important goal; however, full autonomy remains elusive. For completeness, some of the points overlap with the migration section.

As mentioned above, implementing ZT architecture involves addressing various challenges in different areas. Authentication and access requests, for instance, require the automation of these processes at scale, which can be complex. This entails the integration of identity management solutions with applications, APIs, and devices to establish a comprehensive and cohesive authentication framework[95,96].

Similarly, the continuous monitoring of trustworthiness is crucial in ZT; however, it poses a set of challenges. The continuous monitoring of users, devices, and applications in an automated manner requires the integration of various monitoring tools to gather and analyze relevant data[75]. On the other hand, incident response presents a challenge in fully automating the detection, containment, and remediation of security incidents, often requiring some degree of manual intervention[97,98].

Device onboarding in ZT networks involves automatic provisioning of devices and applications while enforcing security policies, which can be a complex process. This requires integration of identity management, configuration management, and network access control. AI can play a crucial role in automating the provisioning of devices and applications and ensuring the enforcement of necessary security policies, configurations, patches, and updates[99–101].

Automating the issuance, renewal, and revocation of credentials such as certificates and tokens at scale is notoriously challenging in ZT. Certificate management requires careful attention to obtain this right[75]. Privileged access management is another area where automation and control of privileged access for administrative activities while maintaining operational efficiency remains an ongoing struggle[102].

Data protection in ZT involves automatically encrypting data at rest and in transit according to security policies, which can be particularly challenging for big data and real-time systems[103]. In addition, automating the generation of audit reports and ensuring compliance with regulations is difficult and often relies on manual reporting, although AI can offer potential solutions in this area[104].

Finally, API management poses a complex endeavor, especially at an enterprise scale, as it requires the automatic management of the full lifecycle of APIs, including discovery, security, monitoring, and deprecation[105]. These challenges emphasize the need for careful consideration, integration, and automation in multiple areas of ZT implementation to achieve a robust and effective security framework.

AI and ML can significantly help with automation in ZT environments. They show great potential for automating many complex components of ZT environments, such as threat detection, dynamic policy management, risk-based access control, device onboarding, accelerated remediation, and verification of trust and compliance. This can streamline the operations and reduce costs.

AI systems can continuously analyze the risk levels associated with different users, devices, applications, locations, and other relevant factors to make automated access control and security decisions based on risk. These capabilities are already emerging today and will likely continue to improve and expand in the coming years to further enable AI-driven automation within ZT architectures.

6.3 Orchestration challenges and how AI can help

As mentioned above, ZT orchestration refers to the ability to automate and coordinate various systems and tools involved in organizational security. Orchestration involves integrating multiple automated systems and technologies involved in the security ecosystem, whereas automation focuses on automating individual ZT tasks and functions without direct human input. Similar to automation, the main orchestration challenges revolve around integrating point solutions, managing policies at scale, achieving visibility in operations, automating processes, and minimizing business disruptions. ZT requires coordinated actions across the full technology stack, and effective orchestration is key to success. Some of the key orchestration challenges for ZT security models include a range of crucial aspects, such as integrating solutions[106,107], management policies[108], scaling operations[109], achieving visibility[92], enforcing trust[110], automating responses[111], automated security workflows[47], checking posture[90], handling incidents[112], minimizing disruptions[113], and reducing costs[90].

Integrating solutions from multiple vendors for tasks such as identity management, access control, device management, network segmentation, and encryption can be difficult owing to the limited interoperability among these solutions[106,107].

In addition, managing various security policies across multiple systems, including access control, device configuration, encryption, and monitoring, requires complex orchestration to ensure dynamic enforcement[108]. Scaling ZT operations to support large-scale authentication, authorization, and monitoring of thousands or millions of users and devices poses further challenges that necessitate scalable solutions[109].

Achieving visibility by orchestrating data from various tools to obtain a unified view of users, devices, applications, networks, and threats is another challenge. Solutions often operate in silos, but AI techniques, such as ML, can analyze data from different ZT tools to provide a unified view of activities within the environment, enabling better orchestration[92]. Enforcing trust and continual verification across dynamic environments, with frequent additions and removals of users, devices, applications, and networks, adds complexity to the orchestration process[110].

Automating responses and coordinating solutions, such as Security Information and Event Management (SIEM), EDR, Network Access Control (NAC), and other relevant solutions in real time pose challenges, as most responses still require human input. However, AI models can be trained to autonomously integrate different ZT solutions from various vendors, minimize manual effort, and facilitate the correlation of data and alignment of policies[111].

Over time, AI may be able to orchestrate entire security workflows within ZT environments autonomously, from continuous monitoring to incident response, with minimal human intervention[47]. Another significant challenge involves effectively orchestrating security posture checks and trustworthiness assessments of devices and applications. This requires seamless coordination of operations across various solutions, including firewalls, antivirus programs, and configuration managers[90]. Furthermore, orchestrating end-to-end workflows to manage security incidents from detection to resolution requires centralized visibility, control, and coordination among teams, tools, and processes[112]. Minimizing disruptions to users and critical business processes during ZT operations requires central governance and policy enforcement for effective orchestration[113]. Finally, effectively orchestrating and automating ZT processes can optimize costs by reducing redundant tooling,

streamlining purchases, and improving the overall efficiency[90].

AI and ML can be instrumental in orchestrating ZT environments and offer significant benefits in several key areas. First, AI is well suited for dynamic policy orchestration, as it can enforce and adapt fine-grained, context-aware access policies that form the foundation of ZT. By leveraging AI, policy changes can be orchestrated in real-time across multiple systems, enabling efficient and agile policy enforcement[111].

AI systems can also play a pivotal role in risk-aware orchestration. Through continuous analysis of the risk levels associated with users, devices, applications, locations, and other relevant factors, AI can dynamically adjust the orchestration and prioritize them based on risk. This proactive approach allows for adaptive and intelligent decision-making in managing security measures within ZT environments[114].

Furthermore, as ZT-related regulations continue to evolve, AI has the potential to automate compliance orchestration. Although this remains a challenge at present, in the future, AI systems may be capable of automatically orchestrating the necessary people, processes, and technologies to ensure compliance with ZT regulations. This would streamline compliance efforts and enhance the overall effectiveness of the ZT security frameworks[41]. The integration of AI and ML technologies into ZT environments empowers organizations with advanced capabilities to dynamically enforce policies, adapt to changing risk levels, and potentially automate compliance-related processes. The synergy between AI and ZT orchestration contributes to the overall efficacy and resilience of security measures in modern digital ecosystems.

AI and automation show great promise for orchestrating the complex components of ZT environments through techniques such as automated solution integration, dynamic policy management, enterprise-wide visibility, risk-aware decision-making, accelerated incident response, automated security workflows, and reduction of alert fatigue. AI can facilitate end-to-end coordination and synchronization within a ZT network.

7. ZERO TRUST AND CYBERSECURITY TECHNOLOGIES FOR DETECTION, PREVENTION, AND RESPONSE

In the previous sections, we mentioned algorithms and an AI approach for supporting the ZT response to attacks. In this section, we discuss the interaction between ZT and technologies, tools, and approaches that provide security solutions for detection, prevention, and response to cyber-attacks. ZT uses and dictates policy for tools and technologies that help organizations interact with the outside world. The definition of ZT provides a comprehensive approach to cybersecurity, helping organizations protect their critical systems and data from cyber threats. By implementing strict access controls, continuous monitoring, and risk-based authentication, organizations can reduce the attack surface and better protect themselves against potential threats. Additionally, the use of detection, prevention, and response tools can provide early warnings of potential threats and enable organizations to respond quickly and effectively to security incidents.

This section provides insight into the interaction between ZT and technologies and solutions such as XDR, EDR, NDR/NTA, Security Orchestration Automation and Response (SOAR) and SIEM[115,116]. The section explains why the aforementioned technologies can work synergistically with ZT and enhance the organizational security level.

The combination of XDR can countermeasure attacks, such as Living Off The Land (LOTL)[117]. XDR is a security approach that aims to integrate multiple security solutions, such as EDR, NDR/NTA, and SIEM, into a unified platform[116].

AI can be a meaningful tool for enhancing XDR and ZT. XDR is based on large volumes of backlogs. Even

a small proportion of false alarms can cause tedious and intensive work for users. An ML-based system can decrease the human labor involved in analyzing a large amount of data. In addition, ML systems can increase the level of accuracy and, hence, decrease the number of false alarms. Combining the ZT policy with the XDR can practically decrease the number of logs by constantly verifying the endpoint online. However, constant verification can slow down the system response[118]. Practically, there is a need to determine the optimal point between the response time and the required threat level. This is a practical compromise between absolute never trust, ZT policy, and organizational needs.

Because there is a high probability that an organization will become a target for cyberattacks, one of the effective ways to handle it is detecting it as soon as possible[5]. Once an attack is detected, a rapid response is required. The effectiveness of an organization in handling an attack is one of the crucial parameters for its success in countermeasuring the attack. Detecting an attack at the endpoints usually indicates the early stage of the attack. Hence, implementing ZT in endpoint devices helps the organization cope with severe stages of attack.

XDR tools are currently attempting to bring together all the relevant security solutions. These are intended to unify multiple security capabilities into a single solution that offers automated analysis, remediation, monitoring, and detection. The organization aims to maximize the detection accuracy while increasing the security operations and remediation efficiency[119]. The benefits of XDR are deemed to be so broad that Gartner called XDR the top security trend to emerge out of 2020. XDR plays a central role in advancing ZT architecture when used together with more targeted Identity and Access Management (IAM)[80]. XDR solutions offer in-depth security monitoring via flexible as-a-service delivery, which addresses identity and data monitoring[119].

As part of XDR, NDR/NTA technologies play a crucial role in monitoring and analyzing network traffic, providing insights into potential threats, and enabling rapid responses within a ZT framework. Another important technology on which XDR relies is EDR. This refers to a category of cybersecurity solutions designed to detect, investigate, and respond to threats at the endpoint level. As part of the ZT architecture, EDR can significantly enhance the security of endpoints and strengthen the overall effectiveness of the ZT model.

An additional solution that enhances the ZT functionality is SOAR. SOAR is a security solution that uses automation and orchestration to streamline security operations and improve the incident response times[115,116]. In the previous section, we elaborated on the relation between ZT and automation and orchestration. By combining ZT and SOAR, organizations can implement a more effective and efficient cybersecurity strategy. ZT provides a strong security foundation by limiting access to critical systems and data and continuously monitoring potential threats. SOAR then builds on this foundation by automating security operations and incident responses, enabling faster and more effective responses to security incidents. For example, a ZT model may limit access to a critical system to only authorized users and devices, and continuously monitor the system for potential threats. If a threat is detected, SOAR can automatically trigger a response, such as isolating the system or blocking access until the threat is resolved. This automated response can significantly reduce incident response times and minimize the impact of potential security breaches.

An additional solution commonly used in the organizational security suitcase is the SIEM. The SIEM is a security solution that collects and analyzes security events from the IT environment to identify potential threats. By combining ZT and SIEM, organizations can implement a more effective and efficient cybersecurity strategy[120]. ZT establishes a robust security foundation by restricting access to critical systems and data while continuously tracking potential threats[115]. SIEM then builds on this foundation by collecting and analyzing security events across the IT environment, providing early warnings of potential threats. For example, a ZT model may limit access to a critical system to only authorized users and devices, and continuously monitor that system for potential threats. If a threat is detected, the SIEM can alert the security teams and provide detailed information about the threat, enabling faster and more effective responses to security incidents.

8. ZERO TRUST AND CHAOS THEORY

Chaos theory has been used in cybersecurity applications to detect cyberattacks. It is a branch of mathematics that studies the behavior of dynamic systems that are highly sensitive to initial conditions, meaning that small changes in the initial conditions can lead to vastly different outcomes.

In the context of cybersecurity, chaos theory can be used similarly to AI to analyze network traffic and detect anomalous patterns that may indicate the presence of a cyberattack[121]. By analyzing the behavior of network traffic over time, chaos theory-based algorithms can detect patterns that deviate from the expected behavior of the system, indicating that cyberattacks may be in progress[122]. An additional approach is to use chaos theory-based algorithms to analyze the behavior of individual network packets and detect anomalous patterns that may indicate the presence of a cyberattack[123].

Moreover, chaos theory can be used to compare the different states of an organization's systems and transferred data. The analysis can indicate a deviation from the normal behavior of the system, and might indicate a cyberattack[124]. The analyzed data can be obtained from various sources, such as logs, EDRs, networks, computers, and every device that is connected to the organization systems.

While chaos theory-based approaches to cyberattack detection are still in the early stages of development and are not widely used in practice, they have shown promise in detecting certain types of cyberattacks such as Distributed Denial-of-Service (DDoS) attacks. However, these approaches also have limitations such as the potential for false positives and the need for extensive training data to develop accurate models. ZT and chaos theory can be used to enhance an organization's security posture. By combining ZT and chaos theory, organizations can implement a more effective and efficient cybersecurity strategy. As explained, by enforcing access control to critical systems and data and maintaining continuous monitoring for potential threats, the ZT approach offers a solid security foundation. Chaos theory analysis can be used to analyze network traffic and detect anomalous patterns that may indicate the presence of a cyberattack, providing an early warning of potential threats.

9. HOW DOES QUANTUM COMPUTING AFFECT ZERO TRUST

Akin to AI, which took many years from its inception to its ubiquitous presence, quantum technology is taking its first steps in general and in the cybersecurity world and has the potential to impact ZT[125]. Although several quantum algorithms, such as Shor's algorithm for integer factorization[126], Grover's algorithm for database search[127–129], Quantum Fourier transform[130,131] and quantum counting algorithms[132], offer promising exponential or quadratic speedups in asymptotic terms, achieving practical speedup on physical quantum computers still encounters significant technological challenges. However, these algorithms do give us a glimpse of the possibilities of overcoming these challenges. As mentioned above, quantum computing remains a speculative technology.

Despite this, it has the potential to revolutionize cybersecurity in several ways. For example, it can strengthen and enable future ZT security models by providing quantum-safe cryptography, scalable policy enforcement, enhanced visibility, accelerated automation, new sensing capabilities, and more resilient network properties that are more difficult to compromise[133]. However, it will likely be many years before these potentials are fully realized. The following are ways in which quantum computing could help strengthen and enable ZT security models in the future.

A quantum can contribute to safe cryptography. Quantum-resistant algorithms are essential for ZT solutions to withstand future attacks by quantum computers[134]. Technologies, such as quantum key distributions, can also enhance trust.

A quantum can enable the detection of anomalies. The pattern-matching and optimization capabilities of quantum computers may accelerate the detection of anomalies within ZT environments. This could help with continuous trust evaluation. Additionally, quantum computing can enhance the visibility of organizational security systems. The massively parallel processing power of quantum computers could potentially provide unprecedented levels of visibility in ZT networks, users, devices, applications, and data. Moreover, quantum technology has the potential to scale policy enforcement. In theory, quantum machines may be able to enforce fine-grained access policies required by ZT at a scale that classical computers cannot match. However, this was impossible for many years.

Existing access control strategies must adapt to the emerging threats and challenges posed by quantum computing[135]. Encryption algorithms such as RSA, built on the complexity of factoring large numbers, face vulnerability to Shor's algorithm on quantum computers, necessitating the evaluation and deployment of post-quantum encryption schemes[136]. Similarly, hash-based signatures such as Elliptic Curve Digital Signature Algorithm (ECDSA) are at risk of being compromised, prompting the adoption of quantum-resistant signature schemes. While symmetric cryptography offers more resilience compared to asymmetric methods, future quantum computers could potentially breach these defenses, underscoring the importance of larger key sizes for enhanced protection.

Access control policies that hinge solely on confidentiality of secrets may require reevaluation to anticipate decryption capabilities, urging the integration of multiple authenticators for fortified security measures. The adequacy of authentication factors, such as passwords and cryptographic one-time passwords, is called into question, urging the adoption of multifactor authentication incorporating physical and behavioral elements for heightened resistance.

Key management strategies must prepare for potential compromise of current keys, necessitating secure transitions as post-quantum alternatives come into play. Vigilance in monitoring for attacks is paramount, with a focus on identifying anomalies and unusual access patterns that could signify early cryptanalysis attempts in the landscape of quantum computing.

An important aspect of quantum technology is its ability to accelerate automation. The futuristic ability of quantum computers to rapidly process vast amounts of data could potentially be leveraged to automate complex ZT tasks such as continuous monitoring, threat detection, and response. When focusing on the EDR, quantum technology can be leveraged to develop sensors. New types of quantum sensors may be able to continuously monitor parameters, such as magnetic fields, vibrations, and temperatures, to help detect threats and anomalies within ZT environments.

Quantum has the potential to strengthen layered defenses. Quantum technologies could augment existing layers of ZT defenses, such as physical security and network segmentation, to make the overall model more resilient against threats. Finally, quantum systems are more difficult to compromise. The quantum properties of superposition and entanglement render quantum systems inherently harder to wiretap or eavesdrop on, potentially enhancing trust within ZT networks.

The advent of quantum computing necessitates fundamental adjustments to access control strategies within a ZT framework[137,138]. Quantum computers pose a threat to current encryption algorithms, demanding the adoption of post-quantum cryptography for secure data protection in transit and at rest. Upgrading cryptographic protocols, deploying quantum-resistant algorithms, and exploring new authentication methods are crucial steps to safeguard against potential quantum threats. Ensuring the integrity of blockchain-based access control systems also requires quantum-resistant cryptographic foundations. Companies must consider the risk of encrypted data compromise in the future and implement preemptive measures to mitigate quantum

computing vulnerabilities.

Exploring quantum components and advanced quantum communication protocols within Zero Trust for Wireless Networks (ZTWN) represents a proactive approach to fortify security against potential cryptographic vulnerabilities posed by quantum computing advancements[137]. These quantum solutions, including Quantum Machine Learning (QML) algorithms and identity authentication techniques, enhance the long-term security objectives of ZTWN by leveraging quantum properties to ensure secure communication and thwart potential attacks.

Quantum computing has the potential to transform cybersecurity through quantum-safe cryptography, scalable policy enforcement, enhanced visibility, accelerated automation, new sensing capabilities, and harder-to-compromise network properties.

10. ZERO TRUST EVALUATION

A crucial aspect of implementing ZT is to compare the organization's security state prior to and after the adoption of ZT principles. Moreover, any change in the ZT policy or architecture affects the organization. An evaluation process is required to assess the impact of these changes. The evaluation process uses metrics as a compass that enables management to understand the changes and progress while using the ZT. In this section, we present several approaches and metrics to evaluate the effectiveness of the organizational ZT security model.

ZT consists of several components and their integration leads to a holistic solution. As shown in Figure 3, the main components are policy enforcement, authentication, authorization, segmentation, monitoring, and response to threats[73,139]. Policy enforcement plays a pivotal role in defining, distributing, and enforcing access policies. It is crucial to strive for consistency across identity management, authorization, and policy control points. In addition, it is important to evaluate how the ZT system enforces a least-privileged access policy for different users. Moreover, ZT uses posture checks to evaluate and continuously verify the health of the devices accessing the network and its applications[35]. These checks also fall into the category of XDR tools.

An important way for ZT to enforce its policy is to use an optimal authentication process. The evaluation of authentication must relate to all entities, such as users, devices, and applications[35,86]. Relevant metrics, such as MFA adoption, can be obtained by investigating the number of users utilizing the MFA. An additional metric relevant for authentication is privileged access usage, which can be calculated by the number of access attempts with elevated privileges. Access policy coverage can be used to identify the roles of defined access policies. In addition, access policy violations can be used to calculate violations of defined access policies. An example of a metric is policy coverage, which measures the number of assets with defined access to configuration policies. The policy compliance metric measures assets compliant with defined access and configuration policies. An additional metric that falls in the policy category is Posture, which checks the failure rate and assesses the number of posture checks that failed to indicate non-compliance.

The next step in the evaluation process is authorization. One of the foundation stones is continuous authorization. The evaluation has to relate to authorization aspects such as continuity and revalidating access permissions over time. This evaluation can predict the ability of ZT to catch privilege escalations and changes.

An additional evaluation aspect of ZT focuses on network segmentation. This evaluation indicates how the network is segmented to restrict lateral movement[140]. Microsegmentation techniques based on application, roles, and environmental configurations can be considered. The relevant metrics for this category include microsegmentation adoption as an indication of the number of applications using microsegmentation and its complementary metric, unmanaged devices, which indicates the number of devices connected without proper

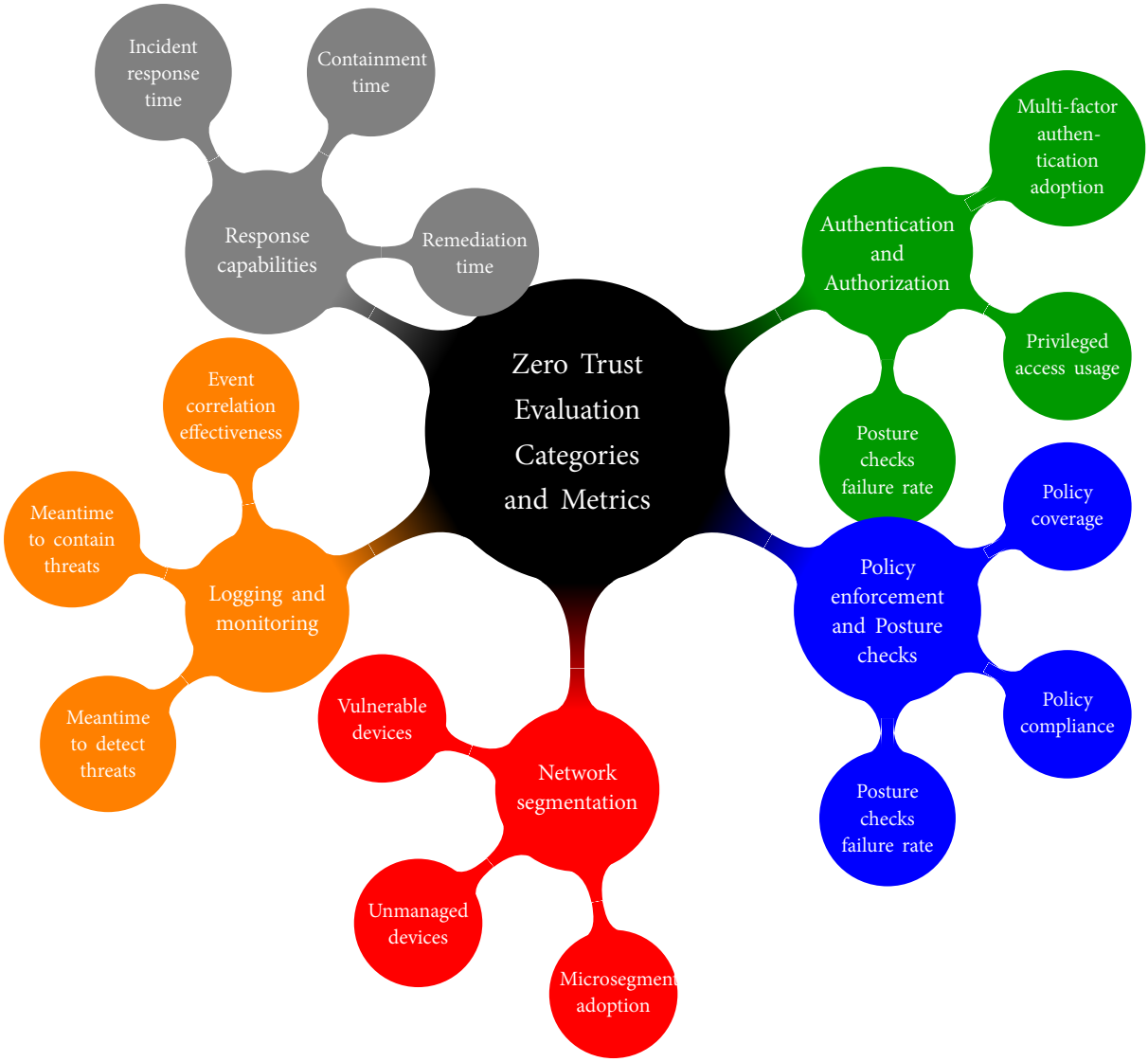


Figure 3. Example for zero trust evaluation approaches and metrics.

registration. An additional metric is a vulnerable device that assesses the number of devices with vulnerabilities identified through the posture checks mentioned above.

Furthermore, the ZT evaluation category relates to the logging and monitoring of organizational systems. This evaluation consists of assessing organizational logs, event monitoring, and SIEM solutions. A high level of performance in this category ensures quick detection of anomalous behaviors. The metrics that can be used for evaluating the logging and monitoring categories are the mean time to detect threats and the average time to detect security incidents. The additional proposed metric is the mean time to contain threats, that is, the average time to isolate and contain security incidents. Another useful metric is event correlation effectiveness, which calculates the percentage of correlated events out of the total events.

The last category in our ZT evaluation process is response capabilities. It measures how quickly an organization responds to threats, revoke access, and remediate incidents. It also evaluates tabletop and red team penetration tests. Incident response metrics include the incident response time, which calculates the average time to begin the incident response after detection [141]. Another relevant metric is the containment time, which calculates

the average time required to contain security incidents after detection. Finally, the remediation time metric calculates the average time required to fully remediate the security incidents after containment.

Additional qualitative metrics such as stakeholder satisfaction surveys, security assessments, and red team penetration test results can also provide valuable insights into the effectiveness of ZT initiatives. This section provides an overview of the main ZT evaluation categories and their metrics. By evaluating these key ZT capabilities, an organization can identify gaps, weaknesses, and areas for improvement to strengthen its overall security posture. Over time, it can track progress and measure the maturity and efficacy of the ZT model.

11. CONCLUSIONS AND FUTURE DIRECTIONS

This paper presents the main ZT issues relevant to the current era of evolving technologies. It also provides an overview of the main events that affect the ZT evolution. This study also compares the traditional ZT approaches with the current ones. In addition, it shows how organizations can implement emerging technologies and algorithms such as AI, quantum computation, and chaos theory, and how they affect the ZT strategy and implementation. Moreover, this study discusses the best practices and main issues in ZT challenges, such as migration, automation, and orchestration. Finally, this paper provides evaluation metrics and approaches for measuring the impact of ZT security on business operations, user experience, and overall security posture.

Future challenges and development directions for ZT architectures include extending policies to edge computing and IoT devices, advancing identity verification with blockchain and passive biometrics, implementing adaptive access authorization through machine learning, integrating ZT into supply chains, emphasizing API security, establishing continuous authorization practices, converging network and security infrastructure, adapting ZT for cloud and serverless applications, and transitioning to quantum-resilient cryptography for enhanced data protection against potential quantum computing threats.

Looking ahead, we predict that the persistent and significant challenges of verification and compliance assurance will continue to evolve alongside ZT architecture. As we delve deeper into the future of ZT security, several critical research and development areas warrant focused attention. These include safeguarding and securing AI and ML workloads, establishing unified access policies across multiple domains, and implementing privacy-preserving access controls. Further, the seamless integration of ZT with DevOps processes and practices represents another promising and essential direction for future exploration and development.

DECLARATIONS

Authors' contributions

Made substantial contributions to conception and design of the study: Weinberg AI, Cohen K
Conceptualization, Methodology, Writing - original draft: Weinberg AI
Conceptualization, Writing - review and editing: Cohen K

Availability of data and materials

Not applicable.

Financial support and sponsorship

None.

Conflicts of interest

Cohen K is an Editorial Board Member of the journal *Complex Engineering Systems*, and Weinberg AI is affiliated with AI-WEINBERG.

Ethical approval and consent to participate

Not applicable.

Consent for publication

Not applicable.

Copyright

© The Author(s) 2024.

REFERENCES

1. IDC. Future of industry ecosystems: shared data and insights. 2021. Available from: https://blogs.idc.com/2021/01/06/future-of-industry-ecosystems-shared-data-and-insights/ [Last accessed on 23 Sep 2024].
2. Business. Cybercrime thrives during pandemic: verizon 2021 data breach investigations report. 2021. Available from: https://www.verizon.com/about/news/verizon-2021-data-breach-investigations-report [Last accessed on 23 Sep 2024].
3. The White House. Executive order on improving the nation's cybersecurity. 2021. Available from: https://www.whitehouse.gov/briefing-room/presidential-actions/2021/05/12/executive-order-on-improving-the-nations-cybersecurity/ [Last accessed on 23 Sep 2024].
4. Syed NF, Shah SW, Shaghaghi A, Anwar A, Baig Z, Doss R. Zero trust architecture (ZTA): a comprehensive survey. *IEEE Access* 2022;10:57143-79. DOI
5. Yampolskiy RV, Spellchecker MS. Artificial intelligence safety and cybersecurity: a timeline of AI failures. 2016. Available from: https://arxiv.org/pdf/1610.07997 [Last accessed on 23 Sep 2024].
6. Wylde A. Zero trust: never trust, always verify. In: 2021 international conference on cyber situational awareness, data analytics and assessment (CyberSA); 2021, pp. 1-4. DOI
7. Paes R, Mazur DC, Venne BK, Ostrzenski J. A guide to securing industrial control networks: Integrating IT and OT systems. *IEEE Ind Appl Mag* 2019;26:47-53. DOI
8. Zanasi C, Magnanini F, Russo S, Colajanni M. A zero trust approach for the cybersecurity of industrial control systems. In: 2022 IEEE 21st international symposium on network computing and applications; 2022, pp. 1-7. DOI
9. Li S, Iqbal M, Saxena N. Future industry internet of things with zero-trust security. *Inf Syst Front* 2022;1-14. DOI
10. Greenberg A. The untold story of NotPetya, the most devastating cyberattack in history. 2018. Available from: https://www.wired.com/story/notpetya-cyberattack-ukraine-russia-code-crashed-the-world/ [Last accessed on 23 Sep 2024].
11. Colombo P, Ferrari E, Tümer ED. Access control enforcement in IoT: state of the art and open challenges in the zero trust era. In: 2021 third IEEE international conference on trust, privacy and security in intelligent systems and applications (TPS-ISA); 2021, pp. 159-66. DOI
12. Chimakurthi VNSS. The challenge of achieving zero trust remote access in multi-cloud environment. *ABC J Adv Res* 2020;9:89-102. Available from: https://www.researchgate.net/publication/357920420_The_Challenge_of_Achieving_Zero_Trust_Remote_Access_in_Multi-Cloud_Environment/fulltext/639b2b3d484e65005b10b3d1/The-Challenge-of-Achieving-Zero-Trust-Remote-Access-in-Multi-Cloud-Environment.pdf [Last accessed on 23 Sep 2024].
13. Dhar S, Bose I. Securing IoT devices using zero trust and blockchain. *J Org Comput Elect Comm* 2021;31:18-34. DOI
14. Samaniego M, Deters R. Zero-trust hierarchical management in IoT. In: 2018 IEEE international congress on internet of things (ICIOT); 2018, pp. 88-95. DOI
15. Cheh C, Chen B. Analyzing openAPI specifications for security design issues. In: 2021 IEEE secure development conference (SecDev); 2021, pp. 15-22. DOI
16. Eckhart M, Ekelhart A. Digital twins for cyber-physical systems security: state of the art and outlook. In: Biffl S, Eckhart M, Lüder A, Weippl E, eds. Security and quality in cyber-physical systems engineering. Cham: Springer; 2019. DOI
17. Lv Z, Li Y, Feng H, Lv H. Deep learning for security in digital twins of cooperative intelligent transportation systems. *IEEE Trans Intell Transp Syst* 2021;23:16666-75. DOI
18. Sellitto GP, Aranha H, Masi M, Pavleska T. Enabling a zero trust architecture in smart grids through a digital twin. In: Dependable computing-EDCC 2021 workshops. 2021. pp. 73-81. DOI
19. Jagannath J, Ramezanpour K, Jagannath A. Digital twin virtualization with machine learning for IoT and beyond 5G networks: research directions for security and optimal control. *arXiv* 2022. pp. 81-6. DOI
20. Marsh SP. Formalising trust as a computational concept. PhD thesis. 1994. Available from: https://www.cs.stir.ac.uk/~kjt/techreps/pdf/TR133.pdf [Last accessed on 23 Sep 2024].
21. Welborn R, Kasten V. The Jericho principle: how companies use strategic collaboration to find new sources of value. John Wiley & Sons; 2003. Available from: https://hbswk.hbs.edu/archive/the-jericho-principle-how-companies-use-strategic-collaboration-to-find-new-sources-of-value [Last accessed on 23 Sep 2024].
22. Flanigan J. Zero trust network model. Medford, MA: Tufts University; 2018.
23. Kindervag J. Build security into your network's DNA: the zero trust network architecture. Forrester Research Inc. 2010.
24. Higgins KJ. Forrester pushes 'zero trust' model for security; 2010.

25. Alagappan A, Venkatachary SK, Andrews LJB. Augmenting zero trust network architecture to enhance security in virtual power plants. *Energy Rep* 2022;8:1309-20. DOI
26. Basim Al-Ruwaii GDM. Basim Al-Ruwaii GDM. Why the time has come to embrace the zero-trust model of cybersecurity; 2021.
27. Cunningham C. The zero trust eXtended (ZTX) ecosystem. Cambridge, MA: Forrester; 2018.
28. Campbell M. Beyond zero trust: trust is a vulnerability. *Computer* 2020;53:110-13. DOI
29. Kerman A, Borchert O, Rose S, Tan A. Implementing a zero trust architecture. National Institute of Standards and Technology; 2020. Available from: https://www.nccoe.nist.gov/sites/default/files/legacy-files/zta-project-description-final.pdf [Last accessed on 23 Sep 2024].
30. Pratt MK. The history and evolution of zero-trust security. Techtarget; 2022.
31. OKTA. The state of zero trust security 2023; 2023.
32. SANS. Building a zero trust framework: key strategies for 2024 and beyond; 2024.
33. MarketsandMarkets. Zero trust security market by solution type. 2023.
34. Chen B, Qiao S, Zhao J, et al. A security awareness and protection system for 5G smart healthcare based on zero-trust architecture. *IEEE Int Things J* 2020;8:10248-63. DOI
35. Stafford V. Zero trust architecture. NIST Special Publication; 2020.
36. Rose S, Borchert O, Mitchell S, Connelly S. Zero trust architecture. National Institute of Standards and Technology; 2020.
37. Gilman E, Barth D. Zero trust networks. O'Reilly Media, Incorporated; 2017.
38. Yan X, Wang H. Survey on zero-trust network security. In: Artificial intelligence and security: 6th international conference, ICAIS 2020. July 17-20, 2020; Hohhot, China; pp. 50-60. DOI
39. Buck C, Olenberger C, Schweizer A, Völter F, Eymann T. Never trust, always verify: A multivocal literature review on current knowledge and research gaps of zero-trust. *Comput Secur* 2021;110:102436. DOI
40. Kim D, Kwon BJ, Dumitraş T. Certified malware: measuring breaches of trust in the windows code-signing pki. In: Proceedings of the 2017 ACM SIGSAC conference on computer and communications security; 2017. pp. 1435-48. DOI
41. Cao Y, Pokhrel SR, ZHU Y, Ram Mohan Doss R, Li G. Automation and orchestration of zero trust architecture: potential solutions and challenges. Elsevier; 2022. DOI
42. Tidjon LN, Khomh F. Never trust, always verify: a roadmap for Trustworthy AI? *arXiv* 2022. DOI
43. Zhou L, Su C, Li Z, Liu Z, Hancke GP. Automatic fine-grained access control in SCADA by machine learning. *Future Gener Comput Syst* 2019;93:548-59. DOI
44. Xiaopeng T, Haohao S. A zero trust method based on BLP and BIBA model. In: 2021 14th international symposium on computational intelligence and design (ISCID); 2021. pp. 96-100. DOI
45. Rousseau TL. Rousseau TL. Insider threat: replacing the trusted security model. Capella University; 2021.
46. Jansen JN, Tokerud S. Jansen JN, Tokerud S. Designing the extended zero trust maturity model a holistic approach to assessing and improving an organization's maturity within the technology, processes and people domains of information security. University of Agder; 2022.
47. Kak S. Kak S. Zero Trust evolution & transforming enterprise security. California State University San Marcos; 2022.
48. Liu N, Yu M, Zang W, Sandhu RS. Cost and effectiveness of trustzone defense and side-channel attack on ARM platform. *J Wirel Mob Netw Ubiquit Comput Depend Appl* 2020;11:1-15. DOI
49. Song M, Wang D. AB-PAKE: achieving fine-grained access control and flexible authentication. *IEEE Trans Inf Forensics Secur* 2024;19:6197-212 DOI
50. He Y, Huang D, Chen L, Ni Y, Ma X. A survey on zero trust architecture: challenges and future trends. *Wirel Commun Mob Com* 2022;2022:6476274. DOI
51. Tian S, Bai F, Shen T, Zhang C, Gong B. Vssb-raft: a secure and efficient zero trust consensus algorithm for blockchain. *ACM Trans Sensor Netw* 2024;20:1-22. DOI
52. Fernandez EB, Brazhuk A. A critical analysis of zero trust architecture (ZTA). *Comput Stand Inter* 2024;89:103832. DOI
53. Botacin M. GPThreats-3: is automatic malware generation a threat? In: 2023 IEEE security and privacy workshops (SPW); 2023. pp. 238-54. DOI
54. Zhao K, Pan L. A machine learning based trust evaluation framework for online social networks. In: 2014 IEEE 13th international conference on trust, security and privacy in computing and communications; 2014. pp. 69-74. DOI
55. El-Sayed H, Ignatious HA, Kulkarni P, Bouktif S. Machine learning based trust management framework for vehicular networks. *Veh Commun* 2020;25:100256. DOI
56. Alanazi R, Aljuhani A. Anomaly detection for industrial internet of things cyberattacks. *Comput Syst Sci Eng* 2023;44:2361-78. DOI
57. Ho S, Al Jufout S, Dajani K, Mozumdar M. A novel intrusion detection model for detecting known and innovative cyberattacks using convolutional neural network. *IEEE Open J Comput Soc* 2021;2:14-25. DOI
58. Saharkhizan M, Azmoodeh A, Dehghantanha A, Choo KKR, Parizi RM. An ensemble of deep recurrent neural networks for detecting IoT cyber attacks using network traffic. *IEEE Int Things J* 2020;7:8852-59. DOI
59. Takiddin A, Ismail M, Zafar U, Serpedin E. Deep autoencoder-based anomaly detection of electricity theft cyberattacks in smart grids. *IEEE Syst J* 2022;16:4106-17. DOI
60. Alaparthi S, Mishra M. Bidirectional encoder representations from transformers (BERT): a sentiment analysis odyssey. *arXiv* 2020. DOI
61. Gao Q, Wang Y, Cheng X, et al. Identification of vulnerable lines in smart grid systems based on affinity propagation clustering. *IEEE Int Things J* 2019;6:5163-71. DOI

62. Wang WT, Wu YL, Tang CY, Hor MK. Adaptive density-based spatial clustering of applications with noise (DBSCAN) according to data. In: 2015 International Conference on Machine Learning and Cybernetics (ICMLC); 2015. pp. 445-51. DOI
63. Nishikaze H, Ozawa S, Kitazono J, et al. Large-scale monitoring for cyber attacks by using cluster information on darknet traffic features. *Proc Comput Sci* 2015;53:175-82. DOI
64. An P, Wang Z, Zhang C. Ensemble unsupervised autoencoders and Gaussian mixture model for cyberattack detection. *Inf Proc Manag* 2022;59:102844. DOI
65. Kiss I, Genge B, Haller P. A clustering-based approach to detect cyber attacks in process control systems. In: 2015 IEEE 13th international conference on industrial informatics (INDIN); 2015. pp. 142-48. DOI
66. Kumar P, Kumar AA, Sahayakingsly C, Udayakumar A. Analysis of intrusion detection in cyber attacks using DEEP learning neural networks. *Peer Peer Netw Appl* 2021;14:2565-84. DOI
67. Lokhande MP, Patil DD. Trust computation model for iot devices using machine learning techniques. In: Proceeding of first doctoral symposium on natural computing research: DSNCR 2020. Springer; 2021. pp. 195-205. DOI
68. Kumari M, Gupta S. Performance comparison between Chaos and quantum-chaos based image encryption techniques. *Multimed Tools Appl* 2021;80:33213-55. DOI
69. Wu YG, Yan WH, Wang JZ. Real identity based access control technology under zero trust architecture. In: 2021 international conference on wireless communications and smart grid (ICWCSG); 2021. pp. 18-22. DOI
70. Wang Zh, Jin Mh, Jiang L, et al. Secure access method of power internet of things based on zero trust architecture. In: International conference on swarm intelligence. Springer; 2023. pp. 386-99. DOI
71. Sheikh N, Pawar M, Lawrence V. Zero trust using network micro segmentation. In: IEEE INFOCOM 2021-IEEE conference on computer communications workshops (INFOCOM WKSHPS); 2021. pp. 1-6. DOI
72. Tyler D, Viana T. Trust no one? a framework for assisting healthcare organisations in transitioning to a zero-trust network architecture. *Appl Sci* 2021;11:7499. DOI
73. Teerakanok S, Uehara T, Inomata A. Migrating to zero trust architecture: reviews and challenges. *Secur Commun Netw* 2021;2021:1-10. DOI
74. Ahmed I, Nahar T, Urmi SS, Taher KA. Protection of sensitive data in zero trust model. In: Proceedings of the international conference on computing advancements; 2020. pp. 1-5. DOI
75. Mehraj S, Banday MT. Establishing a zero trust strategy in cloud computing environment. In: 2020 International conference on computer communication and informatics (ICCCI); 2020. pp. 1-6. DOI
76. Patil AP, Karkal G, Wadhwa J, Sawood M, Reddy KD. Design and implementation of a consensus algorithm to build zero trust model. In: 2020 IEEE 17th India council international conference (INDICON); 2020. pp. 1-5. DOI
77. Garbis J, Chapman JW. Zero trust security: an enterprise guide. Springer; 2021. DOI
78. Vang T, Lind ML. Factors influencing cloud computing adoption in a zero-trust environment. Researchsquare; 2023.
79. Chuan T, Lv Y, Qi Z, Xie L, Guo W. An implementation method of zero-trust architecture. *J Phys Conf Ser* 2020;1651:012010. DOI
80. DeCusatis C, Liengtiraphan P, Sager A, Pinelli M. Implementing zero trust cloud networks with transport access control and first packet authentication. In: 2016 IEEE international conference on smart cloud (SmartCloud); 2016. pp. 5-10. DOI
81. Lookout. Airbus deploys lookout mobile endpoint security to 100,000+ global workforce; 2021.
82. Muncaster P. Capital one breach shines light on cloud security risks, human error, and insider threats. Phil Muncaster; 2022.
83. Mark S, Rachel C. The NASA pathway to zero trust. NASA; 2023.
84. STAMFORD C. Gartner predicts 75fail to implement zero trust security policies through 2026. GARTNER; 2024.
85. D'Silva D, Ambawade DD. Building a zero trust architecture using kubernetes. In: 2021 6th international conference for convergence in technology (i2ct); 2021. pp. 1-8. DOI
86. Bobbert Y, Scheerder J. Zero trust validation: from practice to theory: an empirical research project to improve zero trust implementations. In: 2022 IEEE 29th annual software technology conference (STC); 2022. pp. 93-104. DOI
87. Scott B. How a zero trust approach can help to secure your AWS environment. *Netw Secur* 2018;2018:5-8. DOI
88. Lambert KD. Applications of defense-in-depth and zero-trust cryptographic products in emergent cybersecurity environments. In: Emergent behavior in system of systems engineering. CRC Press; 2022. pp. 93-117.
89. Phiayura P, Teerakanok S. A comprehensive framework for migrating to zero trust architecture. *IEEE Access* 2023;11:19487-511. DOI
90. Adahman Z, Malik AW, Anwar Z. An analysis of zero-trust architecture and its cost-effectiveness for organizational security. *Comput Secur* 2022;122:102911. DOI
91. Greenwood D. Applying the principles of zero-trust architecture to protect sensitive and critical data. *Netw Secur* 2021;2021:7-9. DOI
92. de Weever C, Andreou M. Zero trust network security model in containerized environments. Amsterdam, The Netherlands: University of Amsterdam; 2020.
93. Bodström TT. Strategic cyber environment management with zero trust and cyber counterintelligence. *J Inf Warf* 2022;21:1-12. Available from: https://www.jinfowar.com/journal/volume-21-issue-3/strategic-cyber-environment-management-zero-trust-cyber-counterintelligence [Last accessed on 23 Sep 2024].
94. DeWeaver III LF. Exploring how universities can reduce successful cyberattacks by incorporating zero trust. Colorado Technical University; 2021.
95. Hatakeyama K, Kotani D, Okabe Y. Zero trust federation: sharing context under user control towards zero trust in identity federation. In: 2021 IEEE international conference on pervasive computing and communications workshops and other affiliated events (percom workshops); 2021. pp. 514-19. DOI

96. Yao Q, Wang Q, Zhang X, Fei J. Dynamic access control and authorization system based on zero-trust architecture. In: Proceedings of the 2020 1st international conference on control, robotics and intelligent system; 2020. pp. 123-27. DOI
97. Anson S. Applied Incident Responsee; 2020. DOI
98. Alappat MR. Multifactor authentication using zero trust. Rochester Institute of Technology; 2023.
99. Yeoh W, Liu M, Shore M, Jiang F. Zero trust cybersecurity: critical success factors and a maturity assessment framework. *Comput Secur* 2023;133:103412. DOI
100. Cheng T, Moore P, Samara-Rubio D, Lee S. Universal wellpad control: an open automation and control platform with zero-trust and zero-touch provisioning system. In: Abu Dhabi international petroleum exhibition and conference; 2022. p. D011S027R002. DOI
101. Sanders G, Morrow T, Richmond N, Woody C, PA CMUP. Integrating zero trust and devsecops. Tech. Rep; 2021.
102. Devlekar S, Ramteke V. Identity and access management: high-level conceptual framework. *Cardiometry* 2022;24:393-99. DOI
103. Ahmed G. Improving IoT privacy, data protection and security concerns. *Int J Technol Innov Manag* 2021;1:18-33 DOI
104. Zakaria KN, Zainal A, Othman SH, Kassim MN. Feature extraction and selection method of cyber-attack and threat profiling in cyber-security audit. In: 2019 international conference on cybersecurity (ICoCSec); 2019. pp. 1-6. DOI
105. Kato S, Tanabe R, Yoshioka K, Matsumoto T. Adaptive observation of emerging cyber attacks targeting various IoT devices. In: 2021 IFIP/IEEE international symposium on integrated network management (IM); 2021. pp. 143-51.
106. Bout E, Loscri V, Gallais A. How machine learning changes the nature of cyberattacks on IoT networks: a survey. *IEEE Commun Surv Tut* 2021;24:248-79. DOI
107. Adamsky F, Aubigny M, Battisti F, et al. Integrated protection of industrial control systems from cyber-attacks: the ATENA approach. *Int J Crit Infr Prot* 2018;21:72-82. DOI
108. Perera S, Jin X, Maurushat A, Opoku DGJ. Factors affecting reputational damage to organisations due to cyberattacks. *Informatics* 2022;9:28. DOI
109. Dasawat SS, Sharma S. Cyber security integration with smart new age sustainable startup business, risk management, automation and scaling system for entrepreneurs: an artificial intelligence approach. In: 2023 7th international conference on intelligent computing and control systems (ICICCS); 2023. pp. 1357-63. DOI
110. Qazi FA. Study of zero trust architecture for applications and network security. In: 2022 IEEE 19th international conference on smart communities: improving quality of life using ICT, IoT and AI (HONET); 2022. pp. 111-16. DOI
111. Eidle D, Ni SY, DeCusatis C, Sager A. Autonomic security for zero trust networks. In: 2017 IEEE 8th annual ubiquitous computing, electronics and mobile communication conference (UEMCON); 2017. pp. 288-93. DOI
112. Sheridan O. The state of zero trust in the age of fluid working. *Netw Secur* 2021;2021:15-17. DOI
113. Zanasi C, Russo S, Colajanni M. Flexible zero trust architecture for the cybersecurity of industrial iot infrastructures. *Ad Hoc Netw* 2024;156:103414. DOI
114. Xiao S, Ye Y, Kanwal N, Newe T, Lee B. SoK: context and risk aware access control for zero trust systems. *Secur Commun Netw* 2022;2022:7026779. DOI
115. Selim GEI, Hemdan EED, Shehata AM, El-Fishawy NA. Anomaly events classification and detection system in critical industrial internet of things infrastructure using machine learning algorithms. *Multimed Tools Appl* 2021;80:12619-40. DOI
116. GEORGE DAS, George AH, Baskar T, Pandey D. XDR: the evolution of endpoint security solutions-superior extensibility and analytics to satisfy the organizational needs of the future. *Int J Adv Res Sci Commun Technol* 2021;8:493-501. DOI
117. Hassan WU, Bates A, Marino D. Tactical provenance analysis for endpoint detection and response systems. In: 2020 IEEE symposium on security and privacy (SP); 2020. pp. 1172-89. DOI
118. Zaheer Z, Chang H, Mukherjee S, Van der Merwe J. eztrust: network-independent zero-trust perimeterization for microservices. In: Proceedings of the 2019 ACM Symposium on SDN Research; 2019. pp. 49-61. DOI
119. Ali B, Hijjawi S, Campbell LH, Gregory MA, Li S. A maturity framework for zero-trust security in multiaccess edge computing. *Secur Commun Netw* 2022;2022:3178760. DOI
120. Bertino E, Brancik K. Services for zero trust architectures-a research roadmap. In: 2021 IEEE international conference on web services (ICWS); 2021. pp. 14-20. DOI
121. Khan MS, Ferens K, Kinsner W. A chaotic complexity measure for cognitive machine classification of cyber-attacks on computer networks. *Int J Cogn Inform Nat Intell* 2014;8:45-69. DOI
122. Shaukat S, Arshid A, Eleyan A, et al. Chaos theory and its application: an essential framework for image encryption. *Chaos Theory Appl* 2020;2:17-22.
123. Alabdulkreem E, Alotaibi SS, Alamgeer M, et al. Intelligent cybersecurity classification using chaos game optimization with deep learning model. *Comput Syst Sci Eng* 2023;45:971-83. DOI
124. Okumura M, Tomoki K, Okamoto E, Yamamoto T. Chaos-based interleave division multiple access scheme with physical layer security. In: 2021 IEEE 18th annual consumer communications & networking conference (CCNC); 2021. pp. 1-2. DOI
125. Mogos G. Quantum fingerprint scrambling algorithm based on chaos theory. In: 2023 17th international conference on engineering of modern electric systems (EMES); 2023. pp. 1-4. DOI
126. de Lima Marquezino, F., Portugal, R., Lavor, C. Shor's algorithm for integer factorization. In: A primer on quantum computing. Cham: Springer; 2019. DOI
127. Zhang K, Korepin VE. Depth optimization of quantum search algorithms beyond Grover's algorithm. *Phys Rev A* 2020;101:032346. DOI
128. Long GL. Grover algorithm with zero theoretical failure rate. *Phys Rev A* 2001;64:022307.
129. Lavor C, Manssur LRU, Portugal R. Grover's algorithm: quantum database search. *arXiv*; 2003. Available from: https://arxiv.org/abs/

quant-ph/0301079 [Last accessed on 23 Sep 2024].
130. Weinstein YS, Pravia M, Fortunato E, Lloyd S, Cory DG. Implementation of the quantum Fourier transform. *Phys Rev Lett* 2001;86:1889.
131. Martin A, Lamata L, Solano E, Sanz M. Digital-analog quantum algorithm for the quantum fourier transform. *Phys Rev Res* 2020;2:013012. DOI
132. Aaronson S, Rall P. Quantum approximate counting, simplified. In: Symposium on simplicity in algorithms; 2020. pp. 24-32. DOI
133. Szymanski TH. The "cyber security via determinism" paradigm for a quantum safe zero trust deterministic internet of things (IoT). *IEEE Access* 2022;10:45893-930. DOI
134. Perlner RA, Cooper DA. Quantum resistant public key cryptography: a survey. In: Proceedings of the 8th symposium on identity and trust on the internet; 2009. pp. 85-93. DOI
135. Abdolmaleki B, Blümel H, Fenzi G, Khajeh H, KOpsell S, Zarezadeh M. Post-quantum access control with application to secure data retrieval; 2024. Available from: https://eprint.iacr.org/2024/1160 [Last accessed on 23 Sep 2024].
136. Jemihin ZB, Tan SF, Chung GC. Attribute-based encryption in securing big data from post-quantum perspective: a survey. *Cryptography* 2022;6:40. DOI
137. Farouk A, Al-Kuwari S, Abulkasim H, et al. Quantum computing: a tool for zero-trust wireless networks. *IEEE Netw* 2024;1:1. DOI
138. Jiang J, Wang D. QPASE: quantum-resistant password-authenticated searchable encryption for cloud storage. *IEEE Trans Inf Forensics Secur* 2024;19:4231-46 DOI
139. Simpson WR. Toward a zero trust metric. *Proc Comput Sci* 2022;204:123-30. DOI
140. Basta N, Ikram M, Kaafar MA, Walker A. Towards a zero-trust micro-segmentation network security strategy: an evaluation framework. In: NOMS 2022-2022 IEEE/IFIP Network Operations and Management Symposium; 2022. pp. 1-7. DOI
141. Xiaojian Z, Liandong C, Jie F, Xiangqun W, Qi W. Power IoT security protection architecture based on zero trust framework. In: 2021 IEEE 5th international conference on cryptography, security and privacy (CSP); 2021. pp. 166-70. DOI

Fatorachian *et al. Complex Eng Syst* 2024;4:17
DOI: 10.20517/ces.2024.35

Complex Engineering Systems

Review

Open Access

AI-enhanced fault-tolerant control and security in transportation and logistics systems: addressing physical and cyber threats

Hajar Fatorachian, Hadi Kazemi

Leeds Business School, Leeds Beckett University, Leeds LS1 3HB, UK.

Correspondence to: Dr. Hajar Fatorachian, Leeds Business School, Leeds Beckett University, Portland Crescent, Leeds LS1 3HB, UK. E-mail: h.fatorachian@leedsbeckett.ac.uk

How to cite this article: Fatorachian H, Kazemi H. AI-enhanced fault-tolerant control and security in transportation and logistics systems: addressing physical and cyber threats. *Complex Eng Syst* 2024;4:17. https://dx.doi.org/10.20517/ces.2024.35

Received: 19 Jun 2024 **First Decision:** 16 Aug 2024 **Revised:** 22 Aug 2024 **Accepted:** 6 Sep 2024 **Published:** 30 Sep 2024

Academic Editor: Hamid Reza Karimi **Copy Editor:** Fangling Lan **Production Editor:** Fangling Lan

Abstract

Transportation and logistics systems are becoming increasingly complex and critical to modern infrastructure. This paper proposes a novel AI-enhanced fault-tolerant control framework to address the dual challenges of physical malfunctions and cyber threats. By leveraging advanced machine learning algorithms and real-time data analytics, the proposed methodology aims to enhance the reliability, safety, and security of transportation and logistics systems. This research explores the foundations and practical implementations of AI-driven anomaly detection, predictive maintenance, and autonomous response systems. The findings demonstrate significant improvements in system resilience and robustness, making a substantial contribution to the field of intelligent transportation management.

Keywords: AI-enabled supply chain, predictive maintenance, cybersecurity in logistics, anomaly detection, fault-tolerant control

1. INTRODUCTION

Transportation and logistics systems are essential components of modern infrastructure, enabling the efficient movement of goods and people, which in turn supports economic growth and stability. These systems encompass a vast array of elements, including road networks, railways, ports, airports, and the

© The Author(s) 2024. **Open Access** This article is licensed under a Creative Commons Attribution 4.0 International License (https://creativecommons.org/licenses/by/4.0/), which permits unrestricted use, sharing, adaptation, distribution and reproduction in any medium or format, for any purpose, even commercially, as long as you give appropriate credit to the original author(s) and the source, provide a link to the Creative Commons license, and indicate if changes were made.

underlying logistics networks that manage the flow of products from origin to destination. Each of these components plays a crucial role in ensuring that the global economy functions smoothly. The interconnection and interdependence of these systems mean that a disruption in one part can have significant ripple effects throughout the entire network[1,2].

As transportation and logistics systems become more interconnected and reliant on digital technologies, they face increasing challenges related to complexity, reliability, and security. Deloitte Insights (2024) highlights that the digital transformation of these systems introduces new layers of complexity, making them more efficient but also more vulnerable to disruptions[3]. For instance, the use of Internet of Things (IoT) devices for real-time tracking and autonomous vehicles for delivery has revolutionized logistics but also introduced potential points of failure and security vulnerabilities[4,5]. The dynamic nature of modern transportation networks requires sophisticated control and management techniques that can adapt to changing conditions and emerging threats, as noted by McKinsey & Company (2024) and PwC (2024)[6,7].

The global logistics and transportation sector is a critical enabler of international trade and economic development. The seamless movement of goods across borders is essential for the functioning of global supply chains. However, the increasing complexity of these systems, driven by globalization and technological advancements, has created new challenges. Traditional systems, designed for less dynamic and interconnected environments, are becoming insufficient. They struggle to handle the intricacies of modern transportation networks, where the failure of a single component can lead to significant delays and economic losses[8].

1.1. Gap in knowledge

The significance of transportation and logistics systems in the global economy cannot be overstated. They are integral to international trade, allowing countries to exchange goods and services efficiently. However, the sector is increasingly vulnerable to both physical malfunctions and cyber threats due to its complexity and reliance on interconnected systems. The physical components, such as vehicles and infrastructure, can suffer from wear and tear, leading to malfunctions. Simultaneously, the digital components, such as control systems and communication networks, are susceptible to cyber attacks.

Traditional fault-tolerant control methods are often inadequate for handling the sophisticated nature of these threats. These methods typically involve redundancy and fail-safes that are effective against certain types of physical failures but do not address the complexities introduced by modern digital technologies[9]. Traditional fault-tolerant control approaches rely heavily on redundancy and fail-safes, which are effective to a certain extent but have notable limitations. These methods often fail to address the complexities introduced by modern digital technologies, particularly in detecting and mitigating cyber threats[10]. For instance, redundancy may ensure that a system continues to operate despite a physical fault, but it does not account for cyber vulnerabilities that could be exploited simultaneously[9]. In contrast, the proposed AI-enhanced framework integrates machine learning algorithms that provide real-time anomaly detection and predictive maintenance, which are critical in identifying both physical faults and cyber threats before they escalate[11]. This proactive approach not only improves system resilience but also ensures a higher level of security and reliability compared to traditional methods.

Cyber threats, in particular, pose a new kind of challenge that traditional methods are not equipped to handle. Cyber attacks can disrupt operations, steal sensitive information, and cause widespread damage before they are detected and mitigated.

Current research lacks comprehensive solutions that integrate advanced AI technologies to enhance fault tolerance and cybersecurity simultaneously. While there have been significant advancements in both areas individually, few studies have explored how they can be combined to provide a more robust and resilient framework. This study aims to fill this gap by proposing an AI-enhanced framework that addresses these dual challenges. By leveraging AI, the framework can improve the detection of anomalies, predict potential failures, and respond to cyber threats more effectively, ensuring the integrity and functionality of transportation and logistics systems[12].

The gap in current research is evident in the fragmented approach to addressing physical and cyber threats. Most studies focus on either fault-tolerant control or cybersecurity, but rarely integrate both. This paper aims to bridge this gap by providing a comprehensive framework that leverages AI to enhance both fault tolerance and security in transportation systems. By integrating these aspects, the proposed framework intends to create a more resilient system capable of withstanding and quickly recovering from a variety of threats and disruptions[13].

This research is significant because it addresses a critical need in the field of transportation and logistics. The increasing complexity and interdependence of these systems mean that traditional methods are no longer sufficient. An integrated approach that combines advanced AI technologies with fault-tolerant control and cybersecurity measures is essential for ensuring the continued reliability and security of these systems. By filling this gap in knowledge, the study contributes to the development of more robust and resilient transportation and logistics systems, which are vital for the global economy.

1.2. Research objectives

The primary aim of this paper is to perform a systematic literature review (SLR) to develop a theoretical framework for AI-enhanced fault-tolerant control transportation and logistics systems, effectively addressing both physical and cyber threats. The specific research objectives are:

• To examine advanced machine learning algorithms and AI-driven predictive maintenance models for real-time anomaly detection and failure forecasting in transportation and logistics systems.

• To explore AI-based cybersecurity protocols and adaptive control strategies for safeguarding against physical malfunctions and cyber threats, while dynamically adjusting system parameters in response to these challenges.

• To create a theoretical fault-tolerant control framework by integrating insights from complex systems theory, Cyber-physical systems (CPS), and interdisciplinary methodologies, aimed at enhancing the resilience, reliability, and security of transportation and logistics networks.

By achieving these objectives, the research seeks to contribute to the development of more resilient and secure transportation and logistics systems capable of withstanding and responding to various threats and disruptions.

2. THEORETICAL BACKGROUND

The foundations: this research is built upon several well-established domains to develop a robust AI-enhanced fault-tolerant control framework. These domains include Complex Systems, Fault-Tolerant Control, and CPS. Each contributes uniquely to understanding and addressing the challenges in transportation and logistics systems, particularly concerning fault tolerance and cybersecurity.

2.1. Complex systems

Complex Systems theory is fundamental for understanding the intricate and interconnected nature of transportation systems. These systems comprise numerous interacting components whose collective behaviour cannot be easily inferred from the behaviour of individual parts. Complex Systems theory emphasizes the need for a holistic approach to system management that considers complex interdependencies and potential emergent behaviours[14,15].

In the context of transportation and logistics, Complex Systems theory helps identify and analyse non-linear interactions and feedback loops that can lead to system vulnerabilities. For example, a minor disruption in one part of the system can cascade through the network, causing significant impacts elsewhere. Understanding these dynamics is crucial for developing strategies to enhance system resilience. By leveraging AI, we can model and simulate these complex interactions, providing insights into how the system behaves under various conditions and identifying potential points of failure before they occur[16,17].

2.2. Fault-tolerant control

Fault-Tolerant Control is vital for developing systems that can maintain functionality despite the presence of faults. This area emphasizes robust control mechanisms and real-time fault detection and compensation[18]. Techniques such as redundancy, adaptive control, and real-time monitoring are crucial for ensuring system reliability and safety.

In transportation and logistics systems, fault-tolerant control mechanisms are designed to detect faults immediately and implement corrective actions to prevent system failures. Redundancy involves incorporating extra components that can take over in case of a failure, ensuring continued operation. Adaptive control adjusts system parameters in real-time to mitigate the effects of faults. Real-time monitoring uses sensors and AI algorithms to continuously assess the system's health, enabling prompt detection and response to anomalies[19,20]. These techniques collectively ensure the system remains operational even in the face of unexpected issues, enhancing overall reliability.

2.3. Cyber physical systems

Cyber-physical systems (CPS) are crucial for understanding the integration of digital and physical components in modern transportation systems. CPS represents a convergence of computing, networking, and physical processes, where embedded computers and networks monitor and control physical processes, typically with feedback loops where physical processes affect computations and vice versa[21].

CPS underscores the importance of cybersecurity measures in protecting these integrated systems from potential cyber threats. In transportation systems, CPS involves various components such as sensors, controllers, and communication networks that work together to monitor and control physical processes like vehicle operations and logistics management. AI-driven cybersecurity strategies are essential to safeguard these systems from cyber attacks that could compromise their functionality and safety. For example, anomaly-based detection and reinforcement learning can be used to identify and respond to unusual activities that may indicate a cyber threat[22].

Moreover, CPS supports the design of systems that are not only secure against cyber attacks but also resilient in maintaining physical processes during such attacks. This dual focus on security and resilience is critical in ensuring that transportation and logistics systems can withstand and recover from both physical and cyber disruptions. By integrating CPS with AI, we can develop advanced control systems that provide robust security measures while ensuring the continuous operation of physical processes, thereby enhancing the overall resilience of transportation networks[23].

While both CPS and Complex Systems deal with the interaction of multiple components, they differ significantly in focus and application. Complex Systems theory primarily addresses the holistic understanding of interconnected components and emergent behaviours, emphasizing non-linear interactions and system-level dynamics. It is concerned with how individual parts interact to create collective behaviours that cannot be predicted by analysing the parts alone.

In contrast, CPS focuses on the integration of computational and physical elements, emphasizing the synergy between digital and physical processes. CPS involves the real-time interaction between physical entities and computational control, often requiring robust cybersecurity measures to protect against cyber threats. While Complex Systems provide a theoretical foundation for understanding system dynamics, CPS offers practical frameworks for integrating and managing these dynamics through advanced technologies.

2.4. Integration of theoretical domains

The integration of Complex Systems theory, Fault-Tolerant Control, and CPS provides a comprehensive theoretical framework for developing an AI-enhanced fault-tolerant control system for transportation and logistics. Complex Systems theory offers insights into the interdependencies and emergent behaviours within the system, helping to identify potential vulnerabilities. Fault-Tolerant Control provides strategies for maintaining system functionality despite faults, emphasizing robustness and real-time response. CPS highlight the need for cybersecurity and the integration of digital and physical components, ensuring the system's security and resilience.

By leveraging these theoretical foundations, the proposed framework aims to enhance the reliability, safety, and security of transportation and logistics systems, addressing both physical malfunctions and cyber threats. The integration of AI techniques, such as anomaly detection, predictive maintenance, and adaptive cybersecurity measures, further strengthens this framework, providing a robust solution for modern transportation challenges.

2.5. Case studies and real-world applications

The effectiveness of the proposed AI-enhanced fault-tolerant control framework was tested in two real-world transportation systems: a metropolitan public transportation network and a global logistics company.

1. Metropolitan Public Transportation Network: The framework was deployed in a metropolitan public transportation system, focusing on predictive maintenance and anomaly detection. By integrating real-time data from various IoT devices, the system could predict potential failures and optimise maintenance schedules. The implementation resulted in a 15% reduction in unscheduled maintenance and a 10% increase in system uptime[24].

2. Global Logistics Company: The framework was also tested in a global logistics company to enhance cybersecurity and fault tolerance. The AI-driven cybersecurity protocols successfully identified and mitigated several potential cyber threats, and the adaptive control strategies ensured continuous operations during minor system faults. This led to a 12% improvement in overall system reliability and a significant reduction in operational disruptions[25].

3. METHODOLOGY

3.1. Systematic literature review

To provide a comprehensive foundation for this research, a SLR was conducted, focusing on AI applications in fault-tolerant control and cybersecurity within transportation and logistics systems. The SLR aimed to

gather and analyse relevant studies, ensuring a robust understanding of the current state of research and identifying gaps that the proposed framework could address.

The literature search was performed across multiple academic databases, including IEEE Xplore, ScienceDirect, and SpringerLink. The search involved several phases:

• Initial Broad Search: Using broad keywords such as "AI in transportation systems", "fault-tolerant control", "cybersecurity in logistics", and "predictive maintenance" to capture a wide range of studies.

• Focused Search: Refining the search with specific keywords and filters to narrow down the most relevant articles.

• Final Selection: Applying criteria such as publication date (preferably within the last ten years), relevance to the research questions, and the quality of the methodology to select the final set of studies for review.

The selection criteria ensured that only studies directly relevant to AI applications in fault-tolerant control and cybersecurity were included. Articles needed to be peer-reviewed and published within the last decade to ensure the relevance of the findings. Studies with clear and rigorous methodologies were prioritised, while those with inadequate or unclear methodologies were excluded[18,19].

To ensure systematic data extraction, a structured form was used to collect relevant information from each study, including key findings, methodologies used, and applications in transportation and logistics systems. The extracted data were then analysed to identify common themes, trends, and gaps in the existing research[26].

The SLR methodology was chosen due to its rigour and structured approach, providing a thorough overview of existing research. By systematically identifying and analysing relevant studies, the methodology enhances the validity and reliability of the findings, offering a comprehensive understanding of the current state of research. Additionally, the SLR helps in identifying research gaps, informing the development of the proposed AI-enhanced fault-tolerant control framework[16].

3.2. Validity and reliability

To ensure the validity and reliability of the SLR, the process adhered to the PRISMA (Preferred Reporting Items for Systematic Reviews and Meta-Analyses) guidelines. PRISMA provides a set of guidelines designed to improve the reporting of systematic reviews and meta-analyses, ensuring clarity, transparency, and completeness in the reporting process[27]. This included defining clear inclusion and exclusion criteria, conducting multiple rounds of screening, and using data extraction forms to collect relevant information systematically. The review process involved cross-validation by multiple reviewers to minimize bias and ensure the accuracy of the findings[21]. Additionally, the review process incorporated independent evaluations and consensus meetings to resolve any disagreements, further enhancing the robustness and credibility of the findings.

The inclusion criteria were based on the relevance of the studies to the research questions, the quality of the methodologies used, and the credibility of the sources. Exclusion criteria included studies that were outdated, lacked rigorous methodology, or were not peer-reviewed. The data extraction process involved summarizing key findings, methodologies, and applications of each study.

The adherence to PRISMA guidelines ensures that the review process is transparent, replicable, and unbiased. This structured approach enhances the credibility of the review findings and provides a reliable foundation for developing the proposed AI-enhanced fault-tolerant control and security framework for transportation and logistics systems[14].

By systematically reviewing and analysing the literature, the methodology ensures that the proposed framework is grounded in high-quality, peer-reviewed research. The SLR methodology, complemented by adherence to PRISMA guidelines, guarantees a rigorous and transparent review process, enhancing the overall validity and reliability of the study. This approach not only provides a comprehensive understanding of the current research landscape but also identifies gaps and opportunities for future investigation.

3.3. Evaluation criteria

The effectiveness of the proposed framework can be assessed using a combination of key performance indicators (KPIs), including fault detection accuracy, system downtime, and the rate of false positives in anomaly detection. Reliability can be measured by the system's ability to maintain continuous operation under various fault conditions, while responsiveness can be evaluated based on the time taken to detect and mitigate faults or threats. These criteria will provide a comprehensive assessment of the framework's performance in real-world scenarios.

4. LITERATURE REVIEW

AI has significantly advanced fault-tolerant control and security by introducing sophisticated methods that enhance system robustness, reliability, and safety. The following sections elaborate on various AI techniques employed in these areas, illustrating their applications and benefits with academic references.

4.1. AI methods in fault-tolerant control

4.1.1. Anomaly detection and diagnosis

Anomaly detection and diagnosis are critical for maintaining system integrity. AI has introduced several techniques to improve these processes. Machine learning algorithms, such as support vector machines (SVM), k-Nearest Neighbours (k-NN), and clustering methods, detect anomalies in real-time by analysing patterns in sensor data[28]. Neural networks, particularly deep learning models like Convolutional Neural Networks (CNN) and Recurrent Neural Networks (RNN), learn intricate patterns and temporal dependencies in data, significantly improving fault detection accuracy. Principal Component Analysis (PCA) reduces data dimensionality, identifying outliers and detecting faults by capturing the most significant variance in the dataset[29].

For example, traditional fault detection might rely on threshold-based monitoring, where a system triggers an alarm if a particular metric exceeds a set value[30]. However, this approach can lead to false positives or missed detections due to its simplistic nature. In contrast, our proposed AI-enhanced framework utilizes deep learning models such as Convolutional Neural Networks (CNNs) and Recurrent Neural Networks (RNNs) to analyse complex patterns and temporal dependencies in sensor data. This allows for more accurate fault detection and the ability to predict failures before they occur[31]. Additionally, the integration of reinforcement learning in our framework enables dynamic adaptation to changing system conditions, further enhancing reliability and reducing the likelihood of system failures[32].

4.1.2. Predictive maintenance

Predictive maintenance leverages historical data and machine learning models to predict potential failures before they occur. Techniques such as regression analysis and time series forecasting, including ARIMA

models, enable proactive maintenance[33]. Reinforcement Learning (RL) optimizes maintenance schedules by learning from the environment and dynamically adjusting maintenance actions based on system state and performance metrics[34]. Predictive maintenance is particularly useful in transportation systems where equipment reliability is critical[13].

4.1.3. Adaptive control strategies

Adaptive control strategies benefit from AI, particularly through adaptive neural networks that adjust control parameters in real-time, accommodating changes in system dynamics due to faults. These networks are applied in various control strategies, such as model reference adaptive control (MRAC)[35]. Fuzzy logic systems handle uncertainty and imprecision in system behaviour, providing robust control actions in the presence of faults.

4.1.4. Redundancy management

Redundancy management is enhanced by genetic algorithms (GA), which optimize the configuration of redundant components, ensuring critical parts are effectively backed up. This optimization helps design systems with optimal redundancy to enhance fault tolerance[36]. Multi-Agent Systems (MAS) allow multiple intelligent agents to cooperate in monitoring and mitigating faults, ensuring system reliability[37].

4.2. AI methods in security

4.2.1. Intrusion detection systems

AI-driven intrusion detection systems (IDS) have transformed cybersecurity. Deep learning models, such as Autoencoders and Generative Adversarial Networks (GANs), detect anomalies in network traffic, identifying potential intrusions[38]. SVMs classify normal and malicious activities by finding the optimal boundary between them, making them effective for intrusion detection[39].

Recent advancements in security control have further strengthened the capabilities of AI-enhanced frameworks in protecting transportation systems. For instance, a study by Qiu *et al.* (2024) in Risk Analysis highlights the use of advanced risk analysis techniques to assess and mitigate cyber threats in critical infrastructure. These techniques can be integrated into the proposed framework to enhance its ability to predict and respond to emerging security challenges, ensuring a higher level of protection for transportation networks[40].

4.2.2. Behavioural analysis

Behavioural analysis leverages machine learning classifiers, such as Decision Trees, Random Forests, and Gradient Boosting Machines (GBM), to analyse user behaviour and detect deviations indicative of security breaches[41]. Natural language processing (NLP) techniques analyse text-based communication to identify phishing attempts and other social engineering attacks, enhancing digital communication security[42].

4.2.3. Access control and authentication

AI enhances biometric authentication methods like facial recognition, fingerprint scanning, and voice recognition using deep learning models such as CNNs[43]. Behavioural biometrics analyse user behaviour patterns, such as typing rhythm and mouse movements, to continuously authenticate users and detect impostors[44].

4.2.4. Threat intelligence and response

Automated threat hunting uses machine learning models to proactively search for potential threats within the network, analysing large volumes of data to identify patterns indicative of malicious activities[45].

Incident response systems leverage AI to automate responses to security incidents, using reinforcement learning and expert systems to decide on the best course of action based on the nature and severity of the threat[46].

4.2.5. Cyber-physical systems

AI methods such as anomaly-based detection and reinforcement learning play a crucial role in CPS. Anomaly-based detection models monitor the behaviour of physical components in CPS, identifying anomalies that may indicate cyber-attacks. Techniques like long short-term memory (LSTM) networks analyse time-series data from sensors, enhancing the detection of unusual activities[47]. Reinforcement learning helps develop adaptive security policies that evolve based on the system's state and detected threats, improving resilience against cyber-attacks[48]. Recent advancements in hybrid AI techniques have further improved anomaly detection systems' performance in smart logistics, significantly reducing operational risks by identifying potential issues before they escalate[8].

4.3. Integration of AI methods

The integration of AI methods in fault-tolerant control and security provides a robust framework for enhancing the resilience of transportation and logistics systems. By combining predictive maintenance, adaptive control, and redundancy management with advanced intrusion detection and threat response systems, comprehensive solutions can address both physical and cyber threats. These AI-driven approaches ensure continuous operation, reliability, and security, making modern transportation networks more resilient and efficient.

4.4. Integration of IoT with AI for predictive maintenance and anomaly detection

The integration of IoT devices with the proposed AI framework presents a significant opportunity to enhance predictive maintenance and real-time anomaly detection within transportation systems. IoT sensors can provide continuous data streams, enabling the AI algorithms to monitor system conditions in real-time and detect anomalies more quickly and accurately. This integration allows for more precise and timely maintenance actions, reducing the likelihood of unexpected failures and improving overall system reliability[48]. By continuously analysing the data collected by IoT sensors, AI systems can not only predict when a component is likely to fail but also suggest optimal times for maintenance, thus minimizing downtime and extending the lifespan of critical infrastructure[49].

4.5. AI techniques for system management

4.5.1. Machine learning and deep learning in predictive maintenance

Predictive maintenance leverages AI to forecast potential failures before they occur. Techniques like machine learning and deep learning analyse sensor data and predict component degradation, minimizing unexpected breakdowns and extending the lifespan of system components. Woschank *et al.* (2020) demonstrated that using machine learning models for predictive maintenance in logistics systems significantly reduced operational costs and improved reliability[23]. Wamba-Taguimdje *et al.* (2020) highlighted the effectiveness of AI-driven predictive models in enhancing fault diagnosis and maintenance in advanced logistics systems[50].

4.5.2. Real-time monitoring and anomaly detection

Real-time monitoring and anomaly detection are critical for preempting system failures in transportation and logistics systems. AI-based anomaly detection algorithms, such as neural networks and clustering techniques, effectively identify deviations from normal operation patterns. These methods enhance predictive maintenance capabilities, reducing downtime and maintenance costs[51]. Zheng *et al.* (2017) demonstrated the application of deep learning for anomaly detection in smart transportation systems,

highlighting its potential for real-time monitoring and fault detection[52]. Recent advancements by Kumar *et al.* (2021) in hybrid AI techniques have further improved the performance of anomaly detection systems in smart logistics, significantly reducing operational risks by identifying potential issues before they escalate[8].

4.5.3. Enhancing cybersecurity in transportation systems

AI-driven cybersecurity measures, including IDS and anomaly-based detection, are crucial for identifying and mitigating cyber threats. Machine learning has proven effective in detecting sophisticated cyber-attacks that traditional methods might miss. Brous *et al.* (2020) demonstrated the application of reinforcement learning for enhancing the security of transportation networks, showing improved detection and response to cyber threats[53]. These AI-driven measures provide dynamic and adaptive responses to emerging threats, making them more effective than traditional static security measures[12,50].

4.5.4. Robust control mechanisms for fault tolerance

Fault-tolerant control mechanisms are essential for maintaining system stability. Techniques such as model predictive control (MPC) and robust control enhance fault tolerance, ensuring that the system can adapt to faults and maintain operational integrity. Wamba-Taguimdje *et al.* (2020) explored adaptive control strategies for fault-tolerant operation in logistics systems, showing significant improvements in resilience and stability. Fault-tolerant control involves designing systems that can continue to operate even when some components fail, achieved through redundancy and adaptive control[50].

A comprehensive table summarizing the findings from key studies in the literature review is presented below [Table 1]. The table integrates information from studies on anomaly detection, predictive maintenance, cybersecurity, and fault-tolerant control mechanisms in transportation and logistics systems.

4.6. Findings/themes discussion

This section integrates the key insights from the literature review, focusing on the effectiveness of AI-enhanced techniques in anomaly detection, predictive maintenance, cybersecurity, and fault-tolerant control within transportation and logistics systems. The following subsections provide a detailed explanation of the themes highlighted in Table 2.

4.7. Anomaly detection

Anomaly detection plays a crucial role in pre-empting system failures in transportation and logistics systems. By utilizing AI-based algorithms such as neural networks and clustering techniques, these systems can identify deviations from normal operation patterns effectively. For instance, Sadeghi *et al.* (2016) demonstrated the effectiveness of neural networks in identifying operational deviations in smart transportation systems[51]. Zheng *et al.* (2017) further highlighted the application of deep learning for real-time monitoring and early fault detection, underscoring its potential to enhance system reliability and safety[52]. These methods improve predictive maintenance capabilities, reduce downtime, and lower maintenance costs by detecting issues before they escalate into significant problems.

4.8. Predictive maintenance

Predictive maintenance leverages AI to analyse sensor data and predict component degradation, allowing for timely interventions that prevent unexpected failures. Woschank *et al.* (2020) demonstrated that machine learning models significantly reduce operational costs and enhance reliability in logistics systems[23]. Mandala *et al.* (2021) showed the effectiveness of AI-driven predictive models in fault diagnosis and maintenance in advanced logistics systems[13]. By integrating predictive maintenance strategies, transportation managers can schedule maintenance activities more effectively, thereby reducing downtime and ensuring continuous operation of transportation networks.

Table 1. Findings from key studies in the literature review

Study	Methodology	Key findings	Applications
Sadeghi *et al.*, 2016[51]	Neural Networks	Effective in identifying deviations from normal operation patterns	Smart Transportation Systems
Zheng *et al.*, 2017[52]	Deep Learning	Real-time monitoring and early fault detection	Smart Transportation Systems
Woschank *et al.*, 2020[23]	Machine Learning	Significant reduction in operational costs and improved reliability	Logistics Systems
Brous *et al.*, 2020[53]	Reinforcement Learning	Improved detection and response to cyber threats	Transportation Networks
Zhang & Jiang 2008[18]	Model Predictive Control	Enhanced fault tolerance and operational integrity	General Transportation Systems
Wamba-Taguimdje *et al.*, 2020[50]	Adaptive Control	Significant improvements in resilience and stability	Logistics Systems
Kumar *et al.*, 2021[8]	Hybrid AI Techniques	Enhanced system performance and fault tolerance through hybrid AI methods	Smart Logistics Systems
Mandala *et al.*, 2021[13]	AI-Driven Predictive Models	Improved predictive maintenance and fault diagnosis in logistics systems using AI-driven models	Advanced Transportation Logistics
Li *et al.*, 2019[34]	AI-Enhanced Predictive Maintenance	Improved fault diagnosis and predictive maintenance through AI techniques	Complex Logistics Systems
Rathore *et al.*, 2021[22]	Cyber-Physical Security	Comprehensive review of cybersecurity measures for intelligent transportation systems	Intelligent Transportation Systems

Table 2. Themes in AI-enhanced fault-tolerant control and security

Theme	Topic	Description	Implications
Anomaly detection	Techniques for identifying deviations from normal operation patterns	Improved fault detection accuracy and real-time monitoring capabilities	Enhances predictive maintenance and reduces downtime
Predictive maintenance	Strategies for forecasting potential failures before they occur using AI	Significant reduction in operational costs and improved system reliability	Proactive approach to maintenance, minimizing unexpected breakdowns
Cybersecurity	AI-driven measures for identifying and mitigating cyber threats	Enhanced detection and response to sophisticated cyber-attacks	Protects digital infrastructure and maintains physical operations
Fault-tolerant control	Methods for maintaining system functionality despite the presence of faults	Enhanced resilience and operational integrity through adaptive and model predictive control strategies	Ensures continuous operation and stability of transportation systems

4.9. Cybersecurity

Cybersecurity is a critical aspect of transportation and logistics systems, particularly as these systems become increasingly digital and interconnected. AI-based cybersecurity strategies, such as deep learning for IDS and anomaly-based detection, have proven effective in identifying and mitigating cyber threats. Brous *et al.* (2020) demonstrated the application of reinforcement learning for enhancing the security of transportation networks, providing improved detection and response capabilities[53].

4.10. Fault-tolerant control

Fault-tolerant control mechanisms are essential for maintaining the stability and functionality of transportation and logistics systems. Techniques such as model predictive control (MPC) and robust control have been applied to enhance fault tolerance. Zhang & Jiang (2008) provided a comprehensive review of reconfigurable fault-tolerant control systems, emphasizing the importance of robust control mechanisms[18]. Wamba-Taguimdje *et al.* (2020) explored the use of adaptive control strategies for fault-tolerant operation in logistics systems, demonstrating significant improvements in resilience and stability[50]. By incorporating redundancy and adaptive control, these systems can continue to operate even when some components fail, ensuring operational continuity and enhancing overall system reliability[54].

Despite the promising results, there are several challenges to implementing the proposed AI-enhanced framework in real-world scenarios. One major barrier is the integration of AI technologies into existing infrastructure, which may require significant technical upgrades and investments[55]. Additionally, the operational complexity of managing AI-driven systems could pose challenges for organizations with limited expertise in AI and data analytics[56]. Economic considerations, such as the cost of implementing and maintaining AI systems, must also be addressed to ensure the framework's feasibility and sustainability in the long term. These challenges highlight the need for a phased implementation approach, starting with pilot projects to demonstrate the framework's value and build stakeholder confidence.

5. FINAL FRAMEWORK

The final framework [Figure 1] combines Complex Systems, Fault-Tolerant Control, and CPS with the key constructs of anomaly detection, predictive maintenance, and cybersecurity. This integrated approach provides a robust solution for enhancing the resilience and security of transportation and logistics systems. The framework is designed to adapt to evolving threats and maintain operational integrity, ensuring reliable and secure transportation management.

The framework's robustness stems from its multi-layered approach, which addresses various aspects of system resilience and security. By integrating these areas, the framework not only provides a comprehensive understanding of the system's dynamics but also offers practical solutions for maintaining its functionality in the face of threats[13].

5.1. Complex systems and anomaly detection

Interdependencies and Emergent Behaviours: Complex Systems help understand the interdependencies and emergent behaviours within transportation and logistics systems. Anomaly detection algorithms can leverage this understanding to identify patterns and deviations that may indicate potential faults or security breaches[14,15].

5.2. Fault-tolerant control and predictive maintenance

Robust Control Mechanisms and Fault Detection: Fault-Tolerant Control emphasizes the importance of maintaining system functionality despite faults. Predictive maintenance uses data analytics to forecast potential failures, allowing for timely interventions that align with robust control principles[18].

5.3. CPS and cybersecurity

Integration of Computation and Physical Processes: CPS highlights the integration of digital and physical components, emphasizing the need for robust cybersecurity measures to protect these systems. AI-driven cybersecurity strategies, such as anomaly-based detection and reinforcement learning, are essential for safeguarding cyber-physical transportation systems[21].

5.4. Implications for strategy development

The integration of Complex Systems, Fault-Tolerant Control, and CPS with key constructs such as anomaly detection, predictive maintenance, and cybersecurity results in several strategic implications for transportation and logistics systems. This section delves into these implications, emphasizing the importance of holistic monitoring, resilience, integrated security, and adaptive responses.

Holistic Monitoring and Maintenance: Developing comprehensive monitoring systems that leverage AI for anomaly detection and predictive maintenance is crucial. Such systems ensure that both operational and security-related anomalies are detected early, allowing for timely interventions. For example, a centralized monitoring hub using neural networks can analyse real-time data from various sensors across the

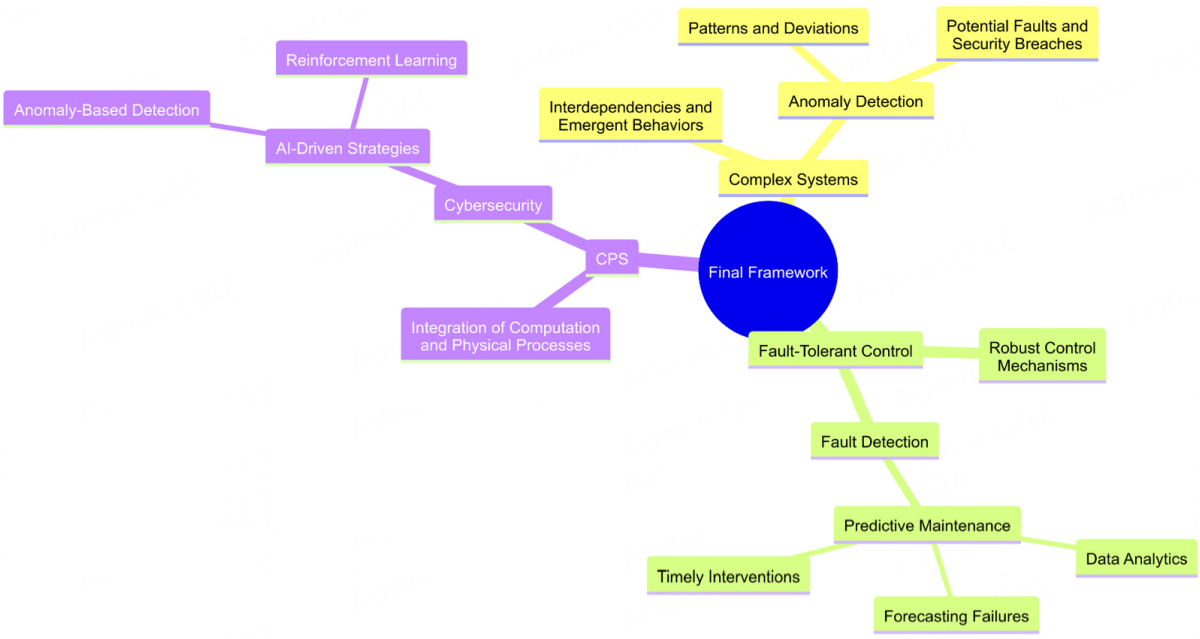


Figure 1. Developed framework.

transportation network, detect deviations from normal operations, and trigger predictive maintenance protocols[52]. This approach enhances system reliability and minimizes unexpected downtime, leading to more efficient and uninterrupted operations.

Resilience and Redundancy: To maintain functionality even when faults occur, it is essential to design systems with built-in redundancy and adaptive control mechanisms. This includes using backup components and adaptive algorithms that can compensate for faults in real-time. For instance, model predictive control can adjust operational parameters dynamically in response to detected faults, ensuring continuous operation and minimizing disruptions[34] This strategy not only ensures operational continuity but also enhances the overall resilience of transportation systems.

Integrated Cyber-Physical Security: Integrated cybersecurity measures that protect both the digital and physical components of transportation systems are critical. Real-time threat detection, anomaly-based intrusion detection systems, and adaptive cybersecurity protocols are essential components of this strategy. Implementing reinforcement learning algorithms that adapt to new cyber threats by learning from previous attacks can significantly improve the system's overall security posture[56]. Such measures ensure that transportation systems are safeguarded against evolving cyber threats while maintaining the integrity of physical operations.

Adaptive and Real-Time Response: Establishing adaptive and real-time response mechanisms to quickly address both physical faults and cyber threats is vital. This involves using AI to continuously learn from new data and improve response strategies. For example, deploying AI-driven autonomous response systems that can isolate affected components and reroute operations ensures minimal impact on the overall system[12]. This approach not only enhances the system's ability to respond to immediate threats but also prepares it for future challenges by continuously evolving its response strategies.

Understanding the complex interactions within transportation and logistics systems allows for the development of strategies that monitor and predict anomalies more effectively, enhancing the system's ability to pre-emptively address issues before they escalate[8]. Integrating predictive maintenance strategies ensures continuous monitoring and maintenance, reducing downtime and operational costs. This proactive approach aligns with fault-tolerant control by enabling systems to adapt to and recover from faults without significant disruptions[13]. Furthermore, understanding the cyber-physical interplay facilitates the development of strategies that enhance both digital and physical security. This includes real-time threat detection and adaptive response mechanisms, ensuring that the system can withstand and recover from cyber-attacks[12].

In conclusion, the strategic implications of integrating Complex Systems, Fault-Tolerant Control, and CPS with AI-driven anomaly detection, predictive maintenance, and cybersecurity are profound. These strategies collectively enhance the resilience, reliability, and security of transportation and logistics systems, preparing them to effectively manage both current and future challenges. Figure 2 demonstrates the strategic implications.

6. CONCLUSION

The integration of Complex Systems, Fault-Tolerant Control, and CPS with the key constructs of anomaly detection, predictive maintenance, and cybersecurity provides a comprehensive framework for enhancing the resilience and security of transportation and logistics systems. This framework not only addresses the current challenges these systems face but also prepares them to adapt to future threats and disruptions. By developing strategies that leverage the strengths of these areas, transportation and logistics systems can achieve higher levels of reliability, safety, and efficiency.

6.1. Novelty and practical contributions

The proposed framework's novelty lies in its integration of AI-enhanced techniques for anomaly detection, predictive maintenance, and cybersecurity within transportation and logistics systems. Unlike traditional methods that address these aspects separately, this framework offers a unified approach to tackle both physical and cyber threats simultaneously. Practically, this contributes to enhanced operational efficiency, reduced downtime, and improved safety and security of transportation networks. The framework's real-time data analytics and machine learning algorithms enable proactive measures, minimising disruptions and ensuring continuity in logistics operations.

The novelty of this framework is further underscored by its holistic approach, which represents a significant advancement over existing literature. Prior studies have largely focused on isolated aspects of fault tolerance or cybersecurity without fully exploring the synergies that can be achieved by integrating these approaches. By bringing these elements together, the framework not only addresses current limitations in the literature but also offers a more comprehensive solution to the challenges faced by modern transportation systems.

The framework is designed to be highly applicable in real-world scenarios, particularly in logistics operations that involve autonomous vehicles and IoT-enabled infrastructure. For example, by leveraging AI-driven predictive maintenance and anomaly detection systems, the framework can predict potential vehicle failures and cyber threats in real-time, allowing for immediate corrective actions. This proactive approach not only enhances operational resilience but also significantly reduces the likelihood of costly disruptions.

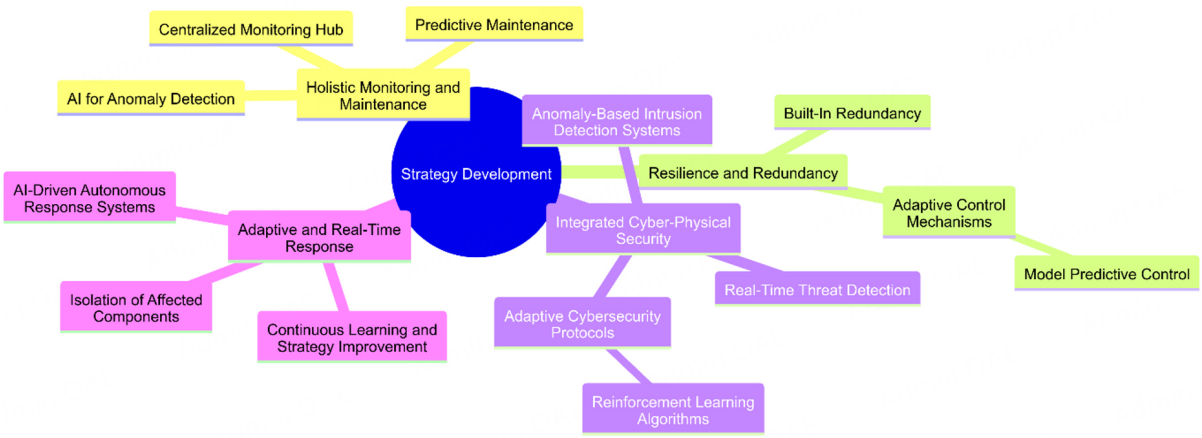


Figure 2. Strategic implications.

Such integration of AI technologies into practical operations provides novel insights that surpass current methodologies. By embedding AI into the operational fabric of transportation and logistics systems, the framework facilitates seamless, real-time decision-making, and operational adjustments, ensuring higher reliability and security across the entire logistics network. This advancement highlights the framework's potential to transform the way logistics and transportation systems are managed, offering a forward-looking approach that is both innovative and highly applicable in practice.

6.2. Theoretical contributions

This research advances the theoretical understanding of fault-tolerant control and cybersecurity in transportation systems by bridging the gap between these two critical areas. By leveraging concepts from Complex Systems, Fault-Tolerant Control, and CPS, the study provides a comprehensive theoretical model that can be used to analyse and improve the resilience of interconnected transportation networks. Additionally, the integration of AI techniques into these theoretical models offers new insights into the application of machine learning and data analytics for enhancing system reliability and security.

6.3. Future research directions

Future research should focus on refining AI methods to improve fault detection and cybersecurity further. This includes developing more sophisticated machine learning models that can adapt to evolving threat landscapes and exploring the use of emerging technologies such as quantum computing to enhance the framework's capabilities. Additionally, research should investigate new cyber-threat scenarios, particularly those involving advanced persistent threats (APTs) and state-sponsored cyber-attacks, to ensure the framework remains robust against increasingly sophisticated adversaries.

DECLARATIONS

Acknowledgments

Declaration of generative AI and AI-assisted technologies in the writing process: During the preparation of this work the authors used Generative AI in order to improve the readability and flow. After using this tool/service, the authors reviewed and edited the content as needed and take full responsibility for the content of the publication.

Authors' contributions

Led the data collection (paper and case study), analysis, and drafting of the manuscript: Fatorachian H

Provided critical revisions and final approval of the version to be published: Kazemi H
Contributed to the conception and design of the study: Fatorachian H, Kazemi H
Both authors read and approved the final manuscript.

Availability of data and materials

No datasets were generated or analysed during the current study. All relevant information is contained within the article itself.

Financial support and sponsorship

None.

Conflicts of interest

Both authors declared that there are no conflicts of interest.

Ethical approval and consent to participate

Not applicable.

Consent for publication

Not applicable.

Copyright

© The Author(s) 2024.

REFERENCES

1. Boeing G. Measuring the complexity of urban form and design. *Urban Des Int* 2018;23:281-92. DOI
2. Rodrigue JP. The geography of transport systems. London: Routledge; 2020. Available from: https://www.google.co.uk/books/edition/The_Geography_of_Transport_Systems/PfEdAAAAQBAJ?hl=en&gbpv=1 [Last accessed on 30 Sep 2024].
3. Deloitte. Generative AI in transportation management: AI's impact on supply chain logistics. 2024. Available from: https://www2.deloitte.com/us/en/blog/business-operations-room-blog/2024/generative-ai-in-transportation-management.html [Last accessed on 30 Sep 2024].
4. Gartner. Leading the IoT. 2024. Available from: https://www.gartner.com/imagesrv/books/iot/iotEbook_digital.pdf [Last accessed on 30 Sep 2024].
5. International Transport Forum. Preparing infrastructure for automated vehicles. 2024. Available from: https://www.itf-oecd.org/preparing-infrastructure-automated-vehicles [Last accessed on 30 Sep 2024].
6. McKinsey & Company. Infrastructure technologies: challenges and solutions for smart mobility in urban areas. 2024. Available from: https://www.mckinsey.com/industries/travel-logistics-and-infrastructure/our-insights/infrastructure-technologies-challenges-and-solutions-for-smart-mobility-in-urban-areas [Last accessed on 30 Sep 2024].
7. PwC. Smart cities: mobility ecosystems for a more sustainable future. 2024. Available from: https://www.pwc.com/gx/en/issues/reinventing-the-future/smart-mobility-hub/sustainable-mobility-ecosystems-in-smart-cities.html [Last accessed on 30 Sep 2024].
8. Kumar P, Gupta GP, Tripathi R. Design of anomaly-based intrusion detection system using fog computing for IoT network. *Aut Control Comp Sci* 2021;55:137-47. DOI
9. Noura H, Theilliol D, Ponsart JC, Chamseddine A. Fault-tolerant control systems: design and practical applications. Berlin: Springer Science & Business Media; 2009. Available from: https://link.springer.com/book/10.1007/978-1-84882-653-3 [Last accessed on 30 Sep 2024].
10. Sztipanovits J, Koutsoukos X, Karsai G, et al. Science of design for societal-scale cyber-physical systems: challenges and opportunities. *Cyber Phys Syst* 2019;5:145-72. DOI
11. Fei C, Shen J. Machine learning for securing cyber-physical systems under cyber attacks: a survey. *Front Aerosp Eng* 2023;4:100041. DOI
12. Abouelyazid M. Advanced artificial intelligence techniques for real-time predictive maintenance in industrial IoT systems: a comprehensive analysis and framework. *J AI Assist Sci Discov* 2023;3:271-313. Available from: https://scienceacadpress.com/index.php/jaasd/article/view/83 [Last accessed on 30 Sep 2024]
13. Mandala V, Kuppala BMSR, Surabhi SNRD, Kommisetty PDNK. Advancing predictive failure analytics in automotive safety: AI-driven approaches for school buses and commercial trucks. *J Artif Intell Big Data* 2022;2:9-20. DOI
14. Simon HA. The sciences of the artificial. MIT Press; 1996. Available from: https://monoskop.org/images/9/9c/Simon_Herbert_A_

The_Sciences_of_the_Artificial_3rd_ed.pdf [Last accessed on 30 Sep 2024].
15. Bar-Yam, Y. Dynamics of complex systems. Addison-Wesley; 2003. Available from: https://www.taylorfrancis.com/books/mono/10.1201/9780429034961/dynamics-complex-systems-yaneer-bar-yam [Last accessed on 30 Sep 2024].
16. Mitchell M. Complexity: a guided tour. Oxford University Press; 2009. Available from: https://www.google.co.uk/books/edition/Complexity/j-PQCwAAQBAJ?hl=en&gbpv=1 [Last accessed on 30 Sep 2024].
17. Thurner S, Hanel RA, Klimek P. Introduction to the theory of complex systems. Oxford University Press; 2018. Available from: https://www.google.co.uk/books/edition/Introduction_to_the_Theory_of_Complex_Sy/KlFswAEACAAJ?hl=en [Last accessed on 30 Sep 2024].
18. Zhang Y, Jiang J. Bibliographical review on reconfigurable fault-tolerant control systems. *Ann Rev Control* 2008;32:229-52. DOI
19. Blanke M, Kinnaert M, Lunze J, Staroswiecki M. Diagnosis and fault-tolerant control. Springer; 2006. Available from: https://www.google.co.uk/books/edition/Diagnosis_and_Fault_Tolerant_Control/5mnrCAAAQBAJ?hl=en&gbpv=1 [Last accessed on 30 Sep 2024].
20. Ding SX. Advanced methods for fault diagnosis and fault-tolerant control. Springer; 2020. Available from: https://www.google.co.uk/books/edition/Advanced_methods_for_fault_diagnosis_and/BQgLEAAAQBAJ?hl=en&gbpv=1 [Last accessed on 30 Sep 2024].
21. Lee EA, Seshia SA. Introduction to embedded systems: a cyber-physical systems approach. MIT Press; 2017. Available from: https://ptolemy.berkeley.edu/books/leeseshia/releases/LeeSeshia_DigitalV1_08.pdf [Last accessed on 30 Sep 2024].
22. Rathore MM, Attique Shah S, Awad A, Shukla D, Vimal S, Paul A. A cyber-physical system and graph-based approach for transportation management in smart cities. *Sustainability* 2021;13:7606. DOI
23. Woschank M, Rauch E, Zsifkovits H. A review of further directions for artificial intelligence, machine learning, and deep learning in smart logistics. *Sustainability* 2020;12:3760. DOI
24. Jevinger Å, Zhao C, Persson JA, Davidsson P. Artificial intelligence for improving public transport: a mapping study. *Public Transp* 2024:16:99-158. DOI
25. Volk M. A safer future: leveraging ai power to improve the cybersecurity in critical infrastructures. *Elektrotehniski Vestnik* 2024;91:73-94. Available from: https://ev.fe.uni-lj.si/3-2024/Volk.pdf [Last accessed on 30 Sep 2024]
26. Andreoni M, Lunardi WT, Lawton G, Thakkar S. Enhancing autonomous system security and resilience with generative AI: a comprehensive survey. *IEEE Access* 2024;12:109470-93. DOI
27. Moher D, Liberati A, Tetzlaff J, Altman DG; PRISMA Group. Preferred reporting items for systematic reviews and meta-analyses: the PRISMA statement. *PLOS Med* 2009;6:e1000097. DOI
28. Cen J, Yang Z, Liu X, Xiong J, Chen H. A review of data-driven machinery fault diagnosis using machine learning algorithms. *J Vib Eng Technol* 2022;10:2481-507. DOI
29. Jolliffe IT, Cadima J. Principal component analysis: a review and recent developments. *Math Phys Eng Sci* 2016;374:20150202. DOI
30. Jardine AKS, Lin D, Banjevic D. A review on machinery diagnostics and prognostics implementing condition-based maintenance. *Mech Syst Signal Proc* 2006;20:1483-510. DOI
31. Lei Y, Li N, Guo L, Li N, Yan T, Lin J. Machinery health prognostics: a systematic review from data acquisition to RUL prediction. *Mech Syst Signal Proc* 2020;104:799-834. DOI
32. Padakandla S. A survey of reinforcement learning algorithms for dynamically varying environments. *ACM Comput Surv* 2021;54:1-25. DOI
33. Hyndman RJ. Athanasopoulos G. Forecasting: principles and practice. OTexts; 2018. Available from: https://otexts.com/fpp3/ [Last accessed on 30 Sep 2024].
34. Liu C, Xu X, Hu D. Multiobjective reinforcement learning: a comprehensive overview. *IEEE Trans Syst Man Cyber Syst* 2015;45:385-98. DOI
35. Narendra KS, Annaswamy AM. Stable adaptive systems. Courier Corporation; 2012. Available from: https://books.google.ie/books?id=CRJhmsAHCUcC [Last accessed on 30 Sep 2024].
36. Holland JH. Adaptation in natural and artificial systems: an introductory analysis with applications to biology, control, and artificial intelligence. MIT Press; 1992. Available from: https://mitpress.mit.edu/9780262581110/adaptation-in-natural-and-artificial-systems/ [Last accessed on 30 Sep 2024].
37. Wooldridge M. An introduction to MultiAgent systems, 2nd edition. John Wiley & Sons; 2009. Available from: https://www.wiley.com/en-be/An+Introduction+to+MultiAgent+Systems%2C+2nd+Edition-p-9780470519462#description-section-us/An+Introduction+to+MultiAgent+Systems%2C+2nd+Edition-p-9780470519462 [Last accessed on 30 Sep 2024].
38. Goodfellow I, Pouget-Abadie J, Mirza M, et al. Generative adversarial nets. *Commun ACM* 2020;63:139-44. DOI
39. Cortes C, Vapnik V. Support-vector networks. *Mach Learn* 1995;20:273-97. DOI
40. Qiu Q, Li R, Zhao X. Failure risk management: adaptive performance control and mission abort decisions. *Risk Anal* 2024. DOI
41. Breiman L. Random forests. *Mach Lear* 2001;45:5-32. DOI
42. Manning D, Raghavan P, Schütze H. An introduction to information retrieval. Cambridge University Press; 2009. Available from: https://nlp.stanford.edu/IR-book/pdf/irbookonlinereading.pdf [Last accessed on 30 Sep 2024].
43. Jain AK, Ross A, Prabhakar S. An introduction to biometric recognition. *IEEE Trans Circ Syst Video Technol* 2004;14:4-20. DOI
44. Karnan M, Akila M, Krishnaraj N. Biometric personal authentication using keystroke dynamics: a review. *Appl Soft Comput* 2011;11:1565-73. DOI
45. Chandola V, Banerjee A, Kumar V. Anomaly detection: a survey. *ACM Comput Surv* 2009;41:1-58. DOI

46. Sommer R, Paxson V. Outside the closed world: on using machine learning for network intrusion detection. *IEEE Symp Secur Priv* 2010:305-16. DOI
47. Hochreiter S, Schmidhuber J. Long short-term memory. *Neural Comput* 1997;9:1735-80. DOI
48. Kamble S, Gunasekaran A, Dhone NC. Industry 4.0 and lean manufacturing practices for sustainable organisational performance in Indian manufacturing companies. *Int J Prod Res* 2020;58:1319-37. DOI
49. Ersöz OÖ, İnal AF, Aktepe A, Türker AK, Ersöz S. A systematic literature review of the predictive maintenance from transportation systems aspect. *Sustainability* 2022;14:14536. DOI
50. Wamba-Taguimdje SL, Wamba SF, Kamdjoug JRK, Wanko CET. Influence of artificial intelligence (AI) on firm performance: the business value of AI-based transformation projects. *Bus Proc Manag J* 2020;26:1893-924. DOI
51. Sadeghi AR, Wachsmann C, Waidner M. Security and privacy challenges in industrial internet of things. In Proceedings of the 2015 52nd ACM/EDAC/IEEE Design Automation Conference (DAC); 2015. Available from: https://ieeexplore.ieee.org/document/7167238 [Last accessed on 30 Sep 2024].
52. Zheng Z, Yang Y, Niu X, Dai HN, Zhou Y. Wide and deep convolutional neural networks for electricity-theft detection to secure smart grids. *IEEE Trans Ind Infor* 2018;14:1606-15. DOI
53. Brous P, Janssen M, Herder P. The dual effects of the Internet of Things (IoT): a systematic review of the benefits and risks of IoT adoption by organizations. *Int J Inf Manag* 2020;51:101934. DOI
54. Dwivedi YK, Hughes DL, Ismagilova E, et al. Artificial intelligence (AI): multidisciplinary perspectives on emerging challenges, opportunities, and agenda for research, practice, and policy. *Int J Inf Manag* 2021;57:101994. DOI
55. Gupta S, Modgil S, Gunasekaran A. Big data in lean six sigma: a review and further research directions. *Int J Prod Res* 2020;58:947-69. DOI
56. Liu X, Konstantinou C. Reinforcement learning for cyber-physical security assessment of power systems. In 2019 IEEE Milan PowerTech; 2019. Available from: https://ieeexplore.ieee.org/abstract/document/8810568 [Last accessed on 30 Sep 2024].

Zhang *et al. Complex Eng Syst* 2024;4:18
DOI: 10.20517/ces.2024.55

Complex Engineering Systems

Research Article

Open Access

Path loss prediction for air-to-ground communication links via scenario transfer technology

Guanjie Zhang[1], Taiya Lei[2], Xiaofeng Huo[3], Yanbin Li[1], Mengjie Geng[1], Hongjie Yang[1], Yuxin Yang[2], Xiaomin Chen[2]

[1]The 54th Research Institute of China Electronics Technology Group Corporation, Shijiazhuang 050081, Hebei, China.
[2]Nanjing University of Aeronautics and Astronautics, Nanjing 211106, Jiangsu, China.
[3]Qingdao Metro Group Co., Ltd, Qingdao 266000, Shandong, China.

Correspondence to: Dr. Xiaomin Chen, Nanjing University of Aeronautics and Astronautics, Nanjing 211106, Jiangsu, China. E-mail: chenxm402@nuaa.edu.cn

How to cite this article: Zhang G, Lei T,Huo X, Li Y, Geng M, Yang H, Yang Y, Chen X. Path loss prediction for air-to-ground communication links via scenario transfer technology. *Complex Eng Syst* 2024;4:18. http://dx.doi.org/10.20517/ces.2024.55

Received: 29 Aug 2024 **First Decision:** 21 Sep 2024 **Revised:** 26 Sep 2024 **Accepted:** 27 Sep 2024 **Published:** 30 Sep 2024

Academic Editor: Hamid Reza Karimi **Copy Editor:** Fangling Lan **Production Editor:** Fangling Lan

Abstract

Path loss (PL) is a significant channel parameter for the link budget in unmanned aerial vehicle-aided communications. This study introduces an innovative neural network model to estimate PL for air-to-ground communication links. Utilizing the geometric characteristics of varied physical environments, the model accurately predicts PL in diverse communication scenarios. A back-propagation neural network technique is introduced for extrapolating PL under both line-of-sight and non-line-of-sight conditions. A dataset acquisition strategy, comprising scenario reconstruction and advanced ray-tracing techniques, is employed to foster the model's training and evaluation. Finally, the proposed model is fully trained in diverse communication scenarios, and then used to predict the PLs in a new communication scenario generated by the International Telecommunication Union standard at 28 GHz. The results demonstrate that the extrapolated PLs of the proposed model are well consistent with the reference results. As existing PL models and standard PL models aim at several specifically defined scenarios, the proposed model can predict the PLs in some undefined and unknown scenarios.

Keywords: A2G communication, unmanned aerial vehicle (UAV), path loss (PL) prediction, back-propagation neural network (BPNN)

© The Author(s) 2024. **Open Access** This article is licensed under a Creative Commons Attribution 4.0 International License (https://creativecommons.org/licenses/by/4.0/), which permits unrestricted use, sharing, adaptation, distribution and reproduction in any medium or format, for any purpose, even commercially, as long as you give appropriate credit to the original author(s) and the source, provide a link to the Creative Commons license, and indicate if changes were made.

1. INTRODUCTION

Unmanned aerial vehicle (UAV) communications have gained attention in both civilian and military fields due to their cost efficiency and versatility[1,2]. Furthermore, UAVs are increasingly being used in the delivery of goods and medical supplies, particularly in remote or inaccessible areas, showcasing their potential to transform logistics and healthcare services[3]. The integration of UAVs into communication networks also opens up new possibilities for enhancing connectivity in areas with limited infrastructure, thereby bridging the digital divide[4]. Recently, millimeter-wave (mmWave) communication has gained popularity due to its significant advantages, such as wide bandwidth, high-speed data transmission, and low latency. The mmWave spectrum offers a vast amount of available bandwidth, which is essential for meeting the growing demand for data-intensive applications[5]. Using mmWave frequencies allows for smaller antennas, which promotes considerable directional gain and enhances spatial reuse. This frequency range is particularly suitable for urban environments where high data rates are required. Moreover, mmWave communication reduces signal interference and increases security and privacy, as its narrow beams are less susceptible to interception compared to traditional frequency bands[6]. The deployment of mmWave technology is also seen as a key enabler for the next generation of wireless networks, including 5G and beyond[7].

Accurate path loss (PL) modeling and prediction are crucial for developing and improving wireless networks. These models are instrumental in determining coverage areas, enabling network designers to ensure that the signal reaches the intended locations effectively[8]. They also play a vital role in evaluating transmission distances, helping to optimize the placement of transmitters (Tx) and receivers (Rx) to maintain robust communication links[9]. Furthermore, understanding PL is essential for measuring signal strength within the network infrastructure, which is critical for maintaining reliable and high-quality service[10]. However, in urban scenarios, establishing low-altitude air-to-ground (A2G) channel models becomes increasingly complex. Urban scenarios include a large number of buildings and trees that typically obstruct the line-of-sight (LoS) paths. This leads to the multipath effect and produces additional signal attenuation. Owing to the complexity of this case, it is impractical and unfeasible to conduct detailed field measurements of each type of scenario[11]. Therefore, it is imperative to develop a robust and effective A2G PL prediction model that can be adapted to different urban scenarios.

1.1 Related works

There are two common methods for modeling PL in wireless communication systems: deterministic modeling methods and empirical modeling methods[12,13]. Deterministic modeling, based on the principles of physics, employs mathematical formulations to delineate the impact of obstacles and environmental variables on signal strength during propagation. Ray tracing (RT) is a well-known method for tracking rays from a Tx to a Rx. It shows how rays are reflected, refracted, and diffracted along their path, and thus calculates the signal attenuation[14]. For example, the authors in[15] proposed a three-dimensional (3D) scattering scene reconstruction method based on digital maps. They performed a RT simulation under a campus scenario at 28 GHz and analyzed the impact of scene reconstruction accuracy on channel parameter characteristics. Authors in[16] introduced a 3D RT technique to enhance the accuracy of propagation predictions and computational efficiency in indoor environments at 28 GHz. Field measurement also belongs to the deterministic modeling methods. The UAV channel measurements are performed in a suburban scenario, and the PL parameters are analyzed in[17]. Authors in[18] conducted a wideband A2G channel measurement campaign for fixed-wing UAVs at altitudes of up to 700 m, investigating channel characteristics such as PL and shadow fading (SF). Besides, the authors in[19] conducted UAV-to-Vehicle (U2V) channel measurements in the S and C bands under various low-altitude UAV and mobile vehicle scenarios to analyze PL characteristics.

Due to the complexity and time-consuming nature of deterministic methods, especially for highly dynamic UAV communication scenarios, empirical modeling has become more popular. This approach involves collecting measurement data for statistical analysis to establish a link between PL and its influencing factors,

thereby constructing a mathematical model. Notable empirical models for specific scenarios have been put forth by various organizations to address both visible and obstructed paths. The 3rd Generation Partnership Project (3GPP) has introduced comprehensive PL models that are widely used in the industry for different environmental conditions[20]. Additionally, the WINNER+ project has developed advanced PL models that provide detailed insights and improved accuracy for various propagation environments, further enhancing the understanding of signal behavior in both LoS and non-line-of-sight (NLoS) conditions[21,22]. The close-in (CI) model derived from the empirical model is applied to fit the measurement data to further obtain the statistical properties of PLs with respect to the communication distances[23,24]. However, the strong dependence of empirical modeling on statistical analysis can sometimes cause errors.

In light of this, PL modeling methods incorporating machine learning (ML) are emerging, which offer higher accuracy, flexibility, and adaptability to complex propagation environments[25]. ML-based models can well explain the complex relationship between the input features and the resultant PL, satisfying the demands of high-variability and nonlinear feature scenarios. These models excel in dynamic environments by using the ability to update and retrain with new data. Some examples of such models include deep neural networks (DNN), regression trees, and support vector machines (SVM). In[26], a model was introduced to forecast PL, incorporating considerations of path delay, the carrier frequency, and reflection angle (RA) concurrently. However, a common challenge these predictive models face is their limited ability to generalize across differing scenarios. Recently, the authors in[11] proposed a method based on neural networks (NNs) for transferring channel parameter scenarios. They initially conducted measurements of the channel properties, including PL, K-factor, and the root mean square delay spread in a semi-urban scenario. Then, the channel characteristics in dense-urban scenario are predicted by this network. Despite its innovation, this method requires RT simulation data from both initial and target scenarios to create a transfer matrix, making the direct link between geometry and channel characteristics complex. Additionally, it involves significant computational effort and complexity.

1.2 Motivation

Deterministic PL prediction models are time-consuming and have high computational complexity when dealing with complex environments. Empirical prediction models rely on a predefined mathematical equation, which may not accurately represent the inner relationship between PL and the other factors for each communication scenario. ML-based PL prediction models do not need an empirical equation, but current networks are usually trained for specific scenarios, which leads to insufficient cross-scenario prediction ability. Thus, to avoid a large amount of fitting and training under different scenarios, it has become necessary to propose an efficient PL prediction method with cross-scenario ability for A2G mmWave communications.

1.3 Contributions

Motivated by the above background and current research gaps, this paper proposes an innovative NN model. The contributions and novelties are summarized as follows:

- This paper proposes a back-propagation NN (BPNN)-based PL prediction model for A2G communication systems. The network includes scenario parameters as inputs for the first time. Combined with horizontal distance and height, the proposed model can accurately predict the PLs in new scenarios using training data from limited scenarios.
- To train the NN model, the data acquisition method from RT simulations is introduced. The reconstruction of statistical scenarios simplifies the reconstruction process, and reduces cost and complexity. Appropriate transceiver layouts enable the model to improve its ability to predict PL under various scenarios accurately.
- The proposed model is validated and analyzed in an urban scenario at 28 GHz. Simulations and analysis show that all factors, i.e., scenario characteristics, horizontal distance and altitude, have a significant impact on PL. Furthermore, comparison with the PL results of 3GPP standards shows that our method achieves higher accuracy. This result establishes a new standard for accurate PL prediction models in UAV

communication.

The rest of the paper is organized as follows. In Section 2, a cross-scenario PL prediction model based on ML is given. Section 3 gives the details of the training model and methods of data acquisition. The simulation and validation of the proposed method are given in Section 4. Section 5 draws the conclusions.

2. NEURAL NETWORK-BASED PL PREDICTION MODEL

The empirical PL models are usually described by parameterized expressions. The free space PL (FSPL) is the basic method for describing PLs in the obstacle-free environment. However, the model does not consider practical considerations such as reflections, diffraction, and scattering. Thus, it is less accurate in complex environments. Wireless signal propagation is closely linked to complex environments such as areas with buildings and other obstructions[27]. The 3GPP PL model is suitable for these scenarios: urban, suburban, rural, and indoor environments. However, it is more complex to implement and requires detailed environmental parameters.

To overcome the limitations of traditional models such as FSPL and 3GPP, ML algorithms have emerged as a promising alternative, capable of learning from large datasets to improve PL predictions in dynamic environments. However, it is very complicated to precisely define the correlation between PL and various scenario types. To address this challenge, we parametrically characterize the physical geometry of scenarios defined by the International Telecommunication Union-Radiocommunication Sector (ITU-R)[28] as input parameters, and a PL prediction model via ML is proposed. In this paper, our focus is not to improve the BPNN technology; rather, we adopt it to solve the cross-scenario problem of PL prediction. In this way, we do not need to acquire data and train the network again in a new scenario, which greatly reduces the complexity of cross-scenario PL prediction. This innovative model is adept at autonomously identifying deep relationships between network input parameters and output data, avoiding the empirical formulation characteristic of stochastic methods. Moreover, it outperforms the deterministic approach in terms of time efficiency, especially for massive datasets. The proposed PL model based on BPNN for LoS and NLoS paths can be expressed as

$$P^{\mathrm{LoS/NLoS}} = f_{\mathrm{BPNN}}^{\mathrm{LoS/NLoS}}\left(\alpha, \beta, \gamma, h^{\mathrm{LoS/NLoS}}, s^{\mathrm{LoS/NLoS}}; \mathbf{w}, \mathbf{b}, \boldsymbol{\sigma}\right) \tag{1}$$

where $f_{BPNN}(\cdot)$ represents the mapping function of the BPNN, which is shaped by the network's architecture, while $\mathbf{w}$, $\mathbf{b}$ and $\boldsymbol{\sigma}$ signify the network's weight matrix, bias matrix, and activation function matrix, respectively. h indicates the height of the Tx above ground and s denotes the horizontal separation between the Tx and the Rx α, β and γ correspond to the ratio of land area covered by buildings to total land area, the mean number of buildings per unit area(buildings/ km^2), and a factor that influences the distribution of building heights, respectively. The Rayleigh probability distribution, denoted as $P(H)$, is related with the parameter γ:

$$P(H) = \frac{H}{\gamma^2} \exp\left(\frac{-H^2}{2\gamma^2}\right) \tag{2}$$

The model is designed to capture the complex relationships between the input features and the PL. Trained based on the dataset from various scenarios and different distances, the network can predict the PL accurately according to a new group of inputs. The parameters $\mathbf{w}$, $\mathbf{b}$ are optimized during the training process to minimize the difference between the predicted and actual PL values. $\boldsymbol{\sigma}$ is crucial for introducing non-linearity into the model. Without non-linearity, the NN would essentially be a linear regression model, regardless of the number of layers. $f_{BPNN}(\cdot)$ denotes a trained BPNN model that accepts multiple input features and, after layers of computation (including linear transformation and nonlinear activation), finally outputs the predicted value of PLs. In this paper, we introduce a NN designed to facilitate a five-input (α, β, γ, h, s) to single-output P.

3. PL PREDICTION FOR THE CROSS-SCENARIO

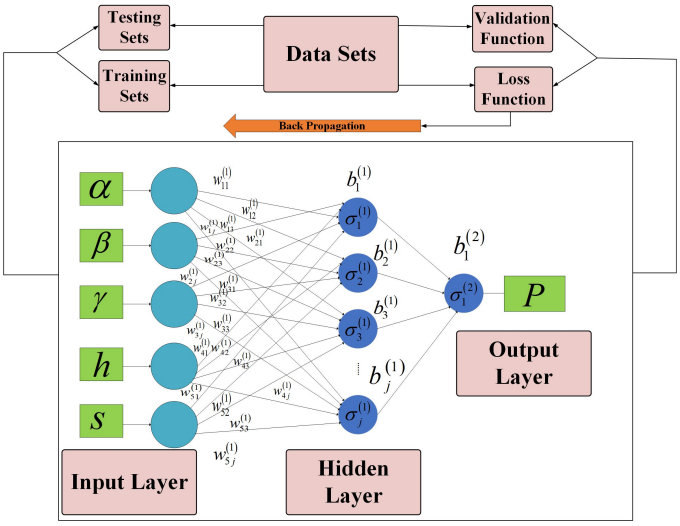


Figure 1. BPNN-based framework of path loss prediction.

3.1 BPNN-based PL prediction

Under the LoS conditions, the PL is predominantly influenced by the distance between the Tx and Rx, given the absence of obstructions along their direct path. The input variables, namely the height h and the horizontal distance s, play a crucial role in determining the P. Consequently, it becomes unnecessary to incorporate an extensive array of scenario parameters such as α, β and γ. By focusing on h and s, we aim to clarify the impact of altitude and horizontal distance on P, and a detailed examination of these parameters is presented in Section 4.

Under NLoS conditions, PL is influenced by either reflection or diffraction phenomena. It is observed that propagation paths of identical distances between the Tx and Rx can exhibit markedly different PL values. This variation underscores the necessity of incorporating a broader range of scenario parameters into the input dataset to enhance the model's capability to discern the intricate relationship between input variables and the resulting PL. The framework for PL prediction utilizing a BPNN for both LoS and NLoS paths is illustrated in Figure 1. Central to the BPNN architecture is the arrangement of an input layer, hidden layers, and an output layer. As depicted in Figure 1, the input layer is designed with five neurons, while the output layer features a single neuron. The original data sets denote $\{P_{all}^{\mathrm{LoS/NLoS}}, \alpha_{all}^{\mathrm{LoS/NLoS}}, \beta_{all}^{\mathrm{LoS/NLoS}}, \gamma_{all}^{\mathrm{LoS/NLoS}}, h_{all}^{\mathrm{LoS/NLoS}}, s_{all}^{\mathrm{LoS/NLoS}}\}$ All of them can be obtained by the data acquisition in Section 3. Then, these data sets are divided into two parts by the proportion of 8:2 randomly, i.e., training set $\{P_{tr}^{\mathrm{LoS/NLoS}}, \alpha_{tr}^{\mathrm{LoS/NLoS}}, \beta_{tr}^{\mathrm{LoS/NLoS}}, \gamma_{tr}^{\mathrm{LoS/NLoS}}, h_{tr}^{\mathrm{LoS/NLoS}}, s_{tr}^{\mathrm{LoS/NLoS}}\}$, and testing set, $\{P_{test}^{\mathrm{LoS/NLoS}}, \alpha_{test}^{\mathrm{LoS/NLoS}}, \beta_{test}^{\mathrm{LoS/NLoS}}, \gamma_{test}^{\mathrm{LoS/NLoS}}, h_{test}^{\mathrm{LoS/NLoS}}, s_{test}^{\mathrm{LoS/NLoS}}\}$, respectively. The data from the training set are used to train the model. The output prediction value of PL can be expressed as

$$P_{trpre}^{\mathrm{LoS/NLoS}} = \sigma\left(\mathbf{w}^{\mathrm{T}}\mathbf{x} + \mathbf{b}\right) \tag{3}$$

where $\mathbf{x}$ represents the input matrix of training set $\{\alpha_{tr}^{\mathrm{LoS/NLoS}}, \beta_{tr}^{\mathrm{LoS/NLoS}}, \gamma_{tr}^{\mathrm{LoS/NLoS}}, h_{tr}^{\mathrm{LoS/NLoS}}, s_{tr}^{\mathrm{LoS/NLoS}}\}$. In this paper, the Tansig function is employed from the input layer to the hidden layer to enhance the network's nonlinear prediction capabilities. For the transition from the hidden layer to the output layer, the Purelin function is applied. These functions are expressed as

$$\sigma_{\mathrm{tansig}}(x) = \frac{2}{1 + e^{-2x}} - 1 \tag{4}$$

$$\sigma_{\mathrm{purelin}}(x) = x \tag{5}$$

At the beginning of the training phase, the weight and bias parameters of each neuron in the network have not yet been optimized, resulting in significant differences between the predicted and reference values. To overcome this difference, it is crucial to establish a suitable loss function. This function helps to continuously refine the neuron parameters through back-propagation, thus minimizing the errors. The loss function utilized in this paper is expressed as

$$L\left(\mathbf{w},\mathbf{b},\sigma\right)=\frac{1}{2R}\sum_{r=1}^{R}\left(P_{trpre,r}^{\mathrm{LoS/NLoS}}-P_{tr,r}^{\mathrm{LoS/NLoS}}\right)^{2} \tag{6}$$

where R is the sum of training set, $P_{tr,r}^{\mathrm{LoS/NLoS}}\in P_{tr}^{\mathrm{LoS/NLoS}}$ and $P_{trpre,r}^{\mathrm{LoS/NLoS}}\in P_{trpre}^{\mathrm{LoS/NLoS}}$. Following the principles of stochastic gradient descent (SGD), the back-propagation algorithm is employed to iteratively adjust the weight and bias matrices, as detailed below

$$w_{ij}^{(k)}=w_{ij}^{(k)}-l\frac{\partial L(\mathbf{w},\mathbf{b},\sigma)}{\partial w_{ij}^{(k)}}+m\Delta w_{ij}^{(k)} \tag{7}$$

$$b_{j}^{(k)}=b_{j}^{(k)}-l\frac{\partial L(\mathbf{w},\mathbf{b},\sigma)}{\partial b_{j}^{(k)}}+m\Delta b_{j}^{(k)} \tag{8}$$

where $\partial(.)$ represents the partial derivatives, $w_{ij}^{(k)}\in\mathbf{w}$ and $b_{ij}^{(k)}\in\mathbf{b}$ are the connection weight values and bias value of the j th neuron in the k th layer of the network and the i th neuron in the previous layer, respectively. l is the learning rate of the NN and m is the momentum factor. the output prediction value of PL from testing dataset can be expressed as

$$P_{testpre}^{\mathrm{LoS/NLoS}}=f_{\mathrm{BPNN}}^{\mathrm{LoS/NLoS}}\left(\alpha_{testpre}^{\mathrm{LoS/NLoS}},\beta_{testpre}^{\mathrm{LoS/NLoS}},\gamma_{testpre}^{\mathrm{LoS/NLoS}},h_{testpre}^{\mathrm{LoS/NLoS}},s_{testpre}^{\mathrm{LoS/NLoS}};\mathbf{w},\mathbf{b},\sigma\right) \tag{9}$$

Root mean square error (RMSE) is proposed as the validation function to evaluate the performance of NN using the testing dataset[29], which can be expressed as

$$RMSE=\sqrt{\frac{1}{T}\sum_{t=1}^{T}\left(P_{testpre,t}^{\mathrm{LoS/NLoS}}-P_{test,t}^{\mathrm{LoS/NLoS}}\right)^{2}} \tag{10}$$

where T is the sum of testing set, $P_{test,r}^{\mathrm{LoS/NLoS}}\in P_{test}^{\mathrm{LoS/NLoS}}$ and $P_{testpre,r}^{\mathrm{LoS/NLoS}}\in P_{testpre}^{\mathrm{LoS/NLoS}}$.

Training concludes and the network stabilizes once any of the following criteria are met: the loss function diminishes to a predetermined threshold, the number of training epochs is reached, or the gradient's decrease meets a predefined value. If the performance is appropriate, this network could be saved and a new group of input parameters; i.e., $\alpha_{new},\beta_{new},\gamma_{new},h_{new},s_{new}$ are used to generate the corresponding prediction value of PL.

3.2 RT-based dataset acquisition

In the BPNN PL prediction model, dataset acquisition is crucial for tuning NN parameters and ensuring accuracy. Due to the complexity of developing an mmWave A2G channel sounder, we are unable to acquire enough training data at the mmWave band. Considering that the RT is one of the accurate channel modeling methods, this paper chooses to acquire the dataset via the RT simulation. The dataset acquisition involves 3D scenario reconstruction and RT simulation.

Traditional methods for scenario reconstruction, such as point-cloud and digital mapping technologies, demand detailed scene information, such as the scatter location, size, shape, and material, making the process complex. To overcome this obstacle, the ITU standard organization has introduced a virtual city-based 3D

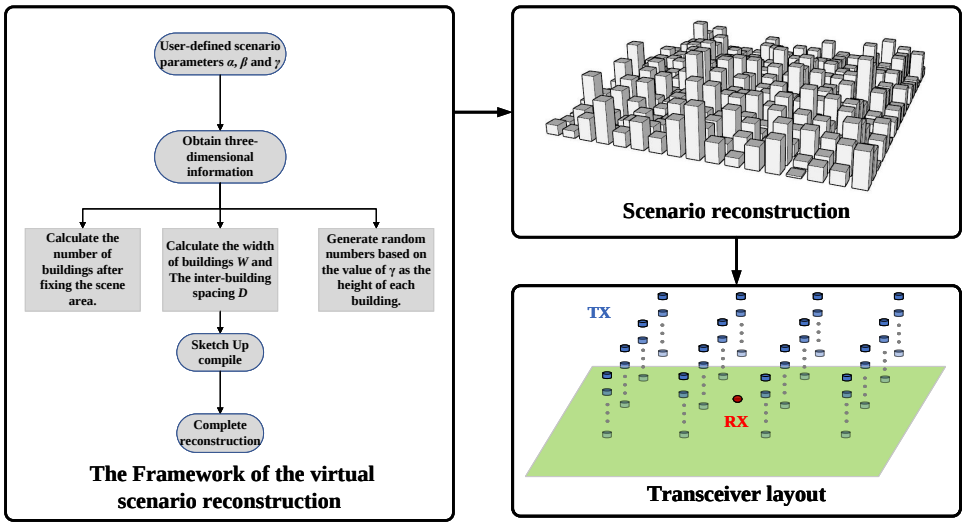


Figure 2. RT simulation setup.

reconstruction technique. This method draws on field measurements and statistical analyses to derive a statistical profile for scatter properties, particularly for buildings in urban scenarios. By acquiring statistical data from real environments, it simplifies the reconstruction process and reduces cost and complexity. Operators only need to specify the parameters, α, β and γ, mentioned in Section 2 to accomplish the 3D scenario reconstruction.

Taking, for example, a city block measuring 1,000 meters by 1,000 meters, the number of buildings per row is calculated as

$$b = floor\sqrt{\beta} \tag{11}$$

where the floor function is applied to guarantee that the quantity of terms in the calculation yields an integer number of buildings. The spacing between buildings D and the width of buildings W can be calculated easily according to the geometric relationship, expressed as

$$W = 1000\sqrt{\alpha/\beta} \tag{12}$$

$$D = \frac{1000}{\sqrt{\beta}} - W \tag{13}$$

Then, a series of random numbers are generated that matched the Rayleigh distribution with a mean value of γ, to the total number of buildings. These random numbers represent the heights of the buildings. With the 3D information of the urban environment, the building modeling can be accomplished using the Ruby Code Editor plugin in SketchUp.

The design of the RT simulation scheme plays a role in ensuring comprehensive and efficient data collection. For every scenario, the Rx is located in the center of the area, and the Txs are at different altitudes on several layers, each with hundreds of Tx uniformly distributed. At last, the building material is set to concrete. The scenario reconstruction and the layout of the transceivers are shown in Figure 2.

A software called Wireless Insite is used for RT simulation. The precision of the reconstructed digital map is 5 m. During the RT simulation, we set the order of reflections to be no more than two, and the order of the diffraction to be one. The channel parameters are computed through three steps, i.e., decomposition of ray source, tracking of rays, and superposition of filed strength [30]. The power received at each RX point is precisely determined and subsequently converted into amplitude as

Table 1. Four typical urban scenarios with characteristic parameters

Scenarios	α	β	γ
Suburban	0.1	750	8
Urban	0.3	500	15
Dense	0.5	300	20
Highrise	0.5	300	50

$$\alpha_o = 10^{\frac{A_o}{10}} \tag{14}$$

where A_o is the power of the oth path. The value of the PL can be expressed as

$$P = 10\log_{10}(\sum_{o=1}^{O} \alpha_o^2) \tag{15}$$

where O is the number of rays.

4. SIMULATIONS AND VALIDATIONS

4.1 Model training in limited scenarios

To validate the accuracy of the proposed PL prediction method, a large number of datasets are obtained through RT simulation, as mentioned in Section 3.2. For the LoS case, four typical urban scenarios are reconstructed for simulations according to the defined parameters in the ITU standard [28], as shown in Table 1. Three stochastic simulations are conducted for each typical scenario to account for the effects of different building heights; i.e., a total of 12 scenarios are considered. However, it is necessary to explore more scenarios for NLoS conditions. To cover more scene types, parameters are varied: α from 0.1 to 0.8 in 0.1 intervals, β from 100 to 800 in 100 intervals, and γ from 8 to 50 in two intervals. This approach includes 176 scenarios, producing a rich dataset. However, due to the delicate and efficient model, only eight of these scenarios are ultimately employed for network training. The Txs are deployed at six different heights, from 30 to 80 m in 10 m intervals, while the Rx is located in the center of the area at 25 m above the ground. In addition, we set the reflection and diffraction counts by RT simulation software to obtain LoS and NLoS datasets, respectively. The details of the specific simulation parameters are presented in Table 2.

Subsequently, the acquired RT simulation data is performed as a dataset for BPNN training. The learning rate is set to 0.0001, the momentum factor is set to 0.95, the number of training epochs is set to 2,000, and the hidden layer is set to a single layer consisting of 20 neurons. For the LoS case, there are 6,078 datasets, of which 4,862 are used for training and 1,216 for testing. Similarly, for the NLoS case, there are 49,230 datasets, of which 39,384 are used for training and 9,846 for testing. For the LoS case, there are 6,078 datasets, of which 4,862 are used for training and 1,216 for testing. Similarly, for the NLoS case, there are 49,230 datasets, of which 39,384 are used for training and 9,846 for testing. This division helps make the training of the network suitable for various scenarios.

In the LoS case, the effect of scenario parameters on PL is found to be minimal. Consequently, we focus on examining the dynamics between horizontal distance s, Tx height h and PL P, as depicted in Figure 3. It is observed that PL intensifies with the distance between the Tx and Rx. Importantly, the impact of horizontal distance on PL is more significant at lower altitudes compared to the effect of vertical separation. Figure 4A illustrates the analysis of the RT simulation data with the PL values predicted by the BPNN model, showing a high degree of correlation and highlighting the accuracy of the model. The deviation results are all less than 3 dB, as shown in Figure 4B. This further validates the reliability of the model and confirms the accuracy of

Table 2. Simulation parameters

Parameters	Value
Scenarios	4 for the LoS case, 8 for the NLoS case
Frequency (Bandwidth)	28 GHz (1 GHz)
Antenna type	Omnidirectional for both Rx and Tx
The height of Tx (interval)	30~80 m (10 m)
The height of Rx	25 m
Building material	Concrete
Maximum number of reflections	0 for LoS and 2 for NLoS
Maximum number of diffraction	0 for LoS and 1 for NLoS

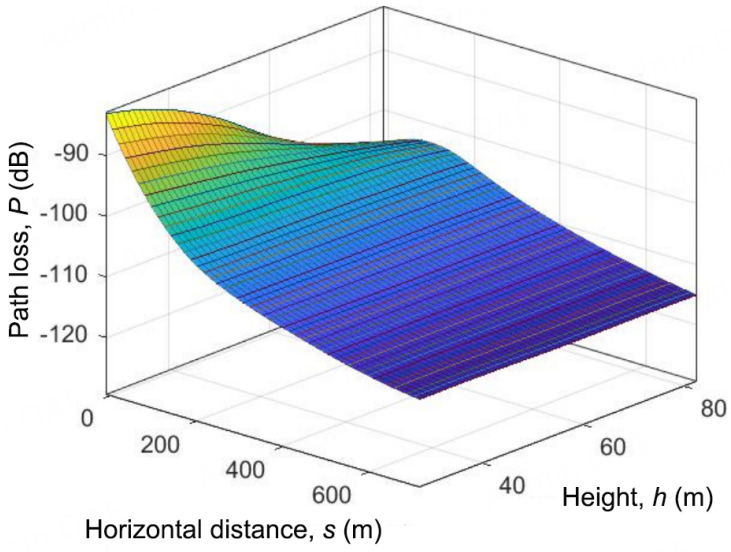


Figure 3. Simulated PL for the LoS case.

our prediction method. Additionally, the RMSE is determined to be 0.2493, following the calculation given in Equation (10).

In scenarios where the LoS path is obstructed, various environmental factors significantly influence PL. Figure 5-Figure 7 illustrate the relationship between the input factors and the PL in this case. Specifically, Figure 5 shows that an increase in Tx height leads to a reduction in PL. This phenomenon can be explained by a reduction in obstacle interference, since increasing the Tx height effectively lengthens the LoS path, thereby reducing signal attenuation caused by physical obstacles. Figure 6 shows that greater building coverage indicates a denser urban environment, where buildings are more likely to obstruct and weaken the signal, thereby increasing PL and negatively affecting signal quality. In addition, the presence of higher buildings increases the likelihood of signal blockage and reflection, further exacerbating PL, as evidenced in Figure 7.

Figure 8 demonstrates the performance of the NN. Obviously, the NN shows good prediction ability. About eighty percent of the deviation results are less than 5 dB and the RMSE is 8.27489.

4.2 Model validation in a new scenario

To further validate the effectiveness of our network, we introduce a new scenario setting with $\alpha = 0.4$, $\beta = 400$ and $\gamma = 18$ ensuring consistency with the network configurations used in previous experiments. Then, we

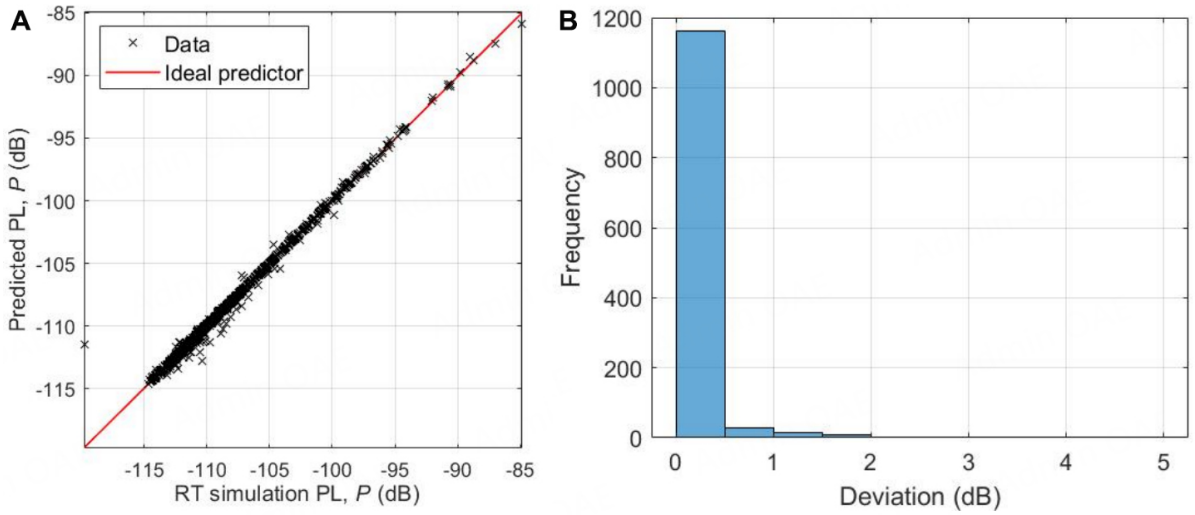


Figure 4. (A) Prediction accuracy and (B) Histogram of prediction error for the LoS case.

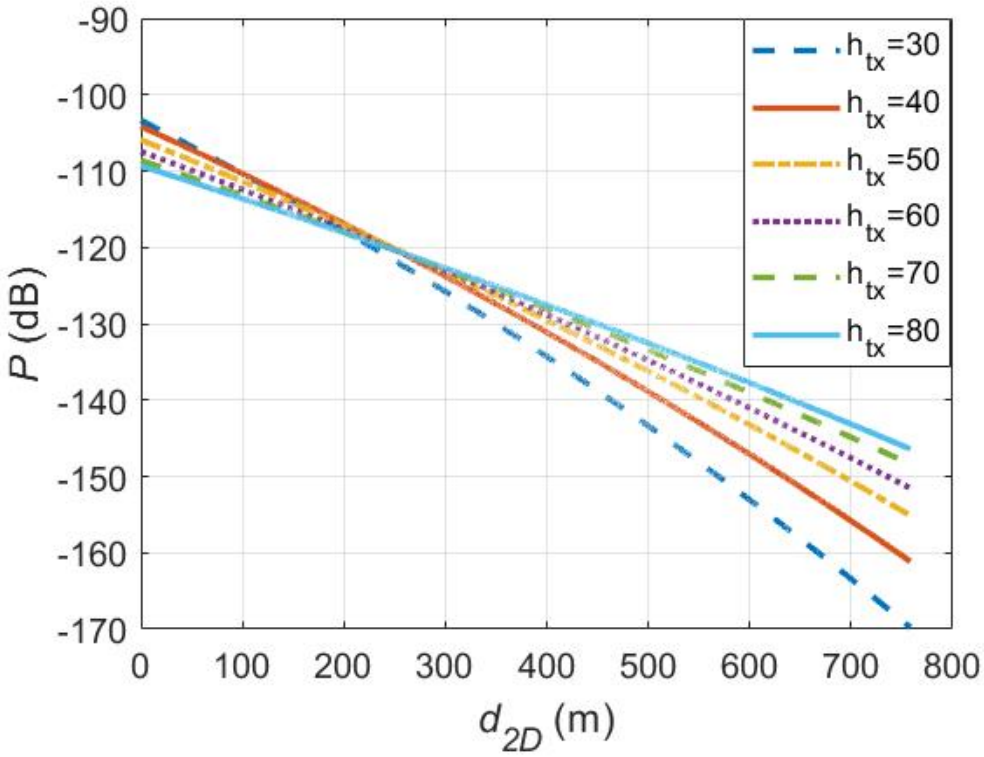


Figure 5. The impact of Tx height on PL for the NLoS case.

compare the PL values derived from the BPNN with RT simulations. The outcomes are depicted in Figure 9. The significant agreement between the BPNN predictions and the RT simulation data highlights the reliability and efficiency of our proposed method. Additionally, we also incorporate the concept of 3D distance between the Tx and the Rx, which is formulated as

$$d_{3D} = \sqrt{s^2 + (h - 25)^2} \tag{16}$$

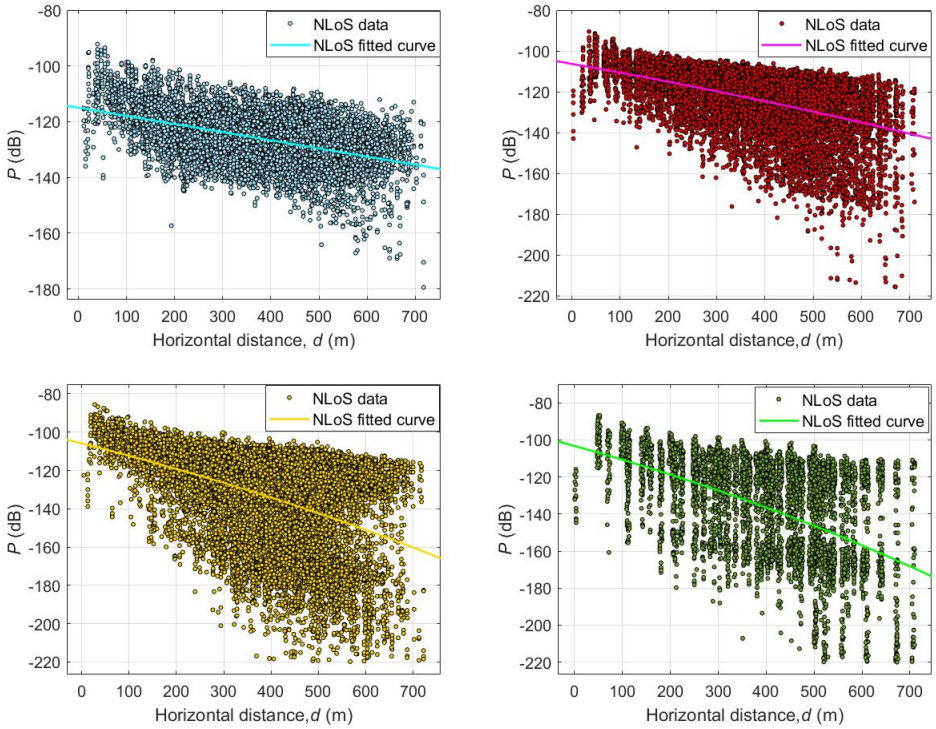


Figure 6. The impact of α on PL for the NLoS case (α=0.1, 0.3, 0.5 and 0.8, respectively).

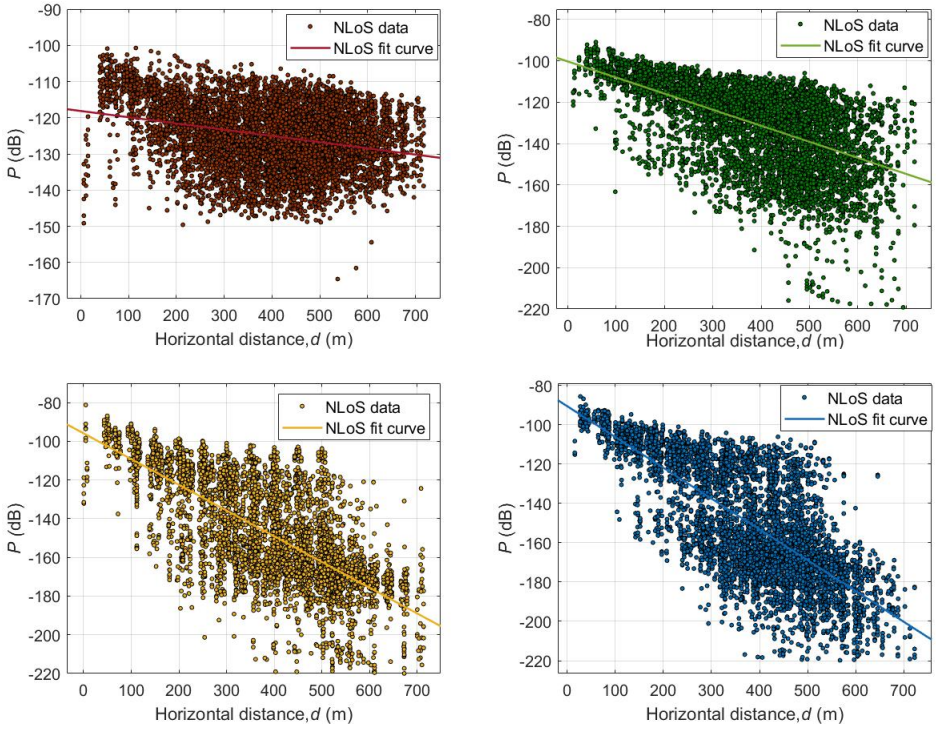


Figure 7. The impact of γ on PL for the NLoS case (γ=10, 30, 40 and 50, respectively).

For comparison, traditional prediction methods such as the 3GPP model were also simulated and the results are shown in Figure 10 and Figure 11. It should be emphasized that the 3GPP PL results are calculated us-

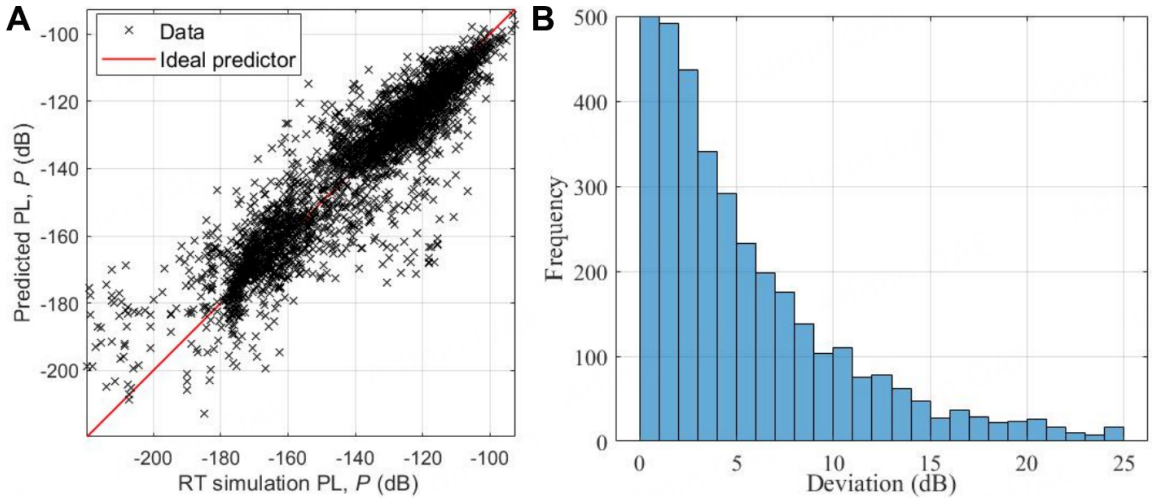


Figure 8. (A) PL prediction accuracy and (B) Histogram of prediction error for the NLoS case.

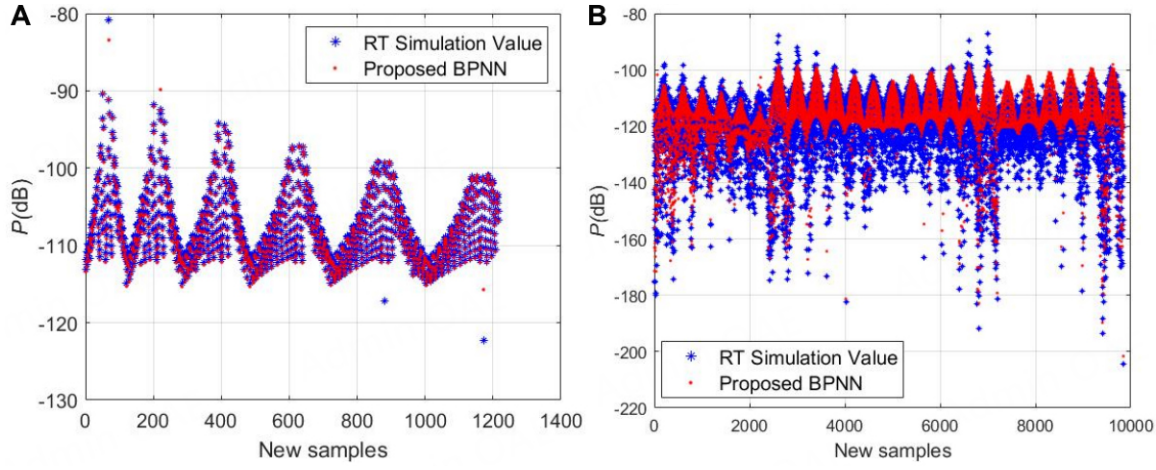


Figure 9. Predicted PL for (A) LoS and (B) NLoS case in the new scenario (α =0.4, β = 400 and γ = 18).

ing the LoS/NLoS path formulae for RMa scenarios[20]. This comparative analysis clearly demonstrates the enhanced performance of our proposed prediction method compared to traditional methods. Our model is tailored to the specific scenario data and utilizes ML techniques, which has a significant correlation with the simulation results. On the contrary, the 3GPP model, which is usually applied to Rx at lower heights (0-10 meters), demonstrates a less accurate predictive capability in specific scenarios. Looking ahead, this comparison underscores the potential of ML-based methods to address limitations in traditional models, particularly in scenarios with higher Rx heights or more complex scenarios. Future research could build on the three scenario parameters in this paper by further exploring additional environmental feature parameters (e.g., terrain relief), integrating them into the ML model, and validating their performance in a wider range of scenarios. This approach may bring more powerful prediction tools and facilitate advances in wireless network planning and optimization.

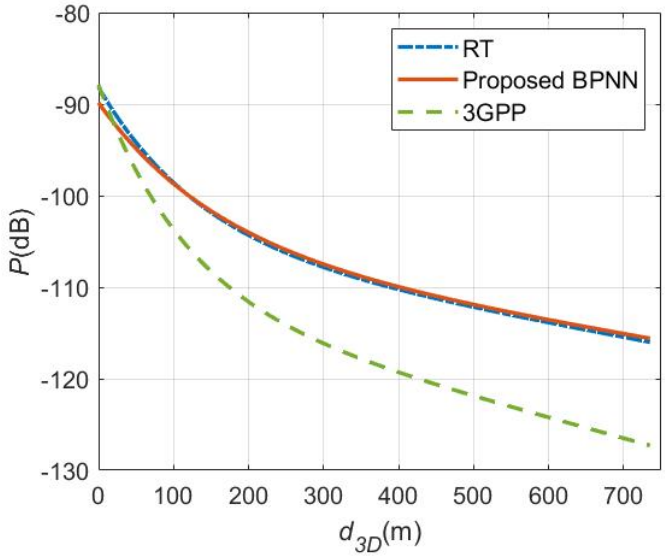


Figure 10. Predicted PL of different methods in the LoS case (α = 0.4, β = 400, and γ =18).

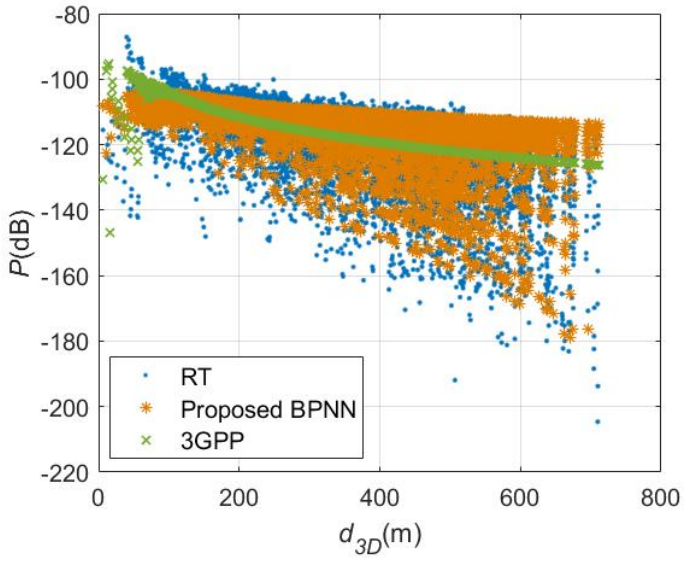


Figure 11. Predicted PL of different methods in the NLoS case (α = 0.4, β = 400, and γ = 18).

5. CONCLUSIONS

This paper has proposed a cross-scenario PL prediction model based on BPNN for A2G communications. The model has demonstrated the ability to accurately forecast the power for both LoS and NLoS paths trained with extensive RT simulation data across a variety of urban environments. A correlation has been established between the PL and scenario parameters, horizontal distance, and altitude. The performance of trained BPNN has been evaluated against a new scenario dataset derived from RT simulations and 3GPP standard model, confirming the superiority of the proposed method over traditional PL prediction approaches. In the future, we will develop an mmWave A2G channel sounder for further validating the proposed method via field measurements.

DECLARATIONS

Authors' contributions

Made substantial contributions to conception and design of the study and performed data analysis and interpretation: Zhang G, Lei T, Huo X

Contributed to approach validation, software simulation, and writing-original draft preparation: Zhang G, Li Y, Geng M, Yang Y

Contributed to the investigation, supervision, and writing-review and preparation: Yang H, Chen X

Availability of data and materials

Not applicable.

Financial support and sponsorship

None.

Conflicts of interest

Huo X is affiliated with Qingdao Metro Group Co., Ltd, while the other authors have declared that they have no conflicts of interest.

Ethical approval and consent to participate

Not applicable.

Consent for publication

Not applicable.

Copyright

© The Author(s) 2024.

REFERENCES

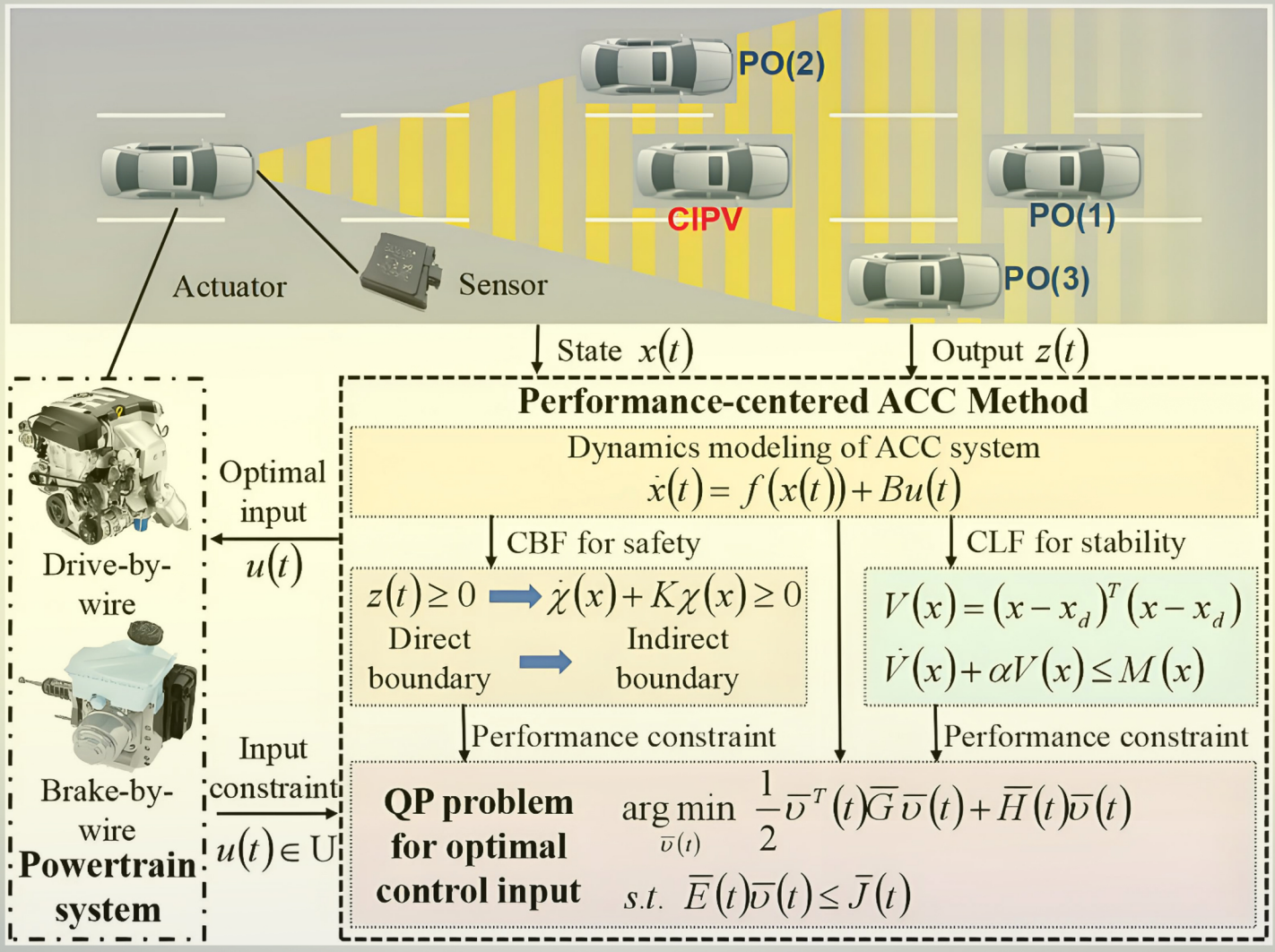
1. Na Z, Liu Y, Shi J, Liu C, Gao Z. UAV-supported clustered NOMA for 6G-enabled internet of things: trajectory planning and resource allocation. *IEEE Int Things J* 2021;8:15041-8. DOI
2. Hua B, Ni H, Zhu Q, et al. Channel modeling for UAV-to-ground communications with posture variation and fuselage scattering effect. *IEEE Trans Commun* 2023;71:3103-16. DOI
3. Mao K, Zhu Q, Qiu Y, et al. A UAV-aided real-time channel sounder for highly dynamic nonstationary A2G scenarios. *IEEE Trans Instrum Meas* 2023;72:6504515. DOI
4. Xiong B, Zhang Z, Jiang H, Zhang J, Wu L, Dang J. A 3D non-stationary MIMO channel model for reconfigurable intelligent surface auxiliary UAV-to-ground mmWave communications. *IEEE Trans Wireless Commun* 2022;21:5658-72. DOI
5. Pi Z, Khan F. An introduction to millimeter-wave mobile broadband systems. *IEEE Commun Mag* 2011;49:101-7. DOI
6. Zhao X, Du F, Geng S, et al. Playback of 5G and beyond measured MIMO channels by an ANN-based modeling and simulation framework. *IEEE J Sel Areas Commun* 2020;38:1945-54. DOI
7. Alkhateeb A, El Ayach O, Leus G, Heath RW. Channel estimation and hybrid precoding for millimeter wave cellular systems. *IEEE J Sel Top Signal Process* 2014;8:831-46. DOI
8. Liu X, Wang J, Zhao N, et al. Placement and power allocation for NOMA-UAV networks. *IEEE Wireless Commun Lett* 2019;8:965-8. DOI
9. Phillips C, Sicker D, Grunwald D. A survey of wireless path loss prediction and coverage mapping methods. *IEEE Commun Surv Tutor* 2013;15:255-70. DOI
10. Ayadi M, Ben Zineb A, Tabbane S. A UHF path loss model using learning machine for heterogeneous networks. *IEEE Trans Antennas Propag* 2017;65:3675-83. DOI
11. Mao K, Zhu Q, Duan F, et al. A2G channel measurement and characterization via TNN for UAV multi-scenario communications. In: GLOBECOM 2022 - 2022 IEEE global communications conference; 2022. pp. 4461-6. DOI
12. Sarkar TK, Ji Z, Kim K, Medouri A, Salazar-Palma M. A survey of various propagation models for mobile communication. *IEEE Antennas Propag Mag* 2003;45:51-82. DOI
13. Mao K, Zhu Q, Wang CX, Ye X, Gomez-Ponce J, et al. A survey on channel sounding technologies and measurements for UAV-assisted communications. *IEEE Trans Instrum Meas* 2024;73:8004624. DOI

14. He D, Ai B, Guan K, Wang L, Zhong Z, Kurner T. The design and applications of high-performance ray-tracing simulation platform for 5G and beyond wireless communications: A tutorial. *IEEE Commun Surv Tutor* 2019;21:10-27. DOI
15. Zhu Q, Mao K, Song M, et al. Map-based channel modeling and generation for U2V mmWave communication. *IEEE Trans Veh Technol* 2022;71:8004-15. DOI
16. Hossain F, Geok TK, Rahman TA, et al. A smart 3D RT method: indoor radio wave propagation modelling at 28 GHz. *Symmetry* 2019;11:510. DOI
17. Cui Z, Guan K, Oestges C, Briso-Rodríguez C, Ai B, Zhong Z. Cluster-based characterization and modeling for UAV air-to-ground time-varying channels. *IEEE Trans Veh Technol* 2022;71:6872-83. DOI
18. Lyu Y, Wang W, Chen P. Fixed-wing UAV based air-to-ground channel measurement and modeling at 2.7GHz in rural environment. *IEEE Trans Antennas Propag* 2024;1. DOI
19. Lyu Y, Wang W, Sun Y, Rashdan I. Measurement-based fading characteristics analysis and modeling of UAV to vehicles channel. *Veh Commun* 2024;45:100707. DOI
20. 3GPP. Evolved Universal Terrestrial Radio Access (E-UTRA); Radio Resource Control (RRC); Protocol specification. 3rd Generation Partnership Project (3GPP); 2017. 36.331. Version 14.2.2.
21. Döttling M, Mohr W, Osseiran A. Radio technologies and concepts for IMT-advanced. John Wiley & Sons; 2010. Available from: http://dx.doi.org/10.1109/pesa.2017.8277746 [Last accessed on 29 Sep 2024]
22. Cui Z, Briso-Rodríguez C, Guan K, Zhong Z, Quitin F. Multi-frequency air-to-ground channel measurements and analysis for UAV communication systems. *IEEE Access* 2020;8:110565-74. DOI
23. Rappaport TS. Wireless Communications: Principles and Practice. USA: Prentice Hall PTR; 2001. Available from: https://telkom2013.wordpress.com/wp-content/uploads/2014/02/wireless-comm-princip-n-practice-theodoresrappaport.pdf [Last accessed on 29 Sep 2024]
24. Cai X, Rodríguez-Piñeiro J, Yin X, et al. An empirical air-to-ground channel model based on passive measurements in LTE. *IEEE Trans Veh Technol* 2019;68:1140-54. DOI
25. Yang G, Zhang Y, He Z, Wen J, Ji Z, Li Y. Machine-learning-based prediction methods for path loss and delay spread in air-to-ground millimetre-wave channels. *IET Microw Antennas Propag* 2019;13:1113-21. DOI
26. Li H, Chen X, Mao K, et al. Air-to-ground path loss prediction using ray tracing and measurement data jointly driven DNN. *Comput Commun* 2022;196:268-76. DOI
27. Huang Y, Cui H, Hou Y, et al. Space-based electromagnetic spectrum sensing and situation awareness. *Space Sci Technol* 2024;4:0109. DOI
28. Union IT. Propagation data and prediction methods for the planning of short-range outdoor radiocommunication systems and radio local area networks in the frequency range 300 MHz to 100 GHz; 2003. pp. 1411-2. Available from: https://www.itu.int/rec/R-REC-P.1411-12-202308-I/en [Last accessed on 29 Sep 2024]
29. Isabona J, Srivastava VM. Hybrid neural network approach for predicting signal propagation loss in urban microcells. In: 2016 IEEE region 10 humanitarian technology conference (R10-HTC); 2016. pp. 1-5. DOI
30. Wang J, Zhu Q, Lin Z, et al. Sparse bayesian learning-based hierarchical construction for 3D radio environment maps incorporating channel shadowing. *IEEE Trans Wirel Commun* 2024;1. DOI

Volume 4, Issue 4, December 2024

COMPLEX ENGINEERING SYSTEMS

Editor-in-Chief: Wenwu Yu



A performance-centered design method for adaptive cruise control system

Siya Zhan, Congzhi Liu*

Open Access
ISSN 2770-6249 (Online)
www.comengsys.com

Chen *et al*. *Complex Eng Syst* 2024;4:19
DOI: 10.20517/ces.2024.37

Complex Engineering Systems

Research Article

Open Access

Tobit Kalman fusion filtering under dynamic event-triggering protocol with token bucket specification

Xiangyu Chen[1,2], Fei Han[1,2,3,4], Yanhua Song[1,2], Jinnan Zhang[1,2,3]

[1]National Key Laboratory of Continental Shale Oil, Northeast Petroleum University, Daqing 163318, Heilongjiang, China.
[2]Artificial Intelligence Energy Research Institute, Northeast Petroleum University, Daqing 163318, Heilongjiang, China.
[3]Heilongjiang Provincial Key Laboratory of Networking and Intelligent Control, Northeast Petroleum University, Daqing 163318, Heilongjiang, China.
[4]Research Center for Mathematics and Interdisciplinary Sciences, Northeast Petroleum University, Daqing 163318, Heilongjiang, China.

Correspondence to: Dr. Yanhua Song, National Key Laboratory of Continental Shale Oil, Northeast Petroleum University, No. 99, Xuefu Street, High-Tech Industrial Development Zone, Daqing 163318, Heilongjiang, China. E-mail: hytsyh@126.com; ORCID: 0000-0002-3649-9160

How to cite this article: Chen X, Han F, Song Y, Zhang J. Tobit Kalman fusion filtering under dynamic event-triggering protocol with token bucket specification. *Complex Eng Syst* 2024;4:19. http://dx.doi.org/10.20517/ces.2024.37

Received: 23 Jun 2024 **First Decision:** 14 Aug 2024 **Revised:** 5 Sep 2024 **Accepted:** 8 Oct 2024 **Published:** 22 Oct 2024

Academic Editor: Hamid Reza Karimi **Copy Editor:** Fangling Lan **Production Editor:** Fangling Lan

Abstract

This paper addresses the multi-sensor fusion filtering problem for a class of linear discrete time-varying systems with censored measurement, described by the Tobit model, and scheduled by dynamic event-triggering protocols with token bucket specification. A dynamic event-triggering mechanism is first used to determine whether to transmit measurements under the token bucket specification, allowing transmission only if there are sufficient tokens and if the event-triggering condition is satisfied. Next, two indicator variables are denoted to represent the combined impact of the dynamic event-triggering protocol and the token bucket specification. A local Tobit Kalman filtering algorithm is then designed for each node by minimizing the trace of the filtering error covariance matrix under censoring and information transmission protocols' influence. Subsequently, all local estimates from each node are transmitted to the fusion center, where global estimates are generated using a federal fusion rule. The global estimates with suitable weights are sent back to every node for predictions at subsequent time instants. Finally, an illustrative simulation example is used to evaluate performance of this fused filtering scheme proposed in this paper.

Keywords: Tobit Kalman filtering, token bucket protocol, censored measurements, multi-sensor filtering fusion

© The Author(s) 2024. **Open Access** This article is licensed under a Creative Commons Attribution 4.0 International License (https://creativecommons.org/licenses/by/4.0/), which permits unrestricted use, sharing, adaptation, distribution and reproduction in any medium or format, for any purpose, even commercially, as long as you give appropriate credit to the original author(s) and the source, provide a link to the Creative Commons license, and indicate if changes were made.

1. INTRODUCTION

As is well known, multi-sensor fusion filtering (MSFF) refers to the integration of information from different sensors to enhance the performance of the filtering scheme[1]. To date, multi-sensor information fusion technology has been extensively applied in a variety of fields, including target localization[2,3], fault detection[4], environmental monitoring[5], signal processing[6], image processing[7], *etc*. In general, multi-sensor fusion falls into two categories: centralized and distributed[8]. In the former, the raw data from each sensor is directly transmitted to the fusion center for filtering processing[9]. In contrast, the latter manner involves the fusion center integrating available estimates from local filters to generate optimal or suboptimal estimates[10]. While the precision of distributed fusion filtering may not match that of centralized fusion, its advantages include reducing the burden on the central processor, lowering communication bandwidth requirements, and enhancing system reliability and robustness. These distinguished advantages have led to widespread attention towards distributed fusion filtering schemes in recent years[11].

In networked control systems, due to harsh environmental conditions, limitations in sensor capabilities, poor signal transmission line quality, and hardware or software failures in sensors, nonlinearities are inevitable in the actual system measurement output. These nonlinearities include, but are not limited to, censoring[12], channel fading[13], quantization[14], saturation[15], *etc*. If not handled properly, these nonlinear factors may even affect the stability of the filtering error system. When designing and implementing filters in networked systems, it is necessary to fully consider the impact of these nonlinear factors and take effective measures to minimize their impact on system performance to ensure system stability and reliability. At present, for addressing nonlinear challenges and improving filtering accuracy and stability, various nonlinear filtering algorithms have been proposed, such as the extended Kalman filtering (EKF)[16], the unscented Kalman filtering (UKF)[17], and the Tobit Kalman filtering (TKF)[18].

Because of the limited sensing abilities of low-cost sensors, the censored measurements are prevalent in practical engineering[19]. The censored measurements are commonly formulated by the Tobit model, which is widely used in data analysis in economics, finance, and social sciences. This model can effectively handle problems involving censored data and provides estimates of unobserved variables. When the measurement noise of a system exhibits non-Gaussian characteristics near the censoring region, traditional Kalman filtering methods cannot handle it. The primary challenge induced by the censored measurements lies in its nonlinearities. A useful method is to introduce the indicator variable to transform the piecewise linear functions into a unified form in[20], which will provide convenience for performance analysis and deal with the scalable distributed H∞-consensus filtering problem. Another challenge in recursive filtering is to calculate the probability of occurrence of censoring measurement[21]. In addition, the TKF surpasses both UKF and EKF in terms of filtering performance when dealing with censored measurements[22].

Allik *et al.* have designed TKF for the first time by using the Tobit model, where the unilateral and bilateral Tobit regression models are integrated into the recursive form of the Kalman filter[23]. In a comparison of TKF and KF, it can be found that when data is not censored, there is no difference between these two filters; when data is censored, the extra computational burden of TKF mainly comes from the calculation of occurrence of censoring measurement. Nevertheless, it fails to fully explore and utilize the useful information contained in the censored region. To address this problem, Han *et al.* have developed a novel conditional expectation approach to study TKF problem for stochastic parameter systems[24]. Subsequent research regarding TKF has been published by combining with other interesting phenomena, such as dynamic bias and Round-Robin protocol[25], fading measurements[26], dynamic event-triggered protocols (DETPs)[27], and so on.

Although there are currently a large number of research results on TKF, the Tobit Kalman fusion filtering (TKFF) has not received sufficient attention due primarily to its complexities in analysis. The core step of this paper is to select an appropriate fusion rule from various existing fusion rules and combine it with local TKFs.

The well-known fusion rules include centralized filtering fusion[28], information filtering fusion[29], weighted filtering fusion[30], covariance intersection fusion[31], federated filtering fusion[10], sequential fusion[32], and robust fusion[33]. In the survey paper[34], these fusion rules are compared in terms of the structure of the fusion, filtering accuracy, and computation burden, respectively. Federated filtering fusion belongs to a distributed structure and has the smallest burden and highest burden. As a result, we choose federated filtering fusion for this paper.

In the past decades, networked systems have gained popularity owing to multiple advantages such as high flexibility, simple installation, and low cost, making them suitable for a range of applications including aerospace, energy monitoring, and telecommunications[35]. Unlike traditional automatic control systems, the focus of networked systems explicitly considers the limitations of the communication medium between the sensor and the controller/filter. Especially when network congestion occurs, where the allocation of requests exceeds the network's sustainable transmission rate, these limitations become even more evident, which would pose a serious impact on the desirable performance. A well-established paradigm for addressing this issue is event-triggered protocol[36]. The idea of event-triggered protocol is to reduce the transmission number only if the event-triggering condition is satisfied. Such a protocol can efficiently save the communication resource[37]. However, it cannot be guaranteed that the transmission network will not be overused, especially when the desired performance level requires a high transmission rate. In the existing references[36,37], the event-triggering protocol (ETP) is introduced to save unilaterally the network bandwidth resource in the premise of a certain performance by reducing the number of information transmissions. Nonetheless, such a protocol cannot be appropriate for practical engineering scenarios. In a shared network with limited bandwidth, when encountering multiple requests of information transmission, it is difficult to have enough bandwidth resources.

It should be noted that the total communication resource cannot be formulated in the existing results and thus the role of the ETP cannot be reflected in a unified framework. Recently, a dynamic model has been used to describe the network resources: the token bucket algorithm[38,39], where the network's communication resources are considered and the signal transmission is triggered only when the network's communication capabilities allow. The level of the bucket reflects the network's current communication capabilities. The objective of these studies is to optimally utilize limited communication resources by combining control inputs with triggering mechanisms[40]. Inspired by such an idea, an interesting problem is to explore how the token bucket algorithm can be integrated with communication protocols, to more reasonably allocate tokens for network requests and achieve optimized resource utilization. In line with this concept, an intriguing issue is to investigate the integration of the token bucket algorithm with DETPs within a unified framework for studying TKFF. This constitutes another motivation for the present paper.

Enlightened by the above arguments, the objective is to investigate the federated TKFF (FTKFF) problem under the schedule of dynamic event-triggered protocols with token bucket specification. The main contributions of this paper are highlighted as follows: (1) an FTKFF problem is studied under the combined schedule of the token buckets and DETPs, where the former characterizes the limited communication resources and the latter determines the necessary information to be transmitted; (2) a recursive local filter is designed, where two indicator variables are introduced to formulate the transmitted censored measurements, and the gain matrix is derived by minimizing the upper bound of the filtering error covariance; (3) the federated fusion criterion is chosen in the fusion center to obtain an optimal estimation by using the local estimates.

Notations: $\|x\| = \sqrt{x^T x}$, where $x \in \mathbb{R}^n$. The notation $X > Y$, where X and Y are real symmetric matrices, means that $X - Y$ is positive-definite. $\mathrm{tr}\{X\}$ stands for the trace of the matrix X. $\mathbb{E}\{\cdot\}$ and $\mathbb{D}\{\cdot\}$ are the mathematical expectation and variance. $\delta(\cdot) \in (0, 1)$ is the Dirac delta function.

2. PROBLEM FORMULATION

2.1. System model

Consider the state-space model for a class of linear discrete time-varying systems and its measurements from l sensor nodes as follows:

$$\begin{cases} x_{t+1} = A_t x_t + B_t \omega_t, \\ z_{m,t} = C_{m,t} x_t + v_{m,t}, m = 1, 2, \ldots, l \end{cases} \tag{1}$$

where $x_t \in \mathbb{R}^{n_x}$ and $z_{m,t} \in \mathbb{R}^{n_y}$ are the state vector and measurement vector, respectively; $\omega_t \in \mathbb{R}^{\omega}$ and $v_{m,t} \in \mathbb{R}^{n_y}$ are white Gaussian noises with $\mathbb{E}\{\omega_t\} = 0$, $\mathbb{E}\{v_{m,t}\} = 0$, $\mathbb{D}\{\omega_t\} = Q_t$, and $\mathbb{D}\{v_{m,t}\} = R_{m,t}$. Furthermore, it is assumed that x_0, ω_t and $v_{m,t}$ are mutually independent for different t and m. A_t, B_t and $C_{m,t}$ are known time-varying matrices with compatible dimensions; the initial state x_0 is a random variable with mean $\bar{x}_0$ and variance P_0. For convenience of later discussion, denote $z_{m,t} \triangleq \begin{bmatrix} z_{m,t}^{(1)} & z_{m,t}^{(2)} & \ldots & z_{m,t}^{(n_y)} \end{bmatrix}^T \in \mathbb{R}^{n_y}$.

The situation where one or multiple sensors cannot perform data measurement or acquisition properly for various reasons is referred to as "censored measurements". To address the issue of censored measurements and mitigate its adverse impact on system monitoring, the Tobit measurement model is used to formulate the one-side censored measurement:

$$y_{m,t}^{(j)} \triangleq \begin{cases} z_{m,t}^{(j)}, & z_{m,t}^{(j)} > \tau_m^{(j)}; \\ \tau_m^{(j)}, & z_{m,t}^{(j)} \leq \tau_m^{(j)} \end{cases} \tag{2}$$

where $y_{m,t}^{(j)}$ is the censored measurement from the m-th sensor and $\tau_m^{(j)}$ is the one-side censoring threshold of $y_{m,t}^{(j)}$.

In light of (2), define a series of Bernoulli random variables $\varrho_{m,t}^{(j)} (m = 1, 2, \ldots, l; j = 1, 2, \ldots, n_y)$ to formulate $y_{m,t}^{(j)}$ as follows:

$$\varrho_{m,t}^{(j)} \triangleq \begin{cases} 1, & z_{m,t}^{(j)} > \tau_m^{(j)}; \\ 0, & z_{m,t}^{(j)} \leq \tau_m^{(j)}, \end{cases} \tag{3}$$

which obeys the distribution law:

$$\begin{cases} \mathbb{P}\{\varrho_{m,t}^{(j)} = 1\} = \bar{\varrho}_{m,t}^{(j)}; \\ \mathbb{P}\{\varrho_{m,t}^{(j)} = 0\} = 1 - \bar{\varrho}_{m,t}^{(j)} \end{cases} \tag{4}$$

where $\bar{\varrho}_{m,t}^{(j)}$ are known non-negative constants. Moreover, $\varrho_{m,t}$ is uncorrelated with other random variables mentioned above.

The censoring probability $\bar{\varrho}_{m,t}$ is approximated by

$$\bar{\varrho}_{m,t}^{(j)} = \Phi\left(\frac{(C_{m,t} x_t)^{(j)} - \tau_m^{(j)}}{\sqrt{R_{m,t}^{(j)}}} \right) \approx \Phi\left(\frac{(C_{m,t} \hat{x}_{m,t|t-1})^{(j)} - \tau_m^{(j)}}{\sqrt{R_{m,t}^{(j)}}} \right) \tag{5}$$

where $\hat{x}_{m,t|t-1}$ represents prediction for x_t from node m, and $\Phi(\cdot)$ is the cumulative distribution function of the standard normal distribution. From (5), it follows that $\bar{\varrho}_{m,t}$ is related to the state x_t, which is replaced with $\hat{x}_{m,t|t-1}$ since x_t is unknown.

Similar to [12], the measurement expectation and variance of $\bar{\varrho}_{m,t}^{(j)}$ are given as follows:

$$\mathbb{E}\{y_{m,t}^{(j)} | x_t\} = \Phi\left(\frac{(C_{m,t} x_t)^{(j)} - \tau_m^{(j)}}{\sqrt{R_{m,t}^{(j)}}} \right) \left[(C_{m,t} x_t)^{(j)} + \sqrt{R_{m,t}^{(j)}} \lambda\left(\frac{\tau_m^{(j)} - (C_{m,t} x_t)^{(j)}}{\sqrt{R_{m,t}^{(j)}}} \right) \right] + \Phi\left(\frac{\tau_m^{(j)} - (C_{m,t} x_t)^{(j)}}{\sqrt{R_{m,t}^{(j)}}} \right) \tau_m^{(j)}, \tag{6}$$

$$\mathbb{D}\{y_{m,t}^{(j)}|x_t\} = R_{m,t}^{(j)}\left[1-\varphi\left(\frac{\tau_m^{(j)}-(C_{m,t}x_t)^{(j)}}{\sqrt{R_{m,t}^{(j)}}}\right)\right] \tag{7}$$

where

$$\lambda(\zeta) \triangleq \frac{\phi(\zeta)}{1-\Phi(\zeta)}, \quad \varphi(\zeta) \triangleq \lambda(\zeta)(\lambda(\zeta)-\zeta).$$

Here, $\phi(\cdot)$ and $\Phi(\cdot)$ are the probability density function and the cumulative distribution function of the standard normal distribution, respectively.

Denote $\varrho_{m,t} \triangleq \text{diag}\left\{\varrho_{m,t}^{(1)}, \varrho_{m,t}^{(2)}, \ldots, \varrho_{m,t}^{(n_y)}\right\}$, $y_{m,t} \triangleq \left[y_m^{(1)}, y_m^{(2)}, \ldots, y_m^{(n_y)}\right]^T$, and $\tau_m \triangleq \left[\tau_m^{(1)}, \tau_m^{(2)}, \ldots, \tau_m^{(n_y)}\right]^T$. Hence, (2) can be rewritten as:

$$y_{m,t} = \varrho_{m,t}z_{m,t} + (I-\varrho_{m,t})\tau_m. \tag{8}$$

Also, the following statistical information can be obtained from (6) and (7):

$$\mathbb{E}\{y_{m,t}|x_t\} = \Phi\left(\frac{C_{m,t}x_t-\tau_m}{\sqrt{R_{m,t}}}\right)\left[C_{m,t}x_t+\sqrt{R_{m,t}}\lambda\left(\frac{\tau_m-C_{m,t}x_t}{\sqrt{R_{m,t}}}\right)\right]+\Phi\left(\frac{\tau_m-C_{m,t}x_t}{\sqrt{R_{m,t}}}\right)\tau_m, \tag{9}$$

and

$$\mathbb{D}\{y_{m,t}|x_t\} = R_{m,t}\left[I-\varphi\left(\frac{\tau_m-C_{m,t}x_t}{\sqrt{R_{m,t}}}\right)\right]. \tag{10}$$

Remark 1. *The censoring measurement is formulated as the Tobit model. The main challenge in dealing with the Tobit model arises from two aspects. Firstly, the Tobit model (2) represents a piecewise linear function, which is inherently nonlinear. To facilitate subsequent analysis, a random variable defined in (3) is introduced to reformulate the censoring measurement into a uniform form (8). Another issue involves determining the probability law and statistical property of the random variable (i.e., (5), (6), and (7)), where (5) is derived by using statistical information of normal distribution of measurement noise $v_{m,t}$, and (6) and (7) are achieved by means of (5).*

2.2. Information transmission protocols

To save precious energy and limited bandwidth, the DETP is used for node m to decide whether to transmit the current measurements to the filter. For this purpose, denote the event-triggering time sequence by $0 \le t_m^1 < \cdots < t_m^n < \cdots$ and define

$$t_m^{n+1} \triangleq \min\left\{t|t>t_m^n, \frac{1}{\chi_m}\eta_{m,t}+\sigma_m-\|\varepsilon_{m,t}\| \le 0\right\}, \tag{11}$$

$$\varepsilon_{m,t} \triangleq y_{m,t_m^n}-y_{m,t}, \tag{12}$$

where σ_m and χ_m are given positive scalars, y_{m,t_m^n} represents the latest transmitted measurement until time t, and the internal dynamic variable $\eta_{m,t}$ satisfies:

$$\eta_{m,t+1} = \lambda_m\eta_{m,t}+\sigma_m-\|\varepsilon_{m,t}\|, \quad \eta_{m,0}=\eta_0, \tag{13}$$

where λ_m is a given positive scalar and $\eta_0 \ge 0$ is the initial value. Moreover, $\lambda_m\chi_m > 1$ and thus ensure $\eta_{m,t+1} \ge 0$. Here, the inequality

$$\frac{1}{\chi_m}\eta_{m,t}+\sigma_m-\|\varepsilon_{m,t}\| \le 0, \tag{14}$$

is referred to as the event-triggering condition. For convenience, define the following indicator variable:

$$\alpha_{m,t} \triangleq \begin{cases} 1, & \text{if (14) holds;} \\ 0, & \text{otherwise.} \end{cases} \tag{15}$$

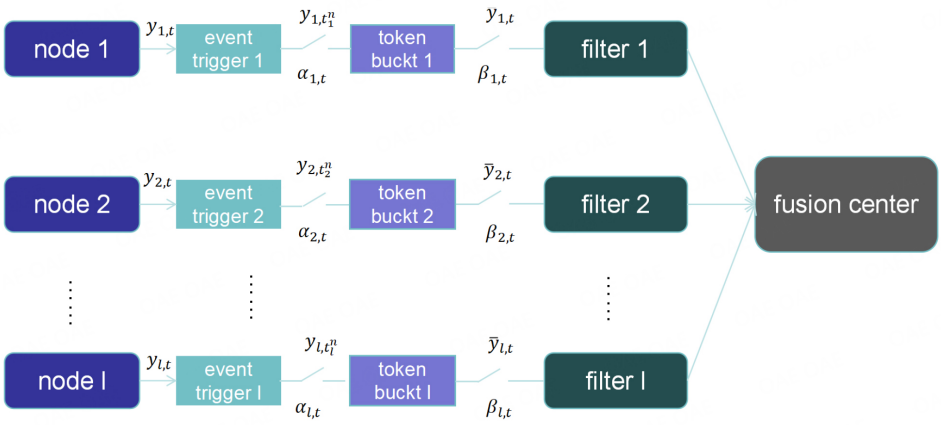


Figure 1. A block diagram of FTKFF under DETP with token bucket.

To cope with the measurement transmission in unexpected situations, such as the need to transfer multiple data at once, a token bucket triggering mechanism is introduced. First, the token bucket is employed to describe the available bandwidth resource, where the integer g and c_m are the token generating rate and transmission cost, respectively. For simplicity, c_m means the total cost for transmitting all elements of $y_{m,t}$ at time instant t of node m.

In order to unify the centralized utilization of the token bucket algorithm, the number of tokens is then evenly allocated to each sensor node, which is given as follows:

$$\xi_{m,t} = \xi_t / l. \tag{16}$$

The internal token change of the token bucket is formulated as follows:

$$\xi_t = \min\left\{\xi_{t-1} + g - \sum_{m=1}^{l} \beta_{m,t}\alpha_{m,t}c_m, b\right\} \tag{17}$$

with initial values $\xi_0 \geq 0$, where b is the token bucket capacity, and

$$\beta_{m,t} \triangleq \begin{cases} 1, & \text{if } c_m \leq \xi_{m,t}; \\ 0, & \text{otherwise.} \end{cases} \tag{18}$$

After scheduled by the DETP with token bucket specification, the measurement received by the filter is formulated as

$$\bar{y}_{m,t} = \begin{cases} y_{m,t_m^n}, & \text{if } \beta_{m,t} = 1 \text{ and } \alpha_{m,t} = 1; \\ \bar{y}_{m,t-1}, & \text{otherwise.} \end{cases} \tag{19}$$

For the convenience of later analysis, (19) is rewritten as

$$\bar{y}_{m,t} = \alpha_{m,t}\beta_{m,t}y_{m,t_m^n} + (1 - \alpha_{m,t}\beta_{m,t})\bar{y}_{m,t-1}. \tag{20}$$

Remark 2. *Different from*[30]*, the introduction of the indicator variable $\alpha_{m,t}$ is utilized to determine whether the conditions are met. This approach provides convenience for subsequent analysis, clearly defining the impact of the ETP. Building on this concept, another indicator variable $\beta_{m,t}$ is implemented to assess whether there are sufficient tokens for information transmission.*

The block diagram of FTKFF is depicted in Figure 1. As for node m, the event trigger is used to determine whether the censored measurement $y_{m,t}$ is transmitted or not, which is formulated by $\alpha_{m,t}$. If the event-triggering condition (14) to be predetermined is met (i.e., $\alpha_{m,t} = 1$), then the measurement to be transmitted is denoted as y_{m,t_m^n}. Next, the token bucket m is employed to formulate the available communication resource, which is formulated by $\beta_{m,t}$. If there exist sufficient tokens (i.e., $\beta_{m,t} = 1$), then the filter can receive the measurement, i.e., $\bar{y}_{m,t}$. Therefore, only when both token and event-triggering conditions are met can information transmission proceed. Such a procedure is expressed as (20).

2.3. Filter design

By using the available measurement $\bar{y}_{m,t}$, construct a recursive filter

$$\hat{x}_{m,t|t-1} = A_{t-1}\hat{x}_{m,t-1|t-1}, \tag{21}$$

$$\hat{x}_{m,t|t} = \hat{x}_{m,t|t-1} + K_{m,t}(\bar{y}_{m,t} - \hat{y}_{m,t|t-1}) \tag{22}$$

with the initial value $\hat{x}_{m,0|0} = \bar{x}_{m,0}$, and for $t \in [t_m^n, t_m^{n+1})(n \geq 0, t \geq 1)$, where $\hat{x}_{m,t|t-1}$ and $\hat{x}_{m,t|t}$ represent the prediction of one step and estimation from node m, respectively; $\hat{y}_{m,t|t-1}$ is the measurement estimate to be discussed later; and $K_{m,t}$ is the filter gain to be designed.

The primary objective of this paper is to design a local filter of the form (21) and (22) for every node under the DETP with token bucket specifications for all censored measurements within the framework of TKF. Moreover, we are devoted to developing an FTKFF framework to address the multiple challenges induced by the censored measurements, the DETP and the token bucket specifications.

3. MAIN RESULTS

This section introduces the recursive bound of the TKF of the filtering error covariance. In addition, the desired filter gain is calculated based on the minimum mean square error criterion.

3.1. Filtering error and covariance matrix

In line with (5) and (6), the estimate of the measurement $\hat{y}_{m,t|t-1}$ is derived as

$$\hat{y}_{m,t|t-1} = \bar{\varrho}_{m,t}(C_{m,t}\hat{x}_{m,t|t-1} + \lambda_{m,t}\sqrt{\mathcal{R}_{m,t}}) + (I - \bar{\varrho}_{m,t})\tau_m \tag{23}$$

where

$$\bar{\varrho}_{m,t} \triangleq \text{diag}\left\{\bar{\varrho}_{m,t}^{(1)}, \bar{\varrho}_{m,t}^{(2)}, \ldots, \bar{\varrho}_{m,t}^{(n_y)}\right\}, \quad \lambda_{m,t} \triangleq \lambda\left(\frac{\tau_m - C_{m,t}\hat{x}_{m,t|t-1}}{\sqrt{R_{m,t}}}\right),$$

$$\mathcal{R}_{m,t} \triangleq \left[R_{m,t}^{(1)} \quad \cdots \quad R_{m,t}^{(n_y)}\right]^T, \quad \sqrt{\mathcal{R}_{m,t}} \triangleq \left[\sqrt{R_{m,t}^{(1)}} \quad \cdots \quad \sqrt{R_{m,t}^{(n_y)}}\right]^T.$$

Let $e_{m,t|t-1} \triangleq x_t - \hat{x}_{m,t|t-1}$. From (1) and (21), one calculates

$$e_{m,t|t-1} = A_{t-1}e_{m,t-1|t-1} + B_{t-1}\omega_{t-1}. \tag{24}$$

Subsequently, from (1), (8), (22) and (23), one has

$$\begin{aligned} e_{m,t|t} =& (I - K_{m,t}\bar{\varrho}_{m,t}C_{m,t})e_{m,t|t-1} - (1-\theta_{m,t})K_{m,t}\varrho_{m,t}v_{m,t} + K_{m,t}\bar{\varrho}_{m,t}\lambda_{m,t}\sqrt{\mathcal{R}_{m,t}} \\ & - (1-\theta_{m,t})K_{m,t}\tilde{\varrho}_{m,t}C_{m,t}x_t + \theta_{m,t}K_{m,t}\bar{\varrho}_{m,t}C_{m,t}x_t - \theta_{m,t}K_{m,t}\bar{y}_{m,t-1} \\ & - (1-\theta_{m,t})K_{m,t}\varepsilon_{m,t} + \theta_{m,t}K_{m,t}(I - \bar{\varrho}_{m,t})\tau_m + (1-\theta_{m,t})K_{m,t}\tilde{\varrho}_{m,t}\tau_m \end{aligned} \tag{25}$$

where

$$\theta_{m,t} \triangleq 1-\alpha_{m,t}\beta_{m,t},\ \tilde{\varrho}_{m,t} \triangleq \varrho_{m,t}-\bar{\varrho}_{m,t},\ \varepsilon_{m,t} \triangleq y_{m,t}^{n}-y_{m,t}.$$

By means of Eqs. (24) and (25), the covariance matrices of the prediction error and filtering error are, respectively, calculated as follows

$$P_{m,t|t-1}=\mathbb{E}(e_{m,t|t-1}e_{m,t|t-1}^{T})=A_{t-1}P_{m,t-1|t-1}A_{t-1}^{T}+B_{t-1}Q_{t-1}B_{t-1}^{T}, \tag{26}$$

and

$$\begin{aligned}
P_{m,t|t}=&(I-K_{m,t}\bar{\varrho}_{m,t}C_{m,t})P_{m,t|t-1}(I-K_{m,t}\bar{\varrho}_{m,t}C_{m,t})^{T}+(1-\theta_{m,t})^{2}K_{m,t}\mathbb{E}\{\varrho_{m,t}v_{m,t}v_{m,t}^{T}\varrho_{m,t}^{T}\}K_{m,t}^{T}\\
&+K_{m,t}\bar{\varrho}_{m,t}\mathbb{E}\{\lambda_{m,t}\sqrt{\mathcal{R}_{m,t}}\sqrt{\mathcal{R}_{m,t}}^{T}\lambda_{m,t}^{T}\}\bar{\varrho}_{m,t}^{T}K_{m,t}^{T}+(1-\theta_{m,t})^{2}K_{m,t}\mathbb{E}\{\tilde{\varrho}_{m,t}C_{m,t}x_{t}x_{t}^{T}C_{m,t}^{T}\tilde{\varrho}_{m,t}^{T}\}K_{m,t}^{T}\\
&+\theta_{m,t}^{2}K_{m,t}\bar{\varrho}_{m,t}\mathbb{E}\{C_{m,t}x_{t}x_{t}^{T}C_{m,t}^{T}\}\bar{\varrho}_{m,t}^{T}K_{m,t}^{T}+\theta_{m,t}^{2}K_{m,t}\mathbb{E}\{\bar{y}_{m,t-1}\bar{y}_{m,t-1}^{T}\}K_{m,t}^{T}+\mathcal{K}_{m,t}^{1}+\mathcal{K}_{m,t}^{1^{T}}\\
&+(1-\theta_{m,t})^{2}K_{m,t}\mathbb{E}\{\varepsilon_{m,t}\varepsilon_{m,t}^{T}\}K_{m,t}^{T}+\theta_{m,t}^{2}K_{m,t}(I-\bar{\varrho}_{m,t})\mathbb{E}\{\tau_{m}\tau_{m}^{T}\}(I-\bar{\varrho}_{m,t})^{T}K_{m,t+1}^{T}\\
&+(1-\theta_{m,t})^{2}K_{m,t}\mathbb{E}\{\tilde{\varrho}_{m,t}\tau_{m}\tau_{m}^{T}\tilde{\varrho}_{m,t}^{T}\}K_{m,t}^{T}+\mathcal{K}_{m,t}^{2}+\mathcal{K}_{m,t}^{2^{T}}-\mathcal{K}_{m,t}^{3}-\mathcal{K}_{m,t}^{3^{T}}-\mathcal{K}_{m,t}^{4}-\mathcal{K}_{m,t}^{4^{T}}\\
&+\mathcal{K}_{m,t}^{5}+\mathcal{K}_{m,t}^{5^{T}}+\mathcal{K}_{m,t}^{6}+\mathcal{K}_{m,t}^{6^{T}}+\mathcal{K}_{m,t}^{7}+\mathcal{K}_{m,t}^{7^{T}}-\mathcal{K}_{m,t}^{8}-\mathcal{K}_{m,t}^{8^{T}}+\mathcal{K}_{m,t}^{9}+\mathcal{K}_{m,t}^{9^{T}}-\mathcal{K}_{m,t}^{10}-\mathcal{K}_{m,t}^{10^{T}}\\
&-\mathcal{K}_{m,t}^{11}-\mathcal{K}_{m,t}^{11^{T}}-\mathcal{K}_{m,t}^{12}-\mathcal{K}_{m,t}^{12^{T}}+\mathcal{K}_{m,t}^{13}+\mathcal{K}_{m,t}^{13^{T}}
\end{aligned} \tag{27}$$

where

$$\begin{aligned}
\mathcal{K}_{m,t}^{1} \triangleq&\mathbb{E}\{(I-K_{m,t}\bar{\varrho}_{m,t}C_{m,t})e_{m,t|t-1}\sqrt{\mathcal{R}_{m,t}}^{T}\lambda_{m,t}^{T}\bar{\varrho}_{m,t}^{T}K_{m,t}^{T}\},\\
\mathcal{K}_{m,t}^{2} \triangleq&\theta_{m,t}\mathbb{E}\{(I-K_{m,t}\bar{\varrho}_{m,t}C_{m,t})e_{m,t|t-1}x_{t}^{T}C_{m,t}^{T}K_{m,t}^{T}\bar{\varrho}_{m,t}^{T}\},\\
\mathcal{K}_{m,t}^{3} \triangleq&\theta_{m,t}\mathbb{E}\{(I-K_{m,t}\bar{\varrho}_{m,t}C_{m,t})e_{m,t|t-1}\bar{y}_{m,t-1}^{T}K_{m,t}^{T}\},\\
\mathcal{K}_{m,t}^{4} \triangleq&(1-\theta_{m,t})\mathbb{E}\{(I-K_{m,t}\bar{\varrho}_{m,t}C_{m,t})e_{m,t|t-1}\varepsilon_{m,t}^{T}K_{m,t}^{T}\},\\
\mathcal{K}_{m,t}^{5} \triangleq&\theta_{m,t}\mathbb{E}\{(I-K_{m,t}\bar{\varrho}_{m,t}C_{m,t})e_{m,t|t-1}\tau_{m,t}^{T}(I-\bar{\varrho}_{m,t})^{T}K_{m,t}^{T}\},\\
\mathcal{K}_{m,t}^{6} \triangleq&(1-\theta_{m,t})^{2}\mathbb{E}\{K_{m,t}\tilde{\varrho}_{m,t}C_{m,t}x_{t}\tau_{m}^{T}\tilde{\varrho}_{m,t}^{T}K_{m,k}^{T}\},\\
\mathcal{K}_{m,t}^{7} \triangleq&\theta_{m,t}\mathbb{E}\{K_{m,t}\bar{\varrho}_{m,t}C_{m,t}x_{t}\sqrt{\mathcal{R}_{m,t}}^{T}\lambda_{m,t}^{T}\bar{\varrho}_{m,t}^{T}K_{m,t}^{T}\},\\
\mathcal{K}_{m,t}^{8} \triangleq&\theta_{m,t}^{2}\mathbb{E}\{K_{m,t}\bar{\varrho}_{m,t}C_{m,t}x_{t}\bar{y}_{m,t-1}^{T}K_{m,t-1}^{T}\},\\
\mathcal{K}_{m,t}^{9} \triangleq&\theta_{m,t}^{2}\mathbb{E}\{K_{m,t}\bar{\varrho}_{m,t}C_{m,t}x_{t}\tau_{m}^{T}(I-\bar{\varrho}_{m,t})^{T}K_{m,t}^{T}\},\\
\mathcal{K}_{m,t}^{10} \triangleq&\theta_{m,t}\mathbb{E}\{K_{m,t}\bar{y}_{m,t-1}\sqrt{\mathcal{R}_{m,t}}^{T}\lambda_{m,t}^{T}\bar{\varrho}_{m,t}^{T}K_{m,t}^{T}\},\\
\mathcal{K}_{m,t}^{11} \triangleq&\theta_{m,t}^{2}\mathbb{E}\{K_{m,t}\bar{y}_{m,t-1}\tau_{m}^{T}(I-\bar{\varrho}_{m,t})^{T}K_{m,t}^{T}\},\\
\mathcal{K}_{m,t}^{12} \triangleq&(1-\theta_{m,t})\mathbb{E}\{K_{m,t}\varepsilon_{m,t}\sqrt{\mathcal{R}_{m,t}}^{T}\lambda_{m,t}^{T}\bar{\varrho}_{m,t}^{T}K_{m,t}^{T}\},\\
\mathcal{K}_{m,t}^{13} \triangleq&\theta_{m,t}\mathbb{E}\{K_{m,t}(I-\bar{\varrho}_{m,t})\tau_{m}\sqrt{\mathcal{R}_{m,t}}^{T}\lambda_{m,t}^{T}\bar{\varrho}_{m,t}^{T}K_{m,t}^{T}\}.
\end{aligned}$$

Next, an upper bound for the filtering error covariance matrix $P_{m,t|t}$ is provided to eliminate the uncertainties in Eq. (27).

Theorem 1. *For the given positive scalars ε_j ($j=1,2,\ldots,14$), it is said that $\bar{P}_{m,t|t}$ is an upper bound of the $P_{m,t|t}$, namely,*

$$P_{m,t|t} \le \bar{P}_{m,t|t}, \tag{28}$$

with the initial value of $P_{0|0}=\bar{P}_{0|0}>0$. Moreover, $\bar{P}_{m,t|t}$ satisfies the following recursions:

$$\bar{P}_{m,t|t-1}=A_{t-1}\bar{P}_{m,t|t}A_{t-1}^{T}+B_{t-1}Q_{t-1}B_{t-1}^{T}, \tag{29}$$

and

$$\begin{aligned}\bar{P}_{m,t|t} &= \kappa_1(I - K_{m,t}\bar{\varrho}_{m,t}C_{m,t})\bar{P}_{m,t|t-1}(I - K_{m,t}\bar{\varrho}_{m,t}C_{m,t})^T + (1-\theta_{m,t})^2 K_{m,t}\{\Omega_{m3,t}\circ R_{m,t}\}K_{m,t}^T \\ &+ \kappa_2 K_{m,t}\bar{\varrho}_{m,t}\lambda_{m,t}\sqrt{\mathcal{R}_{m,t}}\sqrt{\mathcal{R}_{m,t}}^T\lambda_{m,t}^T\bar{\varrho}_{m,t}^T K_{m,t}^T + (1-\theta_{m,t})^2\kappa_3 K_{m,t}C_{m,t}\{\Upsilon_{m,t}\circ\Omega_{m1,t}\}C_{m,t}^T K_{m,t}^T \\ &+ \theta_{m,t}^2\kappa_4 K_{m,t}\bar{\varrho}_{m,t}C_{m,t}\Omega_{m1,t}C_{m,t}^T\bar{\varrho}_{m,t}^T K_{m,t}^T + \theta_{m,t}^2\kappa_5 K_{m,t}\Omega_{m2,t}K_{m,t}^T \\ &+ (1-\theta_{m,t})^2\kappa_6 K_{m,t}\Xi(\bar{G}_{m,t})K_{m,t}^T + \theta_{m,t}^2\kappa_7 K_{m,t}(I-\bar{\varrho}_{m,t})\tau_m\tau_m^T(I-\bar{\varrho}_{m,t})^T K_{m,t+1}^T \\ &+ (1-\theta_{m,t})^2\kappa_8 K_{m,t}\{\Upsilon_{m,t}\circ\tau_m\tau_m^T\}K_{m,t}^T \end{aligned} \tag{30}$$

where

$$\begin{aligned}\kappa_1 &\triangleq 1+\varepsilon_1+\varepsilon_2+\varepsilon_3+\varepsilon_4+\varepsilon_5,\\ \kappa_2 &\triangleq 1+\varepsilon_1^{-1}+\varepsilon_7^{-1}+\varepsilon_{10}^{-1}+\varepsilon_{12}^{-1}+\varepsilon_{13}^{-1},\\ \kappa_3 &\triangleq 1+\varepsilon_6,\\ \kappa_4 &\triangleq 1+\varepsilon_7+\varepsilon_8+\varepsilon_9+\varepsilon_2^{-1},\\ \kappa_5 &\triangleq 1+\varepsilon_3^{-1}+\varepsilon_8^{-1}+\varepsilon_{10}+\varepsilon_{11},\\ \kappa_6 &\triangleq 1+\varepsilon_4^{-1}+\varepsilon_{12},\\ \kappa_7 &\triangleq 1+\varepsilon_5^{-1}+\varepsilon_9^{-1}+\varepsilon_{11}^{-1}+\varepsilon_{13},\\ \kappa_8 &\triangleq 1+\varepsilon_6^{-1},\\ \Upsilon_{m,t} &\triangleq diag\{\bar{\varrho}_{m,t}^{(1)}(1-\bar{\varrho}_{m,t}^{(1)}),\cdots,\bar{\varrho}_{m,t}^{(n_y)}(1-\bar{\varrho}_{m,t}^{(n_y)})\},\\ \Omega_{m1,t} &\triangleq (1+\varepsilon_{14})P_{t|t-1}+(1+\varepsilon_{14}^{-1})\hat{x}_{m,t|t-1}\hat{x}_{m,t|t-1}^T\\ \Omega_{m2,t-1} &\triangleq \bar{y}_{m,t-1}\bar{y}_{m,t-1}^T,\qquad \Omega_{m3,t}\triangleq\Upsilon_{m,t}+\bar{\varrho}_{m,t}\bar{\varrho}_{m,t}^T,\end{aligned}$$

and

$$\begin{aligned}\bar{G}_{m,t+1} &\triangleq \Xi(\bar{G}_{m,t})\\ &= \left((1+d_t)(1+e_t)\lambda_m^2+\frac{(1+\chi_m)(1+d_t^{-1})}{\chi_m^2}\right)\bar{G}_{m,t}+\left((1+d_t)(1+e_t^{-1})+(1+d_t^{-1})(1+\chi_m^{-1})\right)\sigma_m^2\end{aligned}$$

where $\bar{G}_{m,t}$ *is an upper bound of* $G_{m,t}\triangleq\mathbb{E}\{\eta_{m,t}^2\}$ *with the initial condition* $\bar{G}_{m,0}=\eta_{m,0}^2$.

Here, $\circ$ *denotes the Hadamard product, which is defined as* $[A\circ B]_{ij}=A_{ij}\cdot B_{ij}$.

Proof. According to lemma 1 in [36], it follows from Eq. (27) that

$$\begin{aligned}&P_{m,t|t}\\ \le&\kappa_1(I-K_{m,t}\bar{\varrho}_{m,t}C_{m,t})P_{m,t|t-1}(I-K_{m,t}\bar{\varrho}_{m,t}C_{m,t})^T+(1-\theta_{m,t})^2K_{m,t}\mathbb{E}\{\varrho_{m,t}v_{m,t}v_{m,t}^T\varrho_{m,t}^T\}K_{m,t}^T\\ &+\kappa_2K_{m,t}\bar{\varrho}_{m,t}\mathbb{E}\left\{\lambda_{m,t}\sqrt{\mathcal{R}_{m,t}}\sqrt{\mathcal{R}_{m,t}}^T\lambda_{m,t}^T\right\}\bar{\varrho}_{m,t}^TK_{m,t}^T+(1-\theta_{m,t})^2\kappa_3K_{m,t}\mathbb{E}\{\tilde{\varrho}_{m,t}C_{m,t}x_tx_t^TC_{m,t}^T\tilde{\varrho}_{m,t}^T\}K_{m,t}^T\\ &+\theta_{m,t}^2\kappa_4K_{m,t}\bar{\varrho}_{m,t}\mathbb{E}\{C_{m,t}x_tx_t^TC_{m,t}^T\}\bar{\varrho}_{m,t}^TK_{m,t}^T+\theta_{m,t}^2\kappa_5K_{m,t}\mathbb{E}\{\bar{y}_{m,t-1}\bar{y}_{m,t-1}^T\}K_{m,t}^T\\ &+(1-\theta_{m,t})^2\kappa_6K_{m,t}\mathbb{E}\{\varepsilon_{m,t}\varepsilon_{m,t}^T\}K_{m,t}^T+\theta_{m,t}^2K_{m,t}\kappa_7(I-\bar{\varrho}_{m,t})\mathbb{E}\{\tau_m\tau_m^T\}(I-\bar{\varrho}_{m,t})^TK_{m,t+1}^T\\ &+(1-\theta_{m,t})^2\kappa_8K_{m,t}\mathbb{E}\{\tilde{\varrho}_{m,t}\tau_m\tau_m^T\tilde{\varrho}_{m,t}^T\}K_{m,t}^T.\end{aligned} \tag{31}$$

Following the same line, one has

$$\begin{aligned}\mathbb{E}\{x_tx_t^T\} =&\mathbb{E}\{(e_{m,t|t-1}+\hat{x}_{m,t|t-1})(e_{m,t|t-1}+\hat{x}_{m,t|t-1})^T\}\\ \le&\mathbb{E}\{(1+\varepsilon_{14})e_{m,t|t-1}e_{m,t|t-1}^T+(1+\varepsilon_{14}^{-1})\hat{x}_{m,t|t-1}\hat{x}_{m,t|t-1}^T\}\\ \triangleq&\Omega_{m1,t}.\end{aligned} \tag{32}$$

Moreover, given the event-triggering condition (11), we have

$$\varepsilon_{m,t}^T\varepsilon_{m,t} \leq \left(\frac{1}{\chi_m}\eta_{m,t} + \sigma_m\right)^2 \leq (1+\chi_m)\chi_m^{-2}\eta_{m,t}^2 + (1+\chi_m^{-1})\sigma_m^2. \tag{33}$$

In light of lemma 5 and the proof of lemma 4 in [27], one derives

$$\mathbb{E}\{\varepsilon_{m,t}\varepsilon_{m,t}^T\} \leq \Xi(\bar{G}_{m,t}). \tag{34}$$

Substituting Eqs. (32) and (34) into (31), one obtains the following inequality

$$\begin{aligned}
P_{m,t|t} \leq & \kappa_1(I - K_{m,t}\bar{\varrho}_{m,t}C_{m,t})P_{m,t|t-1}(I - K_{m,t}\bar{\varrho}_{m,t}C_{m,t})^T + (1-\theta_{m,t})^2K_{m,t}\{\Omega_{m3,t}\circ R_{m,t}\}K_{m,t}^T \\
& + \kappa_2 K_{m,t}\bar{\varrho}_{m,t}\lambda_{m,t}\sqrt{\mathcal{R}_{m,t}}\sqrt{\mathcal{R}_{m,t}}^T\lambda_{m,t}^T\bar{\varrho}_{m,t}^TK_{m,t}^T + (1-\theta_{m,t})^2\kappa_3K_{m,t}C_{m,t}\{\Upsilon_{m,t}\circ\Omega_{m1,t}\}C_{m,t}^TK_{m,t}^T \\
& + \theta_{m,t}^2\kappa_4K_{m,t}\bar{\varrho}_{m,t}C_{m,t}\Omega_{m1,t}C_{m,t}^T\bar{\varrho}_{m,t}^TK_{m,t}^T + \theta_{m,t}^2\kappa_5K_{m,t}\Omega_{m2,t}K_{m,t}^T \\
& + (1-\theta_{m,t})^2\kappa_6K_{m,t}\Xi(\bar{G}_{m,t})K_{m,t}^T + \theta_{m,t}^2\kappa_7K_{m,t}(I-\bar{\varrho}_{m,t})\tau_m\tau_m^T(I-\bar{\varrho}_{m,t})^TK_{m,t+1}^T \\
& + (1-\theta_{m,t})^2\kappa_8K_{m,t}\{\Upsilon_{m,t}\circ\tau_m\tau_m^T\}K_{m,t}^T.
\end{aligned} \tag{35}$$

By using lemma 2 in [27], one obtains that

$$P_{m,t|t} \leq \bar{P}_{m,t|t}. \tag{36}$$

The proof is now complete. □

Next, the filter gain $K_{m,t}$ is designed such that $\mathrm{tr}\{\bar{P}_{m,t|t}\}$ is minimized at each time instant.

Theorem 2. *Suppose that the positive scalars $\varepsilon_j (j = 1, 2, ..., 14)$ are given. The upper bound of the filtering error covariance $\bar{P}_{m,t|t}$ given by Eq. (30) is minimized by the following filter gain*

$$K_{m,t} = \Psi_{m,t}\Phi_{m,t}^{-1} \tag{37}$$

where

$$\begin{aligned}
\Psi_{m,t} \triangleq & \kappa_1\bar{P}_{m,t|t-1}C_{m,t}^T\bar{\varrho}_{m,t}^T, \\
\Phi_{m,t} \triangleq & \kappa_1\bar{\varrho}_{m,t}C_{m,t}\bar{P}_{m,t|t-1}C_{m,t}^T\bar{\varrho}_{m,t}^T + \kappa_2\bar{\varrho}_{m,t}\lambda_{m,t}\sqrt{\mathcal{R}_{m,t}}\sqrt{\mathcal{R}_{m,t}}^T\lambda_{m,t}^T\bar{\varrho}_{m,t}^T \\
& + \theta_{m,t}^2\left(\kappa_4\bar{\varrho}_{m,t}C_{m,t}\Omega_{m1,t}C_{m,t}^T\bar{\varrho}_{m,t}^T + \kappa_5\Omega_{m2,t} + \kappa_7(I-\bar{\varrho}_{m,t})\tau_m\tau_m^T(I-\bar{\varrho}_{m,t})^T\right) \\
& + (1-\theta_{m,t})^2\left(\Omega_{m3,t}\circ R_{m,t} + \kappa_3C_{m,t}\{\Upsilon_{m,t}\circ\Omega_{m1,t}\}C_{m,t}^T + \kappa_8\{\Upsilon_{m,t}\circ(\tau_m\tau_m^T)\} + \kappa_6\Xi(\bar{G}_{m,t})\right).
\end{aligned}$$

Proof. First, calculate the trace of $\bar{P}_{m,t|t}$ obtained by Eq. (30) as follows

$$\begin{aligned}
& \mathrm{tr}(\bar{P}_{m,t|t}) \\
= & \mathrm{tr}\Big\{\kappa_1(I - K_{m,t}\bar{\varrho}_{m,t}C_{m,t})P_{m,t|t-1}(I - K_{m,t}\bar{\varrho}_{m,t}C_{m,t})^T + (1-\theta_{m,t})^2K_{m,t}\{\Omega_{m3,t}\circ R_{m,t}\}K_{m,t}^T \\
& + \kappa_2K_{m,t}\bar{\varrho}_{m,t}\lambda_{m,t}\sqrt{\mathcal{R}_{m,t}}\sqrt{\mathcal{R}_{m,t}}^T\lambda_{m,t}^T\bar{\varrho}_{m,t}^TK_{m,t}^T + (1-\theta_{m,t})^2\kappa_3K_{m,t}C_{m,t}\{\Upsilon_{m,t}\circ\Omega_{m1,t}\}C_{m,t}^TK_{m,t}^T \\
& + \theta_{m,t}^2\kappa_4K_{m,t}\bar{\varrho}_{m,t}C_{m,t}\Omega_{m1,t}C_{m,t}^T\bar{\varrho}_{m,t}^TK_{m,t}^T + \theta_{m,t}^2\kappa_5K_{m,t}\Omega_{m2,t}K_{m,t}^T \\
& + (1-\theta_{m,t})^2\kappa_6K_{m,t}\Xi(\bar{G}_{m,t})K_{m,t}^T + \theta_{m,t}^2\kappa_7K_{m,t}(I-\bar{\varrho}_{m,t})\tau_m\tau_m^T(I-\bar{\varrho}_{m,t})^TK_{m,t+1}^T \\
& + (1-\theta_{m,t})^2\kappa_8K_{m,t}\{\Upsilon_{m,t}\circ(\tau_m\tau_m^T)\}K_{m,t}^T\Big\}.
\end{aligned} \tag{38}$$

Next, one can derive the derivative of $\mathrm{tr}\left\{\bar{P}_{m,t|t}\right\}$ as follows

$$\begin{aligned}
&\frac{\partial}{\partial K_{m,t}}\mathrm{tr}\left\{\bar{P}_{m,t|t}\right\}\\
=&-2\kappa_1(I-K_{m,t}\bar{\varrho}_{m,t}C_{m,t})\bar{P}_{m,t|t-1}C_{m,t}^T\bar{\varrho}_{m,t}^T+2(1-\theta_{m,t})^2K_{m,t}\{\Omega_{m3,t}\circ R_{m,t}\}\\
&+2\kappa_2K_{m,t}\bar{\varrho}_{m,t}\lambda_{m,t}\sqrt{\mathcal{R}_{m,t}}\sqrt{\mathcal{R}_{m,t}}^T\lambda_{m,t}^T\bar{\varrho}_{m,t}^T+2(1-\theta_{m,t})^2\kappa_3K_{m,t}C_{m,t}\{\Upsilon_{m,t}\circ\Omega_{m1,t}\}C_{m,t}^T\\
&+2\theta_{m,t}^2\kappa_4K_{m,t}\bar{\varrho}_{m,t}C_{m,t}\Omega_{m1,t}C_{m,t}^T\bar{\varrho}_{m,t}^T+2\theta_{m,t}^2\kappa_5K_{m,t}\Omega_{m2,t}\\
&+2(1-\theta_{m,t})^2\kappa_6K_{m,t}\Xi(\bar{G}_{m,t})+2\theta_{m,t}^2\kappa_7K_{m,t}(I-\bar{\varrho}_{m,t})\tau_m\tau_m^T(I-\bar{\varrho}_{m,t})^T\\
&+2(1-\theta_{m,t})^2\kappa_8K_{m,t}\{\Upsilon_{m,t}\circ(\tau_m\tau_m^T)\}.
\end{aligned}\tag{39}$$

By letting (39) be zero, one acquires the filter gain as follows:

$$\begin{aligned}
K_{m,t}=&\kappa_1\bar{P}_{m,t|t-1}C_{m,t}^T\bar{\varrho}_{m,t}^T\Big\{\kappa_1\bar{\varrho}_{m,t}C_{m,t}\bar{P}_{m,t|t-1}C_{m,t}^T\bar{\varrho}_{m,t}^T+(1-\theta_{m,t})^2\{\Omega_{m3,t}\circ R_{m,t}\}\\
&+\kappa_2\bar{\varrho}_{m,t}\lambda_{m,t}\sqrt{\mathcal{R}_{m,t}}\sqrt{\mathcal{R}_{m,t}}^T\lambda_{m,t}^T\bar{\varrho}_{m,t}^T+(1-\theta_{m,t})^2\kappa_3C_{m,t}\{\Upsilon_{m,t}\circ\Omega_{m1,t}\}C_{m,t}^T\\
&+\theta_{m,t}^2\kappa_4\bar{\varrho}_{m,t}C_{m,t}\Omega_{m1,t}C_{m,t}^T\bar{\varrho}_{m,t}^T+\theta_{m,t}^2\kappa_5\Omega_{m2,t}+(1-\theta_{m,t})^2\kappa_6\Xi(\bar{G}_{m,t})\\
&+\theta_{m,t}^2\kappa_7(I-\bar{\varrho}_{m,t})\tau_m\tau_m^T(I-\bar{\varrho}_{m,t})^T+(1-\theta_{m,t})^2\kappa_8\{\Upsilon_{m,t}\circ(\tau_m\tau_m^T)\}\Big\}^{-1}.
\end{aligned}\tag{40}$$

As such, one completes the proof of this theorem. □

Remark 3. *Different from the approach to dealing with the DETP in[6,27,37], an indicator variable is employed to formulate the impact of the DETP. From (37), it can be observed that the filter gain $K_{m,t}$ is dependent on the indicator variable $\theta_{m,t}$, which formulates the combined role of DETP with the token bucket specifications. Meanwhile, the filter gain can be calculated under two cases, i.e., $\theta_{m,t}=1$ (i.e., filter does not receive measurement) and $\theta_{m,t}=0$ (i.e., filter does receive measurement), respectively.*

3.2. Boundedness analysis

In this section, the boundedness of $\bar{P}_{m,t|t}$ will be discussed in the sense of mean square. Before carrying out the performance analysis, an assumption is provided to make some necessary constraints on the corresponding parameters.

Assumption 1. *Suppose that the following inequalities hold*

$$\begin{aligned}
&\|A_t\|\le a,\quad \|B_t\|\le b,\quad \underline{c}\le\left\|C_{m,t}\right\|\le\bar{c},\quad \left\|\Upsilon_{m,t}\right\|\le\pi,\quad \left\|Q_{m,t}\right\|\le q,\quad \left\|\Xi(\bar{G}_{m,t+1})\right\|\le\rho,\\
&\|\tau_m\|\le\bar{\tau},\quad \left\|\Omega_{m1,t-1}\right\|\le\xi,\quad \left\|\Omega_{m2,t-1}\right\|\le\vartheta,\quad \left\|\Omega_{m3,t-1}\right\|\le o,\quad \underline{\varpi}\le\left\|\bar{\varrho}_{m,t}\right\|\le\overline{\varpi},\\
&\left\|R_{m,t}\right\|\le r,\quad \underline{\lambda}\le\left\|\lambda_{m,t}\right\|\le\bar{\lambda},\quad \left\|\sqrt{\mathcal{R}_{m,t}}\right\|\le\mu
\end{aligned}\tag{41}$$

where a, b, c, π, q, r, q, o, ρ, $\bar{\tau}$, ϑ, ξ, $\bar{c}$, $\underline{c}$, $\underline{\varpi}$, $\overline{\varpi}$, μ, and $\bar{\tau}$ are all known positive real numbers.

Theorem 3. *Suppose Assumption 1 holds, in line with the system (1) and censored measurement (2) under Assumption 1, if the following inequality holds:*

$$\kappa_1w_{m,t}a^2<1,\tag{42}$$

where $w_{m,t}\triangleq\left\|I-K_{m,t}\bar{\varrho}_{m,t}C_{m,t}\right\|^2$, then the filtering error (25) is mean-square bounded. Moreover, one has

$$\lim_{t\to+\infty}\|\bar{P}_{m,t|t}\|=\frac{\Delta}{1-\kappa_1w_{m,t}a^2}\tag{43}$$

where

$$\begin{aligned}\Delta \triangleq & \kappa_1 w_{m,t} b^2 q + (1-\theta_{m,t})^2 \bar{k}^2 ro + \kappa_2 \bar{k}^2 \overline{\varpi}^2 \bar{\lambda}^2 \mu^2 + (1-\theta_{m,t})^2 \kappa_3 \bar{k}^2 \bar{c}^2 \pi\xi \\ & + \theta_{m,t}^2 \kappa_4 \bar{k}^2 \overline{\varpi}^2 \bar{c}^2 \xi + \theta_{m,t}^2 \kappa_5 \bar{k}^2 \vartheta + (1-\theta_{m,t})^2 \kappa_6 \bar{k}^2 \rho \\ & + \theta_{m,t}^2 \kappa_7 \bar{k}^2 \bar{\tau}^2 + (1-\theta_{m,t})^2 \kappa_8 \bar{k}^2 \pi \bar{\tau}^2.\end{aligned}$$

Proof. In line with Assumption 1 and Eq. (26), it deduces that

$$\left\|\bar{P}_{m,t|t-1}\right\| \leq a^2 \left\|\bar{P}_{m,t-1|t-1}\right\| + b^2 q. \tag{44}$$

By noting Eqs. (37) with (40), the upper bound of the filter gain $K_{m,t+1}$ is given as

$$\left\|K_{m,t}\right\| \leq \left\|\Psi_{m,t}\right\| \left\|\Phi_{m,t}\right\|^{-1} \leq \frac{\overline{\varpi}\bar{c}}{\underline{\varpi}^2 \underline{c}^2} \triangleq \bar{k}, \tag{45}$$

from which can be gained from Eq. (30):

$$\begin{aligned}\left\|\bar{P}_{m,t|t}\right\| \leq & \kappa_1 \left\|I - K_{m,t}\bar{\varrho}_{m,t} C_{m,t}\right\|^2 \left\|\bar{P}_{m,t|t-1}\right\| + (1-\theta_{m,t})^2 \bar{k}^2 ro + \kappa_2 \bar{k}^2 \overline{\varpi}^2 \bar{\lambda}^2 \mu^2 \\ & + (1-\theta_{m,t})^2 \kappa_3 \bar{k}^2 \bar{c}^2 \pi\xi + \theta_{m,t}^2 \kappa_4 \bar{k}^2 \overline{\varpi}^2 \bar{c}^2 \xi + \theta_{m,t}^2 \kappa_5 \bar{k}^2 \vartheta + (1-\theta_{m,t})^2 \kappa_6 \bar{k}^2 \rho \\ & + \theta_{m,t}^2 \kappa_7 \bar{k}^2 \bar{\tau}^2 + (1-\theta_{m,t})^2 \kappa_8 \bar{k}^2 \pi \bar{\tau}^2.\end{aligned} \tag{46}$$

By means of $w_{m,t} \triangleq \left\|I - K_{m,t}\bar{\varrho}_{m,t} C_{m,t}\right\|^2$, one has

$$\begin{aligned}\left\|\bar{P}_{m,t|t}\right\| \leq & \kappa_1 w_{m,t} a^2 \left\|\bar{P}_{m,t-1|t-1}\right\| + \kappa_1 w_{m,t} b^2 q + (1-\theta_{m,t})^2 \bar{k}^2 ro + \kappa_2 \bar{k}^2 \overline{\varpi}^2 \bar{\lambda}^2 \mu^2 \\ & + (1-\theta_{m,t})^2 \kappa_3 \bar{k}^2 \bar{c}^2 \pi\xi + \theta_{m,t}^2 \kappa_4 \bar{k}^2 \overline{\varpi}^2 \bar{c}^2 \xi + \theta_{m,t}^2 \kappa_5 \bar{k}^2 \vartheta + (1-\theta_{m,t})^2 \kappa_6 \bar{k}^2 \rho \\ & + \theta_{m,t}^2 \kappa_7 \bar{k}^2 \bar{\tau}^2 + (1-\theta_{m,t})^2 \kappa_8 \bar{k}^2 \pi \bar{\tau}^2.\end{aligned} \tag{47}$$

In the following, we can rewrite (47) as follows

$$\|\bar{P}_{m,t|t}\| \leq \kappa_1 w_{m,t} a^2 \|\bar{P}_{m,t-1|t-1}\| + \Delta, \tag{48}$$

which further implies

$$\|\bar{P}_{m,t|t}\| \leq (\kappa_1 w_{m,t} a^2)^t \|\bar{P}_{m,0|0}\| + \frac{1-(\kappa_1 w_{m,t} a^2)^{t-1}}{1-\kappa_1 w_{m,t} a^2} \Delta. \tag{49}$$

If (42) holds, i.e., $\kappa_1 w_{m,t} a^2 < 1$, one then has (43), which implies that the convergence of the upper bound $\left\|\bar{P}_{m,t|t}\right\|$. Meanwhile, it is observed that $\bar{P}_{m,t|t}$ always serves as an upper bound for the true estimation error covariance $P_{m,t|t}$. Consequently, the filtering error is mean-square bounded. Therefore, the proof is now complete. □

Remark 4. *Theorem 3 shows the combined impact of the DETP with the token bucket specifications on the filtering error boundedness and the filtering accuracy. Noticing that $w_{m,t}$ is dependent on filter gain $K_{m,t}$ from sufficient condition (42) and $K_{m,t}$ is dependent on $\theta_{m,t}$ from (37), the DETP with the token bucket specifications will pose an impact on the bounded condition. In addition, as given in (43), $\theta_{m,t}$ and $w_{m,t}$ are involved in the upper bound of the filtering error covariance, showing that $\theta_{m,t}$ would also pose effect on the filtering accuracy.*

3.3. Federated Tobit Kalman fusion filtering

In line with federated filtering fusion, the state estimate and the error covariance are $\hat{x}_{m,t|t}$ and $\bar{P}_{m,t|t}$, respectively, produced by the mth LTKF. Let $\hat{x}^g_{t|t}$ and $\hat{P}^g_{t|t}$ denote the global optimal estimate and covariance obtained at the fusion center under the federated fusion rule.

Theorem 4. *The FTKFF scheme for systems (1)-(2) is expressed as*

$$\begin{cases} P^g_{t|t} = \left(\sum_{m=1}^{l} \bar{P}^{-1}_{m,t|t} \right)^{-1}, \\ \hat{x}^g_{t|t} = P^g_{t|t} \sum_{m=1}^{l} \bar{P}^{-1}_{m,t|t} \hat{x}_{m,t|t} \end{cases} \tag{50}$$

with the resulting updated values

$$\begin{cases} Q_{m,t} = \alpha_m^{-1} Q_t, \\ \bar{P}_{m,t|t} = \alpha_m^{-1} P^g_{t|t}, \\ \hat{x}_{m,t|t} = \hat{x}^g_{t|t} \end{cases} \tag{51}$$

where α_m is the information weight of the m-th local estimator and $\sum_{m=1}^{l} \alpha_m = 1$; $\hat{x}_{m,t|t}$, $\bar{P}_{m,t|t}$, and $Q_{m,t}$ are the local estimates, upper bounds, and process noise covariance to be initialized at time t for predictions at time $t+1$.

It is noted that the role of (51) is to allocate the fused result to the individual sub-filter. The detailed procedure of FTKFF is summarized in Algorithm 1.

In line with the boundedness analysis of Theorem 3, the same argument can be applied to deduce the boundedness.

According to Algorithm 1, one has the computational complexity of the scheme developed in this paper.

Remark 5. *Now, we focus on the computational complexity of the scheme. In light of the system dimensions, such as $x_t \in \mathbb{R}^{n_y}$, $y_{i,t} \in \mathbb{R}^{n_y}$, $w_t \in \mathbb{R}^w$ and the resulting matrix dimensions, such as $A_t \in \mathbb{R}^{n_x \times n_x}$, $B_t \in \mathbb{R}^{n_x \times n_w}$, $C_{i,t} \in \mathbb{R}^{n_y \times n_x}$, one can obtain the computational complexity of the scheme developed in this paper at every fixed time instant. The FLOPS (Floating Point Operations Per Second) of main computational formulas from Algorithm 1 is $7ln_y^3+(10l+1)n_x^3+36ln_y^2n_x+22ln_yn_x^2+(13l+6)n_x^2+18ln_y^2-17ln_xn_y-(2l+1)n_x-ln_y+2ln_xn_w^2-2ln_xn_w+2l+59$. The corresponding complexity is given as $O(7ln_y^3 + (10l + 1)n_x^3 + 36ln_y^2n_x + 22ln_yn_x^2 + 2ln_xn_w^2)$.*

In the following, we will discuss the consistency of the federated fusion.

Theorem 5. *If $P_{m,t|t} \leq \bar{P}_{m,t|t}$, then one has*

$$\mathbb{E}\left\{(x_{t|t} - \hat{x}^g_{t|t})(x_{t|t} - \hat{x}^g_{t|t})^T\right\} \leq P^g_{t|t}. \tag{52}$$

Proof. First of all, one calculates

$$\begin{aligned} &\mathbb{E}\left\{(x_t - \hat{x}^g_{t|t})(x_t - \hat{x}^g_{t|t})^T\right\} \\ =&\mathbb{E}\left\{\left(x_t - P^g_{t|t}\sum_{m=1}^{l}\bar{P}^{-1}_{m,t|t}\hat{x}_{m,t|t}\right)\left(x_t - P^g_{t|t}\sum_{m=1}^{l}\bar{P}^{-1}_{m,t|t}\hat{x}_{m,t|t}\right)^T\right\} \\ =&P^g_{t|t}\mathbb{E}\left\{\left((P^g_{t|t})^{-1}x_t - \sum_{m=1}^{l}\bar{P}^{-1}_{m,t|t}\hat{x}_{m,t|t}\right)\left((P^g_{t|t})^{-1}x_t - \sum_{m=1}^{l}\bar{P}^{-1}_{m,t|t}\hat{x}_{m,t|t}\right)^T\right\}P^g_{t|t}. \end{aligned}$$

Algorithm 1 FTKFF

for m=1:l **do**
  Initialization: $\hat{x}_{m,0|0}$ and $\bar{P}_{m,0|0}$
end for
for t=1:N **do**
  for m=1:l **do**
    Execute information transmission protocols
    determine $\alpha_{m,t}$ by (15)
    determine $\beta_{m,t}$ by (18)
    if $\alpha_{m,t} = 1$ and $\beta_{m,t} = 1$ **then**
      $\bar{y}_{m,t} = y_{m,t_m^n}$
    else
      $\bar{y}_{m,t} = y_{m,t-1}$
    end if
    Execute Local filtering
    Calculate $\hat{x}_{m,t|t-1}$ by (21)
    Calculate $P_{m,t|t-1}$ by (29)
    Compute the filter gain $K_{m,t}$ in line with (37)
    Calculate $\hat{x}_{m,t|t}$ by (22)
    Compute $\bar{P}_{m,t|t}$ by (30)
  end for
  Execute fusion filtering
  Compute $P^g_{t|t}$ and $\hat{x}^g_{t|t}$ by (50)
  Update the number of tokens by (17)
  Tokens are assigned to every node by (16)
  Update $\hat{x}_{m,t|t}$ and $\bar{P}_{m,t|t}$ by (51)
end for

Noting such a fact:

$$\left(P^g_{t|t}\right)^{-1} = \sum_{m=1}^{l} \bar{P}^{-1}_{m,t|t},$$

one derives that

$$\begin{aligned}
&\mathbb{E}\left\{(x_t - \hat{x}^g_{t|t})(x_t - \hat{x}^g_{t|t})^T\right\} \\
=&P^g_{t|t}\mathbb{E}\left\{\left(\sum_{m=1}^{l} \bar{P}^{-1}_{m,t|t}x_t - \sum_{m=1}^{l} \bar{P}^{-1}_{m,t|t}\hat{x}_{m,t|t}\right)\left(\sum_{m=1}^{l} \bar{P}^{-1}_{m,t|t}x_t - \sum_{m=1}^{l} \bar{P}^{-1}_{m,t|t}\hat{x}_{m,t|t}\right)^T\right\} P^g_{t|t} \\
=&P^g_{t|t}\mathbb{E}\left\{\sum_{m=1}^{l} \bar{P}^{-1}_{m,t|t}\left(x_t - \hat{x}_{m,t|t}\right)\sum_{m=1}^{l}(x_t - \hat{x}_{m,t|t})^T\bar{P}^{-1}_{m,t|t}\right\} P^g_{t|t}.
\end{aligned}$$

According to (49), one further has

$$\bar{P}^{-1}_{m,t|t} = \alpha_m (P^g_{t|t})^{-1}, \tag{53}$$

which indicates that

$$\begin{aligned}
&\mathbb{E}\left\{(x_t-\hat{x}^g_{t|t})(x_t-\hat{x}^g_{t|t})^T\right\}\\
=&P^g_{t|t}\mathbb{E}\left\{\sum_{m=1}^{l}\alpha_m(P^g_{t|t})^{-1}\left(x_t-\hat{x}_{m,t|t}\right)\sum_{m=1}^{l}(x_t-\hat{x}_{m,t|t})^T\alpha_m(P^g_{t|t})^{-1}\right\}P^g_{t|t}\\
=&\mathbb{E}\left\{\sum_{m=1}^{l}\alpha_m\left(x_t-\hat{x}_{m,t|t}\right)\sum_{m=1}^{l}\alpha_m(x_t-\hat{x}_{m,t|t})^T\right\}\\
=&\mathbb{E}\left\{\sum_{m=1}^{l}\sum_{s=1}^{l}\alpha_m\alpha_s\left(x_t-\hat{x}_{m,t|t}\right)\left(x_t-\hat{x}_{s,t|t}\right)^T\right\}.
\end{aligned}\tag{54}$$

By resorting to lemma 2 in [41], one derives

$$\begin{aligned}
&\mathbb{E}\left\{(x_t-\hat{x}^g_{t|t})(x_t-\hat{x}^g_{t|t})^T\right\}\\
=&\mathbb{E}\left\{\sum_{m=1}^{l}\sum_{s=1}^{l}\alpha_m\alpha_s\left(x_t-\hat{x}_{m,t|t}\right)\left(x_t-\hat{x}_{s,t|t}\right)^T\right\}\\
\leq&\mathbb{E}\left\{\frac{1}{2}\sum_{m=1}^{l}\sum_{s=1}^{l}\alpha_m\alpha_s\left[\left(x_t-\hat{x}_{m,t|t}\right)\left(x_t-\hat{x}_{m,t|t}\right)^T+(x_t-\hat{x}_{s,t|t})(x_t-\hat{x}_{s,t|t})^T\right]\right\}\\
=&\sum_{m=1}^{l}\alpha_m\sum_{m=1}^{l}\alpha_m\mathbb{E}\left\{\left(x_t-\hat{x}_{m,t|t}\right)\left(x_t-\hat{x}_{m,t|t}\right)^T\right\}\\
=&\sum_{m=1}^{l}\alpha_m\sum_{m=1}^{l}\alpha_m P_{m,t|t}\\
\leq&\sum_{m=1}^{l}\alpha_m\sum_{m=1}^{l}\alpha_m\bar{P}_{m,t|t}\\
=&\sum_{m=1}^{l}\alpha_m P^g_{t|t}\\
=&P^g_{t|t}.
\end{aligned}\tag{55}$$

Now, the proof is complete. □

Remark 6. *The FTKFF scheme is proposed for a class of discrete time-varying systems under the schedule of the DETP with token bucket specifications. This paper embodies the following significant characteristics from two viewpoints: (1) a local Tobit Kalman filter (LTKFs) is elaborately designed based on an enhanced protocol model that gives combined consideration of the impacts incurred by the DETP and token bucket specifications, where two indicator variables are used to formulate their roles; (2) a federated fusion rule is chosen by productively integrating the local estimates from LTKFs.*

4. AN ILLUSTRATION EXAMPLE

In this section, an oscillator simulation example in [10,12] is provided to showcase the effectiveness of the proposed FTKFF algorithm, under the schedule of the dynamic event-triggering with tokens buckets. The system

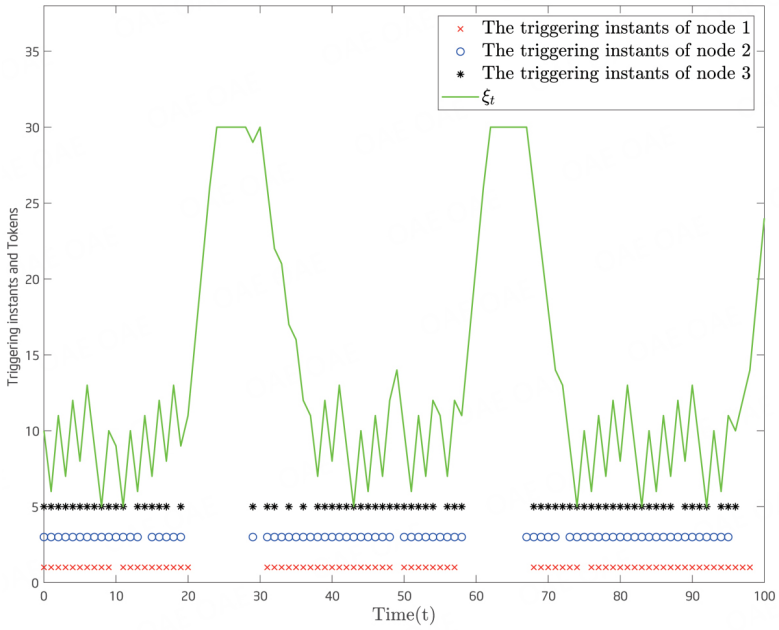


Figure 2. The dynamic change of token and triggering instants of three nodes.

parameters are chosen as

$$A_t = \begin{bmatrix} \cos(w) & \sin(w) \\ -\sin(w) & \cos(w) \end{bmatrix}, \quad B_t = \begin{bmatrix} 0.16 \\ 0.18 \end{bmatrix}, \quad w = 0.052\pi,$$
$$C_{1,t} = \begin{bmatrix} 1 & 0 \\ 0 & 1 \end{bmatrix}, C_{2,t} = \begin{bmatrix} 1 & 0 \\ 0 & 1 \end{bmatrix}, C_{3,t} = \begin{bmatrix} 1 & 0 \\ 0 & 1 \end{bmatrix}, x_0 = \begin{bmatrix} 5 \\ 0 \end{bmatrix},$$
$$Q_t = \text{diag}\{0.05, 0.05\}, \quad R_{1,t} = R_{2,t} = R_{3,t} = 0.5.$$

In terms of the token bucket formulation, choose the following parameters

$$\beta_0 = 10, \quad c_1 = c_2 = c_3 = 3, \quad b = 30, \quad g = 5.$$

The corresponding parameters in the dynamic event-triggering conditions (14) are set to be $d_t = 1.5, e_t = 2$ $\sigma_1 = 0.1, \sigma_2 = 0.2, \sigma_3 = 0.3$, $\lambda_2 = 0.2, \lambda_1 = \lambda_3 = 0.1$, $\theta_1 = \theta_2 = \theta_3 = 5$, $\eta_{1,0} = \eta_{2,0} = \eta_{3,0} = 1.5$, $a_1 = a_2 = a_3 = 1.5$, $b_1 = b_2 = b_3 = 2$. The threshold of τ_m is set to be a zero vector. In addition, set $\varepsilon_1 = \varepsilon_2 = \varepsilon_3 = \varepsilon_4 = \varepsilon_5 = 0.05, \varepsilon_i = 0.7 (i = 6, \cdots, 13)$, and $\varepsilon_{14} = 1$ for Eq. (32). By means of Theorems 2 and 3, one calculates the local filter gains $K_{i,t}$, the local estimates $\hat{x}_{m,t|t}$, and the global estimates $\hat{x}^g_{t|t}$, respectively.

The simulation results are displayed in Figures 2-10. Figure 2 depicts the utilization of communication resources under the schedule of dynamic event-triggered protocol with the token bucket specifications in the network, where the black asterisk, blue circle, and red cross are denoted as the event-triggering time instant of Node $i = 1, 2, 3$, and the green line represents the dynamic change of tokens. Figures 3 and 4 plot the censored measurements before and after the communication protocol scheduling, respectively, which reflects the role of scheduling in the information transmission. Figures 5-7 depict the local estimated values from every node and fusion estimation of state x_t. Figures 8-10 illustrate the logarithm (lg) of $e^T_{m,t|t} e_{m,t|t}$, $\text{Tr}(\bar{P}_{m,t|t})$ for every sensor, $(e^g_{t|t})^T e^g_{t|t}$, and $\text{Tr}(\bar{P}^g_{t|t})$.

In Figures 5-7, the blue curve represents the estimates from the local filters. Due to the existence of censored measurements, there exist obvious fluctuations of the local estimate, especially in the estimation of state $x^2_{3,t}$ in

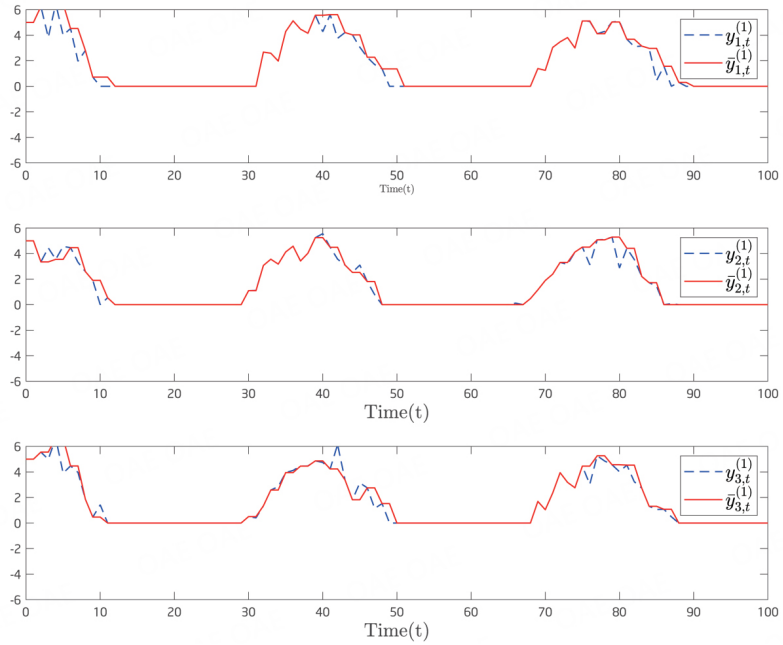


Figure 3. $y_{m,t}^{1}$ and $\bar{y}_{m,t}^{1}$.

Figure 7. However, federated fusion rules are used in this paper to obtain an optimal fusion estimate (shown by the red curve) by fully exploiting the estimates of all local filters. Meanwhile, the optimal fusion estimate can be fed back to the local filter to modify the fluctuations.

In Figures 8-10, the red curve represents the upper bound of the covariance of the local estimation error, while the yellow curve shows that of the filtering error after fusion. It can be observed that the result after fusion is better than that before fusion. Additionally, the blue dashed line represents the mean square error of the local estimator; the black curve indicates that after fusion. It can be noticed that in most cases, the mean square error of fused results is almost smaller than that of the local estimates, and the error curve is relatively smooth. This also demonstrates the superiority of the FTKFF scheme.

Thanks to the regulations of federated fusion filtering, distributed processing is achieved among sensors, where each local filter enhances the real-time performance of the system. Even in cases where a sensor fails or provides inaccurate information, the fusion center can enhance the filter's performance by utilizing data from other nodes and transmitting it to the local filter, resulting in a smoother filtered state value, which implies that the system becomes more resilient. As shown in Figures 8-10, the upper bound of the trace of the fused filtering error covariance matrix is smaller than that of a single node, and there is also an improvement in terms of mean square error. Therefore, the FTKFF scheme developed in this paper is indeed effective.

5. CONCLUSIONS

This paper has proposed a class of FTKFF schemes with censored measurements under the schedule of dynamic event-triggering with token specifications. First, the Tobit model has been used to describe the censored measurements. The token bucket traffic shaping algorithm with DETPs has been integrated to fully utilize limited communication resources. A local recursive filtering scheme has been designed for every node and an upper bound for the covariance matrix of the filtering error has been derived in the sense of trace. By minimizing this upper bound at each time step, the local filter gain has been calculated recursively. Additionally, sufficient conditions for the local filtering error to be mean-square stable are derived by analyzing the bounded-

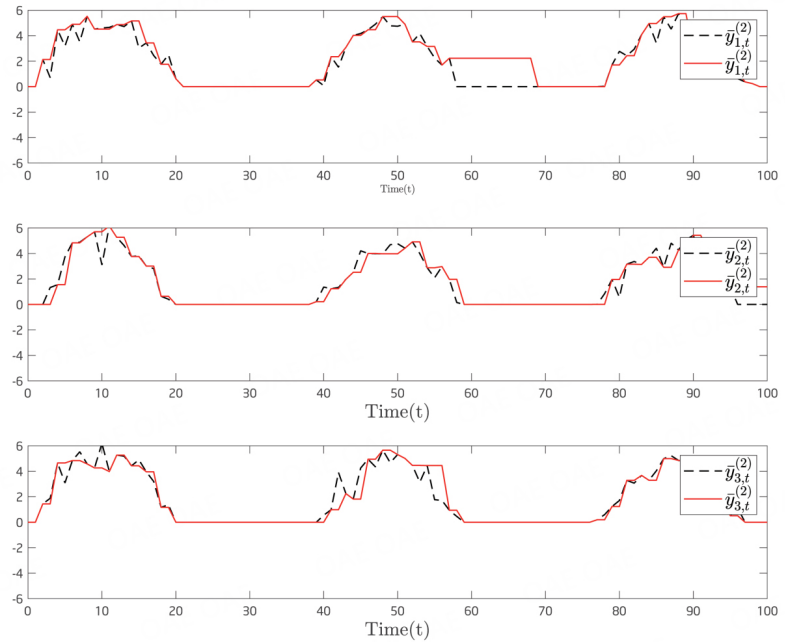


Figure 4. $y_{m,t}^2$ and $\bar{y}_{m,t}^2$.

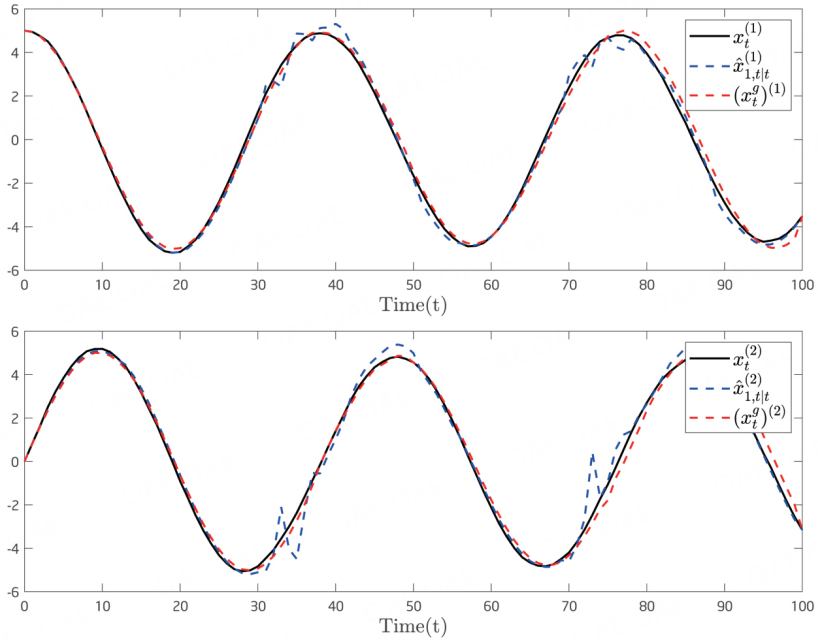


Figure 5. x_t, $\hat{x}_{1,t|t}$, and $\hat{x}_{t|t}^g$.

ness of the local filtering error covariance matrix. The fusion center processes the local filtering values at each time step via the federated fusion rule and distributes the fused results to each local filter. This comprehensive fusion filtering framework provides an effective solution to the censored measurements and information transmission protocol involving the DETP and token bucket specifications. Finally, the performance of the proposed FTKFF scheme is evaluated through a simulation example. In the future, the schemes proposed in this paper could be further developed to deal with more complicated cases such as sensor saturation, uncertain

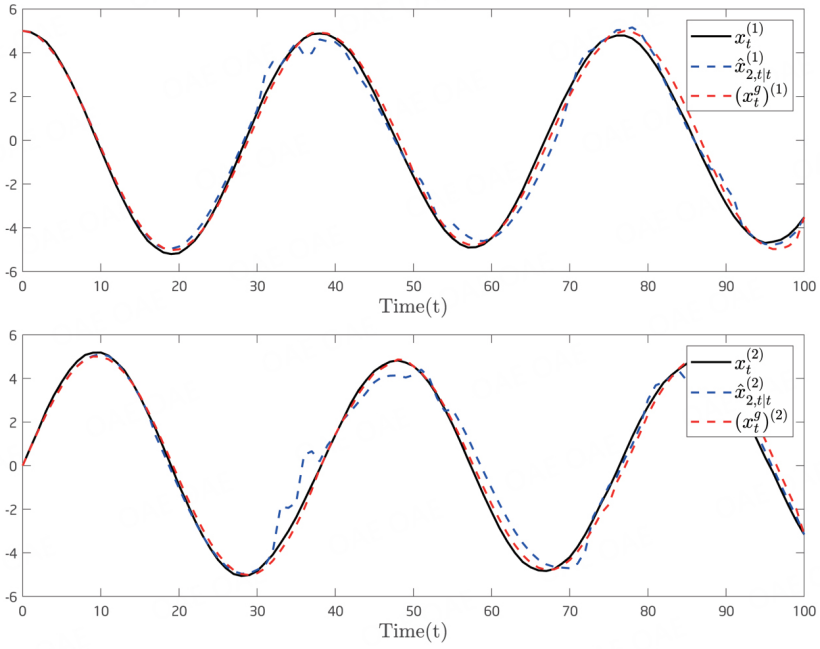


Figure 6. x_t, $\hat{x}_{2,t|t}$, and $\hat{x}_{t|t}^g$.

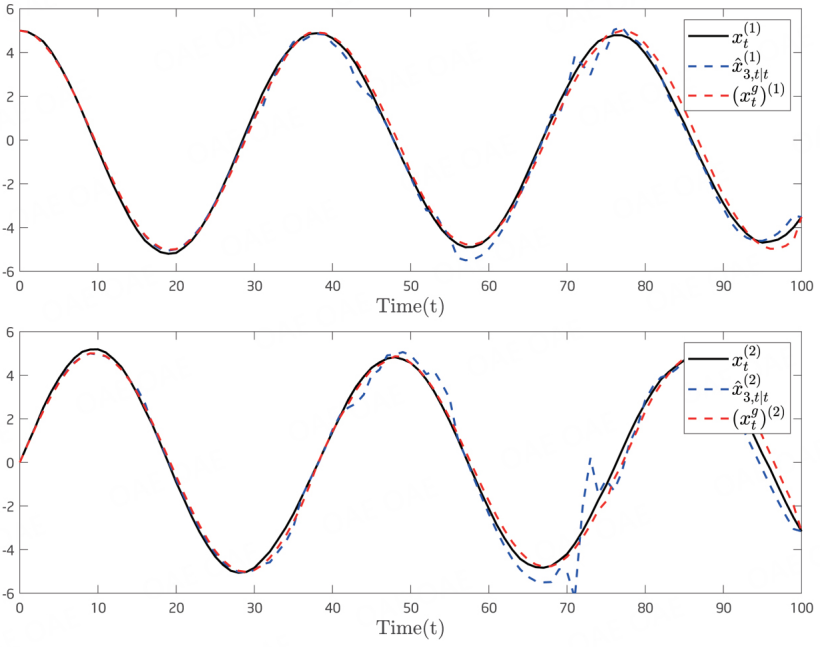


Figure 7. x_t, $\hat{x}_{3,t|t}$, and $\hat{x}_{t|t}^g$.

parameter systems, signal quantization, and time-delay systems or two-side censored measurements.

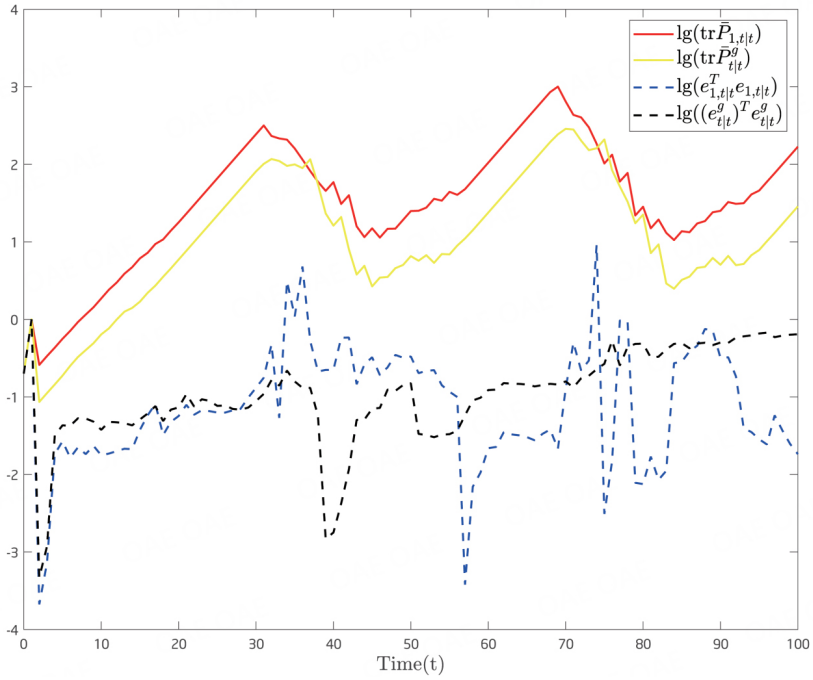


Figure 8. The logarithm of $e^T_{1,t|t}e_{1,t|t}$, $(e^g_{t|t})^T e^g_{t|t}$, $\mathrm{tr}(\bar{P}_{1,t|t})$ and $\mathrm{tr}(\bar{P}^g_{t|t})$.

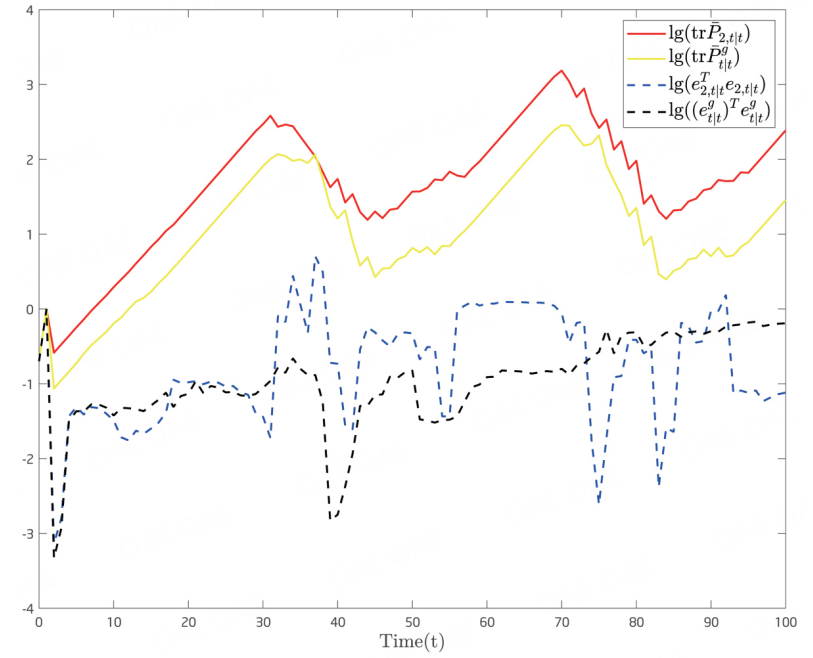


Figure 9. The logarithm of $e^T_{2,t|t}e_{2,t|t}$, $(e^g_{t|t})^T e^g_{t|t}$, $\mathrm{tr}(\bar{P}_{2,t|t})$ and $\mathrm{tr}(\bar{P}^g_{t|t})$.

DECLARATIONS

Authors' contributions

Conceptualization and manuscript drafting: Chen X
Methodology and experiment: Zhang J
Manuscript edition: Song Y
Review and supervision: Han F

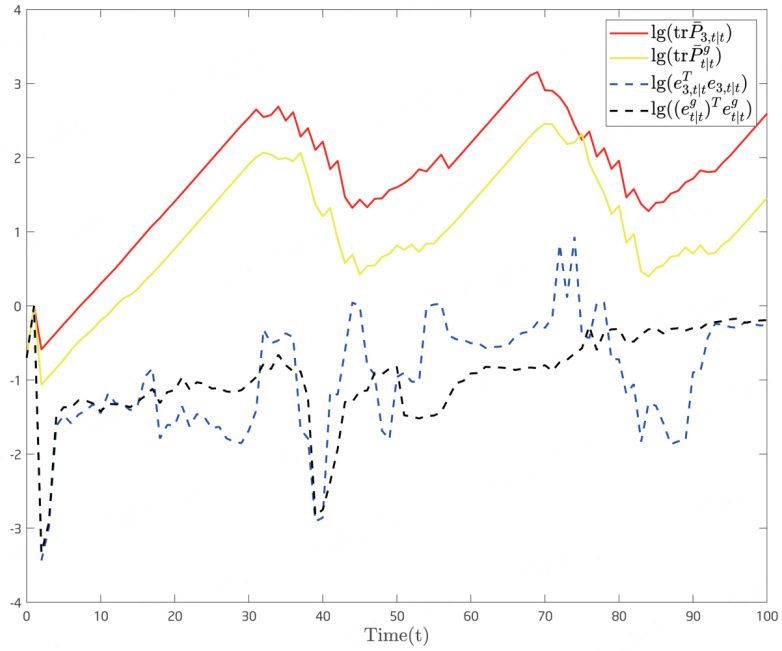


Figure 10. The logarithm of $e^{T}_{3,t|t}e_{3,t|t}$, $(e^{g}_{t|t})^{T}e^{g}_{t|t}$, $\mathrm{tr}(\bar{P}_{3,t|t})$ and $\mathrm{tr}(\bar{P}^{g}_{t|t})$.

Availability of data and materials

Not applicable.

Financial support and sponsorship

This work was supported in part by the National Natural Science Foundation of China under Grants 62073070 and U21A2019.

Conflicts of interest

Han F is a Junior Editorial Board Member of the journal *Complex Engineering Systems*, while the other authors have declared that they have no conflicts of interest.

Ethical approval and consent to participate

Not applicable.

Consent for publication

Not applicable.

Copyright

© The Author(s) 2024.

REFERENCES

1. Li W, Yang F. Information fusion over network dynamics with unknown correlations: an overview. *Int J Netw Dyn Intell* 2023;2:100003. DOI
2. Jiang L, Yan L, Xia Y, Guo Q, Fu M, Lu K. Asynchronous multirate multisensor data fusion over inreliable measurements with correlated noise. *IEEE Trans Aerosp Electron Syst* 2017;53:2427-37. DOI
3. Li S, Deng Z, Feng X, He R, Pan F. Joint parameter and state estimation for stochastic uncertain system with multivariate skew t noises. *Chinese J Aeronaut* 2022;35:69-86. DOI
4. Darvishi H, Ciuonzo D, Eide ER, Rossi PS. Sensor-fault detection, isolation and accommodation for digital twins via modular data-driven architecture. *IEEE Sensors J* 2021;21:4827-38. DOI

5. Chen B, Ho DWC, Zhang WA, Yu L. Networked fusion estimation with bounded noises. *IEEE Trans Automat Control* 2017;62:5415-21. DOI
6. Niu Y, Sheng L, Gao M, Zhou D. Dynamic event-triggered state estimation for continuous-time polynomial nonlinear systems with external disturbances. *IEEE Trans Ind Inf* 2020;17:3962-70. DOI
7. Chen L, Bo K, Lee F, Chen Q. Advanced feature fusion algorithm based on multiple convolutional neural network for scene recognition. *Comput Model Eng Sci* 2020;122:505-23. DOI
8. Yan L, Li XR, Xia Y, Fu M. Optimal sequential and distributed fusion for state estimation in cross-correlated noise. *Automatica* 2013;49:3607-12. DOI
9. Shen Y, Wang Z, Shen B, Alsaadi FE. H_∞ filtering for multi-rate multi-sensor systems with randomly occurring sensor saturations under the p-persistent CSMA protocol. *IET Control Theory Appl* 2020;14:1255-65. DOI
10. Geng H, Wang Z, Alsaadi FE, Alharbi KH, Cheng Y. Federated Tobit Kalman filtering fusion with dead-zone-like censoring and dynamical bias under the round-robin protocol. *IEEE Trans Signal Inf Process Netw* 2020;7:1-16. DOI
11. Hu Z, Hu J, Tan H, Huang J, Cao Z. Distributed resilient fusion filtering for nonlinear systems with random sensor delay under round-robin protocol. *Int J Syst Sci* 2022;53:2786-99. DOI
12. Allik B, Miller C, Piovoso MJ, Zurakowski R. The Tobit Kalman filter: an estimator for censored measurements. *IEEE Trans Control Syst Technol* 2015;24:365-71. DOI
13. Hu J, Wang Z, Gao H. Recursive filtering with random parameter matrices, multiple fading measurements and correlated noises. *Automatica* 2013;49:3440-8. DOI
14. Shen Y, Wang Z, Shen B, Han QL. Recursive state estimation for networked multirate multisensor systems with distributed time-delays under round-robin protocol. *IEEE Trans Cyber* 2020;52:4136-46. DOI
15. Li X, Dong H, Wang Z, Han F. Set-membership filtering for state-saturated systems with mixed time-delays under weighted try-once-discard protocol. *IEEE Trans Circuits Syst II* 2018;66:312-6. DOI
16. Dai D, Li J, Song Y, Yang F. Event-based recursive filtering for nonlinear bias-corrupted systems with amplify-and-forward relays. *Syst Sci Control Eng* 2024;12:2332419. DOI
17. Jiang B, Gao H, Han F, Dong H. Recursive filtering for nonlinear systems subject to measurement outliers. *Sci China Inf Sci* 2021;64:172206. DOI
18. Wang Z, Liu Z, Dai Y, Cai K. Recursive estimation for system with random transmission loss and censored measurement. *IEEE Trans Circuits Syst II* 2022;70:2281-85. DOI
19. LoumponiaS K, Tsaklidis G. Kalman filtering with censored measurements. *J Appl Stat* 2022;49:317-35. DOI
20. Han F, Wang Z, Dong H. Partial-nodes-based scalable H_∞-consensus filtering with censored measurements. In: Distributed filtering, control and synchronization. studies in systems, decision and control. Cham: Springer; 2022. DOI
21. Li W, Jia Y, Du J. Tobit Kalman filter with time-correlated multiplicative measurement noise. *IET Control Theory Appl* 2017;11:122-8. DOI
22. Allik B, Miller C, Piovoso MJ, Zurakowski R. Nonlinear estimators for censored data: A comparison of the EKF, the UKF and the Tobit Kalman filter. In: 2015 American Control Conference (ACC). Chicago, USA, 2015; pp. 5146-51. DOI
23. Allik B, Miller C, Piovoso MJ, Zurakowski R. Estimation of saturated data using the Tobit Kalman filter. In: 2014 American control conference; Portland, OR, USA, 2014; pp. 4151-6. DOI
24. Han F, Dong H, Wang Z, Li G, Alsaadi FE. Improved Tobit Kalman filtering for systems with random parameters via conditional expectation. *Signal Process* 2018;147:35-45. DOI
25. Zou L, Wang Z, Han QL, Zhou D. Moving horizon estimation for networked time-delay systems under round-robin protocol. *IEEE Trans Automat Control* 2019;64:5191-98. DOI
26. Wen C, Wang Z, Liu Q, Alsaadi FE. Recursive distributed filtering for a class of state-saturated systems with fading measurements and quantization effects. *IEEE Trans Syst Man Cyber Syst* 2018;48:930-41. DOI
27. Li Q, Wang Z, Li N, Sheng W. A dynamic event-triggered approach to recursive filtering for complex networks with switching topologies subject to random sensor failures. *IEEE Trans Neural Netw Learn Syst* 2020;31:4381-8. DOI
28. Li XR, Zhu Y, Wang J, Han C. Optimal linear estimation fusion .I. Unified fusion rules. *IEEE Trans Inf Theory* 2003;49:2192-208. DOI
29. Song E, Zhu Y, Zhou J, You Z. Optimal Kalman filtering fusion with cross-correlated sensor noises. *Automatica* 2007; 43:1450-6. DOI
30. Zhang Y, Chen B, Yu L. Fusion estimation under binary sensors. *Automatica* 2020;115:108861. DOI
31. Shen Y, Wang Z, Shen B, Alsaadi FE, Alsaadi FE. Fusion estimation for multi-rate linear repetitive processes under weighted try-once-discard protocol. *Inf Fusion* 2020;55:281-91. DOI
32. Lin H, Sun S. Optimal sequential fusion estimation with stochastic parameter perturbations, fading measurements, and correlated noises. *IEEE Trans Signal Process* 2018;66:3571-83. DOI
33. Shen B, Wang Z, Tan H, Chen H. Robust fusion filtering over multisensor systems with energy harvesting constraints. *Automatica* 2021;131:109782. DOI
34. Geng H, Liu H, Ma L, Yi X. Multi-sensor filtering fusion meets censored measurements under a constrained network environment: advances, challenges and prospects. *Int J Syst Sci* 2021;52:3410-36. DOI
35. Sun J, Shen B, Liu Y. A resilient outlier-resistant recursive filtering approach to time-delayed spatial–temporal systems with energy harvesting sensors. *ISA Trans* 2022;127:41-9. DOI
36. Hu G, Wang Z, Alsaadi FE, Hayat T. Event-based filtering for time-varying nonlinear systems subject to multiple missing measurements with uncertain missing probabilities. *Inf Fusion* 2017;38:74-83. DOI

37. Han F, Wang Z, Dong H, Alsaadi FE, Alharbi KH. A local approach to distributed H_∞-consensus state estimation over sensor networks under hybrid attacks: Dynamic event-triggered scheme. *IEEE Trans Signal Inf Process Netw* 2022;8:556-70. DOI
38. Wildhagen S, Müller MA, Allgöwer F. Predictive control over a dynamical token bucket network. *IEEE Control Syst Lett* 2019;3:859-64. DOI
39. Khashooei AB, Antunes DJ, Heemels WPMH. Output-based event-triggered control with performance guarantees. *IEEE Trans Automat Control* 2017;62:3646-52. DOI
40. Linsenmayer S, Carabelli BW, Wildhagen S, Rothermel K, Allgöwer F. Controller and triggering mechanism co-design for control over time-slotted networks. *IEEE Trans Control Netw Syst* 2021;8:222-32. DOI
41. Liu Y, Wang Z, Liang J, Liu X. Synchronization and state estimation for discrete-time complex networks with distributed delays. *IEEE Trans Syst Man Cyber Part B* 2008;38:1314-25. DOI

Zhan *et al*. *Complex Eng Syst* 2024;4:20
DOI: 10.20517/ces.2024.60

Complex Engineering Systems

Research Article

Open Access

A performance-centered design method for adaptive cruise control system

Siya Zhan[1], Congzhi Liu[2]

[1]College of Mechanical and Vehicle Engineering, Hunan University, Changsha 410082, Hunan, China.
[2]College of Mechanical and Vehicle Engineering, Chongqing University, Chongqing 400030, China.

Correspondence to: Dr. Congzhi Liu, College of Mechanical and Vehicle Engineering, Chongqing University, No. 174, Shazheng Street, Shapingba District, Chongqing 400030, China. E-mail: 15281063684@163.com; ORCID: 0000-0002-2977-1365

How to cite this article: Zhan S, Liu C. A performance-centered design method for adaptive cruise control system. *Complex Eng Syst* 2024;4:20. http://dx.doi.org/10.20517/ces.2024.60

Received: 7 Sep 2024 **First Decision:** 9 Oct 2024 **Revised:** 17 Oct 2024 **Accepted:** 1 Nov 2024 **Published:** 13 Nov 2024

Academic Editor: Hamid Reza Karimi **Copy Editor:** Fangling Lan **Production Editor:** Fangling Lan

Abstract

The adaptive cruise control (ACC) system that can take into account safety and riding comfort has attracted widespread attention. The challenges lie in designing an optimal car-following system with some predefined performance constraints based on the nonlinear dynamics, including being safe with the given certain system constraints, such as safe driving within the system input and output boundaries, also comprising the control stability. In this paper, a novel ACC design approach is proposed by transforming performance boundaries into control input and output constraints, taking into account the need for safe operation. Firstly, a nonlinear dynamics system is modeled for the ACC system based on the vehicle longitudinal dynamics. Then, a performance-centered ACC system is established based on a control barrier function and a control Lyapunov function for safety and stability concerns, respectively. Subsequently, an optimal control strategy with performance constraints is formulated and recast into a standard quadratic programming problem considering the need for stability and reliability. To validate the effectiveness of the proposed method, a real-world experiment is performed, whose results illustrate the safety performance and practical application of the ACC system.

Keywords: Adaptive cruise control, control barrier function, control Lyapunov function, quadratic programming, performance constraints.

© The Author(s) 2024. **Open Access** This article is licensed under a Creative Commons Attribution 4.0 International License (https://creativecommons.org/licenses/by/4.0/), which permits unrestricted use, sharing, adaptation, distribution and reproduction in any medium or format, for any purpose, even commercially, as long as you give appropriate credit to the original author(s) and the source, provide a link to the Creative Commons license, and indicate if changes were made.

1. INTRODUCTION

The adaptive cruise control (ACC) system has been an optional or standard equipment in commercial vehicles[1]. Its key performance is longitudinal collision avoidance and riding comfort, especially for autonomous driving vehicles[2,3]. The challenge is the potential conflicts between comfort, safety and stability, which was usually eliminated by specifying the reasonable performance function and constraint[4–6]. To guarantee driving comfort and safety, the control method with input, state or output constraints is the preferred one, such as the model predictive control (MPC)[7] and control barrier functions (CBFs)[8].

The performance balance and assurance is realized by the optimization objective and constraint condition in the MPC framework[9]. Similarly, the full state and output constraints can be actualized by the predefined CBFs or control Lyapunov functions (CLFs) of the closed-loop control system[10]. The CBF-based method also proves to be effective in the stabilization with safety problems[11], especially for the safety-critical control[12]. A safety-critical control scheme was investigated for unknown structured systems by using the CBF method[13]. An output-dependent universal barrier function was established for the consensus tracking control problem for multiagent systems with prescribed performance constraints[14]. To simultaneously consider the safety, stability, and some other performances, the CBFs and CLFs are integrated together in general, such as the quadratic programming (QP) with CBF and CLF constraints[15,16]. These attempts can balance different kinds of control performances well[17,18]. It has been shown that the optimization problem subject to the control constraints and state convergence for affine control systems can be reduced to a sequence of QPs by using CBF and CLF[15]. For example, a QP was constructed with the unification of CLF for the control objectives and CBF for the admissible state conditions, which were demonstrated on ACC and lane-keeping control problems[4,19]. Then, the optimal control input was incorporated with the performance constraints. An adaptive control scheme was developed based on the barrier Lyapunov function (BLF) for nonlinear stochastic systems with full state constraints[20]. In[21], the MPC and CBF were integrated into a complete stabilizing iteration scheme for linear discrete-time systems subject to polytopic input and state constraints. However, its calculation burden for the practical application is a huge challenge. Moreover, for the specific performance requirements of ACC systems, the safety may conflict with other performance limitations. Therefore, a performance-centered ACC strategy should be considered further for these various performances.

Effectively balancing the potential conflicts among multiple control performances, such as distance tracking, car-following stability, driving comfort, and safety of the ACC system, remains a huge challenge given system nonlinearity[22]. Furthermore, reducing computational requirements and ensuring the desired safety performance is the last important issue of its application. Thus, we explore a safe and reliable control algorithm that can guarantee safety and stability performances, which can be divided into four key parts as shown in Figure 1 and it can be constructed through four corresponding steps: dynamics modeling, CBF for the predefined safety requirement, CLF for the stability performance, and QP problem formation to solve the optimal control input. Therefore, the main contribution here is to provide a performance-centered controller considering the predefined performance requirements for the ACC systems, which lie in the following: (1) Considering the vehicle longitudinal actuator model and car-following strategy, the ACC model is characterized as a nonlinear dynamics system. For its specific model form, a CBF is designed to indirectly establish the relationship between the input and each performance constraint; and (2) An optimal control strategy with various predefined performance constraints is formulated as a standard QP problem with the CBF and CLF constraints for the safety and stability requirements, respectively. Then, a potential practical solution is obtained to enhance the control performance for ACC closed-loop systems.

The outline of this work is as follows. Section 2 establishes the ACC system model considering the input and output constraints. Section 3 describes the proposed method of the performance-centered controller. The experimental results are expressed in section 4. Finally, the main conclusions are summarized in section 5.

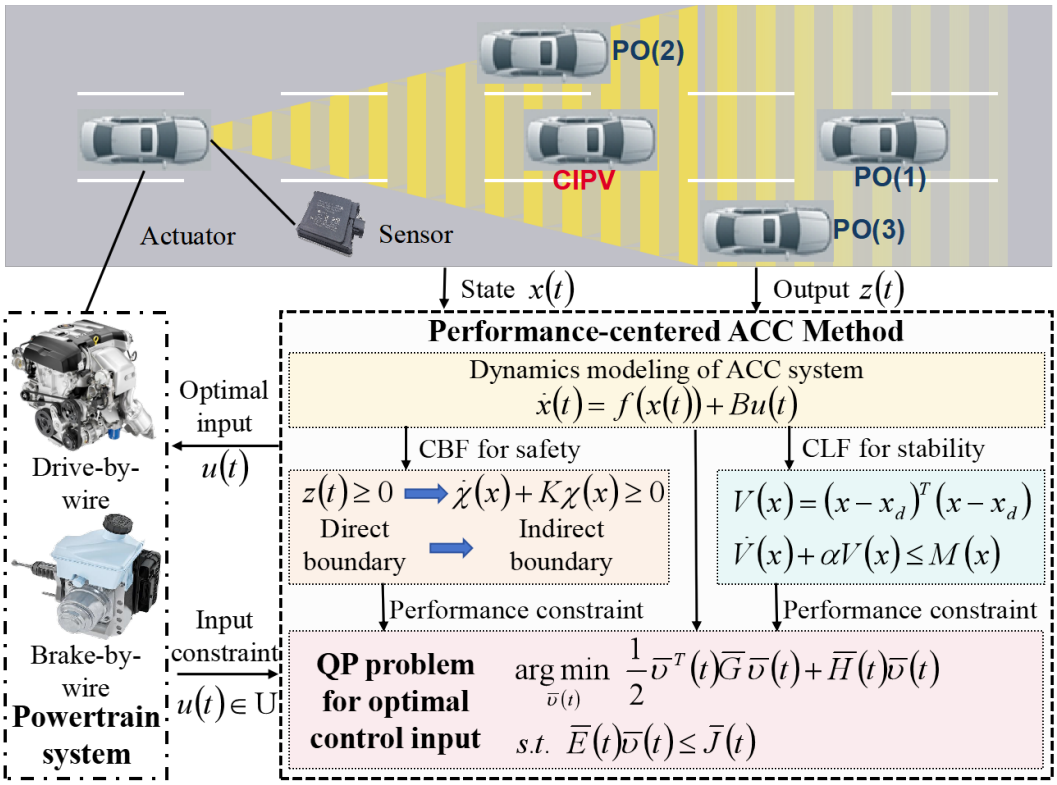


Figure 1. Frame diagram of performance-centered ACC method.

2. ACC SYSTEM MODELING

Actuator model

The actuator of the ACC system is the driving/braking-by-wire subsystem equipped on autonomous driving vehicles. The longitudinal dynamics model is to characterize the steady-state relation between the longitudinal motion and the longitudinal force of the vehicle. When the lateral and yaw motions of a vehicle are ignored, then the vehicle's longitudinal dynamics is given as

$$F_x = \delta m a_{ego} + F_{x0}, \tag{1}$$

where F_x is the total driving/braking force of a vehicle, which consists of two parts. The first one is the whole inertial force (including the rotational and translational motion resistances). The second one represents the main driving resistance which contains the rolling resistance, gradient resistance and wind drag[23], which can be given as

$$F_{x0} = \mu m g \text{sgn}(V_{ego}) \cos\theta + mg \sin\theta + \frac{C_D A}{1.632} V_{ego}^2, \tag{2}$$

where m, C_D, A are the constant weight, drag coefficient, and front face area, respectively. $\delta > 1$ is the scale factor of rotating mass to characterize the inertia of the rotating components of the chassis. $g = 9.81$ m/s^2 is the universal gravitational constant. θ is the longitudinal slope along with the driving direction of a vehicle. μ is the driving friction coefficient. V_{ego}, a_{ego} are the vehicle speed and acceleration, respectively. sgn$(\cdot)$ represents the sign function that is formed for the zero rolling resistance when the vehicle is at a standstill (i.e., $V_{ego} = 0$).

Consider the dynamics of the powertrain system as a first-order process

$$\dot{F}_x(t) = -\frac{1}{\tau} F_x(t) + \frac{1}{\tau} u(t), \tag{3}$$

where u is the external input of a driving/braking-by-wire subsystem which can be interpreted as desired driving/braking force, and τ is the time constant of a drive or brake process. Hence, the vehicle longitudinal dynamics can be characterized by the following system for the actuators:

$$\begin{aligned} &\dot{F}_x(t) = -\tfrac{1}{\tau}F_x(t) + \tfrac{1}{\tau}u(t), \\ &a_{ego} = \tfrac{1}{\delta m}F_x - \tfrac{C_D A}{1.632\delta m}V_{ego}^2 - \tfrac{1}{\delta}(\mu g \operatorname{sgn}(V_{ego})\cos\theta + g\sin\theta). \end{aligned} \tag{4}$$

Assume that the road slope and friction coefficient are slow-varying, and according to (4), the induced dynamics of acceleration can be described as:

$$\dot{a}_{ego} = -\left(\frac{1}{\tau} + \frac{C_D A V_{ego}}{0.816\delta m}\right)a_{ego} + \frac{1}{\delta m \tau}(-F_{x0} + u(t)). \tag{5}$$

Generally, the comfort performance is decided by the acceleration and jerk together, which can be indirectly judged by the input force as given in (5). Hence, the comfort constraint can be transformed into the input constraint. Then, the comfort constraint on the input should be considered and the set of control bounds is designated as follows:

$$u(t) \in \mathbb{U} \triangleq \left\{ u(t) \,\middle|\, \begin{array}{l} -c_d mg \le u(t) \le c_a mg, \\ a_{\min} \le a_{ego}(t) \le a_{\max}, \end{array} \right\}, \tag{6}$$

where the positive coefficients c_d, c_a represent the deceleration and acceleration toleration, respectively. $a_{\max}, a_{\min}$ are the acceptable maximal acceleration and deceleration, respectively.

To introduce the input regulation effect, we define

$$\begin{aligned} a_1(t) &= a_{\max} - a_{ego}(t), \\ a_2(t) &= a_{ego}(t) - a_{\min}, \end{aligned} \tag{7}$$

thus, $a_1 \ge 0, a_2 \ge 0$ is implied in the constraints (6), which can be transformed into the following performance constraints[19,24]:

$$\begin{aligned} &\dot{a}_1(t) + a_1(t) \ge 0, \\ &\dot{a}_2(t) + a_2(t) \ge 0. \end{aligned} \tag{8}$$

Then, the input constraint (6) is equivalent to

$$u(t) \in \mathbb{U} \triangleq \{u(t) : u_{\min}(t) \le u(t) \le u_{\max}(t)\}, \tag{9}$$

where

$$\begin{aligned} u_{\max} &= \min\{c_a mg, F_{x0} + \tau\delta m a_3\}, \\ u_{\min} &= \max\{-c_d mg, F_{x0} + \tau\delta m a_4\}, \\ a_3 &= a_{\max} - \left(1 - \tfrac{C_D A V_{ego}}{0.816\delta m} - \tfrac{1}{\tau}\right)a_{ego}, \\ a_4 &= a_{\min} - \left(1 - \tfrac{C_D A V_{ego}}{0.816\delta m} - \tfrac{1}{\tau}\right)a_{ego}. \end{aligned}$$

Car-following model

The main objective of the car-following mode of ACC systems is to follow the lead car with a desired safety distance which is usually established as the following headway spacing policy[25–27]:

$$d_{rel,d}(t) = d_0 + T_h V_{ego}(t), \tag{10}$$

where T_h is the time headway and d_0 is the standstill distance.

Define the spacing state for the car-following process as

$$\boldsymbol{x}(t) = \begin{bmatrix} e_d(t) \\ e_v(t) \\ a_{ego}(t) \end{bmatrix} = \begin{bmatrix} d_{rel}(t) - d_{rel,d}(t) \\ V_{obj}(t) - V_{ego}(t) \\ a_{ego}(t) \end{bmatrix}, \tag{11}$$

where d_{rel} is the relative distance between the lead car and ego car. V_{obj} is the speed of the tracked object. Then, we use the following three-order nonlinear system representation of the longitudinal dynamics for car-following characteristics [28,29]:

$$\dot{\boldsymbol{x}}(t) = \boldsymbol{f}(\boldsymbol{x}(t)) + Bu(t), \tag{12}$$

where $\boldsymbol{f}(\boldsymbol{x}(t)) = [f_1, f_2, f_3]^T$ exhibits the local Lipschitz continuity and

$$\begin{aligned} f_1 &= V_{obj}(t) - V_{ego}(t) - T_h a_{ego}(t), \\ f_2 &= a_{obj}(t) - a_{ego}(t), \\ f_3 &= -\left(\frac{1}{\tau} + \frac{C_D A V_{ego}}{0.816\delta m}\right) a_{ego} - \frac{1}{\delta m \tau} F_{x0}, \\ B &= [0, 0, \tfrac{1}{\delta m \tau}]^T, \end{aligned}$$

where a_{obj} is the acceleration of the tracked object.

Assume that the system state trajectory is predictable within the neighborhood of its desired state $\boldsymbol{x}_d = 0$ and $\dot{\boldsymbol{x}}_d = 0$ during a short control interval if the ego vehicle is driving. When the vehicle is at a standstill that $V_{ego} = 0, a_{ego} = 0$ and it wants to start driving, we introduce an offset into the desired state as $\boldsymbol{x}_d = [0, 0, a_{ref}]^T$, where a_{ref} is the referenced acceleration during the start process, which is motivated by the structure of matrix B and aims to avoid the undesirable case that the ego vehicle remains in its current standstill state and starts unsuccessfully.

Performance-centered design requirement

The safety constraint is the primary performance evaluation. Generally, a driver cannot easily drive on a narrow road at high speed or adjacent to an obstacle. Similarly, autonomous driving requires a speed reduction on a narrow road to improve the accuracy of the vehicle control. To drive more safely, the target speed should be determined by considering the environment information, such as the proximity of obstacles and collision probabilities. Moreover, the ego vehicle should maintain a safe car-following distance to avoid any potential collisions.

Hence, we define the controlled output as the speed and safe distance evaluations for the safety consideration:

$$\boldsymbol{z}(t) = \begin{bmatrix} d_{rel}(t) - d_{safe}(t) \\ V_{\text{lim}} - V_{ego}(t) \end{bmatrix}, \tag{13}$$

and the output limitations are considered as $\boldsymbol{z}(t) \geq 0$, where $V_{\text{lim}} = \min\{V_{safe}, V_{set}\}$ and $d_{safe}, V_{safe}, V_{set}$ are the safe distance, safe speed and target speed provided by the driver or autonomous driving system, respectively. Assume that $\dot{V}_{\text{lim}} = 0$ within a short time interval and $d_{safe} = 0.5d_0 + T_{safe}V_{ego}(t)$ with the safe headway as T_{safe} to prevent any potential collisions. Then, the safety performance constraint for the output is expressed as

$$\boldsymbol{z}(t) \in \mathbb{Z} \triangleq \{\boldsymbol{z}(t) \geq 0\}. \tag{14}$$

Remark 1 *If the vehicle is driving on a curved road, its safe speed satisfies the following dynamics constraint[30]:*

$$\begin{aligned} a_y &= |\kappa| V_{ego}^2 \le a_{y,\max}, \\ \omega &= |\kappa| V_{ego} \le \omega_{\max}, \end{aligned} \tag{15}$$

where κ and ω are the curvature of the road and the vehicle yaw rate which can be provided by the autonomous driving system and the chassis, respectively. $a_{y,\max}, \omega_{\max}$ are the maximal lateral acceleration and yaw rate to guarantee vehicle stability and safety during a curved road. Hence, a safe speed can be obtained as

$$V_{safe} = \min\left\{\sqrt{\frac{a_{y,\max}}{|\kappa|}}, \frac{\omega_{\max}}{|\kappa|}\right\}. \tag{16}$$

Then, vehicle safety during a curved road is also guaranteed based on the performance constraint (14).

Definition 1 *The set $\mathbb{Z}$ defined by (14) is considered forward invariant for the system (12) if all system output trajectories originating from an initial output $\boldsymbol{z}(0) \in \mathbb{Z}$ remain confined within the set $\mathbb{Z}$ for any $t \ge 0$[31].*

Lemma 1 *If there exits a continuously differentiable CBF $\boldsymbol{\chi}(\boldsymbol{x}) : \mathbb{Z} \to \mathbb{R}$, then the set $\mathbb{Z}$ is forward invariant for the system (12)[19].*

Hence, the ACC system aims to employ an input $u(t) \in \mathbb{U}$ with the output limitation $\boldsymbol{z}(t) \in \mathbb{Z}$ while ensuring that the tracking error satisfies $\|\boldsymbol{x} - \boldsymbol{x}_d\| \le \varepsilon$, where ε is a positive constant. A time-varying CBF is formulated to depict an invariant set for the controlled output of ACC systems (12):

$$\boldsymbol{\chi}(\boldsymbol{x}) = \exp\left\{\frac{\boldsymbol{z}(t)}{\|\boldsymbol{x}\| + r} - \Delta\right\} - 1, \tag{17}$$

where $r > 0, \Delta > 0$ are constants. Then, the performance constraint (14) can be guaranteed by $\chi(\boldsymbol{x}) \ge 0$. Similarly to the input constraint (8), there exists a positive constant K such that the following inequality holds for $\forall \boldsymbol{x}$ [19,24]:

$$\dot{\boldsymbol{\chi}}(\boldsymbol{x}) + K\boldsymbol{\chi}(\boldsymbol{x}) \ge 0. \tag{18}$$

Remark 2 *It is difficult to establish the direct mapping relationship between the input constraint and safety boundaries (defined as $\boldsymbol{z}(t) \ge 0$). Then, it motivates us to find an indirect way to recast the safety requirement $\boldsymbol{z}(t) \ge 0$ into an alternative form as the CBF $\boldsymbol{\chi}(\boldsymbol{x}(0)) \ge 0$, where safety is implicated in its definition (17). According to the performance constraint of the CBF (18), we can have*

$$\boldsymbol{\chi}(\boldsymbol{x}(t)) \ge \boldsymbol{\chi}(\boldsymbol{x}(0)) \exp(-Kt).$$

If the vehicle is safe at the initial sampling, i.e., $\boldsymbol{\chi}(\boldsymbol{x}(0)) \ge 0$, then it means $\boldsymbol{\chi}(\boldsymbol{x}(t)) \ge 0$ for any $t > 0$. However, an activation condition is usually adopted in the ACC system so that the initial safe state of the vehicle can be guaranteed. Hence, a predefined assumption is given here. Then, its safety performance can be maintained based on the CBF condition (18).

Assumption 1 *The initial state of the vehicle is safe when the ACC system is just activated, that is, $\boldsymbol{\chi}(\boldsymbol{x}(0)) \ge 0$.*

Then, the set (14) is forward invariant for (12) based on the definition 1, Lemma 1 and Assumption 1. According to the norm definition $\|\boldsymbol{x}\| = \sqrt{e_d^2(t) + e_v^2(t) + a_{ego}^2(t)}$, we have

$$\dot{\boldsymbol{\chi}}(\boldsymbol{x}) = (\boldsymbol{\chi}(\boldsymbol{x}) + 1) \odot \frac{\dot{\boldsymbol{z}}(\|\boldsymbol{x}\|^2 + r\|\boldsymbol{x}\|) - \boldsymbol{z}\boldsymbol{x}^T(\boldsymbol{f} + Bu)}{(\|\boldsymbol{x}\| + r)^2\|\boldsymbol{x}\|}, \tag{19}$$

where $\odot$ represents the Hadamard product and

$$\dot{\boldsymbol{z}} = C\boldsymbol{x}, C = \begin{bmatrix} 0 & 1 & -T_{safe} \\ 0 & 0 & -1 \end{bmatrix}.$$

According to (18) and (19), it yields

$$(\boldsymbol{\chi}(\boldsymbol{x})+1)\odot\frac{\boldsymbol{z}\boldsymbol{x}^{T}B}{(\|\boldsymbol{x}\|+r)^{2}\|\boldsymbol{x}\|}u(t)\leq(\boldsymbol{\chi}(\boldsymbol{x})+1)\odot\frac{C\boldsymbol{x}(\|\boldsymbol{x}\|^{2}+r\|\boldsymbol{x}\|)-\boldsymbol{z}\boldsymbol{x}^{T}\boldsymbol{f}}{(\|\boldsymbol{x}\|+r)^{2}\|\boldsymbol{x}\|}+K\boldsymbol{\chi}(\boldsymbol{x}). \tag{20}$$

To avoid that the denominator of the differential function $\dot{\boldsymbol{\chi}}(\boldsymbol{x})$ equals to zero, a simplified approximation $\|\boldsymbol{x}\|\approx\|\boldsymbol{x}\|+r$ with a small enough positive number $r=0.01$. Thus, the inequality (20) can be directly recast into the following constraint according to its safety-guaranteed implication:

$$(\boldsymbol{\chi}(\boldsymbol{x})+1)\odot\frac{\boldsymbol{z}\boldsymbol{x}^{T}B}{(\|\boldsymbol{x}\|+r)^{3}}u(t)\leq(\boldsymbol{\chi}(\boldsymbol{x})+1)\odot\frac{C\boldsymbol{x}(\|\boldsymbol{x}\|^{2}+r\|\boldsymbol{x}\|)-\boldsymbol{z}\boldsymbol{x}^{T}\boldsymbol{f}}{(\|\boldsymbol{x}\|+r)^{3}}+K\boldsymbol{\chi}(\boldsymbol{x}). \tag{21}$$

3. PERFORMANCE-CENTERED CONTROLLER

Convergence analysis

Lemma 2 *A continuously differentiable function $V(\boldsymbol{x})$ can be regarded as a CLF that ensures exponential stability of the system (12) if there exist constants $a>0,b>0,c>0$ such that*[32]

$$a\|\boldsymbol{x}\|^{2}\leq V(\boldsymbol{x})\leq b\|\boldsymbol{x}\|^{2},\forall\boldsymbol{x}$$

and

$$\inf_{u\in\mathbb{U}}\left[\dot{V}(\boldsymbol{x})+cV(\boldsymbol{x})\right]\leq 0.$$

We define a CLF for the exponential stability of the ACC system (12) according to the Lemma 2

$$V(\boldsymbol{x})=(\boldsymbol{x}-\boldsymbol{x}_{d})^{T}(\boldsymbol{x}-\boldsymbol{x}_{d})\geq 0, \tag{22}$$

then, there exist positive numbers $\beta,\gamma>0$ such that the following inequality holds for $\forall\boldsymbol{x}$

$$\beta\|\boldsymbol{x}-\boldsymbol{x}_{d}\|^{2}\leq V(\boldsymbol{x})\leq\gamma\|\boldsymbol{x}-\boldsymbol{x}_{d}\|^{2}. \tag{23}$$

Thus, there exist $\alpha>0$ and sufficiently large positive number M such that[32]

$$\dot{V}(\boldsymbol{x})+\alpha V(\boldsymbol{x})\leq M(\boldsymbol{x}), \tag{24}$$

where $M(\boldsymbol{x})\geq 0$ denotes the relaxation of the decision variable. According to the Comparison Lemma[33], it yields that

$$V(\boldsymbol{x}(t))\leq\frac{M}{\alpha}+\left(V(\boldsymbol{x}(0))-\frac{M}{\alpha}\right)\exp\left(-\alpha t\right). \tag{25}$$

According to (23) and (25), it yields

$$\|\boldsymbol{x}-\boldsymbol{x}_{d}\|\leq\sqrt{\frac{1}{\alpha\beta}\left[M+(\alpha V(\boldsymbol{x}(0))-M)\exp(-\alpha t)\right]}. \tag{26}$$

Remark 3 *Define $V_{sup}=\frac{M}{\alpha}+\left(V(\boldsymbol{x}(0))-\frac{M}{\alpha}\right)\exp\left(-\alpha t\right)$, it is clear that $0\leq\min\left\{\frac{M}{\alpha},V(\boldsymbol{x}(0))\right\}\leq V_{sup}\leq\max\left\{\frac{M}{\alpha},V(\boldsymbol{x}(0))\right\}$. Define $\varepsilon=\max\left\{\sqrt{\frac{M}{\alpha\beta}},\sqrt{\frac{V(\boldsymbol{x}(0))}{\beta}}\right\}$, then, we can obtain that $\|\boldsymbol{x}-\boldsymbol{x}_{d}\|\leq\varepsilon$, implying that the system state trajectory remains within the neighborhood of the desired state. The state deviations will be gradually eliminated if there exist some state mutations or bounded disturbances induced by the random driving behaviors of the lead vehicle, i.e., the car-following stability. Hence, the CLF restriction (24) can be employed as a lenient CLF to attain the convergence of the tracking error.*

Performance-centered controller design

The objective of ACC is to design an optimal controller with the input constraint $u(t) \in \mathbb{U}$, output limitation $\boldsymbol{z}(t) \in \mathbb{Z}$ replaced by $\chi(\boldsymbol{x}) \geq 0$ and CLF restriction (24), which possesses the notable advantage of the ability to harmonize various control performances. To achieve this goal and inspired by[15], the optimal control strategy for the ACC system is defined as the energy consumption:

$$\min_{u(t),M(\boldsymbol{x})} \int_0^t [\lambda_1(u(\tau) - F_{x0}(\tau))^2 + \lambda_2 M^2(\boldsymbol{x}(\tau)) - 2(\lambda_3 e_d(\tau) + \lambda_4 e_v(\tau))u(\tau)]d\tau, \tag{27}$$

where the three cost functions represent the energy expenditure of control input and riding comfort during the deceleration and acceleration process, the punishment of the relaxation variable, and the car-following performance trend cost, respectively. $\lambda_i > 0$ are the weight coefficients. Define the optimization variable as $\boldsymbol{\upsilon}(t) = [u(t), M(\boldsymbol{x})]^T$. The optimal objective (27) can be recast to a sequence of instantaneous optimization problems within each sufficiently small sampling interval as follows:

$$\min_{\boldsymbol{\upsilon}(t)} \frac{1}{2}\boldsymbol{\upsilon}^T(t)G\boldsymbol{\upsilon}(t) + H\boldsymbol{\upsilon}(t), \tag{28}$$

where $G = diag\{\lambda_1, \lambda_2\}, H = [-\lambda_1 F_{x0}(t) - \lambda_3 e_d(t) - \lambda_4 e_v(t), 0]$. Moreover, it should satisfy the input constraint (9), performance constraint (20) and (24), which can be transformed into the linear matrix constraint as:

$$E\boldsymbol{\upsilon}(t) \leq J, \tag{29}$$

where

$$E = \begin{bmatrix} 1 & 0 \\ -1 & 0 \\ \vartheta_1 & 0 \\ 0 & -1 \\ 2(\boldsymbol{x} - \boldsymbol{x}_d)^T B & -1 \end{bmatrix}, J = \begin{bmatrix} u_{\max}(t) \\ -u_{\min}(t) \\ \vartheta_2 \\ 0 \\ \vartheta_3 \end{bmatrix},$$

$$\vartheta_1 = (\boldsymbol{\chi}(\boldsymbol{x}) + 1) \odot \frac{z\boldsymbol{x}^T B}{(\|\boldsymbol{x}\|+r)^3},$$

$$\vartheta_2 = (\boldsymbol{\chi}(\boldsymbol{x}) + 1) \odot \frac{C\boldsymbol{x}(\|\boldsymbol{x}\|^2 + r\|\boldsymbol{x}\|) - z\boldsymbol{x}^T \boldsymbol{f}}{(\|\boldsymbol{x}\|+r)^3} + K\boldsymbol{\chi}(\boldsymbol{x}),$$

$$\vartheta_3 = -2(\boldsymbol{x} - \boldsymbol{x}_d)^T \boldsymbol{f}(\boldsymbol{x}(t)) - \alpha(\boldsymbol{x} - \boldsymbol{x}_d)^T(\boldsymbol{x} - \boldsymbol{x}_d).$$

Therefore, the optimal control strategy for the ACC system at each sampling time can be solved by the following QP problem:

$$\begin{aligned} &\arg\min_{\boldsymbol{\upsilon}(t)} \ \tfrac{1}{2}\boldsymbol{\upsilon}^T(t)G\boldsymbol{\upsilon}(t) + H(t)\boldsymbol{\upsilon}(t), \\ &s.t. \ E(t)\boldsymbol{\upsilon}(t) \leq \boldsymbol{J}(t). \end{aligned} \tag{30}$$

In some unusual circumstances, the car-following stability, comfort and safety performances may conflict, leading to a null set due to various system limitations, as given by

$$\{\upsilon(t) : E\boldsymbol{\upsilon}(t) \leq \boldsymbol{J}\} = \varnothing. \tag{31}$$

To avoid the QP problem (30) becoming infeasible and to guarantee its feasibility, a new relaxation variable $\boldsymbol{N} \geq 0$ is introduced and the QP problem (30) is recast to

$$\begin{aligned} &\arg\min_{\boldsymbol{\upsilon}(t),\boldsymbol{N}(t)} \ \tfrac{1}{2}\boldsymbol{\upsilon}^T(t)G\boldsymbol{\upsilon}(t) + \tfrac{1}{2}\lambda_5\boldsymbol{N}^T(t)\boldsymbol{N}(t) + H(t)\boldsymbol{\upsilon}(t), \\ &s.t. \ E(t)\boldsymbol{\upsilon}(t) \leq \boldsymbol{J}(t) + \boldsymbol{N}(t), \end{aligned} \tag{32}$$

which can be transformed into the standard form as

$$\begin{aligned} &\arg\min_{\bar{\boldsymbol{\upsilon}}(t)} \ \tfrac{1}{2}\bar{\boldsymbol{\upsilon}}^T(t)\bar{G}\bar{\boldsymbol{\upsilon}}(t) + \bar{H}(t)\bar{\boldsymbol{\upsilon}}(t), \\ &s.t. \ \bar{E}(t)\bar{\boldsymbol{\upsilon}}(t) \leq \bar{\boldsymbol{J}}(t), \end{aligned} \tag{33}$$

Table 1. Parameters and their effects of ACC system

Parameters	Effects description	Assignment strategy
$d_0 = 4$ m	Standstill distance	Statistics of car-following distance
$T_h = 1.2$ s, $T_{safe} = 0.6$ s	Time headway	Reaction time of driver refereed to RSS model [35]
$a_{ref} = 2$ m/s^2	Referenced acceleration	Empirical value of a comfortable start process
$a_{\max} = 2.5$ m/s^2 $a_{\min} = -5$ m/s^2	Maximal acceleration and deceleration	Acceptable comfort and safety
$c_d = c_a = 0.3$	Deceleration and acceleration toleration	Acceptable comfort and safety
$\tau = 0.18$	Time constant of chassis system	Measured value
$r = 0.01$	Constant of CBF to avoid zero denominator	Small enough positive number
$\Delta = 0.1$	Constant of CBF to guarantee safety	Very small positive number after some attempts
$K = 0.5$	Constant of CBF condition to guarantee safety	Safety condition after some attempts
$\alpha = 10$	Constant of CLF to guarantee convergence	Sufficiently large to guarantee tracking performance
$\lambda_1 = 1, \lambda_2 = 10$ $\lambda_3 = \lambda_4 = 1000, \lambda_5 = 500$	Weight coefficients of optimization objective	Magnitudes and significance of cost function

where $\bar{H}(t) = [H(t), \mathbf{0}], \bar{G} = G \bigoplus \lambda_5 I_7$ and I_7 is an identity matrix with the dimension as 7×7. The optimization variable as $\bar{\boldsymbol{v}}(t) = [u(t), M(\boldsymbol{x}), \boldsymbol{N}^T(t)]^T$. The matrices are

$$\bar{E}(t) = \begin{bmatrix} E(t) & -I \\ 0 & -I \end{bmatrix}, \bar{J}(t) = \begin{bmatrix} J(t) \\ 0 \end{bmatrix}.$$

The QP problem (33) can be solved using the interior-point method by the existing solver or toolbox [34], where the real-time solving process is omitted here.

Remark 4 *The feasibility of the proposed method with various performance constraints is guaranteed based on the penalty variable $\boldsymbol{N}(t)$. Then, the safety and stability performances established by the CBF and CLF can be considered simultaneously and their potential conflict is handled successfully. Moreover, the optimal control input is incorporated with the predefined performance limitations as the established QP problem (33), which is the key to the application of this performance-centered method.*

Remark 5 *A single vehicle ACC model (12) is considered in this paper, which can be extended to the consensus tracking control problem of cooperative adaptive cruise control (CACC) by modifying the ACC model (12) to a CACC model. For some other multiagent systems similar to [6,14], it is also available by using the reconstructed dynamic model and prescribed performance constraints.*

4. EXPERIMENTAL VERIFICATION

The whole parameters and their effects are listed in Table 1. After plenty of attempts and comparative analysis, and also according to practical experiences, the ACC performance parameters and controller parameters are given as Table 1. Then, the QP problem (33) can be solved for its real-time application. According to the magnitudes of the cost function (27), we can select the weights $\lambda_1 = 1, \lambda_2 = 10$. Based on the stability analysis of the system (12) and the characteristic of $\boldsymbol{f}, B$, the weights $\lambda_3 = \lambda_4 = 1,000$ are adopted. As safety is a key constraint, the weight $\lambda_5 = 500$ is selected.

To verify the performance of the proposed method, the field tests are conducted by a modified HAVAL SUV with drive/brake/steer-by-wire systems as shown in Figure 2, and the specification of the vehicle is given in Table 2. The vehicle is equipped with sensors such as a global navigation satellite system (GNSS)/inertial navigation system (INS) with two antennas, a yaw rate gyro equipped near the vehicle centroid, a Mobileye 560 camera installed behind the windshield, a Delphi Electronically Scanning Radar (ESR) and five Rear and Side Detection System (RSDS) Radars equipped around the car. The decision and control platform is established based on a Dspace Micro Autobox II placed in the trunk. Both signals are transmitted by the CAN-bus. The Dspace Micro Autobox II acts as the real-time controller, which receives the feedback information from the

Table 2. Experimental vehicle specifications

Item	Description
Total mass	1,700 kg
Scale factor of rotating mass	1.1
Distance from center of gravity to front axle	1.2 m
Distance from center of gravity to rear axle	1.48 m
Vehicle width	1.86 m
Vehicle length	4.6 m
Drag coefficient	0.389
Front face area	2.86 m^2

sensors and vehicle, and sends the control command to the chassis system. Then, a closed-loop ACC system is established. Because the whole perception, decision, planning and control algorithms (including the proposed method) are implemented in one embedded controller with the sampling period as 10 ms, the real-time performance is implied by the following real car experiments. To make a more intuitive comparison, three test scenarios are adopted and they are implemented in the same microprocessor with the same sampling period of 10 ms, where the first two experiments are performed by the proposed method and the third one is executed by the baseline method.

Test scenario I

To demonstrate the performances of the proposed method, a typical urban test scenario is first performed under a dynamic environment to verify the controller capabilities, which can present the results for the most relevant scenarios. To achieve a convenient and reasonable verification and enhance the applicability to real-world scenarios, the experiment is performed in a real road environment. The relative distance and safe distance of the preceding vehicle are shown in Figure 3. At the beginning (near 60 s), the car ahead is fast decelerated with the deceleration -5 m/s^2. Then, the controlled vehicle is smoothly decelerated with the maximal deceleration -1.54 m/s^2 up to the minimal speed 0.61m/s, where the actual distance is bigger than the safe distance as the partial enlarged detail in Figure 3. It can be seen that the safe car following performance can be guaranteed by the CBF (17) and its constraint condition (18). It is necessary to emphasize that a specific distance of 200 m represents a scenario in which there is no object in front of the ego vehicle. On the other hand, the sudden changing distance represents the scenarios in which there are multiple cut-in or cut-out objects, which implies that there exist some disturbances in this real road environment. According to the results, the safety performance and applicability are verified by real-world scenarios.

In this scenario, the speed limitation is $V_{\text{lim}} = 23.61$ m/s. The corresponding input, acceleration and speed are shown in Figure 4. It is clear that the constraint on the input (6) is satisfied. Moreover, the safety performance constraint (14) is guaranteed based on the CBF framework according to Figure 3 and Figure 4. According to the smooth acceleration responses, excellent riding comfort will be obtained, meaning that the proposed optimal control strategy (27) is reasonable for the ACC system. Because the limited velocity V_{lim} does not ensure safety, the optimal input is obtained by solving the QP problem and then applied to the ACC system. Then, a safe and stable ACC performance is achieved by the proposed QP-based method.

The CLF and its relaxation are shown in Figure 5, which implies that the QP problem (33) can be solved in real time according to the Figure 4 and Figure 5. Moreover, convergence is obtained during every steady car-following process, although there will be some drastic fluctuations when a cut-in or cut-out object occurs. On the contrary, the CLF will be convergent after the car-following process is steady.

The controlled outputs and their CBFs are shown in Figure 6 and Figure 7. Then, the safety performance evaluations $\boldsymbol{z}(t) \geq 0$ as defined in (14) are reflected directly. As given in (13), the output limitations $z_1 \geq 0$ and $z_2 \geq 0$ represent that the relative distance is bigger than its safe distance and the vehicle speed is slower than its limited speed, respectively, which makes it clear that the proposed method can guarantee the vehicle



Figure 2. Test vehicle and scene. (A) Experimental vehicle; (B) Test field with lane markers.

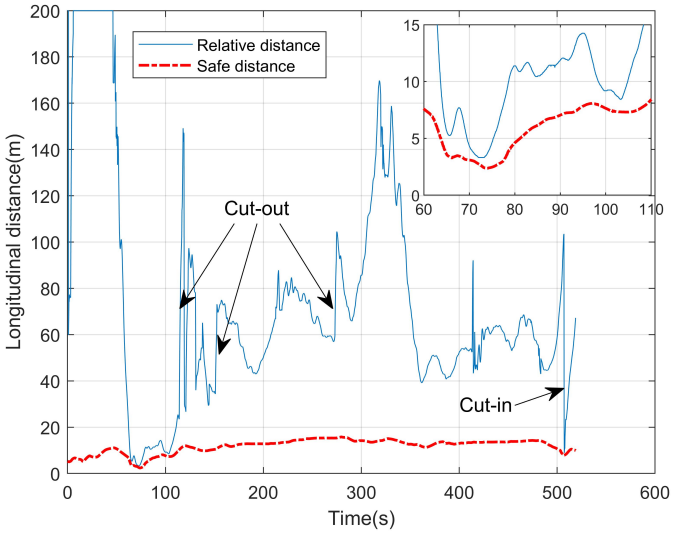


Figure 3. Actual distance and safe distance of scenario I.

collision safety and curve driving safety. The results show that the feasibility of QP problem is guaranteed by the application of CBF, CLF and slack variables, where the predefined safety and stability performances derived from the CBF and CLF are considered simultaneously. Moreover, the proposed method can balance safety, comfort and stability.

Test scenario II

The adopted second test scene is a similar but more complex urban environment with a higher traffic flow to further verify the effectiveness of the proposed method. There exist more curve driving, lane changing and cut-in or cut-out behaviors. The actual distance and safe distance of the preceding vehicle are shown in Figure 8. At the time 167s, the car ahead is fast decelerated and the controlled vehicle is decelerated with the maximal deceleration -1.57 m/s^2 up to the minimal speed of 0.43 m/s, where the minimal distance of 6.12m is also bigger than the safe distance as the partial enlarged detail in Figure 8. Then, the safety performance is guaranteed

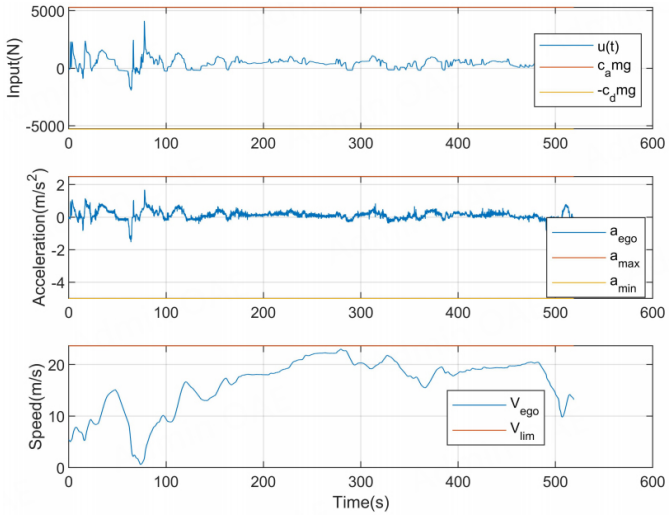


Figure 4. ACC system input and responses of scenario I.

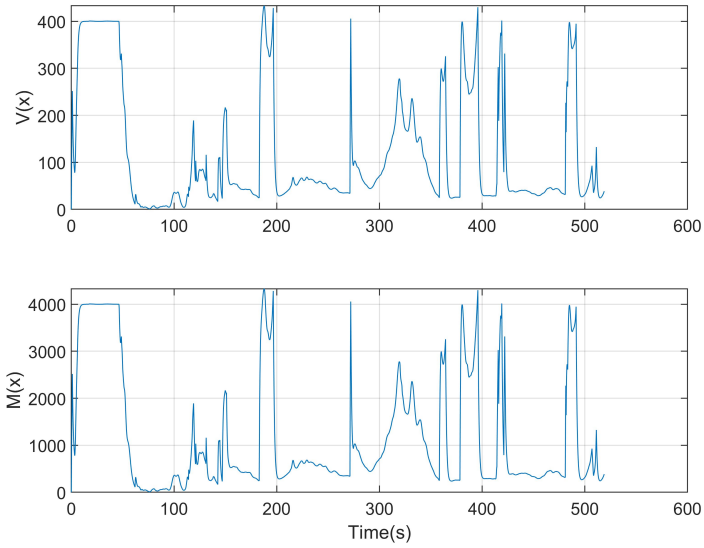


Figure 5. $V(\boldsymbol{x})$ and $M(\boldsymbol{x})$ of ACC system of scenario I.

according to the experimental results.

The input, acceleration and speed of this scenario are shown in Figure 9. It can be seen that there is a provisional parking in front of the red light and a Stop & Go driving behavior. It is obvious that the input constraint (6) is satisfied, where the comfort performance will be obtained. In addition, the vehicle can remain stationary while maintaining a safe distance during the Stop & Go condition. Moreover, the vehicle speed is much lower than its safe speed at the two obvious curve driving moments 222 and 340 s. According to the results in Figure 8 and Figure 9, the safe distance and speed are ensured during the car-following process and curve scene.

The CLF and its relaxation are shown in Figure 10, which can ensure that the QP problem (33) with the CBF and CLF constraints is solvable in real time. The controlled outputs and their CBFs are shown in Figure 11 and Figure 12. Then, the safe distance $z_1 \geq 0$ is maintained during the car-following process and the vehicle is driving with a safe speed $z_2 \geq 0$ on a curved road, which implies that vehicle safety is guaranteed by the

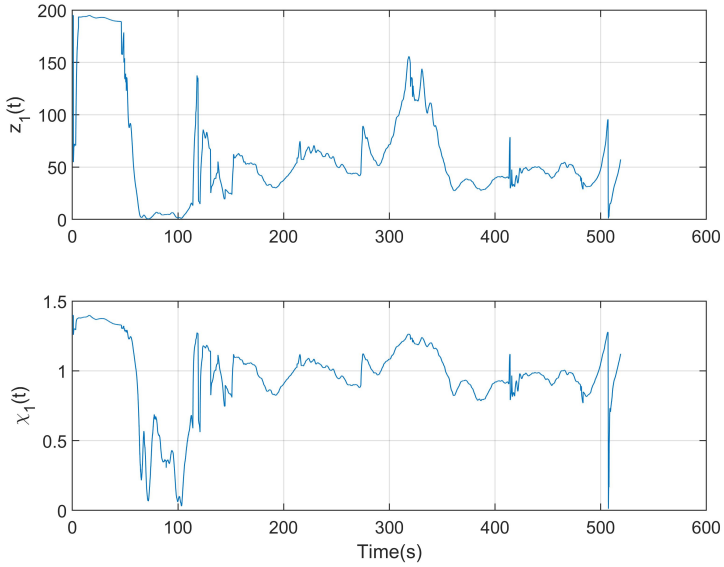


Figure 6. z_1 and its CBF of ACC system of scenario I.

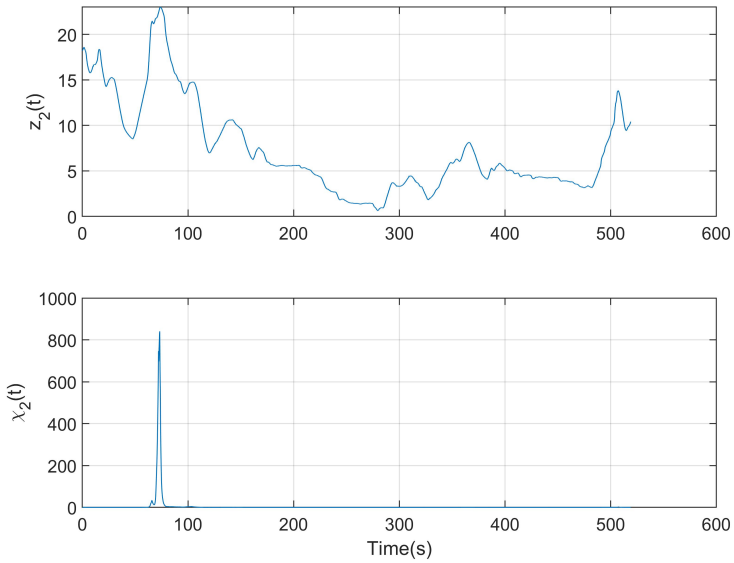


Figure 7. z_2 and its CBF of ACC system of scenario I.

proposed method.

Test scenario III

To make a further horizontal comparison, another well-known method is adopted in this test scene to validate the effectiveness of the proposed method: the intelligent driver model (IDM) method. We know that the IDM approach is a widely used method in vehicle ACC systems due to its stability and excellent calculation efficiency[36], which imitates the driving behavior habits of human drivers and will be employed as a baseline for comparison. The IDM method is a simple empirical model only with the same uncomplicated numerical

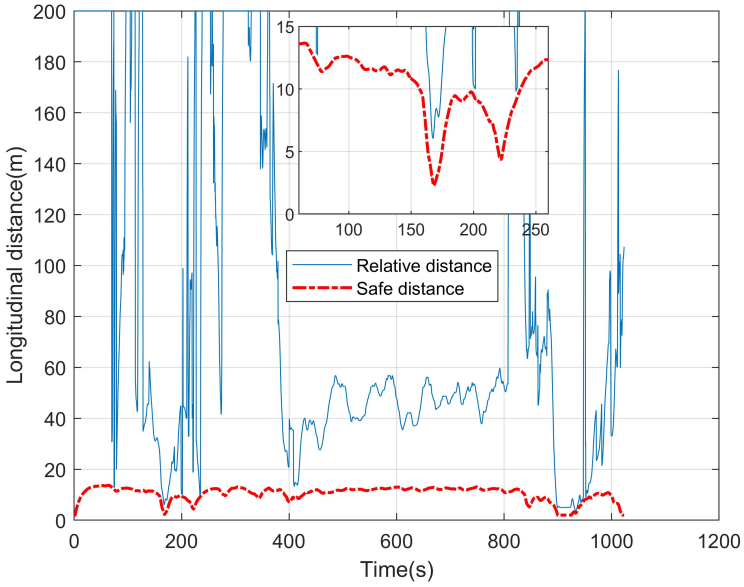


Figure 8. Actual distance and safe distance of scenario II.

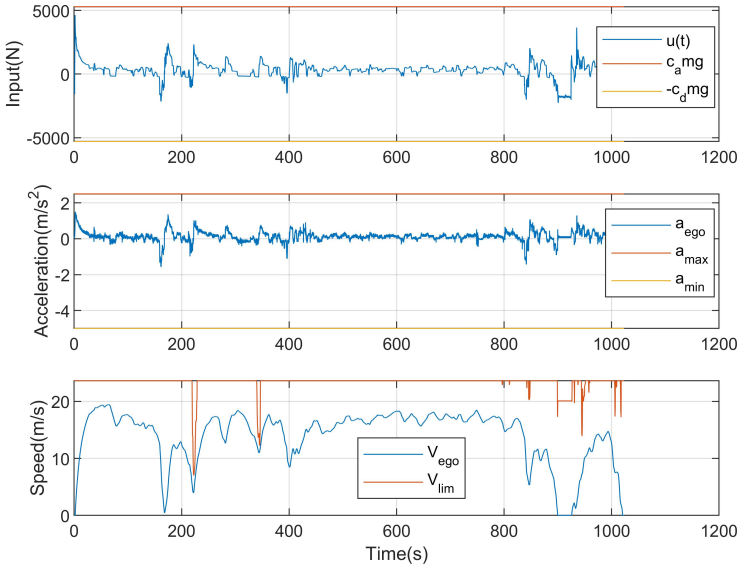


Figure 9. ACC system input and responses of scenario II.

calculation, which is defined as follows:

$$u(t) = F_{x0} + \delta c_a mg \left[1 - \left(\frac{V_{ego}}{V_{\lim}} \right)^4 - \left(\frac{d_{IDM}}{d_{rel}} \right)^2 \right], \tag{34}$$

where the desired headway is given as

$$d_{IDM} = d_0 + T_h V_{ego} + \frac{V_{ego}(V_{ego} - V_{obj})}{2g\sqrt{c_a c_d}}. \tag{35}$$

The IDM method possesses excellent computational efficiency in its practical applications as exhibited as (34). After several attempts, the proposed method and IDM can be executed with the same sampling period as 10

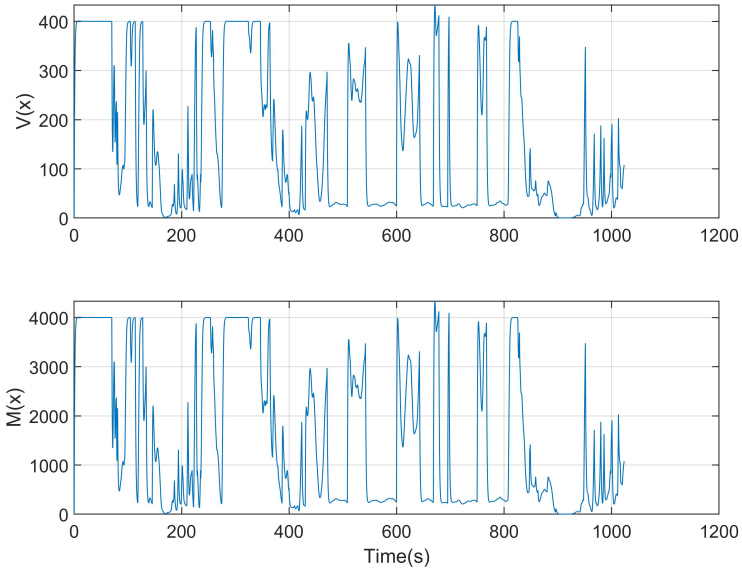


Figure 10. $V(\boldsymbol{x})$ and $M(\boldsymbol{x})$ of ACC system of scenario II.

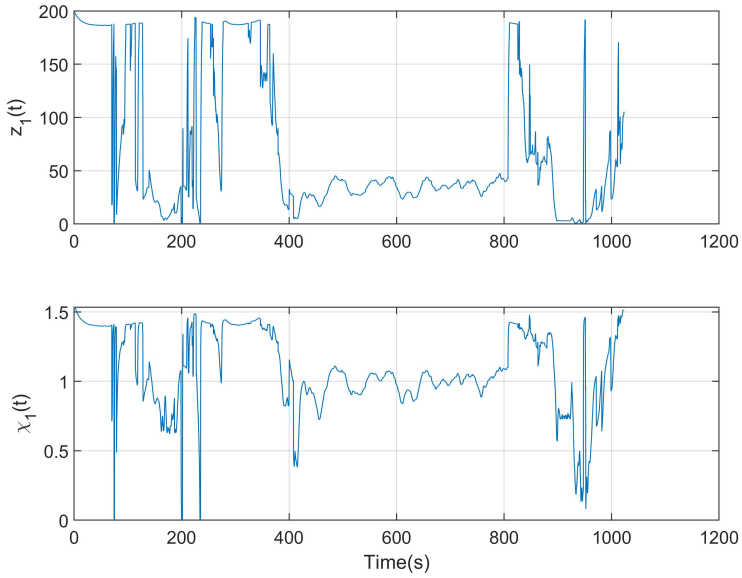


Figure 11. z_1 and its CBF of ACC system of scenario II.

ms in the real microprocessor as shown in Figure 12, which implies that the real-time calculation efficiency of the proposed method is approximate to that of the IDM method and it is satisfying for the practical application as well.

Because the experiment is carried out in real road scenarios, the surrounding vehicles are usually driven by human drivers. It is very hard to repeat the same scenarios 1 and 2 for making a reasonable comparison. Then, we adopt another similar scenario 3 on a real urban road to verify the proposed method. The relative distance and safe distance of the preceding vehicle obtained by the IDM method are shown in Figure 13, where the corresponding input, acceleration and speed are shown in Figure 14. We can see that the car-following distance is closer to its safe distance, even less than the safe distance at 216 s, where safety is hard to guarantee. The

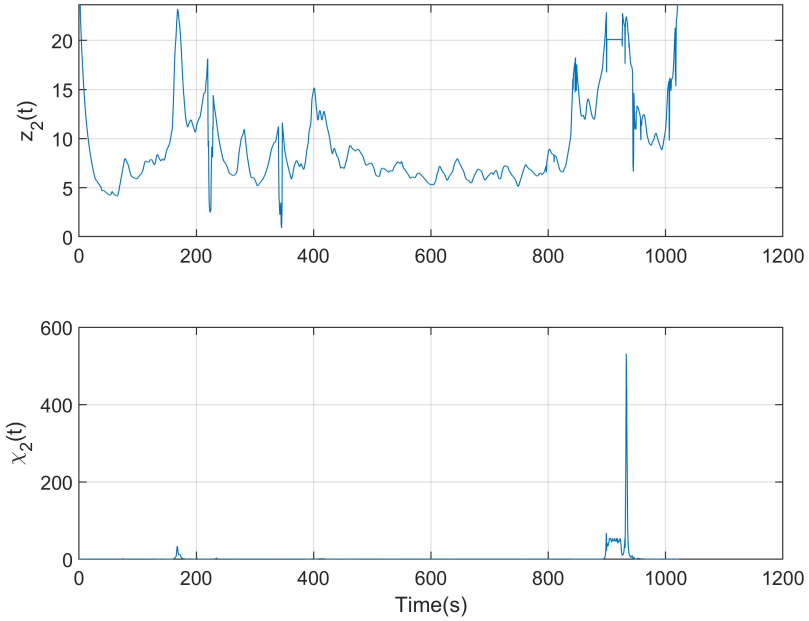


Figure 12. z_2 and its CBF of ACC system of scenario II.

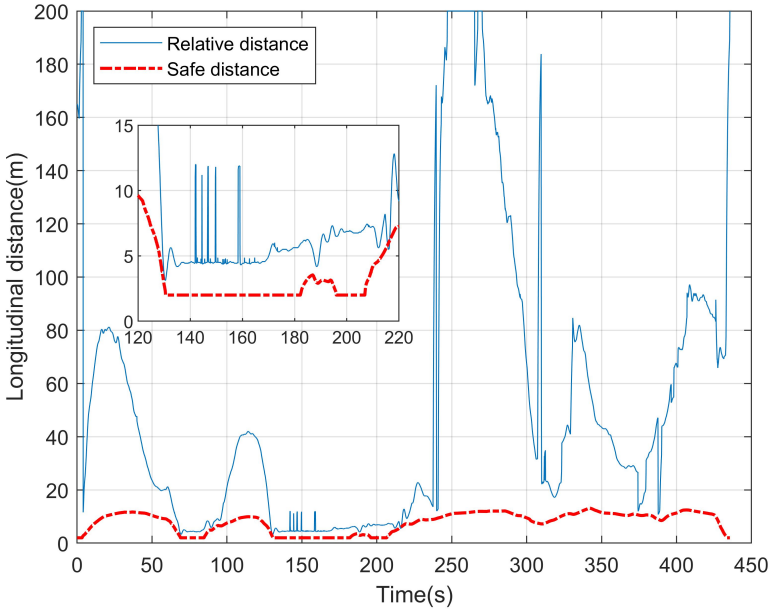


Figure 13. Actual distance and safe distance of scenario III.

maximal acceleration 1.89 m/s^2 is much bigger than that of the first two scenarios, which implies that better comfort performance can be obtained by the proposed method.

The controlled output is shown in Figure 15. It is clear that the output z_1 will be negative; i.e., the actual distance is smaller than its safe distance. Then, the safety performance requirement is not satisfied as defined in (14) since the IDM method is a controller without any constraints. On the contrary, collision safety can be guaranteed by the proposed method due to the consideration of the predefined performance constraints. Therefore, the necessity of the performance-centered design philosophy for the ACC system is verified by the

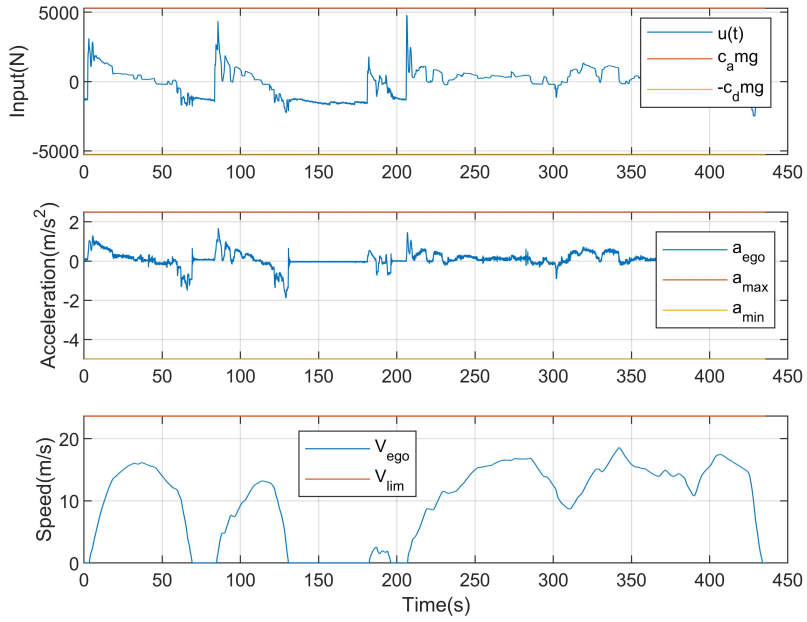


Figure 14. ACC system input and responses of scenario III.

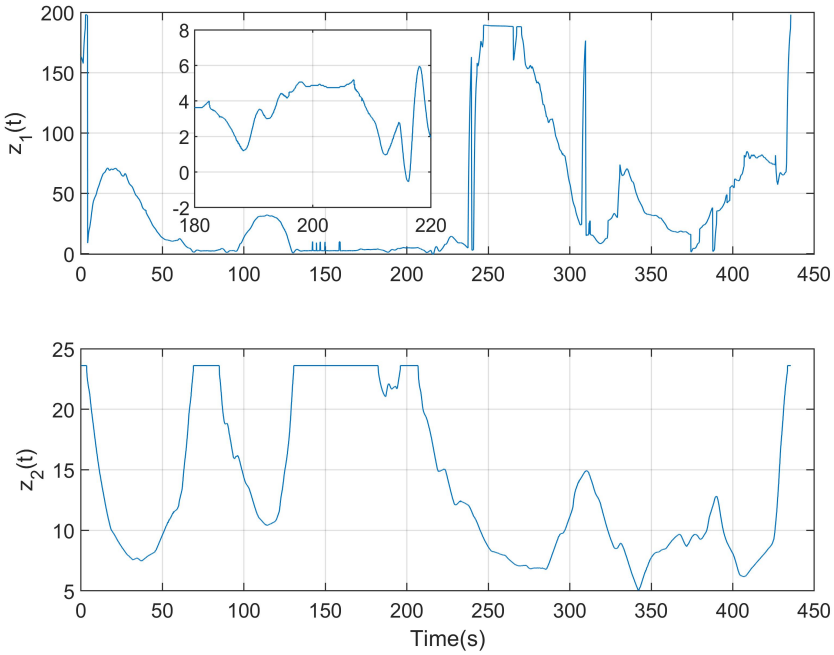


Figure 15. z_1 and z_2 of ACC system of scenario III.

comparison results. Moreover, the safety, comfort and stability performances can be overall considered.

To make a more intuitive comparison, some quantitative analysis of the performance evaluation indicators is listed in Table 3. The scenarios 1 and 2 are performed by the proposed method and the scenario 3 is performed by IDM method [36]. To further evaluate the car-following performance of the proposed controller, the root

Table 3. Experimental results comparison

Scenarios		1	2	3
Methods		Proposed method in this paper		IDM
Safety indexes	$\min(z_1)$	0.5456 m	0.12 m	-0.546 m
	$\min(z_2)$	0.6276 m/s	0.9227 m/s	5.053 m/s
Comfort indexes	$\max(\lvert a_{ego}\rvert)$	1.68 m/s^2	1.575 m/s^2	1.89 m/s^2
	RMS[1]	0.2934 m/s^2	0.3073 m/s^2	0.409 m/s^2

[1] RMS of a_{ego} for judging the comfort of the car-following performance.

mean square (RMS) value of the acceleration a_{ego} is considered, which is defined as:

$$\text{RMS} = \sqrt{\frac{1}{N}\sum_{i=1}^{N} a_{ego}^2(i)}, \tag{36}$$

where N is the sampling number of signal a_{ego}. In Table 3, the evaluation $\min(z_1) \geq 0$ and $\min(z_2) \geq 0$ are used for the safety performance. The indicators $\max(|a_{ego}|)$ and RMS are adopted for comfort and a smaller indicator implies a better comfort performance. These safety-comfort-based indicators produce a reasonable performance margin for the proposed controller. According to the results, the safety, comfort and stability performances are considered simultaneously in the proposed method. Therefore, a safer and more comfortable car-following process will be obtained by the proposed method compared with the IDM method. Moreover, the first two test scenarios are performed by the proposed method and the third one is executed by the IDM method. These experiments are implemented in the same microprocessor with the same sampling period of 10ms. Then, the real-time performance of the proposed method is verified according to the prominent computational efficiency of the IDM method.

It is worth mentioning that the proposed method is finally transformed into a QP-based optimization problem, where its essence is a kind of optimization-based approach. There are two other typical methods: linear quadratic regulator (LQR) and MPC. The LQR is an optimization method without several predefined performance constraints; then, it is hard to ensure the performance requirements. Correspondingly, the MPC is a similar optimization practice, which is usually transformed into a standard QP problem with some performance constraints. However, the MPC method is implemented by the predictive model and iterative optimization, where the calculation burden of the model predictive procedure is a huge challenge that prevents its practical application. Therefore, the proposed method can well balance the potential conflict between the multiple performance requirements, such as safety, comfort, stability and real-time performances. It can outdo the IDM, LQR and MPC methods and be used in practical applications. Then, the effectiveness of the proposed performance-centered ACC method is verified.

5. CONCLUSIONS AND DISCUSSION

In this work, the CBF and CLF are introduced and deployed on the ACC system, which provides a potential practical solution to enhance the control performance for ACC systems. Firstly, the ACC system model is modeled as a nonlinear dynamics system based on the vehicle longitudinal dynamics model and the car-following headway spacing policy. Then, the performance-centered optimal controller is established with the CBF and CLF constraints induced from various predefined performance constraints. The effectiveness of the proposed method is verified by a real road experimental scenario.

Due to the performance-centered design philosophy of the proposed method, it can also be applied in some other autonomous driving systems, such as lane-keeping or other path-tracking systems with similar nonlinear dynamics. For some other vehicle control applications, a similar approach can be adopted step-by-step: dynamics modeling, CBF established for the safety and comfort requirement, CLF established for the stability

performance, and QP problem formation to solve its control input. On the other hand, future studies will focus on the whole autonomous driving system with the safety-centered requirements for the vehicle lateral-longitudinal dynamics integrated control within more traffic scenarios such as traffic jams, also including the vehicle stability control. Moreover, the consensus tracking control and string stable problems will be considered for the CACC system or some other nonlinear multiagent systems.

DECLARATIONS

Authors' contributions

Performed data acquisition and analysis and provided administrative, technical, and material editing: Zhan S
Made substantial contributions to conception and design of the study: Liu C

Availability of data and materials

Not applicable.

Financial support and sponsorship

The authors greatly appreciate the National Science Fund of the People's Republic of China (Grant No. 52102444), the Open Foundation of the National Key Laboratory of Multi-perch Vehicle Driving Systems (Grant No. QDXT-WY-202407-16), the Zhiyuan Laboratory (Grant No. ZYL2024019) and the Central Guidance on Local Science and Technology Development Fund of Hebei Province (Grant No. 226Z2204G).

Conflicts of interest

Liu C is a Junior Editorial Board Member of the journal *Complex Engineering Systems* and the guest editor of the Special Issue of "Generalized Dynamics Modeling and Dynamics Control of Autonomous Driving Vehicle", while the other author has declared that he has no conflicts of interest.

Ethical approval and consent to participate

Not applicable.

Consent for publication

Not applicable.

Copyright

© The Author(s) 2024.

REFERENCES

1. Ampountolas K. The unscented kalman filter for nonlinear parameter identification of adaptive cruise control systems. *IEEE Trans Intell Veh* 2023;8:4094-104. DOI
2. Wei P, Zeng Y, Ouyang W, Zhou J. Multi-sensor environmental perception and adaptive cruise control of intelligent vehicles using kalman filter. *IEEE Trans Intell Transport Syst* 2024;25:3098-107. DOI
3. Li Z, Zhao X, Yang J, Liu M. Model predictive control of multi-objective adaptive cruise system based on extension theory. *Complex Eng Syst* 2023;3:15. DOI
4. Xu X, Grizzle JW, Tabuada P, et al. Correctness guarantees for the composition of lane keeping and adaptive cruise control. *IEEE Trans Autom Sci Eng* 2018;15:1216-29. DOI
5. Liu C, Li L, Chen X, Yong J, Cheng S, Dong H. An innovative adaptive cruise control method based on mixed H_2/H_∞ out-of-sequence measurement observer. *IEEE Trans Intell Transport Syst* 2022;23:5602-14. DOI
6. Pan Y, Ji W, Lam H, Cao L. An improved predefined-time adaptive neural control approach for nonlinear multiagent systems. *IEEE Trans Automat Sci Eng* 2024;21:6311-20. DOI
7. Naus G, Ploeg J, Van de Molengraft M, Heemels W, Steinbuch M. Design and implementation of parameterized adaptive cruise control: an explicit model predictive control approach. *Control Eng Pract* 2010;18:882-92. DOI
8. Wang H, Peng J, Zhang F, Zhang H, Wang Y. High-order control barrier functions-based impedance control of a robotic manipulator with time-varying output constraints. *ISA Trans* 2022;129:361-9. DOI

9. Magdici S, Althoff M. Adaptive cruise control with safety guarantees for autonomous vehicles. *IFAC-PapersOnLine* 2017;50:5774-81. DOI
10. Liu YJ, Tong S. Barrier Lyapunov functions-based adaptive control for a class of nonlinear pure-feedback systems with full state constraints. *Automatica* 2016;64:70-5. DOI
11. Dong Y, Wang X, Hong Y. Safety critical control design for nonlinear system with tracking and safety objectives. *Automatica* 2024;159:111365. DOI
12. Molnar TG, Kiss AK, Ames AD, Orosz G Safety-critical control with input delay in dynamic environment. *IEEE Trans Control Syst Technol* 2023;31:1507-20. DOI
13. Wang S, Lyu B, Wen S, Shi K, Zhu S, Huang T. Robust adaptive safety-critical control for unknown systems with finite-time elementwise parameter estimation. *IEEE Trans Syst Man Cybern Syst* 2023;53:1607-17. DOI
14. Yang S, Pan Y, Cao L, Chen L. Predefined-time fault-tolerant consensus tracking control for multi-UAV systems with prescribed performance and attitude constraints. *IEEE Trans Aerosp Electron Syst* 2024;60:4058-72. DOI
15. Xiao W, Belta CA, Cassandras CG. Sufficient conditions for feasibility of optimal control problems using Control Barrier Functions. *Automatica* 2022;135:109960. DOI
16. Zhang Y, Xu M, Qin Y, Dong M, Gao L, Hashemi E. MILE: multiobjective integrated model predictive adaptive cruise control for intelligent vehicle. *IEEE Trans Ind Inform* 2023;19:8539-48. DOI
17. Gangopadhyay B, Dasgupta P, Dey S. Safe and stable RL (S^2RL) driving policies using control barrier and control Lyapunov functions. *IEEE Trans Intell Veh* 2023;8:1889-99. DOI
18. Hu C, Wang J. Trust-based and individualizable adaptive cruise control using control barrier function approach with prescribed performance. *IEEE Trans Intell Transport Syst* 2022;23:6974-84. DOI
19. Ames AD, Xu X, Grizzle JW, Tabuada P. Control barrier function based quadratic programs for safety critical systems. *IEEE Trans Autom Control* 2017; 62(8): 3861-3876. DOI
20. Liu YJ, Lu S, Tong S, Chen X, Chen CLP, Li DJ. Adaptive control-based Barrier Lyapunov Functions for a class of stochastic nonlinear systems with full state constraints. *Automatica* 2018;87:83-93. DOI
21. Feller C, Ebenbauer C. A stabilizing iteration scheme for model predictive control based on relaxed barrier functions. *Automatica* 2017;80:328-39. DOI
22. Graf Plessen M, Bernardini D, Esen H, Bemporad A. Spatial-based predictive control and geometric corridor planning for adaptive cruise control coupled with obstacle avoidance. *IEEE Trans Control Syst Technol* 2018;26:38-50. DOI
23. Sahlholm P, Johansson KH. Road grade estimation for look-ahead vehicle control using multiple measurement runs. *Control Eng Pract* 2010;18:1328-41. DOI
24. Lindemann L, Dimarogonas DV. Control barrier functions for signal temporal logic tasks. *IEEE Control Syst Lett* 2019;3:96-101. DOI
25. Rajamani R, Zhu C. Semi-autonomous adaptive cruise control systems. *IEEE Trans Veh Technol* 2002;51:1186-92. DOI
26. Naus GJL, Vugts RPA, Ploeg J, van de Molengraft MJG, Steinbuch M. String-stable CACC design and experimental validation: a frequency-domain approach. *IEEE Trans Veh Technol* 2010;59:4268-79. DOI
27. Brugnolli MM, Pereira BS, Angélico BA, Maria Laganá AA. Adaptive cruise control with a customized electronic control unit. *J Control Autom Electr Syst* 2019;30:9-15. DOI
28. Sheikholeslam S, Desoer CA. Longitudinal control of a platoon of vehicles with no communication of lead vehicle information: a system level study. *IEEE Trans Veh Technol* 1993;42:546-54. DOI
29. Stankovic SS, Stanojevic MJ, Siljak DD. Decentralized overlapping control of a platoon of vehicles. *IEEE Trans Control Syst Technol* 2000;8:816-32. DOI
30. Rajamani R. Vehicle dynamics and control. London: Springer Science; 2006.
31. Glotfelter P, Cortes J, Egerstedt M. Nonsmooth barrier functions with applications to multi-robot systems. *IEEE Control Syst Lett* 2017;1:310-5. DOI
32. Ames AD, Galloway K, Sreenath K, Grizzle JW. Rapidly exponentially stabilizing control Lyapunov functions and hybrid zero dynamics. *IEEE Trans Autom Control* 2014;59:876-91. DOI
33. Drazin PG, Drazin PD. Nonlinear systems, 3rd ed. USA: Cambridge University Press; 1992.
34. Jorge Nocedal SW. Numerical Optimization, 2nd ed. Springer series in operations research. Berlin, Germany: Springer; 2006.
35. Chai C, Zeng X, Wu X, Wang X. Evaluation and optimization of responsibility-sensitive safety models on autonomous car-following maneuvers. *Transp Res Rec J Transp Res Board* 2020;2674:662-73. DOI
36. Li Z, Li W, Xu S, Qian Y. Stability analysis of an extended intelligent driver model and its simulations under open boundary condition. *Phys A Stat Mech Appl* 2015;419:526-36. DOI

Tsaimou *et al*. *Complex Eng Syst* 2024;4:20
DOI: 10.20517/ces.2024.28

Complex Engineering Systems

Research Article

Open Access

Mapping cracks on port concrete pavements by analyzing structural health monitoring metadata with computer vision-based techniques

Christina N. Tsaimou[1], Georgios Kagkelis[1], Panagiotis Sartampakos[2], Konstantinos Karantzalos[3], Vasiliki K. Tsoukala[1]

[1]Laboratory of Harbour Works, Department of Water Resources and Environmental Engineering, School of Civil Engineering, National Technical University of Athens (NTUA), Zografou 15780, Greece.
[2]NIREAS Engineering, 8 Katsikogianni Str., Chalkida 34100, Greece.
[3]Remote Sensing Laboratory, School of Rural, Surveying and Geo-Informatics Engineering, National Technical University of Athens (NTUA), Zografou 15780, Greece.

Correspondence to: Christina N. Tsaimou, Laboratory of Harbour Works, Department of Water Resources and Environmen-tal Engineering, School of Civil Engineering, National Technical University of Athens (NTUA), Zografou 15780, Greece. E-mail: ctsaimou@gmail.com; Prof. Vasiliki K. Tsoukala, Laboratory of Harbour Works, Department of Water Resources and Environmental Engineering, School of Civil Engineering, National Technical University of Athens (NTUA), Zografou 15780, Greece. E-mail: tsoukala@mail.ntua.gr

How to cite this article: Tsaimou CN, Kagkelis G, Sartampakos P, Karantzalos K, Tsoukala VK. Mapping cracks on port concrete pavements by analyzing structural health monitoring metadata with computer vision-based techniques. *Complex Eng Syst* 2024;4:20. http://dx.doi.org/10.20517/ces.2024.28

Received: 7 Jun 2024 **First Decision:** 29 Aug 2024 **Revised:** 14 Oct 2024 **Accepted:** 8 Nov 2024 **Published:** 14 Nov 2024

Academic Editor: Hamid Reza Karimi **Copy Editor:** Fangling Lan **Production Editor:** Fangling Lan

Abstract

Ports act as hubs for international trade and transport, strengthening the economies of the regions they serve. To maintain their undisrupted operations, efficient port management systems rely on Structural Health Monitoring practices to detect defects and assess infrastructure performance. Regarding port concrete pavements, condition assessment includes crack detection. Currently, advanced algorithms and methodologies for image processing or machine learning applications are used for surface crack detection with images captured during *in-situ* inspections. The growing urge to employ unmanned aerial vehicles (UAVs) equipped with high-resolution cameras is driving further research into image processing methods. This study provides an insightful approach for real-time crack detection in port concrete pavements that takes advantage of the geospatial information included in UAV imagery. The proposed methodology is based on the synergetic application of programming and Geographic Information System tools. Widely used crack detection methods and algorithms are herein enhanced with geospatial analysis modules that help to manage photogrammetry metadata generated by processing UAV data. Geographic Information System tools are employed to

© The Author(s) 2024. **Open Access** This article is licensed under a Creative Commons Attribution 4.0 International License (https://creativecommons.org/licenses/by/4.0/), which permits unrestricted use, sharing, adaptation, distribution and reproduction in any medium or format, for any purpose, even commercially, as long as you give appropriate credit to the original author(s) and the source, provide a link to the Creative Commons license, and indicate if changes were made.

add a new perspective to crack detection by supporting the visualization and interpretation of geospatial processed images to locate cracks and examine crack propagation. The investigation includes a periodic field test conducted at Lavrio Port, a Greek port located at the southeastern tip of Attica. Overall, the combined methodology returns results with high accuracy (approximately 95%), thus having a practical application in the engineering community that shifts to scalable solutions for mapping cracks in large port concrete surfaces remotely inspected with UAVs.

Keywords: Port pavements, port concrete infrastructure, structural health monitoring (SHM), condition assessment, unmanned aerial vehicles (UAVs), crack detection, image analysis, geographic information systems (GIS)

1 INTRODUCTION

Ports are key nodes having a dynamizing effect on trade, maritime connectivity and transportation, logistics chain, and the blue economy[1]. They are capital-intensive infrastructure assets whose performance is disturbed by natural disasters (e.g., earthquakes and storms), human-induced threats (e.g., human accidents), adverse marine conditions, and climate change impact[2,3],necessitating continuous maintenance and upgrade actions[4–6]. To implement a proactive intervention plan, optimize maintenance resources, and enhance the structural integrity of port infrastructure, port managers are tasked to establish effective asset management programs[7].

Nowadays, Structural Health Monitoring (SHM) of infrastructure is gaining importance in asset management[6,8]. Within the port industry, SHM of constructed port concrete facilities can be measured using an index that requires structural condition data linked to cracking, spalling, corrosion, and other defects[4]. Cracking in port concrete pavements of mooring facilities is often caused by traffic loading conditions (e.g., loading from heavy truck vehicles), inadequate design, construction defects, humidity conditions, *etc.*[9]. Crack detection in such facilities is essential to retain structural and functional performance, ensure public safety, reduce maintenance costs, and prevent operational delays associated with non-targeted repair interventions[9,10].

Computer vision-based techniques for SHM of concrete structures have gained rapid popularity in terms of crack detection[4]. They include both processing-based (i.e., image processing) and learning-based (i.e., deep learning) techniques[11,12]. Digital Image Processing (DIP) is widely used to apply crack detection on concrete surfaces aiming at enhancing the procedures of assessing existing condition[12]. DIP is applied with several methodologies that involve data collection, data pre-processing, and algorithms' implementation for crack detection. Imagery acquisition involves both manual (e.g., handheld cameras) or automated applications (e.g., cameras mounted on Unmanned Aerial Vehicles, UAVs)[10]. The latter can be extremely beneficial for structures that occupy large areas, e.g., the port concrete pavements of mooring facilities, where limited handheld photography may not representatively illustrate the *in-situ* condition of such infrastructure.

Current literature identifies the need to integrate UAV datasets into crack detection practices. The unique characteristics of images captured by cameras mounted on UAVs such as resolution, lighting conditions, image distortion, capturing distance, and lens' characteristics differ from those taken with handheld cameras[13,14]. Hence, different studies have been focused on developing methods for crack detection by adapting to the requirements of analyzing UAV datasets. For example, approaches for pixel-level crack identification[15] and noise reduction[16] have been investigated. Despite the ever-increasing interest in crack detection using UAV imagery, as noted by[17], few studies have focused on localizing cracks in concrete structures with UAV-collected images. In the specific study, the localization was achieved by considering the relative position between objects. Another study focused on locating cracks in the world coordinate system using two UAV-based images[18]. However, the potential of geospatial information in large UAV datasets required to illustrate large structures remains largely untapped.

The growing trend of UAV-driven SHM of port concrete pavements assists in identifying cracks in geospatial output produced by photogrammetry methods and inserted into Geographic Information Systems (GIS)[19]. GIS tools have proven to be promising for manually mapping cracks albeit the lack of engaging automated or semi-automated approaches for crack detection. Although advancing automation in crack detection with coding for image processing and deep learning techniques has occupied several researchers, the synergetic application of programming and GIS tools has not yet been explored. Programming languages can be used to implement algorithms for crack detection[20] while GIS tools allow for managing the geospatial information[21] included in orthophotos that are generated by analyzing UAV imagery. Hence, interrelating both approaches can be quite compelling in terms of assisting an SHM program for port concrete pavements. Except for combining programming and GIS tools for concrete crack detection, proposed practices included in existing works are not tested on UAV imagery acquired on different dates thus searching for changes in crack propagation. While ensuring a reliable output in crack detection is very important, within the framework of civil engineering applications a comprehensive understanding of structural changes is also crucial for managing maintenance interventions.

In light of the above, the present research seeks to contribute to the existing body of knowledge regarding automating crack detection on port concrete pavements by applying current practices in image analysis enhanced with tools for working with geospatial information. Such tools include (a) modules imported in programming languages for managing georeferenced images; and (b) GIS applications for analyzing geospatial metadata acquired by image analysis. The proposed methodology is applied at Lavrio Port, located in the southeastern tip of Attica, Greece. The investigation includes a periodic SHM scheme that encompasses four UAV-based in-situ inspections (ISIs), photogrammetry analyses, python coding, and GIS applications, thus providing a comprehensive outline for facilitating crack detection issues.

To examine the synergistic effect of crack detection algorithms and geospatial tools on advancing structural condition assessment of port concrete pavements, the paper is organized as follows. The current background on crack detection practices is firstly summarized in Section 2 by describing pioneering contributions to algorithm development and later-triggered works. Based on the existing framework a structured methodology is presented that initiates a real-time crack detection approach that utilizes geospatial information of UAV orthophotos to map cracking on port concrete slabs of mooring facilities. The methodology is applied at a pilot area defined within a concrete slab of the domestic ferry mooring facilities of Lavrio port to test its applicability. The analysis of the results [Section 3] includes data validation and change detection during ISIs. The most significant issues noticed while working on the specific case study are further discussed aiming to identify challenges and search for potential ways to address them [Section 4]. Finally, the major findings of the demo application are enclosed in Section 5.

2 MATERIALS AND METHODS

2.1 Background and objectives

UAVs are usually equipped with high-resolution Ultra 4K cameras for capturing digital aerial images[22]. In contrast to the processing of imagery captured with portable cameras, where crack detection can be localized, the analysis of UAV imagery of port concrete infrastructure is compromised by the presence of noise features[16,23]. This is due to the complexity of the surrounding conditions including the shadows of vehicles and passengers, linear joints, manholes, and other defects such as spalling and corrosion. To address these challenges, several scientists have turned their research to deep learning techniques for machine learning applications[24] aiming to classify and recognize cracks with pre-trained algorithms. The efficiency of such techniques is highly dependent on the amount of available imagery and the quality of the representative training dataset. Indicatively, both seasonal and daily time variations in UAV-captured images, the presence of wet pavements, lighting conditions of the sun, and the cracking pattern (e.g., diagonal, transverse, longitudinal,

wide/narrow cracks, *etc.*) may affect the dataset. These issues have motivated studies such as the one of Li *et al.*[23] where a Convolutional Neural Network (CNN)-based methodology has been applied to bridges with different crack patterns.

The combination of machine learning techniques with image processing approaches has proven to deliver promising results[25]. In DIP, color images are represented as a matrix of vector-valued pixels formed by the intensity values of the red, green, and blue components of the image[26]. DIP techniques may involve spatial and frequency domain filtering, segmentation (e.g., thresholding or edge-based techniques), and mathematical methods (e.g., morphological operations)[12,27,28]. Each of these methods encompasses widely accepted techniques. Indicatively, spatial domain filtering is applied by employing mean, median, Winer, and Gaussian methods for denoising converted grayscale images[29]. Thresholding approaches rely on the implementation of image binarization algorithms presented in leading-edge works including the Otsu (1979)[30], Niblack (1986)[31], and Sauvola (2000)[32] algorithms. Moreover, among the most commonly used edge detectors for crack detection are the ones of Sobel (1968)[33] and Canny (1986)[34]. Finally, mathematical methods include morphological operations such as erosion, dilation, or closing to remove irrelevant pixels to cracks or fill the gaps to continue the cracking pattern[35]. All of these image-processing aspects are usually combined to achieve a reliable and accurate cracking output[35] thus triggering several researchers to upgrade practices for DIP crack detection.

Despite the popularity gained in image processing and deep learning techniques, their implementation in UAV-collected data is limited to images captured at a very short distance from the structure (e.g.,[18,23,36]). This is mainly attributed to the specifications of image resolution and pixels required to achieve reliable results. Currently, the issue of pixel-level crack detection has been examined by[37]. The authors reviewed deep-learning-based crack image segmentation techniques and they presented the requirements for their applications.

Within the context of a UAV-based SHM program for civil structures such as port concrete infrastructure, UAV flights are typically conducted at higher altitudes than those currently applied for UAV-based crack detection (e.g.,[19,38]). The flight altitude is optimized to capture a detailed overview of the entire structure while obtaining an acceptable number of images for analysis. The set of individual UAV images can be analyzed with photogrammetry applications to generate surface profiles of the 3D structures (i.e., orthophotos) thus providing geospatial information for detected defects (e.g., cracks)[39]. Once geospatial metadata is acquired, GIS tools can be used to examine structural features[19,39]. Despite the positive feedback from current research on combining UAV-based photogrammetry and GIS applications for assessing the structural condition of concrete structures, this synergy has not yet been integrated into DIP practices. Existing image-based methodologies often overlook geospatial information as their main focus is on a limited and predefined number of UAV images.

Considering the above, the present paper bridges two research gaps in automating crack detection in port concrete pavements. The first one is related to taking advantage of UAV geospatial information and mapping cracks on orthophotos illustrating the entire structure. One of the main challenges is to find suitable UAV flight altitudes that do not compromise accuracy. The second issue is the unexplored implication of GIS tools in assisting automation processes for crack detection and propagation monitoring. Within the framework of this research, an insightful approach is presented to work on geospatial metadata (i.e., orthophotos). A structured methodology is proposed and tested on orthophotos obtained from periodic inspections. The contribution of the present work includes the following:

- Retaining the geospatial information throughout the entire process of crack detection in port concrete pavements while processing orthophotos is achieved by importing specific modules and tools in programming and GIS environments.

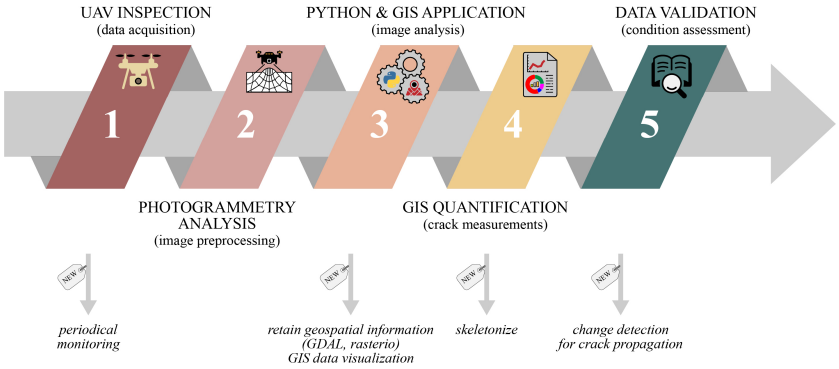


Figure 1. Stages for advanced crack detection in port concrete infrastructure (source: own work).

- The potential of GIS tools in improving crack detection and structural performance assessment is realized. GIS environments offer a range of features that, when combined effectively, enable visualizing, editing, locating, and quantifying cracking results.
- The regular update of the GIS database fed with all comprehensive information on the structural condition of port concrete infrastructure in terms of cracking is encouraged. This enables the identification of variations in crack patterns and propagation issues over the structure's lifespan. Moreover, the causal relationship between crack propagation and forcing factors (e.g., loading conditions) can be examined. Hence, informed decisions regarding maintenance and rehabilitation strategies can be made for effective Life-Cycle Management of the structure.
- The georeferenced output can be combined with structural data related to different port structures and included in GIS databases, thus providing a comprehensive understanding of the vulnerabilities within the entire port system.

2.2 Methodology

The overarching framework for mapping cracks in port concrete infrastructure by combining DIP and GIS modules includes five Stages [Figure 1]. Data acquisition is achieved by employing high-resolution cameras mounted on UAVs following a periodic SHM program (Stage 1). Factors such as the flight altitude, the camera filters, the environmental conditions, etc., affect the quality of the collected imagery. UAV data are processed with photogrammetry analyses to generate geospatial metadata (i.e., orthophotos) (Stage 2). The implementation of Stages 1 and 2 is summarized in Figure 2. Further details regarding the principles and the methods for applying Stages 1 and 2 can be found in the study of[19].

Stages 1 and 2 are crucial for initiating crack detection applications. Once geospatial metadata (i.e., orthophotos) is acquired, Stages 3, 4, and 5 of Figure 1 are applied based on a structured methodology proposed in the present paper [Figure 3]. These Stages include image-based processing techniques and GIS tools. Two open-source environments are employed for the programming and GIS processes: (a) QGIS (version 3.22); and (b) Spyder (version 5.4) for Python language, respectively. QGIS tools are used for visualizing georeferenced metadata and converting raster data (i.e., images) to vector data for mapping and quantifying cracks (Stages 3, 4, and 5). Python language is used for applying image processing algorithms and validation of the proposed methodology (Stages 3 and 5).

The novelty of the proposed methodology is identified in two critical points: (a) working on orthophotos of large surfaces with port concrete pavements and retaining the geospatial information during all steps of image analysis; and (b) integrating GIS tools in automation processes for detecting cracks and monitoring propagation. During the implementation of Stages 3, 4, and 5 working with geospatial data is achieved by integrating the following two libraries into image analysis:

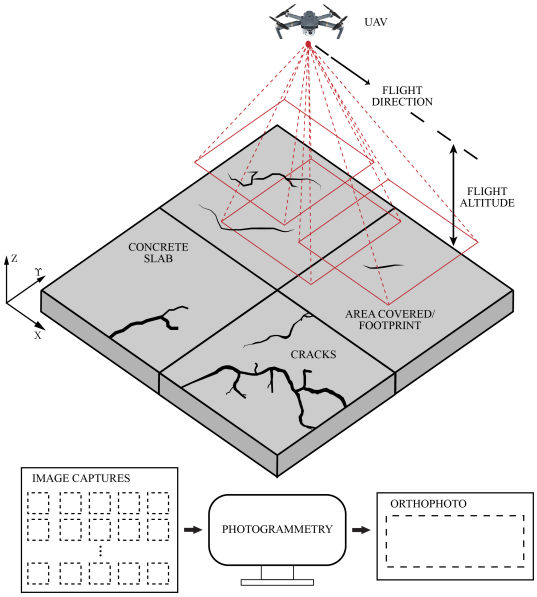


Figure 2. UAV-based data acquisition and photogrammetry applications - Stages 1 and 2 of Figure 1 (source: own work).

- The Geospatial Data Abstraction Library (GDAL) for translating and processing both vector and raster data[40].
- The Rasterio library for reading writing and processing geospatial raster data[41].

The methodology outlined in Figure 3 describes how modules and tools for image processing and GIS applications are interconnected to analyze georeferenced images for crack detection on port concrete pavements. All programming steps of the proposed methodology are summarized in Figure 4. It is noted that the present study does not produce new algorithms and methods for crack detection but rather offers a novel approach for managing orthophotos and leveraging GIS tools. Therefore, existing practices are upgraded with geospatial information analysis. The methodology can be customized to suit specific needs, such as incorporating edge detection algorithms. The primary focus is on preserving the geospatial information throughout the image processing analysis to assess the structural condition of port concrete pavements effectively.

2.2.1 *Study area definition*

Orthophotos typically represent a large part of port infrastructure. To avoid computer crashes and increase the speed of computations, orthophotos are clipped with GIS tools to match the area that will be further examined thus creating a new RGB image. This area is normally defined by considering existing structural conditions (e.g., the presence of cracks that propagate, the occurrence of a sudden event that caused surface cracking, *etc*.), the application of a maintenance scheme, a future upgrade, *etc*.

2.2.2 *Crack digitization*

Crack digitization is essential to verify crack detection results. It is performed in the initial color image of the study area by utilizing GIS tools including changing the layer blending mode, the brightness, the saturation, the contrast, and the Gamma value[19]. The main challenge in this step is to exclude the linear illustrations that are irrelevant to cracks such as marks from dragging equipment or loads.

2.2.3 *Grayscale conversion of the RGB image*

The new georeferenced RGB image is decolorized and converted into a grayscale image with programming modules [Figure 5]. This modification is important to eliminate color information that complicates computational requirements for crack detection[42]. The algorithm used for the conversion is described in Equa-

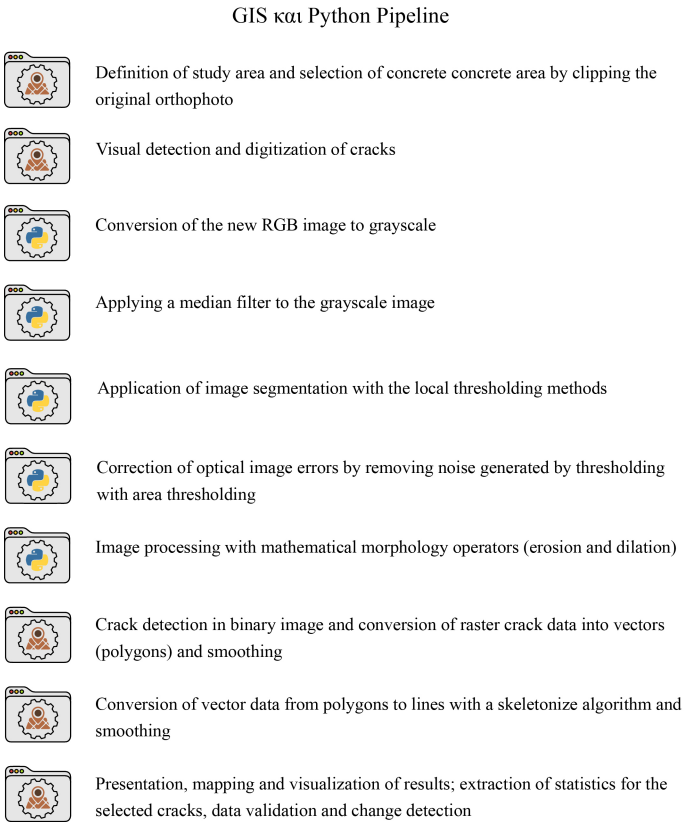


Figure 3. Methodology for mapping cracking in port concrete infrastructure by working on geospatial metadata - Stages 3, 4, and 5 of Figure 1 (source: own work).

tion (1)[43].

$$Y = 0.299 * R + 0.587 * G + 0.114 * B \quad (1)$$

where R, G, and B are a linear representation of the Red, Green, and Blue channels of a pixel, respectively.

2.2.4 *Median filtering*

A common task in DIP is noise removal. Median filtering is applied to the georeferenced grayscale image to reduce the degree of intensity variation between two pixels while avoiding non-realistic values[44]. To apply the median filter, a sliding window (i.e., kernel) is placed at a specific pixel of the image and all pixel values included in this window are placed in ascending order to compute the median value assigned to the pixel[43] [Figure 6].

2.2.5 *Image segmentation with thresholding*

Thresholding is a common segmentation approach for partitioning images into regions based on different ranges of pixel values[26,45]. To achieve this, intensity histograms are built [Figure 7]. The thresholding value t can be either constant for the entire image (global thresholding) or changing over the image (local thresholding). Indicatively, local thresholding with Otsu's algorithm[30] defines different threshold values with block-based or sliding-based windows depending on the lighting conditions and the different features of the image. This algorithm searches for a threshold t that maximizes the variance between the foreground (cracking) and background (no-cracking) groups or minimizes the variance within the group. All pixel values below the

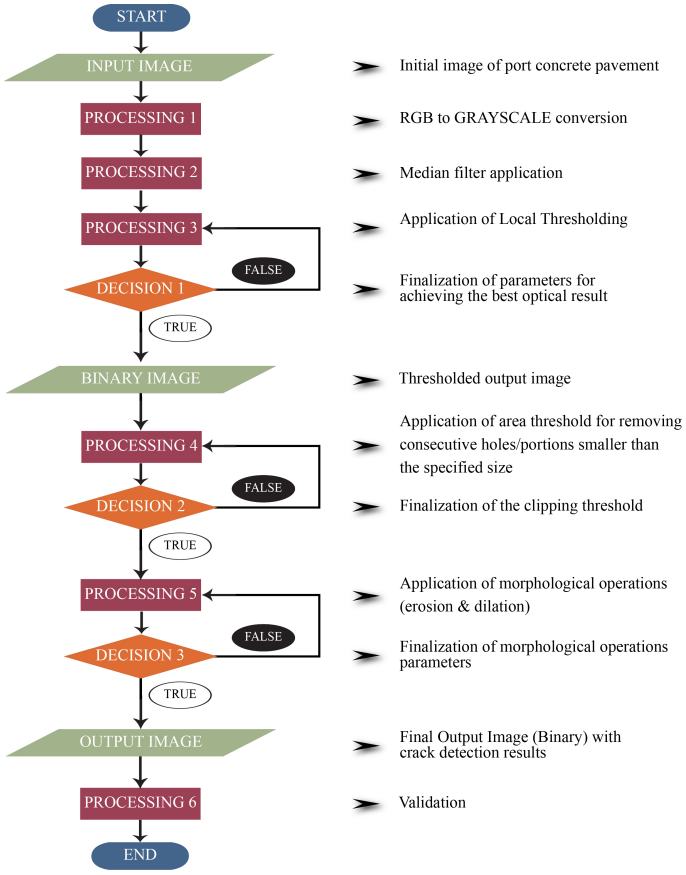


Figure 4. Flow chat of programming-based image processing for crack detection in port concrete pavements (source: own work).

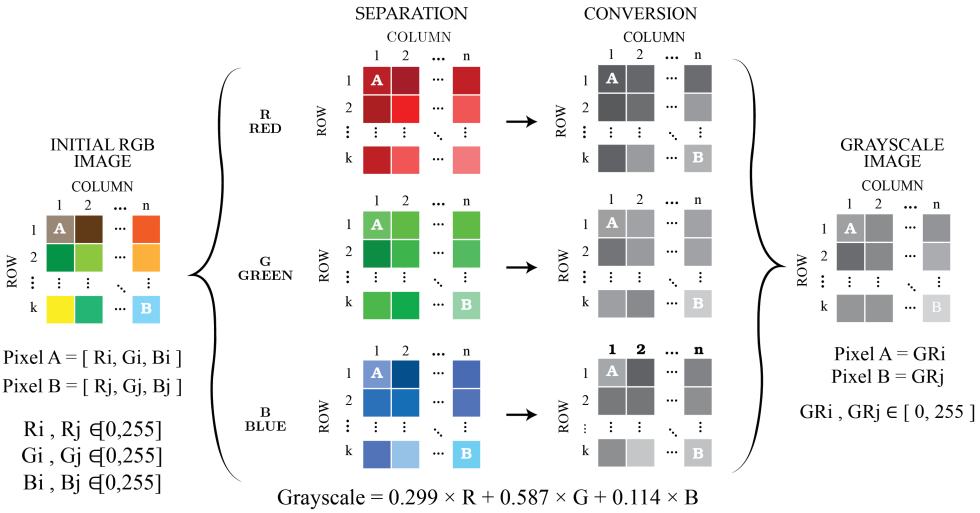


Figure 5. Procedure for converting an RGB image to a grayscale image (source: own work).

threshold are set to zero, while those above the threshold are set to one (image binarization). The variance within the groups v_{within} is given by

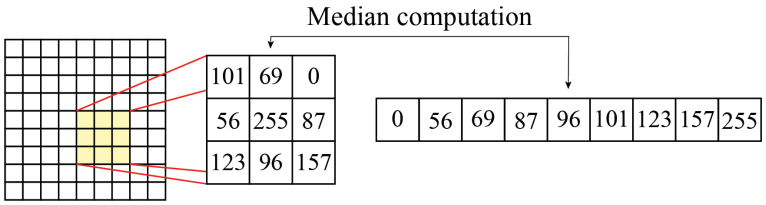


Figure 6. Example of median filtering (source: own work).

$$v_{within} = P_b(t) * v_b + P_f(t) * v_f \tag{2}$$

while the variance in between the groups $v_{\text{inbetween}}$ is given by

$$v_{inbetween} = v - v_{within} = P_b * P_f(m_b - m_f)^2 \tag{3}$$

where $P_b(t) = \sum_{i=0}^{t} p_i$ is the probability of the background pixels, $P_f(t) = \sum_{i=0}^{t} p_i$ is the probability of the foreground pixels, p_i are the probabilities, v_b is the variance of the background, v_f is the variance of the foreground, v is the variance of the entire image, $m_b = \sum_{i=0}^{t} i \cdot p_i$ is the average intensity of the background, and $m_f = \sum_{i=0}^{t} i \cdot p_i$ is the average intensity of the foreground.

2.2.6 Noise removal in the binary image

The presence of shadows, tire marks, and other image noises may be translated as cracking during image thresholding. To address this problem and avoid misinterpretation of results, noise removal is repeated by measuring the properties of the irrelevant-to-cracks black areas in the binary image and isolating them with a new threshold. Label tagging is conducted based on the calculated area represented by the number of irrelevant white pixels.

2.2.7 Morphological operations

Two morphological operations are used in the current research: dilation and erosion [43]. With dilation, small holes in the cracking pattern are filled. A rectangular structural element is placed over every pixel of the binary image and its pixel values are compared with the ones of the image [Figure 8]. Initially, the dilation process identifies the boundary pixels of the crack. Thereafter, it grows the boundary by a specified number of pixels. Multiple iterations are usually required to achieve accuracy in crack detection. On the other hand, erosion is used to remove pixels from the binary image, once dilation is completed. Similar to dilation, erosion places a rectangular structural element over every pixel of the image. However, it shrinks the boundary of the crack by a specified number of pixels.

2.2.8 Vectorization of the detected cracks

The key point of the implementation of all previous steps of the proposed methodology is retaining the geospatial information of the image. Hence, crack detection in port concrete infrastructure is expanded beyond image-based modules in programming and advanced by employing GIS tools. GIS-based vectorization of the binary image enables converting raster data (an array of pixels) to polygons [46] thus identifying crack features. Once achieved, smoothing processing is also applied to enhance the visual display and the continuity of the vectorized cracking data by reducing sharp angles and irregularities. The output of the vectorization step provides geospatial information about the width of the detected cracks [Figure 9].

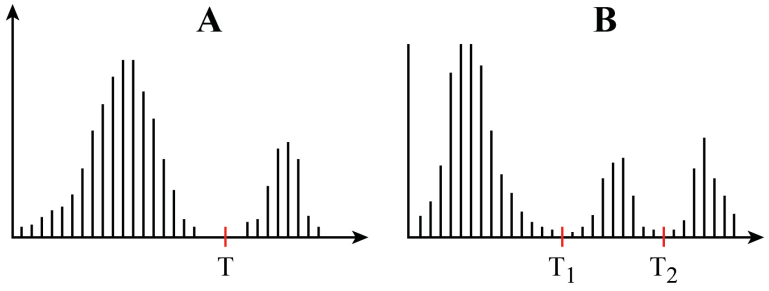


Figure 7. Indicative example of a histogram. A: Use of one threshold and B: use of multiple thresholds (source: own work).

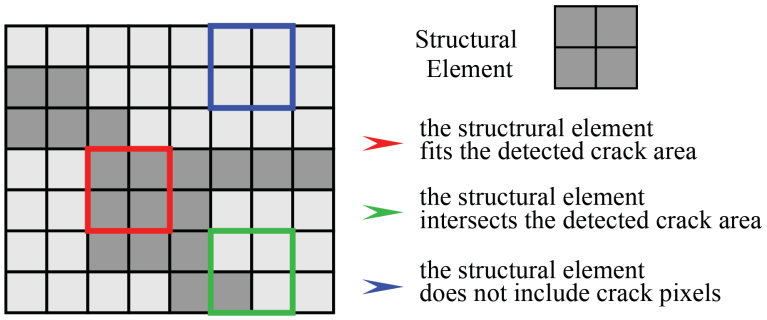


Figure 8. The sliding structural element during morphological operations (source: own work).

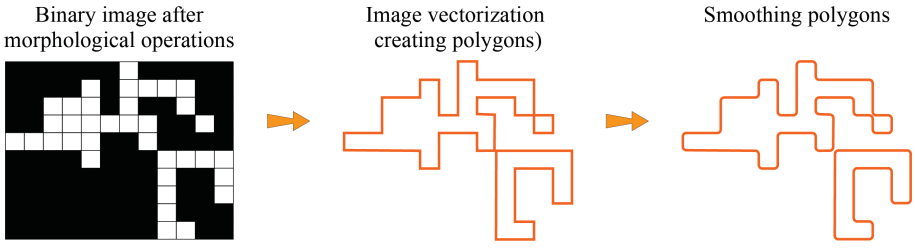


Figure 9. Vectorization of raster data of the binary image once morphological operations are completed (source: own work).

2.2.9 *Skeletonization of vectorized crack data*

Except for the width, additional information regarding the crack length is usually required when inspecting and assessing the condition of concrete structures. GIS-based skeletonization follows vectorization to generate linear illustrations of the detected cracks. The skeletonization algorithm processes the polygon geometry to recognize the pattern of the detected cracks[47]. Similar to the vectorized data, smoothing processing is also applied.

2.2.10 *Crack data validation and change detection*

The validation of the crack detection results is conducted by forming a confusion matrix, i.e., an n × n array that includes information for the automatically detected (predicted) cracks and the manually detected (digitized) ones[48]. The comparison requires raster data. To ensure comparable datasets, digitized cracks are converted to raster data (rasterization). During this process, it is important to ensure that the pixel size of the digitized cracks is equal to the one of the detected cracks. The confusion matrix is used to calculate the sensitivity, specificity, false-positive rate, false-negative rate, positive predictive value, negative predictive value, accuracy, and F1 score[49] [Figure 10]:

- The "Sensitivity" or "Recall" is a measure that indicates to what extent the detection model correctly iden-

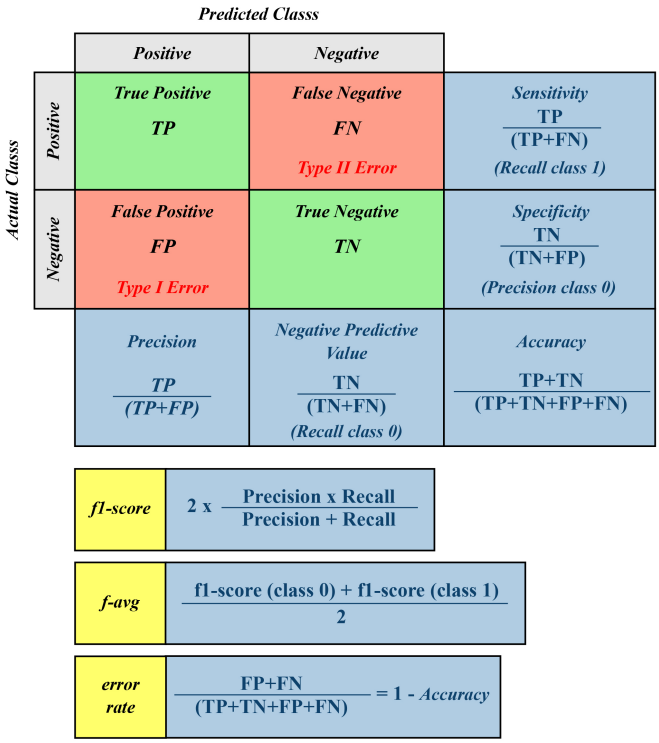


Figure 10. Confusion matrix (Source: Own work based on the studies of Obi [48] and Tharwat [49].

tifies the True positive pixels.

- The "Specificity" or "Precision" is a measure for determining the percentage of positive identifications that are correct.
- The "Accuracy" is a measure that indicates the number of times the detection model correctly identified the data class (i.e., 0 or 1) across the entire dataset.
- The F1-score links "Sensitivity" to "Specificity" by calculating their harmonic mean.

3 RESULTS

Within the context of the current research, the selected study area includes a concrete part of the domestic ferry terminal pavement of a Greek port, namely Lavrio port. Lavrio port is located at the southeastern tip of Attica (37°42′44″ N, 24°3′25″ E) [Figure 11] and is listed as a port of national importance (https://oll.gr/en/). The concrete pavement of the domestic ferry terminal is continuously exposed to loading and environmental conditions, thus threatening its structural integrity. During four UAV-based ISIs conducted on 2020-02-10 (ISI-1), 2020-09-04 (ISI-2), 2021-02-10 (ISI-3), and 2021-07-09 (ISI-4), it was observed that the pavement in the defined concrete area (enclosed within a black outlined rectangle in Figure 11 was severely and continuously cracked. The ISIs were conducted with the DJI MAVIC 2 pro UAV while UAV collected data was analyzed with Agisoft software (version 1.6.4) to generate the orthophotos.

The mean flight altitude of each UAV inspection was 48, 56, 76, and 56 m while the ground resolution was 1.06, 1.21, 1.66, and 1.17 cm/pixel for ISI-1, ISI-2, ISI-3, and ISI-4, respectively. The varying altitudes were applied to investigate the impact of these different flight characteristics on acquiring and analyzing SHM data for port concrete structures. Further details regarding data collection and analysis (Stages 1 and 2 of Figure 1) can be accessed through relevant work [19]. The flight altitude and the ground resolution of ISI-3, as well as the presence of a large shadow within the study area [Figure 12], resulted in the exclusion of the georeferenced

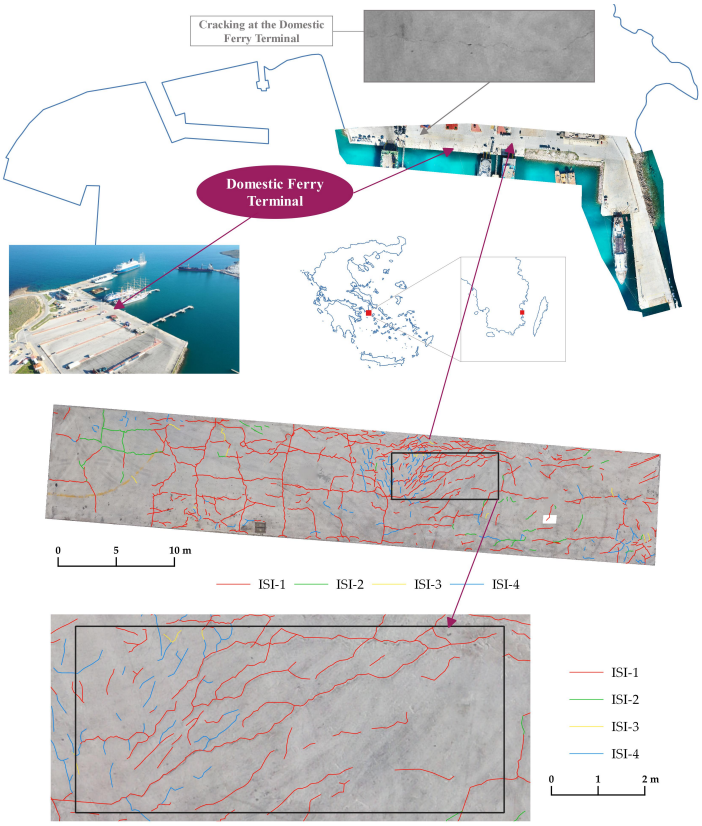


Figure 11. Definition of the study area in Lavrio port, Attica, Greece enclosed within the black outlined rectangle. Red-colored crack lines are digitized based on ISI-1. Green-colored crack lines are the new and/or propagated digitized cracks based on ISI-2 for the time interval between ISI-1 and ISI-2. Yellow-colored crack lines are the new and/or propagated digitized cracks based on ISI-3 for the time interval between ISI-2 and ISI-3. Light blue-colored crack lines are the new and/or propagated digitized cracks based on ISI-4 for the time interval between ISI-3 and ISI-4. The crack digitization process involved using GIS tools to visually detect cracks by working on the orthophotos of each ISI. (source: own work).

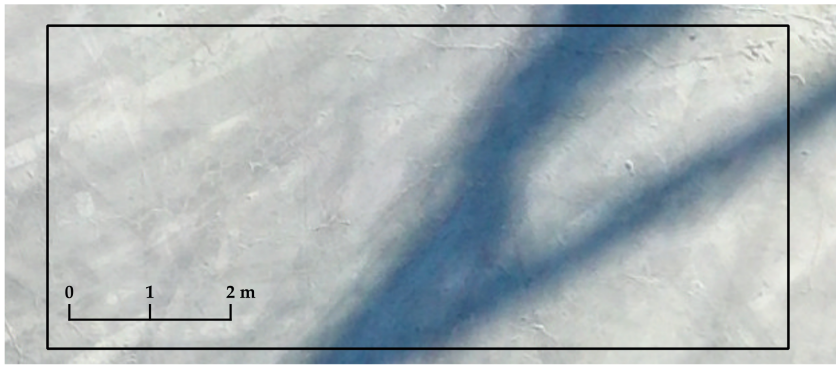


Figure 12. Georeferenced image of the study area based on ISI-3.

image of ISI-3 from the crack detection process.

Once the study area was defined, the georeferenced image clipped from the orthophotos was converted to a grayscale image based on the procedure described in Section 2. A median filter with a 3×3 kernel was implemented in the grayscale image to eliminate noise and local thresholding was applied to binarize the

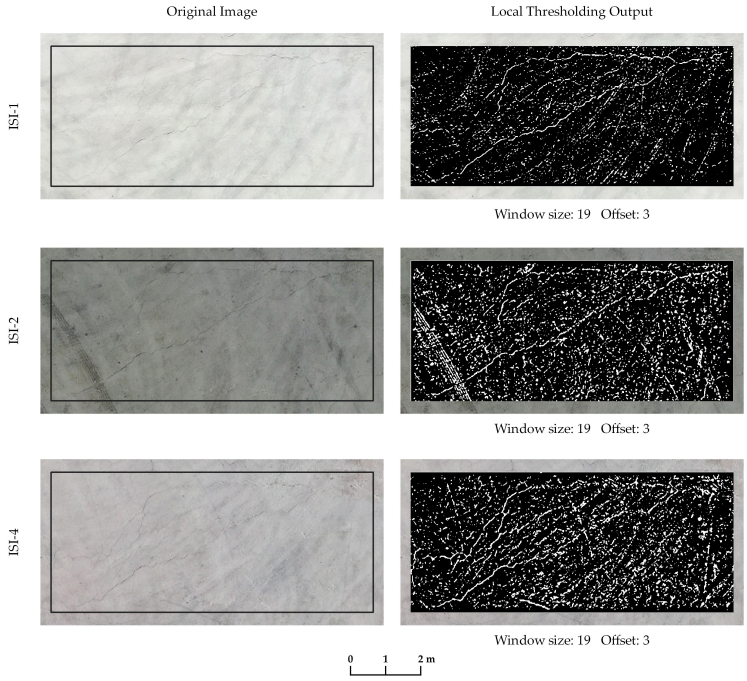


Figure 13. Illustration of the severely cracked area of the examined concrete pavement of Lavrio port once local thresholding was applied for each ISI.

image. Figure 13 shows the image results after the segmentation and the values of the window size and the offset required for the application of the local thresholding algorithm. By examining Figure 13 it is observed that the noise includes not only linear elements/groups of pixels but also circular or ellipsoid shapes. Following similar practices for removing noise after segmentation [30], denoising was applied with a threshold of 15, 25, and 28 pixels for each binary image, respectively [Figure 14].

Although noise removal resulted in improving crack detection, random white pixels remain present. During the digitalization of cracks [Figure 11], it was observed that cracks thinner than 15 mm approximately, detected while conducting visual inspections at Lavrio port, were difficult to identify in the GIS-based visualization. Based on the study of Yang *et al*., the ability to detect thin cracks depends on the image-capturing distance of the camera, the light conditions, the exposure time, and the pixel size [50]. Cracks thinner than one pixel cannot be easily measured. Hence, for the present research, white pixels beyond the area of the main cracking illustrated in Figure 15 were excluded as shown in Figure 16. The cracks shown in Figure 15 were manually digitized using GIS tools, while the cracks in Figure 16 are the result of applying area thresholding.

By examining Figure 16, it was observed that the continuity of the cracks formed by adjacent pixels was interrupted in some areas, while several white irrelevant pixels were present. Based on the described methodology in Section 2, the dilation process was first applied to achieve the optimal filling with white pixels without imperiling over increasing crack width [Figure 17]. A 3×3 structural element was used and the process was repeated twice. Once dilation was completed, erosion was implemented twice with a 3×3 structural element to remove false pixels that existed previously or had occurred during the previous morphological operation [Figure 18]. A more detailed example of the significance of the morphological operations is shown in Figure 19. A crack pattern identified in the initial georeferenced image was effectively detected after the implementation of all steps of the proposed methodology up to the level of completing erosion even though some gaps still exist. Furthermore, although a significant part of the noise was removed, some irrelevant white pixels are still present.

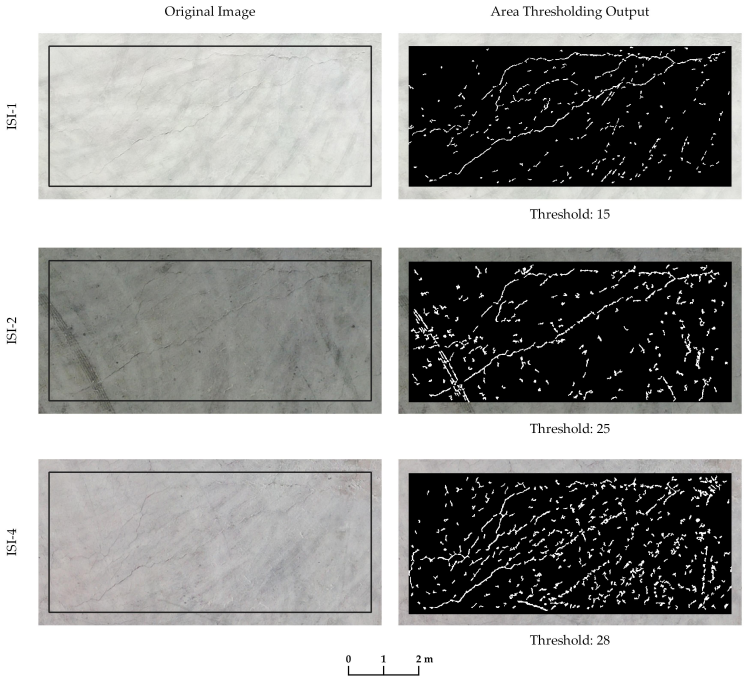


Figure 14. Illustration of the severely cracked area of the examined concrete pavement of Lavrio port once area thresholding was applied to the binary images of each ISI.

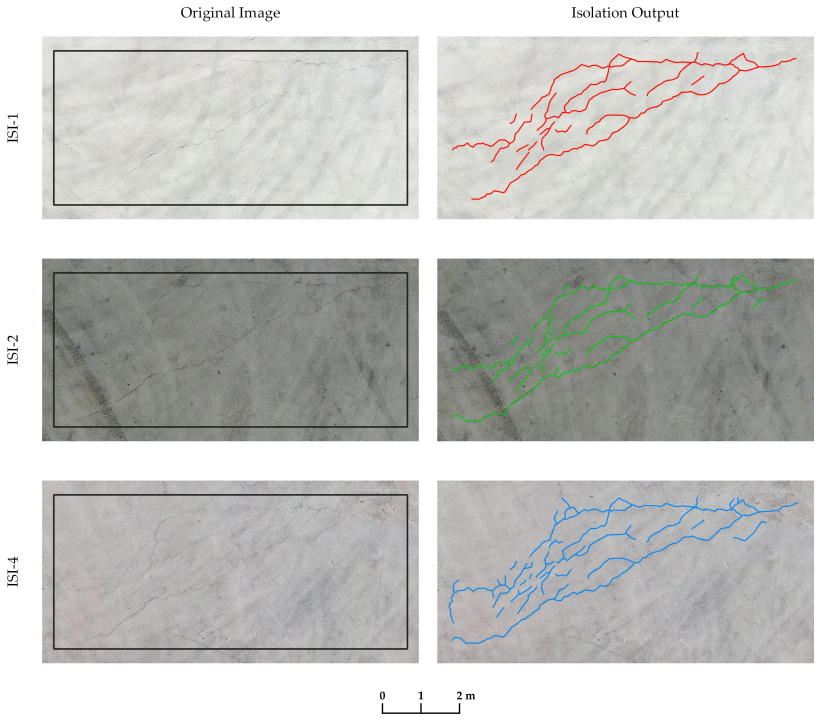


Figure 15. Isolation of the cracked area showing the digitized crack output acquired through visual examination of the orthophotos.

The GIS-based visualized output of crack detection processing in the study area is shown in Figure 20, while the rasterized output generated by the application of the morphological operations was vectorized and the

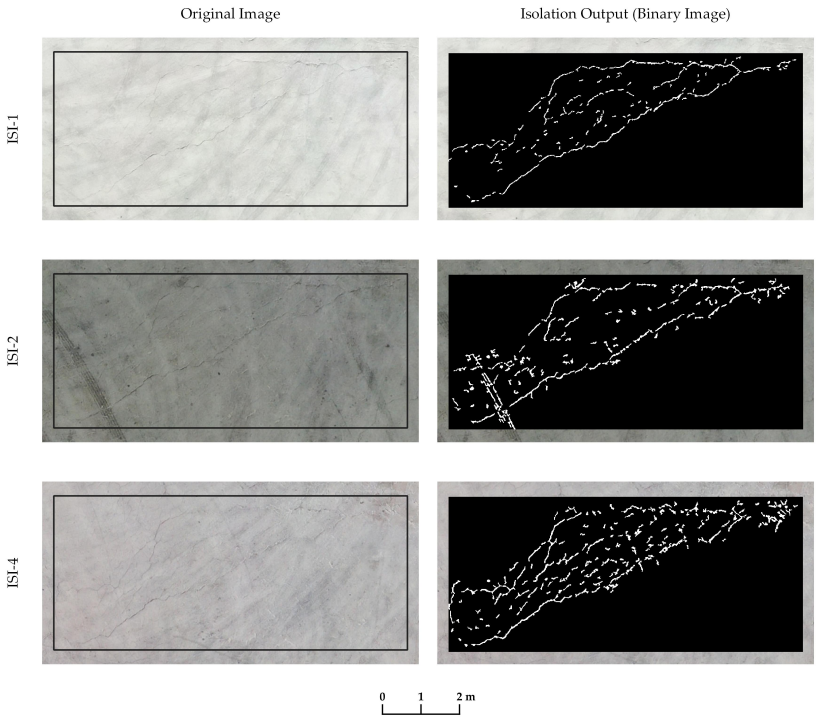


Figure 16. Isolation of the cracked area in the binary image of Figure 14.

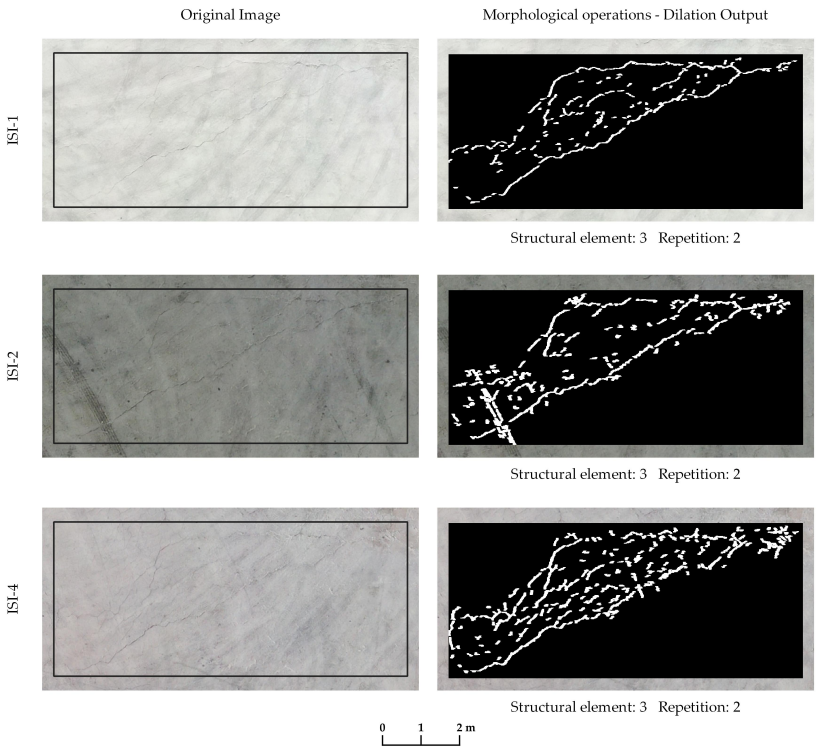


Figure 17. Morphological operations - Dilation output for the considered cracked area.

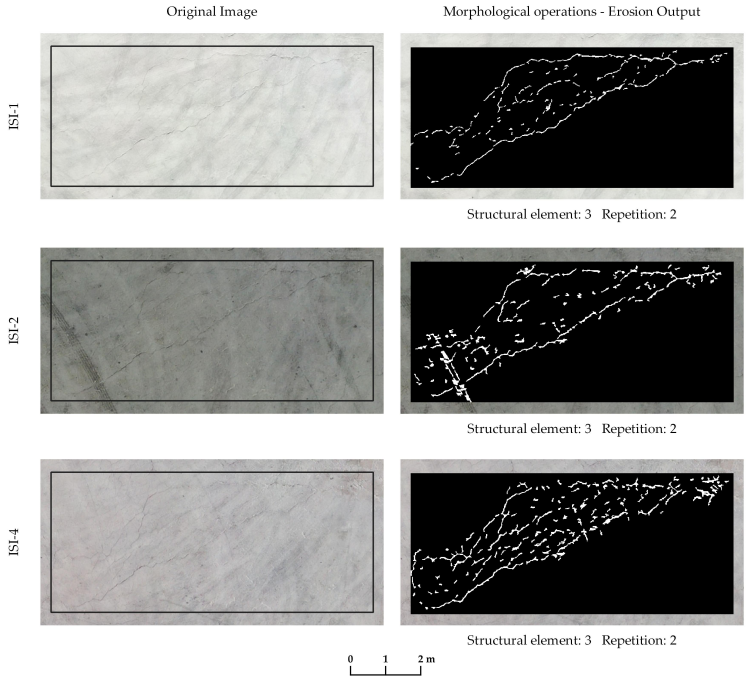


Figure 18. Morphological operations - Erosion output for the considered cracked area.

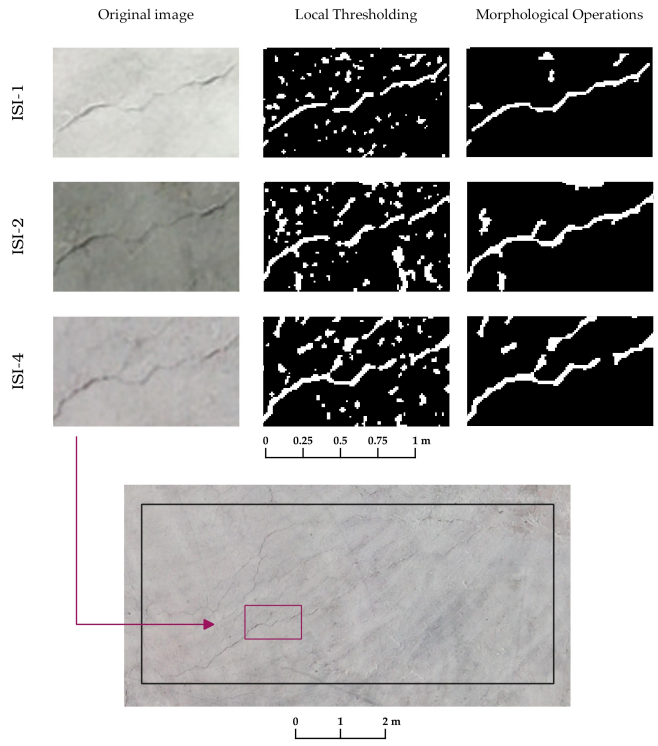


Figure 19. A detailed illustration of the detection of a crack pattern after morphological operations are completed.

final output of the skeletonization is included in Figure 21. Indicatively, the separate steps of subsequently converting raster data to polygons and lines are reflected in Figure 22 for the example of Figure 19. Moreover,

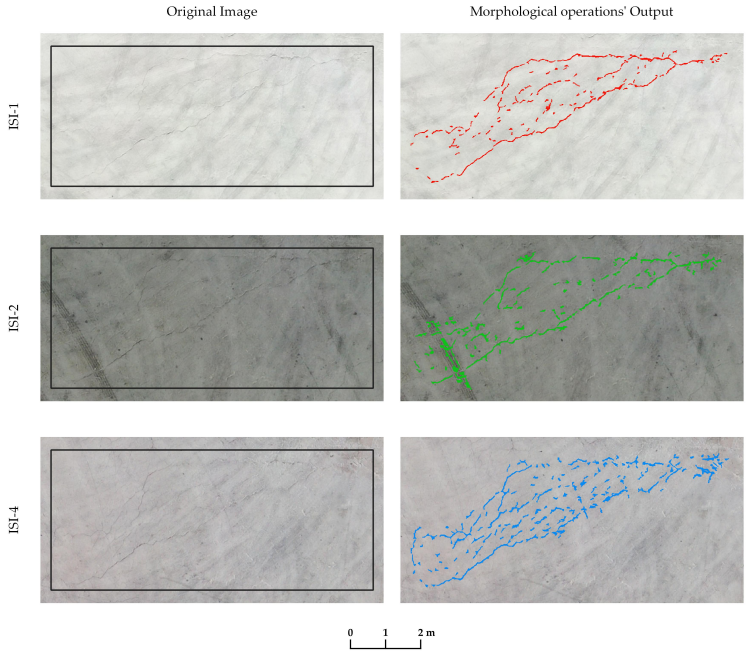


Figure 20. The GIS-based visualized output of crack detection processing after morphological operations are completed. Cracks are depicted as polygons.

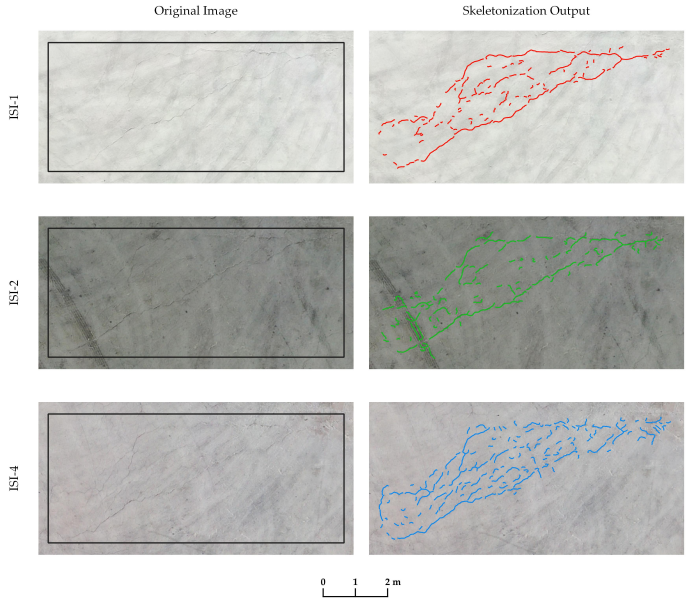


Figure 21. Final output of crack detection based on the proposed methodology. Cracks are depicted as lines with the skeletonization algorithm.

Figure 23 includes a comparison between digitized (i.e., manually detected) and vectorized (i.e., automatically detected) cracks for the same area as in Figure 19.

Based on Figure 23, it is noticed that the digitized primary crack of 28 mm width of ISI-1 is efficiently detected. Both crack features (i.e., width and length) and dark appearance in the original image were the main factors

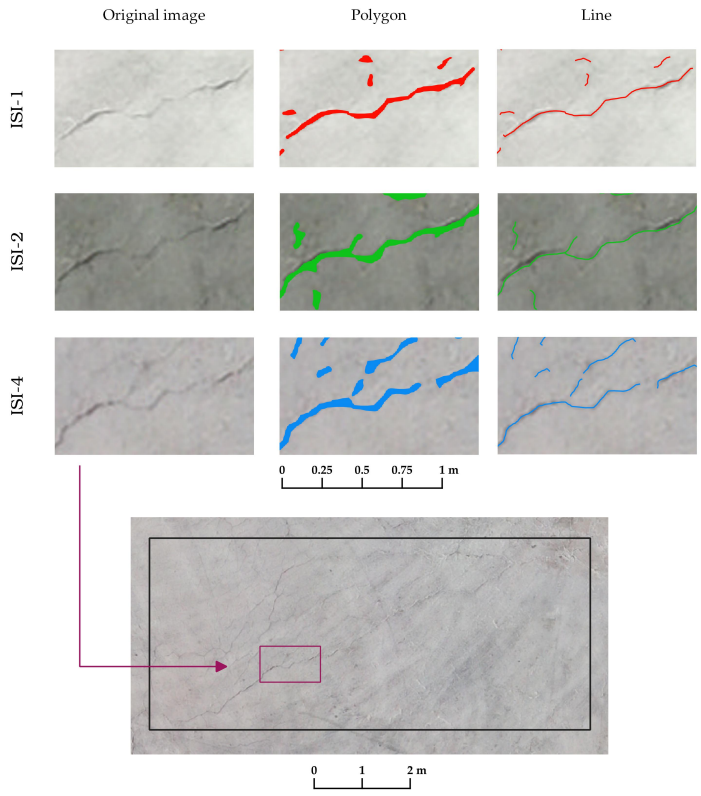


Figure 22. Vectorization of the rasterized output of the example illustrated in Figure 19.

that facilitated crack detection. However, for the remaining cracks thinner than 15 mm crack detection failed. Moreover, three additional lines of 10-15 cm length appeared after image processing mainly due to color tone differentiation from the adjacent pixels. Similar to ISI-1, the primary crack of ISI-2 was also detected along with some false lines. An additional vertical crack was digitized and partially detected. This crack seems to propagate during the time intervals of the ISIs as shown in the results of digitization and detection for ISI-4. Crack detection for ISI-4 resulted in identifying the primary crack and its diagonal propagation, while similar to the inspections ISI-1 and ISI-2 false lines were also present. Considering the above, it is highly interesting that the proposed GIS-based methodology enables detecting structural variations during port concrete pavements' lifetime in terms of crack propagation.

The above observations were validated by building the confusion matrix described in Section 2. Before proceeding with validation, the digitized (i.e., manually detected) crack lines were converted to polygons to measure the crack width with GIS rasterization tools, as indicatively shown in Figure 24. The characteristics of the digitized cracks are included in Table 1. Figure 25 shows a comparative illustration of the digitized and detected width data for the example of Figure 19. It is obvious that for the specific illustration, the crack width is increasing between inspections. This observation indicates a continuous progression of the damage in the concrete pavement, highlighting the need for timely maintenance interventions.

To validate the results for the entire study area, the performance metrics were calculated based on the developed confusion matrix illustrated in Figure 10 [Table 2 and Table 3]. More specifically:

- The high "Sensitivity" percentages of ISI-1 and ISI-4 show that a large amount of the digitized cracks was successfully detected contrary to the digitized cracks of ISI-2 that were partially detected.
- The significantly high "Specificity" percentage of all ISIs indicates the high accuracy in classifying the non-

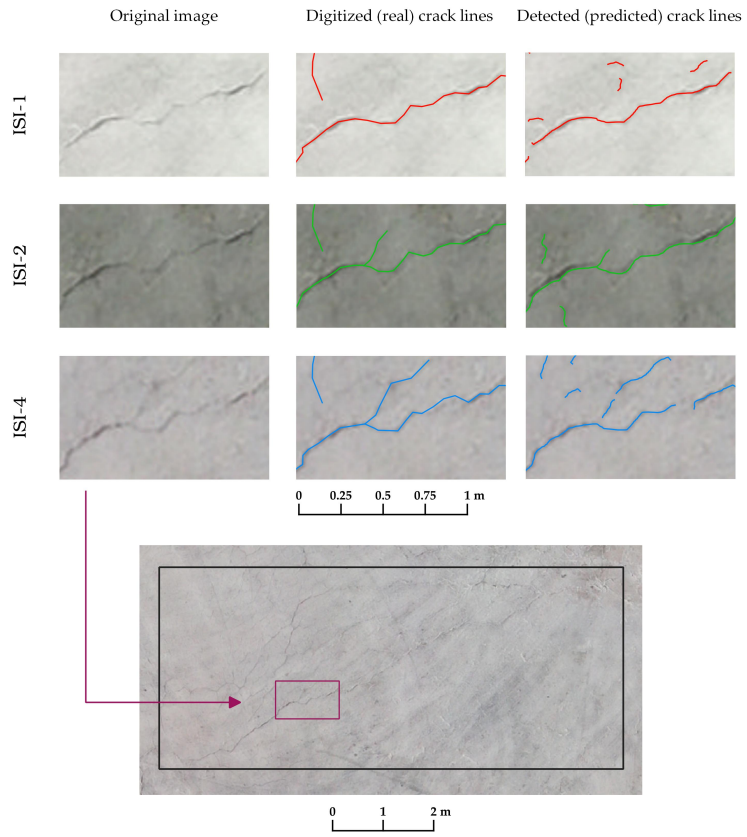


Figure 23. An indicative comparative illustration between digitized (i.e., manually detected) and vectorized (i.e., automatically detected) cracks for the example of Figure 19.

cracked areas.

- The average "Precision" percentage of the order of 68% of all ISIs demonstrates that within the total amount of cracks detected by applying the methodology, approximately 32% of them were false.
- The significantly high "Negative Predictive Value" of all ISIs indicates that the probability that a case is truly negative (non-cracked area) among the cases predicted as negative is very high.
- The high "Accuracy" percentage between 90% and 100% shows that the classification of non-cracked and cracked areas is mainly correct considering the entire sample.
- The F1-score for the class 0 is between 95% and 100% thus demonstrating that the "Sensitivity" and "Specificity" do not deviate from each other and the majority of predictions for the non-cracked areas are correct.
- The F1-score for class 1 is between 74% and 76% for ISI-1 and IS-4 thus demonstrating that the "Sensitivity" and "Specificity" deviate slightly from each other and that 3/4 of predictions for the cracked areas are correct. On the other hand, the F1-score for ISI-2 is reduced up to approximately 57%. Considering this, it seems that the detection model can be improved to avoid F1-scores for class 1 below 70%
- The average F1-score is above 70% thus indicating a total satisfactory balance between "Sensitivity" and "Specificity". In other words, the detection model is performing well.
- The error rate for ISI-1 and ISI-4 ranges between 2% and 3% thus verifying the high accuracy of the model. The increased error rate of ISI-2 is linked to the detection model's liability to falsely detect cracking in some cases where noise is significantly high. This is attributed to the presence of tire marks [Figure 20] which causes the detection model to classify the dark marks as cracks.

Analysis of Table 2 and Table 3 revealed that even though ISI-2 and ISI-4 had the same UAV flight altitude, ISI-4 outperformed ISI-2 in terms of performance metrics and F-score values. The presence of intense noise

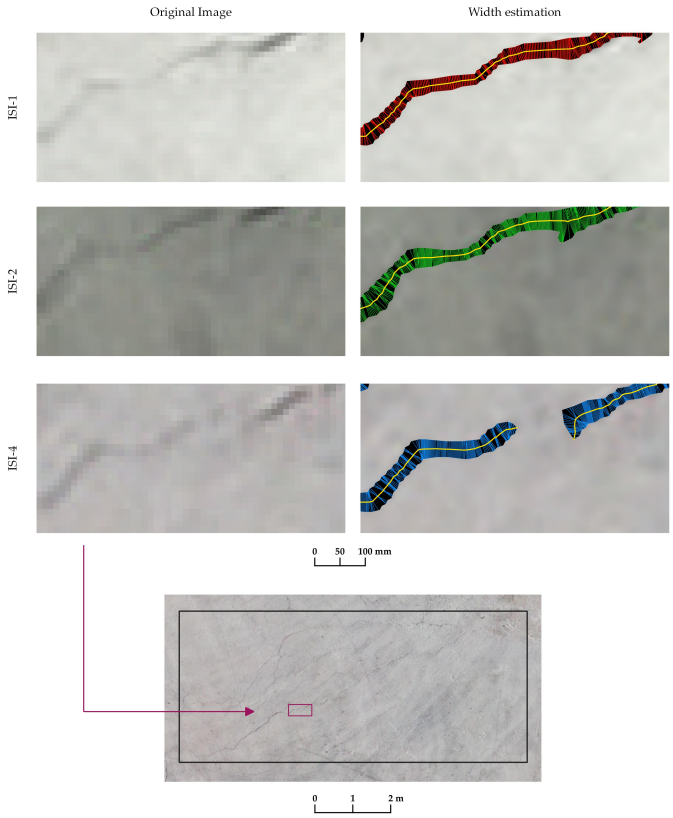


Figure 24. Example of width estimation of digitized crack lines with GIS rasterization tools.

Table 1. GIS-based measurements of the digitized cracks

ISI-i	Total length (m)	Minimum width (mm)	Maximum width (mm)	Average width (mm)
ISI-1	23.65	14.4	82.0	28.5
ISI-2	23.15	13.8	96.0	37.5
ISI-4	27.88	15.2	89.0	36.5

Table 2. Performance metrics for validating crack detection results for the example of Figure 19

ISI-i	Sensitivity	Specificity	Precision	Negative predictive value	Accuracy
	(Recall class 1)	(Precision class 0)	(Precision class 1)	(Recall class 0)	
ISI-1	84.29%	98.12%	66.22%	99.38%	97.62%
ISI-2	56.09%	96.90%	60.81%	95.39%	92.91%
ISI-4	73.53%	98.65%	79.35%	98.17%	97.02%

from the tire marks in ISI-2 had a negative impact on result precision. However, despite this noise, the performance values were still relatively high, indicating that the proposed methodology shows promise even in the presence of noise. Additionally, a variation of 10 m in the UAV flight altitude did not seem to adversely affect the performance of the proposed methodology. Crack detection using data collected from flights at altitudes ranging from 48 to 56 m exhibits high precision. Hence, the methodology maintains its robustness across this range of altitudes.

By combining the GIS-based quantified results for the digitized cracks included in Table 1 and the F-scores of

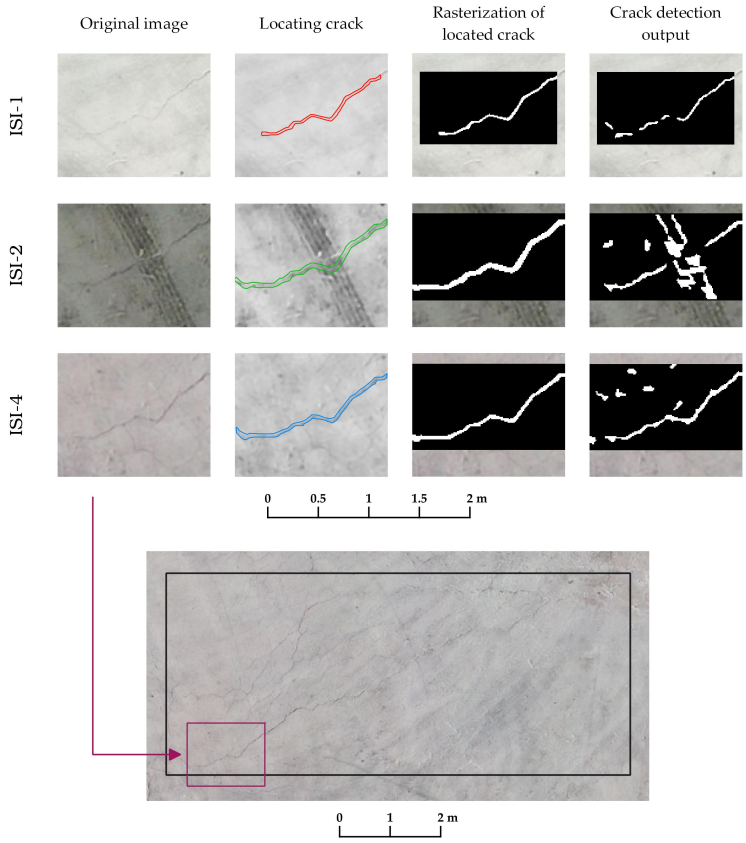


Figure 25. A comparative illustration of the digitized and automatically detected width data for the example of Figure 19.

Table 3. F-score values for validating crack detection results for the example of Figure 19

ISI-i	F1-score - non-crack area (class 0)	F1-score - crack area (class 1)	F1-score Avg	Error rate
ISI-1	98.75%	74.04%	86.39%	2.38%
ISI-2	96.13%	57.44%	76.78%	7.09%
ISI-4	98.41%	76.12%	87.26%	2.98%

Table 3, the measurements of the truly detected cracks can be derived [Table 4]. During the time period from ISI-1 to ISI-4, there was a noticeable increase in the cracked area, which expanded by 3.71 m in length. This time-induced variation can be visually represented with GIS tools as indicatively shown in Figure 25. Therefore, it can be viewed that distressed areas and the extent of damage are identified through GIS-based mapping and assessment by comparing crack detection results from each ISI. In this context, geospatial metadata that changes over time, such as crack propagation, can be efficiently monitored and analyzed using the proposed GIS-based crack detection methodology. The results of ISI-2 were not considered for change detection due to the lower F1-score for class 1.

4 DISCUSSION

Automation in damage detection with structural monitoring data is currently one of the most prominent areas of research in various industry fields (e.g., manufacturing systems[51,52]). Regarding concrete civil infrastructure working on automatically detecting cracks is a growing trend that has occupied several researchers (e.g.,[23,24,36,50]). Their main focus was on advancing current methodologies and improving efficiency in de-

Table 4. Measurements of the truly detected cracks.

ISI-i	Total length (m)	Maximum width (mm)
ISI-1	17.51	60.71
ISI-2	13.30	55.14
ISI-4	21.22	67.75

tecting actual cracks with either image processing or machine learning approaches. The impact of such crack detection approaches can be amplified by the competitive advantages of GIS tools. A GIS-based structural condition assessment of port concrete pavements enables geospatially visualizing cracks, straightforwardly measuring crack features, storing geospatial crack data, and creating databases for gaining a deep insight into the structure's vulnerabilities (e.g., causes of crack propagation)[19]. Hence, the proposed methodology combines image processing programming modules with GIS applications to support SHM of port concrete pavements.

One of the main issues encountered during the entire process was the impact of the UAV flight altitude. Crack detection for the ISIs with the lower flight altitudes (i.e., ISI-1 with 48 m, and ISI-2 and ISI-4 with 56 m) was effective due to the smaller pixel size of the generated orthophotos. Therefore , the GIS-based crack visualization was conducted with more pixels. Except for the UAV flight altitude, the presence of intense noise such as large shadows from vessels or tire marks affected the results. The orthophoto of ISI-3 was excluded from the analysis from the beginning since the large shadowed area was represented with a dark color tone that can be misinterpreted as a cracked area. In contrast to ISI-3, the orthophoto of ISI-2 was included in the crack detection analysis to assess how tire marks on the concrete pavement surface impacted the effectiveness of the proposed methodology. By removing the noise with thresholding and labeling it seemed that the negative effect of the tire marks was limited.

Furthermore, the specific research was based on routine ISIs the main function of which is to gather information for planning future maintenance actions[7]. The inspections dictated the course and the priority for maintaining the herein-examined concrete slab due to the high-density cracking. The latter is mainly attributed to the large dimensions of the slab (i.e., the absence of construction joints within a large part of the concrete surface) thus allowing for the forming of significant cracks due to movements (e.g., shrinkage, thermal contraction, *etc*.). This fact was aggravated by the absence of repair measures. During the routine inspections, UAV flight altitudes were selected so that not only the entire concrete pavement of the mooring facilities but also other structures such as rubble mound structures were depicted by optimizing inspection and computation time[19]. However, flight altitude can be reduced for targeted inspections of the specific concrete slab to further quantify detected deterioration and determine its structural significance[7].

Although the present paper focuses on port concrete pavements, the application of the GIS-based proposed methodology can be valuable for other similar structural systems such as airports with concrete aprons. Factors including tire marks, building or vehicle shadows, passengers' moving, and others are common challenges encountered in both port and airport systems. For a successful SHM program of these systems, the updating of GIS databases with cracking information is crucial.

Finally, it is noted that the methodology used in this research relies on parameter selection based on common practices that were most suitable for the specific case study. A trial and error process is required when applying the methodology for the first time. However, once the parameters are finalized, the methodology can be easily repeated. Based on the overall investigation, the following aspects should be considered for the iterative process of trial and error to maximize accuracy:

- The kernel size in the median filtering should preserve details and edges while controlling noise reduction. Using a smaller kernel (e.g., 3×3) can retain fine details, enhancing the accuracy. Employing a larger kernel

may smooth out or blur fine cracks, potentially causing false negatives that lower accuracy.

- The window size in the local thresholding determines the local area for thresholding. A smaller window size (e.g., 19 × 19) increases sensitivity to local intensity variations, aiding in the detection of fine cracks, thus improving accuracy. A larger window may overlook fine cracks, leading to false negatives and decreasing accuracy.
- The offset in the local thresholding affects the inclusivity or exclusivity of cracks. A positive offset (e.g., 3) increases exclusivity, thus reducing false positives and improving accuracy. On the contrary, negative offset increases inclusivity, potentially mistaking noise for cracks and decreasing accuracy.
- Area thresholding refines the binary output of crack detection by eliminating irrelevant white pixels. During the analysis, it was observed that the optimal area threshold varied for each image of the ISIs due to the presence of noise. A lower area threshold was found to be appropriate for ISI-1 since it preserved finer cracks, whereas, for ISI-2 and ISI-4, the area threshold was increased to improve accuracy by filtering out irrelevant pixels.
- The structural element in morphological operations affects the number of false positives and negatives. A smaller structural element (e.g., 3 × 3) can help preserve fine cracks and increase accuracy. A larger structural element may distort or merge cracks resulting in false positives that can compromise accuracy.
- Repetitions in morphological operations are important to refine cracks. A limited number of repetitions is preferred over excessive repetitions since the latter may thicken, merge or remove cracks leading to false positives or false negatives that reduce accuracy.

5 CONCLUSIONS

The overall investigation indicated the significance of expanding crack detection approaches beyond mathematical computations. Interrelating cracking data with structural issues of port concrete pavements is achieved by retaining the geospatial information throughout the process to support GIS-based structural condition assessment applications. By building a GIS database, it was concluded that despite the small time interval between the ISIs (approximately every half a year), crack propagation was a continuous issue. This ongoing process imperils the structural integrity of the examined concrete slab, highlighting the importance of planning inspection schemes for in-service port concrete pavements.

One of the main challenges during the analysis was the presence of various noises in orthophotos, such as surface scratches or tire marks, unlike images focusing on limited cracked parts of a structure. The implementation of the combined methodology showed that high reliability and accuracy (average 95%) can be achieved while preserving all geospatial information. This finding is significant as it encourages the use of orthophotos for analyzing port concrete pavements without compromising accuracy. Additionally, once the approach is applied for the first time to a specific port structure and the arrangement of the steps is determined, processing data and returning results quickly enhance the real-time performance of the methodology.

Although the proposed methodology was applied to cracks wider than 15 mm, it was concluded that once all steps were completed it was more effective for detecting cracks wider than 20 mm. If required, UAV flight altitude can be reduced to detect thinner cracks. For this task, it is essential to investigate the balance between inspection and computation time, while considering a potential entanglement with port operations. Therefore, further research may include sensitivity analysis to define the optimal UAV flight altitude based on the surrounding height conditions and restrictions, the accuracy of the outcome, and the collected amount of data.

DECLARATIONS

Authors' contributions

Contributed to conceptualization, methodology, software, validation, analysis, investigation, data collection, draft preparation, manuscript editing, and visualization: Tsaimou CN
Contributed to methodology, software, analysis, and manuscript editing: Kagkelis G
Contributed to field data collection and validation: Sartampakos P
Contributed to methodology, software, and validation: Karantzalos K
Contributed to conceptualization, methodology, analysis, investigation, data collection, validation, manuscript editing, review, supervision, project administration, and funding acquisition: Tsoukala VK

Availability of data and materials

Not applicable.

Financial support and sponsorship

The first author was supported for this research by the Special Account for Research Funding of the National Technical University of Athens, Greece (Scholarship grant number 65/219100).

Conflicts of interest

Sartampakos P is from NIREAS Engineering, which declares no conflicts of interest. While the other authors declared that there are no conflicts of interest.

Ethical approval and consent to participate

Not applicable.

Consent for publication

Not applicable.

Copyright

© The Author(s) 2024.

REFERENCES

1. de Langen P, Turró M, Fontanet M, Caballé J. The infrastructure investment needs and financing challenge of European ports; 2018. Available from: https://www.espo.be/media/Port%20Investment%20Study%202018_FINAL_1.pdf [Last accessed on 11 Nov 2024].
2. Lauritzen PN, Reichard J, Ahmed S, Safa M. Review of non-destructive testing methods for physical condition monitoring in the port industry. *J Constr Eng Manag Innov* 2019;2:103-11. DOI
3. Hossain NUI, Nur F, Hosseini S, Jaradat R, Marufuzzaman M, Puryear SM. A Bayesian network based approach for modeling and assessing resilience: a case study of a full service deep water port. *Reliab Eng Syst Saf* 2019;189:378-96. DOI
4. Zhang Y, Kim CW, Tee KF, Lam JSL. Optimal sustainable life cycle maintenance strategies for port infrastructures. *J Clean Prod* 2017;142:1693-709. DOI
5. Rodrigue JP. The geography of transport systems. London: Routledge; 2020. DOI
6. Negi P, Kromanis R, Dorée A, Wijnberg KM. Structural health monitoring of inland navigation structures and ports: a review on developments and challenges. *Struct Health Monit* 2023;23:147592172311707 DOI
7. Heffron RE. Waterfront facilities inspection and assessment. Reston, VA, USA: ASCE; 2015. DOI
8. Klerk WJ, Schweckendiek T, den Heijer F, Kok M. Value of information of structural health monitoring in asset management of flood defences. *Infrastructures* 2019;4:56. DOI
9. Leblouba M, Tarabin M, Zahri M. Probabilistic analysis and simulation of crack propagation in concrete pavements and surfaces. *Sci Rep* 2022;12:14157. DOI
10. Zhang Y, Lu Y, Duan Y, et al. Robust surface crack detection with structure line guidance. *Int J Appl Earth Obs Geoinf* 2023;124:103527. DOI
11. Munawar HS, Hammad AWA, Haddad A, Soares CAP, Waller ST. Image-based crack detection methods: a review. *Infrastructures* 2021;6:115. DOI
12. Gupta P, Dixit M. Image-based crack detection approaches: a comprehensive survey. *Multimed Tools Appl* 2022;81:40181-229. DOI
13. Ding W, Yang H, Yu K, Shu J. Crack detection and quantification for concrete structures using UAV and transformer. *Automat Constr* 2023;152:104929. DOI

14. Jin T, Zhang W, Chen C, Chen B, Zhuang Y, Zhang H. Deep-learning- and unmanned aerial vehicle-based structural crack detection in concrete. *Buildings* 2023;13:3114. DOI
15. Song F, Liu B, Yuan G. Pixel-level crack identification for bridge concrete structures using unmanned aerial vehicle photography and deep learning. *Struct Control Health Monit* 2024;2024:1299095. DOI
16. Li Y, Ma J, Zhao Z, Shi G. A novel approach for UAV image crack detection. *Sensors* 2022;22:3305. DOI
17. Woo HJ, Seo DM, Kim MS, Park MS, Hong WH, Baek SC. Localization of cracks in concrete structures using an unmanned aerial vehicle. *Sensors* 2022;22:6711. DOI
18. Choi D, Bell W, Kim D, Kim J. UAV-driven structural crack detection and location determination using convolutional neural networks. *Sensors* 2021;21:2650. DOI
19. Tsaimou CN, Sartampakos P, Tsoukala VK. UAV-driven approach for assisting structural health monitoring of port infrastructure. *Struct Infrastruct Eng* 2023;1-20. DOI
20. Ali R, Chuah JH, Talip MSA, Mokhtar N, Shoaib MA. Structural crack detection using deep convolutional neural networks. *Autom Constr* 2022;133:103989. DOI
21. Arvidsson B, Johansson J, Guldåker N. Critical infrastructure, geographical information science and risk governance: a systematic cross-field review. *Reliab Eng Syst Saf* 2021;213:107741. DOI
22. Lesiak P. Inspection and maintenance of railway infrastructure with the use of unmanned aerial vehicles. *Probl Kolejn* 2020;115-27. DOI
23. Li R, Yu J, Li F, Yang R, Wang Y, Peng Z. Automatic bridge crack detection using Unmanned aerial vehicle and Faster R-CNN. *Constr Build Mater* 2023;362:129659. DOI
24. Zhao Y, Zhou L, Wang X, Wang F, Shi G. Highway crack detection and classification using UAV remote sensing images based on CrackNet and CrackClassification. *Appl Sci* 2023;13:7269. DOI
25. Azouz Z, Honarvar Shakibaei Asli B, Khan M. Evolution of crack analysis in structures using image processing technique: a review. *Electronics* 2023;12:3862. DOI
26. Sundararajan D. Digital image processing: a signal processing and algorithmic approach. Singapore: Springer; 2017. DOI
27. Liu YF, Cho S, Spencer Jr. BF, Fan JS. Concrete crack assessment using digital image processing and 3D scene reconstruction. *J Comput Civ Eng* 2016;30:04014124. DOI
28. Archana R, Jeevaraj PSE. Deep learning models for digital image processing: a review. *Artif Intell Rev* 2024;57:11. DOI
29. Fan L, Zhang F, Fan H, Zhang C. Brief review of image denoising techniques. *Vis Comput Ind Biomed Art* 2019;2:7. DOI
30. Otsu N. A threshold selection method from gray-level histograms. *IEEE Trans Syst Man Cybern* 1979;9:62-6. DOI
31. Niblack W. An introduction to digital image processing. Englewood Cliffs, NJ: Prentice-Hall International; 1986. Available from: https://archive.org/details/introductiontodi0000nibl [Last accessed on 11 Nov 2024].
32. Sauvola J, Pietikäinen M. Adaptive document image binarization. *Pattern Recognit* 2000;33:225-36. DOI
33. Sobel I, Feldman G. A 3 × 3 isotropic gradient operator for image processing; 1973. Available from: https://www.researchgate.net/publication/285159837_A_33_isotropic_gradient_operator_for_image_processing [Last accessed on 11 Nov 2024].
34. Canny J. A computational approach to edge detection. *IEEE Trans Pattern Anal Mach Intell* 1986;PAMI-8:679-98. DOI
35. Dorafshan S, Maguire M, Qi X. Automatic surface crack detection in concrete structures using OTSU thresholding and morphological operations. UTC Report 01-2016. Utah State University; 2016. DOI
36. Kim IH, Jeon H, Baek SC, Hong WH, Jung HJ. Application of crack identification techniques for an aging concrete bridge inspection using an unmanned aerial vehicle. *Sensors* 2018;18:1881. DOI
37. Li H, Wang W, Wang M, Li L, Vimlund V. A review of deep learning methods for pixel-level crack detection. *J Traffic Transp Eng* 2022;9:945-68. DOI
38. Jofré-Briceño C, Muñoz-La Rivera F, Atencio E, Herrera RF. Implementation of facility management for port infrastructure through the use of UAVs, photogrammetry and BIM. *Sensors* 2021;21:6686. DOI
39. Harris DK, Brooks CN, Ahlborn TM. Synthesis of field performance of remote sensing strategies for condition assessment of in-service bridges in Michigan. *J Perform Constr Facil* 2016;30:04016027. DOI
40. GDAL/OGR geospatial data abstraction software library; 2024. DOI
41. Rasterio/affine's documentation; 2024. Available from: https://affine.readthedocs.io/en/latest/ [Last accessed on 11 Nov 2024].
42. Chen C, Seo H, Jun C, Zhao Y. A potential crack region method to detect crack using image processing of multiple thresholding. *Signal Image Video Process* 2022;16:1673-81. DOI
43. Chityala R, Pudipeddi S. Image processing and acquisition using Python. 2nd ed. Boca Raton: Chapman and Hall/CRC Press; 2020. p. 452. DOI
44. Owotogbe JS, Ibiyemi TS, Adu BA. A comprehensive review on various types of noise in image processing. *Int J Sci Eng Res* 2019;10:388-93. Available from: https://www.ijser.org/researchpaper/A-COMPREHENSIVE-REVIEW-ON-VARIOUS-TYPES-OF-NOISE-IN-IMAGE-PROCESSING.pdf [Last accessed on 11 Nov 2024].
45. Gonzalez RC, Woods RE. Digital image processing. 4th ed. Essex, England: Pearson Education Limited; 2018. Available from: https://dl.icdst.org/pdfs/files4/01c56e081202b62bd7d3b4f8545775fb.pdf [Last accessed on 11 Nov 2024].
46. Xu B, Chen J, Yu P. Vectorization of classified remote sensing raster data to establish topological relations among polygons. *Earth Sci Inform* 2017;10:99-113. DOI
47. Zhang F, Hu Z, Yang K, Fu Y, Feng Z, Bai M. The surface crack extraction method based on machine learning of image and quantitative feature information acquisition method. *Remote Sens* 2021;13:1534. DOI
48. Obi JC. A comparative study of several classification metrics and their performances on data. *World J Adv Eng Technol Sci* 2023;8:308-14.

DOI

49. Tharwat A. Classification assessment methods. *Appl Comput Inform* 2020;17:168-92. DOI
50. Yang YS, Wu Cl, Hsu TTC, Yang HC, Lu HJ, Chang CC. Image analysis method for crack distribution and width estimation for reinforced concrete structures. *Autom Constr* 2018;91:120-32. DOI
51. Feng K, Ji JC, Ni Q, Li Y, Mao W, Liu L. A novel vibration-based prognostic scheme for gear health management in surface wear progression of the intelligent manufacturing system. *Wear* 2023;522:204697. DOI
52. Feng K, Ni Q, Chen Y, Ge J, Liu Z. A cyclostationarity-based wear monitoring framework of spur gears in intelligent manufacturing systems. *Struct Health Monit* 2023;22:147592172211470. Available from: https://www.researchgate.net/publication/367100031_A_cyclostationarity-based_wear_monitoring_framework_of_spur_gears_in_intelligent_manufacturing_systems [Last accessed on 11 Nov 2024].

Zhao *et al. Complex Eng Syst* 2024;4:22
DOI: 10.20517/ces.2024.54

Complex Engineering Systems

Perspective

Open Access

Check for updates

Dynamic reliability decision-making frameworks: trends and opportunities

Xiujie Zhao, Yi Luo

College of Management and Economics, Tianjin University, Tianjin 300072, China.

Correspondence to: Prof. Xiujie Zhao, College of Management and Economics, Tianjin University, 92 Weijin Road, Nankai District, Tianjin 300072, China. E-mail: xiujiezhao@tju.edu.cn

How to cite this article: Zhao X, Luo Y. Dynamic reliability decision-making frameworks: trends and opportunities. *Complex Eng Syst* 2024;4:22. https://dx.doi.org/10.20517/ces.2024.54

Received: 29 Aug 2024 **First Decision:** 10 Oct 2024 **Revised:** 31 Oct 2024 **Accepted:** 26 Nov 2024 **Published:** 30 Nov 2024

Academic Editor: Hamid Reza Karimi **Copy Editor:** Fangling Lan **Production Editor:** Fangling Lan

Abstract

Reliability engineering and management are becoming more important as systems evolve in functionality and complexity. Given various dynamic factors influencing reliability, static one-time decision frameworks can no longer offer optimal reliability decisions. In the paper, we discuss the recent trends in reliability decision-making methods across three stages of reliability issues: reliability testing and optimization, reliability modeling and evaluation, and post-service design. We can find a growing interest in time-dependent dynamic methods in research for all these three stages. Sequential decision modeling methods, such as the Markov decision process and its extensions, can be a resort to solve these problems, while modeling and problem-solving can be quite challenging under certain circumstances. Future research holds promising opportunities in related topics.

Keywords: Reliability, sequential decision models, maintenance optimization, reliability optimization

1. INTRODUCTION

Reliability engineering and management are crucial for product quality and market competitiveness. Demand for high performance and reliability has made decision-making a key research focus in this field.

Traditional static models assume constant conditions, failing to capture dynamic factors such as production, usage, and environment[1-3]. For instance, lithium-ion battery (LiB) reliability in electric vehicles depends on

© The Author(s) 2024. **Open Access** This article is licensed under a Creative Commons Attribution 4.0 International License (https://creativecommons.org/licenses/by/4.0/), which permits unrestricted use, sharing, adaptation, distribution and reproduction in any medium or format, for any purpose, even commercially, as long as you give appropriate credit to the original author(s) and the source, provide a link to the Creative Commons license, and indicate if changes were made.

manufacturing, usage, and maintenance[4,5]. Therefore, dynamic reliability decision-making provides more adaptive solutions across three main stages: reliability testing and optimization, modeling and evaluation, and post-service design.

Reliability testing and optimization face challenges due to complex, long-lasting products[6]. Standard life tests under normal conditions are impractical for highly reliable consumer durables[7]. Accelerated reliability testing (ART) uses stresses such as higher temperatures or humidity to expedite failure[8]. Reliability optimization, once limited to the design phase, now requires ongoing adjustments due to dynamic usage and environments[9,10], involving complex programming and algorithm development[11].

Traditional lifetime prediction methods lack today's needed precision, driving data-driven model growth[12]. The complexity of dynamic environments and varied usage further complicates model development. Peng *et al.* highlight the role of dynamic conditions in reliability modeling[13].

Reliability engineering includes testing, modeling, optimization, and post-service design, linked to degradation and operational environments[14]. For example, Gan *et al.* propose a maintenance optimization strategy for multi-state systems in dynamic environments[15].

The shift towards dynamic decision-making frameworks is driven by the practical needs of industries such as aerospace, automotive, and energy, where systems operate under highly variable conditions. This paper explores trends in dynamic reliability decision-making, addressing challenges and highlighting future research directions for adaptive and responsive management.

2. RELIABILITY TESTING AND OPTIMIZATION

Reliability testing and optimization are typically conducted during product design. However, modern systems' complexity makes system-level testing challenging[16]. Reliability is often assessed by testing the basic units, sometimes performed by suppliers rather than manufacturers. A key challenge in reliability testing is the extrapolation needed for predictions. Long-lasting consumer durables render traditional life tests impractical, making accelerated tests (ARTs) a preferred framework[17,18].

ARTs are typically categorized into accelerated life tests (ALTs) and accelerated degradation tests (ADTs), with some studies combining these methods[19]. Both methods shorten testing time and yield valuable reliability data. ALTs apply higher stress levels to accelerate failure[20], while ADTs track performance degradation over time[21,22]. In ALTs, unit failures and failure times are recorded, whereas ADTs measure periodic degradation. Planning is the first crucial step in ART for reliability assessment. Most existing studies follow a scheme that hinges on large-sample approximation to design ARTs, in which the optimality criteria are established via a function of the Fisher information and other selected variables. Figure 1 shows some key elements to be considered during the planning phase. The scheme is statistically sound, flexible, and adaptable to various scenarios.

Recent literature regarding related topics has implied several possible future directions. First, there are numerous research gaps in formulating new optimality criteria. Classical criteria such as D-, A-, and V-optimality, while statistically robust, often lack practical relevance. Bayesian optimization has been effectively applied to reliability-based design optimization, particularly in estimating design points with high accuracy[23]. Song *et al.* employ the constrained Bayesian optimization method and its variant to adaptively learn design points[24]. Emerging studies have increasingly concentrated on the connections between statistical criteria and the decision-maker's objectives[25,26]. Etemadi and Fotuhi-Firuzabad[27] propose

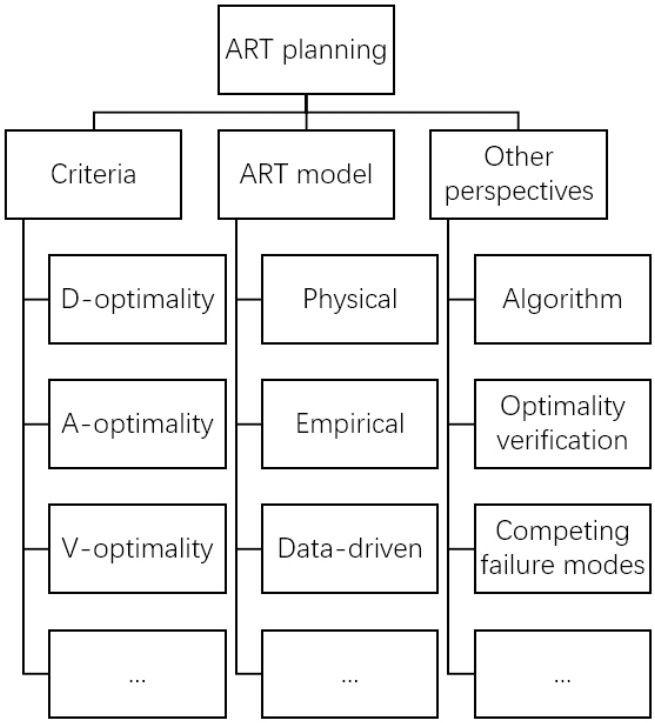


Figure 1. Important aspects in ART plan optimization.

optimizing protection system design by balancing costs and relay failure losses, integrating economic aspects into reliability. Incorporating maintenance and warranty perspectives into these criteria is promising. Second, the enrichment of the ART model and reliability model is always an outlet. Specifically, enhancing the interpretability of such models presents a significant challenge[28]. Last but not least, dynamic methods in ART planning are limited. Most extant works treat the test planning as a static design of experiment problem, yet in practice, tests can be planned and conducted in a dynamic, sequential manner[29,30]. Dynamic decision-making methods such as the Markov decision process (MDP) and reinforcement learning (RL) can be promising tools to tackle such planning problems[31].

Adding redundancy is a traditional yet effective way to boost system reliability, commonly seen in high-safety engineering systems such as airliners and automobiles. Reliability optimization covers various design problems, such as the redundancy allocation problem (RAP)[32], the reliability allocation problem and the reliability RAP (RRAP)[11]. Simply speaking, the problem is selecting the optimal components and quantities to ensure system operation. The uncertainty embedded in the reliability of units can make the problem quite onerous to solve. Risk-aware decision-makers often seek worst-case reliability solutions[33,34], leveraging distributionally robust methods. Nevertheless, the problem usually falls into the category of hard-to-solve mixed integer linear or nonlinear programs. Efficient algorithms remain a research priority, with specific system structures guiding algorithm improvements. Reihaneh *et al.* propose an exact branch-and-price (BP) algorithm for RAP with heterogeneous components under a mixed redundancy strategy[35].

Traditionally, reliability optimization was viewed as a static design-phase problem. However, with modern systems experiencing diverse usage and dynamic environments, system design now spans the entire lifecycle. Peiravi *et al.* introduced a novel Universal Redundancy Strategy (URS) aimed at improving system reliability by dynamically adjusting the configuration of redundant components during system operation[36].

Planning for redundancy upgrades and maintenance interactions is a time-dependent problem that classic methods may not handle effectively. Sequential decision models present a promising approach for tackling such dynamic challenges.

3. RELIABILITY MODELING AND EVALUATION

Data-driven reliability modeling methods have significantly evolved[37], but conventional lifetime-based methods, such as Weibull and Poisson models, remain popular in both research and applications[38]. Meanwhile, degradation modeling that utilizes the health characteristics of products for reliability analysis plays an increasingly important part in related fields[39]. This approach has been used to study reliability through performance loss in batteries, wear in machine tools, and crack growth in turbine blades. Reliability modeling and evaluation is not inherently a decision-making problem, but it provides crucial input for reliability-focused decision-making frameworks.

Dynamic factors can significantly affect system reliability during operation, as most systems function in time-varying environments. Changes in external conditions, such as higher temperatures, can negatively impact electronic products such as batteries and chipsets. Singpurwalla[40] and Eryilmaz and Rıza Bozbulut[41] have explored these effects on reliability modeling. Luo *et al.* propose a statistical model that accounts for both correlated component lifetimes and lifetime ordering constraints under dynamic conditions to show direct impacts on reliability[42]. Dynamic environments are generally modeled as time-varying covariates linked to reliability parameters[1,43]. Zhang *et al.* use a Wiener process for system degradation, treating the dynamic environment as a covariate[44].

Hybrid models have emerged as a transformative approach by integrating the strengths of physics-based models and data-driven techniques to address key challenges in reliability modeling. One such challenge is managing the heterogeneous usage patterns of products, which introduce complex operational variances and significantly affect system reliability. Accurately managing high-dimensional, often correlated, covariates is crucial. Machine learning-based methods can be a resort, yet incorporating the physical principles of reliability into these models can be complex. For a comprehensive review, refer to the study by Xu and Saleh[45]. Physics-informed machine learning methods need more in-depth investigation.

Dependent and Competing Failure Processes (DCFP) are increasingly important in reliability modeling, especially for systems facing multiple, interacting failure mechanisms such as wear, corrosion, and fatigue[46]. In DCFP, one failure process can influence the likelihood of others. This is particularly relevant for industrial applications such as LiB systems[47] and micro-electro-mechanical systems (MEMS)[48]. Additionally, Wu and Ding[49] explore how Markov environments influence systems with DCFP, highlighting dynamic environmental factors. Zhou and Li[50] study interactions between minor and major failures. Future research could integrate DCFP into dynamic decision-making frameworks for a deeper understanding of system reliability in changing conditions.

Reliability modeling for complex multi-component systems is another challenging task especially with component dependencies. Complex systems can be onerous to characterize using classical block diagrams. Network or graph-based characterizations are far more flexible and informative[51]. Combining stochastic models with regression-based methods can enhance the efficiency and accuracy of reliability models.

4. POST-SALE SERVICE DESIGN VIA RELIABILITY MODELS

Maintenance modeling and optimization are crucial post-sale strategies for manufacturers and consumers, with dynamic methods widely studied. MDP-based maintenance optimization dates back to the 1950s when

reliability engineering first emerged. Early research discussed system deterioration without explicitly mentioning "condition-based maintenance", favoring the term "preventive maintenance". In recent decades, condition-based maintenance (CBM) has garnered huge attention[52]. As shown in Figure 2, maintenance schemes often rely on different key state thresholds, which may lead to over-maintenance or unexpected failures. CBM dynamically adjusts maintenance decisions by continuously monitoring the system's degradation state.

Maintenance optimization via MDP and its variants has been studied intensely[53-55]. MDP is a framework for decision-making under uncertainty, representing a system where an agent chooses actions that lead to different states with specific rewards[56,57].

Unlike traditional CBM methods that set a constant threshold, MDP-based approaches use dynamic criteria linked to long-term utility for optimal policies. Semi-MDP (SMDP) and partially observed MDP (POMDP) are among the most commonly used variants of MDP in such problems[58,59]. The decisions are planned as illustrated in Figure 3. Under the MDP framework, system states (S_1 to S_5) are fully observable, while the POMDP framework addresses situations where system states are not directly observable. Instead, the decision-maker relies on observations to update belief states, which serve as probabilistic representations of the system's underlying condition. Mahmoodi *et al.* explore SMDP-based maintenance for parallel unit systems in dynamic environments[60], while Arcieri *et al.* propose a framework for inferring POMDP parameters using Markov Chain Monte Carlo (MCMC) to and address model uncertainty through domain randomization in RL training[61].

Warranty management stands at the interfaces of various engineering and management perspectives, including reliability, quality, marketing, design, *etc*.[62]. Maintenance and warranty policies for sold systems can be optimized jointly using MDP. Developing adaptive, tailored strategies in this context shows great potential.

Maintenance modeling can be expanded by incorporating system dynamics and varied maintenance actions to suit different scenarios. One intriguing direction is to incorporate time-varying dynamic covariates into degradation models, enabling decisions based on both system state and external factors. For example, Zheng *et al.* use an SMDP integrated with lot sizing and maintenance scheduling[63], while Luo *et al.* model the dynamic environment as a time-varying covariate affecting the degradation drift via a Markov process[64]. Joint policies combining maintenance with other decisions, such as production planning and inventory management[65,66], offer significant benefits. Paraschos *et al.* study a stochastic production and inventory system that accounts for multiple deterioration failures and product quality[67]. Zheng *et al.* consider the quality of spare parts supplied by vendors as a critical factor in their model[68]. MDP can facilitate the joint optimization of maintenance and warranty policies, particularly by exploring adaptive and customized strategies, incorporating adaptive approaches and risk-aware criteria, as shown by Xu *et al.*[69].

To tackle sequential decision problems, especially in larger-scale scenarios, algorithms can leverage system reliability characteristics. For example, modern electricity distribution systems consist of intricate networks with interdependent subsystems, presenting significant maintenance challenges due to their scale. RL-driven CBM policies are increasingly popular for their adaptability to dynamic, uncertain systems[70]. However, the dependencies among these subsystems can be limited, allowing for factored MDP modeling to simplify the problem and make the computation of optimal policies more feasible. Furthermore, current RL methodologies applied in CBM optimization primarily focus on determining optimal policies through

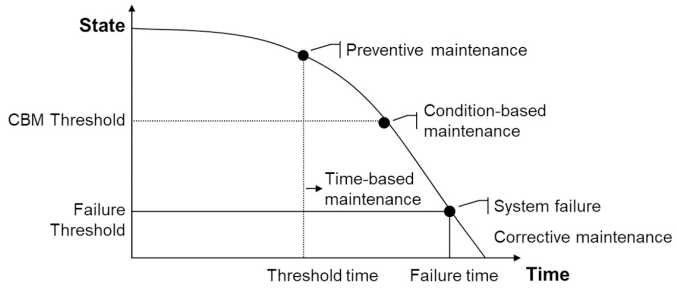


Figure 2. Different maintenance planning schemes.

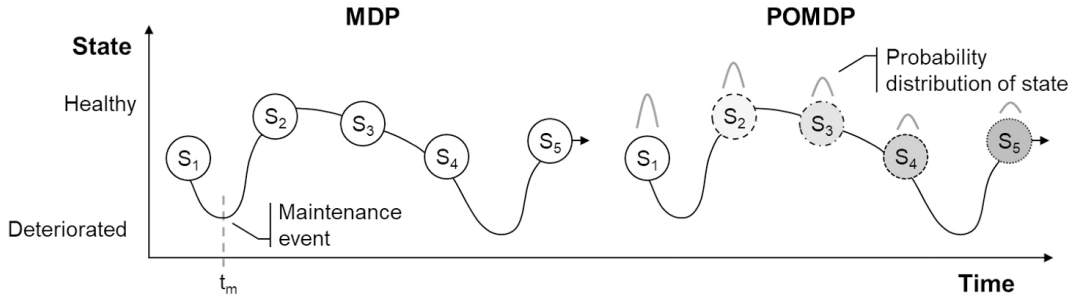


Figure 3. MDP and POMDP in maintenance planning.

numerical approaches. There is a notable gap in research regarding the convergence of regrets, a promising area for exploring CBM policy structures within the RL framework.

5. CONCLUSIONS

The paper highlights progress and future directions in dynamic decision-making for reliability. Advancements in operations research, computer science, and statistics offer valuable tools for modeling and solving dynamic optimization problems. Integrating domain expertise from mechanical and systems engineering enhances applicability. Future research should prioritize physics-informed machine learning to merge physical principles with data-driven reliability models. Transitioning to dynamic ART can yield more realistic simulations, while ensuring model interpretability and computational efficiency is critical as complexity rises. Tailored algorithms for specific systems will enable real-time applications. In CBM, RL can improve policy decisions, addressing challenges such as regret convergence. Developing adaptive maintenance and warranty strategies and new optimality criteria that balance statistical and practical aspects will be essential for practical deployment. The focus on these dynamic approaches signals a promising path for future research across system life cycles.

DECLARATIONS

Authors' contributions

Conceptualization and main drafting of the manuscript: Zhao X
Writing and revision: Luo Y

Availability of data and materials

Not applicable.

Financial support and sponsorship

This work is supported by the National Natural Science Foundation of China [grant numbers 72371182 and 72002149] and the National Social Science Fund of China [grant number 23CGL018].

Conflicts of interest

Zhao X is a Junior Editorial Board member of the journal *Complex Engineering Systems*, while the other author have declared that they have no conflicts of interest.

Ethical approval and consent to participate

Not applicable.

Consent for publication

Not applicable.

Copyright

© The Author(s) 2024.

REFERENCES

1. Hong Y, Duan Y, Meeker WQ, Stanley DL, Gu X. Statistical methods for degradation data with dynamic covariates information and an application to outdoor weathering data. *Technometrics* 2015;57:180-93. DOI
2. Diallo C, Venkatadri U, Khatab A, Bhakthavatchalam S. State of the art review of quality, reliability and maintenance issues in closed-loop supply chains with remanufacturing. *Int J Prod Res* 2017;55:1277-96. DOI
3. Zhang D, Zhang Y. Dynamic decision-making for reliability and maintenance analysis of manufacturing systems based on failure effects. *Enterp Inf Syst* 2017;11:1228-42. DOI
4. Gandoman FH, Jaguemont J, Goutam S, et al. Concept of reliability and safety assessment of lithium-ion batteries in electric vehicles: basics, progress, and challenges. *Appl Energy* 2019;251:113343. DOI
5. Zhao X, Gaudoin O, Doyen L, Xie M. Optimal inspection and replacement policy based on experimental degradation data with covariates. *IISE Trans* 2019;51:322-36. DOI
6. Lobato FS, da Silva MA, Cavalini Jr AA, Steffen Jr V. Reliability-based robust multi-objective optimization applied to engineering system design. *Eng Optim* 2020;52:1-21. DOI
7. Liu L, Li X, Jiang T, Sun F. Utilizing accelerated degradation and field data for life prediction of highly reliable products. *Qual Reliab Eng Int* 2016;32:2281-97. DOI
8. Collins DH, Freels JK, Huzurbazar AV, Warr RL, Weaver BP. Accelerated test methods for reliability prediction. *J Qual Technol* 2013;45:244-59. DOI
9. Baladeh AE, Zio E. A two-stage stochastic programming model of component test plan and redundancy allocation for system reliability optimization. *IEEE Trans Reliab* 2021;70:99-109. DOI
10. Mellal MA, Al-Dahidi S, Williams EJ. System reliability optimization with heterogeneous components using hosted cuckoo optimization algorithm. *Reliab Eng Syst Saf* 2020;203:107110. DOI
11. Coit DW, Zio E. The evolution of system reliability optimization. *Reliab Eng Syst Saf* 2019;192:106259. DOI
12. Li X, Zhang W, Ding Q. Deep learning-based remaining useful life estimation of bearings using multi-scale feature extraction. *Reliab Eng Syst Saf* 2019;182:208-18. DOI
13. Peng W, Hong L, Ye Z. Degradation-based reliability modeling of complex systems in dynamic environments. Singapore: Springer; 2017; pp. 81-103. DOI
14. Li C, Wang X, Li L, Xie M, Wang X. On dynamically monitoring aggregate warranty claims for early detection of reliability problems. *IISE Trans* 2020;52:568-87. DOI
15. Gan S, Hu H, Coit DW. Maintenance optimization considering the mutual dependence of the environment and system with decreasing effects of imperfect maintenance. *Reliab Eng Syst Saf* 2023;235:109202. DOI
16. Friederich J, Lazarova-Molnar S. Reliability assessment of manufacturing systems: a comprehensive overview, challenges and opportunities. *J Manuf Syst* 2024;72:38-58. DOI
17. Meeker WQ, Escobar LA. A review of recent research and current issues in accelerated testing. *Int Stat Rev* 1993;61:147. DOI
18. Limon S, Yadav OP, Liao H. A literature review on planning and analysis of accelerated testing for reliability assessment. *Qual Reliab Eng Int* 2017;33:2361-83. DOI
19. Zhao X, Xu J, Liu B. Accelerated degradation tests planning with competing failure modes. *IEEE Trans Reliab* 2018;67:142-55. DOI
20. Meeker WQ, Escobar LA, Hong Y. Using accelerated life tests results to predict product field reliability. *Technometrics* 2009;51:146-61. DOI

21. Meeker WQ, Escobar LA, Lu CJ. Accelerated degradation tests: modeling and analysis. *Technometrics* 1998;40:89. DOI
22. Ye Z, Chen L, Tang LC, Xie M. Accelerated degradation test planning using the inverse gaussian process. *IEEE Trans Reliab* 2014;63:750-63. DOI
23. Ghaderi A, Hassani H, Khodaygan S. A Bayesian-reliability based multi-objective optimization for tolerance design of mechanical assemblies. *Reliab Eng Syst Saf* 2021;213:107748. DOI
24. Song J, Cui Y, Wei P, Valdebenito MA, Zhang W. Constrained Bayesian optimization algorithms for estimating design points in structural reliability analysis. *Reliab Eng Syst Saf* 2024;241:109613. DOI
25. Fang G, Pan R, Stufken J. Optimal setting of test conditions and allocation of test units for accelerated degradation tests with two stress variables. *IEEE Trans Reliab* 2021;70:1096-111. DOI
26. Zhao X, Chen P, Lv S, He Z. Reliability testing for product return prediction. *Eur J Oper Res* 2023;304:1349-63. DOI
27. Etemadi AH, Fotuhi-Firuzabad M. Design and routine test optimization of modern protection systems with reliability and economic constraints. *IEEE Trans Power Deliv* 2012;27:271-8. DOI
28. Wang R, Xu J, Zhang W, Gao J, Li Y, Chen F. Reliability analysis of complex electromechanical systems: state of the art, challenges, and prospects. *Qual Reliab Eng Int* 2022;38:3935-69. DOI
29. He K, Sun Q, Xie M, Kuo W. Sequential Bayesian planning for accelerated degradation tests considering sensor degradation. *IEEE Trans Reliab* 2023;72:964-74. DOI
30. Lee I, Hong Y, Tseng S, Dasgupta T. Sequential Bayesian design for accelerated life tests. *Technometrics* 2018;60:472-83. DOI
31. Sutton RS, Barto AG. Reinforcement learning: an introduction. MIT Press; 2018. Available from: https://books.google.com/books?hl=zh-CN&lr=&id=uWV0DwAAQBAJ&oi=fnd&pg=PR7&dq=Sutton,+R.+S.+%26+Barto,+A.+G.+Reinforcement+Learning:+An+Introduction+(MIT+Press,+2018).&ots=mjqHm-YYo0&sig=qXB9jA_4jYcn0-4JysHj08ubr1I#v=onepage&q=Sutton%2C%20R.%20S.%20%26%20Barto%2C%20A.%20G.%20Reinforcement%20Learning%3A%20An%20Introduction%20(MIT%20Press%2C%202018).&f=false [Last accessed on 30 Nov 2024]
32. Zhang Z, Yang L, Xu Y, Zhu R, Cao Y. A novel reliability redundancy allocation problem formulation for complex systems. *Reliab Eng Syst Saf* 2023;239:109471. DOI
33. Li J, Huang Y, Li Y, Wang S. Redundancy allocation under state-dependent distributional uncertainty of component lifetimes. *Prod Oper Manag* 2023;32:930-50. DOI
34. Wang S, Li YF. Distributionally robust design for redundancy allocation. *INFORMS J Comput* 2020;32:620-40. DOI
35. Reihaneh M, Abouei Ardakan M, Eskandarpour M. An exact algorithm for the redundancy allocation problem with heterogeneous components under the mixed redundancy strategy. *Eur J Oper Res* 2022;297:1112-25. DOI
36. Peiravi A, Nourelfath M, Zanjani MK. Universal redundancy strategy for system reliability optimization. *Reliab Eng Syst Saf* 2022;225:108576. DOI
37. Meng Z, Zhang Z, Zhou H. A novel experimental data-driven exponential convex model for reliability assessment with uncertain-but-bounded parameters. *Appl Math Model* 2020;77:773-87. DOI
38. Murthy DNP, Xie M, Jiang R. Weibull models. Wiley; 2004. DOI
39. Hajiha M, Liu X, Hong Y. Degradation under dynamic operating conditions: modeling, competing processes and applications. *J Qual Technol* 2021;53:347-68. DOI
40. Singpurwalla ND. Survival in dynamic environments. *Stat Sci* 1995;10:86-103. DOI
41. Eryilmaz S, Rıza Bozbulut A. An algorithmic approach for the dynamic reliability analysis of non-repairable multi-state weighted k-out-of-n:G system. *Reliab Eng Syst Saf* 2014;131:61-5. DOI
42. Luo C, Shen L, Xu A. Modelling and estimation of system reliability under dynamic operating environments and lifetime ordering constraints. *Reliab Eng Syst Saf* 2022;218:108136. DOI
43. Ye Z, Xie M. Stochastic modelling and analysis of degradation for highly reliable products. *Appl Stoch Models Bus & Ind* 2015;31:16-32. DOI
44. Zhang S, Zhai Q, Shi X, Liu X. A wiener process model with dynamic covariate for degradation modeling and remaining useful life prediction. *IEEE Trans Reliab* 2023;72:214-23. DOI
45. Xu Z, Saleh JH. Machine learning for reliability engineering and safety applications: review of current status and future opportunities. *Reliab Eng Syst Saf* 2021;211:107530. DOI
46. Song S, Coit DW, Feng Q, Peng H. Reliability analysis for multi-component systems subject to multiple dependent competing failure processes. *IEEE Trans Reliab* 2014;63:331-45. DOI
47. Han X, Ouyang M, Lu L, Li J, Zheng Y, Li Z. A comparative study of commercial lithium ion battery cycle life in electrical vehicle: aging mechanism identification. *J Power Sources* 2014;251:38-54. DOI
48. Fan M, Zeng Z, Zio E, Kang R. Modeling dependent competing failure processes with degradation-shock dependence. *Reliab Eng Syst Saf* 2017;165:422-30. DOI
49. Wu B, Ding D. A gamma process based model for systems subject to multiple dependent competing failure processes under Markovian environments. *Reliab Eng Syst Saf* 2022;217:108112. DOI
50. Zhou H, Li Y. Optimal replacement in a proportional hazards model with cumulative and dependent risks. *Comput Ind Eng* 2023;176:108930. DOI
51. Zhai Q, Ye Z, Li C, Revie M, Dunson DB. Modeling recurrent failures on large directed networks. *J Am Stat Assoc* 2024:1-15. DOI
52. de Jonge B, Scarf PA. A review on maintenance optimization. *Eur J Oper Res* 2020;285:805-24. DOI

53. Hu J, Huang Y, Shen L. Maintenance optimization of a two-component series system considering masked causes of failure. *Qual Reliab Eng Int* 2024;40:388-405. DOI
54. Sun Q, Chen P, Wang X, Ye Z. Robust condition-based production and maintenance planning for degradation management. *Prod Oper Manag* 2023;32:3951-67. DOI
55. Uit Het Broek MA, Teunter RH, de Jonge B, Veldman J. Joint condition-based maintenance and load-sharing optimization for two-unit systems with economic dependency. *Eur J Oper Res* 2021;295:1119-31. DOI
56. Puterman ML. Chapter 8 Markov decision processes. Elsevier; 1990; pp. 331-434. DOI
57. Wiesemann W, Kuhn D, Rustem B. Robust Markov decision processes. *Math Oper Res* 2013;38:153-83. DOI
58. Deep A, Zhou S, Veeramani D, Chen Y. Partially observable Markov decision process-based optimal maintenance planning with time-dependent observations. *Eur J Oper Res* 2023;311:533-44. DOI
59. Drent C, Drent M, Arts J, Kapodistria S. Real-time integrated learning and decision making for cumulative shock degradation. *Manuf Serv Oper Manag* 2023;25:235-53. DOI
60. Mahmoodi S, Hamed Ranjkesh S, Zhao YQ. Condition-based maintenance policies for a multi-unit deteriorating system subject to shocks in a semi-Markov operating environment. *Qual Eng* 2020;32:286-97. DOI
61. Arcieri G, Hoelzl C, Schwery O, Straub D, Papakonstantinou KG, Chatzi E. POMDP inference and robust solution via deep reinforcement learning: an application to railway optimal maintenance. *Mach Learn* 2024;113:7967-95. DOI
62. González-Prida V, Crespo Márquez A. A framework for warranty management in industrial assets. *Comput Ind* 2012;63:960-71. DOI
63. Zheng R, Zhou Y, Gu L, Zhang Z. Joint optimization of lot sizing and condition-based maintenance for a production system using the proportional hazards model. *Comput Ind Eng* 2021;154:107157. DOI
64. Luo Y, Zhao X, Liu B, He S. Condition-based maintenance policy for systems under dynamic environment. *Reliab Eng Syst Saf* 2024;246:110072. DOI
65. Farahani A, Tohidi H. Integrated optimization of quality and maintenance: a literature review. *Comput Ind Eng* 2021;151:106924. DOI
66. Van Horenbeek A, Buré J, Cattrysse D, Pintelon L, Vansteenwegen P. Joint maintenance and inventory optimization systems: A review. *Int J Prod Econ* 2013;143:499-508. DOI
67. Paraschos PD, Koulinas GK, Koulouriotis DE. Reinforcement learning for combined production-maintenance and quality control of a manufacturing system with deterioration failures. *J Manuf Syst* 2020;56:470-83. DOI
68. Zheng M, Ye H, Wang D, Pan E. Joint decisions of components replacement and spare parts ordering considering different supplied product quality. *IEEE Trans Automat Sci Eng* 2024;21:1952-64. DOI
69. Xu J, Zhao X, Liu B. A risk-aware maintenance model based on a constrained Markov decision process. *IISE Trans* 2022;54:1072-83. DOI
70. Ogunfowora O, Najjaran H. Reinforcement and deep reinforcement learning-based solutions for machine maintenance planning, scheduling policies, and optimization. *J Manuf Syst* 2023;70:244-63. DOI

Monisha *et al*. *Complex Eng Syst* 2024;4:23
DOI: 10.20517/ces.2024.67

Complex Engineering Systems

Research Article

Open Access

Delay-dependent observer based control for uncertain fuzzy-chaotic systems with deception attacks and faulty actuators

Sekaran Monisha[1], Venkatesan Nithya[2], Rathinasamy Sakthivel[1]

[1]Department of Applied Mathematics, Bharathiar University, Coimbatore 641 046, India.
[2]Department of Mathematics, PSG College of Arts & Science, Coimbatore 641 014, India.

Correspondence to: Dr. V Nithya, Department of Mathematics, PSG College of Arts & Science, Coimbatore 641 014, India. E-mail: nithya.ve@gmail.com; Dr. Rathinasamy Sakthivel, Department of Applied Mathematics, Bharathiar University, Coimbatore 641 046, India. E-mail: krsakthivel@buc.edu.in

How to cite this article: Monisha S, Nithya V, Sakthivel R. Delay-dependent observer based control for uncertain fuzzy-chaotic systems with deception attacks and faulty actuators. *Complex Eng Syst* 2024;4:23. http://dx.doi.org/10.20517/ces.2024.67

Received: 30 Sep 2024 **First Decision:** 18 Nov 2024 **Revised:** 22 Nov 2024 **Accepted:** 27 Nov 2024 **Published:** 30 Nov 2024

Academic Editor: Hamid Reza Karimi **Copy Editor:** Fangling Lan **Production Editor:** Fangling Lan

Abstract

In this study, the robust fault-tolerant control problem for T-S fuzzy chaotic systems is studied with the use of a proportional integral observer. Particularly, to accurately consider the real-world scenario, the chaotic system model incorporates the parameter uncertainties, input delay and external disruptions. Furthermore, a fuzzy-based observer is put forward based on analyzed system output with the intent of estimating the states of undertaken chaotic systems. Herein, the system output is susceptible to randomly occurring deception attacks and adheres to the Bernoulli distribution. Precisely, the consideration of deception attacks in the output channel allows for more secure state estimation in a networked setting. Subsequently, we develop a proportional integral observer-based fault-tolerant control that allows for the attainment of goals despite faults and delays in the input channel. Moreover, by setting up the Lyapunov-Krasovskii functional and blending it with Wirtinger's integral inequalities, we put together adequate conditions that ensure the asymptotic stability of the closed-loop systems by establishing conditions in the form of linear matrix inequalities. In the follow-up, based on the established matrix inequalities, the exact procedure for computing the gain matrices is outlined. As a last step, we put forward numerical simulation outcomes that exhibit the viability of the theoretical findings.

© The Author(s) 2024. **Open Access** This article is licensed under a Creative Commons Attribution 4.0 International License (https://creativecommons.org/licenses/by/4.0/), which permits unrestricted use, sharing, adaptation, distribution and reproduction in any medium or format, for any purpose, even commercially, as long as you give appropriate credit to the original author(s) and the source, provide a link to the Creative Commons license, and indicate if changes were made.

Keywords: Chaotic systems, T-S fuzzy technique, fault-tolerant control, proportional-integral observer approach, deception attacks, extended dissipativity

1. INTRODUCTION

Chaos is an inherent nonlinear behavior with significant avenues in various real-world uses, including encrypted communication, processing data, identifying patterns, and chemical processes[1,2]. As a result, there has been a heightened focus on chaos-associated nonlinear behavior in the fields of science and technology. Chaotic systems exhibit unexpected and inconsistent characteristics attributed to initial-value sensitivities, topological temporary nature, pseudo-randomness and the absence of periodicity which can potentially result in functionality degradation or system instability[3–5]. Consequently, chaos control has emerged as an important topic across numerous domains. Numerous intriguing control methodologies have been developed to examine chaotic systems to date, such as feedback control[6], sliding mode control[7], finite-time control[8], and so on. Given these developments and their impact on chaotic systems, this topic has gained our attention.

Additionally, various causes, including unforeseen alterations in operational circumstances, dynamic modifications in system boundaries and behavioral shifts in physical components, might render the nonlinear characteristics of chaotic systems prevalent. Furthermore, when the system is subjected to the nonlinear phenomenon, the control mechanism that was designed for chaotic systems is incapable of producing favorable dynamic outcomes for chaotic systems. For the purpose of resolving the problem discussed above, the concept of fuzzy logic[9] is utilized in this investigation in order to effectively address the nonlinear characteristics of the chaotic system. In detail, the Takagi-Sugeno (T-S) fuzzy model captured growing attention from researchers owing to its outstanding ability to represent intricate dynamical processes. In detail, the T-S fuzzy model employs a collection of fuzzy IF-THEN constraints to depict local linear input-output relationships within a nonlinear system. Upon account of this attribute, the T-S fuzzy model is advantageous for chaotic system analysis and controller design[10]. Moreover, it has been disclosed that many chaotic systems, including Rosler system, Lorenz system and Chua's system, can be precisely represented by T-S fuzzy models[11–14]. Owing to these advantageous attributes, fuzzy model-based control has been extensively utilized in chaotic systems, prompting us to undertake this research.

Besides, control systems are prone to actuator failures, which could substantially affect system operations and, in extreme cases, can cause system instability[15]. Consequently, to preserve the ideal stability and proper operation, it is crucial to take the adverse outcomes of actuator flaws into account while crafting control systems[16]. This premise lends conception to a fault-tolerant control framework for dynamical systems[17]. To put it another way, fault-tolerant control deals with the failed actuators and restores system performance for ensuring the system runs consistently. The beneficial features of fault-tolerant control have prompted substantial research efforts[18,19]. In addition to the actuator fault, if the signal transmission times between the actuator and sensor are prolonged then the control input channel could experience delay and result in unexpected degradation in performance, leading to system instability[20–22]. Consequently, while creating a control protocol, it is relevant and even necessary to consider the input delay[23,24]. Similarly, when there is a discrepancy between the real system and its mathematical model, the performance of the system is likely to suffer[25]. Because of this, embracing uncertainty in system design is important from a theoretical and practical standpoint[26,27]. Furthermore, as a result of unpredictable variables, the external disruptions are pervasive[28,29]. In order to mitigate these impacts, the extended dissipativity concept is used, which reduces the impact of the disturbance in the system model[30–32]. Thus, it is theoretically and practically significant to include parameter uncertainties, actuator faults, external disturbances and input delay in T-S fuzzy chaotic systems.

Meanwhile, estimating the system state in practice gets extremely hard. To address this pressing issue, the researchers have proposed an observer-based state estimation method[33]. It should be noted that the mathe-

matical model of the system being studied determines the structure of the observer. The accuracy of the state estimate is therefore dependent on the mathematical model used and the characteristics of the data that are used. To that end, the proportional integral observer (PIO) has garnered a lot of interest in many real-world systems, since the application of PIO is involved in manufacturing, power circuits, and network communications[34]. The PIO improves the estimate of the system states and boosts the system resiliency which is done by including the proportional and integral feedback term with regard to the output estimation error. As a consequence, the PIO technique has gained a lot of traction among academics[35–37]. It should be noted that the PIO is set up using the system's output signal but in a networked environment, it might be impacted by cyberattacks. Consequently, the observer design should take into account aftermath impacts of cyber attacks in order to obtain a secure estimate of the system states[38,39]. As a consequence of this notion, numerous intriguing findings on secure state estimation for various dynamical systems have been reported in the literature[40–49]. Notwithstanding these many initiatives, the analysis of T-S fuzzy chaotic systems in networked conditions subject to cyber attack scenarios remains an uncharted area and needs exploration.

Driven by above-discussed factors and findings, this study delves into the topic of PIO-based fault-tolerant control for T-S fuzzy chaotic systems that are susceptible to various factors. Additionally, the following is a summary of the research achievements presented in this article:

- A PIO-based fault-tolerant control law is configured for the T-S fuzzy chaotic systems in the case of external disturbances, actuator faults, deception attacks and input delays.
- In detail, with the intent of reconstructing the states of the undertaken model, a PIO is developed with the fuzzy technique. Additionally, to strengthen the model's information security, deception attacks are considered.
- Subsequently, by making use of the estimation information procured from the designed observer along with the feedback control technique, a PIO-based control law is developed, in which actuator faults and input delays are considered to precisely mimic the actual situations.
- By configuring the suitable Lyapunov-Krasovskii functional candidate, a set of adequate constraints is established in the frame of linear matrix inequalities (LMIs) which ensures the asymptotic stability of the investigated system.

At the end of this study, numerical examples accompanied by the simulation findings are offered which substantiate the effectiveness and applicability of the offered control mechanism and the established theoretical findings.

The subsequent sections of this paper are organized as follows: Section 2 outlines the mathematical modeling of the undertaken model and control design and offers the preliminaries. Section 3 presents the adequate constraints that ensure the primary intent of this study. The potential of the proposed findings is summarized in Section 4 through a simulation example. Finally, Section 5 provides a conclusion of our study, presenting insights and emphasizing the significant findings obtained from our investigation.

2. PROBLEM FORMULATION

2.1. Chaotic system description

Consider a class of T-S fuzzy chaotic fuzzy systems subject to multiple vulnerable factors as follows:
rule for the undertaken plant i: IF $\phi_1(t)$ is Φ_1^i and ... and $\phi_h(t)$ is Φ_h^i, THEN

$$\begin{cases} \dot{x}(t) = (\mathcal{A}_i + \Delta\mathcal{A}_i(t))x(t) + \mathcal{B}_i u^f(t - \wp(t)) + \mathcal{D}_i w(t), \quad i \in \omega = \{1, 2, 3, \ldots, l\} \\ y(t) = C_i x(t), \end{cases} \tag{1}$$

where $\phi_1(t), \phi_2(t), \ldots, \phi_h(t)$ are the premise variables, and Φ_1^i, Φ_2^i, Φ_3^i,...,Φ_h^i are the fuzzy sets; l is the number of fuzzy rules; $x(t) \in \mathcal{R}^n$ represents the state vector; $u^f(t) \in \mathcal{R}^m$ signifies the control input; $y(t) \in \mathcal{R}^q$

denotes the measured output vector of the system; $\wp(t)$ indicates the time-varying delay that occurs in the control channel which satisfies $0 \leq \wp(t) \leq \bar{\wp}$ and $\dot{\wp}(t) \leq \varrho$, where $\varrho < 1$; $w(t) \in \mathcal{R}^w$ indicates the external disturbance; $\mathcal{A}_i$, $\mathcal{B}_i$, $\mathcal{D}_i$, C_i are the known constant matrices. Moreover, $\Delta\mathcal{A}_i(t)$ signifies the parameter uncertainty which has the following layout $\Delta\mathcal{A}_i(t) = \mathfrak{B}_i\mathfrak{F}_i(t)\mathfrak{N}_i$, and $\mathfrak{F}_i^T(t)\mathfrak{F}_i(t) \leq I$ is a time-varying matrix that is unknown.

Through the utilization of fuzzy blending techniques, we can attain the underneath the fuzzy chaotic system (1) as

$$\begin{cases} \dot{x}(t) = \sum\limits_{i=1}^{l} \mathfrak{b}_i(\phi(t))\big((\mathcal{A}_i + \Delta\mathcal{A}_i(t))x(t) + \mathcal{B}_i u^f(t - \wp(t)) + \mathcal{D}_i w(t)\big) \\ y(t) = \sum\limits_{i=1}^{l} \mathfrak{b}_i(\phi(t))(C_i x(t)), \end{cases} \tag{2}$$

where $\phi(t) = [\phi_1(t), \phi_2(t), \ldots, \phi_h(t)]$, $\mathfrak{b}_i(\phi(t))$ represents the normalized membership function satisfying:

$$\mathfrak{b}_i(\phi(t)) = \frac{\prod\limits_{j=1}^{h} \Phi_j^i(\phi_j(t))}{\sum\limits_{i=1}^{l}\prod\limits_{j=1}^{h} \Phi_j^i(\phi_j(t))} \geq 0, \quad \sum_{i=1}^{l} \mathfrak{b}_i(\phi(t)) = 1,$$

and $\Phi_j^i(\phi_j(t))$ indicates the grade of membership of $\phi_j(t)$ in Φ_j^i.

2.2. Deception attack model

In the current investigation, the deception attack is taken into account in the measurement output channel. The mathematical configuration of the deception attack is laid out below:

$$y_d(t) = (1 - \theta(t))y(t) + \theta(t)\zeta(y(t)), \tag{3}$$

where $\theta(t) \in \{0, 1\}$ indicates the occurring probability of deception attacks, and $\zeta(y(t))$ illustrates the deceptive signal sent out by the attacker. Further, $\theta(t)$ follows the Bernoulli distribution and it has ensuing probability constraints: $Pr\{\theta(t) = 1\} = \mathbb{E}\{\theta(t)\} = \bar{v}$, $Pr\{\theta(t) = 0\} = 1 - \mathbb{E}\{\theta(t)\} = 1 - \bar{v}$, $\bar{v} \in [0, 1]$ is pre-defined scalar.

2.3. Description of PIO system

In practice, directly measuring the system state (2) is not an easy task. In order to address this issue, a PIO system is developed to estimate the states of the model. Moreover, the observer system is articulated as follows:

$$\begin{cases} \dot{\hat{x}}(t) = \sum\limits_{i=1}^{l} \mathfrak{b}_i(\phi(t))\big(\mathcal{A}_i\hat{x}(t) + \mathcal{B}_i u^f(t - \wp(t)) + \mathcal{L}_i(y_d(t) - \hat{y}(t)) + \mathcal{B}_i x_p(t)\big), \\ \hat{y}(t) = \sum\limits_{i=1}^{l} \mathfrak{b}_i(\phi(t))(C_i\hat{x}(t)), \\ \dot{x_p}(t) = -x_p(t) + \mathcal{L}_{pi}(y_d(t) - \hat{y}(t)) \end{cases} \tag{4}$$

where $\hat{x}(t) \in \mathcal{R}^n$ signifies the estimated states of $x(t)$ and $\hat{y}(t) \in \mathcal{R}^q$ epitomize the estimated output of $y(t)$; L_i and $\mathcal{L}_{pi}$ indicates the proportional and integral gain matrices of the designed observer, which will be reckoned in the later portion of this investigation.

2.4. PIO-based control scheme configuration with delay

Rule for the designed control law j: IF $\phi_1(t)$ is Φ_1^j and ... and $\phi_h(t)$ is Φ_h^j, THEN

By leveraging the estimation data obtained from the established observer configuration and the feedback mechanism, a control rule is provided which includes input delay to align closer with the real-world circumstances.

The dynamic configuration of the control law is given below:

$$u(t-\wp(t)) = \sum_{j=1}^{h} \mathfrak{b}_j(\phi(t))\mathcal{K}_j\,\hat{x}(\tau-\wp(t)), \tag{5}$$

where $\mathcal{K}_j$ is the gain matrices of the controller, which will be determined later.

Apart from this, we consider the controller with faulty actuator model which is defined by $u^f(t) = \mathfrak{G}_f u(t)$. In detail, $\mathfrak{G}_f = \text{diag}\{\mathfrak{g}_1, \mathfrak{g}_2, \ldots, \mathfrak{g}_m\}$, $\mathfrak{g}_s$ $(s = 1, 2, \ldots, m)$ is the fault factor of the s^{th} actuator that is assumed to lie in the interval $[\underline{\mathfrak{g}}_s, \overline{\mathfrak{g}}_s]$ with $0 < \underline{\mathfrak{g}}_s \le \mathfrak{g}_s \le \overline{\mathfrak{g}}_s \le 1$. Furthermore, the fault matrix $\mathfrak{G}_f$ is represented as $\mathfrak{G}_f = \mathfrak{G}_0 + \mathfrak{G}_1\Sigma$, where $\mathfrak{G}_0 = \frac{\overline{\mathfrak{G}}+\underline{\mathfrak{G}}}{2}$, $\mathfrak{G}_1 = \frac{\overline{\mathfrak{G}}-\underline{\mathfrak{G}}}{2}$ with $\overline{\mathfrak{G}}_f = \text{diag}\{\overline{\mathfrak{g}}_1, \overline{\mathfrak{g}}_2, \ldots, \overline{\mathfrak{g}}_m\}$, $\underline{\mathfrak{G}}_f = \text{diag}\{\underline{\mathfrak{g}}_1, \underline{\mathfrak{g}}_2, \ldots, \underline{\mathfrak{g}}_m\}$ and $0 < \Sigma = \text{diag}\{\pi_1, \pi_2, \ldots, \pi_m\} \le I$. Then, in accordance with (5), the control set-up with the actuator fault model can be written as follows:

$$u^f(t-\wp(t)) = \sum_{j=1}^{h} \mathfrak{b}_j(\phi(t))\,(\mathfrak{G}_0 + \mathfrak{G}_1\Sigma)\mathcal{K}_j\,\hat{x}(\tau-\wp(t)). \tag{6}$$

Further, by defining the error system $\mathfrak{e}(t)$ as $\mathfrak{e}(t) = x(t) - \hat{x}(t)$ and making use of relations (3)-(6), the following set-up of a closed-loop system can be obtained.

$$\dot{x}(t) = \sum_{i=1}^{l}\sum_{j=1}^{h} \mathfrak{b}_j(\phi(t))\big((\mathcal{A}_i + \Delta\mathcal{A}_i(t))x(t) + \mathcal{B}_i(\mathfrak{G}_0 + \mathfrak{G}_1\Sigma)\mathcal{K}_j\,\hat{x}(\tau-\wp(t)) + \mathcal{D}_i w(t)\big), \tag{7}$$

$$\begin{aligned}\dot{\mathfrak{e}}(t) = \sum_{i=1}^{j} \mathfrak{b}_i(\phi(t))\big(&\mathcal{A}_i\mathfrak{e}(t) + \Delta\mathcal{A}_i(t)x(t) - \mathcal{L}_i\mathcal{C}_i\mathfrak{e}(t) + \theta(t)\mathcal{L}_i\mathcal{C}_i x(t) - \theta(t)\mathcal{L}_i\zeta(y(t)) + \mathcal{D}_i w(t)) - \mathcal{B}_i x_p(t),\\ \dot{x_p}(t) = \sum_{i=1}^{l} \mathfrak{b}_i(\phi(t))\big(&-x_p(t) + \mathcal{L}_{pi}\mathcal{C}_i\mathfrak{e}(t) - \theta(t)\mathcal{L}_{pi}\mathcal{C}_i x(t) + \theta(t)\mathcal{L}_{pi}f(y(t))\big).\end{aligned} \tag{8}$$

Assumption 1 *For the given real symmetric matrices κ_1, κ_2, κ_3 and κ_4, the following constraints are satisfied:*
1) $\kappa_1 \le 0$, $\kappa_3 > 0$ *and* $\kappa_4 \ge 0$;
2) $(\|\kappa_1\| + \|\kappa_2\|)\kappa_4 = 0$.

Assumption 2 *The nonlinear function $f(y(t))$ satisfies the following constraint*

$$||f(y(t))||^2 \le |\mathcal{H}y(t)|^2$$

where $\mathcal{H}$ is the constant matrix that denotes the upper bound of nonlinear function.

Definition 1 [28] *For the given matrices κ_1, κ_2, κ_3 and κ_4 with Assumption 1, the undertaken system (1) with the controller (6) is extended dissipative if the following inequality holds for $T_f \ge 0$:*

$$\mathbb{E}\left\{\int_0^{T_f} \zeta(t)dt\right\} - \sup_{0\le t\le T_f} \mathbb{E}\left\{y^T(t)\kappa_4 y(t)\right\} \ge \gamma, \tag{9}$$

where $\zeta(t) = y^T(t)\kappa_1 y(t) + y^T(t)\kappa_2 w(t) + w^T(t)\kappa_3 w(t)$.

Lemma 1 [50] *For any positive definite matrix $\mathcal{Z}$, given scalars u and v satisfying $u < v$, the condition given below is satisfied for all continuously differentiable function $\xi : [u, v] \to \mathcal{R}^\alpha$:*

$$(u-v)\int_u^v \xi^T(\mathfrak{s})\mathcal{Z}\xi(\mathfrak{s})d\mathfrak{s} \ge \begin{bmatrix} \int_u^v \xi(k)dk \\ \int_u^v dk\int_u^s \xi(s)ds \\ \int_u^v dk\int_u^s ds\int_u^r \xi(r)dr \end{bmatrix}^T \begin{bmatrix} 9\mathcal{Z} & -\frac{36}{u-v}\mathcal{Z} & \frac{60}{(u-v)^2}\mathcal{Z} \\ * & \frac{192}{(u-v)^2}\mathcal{Z} & -\frac{360}{(u-v)^3}\mathcal{Z} \\ * & * & \frac{720}{(u-v)^4}\mathcal{Z} \end{bmatrix} \begin{bmatrix} \int_u^v \xi(k)dk \\ \int_u^v dk\int_u^s \xi(s)ds \\ \int_u^v dk\int_u^s ds\int_u^r \xi(r)dr \end{bmatrix}.$$

3. MAIN RESULTS

In this section, we focus on deriving sufficient conditions for ascertaining the asymptotic stability of the considered system by configuring Lyapunov-Krasovskii functional and blending it with the extended Wirtinger's integral inequality.

Theorem 1 *For given positive scalars* $\bar{\varphi}$, $\bar{v}$, ϱ, *actuator fault matrix* $\mathfrak{G}_f$ *and controller gain matrices* $\mathcal{K}_j$, $\mathcal{L}_i$, $\mathcal{L}_{pi}$, *system* (7) *is asymptotically stable, if there exist apt dimension matrices* $\mathcal{U}_i > 0$, $(i = 1, 2, 3)$, $\mathcal{W}_g > 0$ $(g = 1, 2, 3, 4)$, $\check{\mathcal{W}}_1$ *and* $\check{\mathcal{W}}_2 > 0$, *such that the following condition is satisfied:*

$$\sum_{i=1}^{l}\sum_{j=1}^{h}\left[\Lambda_{ij}\right]_{15\times 15} < 0, \tag{10}$$

where $\Lambda_{1,1} = sym(\mathcal{U}_{1i}\mathcal{A}_i) + \mathcal{W}_1 + \mathcal{W}_2 + \bar{\varphi}^2\check{\mathcal{W}}_1 + C^T\mathcal{H}^T\mathcal{H}C$, $\Lambda_{1,2} = (\bar{v}\mathcal{U}_{2i}\mathcal{L}_iC_i)^T$, $\Lambda_{1,3} = \bar{v}C_i^T\mathcal{L}_{pi}^T\mathcal{U}_{3i}^T$, $\Lambda_{1,5} = \mathcal{U}_{1i}\mathcal{B}_i\mathfrak{G}_f\mathcal{K}_j$, $\Lambda_{1,7} = -\mathcal{U}_{1i}\mathcal{B}_i\mathfrak{G}_f\mathcal{K}_j$, $\Lambda_{1,9} = \mathcal{U}_{1i}D_i$, $\Lambda_{2,2} = sym(\mathcal{U}_{2i}\mathcal{A}_i - \mathcal{L}_iC_i) + \mathcal{W}_3 + \mathcal{W}_4 + \bar{\varphi}^2\check{\mathcal{W}}_2$, $\Lambda_{2,3} = -\mathcal{U}_{2i}\mathcal{B}_i + C_i^T\mathcal{L}_{pi}^T\mathcal{U}_{3i}^T$, $\Lambda_{2,8} = -\bar{v}\mathcal{U}_{2i}\mathcal{L}_i$, $\Lambda_{2,9} = \mathcal{U}_{2i}D_i$, $\Lambda_{3,3} = -sym(\mathcal{U}_{3i})$, $\Lambda_{3,8} = \bar{v}\mathcal{U}_{3i}\mathcal{L}_{pi}$, $\Lambda_{4,4} = -\mathcal{W}_1$, $\Lambda_{5,5} = -(1-\varrho)\mathcal{W}_2$, $\Lambda_{6,6} = -\mathcal{W}_3$, $\Lambda_{7,7} = -(1-\varrho)\mathcal{W}_4$, $\Lambda_{8,8} = -I$, $\Lambda_{9,9} = -I$, $\Lambda_{10,10} = -9\check{\mathcal{W}}_1$, $\Lambda_{10,11} = \frac{36}{\bar{\varphi}}\check{\mathcal{W}}_1$, $\Lambda_{10,12} = -\frac{60}{\bar{\varphi}^2}\check{\mathcal{W}}_1$, $\Lambda_{11,11} - \frac{192}{\bar{\varphi}^2}\check{\mathcal{W}}_1$, $\Lambda_{11,12} = \frac{360}{\bar{\varphi}^3}\check{\mathcal{W}}_1$, $\Lambda_{12,12} = -\frac{720}{\bar{\varphi}^3}\check{\mathcal{W}}_1$, $\Lambda_{13,13} = -9\check{\mathcal{W}}_2$, $\Lambda_{13,14} = \frac{36}{\bar{\varphi}}\check{\mathcal{W}}_2$, $\Lambda_{13,15} = -\frac{60}{\bar{\varphi}^2}\check{\mathcal{W}}_2$, $\Lambda_{14,14} - \frac{192}{\bar{\varphi}^2}\check{\mathcal{W}}_2$, $\Lambda_{14,15} = \frac{360}{\bar{\varphi}^3}\check{\mathcal{W}}_2$ *and* $\Lambda_{15,15} = -\frac{720}{\bar{\varphi}^3}\check{\mathcal{W}}_2$.

Proof 1 *Let us construct the Lyapunov-Krasovskii functional for systems* (7)-(8) *in the following structure:*

$$\mathcal{V}(t) = \sum_{a=1}^{3}\mathcal{V}_a(t), \tag{11}$$

where

$$\begin{aligned}
\mathcal{V}_1(t) =& x^T(t)\mathcal{U}_{1i}x(t) + \mathfrak{e}^T(t)\mathcal{U}_{2i}\mathfrak{e}(t) + x_p^T(t)\mathcal{U}_{3i}x_p(t),\\
\mathcal{V}_2(t) =& \int_{\tau-\bar{\varphi}}^{\tau} x^T(\mathfrak{m})\mathcal{W}_1x(\mathfrak{m})d\mathfrak{m} + \int_{\tau-\varphi(t)}^{\tau} x^T(\mathfrak{s})\mathcal{W}_2x(\mathfrak{s})d\mathfrak{s} + \int_{\tau-\bar{\varphi}}^{\tau} \mathfrak{e}^T(\mathfrak{m})\mathcal{W}_3\mathfrak{e}(\mathfrak{m})d\mathfrak{m} + \int_{\tau-\varphi(t)}^{\tau} \mathfrak{e}^T(\mathfrak{s})\mathcal{W}_4\mathfrak{e}(\mathfrak{s})d\mathfrak{s},\\
\mathcal{V}_3(t) =& \bar{\varphi}\int_{\tau-\bar{\varphi}}^{\tau}\int_{s}^{\tau} x^T(\mathfrak{v})\check{\mathcal{W}}_1x(\mathfrak{v})d\mathfrak{v}d\mathfrak{s} + \bar{\varphi}\int_{\tau-\bar{\varphi}}^{\tau}\int_{s}^{\tau} \mathfrak{e}^T(\mathfrak{v})\check{\mathcal{W}}_2\mathfrak{e}(\mathfrak{v})d\mathfrak{v}d\mathfrak{s}.
\end{aligned}$$

Then, by taking the derivative of (11) and applying mathematical expectation along with the solutions from

(7)-(8), we get

$$\begin{aligned}\mathbb{E}\{\dot{\mathcal{V}}_1(t)\} =&x^T(t)\mathcal{U}_{1i}\dot{x}(t) + \dot{x}^T(t)\mathcal{U}_{1i}x(t) + \mathfrak{e}^T(t)\mathcal{U}_{2i}\dot{\mathfrak{e}}(t) + \dot{\mathfrak{e}}^T(t)\mathcal{U}_{2i}\mathfrak{e}(t) + x_p^T(t)\mathcal{U}_{3i}\dot{x}_p(t) + \dot{x}_p^T(t)\mathcal{U}_{3i}x_p(t)\\ =&2x^T(t)\mathcal{U}_i\left[\sum_{i=1}^{l}\sum_{j=1}^{h}\mathfrak{b}_j(\phi(t))\big(\mathcal{A}_ix(t) + \mathcal{B}_i\mathfrak{G}_f\mathcal{K}_j\,\hat{x}(\tau-\wp(t)) + \mathcal{D}_iw(t)\big)\right]\\ &+2\mathfrak{e}^T(t)\mathcal{U}_{2i}\left[\sum_{i=1}^{j}\mathfrak{b}_i(\phi(t))\big(\mathcal{A}_i\mathfrak{e}(t) - \mathcal{L}_i\mathcal{C}_i\mathfrak{e}(t) + \theta(t)\mathcal{L}_i\mathcal{C}_ix(t) - \theta(t)\mathcal{L}_i\zeta(y(t)) + \mathcal{D}_iw(t)\big) - \mathcal{B}_ix_p(t)\right]\\ &+2x_p^T\mathcal{U}_{3i}\left[\sum_{i=1}^{l}\mathfrak{b}_i(\phi(t))\big(-x_p(t) + \mathcal{L}_{pi}\mathcal{C}_i\mathfrak{e}(t) - \theta(t)\mathcal{L}_{pi}\mathcal{C}_ix(t) + \theta(t)\mathcal{L}_{pi}\zeta(y(t))\big)\right] \qquad (12)\end{aligned}$$

$$\begin{aligned}\mathbb{E}\{\dot{\mathcal{V}}_2(t)\} =&x^T(t)\mathcal{W}_1x(t) - x^T(\tau-\bar{\wp})\mathcal{W}_1x(\tau-\bar{\wp}) + x^T(t)\mathcal{W}_2x(t) - (1-\varrho)x^T(\tau-\wp(t))\mathcal{W}_2x(\tau-\wp(t))\\ &+\mathfrak{e}^T(t)\mathcal{W}_3\mathfrak{e}(t) - \mathfrak{e}^T(\tau-\bar{\wp})\mathcal{W}_3\mathfrak{e}(\tau-\bar{\wp}) + \mathfrak{e}^T(t)\mathcal{W}_4\mathfrak{e}(t) - (1-\varrho)\mathfrak{e}^T(\tau-\wp(t))\mathcal{W}_4\mathfrak{e}(\tau-\wp(t)), \qquad (13)\end{aligned}$$

$$\mathbb{E}\{\dot{\mathcal{V}}_3(t)\} =\bar{\wp}^2x^T(t)\check{\mathcal{W}}_1x(t) + \bar{\wp}^2\mathfrak{e}^T(t)\check{\mathcal{W}}_2\mathfrak{e}(t) - \bar{\wp}\int_{\tau-\bar{\wp}}^{\tau}x^T(\mathfrak{s})\check{\mathcal{W}}_1x(\mathfrak{s})d\mathfrak{s} - \bar{\wp}\int_{\tau-\bar{\wp}}^{\tau}\mathfrak{e}^T(\mathfrak{s})\check{\mathcal{W}}_2\mathfrak{e}(\mathfrak{s})d\mathfrak{s}. \qquad (14)$$

Now, redrafting the integral term in inequality (14) by making use of Lemma 1, we get

$$-\bar{\wp}\int_{\tau-\bar{\wp}}^{\tau}x^T(t)\check{\mathcal{W}}_1x(t)d(t) \le \Psi^T(t)\begin{bmatrix}-9\check{\mathcal{W}}_1 & \frac{36}{\bar{\wp}}\check{\mathcal{W}}_1 & -\frac{60}{\bar{\wp}^2}\check{\mathcal{W}}_1\\ * & -\frac{192}{\bar{\wp}^2}\check{\mathcal{W}}_1 & \frac{360}{\bar{\wp}^3}\check{\mathcal{W}}_1\\ * & * & -\frac{720}{\bar{\wp}^3}\check{\mathcal{W}}_1\end{bmatrix}\Psi(t), \qquad (15)$$

$$-\bar{\wp}\int_{\tau-\bar{\wp}}^{\tau}\mathfrak{e}^T(t)\check{\mathcal{W}}_2\mathfrak{e}(t)d(t) \le \hat{\Psi}^T(t)\begin{bmatrix}-9\check{\mathcal{W}}_2 & \frac{36}{\bar{\wp}}\check{\mathcal{W}}_2 & -\frac{60}{\bar{\wp}^2}\check{\mathcal{W}}_2\\ * & -\frac{192}{\bar{\wp}^2}\check{\mathcal{W}}_2 & \frac{360}{\bar{\wp}^3}\check{\mathcal{W}}_2\\ * & * & -\frac{720}{\bar{\wp}^3}\check{\mathcal{W}}_2\end{bmatrix}\hat{\Psi}(t), \qquad (16)$$

$$\Psi^T(t) = \left[\int_{\tau-\bar{\wp}}^{\tau}x^T(s)ds \quad \int_{\tau-\bar{\wp}}^{\tau}ds\int_{\tau-\bar{\wp}}^{s}x^T(v)dv \quad \int_{\tau-\bar{\wp}}^{\tau}ds\int_{\tau-\bar{\wp}}^{s}dv\int_{\tau-\bar{\wp}}^{v}x^T(u)du\right] \text{ and}$$

$$\hat{\Psi}^T(t) = \left[\int_{\tau-\bar{\wp}}^{\tau}\mathfrak{e}^T(s)ds \quad \int_{\tau-\bar{\wp}}^{\tau}ds\int_{\tau-\bar{\wp}}^{s}\mathfrak{e}^T(v)dv \quad \int_{\tau-\bar{\wp}}^{\tau}ds\int_{\tau-\bar{\wp}}^{s}dv\int_{\tau-\bar{\wp}}^{v}\mathfrak{e}^T(u)du\right].$$

Moreover, in light of the presumption on deception attack function $\zeta(y(t))$ on (3), the ensuing inequality is attained:

$$x^T(t)\mathcal{C}^T\mathcal{H}^T\mathcal{H}\mathcal{C}x(t) - \zeta^T(y(t))\zeta(y(t)) \ge 0. \qquad (17)$$

Further, by combining (12)-(17), we end up with the hereunder relation:

$$\mathbb{E}\{\dot{\mathcal{V}}(t) - w^T(t)w(t)\} \le \pi^T(t)\left[\sum_{i=1}^{l}\sum_{j=1}^{h}\mathfrak{b}_j(\phi(t))\Lambda_{i,j}\right]\pi(t) \qquad (18)$$

where $\pi^T(t) = \left[x^T(t)\ \mathfrak{e}^T(t)\ x_p^T(t)\ x^T(\tau-\bar{\wp})\ x^T(\tau-\wp(t))\ \mathfrak{e}^T(\tau-\bar{\wp})\ \mathfrak{e}^T(\tau-\wp(t))\ \zeta^T(y(t))\ w^T(t)\ \Psi^T(t)\ \hat{\Psi}^T(t)\right]$ and $\Lambda_{i,j}$ is defined in statement of theorem. Thereafter, if the constraint (10) holds, then in light of the theory of Lyapunov's stability, it is obvious that the closed-loop system (7)-(8) is asymptotically stable. This completes the proof of the theorem.

Next, in the following theorem, the delay-dependent conditions are derived for the uncertain chaotic system given in (1) under the known actuator fault (6) and unknown gain. Added to this, adequate conditions are configured in the form of matrix inequalities with the extended dissipativity theory.

Theorem 2 *Let $\bar{\wp}$, v, ϱ, ε, γ be positive scalars and system (1) with known actuator fault (6) is asymptotically stable with extended dissipativity, if there exist scalars μ, ϑ_1, ϑ_2 and positive definite matrices $\mathfrak{X}_{mi} > 0$, $(m = 1,2,3)$, $\hat{\mathcal{W}}_g > 0$ $(g = 1,2,3,4)$, $\mathring{\mathcal{W}}_1$ and $\mathring{\mathcal{W}}_2 > 0$ such that the following conditions are met:*

$$\begin{bmatrix} -\mu I & C_i\mathfrak{X}_{2i} - \bar{\mathfrak{X}}_{2i}C_i \\ * & -I \end{bmatrix} < 0, \tag{19}$$

$$\Theta_{ij} = \begin{bmatrix} \Pi_{ij\,15\times15} & \daleth & \Xi_1 & \varepsilon\Xi_2^T & \Xi_3 & \varepsilon\Xi_4^T & \Xi_5^T \\ * & -I & 0 & 0 & 0 & 0 & 0 \\ * & * & -\varepsilon I & 0 & 0 & 0 & 0 \\ * & * & * & -\varepsilon I & 0 & 0 & 0 \\ * & * & * & * & -\varepsilon I & 0 & 0 \\ * & * & * & * & * & -\varepsilon I & 0 \\ * & * & * & * & * & 0 & -I \end{bmatrix} < 0, \tag{20}$$

where $\Pi_{1,1} = sym(\mathcal{A}_i\mathcal{X}_{1i}) + \hat{\mathcal{W}}_1 + \hat{\mathcal{W}}_2 + \bar{\wp}^2\mathring{\mathcal{W}}_1$, $\Pi_{1,2} = \bar{v}C_i^T\mathcal{L}_{oi}^T$, $\Pi_{1,3} = \bar{v}C_i^T\mathcal{L}_{pi}^T$, $\Pi_{1,4} = \mathcal{B}_i\mathfrak{G}_f\mathcal{Y}_j$, $\Pi_{1,6} = -\delta_1\mathcal{B}_i\mathfrak{G}_f\mathcal{Y}_j$, $\Pi_{1,9} = D_i - \kappa_2C_i^T$, $\Pi_{2,2} = \delta_1 sym(\mathcal{A}_i\mathcal{X}_{2i}) - \delta_1\mathcal{L}_{oi}C_i + \hat{\mathcal{W}}_3 + \hat{\mathcal{W}}_4 + \bar{\wp}^2\mathring{\mathcal{W}}_2$, $\Pi_{2,3} = -\delta_2\mathcal{B}_i\mathcal{X}_{2i} + \delta_1C_i^T\mathcal{L}_{si}^T$, $\Pi_{2,8} = \bar{v}I$, $\Pi_{2,9} = \mathcal{D}_i$, $\Pi_{3,3} = \delta_2 sym(\mathcal{M}_p\mathcal{X}_{3i})$, $\Pi_{3,8} = \bar{v}I$, $\Pi_{4,4} = -\hat{\mathcal{W}}_1$, $\Pi_{5,5} = -(1-\varrho)\hat{\mathcal{W}}_2$, $\Pi_{6,6} = -\hat{\mathcal{W}}_3$, $\Pi_{7,7} = -(1-\varrho)\hat{\mathcal{W}}_4$, $\Pi_{8,8} = -I$, $\Pi_{9,9} = -\kappa_3 I$, $\Pi_{10,10} = -9\mathring{\mathcal{W}}_1$, $\Pi_{10,11} = \frac{36}{\bar{\wp}}\mathring{\mathcal{W}}_1$, $\Pi_{10,12} = -\frac{60}{\bar{\wp}^2}\mathring{\mathcal{W}}_1$, $\Pi_{11,11} - \frac{192}{\bar{\wp}^2}\mathring{\mathcal{W}}_1$, $\Pi_{11,12} = \frac{360}{\bar{\wp}^3}\mathring{\mathcal{W}}_1$, $\Pi_{12,12} = -\frac{720}{\bar{\wp}^3}\mathring{\mathcal{W}}_1$, $\Pi_{13,13} = -9\mathring{\mathcal{W}}_2$, $\Pi_{13,14} = \frac{36}{\bar{\wp}}\mathring{\mathcal{W}}_2$, $\Pi_{13,15} = -\frac{60}{\bar{\wp}^2}\mathring{\mathcal{W}}_2$, $\Pi_{14,14} - \frac{192}{\bar{\wp}^2}\mathring{\mathcal{W}}_2$, $\Pi_{14,15} = \frac{360}{\bar{\wp}^3}\mathring{\mathcal{W}}_2$ *and* $\Pi_{15,15} = -\frac{720}{\bar{\wp}^3}\mathring{\mathcal{W}}_2$. $\daleth = \begin{bmatrix} \mathcal{X}_{1i}\mathcal{H}_i^TC_i^T & \underbrace{0\cdots0}_{14\ times} \end{bmatrix}^T$, $\Xi_1 = \begin{bmatrix} \mathfrak{B}_i^T & \mathfrak{B}_i^T & \underbrace{0\cdots0}_{13\ times} \end{bmatrix}^T$, $\Xi_2 = \begin{bmatrix} \mathfrak{N}_i\mathcal{X}_{1i} & \underbrace{0\cdots0}_{14\ times} \end{bmatrix}$, $\Xi_3 = \begin{bmatrix} \mathcal{X}_{1i}\mathfrak{B}_i^T & \underbrace{0\cdots0}_{14\ times} \end{bmatrix}^T$, $\Xi_4 = \begin{bmatrix} \mathfrak{N}_i^T\mathcal{X}_{1i} & \underbrace{0\cdots0}_{14\ times} \end{bmatrix}$, $\Xi_5 = \begin{bmatrix} (\mathcal{X}_{1i}C_i^T\tilde{\kappa}_1)^T & \underbrace{0\cdots0}_{14\ times} \end{bmatrix}^T$. *In addition, if the above-offered constraints have a workable solution, then the gain matrices can be computed by using the ensuing connection:* $\mathcal{L}_i = \mathcal{L}_{oi}\bar{\mathfrak{X}}_{2i}^{-1}$, $\mathcal{L}_{pi} = \mathcal{L}_{si}\bar{\mathfrak{X}}_{2i}^{-1}$ *and* $\mathcal{K}_j = \mathcal{Y}_j\mathfrak{X}_{1i}^{-1}$.

Proof 2 *The proof of this theorem follows from the results (10) obtained in Theorem 1 along with system uncertainty and extended dissipative theory. To proceed ahead, let us impose the conditions* $\mathcal{U}_{1i}^{-1} = \mathfrak{X}_{1i}$, $\mathcal{U}_{2i}^{-1} = \mathfrak{X}_{2i}$, $\mathcal{U}_{3i}^{-1} = \mathfrak{X}_{3i}$, $\mathfrak{X}_{1i}\mathcal{W}_1\mathfrak{X}_{1i} = \hat{\mathcal{W}}_1$, $\mathfrak{X}_{1i}\mathcal{W}_2\mathfrak{X}_{1i} = \hat{\mathcal{W}}_2$, $\mathfrak{X}_{2i}\mathcal{W}_3\mathfrak{X}_{2i} = \hat{\mathcal{W}}_3$, $\mathfrak{X}_{2i}\mathcal{W}_4\mathfrak{X}_{2i} = \hat{\mathcal{W}}_4$, $C_i\mathfrak{X}_2 = \bar{\mathfrak{X}}_2C_i$, $\mathfrak{X}_{1i}\breve{\mathcal{W}}_1\mathfrak{X}_{1i} = \mathring{\mathcal{W}}_1$, $\mathfrak{X}_{2i}\breve{\mathcal{W}}_2\mathfrak{X}_{1i} = \mathring{\mathcal{W}}_2$, *along with pre- and post- multiplication by* $\{\mathcal{U}_{1i}^{-1}, \mathcal{U}_{2i}^{-1}, \mathcal{U}_{3i}^{-1}, \mathcal{U}_{1i}^{-1}, \mathcal{U}_{1i}^{-1}, \mathcal{U}_{2i}^{-1}, \mathcal{U}_{2i}^{-1}, \mathcal{U}_{2i}^{-1}, I, \mathcal{U}_{1i}^{-1}, \mathcal{U}_{1i}^{-1}, \mathcal{U}_{1i}^{-1}, \mathcal{U}_{2i}^{-1}, \mathcal{U}_{2i}^{-1}, \mathcal{U}_{2i}^{-1}\}$ *of the matrix* $\Lambda_{i,j}$ *in the previous theorem. As a result of this presumption and by making use of Schur complement, we arrive at the matrix* Θ_{ij} *defined in the theorem statement.*

Further by tracing the similar fashion of Theorem 1, we can attain $\mathbb{E}\{\dot{\mathcal{V}}(t)\} < 0$. *Then, with the extended dissipative criterion* $\zeta(t)$, *we can obtain the following relation:*

$$\mathbb{E}\{\dot{\mathcal{V}}(t)\} - \zeta(t) \le 0.$$

Moreover, by integrating the above inequality from 0 *to* τ, *we obtain*

$$\mathbb{E}\{\mathcal{V}(t)\} \le \mathbb{E}\{\int_0^\tau \zeta(s)ds\}. \tag{21}$$

On the basis of Definition 1, we have

$$\mathbb{E}\left\{\int_0^{T_f} \zeta(t)dt\right\} - \sup_{0\le t\le T_f} \mathbb{E}\left\{y^T(t)\kappa_4 y(t)\right\} \ge \gamma. \tag{22}$$

Subsequently, we need to establish that the above constraint obeys for any matrices $\kappa_1, \kappa_2, \kappa_3$ and κ_4 under the setting of Assumption 1. In this regard, we can characterize the parameter κ_4 into two types.

First, if $\|\kappa_4\| = 0$, then the inequality (22) implies for any $T_f \geq 0$ that

$$\int_0^{T_f} \zeta(s)ds \geq \gamma. \tag{23}$$

If $\|\kappa_4\| \neq 0$, we can have from Assumption 1 that the associated matrices are $\kappa_1 = 0$, $\kappa_2 = 0$, $\kappa_3 > 0$, thus for any $T_f \geq t \geq 0$, we have

$$\int_0^{T_f} \zeta(s)ds \geq \int_0^{t} \zeta(s)ds \geq \gamma. \tag{24}$$

Suppose there exists a scalar $0 < \eta < 1$ such that

$$\int_0^{T_f} \zeta(s)ds \geq \eta x^T(t)\mathcal{U}_{1i}x(t) + \gamma. \tag{25}$$

By letting $C_i^T \kappa_4 C_i < \eta \mathcal{U}_{1i}$, then we have

$$y^T(t)\kappa_4 y(t) = x^T(t)C_i^T \kappa_4 C_i x(t) < \eta x^T(t)x(t). \tag{26}$$

It is clear from (25) and (26) that

$$\int_0^{T_f} \zeta(s)ds \geq y^T(t)\kappa_4 y(t) + \gamma. \tag{27}$$

Thus, the inequality (9) holds for $T_f \geq 0$. Further, if conditions (19)-(20) hold, then we conclude that addressed system (1) is asymptotically stable with the extended dissipative which concludes the proof of this theorem.

At the end of this portion, we prove that the fuzzy chaotic system (1) is asymptotically stable with extended dissipative thorough the designed fault-tolerant controller (6) under the unknown actuator faults.

Theorem 3 *Let $\bar{\wp}$, v, ϱ, ε, γ be given positive scalars. Then, system (1) with the unknown fault controller (6) is asymptotically stable with the extended dissipative, if there exist positive scalars μ, ϑ_1, ϑ_2 and matrices $\mathfrak{X}_{mi} > 0$, $(m = 1, 2, 3)$, $\hat{\mathcal{W}}_g > 0$ $(g = 1, 2, 3, 4)$, $\hat{\mathcal{W}}_1$ and $\hat{\hat{\mathcal{W}}}_2 > 0$ such that the ensuing LMIs hold:*

$$\begin{bmatrix} -\mu I & C_i\mathfrak{X}_{2i} - \bar{\mathfrak{X}}_{2i}C_i \\ * & -I \end{bmatrix} < 0, \tag{28}$$

$$\begin{bmatrix} \Theta_{ij} & \varepsilon\mathfrak{S}_1^T & \mathfrak{S}_2 & \mathfrak{S}_3^T \\ * & -\varepsilon I & 0 & 0 \\ * & * & -\varepsilon I & 0 \\ * & * & * & -\varepsilon I \end{bmatrix} < 0, \tag{29}$$

$$\text{where } \mathfrak{S}_1 = \begin{bmatrix} \mathcal{B}_i^T \mathfrak{G}_1^T & \underbrace{0 \cdots 0}_{20\ times} \end{bmatrix}, \mathfrak{S}_2 = \begin{bmatrix} 0 & 0 & 0 & \mathcal{Y}_j^T & 0 & \mathcal{Y}_j^T & \underbrace{0 \cdots 0}_{15\ times} \end{bmatrix}^T, \mathfrak{S}_3 = \begin{bmatrix} \underbrace{0 \cdots 0}_{15\ times} & \mathcal{B}_i^T \mathfrak{G}_1 & \underbrace{0 \cdots 0}_{5\ times} \end{bmatrix}.$$

Furthermore, the gain matrices of offered controller and observer are obtained by solving the ensuing connection $\mathcal{L}_i = \mathcal{L}_{oi}\tilde{\mathfrak{X}}_{2i}^{-1}$, $\mathcal{L}_{pi} = \mathcal{L}_{si}\tilde{\mathfrak{X}}_{2i}^{-1}$ *and* $\mathcal{K}_j = \mathcal{Y}_j\mathfrak{X}_{1i}^{-1}$.

Proof 3 *The proof of this theorem can be straightforwardly obtained by replacing the actuator fault matrix* $\mathfrak{G}_f$ *with* $\mathfrak{G}_0 + \mathfrak{G}_1\Sigma$ *in the previous theorem. Thus, the proof is omitted here.*

Remark 1 *It should be mentioned that the Lyapunov-Krasovskii functional is specifically designed to handle systems with delays. It accounts for the past states of the system, making it suitable for systems where delay affects stability, which traditional Lyapunov functionals may not address adequately. Further, it allows for a more comprehensive analysis of stability, as it includes integral terms that capture the system's history over a time interval. This inclusion can result in less conservative stability criteria compared to conventional Lyapunov functionals. On the other hand, extended Wirtinger inequality plays a significant role in maximizing the feasible region of stability criteria and obtaining maximum delay bounds of time delays for guaranteeing system stability in a given constraint. Thus, based on these considerations, in our work, Lyapunov-Krasovskii functional with double-integral term is considered. Subsequently, the LMI conditions are derived based on the constructed Lyapunov-Krasovskii functional by properly applying the extended Wirtinger inequality.*

4. SIMULATION VERIFICATION

This section includes an illustrative example demonstrating the effectiveness and superiority of the proposed criterion. Notably, we leverage MATLAB software to aid in the acquisition of simulation results. For this purpose, we consider a chaotic Rossler's system [51] and its dynamics are laid out below:

$$\begin{cases} \dot{x}_1(t) = -x_2(t) - x_3(t), \\ \dot{x}_2(t) = x_1(t) + \mathfrak{a}x_2(t), \\ \dot{x}_3(t) = \mathfrak{b}x_1(t) - (\mathfrak{c} - x_1(t))x_3(t) + u(t), \end{cases} \tag{30}$$

where $x_1(t) \in [\mathfrak{c} - \mathfrak{d} \quad \mathfrak{c} + \mathfrak{d}]$, by using fuzzy modeling method as in [51], we get the system matrices as $\mathcal{A}_1 = \begin{bmatrix} 0 & -1 & -1 \\ 1 & \mathfrak{a} & 0 \\ \mathfrak{b} & 0 & -\mathfrak{d} \end{bmatrix}, \mathcal{A}_2 = \begin{bmatrix} 0 & -1 & -1 \\ 1 & \mathfrak{a} & 0 \\ \mathfrak{b} & 0 & \mathfrak{d} \end{bmatrix}, \mathcal{B}_1 = \mathcal{B}_2 = \begin{bmatrix} 0 \\ 0 \\ 1 \end{bmatrix}, \mathcal{D}_1 = \mathcal{D}_2 = \begin{bmatrix} 0.2 & 0.3 & 0.1 \\ 0.1 & 0.2 & 0.3 \\ 0.1 & 0.7 & 0.4 \end{bmatrix},$

$C_1 = C_2 = \begin{bmatrix} 1 & 0 & 0 \\ 0 & 1 & 0 \\ 0 & 0 & 1 \end{bmatrix}, \mathfrak{B}_1 = \begin{bmatrix} 0.12 & 0.15 & 0 \\ 0.22 & 0 & 0.3 \\ 0.31 & 0.2 & 0.2 \end{bmatrix}, \mathfrak{B}_2 = \begin{bmatrix} 0.12 & 0.1 & 0 \\ 0.32 & 0 & 0.4 \\ 0.3 & 0.2 & 0.3 \end{bmatrix}, \mathfrak{N}_1 = \mathfrak{N}_2 = \begin{bmatrix} 0.1 & 0.4 & 0 \\ 0.3 & 0 & 0.5 \\ 0.2 & 0.3 & 0.1 \end{bmatrix}.$

Further, we have taken the parameters involved in the simulation as $\mathfrak{a} = 0.3$, $\mathfrak{b} = 0.5$, $\mathfrak{c} = 5$, $\mathfrak{d} = 10$, $\bar{\nu} = 0.3$, $\bar{\wp} = 0.5$, $\alpha = 0.6$, $\delta_1 = 1.2$, $\delta_2 = 1.5$, $\gamma = 0.01$, $\kappa_1 = 5$, $\kappa_2 = 0.2$, $\kappa_3 = 0.7$, $\varepsilon = 0.9$, and $\varrho = 1$. The fuzzy membership function to this network transmission is taken as $\mathfrak{b}_1(\phi(t)) = \frac{\mathfrak{c}+\mathfrak{d}-x_1(t)}{2\mathfrak{d}}$ and $\mathfrak{b}_2(\phi(t)) = 1 - \mathfrak{b}_1(\phi(t))$. Moreover, the actuator fault $\mathfrak{G}_f$ is assumed within the interval $(0.2, 0.8)$ and the time-varying delay is selected as $\wp(t) = 0.3 + 0.6(0.9 + 0.5sin(0.3\tau))$. Specifically, the chaotic behavior of the considered system model is supplied in Figure 1.

Moreover, by inputting the aforementioned parameters in Theorem 3 and solving it via standard software, the controller and observer gains are obtained as follows:

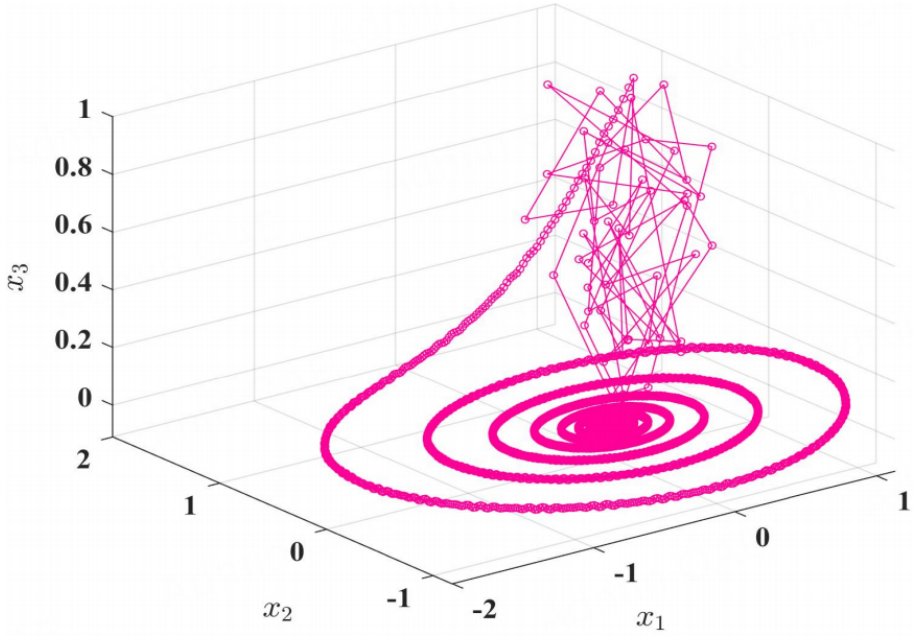


Figure 1. Chaotic behavior of considered system under these parameters.

$$\mathcal{K}_1 = \begin{bmatrix} 0.3703 & 0.0422 & -0.0448 \end{bmatrix}, \qquad \mathcal{K}_2 = \begin{bmatrix} 0.3674 & 0.1812 & 0.0209 \end{bmatrix},$$

$$\mathcal{L}_1 = \begin{bmatrix} 8.3546 & -1.0633 & -1.6445 \\ -1.0633 & 12.0220 & -0.1654 \\ -1.6445 & -0.1654 & 4.5937 \end{bmatrix}, \ \mathcal{L}_2 = \begin{bmatrix} 24.5503 & -7.0704 & -2.3350 \\ -7.0704 & 51.0683 & 0.7260 \\ -2.3350 & 0.7260 & 33.8401 \end{bmatrix},$$

$$\mathcal{L}_{p_1} = \begin{bmatrix} 1.7967 & -0.1956 & 0.0187 \\ -0.1956 & 1.3038 & 0.0149 \\ 0.0187 & 0.0149 & 0.9877 \end{bmatrix}, \ \mathcal{L}_{p_2} = \begin{bmatrix} 3.9617 & 0.1771 & -0.2038 \\ 0.1771 & 2.5764 & -0.0264 \\ -0.2038 & -0.0264 & 0.0819 \end{bmatrix}.$$

For simulation purposes, the external disturbance signal and nonlinear deception attack function are considered as

$$w(t) = \begin{bmatrix} 0.1\sin(0.4\pi\tau) & 0.2\sin(0.4\pi\tau) & 0.3\sin(0.4\pi\tau) \end{bmatrix}^T$$

and

$$f(y(t)) = \begin{bmatrix} 0.01\tanh(0.2x_1(t)) & 0.03\tanh(0.5x_2(t))) & 0.04\tanh(0.2x_3(t)) \end{bmatrix}.^T$$

In the follow-up, by utilizing the gain matrices and the parameters put forward above, the simulation task is carried out under random initial conditions. Specifically, in Figure 2, the response of the state trajectories in the presence and absence of the control is presented. It can be seen that the system trajectories diverge when the controller is absent, whereas, under the developed controller, the intended performance of the system is accomplished. In other words, the system trajectories converge to the equilibrium point, even in the presence of several deteriorating factors. From these figures, the inherent potential of the developed control is straightforwardly exhibited. Furthermore, the significance of the developed observer is demonstrated in Figure 3. Herein, the observer trajectories precisely estimate the system trajectories, showcasing the viability of the observer.

Subsequently, to showcase the impact of actuator faults, Figures 4-6 are provided. Specifically, the trajectories of the system output with and without fault are presented in Figure 4. Likewise, the response of state and

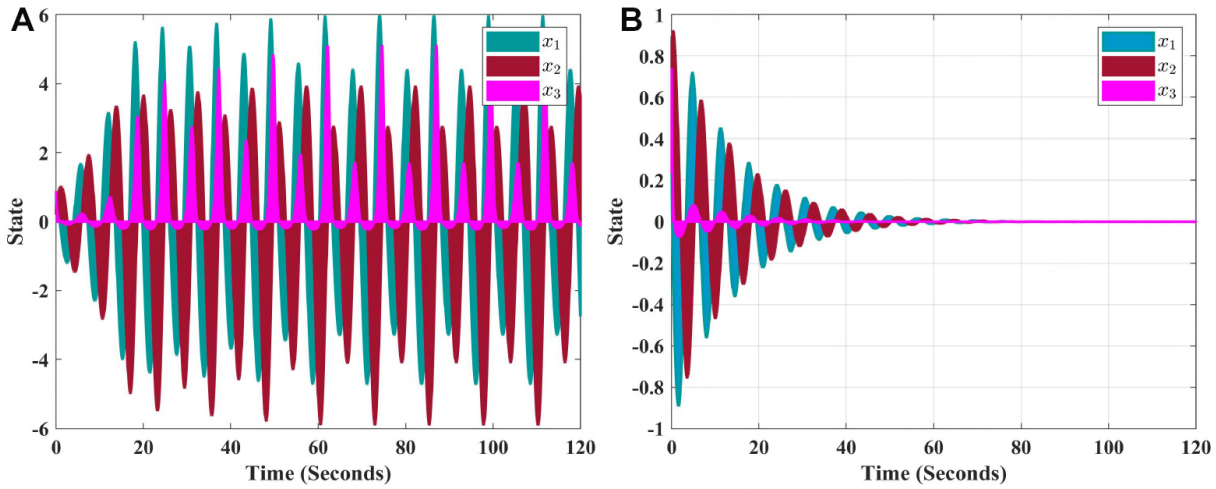


Figure 2. Time evolution of states of the undertaken system. (A) Open loop system; (B) Closed loop system.

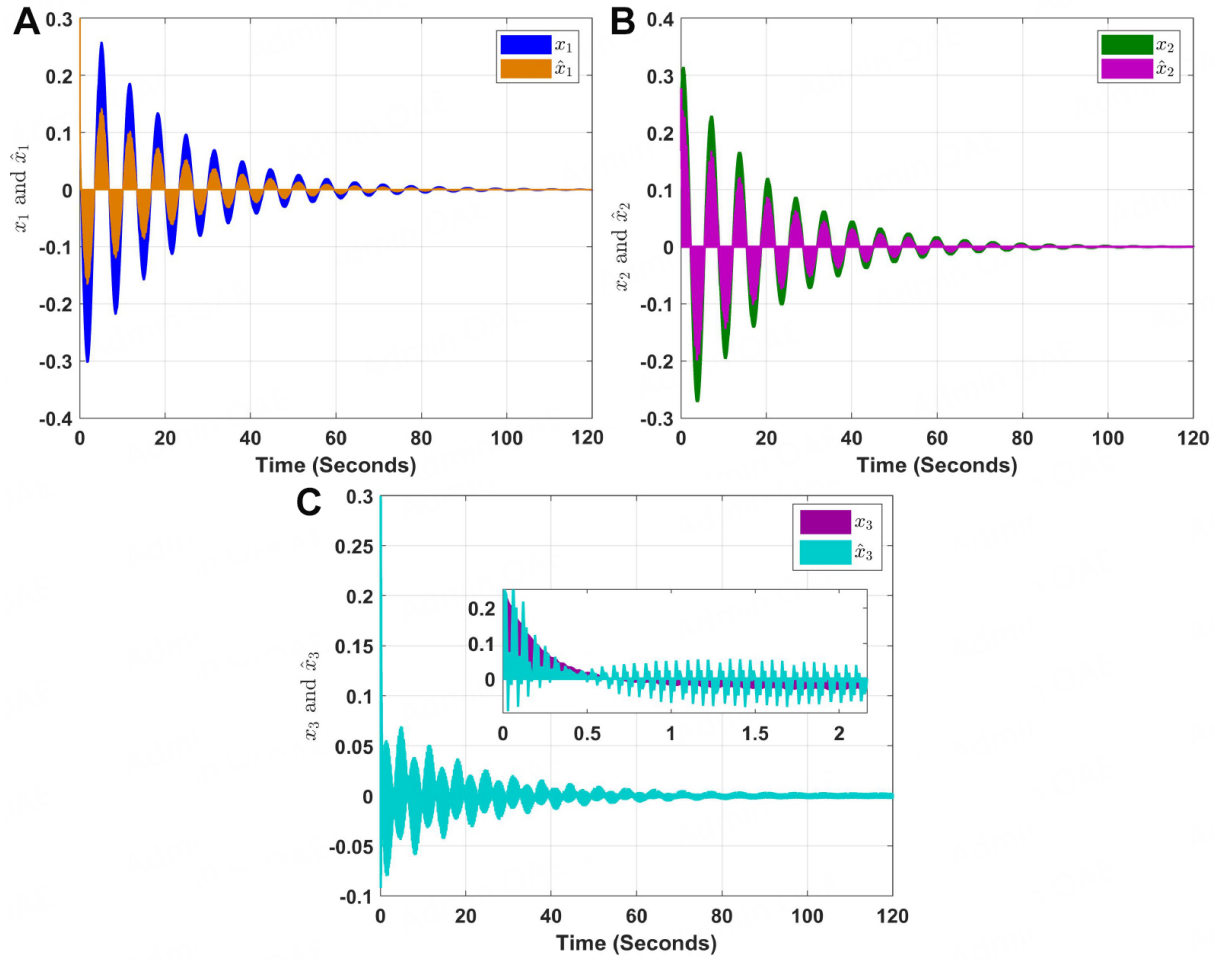


Figure 3. Response of system and its corresponding observer trajectories. (A) $x_1(t)$ *and* $\hat{x}_1(t)$; (B) $x_2(t)$ *and* $\hat{x}_2(t)$; (C) $x_3(t)$ *and* $\hat{x}_3(t)$.

its respective observer response in the situation where the actuator is functioning normally without the fault are presented in Figure 5. It is evidently visible that the estimation performance is better when compared

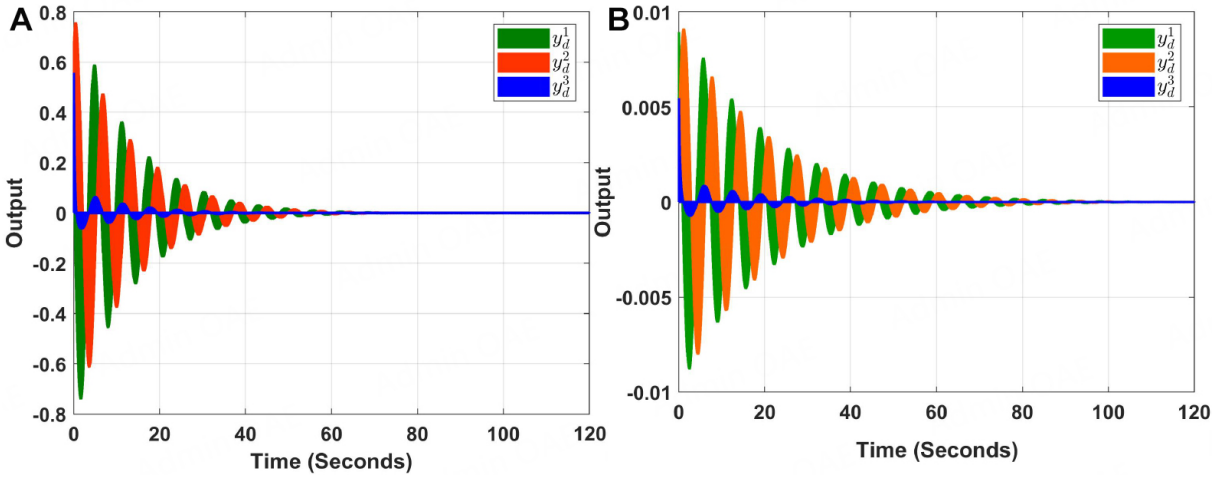


Figure 4. Progression of output trajectories. (A) With actuator faults; (B) Without actuator faults.

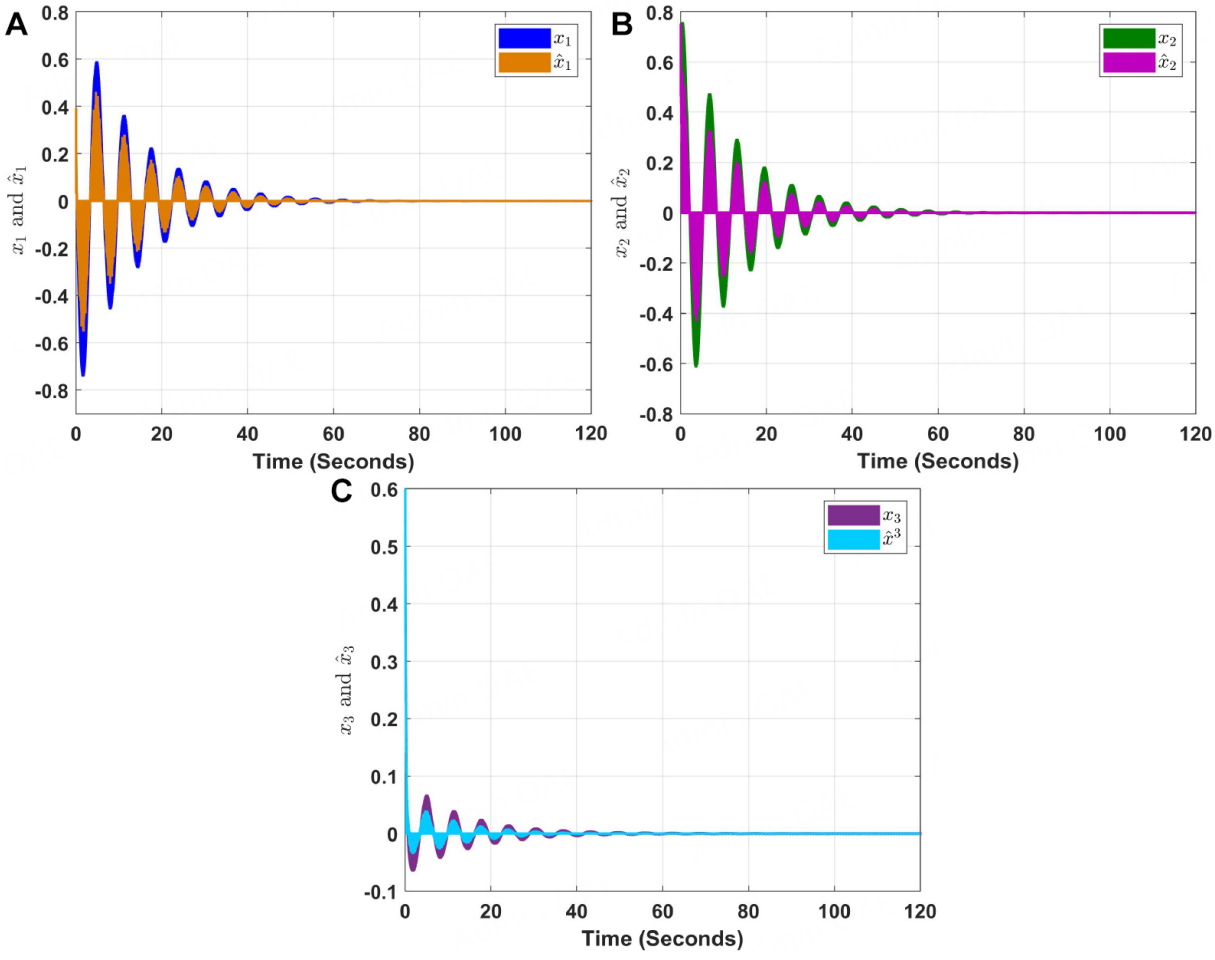


Figure 5. Time profile of system and its corresponding observer without actuator faults. (A) $x_1(t)$ *and* $\hat{x}_1(t)$; (B) $x_2(t)$ *and* $\hat{x}_2(t)$; (C)$x_3(t)$ *and* $\hat{x}_3(t)$.

with Figure 3. Eventually, the pictorial representation of the developed control protocol under the same two scenarios is laid out in Figure 6. Overall, from these figures, the impact of actuator faults of the considered

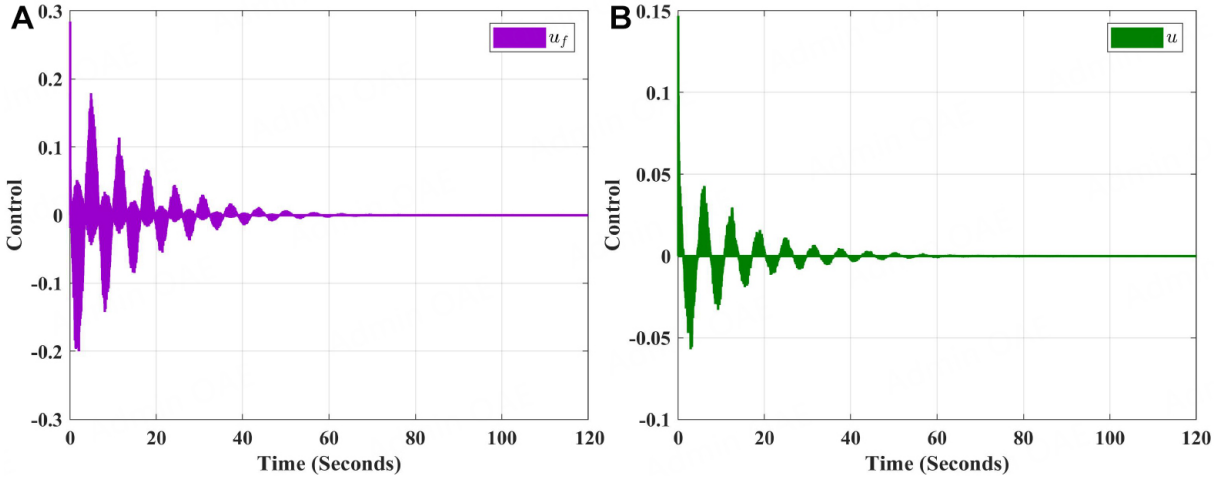


Figure 6. Response of control trajectories. (A) With actuator faults; (B) Without actuator faults.

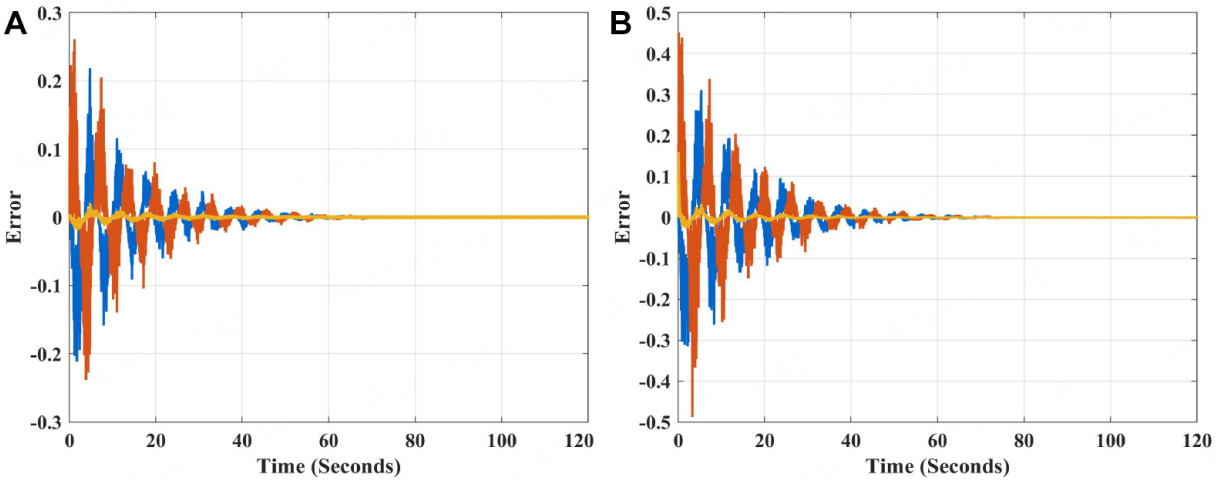


Figure 7. Response of state estimation error. (A) Under PIO; (B) Under Luenberger observer.

system and the observer is clearly exhibited.

Ultimately, to highlight the potential of the configured PIO over the conventional Luenberger observer, Figure 7 is depicted. Specifically, in this figure, the state estimation trajectories for these two observers are offered. It is seen that the estimation error is reduced significantly. In sum, the results of this simulation study indicate that the suggested control mechanism assists the assayed systems in attaining asymptotic stability despite parameter uncertainties, input delay, deception attacks, and external disturbances.

5. CONCLUSION

Over this research endeavor, we have tackled the robust fault-tolerant control issue for the T-S fuzzy chaotic system in the midst of parameter uncertainties, input delay, deception assaults, and external disturbances. To begin, the system states have been estimated by means of configuring fuzzy-based observer and therein, the output measurement of the system model considers deception attacks in the output channel to ensure secure estimation. Therein, it is presupposed that the deception attacks occur at random which considers the Bernoulli distribution. Secondly, the robust fault-tolerant control has been developed by incorporating the

actuator faults and input delays. Here, the system is driven to achieve its goals by substantially mitigating the actuator faults. Thirdly, adequate stability criteria are formed with the assistance of Lyapunov stability theory and the LMI approach and the gain matrices have been emitted based on the derived conditions. In the end, the numerical results are provided to show off the envisaged use of the set-up control technique.

DECLARATIONS

Acknowledgments
The authors would like to thank the reviewers for their valuable comments.

Authors' contributions
Conceptualization, methodology, validation, writing-original draft, writing - review & editing: Monisha S
Conceptualization, validation, software, writing - original draft, writing - review & editing, methodology: Nithya V
Conceptualization, methodology, validation, writing-original draft, writing-review & editing: Sakthivel R

Availability of data and materials
Not applicable.

Financial support and sponsorship
None.

Conflicts of interest
All authors declared that there are no conflicts of interest.

Ethical approval and consent to participate
Not applicable.

Consent for publication
Not applicable.

Copyright
© The Author(s) 2024.

REFERENCES

1. Peng S, Wang Q, Fu B. Exponential stabilization of chaotic systems based on fuzzy time-triggered intermittent control. *Chaos Soliton Fract* 2022;162:112390. DOI
2. Asadollahi M, Ghiasi AR, Badamchizadeh MA. Adaptive control for a class of nonlinear chaotic systems with quantized input delays. *J Franklin Inst* 2020;357:254-78. DOI
3. Chen G. Controlling chaos and bifurcations in engineering systems. Boca Raton: CRC Press; 1999, pp. 412-21. Available from: https://www.amazon.com/Controlling-Chaos-Bifurcations-Engineering-Systems/dp/0849305799 [Last accessed on 28 Nov 2024].
4. Mobayen S, Tchier F. Composite nonlinear feedback control technique for master/slave synchronization of nonlinear systems. *Nonlinear Dyn* 2017;87:1731-47. DOI
5. Ge ZM, Lin GH. The complete, lag and anticipated synchronization of a BLDCM chaotic system. *Chaos Soliton Fract* 2007;34:740-64. DOI
6. Faieghi M, Suwat K, Delavari H, Baleanu D. LMI-based stabilization of a class of fractional-order chaotic systems. *Nonlinear Dyn* 2013;72:301-9. DOI
7. Modiri A, Mobayen S. Adaptive terminal sliding mode control scheme for synchronization of fractional-order uncertain chaotic systems. *ISA Trans* 2020;105:33-50. DOI
8. Rashidnejad Z, Karimaghaee P. Synchronization of a class of uncertain chaotic systems utilizing a new finite-time fractional adaptive sliding mode control. *Chaos Soliton Fract X* 2020;5:100042. DOI
9. Xia Y, Wang J, Meng B, Chen X. Further results on fuzzy sampled-data stabilization of chaotic nonlinear systems. *Appl Math Comput*

2020;379:125225. DOI
10. Chang YC. A robust tracking control for chaotic Chua's circuits via fuzzy approach. *IEEE Trans Circuits Syst I* 2001;48:889-95. DOI
11. Liu YJ, Zheng YQ. Adaptive robust fuzzy control for a class of uncertain chaotic systems. *Nonlinear Dyn* 2009;57:431-9. DOI
12. Ababneh M, Almanasreh AM, Amasha H. Design of digital controllers for uncertain chaotic systems using fuzzy logic. *J Franklin Inst* 2009;346:543-56. DOI
13. Chen L, Chen G. Fuzzy modeling, prediction, and control of uncertain chaotic systems based on time series. *IEEE Trans Circuits Syst I* 2000;47:1527-31. DOI
14. Tanaka K, Ikeda T, Wang HO. A unified approach to controlling chaos via an LMI-based fuzzy control system design. *IEEE Trans Circuits Syst I* 1998;45:1021-40. DOI
15. Wu HN, Bai MZ. Active fault-tolerant fuzzy control design of nonlinear model tracking with application to chaotic systems. *IET Control Theory Appl* 2009;3:642-53. DOI
16. Li X, Ma D, Xie X, Sun Q. Fault-tolerant synchronization of chaotic systems with fuzzy sampled data controller based on adaptive event-triggered scheme. *Int J Fuzzy Syst* 2020;22:917-29. DOI
17. Zhao L, Yang GH. Adaptive sliding mode fault tolerant control for nonlinearly chaotic systems against DoS attack and network faults. *J Franklin Inst* 2017;354:6520-35. DOI
18. Su L, Shen H. Fault-tolerant dissipative synchronization for chaotic systems based on fuzzy mixed delayed feedback. *Neurocomputing* 2015;151:1407-13. DOI
19. Wang H, Liu C, Huang X, Zhong Y, Qu D, Patton RJ. Extended state observer-based fault-tolerant control for an unmanned surface vehicle under asynchronous injection and deception attacks. *Complex Eng Syst* 2024;4:13. DOI
20. Zhu ZY, Zhao ZS, Zhang J, Wang RK, Li Z. Adaptive fuzzy control design for synchronization of chaotic time-delay system. *Inf Sci* 2020;535:225-41. DOI
21. Lam HK, Ling WK, Iu HC, Ling SH. Synchronization of chaotic systems using time-delayed fuzzy state-feedback controller. *IEEE Trans Circuits Syst I* 2008;55:893-903. DOI
22. Sun J, Wang H. Stability analysis for highly nonlinear switched stochastic systems with time-varying delays. *Complex Eng Syst* 2022;2:17. DOI
23. Pai MC. Chaotic sliding mode controllers for uncertain time-delay chaotic systems with input nonlinearity. *Appl Math Comput* 2015;271:757-67. DOI
24. Mobayen S, Ma J. Robust finite-time composite nonlinear feedback control for synchronization of uncertain chaotic systems with nonlinearity and time-delay. *Chaos Soliton Fract* 2018;114:46-54. DOI
25. Zhou J, Er MJ. Adaptive output control of a class of uncertain chaotic systems. *Syst Control Lett* 2007;56:452-60. DOI
26. Zheng W, Zhang Z, Lam HK, Sun F, Wen S. LMIs-based exponential stabilization for interval delay systems via congruence transformation: Application in chaotic Lorenz system. *Chaos Soliton Fract* 2023;176:114060. DOI
27. Bowong S, Kakmeni M, Koina R. Chaos synchronization and duration time of a class of uncertain chaotic systems. *Math Comput Simulat* 2006;71:212-28. DOI
28. Li M, Xia J, Zhao J, Zhang H, Shen H. Event-triggered extended dissipative control for networked singular systems. *Int J Control Autom Syst* 2021;19:382-91. DOI
29. Xia J, Gao H, Liu M, Zhuang G, Zhang B. Non-fragile finite-time extended dissipative control for a class of uncertain discrete time switched linear systems. *J Franklin Inst* 2018;355:3031-49. DOI
30. Li M, Zhao Ji, Xia J, Zhuang G, Zhang W. Extended dissipative analysis and synthesis for network control systems with an event-triggered scheme. *Neurocomputing* 2018;312:34-40. DOI
31. Liu Y, Ma Y. Finite-time non-fragile extended dissipative control for T-S fuzzy system via augmented Lyapunov-Krasovskii functional. *ISA Trans* 2021;117:1-15. DOI
32. Li Y, Zhang J, Li Y. Command filter-based adaptive neural tracking control of nonlinear systems with multiple actuator constraints and disturbances. *Complex Eng Syst* 2024;4:5. DOI
33. Adloo H, Noroozi N, Karimaghaee P. Observer-based model reference adaptive control for unknown time-delay chaotic systems with input nonlinearity. *Nonlinear Dyn* 2012;67:1337-56. DOI
34. Rojas HD, Romero JC. On the equivalence between generalized proportional integral observer and disturbance observer. *ISA Trans* 2023;133:397-411. DOI
35. Ouhib L, Kara R. Proportional observer design based on D-stability and Finsler's Lemma for Takagi-Sugeno systems. *Fuzzy Sets Syst* 2023;452:61-90. DOI
36. Zhong Q, Yang J, Shi K, Zhong S, Li Z, Sotelo MA. Event-triggered H_∞ load frequency control for multi-area nonlinear power systems based on non-fragile proportional integral control strategy. *IEEE Trans Intell Transp Syst* 2022;23:12191-201. DOI
37. Youssef T, Chadli M, Karimi HR, Wang R. Actuator and sensor faults estimation based on proportional integral observer for TS fuzzy model. *J Franklin Inst* 2017;354:2524-42. DOI
38. Sun Y, Yu J, Yu X, Gao H. Decentralized adaptive event-triggered control for a class of uncertain systems with deception attacks and its application to electronic circuits. *IEEE Trans Circuits Syst I* 2020;67:5405-16. DOI
39. Wang D, Chen F, Meng B, Hu X, Wang J. Event-based secure H_∞ load frequency control for delayed power systems subject to deception attacks. *Appl Math Comput* 2021;394:125788. DOI
40. Feng J, Xie J, Wang J, Zhao Y. Secure synchronization of stochastic complex networks subject to deception attack with nonidentical nodes and internal disturbance. *Inf Sci* 2021;547:514-25. DOI

41. Bi Y, Wang T, Qiu J, Li M, Wei C, Yuan L. Adaptive Decentralized finite-time fuzzy secure control for uncertain nonlinear CPSs under deception attacks. *IEEE Trans Fuzzy Syst* 2023;31:2568-80. DOI
42. Hu Z, Deng F, Su Y, Zhang J, Hu S. Security control of networked systems with deception attacks and packet dropouts: a discrete-time approach. *J Franklin Inst* 2021;358:8193-206. DOI
43. Zhang N, Qi W, Pang G, Cheng J, Shi K. Observer-based sliding mode control for fuzzy stochastic switching systems with deception attacks. *Appl Math Comput* 2022;427:127153. DOI
44. Han S, Kommuri SK, Lee S. Affine transformed IT2 fuzzy event-triggered control under deception attacks. *IEEE Trans Fuzzy Syst* 2021;29:322-35. DOI
45. Zhao D, Tian Y, Zhao N. Adaptive neural control for delayed discrete-time switched systems under deception attacks. *Complex Eng Syst* 2024;4:1. DOI
46. Rong N, Wang Z. State-dependent asynchronous intermittent control for IT2 T–S fuzzy interconnected systems under deception attacks. *Nonlinear Dyn* 2020;100:3433-48. DOI
47. Song W, Wang Z, Wang J, Shan J. Particle filtering for a class of cyber-physical systems under Round-Robin protocol subject to randomly occurring deception attacks. *Inf Sci* 2021;544:298-307. DOI
48. Jiang Y, Wu S, Yang H, Luo H, Chen Z, Yin S, Kaynak O. Secure data transmission and trustworthiness judgement approaches against cyber-physical attacks in an integrated data-driven framework. *IEEE Trans Syst Man Cybern Syst* 2022;52:7799-809. DOI
49. Yu K, Chang XH. Quantized output feedback resilient control of uncertain system under hybrid cyber attacks. *Int J Adapt Control Signal Process* 2022;36:2954-70. DOI
50. Samidurai R, Sriraman R, Cao J, Tu Z. Nonfragile stabilization for uncertain system with interval time-varying delays via a new double integral inequality. *Math Methods Appl Sci* 2018;41:6272-87. DOI
51. Wang X, Park JH, She K, Zhong S, Shi L. Stabilization of chaotic systems with T–S fuzzy model and nonuniform sampling: A switched fuzzy control approach. *IEEE Trans Fuzzy Syst* 2019;27:1263-71. DOI

Du *et al. Complex Eng Syst* 2024;4:24
DOI: 10.20517/ces.2024.76

Complex Engineering Systems

Research Article

Open Access

Check for updates

Computation of robust positively invariant set based on direct data-driven approach

Qian Du, Hongli Yang

College of Mathematics and Systems Science, Shandong University of Science and Technology, Qingdao 266590, Shandong, China.

Correspondence to: Prof./Dr. Hongli Yang, College of Mathematics and Systems Science, Shandong University of Science and Technology, Qianwangang Road #579, Huangdao, Qingdao 266590, Shandong, China. E-mail: yhlmath@126.com

How to cite this article: Du Q, Yang H. Computation of robust positively invariant set based on direct data-driven approach. *Complex Eng Syst* 2024;4:24. http://dx.doi.org/10.20517/ces.2024.76

Received: 17 Oct 2024 **First Decision:** 8 Nov 2024 **Revised:** 19 Nov 2024 **Accepted:** 26 Nov 2024 **Published:** 30 Nov 2024

Academic Editor: Duxin Chen **Copy Editor:** Fangling Lan **Production Editor:** Fangling Lan

Abstract

A direct data-driven approach for computing the robust positively invariant sets of a discrete-time system is presented in this study. By transforming the invariance conditions into a set of tractable linear matrix inequality problems and combining them with a semidefinite programming problem, we maximize the volume of invariant sets without violating state constraints. Based on two equivalence conditions of invariance, we investigate two algorithms using the one-step method to maximize the volume of the invariant sets. Ultimately, we opted for Algorithm 1, which is more succinct and effective. To further reduce conservatism, we propose an iterative algorithm based on Algorithm 1. The effectiveness of the proposed algorithm is verified through numerical examples.

Keywords: Direct data-driven, robust positively invariant set, linear discrete-time system, semidefinite programming

1. INTRODUCTION

A set is defined as a robust positively invariant (RPI) set, if every initial state contained within it, the trajectory of the system's state remains confined to that set, regardless of any disturbances or uncertainties in its parameters[1]. In the domain of automatic control, the significance of RPI sets is self-evident. The theories and computational approaches of RPI sets have not only attracted significant interest in the academic community but also demonstrated extensive application values in multiple practical fields such as system stability analysis,

© The Author(s) 2024. **Open Access** This article is licensed under a Creative Commons Attribution 4.0 International License (https://creativecommons.org/licenses/by/4.0/), which permits unrestricted use, sharing, adaptation, distribution and reproduction in any medium or format, for any purpose, even commercially, as long as you give appropriate credit to the original author(s) and the source, provide a link to the Creative Commons license, and indicate if changes were made.

controller design, and nonlinear system theory[1–6]. Moreover, RPI sets offer us a powerful tool for evaluating and resolving a series of issues closely related to external unknown disturbances.

For linear discrete systems, several approaches have been proposed to compute the RPI sets[7–10]. These are model-based approaches that assume the system is usable. However, achieving precise and dependable models in practical applications is challenging, and imprecise models can result in a loss of system invariance and breach associated constraints[11,12], potentially leading to unstable system operation or suboptimal controller performance. To address these limitations, direct data-driven approaches have emerged as a viable alternative, eliminating the need for model identification[12]. As we all know, the two important forms of invariant sets are polyhedral and ellipsoidal sets[4]. Ellipsoidal sets may be more conservative than polyhedral sets. Since polyhedral sets offer more flexible and complex representations, they have an advantage over ellipsoidal sets both in theory and practice[1]. Additionally, polyhedral representations naturally capture physical constraints on state and control variables[3]. Due to these factors, this paper emphasizes the study of polyhedral sets.

In this paper, we propose a direct data-driven method[11,13] for computing polyhedral RPI sets. We assume that the RPI set is a 0-symmetric convex polyhedron of predetermined complexity. The method presented in[14] involves a relatively high number of algorithm optimization variables and linearized matrix inequality constraints, resulting in slow running speeds. Our method expands upon and optimizes the approach recently developed by Mejari *et al*[14]. We have derived a new invariance condition and developed an iterative algorithm based on this condition. In addressing the nonlinear problem of the invariance condition, we ingeniously utilize relevant variable transformations and appropriate scaling techniques. Subsequently, a series of LMIs[15] are employed to precisely represent the constraints and invariance requirements of the system. Finally, we resort to the semidefinite programming (SDP) problem for solution, aiming to maximize the volume of the RPI sets. Notably, our method does not require an accurate system model or system identification steps; it merely requires a state trajectory composed of a finite number of data samples as input. Furthermore, the number of optimization variables and LMIs in this iterative algorithm is less than that in[14], thereby reducing running time and operating costs to some extent.

The primary contribution of this paper lies in the introduction of a novel data-driven methodology tailored for computing systems equipped with RPI sets. This approach holds significant relevance, particularly within the realms of control system design and analysis. A standout feature of our method is its reliance on a limited dataset, bypassing the need for comprehensive mathematical model knowledge-a pivotal advantage in numerous practical applications where precise mathematical models are elusive or challenging to derive. Our work commences by establishing two fundamental equivalence criteria pertaining to invariance properties. Building upon these, we devise two single-step algorithms grounded in LMI frameworks for the computation of RPI sets, denominated as Algorithm 1 and Algorithm 2. A comparative assessment between these algorithms is subsequently undertaken.

Experimental evaluations disclose that although both algorithms converge upon identical RPI sets, Algorithm 1 distinguishes itself through reduced optimization variable requirements and exhibits superior computational efficiency relative to Algorithm 2. This distinction carries substantial weight in practical implementations, as augmented computational speed directly contributes to enhanced real-time system performance and cost efficiency.

Capitalizing on the merits of Algorithm 1, we further propose an iterative refinement strategy aimed at incrementally approximating the target volume of RPI sets over successive iterations. This iterative algorithm ingeniously retains the computational efficiency hallmark of Algorithm 1 while simultaneously alleviating resultant conservatism, thereby striking a balance between precision and performance.

The structure of this paper is as follows: Preliminaries and problem formulation are given in Section 2.1. Section 2.2 presents data-based invariances and constraints. Section 2.3 gives the relevant algorithms to maximize the RPI sets. Numerical examples are given in Section 3. Section 4 provides the discussion. Section 5 gives a summary of this article.

Notations: The following notations are made in this paper. The set of positive real numbers is denoted by R_+; a diagonal matrix with positive members is denoted by D_+^n; the matrix A's transpose is A^T. R^n denotes n-dimensional Euclidean space, and $R^{n\times m}$ denotes a set of $n\times m$-dimensional matrices. A matrix containing zeros in the relevant dimension is written as $\mathbf{0}$. $\mathbf{1}_m$ represents the vector of ones of dimension m. The identity matrix in m dimensions is written as I_m, and the i-th column of the identity matrix is denoted by the symbol e_i. $*$'s represents the matrix element that is uniquely identifiable by symmetry. For the symmetry matrix X, $X \succeq 0$ ($\succ 0$) indicates that the matrix X is a semi-positive definite matrix (positive definite matrix). Let $A \in R^{m\times n}$ be a matrix of n vectors $A = [a_1 \dots a_n]$, we define the vectorization of A as $\vec{A} = [a_1^T \dots a_n^T]^T \in R^{mn}$. For the finite set $\Theta_v = \{\theta^1, \dots, \theta^t\}$ with $\theta^j \in R^n$ for $j = 1, \dots t$, $conv(\Theta_v) = \left\{\theta \in R^n : \theta = \sum_{j=1}^t \alpha_j \theta^j, s.t \sum_{j=1}^t \alpha_j = 1, \alpha_j \in [0,1]\right\}$ denotes the convex-hull of a Θ_v, and $A \otimes B$ denotes the Kronecker product between A and B.

2. METHODS

2.1. Preliminaries and problem formulation

2.1.1 Preliminaries

Lemma 1 ([16]): (Vectorization) For matrices $A \in R^{m\times n}$, $B \in R^{n\times l}$, $C \in R^{l\times k}$ and $D \in R^{m\times k}$, the matrix equation $ABC = D$ is equivalent to

$$\left(C^T \otimes A\right)\vec{B} = \overrightarrow{ABC}, \tag{1a}$$

$$\overrightarrow{ABC} = \left(C^T B^T \otimes I_k\right)\vec{A}. \tag{1b}$$

Lemma 2 ([17]): (Schur complement): Given the matrix $S = \begin{bmatrix} S_1 & S_2 \\ S_3 & S_4 \end{bmatrix}$, where S_1 is a positive definite matrix, and define the Schur complement matrix of S_1 as $M = S_4 - S_3 S_1^{-1} S_2$, then $S \succeq 0(\succ 0) \Leftrightarrow M \succeq 0(\succ 0)$.

Definition 1 ([1]): (Polyhedral set) A convex polyhedral set is a set of the form $\mathcal{P}(F, g) = \{x : Fx \leq g\}$. A polyhedral set includes the origin if and only if $g \geq 0$ and includes the origin as an interior point if and only if $g > 0$.

Definition 2 ([1]): (0–Symmetric convex polyhedral set) A 0–symmetric convex polyhedral set can always be represented in the form $\bar{\mathcal{P}}(F, g) = \{x : -g \leq Fx \leq g\}$. If $\bar{\mathcal{P}}(F, g)$ includes 0 as an interior point, up to a normalization, it can be represented as $\bar{\mathcal{P}}(F, \bar{\mathbf{1}}) = \left\{x : -\bar{\mathbf{1}} \leq Fx \leq \bar{\mathbf{1}}\right\}$, where $\bar{\mathbf{1}}^T = [1 \quad 1 \dots 1]$.

The properties of 0-symmetric convex polyhedral are as follows:

(i) If $x \in \mathcal{P}$, then $-x \in \mathcal{P}$.

(ii) If $x, y \in \mathcal{P}$, then for any $\lambda \in [0,1]$, $\lambda x + (1-\lambda)y \in \mathcal{P}$.

2.1.2 Problem formulation

The following linear discrete-time system with no control inputs

$$x(k+1) = Ax(k) + w(k) \tag{2}$$

is considered in this paper, where $x(k) \in R^n$ and $w(k) \in R^n$ are the system state and the external disturbance at time k, respectively. The matrix A is unknown. A state trajectory of $T+1$ samples $\{x(k)\}_{k=1}^{T+1}$ is generated from the system (2). The generated data is denoted by:

$$X^+ \triangleq [x(2) \;\; x(3) \ldots x(T+1)] \in R^{n \times T}, \tag{3a}$$

$$X \triangleq [x(1) \;\; x(2) \ldots x(T)] \in R^{n \times T}. \tag{3b}$$

The constraints of the system state and disturbances are as follows

$$\mathcal{X} \triangleq \left\{ x \in R^n : Fx \leq \mathbf{1}_{n_x} \right\}, \tag{4a}$$

$$\mathcal{W} \triangleq \left\{ w \in R^n :| Dw \mid \leq \mathbf{1}_{n_w} \right\}, \tag{4b}$$

where $F \in R^{n_x \times n}$ and $D \in R^{n_w \times n}$ are known. Note that the external disturbances of the system are bounded.

Define a set of feasible models as follows:

$$\mathcal{A} \triangleq \left\{ A \in R^{n \times n} : x(k+1) - Ax(k) \in \mathcal{W}, k = 1, \ldots, T \right\} \tag{5}$$

By using the matrices defined in (3) and the disturbance set $\mathcal{W}$ in (4), (5) can be expressed as follows:

$$\mathcal{A} \triangleq \left\{ A \in R^{n \times n} : -\bar{\mathbf{1}} \leq DX^+ - DAX \leq \bar{\mathbf{1}} \in \mathcal{W} \right\}, \tag{6}$$

where $\bar{\mathbf{1}} \triangleq \begin{bmatrix} \mathbf{1}_{n_w} & \mathbf{1}_{n_w} & \ldots \mathbf{1}_{n_w} \end{bmatrix} \in R^{n_w \times T}$. By using Lemma 1, (6) is rewritten as follows,

$$\mathcal{A} \triangleq \left\{ A \in R^{n \times n} : -\bar{\mathbf{1}}_{Tn_w} + d \leq Z\vec{A} \leq \bar{\mathbf{1}}_{Tn_w} + d \in \mathcal{W} \right\}, \tag{7}$$

where

$$Z \triangleq \left(X^T \otimes D \right) \in R^{T_{n_w} \times n^2}, \tag{8a}$$

$$d \triangleq \begin{bmatrix} Dx(2) \\ Dx(3) \\ \vdots \\ Dx(T+1) \end{bmatrix} \in R^{T_{n_w}}. \tag{8b}$$

Proposition 1 [12,18]**:** The set $\mathcal{A}$ in (6) is a bounded polyhedron if and only if $rank\,(X) = n$ and D has a full column rank.

Remark 1: If the condition is not met, then set $\mathcal{A}$ is unbounded, making it difficult to find a feasible RPI set.

To enhance clarity, denote $x(k+1)$ as x^+, then system (2) can be represented by:

$$x^+ = Ax + w. \tag{9}$$

Consider the following set of 0–symmetric convex polyhedral set with predefined complexity n_p, which is given as follows:

$$\mathcal{P} \triangleq \left\{ x \in R^n : -\bar{\mathbf{1}} \leq PW^{-1}x \leq \bar{\mathbf{1}} \right\}, \tag{10}$$

where $P \in R^{n_p \times n}$, $W \in R^{n \times n}$. Assuming that W is reversible, this will be ensured by the invariance conditions in the form of LMIs.

The set $\mathcal{P}$ is the RPI set of system (9), if the following condition is satisfied:

$$x \in \mathcal{P} \Rightarrow x^+ \in \mathcal{P}, \forall w \in \mathcal{W}, \forall A \in \mathcal{A}. \tag{11}$$

The set $\mathcal{P}$ also must adhere to the state constraints, meaning that $\mathcal{P} \subseteq \mathcal{X}$, which leads to the following:

$$x \in \mathcal{P} \Rightarrow x \in \mathcal{X}. \tag{12}$$

From the above (3)-(4), (9)-(12), the problem addressed in this article is formulated as follows:

Problem: Given the data in (3), state constraints in (4) and matrix P, compute W in (10) such that:

(1) The invariance condition in (11) is satisfied;

(2) The set $\mathcal{P}$ satisfies state constraints in (4);

(3) Maximize the volume of the set $\mathcal{P}$.

2.2. Invariance conditions and constraints based on data

To render the state constraints of the system and invariance conditions more manageable, consider the following coordinate transformation [14]:

$$\theta = W^{-1}x \Leftrightarrow x = W\theta. \tag{13}$$

With the coordinate transformation, (10) can be expressed as:

$$\mathcal{P} \triangleq \{W\theta \in R^n : \theta \in \Theta\}, \tag{14}$$

where Θ is a set of 0-symmetric convex polyhedra defined as follows:

$$\Theta \triangleq \left\{\theta \in R^n : -\mathbf{1}_{n_p} \leq P\theta \leq \mathbf{1}_{n_p}\right\}. \tag{15}$$

For a fixed P, the vertices of Θ are known, so Θ can be written as a convex hull of these finite vertices [1].

$$\Theta = conv\left(\left\{\theta^1, \ldots, \theta^{2\sigma}\right\}\right), \tag{16}$$

where $\theta^1, \ldots, \theta^{2\sigma}$ are the vertices of the Θ, and σ is known and determined by matrix P.

Due to the symmetry of the set Θ, there is $\theta^{j+\sigma} = -\theta^j$, for $j = 1, \ldots, \sigma$. And by using (13), the state constraints are rewritten in θ state-space as follows

$$\begin{aligned} HW\theta \leq \mathbf{1}_{n_x}, \forall \theta \in \Theta \Leftrightarrow \\ -\mathbf{1}_{n_x} \leq HW\theta^j \leq \mathbf{1}_{n_x}, j = 1, \ldots, \sigma. \end{aligned} \tag{17}$$

With (13), system (9) can be expressed as:

$$W\theta^+ = AW\theta + w, \tag{18}$$

where $A \in \mathcal{A}$, $w \in \mathcal{W}$.

Two equivalent invariance conditions for system (18) in the θ state space are shown below.

Lemma 3 ([14]): For system (18), where the set Θ in (15) is RPI set, then the following two conditions are equivalent:

(i) for all $\theta \in \Theta$, $\forall w \in \mathcal{W}$ and $\forall A \in \mathcal{A}$,

$$\theta^+ = \left(W^{-1}AW\theta + W^{-1}w\right) \in \Theta \tag{19}$$

(ii) for each vertex θ^j, $j = 1, \ldots, 2\sigma$ of the set Θ, $\forall w \in \mathcal{W}$ and $\forall A \in \mathcal{A}$,

$$\left(\theta^j\right)^+ = \left(W^{-1}AW\theta^j + W^{-1}w\right) \in \Theta \tag{20}$$

2.3. Maximize the volume of the RPI set

In this section, we propose data-driven sufficient LMI conditions for computing the matrix W, ensuring that the set Θ remains invariant.

First, we will consider condition (19) for RPI of the set Θ. Applying (1b), system (18) can be further written as follows:

$$W\theta^+ = \underbrace{\left((W\theta)^T \otimes I_n\right)}_{g(W,\theta)} \vec{A} + w. \tag{21}$$

To achieve fewer conservative LMI conditions, the variables $V_i \in R^{n\times n}$ are introduced and signals $\xi_i = V_i^{-1}W(\theta)^+$, for $i = 1, \ldots, n_p$. The dynamics (21) can then be expressed as follows

$$g(W,\theta)\vec{A} + w - V_i\xi_i = \mathbf{0}. \tag{22}$$

From (15), the invariance condition (19) is given as follows: for all $\theta \in \Theta$,

$$1 - (e_i^T P\theta^+)^2 \geq 0, \forall w \in \mathcal{W}, \forall A \in \mathcal{A}, \tag{23}$$

where e_i is the identity matrix I_{n_p}'s i-th column vector. By using $\xi_i = V_i^{-1}W(\theta)^+$, (23) can be written as follows

$$1 - (e_i^T PW^{-1}V_i\xi_i)^2 \geq 0, \forall w \in \mathcal{W}, \forall A \in \mathcal{A}. \tag{24}$$

We multiply (24) by positive scalar variable $\phi_i > 0$ and lower bound it by terms that are known to be non-negative (S-procedure[15]). This gives

$$\begin{aligned} \phi_i(1 - (e_i^T PW^{-1}V_i\xi_i)^2) \geq\ & \underbrace{2\xi_i^T(g(W,\theta)\vec{A} + w - V_i\xi_i)}_{0} \\ & + \underbrace{((\mathbf{1}+d) - Z\vec{A})^T\Lambda_i((\mathbf{1}+d) + Z\vec{A})}_{\geq 0} \\ & + \underbrace{(\mathbf{1} + Dw)^T\Gamma_i(\mathbf{1} - Dw)}_{\geq 0} \end{aligned} \tag{25}$$

where $\Lambda_i \in D_+^{Tn_w}, \Gamma_i \in D_+^{n_w}$. In this way, we get the sufficient condition of (23), i.e., (25).

Through (22), (4), and (7), it can be proved that the right side of (25) is non-negative for all $w \in \mathcal{W}$, for all $A \in \mathcal{A}$. After that, (25) can be rewritten as the following quadratic form:

$$\mathbf{y}^T T_i(W, \phi_i, \Gamma_i, \Lambda_i, V_i)\mathbf{y} \geq 0, \forall \mathbf{y}, \tag{26}$$

where $\mathbf{y} = [1 \ \vec{A}^T \ w^T \ -\xi_i^T]^T$ and matrix T_i is symmetrical. The invariance condition holds, if $T_i \geq 0$; i.e.,

$$T_i \triangleq \begin{bmatrix} r_i & -d^T\Lambda_i Z & \mathbf{0} & \mathbf{0} \\ * & Z^T\Lambda_i Z & 0 & g^T(W,\theta) \\ * & * & D^T\Gamma_i D & I_n \\ * & * & * & V_i + V_i^T - V_i^T L_i V_i \end{bmatrix} \geq 0, \tag{27}$$

where $L_i \triangleq \phi_i W^{-T} P^T e_i e_i^T P W^{-1}$, $r_i \triangleq \phi_i - \mathbf{1}^T\Lambda_i\mathbf{1} - \mathbf{1}_{n_w}^T\Gamma_i\mathbf{1}_{n_w} + d^T\Lambda_i d$ and $g(W,\theta)$ is as defined in (21). Take note of the nonlinearity of the block(2,4) in (27) and the nonlinear dependence of the block(4,4) on ϕ_i, V_i and W in (27), which will be resolved by introducing new matrix variables and appropriate scaling.

Theorem 1: Given the matrices X, X^+ and P, if there exists $W \in R^{n\times n}$, $W_1 \in R^n$ and variables $\phi_i \in R_+$, $\Lambda_i \in D_+^{Tn_w}, \Gamma_i \in D_+^{n_w}$, $X_i, V_i \in R^{n\times n}$ that satisfy LMIs for $i = 1, \ldots n_p$,

$$\begin{bmatrix} W + W^T - X_i & r_i P^T e_i \\ r_i e_i^T P & r_i \end{bmatrix} \geq 0, \tag{28}$$

$$\begin{bmatrix} r_i & -d^T\Lambda_i Z & \mathbf{0} & \mathbf{0} & \mathbf{0} \\ * & Z^T\Lambda_i Z & 0 & g^T(W_1) & \mathbf{0} \\ * & * & D^T\Gamma_i D & I_n & \mathbf{0} \\ * & * & * & V_i + V_i^T & V_i^T \\ * & * & * & * & X_i \end{bmatrix} \geq 0, \tag{29}$$

where

$$g(W_1) \triangleq (W_1)^T \otimes I_n \in R^{n\times n^2}, \tag{30a}$$

$$W_1 \triangleq W\theta, \tag{30b}$$

$$r_i \triangleq \phi_i - \mathbf{1}^T\Lambda_i\mathbf{1} - \mathbf{1}_{n_w}^T\Gamma_i\mathbf{1}_{n_w} + d^T\Gamma_i d \in R, \tag{30c}$$

then the set $\mathcal{P}$ in (14) is RPI.

proof:

In order to resolve the nonlinearity in the block (2,4) of (27), let us introduce a new matrix variable $W_1 = W\theta$ such that $g(W_1)$ is linear.

First, let us prove the LMI condition (28) stated in Theorem 1. Introduce the positive-definite matrix variable X_i that satisfies

$$X_i^{-1} - L_i \succ 0 \Leftrightarrow X_i^{-1} - \phi_i W^{-T} P^T e_i e_i^T P W^{-1} \succ 0. \tag{31}$$

Applying Lemma 2 to (31), we obtain

$$\begin{bmatrix} X_i^{-1} & \phi_i W^{-T} P^T e_i \\ \phi_i e_i^T P W^{-1} & \phi_i \end{bmatrix} \succ 0, \tag{32}$$

By applying congruence transformation to (32) using the congruence transformation matrix $diag\{W, I_n\}$ which is full rank real matrix, then we get

$$\begin{bmatrix} W^T X_i^{-1} W & \phi_i P^T e_i \\ \phi_i e_i^T P & \phi_i \end{bmatrix} \succ 0. \tag{33}$$

To address the nonlinearity in the block (1,1) of (33), we perform the following steps:

$$\begin{aligned} W^T X_i^{-1} W &= (W - X_i)^T X_i^{-1} (W - X_i) \\ &\quad + W + W^T - X_i \\ &\geq W + W^T - X_i, \end{aligned} \tag{34}$$

then the $W^T X_i^{-1} W$ in (33) can be replaced by $W + W^T - X_i$, and we obtain a sufficient LMI condition for (33) as given in (28).

Next, let us prove the LMI condition (29) stated in Theorem 1. From (31), the condition (27) can be rewritten as

$$\begin{bmatrix} r_i & -d^T \Lambda_i Z & \mathbf{0} & \mathbf{0} \\ * & Z^T \Lambda_i Z & 0 & g^T(W_1) \\ * & * & D^T \Gamma_i D & I_n \\ * & * & * & V_i + V_i^T - V_i^T X_i^{-1} V_i \end{bmatrix} \geq 0, \tag{35}$$

then using the Schur complement, we obtain (29).

Considering the condition (20) of the robust invariance of the set Θ, the following Theorem 2 can be obtained.

Theorem 2 ([14]): Given the matrices X, X^+ and P, if there exists $W \in R^{n \times n}$ and variables $\phi_{ij} \in R_+$, $\Lambda_{ij} \in D_+^{Tn_w}$, $\Gamma_{ij} \in D_+^{n_w}$, $X_{ij}, V_{ij} \in R^{n \times n}$ that satisfy LMIs for $i = 1, \ldots n_p$ and $j = 1, \ldots 2\sigma$,

$$\begin{bmatrix} W + W^T - X_{ij} & r_{ij} P^T e_i \\ r_{ij} e_i^T P & r_{ij} \end{bmatrix} \geq 0, \tag{36}$$

$$\begin{bmatrix} r_{ij} & -d^T \Lambda_{ij} Z & \mathbf{0} & \mathbf{0} & \mathbf{0} \\ * & Z^T \Lambda_{ij} Z & 0 & g^T(W, \theta^j) & \mathbf{0} \\ * & * & D^T \Gamma_{ij} D & I_n & \mathbf{0} \\ * & * & * & V_{ij} + V_{ij}^T & V_{ij}^T \\ * & * & * & * & X_{ij} \end{bmatrix} \geq 0, \tag{37}$$

where,

$$g(W, \theta^j) \triangleq \left(W \theta^j\right)^T \otimes I_n \in R^{n \times n^2}, \tag{38a}$$

$$r_{ij} \triangleq \phi_{ij} - \mathbf{1}^T \Lambda_{ij} \mathbf{1} - \mathbf{1}_{n_w}^T \Gamma_{ij} \mathbf{1}_{n_w} + d^T \Gamma_{ij} d \in R, \tag{38b}$$

then the set $\mathcal{P}$ in (14) is RPI.

We aim to identify the largest set $\mathcal{P}$in (14) that satisfies the state constraints outlined in (4a) and the sufficient conditions for invariance specified in (28) and (29) (or alternatively, (36) and (37)). Given a matrix P, it is

Algorithm 1 Computing RPI set.

Input: F,D,P;
Output: Optimal values for $\mathbf{W}, \mathbf{X_i}$;
Objective function $\underset{Z_{SDP}}{max} \quad log\ det(W)$
Optimization variables $Z_{SDP} \triangleq (W, W_1, X_i, V_i, \phi_i, \Lambda_i, \Gamma_i)$
Symmetry constraint $W = W'$ (in order for the objective function to be concave)
State constraints (17)
Invariance conditions (28), (29)

Algorithm 2 Computing RPI set.

Input: F,D,P;
Output: Optimal values for $\mathbf{W}, \mathbf{X_{ij}}$;
Objective function $\underset{Z_{SDP}}{max} \quad log\ det(W)$
Optimization variables $Z_{SDP} \triangleq (W, X_{ij}, V_{ij}, \phi_{ij}, \Lambda_{ij}, \Gamma_{ij})$
Symmetry constraint $W = W'$ (in order for the objective function to be concave)
State constraints (17)
Invariance conditions (36), (37)

known that the volume of P is proportional to its determinant, denoted as $|det(W)|$[19]. Consequently, we can determine the largest set P by formulating a SDP problem. Algorithms 1 and 2 based on the one-step method are given below.

Therefore, in order to obtain the desired large volume of RPI sets, we need to solve the determinant maximization problem under LMI conditions. However, this problem is easy to solve only if W is symmetric[20]. The symmetry of W would introduce conservatism[21]; thus, we introduce an iterative algorithm based on Algorithm 1. In an iterative algorithm, W does not need to maintain symmetry, and the algorithm also reduces the conservatism caused by the introduction of (34)[19]. At the k-th iteration, let W_k and X_{ik} be the values of the variables W, X_i. At each subsequent iteration, the volume of the RPI set increases, i.e., $|det(W_{k+1})| \geq |det(W_k)|$, if the following LMI condition is imposed,

$$W^T W_k + W_k^T W - W_k^T W_k \geq Z > 0, \tag{39}$$

where $Z = Z^T \in R^{n \times n}$ is the new matrix variable.

From[22], we get

$$\begin{aligned}(W - X_i Z_{ik})^T X_i^{-1} (W - X_i Z_{ik}) = W^T X_i^{-1} W \\ -W^T Z_{ik} - Z_{ik}^T W + Z_{ik}^T X_i Z_{ik} \geq 0,\end{aligned} \tag{40}$$

thus we can obtain:

$$W^T X_i^{-1} W \geq W^T Z_{ik} + Z_{ik}^T W - Z_{ik}^T X_i Z_{ik}, \tag{41}$$

where $Z_{ik} \triangleq X_{ik}^{-1} W_k$, and then the linear term to the right of (41) can be used to substitute for the nonlinear term $W^T X_i^{-1} W$ in (29). From (41), the condition (28) can be rewritten as follows,

$$\begin{bmatrix} W^T Z_{ik} + Z_{ik}^T W - Z_{ik}^T X_i Z_{ik} & r_i P^T e_i \\ r_i e_i^T P & \phi_i \end{bmatrix} \geq 0. \tag{42}$$

Therefore, we can obtain the following iterative algorithm based on Algorithm 1:

iterative algorithm Computing RPI set.

Input: F,D,P,W^q, X_i^q;
Output: Optimal values for **W**;
Objective function $\max_{Z_{SDP}} \quad log\ det(Z)$
Optimization variables $Z_{SDP} \triangleq (W, X_i, V_i, \phi_i, \Lambda_i, \Gamma_i, Z)$
State constraints (17)
Invariance conditions (28), (42)

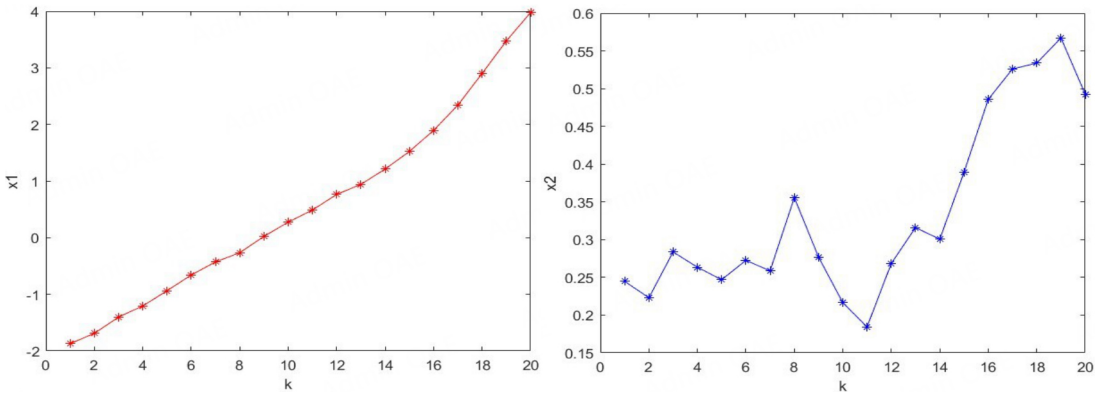


Figure 1. The data samples collected from the liner discrete-time system (43).

Remark 2: Algorithm 2 has $10\sigma n_p + 1$ optimization variables, the invariance conditions (36), (37) consist of $2\sigma n_p$ linear matrix inequalities respectively. The iterative algorithm has $5n_p + 2$ optimization variables; the invariance conditions (28), (42) consist of n_p linear matrix inequalities respectively. This suggests that both the iterative algorithm has fewer optimization variables and fewer LMIs for invariant conditions than Algorithm 2. In addition, Algorithm 1 is more conservative than iterative algorithm (see Example 2).

3. RESULTS

The algorithms in the experiments are implemented in Matlab by using CVX[23] and solver SeDuMi. And the MPT toolbox is used to manage polytopes[24]. The following liner discrete-time system is considered:

$$x(k+1) = \underbrace{\begin{bmatrix} 1 & 1 \\ 0 & 1 \end{bmatrix}}_{A} x(k) + w(k). \tag{43}$$

The matrice A is unknown, but it is only used to gather data. $T = 20$ samples of data are collected by system (43), as shown in Figure 1. Assume the disturbance w in system (43) ranges between -0.1 and 0.1, with the state constraints being $(x_1, x_2) \in [-2, 2] \times [-2, 2]$.

Example 1: By taking different matrices P, the complexity of the RPI set is denoted as $n_p = 2, 3, 4$ respectively, and the corresponding matrices are computed as follows

Table 1. $|det(W)|$ **(Algorithm 1)** $vs.$ **complexity of the matrix** P

complexity	$n_p = 2$	$n_p = 3$	$n_p = 4$
$\lvert det(W)\rvert$	3.5	384.0	8001.2

$$P_2 = \begin{bmatrix} 1 & 0 \\ 0 & 1 \end{bmatrix}, P_3 = \begin{bmatrix} 10 & 10 \\ 10 & 0 \\ 1 & 11 \end{bmatrix}, P_4 = \begin{bmatrix} -18 & -55 \\ 18 & 55 \\ 55 & -18 \\ 55 & 18 \end{bmatrix}.$$

The matrice W is computed by running Algorithms 1 and 2 as follows:

$$W_{21} = \begin{bmatrix} 3.5 & 0 \\ 0 & 1 \end{bmatrix} \text{(Algorithm 1, 2.039 s)}, W_{22} = \begin{bmatrix} 3.5 & 0 \\ 0 & 1 \end{bmatrix} \text{(Algorithm 2, 2.770 s)},$$

$$W_{31} = \begin{bmatrix} 35 & 1 \\ 1 & 11 \end{bmatrix} \text{(Algorithm 1, 2.418 s)}, W_{32} = \begin{bmatrix} 35 & 1 \\ 1 & 11 \end{bmatrix} \text{(Algorithm 2, 4.552 s)},$$

$$W_{41} = \begin{bmatrix} 151.4106 & 18.1135 \\ 18.1135 & 55.0114 \end{bmatrix} \text{(Algorithm 1, 2.410 s)}, W_{42} = \begin{bmatrix} 151.4106 & 18.1135 \\ 18.1135 & 55.0114 \end{bmatrix} \text{(Algorithm 2, 4.725 s)},$$

where W_{21} and W_{22} are obtained from P_2; W_{31} and W_{32} are obtained by taking P_3; W_{41} and W_{42} are obtained by taking P_4.

It is discovered from experiment results that while Algorithm 2 yields the same results, Algorithm 1 runs faster and requires fewer optimization variables (see Remark 2) than Algorithm 2.

Example 2: The RPI sets with complexities $n_p = 2, 3, 4$ (i.e., P_2, P_3, P_4 are selected respectively) which are obtained by Algorithm 1 are as follows

$$W_2 = \begin{bmatrix} 3.5 & 0 \\ 0 & 1 \end{bmatrix}, W_3 = \begin{bmatrix} 35 & 1 \\ 1 & 11 \end{bmatrix}, W_4 = \begin{bmatrix} 151.4106 & 18.1135 \\ 18.1135 & 55.0114 \end{bmatrix}.$$

The corresponding RPI sets obtained by Algorithm 1 are shown in Figure 2.

After five times iterations of the iterative algorithm, the RPI sets $\mathcal{P}$ with complexities $n_p = 2, 3, 4$ are obtained as

$$W_2 = \begin{bmatrix} 3.5 & 0 \\ 0 & 1 \end{bmatrix}, W_3 = \begin{bmatrix} 35 & 1 \\ 1 & 11 \end{bmatrix}, W_4 = \begin{bmatrix} 192.5402 & -63.3969 \\ 18.1136 & 55.0115 \end{bmatrix}.$$

The corresponding RPI sets obtained by iterative algorithm are shown in Figure 3.

We find that the volume of RPI sets obtained by the iterative algorithm is larger than that obtained by Algorithm 1 (see Table 1 and Table 2), which indicates that Algorithm 1 is more conservative than the iterative algorithm. For the given matrix P, the volume of $\mathcal{P}$ is proportional to the determinant $|det(W)|$ [19]. And as n_p rises, the absolute value of the determinant of W grows; thus, the volume of the RPI set increases (see Table 1 and Figure 4), so that an invariant set with a higher volume can be obtained by adding n_p as a parameter.

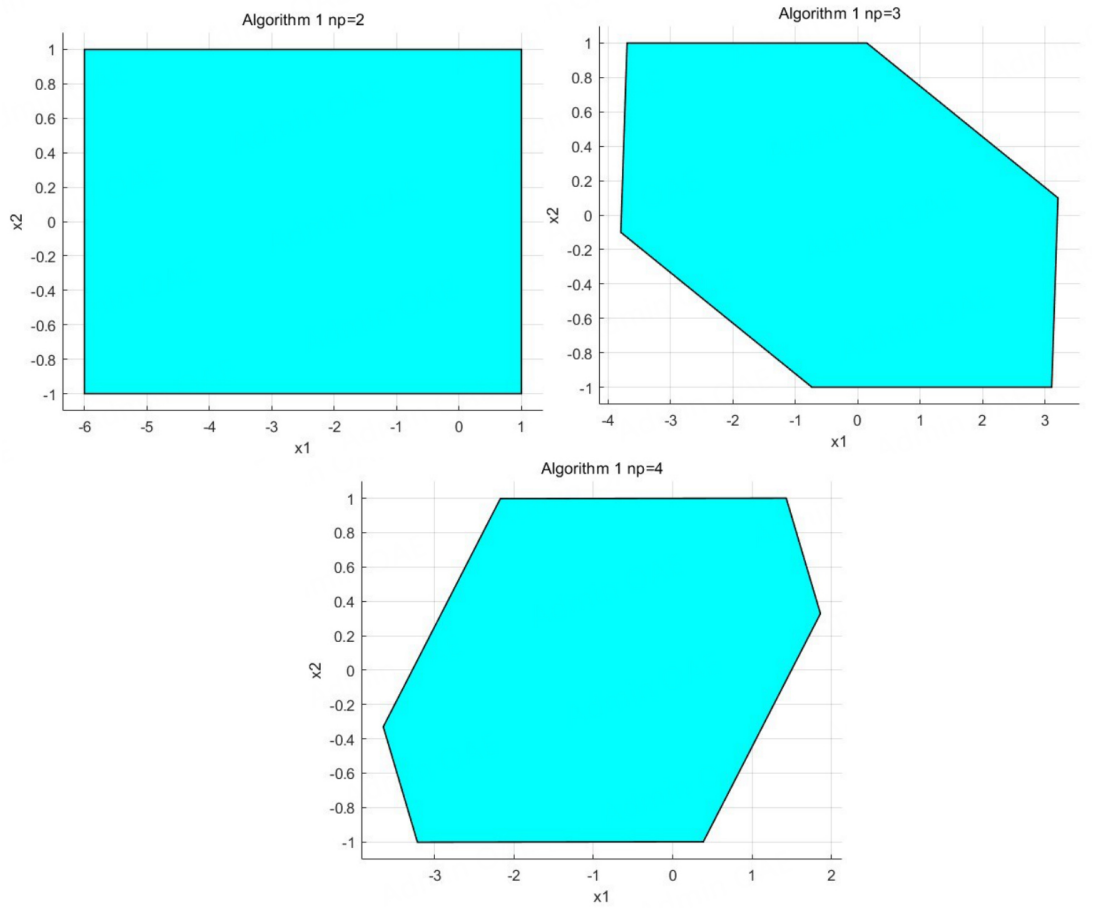


Figure 2. Maximum volume RPI sets $\mathcal{P}$ with different complexities: n_p = 2 (left), n_p = 3 (right), n_p = 4 (bottom).

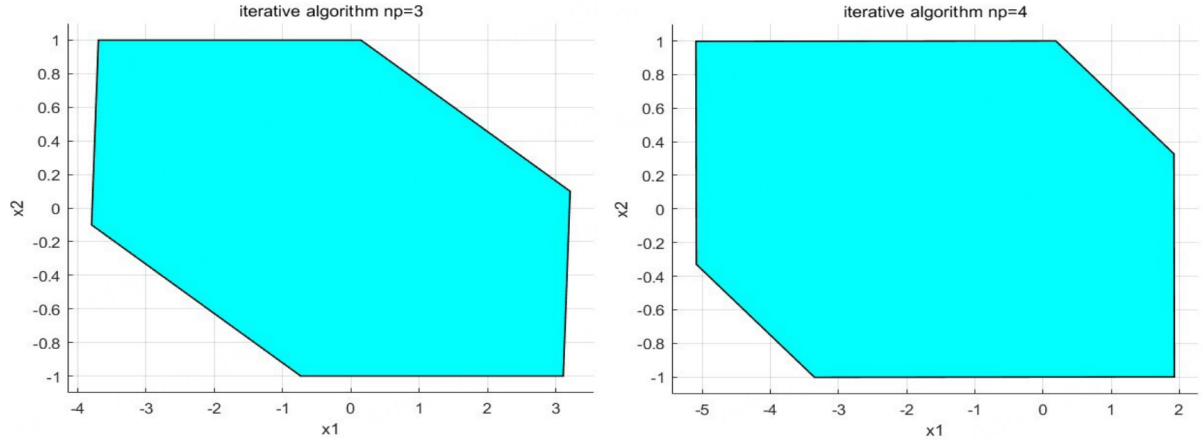


Figure 3. Maximum volume RPI sets $\mathcal{P}$ with different complexities: n_p = 3 (left), n_p = 4 (right).

Table 2. $|det(W)|$ **(iterative algorithm)** $vs.$ **complexity of the matrix** P

complexity	$n_p = 2$	$n_p = 3$	$n_p = 4$
$\lvert det(W)\rvert$	3.5	385.0	11740.3

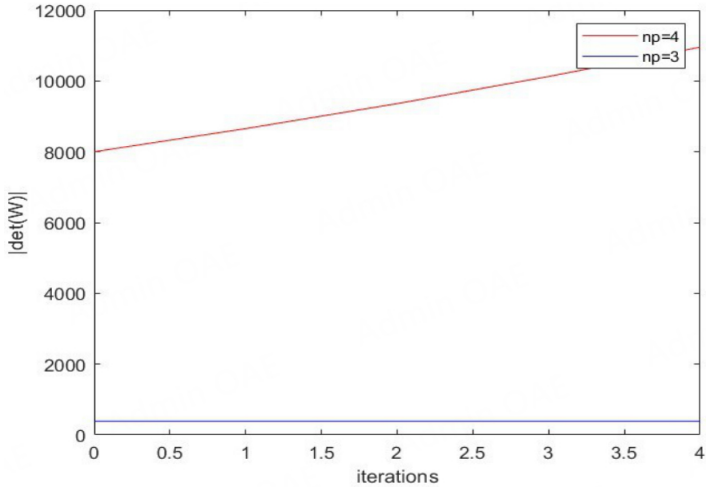


Figure 4. $|det(W)|$ *vs*. iterations of iterative algorithm.

4. DISCUSSION

A direct data-driven method is proposed to calculate the robust positive invariant (RPI) sets for discrete-time systems. To further reduce conservatism, an iterative algorithm based on Algorithm 1 is introduced. This approach does not require prior knowledge of the model or system identification. Future research could extend this methodology to nonlinear systems. Additionally, while the RPI sets discussed here are symmetric, the exploration of asymmetric RPI sets is another potential area for investigation.

5. CONCLUSIONS

This paper proposes a direct data-driven method to calculate RPI sets for discrete-time systems by deriving a set of invariance conditions expressed as linear matrix inequalities (LMIs). Subsequently, we maximize the volume of the invariant set using a SDP problem. We have developed two one-step algorithms based on LMIs to compute the RPI sets; experimental results indicate that Algorithm 1 requires fewer optimization variables compared to Algorithm 2 and demonstrates superior computational efficiency. Additionally, we have introduced an iterative approach based on Algorithm 1 to further reduce conservatism. Numerical examples have verified the effectiveness of the proposed algorithm.

DECLARATIONS

Acknowledgments

We would like to express our great appreciation to the editors and reviewers.

Authors' contributions

Conceptualization, methodology, resources, supervision: Yang H
Software, validation, writing - original draft preparation: Du Q
Formal analysis, investigation, writing - review and editing, visualization: Yang H, Du Q
All authors have read and agreed to the published version of the manuscript.

Availability of data and materials

The data cannot be shared publicly as the partner (company) does not permit public disclosure. It is available from the corresponding author upon reasonable request.

Financial support and sponsorship

None.

Conflicts of interest

Both authors declared that there are no conflicts of interest.

Ethical approval and consent to participate

Not applicable.

Consent for publication

Not applicable.

Copyright

© The Author(s) 2024.

REFERENCES

1. Blanchini F, Miani S. Set-theoretic methods in control, 3th ed. Springer, 2008. Available from: https://link.springer.com/book/10.1007/978-3-319-17933-9 [Last accessed on 28 Nov 2024].
2. Castelan EB, Tarbouriech S. Positively invariant polyhedral sets for discrete-time singular systems with additive perturbations. In Proceedings of the 35th IEEE Conference on Decision and Control; 13 December 1996; Kobe, Japan. DOI
3. Blanchini F. Set invariance in control. *Automatica* 1999;35:1747-67. DOI
4. Kolmanovsky I, Gilbert EG. Theory and computation of disturbance invariant sets for discrete-time linear systems. *Math Probl Eng* 1998;4:317-67. DOI
5. Raković SV, Kerrigan EC, Mayne DQ, Kouramas KI. Optimized robust control invariance for linear discrete-time systems: theoretical foundations. *Math Probl Eng* 2007;43:831-41. DOI
6. Wang P, Feng X, Li W. Design of robust positively invariant set for nonholonomic vehicle. In Proceedings of the 2016 Chinese Control and Decision Conference (CCDC); 28-30 May 2016; Yinchuan, China. DOI
7. Esterhuizen W, Aschenbruck T, Streif S. On maximal robust positively invariant sets in constrained nonlinear systems. *Automatica* 2020;119:109044. DOI
8. Rakovic SV, Kerrigan EC, Kouramas K, Mayne DQ. Invariant approximations of the minimal robust positively invariant set. *IEEE Trans Automat Contr* 2005;50:406-10. DOI
9. Trodden P. A one-step approach to computing a polytopic robust positively invariant set. *IEEE Trans Automat Contr* 2016;61:4100-5. DOI
10. Xue B, Zhan N. Robust invariant sets computation for discrete-time perturbed nonlinear systems. *IEEE Trans Automat Contr* 2022;67:1053-60. DOI
11. Hou ZS, Wang Z. From model-based control to data-driven control: survey, classification and perspective. *Inf Sci* 2013;235:3-35 DOI
12. Zhong B, Zamani M, Caccamo M. Synthesizing safety controllers for uncertain linear systems: a direct data-driven approach. In Proceedings of the 35th IEEE Conference on Decision and Control; 23-25 August 2020; Trieste, Italy. DOI
13. Bisoffi A, De Persis C, Tesi P. Data-based guarantees of set invariance properties. *IFAC-PapersOnLine* 2020;53:3953-8 DOI
14. Mejari M, Gupta A. Direct data-driven computation of polytopic robust control invariant sets and state-feedback controllers. In Proceedings of the 62nd IEEE Conf. on Decision and Control (CDC); 13-15 December 2023; Singapore, Singapore. DOI
15. Scherer CW. A full block S-procedure with applications. In Proceedings of the 36th IEEE Conf. on Decision and Control; 12 December 1997; San Diego, CA, USA. DOI
16. Abadir KM, Magnus JR. Matrix algebra, 3th ed. Cambridge University Press; 2005. DOI
17. Cottle RW. Manifestations of the Schur complement. *Linear Algebra Appl* 1974;8:189-211. DOI
18. Willems JC, Markovsky I, Rapisarda P, De Moor BLM. A note on persistency of excitation. *Syst Control Lett* 2005;54:325-9. DOI
19. Gupta A, Köroğlu H, Falcone P. Computation of robust control invariant sets with predefined complexity for uncertain systems. *Intl J Robust Nonlinear* 2021;31:1674-88. DOI
20. Vandenberghe L, Boyd S, Wu SP. Determinant maximization with linear matrix inequality constraints. *SIAM J Matrix Anal Appl* 1998;19:499-533. DOI
21. Gupta A, Köroğlu H, Falcone P. Restricted-complexity characterization of control-invariant domains with application to lateral vehicle dynamics control. In Proceedings of the 2017 IEEE 56th Annual Conference on Decision and Control (CDC); 12-15 December 2017; Melbourne, VIC, Australia. DOI
22. Gupta A, Köroğlu H, Falcone P. Computation of low-complexity control-invariant sets for systems with uncertain parameter dependence. *Automatica* 2019;101:330-7. DOI
23. CVX: matlab software for disciplined convex programming; 2020. Available from: http://cvxr.com/cvx [Last accessed on 28 Nov 2024].
24. Herceg M, Kvasnica M, Jones CN, Morari M. Multi-parametric toolbox 3.0. In Proceedings of the 2013 European Control Conference (ECC); 17-19 July 2013; Zurich, Switzerland. DOI

Chen *et al*. *Complex Eng Syst* 2024;4:25
DOI: 10.20517/ces.2024.69

Complex Engineering Systems

Review

Open Access

Autonomous vehicles in mixed-autonomy traffic: game theoretic human-like decision making countermeasures

Qitong Chen[1], Dong Zhao[1], Congzhi Liu[2], Meng Yang[3], Yehui Shi[3]

[1]The School of Technology, Beijing Forestry University, Beijing 100083, China.
[2]The State Key Laboratory of Mechanical Transmission, College of Mechanical and Vehicle Engineering, Chongqing University, Chongqing 400044, China.
[3]Zhiyuan Laboratory, Hangzhou 310020, Zhejiang, China.

Correspondence to: Prof. Congzhi Liu, The State Key Laboratory of Mechanical Transmission, College of Mechanical and Vehicle Engineering, Chongqing University, 174 Shazheng Street, Chongqing 400044, China. E-mail: 15281063684@163.com; ORCID: 0000-0002-2977-1365

How to cite this article: Chen Q, Zhao D, Liu C, Yang M, Shi Y. Autonomous vehicles in mixed-autonomy traffic: game theoretic human-like decision making countermeasures. *Complex Eng Syst* 2024;4:25. http://dx.doi.org/10.20517/ces.2024.69

Received: 9 Oct 2024 **First Decision:** 21 Nov 2024 **Revised:** 13 Dec 2024 **Accepted:** 23 Dec 2024 **Published:** 30 Dec 2024

Academic Editor: Zhaojing Wu **Copy Editor:** Fangling Lan **Production Editor:** Fangling Lan

Abstract

Human-like decision-making plays a pivotal role in enhancing the human-likeness of autonomous vehicles and ensuring seamless blending into human-driven vehicles-dominated traffic. Due to the ability to capture the interaction between drivers, it has great potential to apply game theory in the development of human-like decision-making algorithms. However, there are few reviews that systematically focused on the human-like decision-making strategy based on game theory. To this end, this paper is targeted to present a comprehensive and up-to-date summary of game theoretic human-like decision-making methods for autonomous vehicles in mixed-autonomy traffic by reviewing cutting-edge research conducted for various scenarios. The questions discussed in this article include: (1) What are the implications of social interactions for human-like decision-making development; and (2) How to establish the human-like decision-making algorithm with game theory, satisfying personalized requirements and coping with the uncertainty and randomness of complex traffic environment. To provide sound answers, the pivotal factors influencing decision performance are concluded based on the existing social interaction research and human-like decision methods. Through a comprehensive analysis, the development framework of the human-like game theoretic algorithm is proposed. Finally, the critical academic issues are concluded for indicating the future research directions.

Keywords: Mixed autonomy, social interaction, game theoretic scheme, human-like decision-making, socially compatible

© The Author(s) 2024. **Open Access** This article is licensed under a Creative Commons Attribution 4.0 International License (https://creativecommons.org/licenses/by/4.0/), which permits unrestricted use, sharing, adaptation, distribution and reproduction in any medium or format, for any purpose, even commercially, as long as you give appropriate credit to the original author(s) and the source, provide a link to the Creative Commons license, and indicate if changes were made.

1. INTRODUCTION

Statistics about traffic safety have indicated that 94% of crashes are provoked by human errors, for example, inattention, distractions, and decision errors[1]. With the rapid development of vehicle automation, autonomous vehicles (AVs) have shown great promise to eliminate human error-induced accidents due to accurate and timely execution, further improving traffic safety[2]. However, before fully automated driving becomes widespread, AVs will blend into roads populated with human-driven vehicles (HDVs) in the near future which results in a mixed-autonomy traffic context. Similar to HDV-HDV social interaction, AVs will interact with surrounding vehicles (SVs), either AVs or HDVs, forming different configurations. AV-HDV interaction is more complex owing to human uncertainty. Also, driven by the personalized needs of passengers, human-like decision-making considering social interaction is proposed to enable AVs to make more informed and human-like decisions. However, humans, vehicles, and traffic environments are closely intertwined in reality which makes social interaction exhibit dynamicity and continuity, uncertainty and variability, interdependence and mutual influence. Thus, qualitatively understanding the social interaction mechanism and evolution law contributes to developing high-fidelity interactive models and making human-like decisions. Based on the interaction mechanism, how to develop a human-like decision-making algorithm is the core problem discussed in this paper. Human-like decision-making algorithms are supposed to be equipped with at least one of the following characteristics: (1) scene adaptation; (2) personalized adjustment; (3) decision interpretability; and (4) reasoning and learning abilities[2]. Additionally, the close linkage nature increases the computational complexity, which poses a new challenge to the real-time performance of the decision-making algorithm. Achieving real-time receding horizon optimization and adjustment is pivotal to ensuring safe driving.

Game theory, possessing an inherent ability to analyze decision dependence among entities, has exhibited a superior understanding of complex interactive decisions and uncertain behaviors. Motivated by this, it has been widely introduced into the transportation field to tackle conflict or coordination problems[3,4]. Article[5] reviewed the use of game theory for autonomous system decisions from a risk perspective, but lacked a specific approach to self-driving vehicles. In contrast, reviews[6,7] concluded applications of game theory in transportation for security assessment and traffic congestion resolution, respectively. In recent years, game theory has been adopted to develop AVs' decision-making algorithms, aiming to mimic the dynamic and interactive decision-making process of human drivers. In this sense, game theoretic decision methods hold significant potential for augmenting the social decision-making prowess of AVs, and further facilitating a seamless blending of AVs into the HDV-populated traffic. It should be noted that the interactive vehicles are referred to as "agents" or "players" in the game theoretic framework, which is applicable in this paper. Di and Shi[8] overviewed the effective control models from artificial intelligence in the domain of transportation engineering in the era of mixed autonomy, but did not give a systematic discussion of game-based control. The ref.[9] reviews the game theory-based methods for modeling driver behavior, but focuses only on the lane-changing (LC) process and does not investigate the decision-making methods in more complex scenarios, such as roundabouts and unsignalized intersections. The ref.[10] reviewed the game theoretic models for explaining road user behavior, but neglected the influence of heterogeneous factors, such as gender, age and experience, on different driving behaviors. However, the application of the models in multi-vehicles and their scalability in other scenarios are limited. While they address the issues outlined in the abstract, they fail to account for the dynamics and uncertainty of interactions. Moreover, real-time solutions are not discussed. In practice, AVs are expected to make distinguished behavior responses to HDVs with diverse driving characteristics. The fast and accurate recognition of the driving characteristics of the interactive objects is also a significant component of human-like decision-making strategies.

In conclusion, given the complexity of AV-HDV interaction, it is expected that AVs will be equipped with well-designed human-like decision-making strategies with adaptation and learning capabilities. Hence, this paper reviews and analyzes the latest research in the field of game theoretic decision-making of AVs. Particularly, we

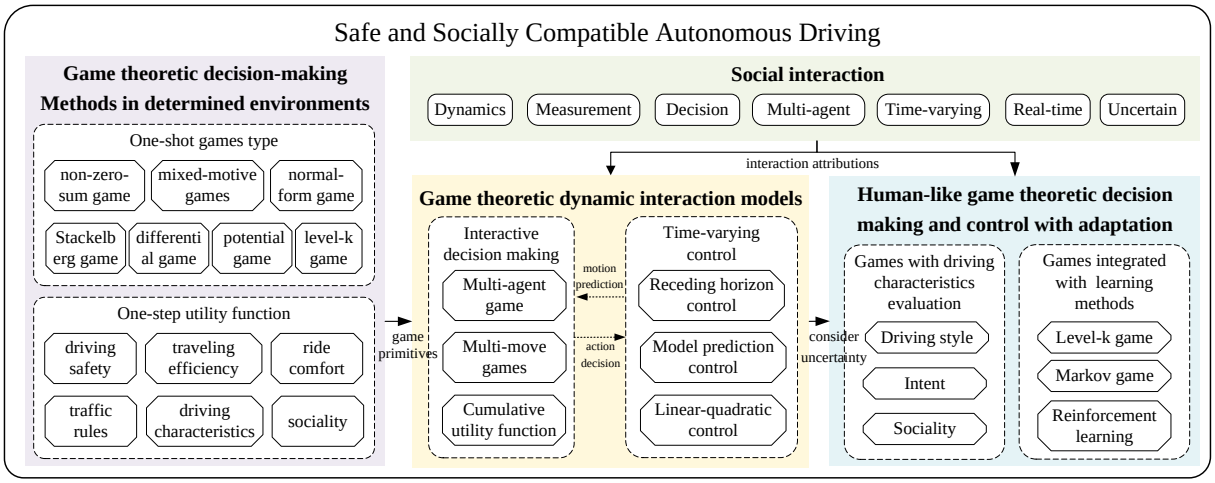


Figure 1. Paper framework.

explore game theory-based human-like methods considering the dynamic and uncertain interaction among on-road vehicles including AVs and/or HDVs. The human-like decision strategy could be broken down into two main components: social interaction understanding and game theoretic interaction modeling. These components give rise to two critical questions: The first is what the implications of social interactions are for the development of human-like decision-making. The second concerns how to establish a human-like decision-making algorithm with game theory, satisfying personalized requirements and coping with the uncertainty and randomness of complex traffic environments. The contributions of this paper lie in twofold: (1) With a view to AV-HV interaction in mixed-autonomy traffic, we comprehensively review the game theoretic human-like decision-making methods, presenting the results of this review and future research directions; and (2) The influencing factors considered in game theoretic decision-making methods are summarized systematically.

To provide more reasoned answers to these questions, we review the status quo of related studies according to the logic structure shown in Figure 1. Firstly, we investigate the existing definitions of social interaction and explore its intrinsic properties in section 2. Building upon these attributions, pivotal factors affecting the human-like performance of the AV decision-making algorithm are analyzed and summarized in section 3. Then, starting with the definition of deterministic environment, section 4 discusses the game theoretic decision-making algorithms in deterministic environments including the existing design methods of utility function. The overview of game theoretic decision frameworks in deterministic environments provides fundamental knowledge for the development of more complex interactive decision strategies. section 5 covers state-of-the-art dynamic game theoretic techniques used for dynamic interaction modeling and the integrated methods of decision making and control considering time-varying characteristics in dynamic interaction scenarios. In section 6, we review human-like decision-making and control methods with adaptation, such as those employing Markov or level-k games and reinforcement learning (RL), along with estimation methods of incomplete information such as driving style, driving intentions, and social factors. Finally, in section 7, we conclude by summarizing the challenges and insights from existing human-like game theoretic decision and control methods, and suggest future research directions.

2. DEFINITION AND ATTRIBUTES OF SOCIAL INTERACTION IN ROAD TRAFFIC

Human driving behaviors generally involve both social interactions among drivers and their physical interactions with the driving environment[11]. Rational human drivers can make socially compatible decisions in dynamically complex scenes by performing efficient negotiation with their neighbors using non-linguistic communications such as gesture language (e.g., waving hands to the other car to give way), deictics (e.g., using turn signals to indicate intentions), and motion cues (e.g., accelerating/decelerating/turning)[12]. Due to the

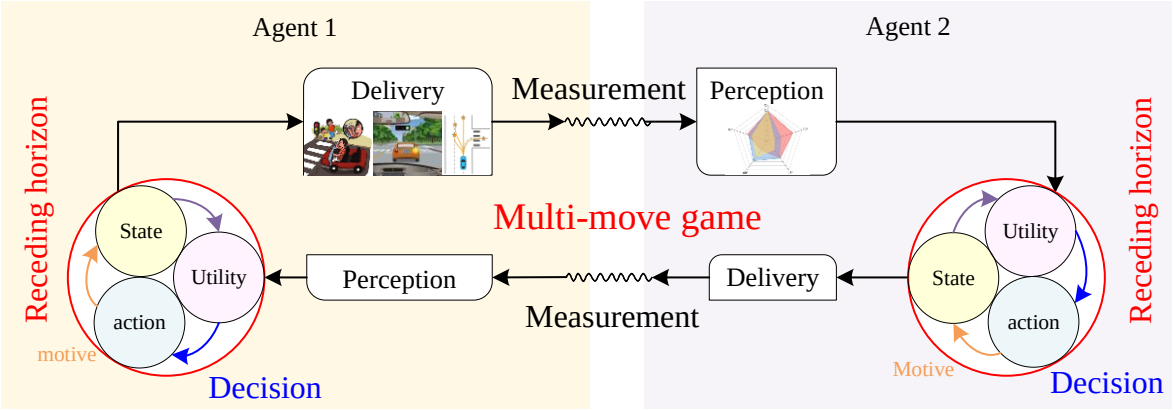


Figure 2. Illustration of Interaction attribute-oriented game theoretic decision-making process.

uncertainties and continuous closed-loop feedback among human drivers, social interactions are more intricate to quantify than physical interactions. Markkula *et al.* pointed out that the conceptual understanding of social interaction would facilitate the development of accurate theoretical models, high-fidelity simulation tools, and stringent technical requirements for vehicle automation[13]. Thus, a review of mainstream definitions of social interaction is undertaken first.

2.1 Definition and attribution of social interaction

The research about interaction covers multiple academic disciplines, each with varying definitions. In the fields of artificial intelligence and robotics, the study of interactions in transportation has attracted significant academic attention and effort. Review[13] provided a general understanding and interpretation of road traffic interaction in a cross-theoretical sense, which emphasized the interactive objectives, condition of interaction occurrence and the reciprocality of coordination, but at a loss to reveal the underlying dynamic process of road traffic interaction. Many scholars hold that road traffic interactions share fundamental features similar to human interactions, such as coordination, collaboration, competition, negotiation,[10,14,15] and communication[16]. Inspired by this, three fundamental characteristics of social interaction, i.e., dynamics, measurement, and decision, were excavated[11]. Revolving around these interaction attributes, we illustrate the two-agent interaction process from the perspective of game theory in Figure 2, with reference to the closed-loop formalism of interaction[11]. Each attribute provides irreplaceably constructive guidance for mimicking real-world social interaction with high fidelity.

Dynamics: As shown in Figure 2, every road user continuously adjusts their actions based on social perception of neighbors' current and future reactions and then conveys their state in a recognizable manner. The mutual dependence during interactions forms a continuous closed-loop feedback system, where each road user contributes to and is affected by the aggregated dynamics of the traffic system. Furthermore, each road user could be treated as a closed-loop feedback optimizer, where each alternative action would facilitate a corresponding update in the motion state, resulting in a specific reward or cost that further guides strategy selection. The review[11] argues that comprehending the principles and mechanisms of the dynamic interaction among human drivers in complex traffic scenarios would allow (1) generating various social driving behaviors that leverage beliefs and expectations about others' actions or reactions[17]; (2) predicting the future states of the aggregated system involving moving obstacles is essential to enhance safety by detecting potential collisions[18]; and (3) devising realistic driving simulators and virtual testing platforms[19,20]. In conclusion, understanding and modeling dynamic social interactions in mixed-traffic environments are pivotal for predicting scene dynamics and ensuring safe AV behavior decisions[21]. Moreover, it is widely acknowledged that model-based methods outperform implicit modeling approaches, such as learning-based algorithms, in terms of interpretability. Consequently, the main challenge in human-like decision algorithms is how to explicitly

model the dynamic interaction between multi-vehicles while fully considering the evolution of dynamics over a temporal horizon.

Measurement: Interaction uncertainty is a critical factor influencing the safety and human-like performance of autonomous driving. Motivated by internal social driving characteristics, road users may respond with various reactions and actions through both explicit and implicit communication. Due to the bidirectional nature of information exchange, the road user not only acts as a deliver, but also as a receiver, which requires the information to be recognizable and measurable. Quantitative evaluation of social driving characteristics helps mitigate the impact of interaction uncertainty and address the "incompleteness" of game information.

Decision: Based on dynamics and measurements, road users are regarded as rational agents who make decisions by maximizing/minimizing their utility/cost. What needs to be considered is how to incorporate information such as physical interactions, social interactions and driving characteristics into computational models while ensuring their fidelity. Additionally, the decision-making algorithms should maintain manageable computational complexity when applied to multi-vehicle interaction problems.

2.2 Summary

In conclusion, a unified definition of social interaction in road traffic has been presented by Wang[11], which provides a computational framework that connects the fields of psychology and robotics. In terms of communication among human drivers, implicit signals such as vehicle kinematics are widely accepted, pervasive, common, and reliable communication methods; their critical roles cannot be ignored[22]. Although researchers have made initial attempts to influence HDVs by manipulating implicit signals, such as vehicle deceleration rate and a lateral move[23,24], these efforts are insufficient to ensure safe and efficient communication. These communication methods lack relevant theoretical support to demonstrate the accurate and effective delivery of communication information.

3. OVERVIEW OF PIVOTAL FACTORS IN GAME THEORETIC DECISION-MAKING AND CONTROL ALGORITHMS

The realm of AV decision-making strategies based on game theory has witnessed extensive exploration, ranging from the discrete decision procedure modeling methods during the interaction only by game theory to the integrated decision-making and control strategies by combining other control theories and learning methods. We collect the latest research progress and systematically summarize the key factors affecting the human-like performance of the game theoretic decision-making system of AVs in Table 1. The factors are divided into three broad categories: interaction-related, game theory-related and control-related.

In reality, human drivers mostly react to the physical environment without interacting with the other road users in most driving cases. Generally speaking, the interactions occur in scenes without explicit traffic lights for guiding, such as unprotected left turns, ramp merging, passing through roundabouts, and lane changing (LC) in a multilane highway or urban environment. Road users need to negotiate among themselves to determine the right-of-way, which is a challenge for AVs due to the partially observable environmental states. Also, there are various uncertainties in the interactive environment that can exert influences on driving behaviors, including multifarious road types, unpredictable speed and direction of HDVs, unknown intentions and dispositions of the interactive agents and uncertain perception[19]. The interactive environments with uncertainty could be called stochastic environments.

Among all kinds of uncertainties, the social driving characteristics of other agents directly influence the cooperativeness of HDVs. The ref.[25] pointed out that individual social driving features could be sorted into long-term style features and short-term interactive characteristics. Personal traits and behavioral styles are pre-

Table 1. Pivotal factors in game theoretic decision-making and control algorithms

Interaction-related factors					
Algorithm function	**Interactive scene**		**Uncertainty**	**Environment**	**Social driving feature**
Model discrete decision Process during interaction Mimic entire decision and control of interaction	Left turn in uncontrolled intersection Merging on highway on-ramps LC in highway or urban environment Passing through roundabout		Road types Speed and direction Intention Perception	Determined Stochastic	Intention Driving style Sociality
Game theory-related factors					**Control-related**
Interaction	**Role assignment**	**Reward**	**Incomplete information**	**Adaptation**	**Factors**
Two-agent Multi-agent One-shot Multi-move	Rational follower Mutual-dependence actor	One-step Cumulative Rule-based formulation Demonstration learning	Irrational agent Social driving feature Reward of HDVs Partially available states	Asynchronous Synchronous	One-step Receding-Horizon Uncertainty

dominant in the former's formation while the latter is influenced by the interactive environment and driving behaviors of other agents. The long-term style of drivers can be characterized by driving style on a behavioral level [26–28] or captured by social value orientation (SVO) from the view of sociality [17,29]. As for the short-term interactive features, certain characteristic variables (e.g., reference acceleration [30], impact intensity related to acceleration, and kinematic indicators related to acceleration and speed) are usually presented to reflect the real-time traits of other agents [31]. Evaluating the social driving characteristics of other agents quantitatively helps AVs augment the interaction understanding abilities and enhance the social decision-making prowess of AVs [32].

Through a comprehensive literature analysis, the development process of game theoretic decision-making methods is illustrated in Figure 3. The horizontal axis represents the randomness of the interactive environment while the vertical one indicates the number of interactive agents. The evolution of game theoretic models is fundamentally driven by control theory and learning methods, based on which the development process is roughly divided into three stages as represented by the differently colored areas in Figure 3. In the first stage, researchers focus on high-fidelity decision-making modeling by exploring various types of game theory and integrating social driving characteristics into computational models. Usually, the following assumptions are made: for example, the interactive environment is treated as deterministic; (2) the interaction takes place only once; (3) the game played by AVs and HDVs has complete information. As research progresses, more realistic factors are considered. To address the computational complexity problem arising from the multi-agent coupling relationships, real-time methods for solving combinatorial optimization problems have also been investigated. Considering the dynamics of social interaction and time-varying control, a multi-move dynamic game scheme is presented by combining control theories to enable AVs to make decisions based on predictions of SVs' motion. Furthermore, to handle the incomplete information induced by uncertain driving intentions, social driving characteristics are quantitatively assessed based on the observed trajectories. Driven by the rise of artificial intelligence, learning methods are incorporated into the game theoretic scheme, equipping AVs with the ability to learn from interactions and further enhancing the adaptability of the autonomous decision-making system.

4. GAME THEORY-BASED DECISION-MAKING STRATEGY IN DETERMINISTIC ENVIRONMENT

In mixed-autonomy traffic, if AVs are driving in certain scenarios such as in a vehicle platoon or in a closed environment, a deterministic environment is usually assumed. Also, the common scenarios in reality, namely highways or urban streets, become deterministic under the assumption that the stochasticity of human driving behavior is ignored and all states of HDVs are fully observable. Therefore, without considering randomness and uncertainty, early research primarily focuses on constructing game theoretic decision-making frameworks,

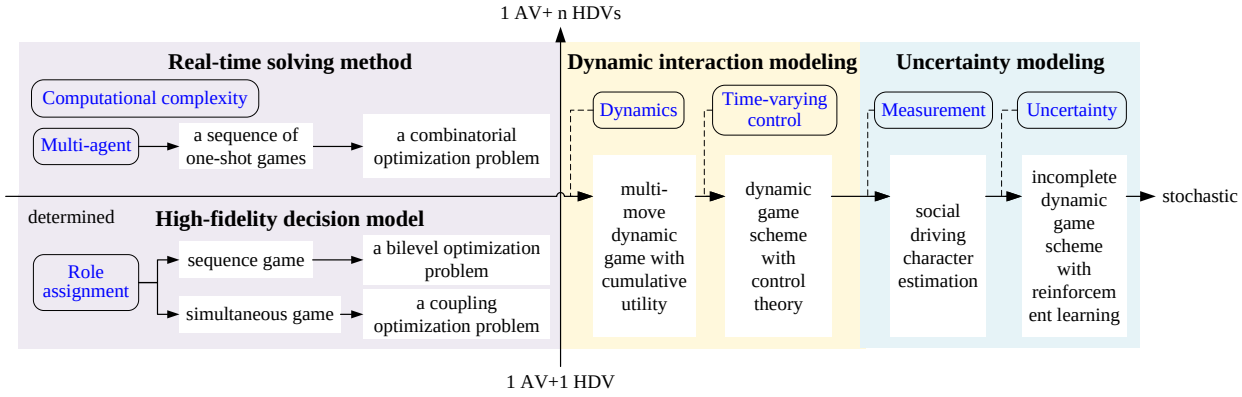


Figure 3. Development process of game theoretic decision-making and control methods driven by influencing factors.

particularly the selection of game-theory types based on a different understanding of interactive agents' impact and the design of utility functions that account for human driving behavior. Additionally, under a deterministic environment, vehicle states are updated according to a deterministic kinematic state-space model, which is in charge of calculating the change of positions, velocities, and accelerations. Considering the complexity of the vehicle dynamics model, the point-mass (which treats a car as a particle) and bicycle or front wheel steering (which treats a car as a 2D) models are commonly used[33].

Essentially, the driving behavior decision of human drivers is a game theoretical problem where drivers make real-time decisions by considering the effects of mutual interaction[34]. Game theory has been a mature field for modeling strategic interactions of rational players and can offer versatile and adaptive solutions for interactive decision problems in various scenarios without relying on specific data distributions[21,35]. The game theoretic decision-making methods establish the mapping relationship from the driving environment to driving behavior. Human driving behaviors or actions are theoretically the optimal or approximate optimal solution that maximizes certain rewards/utility related to the driving environment[36]. Toward this point, researchers formulate the social interactions as optimization problems by integrating the vehicle states-related information into the reward/cost function, where the game equilibrium is exactly the optimal outcome[37].

4.1 One-shot games in determined environment

The most commonly encountered interactive scenarios in our daily traffic are car-following, merge-in/out, and lane change in urban environments and highways, which is assumed as determined in the early studies. Without considering interaction uncertainty, researchers focus on modeling the decision-making process during the one-stage interaction by one-shot games. Without loss of generality, the one-stage interaction could be regarded as one turn of the dynamic interaction. Studying the behavioral decision during one-stage interaction helps to facilitate a deeper exploration of the dynamic interaction process imitation. Additionally, either simultaneous one-shot games or multi-move games could be viewed as a combination of one-shot games. Therefore, the typical one-shot game-based methods (e.g., Stackelberg game and simultaneous game) are discussed hereinafter, followed by the approaches of game reward/utility function construction.

For the case that an AV interacts with only one HDV in a determined environment, game theoretic models are developed based on a one-shot game to delineate the strategic actions of both vehicles at a single step. For instance, driver behavior of merging[38,39], LC[23,40–47] and unprotected left-turning[48] is modeled as either a two-person non-zero-sum non-cooperative game[49,50], a normal-form game[28], a Stackelberg game[23,26,38,39,43–47] or a simultaneous game[27,32,40] depending on the role assignment of the other agent and game equilibrium. The outcome of simultaneous games can be a pure or mixed-strategy Nash equilibrium, derived from the utility function maximization/minimization. The optimization problem built based on one-shot

games with two agents could be solved using the off-the-shelf dynamic and linear programming algorithms. If the mixed-traffic environment is assumed to be deterministic and multiple vehicles interact with each other in a game theoretic framework, a simultaneous one-shot game or a differential game would be modeled between one AV and multiple HDVs.

In games, how the ego AV accounts for the influence of interactive HDVs would impact the decision-making capability of game theoretic models. The role of other agents could be categorized as moving obstacles, rational followers, or mutual-influence actors, each of which follows a progressive logic. The interaction with moving obstacles is one-way, where obstacles are deemed to be unaffected by AVs. In the ref.[39], vehicles on the main road were assumed to move along the current lane at a constant speed. The trajectories of interactive vehicles predicted on this assumption were fed into the planning level. This simplification works in a one-shot game due to longer reaction time of HDVs. However, human driver heterogeneous characteristics may give rise to conservative action of AVs or even risky situations in reality. To avoid this, the roles of rational followers and further mutual-dependency actors are assigned to HDVs, facilitating Stackelberg game theoretic methods and simultaneous game theoretic methods, respectively, as detailed below.

4.1.1 Stackelberg game theoretic decision-making

In Stackelberg games, HDVs are regarded as rational followers who would respond rather than influence the leader AV. The leader-follower relationship entails a bi-level optimization where a lower-level optimization is contained in an optimization for the leader's objective on the higher level. Yoo and Langari[38,39] presented an interaction model between vehicles during LC and lane merging based on a Stackelberg game, where the ego AV was assumed to know the cost function of the competing vehicle beforehand. Based on the same assumption, Hang[26] modeled the lane-change decision-making procedure using a Stackelberg game, considering two-agent interaction. The upper layer was to optimize the follower's behavior decision grounded on predictions about the follower's strategy while the lower layer optimized the decision-making process of the follower given the leader's choice.

To address the challenge in modeling a large amount of HDVs simultaneously, Liu and Tomizuka[51,52] combined multiple HDVs as one effective agent and assumed a sequential game in which HDVs led and the AV played reactive strategies. By mapping a baseline control law to a set of safe controls, an online algorithm was developed for the AV controller to incorporate human intentions as safety constraints. Coskun and Zhang[41,43,46] exploited a sequence of one-shot Stackelberg games to deal with multi-vehicle interaction in the HDV-dominated mixed-traffic environment. The goal was to train autonomous driving with human-like performance in gap acceptance and lane change. We noticed that the ego AV was regarded as the leader in the above works while the leader-follower role was determined based on the right-of-way in[19]. There is no doubt that the role allocation of leader and follower deserves more discussion due to its importance in applications. One effective method is to directly assign the leader role to the ego AV[23,26,39,46,47], which is valid because the AV deserves to be endowed with the advantage of active pursuit as the initiator of the LC interaction. Also for the LC scenarios, the pairwise leader-follower relationships were dealt with as a priori uncertain and modeled as latent variables, which were estimated online predicated on observed trajectories[53]. Another alternative logic to determine the sequence order is based on traffic rules. For instance, Li *et al.* applied the "right-of-way" rules to artificially formulate role assignment rules at uncontrolled intersections[19]. So far, a unified method for leader-follower role allocation has not been proposed for various interactive scenarios. Besides, a rational follower could only derive the best response to the leader passively instead of actively exerting influence on it[54,55], which might cause an inevitable shortcoming that dynamic mutual influences between the AVs and HDVs are neglected.

4.1.2 Simultaneous game theoretic decision-making

To consider the coupling influence among agents, simultaneous games are used to capture their dependence[27,32,40], where every agent makes decisions simultaneously without knowing the others. Usually, a two-agent interaction problem is modeled as a coupling optimization problem[27]. Hang[27] adopted Nash game to handle the non-cooperative decision-making problem in common LC scenarios by combining with the potential field method to provide a collision-free reference path. Under the scheme of a simultaneous game, Nash equilibrium was derived for the pure strategy by solving the optimization problem. A deterministic strategy provides a complete plan of how a player will take action in a game. However, a deterministic strategy is not always feasible, consequently necessitating a probabilistic analysis of all the likely responses. If each player selects the optimal strategy probability distribution given the fixed strategies of others, a mixed-strategy Nash equilibrium would be computed as the game outcome[32,40]. Meanwhile, multi-vehicle decision-making is formulated as a combinatorial optimization problem in the distributed or centralized form[56]. Under the distributed frame, only the closest n SVs in the neighborhood are considered. In the centralized formulation, the objective function is a weighted sum of the cost functions for every participant[11]. Directly solving the optimization problem might lead to a trapped situation where all vehicles decide to slow down to yield. To solve this problem, Liu *et al*. proposed a communication-enabled conflict resolution[57].

4.2 Utility function construction

The game theoretic models for interaction problems formulate various optimization problems, which require specified objective functions (also known as utility/reward/payoff) to be optimized. The utility value represents the outcome obtained by selecting a particular action. To guarantee the complete information of the game, the assumption that the ego AV has access to others' utility functions has been made[17,23,53,58–60]. Generally, utility functions of AVs and HDVs are contrivedly designed to realize human-like driving performance according to the prior domain knowledge of traffic regulation and driving tasks[26,27,61–63]. However, the interaction among human drivers in natural traffic environments suffers not only physical (e.g., kinematics and geometry) but also social (e.g., driving style, intention, and social preference) constraints. For example, driving safety can always be guaranteed by a safe gap ideally. Nevertheless, it is difficult for the ego AV to perfectly predict the actions of the interactive vehicles due to their uncertain driving intentions. As traffic psychologists held that the social interaction of human drivers was characterized by the orientation of social habits and values, social preferences and social interaction patterns[64,65], which could be collectively called social driving characteristics[11]. These representation parameters could be parameterized and then embedded into the cost functions of interactive agents involved in a game, which would help improve the adaptation of AV's decision. Herein, how social driving characteristics are considered in utility function design is primarily introduced, and how to quantify them would be discussed later. The mainstream individual utility functions can be summed up as three categories, as shown in Figure 4.

In LC environments, Hang[26,27] formulated the cost function of LC behavior as a linear weighted sum of tripartite costs on driving safety, ride comfort and travel efficiency. The cost of driving safety was calculated by a function of gap and relative velocity, while the ride comfort and travel efficiency were evaluated by the jerk-related expression and relative velocity, respectively. The HDV was supposed to be an optimizer with the same formulation principle for cost function as an AV, based on which the integrated decision-making and motion planning framework was established as a two-level multi-objective optimization problem through Stackelberg game and model predictive controller (MPC). Similarly, a multi-factor-enabled interactive decision-making method was presented to align decision-making with human logic while ensuring driving safety[66]. The multiple complementary factors included driving performance requirements - such as safety, smoothness, comfort, speed and available space - as well as diverse driving styles suitable for different driver groups. The driver's driving style was incorporated into the goal function by assigning different weights, although it was assumed as a priori and fixed variable. In contrast, the aggressive level was deemed to follow the Gaussian distribution and there was a one-to-one mapping between the driver's aggressiveness and weight[23,67]. Through the cumu-

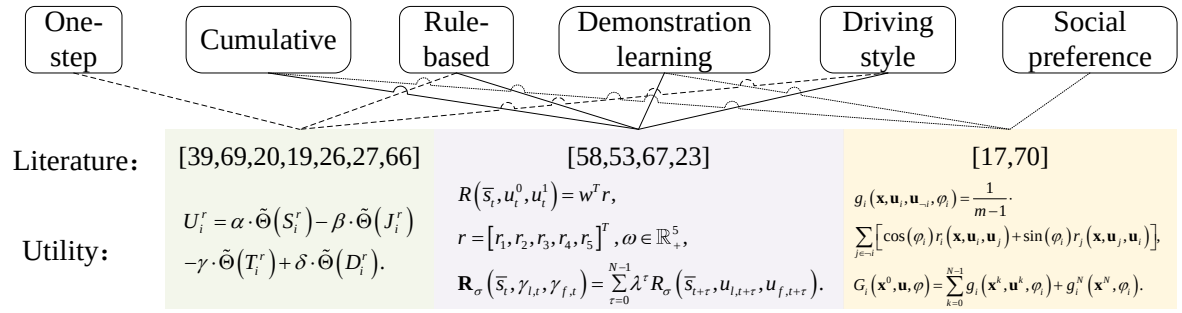


Figure 4. Mainstream utility functions classification.

lative distribution function of aggressiveness, the safety and space payoffs were linearly combined as the total optimization objective[23].

Due to the uniqueness of each driving task, additional considerations were represented in utility functions. As for merging scenarios, Langari[39,41] considered the limitations of on-ramps' length and driver's visibility in addition to the factors of speed advantage and unacceptable collision risk. Also, different drivers with varying levels of sensibility were distinguished by introducing a parameter called "aggressiveness" into the utility functions. With the utilities that originated from drivers' intentions, a driver merging model was established that can judge the merging instant and acceleration/deceleration according to the driver's aggressiveness[39]. In unsignalized intersections (e.g., four-way and roundabout), traffic rules were introduced to motivate vehicles to drive into the right lane[19,20,68,69]. Driving styles were reflected by choosing distinct weighting coefficients. Liu *et al.* formulated the reward function accounting for safety and the adherence to or violation of "soft" traffic rules[28].

Similarly, payoffs developed in[28] consisted of safety utility and traffic rule-related rewards. But differently, the parameters used to adjust the ego AV's behaviors were designed to rely on the driving style of the counterpart based on supervised learning mechanisms. Furthermore, the multi-vehicle interaction was modeled based on a normal-form game, facilitating a clear representation of players' strategy space and payoff. Coincidentally, SVO can be learned from observed trajectories using inverse RL (IRL)[17,70]. As an effective tool to quantify the social preferences of human drivers, SVO can assess how one driver weights its rewards against the rewards of other agents[71]. Many researchers have adopted the SVO concept to conduct extensive investigations about human-like decision-making of autonomous driving[17,72–74]. By introducing human-like elements into utility functions, mainly indicated by intention, driving style and social preference, AVs are promised to generate socially-compatible driving behaviors.

4.3 Summary

Naturally, game theory has exhibited great superiority in modeling the interdependence of actions and some exact real-time solutions exist for a limited number of problems. Research on game theoretic decision-making in a deterministic environment emphasizes the construction of decision schemes with game theory. This mainly involves game type selection considering the role of HDVs during the interaction process, as well as the number of interactive agents and the design of individual and total utility functions. Concretely, depending on whether HDVs are followers or mutual influencing agents, either a sequential or simultaneous game is employed to model the interaction. Besides, a deterministic kinematic state-space model is specified to update states, based on which the utility function is constructed focusing more on individual driving performance than traffic performance. The effectiveness of the proposed methods in a deterministic environment has been verified in simulations and hardware-in-loop experiments. However, game theoretic approaches in a deterministic environment suffer from the following issues: (1) it is assumed that the AV can access the utility

function that justifies other agents' actions and that the players act rationally according to those contrived goal functions. Nevertheless, the assumption is too ideal to come true in realistic traffic; (2) the numerical computation complexity expands exponentially in the number of players and with the growing temporal horizon; and (3) the HDVs' behavior might be stochastic which makes the computations of solving for mixed or behavioral strategies even more intractable. Consequently, to alleviate those issues, many papers in the field of game theoretic autonomous driving try to simulate the dynamic interaction and handle the stochasticity of human behavior in the development of decision-making algorithms.

5. HUMAN-LIKE DECISION-MAKING CONSIDERING DYNAMIC INTERACTION MODELING

Human drivers handle interactions not only considering immediate benefits related to driving performance such as safety and comfort efficiency but also involving reasoning about future states. Moreover, Lee *et al*. argued that the interaction among human drivers should gain an optimal accumulated utility over a short future horizon [75]. As exhibited in Figure 2, the dynamics of interaction can be summed up in two aspects: (1) the multi-turn closed-loop feature; and (2) dynamic evolution of each agent's state over time. The evolution and update of system states lead to the accumulation of each-step utility over the future horizon [19,53,68,69]. However, the abovementioned one-shot games cannot model drivers' dynamic driving actions; by contrast, multi-move games considering the mutual dependence among interactive agents have exhibited great potential in dynamic interaction modeling. Thus, most of the current works switch on multi-move games with cumulative utility by translating interactive behavior into an iterative optimization problem [17,43,53]. Considering the dynamic and uncertainty of the interaction process, as well as the potential reasoning of human drivers about future risks and situation evolution, Liu [32] first modeled the future state extrapolation of environmental risks and incorporated efficiency, safety, and stochastic disturbance benefits into the payoff function. If the game involves multiple decisions where the order is important, it is dynamic. Furthermore, it becomes non-cooperative if each player pursues their own utility partly conflicting with the utilities of others.

Another method capable of capturing dynamic mutual dependence is the hierarchical game theoretic planning where the AV's planning and its predictions of HDVs' behaviors are decoupled [76]. The higher strategic planner level was featured by a long-horizon feedback Stackelberg game with simplified dynamics and full information structure. By successive application of dynamic programming, driving actions of interactive agents were recursively solved. The optimal Q-value was utilized to inform the tactical planner, who applied a short-horizon "tactical" game with full dynamics and a simplified information structure. The trajectory of the AV was output by iteratively solving a nested optimization problem, i.e., estimating the human's best trajectory response to each candidate plan in the short-term planning horizon.

5.1 Human likeness evaluation metrics

The review [2] suggested that human-like decision-making could empower automated systems to make correct judgments and decisions in complex traffic scenes. Achieving human-like performance requires algorithms to manage diverse uncertain factors in dynamic traffic environments, meet the demands of passengers and other road users, and guarantee efficiency and safety. Therefore, the human similarity of decision-making algorithms can be assessed from two perspectives: the algorithm's principles and its driving performance. In terms of the former, the human likeness evaluation methods include (1) a combination of deterministic and fuzzy logic; (2) capability to unknown scenes; (3) consideration of randomness; (4) learning ability; and (5) interpretability. Driving performance metrics, i.e., driving comfort, driving safety, similarity with human demonstration trajectories, and characteristics relative to other traffic participants, are used to directly compare human driving data with intelligent decision-making algorithms, demonstrating their similarity.

Table 2. Typical human-like decision methods combining dynamic game and control

Ref.	Scenes	Game theory	Control	Contributions
[43,47]	Mandatory Merging	Stackelberg Game	MPC	Development of game theoretic model predictive Controller with online aggressiveness estimation
[26,27]	Lane change In highways	Stackelberg Game	MPC with Potential filed	Integration of decision and motion Planning considering social behaviors
[79]	Uncontrolled Intersections	Differential Game	LQ	Enable real-time decision in Continuous action spaces
[19]	Uncontrolled Intersections	Leader-follower Game	RHC	Application to various interactions With up to 10 vehicles
[77,83]	Diverse multi-Agent scenarios	Potential Game	RHC	Computationally scalable and actual NE Approximation despite unknown others' cost

5.2 Human-like decision-making methods considering time-varying controls

In general, the game theoretic models could accomplish an expected performance in similar scenarios with elaborative parameter tuning, yet have low generalization capability in the unseen traffic scenarios. Therefore, model predictive control (MPC)[26,27,42,53], receding horizon control (RHC)[19,20,77,78] and linear quadratic (LQ)[79–81] techniques have been introduced to solve time-varying control problems. The main research and their contributions are summarized in Table 2.

Real traffic environments are characterized by highly dynamic variations, meaning that actions computed at the current time step may become obsolete by the next time step. In order to avoid this issue, the idea of RHC[42], widely implemented in MPC theory, was borrowed into game theoretic decision-making methods. Coskun *et al.*[41] developed a dynamic decision strategy combining Markov games with a receding horizon approach to handle new information received as time progresses. The human-in-the-loop (HIL) experiment results demonstrated that the proposed receding horizon Markov game could determine a safe gap in multi-move traffic. Moreover, Li *et al.*[19,20,53,58,82] have carried out much research focused on interaction problems in various unsignalized intersections by combining game theory with receding horizon optimal control. In these works, the rewards were an accumulation of the one-step reward constructed in[61,62,68,69]. Particularly, Tian *et al.*[20] presented a general interaction modeling method with level-k game and receding-horizon optimization, which could be scalable in urban environments with many intersections and vehicles. To resolve the computation challenges posed by large state space of urban traffic, an imitation learning (IL) algorithm was used to obtain control policies.

In the integrated framework of decision-making and motion planning[26], MPC was used to predict the state over the future horizon. Based on the idea of optimization, the decision-making and motion planning problem was transformed into a closed-loop iterative optimization process with multiple constraints by combining Stackelberg game theory, potential field method and MPC. Since only current states were considered in the game theoretic decision process, the multi-constraint interactive optimization could be iteratively solved with an evolutionary algorithm in real time. To handle constraints in different lanes during instantaneous LC, hybrid MPC was introduced into the development of behavioral decision methods[43,46,47]. The higher-level controller evaluated the proper times to initiate/complete a lane-change maneuver by continuously playing a Stackelberg game with surrounding HDVs. The four-stage hybrid MPC in the lower controller was responsible for prediction and update of HDV's longitudinal position and lane decision. The pure equilibrium was readily obtained by a sweeping search of all the solution candidates because of the small scale of the game.

5.3 Real-time solution for multi-vehicle dynamic interactive decision making

The game theoretic framework has been proven to provide an explainable explicit solution to model the dynamic interactions among human drivers. However, if the AV could predict the actions of HDVs in the entire planning horizon, it would optimize its own objective function based on both current and future strategies to bring about a continuous sequence of control strategies to implement. The same process holds for HDVs. Due to dynamic coupling, it remains a challenge to satisfy the real-time constraint regarding computational

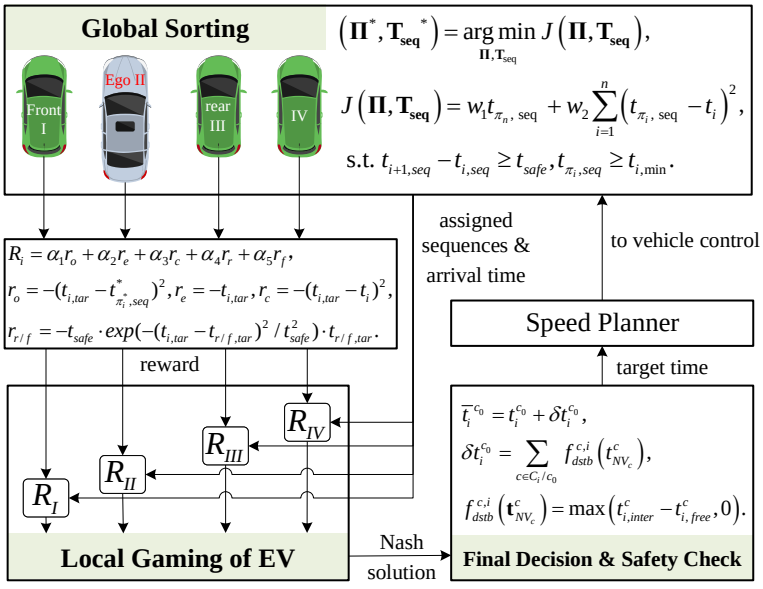


Figure 5. The decision framework of global sorting and local gaming (GLOSO-LOGA)[86].

tractability although progress has been made with simplified system dynamics and information structures[76].

With such restrictions, most of the current game theoretic interactive decision-making and control methods have difficulty in algorithm scalability, thus being trapped in two-vehicle settings and simulation tests or handling multi-agent interaction pairwisely[17,43,55,70,84,85]. For instance, dynamic games with concurrent pairwise leaders/followers were adopted to capture dynamic interaction among multiple agents at uncontrolled intersections[19]. Each pair of lead-follower games formed a bi-level optimization problem, which could be computed in real time by (1) reformulating it as a local single-level optimization problem[17,86]; (2) approximating an optimal solution of the follower[54,87]; and (3) setting assumptions on the uniqueness of each optimizer that maximizes rewards[19]. Simulation results indicated that the interactive model demonstrated reasonable behavior and manageable computational complexity. As displayed in Figure 5, Li *et al.* proposed a global sorting-local gaming framework to solve the complex multi-vehicle interactions with comprehensive consideration of the advantages of multi-vehicle collaboration and single-vehicle intelligence approaches[86]. Moreover, an interaction disturbance function is used to quantify the impact of indirect interactions on ego vehicles. Additionally, Schwarting *et al.* developed a game theoretic control policy for AVs by solving a locally equivalent formulation[17]. The two-agent Stackelberg game created a constrained bi-level optimization, which was then reformulated as a local single-level optimization problem using Karush-Kuhn-Tucker (KKT) stationarity conditions, allowing the solving method to propagate the constraints. However, it may be desirable to have back-and-forth tacit negotiation even if two agents interact, which removes the leader-follower dynamics and entails a simultaneous game. Regarding the constrained multi-agent Nash equilibrium, Schwarting *et al.* reformulated the multi-level optimization problem with KKT condition and applied existing nonlinear optimizer to solve it, as shown in Figure 6[17].

As pointed out in the ref.[78], a differential game arises when two interacting agents with conflicting goals solve their own optimal control problems. The classical differential game basically concerns two agents and gets intractable for an equilibrium of more than two agents. Sadigh[87] predigested the original two-agent differential game to a Stackelberg game played at discretized time steps. This framework was extended to a multi-agent Stackelberg game, but with assumptions that the ego AV only affected one HDV and the actions of other HDVs were fixed[88]. In order to facilitate interactive decision-making in continuous action spaces, iterative LQ technique was blended with differential games to compute a discrete-time linear dynamics approximation

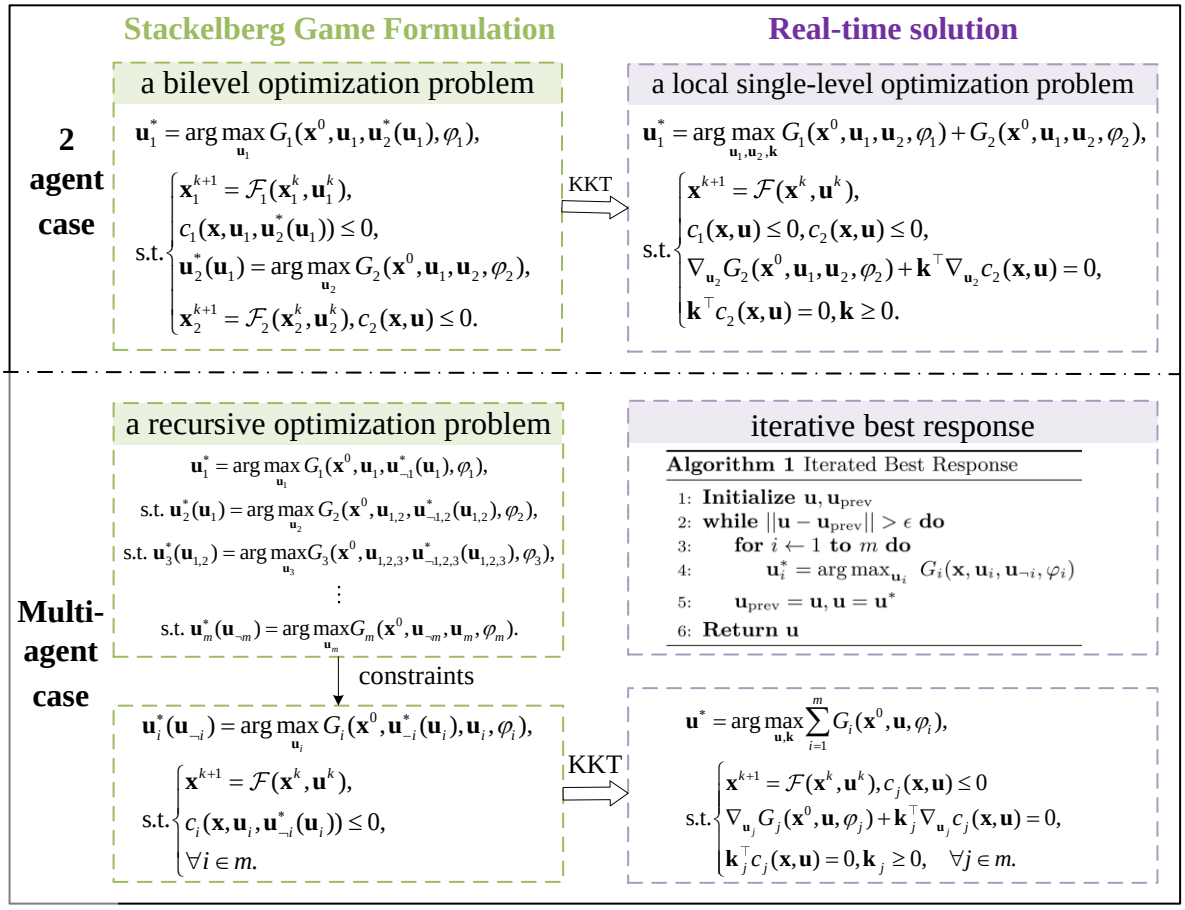


Figure 6. Real-time solving methods for multi-agent interactive decision-making problems[17].

and quadratic cost approximation[79–81]. Fridovich[80,81] developed an efficient iterative LQ approximation for nonlinear multi-agent general-sum differential games. Based on the feedback-loop LQ differential game, a planning and decision-making framework was built for unprotected left-turning handling[79]. To enhance the accuracy of the interaction model, real-world human behavior was extracted and evaluated from a naturalistic driving dataset to help construct a more realistic behavior model.

Another special class of multi-player games, called potential games, has also been integrated with receding horizon optimization to address decision-making[77,83]. Motivated by the need for real-time solutions, Liu *et al.* performed an in-depth investigation on finite and continuous potential game frameworks and formulated practical and reliable models with adaptation to specific traffic scenarios[83]. Additionally, a potential game consisting of Predictor and Corrector was investigated[77], where the former was responsible for heuristically predefining agents' cost functions, and the latter handled action deviation measurement, feedback and correction. This framework successfully fulfilled the requirements of interpretability, computational scalability, applicability to distinct scenarios, and human-like intelligence.

5.4 Summary

In this section, dynamic interaction modeling over the receding horizon is achieved by applying multi-move game or potential game and control methods. To ensure tractable computation, researchers have put forth several strategies to enhance game theoretic solutions. However, these solutions might be inaccurate in environments with high clutter or uncertainty. Uncertainty seeps in from unpredictable behaviors in surrounding traffic participants, as well as sensor noise and vehicle models[21]. In particular, the diversity and unpredictabil-

ity of human driver behaviors present a major challenge for adapting decision-making algorithms[24].

6. GAME THEORETIC DECISION-MAKING AND CONTROL METHODS WITH ADAPTATION

To enhance human-like performance, AVs should be equipped with the capabilities to handle unseen scenarios, adapt to various human drivers, and even manage potential accidents. However, game theoretic decision-making methods that just consider the dynamics of social interaction may not address the uncertainties resulting from the actions of other drivers. Additionally, most game theoretic methods mentioned above assume a complete-information framework, where (1) all HDVs are rational agents; and (2) each agent has full knowledge of others' information, such as states, intentions and utility/cost functions. However, this symmetric information structure is too idealistic to be realized in practice, as it overlooks the uncertainties that naturally exist in complex interactive environments.

The uncertainties influencing human drivers' driving behaviors mainly include (1) multifarious road types[20]; (2) uncertain prediction caused by noisy sensor data and directly unmeasured intention of HDVs[89]; (3) interaction uncertainties due to varied cooperation intents and dispositions of other vehicles[58]; (4) unpredictable of speed and direction of HDVs[30]; and (5) perception uncertainty[39,90]. Essentially speaking, the uncertainty that has the greatest impact on social interaction ultimately stems from unknown driving/cooperation intent. Without prior information about intentions, incomplete games are formulated. Most works deal with incomplete information by converting them to complete ones based on estimations of driving intentions or social cooperation level of HDVs[23]. Another effective train of thought for uncertainty resolution is to combine game theory with other learning methods, such as RL and Markov decision process (MDP). In the following subsections, we will provide an in-depth discussion of methods integrating dynamic games and learning techniques, and dynamic incomplete game theoretic methods considering the estimation of social driving characteristics.

6.1 Game theoretic decision-making and control methods combining reinforcement learning

Thanks to the ability to handle uncertainties, RL has become a powerful tool to help AVs realize socially compatible autonomous driving. Details on the principle of RL control can be found in[11,91]. Herein, we focus on the application of RL on game theoretic human-like decisions. In recent years, the application of AI technology has allowed AVs to break through the assumption that interactive agents are "rational". Algorithms such as RL[92] and IL could be utilized to directly learn driving policies from driving datasets or environmental interactions. Instead of treating every individual HDV as an intelligent agent, researchers regard all these HDVs as part of the stochastic environment in the RL scheme, which produces two types of game formulations of modeling interactions, i.e., synchronous Markov/stochastic scheme and asynchronous level-k scheme[11]. We summarize a list of typical game theoretic decision-making methods combining RL in Table 3.

6.1.1 Integrated methods of Markov/stochastic game and RL

Markov models can represent uncertainty in a stochastic manner[89]. In mixed-autonomy traffic, the driving strategy selection of an AV can be regarded as a sequence of decision-making processes in a fully or partially observable random environment. MDP makes an assumption that the state dynamics is fully observable to the ego agent[97]. Zhang[47] made an assumption that the ego vehicle had access to the full information and system state of other vehicles through vehicle-to-vehicle (V2V) communication. Based on this, a fuzzy Markov chain was used to predict the future motion of SVs to deal with the uncertainties in their behavior. As demonstrated in Figure 7, Li *et al.* combined MDP and matrix game with deep neural network (DNN) and a deep maximum entropy-IRL to model the behavior of background vehicles for simulating the game and interaction processes[95]. In the proposed scheme, a standard MDP with states of horizontal and vertical coordinates, velocity and acceleration was used to describe the merging decision process. The comparative results denoted that the data-driven method accurately reflected human driving behavior in real-world scenes.

Table 3. Typical game theoretic decision-making methods combining RL

Ref.	Interactive scene	Theories of game and RL	Uncertainty	Computational complexity	Verification
[53]	n , Merging	POMDP, Bayesian Inference, LFG, IL	A priori uncertain Driving intentions	Tractable Computation	Simulation, NGSIM data
[93]	10, LC	Matrix game BMPC	Unknown cost Functions	A tailored Numerical solver	Using real Traffic data
[24]	n,multimodal, Merging	Bayesian game Markov	Incomplete Information	Proportional To n	HIL, Turing tests
[94]	2,UI, Highway	Markov game DQN, WolF-PHC	Trains a Stochastic policy	Fastest Convergence	Simulation
[95]	n Merging	MDP, matrix Game, DQN	The impact of indirect Interactions on ego vehicles	-	Simulation NGSIM data
[96]	Complex Traffic Scenarios	Markov game, Level-k reasoning, TSA-DQN	Infer SV's Decision-making Ability	Increase by 12.8% in Efficiency	Simulation, Real-world Hardware test

Note: n refers to multiple vehicles; LFG and UI indicate leader-follower game and unsignalized intersection, respectively.

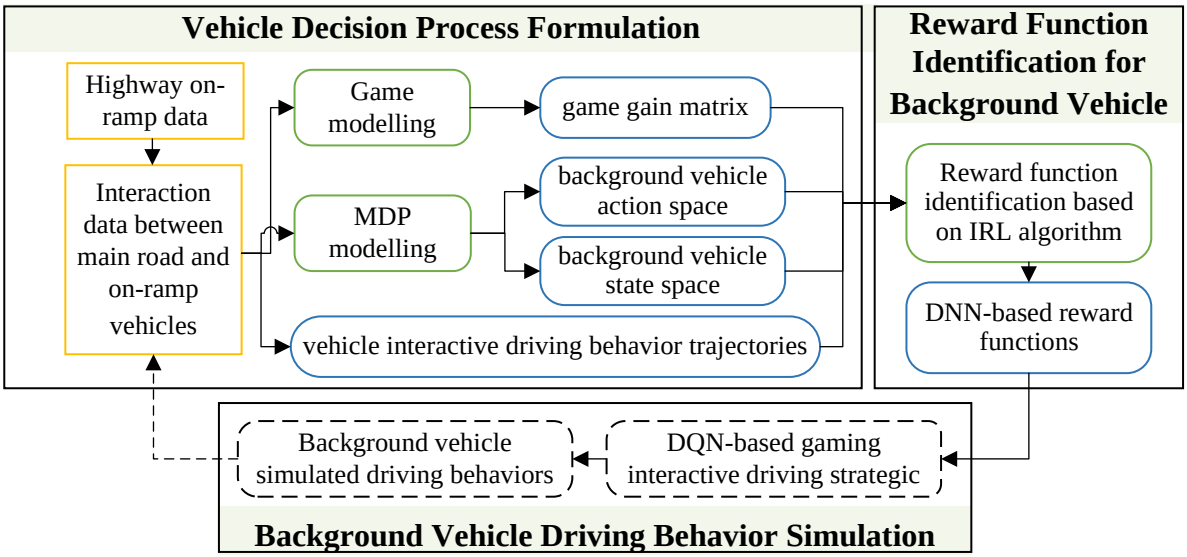


Figure 7. Data-driven game theoretic model framework with the integration of MDP, DQN, DNN, and IRL [95].

More realistically, human drivers can only observe a partial state of the traffic around them [51,52,63,98]. For example, they can observe locations and orientations, and occasionally the velocity of other vehicles, but acceleration remains unobservable. In addition, direct identification of other agents' driving intentions is still a challenge. As a result, the ego agent holds a belief state space over all alternative states in partially observable Markov decision process (POMDP). A stochastic predictive control algorithm for POMDP with time-joint chance constraints was proposed for behavior planning of AVs in dynamic and uncertain environments [99]. Hubmann [89] considered perception uncertainty caused by the unmeasured intentions in POMDP. In the studies [53,58], the interactions between the autonomous ego vehicle and other vehicles with a priori uncertain driving intentions were modeled as a partially observable leader-follower game. Additionally, the interaction uncertainty led by varied cooperation intentions was modeled as latent variables in the POMDP framework and an online estimation was conducted based on observed trajectories.

It has been found that POMDP is suitable for autonomous driving to make real-time decisions [100]. Compared with the study [58], a continuous state space was assumed in [53] where vehicle motion was predicted and planned using two much larger sets of trajectories instead of a small number of actions (or motion primitives) to represent vehicle behavior. A game theoretical traffic model considering human behavior was developed to provide a computationally tractable solution for a POMDP by using hierarchical reasoning and RL [61]. How-

ever, obtaining a general solution to a specific problem is difficult with the original POMDP. Therefore, the multi-policy decision-making method has received extensive attention [101,102].

In a stochastic environment with adversarial risks, an adversarial learning game has been used to model human-robotic interaction and train robust AV controllers. Assuming that the HV was an adversary attempting to falsify the AV's actions, Sadigh *et al.* first learned the HV's reward underlying its actions using maximum entropy IRL and then computed sequential AV controls with nested optimization [103].

6.1.2 Integrated methods of Level-k game and RL

The multi-agent interaction can be captured by the level-k reasoning on the strength of its easy extensibility to multiple vehicles. Level-k game theory relies on a hierarchical cognitive structure to model human reasoning in games [77]. Hierarchical reasoning for multi-agent interaction modeling has been applied in a series of time-extended and interactive scenarios, ranging from three-lane highways [61–63,104], unsignalized intersection networks (e.g., the most common types of three/four/five-way, T-shaped, and roundabout) [19,20] to forced merging scenarios [53,58,82].

In highways, an adaptive robust level-k reasoning was combined with game theory to develop the decision-making strategy in order to avoid undesirable behavior induced by uncertainties, such as dynamic model mismatch and improper agent classification [104]. Besides, the evolving of the dynamic scenario with multiple actions was taken into account in the level-k game-based interaction model [61–63]. The underlying aggregated dynamics of the traffic system conformed to Markov characteristics. However, the studied problem was formulated as a POMDP because not all of the system states were observable to the agents. Therefore, Jaakkola RL was adopted to simulate the time-extended scenario, with the preponderance of convergence to at least a local maximum in POMDP. Based on the theoretical frame constructed in [61,62], the research [63] enhanced the fidelity of the interaction model by two improvements: (1) designing a more realistic action space containing harder brakes and faster accelerations; and (2) exploiting a more realistic traffic model with the consideration of more representative constraint violation. With the designed simulator, two AV control algorithms were tested and quantitatively evaluated for their safety and performance.

Compared with highway scenarios, urban unsignalized intersections are more challenging since much larger state space brings difficulty in real-time policy resolution [20,68,69]. One approach to achieving real-time resolution is to make reasonable simplifications. In [69], the action sequence of the level-(k-1) agent was assumed to be independent of that of the level-k ego vehicle, which eliminated the need for nested back-and-forth calculations and made the computation more manageable. Another alternative approach is IL [105], a method for autonomous agents to imitate expert's behavior by learning a control policy from pre-collected expert demonstrations. For example, Tian *et al.* proposed an explicit online implementation scheme to acquire an explicit approximation of expert policy [68]. With the function approximation techniques, the computations required for solving the optimization problems could be moved from online to offline. However, the control policy entirely relies on the expert policy, which would generate a sampling bias, further probably inducing the propagation of error between policy and expert policy in time. To avoid this, an iterative algorithm called DAgger was developed to train the policy under its induced state distribution [20]. Benefiting from the DAgger algorithm, the level-k game theoretic formalism was successfully generalized to model the multi-vehicle dynamic interactions, and to larger urban road systems (including four-way, roundabout, and T-shaped intersections) with manageable online computational effort. To ensure the safe and efficient navigation of AVs in complex traffic scenarios, Zhou *et al.* proposed a game theoretic driver model based on level-k reasoning, which is characterized by mixed decision levels. Compared with the widely used intelligent driver model (IDM) [33,43,106], the proposed driver model could effectively capture the behaviors of diverse drivers [96]. Following this, a temporal-spatial attention-based deep Q-learning (TSA-DQN) algorithm was developed to approximate the optimal policy for interactive agents, whose outperformance in success rate, efficiency, and safety in driving

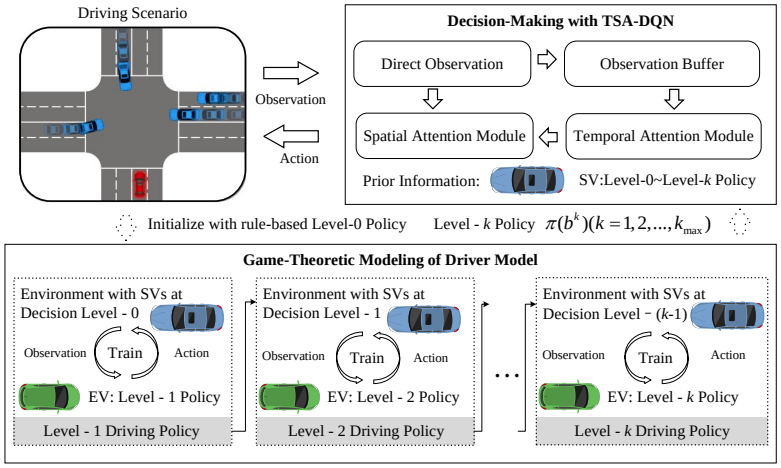


Figure 8. Overview of the decision-making framework based on level-k game theoretic driver model for autonomous driving [96].

tasks has been validated. The framework of the TSA-DQN decision-making method is shown in Figure 8.

There is no doubt that the level-k reasoning framework contributes a lot to formulating a dynamically-evolving interactive decision strategy. However, this type of cognitive hierarchy theory has a strong dependence on the accuracy of the (k-1)-assumption about the interactive environment's cognitive level. To avoid poor decision performance, cognitive hierarchy framework, Bayesian inference of cognitive level and receding-horizon optimization were introduced to formulate a constrained partially observable MDP [82]. The Bayesian network not only utilizes the probability description of the time-space relationship between vehicles but also incorporates the uncertainty of input data into the threat assessment of vehicles. It can efficiently represent uncertain events, such as estimating the probability of a vehicle collision [82,107].

6.2 Dynamic games with incomplete information

In the safety-paramount transportation system, AVs are expected to assimilate seamlessly into HDVs, which necessitates AVs to better understand HDVs' driving intention for a human-like interactive performance. In early studies, Talebpour *et al.* have considered the concept of incomplete information as part of the game formulation process, and developed a two-person non-zero-sum non-cooperative model that could cope with the stochastic nature of LC maneuver [50,108]. In the study [23], the incomplete information, i.e., the aggressiveness of interactive HDVs, was estimated and updated, further prompting the transformation from incomplete game to complete game. Motivated by the fact that quantifying the driving intention contributes to the reduction of interaction uncertainties, social driving characteristics estimation methods are necessary to be investigated.

Modeling and quantifying the driving characteristics of interactive agents is critical for AVs to better discern these agents and dynamically adjust their actions based on these characteristics, thereby enhancing the social decision-making capabilities of AVs in mixed-traffic environments. A great deal of endeavor has been devoted to embedding social driving characteristics in game theory-based decision-making models as recommended in Section 4.2. However, the fly in the ointment is that driving characteristics of other agents are usually known and fixed which removes the 'incompleteness' of games. Therefore, the main methods for recognizing and evaluating driving characteristics are presented here. Social driving characteristics are typically captured through intention, driving style and social preference, along with their evaluation metrics, as shown in Table 4.

Table 4. Methods for estimating social driving characteristics

Social driving characteristics	Ref.	Metric	Measure method
Driving Style	[23,43,109]	Aggressiveness	By online observation of real-time behavior in tentative interaction
	[79]		A behavior model estimation based on accepted time gap
	[30]	Weightings on safety and speed	Compare actual acceleration with predicted acceleration
Intention	[53,58]	A posterior belief of HDV's leader or follower role	Leader-follower game theoretic behavioral model
	[110]		With latent variables indicating the intention uncertainties
	[32]	Politeness	Based on observed actual acceleration of HDV
	[111]	IO	Based on environmental factors and trajectory characteristics
Sociality	[71,112,113]	Courteous and rude	Quantitatively analyzing the interaction process based on dataset
		SVO	Compare a candidate trajectory to the actual observed Trajectory for the most likely SVO

6.2.1 Dynamic games with driving style estimation

With the integration of driver's psychological thinking and behavioral mode, driving style reflects comparatively stable, long-term, and intrinsic behavioral tendencies[2]. Under the optimization scheme, human drivers make decisions by balancing the different utility terms over the future. Depending on the driving tasks and incentives, different drivers may concentrate more on different terms, thus exhibiting disparate interactive styles with their surroundings, such as aggressive, conservative, courtesy, and selfishness[111]. Aggressive driving style takes some risks to pursue the driving goal with violent or frequent acceleration and deceleration, and exhibits relatively more radical driving behavior for the right-of-way. In a conservative driving style, safety takes precedence over driving goals in this style, resulting in more conservative acceleration and deceleration. This style usually shows a tendency to stay in the current lane or give way to other vehicles. Moderate driving style lies somewhere in between. For this reason, the interactive styles can be formulated as the weighted outcomes of different features in generating trajectories. When human driving behavior is modeled, driver data is collected to rank objective functions from trajectories[75], or learn the weights of such features, using IRL[55,70], bi-level optimization[49], simulated moments[50], and maximum likelihood[114].

To model mathematical interaction accurately, real-world human behavior was extracted from a naturalistic driving dataset, based on which the driving style of the human participant was estimated[79]. Further, a planning and decision-making framework was proposed by formulating the problem as a LQ differential game. A human-like game theoretic controller was developed to determine the optimal timing and acceleration for LC where AVs interacted with HVs by a small lateral move to imitate human behavior[23]. To ensure the complete information of the game, the aggressiveness of HVs was estimated first based on their reaction. Considering the several SVs within the game scope, Stackelberg games were constantly built and solved by the proposed game-based MPC to select the interactive vehicle. The vehicle's aggressiveness was then estimated online according to its interactive behavior, followed by the execution of LC maneuvers through MPC[43]. Regarding the time and effort spent on real-world driving tests, a game theoretic traffic model with reasonable fidelity was presented, incorporating interaction to test performance and calibrate parameters of various AV decision-making and control systems[63]. Additionally, a game theoretic traffic model with heterogeneous driving styles was designed to model interactions at unsignalized intersections for virtual testing, performance evaluation, and parameter calibration of AV automation systems[20].

6.2.2 Dynamic games with intention estimation

In addition to driving styles, driving behavior is also affected by the short-term interactive features usually represented by certain parameters related to acceleration or speed[30,31,58]. For the lane-merging task in dense traffic, the HDVs' intentions were inferred from their behaviors, such as speed changes of the human driver in the next lane. The predicted reaction of the interacting HDV was then introduced in the Stackelberg-based decision-making strategy to determine whether the AV should merge or not[110]. Due to the priori uncertain driving intentions, the interaction between vehicles was modeled as a partially observable Stackelberg game. SVs' intentions were recognized online by observed trajectories; thus, their desired trajectories were

predicted[53]. Under the framework of Markov, intent uncertainties were modeled as latent variables. Furthermore, a novel decision-making algorithm based on a partially observable leader-follower game was presented to model the interaction and a receding-horizon optimization-based control strategy was proposed to simultaneously achieve safety and liveness with the adaptation to online estimated other vehicles' driving intents[58]. Nash game theoretical structure was created to predict the trajectories of human actors[115].

6.2.3 Dynamic games with sociality estimation

Recent studies have begun integrating social interaction concepts from human sociology into AV-HV interactions. Wang *et al.* performed a quantitative analysis of merging behavior to extract courteous and rude social interaction scenarios by virtue of the social preference of other agents[111]. Building on this, two instructive mechanisms for developing an interactive decision-making approach were identified: incorporating social preferences and selecting relevant variables during the decision-making process. In order to realize smooth interaction and the consequent human-expected driving decision, social compatibility was represented by social fitness and reciprocal altruism in the proposed game theory-based decision method[90]. As one of the social preferences, Social Value Orientation (SVO) reflects the preference of utility assignment between the ego agent and the other agents, which could be used to anticipate cooperative motives and negotiation strategies[17,71–74,112,113]. In[17], SVO was represented in angular notation and regarded as the one that best matched predicted trajectories to the actual human driver trajectories. The recognized SVO was then combined with a human-imitating control policy to improve social compliance of AVs in mixed transportation. To adeptly and dynamically measure surrounding agents' social tendencies during interaction, a novel metric named interaction orientation (IO) was defined as a quantified prediction of the probability that an interaction object will exhibit certain behaviors[32]. IO was predicated on environmental contexts and trajectory motion characteristics observed over a time period, based on which a mixed-strategy game model combined with a dynamic optimization framework was deployed to learn from expert human driving policies and make informed, social coherent decisions.

6.3 Summary

To address uncertainties and enhance the learning capabilities of AVs, MDP and level-k reasoning are incorporated with game theory. Although more advanced Multi-Agent Reinforcement Learning (MARL) algorithms have been explored, most researchers still rely on basic deep RL algorithms such as deep Q networks[94–96]. Obviously, the application of MARL to the autonomous driving domain has lagged behind the fast evolving technique, which may affect the algorithm's performance in more complex problems involving multiple agents. To integrate seamlessly into human-dominated traffic, it is essential for AVs to understand HDVs' intentions correctly and make human-like decisions. Quantifying and modeling personal social characteristics in the decision-making and control algorithms is expected to improve autonomous driving safety and passenger acceptance[116].

7. CONCLUSION AND OUTLOOK

This paper discusses the definition of social interaction in road traffic and reviews the game theoretic decision-making and control methods considering social interaction. Based on the above systematic analysis, the dominant implications of social interactions can be summarized as the following attributes, i.e., (1) dynamics; (2) measurability; (3) time-varying nature; (4) uncertainty; (5) real time considerations; and (6) decision-making. Instructed by these features, we construct the development framework for human-like game theoretic decision-making methods with adaptation in Figure 9.

The method development begins with the social driving features estimation module, which performs online measurements of social features based on observed trajectories. The representation parameters are then transmitted to the planning and prediction module for further behavior prediction and motion control. Then, the

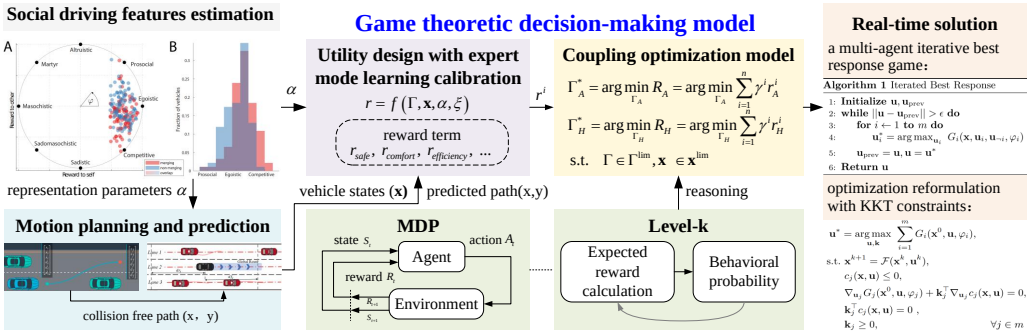


Figure 9. Development framework of human-like decision-making and control methods. Methods for estimating social driving features and providing real-time solutions[17]. α, $\mathbf{x}$, Γ, ξ and γ denote characterization parameters for social interaction, the vehicle state matrix, strategy set for game, stochastic disturbance, and the future discount factor, respectively.

utility function is designed based on the information of predicted vehicle states and social driving features considering safety, comfort and traveling efficiency. Usually, expert mode learning is adopted to derive driving patterns from real expert data for high fidelity. Additionally, MDP and learning methods could be combined with game theory to model interaction uncertainties and cognitive reasoning, respectively. Finally, to resolve the high computational complexity induced by multi-agent interdependence and continuous state space, a real-time calculation method is required for the complex optimization model, further guaranteeing the real-time decision. With these function modules, the automated decision-making system developed based on game theory and learning methods achieves a certain level of humanness, but has not yet reached the performance level of an experienced driver. Despite the progress made, some unresolved issues remain, and the corresponding future study directions are presented.

(1) **Implicit interaction mechanism:** In dynamic traffic environments, human drivers intentionally or unintentionally convey signaling information to one another through their movements and spatial cues, giving rise to both explicit and implicit communication[12,117]. However, current implicit communication methods lack relevant theoretical support to demonstrate the accurate and effective delivery of communication information. Besides, the decision-making and behavioral patterns of human drivers are influenced by the diversity of interaction situations and traffic environments. However, existing studies often focus on specific interaction scenarios. Consequently, aiming to discover insights that may facilitate the development of human-like decision algorithms, the future investigation can explore the theoretical models of implicit communication and the adequate understanding of the underlying mechanisms of human interactive behavior.

(2) **Social optima-based decision and control framework:** Game theoretical models have solid psychological and behavioral foundations, and their behavioral decision-making logic is clear and interpretable. Nevertheless, algorithmic designers tend to program AVs for individual welfare, such as the ride comfort and traveling efficiency of the ego vehicle, with no incentive for improved traffic performance. These individualistic control models may induce suboptimal traffic flow or even traffic safety issues[118]. Thus, a socially optimal control scheme needs to be devised for city planners to guide autonomous driving technology toward social optima.

(3) **Real-time cluster decision-making considering interaction:** A key advantage of game theoretic solutions for decision-making problems is the ability to address planning and prediction for agents in a given situation. However, as the number of agents and the time horizon grow, the computational burden increases, which necessitates a trade-off in terms of computation. To scale the decision-making methods to scenarios involving

a large number of AVs, real-time solving algorithms need to be developed.

(4) Personalized and human-like decision-making: The existing game theoretic decision model could account for a single heterogeneous factor. However, drivers are highly heterogeneous because of personal preference, randomness or aggressiveness, and driving experience. For human drivers, the heterogeneities are manifested in different capabilities and risk profiles while in varied acceleration/braking capacities and manufacturer's choice of risk tolerance in the case of self-driving cars[119]. To achieve personalized requirements, an accurate and real-time estimation of SVs' driving characteristics is needed. Besides, a robust model with comprehensive consideration of heterogeneous features needs further development for predicting a distribution of actions that is consistent with real-world observations.

(5) Self-learning and self-evolving interactive decision-making for real-world applications: The mixed transportation, composed of AVs, HDVs, other road users and road traffic environments, is a dynamically coupled system, which exhibits dynamicity and randomness. However, most of the existing interactive models have only been validated on limited datasets or are still in the stage of laboratory validation, lacking extensive engineering practice. Hence, the game theoretic models need to be further refined and extensively verified on a large number of real datasets in the future. Additionally, as for a multi-agent system, a social learning scheme allows independent agents to learn through interactions with agents randomly selected from a pool[94,120]. Such a scheme is vital for AVs to navigate complex traffic environments with numerous road users, which deserves more exploration.

DECLARATIONS

Authors' contributions

Performed references search, research and analysis, and article writing: Chen Q
Provided technical support: Zhao D, Yang M, Shi Y
Made substantial contributions to conception and design of the study: Liu C

Availability of data and materials

Not applicable.

Financial support and sponsorship

The authors greatly appreciate the National Natural Science Foundation of China (Grant No. 52102444), the Open Foundation of National Key Laboratory of Multi-perch Vehicle Driving Systems (Grant No. QDXT-WY-202407-16), the Zhiyuan Laboratory (Grant No. ZYL2024019), the Major Program of University Natural Research Program of Anhui Province (Grant No. 2022AH040278), and the Central Guidance on Local Science and Technology Development Fund of Hebei Province (Grant No. 226Z2204G).

Conflicts of interest

Liu C is a Junior Editorial Board Member of the journal *Complex Engineering Systems* and Guest Editor of the Special Issue of "Generalized Dynamics Modeling and Dynamics Control of Autonomous Driving Vehicle". He is not involved in any steps of editorial processing, notably including reviewers' selection, manuscript handling and decision-making, while the other authors have declared that they have no conflicts of interest.

Ethical approval and consent to participate

Not applicable.

Consent for publication

Not applicable.

Copyright

© The Author(s) 2024.

REFERENCES

1. NHTSA. Critical Reasons for Crashes Investigated in the National Motor Vehicle Crash Causation Survey; 2018. Available from: https://crashstats.nhtsa.dot.gov/Api/Public/ViewPublication/812506.
2. Zhang T, Zhan J, Shi J, Xin J, Zheng N. Human-like decision-making of autonomous vehicles in dynamic traffic scenarios. *IEEE-CAA J Automatic* 2023;10:1905–17. DOI Pubmed
3. Hafner MR, Cunningham D, Caminiti L, Del Vecchio D. Cooperative collision avoidance at intersections: algorithms and experiments. *IEEE Trans Intell Transp Syst* 2013;14:1162–75. DOI Pubmed
4. Dario B. Game theory: models, numerical methods and applications. *Found Trends Syst Co* 2014;1:379–522. DOI Pubmed
5. Ramos M, Moura M, Lins I, Ramos F. The Use of Game Theory for Autonomous Systems Safety: An Overview. In: Castanier B, Cepin M, Bigaud D, Berenguer C, editors. ESREL 2021: Proceedings of the 31st European Safety and Reliability Conference; 2021 Sep; Angers, Ireland. Singapore: Research Publishing; 2021. pp. 2494–501.
6. Qurashi JM, Ikram MJ, Jambi K, Eassa FE, Khemakhem M. Autonomous Vehicles: Security Challenges and Game theory-based Countermeasures. In: 2023 1st International Conference on Advanced Innovations in Smart Cities (ICAISC); 2023 Jan 23-25; Jeddah, Saudi Arabia. USA: IEEE; 2023. pp. 1–6.
7. Li Y. A review of how game theory is applied in transportation analysis. In: Proceedinds of 2022 5th International Conference on Financial Management, Education and Social Science (FMESS 2022); 2022 Sep 3-5; Hohhot, China. UK: Cambridge Scholars Publishing; 2022. pp. 321–29.
8. Di X, Shi R. A survey on autonomous vehicle control in the era of mixed-autonomy: From physics-based to AI-guided driving policy learning. *Transport Res Part C: Emerg Technol* 2021;125:103008. DOI Pubmed
9. Ji A, Levinson D. A review of game theory models of lane changing. *Transportmetrica A* 2020;16:1628–47. DOI
10. Rune E. A review of game-theoretic models of road user behavior. *Accid Anal Prev* 2014;62:388–96. DOI Pubmed
11. Wang W, Wang L, Zhang C, Liu C, Sun L. Social interactions for autonomous driving: A review and perspectives. *Foundations and Trends in Robotics* 2022;10:198–376. DOI Pubmed
12. Kauffmann N, Winkler F, Naujoks F, Vollrath M. What Makes a Cooperative Driver?" Identifying parameters of implicit and explicit forms of communication in a lane change scenario. *Transport Res Part F: traffic psychology and behavior* 2018;58:1031–42. DOI
13. Markkula G, Madigan R, Nathanael D, Portouli E, Lee Y, et al. Defining interactions: a conceptual framework for understanding interactive behavior in human and automated road traffic. *Theor Iss Ergon Sci* 2020;21:728–52. DOI
14. Choudhury CF, Ben-Akiva ME, Toledo T, Lee G, Rao A. Modeling cooperative lane changing and forced merging behavior. In: 86th Annual Meeting of the Transportation Research Board; 2007 Jan; Washington, DC; 2007. pp. 1–23.
15. Risser R. Behavior in traffic conflict situations. *Accid Anal Prev* 1985;17:179–97. DOI
16. Domeyer J, Dinparastdjadid A, Lee JD, Douglas G, Alsaid A, et al. Proxemics and kinesics in automated vehicle–pedestrian communication: Representing ethnographic observations. *Accid Anal Prev* 2019;2673:70–81. DOI
17. Schwarting W, Pierson A, Alonso-Mora J, Karaman S, Rus D. Social behavior for autonomous vehicles. *Proceedings of the National Academy of Sciences* 2019;116:24972–78. DOI
18. Roy D, Winkler D, Mohan C, Fukuda A. Detection of Collision-Prone Vehicle Behavior at Intersections using Siamese Interaction LSTM. *IEEE Transactions on Intelligent Transportation Systems* 2022;23:1031–42. DOI
19. Li N, Yao Y, Kolmanovsky I, Atkins E, Girard AR. Game-theoretic modeling of multi-vehicle interactions at uncontrolled intersections. *IEEE Trans Intell Transp Syst* 2020;23:1428–42. DOI
20. Tian R, Li N, Kolmanovsky I, Yildiz Y, Girard AR. Game-theoretic modeling of traffic in unsignalized intersection network for autonomous vehicle control verification and validation. *IEEE Trans Intell Transp Syst* 2020;23:2211–26. DOI
21. Crosato L, Tian K, Shum H, Shum H, Ho E. Social Interaction-Aware Dynamical Models and Decision-Making for Autonomous Vehicles. *Adv Intell Syst* 2024;6:2300575. DOI
22. Tabone W, de Winter J, Ackermann C, Bärgman J, Baumann M, et al. Vulnerable road users and the coming wave of automated vehicles: Expert perspectives. *Transp Res Interdiscip Persp* 2021;9:100293. DOI
23. Yu H, Tseng HE, Langari R. A human-like game theory-based controller for automatic lane changing. *Transport Res C-EMER* 2018;88:140–58. DOI
24. Zhang Y, Hang P, Huang C, Lv C. Human-Like Interactive Behavior Generation for Autonomous Vehicles: A Bayesian Game-Theoretic Approach with Turing Test. *Adv Intell Syst* 2022;4:2100211. DOI
25. Chen X, Sun J, Ma Z, Sun J, Zheng Z. Investigating the long-and short-term driving characteristics and incorporating them into car-following models. *Transport Res Part C: Emerg Technol* 2020;117:102698. DOI Pubmed
26. Hang P, Lv C, Huang C, Cai J, Hu Z, et al. An integrated framework of decision making and motion planning for autonomous vehicles considering social behaviors. *IEEE Trans Veh Technol* 2020;69:14458–69. DOI

27. Hang P, Lv C, Xing Y, Huang C, Hu Z. Human-like decision making for autonomous driving: A noncooperative game theoretic approach. *IEEE Trans Intell Transp Syst* 2020;22:2076–87. DOI
28. Liu M, Wan Y, Lewis FL, Nageshrao S, Filev D. A three-level game-theoretic decision-making framework for autonomous vehicles. *IEEE Trans Intell Transp Syst* 2022;23:20298–308. DOI
29. Hang P, Huang C, Hu Z, Lv C. Decision Making for Connected Automated Vehicles at Urban Intersections Considering Social and Individual Benefits. *IEEE Trans Intell Transp Syst* 2022;23:22549–62. DOI Pubmed
30. Li D, Liu G, Xiao B. Human-like driving decision at unsignalized intersections based on game theory. *P I Mech Eng D-J Aut* 2023;237:159–73. DOI
31. Sagberg F, Selpi, Bianchi Piccinini GF, Engström J. A review of research on driving styles and road safety. *Human factors* 2015;57:1248–75. DOI
32. Liu J, Qi X, Hang P, Sun J. Enhancing Social Decision-making of autonomous vehicles: A mixed-strategy game approach with interaction orientation identification. *IEEE Trans Veh Technol* 2024;73:12385–98. DOI
33. Negash N, Yang J. Driver Behavior Modeling Toward Autonomous Vehicles: Comprehensive Review. *IEEE Access* 2023;11:22788–821. DOI
34. Qin Z, Ji A, Sun Z, Wu G, Hao P, et al. Game Theoretic Application to Intersection Management: A Literature Review. *IEEE Transactions on Intelligent Vehicles* 2024:1–19. DOI
35. Farooqui AD, Niazi MA. Game theory models for communication between agents: a review. *Complex Adapt Syst Model* 2016;4:1–31. DOI
36. Li J, Niazi D, Zhang M. Equilibrium modeling of mixed autonomy traffic flow based on game theory. *Transportation Research Part B: Methodological* 2022;166:110–27. DOI
37. Nan J, Deng W, Zheng B. Intention Prediction and Mixed Strategy Nash Equilibrium-Based Decision-Making Framework for Autonomous Driving in Uncontrolled Intersection. *IEEE Transactions on Vehicular Technology* 2022;71:10316–26. DOI
38. Yoo JH, Langari R. Stackelberg game based model of highway driving. In: ASME 2012 5th Annual Dynamic Systems and Control Conference joint with the JSME 2012 11th Motion and Vibration Conference; 2012 Oct 17–19; Florida, USA. USA: ASME; 2012. pp. 499–508.
39. Yoo JH, Langari R. A stackelberg game theoretic driver model for merging. In: Proceedings of the ASME 2013 Dynamic Systems and Control Conference; 2013 Oct 21-23; Palo Alto, California, USA. USA: ASME; 2013. p. V002T30A003.
40. Kim C, Langari R. Game theory based autonomous vehicles operation. *Int J Vehicle Des* 2014;65:360–83. DOI
41. Coskun S, Zhang Q, Langari R. Receding horizon markov game autonomous driving strategy. In: 2019 American Control Conference (ACC); 2019 Jul 10-12; Philadelphia, PA, USA. USA: IEEE; 2019. pp. 1367–1374.
42. Yoo J, Langari R. A predictive perception model and control strategy for collision-free autonomous driving. *IEEE Trans Intell Transp Syst* 2019;20:4078–91. DOI
43. Zhang Q, Langari R, Tseng HE, Filev D, Szwabowski S, et al. A game theoretic model predictive controller with aggressiveness estimation for mandatory lane change. *IEEE Trans Intelligent Vehicles* 2019;5:75–89. DOI
44. Yoo J, Langari R. A game-theoretic model of human driving and application to discretionary lane-changes; 2020. ArXiv preprint arXiv:2003.09783.
45. Yoo J, Langari R. A Stackelberg Game Theoretic Model of Lane-Merging; 2020. 10.48550/arXiv.2003.09786.
46. Zhang Q, Filev D, Tseng HE, Szwabowski S, Langari R. A game theoretic four-stage model predictive controller for highway driving. In: 2019 American Control Conference (ACC); 2019 Jul 10-12; Philadelphia, PA, USA. USA: IEEE; 2019. pp. 1375–1381.
47. Zhang Q, Filev D, Tseng HE, Szwabowski S, Langari R. Addressing Mandatory Lane Change Problem with Game Theoretic Model Predictive Control and Fuzzy Markov Chain. In: 2018 Annual American Control Conference (ACC); 2010 Jun 27-29; Milwaukee, WI, USA. USA: IEEE; 2018. pp. 4764–71.
48. Banjanovic-Mehmedovic L, Halilovic E, Bosankic I, Kantardzic M, Kasapovic S. Autonomous vehicle-to-Vehicle (V2V) decision making in roundabout using game theory. *International journal of advanced computer science and applications* 2016;7. DOI
49. Liu H, Xin W, Adam Z, Ban J. A game theoretical approach for modeling merging and yielding behavior at freeway on-ramp sections. *Transport Traffic Theory* 2007;3:197–211.
50. Talebpour A, Mahmassani HS, Hamdar SH. Modeling lane-changing behavior in a connected environment: A game theory approach. *Transport Res Procedia* 2015;7:420–40. DOI
51. Liu C, Tomizuka M. Safe exploration: Addressing various uncertainty levels in human robot interactions. In: 2015 American Control Conference (ACC); 2015 Jul 01-03; Chicago, IL, USA. USA: IEEE; 2015. pp. 465–70.
52. Liu C, Tomizuka M. Enabling safe freeway driving for automated vehicles. In: American Control Conference (ACC); 2016 Jul 06-08; Boston, MA, USA. USA: IEEE; 2016. pp. 3461–3467.
53. Liu K, Li N, Tseng HE, Kolmanovsky I, Girard A. Interaction-aware trajectory prediction and planning for autonomous vehicles in forced merge scenarios. *IEEE Trans Intell Transp Syst* 2022;24:474–88. DOI
54. Sadigh D, Landolfi N, Sastry SS, Seshia SA, Dragan AD. *Planning for cars that coordinate with people: leveraging effects on human actions for planning and active information gathering over human internal state* 2018;42:1405–1426. DOI
55. Sun L, Zhan W, Tomizuka M, Dragan AD. Courteous autonomous cars. In: 2018 IEEE/RSJ International Conference on Intelligent Robots and Systems (IROS); 2018 Oct 01-05; Madrid, Spain. USA: IEEE; 2018. pp. 663–670.
56. Murgovski N, de Campos G, Sjoberg J. Convex modeling of conflict resolution at traffic intersections. In: 2015 54th IEEE conference on decision and control (CDC); 2015 Dec 15-18; Osaka, Japan. USA: IEEE; 2015. pp. 4708–13.

57. Liu C, Lin CW, Shiraishi S, Tomizuka M. Distributed conflict resolution for connected autonomous vehicles. *IEEE Trans Veh Technol* 2017;3:18–29. DOI
58. Liu K, Li N, Tseng HE, Kolmanovsky I, Girard A, et al. Cooperation-aware decision making for autonomous vehicles in merge scenarios. In: 2021 60th IEEE Conference on Decision and Control (CDC); 2021 Dec 14-17; Austin, TX, USA. USA: IEEE; 2021. pp. 5006–12.
59. Espinoza JLV, Liniger A, Schwarting W, Rus D, Van Gool L. Deep Interactive Motion Prediction and Planning: Playing Games with Motion Prediction Models. In: Proceedings of The 4th Annual Learning for Dynamics and Control Conference; 2022 Jun 23-24. New York: PMLR; 2022. pp. 1006–1019.
60. Ozkan MF, Ma Y. Socially Compatible Control Design of Automated Vehicle in Mixed Traffic. *IEEE Control Systems Letters* 2022;6:1730–35. DOI Pubmed
61. Oyler DW, Yildiz Y, Girard AR, Li NI, Kolmanovsky IV. A game theoretical model of traffic with multiple interacting drivers for use in autonomous vehicle development. In: 2016 American Control Conference (ACC); 2016 July 6-8; Boston, MA, USA. USA: IEEE; 2016. pp. 1705–10.
62. Li N, Oyler D, Zhang M, Yildiz Y, Girard A, et al. Hierarchical reasoning game theory based approach for evaluation and testing of autonomous vehicle control systems. In: 2016 IEEE 55th Conference on Decision and Control (CDC); 2016 Dec 12-14; Las Vegas, NV, USA. USA: IEEE; 2016. pp. 727–33.
63. Li N, Oyler DW, Zhang M, Yildiz Y, Kolmanovsky I, et al. Game theoretic modeling of driver and vehicle interactions for verification and validation of autonomous vehicle control systems. *IEEE Trans Contr Syst Technol* 2017;26:1782–97. DOI
64. Wilde GJ. Social interaction patterns in driver behavior: An introductory review. *Human factors* 1976;18:477–92. DOI
65. Wilde GS. Immediate and delayed social interaction in road user behaviour. *Applied Psychology* 1980;29:439–60. DOI
66. Jia S, Zhang Y, Li X, Na X, Wang Y, et al. Interactive Decision-Making With Switchable Game Modes for Automated Vehicles at Intersections. *IEEE Transactions on Intelligent Transportation Systems* 2023;24:11785–99. DOI
67. Huang S, Chan S, Ren W. Mixed traffic control involving manually-controlled and automatically-controlled vehicles in IVHS. *Advances in Intelligent Autonomous Systems* 1999;18:507–528. DOI
68. Tian R, Li S, Li N, Kolmanovsky I, Girard A, et al. Adaptive Game-Theoretic Decision Making for Autonomous Vehicle Control at Roundabouts. In: 2018 IEEE Conference on Decision and Control (CDC); 2018 Dec 17-19; Miami, FL, USA. USA: IEEE; 2018. pp. 321–26.
69. Li N, Kolmanovsky I, Girard A, Yildiz Y. Game theoretic modeling of vehicle interactions at unsignalized intersections and application to autonomous vehicle control. In: 2018 Annual American Control Conference (ACC); 2018 Jun 27-29; Milwaukee, WI, USA. USA: IEEE; 2018. p. V002T30A003.
70. Sun L, Zhan W, Tomizuka M. Probabilistic prediction of interactive driving behavior via hierarchical inverse reinforcement learning. In: 2018 21st International Conference on Intelligent Transportation Systems (ITSC); 2018 Nov 04-07; Maui, HI, USA. USA: IEEE; 2018. pp. 2111–17.
71. McClintock CG, Allison ST. Social value orientation and helping behavior. *J Appl Soc Psychol* 1989;19:353–62. DOI
72. Zhao X, Tian Y, Sun J. Yield or Rush? Social-Preference-Aware Driving Interaction Modeling Using Game-Theoretic Framework. In: 2021 IEEE International Intelligent Transportation Systems Conference (ITSC); 2021 Sep 19-22; Indianapolis, IN, USA. USA: IEEE; 2021. p. 453–459.
73. Toghi B, Valiente R, Sadigh D, Pedarsani R, Fallah YP. Social Coordination and Altruism in Autonomous Driving. *IEEE Trans Intell Transp Syst* 2022;23:24791–804. DOI Pubmed
74. Toghi B, Valiente R, Sadigh D, Pedarsani R, Fallah Y. Altruistic Maneuver Planning for Cooperative Autonomous Vehicles Using Multi-agent Advantage Actor-Critic; 2021. ArXiv preprint arXiv:2107.05664.
75. Lee N, Choi W, Vernaza P, Choy CB, Torr PH, et al. Desire: Distant future prediction in dynamic scenes with interacting agents. In: Proceedings of the IEEE conference on computer vision and pattern recognition(CVPR); 2017; Honolulu, HI, USA. USA: IEEE; 2017. pp. 336–45.
76. Fisac JF, Bronstein E, Stefansson E, Sadigh D, Sastry SS, et al. Hierarchical game-theoretic planning for autonomous vehicles. In: 2019 International Conference on Robotics and Automation (ICRA); 2010 May 20-24; Montreal, QC, Canada. USA: IEEE; 2019. pp. 9590–9596.
77. Liu M, Tseng HE, Filev D, Girard A, Kolmanovsky I. Safe and human-like autonomous driving: A predictor-corrector potential game approach. *IEEE Trans Contr Syst Technol* 2024;32:834–48. DOI
78. Wang M, Hoogendoorn SP, Daamen W, van Arem B, Happee R. *Game theoretic approach for predictive lane-changing and car-following control* .
79. Shu K, Mehrizi RV, Li S, Pirani M, Khajepour A. Human inspired autonomous intersection handling using game theory. *IEEE Trans Intell Transp Syst* 2023;24:11360–71. DOI
80. Fridovich-Keil D, Ratner E, Peters L, Dragan AD, Tomlin CJ. Efficient iterative linear-quadratic approximations for nonlinear multi-player general-sum differential games. In: 2020 IEEE Int. Conf. Robot. Autom. (ICRA); 2020 May 31; Paris, France. USA: IEEE; 2020. pp. 1475–81.
81. Fridovich-Keil D, Ratner E, Peters L, Tomlin CJ. An iterative quadratic method for general-sum differential games with feedback linearizable dynamics. In: 2020 IEEE Int. Conf. Robot. Autom. (ICRA); 2020 May 31; Paris, France. USA: IEEE; 2020. p. 2216–2222.
82. Li S, Li N, Girard A, Kolmanovsky I. Decision making in dynamic and interactive environments based on cognitive hierarchy theory, Bayesian inference, and predictive control. In: 2019 IEEE 58th Conference on Decision and Control (CDC); 2019 December 11-13; Nice, France. USA: IEEE; 2019. pp. 2181–87.

83. Liu M, Kolmanovsky I, Tseng HE, Huang S, Filev D, et al. Potential Game-based decision-making for autonomous driving. *IEEE Trans Intell Transp Syst* 2023;24:8014–27. DOI
84. Ozkan MF, Ma Y. Socially-compatible behavior design of autonomous vehicles with verification on real human data. *IEEE Robotics and Automation Letters* 2021;6:3421–28. DOI Pubmed
85. Lopez VG, Lewis FL, Liu M, Wan Y, Nageshrao S, et al. Game-Theoretic Lane-Changing Decision Making and Payoff Learning for Autonomous Vehicles. *IEEE Trans Veh Technol* 2022;71:3609–20. DOI Pubmed
86. Li D, Zhang J, Liu G. Autonomous Driving Decision Algorithm for Complex Multi-Vehicle Interactions: An Efficient Approach Based on Global Sorting and Local Gaming. *IEEE Transactions on Intelligent Transportation Systems* 2024;25:6927–37. DOI
87. Sadigh D, Sastry S, Seshia SA, Dragan AD. Planning for autonomous cars that leverage effects on human actions. *Robotics: Science and systems* 2016;2:1–9.
88. Lazar DA, Pedarsani R, Chandrasekher K, Sadigh D. Maximizing road capacity using cars that influence people. In: 2018 IEEE Conference on Decision and Control (CDC); 2018 Dec 17–19; Miami, FL, USA. USA: IEEE; 2018. pp. 1801–8.
89. Hubmann C, Becker M, Althoff D, Lenz D, Stiller C. Decision making for autonomous driving considering interaction and uncertain prediction of surrounding vehicles. In: Proc. 2017 IEEE Intelligent Vehicles Symposium; 2017 Jun 11-14; Los Angeles, CA, USA. USA: IEEE; 2017. pp. 1671–78.
90. Li D, Liu A, Pan H, Chen W. Safe, efficient and socially-compatible decision of automated vehicles: A case study of unsignalized intersection driving. *Automotive Innovation* 2023;6:281–96. DOI
91. Jain G, Kumar A, Bhat SA. Recent developments of game theory and reinforcement learning approaches: A systematic review. *IEEE Access* 2024;12:9999–0011. DOI Pubmed
92. Sutton R, Barto A. Introduction to Reinforcement Learning. 1st ed. Cambridge: MIT Press; 1998.
93. Zhang L, Han S, Grammatico S. Automated Lane Merging via Game Theory and Branch Model Predictive Control. *IEEE Transactions on Control Systems Technology* 2024:1–12. DOI
94. Chen X, Li Z, Di X. Social Learning In Markov Games: Empowering Autonomous Driving. In: 2022 IEEE Intelligent Vehicles Symposium (IV). USA: IEEE; 2022. pp. 78–483.
95. Li W, Qiu F, Li L, Zhang Y, Wang K. Simulation of Vehicle Interaction Behavior in Merging Scenarios: A Deep Maximum Entropy-Inverse Reinforcement Learning Method Combined With Game Theory. *IEEE Transactions on Intelligent Vehicles* 2024;9:1079–93. DOI
96. Zhou X, Peng Z, Xie Y, Liu M, Ma J. Game-Theoretic Driver Modeling and Decision-Making for Autonomous Driving with Temporal-Spatial Attention-Based Deep Q-Learning. *IEEE Transactions on Intelligent Vehicles* 2024:1–17. DOI
97. Littman ML. Markov games as a framework for multi-agent reinforcement learning. In: Machine learning proceedings. Amsterdam: Elsevier; 1994. pp. 157–63.
98. Liu C, Lin CW, Shiraishi S, Tomizuka M. Improving efficiency of autonomous vehicles by v2v communication. In: 2018 Annual American Control Conference (ACC); 2018 Jun 27-29; Milwaukee, WI, USA. USA: IEEE; 2018. pp. 4778–4783.
99. Li N, Girard A, Kolmanovsky I. Stochastic predictive control for partially observable markov decision processes with time-joint chance constraints and application to autonomous vehicle control. *J Dyn Sys, Meas, Control* 2019;141:071007. DOI
100. Qiao Z, Muelling K, Dolan J, PNovalanisamy P, Mudalige P. Pomdp and hierarchical options MDP with continuous actions for autonomous driving at intersections. In: Proc. 21st Int. Conf. Intelligent Transportation Systems; 2018 Nov 04-07; Maui, HI, USA. USA: IEEE; 2018. pp. 2377–82.
101. Cunningham AG, Galceran E, Mehta D, Ferrer G, Eustice RM, et al. Mpdm: Multi-policy decision-making from autonomous driving to social robot navigation. 1st ed. Cham: Springer International Publishing; 2019.
102. Nishi T, Doshi P, Prokhorov D. Merging in congested freeway traffic using multipolicy decision making and passive actor-critic learning. *IEEE Trans Intelligent Vehicles* 2019;4:287–97. DOI
103. Sadigh D, Sastry SS, Seshia SA. Verifying robustness of human-aware autonomous cars. *IFAC-PapersOnLine* 2019;51:131–38. DOI
104. Sankar GS, Han K. Adaptive robust game-theoretic decision making strategy for autonomous vehicles in highway. *IEEE Trans Veh Technol* 2020;69:14484–93. DOI
105. Ho J, Ermon S. Generative Adversarial Imitation Learning. In: Lee D, Sugiyama M, Luxburg U, Guyon I, Garnett R, editors. Advances in Neural Information Processing Systems. Curran Associates, Inc.; 2016. .
106. Treiber M, Hennecke A, Helbing D. Congested traffic states in empirical observations and microscopic simulations. *Physical Rev E* 2000;62:1805–24. DOI
107. Makaba T, Doorsamy W, Paul B. Bayesian network-based framework for cost-implication assessment of road traffic collisions. *Int J ITS Res* 2021;19:240–53. DOI
108. Talebpour A, Mahmassani HS, Hamdar SH. Multiregime sequential risk-taking model of car-following behavior: Specification, calibration, and sensitivity analysis. *Transportation research record* 2011;2260:60–66. DOI
109. Wei C, He Y, Tian H, Lv Y. Game theoretic merging behavior control for autonomous vehicle at highway on-ramp. *IEEE Transactions on Intelligent Transportation Systems* 2022;23:21127–36. DOI
110. Ji K, Orsag M, Han K. Lane-Merging Strategy for a Self-driving car in dense traffic using the stackelberg game approach. *Electronics* 2021;10:894. DOI
111. Wang H, Wang W, Yuan S, Li X, Sun L. On social interactions of merging behaviors at highway on-ramps in congested traffic. *IEEE Trans Intell Transp Syst* 2021;23:11237–48. DOI
112. De Dreu CK, Van Lange PA. The impact of social value orientations on negotiator cognition and behavior. *Pers Soc Psychol B* 1995;21:1178–88. DOI

113. Pletzer JL, Balliet D, Joireman J, Kuhlman DM, Voelpel SC, et al. Socal value orientation, expectations, and cooperation in social dilemmas: A meta-analysis. *Eur J Personality* 2018;32:62–83. DOI
114. Rahmati Y, Talebpour A. Towards a collaborative connected, automated driving environment: A game theory based decision framework for unprotected left turn maneuvers. In: 2017 IEEE Intelligent Vehicles Symposium (IV); 2017 Jun 11–14; Los Angeles, CA, USA. USA: IEEE; 2017. pp. 1316–21.
115. Rahmati Y, Talebpour A, Mittal A, Fishelson J. Game Theory-Based Framework for Modeling Human–Vehicle Interactions on the Road. *Transportation research record* 2020;2674:701–13. DOI
116. Gkartzonikas C, Gkritza K. What have we learned? A review of stated preference and choice studies on autonomous vehicles. *Transport Res Part C: Emerg Technol* 2019;98:323–37. DOI
117. Lemmer M, Shu J, S S, Hohmann S. Maneuver Based Modeling of Driver Decision Making using Game-Theoretic Planning. In: 2021 IEEE International Conference on Systems Man, and Cybernetics (SMC). USA: IEEE; 2021. p. 1332–1338.
118. Zhu L, Yang D, Cheng Z, Yu X, Zheng B. A Model to Manage the Lane-Changing Conflict for Automated Vehicles Based on Game Theory. *Sustainability* 2023;15:3063. DOI
119. Huang H, Zheng X, Liu Y, Zhao S, Wang Y, et al. Intelligent Adaptive Decision-Making for Autonomous Vehicles: A Learning-Enhanced Game-Theoretic Approach in Interactive Scenarios. In: 2023 3rd International Conference on Digital Society and Intelligent Systems (DSInS). USA: IEEE; 2023. pp. 258–64.
120. Dai S, Bae S, Isele D. *Game Theoretic Decision Making by Actively Learning Human Intentions Applied on Autonomous Driving* 2023:1–6. DOI

Li *et al. Complex Eng Syst* 2024;4:26
DOI: 10.20517/ces.2024.64

Complex Engineering Systems

Review

Open Access

A meta-learning approach for predicting asphalt pavement deflection basin area

Zhuoxuan Li[1,2], Xin Jin[3], Xinli Shi[2,3], Jinde Cao[1,2]

[1]School of Mathematics, Southeast University, Nanjing 210096, Jiangsu, China.
[2]Nanjing Modern Multimodal Transportation Laboratory, Ministry of Transport, Nanjing 211135, Jiangsu, China.
[3]School of Cyber Science and Engineering, Southeast University, Nanjing 210096, Jiangsu, China.

Correspondence to: Prof. Xinli Shi, School of Cyber Science and Engineering, Southeast University, Southeast University Road, No. 2, Nanjing 211189, Jiangsu, China. E-mail: xinli_shi@seu.edu.cn; ORCID: orcid.org/0000-0002-4443-608X

How to cite this article: Li Z, Jin X, Shi X, Cao J. A meta-learning approach for predicting asphalt pavement deflection basin area. *Complex Eng Syst* 2024;4:26. http://dx.doi.org/10.20517/ces.2024.64

Received: 25 Sep 2024 **First Decision:** 12 Nov 2024 **Revised:** 7 Dec 2024 **Accepted:** 24 Dec 2024 **Published:** 31 Dec 2024

Academic Editor: Ding Wang **Copy Editor:** Fangling Lan **Production Editor:** Fangling Lan

Abstract

To address the urgent need for accurate pavement performance modeling in pavement design, this study proposes a meta-learning-based few-shot learning method for predicting the Deflection Basin Area (DBA) of asphalt pavements. The method utilizes features such as pavement temperature and load pressure, and applies cyclic DBA data from various pavement types subjected to different pressures. The objective is to predict the trend of DBA changes over cycles at a specific pressure. By leveraging pre-training on diverse pavement datasets, the proposed meta-learning model reduces the training data required for target pavement DBA prediction, enabling better generalization to the target pavement. This approach enhances DBA prediction accuracy even with a small sample size. Compared to traditional machine learning and pre-training methods using data from a single pavement type, the proposed method achieves a Mean Square Error of 13.26 and a Mean Absolute Error of 2.85, demonstrating superior performance. Furthermore, it achieves high prediction accuracy with fewer iterations. Overall, the proposed method effectively predicts DBA across various pavement structures with a few data.

Keywords: Meta-learning, deflection basin area, pre-training, few-shot learning, time series prediction

© The Author(s) 2024. **Open Access** This article is licensed under a Creative Commons Attribution 4.0 International License (https://creativecommons.org/licenses/by/4.0/), which permits unrestricted use, sharing, adaptation, distribution and reproduction in any medium or format, for any purpose, even commercially, as long as you give appropriate credit to the original author(s) and the source, provide a link to the Creative Commons license, and indicate if changes were made.

1. INTRODUCTION

Highway infrastructure in China has undergone rapid development in recent years, with asphalt pavement (AP) structures being widely adopted across roads of all grades. The majority of these structures use semi-rigid base pavement designs[1]. However, the long-term service of operating highways, subjected to traffic loads and environmental factors, often leads to various degrees of structural damage, including cracking and subsidence. In this context, pavement deflection has emerged as a critical parameter for assessing the bearing capacity of subgrade pavements and plays a pivotal role in evaluating overall pavement conditions[2].

The Falling Weight Deflectometer (FWD) has become the standard tool for non-destructive pavement testing. While FWD detection results contain a wealth of pavement characteristic information, current engineering practices typically rely solely on the maximum deflection at the load center to characterize the surface deflection of the structural layer. This approach, however, underutilizes the comprehensive data provided by FWD testing[3]. Recognizing this limitation, researchers have increasingly focused on establishing correlations between the pavement Deflection Basin Area (DBA) and the structure's bearing capacity. This approach aims to predict pavement usage indicators and evaluate overall structural integrity more comprehensively[4–7]. The DBA, which considers the entire deflection profile rather than a single point, offers a more holistic representation of pavement response to loading.

However, the collection of FWD testing data presents significant challenges. The process is resource-intensive, time-consuming, and costly, making it difficult to conduct repeated measurements across large road networks. These limitations underscore the need for predictive models that can accurately estimate the DBA for various pavement structures without extensive field testing.

Recent advancements in artificial intelligence (AI) have opened new avenues for addressing this challenge. AI methods have been successfully applied across various domains of traffic engineering[8–10], demonstrating their potential for complex prediction tasks. In the context of pavement engineering, AI offers the promise of high-accuracy DBA prediction, potentially revolutionizing how we assess and manage road infrastructure. The motivation behind this research lies in the critical need for more efficient and cost-effective methods of pavement assessment. By developing accurate predictive models for DBA, we aim to enhance the ability of road authorities to monitor pavement conditions, plan maintenance activities, and optimize the allocation of resources. This approach promises to reduce the reliance on extensive field testing and provide a more nuanced understanding of pavement behavior under various conditions.

Despite the potential benefits, achieving high-accuracy DBA prediction remains a significant challenge. This research seeks to address this gap by exploring advanced AI techniques and their application to pavement engineering. By doing so, we aim to contribute to developing more robust and reliable methods for assessing pavement structural integrity, ultimately leading to improved road infrastructure management and longevity. This research aims to develop and design a meta-learning-based prediction model for DBA of APs, which uses measured cyclic data of pavement DBA under different pressures to predict the trend of rebound deflection basin area changes throughout all cycles at a specific pressure. The contributions of this research are as follows.

- This study applies meta-learning algorithms to predict the AP DBA over the entire cycle at a specific pressure for the first time, achieving better performance than traditional machine learning algorithms as measured by Mean Square Error (MSE) and Mean Absolute Error (MAE). These results demonstrate the effectiveness of meta-learning algorithms in small sample regression tasks.
- The proposed meta-learning prediction approach can reduce the need on the amount of target pavement data by reusing relevant data acquired from other pavement structures for training, which is crucial given the challenge of obtaining long-term cyclic data for target pavements in the early stages.
- Compared with the pre-training-based transfer learning method, the proposed meta-learning prediction

uses a limited dataset specific to the target pavement to fine-tune the parameters from pre-training. This strategy not only ensures stability, but also produces better performance in predicting the DBA.

2. RELATED WORK

Machine learning methods can be widely used for data regression prediction tasks[11], and in recent years, they have been increasingly applied to pavement performance prediction tasks. The primary hurdle in pavement performance prediction arises from extracting crucial spatiotemporal features from multidimensional coupled data. Early work, including Artificial Neural Network (ANN)[12], stacked autoencoders[13], and Long Short-term Memory (LSTM)[14], predominantly focused on extracting temporal features but encountered challenges in unveiling latent spatial features within traffic data, leading to suboptimal performance. Yang *et al.*[15] use K-nearest neighbor to characterize crack type and crack width information derived from FWD test data for applied statistical techniques, including ANN and multiple nonlinear regression, to proficiently rut distress in AP using an AP analyzer[16].

Recently, sophisticated learning algorithms have been integrated into engineering modeling applications. Tang *et al.* use genetic algorithms to develop a reverse analysis program that combines finite element analysis and population-based optimization techniques to infer the modulus of the pavement layer[17]. Mabrouk *et al.* use ANNs to calculate the pavement layer modulus as a function of traffic speed deviation, thus predicting the pavement modulus[18]. Zhang *et al.* propose a brand-new framework for predicting time series of ruts, based on multi-level discrete wavelet decomposition and multivariate transfer entropy for feature selection, to achieve higher prediction accuracy[19]. Li *et al.* compare random forest and gradient boosting regression methods for predicting the pavement Asphalt Concrete (AC) layer and use grid search and cross-validation for optimization[20].

In addition, the frequent collection of pavement structure data is very time-consuming, disrupts traffic flow, and is costly, making it hard to duplicate. These factors might contribute to the oversight of pavement structure aspects in maintenance or repair decisions. Consequently, researchers have invested considerable effort in identifying relatively expedient alternative analysis methods to overcome these limitations. Li *et al.* propose a Chaotic Particle Swarm Optimization (CPSO) to optimize the Extreme Gradient Boosting (XGBoost) model, decreasing the frequency of deflection tests while maintaining estimation accuracy[21]. Zhang *et al.* propose a model for predicting ruts based on multi-source transfer entropy and graph neural networks, which can adapt to sufficient predictive performance and the generalization ability of various complex pavement design data[22]. Shen *et al.* employ LSTM to construct a predictive model for estimating the technical condition score of bridge components[23].

Nevertheless, traditional machine learning methods still face a practical challenge: the accuracy of deep learning regression prediction algorithms heavily depends on the availability of a substantial amount of training data[24]. For tasks such as pavement performance prediction, a large volume of pavement structure data is required, which presents a significant drawback. Collecting such extensive data is time-consuming and resource-intensive, but it remains essential for training deep learning models[25,26]. Furthermore, if the pavement structure used for training does not align with the target pavement structure, retraining the model becomes necessary, which again requires considerable time and effort. These issues highlight a major limitation of traditional machine learning methods: developing accurate performance prediction models for various pavement structures demands both significant time and financial investment.

Given these challenges, alternative approaches such as Model-Agnostic Meta-Learning (MAML)[27] have gained attention in the field. MAML is a powerful meta-learning algorithm designed for few-shot learning, and it has demonstrated superior performance in addressing problems with limited data[28–32]. As a member of optimization-based meta-learning algorithms, MAML differs from traditional methods by enabling mod-

els to learn in a way that generalizes quickly to new tasks with minimal data. Other meta-learning algorithms have introduced various modifications for learning weights in task-specific classifiers [33,34]. For example, methods in [35–38] first learn a function to embed the support set and target examples of a few-shot task, and then use the test support set to fine-tune task-specific weights for embedding the target examples. On the basis of meta-learning, Aguiar *et al.* propose selecting meta-features for extracting optimal dataset descriptions, which enhances multi-target regression with high predictive accuracy [39]. Additionally, Jeong *et al.* introduce a meta-learning approach for State-Of-Charge (SOC) estimation in batteries, aiming to reduce the amount of target data needed for training by leveraging deep learning [40]. By overcoming the data limitations inherent in traditional machine learning methods, meta-learning provides a more efficient framework for addressing pavement performance prediction tasks, particularly in situations with scarce or inconsistent data.

Building upon optimization-based meta-learning algorithms, MAML, in particular, has exerted significant influence, inspiring numerous direct extensions in [41–44]. Many of these extensions heavily depend on the foundational structure of the MAML algorithm, encompassing the outer loop (for meta-training) and the inner loop (for task-specific adaptation). However, scant prior research has thoroughly examined the reasons for the success of this core aspect of MAML. To investigate how and why MAML achieves effective few-shot learning [45–47], employs analytical tools such as centered kernel alignment to scrutinize the neural network representations learned by the MAML. This analysis also highlights the proficiency of this algorithm in acquiring practical few-shot learning features.

Meta-learning is sensitive to the choice of initial model parameters. In certain situations, different initial parameters may result in significant performance variations of the model across various tasks. Additionally, the performance of meta-learning may be affected by noise and distribution changes in the input data. When there is considerable noise or shifts in the data distribution within the meta-learning tasks, it can decline the model's generalization performance.

In addition, some robust meta-learning algorithms have been developed for noise rejection. The most effective robust training methods include adversarial training and robustness which establishes a theoretical foundation between accuracy and robustness, and many of their variants such as fast adversarial training methods [48–50], semi-supervised robust training [51,52], adversarial transfer learning. Furthermore, recent research [53–55] has explored the transferability of robustness within the realms of transfer learning and representation learning. Nevertheless, the conventional robust training methods mentioned earlier need to be better suited for MAML in few-shot learning, given the dual optimization characteristics inherent in MAML.

In summary, meta-learning exhibits significant advantages over traditional machine-learning methods when handling small-sample classification and regression tasks. Firstly, meta-learning achieves rapid model adaptation by learning across multiple relevant tasks, enabling it to adjust its parameters to accommodate new tasks quickly. Secondly, meta-learning enhances sample efficiency by acquiring general task-related knowledge, allowing the model to utilize limited samples for learning more effectively. Thirdly, emphasizing the transfer learning concept in meta-learning enables models to share knowledge between tasks, facilitating robust generalization performance. These capabilities represent a notable advantage that traditional machine-learning algorithms lack.

3. FUNDAMENTAL ALGORITHMS

3.1. Gradient boosting decision trees and random forests

Breiman [56] proposed the Random Forests (RF) algorithm, which builds upon the Bagging algorithm by incorporating Bootstrap sampling to construct multiple decision trees. The final prediction of the random forest is made through a majority voting mechanism. The use of Bootstrap sampling enhances the algorithm's accuracy

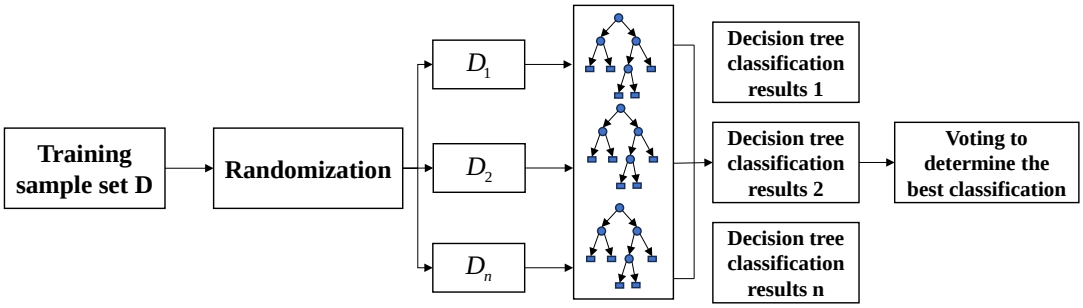


Figure 1. The structure of RF.

and helps mitigate the overfitting issues commonly associated with single decision trees. The structure of RF is shown in Figure 1.

The Gradient Boosting Decision Tree (GBDT)[57] is an ensemble machine learning algorithm based on the Boosting strategy proposed by Friedman. The core idea is to sequentially train multiple weak learners to improve performance iteratively. In each iteration, except for the first decision tree, the objective is to minimize the loss function of the current learner by updating it in the direction of the gradient, ensuring that the loss function decreases with each step. Through continuous iterations, the residuals approach zero, and the results of all trees are combined to generate the final prediction. The specific implementation process of GBDT is as follows:

(1) Initialize weak learner

$$f_0(x) = \text{argmin} \sum_{i=1}^{N} L(y_i, c),$$

where e is the value of the leaf node after the node is divided by the least squares method.

(2) Calculate negative gradient

For each tree $m = 1, 2, \cdots, M$, and for each sample $i = 1, 2, \cdots, N$, calculate the negative gradient, which is the residual:

$$r_{im} = -\left[\frac{\partial L(y_i, f(x_i))}{\partial f(x_i)}\right],$$

where $f(x_i)$ is the predicted value of the weak learner, and y_i is the true value of the weak learner.

The obtained residual is used as the true value of the new sample, and the data (x_i, r_{im}), $i = 1, 2, \cdots, N$, is used as the training data of the next tree to obtain a new regression tree $f_m(x)$, whose corresponding leaf node area is R_{jm}, $j = 1, 2, \cdots, J$ is the number of leaf nodes of the regression tree t, and the best fitting value is calculated for the leaf area $j = 1, 2, \cdots, J$, and we have

$$\gamma_{jm} = \text{argmin} \sum_{x_i \in R_{jm}} L(y_i, f_{m-1}(x_i) + \gamma).$$

Update the strong learner, then we have

$$f_m(x) = f_{m-1}(x) + \sum_{j=1}^{J} \gamma_{jm} I(x \in R_{jm}).$$

Get the final learner

$$f(x) = f_0(x) + \sum_{m=1}^{M} \sum_{j=1}^{J} \gamma_{jm} I(x \in R_{jm}).$$

3.2. Convolutional neural networks for solving regression problems

The network structure of Convolutional Neural Networks (CNNs) consists of an input layer, convolutional layers, pooling layers, and output layers, among others. CNNs are widely used for image classification tasks due to their ability to effectively capture spatial hierarchies in image data. However, when adapted for regression tasks involving numerical data, significant differences arise in various aspects, such as input data handling, the design of convolution and pooling layers, output layer configuration, and the choice of loss function.

In regression tasks, the input data typically takes the form of a numerical feature vector or matrix, denoted as $\mathbf{X}$, where $\mathbf{X} \in \mathbb{R}^{m \times n}$. The convolution layer extracts features from the input data through convolution operations. Mathematically, the output of the convolution layer can be given as:

$$\mathbf{C} = \mathbf{X} * \mathbf{W},$$

where $*$ represents the convolution operation. $\mathbf{X}$ is the input feature matrix, $\mathbf{W}$ represents the convolution kernel (also known as the filter), s denotes the stride of the convolution operation, and p refers to the padding size. The convolution operation involves sliding the kernel $\mathbf{W}$ over the input matrix $\mathbf{X}$, performing element-wise multiplications, and summing the results to produce the output feature matrix $\mathbf{C}$. The choice of s and p directly affects the dimensions of $\mathbf{C}$ and influences how much of the input matrix's boundary information is retained in the output. By adapting these components, CNNs can be effectively utilized for regression tasks, making them versatile tools for a wide range of applications beyond image classification.

Activation functions introduce non-linear transformations, increasing the expressive ability of the model. Commonly used activation functions include the rectified linear unit (ReLU) function. The output of the activation function is given by: $\mathbf{A} = \text{ReLU}(\mathbf{C})$, where $\text{ReLU}(x) = \max(0, x)$. Pooling layers reduce the size of the feature maps through down-sampling while preserving the main features. Common pooling operations include max pooling and average pooling. Assuming the size of the pooling operation is $k \times k$ and the stride is s, the output of the pooling layer can be expressed as:

$$\text{MaxPooling}\left(x_{ij}\right) = \max\left(x_{(i-1)k+1:ik,(j-1)k+1:jk}\right), \tag{1}$$

where x_{ij} represents the value of the pooled output at position (i, j) in the feature map, while k denotes the size of the pooling window, such as $k \times k$. The expression $x_{(i-1)k+1:ik,(j-1)k+1:jk}$ specifies the submatrix of the input feature map covered by the pooling window for the output position (i, j). The max pooling operation extracts the maximum value within this submatrix, effectively reducing the spatial dimensions of the feature map while retaining the most salient features. This dimensionality reduction enhances computational efficiency and helps mitigate overfitting by summarizing the key information from each region of the feature map.

Fully connected layers flatten the output of the pooling layer into a vector and perform linear transformations through matrix multiplication and bias terms. The output of the fully connected layer is given as

$$\mathbf{F} = \text{ReLU}\left(\mathbf{P} \cdot W_f + b_f\right), \tag{2}$$

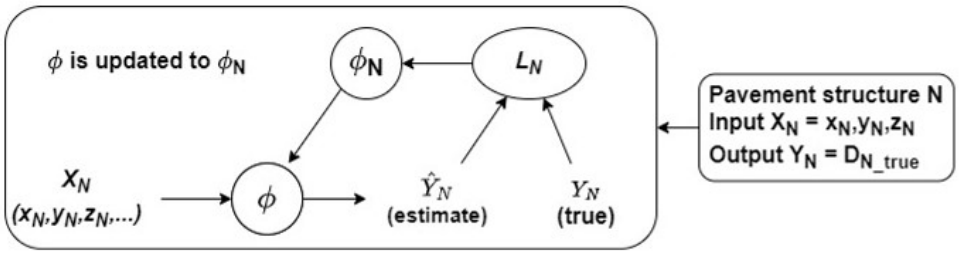


Figure 2. General deep-learning training methods.

where $\mathbf{P} = \text{MaxPooling}(A)$, the weight matrix of the fully connected layer is denoted as W_f, and the bias term is b_f. Activation functions introduce non-linear transformations, increasing the expressive ability of the model and allowing it to learn complex patterns. Commonly used activation functions include the sigmoid, tanh, and ReLU functions. The ReLU function is often chosen for its simplicity, computational efficiency, and ability to mitigate the vanishing gradient problem, making it a popular choice for deep networks.

Finally, the output layer maps the output of the fully connected layer to the range of the predicted values through linear transformations and activation functions, resulting in the output

$$\mathbf{Y} = \mathbf{F} \cdot W_o + b_o, \tag{3}$$

where W_o represents the weight matrix, b_o is the bias term, and Y indicates the predicted data.

In regression tasks, the MSE is a commonly employed loss function. The network parameters are then updated through the backpropagation algorithm based on this loss function to minimize the overall loss. This iterative process allows the CNN algorithm to learn the relationship between input features and regression targets, enabling it to make numerical regression predictions.

Traditional machine learning methods rely on a substantial amount of data for training. When faced with small sample data, it is often unable to train a model with excellent performance. The model parameter update process for the service performance prediction of different pavement structures is shown in Figure 2, where each type of pavement structure must be trained separately as a model to perform regression tasks.

3.3. Pre-training for the prediction of pavement deflection basin area

Pre-training method is an effective approach for few-shot learning, which is an unsupervised learning method. Before predicting the DBA of the target pavement structure data, we use other types of pavement surface data for the usual optimization pre-training. This approach is applicable to deep learning models trained through gradient descent. The comprehensive pre-training process is given in

$$\phi_i \leftarrow \phi_i - \alpha \nabla_{\phi_i} L_i \left(\phi_i, D_i^{\text{pre-train}} \right), \tag{4}$$

where $D_i^{\text{pre-train}}$ is the dataset used for training the DBA, and D_i^{test} is the dataset used for testing. The pre-training is performed on $D_i^{\text{pre-train}}$, updating the parameters ϕ_i using the deep learning model. α denotes a weighting factor, representing the learning rate at which ϕ_i will traverse in the gradient direction. The parameter ϕ_i is set with a random number initially. $D_i^{\text{pre-train}}$ is used to pre-train ϕ_i to minimize the loss function L_i. By repeating Equation (4), the parameter ϕ_i obtained through pre-training serves as the initial parameter for training the model with target pavement data. Then, fine-tuning is performed using target pavement training data to calculate the loss function L_T. The final parameter ϕ_i of the model is initialized as ϕ_T, resulting in a fine-tuned model. Finally, the target data to be trained is input into the final model for prediction. The overall

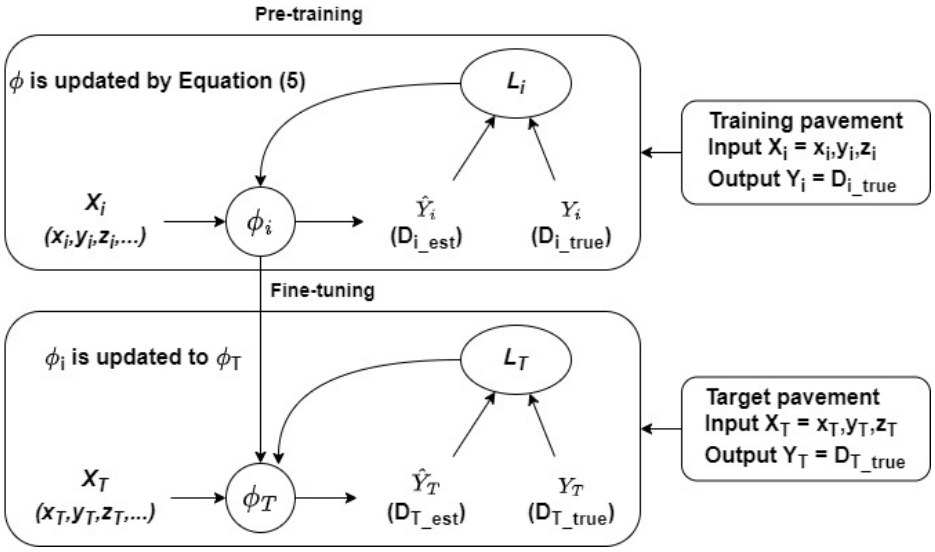


Figure 3. Pre-training methods.

parameter update process is illustrated in Figure 3, where $D_{\text{T_est}}$ represents the estimated value obtained by the pre-training method, and $D_{\text{T_true}}$ stands for the true value.

The purpose of pre-training models is to determine the optimal initial parameters ϕ_i for all tasks. However, pre-training does not ensure that employing this ϕ_i for fine-tuning in other tasks will yield a favorable ϕ_T. In essence, the pre-training algorithm concentrates on evaluating the performance of ϕ_i within the current model.

3.4. MAML for the prediction of pavement deflection basin area

The meta-learning algorithm stands out as one of the most effective approaches for addressing few-shot learning challenges. Figure 4 shows the overall process of using meta-learning methods to predict the DBA. The meta-model leverages the related datasets of 18 pavement structures, excluding the target pavement structure, for the training task, while the target pavement data serves as the testing task. Furthermore, each task is subdivided into a query set and a support set, utilized for training and testing in the inner loop, respectively. Algorithm 1 showcases the entire pre-training procedure of meta-learning.

First, meta-learning initializes a model with random parameters ϕ. The meta-model uses pavement data from tasks other than the target pavement, referred to as $D_i^{\text{meta-train}}$. The parameter update is expressed as follows:

$$\phi_i = \phi - \alpha \nabla_\phi L_i \left(\phi, D_i^{\text{support}}\right), \tag{5}$$

where ϕ represents the initial model parameters, and ϕ_i denotes the updated parameters after performing gradient descent on the support data D_i^{support}. The learning rate α controls the step size for each update, and $\nabla_\phi L_i \left(\phi, D_i^{\text{support}}\right)$ refers to the gradient of the loss function L_i with respect to ϕ, computed using the support dataset.

For each class of AP data, the data is further divided into D_i^{support} and D_i^{query}. In the inner loop, the model's parameters are updated using a small number of training samples, enabling the model to quickly adapt to the task. D_i^{support} is used for training, and one or more gradient descent steps are performed to update the model's parameters from ϕ to ϕ_i. Multiple D_i^{query} sets are used during the inner loop, with each gradient update applied

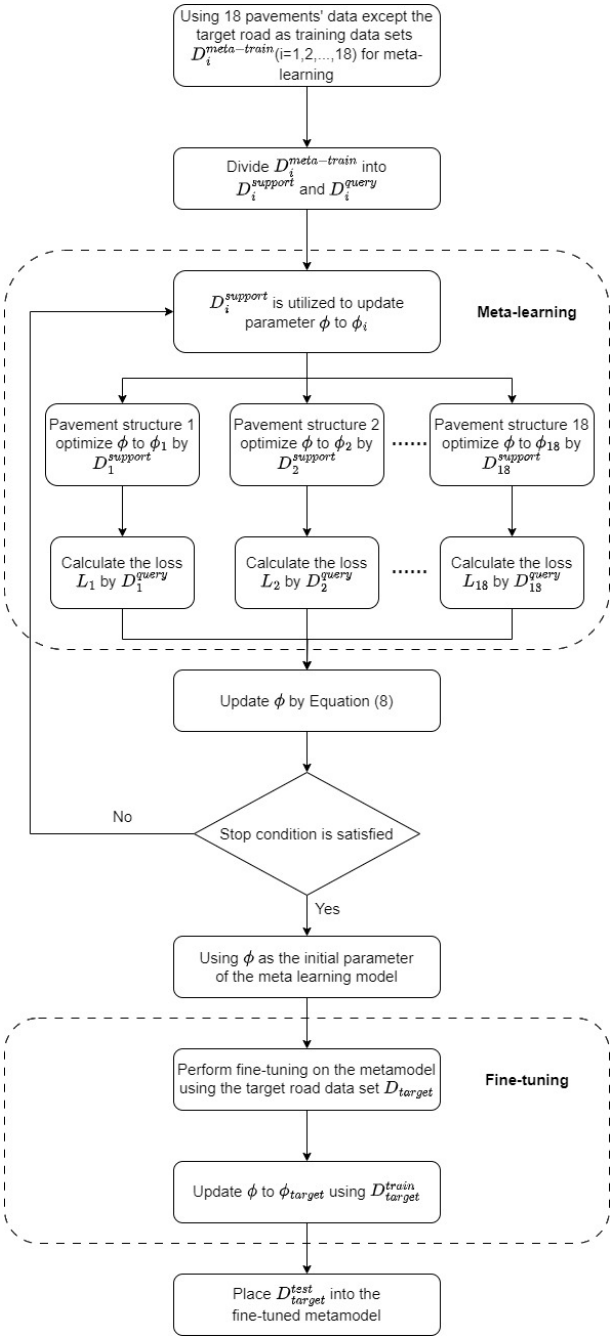


Figure 4. Meta learning algorithm flowchart

to the model with the original parameters ϕ. After the inner loop ends, n updated ϕ_i parameters are obtained.

In the outer loop, the MAML algorithm improves the initial parameters of the model by learning through inner loop iterations on multiple small-sample tasks, enabling it to quickly adapt to new tasks. For each update in the inner loop, the obtained parameters are used as the initial parameters of the new model. The model is then tested using the corresponding test set D_i^{query}, resulting in n loss values. These losses are weighted and averaged to obtain the overall loss function of the meta-model, as given in

$$L_{sum} = \sum_i L_i \left(\phi_i, D_i^{\text{query}} \right). \tag{6}$$

Using the sum of the loss L_{sum}, we perform gradient descent on the initial parameters of the target meta-model. Throughout the entire training process, we continuously perform inner and outer loops on multiple tasks to iteratively optimize the model's parameter ϕ. In this way, when encountering a new task, we only need to use the updated model from the outer loop to rapidly adapt to this task using a small quantity of training data. Ultimately, the MAML algorithm achieves fast learning and adaptation on few-slot tasks by updating the meta-model parameters ϕ, resulting in a well-trained final model, as given in

$$\phi \leftarrow \phi - \beta \nabla_{\phi} L_{sum}. \tag{7}$$

During the prediction phase, we use a portion of the target pavement data as training data ($D_{\text{target}}^{\text{train}}$), which is input into the newly learned meta-model for fine-tuning. Fine-tuning is performed using target pavement training data to calculate the loss function L_T. The initial parameters of the model are updated to ϕ_T to initialize ϕ. Finally, we use the test data ($D_{\text{target}}^{\text{test}}$) for prediction and obtain the predicted results. A flowchart is shown in Figure 5 to illustrate the parameter updates of meta-learning.

Algorithm 1 Meta-learning

Input: $D_i^{\text{meta-train}}$: meta-training data
α, β : step size hyperparameters

Initialize ϕ with a random number
Divide $D_i^{\text{meta-train}}$ into D_i^{support} and D_i^{query}
while not done **do**
  for all $D_i^{\text{meta-train}}$ **do**
    Compute adapted parameters : $\phi_i = \phi - \alpha \nabla_{\phi} L_i \left(\phi, D_i^{\text{support}}\right)$
  end for
  Calculate the loss value : $L_{sum} = \sum_i L_i \left(\phi_i, D_i^{\text{query}}\right)$
  Update $\phi \leftarrow \phi - \beta \nabla_{\phi} L_{sum}$
end while

As observed, in the training process of the MAML model, compared to the impact of ϕ on training task performance, the impact of the parameter ϕ_T trained with ϕ on task performance should be of greater concern. In other words, the MAML algorithm is used to find an initial model parameter ϕ that is more adaptable to other tasks.

4. RIOHTRACK STRUCTURE AND DATA SET

4.1. RIOHTrack structure

The data used by the meta-learning model in this experiment is the AP DBA. The measured data about the DBA is derived from the Ministry of Transport's full-scale pavement test loop project. This project is situated in Beijing and encompasses 25 AP structures. It has a full-scale on-site acceleration road test track called RIOHTrack, which is 2.038 km long. The arrangement of these pavement structures is illustrated in Figure 6.

The data used in this article was measured from different pavement structures. A total of 19 primary experimental pavement structures were established on the test circuit to investigate and compare the long-term performance and evolution of AC structures with varying combinations of structural stiffness. The asphalt concrete layer thickness for these pavement structures ranges from 12 to 48 cm (or 52 cm), covering the spectrum of asphalt concrete layer thicknesses found in highways across China, including the thickness of flexible base layers for thick AP.

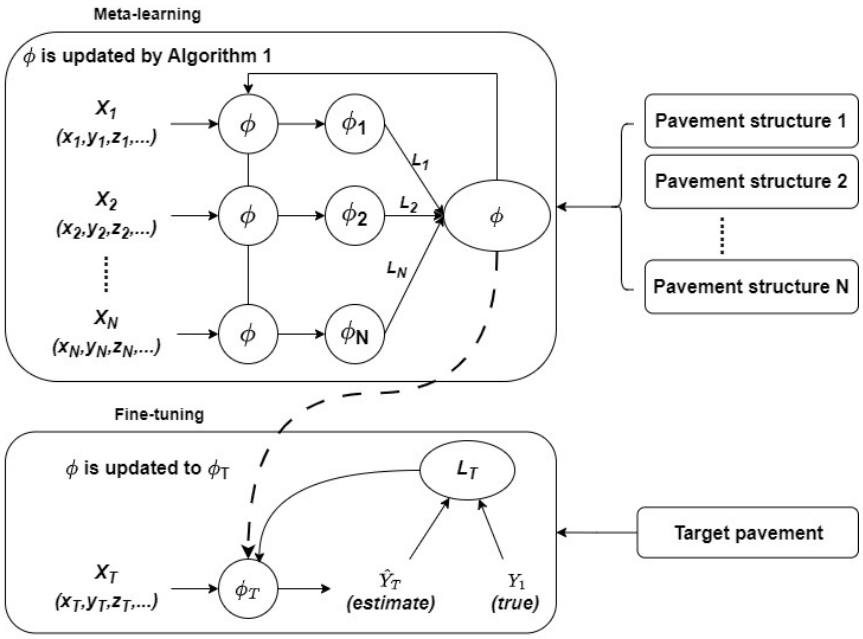


Figure 5. Meta learning method for the performance prediction of the pavement.

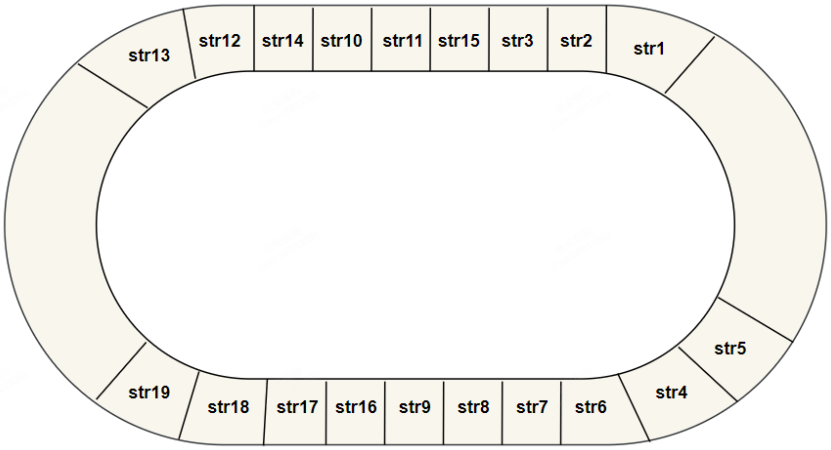


Figure 6. RIOHTRACK test loop pavement.

4.2. Acquisition of datasets

The DBA is measured using a FWD, which mainly consists of a heavyweight (falling weight) and a measuring instrument (usually a level or optical instrument). The FWD is dropped freely from a certain height, causing it to impact the pavement. After that, the pavement undergoes a slight deformation, forming a depression area, the settlement basin. Based on the shape and size of the observed depression area, mathematical formulas or calculation methods can be used to determine the area of the settlement basin.

The measured settlement basin area data has the following characteristics: axle load times, load level, pavement temperature, atmospheric temperature, etc. The data used in the article comes from the DBA measured at pressures of 5, 7, 9, and 11 tons in multiple cycles, respectively. Taking the data of STR1 pavement structure under a pressure of 5 tons as an example, the partial data of the settlement basin area measured by the FWD are shown in Table 1. These variables were selected based on their direct relevance to pavement performance and

Table 1. The pavement feature data(part)

Cycle number	Axle load times	Load level	Pavement temperature (⊠)	Atmospheric temperature (⊠)
N1	4.4533	56.47	12.77	9.17
N2	5.0184	56.47	8.05	11.34
N3	5.4729	56.47	11.66	7.81
N4	5.6846	56.47	26.92	21.85
N5	5.8265	56.47	30.2	25.32
...	...	...	...	...
N111	7.7491	48.09	1.75	3.34

degradation. Axle load times and load level are crucial as traffic load frequency and intensity affect pavement durability. Pavement temperature influences the stiffness and cracking susceptibility of asphalt, while atmospheric temperature affects thermal expansion and environmental wear, all contributing to the pavement's long-term performance.

This text leverages measurement data from the pavement of 19 types of AP as the primary data source. The objective is to regressively predict the area of a particular pavement type's DBA. Due to the brief construction time of the pavement, the data is limited. The deflection basin measurement data is categorized under four distinct pressure conditions, amounting to only 1,792 data cycles. To address the scarcity, we utilize the data under three pressure conditions as the training set to predict pavement data under the remaining pressure conditions. Traditional machine learning methods are less effective for this regression task due to the limited dataset. To overcome the challenge, this paper employs a meta-learning method, using an additional 18 pavement datasets for meta-training, effectively expanding the dataset. The trained meta-learning model is subsequently used to predict the target pavement, achieving regression prediction of the DBA with only a small quantity of training data. Model evaluation is performed using MSE, Root Mean Squared Error (RMSE), and MAE. These metrics gauge the algorithm's performance by reflecting the differences between actual and predicted values, serving as commonly used performance indicators in regression tasks. Smaller values of these indicators indicate more accurate predictions. The metrics are defined in:

$$MSE = \frac{1}{n}\sum_{i=1}^{n}(y_i - \hat{y}_i)^2, \tag{8}$$

$$RMSE = \sqrt{\frac{1}{n}\sum_{i=1}^{n}(y_i - \hat{y}_i)^2}, \tag{9}$$

$$MAE = \frac{1}{n}\sum_{i=1}^{n}|y_i - \hat{y}_i|, \tag{10}$$

$$R^2 = 1 - \frac{\sum_{i=1}^{n}(y_i - \hat{y}_i)^2}{\sum_{i=1}^{n}(y_i - \bar{y})^2}. \tag{11}$$

5. EXPERIMENTAL RESULTS

This section uses meta-learning to experimentally estimate the DBA of pavement to verify its estimation performance compared to pre-training. It also compares the performance of pre-training with other deep learning models that do not use pre-training. It verifies the impact of pre-training on predicting the DBA of the pavements. The purpose of the experiments in this paper is to utilize measured cyclic data of pavement DBA under

Table 2. Comparison of model performance after 10 to 100 iterations

Iterations	10	20	30	40	50	60	70	80	90	100
MSE	172.38	107.33	106.61	55.66	68.56	36.04	63.76	46.35	49.52	40.10
MAE	9.12	9.41	8.17	5.65	6.62	4.74	6.17	5.09	5.41	4.73

different pressures to predict the trend of rebound DBA changes and its variation trend throughout all cycles at a specific pressure. Specifically, the training involves using DBA cyclic data under pressures of 5, 9, and 11 tons, and the goal is to predict the DBA and its variation trend over the entire cycle at a pressure of 7 tons.

5.1. Performance after a small number of iterations

A meta-learning prediction model trained on multiple pavement data (excluding the target pavement) can predict the target pavement DBA by fine-tuning a small quantity of pavement data in several gradient steps. To assess the effectiveness of meta-learning in DBA prediction, this study conducted a performance comparison based on gradient steps. A limited dataset specific to the target pavement was employed to fine-tune pre-trained DBA prediction models constructed using DNNs. In addition, this study also uses calibrated linear unit activation functions and the Adam optimizer. Multiple error measurement indicators, including the coefficient of determination (R^2), MSE, etc., are used to evaluate the prediction performance of the basin area of AP for meta-learning, pre-training, and traditional deep learning methods without pre-training. The basin area of the AP estimation model is trained using an NVIDIA 3060 graphics processing unit and Pytorch deep learning framework. Taking road surface STR19 as an example, the MAML algorithm is tested and the results are shown in Table 2.

Table 2 illustrates a noteworthy reduction in MSE and MAE after ten to 100 iterations, underscoring that DNN models with meta-learning can rapidly adapt to accurately predict the pavement DBA.

5.2. Prediction of the area of pavement deflection basin

The CNN model used in this experiment consists of one convolutional layer and two fully connected layers. The convolutional layer has 1 input channel, 10 output channels, and a kernel size of 2. The first linear layer has an input dimension of 10 and an output dimension of 10, containing ten neurons. The second linear layer has an input dimension of 10 and an output dimension of 1, containing 1 neuron. The learning rate is 0.001. The GBDT model uses a parameter *n_estimators* of 500, which indicates the number of trees, and the learning rate as 0.01. The RF regression model used in this experiment has a parameter n_estimators of 200, the loss function is selected as MSE, max_depth is set to None, and min_samples_split is 2. The pre-trained deep learning models studied include meta-learning and pre-training learning. The Deep Neural Network (DNN) structure studied in this research consists of 40 neurons and three hidden layers. The specific parameters are shown in the Table 3.

The performance of meta-learning in predicting the area of deflection basins using data from different pavement structures. To test the exactitude of meta-learning in predicting the area of deflection basins, experiments are conducted on pre-training data involving various pavement conditions without considering the similarity between targets. Table 4 summarizes the DBA estimation errors for each method. As observed, among the studied methods, the deflection basin area estimation using meta-learning achieves the most accurate results (MSE = 13.262, MAE = 2.854) despite using a pre-trained pavement structure different from the target pavement. Among the compared ML methods, the RF model has the least accurate prediction results, with MSE = 372.982 and MAE = 17.161, as it did not receive sufficient training (only using 424 target data points).

Taking the STR19 road as an example, the MAML algorithm uses the data of STR19 as the target road and performs meta-training on other roads. We intend to forecast the DBA of STR19 within one cycle. The MAML model uses parameters of 0.01 for the inner loop learning rate, 0.001 for the outer loop learning rate, and 1 for

Table 3. Model Parameters Summary

Model	Parameter	Value
CNN	Convolutional layer	1 input channel, 10 output channels, kernel size = 2
	First linear layer	Input dimension = 10, Output dimension = 10
	Second linear layer	Input dimension = 10, Output dimension = 1
	Learning rate	0.001
GBDT	Number of estimators	500
	Learning rate	0.01
RF	Number of estimators	200
	Loss function	MSE (Mean Squared Error)
	Max depth	none
	Min samples split	2
DNN	Number of neurons	40 (3 hidden layers)

Table 4. Comparison of model performance

Model	MSE	MAE	R^2
RF	372.982	17.161	-
GBDT	228.281	14.651	-
CNN	151.741	10.144	0.745
Pre-training	16.645	3.253	0.902
MAML	13.262	2.854	0.922

Table 5. Comparison of model performance

Pavement	STR1	STR2	STR3	STR4	STR5	STR6	STR7	STR8	STR9
MSE	20.132	13.830	57.710	63.206	50.844	63.216	60.360	14.453	36.942
MAE	3.394	2.805	5.677	3.680	3.757	4.622	3.895	3.075	4.765
R^2	0.933	0.843	0.791	0.622	0.604	0.630	0.696	0.855	0.776
Pavement	STR10	STR11	STR12	STR13	STR14	STR15	STR16	STR17	STR18
MSE	56.620	11.873	52.740	50.941	69.873	20.132	39.535	23.012	19.111
MAE	5.658	2.788	5.480	4.917	5.045	3.394	4.946	3.863	5.335
R^2	0.840	0.888	0.644	0.781	0.787	0.933	0.895	0.885	0.914

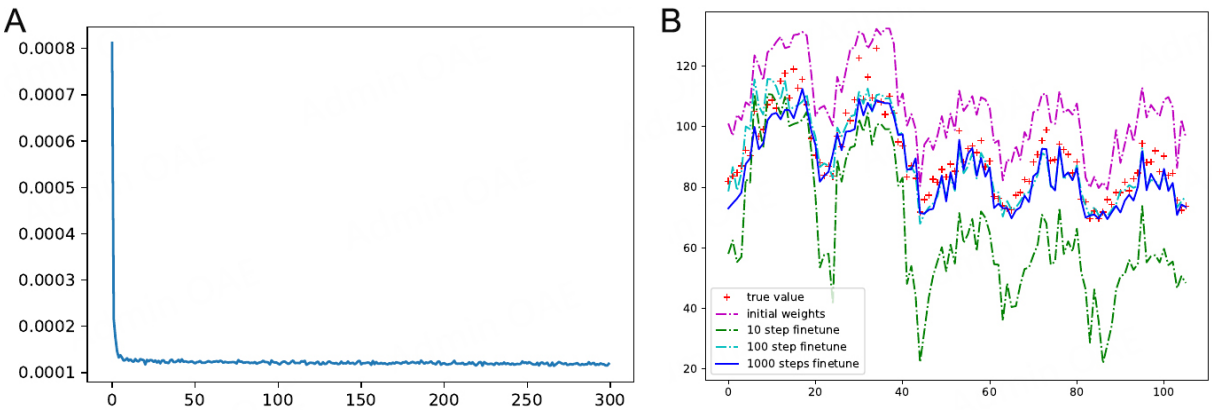


Figure 7. (A) The training loss values of the MAML model, (B) The model prediction performance after different steps.

the inner steps. The experimental results are shown in Figure 7.

5.3. Predictions with various pavement types

This section outlines the prediction performance of meta-learning when utilizing pavement data with diverse structures. To validate the exactitude of meta-learning in predicting the DBA, the subsequent experiments are conducted under the condition that the meta-training data is composed of pavement data with diverse structures without considering the similarity between targets.

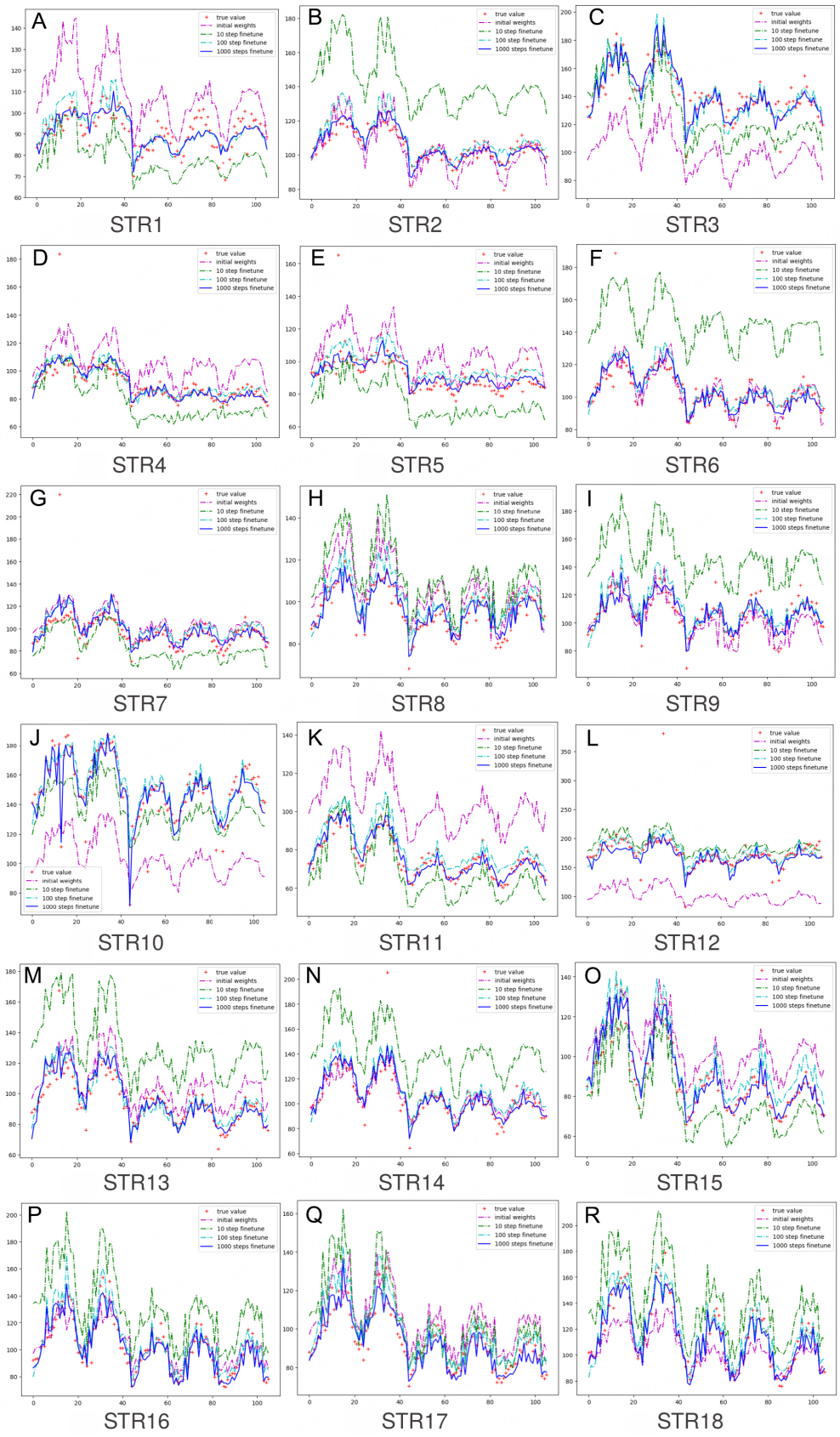


Figure 8. The results of estimating the deflection basin area of the remaining 18 pavements through meta-learning.

This experiment aims to verify that the meta-learning algorithm can have a good estimation performance when facing pavement data with different structures rather than being only applicable to specific data. The specific process of the experiment is similar to Section 5.2. The experiment is conducted on 19 pavements, with one target structure to be predicted and the other 18 pavements as the training data for meta-learning.

Table 5 lists the DBA prediction results for 18 different pavement structures. The MSE and MAE are significantly lower than those of the CNN, GBDT, and other models used in the comparative experiments. The estimation performance of the meta-learning algorithm is superior. Apart from the different data on the target pavement, the same conditions are applied in this experiment. As shown in Figure 8A-R, the fitting and estimation effects for different structures of the pavement are generally sound. Therefore, it is concluded that the meta-learning method could achieve good estimation performance for different types of pavement structures.

6. CONCLUSIONS

This paper proposes a meta-learning-based approach to predict the DBA of AP. By leveraging data from multiple pavement structures, excluding the target pavement, the proposed method significantly reduces the required training data volume, enabling accurate DBA prediction with small sample sizes. Traditional machine learning methods, which rely on training with data from a single pavement type, are less effective in estimating the DBA of the target pavement. In contrast, the proposed meta-learning method effectively reuses data from different pavement structures to pre-train deep learning models, improving the model's generalization capabilities.

Through experiments, we demonstrated that the meta-learning approach outperforms traditional machine learning, neural networks, and pre-training methods in predicting the DBA of APs. The results show that the proposed method is effective and resource-efficient for estimating pavement performance, especially in the early stages of pavement development.

However, the study also has limitations. One potential limitation is the impact of sample size on the model's prediction accuracy. Further research could explore how variations in sample size affect model performance and investigate ways to mitigate the effects of limited data. Additionally, the applicability of the proposed method to different pavement types and conditions remains an area for future exploration. Future studies could also focus on extending the model's capabilities to include real-time data integration and testing in various environmental conditions.

DECLARATIONS

Authors' contributions

Methodology, validation, visualization, and writing-original draft: Li Z, Jin X
Conceptualization, writing-reviewing, supervision, and editing: Shi X, Cao J

Availability of data and materials

The data cannot be shared publicly as the partner (company) does not permit public disclosure. It is available from the corresponding author upon reasonable request.

Financial support and sponsorship

This work was supported by the National Key Research and Development Project of China under Grant (No. 2020YFA0714300) and the Open Project of Nanjing Modern Multimodal Transportation Laboratory (MTF2023004).

Conflicts of interest

Cao J is an Advisory Board Member of the journal *Complex Engineering Systems*. Shi X is an Junior Editorial Board Member of the same journal. Cao J and Shi X were not involved in any steps of editorial processing, notably including the selection of reviewers, manuscript handling and decision-making, while the other authors have declared that they have no conflicts of interest.

Ethical approval and consent to participate

Not applicable.

Consent for publication

Not applicable.

Copyright

© The Author(s) 2024.

REFERENCES

1. Wang X. Design of pavement structure and material for full-scale test track. *J Highw Transp Res Dev* 2017;34:30-7. DOI
2. Fu G, Zhao Y, Zhou C, Liu W. Determination of effective frequency range excited by falling weight deflectometer loading history for asphalt pavement. *Constr Build Mater* 2020;235:117792. DOI
3. Habbouche J, Hajj EY, Sebaaly PE, Morian NE. Damage assessment for M-E rehabilitation design of modified asphalt pavements: challenges and findings. *Transp Res Rec* 2018;2672:228-41. DOI
4. Huang W, Liang S, Wei Y. Surface deflection-based reliability analysis of asphalt pavement design. *Sci China Technol Sci* 2020;63:1824-36. DOI
5. Vyas V, Singh AP, Srivastava A. Prediction of asphalt pavement condition using FWD deflection basin parameters and artificial neural networks. *Road Mater Pavement Des* 2021;22:2748-66. DOI
6. Liu H, Cao J, Huang W, Shi X, Zhou X, Li Z. A multidimensional framework for asphalt pavement evaluation based on multilayer network representation learning: a case study in RIOHTrack. *Expert Syst Appl* 2024;237:121370. DOI
7. Wang W, Zhang H, Li T, et al. An interpretable model for short term traffic flow prediction. *Math Comput Simul* 2019;171:264-78. DOI
8. Li Z, Korovin I, Shi X, Gorbachev S, Gorbacheva N, Huang W. A data-driven rutting depth short-time prediction model with metaheuristic optimization for asphalt pavements based on RIOHTrack. *IEEE/CAA J Autom Sin* 2023;10:1918-32. DOI
9. Li Z, Cao J, Shi X, Huang W. QPSO-AHES-RC: a hybrid learning model for short-term traffic flow prediction. *Soft Comput* 2023;97:9347-66. DOI
10. Yang Y, Li Z, Chen J, Liu Z, Cao J. TRELM-DROP: an impavement non-iterative algorithm for traffic flow forecast. *Physica A* 2024;633:129337. DOI
11. Pan JS, Zhang Z, Chu SC, Zhang SQ, Wu JMT. A parallel compact marine predators algorithm applied in time series prediction of Backpropagation neural network (BNN) and engineering optimization. *Math Comput Simulat* 2024;220:65-88. DOI
12. Saltan M, Terzi S. Modeling deflection basin using artificial neural networks with cross-validation technique in backcalculating flexible pavement layer moduli. *Adv Eng Softw* 2008;39:588-92. DOI
13. Lv Y, Duan Y, Kang W, Li Z, Wang FY. Traffic flow prediction with big data: a deep learning approach. *IEEE Trans Intell Transp Syst* 2015;16:865-73. DOI
14. Ma X, Tao Z, Wang Y, Yu H, Wang Y. Long short-term memory neural network for traffic speed prediction using remote microwave sensor data. *Transp Res Part C Emer Technol* 2015;54:187-97. DOI
15. Yang Q, Deng Y. Evaluation of cracking in asphalt pavement with stabilized base course based on statistical pattern recognition. *Int J Pavement Eng* 2019;20:417-24. DOI
16. Karballaeezadeh N, Ghasemzadeh Tehrani H, Mohammadzadeh Shadmehri D, Shamshirband S. Estimation of flexible pavement structural capacity using machine learning techniques. *Front Struct Civ Eng* 2020;14:1083-96. DOI
17. Tang X, Yang X. Inverse analysis of pavement structural properties based on dynamic finite element modeling and genetic algorithm. *Int J Transp Sci Technol* 2013;2:15-30. DOI
18. Mabrouk GM, Elbagalati OS, Dessouky S, Fuentes L, Walubita LF. Using ANN modeling for pavement layer moduli backcalculation as a function of traffic speed deflections. *Constr Build Mater* 2022;315:125736. DOI
19. Zhang J, Cao J, Huang W, Shi X, Ji X, Zhou X. A hybrid framework for asphalt pavement rutting prediction modeling and influencing factors analysis based on multilevel wavelet decomposition and transfer entropy. *Appl Math Model* 2023;121:714-30. DOI
20. Li M, Dai Q, Su P, You Z, Ma Y. Surface layer modulus prediction of asphalt pavement based on LTPP database and machine learning for Mechanical-Empirical rehabilitation design applications. *Constr Build Mater* 2022;344:128303. DOI
21. Li Z, Shi X, Cao J, Wang X, Huang W. CPSO-XGBoost segmented regression model for asphalt pavement deflection basin area prediction. *Sci China Technol Sci* 2022;65:1470-81. DOI

22. Zhang J, Cao J, Huang W, Shi X, Zhou X. Rutting prediction and analysis of influence factors based on multivariate transfer entropy and graph neural networks. *Neural Netw* 2023;157:26-38. DOI
23. Shen C, Jiang B, Yue L. LSTM combined with BIM technology in the management of small and medium-sized span highway concrete beam bridges. *Results Eng* 2023;20:101539. DOI
24. Sharma A, Sachdeva SN, Aggarwal P. Predicting IRI using machine learning techniques. *Int J Pavement Res Technol* 2023;16:128–37. DOI
25. Tommasi T, Orabona F, Caputo B. Learning categories from few examples with multi model knowledge transfer. *IEEE Trans Pattern Anal Mach Intell* 2013;36:928-41. DOI
26. Pan SJ, Yang Q. A survey on transfer learning. *IEEE Trans Knowl Data Eng* 2010;22:1345-59. DOI
27. Finn C, Abbeel P, Levine S. Model-agnostic meta-learning for fast adaptation of deep networks. *arXiv* 2017. pp. 1126-35. DOI
28. Vinyals O, Blundell C, Lillicrap T, Kavukcuoglu K, Wierstra D. Matching networks for one shot learning. *arXiv* 2016. DOI
29. Snell J, Swersky K, Zemel RS. Prototypical networks for few-shot learning. *arXiv* 2017. DOI
30. Santoro A, Bartunov S, Botvinick M, Wierstra D, Lillicrap T. Meta-learning with memory-augmented neural networks; 2016. Available from: https://proceedings.mlr.press/v48/santoro16.pdf [Last accessed on 28 Dec 2024]
31. Ravi S, Larochelle H. Optimization as a model for few-shot learning; 2016. Available from: https://openreview.net/forum?id=rJY0-Kcll [Last accessed on 28 Dec 2024].
32. Nichol A, Schulman J. Reptile: a scalable metalearning algorithm. *arXiv* 2018. Available from: https://yobibyte.github.io/files/paper_notes/Reptile___a_Scalable_Metalearning_Algorithm__Alex_Nichol_and_John_Schulman__2018.pdf [Last accessed on 28 Dec 2024]
33. Chu X, Cai F, Cui C, Hu M, Li L, Qin Q. Adaptive recommendation model using meta-learning for population-based algorithms. *Inf Sci* 2019;476:192-210. DOI
34. Yu H, Zhang Q, Liu T, Lu J, Wen Y, Zhang G. Meta-ADD: a meta-learning based pre-trained model for concept drift active detection. *Inf Sci* 2022;608:996-1009. DOI
35. Lee Y, Choi S. Gradient-based meta-learning with learned layerwise metric and subspace. *arXiv* 2018. pp. 2927-36. DOI
36. Gordon J, Bronskill J, Bauer M, Nowozin S, Turner RE. Meta-learning probabilistic inference for prediction. *arXiv* 2018. DOI
37. Bertinetto L, Henriques JF, Torr PHS, Vedaldi A. Meta-learning with differentiable closed-form solvers. *arXiv* 2018. DOI
38. Lee K, Maji S, Ravichandran A, Soatto S. Meta-learning with differentiable convex optimization. In Proceedings of the 2019 IEEE/CVF Conference on Computer Vision and Pattern Recognition (CVPR); 15-20 June 2019; Long Beach, CA, USA. pp. 10657-65. DOI
39. Aguiar GJ, Santana EJ, de Carvalho ACPFL, Barbon Junior S. Using meta-learning for multi-target regression. *Inf Sci* 2022;584:665-84. DOI
40. Jeong D, Bae S. Estimating battery state-of-charge with a few target training data by meta-learning. *J Power Sources* 2023;553:232238. DOI
41. Antoniou A, Edwards H, Storkey A. How to train your MAML. *arXiv* 2018. DOI
42. Finn C, Xu K, Levine S. Probabilistic model-agnostic meta-learning. *arXiv* 2018. DOI
43. Grant E, Finn C, Levine S, Darrell T, Griffiths T. Recasting gradient-based meta-learning as hierarchical bayes. *arXiv* 2018. DOI
44. Rusu AA, Rao D, Sygnowski J, et al. Meta-learning with latent embedding optimization. *arXiv* 2018. DOI
45. Morcos AS, Raghu M, Bengio S. Insights on representational similarity in neural networks with canonical correlation. *arXiv* 2018. DOI
46. Kornblith S, Norouzi M, Lee H, Hinton G. Similarity of neural network representations revisited. *arXiv* 2019. pp. 3519-29. DOI
47. Yang J, Wang X, Luo Z. Few-shot remaining useful life prediction based on meta-learning with deep sparse kernel network. *Inf Sci* 2024;653:119795. DOI
48. Shafahi A, Saadatpanah P, Zhu C, et al. Adversarially robust transfer learning. *arXiv* 2019. DOI
49. Wong E, Rice L, Kolter JZ. Fast is better than free: Revisiting adversarial training. *arXiv* 2020. DOI
50. Andriushchenko M, Flammarion N. Understanding and improving fast adversarial training. *arXiv* 2020. DOI
51. Carmon Y, Raghunathan A, Schmidt L, Liang P, Duchi JC. Unlabeled data improves adversarial robustness. *arXiv* 2019. DOI
52. Uesato J, Alayrac JB, Huang PS, Stanforth R, Fawzi A, Kohli P. Are labels required for improving adversarial robustness? *arXiv* 2019. DOI
53. Chan A, Tay Y, Ong YS. What it thinks is important is important: Robustness transfers through input gradients. In Proceedings of the 2020 IEEE/CVF Conference on Computer Vision and Pattern Recognition (CVPR); 13-19 June 2020; Seattle, WA, USA. pp. 332-41. DOI
54. Utrera F, Kravitz E, Erichson NB, Khanna R, Mahoney MW. Adversarially-trained deep nets transfer better: Illustration on image classification. *arXiv* 2020. DOI
55. Salman H, Ilyas A, Engstrom L, Kapoor A, Madry A. Do adversarially robust imagenet models transfer better? *arXiv* 2020. DOI
56. Breiman L. Random forests. *Mach Learn* 2001;45:5-32. DOI
57. Friedman JH. Greedy function approximation: a gradient boosting machine. *Ann Statist* 2001;29:1189-232. DOI

AUTHOR INSTRUCTIONS

1. Submission Overview

Before you decide to publish with us, please read the following items carefully and make sure that you are well aware of Editorial Policies and the following requirements.

1.1 Topic Suitability

The topic of the manuscript must fit the scope of the journal. Please refer to Aims and Scope for more information.

1.2 Open Access and Copyright

The journal adopts Gold Open Access publishing model and distributes content under the Creative Commons Attribution 4.0 International License. Copyright is retained by authors. Please make sure that you are well aware of these policies.

1.3 Publication Fees

CES is an open access journal. When a paper is accepted for publication, authors are required to pay Article Processing Charges (APCs) to cover its editorial and production costs. The APC for each submission is $1600. There are no additional charges based on color, length, figures, or other elements. For more details, please refer to OAE Publication Fees.

1.4 Language Editing

All submissions are required to be presented clearly and cohesively in good English. Authors whose first language is not English are advised to have their manuscripts checked or edited by a native English speaker before submission to ensure the high quality of expression. A well-organized manuscript in good English would make the peer review even the whole editorial handling more smoothly and efficiently.

If needed, authors are recommended to consider the language editing services provided by OAE to ensure that the manuscript is written in correct scientific English before submission. An extra charge is required to enjoy this service. Please visit https://www.oaepublish.com/index/author_services or contact English-Editing@oaepublish.com for more details.

1.5 Work Funded by the National Institutes of Health

If an accepted manuscript was funded by National Institutes of Health (NIH), the author may inform Editors of the NIH funding number. The Editors are able to deposit the paper to the NIH Manuscript Submission System on behalf of the author.

2. Submission Preparation

2.1 Cover Letter

A cover letter is required to be submitted accompanying each manuscript. Here is a guideline of a cover letter for authors' consideration:

List the highlights of the current manuscript and no more than 5 short sentences;

All authors have read the final manuscript, have approved the submission to the journal, and have accepted full responsibilities pertaining to the manuscript's delivery and contents;

Clearly state that the manuscript is an original work on its own merit, that it has not been previously published in whole or in part, and that it is not being considered for publication elsewhere;

No materials are reproduced from another source (if there is material in your manuscript that has been reproduced from another source, please state whether you have obtained permission from the copyright holder to use them);

Conflicts of interest statement;

If the manuscript is contributed to a Special Issue, please also mention it in the cover letter;

If the manuscript was presented partly or entirely in a conference, the author should clearly state the background information of the event, including the conference name, time, and place in the cover letter.

2.2 Types of Manuscripts

There is no restriction on the number of figures, tables and references, provided that the manuscript is concise and comprehensive. The journal publishes Research Article, Review, Technical Note, etc. For more details about paper type, please refer to the following table.

Manuscript Type	Definition	Word Limit	Abstract	Keywords	Main Text Structure

Research Article	A Research Article is a seminal and insightful research study and showcases that often involves modern techniques or methodologies. Authors should justify that their work is of novel findings	8 0 0 0 max	The abstract should state briefly the purpose of the research, the principal results andmajor conclusions. No more than 250 words	3-8 keywords	The main text may consist of several sections with unfixed section titles. We suggest that the author include an "Introduction" section at the beginning, several sections with unfixed titles in the middle part, and a "Conclusions" section at the end
Review	A review article should provide readers with an in-depth understanding of a field by summarizing existing literature, and highlight key gaps and challenges to address future research.	1 0 0 0 0 max	Unstructured abstract. No more than 250 words	3-8 keywords	The main text may consist of several sections with unfixed section titles. We suggest that the author include an "Introduction" section at the beginning, several sections with unfixed titles in the middle part, and a "Conclusions" section at the end
Technical Note	A Technical Note is a short article giving a brief description of a specific development, technique, or procedure, or it may describe a modification of an existing technique, procedure or device applied in research	3 5 0 0 max	Unstructured abstract. No more than 250 words	3-8 keywords	/
Editorial	An Editorial is a short article describing news about the journal or opinions of senior Editors or the publisher	1 0 0 0 max	None required	None required	/
Commentary	A Commentary is to provide comments on a newly published article or an alternative viewpoint on a certain topic	2 5 0 0 max	Unstructured abstract. No more than 250 words	3-8 keywords	/
Perspective	A Perspective provides personal points of view on the state-of-the-art of a specific area of knowledge and its future prospects	2 0 0 0 max	Unstructured abstract. No more than 250 words	3-8 keywords	/

2.3 Manuscript Structure

2.3.1 Front Matter

2.3.1.1 Title

The title of the manuscript should be concise, specific and relevant, with no more than 16 words if possible.

2.3.1.2 Authors and Affiliations

Authors' full names should be listed. The initials of middle names can be provided. The affiliations and email addresses for all authors should be listed. At least one author should be designated as the corresponding author. In addition, corresponding authors are suggested to provide their Open Researcher and Contributor ID upon submission. Please note that any change to authorship is not allowed after manuscript acceptance. The authors' affiliations should be provided in this format: department, institution, city, postcode, country.

2.3.1.3 Abstract

The abstract should be a single paragraph with word limitation and specific structure requirements (for more details please refer to Types of Manuscripts). It usually describes the main objective(s) of the study, explains how the study was done, including any model organisms used, without methodological detail, and summarizes the most important results and their

significance. The abstract must be an objective representation of the study: it is not allowed to contain results that are not presented and substantiated in the manuscript, or exaggerate the main conclusions. Citations should not be included in the abstract.

2.3.1.4 Graphical Abstract

The graphical abstract is essential as this can catch first view of your publication by readers. We recommend you submit an eye-catching figure. It should summarize the content of the article in a concise graphical form. It is recommended to use it because this can make online articles get more attention.

The graphical abstract should be submitted as a separate document in the online submission system. Please provide an image with a minimum of 531 × 1,328 pixels (h × w) or proportionally more. The image should be readable at a size of 5 cm × 13 cm using a regular screen resolution of 96 dpi. Preferred file types: TIFF, PSD, AI, JPEG, and EPS files.

2.3.1.5 Keywords

Three to eight keywords should be provided, which are specific to the article, yet reasonably common within the subject discipline.

Sections 2.3.1.1 and 2.3.1.2 should appear in all manuscript types.

2.3.2 Main Text

Manuscripts of different types are structured with different sections of content. Please refer to Types of Manuscripts to make sure which sections should be included in the manuscripts.

2.3.2.1 Introduction

The introduction should contain background that puts the manuscript into context, allow readers to understand why the study is important, include a brief review of key literature, and conclude with a brief statement of the overall aim of the work and a comment about whether that aim was achieved. Relevant controversies or disagreements in the field should be introduced as well.

2.3.2.2 Methods

The methods should contain sufficient details to allow others to fully replicate the study. New methods and protocols should be described in detail while well-established methods can be briefly described or appropriately cited. Statistical terms, abbreviations, and all symbols used should be defined clearly. Protocol documents for clinical trials, observational studies, and other non-laboratory investigations may be uploaded as supplementary materials.

2.3.2.3 Results

This section contains the findings of the study. Results of statistical analysis should also be included either as text or as tables or figures if appropriate. Authors should emphasize and summarize only the most important observations. Data on all primary and secondary outcomes identified in the section Methods should also be provided. Extra or supplementary materials and technical details can be placed in supplementary documents.

2.3.2.4 Discussion

This section should discuss the implications of the findings in context of existing research and highlight limitations of the study. Future research directions may also be mentioned.

2.3.2.5 Conclusion

It should state clearly the main conclusions and include the explanation of their relevance or importance to the field.

2.3.3 Back Matter

The following sections should appear in all manuscript types.

2.3.3.1 Acknowledgments

Anyone who contributed towards the article but does not meet the criteria for authorship, including those who provided professional writing services or materials, should be acknowledged. Authors should obtain permission to acknowledge from all those mentioned in the Acknowledgments section. This section is not added if the author does not have anyone to acknowledge.

2.3.3.2 Authors' Contributions

Each author is expected to have made substantial contributions to the conception or design of the work, or the acquisition, analysis, or interpretation of data, or the creation of new software used in the work, or have drafted the work or substantively revised it.

Please use Surname and Initial of Forename to refer to an author's contribution. For example: made substantial contributions to conception and design of the study and performed data analysis and interpretation: Salas H, Castaneda WV; performed

data acquisition, as well as providing administrative, technical, and material support: Castillo N, Young V.
If an article is single-authored, please include "The author contributed solely to the article." in this section.

2.3.3.3 Availability of Data and Materials

In order to maintain the integrity, transparency and reproducibility of research records, authors should include this section in their manuscripts, detailing where the data supporting their findings can be found. Data can be deposited into data repositories or published as supplementary information in the journal. Authors who cannot share their data should state that the data will not be shared and explain it. If a manuscript does not involve such issues, please state "Not applicable." in this section.

2.3.3.4 Financial Support and Sponsorship

All sources of funding for the study reported should be declared. The role of the funding body in the experiment design, collection, analysis and interpretation of data, and writing of the manuscript should be declared. Any relevant grant numbers and the link of funder's website should be provided if any. If the study is not involved with this issue, state "None." in this section.

2.3.3.5 Conflicts of Interest

Authors must declare any potential conflicts of interest that may be perceived as inappropriately influencing the representation or interpretation of reported research results. If there are no conflicts of interest, please state "All authors declared that there are no conflicts of interest." in this section. Some authors may be bound by confidentiality agreements. In such cases, in place of itemized disclosures, we will require authors to state "All authors declared that they are bound by confidentiality agreements that prevent them from disclosing their conflicts of interest in this work.". If authors are unsure whether conflicts of interest exist, please refer to the "Conflicts of Interest" of *Complex Engineering Systems* (*CES*) Editorial Policies for a full explanation.

2.3.3.6 Ethical Approval and Consent to Participate

Research involving human subjects, human material or human data must be performed in accordance with the Declaration of Helsinki and approved by an appropriate ethics committee. An informed consent to participate in the study should also be obtained from participants, or their parents or legal guardians for children under 16. A statement detailing the name of the ethics committee (including the reference number where appropriate) and the informed consent obtained must appear in the manuscripts reporting such research.

Studies involving animals and cell lines must include a statement on ethical approval. More information is available at Editorial Policies.

If the manuscript does not involve such issues, please state "Not applicable." in this section.

2.3.3.7 Consent for Publication

Manuscripts containing individual details, images or videos, must obtain consent for publication from that person, or in the case of children, their parents or legal guardians. If the person has died, consent for publication must be obtained from the next of kin of the participant. Manuscripts must include a statement that written informed consent for publication was obtained. Authors do not have to submit such content accompanying the manuscript. However, these documents must be available if requested. If the manuscript does not involve this issue, state "Not applicable." in this section.

2.3.3.8 Copyright

Authors retain copyright of their works through a Creative Commons Attribution 4.0 International License that clearly states how readers can copy, distribute, and use their attributed research, free of charge. A declaration "© The Author(s) 2024." will be added to each article. Authors are required to sign a License to Publish before formal publication.

2.3.3.9 References

References should be numbered in order of appearance at the end of manuscripts. In the text, reference numbers should be placed in square brackets and the corresponding references are cited thereafter. List all authors when the number of authors is less than or equal to six, if there are more than six authors, only the first three authors' names should be listed, other authors' names should be omitted and replaced with "et al.". The journal's name should be required to be italicized and the journal references should have corresponding DOI numbers. Information from manuscripts accepted but not published should be cited in the text as "Unpublished material" with written permission from the source. Journal names should be abbreviated according to the List of Title Word Abbreviations.

References should be described as follows, depending on the types of works:

Types	Examples

Journal articles by individual authors	Weaver, D. L.; Ashikaga, T.; Krag, D. N. Effect of occult metastases on survival in node-negative breast cancer. *N. Engl. J. Med.* **2011**, 364, 412-421. DOI: 10.1056/NEJMoa1008108
Organization as author	Diabetes Prevention Program Research Group. Hypertension, insulin, and proinsulin in participants with impaired glucose tolerance. *Hypertension* **2002**, 40, 679-686. DOI: 10.1161/01.HYP.0000035706.28494.09
Both personal authors and organization as author	Vallancien, G.; Emberton, M.; Harving, N.; van Moorselaar, R. J.; Alf-One Study Group. Sexual dysfunction in 1,274 European men suffering from lower urinary tract symptoms. *J. Urol.* **2003**, 169, 2257-2261. DOI: 10.1097/01.ju.0000067940.76090.73
Journal articles not in English	Zhang X.; Xiong H.; Ji T. Y.; Zhang Y. H.; Wang Y. Case report of anti-N-methyl-D-aspartate receptor encephalitis in child. J. *Appl. Clin. Pediatr.* **2012**, 27, 1903-1907. (in Chinese)
Journal articles ahead of print	Odibo, A. O. Falling stillbirth and neonatal mortality rates in twin gestation: not a reason for complacency. *BJOG.* **2018**, Epub ahead of print [DOI: 10.1111/1471-0528.15541]
ebook	Hammond, C. *The Basics of Crystallography and Diffraction,* 4th ed.; Oxford University Press, 2015. DOI: 10.1093/acprof:oso/9780198738671.001.0001
Book in print	Frankel, F. *Picturing Science and Engineering*; MIT Press, 2018..
ebook chapter	Hammond, C. Crystal Symmetry. In The Basics of Crystallography and Diffraction, 4th ed.; International Union of Crystallography Texts on Crystallography, Vol. 21; Oxford University Press, 2015; pp 99−134. DOI: 10.1093/acprof:oso/9780198738671.003.0004
ebook with editors	Mom the Chemistry Professor: Personal Accounts and Advice from Chemistry Professors Who Are Mothers, 2nd ed.; Woznack, K., Charlebois, A., Cole, R. S., Marzabadi, C. H., Webster, G., Eds.; Springer, 2018. DOI: 10.1007/978-3-319-78972-9
ebook series	Gaede, H. C. Professional Development for REU Students. In *Best Practices for Chemistry REU Programs*; Griep, M. A, Watkins, L., Eds.; ACS Symposium Series, Vol. 1295; American Chemical Society, 2018; pp 33−44. DOI: 10.1021/bk-2018-1295.ch003
Thesis or dissertation	Cable, M. L. Life in Extreme Environments: Lanthanide-Based Detection of Bacterial Spores and Other Sensor Design Pursuits. Ph.D. Dissertation, California Institute of Technology, Pasadena, CA, 2010. http://resolver.caltech.edu/CaltechTHESIS:05102010-145436548 (accessed 2019-09-10).
Thesis or dissertation in print	Enander, R. T. Lead particulate and methylene chloride risks in automotive refinishing. Ph.D. Thesis, Tufts University, Medford, MA, 2001.
Website	*World Health Organization Home Page*. https://www.who.int/ (accessed 2019-02-21).
Newspaper	Beauge, J. School district sued over burns girl suffered during chemistry class demonstration. *PennLive (Harrisburg, PA)*, November 17, 2018, updated November 17, 2018. https://www.pennlive.com/news/2018/11/school_district_sued_over_burn.html (accessed 2019-02-22).
Conference abstract	Okita, J.; Iwamoto, T.; Kira, M. Novel synthetic route for hydrosilyllithiums. In *Book of Abstracts, 2000 International Chemical Congress of Pacific Basin Societies (PACIFICHEM 2000)*, Honolulu, HI; Paper INOR 216.
Conference proceedings	Nilsson, A.; Petersson, F.; Persson, H. W.; Jönsson, H.; Laurell, T. Manipulation of suspended particles in a laminar flow. In *Micro Total Analysis Systems 2002, Proceedings of the μTAS 2002 Symposium*, Nara, Japan, November 3−7, 2002; Baba, Y., Shoji, S., van den Berg, A., Eds.; Kluwer Academic Publishers: Dordrecht, The Netherlands, 2002; Vol. 2, pp 751−753. DOI: 10.1007/978-94-010-0504-3_50
Database	*SpectraBase*. Bio-Rad Laboratories. https://spectrabase.com/ (accessed 2020-01-05).
Patent	Stern, M. K.; Cheng, B. K. M. Process for preparing N-(p-nitroaryl)amides via reaction of nitrobenzene with nitriles. US 5380946, 1995.
Preprint	Yamamoto T. S.; Inui R.; Tada Y.; Yokoyama S. Prospects of detection of subsolar mass primordial black hole and white dwarf binary mergers. *arXiv* 2004, arXiv:2401.00044. Available online: https://arxiv.org/abs/2401.00044 (accessed 29 December 2023).

2.3.3.10 Supplementary Materials

Additional data and information can be uploaded as Supplementary Materials to accompany the manuscripts. The supplementary materials will also be available to the referees as part of the peer-review process. Any file format is acceptable, such as data sheet (word, excel, csv, cdx, fasta, pdf or zip files), presentation (powerpoint, pdf or zip files), image (cdx, eps, jpeg, pdf, png or tiff), table (word, excel, csv or pdf), audio (mp3, wav or wma) or video (avi, divx, flv, mov, mp4, mpeg, mpg or wmv). All information should be clearly presented. Supplementary materials should be cited in the main text in numeric order (e.g., Supplementary Figure 1, Supplementary Figure 2, Supplementary Table 1, Supplementary Table 2, *etc*.). The style of supplementary figures or tables complies with the same requirements on figures or tables in main text. Videos and audios should be prepared in English, and limited to a size of 500 MB.

2.4 Manuscript Format

2.4.1 File Format

Manuscript files can be in DOC and DOCX formats and should not be locked or protected.

Manuscript prepared in LaTex must be collated into one ZIP folder (including all source files and images, so that the Editorial Office can recompile the submitted PDF).
When preparing manuscripts in different file formats, please use the corresponding Manuscript Templates.

2.4.2 Length
The word limit is specified in the item "Types of Manuscripts". There are no restrictions on number of figures or number of supporting documents. Authors are encouraged to present and discuss their findings concisely.

2.4.3 Language
Manuscripts must be written in English.

2.4.4 Multimedia Files
The journal supports manuscripts with multimedia files. The requirements are listed as follows:
Video or audio files are only acceptable in English. The presentation and introduction should be easy to understand. The frames should be clear, and the speech speed should be moderate;
A brief overview of the video or audio files should be given in the manuscript text;
The video or audio files should be limited to a size of up to 500 MB;
Please use professional software to produce high-quality video files, to facilitate acceptance and publication along with the submitted article. Upload the videos in mp4, wmv, or rm format (preferably mp4) and audio files in mp3 or wav format.

2.4.5 Figures
Figures should be cited in numeric order (e.g., Figure 1, Figure 2) and placed after the paragraph where it is first cited;
Figures can be submitted in format of TIFF, PSD, AI, EPS or JPEG, with resolution of 300-600 dpi;
Figure caption is placed under the Figure;
Diagrams with describing words (including, flow chart, coordinate diagram, bar chart, line chart, and scatter diagram, *etc*.) should be editable in word, excel or powerpoint format. Non-English information should be avoided;
Labels, numbers, letters, arrows, and symbols in figure should be clear, of uniform size, and contrast with the background;
Symbols, arrows, numbers, or letters used to identify parts of the illustrations must be identified and explained in the legend;
Internal scale (magnification) should be explained and the staining method in photomicrographs should be identified;
All non-standard abbreviations should be explained in the legend;
Permission for use of copyrighted materials from other sources, including re-published, adapted, modified, or partial figures and images from the internet, must be obtained. It is authors' responsibility to acquire the licenses, to follow any citation instruction requested by third-party rights holders, and cover any supplementary charges.

2.4.6 Tables
Tables should be cited in numeric order and placed after the paragraph where it is first cited;
The table caption should be placed above the table and labeled sequentially (e.g., Table 1, Table 2);
Tables should be provided in editable form like DOC or DOCX format (picture is not allowed);
Abbreviations and symbols used in table should be explained in footnote;
Explanatory matter should also be placed in footnotes;
Permission for use of copyrighted materials from other sources, including re-published, adapted, modified, or partial tables from the internet, must be obtained. It is authors' responsibility to acquire the licenses, to follow any citation instruction requested by third-party rights holders, and cover any supplementary charges.

2.4.7 Abbreviations
Abbreviations should be defined upon first appearance in the abstract, main text, and in figure or table captions and used consistently thereafter. Non-standard abbreviations are not allowed unless they appear at least three times in the text. Commonly-used abbreviations, such as DNA, RNA, ATP, *etc*., can be used directly without definition. Abbreviations in titles and keywords should be avoided, except for the ones which are widely used.

2.4.8 Italics
General italic words like vs., et al., *etc*., in vivo, in vitro; t test, F test, U test; related coefficient as r, sample number as n, and probability as P; names of genes; names of bacteria and biology species in Latin.

2.4.9 Units
SI Units should be used. Imperial, US customary and other units should be converted to SI units whenever possible. There is a space between the number and the unit (i.e., 23 mL). Hour, minute, second should be written as h, min, s.

2.4.10 Numbers
Numbers appearing at the beginning of sentences should be expressed in English. When there are two or more numbers in a paragraph, they should be expressed as Arabic numerals; when there is only one number in a paragraph, number < 10

should be expressed in English and number > 10 should be expressed as Arabic numerals. 12345678 should be written as 12,345,678.

2.4.11 Equations

Equations should be editable and not appear in a picture format. Authors are advised to use either the Microsoft Equation Editor or the MathType for display and inline equations.
Display equations should be numbered consecutively, using Arabic numbers in parentheses;
Inline equations should not be numbered, with the same/similar size font used for the main text.

2.4.12 Headings

In the main body of the paper, three different levels of headings may be used.
Level one headings: they should be in bold, and numbered using Arabic numbers, such as **1. INTRODUCTION**, and **2. METHODS**, with all letters capitalized;
Level two headings: they should be in bold and numbered after the level one heading, such as **2.1 Statistical analyses, 2.2 ..., 2.3...**, *etc*., with the first letter capitalized;
Level three headings: they should be italicized, and numbered after the level two heading, such as 2.1.1 Data distributions,and 2.1.2 outliers and linear regression, with the first letter capitalized.

2.4.13 Text Layout

As the electronic submission will provide the basic material for typesetting, it is important to prepare papers in the general editorial style of the journal.
The font is Times New Roman;
The font size is 12pt;
Single column, 1.5x line spacing;
Insert one line break (one Return) before the heading and paragraph, if the heading and paragraph are adjacent, insert a line break before the heading only;
No special indentation;
Alignment is left end;
Insert consecutive line numbers;
For other details please refer to the Manuscript Templates.

2.5 Submission Link

Submit an article via https://www.oaecenter.com/login?JournalId=comengsys.

3. Research and Publication Ethics

3.1 Research Involving Human Subjects

All studies involving human subjects must be in accordance with the Helsinki Declaration and seek approval to conduct the study from an independent local, regional, or national review body (e.g., ethics committee, institutional review board, *etc*.). Such approval, including the names of the ethics committee, institutional review board, *etc*., must be listed in a declaration statement of Ethical Approval and Consent to Participate in the manuscript. If the study is judged exempt from ethics approval, related information (e.g., name of the ethics committee granting the exemption and the reason for the exemption) must be listed. Further documentation on ethics should also be prepared, as Editors may request more detailed information. Manuscripts with suspected ethical problems will be investigated according to COPE Guidelines.

3.1.1 Consent to Participate

For all studies involving human subjects, informed consent to participate in the studies must be obtained from participants, or their parents or legal guardians for children under 16. Statements regarding consent to participate should be included in a declaration statement of Ethical Approval and Consent to Participate in the manuscript. If informed consent is not required, the name of the ethics committee granting the exemption and the reason for the exemption must be listed. If any ethical violation is found at any stage of publication, the issue will be investigated seriously based on COPE Guidelines.

3.1.2 Consent for Publication

All articles published by OAE are freely available on the Internet. All manuscripts that include individual participants' data in any form (i.e., details, images, videos, *etc*.) will not be published without Consent for Publication obtained from that person(s), or for children, their parents, or legal guardians. If the person has died, Consent for Publication must be obtained from the next of kin. Authors must add a declaration statement of Consent for Publication in the manuscript, specifying written informed consent for publication has been obtained.

3.1.3 Trial Registration

OAE requires all authors to register all relevant clinical trials that are reported in manuscripts submitted. OAE follows the World Health Organization (WHO)'s definition of clinical trials: "A clinical trial is any research study that prospectively assigns human participants or groups of humans to one or more health-related interventions to evaluate the effects on

health outcomes. Interventions include but are not restricted to drugs, cells, other biological products, surgical procedures, radiologic procedures, devices, behavioral treatments, process-of-care changes, preventive care, *etc*.".
In line with International Committee of Medical Journal Editors (ICMJE) Recommendations, OAE requires the registration of clinical trials in a public trial registry at or before the time of first patient enrollment. OAE accepts publicly accessible registration in any registry that is a primary register of the WHO International Clinical Trials Registry Platform or in ClinicalTrials.gov. The trial registration number should be listed at the end of the Abstract section.
Secondary data analyses of primary (parent) clinical trials should not be registered as a new clinical trial, but rather reference the trial registration number of the primary trial.
Editors of OAE journals will consider carefully whether studies failed to register or had an incomplete trial registration. Because of the importance of prospective trial registration, if there is an exception to this policy, trials must be registered and the authors should indicate in the publication when registration was completed and why it was delayed. Editors will publish a statement indicating why an exception was allowed. Please note such exceptions should be rare, and authors failing to prospectively register a trial risk its inadmissibility to OAE journals.
Authors who are not sure whether they need trial registration may refer to ICMJE FAQs for further information.

3.2 Research Involving Animals

Experimental research on animals should be approved by an appropriate ethics committee and must comply with institutional, national, or international guidelines. OAE encourages authors to comply with the AALAS Guidelines, the ARRIVE Guidelines, and/or the ICLAS Guidelines, and obtain prior approval from the relevant ethics committee. Manuscripts must include a statement indicating that the study has been approved by the relevant ethical committee and the whole research process complies with ethical guidelines. If a study is granted an exemption from requiring ethics approval, the name of the ethics committee granting the exemption and the reason(s) for the exemption should be detailed. Editors will take account of animal welfare issues and reserve the right to reject a manuscript, especially if the research involves protocols that are inconsistent with commonly accepted norms of animal research.

3.3 Research Involving Cell Lines

Authors must describe what cell lines are used and their origin so that the research can be reproduced. For established cell lines, the provenance should be stated and references must also be given to either a published paper or to a commercial source. For de novo cell lines derived from human tissue, appropriate approval from an institutional review board or equivalent ethical committee, and consent from the donor or next of kin, should be obtained. Such statements should be listed on the Declaration section of Ethical Approval and Consent to Participate in the manuscript.
Further information is available from the International Cell Line Authentication Committee (ICLAC). OAE recommends that authors check the NCBI database for misidentification and contamination of human cell lines.

3.4 Research Involving Plants

Experimental research on plants (either cultivated or wild), including collection of plant material, must comply with institutional, national, or international guidelines. Field studies should be conducted in accordance with local legislation, and the manuscript should include a statement specifying the appropriate permissions and/or licenses. OAE recommends that authors comply with the IUCN Policy Statement on Research Involving Species at Risk of Extinction and the Convention on the Trade in Endangered Species of Wild Fauna and Flora.
For each submitted manuscript, supporting genetic information and origin must be provided for plants that were utilized. For research manuscripts involving rare and non-model plants (other than, e.g., Arabidopsis thaliana, Nicotiana benthamiana, Oriza sativa, or many other typical model plants), voucher specimens must be deposited in a public herbarium or other public collections providing access to deposited materials.

3.5 Publication Ethics Statement

OAE is a member of the Committee on Publication Ethics (COPE). We fully adhere to its Code of Conduct and to its Best Practice Guidelines.

The Editors of this journal enforce a rigorous peer-review process together with strict ethical policies and standards to guarantee to add high-quality scientific works to the field of scholarly publication. Unfortunately, cases of plagiarism, data falsification, image manipulation, inappropriate authorship credit, and the like, do arise. The Editors of CES take such publishing ethics issues very seriously and are trained to proceed in such cases with zero tolerance policy.
Authors wishing to publish their papers in CES must abide by the following:
The author(s) must disclose any possibility of a conflict of interest in the paper prior to submission;
The authors should declare that there is no academic misconduct in their manuscript in the cover letter;
Authors should accurately present their research findings and include an objective discussion of the significance of their findings;
Data and methods used in the research need to be presented in sufficient detail in the manuscript so that other researchers can replicate the work;
Authors should provide raw data if referees and the Editors of the journal request;
Simultaneous submission of manuscripts to more than one journal is not tolerated;
Republishing content that is not novel is not tolerated (for example, an English translation of a paper that is already published in another language will not be accepted);
The manuscript should not contain any information that has already been published. If you include already published figures or images, please get the necessary permission from the copyright holder to publish under the CC-BY license;

Plagiarism, data fabrication and image manipulation are not tolerated;
Plagiarism is not acceptable in OAE journals.
Plagiarism involves the inclusion of large sections of unaltered or minimally altered text from an existing source without appropriate and unambiguous attribution, and/or an attempt to misattribute original authorship regarding ideas or results, and copying text, images, or data from another source, even from your own publications, without giving credit to the source.
As to reusing the text that is copied from another source, it must be between quotation marks and the source must be cited.
If a study's design or the manuscript's structure or language has been inspired by previous studies, these studies must be cited explicitly.
If plagiarism is detected during the peer-review process, the manuscript may be rejected. If plagiarism is detected after publication, we may publish a Correction or retract the paper.
Falsification is manipulating research materials, equipment, or processes, or changing or omitting data or results so that the findings are not accurately represented in the research record.
Image files must not be manipulated or adjusted in any way that could lead to misinterpretation of the information provided by the original image.
Irregular manipulation includes: introduction, enhancement, moving, or removing features from the original image; grouping of images that should be presented separately, or modifying the contrast, brightness, or color balance to obscure, eliminate, or enhance some information.
If irregular image manipulation is identified and confirmed during the peer-review process, we may reject the manuscript.
If irregular image manipulation is identified and confirmed after publication, we may publish a Correction or retract the paper.
OAE reserves the right to contact the authors' institution(s) to investigate possible publication misconduct if the Editors find conclusive evidence of misconduct before or after publication. OAE has a partnership with iThenticate, which is the most trusted similarity checker. It is used to analyze received manuscripts to avoid plagiarism to the greatest extent possible.
When plagiarism becomes evident after publication, we will retract the original publication or require modifications, depending on the degree of plagiarism, context within the published article, and its impact on the overall integrity of the published study. Journal Editors will act under the relevant COPE guidelines.

4. Authorship

Authorship credit of CES should be solely based on substantial contributions to a published study, as specified in the following four criteria:
1. Substantial contributions to the conception or design of the work, or the acquisition, analysis, or interpretation of data for the work;
2. Drafting the work or revising it critically for important intellectual content;
3. Final approval of the version to be published;
4. Agreement to be accountable for all aspects of the work in ensuring that questions related to the accuracy or integrity of any part of the work are appropriately investigated and resolved.

All those who meet these criteria should be identified as authors. Authors must specify their contributions in the section Authors'' Contributions of their manuscripts. Contributors who do not meet all the four criteria (like only involved in acquisition of funding, general supervision of a research group, general administrative support, writing assistance, technical editing, language editing, proofreading, *etc*.) should be acknowledged in the section of Acknowledgement in the manuscript rather than being listed as authors.
If a large multiple-author group has conducted the work, the group ideally should decide who will be authors before the work starts and confirm authors before submission. All authors of the group named as authors must meet all the four criteria for authorship.
AI and AI-assisted technologies should not be listed as an author or co-author.

5. Reviewers Exclusions

You are welcome to exclude a limited number of researchers as potential Editors or reviewers of your manuscript. To ensure a fair and rigorous peer review process, we ask that you keep your exclusions to a maximum of three people. If you wish to exclude additional referees, please explain or justify your concerns—this information will be helpful for Editors when deciding whether to honor your request.

6. Editors and Journal Staff as Authors

For all studies involving human subjects, informed consent to participate in the studies must be obtained from participants, or their parents or legal guardians for children under 16. Statements regarding consent to participate should be included in a declaration statement of Ethical Approval and Consent to Participate in the manuscript. If informed consent is not required, the name of the ethics committee granting the exemption and the reason for the exemption must be listed. If any ethical violation is found at any stage of publication, the issue will be investigated seriously based on COPE Guidelines.

7. Policy of the Use of AI and AI-assisted Technologies in Scientific Writing

7.1 AI Authorship

Generative AI and AI-assisted technologies (e.g., large language models) are increasingly employed in content creation. However, their use in manuscript preparation is strictly limited:

• Prohibited applications: These tools must not be used to perform core research tasks, including generating scientific insights, analyzing/interpreting data, or drawing scientific conclusions.
• Permitted applications: They may only be used to enhance manuscript readability and language quality.
All AI technologies must be used under human oversight, as they may produce inaccurate or biased content. AI tools cannot be listed as authors/co-authors or cited as such. Authors retain full responsibility for all content, including AI-generated material.
Exceptions for methodological use:
If AI tools are integral to the research design/methodology, authors must:
1. Document usage transparently in the *Materials and Methods* section, specifying:
• Tool/model name
• Version/extension number
• Manufacturer
2. Include a declaration titled "*Declaration of Generative AI Use*" before the reference section, stating:
"*During the preparation of this work, the author(s) used [TOOL NAME] due to [reason]. The author(s) reviewed and edited all AI-generated content and accept full responsibility for the published material."*
Note: No declaration is required for basic grammar/spelling checkers or reference managers.

7.2 Generative AI in Visual Content
OAE prohibits the use of generative AI/AI-assisted tools to create or modify images, including:
• Graphical abstracts
• Cover images
• Figures within manuscripts
Permitted adjustments limited to:
• Brightness/contrast correction
• Color balance optimization
provided these edits do not obscure, delete, or misrepresent original image data.

7.3 AI Use in Peer Review
Confidentiality requirements:
• Reviewers must not upload manuscripts/materials to AI platforms, as this:
1. Violates OAE's confidentiality policies
2. Risks intellectual property infringement
3. May compromise personal data in identifiable content
Review integrity standards:
• Peer review must remain human-driven – AI tools cannot replace critical scholarly judgment.
• Reviewers must not use AI for manuscript evaluation due to risks of:
1. Inaccurate/incomplete assessments
2. Algorithmic bias
Declaration requirement: Reviewers retain full accountability for their reports, if any aspect of the manuscript's evaluation was supported in any way by an AI tool, reviewers must explicitly disclose it in their report.
OAE will periodically reassess this policy to align with technological advancements and academic standards.

8. Conflict of Interests
OAE journals require authors to declare any possible financial and/or non-financial conflicts of interest at the end of their manuscript and in the cover letter, as well as confirm this point when submitting their manuscript in the submission system. If no conflicts of interest exist, authors need to state "All authors declared that there are no conflicts of interest". We also recognize that some authors may be bound by confidentiality agreements, in which cases authors need to state "All authors declared that they are bound by confidentiality agreements that prevent them from disclosing their competing interests in this work".

9. Editorial Process
9.1 Pre-Check
New submissions are initially checked by the Managing Editor from the perspectives of originality, suitability, structure and formatting, conflicts of interest, background of authors, etc. Poorly prepared manuscripts may be rejected at this stage. If your manuscript does not meet one or more of these requirements, we will return it for further revisions.
Once your manuscript has passed the initial check, it will be assigned to the Assistant Editor, and then the Editor-in-Chief, or an Associate Editor in the case of a conflict of interest, will be notified of the submission and invited to review. Regarding Special Issue paper, after passing the initial check, the manuscript will be successively assigned to the Assistant Editor, and then to the Editor-in-Chief, or an Associate Editor in the case of conflict of interest for the Editor-in-Chief to review. The Editor-in-Chief, or the Associate Editor may reject manuscripts that they deem highly unlikely to pass peer review without further consultation. Once your manuscript has passed the Editorial assessment, the Associate Editor will start to organize peer-review.
All manuscripts submitted to CES are screened using CrossCheck powered by iThenticate to identify any plagiarized content. Your study must also meet all ethical requirements as outlined in our Editorial Policies. If the manuscript does not pass any of these checks, we may return it to you for further revisions or decline to consider your study for publication.

9.2 Peer Review
CES operates a single-blind review process, which means that reviewers know the names of authors, but the names of the reviewers are hidden from the authors. The scientific quality of the research described in the manuscript is assessed by a minimum of three independent expert reviewers. The Editor-in-Chief is responsible for the final decision regarding acceptance or rejection of the manuscript.
All information contained in your manuscript and acquired during the review process will be held in the strictest confidence.

9.3 Decisions
Your research will be judged on scientific soundness only, not on its perceived impact as judged by Editors or referees. There are three possible decisions: Accept (your study satisfies all publication criteria), Invitation to Revise (more work is required to satisfy all criteria), and Reject (your study fails to satisfy key criteria and it is highly unlikely that further work can address its shortcomings). All of the following publication criteria must be fulfilled to enable your manuscript to be accepted for publication:
Originality
The study reports original research and conclusions.
Data availability
All data to support the conclusions either have been provided or are otherwise publicly available.
Statistics
All data have been analyzed through appropriate statistical tests and these are clearly defined.
Methods
The methods are described in sufficient detail to be replicated.
Citations
Previous work has been appropriately acknowledged.
Interpretation
The conclusions are a reasonable extension of the results.
Ethics
The study design, data presentation, and writing style comply with our Editorial Policies.

9.4 Revisions
Authors are required to submit the revised manuscript within one week if minor revision is recommended while two weeks if major revision recommended or one month if additional experiments are needed. If authors need more than one month to revise their manuscript, we usually require the authors to resubmit their paper. We request that a document of point-to-point response to all comments of reviewers and the Editor-in-Chief or the Associate Editor should be supplied along with the revised manuscript to allow quick assessment of your revised manuscript. This document should outline in detail how each of the comments was addressed in the revised manuscript or should provide a rebuttal to the criticism. Manuscripts may or may not be sent to reviewers after revision, dependent on whether the reviewer requested to see the revised version. Apart from in exceptional circumstances, *CES* only supports a round of major revision per manuscript.

10. Contact Us
Journal Contact

Complex Engineering Systems Editorial Office
Suite 1504, Tower A, Xi'an National Digital Publishing Base, No. 996 Tiangu 7th Road, Gaoxin District, Xi'an 710077, Shaanxi, China.

Lyric Zhang
Managing Editor
editorial@comengsys.com

Last updated on 5 September, 2024



Complex Engineering Systems
(*CES*)
Suite 1504, Tower A, Xi'an National Digital Publishing Base,
No. 996 Tiangu 7th Road, Gaoxin District, Xi'an 710077,
Shaanxi, China.
E-mail: editorial@comengsys.com
Website: https://www.oaepublish.com/comengsys

